TOHOKU UNIVERSITY

# Eleventh International Conference on Flow Dynamics

October 8-10, 2014

Sendai International Center, Japan

Institute of Fluid Science Tohoku University IFS

## Proceedings

Institute of Fluid Science, Tohoku University

# Preface

Welcome to the Eleventh International Conference on Flow Dynamics (ICFD2014) at the Sendai International Center, Sendai, Japan, hosted by the Institute of Fluid Science, Tohoku University.

Flow Dynamics is a comprehensive scientific field which deals with the flow and transport phenomena concerning atoms, molecules and nano-scale particle, any fluids, any materials, energy, information, economic activities and so forth. ICFD is now recognized by world researchers, engineers and academicians as the biggest and the most important international conference in field of Flow Dynamics. It has also played an important role of initiating international research collaborations and scientific exchange.

Another significance of this conference is that it provides young researchers and students with unique opportunities to be educated and self-developed through participation and presentation in the Student Session and events.

The technical program consists of 3 plenary lectures, 1 General Session, 10 Organized Sessions, 5 Colloquium Sessions, and 1 Special Session, starting in the morning on Wednesday, October 8. About 390 papers will be presented and it is our pleasure to meet a large number of presenters and participants during the conference.

In addition to the technical program, we have organized the event named the Students / Young Birds Friendship Night for students and young researchers participating in ICFD2014 on Wednesday evening, as well as the Conference Banquet on Thursday evening.

On behalf of the organizing committee of the Eleventh International Conference on Flow Dynamics, we wish you will enjoy fruitful discussions and exchanges of information, and we want you to have the opportunity to strengthen old friendships all over the world and enjoy the beautiful scenery and comfortable atmosphere of autumn in Sendai.

Hideaki Kobayashi, Professor
Institute of Fluid Science, Tohoku University
and
Fredrik Lundell, Associate Professor
KTH Mechanics, Royal Institute of Technology
General Co-Chairs, Eleventh International Conference on Flow Dynamics (ICFD2014)

# Eleventh International Conference on Flow Dynamics

**Hosted by:**

- Institute of Fluid Science, Tohoku University

**In cooperation with:**

- Combustion Society of Japan
- Cryogenics and Superconductivity Society of Japan
- The Electrochemical Society of Japan
- The International Centre for Heat and Mass Transfer (ICHMT)
- Japan Aerosapce Exploration Agency (JAXA)
- The Japan Society of Aeronautical and Space Sciences
- The Japan Society of Applied Electromagnetics and Mechanics
- The Japan Society for Computational Engineering and Science
- The Japan Society of Fluid Mechanics
- Japan Society of Maintenology
- The Japan Society of Mechanical Engineers
- The Japan Society of Microgravity Application
- Japan Society of Thermophysical Properties
- Turbomachinery Society of Japan
- Aoba Foundation for the Promotion on Engineering
- Fluid Sciences Foundation

**SCOPE:**

The eleventh International Conference on Flow Dynamics (ICFD2014), in the annual series hosted by the Institute of Fluid Science, Tohoku University, will be held on October 8th through 10th at the Sendai International Center, Sendai, Japan. The objectives of this conference are to explore new horizons in science by discussing and exchanging information related to the most advanced scientific fields and to cutting edge technologies in Flow Dynamics. ICFD is now recognized by world researchers, engineers and academicians as the biggest and the most important international conference in field of Flow Dynamics. It has also played an important role of initiating international research collaborations. It should be noted that another significance of this conference is that it provides young researchers and students with unique opportunities to be educated and self-developed through proactive participation in the conference.

The first nine ICFDs were hosted by two Tohoku University COE Programs, "The 21st Century International COE on Fluid Dynamics (21COE, Year 2003 - Year 2007)" and its successor "Global COE Program World Center of Education and Research for Trans-disciplinary Flow Dynamics (the GCOE, Year 2008 - Year 2012)". The Institute of Fluid Science (IFS) was the principal operating body for both 21COE and GCOE, the latter which came to end in March 2013. Also, last year, on the occasion of its 70th anniversary, IFS was regenerated as an even more powerful research institute, particularly in energy-related research. Its reorganization has led to the creation of three new flow research divisions and the Innovative Energy Research Center. In this new context, IFS decided to continue to host the conference, and ICFD2013 was held in November of last year. We pledge to maintain ICFD's dynamism and spirit as a meeting for present-day distinguished scientists of Flow Dynamics as well as for future generations of scientists.

Flow Dynamics is a comprehensive scientific field which deals with flow and transport phenomena concerning atoms, molecules and nanoscale particles, any fluid, any material, energy, information, economic activities and so forth. It addresses multiscale and multidisciplinary problems and deals with all natural phenomena (biochemical processes, corrosion, weather, volcanic eruptions, earth magnetic field and tectonic motions, etc.) and in most human activities (industrial processes, energy production and saving, transportation, etc.). The ICFD conferences have played a significant role in helping Flow Dynamics to become a major academic discipline which is dealing with various difficult tasks faced by human society, such as control of nuclear power generators, global warming, energy resource depletion, diseases, and so on. Flow

Dynamics is playing major roles in the realization of the advanced medicine and medical treatment, aerospace technology, robotics, IT technology accessible by anybody, anytime, anywhere, and so forth. Scientists and engineers, who are working and/or interested in such areas, please participate in the ICFD2014 and extend your domains and databases.

We cordially invite scholars, researchers, educationists, students and planners exploring and studying in the relevant research and development fields of bio-, nano-, material, energy, environmental, planetary and earth sciences and technologies, particularly in the academic fields of mechanical engineering, aerospace engineering, nuclear engineering, physics, medical science and engineering, chemistry, chemical engineering and so forth, to join the conference.

After the East Japan Great Earthquake and Disaster in March, 2011, Sendai and the vicinities are definitely recovering, although the speed of recovery depends on the area. Fortunately, activities of Tohoku University as well as the lives of people living in the city are already at the pre-disaster level. We believe that you will enjoy the beautiful season and comfortable atmosphere of autumn in Sendai in October.

## CONFERENCE COMMITTEE:

### Executive Committee Members:

Hideaki Kobayashi (ICFD2014 General Co-Chair, Tohoku University)
Fredrik Lundell (ICFD2014 General Co-Chair, Royal Institute of Technology)
Shigeru Obayashi (IFS Director, Tohoku University)

### International Scientific Committee Members:

Chair: Shigenao Maruyama (Tohoku University)

Australia
- Masud Behnia (The University of Sydney)
- Gary Rosengarten (RMIT University)
- Victoria Timchenko (The University of NSW)

Canada
- Javad Mostaghimi (University of Toronto)

China
- Zhenmao Chen (Xi'an Jiaotong University)
- XinGang Liang (Tsinghua University)

France
- Patrick Bourgin (ECL)
- Jean-Yves Cavaillé (INSA de Lyon)
- Philippe Kapsa (ECL)

Germany
- Gerd Dobmann (Fraunhofer-IZFP)
- Serge A. Shapiro (Freie University Berlin)

Hungary
- Miklos Zrinyi (Semmelweis University)

India
- Subhash C. Mishra (Indian Institute of Technology Guwahati)

Italy
- Gian Piero Celata (ENEA)

Japan
- Keisuke Asai (Tohoku University)
- Yu Fukunishi (Tohoku University)
- Masato Furukawa (Kyushu University)
- Toshiyuki Hayase (Tohoku University)
- Nobuhide Kasagi (The University of Tokyo)

Chisachi Kato (The University of Tokyo)
Hideaki Kobayashi (Tohoku University)
Junichiro Mizusaki (Tohoku University)
Kazuhiro Nakahashi (Japan Aerospace Exploration Agency)
Masami Nakano (Tohoku University)
Tomohide Niimi (Nagoya University)
Hideya Nishiyama (Tohoku University)
Shigeru Obayashi (Tohoku University)
Masaki Sano (The University of Tokyo)
Akihiro Sasoh (Nagoya University)
Toshiyuki Takagi (Tohoku University)
Michio Tokuyama (Tohoku University)
Satoru Yamamoto (Tohoku University)

Korea
Sung-Jin Kim (Korea Advanced Institute of Science and Technology)
Hyung Jin Sung (Korea Advanced Institute of Science and Technology)

Russia
Oleg P. Solonenko (Insitute of Theoretical and Applied Mechanics SB RAS)
Alexander Vasiliev (Moscow State University)

Sweden
Fredrik Lundell (Royal Institute of Technology)

Switzerland
Bastien Chopard (University of Geneve)
Dimos Poulikakos (ETH Zurich)

Taiwan
Chingyao Chen (National Chiao Tung University)
Wu-Shung Fu (National Chiao Tung University)
Jongshinn Wu (National Chiao Tung University)

UK
Yiannis Ventikos (University of Oxford)

USA
Louis N. Cattafesta III (University of Florida)
Yiguang Ju (Princeton University)
Ishwar K. Puri (Virginia Tech)
Kozo Saito (Kentucky University)
John P. Sullivan (Purdue University)
Rongia Tao (Temple University)
Satish Udpa (Michigan State University)

**Advisory Board Members:**

| | |
|---|---|
| China | Xing Zhang (Tsinghua University) |
| Japan | Yoichiro Matsumoto (The University of Tokyo) |
| | Masaaki Sato (Tohoku University) |
| | Takashi Yabe (Tokyo Institute of Technology) |
| Korea | Joon-Hyun Lee (KETEP) |
| | Joon Sik Lee (Seoul National University) |

**Organizing Committee Members:**

Shigeru Yonemura (Chair), Keisuke Asai, Hisanori Masuda, Kazushi Miyata, Taku Ohara, Fukuo Ohta, Fumio Saito, Hiroyuki Shimizu, Hidemasa Takana
(Observer) Yoshinori Sasaki, Atsushi Shirai, Toshiyuki Takagi

# Plenary Lectures

**Recent Advances in High Reynolds Number Partially-premixed Combustion Research**

James F. Driscoll (University of Michigan, USA)
(9:20-10:10, October 8 at TACHIBANA)

**Means of Stabilization of Flying Inspection Vehicles to Enhance Data Flow in Image Processing**

Christian Boller (Saarland University / Fraunhofer IZFP, Germany)
(10:15-11:05, October 8, at TACHIBANA)

**Wettability Engineering for Heat Transfer Applications**

Constantine Megaridis (University of Illinois at Chicago, USA)
(11:10-12:00, October 8, at TACHIBANA)

# Sessions

General Session:

- GS1: General Session
  Co-Organizers: H. Kobayashi, S. Yonemura (Tohoku University)

Organized Sessions & Symposia:

- OS1: The Second International Symposium on Innovative Energy Research Ⅰ
  Core Technology for Advanced Energy Devices
  Organizer: S. Samukawa (Tohoku University)

- OS2: The Second International Symposium on Innovative Energy Research Ⅱ
  State-of-the-art Combustion Research
  Co-Organizers: K. Maruta (Tohoku University), S. Minaev (Far-Eastern Federal University)

- OS3: The Second International Symposium on Innovative Energy Research Ⅲ
  Multiphase Energy Science and Risk Mitigation
  Organizer: J. Ishimoto (Tohoku University)

- OS4: International Symposium on Smart Layered Materials and Structures for Energy Saving (Joint Symposium)
  Co-Organizers: T. Takagi, T. Uchimoto (Tohoku University), J. Y. Cavaillé (INSA de Lyon), C. Boller (Saarland University / Fraunhofer IZFP), J. Qiu (Nanjing University of Aeronautics and Astronautics), F. Lundell (Royal Institute of Technology)

- OS5: Biomedical Flow Dynamics
  Co-Organizers: H. Anzai, T. Nakayama, M. Ohta (Tohoku University)

- OS6: Advanced Physical Stimuli and Biological Responses
  Co-Organizers: T. Sato (Tohoku University), T. Ohashi (Hokkaido University), S. Kawano (Osaka University), R. Shirakashi (The University of Tokyo)

- OS7: Cutting Edge of Thermal Science and Engineering
  Co-Organizers: S. Maruyama, A. Komiya (Tohoku University)

- OS8: Flow Dynamics and Combustion in Hybrid Rockets
  Co-Organizers: T. Shimada (Japan Aerospace Exploration Agency), K. Sawada (Tohoku University)

- OS9: Advanced Control of Smart Fluids and Fluid Flows
  Co-Organizers: M. Nakano, Y. Fukunishi (Tohoku University)

- OS10: The Tenth International Students / Young Birds Seminar on Multi-scale Flow Dynamics
  Co-Organizers: Y. Takahashi, H. Sato, R. Kikuchi (Tohoku University),
  Supervisors: K. Miyata, H. Shimizu, A. Hayakawa, K. Sato (Tohoku University)

Colloquium Sessions:

- CS1: The Second International Workshop on Fluid and Material Sciences in Cooperation between Tohoku University and KTH
  Co-Organizers: T. Hayase (Tohoku University), F. Lundell (Royal Institute of Technology)

- CS2: Heat and Fluid Flow
  Co-Organizers: Y. H. Liu, M. C. Lu (National Chiao Tung University)

- CS3: Global / Local Innovations for Next Generation Automobiles (Joint Session) (Tentative)
  Co-Organizers: A. Miyamoto (Tohoku University), P. Kapsa (Ecole Central de Lyon), M. C. Williams (URS Corporation), K. Nakatsuka (Intelligent Cosmos Research Institute)

- CS4: IFS Collaborative Research Forum (AFI-2014)
  Co-Organizers: H. Kobayashi, H. Masuda (Tohoku University)

- CS5: Fluids Science Research Award Lectures
  Co-Organizers: T. Hayase, H. Masuda (Tohoku University)

Special Session

- SS1: Liaison Office Session
  Co-Organizers: T. Takagi, M. Ohta (Tohoku University)

Eleventh International Conference on Flow Dynamics

# Proceedings

## Plenary Lectures

## GS1: General Session

## OS1: The Second International Symposium on Innovative Energy Research I
## Core Technology for Advanced Energy Devices

## OS2: The Second International Symposium on Innovative Energy Research II
## State-of-the-art Combustion Research

## OS3: The Second International Symposium on Innovative Energy Research Ⅲ Multiphase Energy Science and Risk Mitigation

## OS4: International Symposium on Smart Layered Materials and Structures for Energy Saving (Joint Symposium)

## OS5: Biomedical Flow Dynamics

## OS6: Advanced Physical Stimuli and Biological Responses

## OS7: Cutting Edge of Thermal Science and Engineering

## OS8: Flow Dynamics and Combustion in Hybrid Rockets

## OS9: Advanced Control of Smart Fluids and Fluid Flows

## OS10: The Tenth International Students / Young Birds Seminar on Multi-scale Flow Dynamics

## CS1: The Second International Workshop on Fluid and Material Sciences in Cooperation between Tohoku University and KTH

## CS2: Heat and Fluid Flow

## CS3: Global / Local Innovations for Next Generation Automobiles (Joint Session)

## CS4: IFS Collaborative Research Forum (AFI-2014)

(For details, please refer to the separate volume.)

CRF-1 **Study on Improvement of Aerodynamic Performance for an Airborne Projectile —Effect of Air Permeability of Ski Jumpsuit on Aerodynamic Characteristics—**
Shigekazu Tekuramori, Hiroaki Hasegawa (Akita University, Japan), Shigeru Obayashi (Tohoku University, Japan)

CRF-2 **Low Reynolds Number Flow Analysis of Flat Plate**
Yuya Kojima, Daisuke Sasaki, Takeshi Akasaka, Masato Okamoto (Kanazawa Institute of Technology, Japan), Kazuhiko Komatsu, Shigeru Obayashi, Koji Shimoyama (Tohoku University, Japan)

CRF-3 **Optimization of Influential Factors for Practical Application of an Ornithopter**
Tadateru Ishide, Shinsuke Seiji, Hiroyuki Ishikawa, Kazuya Naganuma, Ryo Fujii (Kisarazu National College of Technology, Japan), Shigeru Obayashi, Koji Shimoyama (Tohoku University, Japan)

CRF-4 **Investigation of Flow Characteristics around an Oscillating Airfoil at Large Reduced Frequency**
Ryohei Serizawa, Shun Takahashi (Tokai University, Japan), Daisuke Sasaki, Masato Okamoto (Kanazawa Institute of Technology, Japan)

CRF-5 **Pressure Drop of Vapor-Liquid Nitrogen Flow in a Corrugated Pipe**
Jumpei Ohta, Katsuhide Ohira, Kazushi Miyata, Koichi Takahashi (Tohoku University, Japan), Hiroaki Kobayashi, Hideyuki Taguchi, Motoyuki Hongo, Takayuki Kojima (Japan Aerospace Exploration Agency, Japan)

CRF-6 **Numerical Study of Thermal and Chemical Non-Equilibrium Effects in Near-Continuum Hypersonic Flows**
Georgy Shoev, Yevgeniy Bondar (Khristianovich Institute of Theoretical, Applied Mechanics, Russia), Shigeru Yonemura (Tohoku University, Japan)

CRF-7 **Numerical Studies of Rarefied Chemically Reacting Flows about Space Vehicles**
Alexander Shevyrin, Yevgeniy Bondar, Anton Shershnev, Pavel Vashchenkov (Khristianovich Institute of Theoretical, Applied Mechanics, Russia), Shigeru Yonemura (Tohoku University, Japan)

CRF-8 **Atomizing Characteristics of Water and Liquid Nitrogen Jets under High Pressure Environment**
Rikio Watanabe, Narumi Hiramoto, Hiroki Ishii (Tokyo City University, Japan), Hideaki Kobayashi (Tohoku University, Japan)

CRF-9 **Development of PSP technique for Ballistic Range Experiments**
Daiju Numata, Keisuke Asai, Kiyonobu Ohtani (Tohoku University, Japan)

CRF-10 **Numerical Investigation of Wave Reflections at the Centerline of Stunted Busemann Intakes**
Hideaki Ogawa (RMIT University, Australia), Sannu Mölder (Ryerson University, Canada), Evgeny V. Timofeev (McGill University, Canada), Hans Hornung (California Institute of Technology, USA), Georgy Shoev, Yevgeniy Bondar (Russian Academy of Sciences, Russia), Kiyonobu Ohtani, Shigeru Obayashi (Tohoku University, Japan)

CRF-11 **Elementary Experiments of Air-Leakage Detection for Space-Debris Impact using Photoluminescent Substance**
Norihiko Matsumoto, Yoshihiro Oki, Kiyonobu Ohtani (Tohoku University, Japan), Sunao Hasegawa (Japan Aerospace Exploration Agency, Japan), Miki Hasegawa (Aoyama Gakuin University, Japan), Kanjuro Makihara (Tohoku University, Japan)

CRF-12 **Electron Density Measurements behind a Hypersonic Shock Wave in Argon**
Gouji Yamada, Shunpei Maruyama, Hiromitsu Kawazoe (Tottori University, Japan), Shigeru Obayashi (Tohoku University, Japan)

CRF-13 **Aerodynamic Force Measurements in Supersonic Flow Conditions using a Sensitivity-Adjustable Three Component Force Balance**
Aya Miyazaki, Takahiro Mizuguti, Gouji Yamada, Hiromitsu Kawazoe (Tottori University), Shigeru Obayashi (Tohoku University, Japan)

CRF-14 **Advanced LES of Aircraft Wake Vortices**
Shigeru Obayashi, Takashi Misaka (Tohoku University, Japan), Anton Stephan, Frank Holzäpfel, Thomas Gerz (Deutsches Zentrum für Luft- und Raumfahrt, Germany)

CRF-15 **Stratum-Type Association Analysis for Conceptual Design of Hybrid Rocket in View of Fuels**
Kazuhisa Chiba (Hokkaido University of Science, Japan), Shin'ya Watanabe (Muroran Institute of Technology, Japan), Masahiro Kanazaki (Tokyo Metropolitan University, Japan), Shigeru Obayashi (Tohoku University, Japan)

CRF-16 **Global Design Optimization of Winglet/ Wingtip Shape for Furture Aircraft**
Yosuke Tuchiya, Taichi Sugiyama, Masahiro Kanazaki (Tokyo Metropolitan University, Japan), Mitsuhiro Murayama, Mitsuru Kurita, Masataka Kozai (Japan Aerospace Exploration Agency, Japan)

CRF-17 **A Comparative Visualization Technique for Fluid Simulation Results**
Anna Kuwana, Kaori Hattanda, Takayuki Itoh (Ochanomizu University, Japan), Shigeru Obayashi, Yuriko Takeshima (Tohoku University, Japan)

CRF-18 **Research of Friction and Drilling on Bio-composite Model (Second report)**
Makoto Ohta, Kei Ozawa (Tohoku University, Japan), Vincent Fridrici (École Centrale de Lyon,France), Kaihong Yu (Tohoku University, Japan), Philippe Kapsa (École Centrale de Lyon,France)

CRF-19 **Development of a Program for Blood Flow and Cell Behaviors Based on LBM Method (Second report)**
Makoto Ohta, Sho Matsumoto, Xiaobo Han (Tohoku University, Japan), Bastien Chopard (Geneva University, Switzerland), Mingzi, Zhang, Yujie Li, Yuuki Yoshida, Hitomi Anzai (Tohoku University, Japan)

CRF-20 **Numerical Analysis of Dual-Phase Lag Conduction in a Long Cylindrical Medium Using Lattice Boltzmann Method**
Rahul Chaurasia, Subhash C. Mishra (Indian Institute of Technology Guwahati, India), Junnosuke Okajima, Shigenao Maruyama (Tohoku University, Japan)

CRF-21 **Numerical Study on Vehicles Aerodynamic Performances During Straight and Curve Crossings**
Chenguang Lai, Chao Man, Kaiping Wen (Chongqing University of Technology, China)

CRF-22 **Reduction of Radiative Heat Transfer between Two Metallic Plates due to Interferences**
Yoichiro Tsurimaki (Tohoku University, Japan / INSA de Lyon, France), Pierre-Olivier Chapuis, Rodolphe Vaillon (INSA de Lyon, France), Junnosuke Okajima, Atsuki Komiya, Shigenao Maruyama (Tohoku University, Japan)

CRF-23 **Theoretical and Experimental Studies of Local Heating of Biological Tissue for Laser Therapy**
Tessai Sugiura, Takahiro Okabe, Junnosuke Okajima, Atsuki Komiya (Tohoku University, Japan), Victoria Timchenko (University of New South Wales, Australia), Tetsuya Kodama, Shigenao Maruyama (Tohoku University, Japan)

CRF-24 **Researches on a Sensing-Based Dynamic Forced Ventilation Control of Leaking Hydrogen**
Kazuo Matsuura (Ehime University, Japan), Masami Nakano, Jun Ishimoto (Tohoku University, Japan)

CRF-25 **Numerical Prediction of Compressible Vapor Flow with LDI Erosion**
Jun Ishimoto (Tohoku University, Japan), Kazuo Matsuura (Ehime University, Japan), Kozo Saito (University of Kentucky, USA)

CRF-26 **Investigation of Mixing of Plasma Species in the Hybrid-Stabilized Argon-Water Electric Arc**
Jiří Jeništa (Institute of Plasma Physics ASCR, Czech Republic), Hidemasa Takana, Satoshi Uehara, Hideya Nishiyama (Tohoku University, Japan), Milan Hrabovský (Institute of Plasma Physics ASCR, Czech Republic)

CRF-27 **Titanium Oxide Film Deposition by SPPS using Vortex Ar/$N_2$ Plasma Jet**
Yasutaka Ando, Yoshimasa Noda (Ashikaga Institute of Technology, Japan)
Satoshi Uehara, Hideya Nishiyama (Tohoku University, Japan)

CRF-28 **Instability Analysis of Natural Convection in Closed Cavity Configuration**
Juan F. Torres (Tohoku University, Japan / Ecole Centrale Lyon, France), Atsuki Komiya (Tohoku University, Japan), Daniel Henry (Ecole Centrale Lyon, France), Junnosuke Okajima, Shigenao Maruyama (Tohoku University, Japan)

CRF-29 **On Numerical Modeling of Some Features of Heterogeneous Combustion Waves in Porous Media under Free Convection**
Nickolay A. Lutsenko (IACP FEB RAS / Far Eastern Federal University, Russia), Kaoru Maruta (Far Eastern Federal University, Russia / Tohoku University, Japan)

CRF-30 **Nucleate Pool Boiling Heat Transfer and Critical Heat Flux of Liquid Nitrogen on the Surface Composed of a High and a Low Thermal Conductivity Materials**
Kazushi Miyata, Katsuhide Ohira (Tohoku University, Japan), Hideo Mori (Kyushu University, Japan)

CRF-31 **The Effects of Intermediate Product on the Intrinsic Instability of Premixed Flames with High Lewis Number Reactant**
Satoshi Kadowaki, Thwe Thwe Aung, Wataru Yamazaki (Nagaoka University of Technology, Japan), Hideaki Kobayashi (Tohoku University, Japan)

CRF-32 **Numerical Studies of Ignition in ABC-Flow Modeling 3D Turbulence**
Evgeniy Sereshchenko, Roman Fursenko, Sergey Minaev (Institute of Theoretical and Applied Mechanics Russia / FEFU, Russia), Shenqyang Shy (National Central University, Taiwan), Kaoru Maruta, Hisashi Nakamura (Tohoku University, Japan)

CRF-33 **Development of Radiometer-sonde for Flux Measurement of Solar and Thermal Radiation in Earth's Atmosphere**
Noboru Yamada, Takanori Yoshida (Nagaoka University of Technology, Japan), Junnosuke Okajima, Shigenao Maruyama (Tohoku University, Japan)

CRF-34 **Low-Lewis-Number Premixed Flames Stabilization in Stretched Flow of Two Slot Burners**
Roman Fursenko (FEFU, Russia / ITAM SB RAS, Russia), Sergey Minaev (FEFU, Russia), Kaoru Maruta (FEFU, Russia / Tohoku University, Japan)

CRF-35 **Lattice Boltzmann Simulation on MHD Energy Conversion for Efficient Wind Utilization**
Yuhiro Iwamoto (Doshisha University, Japan), Hidemasa Takana (Tohoku University, Japan), Kenta Taki, Hiroshi Yamaguchi (Doshisha University, Japan)

CRF-36 **Master Equation Modeling of a Nanosecond Pulse Discharge in Nitrogen in a Pin-to-Pin Geometry**
Zak Eckert (The Ohio State University, USA), Hidemasa Takana, Hideya Nishiyama (Tohoku University, Japan), Igor Adamovich (The Ohio State University, USA)

CRF-37 **Oxygen Ion Transport Phenomena in a Ceramic Membrane**
Hiroki Nagashima, Takashi Tokumasu (Tohoku University, Japan), Jeongmin Ahn (Syracuse University, USA)

CRF-38 **Characterization of Plastic Deformation by using Electromagnetic NDT Methods**
Zhenmao Chen, Hong-En Chen, Shejuan Xie (Xi'an Jiaotong University, China), Tetsuya Uchimoto, Toshiyuki Takagi (Tohoku University, Japan)

CRF-39 **Magnetic Simulation for Localized Structure of Stressed Stainless Steel**
Kenichi Terashima, Katsuhiko Yamaguchi, Kenji Suzuki (Fukushima University, Japan), Tetsuya Uchimoto, Hiroyuki Kosukegawa, Toshiyuki Takagi (Tohoku University, Japan)

CRF-40 **Microscopic Observation of Jumping Organ of Collembola**
Seiichi Sudo, Toshiya Kainuma (Akita Prefectural University, Japan), Atsushi Shirai, Kosuke Inoue, Toshiyuki Hayase (Tohoku University, Japan)

CRF-41 **Attenuation and Reduction Effect of Underwater Explosion by Porous Materials(2nd report)**
Kazutaka Kitagawa (Aichi Institute of Technology, Japan), Kiyonobu Ohtani (Tohoku University, Japan), Atsushi Abe (ITOCHU Techno-Solutions Corporation (CTC), Japan)

CRF-42 **Biological Actuation with the Magnetic Stimulation**
Hitoshi Mori (IFG Corporation, Japan), Kenji Yashima, (IFG Corporation / Tohoku University, Japan), Toshiyuki Takagi, Shinichi Izumi, Ryoichi Nagatomi , Hiroyuki Kosukegawa, Genji Abe (Tohoku University, Japan), Toshihiko Abe (IFG Corporation, Japan)

CRF-43 **Localization of Protein Tyrosine Phosphatase in Endothelial Cells under Shear Flow**
Daisuke Yoshino (Tohoku University, Japan), Naoya Sakamoto (Kawasaki University of Medical Welfare, Japan), Masaaki Sato (Tohoku University, Japan)

CRF-44 **Sterilization Mechanism of Plasma Discharge against Biofilm-producing *Pseudomonas aeruginosa* on Contact Lenses**
Yoshihisa Nakano (Tohoku University, Japan), Shigeru Fujimura (Tohoku University, Japan / Tohoku Pharmaceutical University, Japan) , Takehiko Sato, Daisuke Yoshino, Akira Watanabe (Tohoku University, Japan)

CRF-45 **Correlation between Physicochemical Properties of Protein Signal Sequence Variation and Subcellular Transportation**
Kota Hamada, Naoyuki Takachio, Hiromu Sugita, Noritaka Kato (Meiji University, Japan), Makoto Ohta (Tohoku University, Japan), Kenji Etchuya, Yuri Mukai (Meiji University, Japan)

CRF-46 **Study of 3D Recognition by Glycosyltransferase in Protein Sugar Modification**
Kenji Etchuya (Meiji University, Japan), Makoto Ohta (Tohoku University, Japan), Yuri Mukai (Meiji University, Japan)

CRF-47 **Cardiac Evaluation of Fetal Mice by ECG and Ultrasound**
Rika Sugibayashi (National Center for Child Health and Development, Japan), Takuya Ito, Kenichi Funamoto, Toshiyuki Hayase, Yoshitaka Kimura (Tohoku University, Japan)

CRF-48 **Generation and Transport of Chemical Species in Low-Temperature Atmospheric Plasma for Sanitization Device**
Tetsuji Shimizu (terraplasma GmbH, Germany), Masahi Hara (Tohoku University, Japan), Gregor E. Morfill (terraplasma GmbH, Germany), Daisuke Yoshino, Takehiko Sato (Tohoku University, Japan)

CRF-49 **Observation of Hypoxia Cellular Response by using Microfluidic Devices**
Shuichiro Fukushima (Osaka University, Japan), Kenichi Funamoto (Tohoku University, Japan)

CRF-50 **Elucidation of Mechanisms of the Frictional Characteristics of Erythrocytes under inclined Centrifugal Force**
Kenichi Funamoto (Tohoku University, Japan), Luca Brandt (KTH Mechanics, Sweden), Akira Yatsuyanagi, Kosuke Inoue, Toshiyuki Hayase (Tohoku University, Japan)

CRF-51 **Evaluation of Permeability of Endothelial Cell Monolayer under Controlled Oxygen Tension**
Kenichi Funamoto (Tohoku University, Japan), Ioannis K. Zervantonakis (Harvard Medical School, USA), Kento Matsubara, Kiyoe Funamoto, Takuya Ito, Yoshitaka Kimura (Tohoku University, Japan), Roger D. Kamm (Massachusetts Institute of Technology, USA)

CRF-52 **Application of MR-Measurement-Integrated Hemodynamic Simulation to Cerebrovascular Diseases**
Shin-ichiro Sugiyama (Kohnan Hospital, Japan), Kenichi Funamoto, Daichi Suzuki, Toshiyuki Hayase, Teiji Tominaga (Tohoku University, Japan)

CRF-53 **Characteristics of a Plasma-induced Flow using a Mesh Electrode for Viral Inactivation**
Yuji Kudo, Michiko Okamoto, Takehiko Sato, Daisuke Yoshino (Tohoku University, Japan), Akira Suzuki (Sendai Medical Center, Japan), Hitoshi Oshitani (Tohoku University, Japan)

CRF-54 **Visualization of the Formation of Shock Waves at the Collapse of a Laser-induced Bubble**
M. Tinguely (Swiss Federal Institute of Technology Lausanne, Switzerland / Imperial College London, United Kingdom), T. Sato, K. Ohtani (Tohoku University, Japan), M. Farhat (EPFL, Switzerland)

CRF-55 **Hydrophilization of Metal Surface Using Thermal-Nonthermal Coupled Plasma Flow System**
Juyong Jang (University of Minnesota, USA), Hidemasa Takana (Tohoku University, Japan), Oleg P. Solonenko (Siberian Branch of Russian Academy of Science, Russia), Hideya Nishiyama (Tohoku University, Japan)

CRF-56 **Molecular Dynamics Study of Static and Dynamic Density Fluctuation of Diatomic Fluids around the Critical Points**
Shohei Ikawa (Shinshu University, Japan), Takashi Tokumasu (Tohoku University, Japan), Nobuyuki Tsuboi (Kyushu Institute of Technology, Japan), Shin-ichi Tsuda (Kyushu University, Japan)

CRF-57 **Development of Micro-motor Using Electrorotation of Smart Polymer**
Miklos Zrinyi (Semmelweis University, Hungary), Masami Nakano (Tohoku University, Japan)

CRF-58 **Particle Structural Formations of Colloidal MR Fluid and Their Influences on Magnetic Rheological Response**
Hiroya Abe (Osaka University, Japan), Masami Nakano (Tohoku University, Japan)

CRF-59 **Photoluminescence of Ge Nanodisk Array Structure Fabricated by Bio-template and Neutral Beam Etching**
Daisuke Ohori, Yuki Murayama, Kiyofumi Kondo (University of Miyazaki, Japan), Fujii Takuya, Takeru Okada, Seiji Samukawa (Tohoku University, Japan), Atsuhiko Fukuyama, Tetsuo Ikari (University of Miyazaki, Japan)

CRF-60 **Gate-Voltage Tunable Coupling Capacitance of Si Double-Quantum-Dots with Multiple Gates**
Takafumi Uchida, Masashi Arita (Hokkaido University, Japan), Akira Fujiwara (NTT Basic Research Laboratories, Japan), Yasuo Takahashi (Hokkaido University, Japan), Seiji Samukawa (Tohoku University, Japan)

CRF-61 **Intelligent Information Processing Circuits Using Nanodisk Array Structure**
Takashi Morie, Takashi Tohara, Yoshiaki Kuramitsu (Kyushu Institute of Technology, Japan), Kazuhiko Endo (National Institute of Advanced Industrial Science and Technology, Japan), Takeo Ohno, Seiji Samukawa (Tohoku University, Japan)

CRF-62 **Numerical Study on Charge Transfer by Collision of Particle from Plasma against Surface**
Satoshi Hamaguchi (Osaka University, Japan), Tomohiro Kubota, Seiji Samukawa (Tohoku University, Japan)

CRF-63 **Propagation Processes of Primary and Secondary Streamers by Pulsed Discharge in Water**
Hidemasa Fujita (Tohoku University, Japan) , Seiji Kanazawa (Oita University, Japan), Kiyonobu Ohtani, Atsuki Komiya, Toshiro Kaneko, Takehiko Sato (Tohoku University, Japan)

CRF-64 **Computational Study of Bubble Behavior for Clarification of Particle Removal Mechanism in Megasonic Cleaning**
Naoya Ochiai, Jun Ishimoto (Tohoku University, Japan), Jin-Goo Park (Hanyang University, Korea)

CRF-65 **Development of Thermomechanical Resist Removal-Cleaning Technology Using Cryogenic Micro-Solid Nitrogen Spray**
Jun Ishimoto (Tohoku University, Japan), Hideo Horibe (Osaka City University, Japan)

CRF-66 **Investigation of Shock Waves Propagation on Microscale**
Dmitry Khotyanovsky, Georgy Shoev, Yevgeniy Bondar (Khristianovich Institute of Theoretical and Applied Mechanics, Russia), Kaoru Maruta (Tohoku University, Japan)

CRF-67 **Thermal Resistance between Nano-Structured Surfaces and Liquids**
Taku Ohara (Tohoku University, Japan), Masahiko Shibahara (Osaka University, Japan), Gota Kikugawa, Chilukoti Hari Krishna (Tohoku University, Japan)

CRF-68 **Construction of Lattice Constant in Aluminum Nitride Prepared by ECR Sputtering**
Satoru Kaneko (Kanagawa Industrial Technology Center, Japan), Hironori Torii (JSW-AFTY, Japan), Manabu Yasui, Takeshi Ito (Kanagawa Industrial Technology Center, Japan), Shigeo Yasuhara (Japan Advanced Chemicals, Japan), Rieko Sudo (Sagamihara Surface Technology Laboratry, Japan), Takashi Tokumasu (Tohoku University, Japan)

CRF-69 **Fabrication of Al/Ti Composite Material by Compression Shearing Method at Room Temperature**
Shota Sakagami, Masaomi Horita, Noboru Nakayama (Shinshu University, Japan), Hiroyuki Miki, Toshiyuki Takagi, Hiroyuki Kosukegawa (Tohoku University, Japan), Hiroyuku Takeishi (Chiba Institute of Technology, Japan)

CRF-70 **Molecular Dynamics Study of the Droplet Shearing by Solid Walls**
Akinori Fukushima (Tohoku University, Japan), Nicolas Fillot, Marie-Hélène Meurisse (Université de Lyon, France), Takashi Tokumasu (Tohoku University, Japan), Philippe Vergne (Université de Lyon, France)

CRF-71 **Research on the Physical and the Tribological Properties of a Soft Metal Layer Originating in Me-DLC on Sliding Surface**
Minoru Goto (Ube National College of Technology, Japan), Toshiyuki Takagi (Tohoku University, Japan), Kosuke Ito (Nihon University, Japan), Takanori Takeno, Hiroyuki Miki, Hiroyuki Kosukegawa (Tohoku University, Japan)

CRF-72 **Study on the High-Performance and High-Mobility MOS Transistor by the Neutral Beam Process**
Kazuhiko Endo, Wataru Mizubayashi, Meishoku Masahara (National Institute of Advanced Industrial Science and Technology, Japan), Seiji Samukawa (Tohoku University, Japan)

CRF-73 **Adsorption Control of Ferritin Molecules with Nano Particles**
Ichiro Yamashita (Nara Institute of Science and Technology, Japan), Rikako Tsukamoto, Seiji Samukawa (Tohoku University, Japan)

CRF-74 **Photoluminescence Properties of InAs Quantum Dots on Nitrogen δ-doped GaAs**
Toshiyuki Kaizu, Takashi Kita (Kobe University, Japan)

CRF-75 **Bottom-up Construction of Coarse-grained Interaction Models from Molecular Dynamics Simulations**
Ikuya Kinefuchi, Yuta Yoshimoto, Toshiki Mima (The University of Tokyo, Japan), Akinori Fukushima, Takashi Tokumasu (Tohoku University, Japan), Shu Takagi (The University of Tokyo, Japan)

CRF-76 **Development and Micro-Channel Flow Evaluation of Electro-Rheological Nano-Suspensions**
Katsufumi Tanaka, Seiya Robson, Keita Kitaura, Haruki Kobayashi (Kyoto Institute of Technology, Japan), Masami Nakano, Atsushi Totsuka (Tohoku University, Japan)

CRF-77 **Structural and Transformational Properties of $Ni_{46.4}Mn_{38.8}In_{12.8}Co_2$ Thin Films**
Anna Kosogor (National University of Science and Technology, Russia / Institute of Magnetism, Ukraine), Maria Lyange, Michail Gorshenkov (National University of Science and Technology, Russia), Vladimir Khovaylo (National University of Science and Technology, Russia / ITMO University, Russia), Makoto Ohtsuka, Hiroyuki Miki, Toshiyuki Takagi (Tohoku University, Japan)

CRF-78 **Measurement on Wake Flow Induced by Soft Fins' Vibration**
Akira Rinoshika, Shunya Suzuki (Yamagata University, Japan), Masami Nakano (Tohoku University, Japan)

CRF-79 **Manipulation of 3-D Boundary-Layer Transition on a Swept NLF Wing**
Shohei Takagi (Tokyo Metroplitan University, Japan), Yusuke Fushikida, Tsutomu Saito (Muroran Institute of Technology and Aerospace Plane Research Center, Jpan), Shigeru Obayashi, Yasufumi Konishi (Tohoku University, Japan)

CRF-80 **Quantitative Visualization of Unsteady High-speed Fluid Phenomena in Nature Environment**
Toshiharu Mizukaki (Tokai University, Japan), Shigeru Obayashi (Tohoku University, Japan)

CRF-81 **The Dynamic Behavior of Magnetic Fluid Adsorbed on the Cylindrical Permanent Magnet in Water Container Subjected to Alternating Magnetic Field**
Masato Nakanishi, Seiichi Sudo (Akita Prefectural University, Japan), Hideya Nishiyama (Tohoku University, Japan)

CRF-82 **Rheology of MR Shear Thickening Fluids under Instantaneous Flow**
Gangrou Peng, Weihua Li, Tongfei Tian (University of Wollongong, Australia), Masami Nakano (Tohoku University, Japan)

CRF-83 **Researches on the Suppression Control of Hole Tone Phenomena**
Kazuo Matsuura (Ehime University, Japan), Masami Nakano (Tohoku University, Japan)

CRF-84 **Numerical and Experimental Research on Active Control of Self-Sustained Flow Oscillations with Sound Interaction**
Mikael A. Langthjem (Yamagata University, Japan), Masami Nakano (Tohoku University, Japan)

CRF-85 **Effects of External Disturbances on Spatial Development of Turbulence and toward the Control of Thermo-Fluid Dynamics (Cases of Boundary Layer, Wake, and Jet)**
Yasuhiko Sakai, Kouji Nagata, Yasumasa Ito (Nagoya University, Japan), Toshiyuki Hayase (Tohoku University, Japan), Shuang Xia, Zhou Yi, Tomoaki Watanabe, Akihiro Sasoh, Nannan Wu, Kousuke Takeuchi (Nagoya University, Japan)

CRF-86 **Analysis of Complex Spatiotemporal Structures of Vortices in Turbulence: Extraction of Strong Vortical Clusters in High-Reynolds-Number Turbulence**
Takashi Ishihara (JST, Japan / Nagoya University, Japan), Yuji Hattori (Tohoku University, Japan)

CRF-87 **Vortex Dynamics of the High Energy (Negative Temperature) State in Quasi-Geostrophic Turbulence**
Masaya Ishihara (University of Electro-Communications, Japan), Naoya Takahashi (Tokyo Denki University, Japan), Takeshi Miyazaki (University of Electro-Communications, Japan), Nozomu Hatakeyama, Yuji Hattori (Tohoku University, Japan)

CRF-88 **Stability Analysis of Vortices with Axial Flow based on Energetics and its Application**
Yasuhide Fukumoto (Kyushu University, Japan), Makoto Hirota, Yuji Hattori (Tohoku University, Japan)

CRF-89 **The Continuous Spectrum in the Moore–Saffman–Tsai–Widnall Instability**
Yuji Hattori, Makoto Hirota (Tohoku University, Japan), Stefan G. Llewellyn Smith (UCSD, USA)

CRF-90 **Serial Recalculation of Velocities of Quasiparticles in Kinetic Force Method**
Vladimir Saveliev (Institute of Ionosphere, National Center of Space Researches and Technologies, Kazakhstan), Svetlana Filko (Institute of Ionosphere, National Center of Space Researches and Technologies / Zhetysu State University, Kazakhstan), Shigeru Yonemura (Tohoku University, Japan)

CRF-91 **Generation Mechanism of Rising Film Flow along the Rotating Conical Outer Surface and the Subsequent Atomization Characteristics**
Keisuke Matsuda, Takahiro Adachi (Akita University, Japan), Junnosuke Okajima (Tohoku University, Japan), Takeshi Akinaga (Aston University, United Kingdom)

CRF-92 **Hopf Bifurcation of 2D Driven Cavity Flows**
Reima Iwatsu, Kazuyuki Itoi (Tokyo Denki University, Japan)

CRF-93 **Development of New Visualization Method for Plasma-generated Nano-micro Bubbles**
Takehiko Sato, Yuki Yamaguchi, Kiyonobu Ohtani (Tohoku University, Japan), Takashi Miyahara (Shizuoka University, Japan), Tatsuyuki Nakatani (Okayama University of Science, Japan)

CRF-94 **Development of CFD Code for Tsunami using Shallow Water Equations**
Fumiya Togashi (Applied Simulations Inc., USA), Rainald Lohner (George Mason University, USA), Masuhiro Beppu (National Defense Academy of Japan, Japan), Hiroshi Tatesawa (Bousai Consultant Co., Ltd., Japan), Shigeru Obayashi (Tohoku University, Japan)

CRF-R1 **Numerical Study of Flotsam Mixed Tsunami and Tsunami Scale Modeling**
Jun Ishimoto (Tohoku University, Japan), Kozo Saito (University of Kentucky, USA),

CRF-R2 **Investigation on Advanced Medical Ultrasound Imaging Technology**
Masayuki Tanabe (Kumamoto University, Japan), Hiroshi Hashimoto (GE Healthcare Japan, Japan), Kenichi Funamoto, Yoshiki Chiba, Toshiyuki Hayase (Tohoku University, Japan)

# Plenary Lectures

Eleventh International Conference on Flow Dynamics
October 8-10, 2014, Sendai, Miyagi, Japan

# Recent advances in high Reynolds number partially-premixed combustion research

James F. Driscoll, A. B. Modine Professor of Aerospace Engineering
University of Michigan, 3120 Beal Ave. Ann Arbor MI, USA

**ABSTRACT**

Jet engines and liquid propellant rockets suffer from "growl", "screech" and heat transfer problems that can be triggered by flame liftoff, requiring better understanding and new models of liftoff. The Takeno flame index [1, 2] is important to identify premixed and non-premixed flamelets; our new method provides measurements of flame index that are compared to simulations of Mizobuchi [1, 2], Pitsch [4] and Vervisch [5]. PLIF images of internal structure of flames in the flamelet and distributed reaction regime are compared to results of Dunn [6], Kobayashi [7-8] and others [9-12].

## 1. Introduction

Partially-premixed turbulent combustion consists of both premixed flamelets along with non-premixed flamelets; for example this occurs in the base region of a lifted flame that is downstream of a fuel jet [1, 2] or a gas turbine fuel injector [3]. To model and understand lifted flames, it is useful to measure the fraction of flamelets that are premixed (versus non-premixed), and the locations of high probability of premixed (versus non-premixed) flamelets. Flame index is +1 where a premixed flamelet exists and is -1 where a non-premixed flamelet is located. A new method to measure flame index was developed that adds 5000 ppm $NO_2$ to the air; acetone is used as one component of the fuel. Laser induced fluorescence images indicate the locations of flamelets and whether the gradients of the fuel and $O_2$ are in the same direction (premixed) or not (non-premixed flamelet).

## 2. Flame Index measurements

The Siemens DLR gas turbine model combustor design is shown in Fig. 1a and one of our instantaneous flame index images is Fig. 1b. Red layers are measured premixed flamelets while blue layers are non-premixed flamelets. Contours in Fig. 1c show where there is a large probability that a flamelet is premixed. In contrast to this model gas turbine device, the Sandia jet flame D is long and narrow and has a small amount of premixed combustion near its base due to a pilot flame. It was found that one parameter that controls the fraction of flamelets that are premixed is the fuel injection velocity (relative to the air velocity). Increasing this parameter increases the distance that the fuel penetrates into the mixing region, which favors premixed flamelets. Near the fuel injector in Fig. 1 the flamelets are mostly non-premixed.

In an LES simulation of lifted, partially-premixed flames in jet engines, IC engines or rockets, for example, the reaction rate of hydrogen [4, 5] can be set equal to:

$$\bar{\omega}_{H2} = \int_{-\infty}^{\infty} \omega_{H2}\, P(\xi) d\xi \;\; = A\, \omega_{H2\ nonpre} \; + \; C\, \omega_{H2\ pre}$$

Submodels [4, 5] provide the probabilities of premixed (A) and non-premixed (C) flamelets, and the reaction rates (ω) of each. Measurements are being used to assess these new submodels.

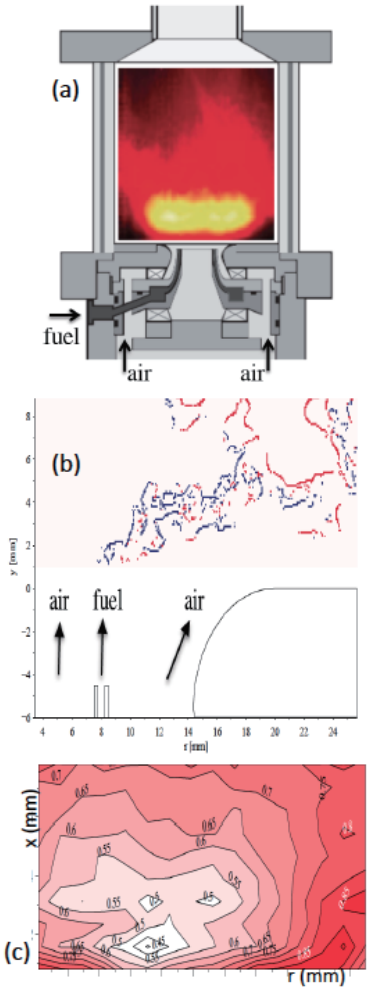


Figure 1. (a) Siemens / DLR gas turbine model combustor, (b) Premixed (red), non-premixed flamelets (blue) (c) Probability that a flamelet is premixed

Corresponding author: James F. Driscoll
*E-mail address*: jamesfd@umich.edu

### 3. Flame structure at high Reynolds number

High Reynolds number premixed flames are of interest because they have both large turbulence levels and large integral scales and have not been studied enough to understand their new physics. High Re leads to a larger range of eddy sizes, local flame extinction due to large, strong eddies, and distributed reactions. We discuss several recent results: the high-pressure flames of Kobayashi [7, 8], the high velocity flames of Dunn and Masri [6] and Shy [11] and some PLIF images of the thickening of the preheat zone and reaction layer in our flames. Our fully-premixed experiment is a 25 mm diameter Bunsen burner is operated at reactant velocity up to 106 m/s. PLIF images of formaldehyde show that the preheat layer is thickened. Images of the overlap of the OH-formaldehyde signals indicate the thickening of the reaction layer, as seen in Fig. 2. Results from several high Reynolds number studies are being used to infer the boundaries of the Borghi regime diagram that indicates where flamelet and distributed reaction models are appropriate. The PLIF images are useful for assessing basic assumptions in various models [4, 5, 13].

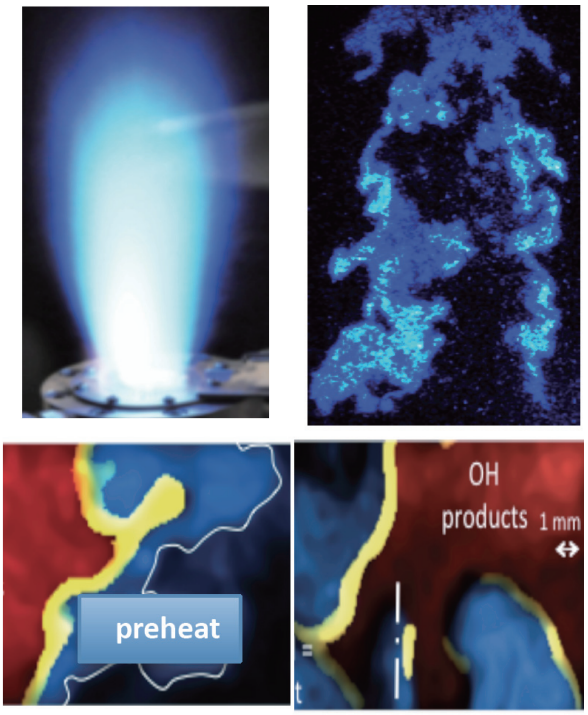


Figure 2. U. of Michigan high Reynolds number PLIF images of thick preheat regions and thick reaction layers in premixed turbulent flames.

A new regime was found (called "distributed - thickened) that contains distributed preheat zones and thickened reaction layers. Distributed preheat zones are seen to be 20 times thicker than the laminar case. They first occur when local extinction first creates "holes" that allow hot product to rapidly mix with the reactants. A second new regime was identified that is called "distributed-distributed"; it occurs when the reaction zones also become distributed and are no longer layer-like. The upper boundary of this regime is caused by global extinction, which competes with local extinction. For certain conditions when global extinction dominates, reactions cannot become distributed, but for other conditions they can. An analysis is presented that suggests that the slope of the new regime boundaries should depend on the Stretch Efficiency Function of Meneveau and Poinsot [14], which predicts the first occurrence of local extinction.

The boundaries of the Borghi regime diagram are being measured in order to provide guidance as to when a flamelet model is realistic, and when a distributed reaction model is necessary. A previous series of papers by Kobayashi and colleagues [7, 8] showed how flame structure becomes thinner and with finer small scale wrinkles as the Reynolds number is increased by increasing the gas pressure and gas density. Shy and co-workers [11] have achieved very high turbulence intensity to determine boundaries of different regimes, while Kido et al. [12] studied spherical flames that represent IC engine conditions. These results also are compared to our measurements [9] using a single GE-TAPS Lean Premixed Pre-vaporized fuel injector operated at realistic high-pressure, preheated air conditions with Jet-A fuel. PLIF of formaldehyde identifies the flame location and flame surface density, while PIV was used to measure the recirculation zones and flow pattern.

### References


1. H. Yamashita, M. Shimada, T. Takeno, Proc. Combust. Inst. 26 (1996) 27–34.
2. Y. Mizobuchi, J, Shinjo, S. Ogawa, T. Takeno, Proc. Comb. Inst. 30 (2005) 611–619
3. D. A. Rosenberg, P, M. Allison, J. F. Driscoll, AIAA paper 2013-1181.
4. E. Knudsen, H. Pitsch, Combust. Flame 159 (2012) 242–264.
5. P. Domingo, L. Vervisch, K. Bray, Combust. Theor. Model. 6 (2002) 529–551.
6. M. J. Dunn, A. R. Masri, R. Bilger, R. S. Barlow, Flow Turb. Comb. 85 (2010) 621.
7. H. Kobayashi, T. Tamura, K. Maruta, T. Niioka, F. Williams, Proc. Comb Inst 26 (1996) 389.
8. G.G. Lee, K. Y. Huh, H. Kobayashi, Comb. Flame 122 (2000) 43.
9. J. E. Temme, P. M. Allison, J. F. Driscoll, Comb. Flame 161 (2014) 958.
10. P. M. Allison, J. F. Driscoll, M. Ihme, Proc. Comb. Inst. 34 (2013) 3145.
11. C. C. Liu, S. S. Shy, Y. C. Dong, M. W. Peng, Comb. Sci. Technol., 184 (2012) 1916–1933.
12. H. Kido, M. Nakahara, K. Nakashima, J. Hashimoto, Proc. Comb. Inst. 29 2002, 1855.
13. K.N.C. Bray, P. Libby, G. Masuya, J. B. Moss, Comb. Sci. Tech. 25 (1981) 127.
14. C. Meneveau, T. Poinsot, Combust. Flame 86 (1991) 311.

Eleventh International Conference on Flow Dynamics
October 8-10, 2014, Sendai, Miyagi, Japan

# Means of Stabilization of Flying Inspection Vehicles to Enhance Data Flow in Image Processing

Christian Boller, Chung-Hsin Kuo, and Chen-Ming Kuo
Chair in Non-Destructive Testing and Quality Assurance (LZfPQ)
Saarland University
Campus E3.1, 66123 Saarbrücken, Germany

**ABSTRACT**

The presentation will deal with means for stabilizing the flight performance of a micro-aerial vehicle (MAV) and what impact this has on the image flow and resolution of images obtained in general. The means to be discussed will include a vector thrust propulsion system for the MAV as such as well as a fuzzy logic controlled device to control stability of a gimbaled camera system on a MAV.

## 1. Introduction

The increasing amount of civil infrastructure ageing has given rise to enhanced monitoring. Monitoring of civil infrastructure is done visually in most of the cases. Human beings are usually making the inspections in person, which can make the task dangerous, time consuming and costly. A way to ease this process is by applying robotic systems such as MAVs which record a continuous flow of images at a very high resolution such that damage of an infrastructure can be observed and analysed at even millimetre scale. These images need to be combined and hence 'stitched' which is a process becoming increasingly difficult the more images have to be processed. The number of images taken is a function of the images' resolution and quality hence the better the quality of the images taken become the less the number of images have to be processed.

Since MAVs are flying vehicles they are subject to gusts which can occur at different intensities and lead to a distortion of the images taken in different regards. A motivation is therefore to look for means that allow flight performance of the MAV to be stabilised such that the quality of the image can be maximised. Two options that have been explored include the application of a vector thrust and a fuzzy logic image control system that are briefly explained throughout the following.

## 2. MAV Considered

There are different types of MAV including fixed, rotary and flapping wing where rotary wing MAVs are possibly the most suitable with regard to scanning infrastructure due to the vehicle's ability to hover and hence to keep attitude to a comparatively satisfying degree. However with respect to recognising details such as damage in the millimetre range as well as stitching large numbers of images together in a preferably automated way, requirements in attitude control become quite high.

Fig. 1 shows the MAV system considered which has been a quadrocopter system in the respective case. Operation of the quadrocopter is done by variation of the speed of the different rotors as it is shown schematically in Fig. 2. Whenever the MAV flies forward at a constant altitude a slight pitch angle is generated which may lead the photograph taken to be distorted.

Fig. 1 Quadrocopter-based MAV

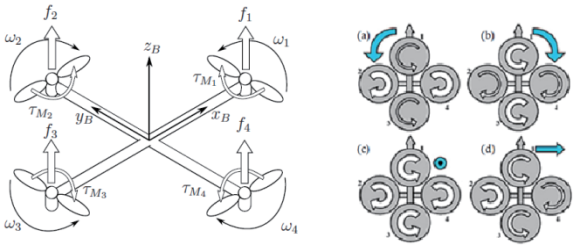


Fig. 2 Left: Free force diagram of the multi-rotor robot. Right: Motion diagram, a) yaw anti-clockwise, b) yaw clockwise, c) increase altitude (movement in Z direction only), d) roll positively to create motion in y direction (negatively).

## 3. Vector Thrust Control

To further enhance this control a vector thrust solution has been developed based on a concept already successfully applied in the past [1]. Vector thrust in the type of rotary wing vehicle shown above can be realized by twisting the rod along which the rotor is attached, hence around the x- and y-axis respectively when taking the definitions provided in Fig. 2 (left). To describe the direction of motion of the aerial vehicle itself the position of rotors versus the direction of motion of the aerial vehicle becomes important. In the case of four rotors and when the aerial vehicle moves in the direction of

Corresponding author: Christian Boller
*E-mail address*: c.boller@mx.uni-saarland.de

either the x- or y-axis within the x-y-plane the configuration will be called a plus-configuration while when the aerial vehicle moves in a direction between the x- and y-axis it will be called an x-configuration. When comparing the two configurations it already becomes obvious that the efficiency of the vector thrust propulsion with respect to vehicle stabilization becomes less in the plus-configuration since two of the vector thrust rotors operating along the direction of motion basically do not show any effect. Background of the mathematical modelling has been described in [2].

Control of the vector thrust has been implemented into the flight control of the MAV which has allowed vector thrust control to be switched on as an automated feature. Fig. 3 shows the attitude reading from the flight where the lighter (red) line indicates the actual roll angle and the black line indicates the input signal from pilot command (roll angle in this case). "Normal" flight is the region in the left hand rendered box, where the large roll angle can be seen when the pilot applies a roll (side way) displacement command. However, the performance becomes completely different and hence stable once the MAV enters into the vector thrust mode. The roll angle in the right hand rendered box (vector thrust mode) stays at a minimum when the pilot gives a side way (roll) command, which means the vehicle is moving sideways without any attitude change, becoming much more stable with a significant improvement of the image captured.

This measure has allowed images taken to be much more stable leading to a much smaller variation in image distortion and an enhanced 50% better output of images to be used for the subsequent image stitching process.

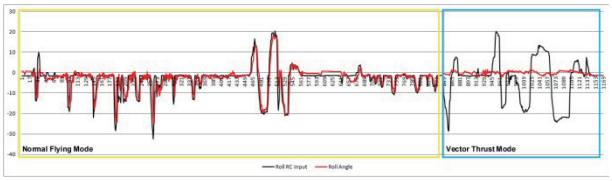


Fig. 3 On board accelerometer roll reading (black) and RC roll input (red/light); no vector thrust (box left) with vector thrust (box right)

## 4. Fuzzy Logic Controlled Imaging

Although the vector thrust option very much helps to improve image quality in terms of image distortion with respect to pitch and yaw there is still a variation with respect to the waypoint where an image should be taken.

The minimum number of images to be taken from an object is defined by

$$\text{scale} = \frac{\text{distance of object from camera}}{\text{focal length}}$$

and

$$\text{actual width on photo} = \text{scale} \times \text{sensor width}$$

$$\text{actual height on photo} = \text{scale} \times \text{sensor height}$$

where the number of pixels is considered to be sensor width and sensor height respectively. Since the scale is subject to scatter due to variation in yaw and pitch of the MAV a fuzzy logic approach can be used to define the waypoint where/when an image has to be taken best. To get such a system operational it first needs to be trained in accordance to the operational conditions the MAV has to go through. This leads to some input functions such as the example shown in Fig. 4 below. A respective output function is then determined as to Fig. 5, which is the basis on automatically triggering the camera on the MAV along its flight path.

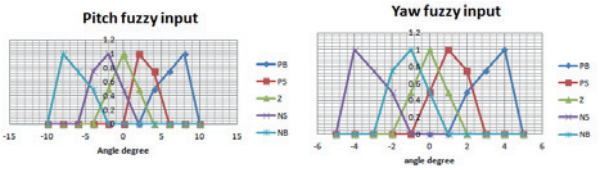


Fig. 4 Fuzzy input; Left: pitch noise. Right: heading (yaw) noise

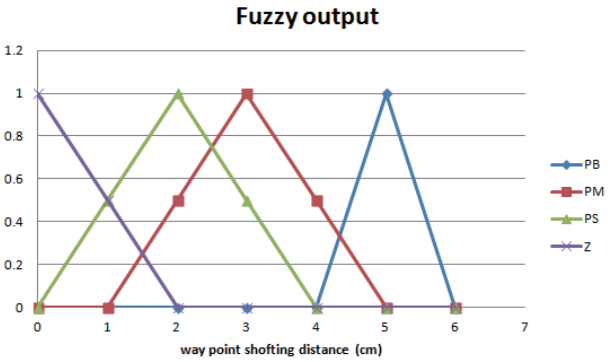


Fig. 5 Fuzzy output waypoint correction functions

Following first tests made an improvement in images to be used for stitching has been improved by a factor of four which is another important measure to improve image quality.

## 5. Concluding Remarks

Measures taken in controlling flight attitude of a MAV as well as the sensor system to be used for monitoring can become significantly rewarding with respect to the quality of the sensing output which has been images in the case reported here. With the measures described and possibly even others such as optical data flow high resolution monitoring of civil infrastructure can be made possible in the longer term even on an increasingly automated basis.

## References

[1] C.-M. Kuo and C. Boller, 2013: Adaptive aeronautical structures demonstration on a modular designed micro aerial vehicle; in C. Boller & H. Janocha (Ed.s): New trends in smart technologies; Fraunhofer Verlag, pp. 255 – 271 (open source)

[2] C.-H. Kuo, C.-M. Kuo, A. Leber and C. Boller, 2013: Vector thrust multi-rotor copter and its application for building inspection; Proc. of the Internat MAV Conf. & Flight Competition, Toulouse/France

# Wettability Engineering for Heat Transfer Applications

D. Attinger[1], C. Frankiewicz[1], A. Betz[2], T. M. Schutzius[3], R. Ganguly[3], A. Das[3], C.-J. Kim[4] and C. M. Megaridis[3]
[1] Mechanical Engineering, Iowa State University
Ames, Iowa 50011, USA
[2] Department of Mechanical and Nuclear Engineering, Kansas State University
Manhattan, KS 66506, USA
[3] Mechanical and Industrial Engineering, University of Illinois at Chicago
Chicago, Illinois 60607-7022, USA
[4] Department of Mechanical and Aerospace Engineering, University of California, Los Angeles
Los Angeles, CA 90095-1597, USA

**ABSTRACT**

The design of surfaces for phase change heat transfer applications is critical for supplying energy with higher efficiency. Efforts in this area have been invigorated by the emergence of novel mini-, micro- and nano-scale methods for surface manufacturing/modification, which can control the relevant length scales and assist in fluid phase management. We review historical developments in texturing/chemical modification of surfaces aiming to maximize energy transport and thermodynamic efficiency in boiling, condensation and icing/frosting applications, and present examples in each area.

## 1. Introduction

We discuss the increasingly important contributions of advanced materials and novel fabrication techniques in enhancing phase change heat transfer and related energy applications. Phase change is essential to energy applications, where it drastically enhances heat transfer (latent heat is typically much larger than sensible heat). In addition, phase change is frequently accompanied by large and rapid changes in specific volume, which result in enhanced heat transfer due to induced convection.

## 2. Industrial Relevance

The rate of heat exchange in the presence of phase transformations is much higher compared to single-phase systems. Thus, phase change benefits many industrial applications, ranging from thermal generation of electricity, desalination and metallurgy, to electronics cooling and food processing. Industrial applications with phase change typically use water-based fluids or refrigerants, depending on the amount of heat to be transferred, operating conditions, and interactions of the fluid with device components. Three phase-change processes with industrial relevance are reviewed: boiling (liquid to vapor phase change), condensation (vapor to liquid) and ice/frost formation (gas/liquid to solid). The properties of an optimum surface for each of these three modes of phase change are described; then some fabrication/manufacturing techniques to modify surface texture and chemistry are presented; next, the ways that these techniques have been used to enhance phase change heat transfer are reviewed. An emphasis is placed on the fast-developing area of wettability engineering, which relies on manipulating both surface texture and chemistry using special attributes, such as advanced materials. The present review bridges the gap between the heat transfer and material science communities towards the common goal of designing and deploying optimum material systems to enhance phase change heat transfer performance and minimize thermodynamic inefficiencies, thus facilitating sustainable energy transmission and production.

Corresponding author: Constantine Megaridis
*E-mail address*: cmm@uic.edu

## 3. Thermodynamic Considerations

A first measure of phase change heat transfer performance is the maximum heat flux exchanged between a solid surface and the fluid. For a boiling fluid, the critical heat flux (CHF) is the highest heat flux that can be exchanged before vapor bubbles merge into a vapor layer that insulates the surface from the liquid, thus reducing subsequent heat transfer. A second measure of performance is the heat transfer coefficient (HTC), namely the ratio of the heat flux to the driving temperature difference, $\Delta T$, between the solid surface and the fluid. HTCs associated with phase change are typically one to two orders of magnitude larger than HTCs in single-phase systems, because the latent heat minimizes $\Delta T$. An optimum surface for phase change heat transfer is therefore a surface that optimizes heat transport in terms of maximizing both CHF and HTC.

## 4. Wettability Engineering

Boiling: Engineering surfaces to achieve higher boiling performance dates back to more than 80 years. Fundamental studies in this area began to appear in the mid-twentieth century, when fabrication techniques started developing to allow more precise manufacturing of the geometries considered for enhanced heat transfer. Several reviews have been published in this area, exemplified by those of Webb [1,2] and more recently by Bergles and Manglik [3]. We describe the main engineering attempts to produce surfaces with high boiling performance, i.e., high HTC and CHF. An ideal boiling surface requires hydrophobicity to promote nucleation and HTC at low heat flux, and hydrophilicity to maintain water contact with the hot surface for preventing the onset of CHF [4]. More recently, attempts have been made to engineer multifunctional surfaces which feature both wettable and non-wettable

domains with the goal to increase HTC and CHF simultaneously [5].

Condensation: Early review of methods to enhance heat transfer in condensing equipment and technical approaches to favor dropwise condensation (DwC) has been provided by Williams et al. [6]. The use of micro- and nanostructures to enhance DwC on surfaces has recently been reviewed by Enright et al. [7]. Surface wettability engineering aims to improve condensation heat transfer by: (i) maximizing the DwC HTC by encouraging nucleation and early removal of droplets, (ii) ensuring adequate drainage of condensate to avoid the transition to filmwise condensation (FwC), and (iii) sustaining DwC over prolonged periods by minimizing surface degradation. The design requirements for surfaces addressing the above three criteria are distinct. Enhancing DwC HTC requires that the surface be hydrophobic enough to shed the condensate droplets at a small size and at the same time allow better surface rejuvenation. Enhanced droplet mobility on a hydrophobic condenser surface also facilitates condensate drainage, thus delaying the transition from the DwC to the FwC mode. Multiscale wettability patterning is investigated to enhance the removal of condensate and prevent formation of liquid film on the surface. We describe how current wettability engineering strategies are implemented through homogeneous (monophilic) and heterogeneous (biphilic) chemical coatings, homogeneous and heterogeneous physical texturing, or a combination of chemical coating and physical texturing.

Icing/Frosting: A passive strategy to avoid ice formation/deposition includes delaying ice nucleation and the onset of mass solidification. This can be achieved by modifying the chemistry of the surface or its micro- and nanoscale texture [8]. However, this approach is limited under many technical circumstances, e.g. when a cold surface encounters supercooled water droplets in a humid atmosphere, where icing is ultimately inevitable. In this situation, ice adhesion hinders the effort to rid a surface of the ice. Thus, engineering attempts to prevent ice/frost formation or prolong machinery operation in ice-promoting environments have concentrated on ice/frost delay, ice adhesion reduction or both. We review engineering attempts to produce surfaces that delay ice/frost nucleation and reduce ice adhesion.

## 5. Concluding Remarks

This review is based on material drawn from [9] and illustrates the rationale, techniques and challenges of engineering the texture and chemistry of surfaces for phase change heat transfer. While the idea of engineering surfaces for enhanced phase change heat transfer is not new, the degree of sophistication with which surfaces can be engineered today—owing to advances in micro- and nano-fabrication methods over the last two decades—has caused a resurgence of interest in this subject. Examples of the variety of methods available have been presented, and a large choice of modifications of surface energy and texture is possible, all the way from the nanoscale to the centimeter scale.

## Acknowledgement

Funding from the U.S. National Science Foundation under Grants CBET-1066426, 1236030 and 1235867 is acknowledged.

## References

[1] R. L. Webb, *Heat Transfer Eng.* 2 (1981) 46-69.
[2] R. L. Webb, *J. Heat Transfer* 126 (2004) 1051-1059.
[3] A. E. Bergles and R. M. Manglik, *J. Enhanced Heat Transfer* 20 (2013) 1-15.
[4] C. H. Wang and V. K. Dhir, *J. Heat Transfer-Transactions of the ASME* 115 (1993) 659-669.
[5] A. R. Betz, J. Xu, H. Qiu and D. Attinger, *Applied Physics Letters* 97 (2010) 141909.
[6]A. G. Williams, S. S. Nandapurkar and F. A. Holland, *Transactions of the Institution of Chemical Engineers and the Chemical Engineer* 46 (1968) CE367-CE373.
[7] R. Enright, N. Miljkovic, J. L. Alvarado, K. Kim and J. W. Rose, *Nanoscale and Microscale Therm. Eng.* 18 (2014) 223-250.
[8] S. Jung, M. Dorrestijn, D. Raps, A. Das, C. M. Megaridis and D. Poulikakos, *Langmuir* 27 (2011) 3059-3066.
[9]D. Attinger, C. Frankiewicz, A. Betz, T.M. Schutzius, R. Ganguly, A. Das, C.-J. Kim and C. M. Megaridis, *MRS Energy & Sustainability* (2014).

# GS1: General Session

# Thickening of $CO_2$ Using Copolymer- Application in $CO_2$ Management

Botchu Vara Siva Jyoti, Seung Wook Baek, N.Purushothaman, Dong Gi Lee
Korea Advanced Institute of Science and Technology
Daejeon, 305701, South Korea

**ABSTRACT**

The objective of this research was the design, synthesis and evaluation of fluorous $CO_2$ thickening agent for the better understanding and development of inexpensive non-fluorous $CO_2$ thickening agents. Firstly a highly $CO_2$-philic, hydrocarbon-based monomer was identified for soluble in $CO_2$. Secondly, synthesis of copolymer in which $CO_2$-philic monomer was combined with a small proportion of $CO_2$-phobic and philic (3-vinylaniline) associating groups for viscosity-enhancing intermolecular interactions to occur and a primary amine $CO_2$-philic group for capturing $CO_2$.

## 1. Introduction

Environmental issues are a major cause for concern in the world of today. Greenhouse gases are an environmental concern that is continuously increasing in importance, especially the emissions of carbon dioxide. Fossil fuel burning results in the emission of carbon dioxide. This additional carbon dioxide is upsetting the delicate balance that the earth manages naturally. In order to reduce the amount of carbon dioxide released into atmosphere, the carbon dioxide must be captured and stored, or sequestered. In order to store carbon dioxide, the gas must be captured prior to release into the atmosphere. One of the methods could be thickening/gelation of $CO_2$.

The identification of highly $CO_2$-soluble polymers composed of only Carbon, hydrogen, oxygen and nitrogen could facilitate the design of safe, inexpensive, environmentally benign "$CO_2$-philes". These compounds could enhance the performance and economics of $CO_2$-based technologies that require the dissolution of amphiphiles, such as surfactants, chelating agents, thickeners, and dispersants and homopolymers or copolymers for $CO_2$ thickening applications. An extensive review of polymer solubility in dense carbon dioxide was previously conducted in an attempt to identify a thickener that would reduce the mobility of supercritical $CO_2$ flowing through porous media (Heller, et al. 1985). Although very little work on viscosity-enhancing associative thickener or polymer has been done. Therefore, the objective of the current work was to determine whether the fluoroacrylate-3-vinylaniline copolymer would be sufficiently soluble in $CO_2$ in the 298 to 373 K temperature range to increase the viscosity and decrease the mobility of carbon dioxide.

## 2. Experimental

**Copolymer Synthesis:** 3-vinylaniline [Aldrich, 97%] was purified under vacuum distillation to remove KOH inhibitor. 1H,1H,2H,2H-perfluorodecyl acrylate [Aldrich, 97%] was used after the inhibitor, 100 ppm tert-butylcatechol, was removed by adding the monomer Drop wise to an inhibitor removal column (Fig.1). Bulk, free radical polymerization, with AIBN as initiator, was used to obtain a random copolymer product.

Corresponding author: Seung Wook Baek
*E-mail address*: swbaek@kaist.ac.kr


Fig. 1 Experimental setup

## 3. Results and Discussion

In a typical synthesis of the 71% fluoroacrylate, 29% 3-vinylaniline copolymer, 0.91 g (0.007873 mol) 3-vinylaniline, 10.00 g (0.01929 mol) fluoroacrylate, and $8.93*10^{-3}$ g ($5.44*10^{-5}$ mol) of AIBN were added to a 50-ml glass ampule under an inert $N_2$ atmosphere. The ampule was sealed and placed in an oil bath at 338 K for 12 hours to promote polymerization. The reaction products were then dissolved in 100 g 1,1,2-trichlorotrifluoroethane. The copolymer was then precipitated by washing with 300 g methanol, while the unreacted monomer remained in solution. The copolymer produced, a white solid was recovered by filtration. The copolymer was washed two more times in a similar manner and dried under vacuum overnight (Fig.1). The structure of the copolymer will be confirmed using standard IR and NMR techniques. The resultant copolymer could be a random copolymer of these two monomers (Fig. 2).

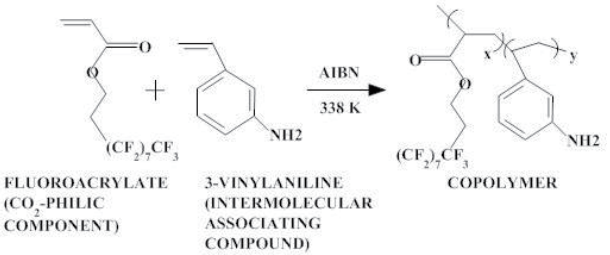


Fig. 2 Free radical polymerization synthesis process

The fluoroacrylate functional groups in these copolymer imparted $CO_2$-philicity to the candidate thickening agent, thereby facilitating its dissolution in dense $CO_2$. The carbon dioxide insoluble 3-vinylaniline group in the thickener enhanced intermolecular associations with similar groups in neighboring molecules. These intermolecular associations led to the formation of macromolecular structures in solution that were capable of inducing viscosity increase or gelation when present in dilute concentration. At the same time the secondary amine group on 3-vinylaniline could act as chemical absorbent and can help in capture of $CO_2$ by binding with $CO_2$ through carbonate or bicarbonate chemical bonding. Further work has to be done for better understanding of such copolymers and their affinity towards $CO_2$ as a thickening agent.

## 4. Concluding Remarks

This study showed the feasibility to design a polymer that exhibit both high carbon dioxide solubility and the ability to enhance carbon dioxide through intermolecular associations and chemical absorption using a fluorinated copolymer. A 71 mol% fluoroacrylate-29 mol% 3-vinylaniline random copolymer was synthesized through bulk, free-radical polymerization. The thickening capability of the copolymer over the 298 to 373 K temperature range has to be performed, however, this thickening could be attributed to intermolecular stacking of the aromatic rings associated with the 3-vinylaniline monomer. Although this copolymer might be successfully thickened $CO_2$, fluorinated polymers are expensive, unavailable in bulk quantities, and environmentally persistent. Therefore, we are currently also investigating non-fluorous thickeners, which are composed solely of carbon, hydrogen, oxygen, and nitrogen.

## Acknowledgements

This work was supported by ARAMCO Research Project of the office of KAIST-ARAMCO Initiative.

## References

[1] D. Xing, R. Enick, *Increasing The Viscosity of CO2 with Surfactants to Improve EOR Performance*.

[2] Robert. M. Enick, Eric. J. Beckman, Andrew Hamilton, *Inexpensive CO2 Thickening Agents for Improved Mobility Control of CO2 Floods,* DOE-FC26-01BC15315, (2009) June 18.

# Multi-Scale FEM Modeling Effective Thermal Conductivity of Composite Medium

Ella P. Shurina[1,3], Oleg P. Solonenko[2], Natalia B. Itkina[3], Alexandr A. Agafontsev[3]
[1]Trofimuk Institute of Oil and Gas Geology and Geophysics, Siberian Branch of RAS,
Academician Koptyug Av, 3, Novosibirsk, 630090, Russia
[2]Khristianovich Institute of Theoretical and Applied Mechanics, Siberian Branch of RAS,
Institutskaya str. 4/1, Novosibirsk, 630090, Russia
[3]Novosibirsk State Technical University, Karl Marks Av. 20, Novosibirsk, 630073, Russia

**ABSTRACT**

On the example of the heterogeneous compact "carbon matrix - ultrafine inclusions of magnesia" a boundary value problem is formulated and calculations of effective thermal conductivity of composite are carried out with use of the developed multi-scale finite element method ($M_s$FEM). Comparison of the calculated coefficient of thermal conductivity of the heterogeneous medium depending on volume concentration of inclusions and their size with the values obtained by means of analytical approximations widely used in calculations is given.

## 1. Introduction

Currently topical problems of studying the composite nano- submicro- and microstructured materials properties and their behavior at interaction with high-concentrated energy flows belong to type of multi-scale problems. When solving such problems the main difficulties arise already at the stage of creation of the physical model of process when it is necessary to set authentically properties of the heterogeneous medium that causes "heterogeneity" of the coefficients of a mathematical model. There are some methods of representation of coefficients for such models [1-3]: (*i*) averaging and (*ii*) homogenization. After definition of their form it is necessary to choose an adequate method of the model discretization, considering the features of physical process. The finite element method (FEM) is most widely used for discretization. However, for creation of the stable computational scheme approximating the initial continuous model with adequate accuracy, when solving multi-scale problems, it is necessary to consider "small" inclusions. This results in necessity of creation of an adaptive detailed mesh. It significantly increases dimension of the system of linear algebraic equations (SLAE) which solution is rather laborious even on the modern supercomputers. The specified difficulties of the multi-scale problems solution led to appearance of the $M_S$FEM. The main idea of the $M_S$FEM is obtaining the large-scale solution taking into account small-scale, but without excessive detalization [4]. In the present work realization of the $M_S$FEM for studying the stationary heat conduction problem and construction of an assessment of effective thermal conductivity coefficient of composite medium with small-scale inclusions is offered. The offered realization of $M_S$FEM is the further development of the method [5] and consists of two main parts: (*i*) definitions of multi-scale basic functions, and (*ii*) general variational formulation using these functions, taking into account a finite-element discretization of original domain. Basic functions are formed in a special way taking into account multi-scale of the solution while the global formulation (numerical) is formed so that they provide necessary accuracy of the numerical solution [5]. Comparison of the calculated coefficient of thermal conductivity of the heterogeneous medium depending on volume concentration of inclusions and their size with the results obtained by means of analytical approximations widely used in calculation practice is given.

Corresponding author: Oleg P. Solonenko
*E-mail address*: solo@itam.nsc.ru

## 2. Brief Description of Method Developed

In order to illustrate the developed approach we assume that it is necessary to calculate thermal conductivity of the infinite flat layer "matrix C - ultrafine spherical inclusions of MgO" of thickness $L$. Diameter $d$ of spherical inclusions meets condition $d<<L$, and inclusions themselves are evenly distributed in volume of the layer. For simplicity we consider that porosity in heterogeneous material is absent, and contact between inclusions and matrix is ideal. Given problem has direct relation to carbothermal reduction of magnesium from magnesia, according to reaction MgO+C=Mg+CO at plasma treatment of particles - mechanocomposites. Densities of the materials are $\rho_C$=1950 kg/m$^3$, $\rho_{MgO}$=3580 kg/m$^3$, and their thermal conductivities are $\lambda_C$=1.6 W/m·K, $\lambda_{MgO}$=36 W/m·K.

The mathematical model of stationary heat conduction problem can be written as:

$$-\nabla\cdot[a^\varepsilon(z)\nabla u^\varepsilon(z)] = f(z)\ \text{in}\ \Omega,\ u^\varepsilon(z) = g(z)\ \text{on}\ \partial\Omega, \quad (1)$$

where $\varepsilon<<1$ is the small parameter characterizing the subdomains with various physical properties. Considering uniformity of the temperature field along coordinates $x$ and $y$, the compact sample can be represented in the form of a cube with an edge $L$.

Let assume $\Xi = \{K\}$ is subdividing the domain $\Omega$ into macrocells (crude mesh). Let's associate standard bilinear basic functions $\{\varphi_i^0\} \in K$, $i$=1,..,4 with finite elements of the crude mesh (macrocells) $\{K\}$. Multi-scale basic functions $\{\varphi_i\} \in K$, $i$=1,..,4 are defined on a macrocell as follows:

$$-\nabla\cdot[a^\varepsilon(z)\nabla\varphi_i(z)] = 0 \quad \text{in}\ K, \varphi_i(z) = \varphi_i^0(z)\ \text{on}\ \partial K. \quad (2)$$

The general variational formulation with use of multi-scale basic functions assumes decrease in number of calculations and dimension of SLAE to be solved.

Let's search for the solution of the discrete problem in form $u_h = \sum_{i=1}^{i=N} u_i \varphi_i$, where $N$ is quantity of macrocells, $\varphi_i$ are multi-scale basic functions defined on macrocells (crude mesh), $u_i$ are the coefficients of expansion of solution $u_h$ by the basis $\{\varphi_i\}$. The above-mentioned variational problem will look as follows:

$$\sum_K \int_K a^\varepsilon(z)(\sum_{i=1}^{i=4} u_j \nabla\varphi_j)\cdot\nabla\varphi_i^0 dz = \int_\Omega \varphi_i^0 dz . \quad (3)$$

The problem (2) is solved on each macrocell with the use of internal subdividing the element $K$ - fine mesh, basic functions on the support $K^{loc}$ are the bilinear functions $\{\varphi_i^{loc}\}$, $i$=1,..,4. Dimension of the "fine" mesh (of finite element $K^{loc}$) is usually conformed with dimension of inclusions. Multi-scale basic functions are determined in the form $\varphi_i = \sum_{j=1}^{j=M} \alpha_j \varphi_j^{loc}$, where $\varphi_j^{loc}$ are the bilinear basic functions on the fine mesh, $\alpha_j$ are the weights in function $\varphi_i$ expansion by the basis $\{\varphi_j^{loc}\}$. Similarly, each multi-scale function can be presented as the linear combination of basic functions of the element $K$: $\varphi_i = \sum_{j=1}^{j=4} \beta_j \varphi_j^0$. For definition of elements of discrete analog matrix of the variation equation (3) we use quadrature formulas for calculation of integrals:

$$\int_K a^\varepsilon(z)\nabla\varphi_i\cdot\nabla\varphi_j^0 dz \approx \sum_{\tau\in K} a^\varepsilon(z)\nabla\varphi_i\cdot\nabla\varphi_j^0 \Delta z_\tau ,$$

where $\tau$ is the fine mesh (subdividing the macrocell $K$).

Let's consider a problem (1) without source term ($f = 0$), with the first boundary conditions on top and bottom cube faces ($T_1$=20°C, $T_2$=100°C) and the second homogeneous boundary conditions on other sides. Length of an edge of the sample is $L$=10$^{-4}$m. Calculation of the effective coefficient of thermal conductivity according to results of the solution of the problem (1) by means of M$_S$FEM is made under an average formula:

$$\lambda_{eff} = \iiint_V \lambda\nabla T\cdot\nabla T / \{[(T_2 - T_1)/L]^2 L^3\} dV ,$$

where values of the heat flux and temperature are calculated by means of the M$_S$FEM.

## 3. Results of Computing Experiments

The composite material can conventionally be considered as the system consisting of alternating flat layers of materials with various physical properties. For such model of the medium there are analytical formulas for definition of $\lambda_{eff}$. In the case when the heat flux is directed to layers:

1) parallel $\lambda_{eff\,1} = \lambda_m(1-\xi) + \lambda_i\xi$,

2) perpendicularly $\lambda_{eff\,2} = \lambda_m\lambda_i / [\lambda_i(1-\xi) - \lambda_m\xi]$,

where $\lambda_m$ and $\lambda_i$ are coefficients of thermal conductivity of the matrix of the composite and the inclusions, which volume ratio is $\xi$. For the analysis of the influence of the inclusions diameter on $\lambda_{eff}$, at their constant volume ratio, the uniform layered distributions of inclusions were considered with diameter of $d$=10$^{-5}$ and 10$^{-6}$ m when each subsequent layer was placed: 1) strictly under the previous layer without shift; 2) with shift on $d$/2 relatively to previous layer. It is shown that on the effective thermal conductivity $\lambda_{eff}$ obtained as a result of numerical homogenization, influences not only the amount of inclusions, but also the way of their laying. For the analysis of influence of $d$ and $\xi$ on the value $\lambda_{eff}$ by means of the developed M$_S$FEM computing experiments at the uniform layering of inclusions were executed. Graphs of the dependence of $\lambda_{eff}$ on volume ratio of inclusions ($d$=10$^{-6}$m) at their uniform laying are presented in Fig. 1.

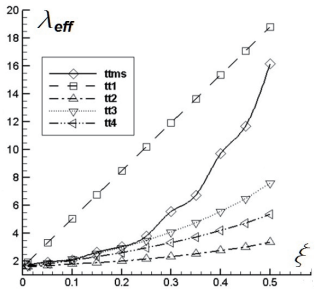


Fig. 1 The coefficient of thermal conductivity (W/m·K) vs volume concentration of the inclusions ($d$=10$^{-6}$ m).

The agreed notations: tt1 - $\lambda_{eff\,1}$, tt2 - $\lambda_{eff\,2}$, ttms - $\lambda_{eff}^{MsFEM}$. Besides, in Fig. 1 are also presented results of calculations for additional analytical dependences:

tt3 - $\lambda_{eff\,3} = (\lambda_i)^\xi (\lambda_m)^{1-\xi}$ is the geometric mean value;

tt4 - $\lambda_{eff\,4} = \lambda_m \dfrac{\lambda_i + 2\lambda_m + 2\xi(\lambda_i - \lambda_m)}{\lambda_i + 2\lambda_m - \xi(\lambda_i - \lambda_m)}$ is the Maxwell formula.

## 4. Concluding Remarks

M$_S$FEM application for definition of the thermal conductivity of composite materials $\lambda_{eff}$ allows to considerably increase the accuracy of its determination (in comparison with analytical formulas) and to reduce the calculation time up to an order of magnitude in comparison with the reference FEM demanding detailed subdividing the computational domain.


## Acknowledgement

This work was supported in part in the framework of Interdisciplinary Integration Project 98 of Siberian Branch of the RAS for 2012-2014.


## References


[1] S.M. Kozlov, *Mathematical Collection*, 107(149) (1978) 199-217.

[2] R.P. Fedorenko, *Introduction in Computational Physics*, Moscow, MFTI Publ., 1994.

[3] Y.R. Efendiev, T.Y. Hou, *Multiscale Finite Element Methods. Theory and Application*. Springer, 2009.

[4] B. Engquist, *Notices of the American Math. Soc.*, 50 (2003), 1062-1070.

[5] M.I. Epov, E.P. Shurina, M.K. Artemiev, *Reports of RAS*, 442 (2012), 118-120.

# Multi-Level Structure of High-Temperature Synthesized NiCr-TiC Cermet Versus Liquid Inert Binder Content

Oleg P. Solonenko[1], Vladimir E. Ovcharenko[2], Anton E. Chesnokov[1]
[1]Khristianovich Institute of Theoretical and Applied Mechanics, Siberian Branch of RAS,
4/1 Institutskaya str., Novosibirsk, 630090, Russia
[2]Institute of Strength Physics and Material Science, Siberian Branch of RAS, Tomsk, 634021, Russia

**ABSTRACT**

Through the example of mechanically activated Ti-C-NiCr powder composition, for the first time the influence of volume ratio of the inert component (NiCr) on the evolution of the TiC inclusions size distribution in the TiC-NiCr cermets synthesized both in the free mode of combustion, and under pressure is studied. It was established that at increase in volume content of nickel-chrome binder, there is a gradual redistribution of number of ultra-fine carbide inclusions towards the smaller sizes (up to nanodimensional level). Justification to the found phenomenon is given.

## 1. Introduction

The use, in thermal spraying and, in particular, plasma spraying of composite powders with particles formed by very hard inclusions in a metal alloy matrix presents a promising strategy in synthesis of wear- and corrosion resistant coatings. At present spraying of cermet powders WC-Me (Me=Co, CoCr, etc.) with the help of HVOF became widely spread. But, usage of such powders in plasma spraying is very problematic due to tungsten carbide degradation ($WC \rightarrow W_2C \rightarrow W$) at increased temperatures [1]. At the same time, great prospects open when using the tungsten-free cermet powders (TiC-Ni, TiC-NiCr, etc.) for plasma spraying of wear- and corrosion resistant coatings as compound of titanium carbide is stable up to its melting point.

One of the main characteristics of cermet powder is the dispersion of their internal structure at specific volume content of the highly rigid components, which in many aspects determines the properties of the cermet coatings and their service life. The increase of dispersion of the highly rigid component of the cermet composite down to submicron-sized and nano-sized levels is a promising direction in the development of long-service life ceramic-metal coatings operated under extreme conditions. Greater prospects at production of the composite powders open when using self-propagating high-temperature synthesis (SHS) initiated in powders component, uniformly mixed with inert powder of given volume content. Synthesis of cermet powder for thermal spraying is possible both in a free mode of combustion of powder composition of initial elements, and in the mode of combustion under simultaneous dynamic loading. The final powder is obtained by subsequent mechanical grinding of synthesized compact and sizing.

In the present work it is shown that increase in dispersion of structure of cermet, synthesized both in free mode, and under pressure, other things being equal, is provided due to acceleration of reaction of titanium carbides high-temperature synthesis in the original powder composition of titanium with carbon and metal binder. The latter is reached by the preliminary mechanical activation (MA) of metal components of the original powder composition. For the first time the influence of volume ratio of the inert component (NiCr) on the evolution of the TiC inclusions size distribution in the TiC-NiCr cermets synthesized both in the free mode of combustion, and under pressure is studied.

Corresponding author: Oleg P. Solonenko
*E-mail address*: solo@itam.nsc.ru

## 2. Experimental Conditions

The cycle of model experiments on studying the evolution of dispersion of TiC inclusions in synthesized TiC-NiCr cermet was executed with change of volume content of nickel-chrome binder (30-50vol%). In these experiments SHS of cermet compact in the mode of free combustion as well as under pressure was carried out in powder composition of titanium (PTOM2 brand), lampblack (P803 brand) and nickel-chrome alloy (PCr20Ni80-56-24 brand). According to [3], for grinding of initial powders of titanium and nickel-chrome alloy their preliminary MA was carried out in high-energy planetary mill "Activator – 2SL" (acceleration 100g, diameter of balls 5mm) [2]: titanium powder with 10%wt. addition of lampblack, as surface-active substance, within 90s; nichrome powder - within 120s. When carrying out SHS of TiC-NiCr, mixtures of powders with particle sizes of nichrome and titanium $\leq 40$ μm were used. The original stoichiometric powder compositions of Ti-C with various volume content of NiCr binder (30, 40 and 50%) were used in the model experiments. These powder compositions just before carrying out SHS were undergone to additional joint MA within 60s for ensuring their uniform mixing. Before carrying out SHS the reactor was blown by argon for 5min at flow rate of 36nl/min.

## 3. Multi-Level Structure of Synthesized Products Versus Binder Volume Content

For study of evolution of the number distributions of TiC inclusions by sizes in the synthesized cermet articles vs volume content of NiCr binder the empirical histograms were built (see Fig. 1). The analysis of the histograms allows to draw the following conclusions. At increase in volume content of nickel-chrome binder from 30% to 50% there is a gradual redistribution of number of inclusions towards the submicron sizes.

In order to explain this phenomenon we will use the considerations based on the assumption of one-dimensional nature of propagation of combustion front in a powder filling.

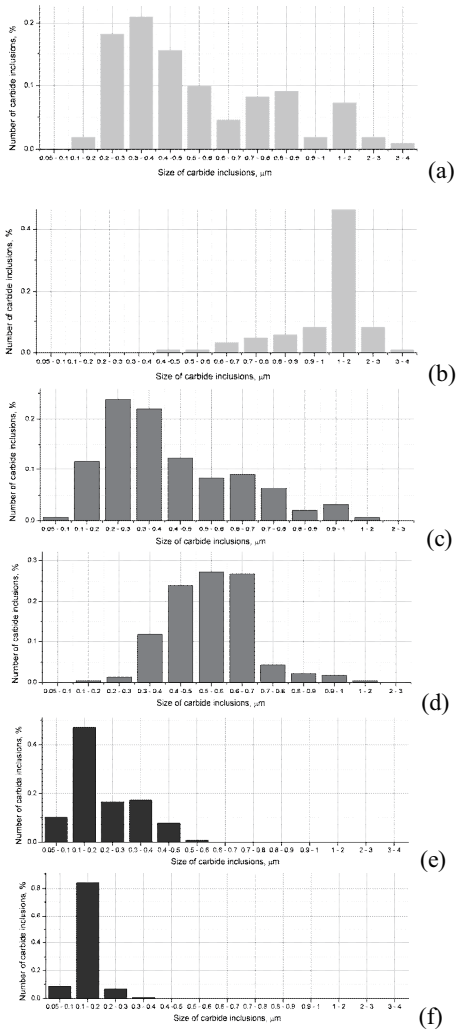


Fig. 1 The histograms characterizing the number distributions by size of carbide inclusions in synthesized powders vs volume binder content (*a, b* - 30%, *c, d* - 40%, *e, f* - 50%). *a, c, e* - SHS under free combustion, *b, d, f* - SHS under pressure.

Initial ultra-fine MA particles of titanium possess high surface activity that can lead to their agglomeration at the stage of preparation of powder compositions. According to [4], synthesis of pure titanium carbide in powder mixture of Ti-C is realized in conditions, when in the combustion wave, the titanium particles, characterized by melting point $T_{m,Ti}$=1958 K, are in a molten state. But, formed product, which is titanium carbide, having melting point of $T_{m,TiC}$=3290 K, is in solid-phase as combustion temperature does not surpass 3210 K. Therefore, in front of the combustion wave propagating in powder mixture of Ti-C, as a result of thermal conductivity of the heterogeneous media, there is a thin layer of powder in which the titanium ultra-fine particles and also their agglomerates are exposed to melting. Melting of agglomerates leads to formation of larger blocks of titanium carbide in synthesized compact which has cellular-porous frame. By-turn, when movement of combustion front in powder mixture in presence of inert binder of NiCr with melting point of $T_{m,NiCr}$=1663K which is lower than melting point of titanium $T_{m,Ti}$=1958 K, in front of combustion wave, propagating in the Ti-C-NiCr powder filling, originally appears a layer in which inclusions of NiCr undergo melting while ultra-fine titanium particles and their agglomerates remain solid. Preliminary MA of metal components significantly increases the wettability of solid titanium inclusions by nichrome melt that, along with volume expansion of inclusions of nichrome at their melting, promotes disintegration of agglomerates consisting of solid titanium ultra-fine particles, acceleration of melting of the latter and, as a result, leads to decrease in size of the TiC inclusions in final cermet compact. Besides, melting of ultra-fine particles of nichrome and titanium agglomerates (average size ~ 2 μm), surrounded with layers of lampblack solid particles (average size ~ 0.3 μm), leads to their local compaction and increase in the area of contact border between the lampblack and titanium particles that accelerates synthesis reaction. However, the poor content of the binder metal results in residual distributed porosity in synthesized cermet product, as the microvoids formed because of dissolution and absorption of ultra-fine lampblack particles which density is significantly less than density of titanium carbide, cannot be completely filled with binder metal. At increase in volume content of binder metal to 40% the porosity of synthesized compact, and, consequently, of powder particles, considerably reduces as the melt of NiCr is rather uniformly distributed in cermet void space. At further increase in volume content of NiCr binder up to 50%, the noted tendency remains, i.e. there is further decrease of size of TiC inclusions (Fig. 1) uniformly distributed in NiCr. This tendency is shown more clearly at SHS under pressure (Fig . 1,*b,d,f*).

.

## 4. Concluding Remarks

It was established that at increase in volume content of nickel-chrome binder, there is a gradual redistribution of number of ultra-fine carbide inclusions towards the submicron sizes (up to nanodimensional level).

Simultaneously, the increase in volume content of metal binder leads to refinement of crystal structure. Justification to the found phenomenon is given.

**Acknowledgement**

This work was supported in part in the framework of Interdisciplinary Integration Project 2 of SB RAS for 2012-2014.

**References**

[1] A. Koutsomichalis, N. Vaxevanidis, G. Petropoulos, E. Xatzaki, A. Mourlas, and S. Antoniou, *Tribology in Industry*, 31, 1-2 (2009) 37－42.

[2] A.A. Leutkin: RF Patent No. 33037 U1, 2003.

[3] V.A. Poluboyarov, O.P. Solonenko, A.E. Chesnokov, A.A. Zhdanok, *Proc. of Intern. Theoretical and Practical Conf. "Powder Metallurgy: Its Present and Future"*, Kiev, Ukraine, (2012), 190.

[4] A.G. Merzhanov, *Solid-Flame Combustion*, Chernogolovka, Institute of Structural Macrokinetics and Material Sciences RAS, (2000), 224 p.

# Application of Lock-in Thermography to Detect Debonding in Welding Joints of Metallic Lattice Sandwich Plate

Haochen Liu and Zhenmao Chen*
State Key Laboratory for Strength and Vibration of Mechanical Structures, Xi'an Jiaotong University, 28 West Xianning Road, Xi'an, 710049, China

**ABSTRACT**

Lattice sandwich metallic plate (LSMP) plays an important role in many industries due to its features of superlight and high specific strength etc. A typical defect in LSMP is the debonding occurred at the welding joints of the truss inner layer and the surface layers. To detect debonding defects, the validity of the Lock-in Thermography (LIT) method is investigated through experiments in this study. It is found that the phase images at proper frequency are suitable to detect debonding defects in a LSMP of stainless steel, which demonstrated the validity of LIT for LSMP.

## 1. Introduction

Lattice sandwich metallic plate (LSMP) is a new kind of multifunctional material, which plays an important role in many industries due to its features such like superlight, high specific strength, high mechanical energy absorption etc [1]. LSMP is made of two surface plates and an inner truss layer bonded together by welding technique. The mechanical behaviors of LSMP highly depend on the quality of welding joints. Miswelding and debonding in welding joints may result in significant strength reduction in LSMP and may cause structural failure consequently. The debonding may occurs during service and during fabrication. A proper NDT technique is very important to guarantee the quality of the LSMP. There are some NDT methods, such as ECT and DCPD techniques, which are proved applicable to debonding inspection through numerical simulation and experiments. In view of efficiency, however, the ECT and DCPD methods are not fast as the probe has to be scanned point by point. A rapid and intuitive NDT method is expected by industries.

Infrared thermography (IRT) provides images of specimens in which local changes of temperature on surface indicate internal defects. IRT is widely used in material characterization and defect inspection etc. due to its intuitive, non-contacting and rapid features. The lock-in thermography (LIT) allows a better defect inspection than pulsed IRT as it is less sensitive to noise and environmental influence.

## 2. Lock-in Thermography

In LIT, the absorption of modulated optical radiation results in a temperature modulation that propagates as a thermal wave into the inspection target. Usually, the modulated heat wave has to be calibrated to sinusoidal. The temperature at the surface (z=0) is periodical and is given by [1]

$$T(z,t) = T_0 \exp(-\frac{z}{\mu}) \exp i([\omega t - \frac{z}{\mu}]) = T(z) \exp i[\omega t - \phi(z)], \quad (1)$$

where $\mu$ is the thermal diffusion depth with

$$\mu = \sqrt{\frac{k}{\pi f \rho c}} \quad (2)$$

where $k$ is the thermal diffusivity, T(z) is the decay of thermal wave with depth, $\Phi(z)$ is the phase shift.

By extracting four thermal images with interval of $T/4$ phase step, the magnitude image $A(x,y)$ and phase image $\Phi(x,y)$ of surface temperature can be calculated by [6]:

$$A(x,y) = \sqrt{(S_1(x,y) - S_3(x,y))^2 + (S_2(x,y) - S_4(x,y))^2}, \quad (3)$$

$$\phi(x,y) = \tan^{-1}\left(\frac{S_1(x,y) - S_3(x,y)}{S_2(x,y) - S_4(x,y)}\right), \quad (4)$$

where $S(x,y)$ is the gray scale value at each pixel.

## 3. Specimen and Experimental Procedure

Experiments were carried out for a rectangle stainless steel LSMP. The welding joints between the two surface plates are approximately of 5×5mm square area. The debonding defect is simulated by a lack welding but adjoin point as shown in Fig.1.

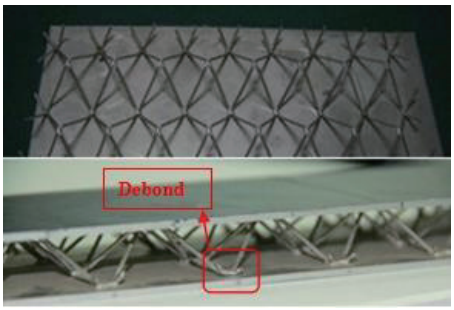


Fig.1 Structure and debonding defect example of LSMP.

The target specimen is a rectangle plate of 290 mm by 70mm side length and 2mm thickness plate. There are 3×9 welding joints on each side. Since the view area of the IRT camera is limited, the camera is zoomed-in on few welding joints. The sketch to obtain the thermal view is shown in Fig.2. There are 3×4 welding points in the selected thermal images, including two debonding points in column 2 and 3 of line 1.

Corresponding author: Zhenmao Chen
*E-mail address*: chenzm@mail.xjtu.edu.cn

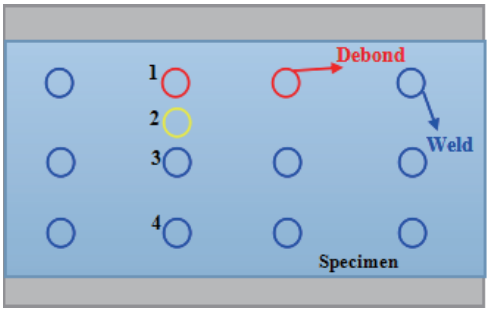


Fig2. The sketch of inspection thermal view

In this study, an IRT heating system consisting of signal generator, low frequency amplifier and two halogen lamps is constructed. A NEC Infrec R300 infrared camera, which is set on the same side with the heating lamps, is used to detect the temperature distribution , as shown in Fig.3.

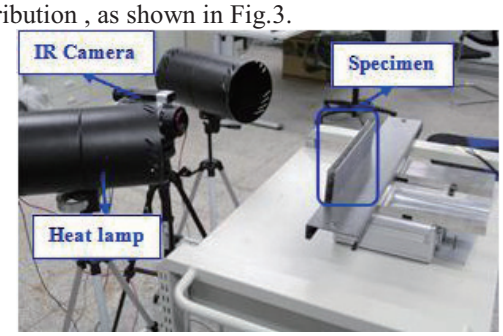


Fig.3 Lock-in Thermography Experiment System

## 4. Results and Discussions

Fig.4 shows the phase images of different frequency sinusoidal heat wave.The frequency we used decrease from 100mHz to 20mHz. The welding points inside the surface plate can be recognized clearly from the phase images except the 100mHz one. The debonding defects in the middle of first line can be detected in images of 50mHz and 20mHz. In 20mHz image, compared to others, all the welding points are more clear to see and debonding are distinct in contrast to welding points. Whereas, 20mHz is selected as optimum frequency.

Since the surface temperature is not quite uniform, four vertical circle areas at the column 2 (shown in Fig.2) are selected to calculate the phase values. The average phase values of these areas represent the phases in areas of debonding defect, plate, and healthy weld joints. The images of frequency 20mHz and 50mHz are selected to calculate the average phase angle, as shown in Table.1

Table.1 Average phase of four circles in image

| Average phase (degree) | Area 1 (debond) | Area 2 (Plate) | Area 3 (Weld) | Area 4 (Weld) |
|---|---|---|---|---|
| 20mHz | 10.45 | 12.58 | 5.78 | 4.35 |
| 50mHz | 24.41 | 25.53 | 19.43 | 16.09 |

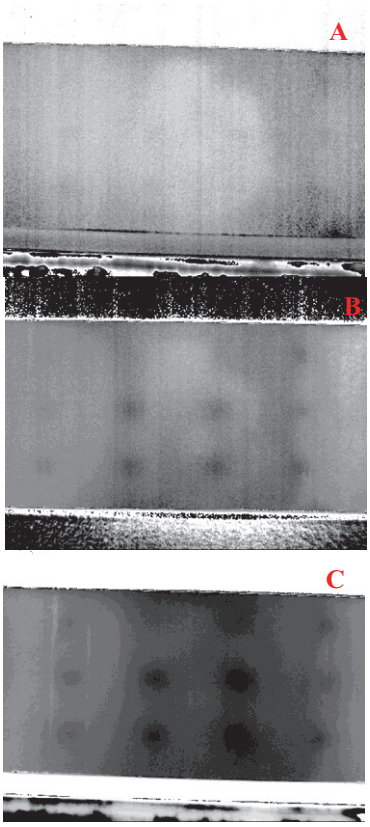


Fig.4 Phase images: a) 100 mHz; b) 50 mHz; c) 20 mHz;

The table 1 indicates that the image at the debonding area has big difference with that of the weld joints in phase. In addition, the image at debonded welding joints also has clear distinction with that of the plate area. The reason can be explained as that debonded welding joint still contact with the surface plate and cause smaller temperature change at the welding points.

## 5. Concluding Remarks

In this study, the lock-in thermography method is applied to detect the debonding defect in the LSMP. IR thermography inspection system is established and is adopted to detect debonding defect at different heating frequency. According to phase images of temperature distribution, 20mHz frequency is the best heating frequency for debonding detection. Although it still needs improvements, the lock-in thermography is a feasible to detect debonding defect in the LSMP.

## References

[1] Zhang, D., Chen, Z., Xu, M., & Lu, T. J. Quantitative NDE of welding defects in lattice sandwich metallic plate by using DC potential drop method. *Int. J. of Appl. Electromagn. Mech*, *33*(3)(2010)1109-1117.

[2] Busse, G.. Optoacoustic and photothermal material inspection techniques. *Applied Optics*, *21*(1)(1982)107-110.

[3] Choi, M., Kang, K., Park, J., Kim, W., & Kim, K. (2008). Quantitative determination of a subsurface defect of reference specimen by lock-in infrared thermography. *NDT&E Int.*, *41*(2)(2008)119-124.

Eleventh International Conference on Flow Dynamics
October 8-10, 2014, Sendai, Miyagi, Japan

# An Aspect in Flight Morphology of the Butterfly

Seiichi Sudo[1], Ryosuke Tanaka[1], Kosuke Inoue[2], Atsushi Shirai[2] ,Toshiyuki Hayase[2]
[1]Faculty of Systems Science and Technology, Akita Prefectural University
Ebinokuchi 84-4, Yurihonjo, Akita 015-0055, Japan
[2]Institute of Fluid Science, Tohoku University
Katahira 2-1-1, Sendai, Miyagi 980-8577, Japan

**ABSTRACT**

Insect flight is an extraordinary phenomenon compared to other forms of animal movement. This paper describes the details of the movement of wings and body in climbing flight during take-off of a butterfly *Colias erate* Esper. Free flight of the butterfly was observed by a high-speed video camera system. The butterfly generates a climbing force in the air even in the upstroke of wing flapping motion. The importance of aerodynamic forces produced by the upstroke motion in wing flapping and rotational movement of the butterfly body axis was revealed.

## 1. Introduction

In the development of Biomimetics, the study of various functions of animals is of fundamental interest and importance with respect to a variety of application on innovative engineering. Therefore, extensive investigations on the motion of great many animals have been conducted by a number of researchers [1, 2]. For example, Ligthill has devised an ingenious explanation for the fluid dynamic processes whereby certain insects are able to generate large lift coefficients by use of so-called “clap and fling “mechanism [3]. Ellington re-examined the aerodynamics of hovering insect flight, and presented new morphological and kinematic data for a variety of insects [4]. In spite of many investigations, however, there still remains a wide unexplored domain. Research data on flight characteristics of butterflies are scanty, and there are many points which must be clarified.

In this paper, the climbing flight behavior of a butterfly *Colias erate* Esper was analyzed by using a digital high-speed video camera system. Details of the wing movement during downstroke and upstroke of butterfly flapping and details of the aerodynamic force generation mechanism were revealed.

## 2. The butterfly *Colias erate* Esper

Butterflies are a group of specialized, day-flying Lepidoptera, and they are probably the most popular in Japan. They can be recognized by their beautiful colors and clubbed antennae as shown in Fig.1. Figure 1 shows the photograph of a butterfly and its morphology. The butterfly called, Pale Clouded Yellow (*Colias erate*), is a butterfly in the Pieridae family. The pale clouded yellow is observed from spring to the autumn in Japan. The butterfly flies in two generations.

Butterflies rest with the wings held together over the back as shown in Fig.2. This posture of butterflies is very important in their take-off flight.

In many insects, jumping is a widely used form of locomotion that enables an animal to escape imminent predation by moving rapidly from one place to another, to escape from unfavorable conditions, to leap from one food source to another, to circumvent obstacles in a difficult terrain and to launch into flight [5].

However, butterflies rely neither on leaping nor on gravitational assistance. They can take-off like lightning. They can climb straight up into the air. Such a vertical take-off fight is only one of the many remarkable characteristics of butterfly flight.

In this paper, such a vertical take-off flight of the butterfly *Colias erate* Esper was analyzed by using of high-speed video camera system.

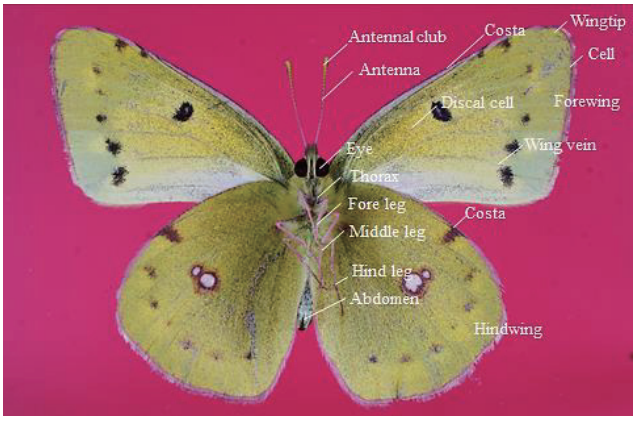


Fig. 1 Photograph of test butterfly *Colias erate* Esper and its body parts.

Fig. 2 Photograph of test *Colias erate* Esper which is in rest state with the wings held together over the back.

Corresponding author: Seiichi Sudo
*E-mail address*: sudo@akita-pu.ac.jp

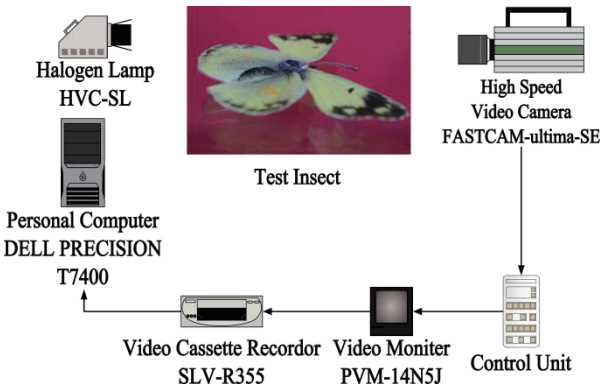


Fig. 3 Schematic diagram of experimental apparatus.

## 3. Experimental Apparatus and Procedures

A schematic diagram of the experimental apparatus to study of a butterfly flight is shown in Fig.3. The experiment was performed using a high-speed video camera system. The system is composed of a high-speed video camera, a control unit, a video cassette recorder, a video monitor, and a personal computer. In the preceding experiment, the scales were recorded in the view field of the camera. Most view fields for recording the flight behavior of butterfly were set in the region of 162 mm×114 mm. The test butterflies were collected in the field. In the experiment of the free flight test, the butterfly was released from the horizontal plate. The take-off flight of the butterfly was recorded by the high-speed video camera. It was recorded with 4,500 frames per second (fps). A series of frames of free flight of the butterfly were analyzed by the personal computer. The experiment was performed in the laboratory under the condition of the room temperature in summer. A large number of samples were examined in the experiment, but one sample with good records was chosen for a description. The records on the butterfly flight show typical and universal facts.

## 4. Experimental Results and Discussion

The climbing flight of the butterfly from the ground was observed. Figure 4 shows a sequence of photographs showing the take-off phase of the butterfly flight. In Fig.4, $L$ is the body length of test butterfly. The time interval of each picture is $\delta_t = 3.33$ ms. It can be seen from Fig.5 that the butterfly takes off by beating down of wing flapping. In general, the jumping propulsion such as leafhopper insects was delivered by rapid and synchronous movements of the hind legs that are twice the length of the other legs, and the wings were not moved before take-off [5]. However, in the take-off flight, the butterfly extends all legs during the downstroke of wings, but does not jump. The butterfly spends about 50 ms for beating down of wings. Figure 5 shows the change in the butterfly position which corresponds to Fig.4. The two-dimensional coordinate system fixed on the camera view is set. The coordinate system is chosen as the $x$-axis in the horizontal direction and the $z$-axis in the vertical direction. The marks in Fig.5 represent the position of the butterfly head in the $x$-$z$ plane.Two straight lines represent

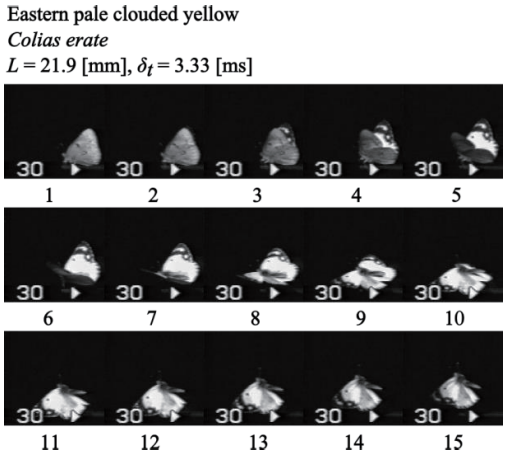


Fig. 4 Take-off phase in butterfly wing flapping

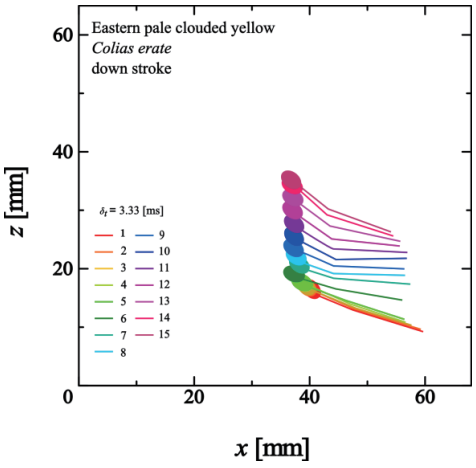


Fig. 5 Position change of the body of the butterfly

the body axis of the thorax and abdomen. The butterfly is climbing by the downstroke of wings. In the latter half of the downstroke during wing flapping, the butterfly bends the abdomen upward. Bending motion of the abdomen is conducted to shift the center of gravity of the body to higher position, and helps with the following actions in wing beating. The butterfly shows a larger movement in the second half of the downstroke in wing flapping.

## 5. Concluding Remarks

The vertical takeoff flight of the test butterfly *Colias erate* Esper was discussed based on the high-speed motion analysis. Three consecutive stages in the take-off maneuver were revealed.

## References

[1] R.M. Alexander, *Exploring Biomechanics*, W.H. Freeman and Company, New York (1992), 1-237.
[2] A. Azuma, *The Biokinetics of Flying and Swimming,* Springer-Verlag (1992), 1-265.
[3] M.J. Lighthill, *J. Fluid Mech.*, 60(1973)1-17.
[4] C.P. Ellington, *Phil. Trans. R. Soc. Lond.*, B305(1984)1-15.
[5] M. Burrows, V. Hartung, H. Hoch, *J. Exp. Biol.*, 210(2007)3311-3318.

# Microscopic Observation of Surface Cell Shape in a Catsear Petal

Maki Sato[1], Seiichi Sudo [1]
[1]Faculty of Systems Science and Technology, Akita Prefectural University
Ebinokuchi 84-4, Yurihonjo, Akita 015-0055, Japan

**ABSTRACT**

The plant functions for petal movement of a catsear flower were examined from the microscopic view point. The petal surface of a catsear flower head was observed with the confocal laser scanning microscope. Non-contact measurements of surface roughness on the catsear petal with laser acquisition of three-dimensional data were conducted over a long period of time. The measurements were carried out through the opening and closing of the catsear flower head. It was found that the surface cell shape changes according to progress in the opening or closing of flower head.

## 1. Introduction

Recently, the development of artifacts that follow the function and morphology excellent with the plant has attracted attention [1,2]. To elucidate the morphological structure, the self-organization, the self-repair function, the survival and growth function of the plant-specific can be expected applications of innovative engineering follow the plant system. Extensive investigations on the plant physiology and the structures of a great many plants have been conducted and reported by a number of researchers. For example, Taiz reviewed on cell wall mechanical properties to integrate some of the major biophysical and biochemical components of wall extension, with an emphasis on the events occurring within the wall itself [3]. Cosgrove examined the prevailing concept that plant cell growth results from turgor-driven yielding of the cell wall in his review paper [4]. Gibson et al. reviewed the structure of the leaf of the bearded iris and showed that its flexural stiffness can be explained in terms of the mechanics of sandwich beams [5]. Kobayashi et al. reported a morphological study on the unfolding of a leaf with a straight central vein and symmetrically arranged parallel lateral veins that generate a corrugated surface [6]. In spite of many investigations, however, there still remains a wide unexplored domain. No study has been published on the petal surface cell shapes. This study is related to special fluid mechanics problem based on physiological function of plants.

In this paper, the petal surface cell shape in the opening and closing of catsear flower head was observed with the confocal laser scanning microscope. Measurement results of the surface roughness in the petal cells were discussed from the view point of hydrodynamics.

## 2. Experimental Apparatus and Procedures

Mechanism of movement in the opening and closing of catsear petals was examined in this paper. The live petal surface was observed microscopically. Schematic diagram of experimental apparatus is shown in Fig.1. Microscopic observation of the petal surface was conducted using the color 3D laser scanning microscope. The sample catsear were *Hypochaeris radic ata*. Figure 2 shows a photograph of catsear flower head which is in the state of opening. Figure 3 shows also a photograph of catsear flower which is in the state of closing. This kind of capital motion was examined. Test catsear were collected in the field in Yurihonjo, Japan. One piece of petal was set in the observation area in the laser scanning microscope. The catsear stem was cut,

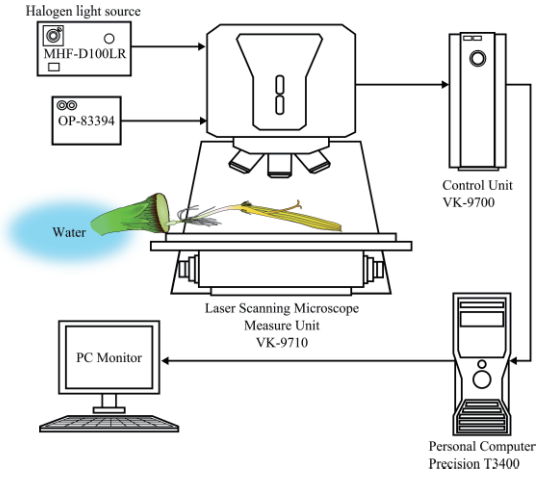


Fig. 1 Schematic diagram of experimental apparatus.

Fig. 2 Photograph of catsear flower head in the opening state.

Fig. 3 Photograph of catsear flower head in the closed state.

Corresponding author: Seiichi Sudo
*E-mail address*: sudo@akita-pu.ac.jp

and water was supplied through the stem. The petal surface was observed for a long time (for 5 hours). The time change of surface roughness of the petal was analyzed with the observed laser images. The experiment was performed under the condition of the room temperature.

## 3. Experimental Results and Discussion

*3.1 Microscopic observation of upper surface in petal*

Microscopic observations of the upper surface in the catsear petals were conducted in order to examine the movement of plant from the microscopic point of view. Non-contact observations of the petal surface of live catsear were conducted by using the laser scanning microscope. Figure 4 shows the three-dimensional description of shape measurement for the petal surface. It is clear that the petal surface is not a flat plane. A large number of longitudinal mountains are observed in Fig.4. Each mountain corresponds to one surface cell. The size of each cell is about 23 μm×47 μm in Fig.4. The aspect ratio of the cell, shape was $\sigma_c$=1-3 in this measurement in the state of Fig.4. In this state, each cell fills the vacuole with enough water.

*3.2 Measurement of surface roughness*

Surface roughness profile parameters were analyzed from the measurement of the surface shape. Figure 5 shows the change of surface roughness profile parameters with time. In the definitions of surface roughness, $R_p$ is the maximum profile peak height, $R_v$ is the maximum profile valley depth, $R_z$ is the maximum height of the roughness profile, and $R_a$ is the arithmetic average of the absolute values of the roughness profile ordinates. In this study, $R_p$, $R_v$, $R_z$, and $R_a$ were measured in 282 μm×212 μm area of the petal surface. It can be seen from Fig.5 that surface roughness $R_a$ moves toward higher value gradually.

*3.3 Observation of lower surface in petal*

The lower surface of a catsear petal was observed by the laser scanning microscope. Figure 6 shows the optical image the lower surface of petal tip. There are a lot of stomata on the petal surface. The stomata are an essential structure for plant photosynthesis. Stomata consist of two guard cells. Two guard cells are responsible for opening and closing of the stoma. The main function of the stomata is to control gas exchange. The existence of many stomata in lower petal surface means that the catsear petal exchanges gases such as carbon dioxide, water vapor and oxygen.

## 4. Conclusion

The upper and lower surfaces of catsear petal were observed with the confocal laser scanning microscope.

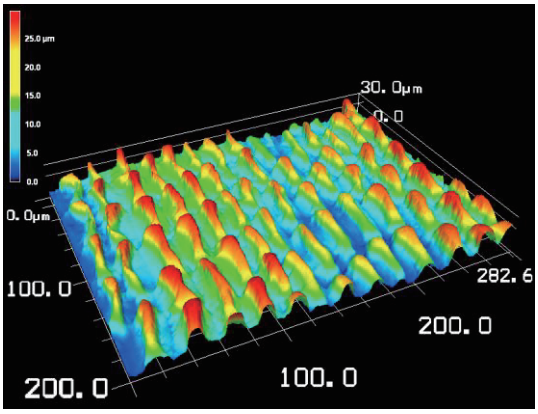


Fig. 4 Three-dimensional description of petal surface shape (at $t$=0 h).

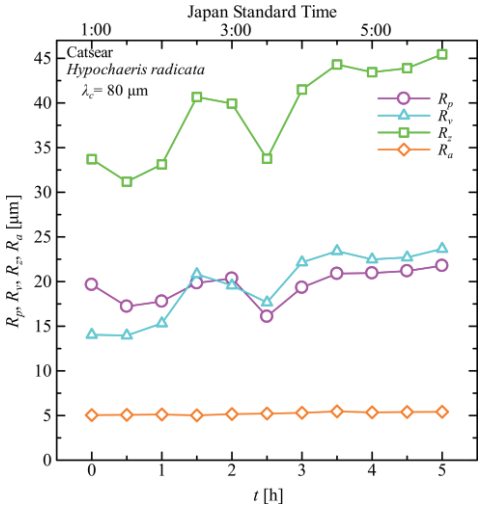


Fig. 5 Changes of surface roughness profile parameters.

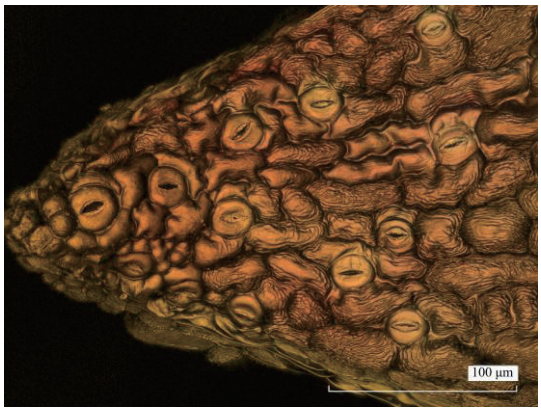


Fig. 6 Microscopic optical image of catsear petal tip surface (lower surface).

## References


[1] M. Milwich, T. Speck, O. Speck, T. Stegmaier, H. Planck, *American Journal of Botany*, 93-10(2006), 1455-1465.

[2] K.J. Niklas, H.-C. Spatz, J. Vincet, *American Journal of Botany*, 93-10(2006), 1369-1378.

[3] L. Taiz, *Annual Review of Plant Physiology*, 35(1984), 585-657.

[4] D. Cosgrove, *Annual Review of Plant Physiology*, 37(1986), 377-405.

[5] L.J. Gibson, M.F. Ashby, K.E. Easterling, *Journal of Materials Science*, 23(1988), 3041-3048.

[6] H. Kobayashi, B. Kresling, J.F.V. Vincent, *Proceedings of Royal Society London B*, 265(1998), 147-154.

Eleventh International Conference on Flow Dynamics
October 8-10, 2014, Sendai, Miyagi, Japan

# Dependence of Axial Flow inside Wing Tip Vortices on Wing Planforms

Hiroshi Koizumi[1], Yuji Hattori[2]
[1]Department of Applied Information Sciences, Graduate School of Information Science, Tohoku University
6-3-09 Aramaki Aoba Aoba-ku, Sendai, Miyagi, 980-8579, Japan
[2]Institute of Fluid Science, Tohoku University
2-1-1 Katahira Aoba-ku, Sendai, Miyagi, 980-8577, Japan

**ABSTRACT**

The vorticity field of the wing tip vortex has been calculated for different wing planforms at the Reynolds number 1000 by the direct numerical simulation. The radial profiles of the vorticity and the axial velocity are compared to the theoretical model of Moore and Saffman[3]. The vorticity shows different radial profiles depending on its wing planforms and it agrees well with the theoretical model. On the other hand the axial flow is not in good agreement with the theoretical model, while numerical results decay and dissipate more slowly than the theoretical model.

## 1. Introduction

Wing tip vortices are generated at the edge of wing tips and cause hazardous phenomen for the trailing aircrafts. Once wing tip vortices are shed to the downstream, they form the large rotational flow field. It is called wake turbulence and it strongly affects the frequencies of taking off and landing of aircrafts in an airport. To increase the efficiency of the air traffic control, recent studies are focused on the role of vortex instability. Many instability studies assume the vortex models. However, hydrodynamic stability characteristics depend on the precise distribution of the vorticity and axial velocity. Unfortunately the mechanism of formation of axial velocity distribution is not completely revealed. In this paper, we perform the direct numerical simulation and assess dependence of axial velocity on the wing planforms by comparing to the theoretical models.

The structure of wing tip vortices has been studied experimentally and theoretically. For the experimental study, Chow et al[1] investigated the velocity field of wing tip vortices by using triple-wire probes at the Reynolds number 46000. They reported that axial velocity excesses the free stream velocity as a low pressure region is formed around the vortex center when vortices roll up on the wing surface. Lee et al[2] studied dependence of the axial flow on the angle of attack by using seven hole pressure probes at the Reynolds number 307000. They concluded that the axial velocity excess and deficit compared to the uniform flow velocity changes at the angle when the lift-drag ratio becomes maximum. And they also noted that axial velocity deficit occurs when low momentum boundary layer flow is entrained to the wing tip vortex. For the theoretical study, Moore and Saffman[3] constructed a theoretical model of wing tip vorticies considering Plandtl's lift line theory and momentum deficit due to the boundary layer on the wing surface. As to their study, axial flow distribution is determined by the spanwise lift distribution on the wing. In this study, we investigate the axial velocity distribution for different types of wing planform and compare it to Moore's theoretical model.

Corresponding author: Hiroshi Koizumi
*E-mail address*: koizumi@dragon.ifs.tohoku.ac.jp

## 2. Method

We solve the three-dimensional incompressible Navier-Stokes equations by the volume penalization method (VPM).

$$\frac{\partial \boldsymbol{u}}{\partial t} + (\boldsymbol{u} \bullet \nabla)\boldsymbol{u} = -\nabla p + \frac{1}{\mathrm{Re}} \nabla^2 \boldsymbol{u} + \frac{\chi(\boldsymbol{x})}{\eta}(\boldsymbol{u} - \boldsymbol{u_b}) \quad . \tag{1}$$

$$\nabla \bullet \boldsymbol{u} = 0 \quad . \tag{2}$$

The last term of equation (1) is called the VP term which is the key ingredient of VPM. VPM is one of the immersed boundary methods. The boundary conditions are automatically satisfied thanks to the VP term. $\boldsymbol{u_b}$ denotes moving velocity of objects, in this study we set $\boldsymbol{u_b} = 0$. We classify the whole region into the flow region and the wing region by the mask function $\chi$; $\chi = 0$ in the flow region, and $\chi = 1$ in the wing region.

We simulate the flow past a fixed wing at the Reynolds number 1000. The airfoil is NACA0012 and the angle of attack is 8 degree. The length of the cord is c=1 and the aspect ratio is 2.

We set the x, y and z axes as the flow, spanwise and vertical directions, respectively. The origin of the coordinate system is set at the center of the trailing edge. We use the uniform grid in the y and z directions and non-uniform grid in the x direction. In the x direction, grid resolution becomes the highest in the wing region. The grid resolution is (dx, dy, dz)=(0.003, 0.002, 0.004) and the number of grid points is (nx, ny, nz)=(1100, 512, 1024).

We use the 2th-order Adams-Bashforth method for time development except that the VP term is integrated exactly. For spatial derivatives the 6th-order compact scheme is used in the x direction and the Fourier collocation method is used in the y and z directions.

Moore and Saffman's theoretical model[3] takes into account the roll up process of vortex sheet shed from the trailing edge. In Plandtl's lift line theory, vortex sheet strength is determined by the spanwise lift distribution. Spanwise distribution is also related to the wing planforms, so we choose different wing planforms and assess whether vortex structure is close to the theoretical model or not.

We use three wing planforms. First is a rectangular

wing. Second and third are a delta and an elliptic wing whose wing width becomes the largest at the center of the wing cord length.

## 3. Results and Discussion

We show the vorticity field by contours of the magnitude of vorticity in the wing region and wake region in Fig. 1. A wing tip vortex is formed at the edge of the wing tip. Once it is released in the wake region, vortex sheet which exists on the wing trailing edge rolls up and absorbed into the main wing tip vortex. In this study, vortex sheet roll up is completed before the vortex reaches x=2.

The radial profile of vorticity is shown in Fig. 2. In this graph, the horizontal and vertical axis are normalized by the radius at which the tangential velocity becomes maximum and the maximum vorticiy at the vortex center. Vorticity distribution is self-similar in the downstream region for each wing planforms. But differences of wing planforms affect the radial profile of vorticity. The rectangular wing shows the high vorticiy value in the vortex core region while the delta wing becomes high at outer core region. This result is consistent with the Moore and Saffman model. More steep gradient lift distribution makes wing tip vortices with higher concentration of vorticity.

Fig. 3 shows the radial profile of the axial velocity. Free stream velocity is U=1. Axial velocity has deficit compared to the free stream velocity for all wing planforms. This is because the boundary layer decelerates the flow drawn into the wing tip vortex core. For the wing tip vortex, boundary layer thickness on the wing tip region affects the core axial velocity significantly. In this study, rectangular wing's cord length at the wing tip region is the highest, so the axial flow is most decelerated for this planform. Comparison between theoretical models and numerical results for the rectangular wing is shown in Fig. 4. For the axial velocity distribution, the theoretical model fails to approximate the numerical results. Numerical result shows slower dissipation of velocity in the vortex core and larger velocity in the outer core region. Accelerated flow in the outer core region is caused by the flow passing through the wing upper surface. The reason of decelerated flow in the core region is under investigation. It may be due to more complex initial conditions at the wing trailing edge than the theoretical model.

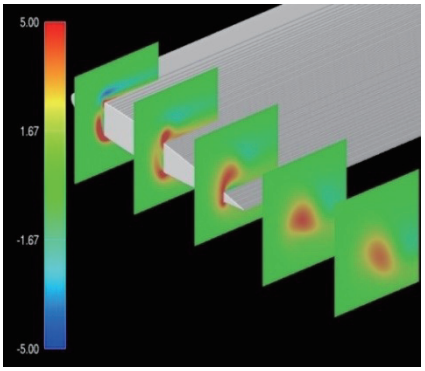

Fig.1 Contours of vorticity near the wing region.

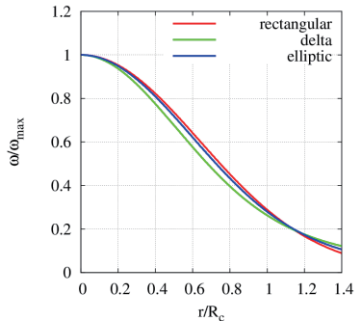

Fig. 2 Radial profile of vorticity at x=6.0. Horizontal axis is normalized by the radius at which the tangential velocity becomes maximum, and the vertical axis is normalized by the core voriticity.

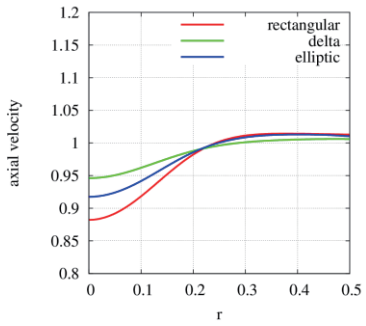

Fig. 3 Radial profile of axial velocity at x=6.0.

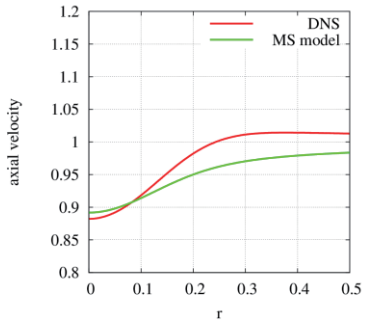

Fig. 4 Radial profile of axial velocity compared with theoretical model at x=6.0. DNS: Numerical result for rectangular wing, MS: Moore and Saffman model.

## 4. Concluding Remarks

Wing tip vortices are calculated at the Reynolds number 1000 by DNS. The effect of wing plamforms on the vorticity and axial velocity are examined. They are shown to depend on the wing planforms. Moore and Saffman's theoretical model is in good agreement with the numerical results for vorticiy distribution, but fails to approxiate the axial velocity characteristics.

## References

[1] J.S. Chow, G.G. Zilliac, P. Bradshaw, *AIAA Journal*, 35(1997), 1561-1567.
[2] T. Lee, J. Pereira, *Journal of Aircraft*, 47(2010), 1946-1954.
[3] D.W. Moore, P.G. Saffman, *Proc. R. Soc. London. A*, 333(1973), 491-508.

Eleventh International Conference on Flow Dynamics
October 8-10, 2014, Sendai, Miyagi, Japan

# Nonlinear Evolution of Disturbed Compressible Vortex Pair

Tomohiro Ushiki[1], Makoto Hirota[2], Yuji Hattori[2]
[1] Department of Applied Information Sciences, Graduate School of Information Science, Tohoku University
Aramaki Aoba 6-3-09, Sendai, Miyagi, 980-8579, Japan
[2]Institute of Fluid Science, Tohoku University

**ABSTRACT**

We analyze instability of two counter-rotating vortices in compressible flow. It is important to study the effects of compressibility on the instability of vortices since current aircrafts fly at subsonic speed so that the wingtip vortices become strong. In this paper, we investigate nonlinear growth taking account of the compressible effects using direct numerical simulation, and clarify the differences from incompressible case.

## 1. Introduction

Pressure difference occurs between the upper surface and the lower surface of the wing of aircrafts so that wing tip vortices are generated. The wing tip vortices develop into wake turbulence at downstream. It causes troubles such as loss of control or fatal accident when an aircraft is trapped. In order to take off and land on safely, it is necessary to keep an interval long enough for the turbulence to decay at an airport.

The development of aviation industry in recent years and the emergence of new companies such as LCC are demanding increase of the number of flights. Therefore, efficient operation at airports is required. One possible method for achieving it lies in the instability of the wing-tip vortex. By adding a suitable small disturbance to vortices the instability can make them collapse. It is possible to destroy the wing tip vortex and thereby decrease the intervals between flights for efficient operation of the airport.

A number of studies of vortex instability have been carried out. However, most of the previous studies are performed assuming incompressibility. It is necessary to consider compressible flow because current aircrafts are large and fly at subsonic speed and the resulting wing-tip vortices are strong.

In this study, we investigate the non-linear growth of a disturbed vortex pair in compressible flow using direct numerical simulation.

## 2. Method

First, in order to obtain the basic flow, we perform simulation in two dimensions. The initial vortex pair has Gaussian distribution of vorticity

$$\omega_G = \frac{\Gamma}{\pi r_c^2} e^{-r^2/r_c^2}$$

$$v_G = \frac{\Gamma}{2\pi r}\left(1 - e^{-r^2/r_c^2}\right)$$

We solve the two-dimensional compressible Navier-Stokes equations by DNS

$$\frac{\partial \rho}{\partial t} = \frac{\partial m_j}{\partial x_j}$$

$$\frac{\partial m_j}{\partial x} = -\frac{\partial}{\partial x_j}\left(m_i u_j\right) - \frac{\partial p}{\partial x_j} + \frac{\partial \tau_{ij}}{\partial x_j}$$

$$\frac{\partial e}{\partial t} = -\frac{\partial}{\partial x_j}\left[(e+p)u_j\right] + \frac{\partial}{\partial x_j}\left(u_j \tau_{ij}\right) + \frac{\partial}{\partial x_j}\left(k\frac{\partial T}{\partial x_j}\right)$$

Calculation is performed until the vortex pair reaches a quasi-steady state. We use scatter plot of the stream function and vorticity to obtain a quasi-steady state. When the vortex pair becomes quasi-steady, the vorticity becomes a function of the stream function as shown in Fig.1. In order to characterize the scatter plot, we calculate the area of Fig.1. Fig.2 shows the result. It is seen that the area decreases as time proceeds and the rate of decrease is small after t=15. Fig.3 shows a vortex pair in quasi-steady state obtained in this way. It is used as a basic flow in DNS of non-linear growth of the vortex pair.

Next, we seek the most unstable mode by numerical calculation. We solve the linearized three-dimensional Navier-Stokes equations by direct numerical simulation. The vortex pair obtained by two-dimensional simulation is used as the base flow. The initial condition consists of randomized modes. After a long time the most unstable mode becomes dominant.

The growth rate is defined as

$$\sigma = \frac{log_e E^{n+1} - log_e E^n}{\Delta t}$$

where

$$E = u^2 + v^2 + w^2$$

Corresponding author: Tomohiro Ushiki
*E-mail address*: ushiki@dragon.ifs.tohoku.ac.jp

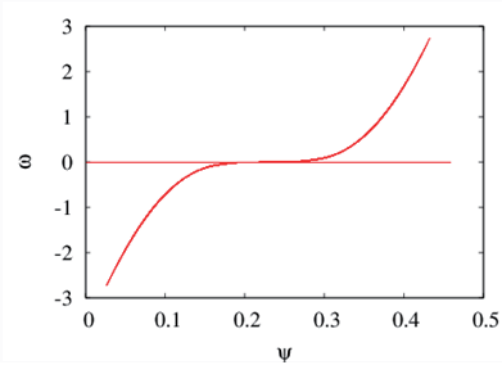


Fig.1 Scatter plot of vorticity ω and stream function ψ

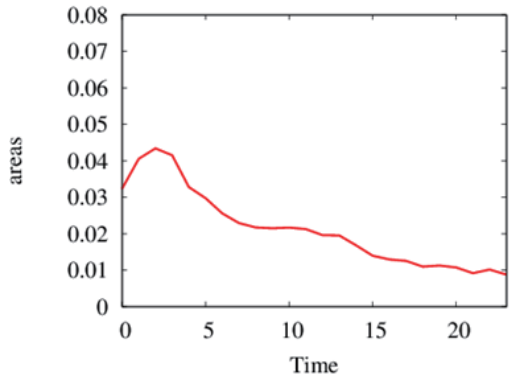


Fig.2 Time evolution of the area of scatter plot.

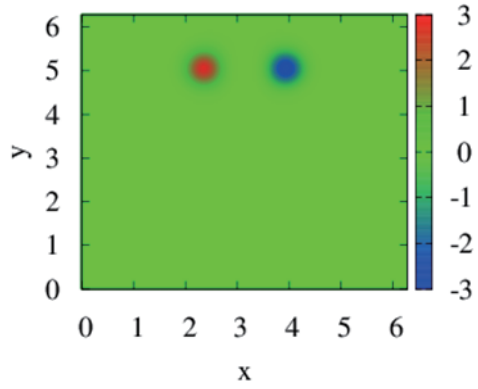


Fig.3 Vorticity distribution of a vortex pair in quasi-steady state.

### 3. Results and Discussion

Fig.4 shows the energy growth rate of the most unstable mode as a function of wavenumber. Fig. 5 shows the vorticity distribution of the disturbance of the mode which has the largest growth rate. In Fig. 4, sharp peaks of growth rate are observed. They are most likely caused by the elliptical instability which is due to parametric resonance. However, there are no sharp peaks for $k_z$>8; this region seems to correspond to the hyperbolic instability. The overall trend is similar to incompressible results by Laporte and Corjon [1] and Schaffer and Le Dizes [2], but the value of the peak is different from them. The basic flow and the disturbances of the most unstable mode obtained above will be used in investigating the destabilization process of a compressible vortex pair.

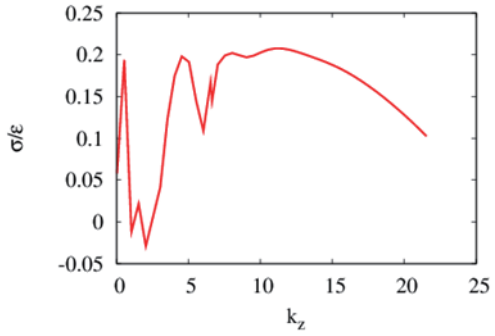


Fig.4 Growrh rate of each mode.

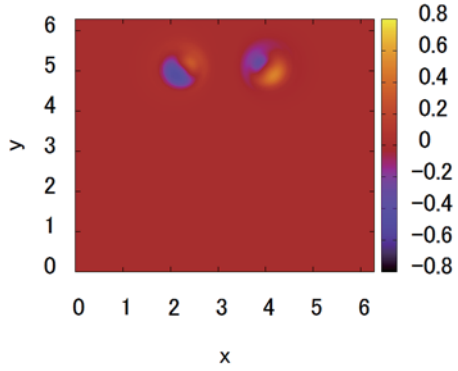


Fig.5 Vorticity distribution of disturbance.

### 4. Concluding Remarks

We have prepared a quasi-steady vortex pair and unstable modes of disturbance. Some features of elliptic and hyperbolic instabilities are captured. The destabilization process of a compressible vortex pair using the vortex pair as the base flow and the disturbance will be investigated in the near future.

### References

[1] F. Laporte and A. Corjon, *Direct numerical simulations of the elliptic instability of a vortex pair, Phys. Fluids* 12, (2000) 1016.

[2] N. Schaffer and S. Le Dizes, *Nonlinear dynamics of the elliptic instability, J. Fluid Mech*. 646, (2010) 471-480.

Eleventh International Conference on Flow Dynamics
October 8-10, 2014, Sendai, Miyagi, Japan

# Improved Compressor Corner Separation Prediction with the Quadratic Constitute Relation

Xinrong Su[1], Xin Yuan[1]
[1] Key Laboratory for Thermal Science and Power Engineering of Ministry of Education, Tsinghua University
Haidian District, Beijing 100084, P. R. China

**ABSTRACT**

In this work the compressor corner separation is predicted with a simple nonlinear eddy-viscosity model, the Quadratic Constitutive Relation (QCR) model. Compared to the linear Boussinesq mode, a correction tensor term is added to resolve the turbulent anisotropy. Numerical results show that improved pressure distribution is obtained at various incidents and the results agree better with the experiment. The flow details in the corner separation region are discussed for better understanding of the flow physics that results in the improved prediction.

## 1. Introduction

For complex turbomachinery flows the turbulence model is among one of the key parameters required for accurate numerical predictions. Currently the most popular turbulence models, including the Spalart Allmaras model and the Shear Stress Transport model, are based on the linear eddy viscosity formulation where the Reynolds stress is assumed to be proportional to the rate-of-strain tensor. These models work well in simple flows like boundary layer; however, for complex flows of importance to turbomachinery, such as secondary flow structure and the corner separation, they may give unsatisfying results. One solution is to use the costly Reynolds stress turbulence model which contains at least 7 partial-differential equations and another method is to conduct the more costly Detached Eddy Simulation. However, this represents a dramatic increase in the computation cost which prevents the extensive application of these methods in routine use.

In this work we are interested in the corner separation of the highly-loaded compressor and its accurate numerical prediction. The corner separation induces a large area of flow blockage and the resulted loss. In the separation area the flow is highly anisotropic and far from equilibrium, which violates the assumptions in the currently widely linear eddy-viscosity turbulence model. In this work we are interested whether we can improve the fidelity of RANS simulation of compressor corner separation by using advanced turbulence model which is also less cost-extensive, compared to the Reynolds stress model and the DES simulation. The QCR model, a nonlinear eddy-viscosity model developed by Spalart [1], is tested in this work with emphasis on the compressor corner separation. Results show that with the QCR nonlinear eddy-viscosity model, the fidelity of predicted corner separation is much improved. The improvement mostly takes place in the separation area, where the linear model fails to give accurate the pressure distribution and the starting point of separation. With the QCR model much improved results are obtained. The improvement comes from the capturing of the anisotropic turbulent stress. Ac-cording to our results, the QCR model is low cost and can be easily implemented. As a result it is a promising model worth further research.

Corresponding author: Xinrong Su
*E-mail address*: suxr@mail.tsinghua.edu.cn

## 2. Numerical Method

The compressible Navier-Stokes equation in the conservative form can be expressed as

$$\frac{\partial}{\partial t}\int \mathbf{U}dV + \oint (\mathbf{F}i + \mathbf{G}j + \mathbf{H}k)\cdot d\mathbf{S} = \oint (\mathbf{F}_v i + \mathbf{G}_v j + \mathbf{H}_v k)\cdot d\mathbf{S} \quad (1)$$

where $\mathbf{U}$ denotes the conservative variable; $\mathbf{F}$, $\mathbf{G}$ and $\mathbf{H}$ denote the convective fluxes; $\mathbf{F}_v$, $\mathbf{G}_v$ and $\mathbf{H}_v$ denote the viscous fluxes. The governing equation is completed with the equation of state and in this work the perfect gas property is assumed.

In this work a suite of well-proved research code is used in the numerical studies. Multi-block structured meshes are used to mesh the computation domain and the finite volume method is employed to discrete the RANS equation. Let $\mathbf{n} = (n_x, n_y, n_z)^T$ be the unit normal of the surface and the convective flux across this surface is denoted by $\mathbf{F}_n = \mathbf{F}n_x + \mathbf{G}n_y + \mathbf{H}n_z$. In this code a series of high accuracy methods are available to approximate $\mathbf{F}_n$ and in this work the upwind flux together high order reconstruction is employed to obtain as small numerical dissipation as possible. With upwind method, the numerical flux is computed with the Roe scheme and has the form of $\mathbf{F}_n = \mathbf{F}_n(\mathbf{U}_L, \mathbf{U}_R)$. High order accurate reconstruction should be used to reconstruct the left and right state variables, $\mathbf{U}_L$ and $\mathbf{U}_R$, for high order accuracy. In this work a fifth order Weighted Essentially Nonoscillatory scheme is used.

For high Reynolds flow, currently the RANS framework still serves as the workhorse in daily use. With turbulence model the Reynolds stress is completed. For most of the widely used turbulence models, such as the one-equation Spalart-Allmaras model, or the two-equation Shear Stress Transport model, the Reynolds stress is formed based on the Boussinesq assumption where the Reynolds stress is assumed to be proportional to the rate-of-strain tensor

$$-\rho\overline{u_i'u_j'} = 2\mu_t\left(S_{ij} - \frac{1}{3}\nabla\cdot\mathbf{u}\delta_{ij}\right) - \frac{2}{3}\delta_{ij}k \quad (2)$$

where $\mu_t$ is the turbulent viscosity which is obtained by solving the turbulence model equation. In this work the one-equation Spalart-Allmaras model is used.

A new nonlinear model was proposed by Spalart [1]

and it is named as Quadratic Constitutive Relation (QCR). In the QCR model the nonlinear term is added to the stress-strain relation as a correction, in that the turbulent stress in first computed with the Boussinesq relation and then augmented with a nonlinear term as:

$$\tau_{ij,QCR} = \tau_{ij} - C_{cr1}\left(O_{ik}\tau_{jk} + O_{jk}\tau_{ik}\right) \qquad (3)$$

where $O$ is the normalized rotation tensor. From Eq. (3) it is easily seen that the QCR model can be implemented into existing code with the addition of the nonlinear term. In this work we are interested in the applicability of this model in the complex turbomachinery flow.

## 3. Results and Discussion

The numerical study is conducted with a linear compressor cascade which was experimentally studied by Ma et al. [2]. For the half span model, after several circles of mesh adaption targeted for mesh independence, the final mesh is composed of about one million points.

Five angle-of-attacks (AoA) ranging from -2° to 6° are studied and compared with the experiment.

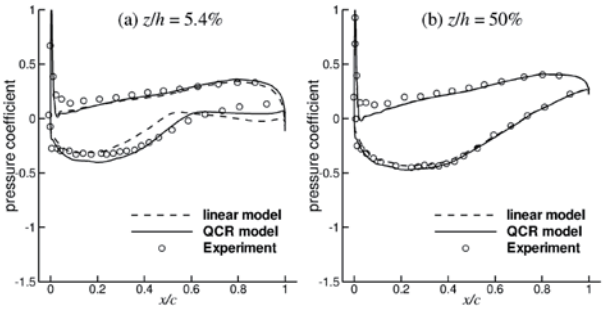


Fig. 1 Comparison of pressure coefficients at: (a). *z/h*=5.4% and (b). *z/h*=50% spanwise sections, AoA=-2°.

The pressure coefficients at two spanwise sections, *z/h*=5.4% and *z/h*=50% are obtained from the experiment and are compared with the numerical results. Due to the space constraints, only the results at two AoA are given in Fig. 1 and Fig. 2 and more results will be presented in the conference.

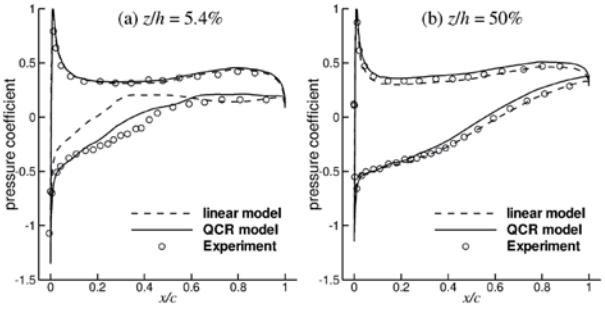


Fig. 2 Comparison of pressure coefficients at: (a). *z/h*=5.4% and (b). *z/h*=50% spanwise sections, AoA=4°.

From the comparison at *z/h*=50%, the difference between two viscosity models is rather small and all numerical results agree well with the experiment. In this region the flow is free of separation and Boussinesq linear model works well. At the near-hub spanwise section *z/h*=5.4%, the QCR model yields better results compared to the linear model. From the pressure distribution at this near-hub section, it can be seen that with increasing AoA, the starting point of the corner separation also moves further upstream and the size of the corner separation also increases. At every AoA, these turbulence models fail to reproduce the pressure distribution and the numerical results from the linear model are quite inaccurate, in that it predicts earlier flow separation, thus larger area of flow separation.

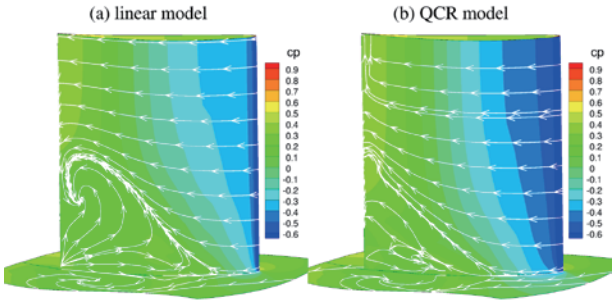


Fig. 3 Comparison of surface limiting streamlines of (a). linear model and (b). QCR model, AoA=4°.

The limiting streamlines obtained from both viscosity models are given from Fig. 3. It is clear there is a large area of corner separation which causes flow blockage and a large amount of loss. We can see that with the widely used linear viscosity model, the maximum streamwise extent of the separation area is larger than that predicted by the QCR linear model.

## 4. Concluding Remarks

In this work the compressor corner separation is numerically simulated with the QCR nonlinear eddy-viscosity model. Results show that with this model the prediction of corner separation size and the pressure coefficients is improved and agrees better with the experiment. As a result the flow in the corner region has large velocity and the earlier corner separation predicted by linear eddy-viscosity model is improved.


## Acknowledgement

This work is supported by the Key Project of the National Natural Science Foundation of China (Grant No. 51136003). Professor Lipeng Lu of Beihang University kindly provided the cascade geometry and the experiment results.


## References


[1] P. Spalart, *Int. J. Heat and Fluid Flow*, 21 (2000) 252－263.

[2] W. Ma, O. Xavier, L. Lu, F. Leboeuf, F. Gao, *Chinese J. Aeronaut*, 24 (2011) 235－242.

Eleventh International Conference on Flow Dynamics
October 8-10, 2014, Sendai, Miyagi, Japan

# Experimental Study on Sound from Two Side-by-side Rectangular Cylinders with Slightly Different Aspect Ratios

Ressa Octavianty and Masahito Asai
Department of Aerospace Engineering, Tokyo Metropolitan University
6-6 Asahigaoka, Hino,Tokyo 191-0065, Japan

**ABSTRACT**

Sound radiation and vortex shedding from two side-by-side rectangular cylinders with slightly different aspect ratios, $AR = 1.0$ and 1.2 were investigated experimentally for gap ratios ($g/h$) of 3.6, 4.5 and 6.0 for $Re \leq 3.3 \times 10^4$ and $M \leq 0.14$. It was found that the vortex shedding and the associated sound generation occurred at a locked-on frequency for $g/h = 3.6$ and 4.5, while not for $g/h = 6.0$. A coupled vortex street in synchronized anti-phase mode was also observed similar to the two square-cylinders case.

## 1. Introduction

There have been extensive investigations in side-by-side configuration of cylinders due to its practical important in engineering applications. For two square cylinders in side-by-side arrangement, Alam et al. [1] did comprehensive study on flow characteristics and categorized specific patterns corresponding to the gap size for which coupled vortex street generated at gap ratio between $3.0 - 6.0$. The spacing ratio effect also has been studied computationally by Inoue et al. [2] at $Re = 150$ to understand the characteristic of sound radiation for this configuration.

In the present experimental study, we examined vortex shedding and the associated sound radiation from two rectangular cylinders with slightly different aspect ratios in side-by-side arrangement. In such a configuration, we are able to expect the so-called locked-on phenomenon if strong sound radiation occurs so that it operates as an external disturbance. In case of a single cylinder, the frequencies of vortex shedding and sound are slightly different for $AR = 1.0$ and 1.2 [3]. Therefore, it is of interest how sound radiation occurs in this case. The present experiment is in contrast to the forced locked-on phenomenon observed by Mahir and Rockwell [4] who investigated the locked-on response of the side-by-side circular-cylinder wake due to forced cylinder oscillations.

## 2. Experimental setup and Procedure

The whole experiment was conducted in a low-turbulence and low-noise wind tunnel of the open-return type. A 1.6-m-long test section was placed after nozzle whose dimension was 500 mm × 500 mm. Two large plates made of wood and Plexyglass with 1-m streamwise length were set to maintain the two-dimensionality of the flow. Two rectangular cylinders made of aluminium were carefully mounted perpendicular to the oncoming free-stream flow. The transverse length ($h$) of cylinders was 10 mm, hence the maximum $Re$ based on $h$ was $3.3 \times 10^4$. The aspect ratio ($AR$) was defined as the ratio between streamwise and transverse length ($w/h$). In the experiment, two pairs of rectangular cylinder, $ARs = 1.0$ and 1.0 and $ARs = 1.0$ and 1.2, were investigated at several gap ratios, $g/h = 3.6,\ 4.5,$ and 6.0 which was defined as the ratio of center-to center distance to cylinder's transverse length. The schematic diagram of the test section is illustrated in Fig. 1. The sound measurement was conducted with two precise microphones placed in opposite side of cylinder's configuration. A PIV system (DANTEC) consisting of a double-pulsed Nd:Yag laser and a CCD camera of 2048 × 2048 pixels was also utilized to measure the instantaneous velocity field at downstream region of the cylinders.

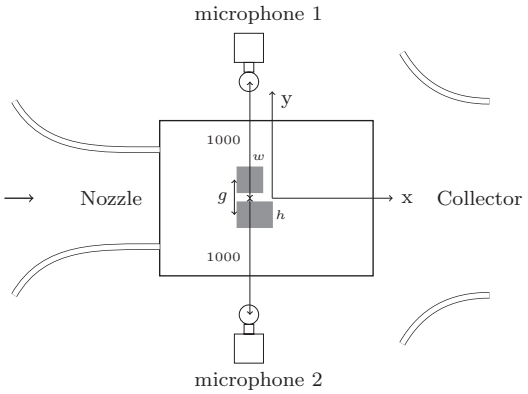


Fig. 1 Schematic of test section (dimensions in mm).

## 3. Results and Discussion

Two sound spectra measured by both the microphones at $U_\infty = 50$ m/s ($Re = 3.3 \times 10^4$) are shown in Figs. 2 - 4 for $g/h = 3.6$, $g/h = 4.5$, and $g/h = 6.0$, respectively. For $g/h = 3.6$, a very sharp spectral peak occurred at $St = 0.131$. For a single cylinder of $AR = 1.0$ and 1.2, the Strouhal number was obtained as 0.128 and 0.120, respectively, in the same free-stream condition. For this gap ratio, locked-on phenomenon occurred with a single dominant frequency. For wider gap ratio ($g/h = 4.5$), locked-on still contributed to the emitted sound but the spectrum became slightly broad compared to the case

Corresponding author: Ressa Octavianty
*E-mail address*: ressa-octavianty@ed.tmu.ac.jp

of $g/h = 3.6$. On the other hand, for the widest gap ratio, $g/h = 6.0$, two distinguished peaks appeared at $St = 0.121$ and $St = 0.129$ as shown in Fig. 4. Those frequencies were close with those of Aeolian tone generated from a single configuration of $AR = 1.0$ ($St = 0.128$) and $AR = 1.2$ ($St = 0.12$).

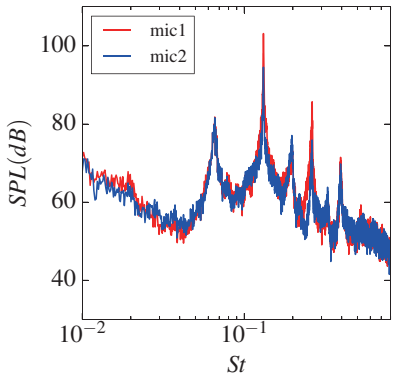


Fig. 2 SPL vs $St$ for $AR = 1.0$ and 1.2 with $g/h = 3.6$

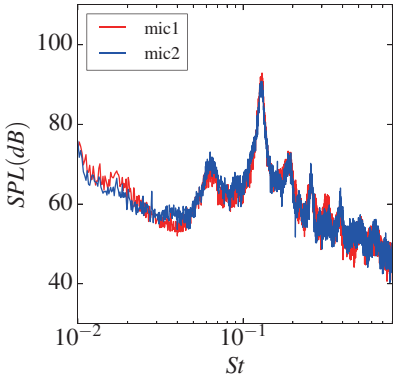


Fig. 3 SPL vs $St$ for $AR = 1.0$ and 1.2 with $g/h = 4.5$

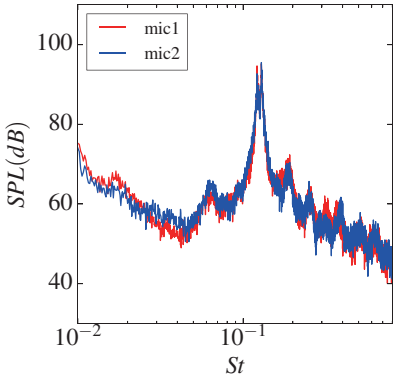


Fig. 4 SPL vs $St$ for $AR = 1.0$ and 1.2 with $g/h = 6.0$

Typical vorticity contours for $AR = 1.0$ and 1.0 at $Re = 3.3 \times 10^4$, which were obtained by PIV, are given in Fig. 5. Blue and red colors represent the clockwise and counter-clockwise directions, respectively. For $g/h = 3.6$, the shed vortices exhibit 'coupled vortex street' with anti-phase pattern. Similar with the square cylinder configuration, the vortex street from the cylinder pair of $AR = 1.0$ and 1.2 also generate the wake structure with synchronized anti-phase vortex-shedding pattern as seen from Fig.6. The difference in the shedding frequency for a single cylinder between $AR = 1.0$ and $AR = 1.2$ still lied in the range of locked-on frequency [4].

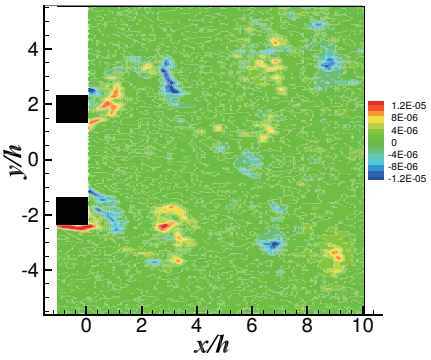


Fig. 5 Instantaneous vorticity of $AR = 1.0$ and 1.0 with $g/h = 3.6$

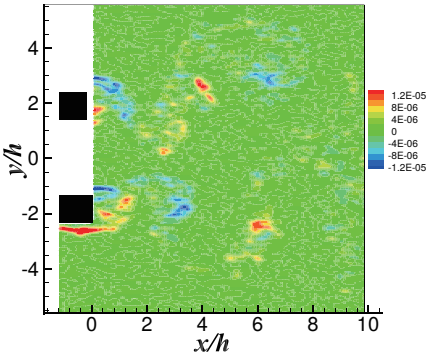


Fig. 6 Instantaneous vorticity of $AR = 1.0$ and 1.2 with $g/h = 3.6$

## 4. Conclusion

Two cylinders with slightly different aspect ratios ($AR = 1.0$ and 1.2) of side-by-side arrangement with $g/h = 3.6 - 6.0$ was studied experimentally at $Re \leq 3.3 \times 10^4$. Vortex shedding and the associated sound generation were locked-on at a single frequency for $g/h = 3.6$ and 4.5, while the vortex shedding occurred at different frequencies for $g/h = 6.0$. Thus,when the gap ratio was not large, sound radiation is governed by the frequency-lock-on phenomenon. Correspondingly, the coupled vortex street with anti-phase pattern of the same periodicity was observed even for two different-aspect-ratio rectangular-cylinders for $g/h = 3.6$.

## References


[1] M. M. Alam, Y. Zhou, and X. W. Wang, *J.Fluid Mech.,* 669 (2011), 432–471.

[2] O. Inoue, W. Iwakami, and N. Hatakeyama, *Phys. Fluids,* 18.046104 (2006).

[3] R. Octavianty, A. Inasawa, and M. Asai, *Proc.14th Asian Congress of Fluid Mech.,* (2013), 106–109.

[4] N. Mahir and D. Rockwell, *J. Fluids & Struct.,* 10 (1996), 491–500.

Eleventh International Conference on Flow Dynamics
October 8-10, 2014, Sendai, Miyagi, Japan

# Experimental Investigation of the Influence of Roughness Receptivity on Protuberance Noise

Masashi Kobayashi[1], Masahito Asai[1]
[1]Department of Aerospace Engineering, Tokyo Metropolitan University
6-6 Asahigaoka, Hino, Tokyo, 191-0065, Japan

**ABSTRACT**

Influences of roughness receptivity on the protuberance noise were examined experimentally in a zero-pressure-gradient boundary layer at low Mach numbers. When a small-height roughness element was glued upstream of the protuberance, the competition between the leading-edge-generated and roughness-generated T-S waves occurred, and the peak frequency of radiated sound was dominated by such a competition. When the roughness height was larger than 20 % of the boundary-layer displacement thickness, tonal sound due to the roughness receptivity became dominant.

## 1. Introduction

In order to clarify the generation mechanism of vortex sound in a laminar boundary layer, we have been studying possible interactions between the instability waves and roughness element(s). Our recent experimental study [1] on sound radiation from a two-dimensional (2D) protuberance in laminar boundary layer demonstrated that when the protuberance height was as high as the thickness of Blasius boundary layer, a feedback-loop mechanism set in. The feedback model proposed is illustrated in Fig. 1. The acoustic feedback mechanism required occurrence of separation bubble immediately upstream of the protuberance, in addition to the receptivity to acoustic waves (stage I), growth of T-S waves (stage II) and sound radiation at the protuberance (stage IV). This is different from the theoretical model proposed for very high Reynolds number flows by Wu [2, 3], in which 2D T-S waves can be amplified sufficiently in the boundary layer (without separation bubble) upstream of the protuberance to interact directly with the protuberance even though it is sufficiently lower than the boundary-layer thickness. In the actual boundary layer, on the other hand, the 2D T-S waves cannot directly interact with the protuberance because the secondary instability occurs once the T-S amplitude exceeds a threshold amplitude.

In order to further understand the feedback mechanism, it is important to clarify how strongly the receptivity coefficient affects the sound generation at the protuberance. To examine the effect of the receptivity, in the present study, a small-height roughness element was introduced upstream of the protuberance, expecting that the introduction of the additional receptivity region can control the process of tonal noise generation.

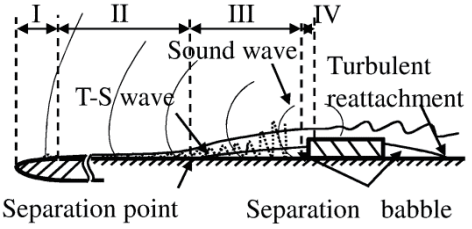


Fig. 1 Mechanism of protuberance noise generation

Corresponding author: Masashi Kobayashi
*E-mail address*: kobayashi-masashi@ed.tmu.ac.jp

## 2. Experimental set-up and procedure

The experiment was conducted in a low-turbulence and low-noise wind tunnel with square exit cross-section of 500 mm × 500 mm. The test section with a streamwise length of 1.5 m is placed in an anechoic chamber 4.8 m long, 3.6 m wide and 3.3 m high. The turbulence intensity measured at the tunnel exit was 0.1% of the freestream velocity $U_\infty$ in terms of the rms value of the steamwise velocity fluctuation, and the background noise level was 65 dB(A) at $U_\infty$ = 50 m/s. A boundary-layer plate of 1000 mm long and 5 mm thick with a sharp leading edge was set between a pair of Plexiglas walls which maintained two-dimensionality of the mainstream in the test section though the upper and lower areas were opened.

A two-dimensional protuberance, a resin tape with a width of 20 mm was glued perpendicular to the flow direction on the boundary-layer plate, as illustrated in FIG. 2. A two-dimensional small-height roughness element, a 7.5-mm-wide cellulose tape, was also glued upstream of the protuberance, which produced an additional receptivity region (other than the leading edge region). The streamwise distance $x$ is measured from the leading edge and the distance $y$ is normal to the wall. A microphone set on the upstream side 1000 mm apart from the protuberance (145° rotated from $x$-axis) measured sound radiated from the protuberance. A constant-temperature hot-wire anemometer (Dantec) was used to measure the mean and fluctuation streamwise velocity denoted by $U$ and $u$, respectively.

In the experiment, the freestream velocity $U_\infty$ was fixed at 30 m/s. The displacement thickness of the Blasius boundary layer without a protuberance ($\delta^*$) was used to define the Reynolds number as $R^* = \delta^* U_\infty / \nu$.

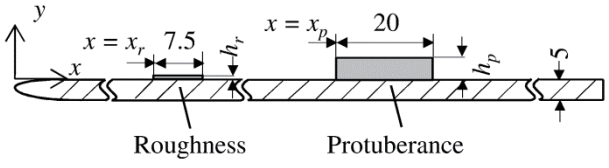


Fig. 2 Boundary-layer plate with a protuberance and a roughness element (dimensions in mm).

## 3. Results and Discussion

The protuberance of $h_p$ = 4.9 mm was fixed at $x$ = 450 mm, where $R^*_p$ = 1432 and $h_p/\delta^*_p$ was 6.0 at $U_\infty$ = 30

m/s. Fig. 3(a) displays the spectra of SPL without the roughness element ($h_r/\delta^*_r$ = 0.21). Multiple discrete spectra are observed between 600 Hz and 900 Hz. On the other hand, Fig. 3(b) displays the spectra of SPL with the roughness element, showing two prominent peaks at 620 Hz and 754 Hz. The latter frequency corresponds to the center frequency of the multiple discrete components in Fig .3(a). When the roughness height was increased, the spectral peak of 620 Hz became more dominant while the 754 Hz peak originating from the leading-edge receptivity only was diminished: It should also be noted that the total SPL was little changed even when the roughness was introduced. Thus, when there are two receptivity regions, a competition between the T-S waves excited in these two receptivity regions.

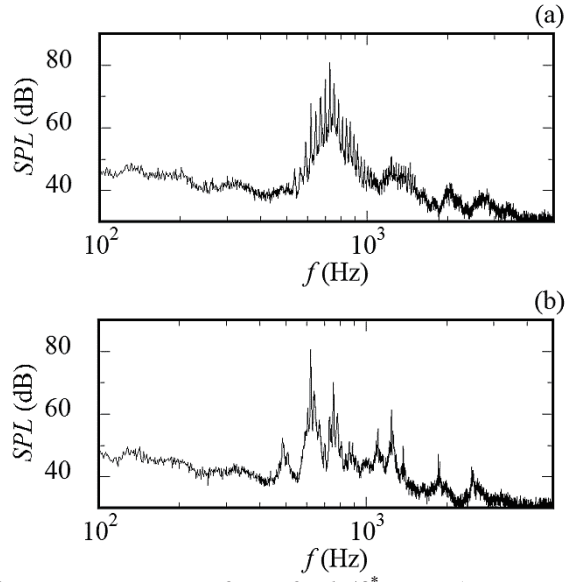


Fig. 3 Power spectra of SPL for $h_p/\delta^*_p$ = 6.0 ($x_p$ = 450 mm) at $U_\infty$ = 30 m/s. (a) without roughness, (b) with roughness ($h_r/\delta^*_r$ = 0.21 and $x_r$ = 350 mm).

Fig. 4 displays the lower and higher frequencies of spectral peaks ($f_0$) against the roughness $x$-location, $x_r$. Here the roughness height $h_r$ was fixed at 0.05 mm in all the cases. Note that the wavelength of the T-S wave of 650 Hz was about 15 mm. The frequencies of the two peaks exhibited discontinuous variations with $x_r$. For instance, the lower frequency jumped between $x_r$ = 260.0 mm and 267.5 mm by 28 Hz. It is also noted that each peak frequency corresponded to one of the multiple discrete peaks observed in the spectra without roughness.

Fig. 5 displays the rms value of $u$-fluctuation of higher- and lower-frequency peaks in the region from $x$ = 327.5 mm to 401.0 mm. Here the roughness was located at $x$ = 275 mm ($R^*$ = 1252) and the separation bubble started around $x$ = 390 mm ($R^*$ = 1491). Upstream of the separation bubble, the oscillating stokes-layer due to acoustic wave radiated from the protuberance was more dominant than the T-S wave, so that each rms-amplitude exhibited a wavy variation (with the T-S wavelength ~ 15 mm) around the almost constant value. In this condition, the T-S wave component of the lower frequency (648 Hz) superposed to the sound-induced Stokes layer grew faster than that of the higher frequency (728 Hz) for $x$ > 370 mm. This is because the T-S wave of the higher-frequency turned to decay for $x$ > 380 mm which corresponds to $R^*$ > 1473, as seen from the neutral stability diagram of Blasius flow in Fig. 6.

**References**


[1] M. Kobayashi, A. Inasawa, M. Asai, *Proc. 14th Asia Cong. Fluid Mech.*, (2013) 268-271.

[2] X. Wu and L. W. Hogg., *J. Fluid Mech.*, 550 (2006) 307-347.

[3] X. Wu, *J. Fluid Mech.*, 689 (2011) 279-315.


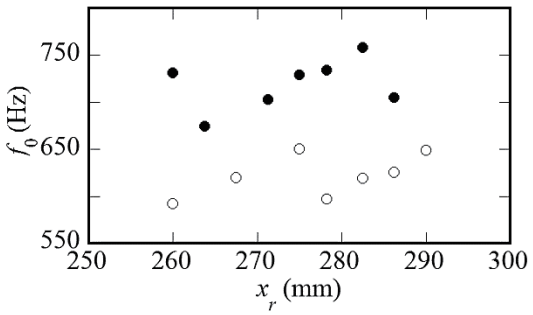


Fig. 4 Frequency variation of the dominant tonal sound with $x_r$ at $U_\infty$ = 30 m/s ($x_p$ = 450 mm, $h_p/\delta^*_p$ = 5.9). ○, lower-frequency peak; ●, higher-frequency peak.

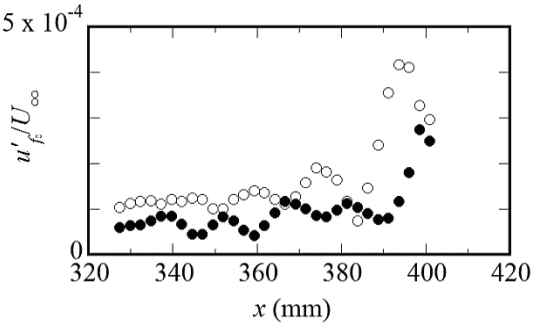


Fig. 5 The streamwise distributions of $u'_{fi}$ at a constant $y$-position at $U_\infty$ = 30 m/s ($x_r$ = 275 mm, $x_p$ = 450 mm). ○, 648 Hz ($F$ = 70.5); ●, 728 Hz ($F$ = 79.2), where $F = 2\pi f_0 \nu/U_\infty^2 \times 10^6$. Each component was extracted with bandwidth of ±5 Hz.

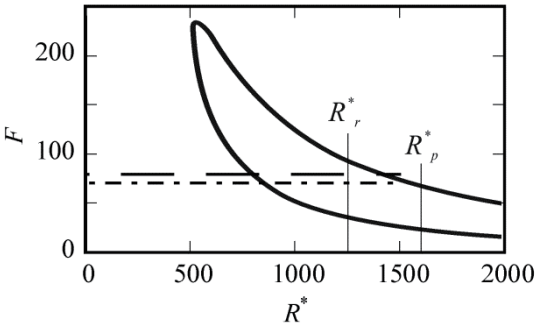


Fig. 6 Neutral stability diagram of Blasius flow. Non-dimensional values $F$ of dominant sound frequencies in Fig. 5 are -.- 70.5 and - - -79.2.

# Numerical Analysis of Sound Propagation for Acoustic Phased Array

Kei Fujisawa[1], Akira Asada[2]
[1] Department of Ocean Technology, Policy, and Environment, University of Tokyo
4-6-1 Komaba Meguro-ku, Tokyo, Japan
[2] Institute of Industrial Science, University of Tokyo
4-6-1 Komaba Meguro-ku, Tokyo, Japan

**ABSTRACT**

This paper presents the analysis of acoustic array with variable phase signals called “acoustic phased array”. To understand the sound field of acoustic phased array, the governing equations of compressible Navier stokes equation, energy equation and state equation are solved by finite difference time domain based method. The numerical analysis is applied to the sound propagation of different phase signals emitted from two different transducer element arrays. The result shows the capability of variable focusing control of the sound field using the acoustic phased array.

## 1. Introduction

Acoustic array using variable phase signal control function is called “acoustic phased array”. This has been applied to the some underwater technology, such as nondestructive inspection and detection, due to its adjustability of beam angle and focusing distance of acoustic sound beam. The acoustic phased array consists of two different sound emitting elements, which control the sound phase independently, as illustrated in Figure1.

Acoustic sound propagation has been numerically studied by solving KZK (Khokhlov - Zabolotskaya - Kuznetsov) equation [1], which is a parabolic approximation of the Westervelt equation [2]. Therefore, the application of this approach is limited to a far field apart from the acoustic array. More recently, fluid dynamics approaches using the compressible form Navier-Stokes equations combined with energy equation have been proposed by Nomura [3] and this direct approach is also applied to the sound propagation in the near-field of parametric array [4]. To understand the acoustic sound propagation of the acoustic phased array, it is important to consider the sound field without parabolic approximation and all the local nonlinear effects have to be included in the numerical analysis.

The purpose of this paper is to study sound propagation of acoustic phased array using direct numerical approach using compressible Navier-Stokes based method.

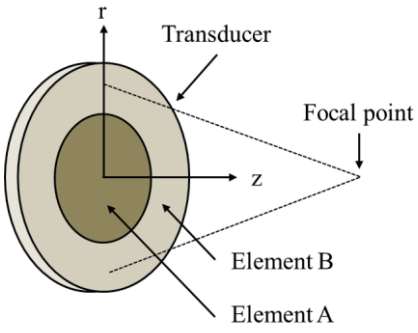


Figure1 Phased array

## 2. Method

The governing equations are based on compressible viscous fluid, which is described by Navier-Stokes equations (eq. 1, 2), the mass conservation (eq. 3), energy equation (eq. 4) and state equation (eq. 5), which can be written in the following form in cylindrical coordinate system under the axisymmetric assumption.

$$\frac{\partial u^*}{\partial t} = -\frac{1}{\gamma}\frac{\partial p^*}{\partial z^*} + \frac{1}{\gamma}\frac{\rho^*}{1+\rho^*}\frac{\partial p^*}{\partial z^*} - \left(u^*\frac{\partial u^*}{\partial z^*} + v^*\frac{\partial u^*}{\partial r^*}\right) + \frac{1}{\mathrm{Re}}\frac{1}{1+\rho^*}\left(\frac{\partial \tau_{zz}^*}{\partial z^*} + \frac{\partial \tau_{rz}^*}{\partial r^*} + \frac{\tau_{rz}^*}{r^*}\right) \quad (1)$$

$$\frac{\partial v^*}{\partial t^*} = -\frac{1}{\gamma}\frac{\partial p^*}{\partial r^*} + \frac{1}{\gamma}\frac{\rho^*}{1+\rho^*}\frac{\partial p^*}{\partial r^*} - \left(u^*\frac{\partial v^*}{\partial z^*} + v^*\frac{\partial v^*}{\partial r^*}\right) + \frac{1}{\mathrm{Re}}\frac{1}{1+\rho^*}\left(\frac{\partial \tau_{zr}^*}{\partial z^*} + \frac{\partial \tau_{rr}^*}{\partial r^*} + \frac{\tau_{rr}^* - \tau_{\theta\theta}^*}{r^*}\right) \quad (2)$$

$$\frac{\partial \rho^*}{\partial t^*} = -\left(\frac{\partial u^*}{\partial z^*} + \frac{\partial v^*}{\partial r^*} + \frac{v^*}{r^*}\right) - \rho^*\left(\frac{\partial u^*}{\partial z^*} + \frac{\partial v^*}{\partial r^*} + \frac{v^*}{r^*}\right) - \left(u^*\frac{\partial \rho^*}{\partial z^*} + v^*\frac{\partial \rho^*}{\partial r^*}\right) \quad (3)$$

$$\frac{\partial s^*}{\partial t^*} = -\left(u^*\frac{\partial s^*}{\partial z^*} + v^*\frac{\partial s^*}{\partial r^*}\right) + \frac{\gamma}{\mathrm{Re}}\frac{D^*}{(1+\rho^*)(1+T^*)} \quad (4)$$

$$p^* = \gamma\rho^* + \gamma\frac{B}{2A}\rho^{*2} + \frac{\beta_0 c_0^{\,2}}{C_{p0}}s^* \quad (5)$$

where D* denotes the dissipation term and $\gamma=\rho_0 c_0/P_0$. Note that the variables with * and 0 are non-dimensional variables and reference quantities, respectively. T:temperature, $c_0$: sound velocity, p:pressure amplitude, s:entropy variation, t: time, u and v are velocity components in axial and radial direction, respectively, $\boldsymbol{\tau}$:stress tensor, ρ:dencity variation, $C_p$: specific heat at constant pressure, $\beta_0$: coefficient of thermal expansion, κ:thermal conductivity, Re: Reynolds number and Pr: Prandtl number. B/A is parameter of nonlinearity. These equations are solved using finite difference time domain based method [5]

Corresponding author: Kei Fujisawa
*E-mail address*: fujisawa_ocean_eng@yahoo.co.jp

## 3. Computational condition

The numerical simulation is carried out for the sound propagation from annular type array in a fluid of water at temperature 293.15 K, as shown in Figure 1. Computational area is 10 cm in axial direction and 10 cm in radial direction which is surrounded by Mur1st absorbing boundary condition [6]. The cell size is set to $\Delta z=\Delta r=\lambda/40$ ($\lambda$: wavelength of sound) and the increment of time step (=0.014 μs) is determined to satisfy Courant-Friedrichs-Lewy (CFL) condition. The physical parameters used in this study are $\rho_0$=998.2kg/m$^3$, $c_0$=1482 m/s, $\beta_0=2.1\times10^{-4}$ 1/K, $C_p=4.18\times10^3$ J/(kg/K), $\kappa$=0.602 W/(m K). The continuous sinusoidal waves are emitted from each element of array, which is expressed by following equation,

$$p = p_m \sin\{2\pi ft + \alpha_p\} \tag{8}$$

where f is frequency, $p_m$ is pressure amplitude of sound source, $\alpha_p$ is phase shift which is set for each element. Frequency and pressure amplitude of both elements are set to be 500kHz and 30kPa, respectively, while the different phases are applied. In the present computation, two cases are considered, that is $\alpha_p$=0 for in phase and $\alpha_p=\pi$ for the out-of phase. The radius of element A is assumed 1cm and the width of element B is 1cm.

## 4. Results and Discussion

Figure 2 shows the pressure distribution along beam axis of the acoustic phased array. The time step is at 2500 steps, which corresponds to the time t = 0.0706 ms after the sound emission. The observation of the sound propagation for phased array sound indicates that beam focusing occurs at the 0.08 m apart from the acoustic phased array. This is due to the result of sound interference generated by different phased sound wave emitted from each array element. On the other hand, the sound propagation of the array oscillating in phase indicates almost uniform sound wave propagation in axial and radial direction. Note that the magnitude of sound pressure on beam axis is smaller than that of phased array.

Figure 3 shows the two-dimensional sound pressure fields of the acoustic phased array operating out-of phase (a) and in phase (b). These results indicate that the sound focusing in the out-of phase operation is due to the result of sound interference. Therefore, the emitted

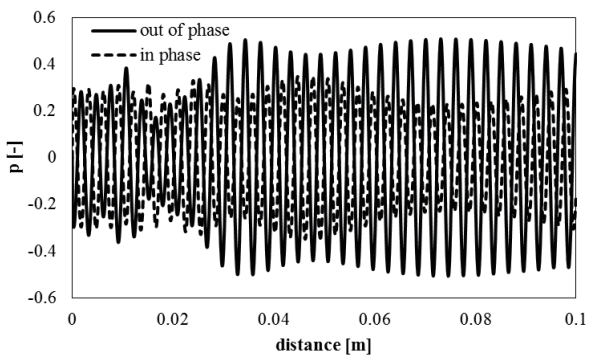


Figure 2. Pressure distribution along beam axis

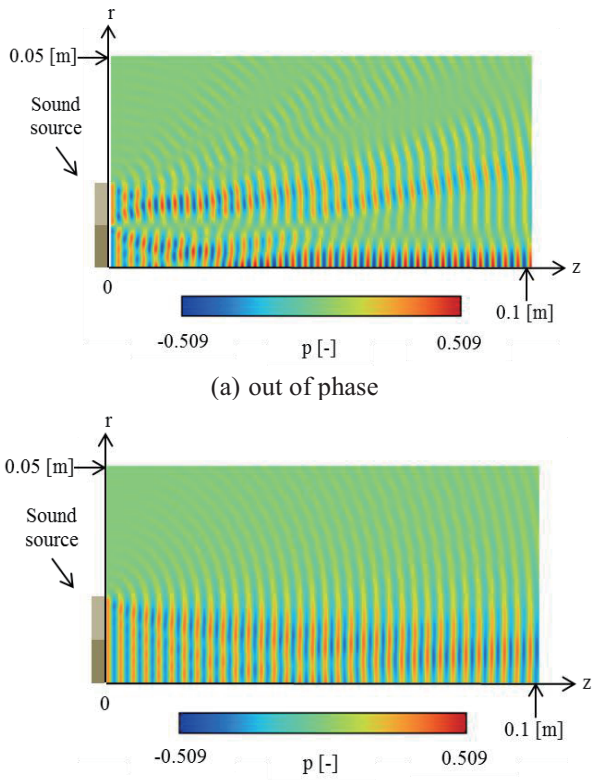


(a) out of phase

(b) in phase

Figure 3. Sound propagation from acoustic array

sound from outer array is directed outward in the out-of phase operation, while the it is inclined to the beam axis in the in phase operation.

## 5. Concluding Remarks

The propagation of sound emitted from the phased array is numerically studied by solving compressible Navier-Stokes based method. The result shows the sound focusing occurs for the out-of phase operation due to the sound interference.


## Acknowledgement

The authors would like to thank to Prof. H. Nomura from The University of Electro-Communications for helpful suggestion on this research.


## References


[1] T. Kamakura, S. Sakai, *IEICE Technical Report*, (2006) US2005-116 EA2005-100.

[2] Y. Jing, D. Shen, G.T. Clement, *IEEE Transactions on Ultrasonics, Ferroelectrics, and Frequency Control*, **58** 5 (2011) 1097-1101.

[3] H. Nomura, H. Adachi, T. Kamakura, G.T. Clement, *Japanese Journal of Applied Physics*, **53** (2014) 07KC03.

[4] K. Fujisawa, *Journal of Flow Control, Measurement & Visualization*, **2** (2014), in press.

[5] H. Nomura, C. M. Hedberg, T. Kamakura, *Applied Acoustics*, **73** (2012) 1231-1238.

[6] Mur, G., *IEEE Transaction on Electromagnetic Compatibility*, EMC-23 (1981) 377-382.

Eleventh International Conference on Flow Dynamics
October 8-10, 2014, Sendai, Miyagi, Japan

# Numerical Modeling of Heat Transfer in the Cooling System Using Phase Change Material and Heat Pipes for Power Battery of Electric Vehicles

Takuya Ojiro[1], Kosuke Nonaka[1], Kazuhiro Kudo[1] , Tatsuya Yamada[1], Takashi Yamada[1] and Naoki Ono[1]
[1]Shibaura Institute of Technology
3-7-5, Toyosu, Koto-ku, Tokyo, 135-8548, Japan

**ABSTRACT**

The lithium-ion battery which is used for electric vehicles has safety risk when it is used in more than 45℃. The performance deteriorates rapidly, and burning or explosion may occur because of abnormal heat generation. Therefore, thermal management technology is required for the optimization of battery properties. We studied the most suitable design of PCM and heat pipes by applying lumped model. We examined the steady-state temperature in normal heat generation and the time to reach 80℃ in abnormal heat generation and investigated the optimal number of heat pipes.

## 1. Introduction

In recent years, it is expected that electric vehicles having a high-performance battery is required to use energy in high efficiency. As the development of the battery advances, its high output and capacity is progressed rapidly. However, the establishment of thermal management technology of the battery for the optimization of its properties, long life and improvement of safety. Also there is the risk of overheating and deterioration of its performance because the temperature of the cell is increased by the heat generated at discharge and charge. It is reported that its cycle life and capacity was decreased when the temperature of the battery cell becomes more than 45℃[1]. Thus, the cell has to be kept under the particular temperature. As a cooling method, there are air cooling or liquid cooling types. However, it is not yet assured that those systems are particularly superior form in terms of cost or space.

In this study, the thermal management system of power battery is based on using phase change material (PCM) [2], [3] with some heat pipes for safety improvement are long life. We investigate the optimal number of heat pipes on the thermal management system, we expect that the temperature of the cells are kept within 15℃ to 45℃ at normal usage and that the time to reach 80℃ is extended so that the human can evacuate from the vehicle at abnormal heat generation, because the hybrid type thermal management technology[4] with heat pipes was very effective.

## 2. Numerical model

Several kinds of the lithium-ion battery cell are already used. In this study it is expected to use them from the viewpoint of cooling performance in the future. But internal short-circuit in the battery or the lack of management of the temperature cause abnormal heat generation in the cell. Thus, this study focused on laminating type of lithium-ion battery. We investigated heat transportation of cooling system with PCM and heat pipes by using lumped model. Input power was changed to simulate normal heat generation (1C, 2C, 3C or 5C) and abnormal heat generation, 1C is a current value when the battery was discharged the capacity in one hour, 2C is 30 minutes, 3C is 20 minutes and 5C is 12 minutes.

Corresponding author: Naoki Ono
*E-mail address*: naokiono@shibaura-it.ac.jp

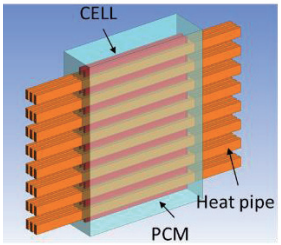


Fig. 1 Apparatus model

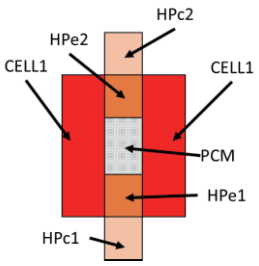


Fig. 2 Lumped model

This model adopted one-dimension heat transfer and calculated transported heat neighboring between. The heat influx or outflow was calculated between lumps; (1) and (2). The temperature of a lump was deduced by heat balance; (3). The melting of PCM was simulated by using the temperature recovery method[5].

$$\dot{Q_{i,J}} = A_{i,j} k_{i,j} \frac{T_i - T_j}{L_{i,j}} \tag{1}$$

$$\dot{Q_{i,J}} = A_{i,j} h_{i,j} (T_i - T_j) \tag{2}$$

$$T_i^{t+1} = \frac{\sum \dot{Q_{in}} - \sum \dot{Q_{out}}}{\rho_i C_{p_i} V_i} \Delta t + T^t{}_i \tag{3}$$

We modelled an actual module system of two battery cells with PCM and heat pipes, in Fig.2. Fig. 3 shows a lumped model for represent the module system. This model was divided to some blocks, PCM, the evaporator and condenser of heat pipes and air. To compare it with the experiment, we examined the heater on 1/4 scale of the real battery size. The heater was a substitute of the real cell. Therefore, input power was assumed to be 0.75W at charge and discharge of 1C, 2.5 W at 2C, 5 W at 3C, 12.5 W at 5C, 100 W at the abnormal heat generation, respectively. RT-50 (Melting point is 49℃) developed by the company Rubithrem Technologies GmbH and was used as PCM, their physical property was adopted in the analysis. Flat type heat pipe of 6mm in diameter was used, and its axial thermal conductivity was assumed to be 100 times larger than that of copper. The

heat transfer coefficient of their condenser was assumed to be in the order of air cooling.

## 3. Results and Discussion

First of all, we inspected the model in comparison with the experiment. In this experiment, condenser of heat pipes was cooled by using water. The temperature was calculated by changing the number of heat pipes between the cells. The heat transfer coefficient of the condensation area was assumed to being the order of air-cooling. The results of the temperature change in the battery at the time of heat generation of 1C and abnormal heat generation were shown in Fig. 4 and Fig. 5.

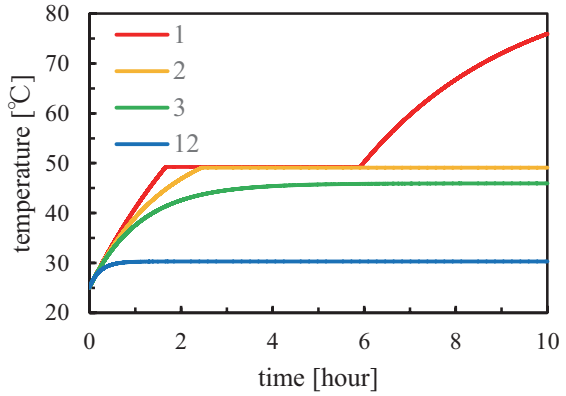


Fig. 3 Temperature change of the cell at 1C heat generation vs. number of heat pipes

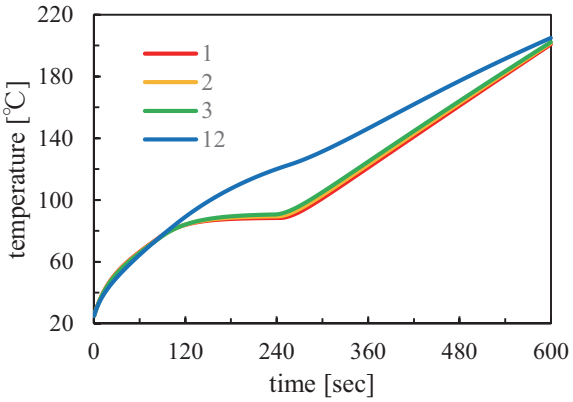


Fig. 4 Temperature change of the cell at abnormal heat generation vs. number of heat pipes

In the case of 1C, the temperature reached melting point when one or two heat pipes existed between the cells. Later also the temperature was rising. However it became 45℃ or less when the number was larger than two. In the case of abnormal heat generation, the temperature kept increasing in the all number of heat pipes. Thus, we examined the temperature when it became the steady-state in the case of normal heat generation and the time to reach 80℃ in the case of abnormal heat generation. An evaluation was attempted by making each temperature and time nondimensional, from 1 as a good condition to 0 as a bad condition. The result is shown in Fig.6.

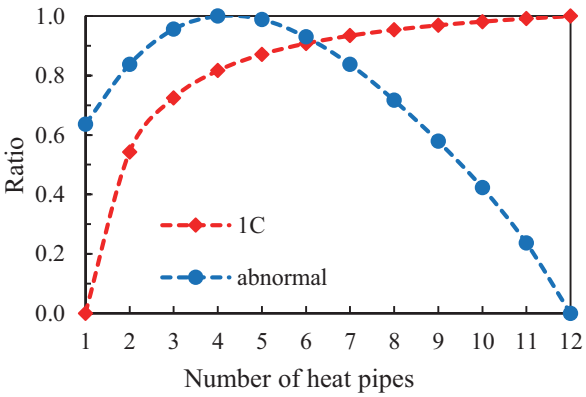


Fig. 5 Optimization of the number of heat pipes

A shown in Fig. 6, two curbs are overlapped at six heat pipes. Thus, by studying with lumped model, it is thought the most suitable number of heat pipes at both of normal and abnormal heat generation were six.

## 4. Concluding Remarks

In this study the temperature of the cell was calculated by using a lumped model. The temperature change in varying the number of heat pipes was simulated and we made the results nondimensional. As a result when there are six heat pipes between cells, we think an optimal state was realized.

## 5. Future Prospects

We will compare the calculation by a lumped model with the detailed experiment and revise the most suitable number of the heat pipes.


## Acknowledgement

This research was supported by the strategic international cooperative program of JST in the field of highly-efficient energy utilization.


## References


[1] P.Romadass, “Capacity fade of Sony 18650 cells cycled at elevated temperatures”, *J.Power Sorces,* 112(2): (2002), 614-620.

[2] Zhonghao Rao, Shuangfeng Wang, Maochun Wu, Zirong Lin, Fuhuo Li, “Wxperimental investigation on thermal management of electric vehicle battery with heat pipe”, *Energy Conversion and Management, 65* (2013), 92-97.

[3] X.Duan, G.F Naterer, “Heat transfer in phase change materials for thermal management of electric vehicle battery modules”, *InternationalJournal of Heat and Mass Transfer, 53* (2010), 5176-5182.

[4] Takuya Ojiro, Keisuke Kambara, Takashi Yamada, Naoki Ono, “Development of a new cooling system using phase change material for power battery thermal management of electric vehicles,” Proceeding of *51th Japan Heat Transfer Symposium*, (2014), F321.

[5] Ohnaka I, Fukusako T, *Trans. ISIJ, 17* (1977), 410.

# Experimental Analysis of Heat Transfer in the Cooling System Using Phase Change Material and Heat Pipes for Power Battery of Electric Vehicles

Kosuke Nonaka, Takuya Ojiro, Kazuhiro Kudo, Tatsuya Yamada, Takashi Yamada and Naoki Ono
Shibaura Institute of Technology
3-7-5, Toyosu, Koto-ku, Tokyo, 135-8548, Japan

**ABSTRACT**

About lithium ion battery used for an electric vehicle, the battery deterioration by temperature rise of the battery cell and thermal runaway are considered to be a serious problem. The aim of this study is the development of the heat control technology that can keep the temperature of the battery cell at the most suitable temperature by using PCM (Phase Change Materials) and heat pipes. We here report the fundamental results by performing the model experiment which used two plates of heated to simulate lithium ion battery.

## 1. Introduction

In a battery used for an electric vehicle, the lithium ion battery is now used by many electric vehicles because it has the high electric capacity and the high output. However, in the case of charge and discharge of the battery, it is considered to be a problem that the battery cell becomes hot, and that the battery deteriorates by the temperature rise. It is thought that there is little deterioration and that stable electricity can be supplied when the battery is used in the range of 15℃ to 45℃[1].

Furthermore, by the further temperature rise of the battery cell, there is a problem of safety risk of burning and explosion of the battery cell in worst case as shown Fig. 1. Burning and explosion of the battery are caused by an internal short circuit, and they can be prevented by keeping the battery temperature at less than 80℃. For these problems, the battery heat control technology is required to obtain longer life and safety of a battery cell.

Fig. 1 Burning accident of electric vehicle[2]

The aim of this study is the development of the heat control technology by using PCM and heat pipes. We explored a cooling system which filled PCM around lithium ion battery and inserted a heat pipes in PCM. By this cooling system, the heat of the battery is absorbed by the PCM. The heat that the PCM absorbed and that the battery generates are transported to a heat sink by heat pipes and are radiated by a heat sink. As a result, the temperature rise of the battery is controlled. By this heat control technology, we will develop an electric module which has high efficiency, safety, compactness and reduced cost. By the experiment, we will investigate the ratio of PCM and heat pipes for cooling the battery effectively and their placement. We made an equipment which physically simulates a real battery module, and performed heat transfer measurement[3].

Corresponding author: Naoki Ono
*E-mail address*: naokiono@shibaura-it.ac.jp.ac.jp

## 2. The outline of the experiment

As fundamental experiment, we performed the experiment which used the polyimide heater of the 1/4 scale as a substitute of lithium ion battery. By this experiment, temperature change of the heater and heat transported to the heat sink were measured. In PCM, paraffin(Rubitherm “RT-50”) of melting point 50℃ and thermal conductivity 0.2W/(m・K) were used for the experiment. 48 flat heat pipes of 3mm×8mm×116mm were used. Heat pipes was cooled by water at the heat sink. The temperature of the heater surface was measured by K type sheath thermocouples. In addition, the water temperature in the inlet and the outlet of the heat sink was measured. The heater was sandwiched with two pieces of aluminum plates of thickness 1mm. The aluminum plates were covered by the aluminum laminate film. We think it can simulates real lithium ion battery physically. The experiment situation is shown in Fig. 2 (a)-(c).

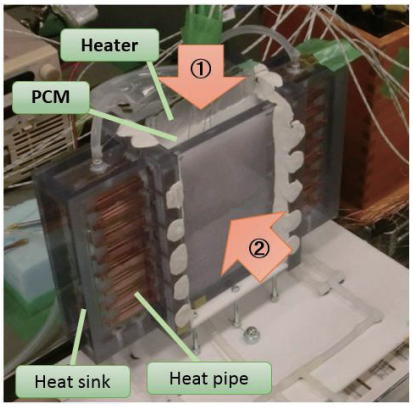


(a) Overview

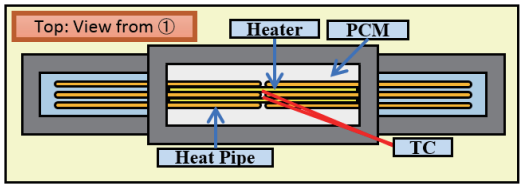


(b) View from ① in (a)

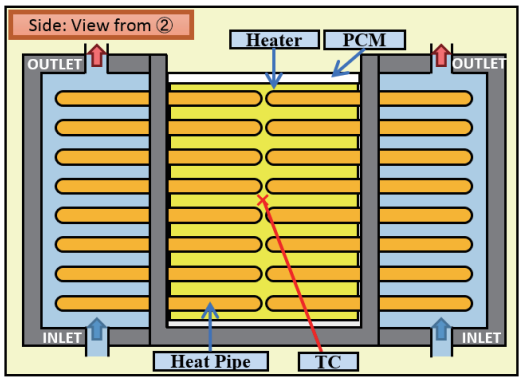


(c) View from ② in (a)

Fig. 2 Experimental apparatus

The input power of the heater was 0.75W(1C), 2.5W(2C), 5W(3C) and 12.25W(5C), in the case of the experiment for the normal heat generation. This C is an index value to express a ratio of the electric current in the battery capacity. For example, 1000mAh battery that is charged or discharged at 1C rate provides a current of 1000mA for one hour under ideal conditions. In addition, the input power of the heater was 100W, in the case of the experiment for the abnormal heat generation by thermal runaway of the battery.

## 3. Results and Discussion

The change of the temperature of the heater surface is shown in Fig. 3 and Fig. 4. In the case of input power 0.75W(1C) - 12.25W(5C) which assumed normal heat generation, it was confirmed that the temperature of the heater surface was controlled to be under 45 ℃ or less, which was appropriate temperature by PCM and heat pipes. In the case of input power 100W which assumed abnormal heat generation by thermal runaway, the temperature of the heater surface was not controlled to be under 45℃. However, it was confirmed that the temperature of the heater surface was controlled to be under 80 ℃, which prevents burning and explosion.

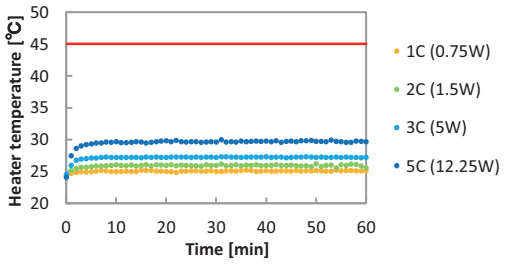


Fig. 3 The surface temperature of the heater (normal)

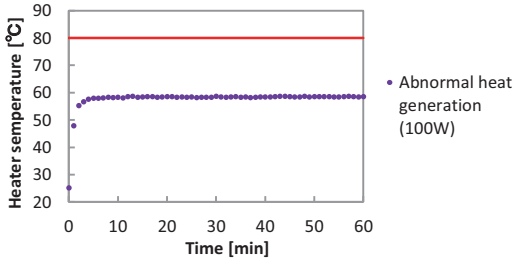


Fig. 4 The surface temperature of the heater (abnormal)

In addition, it is thought that there is almost no temperature change of the heater surface during 60 minutes from 20 minutes. During this period, the heat transported to the heat sink in each input power is shown in Table 1. It was calculated from the difference of temperature at the inlet and the outlet of cooling water of heat sink. From Table 1, it was confirmed that most of heat of the heater was transported by heat pipes and was removed by a heat sink.

Table 1 Heat removed by the heat sink
(Time: 20-60 minutes)

| | 1C 1.5W | 2C 5W | 3C 10W | 5C 25W | Abnormal 100W |
|---|---|---|---|---|---|
| Removed heat (W) | (-0.1) | 3.7 | 9.2 | 24.3 | 97.0 |
| Proportion (%) | - | 74.0 | 92.0 | 97.2 | 97.0 |

From these results, it was confirmed that the present system with 48 heat pipes was a little too strong for cooling the battery cell. Optimized number of heat pipes with air-cooling heat sink has to be investigated.

## 4. Concluding remarks

The temperature of the heater surface was a little too much lowered by using PCM and 48 flat heat pipes with water-cooling heat sink. Optimized number of heat pipes with air-cooling heat sink has to be investigated.

## 5. Future plans

(1) We will perform the experiment which changed a ratio of PCM and heat pipes. From the result, we will develop the system effective for both situations of normal and abnormal heat generation.

(2) We will perform the experiment using the real lithium ion battery and the battery charger and discharger.

## Acknowledgement

This research was supported by the strategic international cooperative program of JST in the field of highly-efficient energy utilization.

## References

[1]P.Romadass, *J.Power Sorces 112(2)*, (2002) 614-620.

[2]*Hangzhou Halts All Electric Taxis as a Zotye Langyue (Multipla) EV Catches Fire – China Auto Web*, http://chinaautoweb.com/2011/04/hangzhou-halts-all-electric-taxis-as-a-zotye-langyue-multipla-ev-catches-fire/, (2014/7/7).

[3]Kosuke Nonaka, *The 51st Japan heat transfer symposium*, F322(2014).

# Improvement of Startup Characteristics of a Loop Heat Pipe using Secondary Wicks

Masahiko Taketani, Hiroki Nagai
Department of Aerospace Engineering, Tohoku University, Japan
6-6-01 Aramakiazaaoba, Aoba-Ku, Sendai-Shi, Miyagi prefecture, Japan

**ABSTRACT**

A Loop Heat Pipe (LHP) is an efficient heat transfer device utilizing the phase change of fluid. However, LHPs have problematic startup behavior in certain situations. One of the proposed solutions for this problem is the use of secondary wick. However, it has not yet been verified that a secondary wick can actually improve the startup process of an LHP. In this study, we experimentally studied the effects of a secondary wick on the thermal performance of the LHP. We find that (1) using a secondary wick improves the startup process and (2) certain types of secondary wicks have an adverse effect on the maximum heat inputs.

## 1. Introduction

Thermal control on the spacecraft is necessary to operate its equipment surely under strict thermal environment, in which ambient temperature changes greatly. In addition, recent spacecraft need large length of heat transfer from inside to outside of its structure. Loop Heat Pipes (LHPs) are promising heat transfer devices that utilize phase change of working fluid, and meet these requirements [1].

However, in certain conditions, LHP has problems on its startup performance: unstable behavior and slow startup. The startup performance depends on initial vapor-liquid distribution in LHP. If enough amount of liquid is not supplied to evaporator core, the startup process becomes unstable and slow.

One of the solutions for improvement of startup performance is using a secondary wick [1]. By attaching a secondary wick, enough amount of liquid is supplied to the evaporator core, and as a result, the startup performance is expected to be stabilized. Nevertheless, optimum shape of secondary wick is not proposed. In this research, we prepared three types of secondary wicks, and conduct experiments to find desirable characteristics of secondary wicks.

## 2. Experimental set up

### 2.1 Design of miniature LHP

Fig.1 shows a miniature LHP designed for this study. The material for this LHP is stainless.

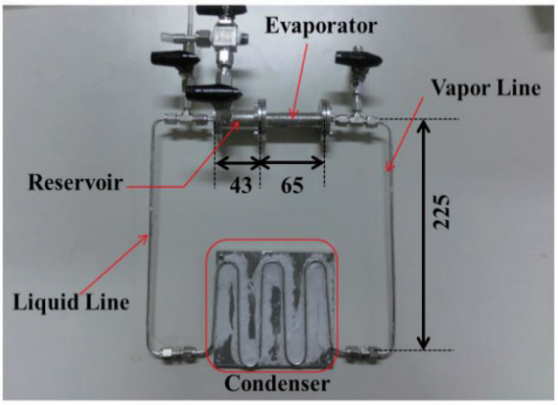


Fig.1 Miniature LHP

### 2.2 Attaching secondary wick

Fig.2 shows the schematics of attached secondary wicks. The material is stainless mesh (#300)

Corresponding author: Hiroki Nagai
*E-mail address*: nagai.hiroki@aero.mech.tohoku.ac.jp

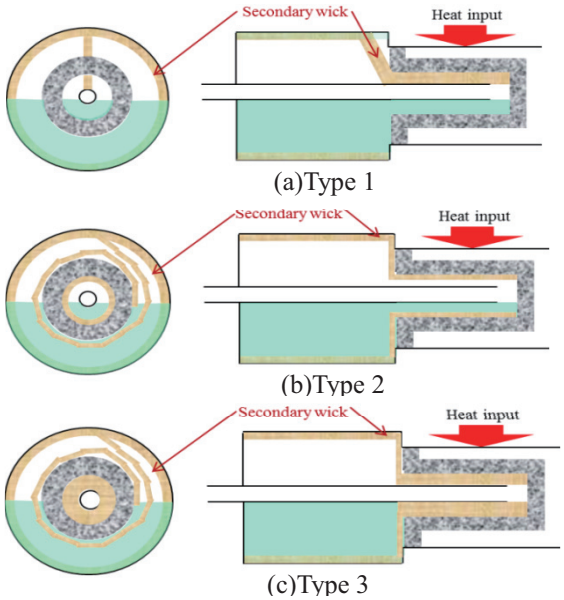


Fig.2 Attachment of secondary wicks

### 2.3 Experimental set up and condition

Temperature data was measured by thermocouples (T-type), and the experimental condition in this study is following:

・Working fluid: Acetone
・Temperature of cooling plate: 10 [deg *C*]
・Heat input: 5-100 [W]

## 3. Result and Discussion

### 3.1 Startup characteristics at low heat input

Fig.3 shows temperature time-histories during startup with a heat input of 5 W in conditions without secondary wick and with secondary wick (Type 1). In condition without a secondary wick, the evaporator temperature began increasing as soon as the evaporator was heated. However, there was a temperature difference in the vapor line. The temperature of vapor line decreased from the evaporator side to the condenser side. Therefore, it was considered that the amount of vapor generated was not sufficient to operate the LHP.

In contrast, with type 1 of secondary wick, the temperature difference in the vapor line was smaller, and the time taken for startup was shorter compared with the case without the secondary wick. In addition, the steady–state temperature was lower than that of in the condition without secondary wick. These results suggest that the secondary wicks improved the startup behavior

of LHPs. In condition with type 2 and type3 of secondary wicks, startup behaviors were similar to that with type 1 of secondary wick.

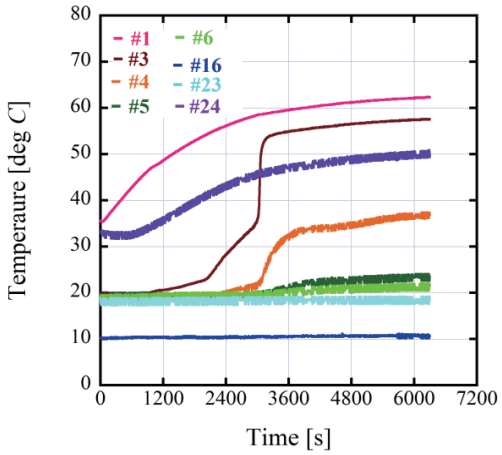


(a)Without secondary wick

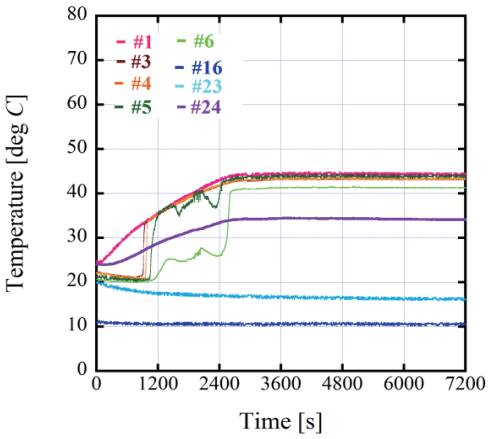


(b)With secondary wick (Type 1)

**#1: Evaporator** **#23: Liquid line**
**#3-6: Vapor line** **#24: Reservoir**
**#16: Condenser**

Fig.3 Startup characteristics at 5 W

### 3.2 Performance at high heat input

Fig.4 shows the temperature time-histories at high heat inputs in conditions without secondary wick and with type 1 and type 2 of secondary wicks. In conditions without secondary wick and with type 2 of secondary wick, LHP operated from 10 to 100 W. However, in the condition with type 1 of secondary wick, dry-out occurred at 80 W. Moreover, in the condition with type 3 of secondary wick, dry-out also occurred at 80 W. Hence, it was found that using certain types of secondary wicks had an adverse effect on the maximum heat input. In type 1 and 3, the vapor path from the evaporator core to the reservoir was blocked, thus it was considered that gathered vapor at the evaporator core prevented flow circulation.

### 4. Conclusion

In this study, we studied effects of three types of secondary wicks on LHP performance. Experimental results indicated that secondary wick improved startup process of LHP. However, certain types of secondary wicks had an adverse effect on maximum heat input.

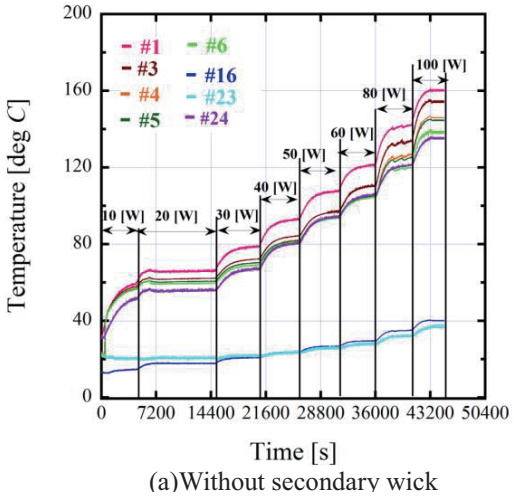


(a)Without secondary wick

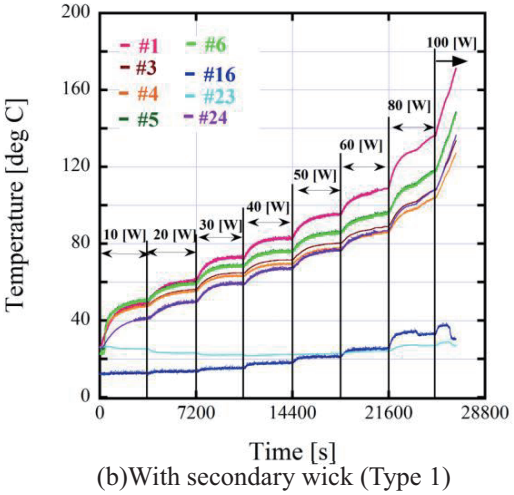


(b)With secondary wick (Type 1)

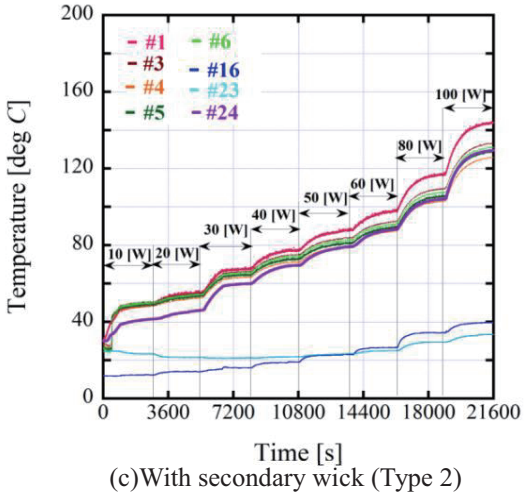


(c)With secondary wick (Type 2)

Fig.4 Operations at 10-100 W

Experimental results indicated that the vapor path from the evaporator core to the reservoir is necessary to operate LHPs. Thus, when a secondary wick is attached, it is necessary that a secondary wick does not block the vapor path from the evaporator core to the reservoir.

### References

[1]Yuki Mase, “Gravity Effect on Thermal Performance of Miniature Loop Heat Pipes”, *Master’s Thesis, University of Tsukuba, Japan* (2008).

Eleventh International Conference on Flow Dynamics
October 8-10, 2014, Sendai, Miyagi, Japan

# Numerical Investigation of the Effects of Initial Liquid-Vapor Distribution in Oscillating Heat Pipes

Takurou Daimaru[1], Shuhei Yoshida[1], Hiroki Nagai[1], Atsushi Okamoto[2], Makiko Ando[2], Hiroyuki Sugita[2]
[1]Department of Aerospace Engineering, Tohoku University
6-6-01, Aoba-Aza-Aramaki, Aoba-ku, Sendai, Miyagi, 980-8579, Japan
[2]Japan Aerospace Exploration Agency
2-2-1, Sengen, Tsukuba, Ibaraki, 305-8505, Japan

**ABSTRACT**

Effects of initial liquid-vapor distribution on startup behavior of Oscillating Heat Pipes (OHPs) were studied. A numerical model of OHPs was constructed to evaluate the effect. In the model, movement of liquid slugs was governed by pressure differences between each vapor plug and pressure drops in the tubes. Three conditions of initial liquid-vapor distributions were simulated. The results showed that initial conditions of the working fluid affected the startup behavior of OHPs. The trigger of oscillating was the different void fraction between turns.

## 1. Introduction

In recent years, Oscillating Heat Pipes (OHPs) have attracted attention as next-generation thermal control devices for spacecraft. OHPs consist of only meandering metal capillary tube and working fluid as shown in Fig. 1. In OHPs, liquid phase splits into several short slugs due to capillary force and vapor plugs exist between them. Once heat is applied into heating section, liquids start oscillating by pressure difference between turns. OHPs transport heat from the heating section to the cooling section with high conductivity by combination of sensible heat and latent heat.

For utilization in space, robustness of startup behavior is necessary, because high reliability of device is required. As one of the factors, which could affect startup behavior, initial liquid-vapor distribution is possible, because it can change easily due to micro gravity, vibration at launch and thermal environment in space [1]. Therefore, in this research, effects of initial condition of working fluid on startup-behavior of the OHP are evaluated by numerical simulation.

## 2. Numerical Model

The numerical model is a one-dimensional model along flow path. The inner flow regime is assumed to be slug flow. Fig. 2 shows the back and the front menisci locations for the *i*-th liquid and the main heat transfer path. The primary governing equations are the energy equations and the momentum equation for liquid slugs.

The energy equation of tube wall is a one dimensional heat equation with heat transfer with the ambient and working fluid.

$$c_{p,w}\rho_w A_w \frac{\partial T_w}{\partial t} = q_{ex} p_{out} - q_{w-f} p_{in} + k_w A_w \frac{\partial^2 T_w}{\partial z^2} \quad (1)$$

The energy equation for liquid slugs is also one-dimensional equation considering heat transfer with tube wall.

$$\left[ c_{p,l}\rho_l A_{cr} \frac{\partial T_l}{\partial t} = q_{w-f} p_{in} + k_l A_{cr} \frac{\partial^2 T_l}{\partial z^2} \right]_i \quad (2)$$

Corresponding author: Takurou Daimaru
*E-mail address*: daimaru.takurou@aero.mech.tohoku.ac.jp

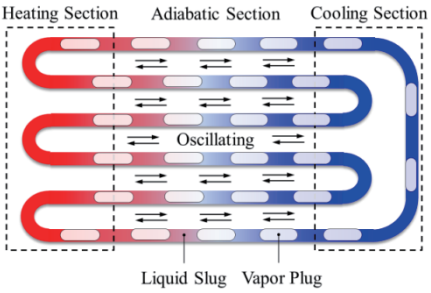


Fig. 1 Schematic of Oscillating Heat Pipes.

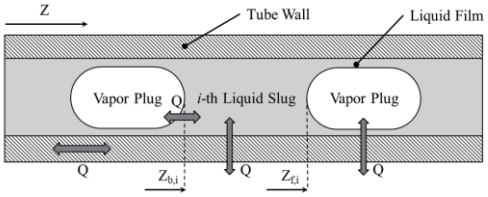


Fig. 2 Schematic of flow pattern and heat transfer path.

Temperature within each vapor plug assumed to be uniform. Temperature is calculated by energy balance equation.

$$dQ_{v,j} = q_{w-f} p_{in}\left(z_{f,j} - z_{b,j}\right) + k_l A_{cr} \left.\frac{\partial T_l}{\partial z}\right|_{z_{f,i-1}} - k_l A_{cr} \left.\frac{\partial T_l}{\partial z}\right|_{z_{b,i}} \quad (3)$$

$$\left[ T_v^{t+1} = T_v^t + \frac{dQ_v}{c_{v,v}\rho_v V_v} \right]_j \quad (4)$$

Movement of liquid slugs is governed by pressure difference between adjacent vapor plugs and pressure loss in tubes.

$$\left[ \frac{d\dot{m}_l}{dt} = A_{cr}\left(dP_v - dP_\tau - dP_K\right) \right]_i \quad (5)$$

The moving distance of the liquid slug is calculated from mass flow rate of the liquid slug at each time step.

$$\dot{m}_i^{t+1} = \dot{m}_i^t + d\dot{m}_i \quad (6)$$

$$\Delta z_i = \frac{\dot{m}_i^{t+1}}{A_{cr}\rho_{l,i}} dt \quad (7)$$

Table 1. Major specifications of OHP.

| | | |
|---|---|---|
| Material of tube | Copper | |
| I.D. / O.D. | 2 / 3 | [mm] |
| Number of turns | 16 | |
| Length of evaporator section | 100 | [mm] |
| Length of adiabatic section | 160 | [mm] |
| Length of condenser section | 100 | [mm] |

Table 2. Simulation Conditions.

| | | |
|---|---|---|
| Working fluid | Ethanol | |
| Charging ratio of fluid | 55 | [%] |
| Inclination angle | 0 | [ ° ] |
| Heat input | 80 | [W] |
| Temperature of cooling plate | 20 | [°C] |

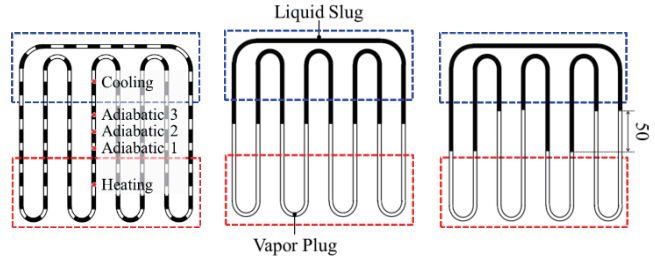


(1) Equal distribution of 100 slugs. (2) Localization in cooling section. (3) Localization with gaps.

Fig. 3 Conceptual diagrams of initial distribution.

## 3. Simulation Condition

Table 1 shows major specifications of simulated OHP. Also, simulation conditions are shown in Table 2. As condition of initial distribution, three patterns are simulated as shown in Fig. 3.

## 4. Results and Discussion

Temperature histories of each condition of initial distribution are shown in from Fig. 4 to 6. In results, temperature oscillation occurred in the cases (1) and (3). In these cases, temperature in heating section converged at approximately 90 ~ 100 [°C]. These results indicate that oscillating of liquids occurred and OHP transported heat from the heating section to the cooling section successfully. However, temperature oscillation did not occur in the case (2) and temperature increased up to 240 [°C]. This result means that OHP could not startup, when liquid slugs completely localize in the cooling section without gaps. These different startup behaviors can be caused by void fractions. Void fraction means the ratio of the vapor volume to the total volume. The difference of initial distribution between the case 2 and 3 is the presence of gaps in liquid slug's positions. When liquid slugs are localized in the cooling section without gaps (case 2), the void fractions are same in each turn completely. On the other hand, when there are gaps in positions of liquid slugs (case 3), the void fraction has different values in each turn. In this case, difference of pressure in each vapor should be generated, because heat which enters vapors is different values. Therefore, liquids are driven by pressure difference. On the other hand, in the case 1, short liquid slugs started merging right after heating and formed long liquids which are different length individually. Thus, difference of void fractions was caused spontaneously by merging in the case 1 and the OHP could start up.

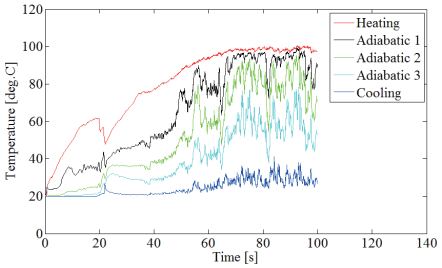


Fig. 4 Temperature history of case (1).

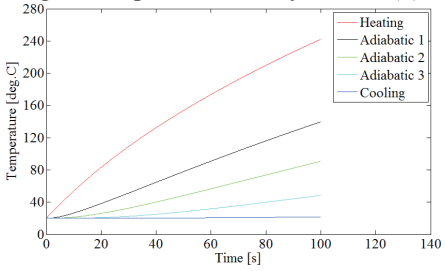


Fig. 5 Temperature history of case (2).

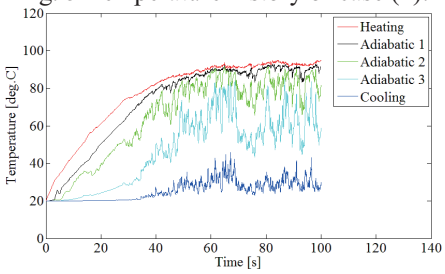


Fig. 6 Temperature history of case (3).

## 5. Concluding Remarks

Effects of initial liquid-vapor distribution on startup behavior were investigated. Results showed that difference of void fraction between turns is the trigger oscillating of liquid slugs.

## Nomenclature

| | | |
|---|---|---|
| $A$ | : cross section | [m$^2$] |
| $c_p$ | : specific heat at constant pressure | [J/K/kg] |
| $c_v$ | : specific heat at constant volume | [J/K/kg] |
| $dP$ | : pressure gradient | [Pa/m] |
| $\dot{m}$ | : mass flow rate | [kg/s] |
| $p$ | : perimeter | [m] |
| $z$ | : axial location | [m] |

### *Subscripts*

| | |
|---|---|
| $b$ | : back menisci |
| $cr$ | : channel cross section |
| $f$ | : front menisci, working fluid |
| $i$ | : liquid slug index |
| $j$ | : vapor plug index |
| $K$ | : turn |
| $l$ | : liquid slug |
| $v$ | : vapor plug |
| $w$ | : tube wall |
| $\tau$ | : shear stress |

## References

[1] A. Okamoto, M. Ando, H. Sugita, *Proc. 17th Int. Heat Pipe Conf.*, (2013), Paper No. 115.

# Combustion Characteristics of Ethylene in a Dual-Mode Combustor

Kiyoshi Nojima[1], Sadatake Tomioka[2], Noboru Sakuranaka[2]
[1]Tohoku University, Department of Aerospace Engineering
Sendai, Miyagi 980-8579, Japan
[2]Japan Aerospace Exploration Agency
Kakuda, Miyagi 981-1525, Japan

**ABSTRACT**

Combustion tests were carried out for a dual-mode combustor with ethylene fuel and hydrogen fuel in a direct-connect wind-tunnel facility to acquire the basic data for performance estimation of a hydrocarbon-fueled dual-mode combustor. At a low fuel equivalence ratio, the combustion efficiency of ethylene could be estimated from the incomplete combustion loss derived from gas sampling measurement.

## 1. Introduction

A combined cycle engine is one of promising candidates of the propulsion system for a more reliable and lower cost launch vehicle than rocket systems. A well-known combined cycle engine is the rocket-based combined cycle engine (RBCC). In RBCC engines, both ramjet-mode (i.e., dual-mode) and scramjet-mode operations are vital parts to reduce the onboard oxygen consumption. As the incoming flow speed to the combustor is supersonic, and thus, residence time of the fuel in the combustor is of the order of milliseconds, the key technological challenges of the engine are to attain high fuel-air mixing, ignition and sufficient flame holding in high-speed flows. In many studies, hydrogen, which are high reactive, contain high energy per unit mass and have high heat capacity for use as coolant, was used as fuel for the ramjet (scramjet) engine. However, hydrogen has a lower energy density than typical storable hydrocarbons, and it is difficult to store and handle on a routine basis. In contrast, hydrocarbon fuels package better, exhibiting a greater energy per unit volume, so that they require less room onboard than hydrogen fuel for an equivalent amount of energy [1]. And now, to model the performance of a dual-mode scramjet engine, the heat release distribution must be accurately predicted, because the heat release have an influence on the thermal choking point, the profiles of pressure and Mach number, etc. Tomioka et al. carried out dual-mode combustion tests with hydrogen fuel injection in diverging section and a one-dimensional calculation to estimate combustion efficiency [2]. In hydrogen fuel, the combustion efficiency can be expressed as fuel consumption rate, because most of combustion products of hydrogen fuel are water vapor. On the other hand, the combustion products of hydrocarbon fuel contain many intermediate products, so the combustion efficiency expressed as fuel consumption rate may overestimate the heat release.

In our present study, we have investigated the combustion characteristics of ethylene to estimate performances of a dual-mode combustor. We have also investigated the heat flux distribution from the combustor to estimate cooling requirement.

Corresponding author: Kiyoshi Nojima
*E-mail address*: nojima@scrj.mech.tohoku.ac.jp

## 2. Experimental Apparatus and Measurements

### 2.1 Experimental Apparatus

We used a blowdown type wind-tunnel facility, shown in Fig. 1. A high-enthalpy airflow with total temperature $T_0$ of 1950 ± 50 K and total pressure $P_0$ of 0.96 ± 0.02 MPa was supplied from a vitiation air heater. The vitiated airflow was accelerated to Mach 2.44 through a rectangular nozzle with the exit cross-section area of 51 mm high and 94.3 mm wide.

A rectangular combustor was directly connected to the nozzle. The combustor was divided into two sections; a 742 mm long constant-area section where cross sectional area remained constant from nozzle exit and 635 mm long diverging section. The diverging section had half expansion angle of 1.66 deg. in its height direction and constant width. The resulting exit area of the diverging section was 87.8 mm high and 94.3 mm wide. The combustor was paced in the atmosphere, and the combustion flow was exhausted to atmospheric pressure. As shown in the figure, the streamwise x coordinate was from the onset of the diverging section (defined as x = 0). The y coordinate was in the spanwise direction from the center of the combustor, and the z coordinate was in the height direction from the center of the combustor.

The combustor was equipped with an injector block assembly and a flame-holding device (cavity) in each of the constant-area section and the diverging section. These devices were installed on opposite walls of each section. In the present study, the injector-side in the constant area section was called as the cowl side and the

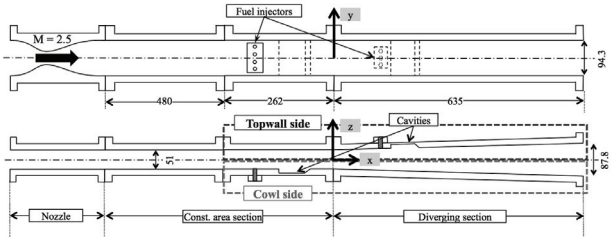


Fig. 1 Schematic diagram of facility and combustor.

Table. 1 Injectors and cavities configuration

| | Injector | | | Cavity | | | |
|---|---|---|---|---|---|---|---|
| | location, mm | Diameter, mm | Geometry | Upstream-end step location, mm | Depth, mm | Length, mm | Aft angle, deg. |
| Topwall | 129.5 | 2 or 3 | 3 circular holes | 170.5 | 11 | 70.6 | 22.5 |
| Cowl | -186 | 3 | 4 circular holes | -131 | 15 | 76 | 30 |

injector-side in the diverging section was called as the topwall side. The detailed shape of these injectors and cavities was shown in Table 1.

For comparison, room temperature, gaseous ethylene or hydrogen was injected perpendicularly though sonic orifice on the injector to the crossflow. In the present study, flow restrictors of a converging-diverging shape ware installed within the feed line to control fuel flow rate. Fuel flow rate (indicated with bulk equivalence ratio $\Phi$ in the present study) was monitored with a sharp-edge orifice flowmeter.

### 2.2 Measurements and Data Reduction

We measured wall pressure $P_w$ on both the topwall side and the cowl side using electrical scanning-type pressure sensors. As the wall pressure distributions on the topwall side and cowl side walls showed little discrepancies, those on the topwall side wall were shown and were used for the following data reduction in the present study.

We sampled gas at the exit of the combustor using a water-cooled sampling probe rakes to evaluate the local equivalence ratio and combustion efficiency. The probe ensured reaction quenching during the sampling process. Sampling probes rakes had 10 mm interval and nine probes in the height z direction. Gas sampling was carried out at three-five positions in the width y direction (y = ±42, ±21, 0). We also measured the pitot pressure at the same position as sampling points.

The sampled gases were analyzed with gas chromatography, which determined the mole fraction of $H_2$, $N_2$, $O_2$, CO, CO2 and $C_2H_4$. The sampled gas composition derived the local equivalence ratio $\phi$ including the deduced reacted fuel from the conservation of atoms and on the assumption that the molar concentration of nitrogen is uniformity. The local combustion efficiency $\eta_c$ was derived from the incomplete combustion loss $\Delta H$ (defined as the difference of lower heating value of supplied fuel $H$ and actual combustion heat release). These local values were representative value in divided area $dA$ around the sampling points. Note that the measured compositions were time-averaged values over the sampling duration (3.0 s), and were spatially averaged values over the probe inlet area (diameter of 0.3 mm).

We measured wall heat flux on both the topwall side and the cowl side using circular-foil heat flux transducers: Gardon gages sensors. Their sensors were mounted flush with the combustor inner wall.

### 3. Results and Discussion

Figure 2 shows the distributions of wall pressure and heat flux with ethylene fueled at $\Phi_1 = 0.27$ and hydrogen fueled at $\Phi_1 = 0.25$. With ethylene fueled, the pressure level downstream of the injector location was almost the same as that with hydrogen fueled, whereas the pressure level upstream of the location with ethylene injection resulted in a slightly lower than that with hydrogen injection. The heat flux level with ethylene injection was almost the same as that with hydrogen injection. In the diverging section, the pressure and heat flux decreased monotonically.

Figure 3 shows relation between the local fuel equivalence ratio and the local combustion efficiency at each probing location. The relation with ethylene injection was almost the same as that with hydrogen injection. The local combustion efficiency decreased with the increasing local equivalence ratio. As the fuel flow rate was controlled to match heat release for complete combustion, the same combustion efficiency resulted in the same heat release. This result was confirmed by the same pressure and heat flux distribution.

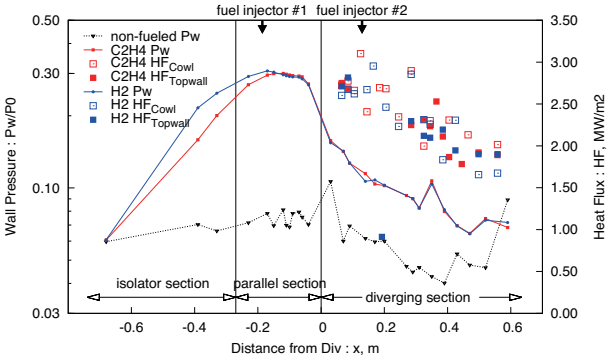


Fig. 2 Distributions of wall-pressure and heat flux.

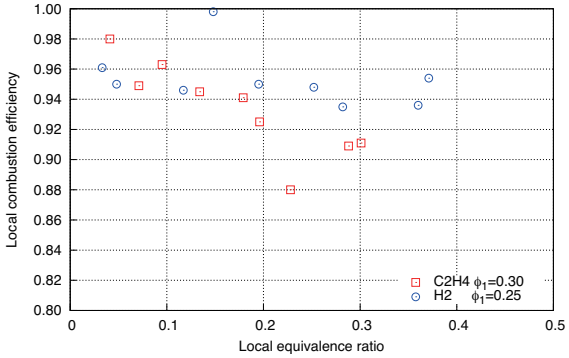


Fig. 3 Relation between local fuel equivalence ratio and local combustion efficiency.

### 4. Conclusion

Combustion tests were carried out with a direct connected dual-mode combustor with ethylene fuel and hydrogen fuel.

The basic data to estimate performance of a hydrocarbon-fueled dual-mode combustor was acquired.

The combustion efficiency of ethylene could be estimated from the incomplete combustion loss derived from gas sampling measurement.

### References


[1] Waltrup, P., J., "Upper Bounds on the Flight Speed of Hydrocarbon-Fueled Scramjet-Powered Vehicles," *Journal of Propulsion and Power*, Vol. 17, No. 6, (2001) 1199-1204.

[2] Tomioka, S., Kouchi, T., Masumoto, R., Izumikawa, M., Matsuo, A., "Supersonic Combustion with Supersonic Injection Through Diamond-Shaped Orifices," *Journal of Propulsion and Power*, Vol. 27, No. 6, (2011) 1196-1203.

# Mixture Evaluation in a RBCC Engine at Scramjet Mode

Ryosuke Nakano[1], Sadatake Tomioka[2], Kenji Kudo[2], Atsuro Murakami[2], Shuichi Ueda[2]
[1]Department of Aerospace Engineering, Tohoku University
980-8579, Sendai, Japan
[2]JAXA-Kakuda Space Center
981-1525, Kakuda, Japan

**ABSTRACT**

The purpose of this study is to improve the mixing efficiency in RBCC engine operating in hypersonic flow at of the rocket exhaust and the airflow, and to evaluate the mixing enhancement performance. In this experiment, gas sampling and Schlieren measurement was carried out to investigate the effect of slit provided in the rocket part. The resulting mixing performance in the case with slit was better than in the case without slit.

**Nomenclature**

$U$ : velocity
$M$ : Mach number
$M_c$ : convective Mach number
$p$ : pressure
$\rho$ : density
$X$ : Stream wise location from the rocket base

*Subscripts*

0 : stagnant
a : air flow
r : rocket exhaust

## 1. Introduction

Rocket Based Combined Cycle (RBCC) engine is expected to be the most effective propulsion system for booster stage of launch vehicles. RBCC engine combine elements of rocket and airbreathing propulsion into a single engine, and are capable of multi-mode operations including ejector mode (flight Mach number 0~3), ramjet mode (flight Mach number 3~7), scramjet mode (flight Mach number 7~11) and rocket mode (flight Mach number 11~). The subject of this research is to accomplish combustion in scramjet mode operation of RBCC engine. In the scramjet mode operation, the incoming airflow and the residual fuel in the rocket exhaust run downstream at high speed. Therefore, accomplishment of combustion is very difficult due to insufficient combustion velocity. This is the major problem of the scramjet mode operation.

In the previous studies, the combustion test was carried out in the Mach 11 flight condition by Tomioka, Kobayashi, and Takagi [1][2][3], but the combustion efficiency between incoming air and the residual fuel in the rocket exhaust was low. The cause was concluded that mixing efficiency of the airflow and the residual fuel is low.

The purpose of this study is to improve the mixing efficiency of the rocket exhaust and the airflow, and to evaluate the mixing enhancement performance.

## 2. Test apparatus and Measurements

Figure 1 shows schematics of the test apparatus. Experiments were carried out in the M2.3 blow-down wind tunnel with a rectangular test section.

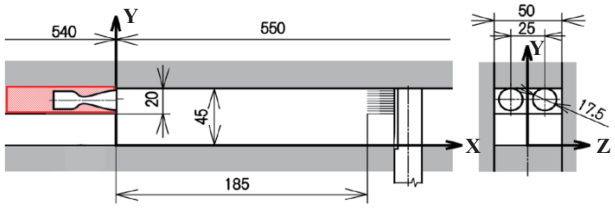


Fig.1. Mixing study apparatus

Room temperature air was accelerated to Mach 2.3 though a rectangular nozzle. Rocket exhaust was simulated with room temperature nitrogen.

Rocket nozzle Mach number was 4. The airflow and the rocket exhaust conditions were fixed at total pressure of 385kPa, 4000kPa. Table 1 show mixing parameters in this test.

Table.1 Mixing parameters

| | |
|---|---|
| $U_a/U_r$ | 0.81 |
| $\rho_a/\rho_r$ | 0.58 |
| $M_c$ | 0.32 |
| $p_a/p_r$ | 1.15 |
| Shear growth rate (Eq.5 [4]) | 0.028 |

In this experiment, the effect of slit provided in the rocket part (with slit) was investigated to compere with the base rocket part (without slit). Figure 2 shows the design of slit provided in the rocket part. This rocket part was composed of three slits which were expansion ramps and two rockets. The ramp angle was 14 deg, and the thickness of slit was 3 mm (at side wall) and 6 mm (at Z = 0).

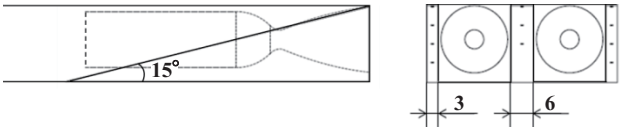


Fig.2 Rocket part with slit

Gas sampling was carried out at (X : Y : Z) = (185 mm : 2～44mm : 0, 12.5, 19 mm) downstream of the using gas chromatography. As for the data reduction, 1) Local rocket nitrogen to air mole ratio was deduced

Corresponding author: Sadatake Tomioka
*E-mail address*: sadatake.tomioka@jaxa.jp

from measured composition. 2) Local rocket gas to air mole ratio was normalized with overall rocket to airflow mole flow ratio. 3) Hydrogen mole concentration was calculated assuming water vapor and hydrogen was contained in the exhaust 2:1 and equivalent ratio of the single rocket exhaust was 1.5. Mass flux was calculated based on pitot pressure and wall pressure data as well as the measured composition. Then the mass-flux-weighted local fuel fraction was integrated over the measured cross-section to attain average over the cross-section.

Wall pressure distributions were measured by using a scanning type sensor (Scannivalve, range; 350 kPa, error; ± 1.4 kPa) and Schlielen images were taken.

## 3. Results and discussion

### 3.1 Schlieren Photographs

Figure 3 shows two Schlieren photographs at X = -75~195mm, and the flow direction is from left to right.

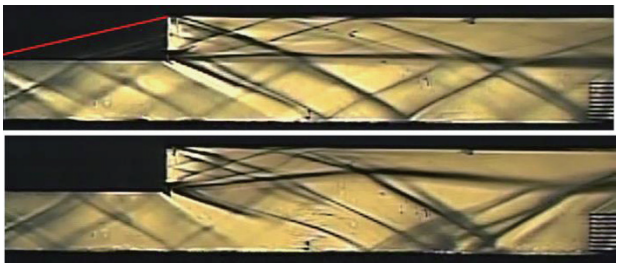

Fig.3. Schlieren photographs in case with slit (upper) and without slit (lower)

In the case with slit, the rocket exhaust is injected straight. The shear layer also grew along the downstream. Further, the expansion wave occurred from the X = - 80 mm was also observed. On the other hand, in the case without slit, the rocket exhaust is bent in the vicinity of X = 90 mm. In the case without slit, the nozzle exit was a full-back step shape, so the static pressure of the airflow became low in the rocket nozzle exit. And because the rocket exhaust became under-expansion, the static pressure of the rocket exhaust was much lower than the airflow. Meanwhile in the case with slit, because the airflow entered the slit and reached the rocket nozzle exit, the rocket exhaust became a state close to correct expansion.

From the Schlieren photographs, there is almost no difference in the thickness of the shear layer.

### 3.2 Molar Concentration Distribution

Figure 4 shows the molar concentration distribution with slit (right side of the figure) and without slit (left side of the figure). In the case without the slit, the rocket exhaust are distributed overall in the Y = 25 mm or more. On the other hand, in the case with the slit, region of low concentration can be found in the rocket side wall and Z = 0 mm. This is because the airflow entered from the slit. Because the airflow got into the slit on both sides, the expansion of rocket exhaust was suppressed. In addition, the concentration gradient became tough at Y = 25 ~ 30 mm. The effect of the streamwise vortices generated from expansion ramp through the baroclinic torque mechanism was hardly observed.

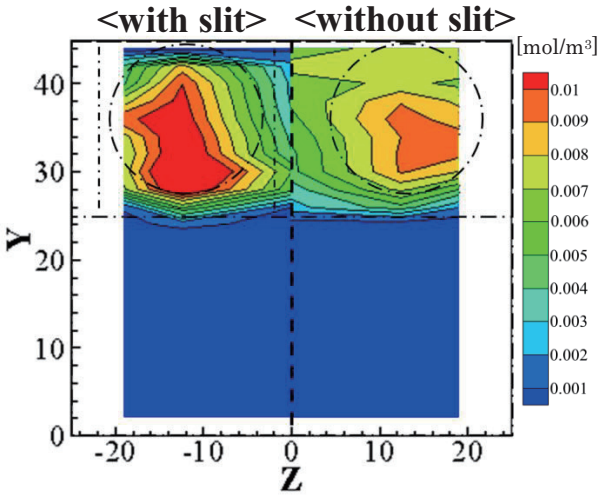


Fig.4. Comparison of concentration distribution (left: with slit right: without slit)

### 3.3 Mixing Efficiency

The resulting mixing efficiency was 34.4% in the case with slit and 15.4% in the case without slit. From the Schlieren photographs, there is no difference in the thickness of the shear layer. From the results of gas sampling, the airflow entered around the rocket exhaust. So, it was suggested that the mixing efficiency was improved in the case with slit as compared to without slit resulted from the contact area with the airflow increased.

## 4. Conclusions

1) In the case with slit, the shear layer grew straight. Meanwhile, in the case without slit, the shear layer grew bent.

2) The airflow entered slit prevented the rocket exhaust from expanding, but increased the contact area with the airflow.

3) In case with slit, the mixing efficiency was improved more than twice better than without slit.

## References

[1] S. Tomioka, K. Kenji, K. Kato, A. Murakami, and T. Kanda, *41st. AIAA/ASME/SAE/ASEE Joint Propulsion Conference and Exhibit*, (2005), 4284.

[2] S. Tomioka, R. Kobayashi, A. Murakami, S. Ueda, T. Komuro, and K. Itoh, *Transactions of the Japanese Society for Artificial Intelligence, Aerospace Technology Japan*, Vol. 10, (2012) 55－61.

[3] T. Komuro, S. Tomioka, S. Takagi, M. Takahasi, S. Ueda, and K. Itoh, *29th International Symposium on Space Technology and Science*, (2013), a－38.

[4] D. Papamosh, *AIAA Jornal*, 31(1993) 1643－1650.

# Development Of The Fuel Heating Device For Component Test Of Aerospace Propulsion Systems

Mitsuhiro Soejima[1], Kiyoshi Nojima[1], Sadatake Tomioka[2], Noboru Sakuranaka[2]
[1]Tohoku University,
6-6 Aoba, Aramaki, Aoba-ku, Sendai, Miyagi, 980-8579, Japan
[2]Japan Aerospace Exploration Agency,
1, Koganezawa, Kimigaya, Kakuda, Miyagi, 981-1525, Japan

**ABSTRACT**

For the future space transporter, using a hydrocarbon (HC) fuel is proposed to reduce the propellant tank volume and the cost. So, the component tests of the next generation space propulsion systems using HC fuels are running. However, these tests are run using the ordinary temperature HC fuels. In actual system, the fuels are heated up by regenerative cooling combustor. Therefore, some of the component tests should use the heated HC fuel. We developed a fuel heating device for these tests. We report in this paper that the result of the test run.

## 1. Introduction

The fully reusable spaceplane is proposed as a next generation space transporter; because they may reduce the cost carrying the cargo to the orbit. The spaceplane requires closing the system without external tank or boosters. Therefore, the propulsion system need to reduce the propellant mass and tank volume compared with conventional rocket engine using LOX/LH2.

JAXA suggest that Rocket Based Combined Cycle (RBCC) Engine using LOX/Hydrocarbon fuel for the propulsion system of the spaceplane.[1] Ethanol is regarded as the first choice for the fuel, because it has some advantages to the other fuels, such as the better density specific impulse, non-toxic, and storable at normal temperature.

For this reason, the variety of component tests of the propulsion systems are practiced.[2] Some of these test should use the fuel at high temperatures and pressures. However, it was difficult to supply such high temperature fuel for the component test because of the fuel feed system is required enormous thermal capability of 300 kW class to elevate fuel temperature.

Therefore, we developed a fuel heating device for component test of aerospace propulsion systems.

In this paper, we describe the results of test run of our fuel heating device.

## 2. Heating device design

The target performance of the fuel heating device is shown in table1. The fuel pressure and temperature were determined based on the ethanol's critical point. The fuel mass flow rate and duration time of supply were determined based on some component test conditions of scramjet combustor.[3]

We designed the heating device using combinations of two heating methods.

- Thermal storage heater(Storage heater)
- Electric heated tube

The first has the most of heat load. And, the latter has compensation for the fuel temperature change by the temperature drop of the first.

The storage heater is a copper block (a cubic with one side 250 mm). The fuel channel of storage heater is constructed into the block. The channel inner diameter is 12 mm and the length is about 6 meters. The block mass is about 130 kg, and the heat capacity is 50 kJ/K.

The electric heated tube is a 3 meters length 1/2inches copper tube with 6 × 1.2 kW electric heaters. These heaters are controlled to maintain the set temperature of the tube.

This system pressurizes the fuel by compressed nitrogen gas. And, the relationship between the fuel flow rate and pressure are controled by the throttling orifice.

The priming valve and orifice operate in advance of the main valve, and supplies the storage heater a small amount of fuel. Thereby, the downstream of main valve are pre-pressurized to prevent excessive fuel is supplied.

Table 1 Target capacity of the heating device

| | | |
|---|---|---|
| Fuel type | | Ethanol, Kerosene, etc. |
| Fuel Pressure | MPa | > 7 |
| Fuel Temperature | K | > 550 |
| Fuel flow rate | kg/s | 0.05~0.200 (Ethanol) |
| Duration of supply | sec | > 10 |

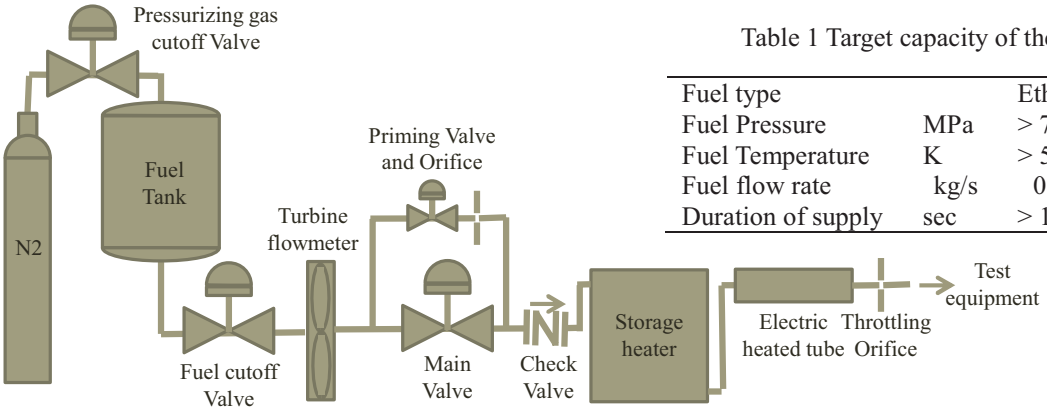


Fig.1 Description of fuel heating device

Corresponding author: Mitsuhiro Soejima
*E-mail address*: soejima@scrj.mech.tohoku.ac.jp

## 3. Results and Discussion

We ran the heating device at some different condition using ethanol. In these test, the fuel temperature and pressure were measured upstream and downstream of the throttling orifice. The fuel flow rate was measured using turbine flow meter.

Figure 2 show the principal result of the test run under supercritical condition (heated ethanol was supplied to 80 seconds from 70 seconds). In this case, we aimed to make supercritical condition ethanol. The representative heating device setting data is shown table 2. Comparing with the ethanol critical point (6.3 MPa, 513 K), the exit condition of the test is 6.9 MPa, 520 K, therefore, we determined our fuel heating device achieved the goal. However, the fuel mass flow rate changed about 10 % in the run. We estimated that the storage heater's temperature drop caused the flow rate change. That is, the decrease of the flow resistance to attendant on cubical expansion by the heating caused the flow rate increasing in the test.

Figure 3 show the result of a test under subcritical condition (heated ethanol was supplied to 78 seconds from 68 seconds). The heating device setting data is shown table 3. In this case, the fuel pressure was stable, too. On the other hand, the fuel mass flow rate fluctuated somewhat. We estimated that was due to boiling flow in the electric heated tube.

After this, we investigate an improvement plan of these mass flow rate changes.

## 4. Concluding Remarks

- The heating device achieved the main goal to feed ethanol at supercritical condition.
- Ethanol temperature and pressure was stabled in the test run under supercritical condition.
- Ethanol mass flow rate increased gradually in the test run under supercritical condition.
- Using ethanol at subcritical pressure, the heating device worked without pressure oscillation under subcritical condition.
- Ethanol mass flow rate fluctuated somewhat under subcritical condition.

## References


[1] Kanda T. and Kudo K., Conceptual Study of a Combined-Cycle Engine for an Aerospace Plane, *Journal of Propulsion and Power* Vol. 19, No. 5, September–October (2003).

[2] Masao Takegoshi at.el, Effect of Triangular Fins on Critical Heat Flux of Ethanol , *47th AIAA/ ASME/ SAE/ ASEE Joint Propulsion Conference & Exhibit*, California, (2011).

[3] Y. Suzuki, K. Nojima, S. Tomioka, N.Sakuranaka, Heat Flux Distribution of Ethylene Fueled Combustion in Supersonic Flow, *AJCPP2014*, Korea.


Table 2 Heating device setting(Supercritical condition)

| | | |
|---|---|---|
| Fuel tank set pressure | MPa | 7.5 |
| Storage heater initial temperature | K | 520 |
| Electric heated tube temperature | K | 520 |
| Throttling orifice diameter | mm | 2.0 |

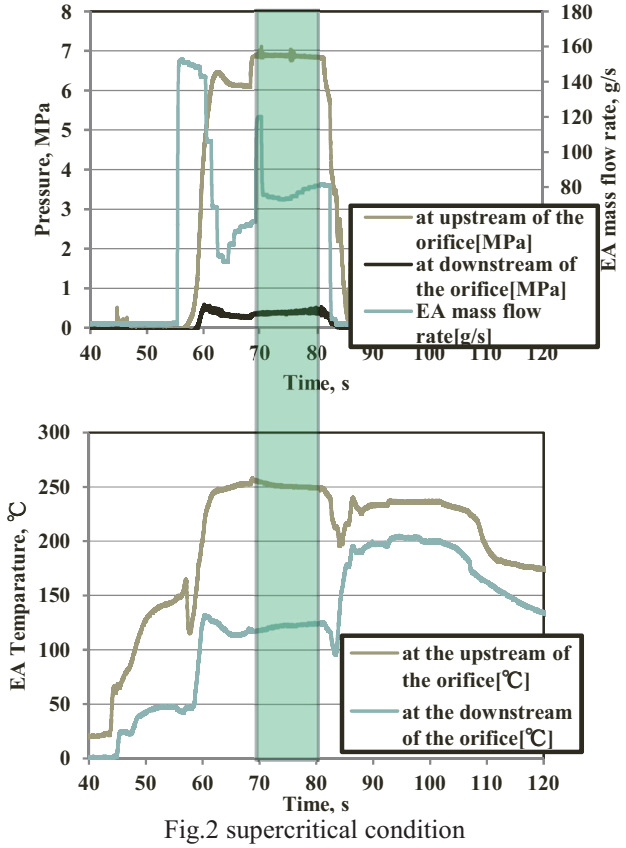


Fig.2 supercritical condition

Table 3 Heating device setting(Subcritical condition)

| | | |
|---|---|---|
| Fuel tank set pressure | MPa | 4.0 |
| Storage heater initial temperature | K | 460 |
| Electric heated tube temperature | K | 530 |
| Throttling orifice diameter | mm | 2.0 |

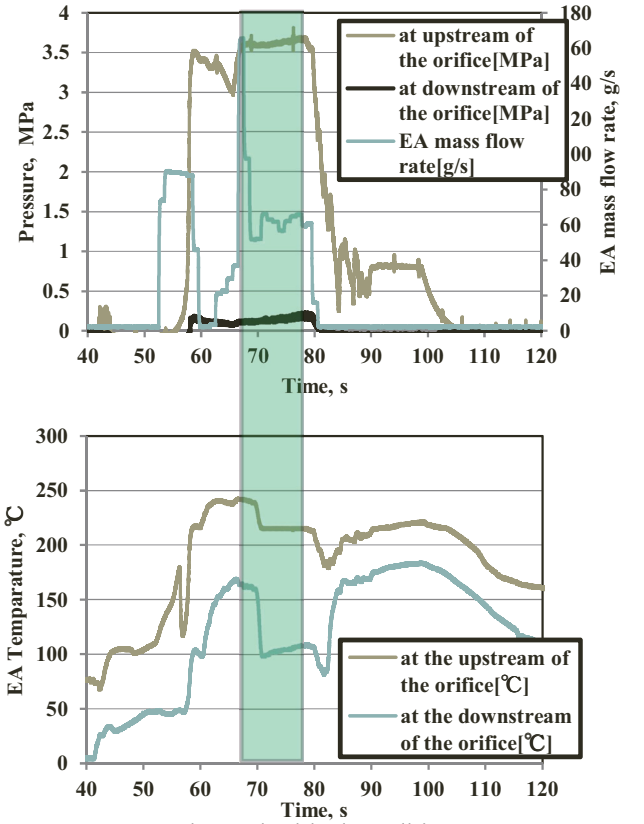


Fig.3 subcritical condition

# Examination of Options for Space Disposal of Nuclear Waste

C. Park[1], W. S. Jeong[1], J. Jerin[1], D. Lee[1], H. J. Kim[1], H. T. Kim[1], and N. Purushothaman[1]
[1]Korea Advanced Institute of Science and Technology
291 Daehak-ro, Yuseong-gu, Daejeon, 305-701, Republic of Korea

**ABSTRACT**

A proposal is made that the radioactive nuclear waste material be disposed of into space. NASA proposed that this technology be used for the disposal of nuclear waste. We propose this idea again. Strongly radioactive nuclear waste (fission products) will be extracted and packaged to form a spherical ball. The package will consist of steel casing, heat-shield, graphitic foam and thermopile junction. The package will be launched from the equator, and delivered either to geo-lunar $L_4$ or $L_5$. In case an asteroid threatens, an orbital transfer vehicle will be needed

## 1. Introduction

Nuclear power plants produce toxic radioactive materials that need to be disposed of to somewhere for thousands of years. In essence approximately 4.6% (0.5% hot elements and 4.1% fast decayer) of the mass of the spent fuel becomes highly radioactive waste and must be disposed of semi-permanently. One batch of such waste weighs typically 23kg.

The preferred method of disposal of this waste material is to store underground. However, for certain countries, such as Korea or Japan, there are no such suitable sites. Here in this work, we propose that the radioactive material be launched into space, and taken to and kept in a stable lunar orbit or on the planet Venus.

## 2. Proposed Method

The spent fuel will be chemically processed to extract the radioactive material (fission products). Fission products will be packaged inside a strong metal casing such as Inconel-625. The casing having waste will be further covered with a thick heat-shield material made of carbon-carbon composite. Also, it will be further surrounded by a layer of light graphitic foam about 0.5m thick to provide a large drag that will reduce ground impact speed. The casing will have to withstand the accidental reentry into Earth's atmosphere to an entry speed of 12 km/s or more and for entry angles of $0 \sim 90^\circ$. Not only that the package must survive the reentry flight but also they must survive the ground impact. Such casing will consequently survive collisions with space objects.

The launching will preferentially be carried out from an artificial island floating over the Pacific Ocean, located along the equator. The launch direction will be due east, so that the flight path will along the equator.

Two options are being considered for the site for disposing the nuclear waste: one of the two lunar Lagrangian points $L_4$ and $L_5$, or the planet Venus. As is well known, the lunar Lagrangian points $L_4$ and $L_5$ are energetically stable locations. The spaces they occupy are very large. Out of the two points, $L_4$ and $L_5$, only one will be used for nuclear waste dump. The other will be reserved for other uses. The planet Venus is known to be hellish place: atmospheric pressure is some 60 times larger than that on Earth, temperature exceeds 200 ºC, and the atmosphere consists of carbon-dioxide and sulfuric acid. There should be no opposition to the idea of dumping hazardous material on this planet.

Corresponding author: H. J. Kim
*E-mail address*: consolike@kaist.ac.kr

### *Package Design*

In case of malfunction during launch and inadvertent mission abort, in which the waste package falls to the ground, radioactivity should not leak under all circumstances. The package should also withstand ground impact and the harsh seabed environments.

The first stage of package design is shielding analysis. Following the prevailing nuclear safety standard, the radiation level must not exceed 2 mSv/h at any point and 0.1 mSv/h at 2m away from the object. This requirement results in a design of the metal shield thickness and the overall weight of the package (excluding the light-weight foam) shown in table 1. As shown, the required thickness ranges from 21 cm to 24 cm.

Table 1. The mass and thickness of package

| Waste(kg) | Payload(kg) | Thickness(cm) |
|---|---|---|
| 100 | 2219.2 | 24 |
| 400 | 4515.9 | 25.68 |
| 800 | 5344 | 22.5 |
| 4000 | 13841.8 | 21.54 |
| 10000 | 26445 | 21.45 |
| 20000 | 44238.4 | 21.11 |

According to the thickness obtained from shielding calculation, the ground impact and seabed test should be performed. Fig. 1 represents the impact test results of the nuclear waste package made by NASA [1].

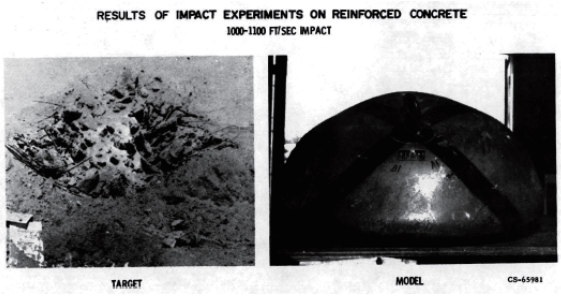


Fig. 1 Impact experiments on reinforced concrete.

***Dump Site management***

When the $L_4/L_5$ site is filled with many such nuclear waste packages, it is desirable that they would be at one location and form a single body. This can be achieved by magnetizing each package. Each package will be weakly magnetized using the electrical power generated onboard the nuclear waste using its heat by a radioisotope thermoelectric generator(RTG).

In case an asteroid comes by and is predicted to collide with this pile of waste packages, a standing-by orbital transfer vehicle can move the pile out of the way of the collision. The towing will be accomplished by an umbrella-shaped-structure. Mission velocity $\Delta V$ needed for this operation should be only of the order 0.1 m/s. The radius of structure is 5m during towing the pile. Fig. 2 shows the concept of orbital transfer vehicle.

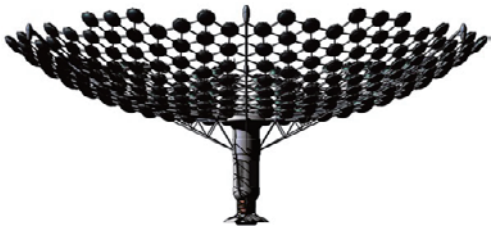

Fig. 2 An orbital transfer vehicle pushing the nuclear waste pile.

***Mission Velocity for L point and Venus***

The velocity to escape Earth at surface is 11.1 km. Therefore, mission velocity for Lagrangian $L_4$ and $L_5$ is smaller than 3.2 km due to 7.9 km for centrifugal velocity at surface.

For interplanetary mission, Earth departure energy ($C_3L$); same as the square of departure hyperbolic excess velocity, is considered. Mission opportunity data based on Lambert theorem provides energy minima and $C_3L$ [2]. Table 2 lists the maximum, minimum and average of $C_3L$ for Venus.

Table 2. $C_3L$ for Venus

| $C_3L$ among 10 consecutive missions | | |
|---|---|---|
| Max($km^2/s^2$) | Min($km^2/s^2$) | Ave.($km^2/s^2$) |
| 8.718 | 6.818 | 7.314 |

Comparison with mission velocity for L point and Venus shows that the difference of mission velocity between them occurs slightly. Therefore the rocket for disposing waste to $L_4$ or $L_5$ point can be also used to dispose it at Venus.

***Launch Location***

As mentioned, the preferred launch site is a floating island located on the equator over the Pacific Ocean. Along the equator, there are not many inhabited cities, and so the risk to humans is minimal. The alternative launch site is India, from which the launch can be made into the polar orbit. This trajectory is also free from inhabited cities.

**3. Safety and Risks**

The most important aspect of the present proposal is the issue of safety and risks. But here, the early works of the U.S. becomes relevant. The U.S. made a concerted effort prior to 1980 to realize this space disposal of nuclear waste. In those early studies, the launch was to be made by the Space Shuttle.

The U.S. was quite confident about the safety of the proposed system because of its experience with the RTGs. An RTG is a device to generate electrical power using the heat generated by the decaying radioisotope material. Many spacecraft used an RTG. Soviet Union is also known to have used many RTGs. Militarily, both U.S. and Soviet Union are known to have used RTGs additionally.

In the case of Apollo 13, the RTG had returned to Earth and reentered the atmosphere and fell into the Pacific Ocean. No radiation leakage was ever found. A detailed safety analysis was made in 1997 for the Cassini mission [3], and the mission was declared safe.

**4. Discussion and Conclusion**

When NASA proposed this space disposal of nuclear waste in the late 1970s, it was not accepted because of three reasons. First, the cost of space launch was expensive: the cost of lifting 1 kg of payload to space was about $20,000 at that time. Second, the cost of extracting the fission products from the spent fuel was expensive. Thirdly, there was really no urgency to dispose the nuclear waste. Today, situation is very different. First, the cost of space launch has declined by at least an order of magnitude: Space-X's quoted price for launching 1 kg of payload to space is approximately $2000. Second, the cost extracting the fission products from the spent fuel is also lowered greatly, thanks to the advancement in technology. Thirdly, there is urgency for disposing of the nuclear waste. The U.S., Russia, and China all have large deserts where they should be able to deposit the nuclear waste. However, Korea, Japan, and Europe do not have such deserts. The nuclear waste has accumulated over the years. Today, space disposal of nuclear waste looks to be economically viable, can be done safely, and there is urgency for doing it.

One might argue that other celestial locations are better suited than $L_4/L_5$ or Venus. However, in such an argument, one must think the possibility that the nuclear package may not reach the destination by equipment malfunction. In such a case, the lunar L points give the best chance of recovery: an orbital transfer vehicle can be sent to retrieve the package to the lost spacecraft.

**References**


[1] NASA, *Summary of the Study of Disposal of Nuclear Waste into Space*, NASA TM X-68235 (1973).

[2] NASA, *Interplanetary Mission Design Handbook Vol.1 Part 1 : Earth to Venus Ballistic Mission Opportunity 1991-2005* (1983).

[3] JPL, *Cassini Program Environmental Impact Statement Supporting Study*, D-10178-1 (1993).

# Numerical Simulation of High-Altitude Aerothermodynamics of Prospective Spacecraft by the DSMC Method

Pavel Vashchenkov[1], A. Kashkovsky[1], A. Shevyrin[1], and Shigeru Yonemura[2]
[1]Institute of Theoretical and Applied Mechanics SB RAS
Institutskaya 4/1, Novosibirsk, 630090, Russia
[2]Institute of Fluid Science, Tohoku University
1-1 Katahira, Aoba Ward, Sendai, Miyagi Prefecture 980-8577, Japan

**ABSTRACT**

The paper describes the computations of aerothermodynamic characteristics of a promising spacecraft (Prospective Piloted Transport System) at the initial part of its descent trajectory at altitudes from 90 to 75 km. The computations are performed by the DSMC method with the use of the SMILE software system. The influence of real gas effects (excitation of rotational and vibrational energy modes and chemical reactions) on aerothermodynamic characteristics of the vehicle is studied.

## 1. Introduction

During de-orbiting, the vehicle passes through the free-molecular flow, then through the transitional zone, and the flight is finalized in the continuum flow. The most difficult regime for computations is the transitional regime at altitudes of 110-75 km. At these altitudes nonequilibrium effects and chemical reactions appear. The gas cannot be considered as a continuous medium. Intermolecular collisions have to be taken into account. The most effective numerical method to simulate free-molecular, transitional, and near-continuum flows is the Direct Simulation Mote Carlo (DSMC) method. It is widely used in scientific and engineering problems of space industry. In the present work, the DSMC method is used for computations of aerothermodynamic characteristics of the model of reentry module of the Prospective Piloted Transport System. The real gas effects (chemical reactions, translational, rotational and vibrational nonequilibrium) on changing of the flow around the model and thermodynamic characteristics are investigated.

## 2. Free-stream conditions

The free-stream parameters are listed in Table 1. The free stream was a mixture of N, $N_2$, O, $O_2$, and NO. The species concentrations correspond to altitudes for which the computations were performed. The gas/surface interaction was simulated by the diffuse law. The thermodynamic characteristics were obtained for two cases of wall temperature distributions: constant wall temperature of 1000 K and adiabatic surface.

Table 1. Free stream conditions

| H, km | M | $T_\infty$ | $\rho_\infty, kg/m^3 \cdot 10^6$ |
|---|---|---|---|
| 75 | 25.9 | 208 | 39.9 |
| 80 | 26.5 | 199 | 18.5 |
| 85 | 27.2 | 189 | 8.21 |
| 90 | 27.3 | 187 | 3.42 |
| 100 | 26.3 | 197 | 0.56 |
| 110 | 22.5 | 256 | 0.093 |

Corresponding author: Pavel Vashchenkov
*E-mail address*: vashen@itam.nsc.ru

## 3. Numerical method

The SMILE software system [1,2] was used in our numerical study. This software system allows modeling two-dimensional, axisymmetric, and three-dimensional flows by the DSMC method with allowance for real gas effects, such as nonequilibrium and chemical reactions. The number of collisions was found by the majorant collision frequency scheme. The energy exchange between the transitional and internal modes was defined using the Larsen-Borgnakke phenomenological model with temperature depending on the rotational and vibrational relaxation collision numbers. The Variable Hard Sphere (VHS) model was used for intermolecular collisions, and reflection of molecules from the spacecraft surface was simulated in accordance with the Diffuse reflection model with complete accommodation of translational and internal energies. The Total Collision Energy (TCE) model [3] was applied to simulate chemical reactions.

## 4. Geometry

The nose part of the simplified geometrical model of the prospective spacecraft is spherical (see Fig. 1), and the rear part is beveled at an angle of 20º. There are two trim flaps on the rear part of the spacecraft. The temperature of the entire body surface was assumed to be constant and equal to 1000 K. The other case had an adiabatic surface, and its temperature was assumed to be equilibrium.

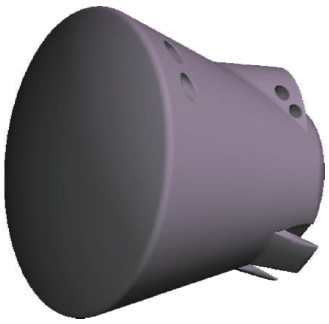

Fig. 1 Geometry of the spacecraft

## 5. Results and Discussion

The effect of chemical reactions on the flow field is

illustrated in Fig. 2, which shows the translational temperature fields around the spacecraft obtained in a chemically reacting flow (upper figure) and in a chemically inert gas (lower figure) for the flap deflected by 30º. The calculations were performed for an altitude of 75 km. It is seen that the flow fields are drastically different in the entire computational domain. The flow temperature in the case of a chemically reacting gas is substantially lower than the temperature obtained with the chemical reactions being ignored. Therefore, we can conclude that the entire flow structure and the shock waves near the spacecraft are formed in a different manner. In a chemically reacting gas, some part of the free-stream energy is spent on dissociation of

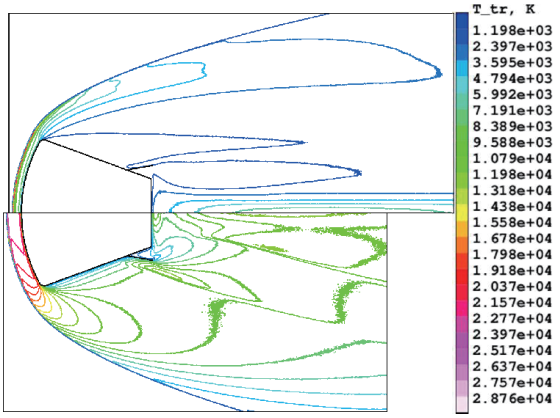


Fig. 2 Translational temperature flowfield. Altitude 75 km. Upper – chemically reacting gas, lower – chemically inert gas

polyatomic molecules. As a result, the mass fractions of atomic species (N and O) behind the bow shock wave substantially increase. For instance, at an altitude of 75 km, the free-stream mass fractions of atomic nitrogen N and molecular nitrogen $N_2$ are $5.46\cdot10^{-4}$ and $0.79$, respectively. Behind the bow shock wave, in the vicinity of the stagnation point, the fraction of N appreciably increases (by three orders of magnitude) up to $C_N \approx 0.46$, while the fraction of $N_2$ noticeably decreases to $C_{N_2} \approx 0.3$.

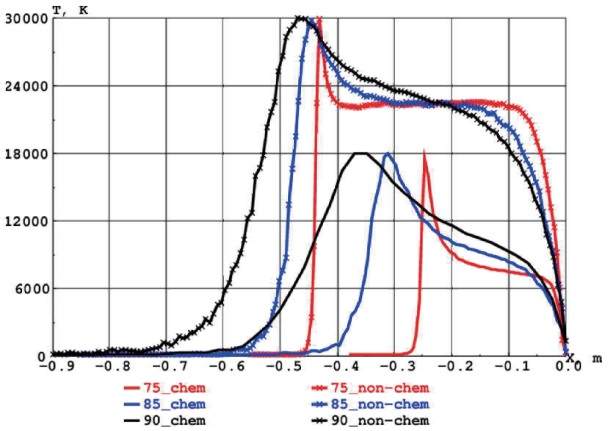


Fig. 3 Temperature along the stagnation line at different altitudes.

Figure 3 shows the distributions of temperature over the stagnation lines at altitudes of 90, 85, and 75 km for chemically reacting and chemically inert gases (the stagnation point has the coordinate X = 0). It is seen that the temperature of the flow behind the bow shock wave is substantially lower if chemical reactions are taken into account. In addition, the stand-off distance of the bow shock wave is changed. The influence of chemical reactions becomes attenuated with increasing flight altitude. Thus, for instance, the difference in the shock-wave stand-off distance is 0.09 m at an altitude of 90 km, 0.13 m at 85 km, and 0.19 m at 75 km.

At altitudes from 90 to 75 km, the flow is close to the near-continuum regime (the Knudsen number changes from $3.7\cdot10^{-4}$ to $4.3\cdot10^{-3}$). The drag coefficient $C_D$ is almost independent of the flight altitude and the presence of chemical reactions; its value is approximately 1.55. The total heat-transfer coefficients $C_h = \dfrac{Q}{\dfrac{\rho_\infty V_\infty^3}{2} S_{ref}}$ and heat going to the spacecraft surface the spacecraft in computations with and without chemical reactions are listed in Table 2. It is seen from Table 2 that the heat-transfer coefficient decreases by more than a factor of 3 at an altitude of 75 km and by a factor of 2 at an altitude of 90 km if chemical reactions are taken into account.

The effect of chemical reactions decreases with increasing Knudsen number.

Table 2. Heat transfer coefficient of the spacecraft model

| H, km | $C_h$, chem | $C_h$, inert | Q (W), chem | Q (W), inert |
|---|---|---|---|---|
| 75 | $1.30\cdot10^{-2}$ | $4.30\cdot10^{-2}$ | $1.66\cdot10^{6}$ | $5.50\cdot10^{6}$ |
| 80 | $2.11\cdot10^{-2}$ | $6.22\cdot10^{-2}$ | $1.25\cdot10^{6}$ | $3.69\cdot10^{6}$ |
| 85 | $3.38\cdot10^{-2}$ | $9.47\cdot10^{-2}$ | $0.89\cdot10^{6}$ | $2.49\cdot10^{6}$ |
| 90 | $6.18\cdot10^{-2}$ | $1.36\cdot10^{-1}$ | $0.68\cdot10^{6}$ | $1.49\cdot10^{6}$ |

**Acknoledgements**

This work was supported by the Collaborative Research Project IFS J14019

**References**

[1] M.S. Ivanov and G.N. Markelov and S.F. Gimelshein, *Proc. 7th Joint Thermophysics and Heat Transfer Conf.* (1998).

[2] M. S. Ivanov, A. V. Kashkovsky, P. V. Vashchenkov and Ye. A. Bondar, *AIP Conf. Proc.* 1333, 211 (2011).

[3] Bird, G.A., *Molecular gas dynamics and the direct simulation of gas flows*, Clarendon Press, Oxford (1994).

# Study of Motion Modeling for a Capsule Shaped Projectile in Free Flight Testing at Transonic

Akiho Ishida[1], Hiroki Nagai[1], Tanno Hideyuki[2], Tomoyuki Komuro[2]
[1]Department of Aerospace Engineering, Graduate School of Engineering, Tohoku University
6-6-01 Aramaki Aza Aoba, Aoba-ku, Sendai, Miyagi, 980-8579, Japan
[2]Japan Aerospace Exploration Agency
1 Kimigaya Aza Koganesawa, Kakuda, Miyagi, 981-1525, Japan

**ABSTRACT**

Free flight testing for the HTV Return Vehicle (HRV) shaped projectile was conducted in the JAXA HEK-G Ballistic Range. The motion in free flight was measured by four acceleration sensors for the pitching and yawing directions. The motion modeling is being studied for aerodynamic control the oscillation caused by the dynamic instability at transonic.

## 1. Introduction

HTV Return Vehicle (HRV) is being considered as a new spaceship by Japan Aerospace Exploration Agency (JAXA). HRV is a re-entry lifting capsule which is planned to carry the various cargos from International Space Station (ISS) to the ground [1]. Generally, it is known that a blunt body causes dynamic instability at transonic with a limit cycle that involves large and constant amplitude. The dynamic instability must be clarified for the design of the HRV, in addition to the trajectory and stable parachuting.

In a single degree-of-freedom (1 DOF) wind tunnel test, pressure measurement was conducted by Hiraki and revealed that the pressure change on the backside induces the dynamic instability [2]. Although the influence of the sting, which holds the model, must be assessed accurately, support construction is required in normal wind tunnel tests. Ballistic ranges can operate without restrictions on the DOF of the model's motion and support construction interference by launching the projectile with high pressure gas.

In this study, the HRV shaped projectile was tested in the ballistic range. Four accelerometers were used to measure the pitching and yawing motions during free flight. Based on the angular acceleration data, the capsule motion modeling during free flight is being studied.

## 2. Motion Equation and Damping Coefficient

A confirmed capsule motion model based on the ground tests is required for aerodynamic control during dynamic instability, and the damping coefficient of the oscillating motion is the most important parameter.

The motion equation for 1 DOF rotation is expressed by Eq.1. The damping coefficient, $\left(C_{mq}+C_{m\dot{\alpha}}\right)$, relates directly to the dynamic characteristics and is solved by partially differentiating the moment coefficient by the angular acceleration and assigning zero to the angular acceleration.

Hiraki calculated the damping coefficient in the pitching direction with wind tunnel test results and modeled the pitching instability motion at transonic speeds. The damping coefficient is expressed as a function of the pitching angle, $\theta$, and the motion model is defined by the Van der Pol equation (Eq. 2) [2].

Corresponding author: Akiho Ishida
*E-mail address*: ishida.akiho@aero.mech.tohoku.ac.jp

Koga et al expressed the motion model for control by a linear equation by using data acquired in a 1 DOF free-rotation wind tunnel test. The damping coefficient was expressed by Eq. 3 [1].

All these motion models were constructed by using the data acquired in the wind tunnel tests. Thus, the motion model based on the free flight tests, without support construction interference, has been required.

$$I\ddot{\theta}=\frac{1}{2}\rho_\infty {U_\infty}^2 SD\cdot\{C_{m\alpha}(\theta)\cdot(\theta-\theta_0)+\left(C_{mq}+C_{m\dot{\alpha}}\right)(\theta,\dot{\theta})\cdot\frac{D}{U_\infty}\cdot\dot{\theta}\} \quad (1)$$

$$\ddot{\theta}=\hat{\varepsilon}\left(1-\frac{\theta^2}{\delta^2}\right)\cdot\dot{\theta}-\theta \quad (2)$$

$\hat{\varepsilon}$, $\delta$ : constant

$$\left(C_{mq}+C_{m\dot{\alpha}}\right)(\theta,\dot{\theta})=\frac{2I}{\rho_\infty U_\infty SD^2\dot{\theta}}\cdot\{\ddot{\theta}-(c_0+c_1\theta+c_2\theta^2+c_3\theta^3)\} \quad (3)$$

$c_0$, $c_1$, $c_2$, $c_3$ : constant

## 3. Experimental Set-up and Conditions

The free flight tests were conducted in the JAXA HEK-G Ballistic Range (Figure.1). On the end of the tube, a disturbance plate was placed to create an initial disturbance for the projectile. The projectile continues through 22.5 m free flight after contact with the plate and subsequently contacts the recovery cushion. The charging pressure of the compression tube was regulated to launch at the nominal Mach number (M) of 0.4, which was estimated to subject the projectile to dynamic instability with the largest amplitude [3]. The actual launch velocity was measured by two laser sensors at the end of the tube.

Figure.2 shows the HRV shaped model used in this test designed with a body and base that can be separated to mount the four accelerometers and data logger inside the unit for aerodynamic measurements. Two accelerometers [B] and [C] are placed in the vertical direction in the launching (axial) direction for the pitching motions, and the other two [A] and [D] are placed horizontally for the yawing motions. The data logger has a 500 kHz response performance and a 16-bit processing ability.

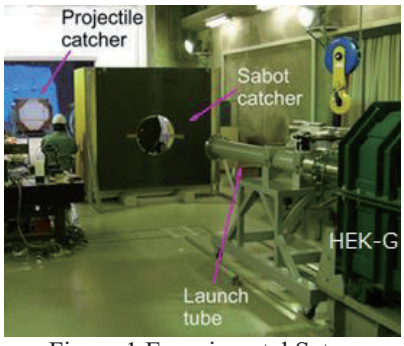

Figure.1 Experimental Setup


Figure.2 Experimental Setup

## 4. Results

Figure.3 shows the angular acceleration time history during free flight recorded by [B] with launch at M = 0.32 (Shot1). The effects of gravity and translation acceleration were omitted in this Figure by subtracting the average of all acceleration results from each result.

Fast Fourier transform (FFT) was applied to the angular acceleration data during free flight acquired by Shot1, launch at M = 0.32. The lower frequencies dominated for all positions, especially pitching directions. A low-pass filter was created from this analysis. Figure.4 shows the filtered angular acceleration time history. From the pitching results, an oscillation with about one and a half period of was observed. An oscillation with a smaller amplitude and higher frequency was observed from the yawing result.

Figure.5 shows the filtered angular acceleration time history with launch at M = 0.35 without disturbance plate (Shot2). Similar to Shot1, about one and a half period of oscillation was observed in the pitching direction. However, the amplitude was smaller and the period was shorter for the pitching than Shot1.

The angular rate and angle time history was calculated from these results.

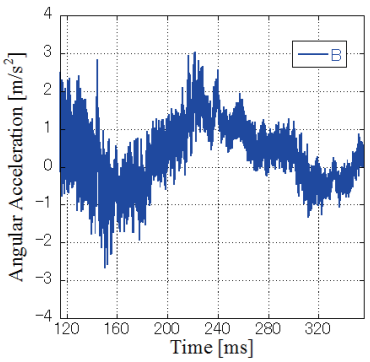

Figure.3 Free Flight B (Shot1)

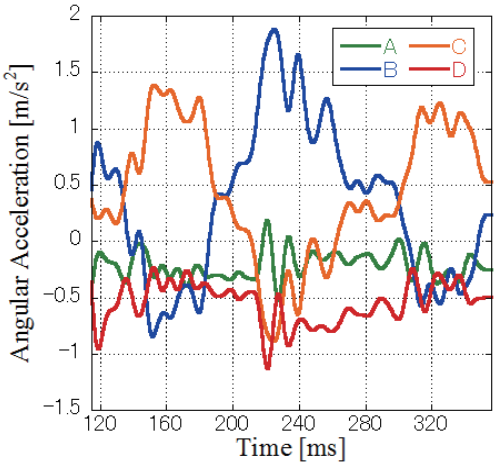

Figure.4 Filtered Angular Acceleration (Shot1)

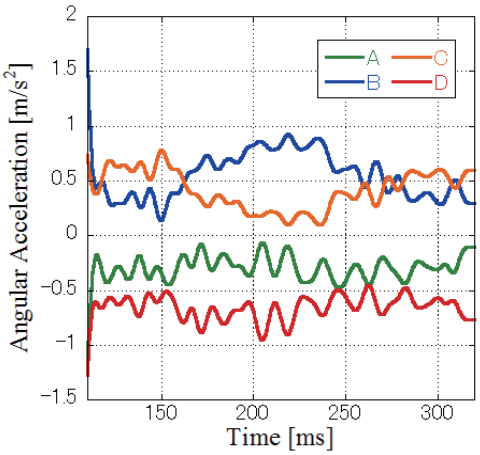

Figure.5 Filtered Angular Acceleration (Shot2)

## 5. Summary

In this study, the angular acceleration time history of the HRV capsule shaped projectile during free flight was clarified by acceleration meters at four positions for the pitching and yawing directions. The model was launched using the HEK-G Ballistic Range in JAXA. The pitching oscillation dominated and about one and a half period was obtained in the 22.5 m free flight. Differences of amplitude, frequency, and period between the launches at Shot1 and Shot2 were observed. The angular rate and angle was calculated from these results.

## References

[1] Seigo Koga, Akiko Hidaka, Takeshi Kimura, Takashi Yoshinaga, Shinji Nagai, Dynamic Stability Testing of a Reentry Lifting Capsule in a Transonic Wind Tunnel, *AIAA SciTech2014*, AIAA 2014-1119.

[2] Koju Hiraki, Experimental Study on Dynamic Instability of Capsule-shaped Body, *Institute of Space and Astronautical Science Report*, Vol.103, Japan (1999).

[3] Akiko Hidaka, Seigo Koga, Takeshi Kimura, Shinji Nagai, Takeshi Yoshinaga, Hironori Nishijima, Dynamic Testing of HTV Re-Entry Vehicle at the Transonic Wind Tunnel, *56th Conference on Space Science and Technology*, JSASS-2012-4641.

Eleventh International Conference on Flow Dynamics
October 8-10, 2014, Sendai, Miyagi, Japan

# Optical Diagnostics of $CO_2$-$N_2$-Ar Plasma in the Hollow Electrode Arc Heater

Gouji Yamada, Genki Nishida, Motohiro Nakanishi, Hiromitsu Kawazoe
Tottori University
4-101 Koyama-minami, Tottori, Tottori, 680-8552, Japan

**ABSTRACT**

The purpose of the present study is to characterize the properties of $CO_2$-$N_2$-Ar plasma in the hollow electrode arc heater by optical diagnostics. Spectroscopic measurements are conducted in the region of the arc heated part. The rotational and vibrational temperatures are determined from the measured spectrum using a spectrum fitting technique. It is found that the rotational and vibrational temperatures are almost same, showing the plasma in the arc heater is under equilibrium. Finally, the chemical composition of the plasma is determined using the NASA-CEA program.

## 1. Introduction

Recent space missions pay much attention to Mars explorations. In proposed missions, new challenging technologies such as Mars airplane and Mars Aeroflyby Sample Collection (MASC) will be planned. For the success of these missions, the Mars entry flight is main concerned. Space vehicles receive severe heat loads during atmospheric entry flights. Therefore, thermal protection materials are required to shield space vehicles from the heat loads. The thermal protection materials are developed through heat tests using an arcjet facility which generates high enthalpy plasma flows corresponding to entry flight conditions. It has been pointed out that the flow properties have a great influence on the test results. However, the flow properties of the test flows have been not yet clarified, degrading the accuracy of the heat tests. To improve the accuracy of the heat tests, the characterization of the test flows is necessary. The authors have conducted optical diagnostics of $CO_2$-$N_2$ plasma flows in an arc heated wind tunnel and deduced temperature distribution along the stagnation streamline around a blunt body [1]. The result showed that the plasma flow was in the vibrational nonequilibrium state. For complete characterization, we focus on the plasma properties in the arc heater where the plasma is generated. The information of the plasma properties in the arc heater is helpful for further analysis of the plasma flows at the test section. The purpose of the present study is to characterize plasma properties in the arc heater.

## 2. Experimental setup

In the present study, a hollow-electrode type arcjet facility is used to generate an arc-heated plasma. The facility is composed of the hollow-electrode type arc heater, a test section, a vacuum tank, and a vacuum pumping system. A schematic drawing of the arc heater is shown in Fig. 1. The arc heater consists of hollow-type cathode and anode electrodes connected to a convergent-divergent nozzle. Each component of the electrodes and nozzle are independently cooled by cooling water. The anode electrode and the outer case have holes for spectroscopic measurements. A quartz window is located between the anode electrode and the outer case. The optical system is arranged so that the radiation from the downstream end of the anode electrode can be measured through the quartz window. In the present measurement, the arc heater is operated with a plenum chamber pressure of $3.5\times10^5$ Pa, an arc current of 60 A, and a voltage of 150 V. To simulate the Mars entry flight, a mixture of 95.7% $CO_2$, 2.7% $N_2$, and 1.6% Ar should be used as a test gas. However, the generated arc plasma flow is unstable using the actual composition as a test gas. The increase of the amount of Ar enables us to observe a stable arc plasma flow. Therefore, in this study, a mixture of $CO_2$-$N_2$ diluted in Ar is used as a test gas with the respective mass flow rates of 0.131 g/s, 0.0042 g/s, and 0.743 g/s. In this condition, the specific enthalpy of the arc plasma flow is about 7.2 MJ/kg at the nozzle exit.

Corresponding author: Gouji Yamada
*E-mail address*: yamada@mech.tottori-u.ac.jp

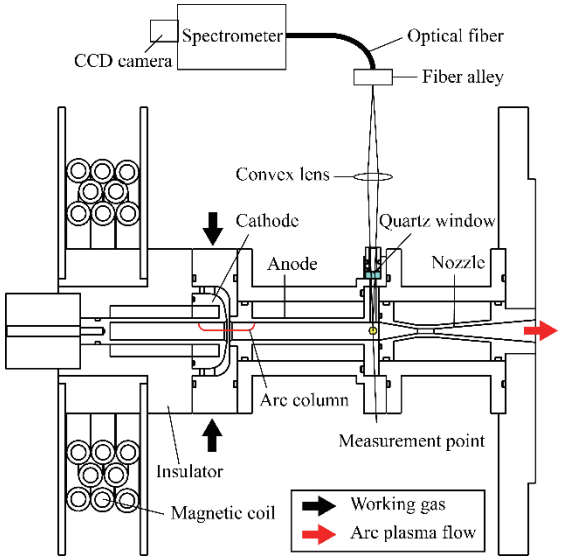


Fig. 1 Schematic of the hollow electrode arc heater

## 3. Results and Discussion

Figure 2 shows the overall spectrum of emission intensity in the arc heater. CN violet and $C_2$ Swan bands are prominent in the overall spectrum. Most intense emission is seen to originates from CN violet $\Delta v$ =0. Atomic lines of Oxygen, argon, and carbon are seen in the long wavelength range above 700 nm. Atomic carbon is considered to come from the contaminated electrode surface because the water-cooled electrodes are polluted with a black layer of carbon or carbonic compounds. Atomic lines of copper are seen in the near-ultraviolet

region due to the erosion of electrodes by arc heating.

Figure 3 shows the high-resolution spectrum of CN violet Δv =0 observed using a 1200-lines/mm grating. Five bandheads are clearly identified by referring to standard tables of molecular spectra. This band structure depends on the rotational and vibrational temperatures of the plasma. In this study, a spectrum fitting method using SPRADIAN 2 is applied for the temperature evaluation of CN. The spectrum fitting result is shown in Fig. 3. A good agreement between the measured and computed spectra can be obtained. The rotational and vibrational temperatures are deduced to be 6500 K, respectively, showing that the plasma in the arc heater is close to thermal equilibrium. Based on this result, the chemical composition of $CO_2$-$N_2$-Ar mixture gas is calculated using the NASA computer program Chemical Equilibrium with Applications (CEA).

Figure 4 shows the chemical composition of $CO_2$-$N_2$-Ar mixture gas at temperatures from 2000 to 10000 K. The chemical composition varies as a function of temperature. In the low temperature range below 4000 K, the mole fraction of $CO_2$ rapidly decreases as the temperature increases. In contrast, the mole fractions of CO and O increases and become higher than that of $CO_2$. This is because that the $CO_2$ dissociation mainly occurs, producing CO and O. At the temperature around 4000 K, the mole fraction of N starts to increase due to the $N_2$ dissociation. In the temperature range between 4000 and 8000 K, the CO dissociation becomes prominent as well as $CO_2$ dissociation, increasing the mole fractions of $C_2$ and O. In the temperature range between 5000 and 10000 K, The formation reaction of CN follows the CO dissociation, producing CN. The mole fraction of CN is relatively low in the chemical composition under consideration. However, the CN radiation is most intense as seen in Fig. 2. The result shows that the temperature evaluation using emission spectrum of CN is effective in the high temperature range between 5000 and 10000 K. In the entire temperature range, the mole fraction of Ar is high and almost unchanged. Table 1 shows the chemical composition of $CO_2$-$N_2$-Ar plasma at the estimated temperature of 6500 K. It is found that Ar, CO and O are dominant species in the plasma under investigation. Since the mole fractions of CN and $C_2$ are extremely low, they are found to be strong radiators in the $CO_2$-$N_2$-Ar plasma.

## 4. Concluding Remarks

In the present study, characteristics of $CO_2$-$N_2$-Ar plasma in the hollow electrode arc heater have been investigated by optical diagnostics. Temperatures of the plasma have been evaluated by the spectrum fitting method from the CN violet Δv=0. It is found that the rotational and vibrational temperatures are same and estimated to be 6500K, showing that the plasma is under equilibrium in the arc heater. Based on the result, the chemical composition is deduced using the NASA-CEA program. Since the mole fractions of CN and $C_2$ are extremely low, they are found to be strong radiators in the $CO_2$-$N_2$-Ar plasma.

## Reference

[1] G. Yamada, S. Otsuta, T. Matsuno, H. Kawazoe, *Trans. JSASS, Aerospace Tech. Japan*, 11 (2013) 87－91.

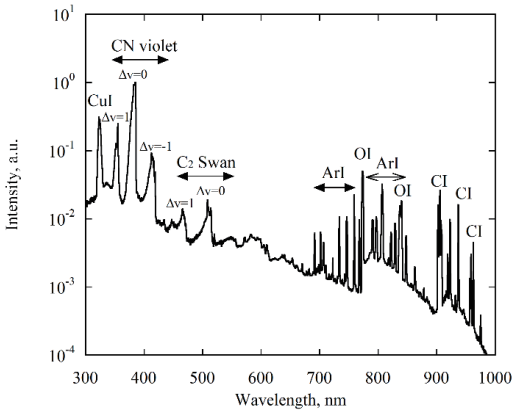


Fig. 2 Overall spectrum of emission intensity

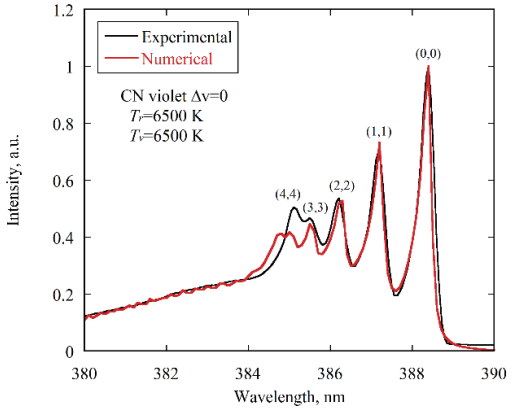


Fig. 3 High resolution spectrum of the CN violet Δv=0

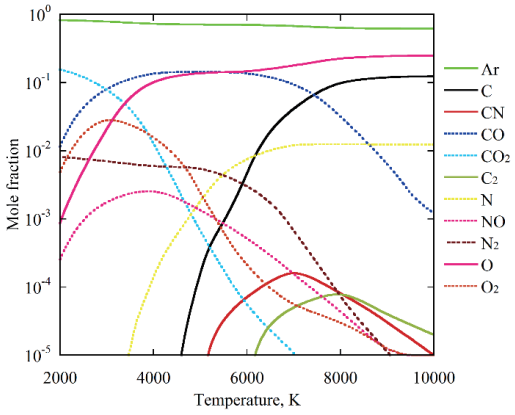


Fig, 4 Chemical composition of $CO_2$-$N_2$-Ar

Table 1 Chemical composition at 6500 K

| Species | Mole fraction, % |
|---|---|
| Ar | 68.8685 |
| C | 2.1535 |
| CN | 0.012 |
| CO | 11.7335 |
| $CO_2$ | 0.0025 |
| $C_2$ | 0.0025 |
| N | 0.9885 |
| NO | 0.0315 |
| N2 | 0.173 |
| O | 16.0225 |
| $O_2$ | 0.0105 |

Eleventh International Conference on Flow Dynamics
October 8-10, 2014, Sendai, Miyagi, Japan

# Experimental Study Of Effects Of Mini Flaps At Low Reynolds Number

Daisuke Oshiyama, Daiju Numata, Keisuke Asai
Department of Aerospace engineering, Tohoku University
Aoba 6-6-01, Aoba-ku, Sendai-shi, Miyagi-ken, 980-8579, Japan

**ABSTRACT**

The objective of this study is to evaluate effects of mini flaps on a NACA0012 airfoil at low Reynolds number. Force, skin friction and wake distribution measurements were conducted. Results reveal that airfoil with mini flaps gain higher lift and give more separation area both upper and lower surface. This suggests that these separation areas might have some relationships with flow behind the flaps.

## 1. Introduction

Recently, the mars airplane has been focused on as a new method to observe the mars. It can obtain high quality information from huge area. Flight condition of the Mars airplane becomes low Reynolds number (*Re*) because Martian atmospheric pressure is almost one - hundredth of the one of the Earth. In this Reynolds number range, laminar separation occurs easily, so characteristics of conventional airfoil becomes worse, and it is difficult to keep on gaining constant lift because of non-liner behavior of lift which originates in occurrence of laminar separation bubble[1]. Thus, new solution is needed to acquire higher and constant lift.

In this study, mini flaps are picked up as high lift devices. Basically, these look like Gurney Flap which is known to enhance lift at high *Re*. However, effects of that are not well-known at low *Re*.

Thus, the objective of this study is to evaluate the effects of mini flaps experimentally at low *Re*. In addition to force measurements, skin friction measurements are conducted in order to visualize flow around the airfoils. Moreover, wake distributions were measured to figure out how mini flaps affect flow.

## 2. Method

### 2.1. Wind Tunnel

Tohoku-University Basic Aerodynamic Research Tunnel (T – BART) was used. Test section is 300 mm x 300 mm, and turbulence intensity is less than 0.5 %.

### 2.2. Force Measurement

Three components balance system (Nissho Electric Works, LMC-3531-50NS) was used. The range of the load cells for lift, drag and pitching moment are 50 N, 50 N and 5 N-m, respectively.

### 2.3. Skin Friction Measurement

In this study, Global Luminescent Oil Film (GLOF) was used as a visualization method. This is optical skin friction measurement technique developed by Liu et al[2]. Silicon oil doped with luminescent molecules is used and exited by excitation light. For a thin film of the luminescent oil, the emitted light intensity is proportional to the thickness. So, oil film thickness can be obtained by measuring oil film luminescence intensity, and skin friction is measured by chasing the fluctuation of the thickness.

Corresponding author: Daisuke Oshiyama
*E-mail address*:
oshiyama.daisuke@aero.mech.tohoku.ac.jp

### 2.4. Wake Distribution Measurement

Hot wire anemometer was used to measure wake velocity distribution. The hot wire was controlled by Constant Temperature Anemometer. Analog filter was operated before saving data.

### 2.5. Test Model

#### 2.5.1. Airfoil

In all experiments, NACA0012 made with ABS resins was used, and chord length is 50 mm and span length is 300 mm.

#### 2.5.2. Mini Flaps

Mini flaps used in this study are illustrated in the Fig. 1. Material of that was aluminum (AL1050). The symbol *h* [%C] in the figure means the height of mini flaps.

### 2.6. Experiment Conditions

All experimental conditions are in Table.1.

Table. 1 Experimental conditions

| Measurement | Force | Skin friction | Wake distribution |
|---|---|---|---|
| *Re* | 25,000 | | |
| *h* [%C] | 6,8,10,12 | 10 | |
| Angle of Attack [deg] | -5~16 | 0,3,6,9 | |

Wake distributions were measured, traversing between y/c = +1.0 and -1.0 at x/c = 0.1 behind the T.E. RMS and mean velocity profile were calculated by the obtained data.

## 3. Results

### 3.1. Force Measurements

Fig. 2 shows lift curve of both clean and mini flap airfoils. As for clean airfoil, almost no lift is measured at low Angle of Attack (AoA). After AoA 3 deg, lift goes up suddenly, and maximum lift coefficient is obtained at AoA 6 deg. After that, stall occurs little by little. Once mini flap is attached to the airfoil, it is obvious that much higher lift is achieved for all cases. Moreover, as flap height increases, higher lift coefficient is observed. In

addition, non-liner behavior of clean airfoil at low AoA disappears, attaching mini flaps to the airfoil.

### 3.2. Skin Friction Measurements

Results of GLOF of AoA 0 deg are in Fig. 3. Flow comes from left to right. Diagrams of first and third from top show skin friction of upper and lower surfaces, and middle schemes mean flow fields expected by diagrams. The direction of arrows on the diagram implies the direction of skin friction force, i.e. if the arrow points left, this means adverse flow. From these results, separation occurs at x/c = 0.7 on both sides for clean airfoil, but separation on upper and lower surface are happed at x/c = 0.4 and 0.3 respectively for the airfoil with mini flap. This result means that flap makes separation points both upper and lower surface occurs closer to leading edges.

### 3.3. Wake Distribution Measurements

Fig. 4 shows the wake distribution with and without mini flaps. This says that RMS and wake distributions of clean airfoil are symmetric in terms of y/c. However, RMS of mini flap airfoil has two peaks asymmetrically both upper and lower surface, meaning that shear layers are generated on both sides at these peaks. This suggests the same results with the one of GLOF. The wake distribution is also asymmetry. Flow velocity on upper surface is faster than the one of lower surface. This must be the reason why airfoil with mini flap gives much higher lift coefficient.

## 4. Conclusions

This study aims to evaluate effects of mini flaps at low *Re*. Three kinds of measurements were conducted. These results say that mini flap enhances lift dramatically based on how height mini flap is, and airfoil with mini flap makes larger separation area both upper and lower surface. Then, these separation areas also give rises to unsteady vortices, especially upper surface, suggesting existence of big vortex area behind the mini flap. This pull the upper surface flow down, and flow on upper surface is accelerated. This is the reason why high lift is caused.

## References


[1] P. B. S. Lissaman, “Low Reynolds Number Airfoils”, *Ann. Rev. Fulid Mech*, vol. 15 (1983) 223-239.

[2] T. Liu, J. Montefort, S. Woodiga and P. Merati, “Global Luminescent Oil-Film Skin-Friction Meter”, *AIAA Journal*, Vo. 46, No. 2 (2008) 1-11.

[3] J. J. Wang, Y. C. Li and K. S. Choi, “Gurney flap Lift enhancement, mechanisms and applications”, *Progress in Aerospace Science* 44 (2008) 22-47.


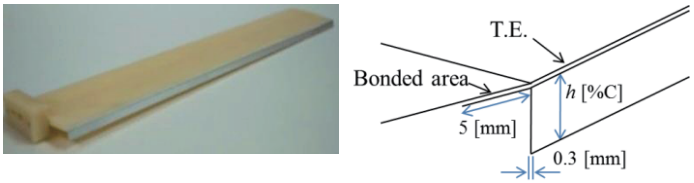


(a) Picture (b) Scheme

Fig. 1 Mini flap

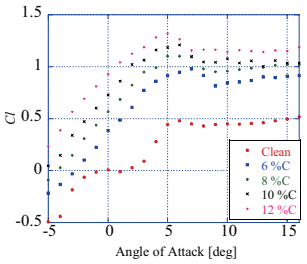


Fig. 2 Lift curve

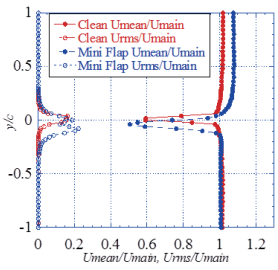


Fig. 4 Wake distribution at AoA 0 deg

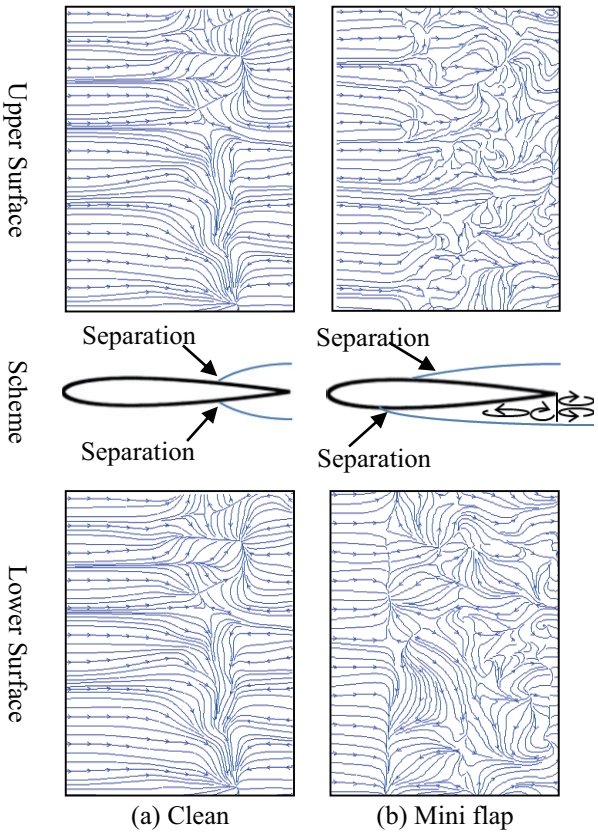


(a) Clean (b) Mini flap

Fig. 3 GLOF AoA 0 deg results

Eleventh International Conference on Flow Dynamics
October 8-10, 2014, Sendai, Miyagi, Japan

# PIV Flowfield Analysis around Flapping Wing Object via Proper Orthogonal Decomposition

Yuya Fujii, Kazunosuke Hirayama, Wataru Yamazaki
Department of Mechanical Engineering, Nagaoka University of Technology,
Kamitomioka-machi 1603-1, Nagaoka, Niigata, 940-2188, Japan

**ABSTRACT**

In this research, particle image velocimetry (PIV) data around a flapping wing object are reconstructed/analyzed by a proper orthogonal decomposition (POD) approach. At hovering (no uniform flow) condition we have interests, it is difficult to measure the PIV velocity vector in its entire flowfield. A POD-based gappy data reconstruction approach is applied to recover the gappy PIV data. The flowfields around a flapping wing with a feathering motion are investigated.

## 1. Introduction

Flapping wing micro air vehicles (MAV) are watched with keen interest since these are promising for advanced unmanned MAV for exploration/observation under risky/ultimate environments. The fluid mechanics of flapping wing are more difficult than traditional fixed wing due to its complex unsteady fluid physics at low Reynolds numbers. Recently, a flapping wing object has been self-developed by the present authors [1-2] to investigate the flowfields around the flapping wing object by PIV measurements. However, it is difficult to control the scatter of smoke particles with a certain level of repeatability in its hovering condition, which requires some other approaches to obtain PIV data in the entire flowfield. To reconstruct incomplete data which is often referred to as gappy data, several approaches have already been developed in the literature. A gappy POD approach is an efficient reconstruction method which can treat spatial/temporal gappy data.

In this research, we aim to reconstruct gappy PIV data around a flapping wing object by using the POD approach. Furthermore, the flowfields around the flapping wing object are discussed in the reconstructed flowfields.

## 2. PIV measurement around flapping wing object

In this section, our flapping wing object as well as the brief overview of the PIV measurements is introduced concisely. The developed flapping wing object is shown in Fig.1. By transferring the rotational motion of a D.C. motor into a simple harmonic motion by using gears, the flapping motion at 5[Hz] can be achieved. The Reynolds number based on the chord length and the averaged flapping velocity at the wingtip is about 8800. Since the wing portion has the degree of rotational freedom along the leading edge beam axis, the feathering angle (α) passively shifts towards 90[deg] (vertical) at the upstroke and towards 0[deg] (horizontal) at the downstroke by the effect of aerodynamic force acting on the flapping wing. The PIV data at 60% semi-span section with the feathering motion of $0<\alpha<90$[deg] is investigated in this paper. In Fig.1, the definition of the PIV measurement region is schematically indicated.

Corresponding author: Yuya Fujii
*E-mail address*: s091064@stn.nagaokaut.ac.jp

## 3. Proper orthogonal decomposition

### 3-1. POD-based data reconstruction approach

We assume that $\mathbf{F} \in \Re^{n\times m}$ is a large scale spatial/temporal data where $n$ and $m$ are the numbers of data points and of temporal steps (snapshots), respectively. The spatial/temporal data can be decomposed as the linear combination of POD modes $\Phi \in \Re^{n\times m}$ and POD coefficients $\xi \in \Re^{m\times m}$. When all POD modes and POD coefficients are obtained, the large scale data can be reconstructed. Since several dominant POD modes of smaller indicies are approximately enough to reconstruct the large scale data, the number of POD modes can be limited as:

$$\mathbf{F} = \sum_{i=1}^{m} \Phi_i(\mathbf{x})\xi_i(t) \cong \sum_{i=1}^{r} \Phi_i \xi_i \tag{1}$$

The gappy PIV data is reconstructed by applying the POD approach using the dominant POD modes of the gappy PIV data itself. Firstly, tentative values (time-averaged values) are inserted on the missing components of $\mathbf{F}$ and then an initial complete data matrix is constructed. Then, (approximate) POD modes $\widetilde{\Phi}$ can be obtained by performing the POD analysis. Appropriate POD coefficients $\widetilde{\xi}$ are separately estimated by minimizing the following function at each time step:

$$J_t = \left\| \mathbf{u}_t - \sum_{i=1}^{r} \widetilde{\Phi}_i \widetilde{\xi}_{ti} \right\|^2 \qquad (t = 1, \cdots, m) \tag{2}$$

where $\mathbf{u}_t$ is the PIV velocity data at the time step of $t$. Finally, the missing components of $\mathbf{F}$ are overwritten by the estimations from $\widetilde{\Phi}$ and $\widetilde{\xi}$. By performing the above procedure iteratively, more accurate estimation of the missing PIV data can be achieved. The representative parameters of this approach are the number of considering POD modes $r$ and the number of iterations $i_{\max}$, which can be specified by users.

### 3-2. Cross validation analysis

For the POD-based data reconstruction approach, the two parameters of $r$ and $i_{\max}$ have to be determined beforehand. In this research, the effect of these input parameters is investigated by a cross validation approach. In this approach, some parts of the data available regions are considered as “dummy” missing

regions and then those dummy missing regions are also reconstructed by the POD approach from the remaining available data. The accuracy of the reconstruction can be evaluated as follows:

$$Error = \frac{1}{2N\overline{V}} \sum_{i=1}^{N} \left[ \left| u_i^{PIV} - u_i^{POD} \right| + \left| v_i^{PIV} - v_i^{POD} \right| \right] \quad (3)$$

where $\overline{V}$ is the mean velocity of the flapping motion at 60% semi-span section. $N$ is the number of dummy missing points. $u^{PIV}$ and $u^{POD}$ are respectively the exact PIV measurement velocity data and POD-based reconstructed velocity data. The dummy missing regions are randomly selected in the entire flowfield with the probability factor of $p_{cv}$.

## 4. Results and discussion

The original PIV data at the 60% semi-span location is shown in Fig.2. It can be observed that complicated vortex structures are captured some extent, although the PIV measurements failed at considerable regions. In the rightmost side of Fig.2, the PIV data available regions are visualized in which red/blue regions respectively correspond to the data available/missing regions. Since the percentage of the missing in this data is about 52% in total (there are about 600 snapshots for three flapping cycles in this PIV data), it can be considered that the missing regions are still significant to understand the detailed flow structures around the flapping wing object.

Therefore, the developed POD based reconstruction approach is applied to the gappy PIV data. The result of the cross validation analysis ( $p_{cv}$ =10%, $i_{\max}$ =10) is shown in Fig.3. It is confirmed that the optimal number of considering POD modes is approximately 190 in this case.

The reconstructed flowfields are also shown in Fig.2. When the flapping wing is horizontal at the downstroke motion, clockwise trailing edge vortex (TEV) and counterclockwise leading edge vortex (LEV) are observed at the upper side of the flapping wing. When the flapping wing is vertical at the upstroke motion, the LEV and TEV are detached from the flapping wing, and then downward induced velocities are observed at the lower side of the wing. It is confirmed that complicated vortex structures are reconstructed qualitatively well. This result indicates the effectiveness of the developed POD-based PIV data recovery approach.

## 5. Concluding remarks

In this research, the PIV data around a flapping wing object were reconstructed/analyzed by a proper orthogonal decomposition (POD) approach. The LEV and TEV, that are typical flow structures for flapping wings were observed in the reconstructed flowfields. Therefore, the effectiveness of the present data reconstruction approach can be confirmed. As future works, PIV measurements will be performed at multiple sections to understand the 3D flowfields around the flapping wing object.

## References


[1] Yamazaki, W., Yamada, H., *AIAA Paper 2013*, (2013) 2473.

[2] Yamada, H., Fujii, Y., Hashiguchi, R., Yamazaki, W., *Proceedings of 10th International Conference on Flow Dynamics*, (2013) 144－145.


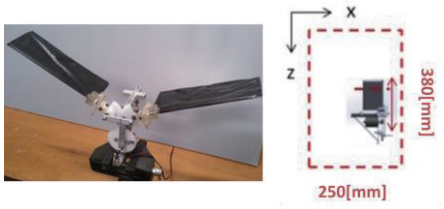


Fig.1 Left: Developed flapping wing object, Right: Definition of PIV measurement region

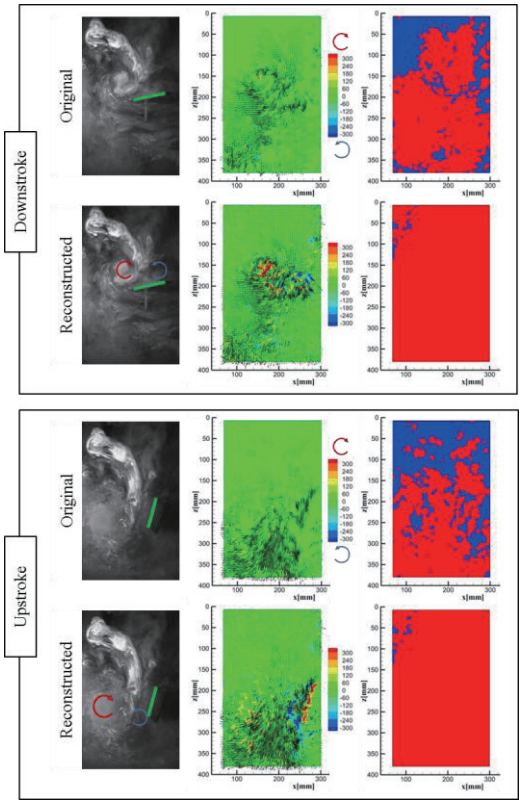


Fig.2 Gappy/Reconstructed PIV data at downstroke moment (upper) and upstroke moment (lower), Left: Raw image, Middle: Velocity vector with vorticity magnitude, Right: Data available (red) and missing (blue) regions, Green line: flapping wing location, Red/blue arrows: typical vortices

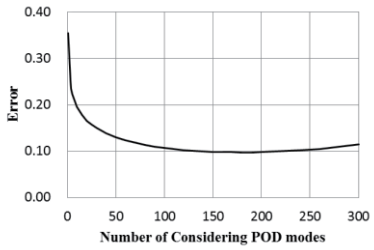


Fig.3 Result of cross validation analysis ( $p_{cv}$ =10%, $i_{\max}$ =10)

Eleventh International Conference on Flow Dynamics
October 8-10, 2014, Sendai, Miyagi, Japan

# Investigation of Dynamic Characteristics of Pitching Flat-plate by Dynamic Wind-Tunnel Testing

Takumi Ambo, Takahiro Senzaki, Daiju Numata and Keisuke Asai
Department of Aerospace Engineering, Graduate School of Engineering, Tohoku University
6-6-01 Aramaki Aza Aoba, Aoba-ku, Sendai, Miyagi, 980-8579 JAPAN

**ABSTRACT**

In order to investigate unsteady aerodynamic characteristics of a three-dimensional rectangular flat-plate wing, a wind-tunnel test of a flat-plate wing model in pitching motion was performed. To examine the effects for aerodynamic performance, pitching frequency was changed. Difference of aerodynamic force between upstroke and downstroke of pitching motion was observed. To consider relationship of flow field to aerodynamic force, visualization on surface of wing model by Fluorescent minitufts method and oil flow method were carried out.

## 1. Introduction

Recently, an interest to aircrafts flying in low *Re* number circumstance like micro air vehicles (MAVs) is increasing. At low *Re* number cruise conditions, MAV's flight stability is influenced by unsteady aerodynamic phenomena such as Dynamic Stall. This phenomenon influences lift force and pitching moment. Several studies about Dynamic Stall using a two-dimensional model have been examined [1]. However, MAVs have three-dimensional wings. It is necessary to know Dynamic Stall phenomenon on the three-dimensional wing. There are few studies about Dynamic Stall using the three-dimensional wing [2], especially there are little to no study in low *Re* conditions. Hence, it is necessary to investigate Dynamic Stall phenomenon in low *Re* number conditions for improving MAV's flight stability.

In this study, to clarify Dynamic Stall on the three dimensional wing, a wind-tunnel test of a flat-plate wing model in pitching motion was performed. To consider relationship of flow field to aerodynamic force, visualization on surface of wing model by Fluorescent minitufts method and oil flow method were carried out.

## 2. Experimental Setup

### 2.1. Wind Tunnel

Experiments were conducted in the Low-Turbulence Wind Tunnel at Institute of Fluid Science (IFS), Tohoku University. This is a closed circuit wind-tunnel with an open-type octagonal test section with the cross distance of 0.8 m.

### 2.2. Robot Manipulator

An intelligent serial-type robot manipulator (PA-10, Mitsubishi Heavy Industries, Ltd.) was used to set the model attitude and to produce motion of the model.

### 2.3. Test Model

Figure 1 shows the rectangular flat-plate wing test model. The chord length, span length and thickness of the test model is 75 mm, 400 mm and 4 mm, respectively. The material of wing is Medium-density fiberboard (MDF). Test model is connected Robot manipulator by sting. Its diameter is 20 mm and length is 300 mm. The sting is made of aluminum.

Corresponding author: Takumi Ambo
*E-mail address*: ambo.takumi@aero.mech.tohoku.ac.jp

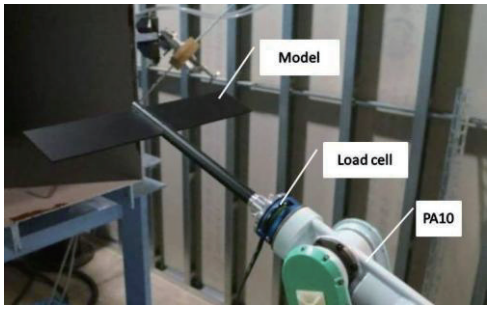


Fig. 1 Robot manipulator and Test model

### 2.4. Surface Flow Visualization Method

Fluorescent minitufts method and oil flow method were carried out. The material of minitufts is polyester monofilament with the diameter of 50 μm. The minitufts were glued on the model surface. Flow direction is estimated by direction of tufts. Painted oil on model surface is flowing by shear force, and time-averaged flow pattern is observed.

### 2.5. Test Condition

In this experiment, the robot manipulator made a single-DoF forced pitching motion. Rotation axis is quarter-chord line. Figure 2 shows location of axis. Table 1 and Table 2 show test conditions.

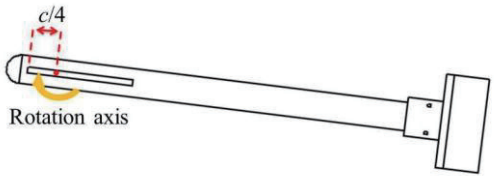


Fig. 2 Diagram of model

Table 1. Test conditions (Force measurement, Fluorescent minitufts method)

| | |
|---|---|
| Flow velocity $U$ [m/s] | 15 |
| Mean angle of attack $\alpha_0$ [deg] | 5 |
| Amplitude $A$ [deg] | 4 |
| Frequency $f$ [Hz] | 0.5, 1.0 |
| Reduced frequency $k$ | 0.008, 0.016 |

Table 2. Test conditions (Oil flow method)

| | |
|---|---|
| Flow velocity $U$ [m/s] | 15 |
| Angle of attack $\alpha$ [deg] | 0, 1, …, 11 |

## 3. Results and Discussion

Figure 3 shows unsteady lift coefficient curves. Black circles in figure shows lift coefficients in static condition. Blue line shows the case of $f$ = 0.5 Hz, and red line shows the case of $f$ = 1.0 Hz. In static condition, lift slope is equal to theoretical slope under $\alpha$ = 6 deg, and lift slope changes over $\alpha$ = 6 deg. Therefore, it is considered that stall occurs in $\alpha$ = 6 deg. In dynamic condition of $f$ = 0.5 Hz, stall angle is rarely different from static condition. However, lift coefficient on upstroke is larger than static case. Lift force between upstroke and downstroke motions are different and clockwise hysteresis loop appears. In $f$ = 1.0 Hz case, stall angle shifts to 7 deg. Lift coefficient on upstroke is also larger than static condition. However, lift coefficient on downstroke is lower than static condition. Hysteresis loop in $f$ = 1.0 Hz case is larger than $f$ = 0.5 Hz case.

Figure 4 shows unsteady regions on surface of right wing of model in $f$ = 1.0 Hz case. To process raw images, the technique formulated by Nakajima [3] is used. As a result, difference of unsteady area between before and after stall is observed.

Figure 5 shows results of oil flow visualization on surface of right wing of model. In before stall case, the separation bubble is distributed evenly on spanwise direction, and most of flow field is dominated by forward flow. However, after stall condition, most of flow field is dominated by reverse flow. Three dimensional structure is observed on wing.

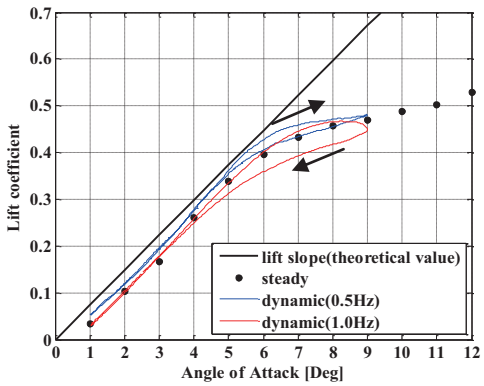


Fig. 3 Lift curve at condition of $U$ = 15 m/s, $\alpha_0$ = 5 deg, $A$ = 4 deg

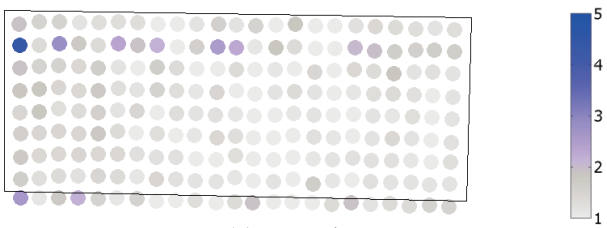

(a) $\alpha$ = 1 deg

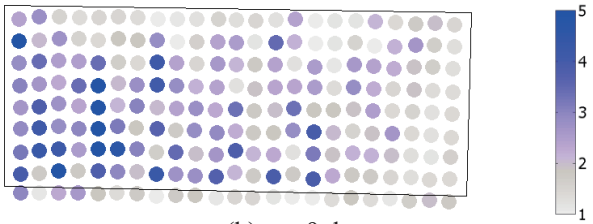

(b) $\alpha$ = 9 deg

Fig. 4 Processed image on right wing of model at condition of $U$ = 15 m/s, $\alpha_0$ = 5 deg, $A$ = 4 deg, $f$ = 1.0 Hz (index of flow unsteadiness)

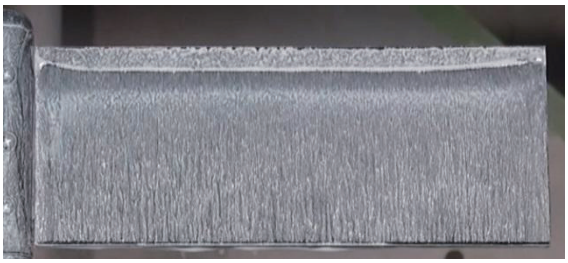

(a) $\alpha$ = 1 deg

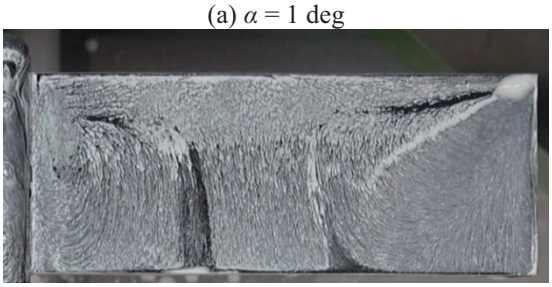

(b) $\alpha$ = 9 deg

Fig. 5 Oil flow visualization on right wing of model at condition of $U$ = 15 m/s

## 4. Concluding Remarks

To investigate unsteady aerodynamic characteristics of the three dimensional rectangular flat-plate wing, a wind-tunnel test of a flat-plate wing model in pitching motion was performed. In dynamic conditions, stall characteristics changed as compared with static condition. Lift coefficients on upstroke were larger than static condition. Lift coefficients between upstroke and downstroke were different and hysteresis loop appeared.

Visualization on surface of wing model by Fluorescent minitufts method and oil flow method were carried out. Different flow structures between before and after stall were observed.

## References


[1] Lawrence W.Carr, *Journal of Aircraft*, 25(1), (1987) 6-17.

[2] D.M.Tang, E.H.Dowell, *Journal of Aircraft*, 32, (1995) 1062-1071.

[3] Nakajima R, *Master Thesis, Department of Aerospace Engineering, Tohoku University*, (March 2014)

# The Development of the 0.3-m Magnetic Suspension and Balance System

Daiju Noguchi, Shuhei Taniguchi, Takumi Ambo, Daiju Numata and Keisuke Asai
Department of Aerospace Engineering, Graduate School of Engineering, Tohoku University
6-6-01 Aramaki Aza Aoba, Aoba-ku, Sendai, Miyagi, 980-8579 JAPAN

**ABSTRACT**

The purpose of this study is the development of the Magnetic Suspension and Balance System (MSBS) which can be applicable to dynamic wind tunnel testing in multi degrees of freedom. The first stage of this study is to support the model stably under windless condition. We developed the optical position sensing system and the control simulator for the 0.3-m MSBS. The resolutions of sensing system are as much or more than accurate compared with existing MSBS. Besides, the results of the control simulator suggest this system has enough stability margins. As a result, it is expected that this MSBS could support the model stably.

## 1. Introduction

Recently, evaluation of flight stability when an aircraft caught disturbance comes to be important as maneuverability of it improves. It is unsteady flow field where the dynamic stability of the aircraft is important to affect aerodynamics. Dynamic wind tunnel testing (DWT) is one of ways of modeling such field. DWT is the wind tunnel testing method to simulate unsteady aerodynamic behavior of the aircraft by oscillating or moving an aircraft model, and currently needs the model to move in multi degrees of freedom (D.O.F.). DWT uses mainly robotic manipulator generating movements like large swing in multi D.O.F. [1]. However, the movable range has some limits due to the number or length of the joints of the support device. Besides, the flow interference between model and support cannot ignore.

The Magnetic Suspension and Balance System (MSBS), which supports the model using magnetic force generated by interaction between magnet inside the model and magnetic field provides an ideal way of wind tunnel testing without support interference [2]. Moreover, aerodynamic forces acting on the model can be evaluated by the control condition. It is also possible to move the model in multi D.O.F..

The purpose of this study is the development of the Magnetic Suspension and Balance System (MSBS) which can be applicable to dynamic wind tunnel testing in multi D.O.F.. The first stage of this study is to support the model stably under windless condition. Even if it is under windless condition, external force from the holding tool setting the model on before levitation is acting on it. This force causes divergence behavior of the model without enough stability margins. In addition, such behavior is also caused by inaccurate position sensing.

In this paper, we report recent activities, mainly development of the position sensing system and the control simulator, towards supporting the model stably under windless condition.

## 2. The Principle of the MSBS

Figure 1 shows the coil configuration of the 0.3-m MSBS. The coordinate system of the MSBS is defined in the center of the coil system in the same figure.

Corresponding author: Daiju Noguchi
*E-mail address*: noguchi.daiju@aero.mech.tohoku.ac.jp

The coil system consists of eight electromagnets (#1 ~ #8) and two air-cored coils (#0, 9). The coils are placed at point-symmetric with respect to the origin. The magnet inside model is suspended against the aerodynamic force, moment and gravity force. Each coil is connected by yoke made of SS400 to forms the magnetic circuit.

The magnetic force $\boldsymbol{F}$ [N] and moment $\boldsymbol{N}$ [N·m] acting on the model installing cylindrical magnet can be expressed as following Eqs. (1) and (2). Where $\boldsymbol{M}$ [Wb·m] is magnetic moment of the magnet and $\boldsymbol{H}$ [AT/m] is magnetic field intensity around the magnet. $\boldsymbol{H}$ is controllable with the control current.

$$F = \int_V (M \cdot \nabla) H dV \tag{1}$$

$$N = \int_V M \times H dV \tag{2}$$

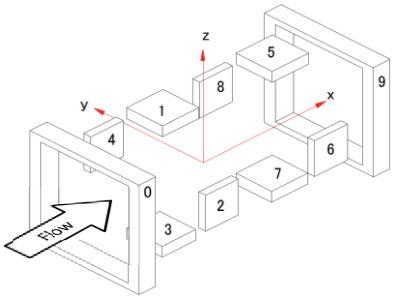


Fig. 1 Coil configuration of the MSBS

## 3. The Development of the Position Sensor

The optical position sensing system of the MSBS is developed based on the system at JAXA using CCD line sensors. As shown in figure 2, the line sensors are located in five places. These line sensors detect the outline around the model and the black-line marker on the surface. Using line sensors, this sensor system has characteristics such as high speed and accurate. The detected signals are converted to digital values which are defined as “count number” by counter board. The count numbers are in proportion to the number of CCD elements. Hence the position of the model can be detected by the count number.

Figure 3 shows the result of the calibration test between position of model and the count number. The vertical axis is for position of the model along $x$ direction, and the horizontal for count number of $x$ direction in the same figure. Standard deviations were taken at each point. This figure shows liner relationship

between the model position and the count number. Moreover, the errors were very smaller than the displacement of the model. Even the biggest error was approximately 7.08 μm when it was converted into the displacement of the model. It can be expected that magnetic suspension in windless condition is stable considering that the resolution of displacement of JAXA is about 50 μm.

## 4. The Development of Control Simulator

As position and attitude angle of the model detected by sensors include some delays due to signal transmission and low pass filter generally, there is some gap between real position and detected value. The control system of MSBS compensates these delays using double phase advancer. MSBS controls position of the model using PI controller after obtaining the difference between the compensated position and the target position. The calculated control currents are outputted from DA converter, and the currents flow in the coils. Thus, magnetic force acts on the model by generated magnetic field.

In order to support model securely using MSBS, it is necessary to estimate the control constant of the PI controller and the double phase advancer in advance. The simulator of the MSBS which simulates the model motion is developed using Simulink. Figure 4 shows block diagram of the control simulator. All blocks in the simulator are substituted transfer functions obtained by measurement and modeling.

Stability of the control system can be determined by stability of the open loop transfer function surrounded by the red dashed line in figure 4. The index of stability is satisfying both of more than 10 dB gain margin and 40 dB phase margin. This index is based on experience using follow-up control.

Figure 5 shows bode plot of the transfer function of $x$ direction after tuning of the control constant. As shown the same figure, this system has 13.9 dB gain margin and 63.4 deg phase margin. Similarly, other directions also have enough stability margins.

As the simulation includes the uncertainty in the modeling due to measuring error and nonlinearity generally, the accuracy of this simulation is unknown. It is necessary to optimize the control constant in the future observing step response of the real MSBS.

## 5. Summary

In this paper, we reported recent activities, mainly development of the position sensing sensor and the control simulator, towards supporting the model stably for the 0.3-m MSBS. The resolutions of displacement and attitude angle are as much or more than accurate compared with existing MSBS. According to estimation of the stability on the control simulator, control system of the MSBS has enough stability margins. In the future, we will conduct the levitation test, and optimize the control constant in the future observing step response of the real MSBS.

## References


[1] A. Bergmann, A. Huebner, T. Loeser, *Progress in Aerospace Sciences*, 44 (2008) 121－137.

[2] H. Sawada, T. Kunimasu, *Journal of the Japan Society for Aeronautical and Space Sciences*, 50 (2004) 188－195


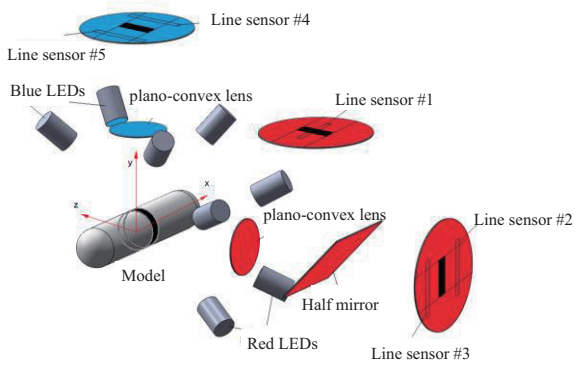


Fig. 2 Configuration of optical position sensors

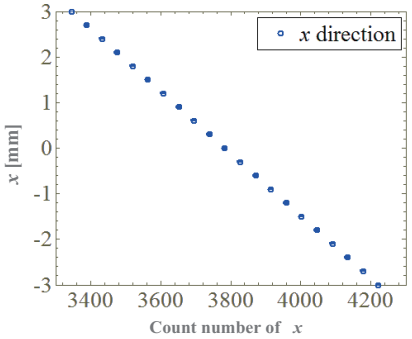


Fig. 3 Sensor calibration test result of $x$ direction

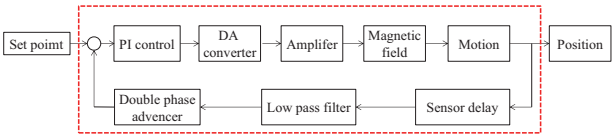


Fig. 4 Block diagram of the control simulation

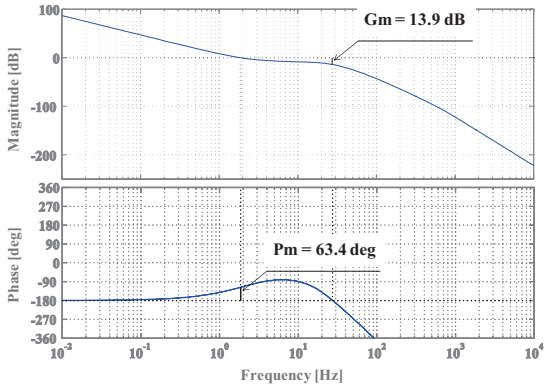


Fig. 5 Bode plot of the open loop transfer function of $x$ direction

# Conceptual Design of the Blended Wing Body Type Business Jet

Hyunmin Choi[1], Minhyung Ryu[1], Jinuk Kim[1], Jinsoo Cho[2]
[1]Department of Mechanical Engineering, Hanyang University
222 Wangsimni-Ro, Seongdong-Gu, Seoul, 133-791, Rep. of Korea
[2]School of Mechanical Engineering, Hanyang University
222 Wangsimni-Ro, Seongdong-Gu, Seoul, 133-791, Rep. of Korea

**ABSTRACT**

The demand on the business jet is growing fast. Conceptual study of the high efficient transonic business jet is carried out by using Blend-Wing-Body (BWB) configuration. The aerodynamic analysis of the BWB type transonic business jet is performed to understand the flow field around the aircraft at high subsonic flight speed. Commercial CFD code, ANSYS Fluent, is used for aerodynamic analysis of the BWB type business jet. As the results of aerodynamic study, the Mach number and pressure coefficient distribution around the BWB type business jet is presented.

## 1. Introduction

The global air traffic is growing explosively. Not only the demand for large commercial aircrafts is rising, but also the demand for smaller business jet is getting huge and the business jet market is growing fast. The business jet can provide the convenience of scheduling of the flight and more private space[1].

The large BWB aircrafts for the commercial airliners have been studied by many researchers. The BWB configuration has many advantages for aerodynamic performance. Smaller wetted area reduces surface drag and additional lift of center body increases total lift. High lift-to-drag ratio is benefit for high fuel efficiency and low emission[2-11].

Osterheld et al[4], Qin et al[5] and Liebeck[6] design the large scale commercial BWB aircraft by using high-fidelity CFD solver and multidisciplinary design optimization techniques. Qin et al[7] study about twist angle of the wing and spanwise lift distribution of the large BWB aircraft to reduce the drag.

Nara and Kanazaki [8] and Kanazaki et al[9] perform the conceptual design and aerodynamic shape optimization of a 150PAX class BWB type aircraft named Novel-Wing-Body (NWB). They use the unstructured Navier–Stokes flow solver for aerodynamic analysis and optimization technique to evaluate optimized NWB.

Harijono and Alvin[10] and Mulyanto and Nurhakim[11] are carried out conceptual study on the large category BWB business jet. By applying the BWB configuration to the business jet, not only the business jet takes advantages of the BWB configuration, but also the advantage of wide cabin space from wide center body is provided. But aerodynamic analysis at high subsonic speed for design the transonic BWB business jet is not presented yet.

In this paper, the conceptual design and aerodynamic analysis of the medium category BWB type business jet are performed to understand the flow field around the BWB type business jet at high subsonic speed. For the aerodynamic analysis, commercial CFD tool, ANSYS Fluent is used.

Corresponding author: Jinsoo Cho
*E-mail address*: jscho@hanyang.ac.kr

## 2. Method

### 2.1 Design requirements

The design target of the BWB type business jet is medium category business jet with transonic cruise speed. The large category business jet is typically define as prices from $49M to $71M, offering ranges over 5,000 NM and cabin volume of 42.5 $m^3$ (1,500 $ft^3$) to 85.0 $m^3$ (3,000 ft3) [1].

The target performance of the BWB type business jet is listed in Table 1. The target maximum-take-off-weight is about 40,000 kg with over 12 pax and the target cruise speed is Mach 0.85. The target cruise altitude is over 11 km.

Table 1. Target performance of the BWB type business jet

| | |
|---|---|
| MTOW | 40,000 kg |
| Cruise speed | M 0.85 |
| Range | Over 5,000 NM |
| Cruise altitude | Over 11 km |
| Passengers | 2 + over 12 pax |

### 2.2 Airfoil selection

The thickness and camber distribution of the airfoil are critical to the aerodynamic characteristics such as lift-to-drag ratio, moment coefficient and shock strength for high speed flight.

The fuselage of BWB aircraft is considered as low aspect ratio wing and the cross section of the fuselage is designed as an airfoil. The airfoils used for the BWB type business jet is shown in Fig. 1. For the center body, an arbitrary reflexed airfoil is designed. For enough cabin height, thickness of center body airfoil is designed to 2.3 meters and chord length of center body airfoil is designed for 18 meters for reducing thickness ratio to not exceed 13%. The REA 2822 transonic airfoil is selected for the wing section.

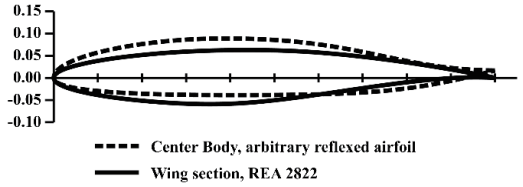


Fig. 1 Airfoils shape for the BWB type business jet

### 2.3. Platform design

The BWB business jet platform is consist of center body, wing-section and mid-section. The center body is defined with two airfoil section and span like the very low aspect ratio wing. The wing-section is a simple taper ratio wing.

The mid-section blends the center body and wing-section. The leading edge and tailing edge of the center body and mid-section are designed with spline curve to smoothly connect the leading and trailing edges of each section. The design parameters are shown in Fig. 2. Total span, width of center body, span of wing, the chord length, sweep back angles and incidence angles of each airfoil section are selected as geometric parameter and design variables. The wing span and chord length of each wings are fixed. The total wing span and wing area are fixed as 28 meters and 90 $m^2$ each based on average span and wing area of the large category business jet.

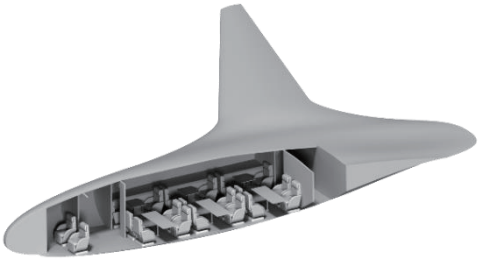

Fig. 2 Conceptual modeling of cabin space of the BWB type business jet

### 2.4. Aerodynamic analysis

Aerodynamic analysis of the BWB type business jet is performed by using commercial CFD tool, ANSYS Fluent. For the aerodynamic analysis, half sphere of computational domain is generated. The radius of computational domain is 20 times of the MAC. The density-based coupled solver is used as solver and SST k-e turbulent model is applied. The half spheral far boundary surface is set as pressure far field and circular center section is set as symmetric plane. Free stream Mach number of 0.85 and standard atmosphere condition at altitude of 11km are applied to the pressure far field boundary condition.

## 3. Results and Discussion

The aerodynamic analysis result is shown in Fig. 3. Weak shock occurs on the upper surface of the BWB type business jet.

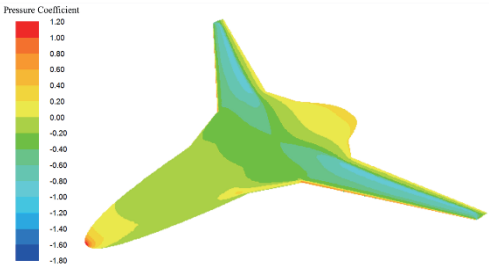


Fig. 3 Pressure coefficient distribution on the BWB type business jet

## 4. Concluding Remarks

As result of conceptual design of the BWB type business jet, the BWB configuration introduces not only aerodynamic efficiency but also advantage of large cabin space.

## References


[1] Bombardier Aerospace: Market Forecast 2013-2032, (2013).

[2] M. A. Potsdam, Blended wing body analysis and design, *AIAA Applied Aerodynamics Conference*, (1997) 799-805.

[3] R. H. Liebeck, M. A. Page, B. K. Rawdon, Blended-Wing-Body Subsonic Commercial Transport, *36th AIAA Aerospace Sciences Meeting and Exhibit*, (1998).

[4] C. M. Osterheld, W. Heinze, P. Horst. Preliminary design of a blended wing body configuration using the design tool PrADO, *DGLR BERICHT*, 5(2001) 119-128.

[5] N. Qin, A. Vavalle, A. Le Moigne, M. Laban, K. Hackett, P. Weinerfelt, Aerodynamic considerations of blended wing body aircraft, *Progress in Aerospace Sciences*, 40 (2004) 321-343.

[6] R. H. Liebeck, Design of the blended wing body subsonic transport, *Journal of Aircraft*, 41 (2004) 10-25.

[7] N. Qin, A. Vavalle, A. Le Moigne, Spanwise Lift Distribution for Blended Wing Body Aircraft, *Journal of Aircraft*, 42 (2005) 356-365.

[8] T. Nara, M. Kanazaki, Initial Design and Evaluation of a Novel Concept Regional Aircraft, *2010 Asia-Pacific International Symposium on Aerospace Technology*, (2010)

[9] M. Kanazaki, R. Hanida, T. Nara, M. Shibata, T. Nomura, M. Murayama, K. Yamamoto, Challenge of design exploration for small blended wing body using unstructured flow solver, *Computers & Fluids*, 85 (2013) 71–77.

[10] D. Harijono, K. L. W. Alvin, Conceptual Design and Aerodynamic Study of Blended Wing Body Business Jet, *ICAS 2012*, (2012)

[11] T. Mulyanto, M. L. I. Nurhakim, Conceptual Design of Blended Wing Body Business Jet Aircraft, *Journal of KONES Powertrain and Transport*, 20 (2013) 299-306.

# A Priori Test of Subgrid-scale Model by Machine Learning in a Turbulent Channel Flow

Masataka Gamahara[1], Yuji Hattori[2]
[1]Department of Applied Information Sciences, Tohoku University
Aramaki aza Aoba 6-3-09, Sendai, Miyagi, 980-8579, Japan
[2]Institute of Fluid Science, Tohoku University
Sendai, 980-8577, Japan

**ABSTRACT**

The SGS model in LES is estimated by neural network (NN model), which is one of the methods in machine learning. Training data for learning are obtained by direct numerical simulation (DNS) of turbulent channel flow. The SGS stress tensor obtained by NN model is in good agreement with that by DNS. The correlation coefficients are shown to depend on the filter size.

## 1. Introduction

Large eddy simulation (LES) is a method in which only large-scale eddies in turbulence are calculated and the effects of small-scale eddies are modeled as subgrid scale (SGS) stress. LES enables us to use coarser grid than DNS which uses no model. Hence, computational costs are reduced.

Many existing SGS models are based on the eddy viscosity. In this theory turbulent diffusion is regarded to be analogous to molecular diffusion. The Smagorinsky model [1] which is the most famous SGS model approximates well dissipation of energy in turbulence. However, it is known that the SGS stress tensor obtained by the Smagorinsky model is poorly approximated. The dynamic Smagorinsky model proposed by Germano [2], in which the model coefficient is dynamically calculated from the velocity field, sometimes gives negative viscosity. This represents energy transfer from subgrid-scale to grid scale (GS), but overestimation induces instability. Therefore, more accurate turbulence model is required. In addition, models taking account of the effects of vorticity are proposed after coherent structures are discovered [3].

In this study as a new approach of proposing a turbulence model, we try to construct a SGS model by neural network which is one of the methods in machine learning. Training data which are used for learning are obtained by DNS of turbulent channel flow. We are interested in whether it is possible to learn the effects of small-scale turbulence by machine learning. We investigate correlation between SGS stress tensor obtained by DNS and that estimated by NN model. (a priori test)

## 2. Method

In LES, the filtered Navier-Stokes equations are solved. For incompressible flow, the equations are

$$\frac{\partial \bar{u}_i}{\partial t} = -\frac{\partial \bar{u}_i \bar{u}_j}{\partial x_j} - \frac{\partial \bar{p}}{\partial x_i} + \frac{1}{Re}\frac{\partial^2 \bar{u}_i}{\partial x_j \partial x_j} + \frac{\partial \tau_{ij}}{\partial x_j} \qquad (1)$$

where $\tau_{ij}$ is the subgrid-scale stress tensor and modeled by filtered variables. It represents contribution to GS from SGS. $\bar{f}$ is the grid-scale component obtained by filtering operation.

Corresponding author: Masataka Gamahara
*E-mail address*: gamahara@dragon.ifs.tohoku.ac.jp

One-dimensional filtering is

$$\bar{f} = \int_{-\infty}^{\infty} G(x - x') f(x') dx', \qquad (2)$$

where $G$ is a filter function. We use top hat filter as the filter function.

We use neural network for machine learning since it is easy to implement and known to give good approximation of function. An example of network and one neuron in the entire network are shown in Fig.1. In NN, many inputs are weighted and summed. The output which becomes n[th] input is calculated as

$$X_i^n = f(u_i^n - h_i^n), \quad u_i^n = \sum_j w_{ij}^n X_i^{n-1}, \qquad (3)$$

where $X_i^n$ is n[th] input, $w_{ij}^n$ is weight, $h_i^n$ is threshold and $f$ is the basis function. We use error back-propagation method for the learning method which determines weight and thresholds. This method puts repetitively input and training data and then modifies the weight and thresholds.

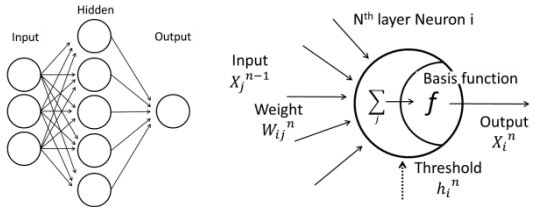


Fig.1 Network and structure of one neuron

We use velocity gradient tensor as inputs aiming at improving conventional SGS model. In the eddy viscosity approximation, turbulent diffusion is considered as analogous to molecular diffusion. Hence, the rate of strain tensor is used. In this study we include vorticity since we take account of its effects. The velocity gradient tensor is equal to the sum of rate of strain tensor and vorticity. Furthermore, we consider the effects of the wall. We add the distance from the wall to the input. This model recurs on point to point and uses no test filter. Hence, it corresponds to a simple Smagorinsky model.

This NN consists of three layers with the number of the input unit, hidden unit and output unit being 10, 100 and 1, respectively. Since the number of the output is one we construct each component of the SGS model independently. Training data are obtained from DNS of turbulent channel flow. The Reynolds number based on the friction velocity $u_\tau$ and the channel half width $\delta$ is

$Re_\tau$=180. The streamwise, spanwise and wall normal sizes of the computational domain are 4πδ, 2πδ and 2δ respectively. DNS is performed on 192×128×160 (Nx×Ny×Nz) grid points to resolve the smallest eddies. Exact SGS stress tensor is obtained as follows by filtering velocity field from DNS

$$\tau_{ij} = \overline{u}_i\overline{u}_j - \overline{u_i u_j}, \quad (4)$$

In this study, we investigate dependence on filter size. We use four values of filter size as shown in Table.1.

Table 1. Filter size

| Name | Nx | Ny | Nz | Δx | Δy(ave.) | Δz |
|---|---|---|---|---|---|---|
| Filter48 | 48 | 48 | 48 | 0.262 | 0.042 | 0.131 |
| Filter52 | 52 | 52 | 52 | 0.242 | 0.038 | 0.121 |
| Filter64 | 64 | 64 | 64 | 0.196 | 0.031 | 0.098 |
| Filter96 | 96 | 96 | 96 | 0.131 | 0.021 | 0.065 |

## 3. Results and Discussion

First, results of Filter64 are shown. Fixing y coordinates, correlation coefficients are obtained on the xz plane. Fig.2 shows correlation coefficients along y coordinates between SGS stress tensor form DNS and that obtained by NN. All components are well correlated. Especially, $\tau_{11}$, $\tau_{12}$ and, $\tau_{31}$are larger than 0.8 in most of y values. Correlation coefficients between the Smagorinsky model and DNS are about 0.3 which is low. Hence higher correlation coefficients than the Smagorinsky mode are obtained by NN model. Near the wall all correlation coefficients are small. It seems that viscosity is dominant and fluctuations are too small to be learned.

Fig.3 compares spatial distribution of $\tau_{11}$ at y = 0.1 of the SGS stress obtained by DNS and NN model; note that the fluctuations are the largest at y=0.1. It shows that NN model approximates the SGS stress well, while it underestimates the SGS stress a little. We have tried learning and recurring using different five sets of training data. High correlation coefficients are obtained from each set. It is not coincidental that NN works well. NN model learns some important statistical properties of wall turbulence.

The total correlation coefficient is defined as

$$R = \frac{1}{2\delta}\int_{-\delta}^{\delta} C(y)dy, \quad (5)$$

where C is the correlation coefficients at xz plane. $R$ shows correlation coefficients in the entire channel. Fig.4 shows correlation coefficients for different filter size. The finer the filter size, the better are the correlation coefficients. It turns out that NN model using Filter48 is low performance. It is reasonable that LES coincides with DNS when the grid becomes fine enough. In order that NN model learns the turbulent statistics successfully the grid size should be smaller than a certain length scale.

## 4. Concluding Remarks

We have tried to construct an SGS model by NN. We used velocity gradient tensor and y coordinate as input and SGS stress tensor obtained by DNS as output, and then executed machine learning. High correlation coefficients of all components are obtained between SGS stress tensor by DNS and that obtained by NN. Spatial distributions of SGS stress obtained by NN model are similar to those obtained by DNS. The correlation coefficients depend on the filter size.

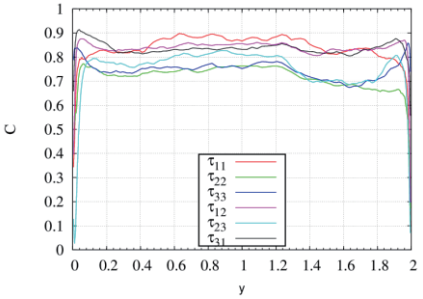


Fig.2 Correlation coefficients along wall normal direction

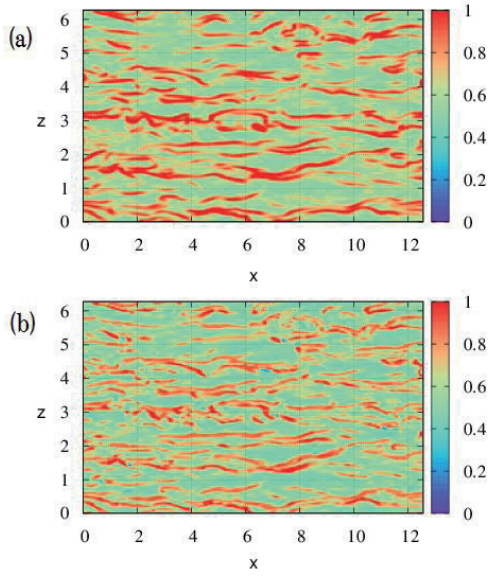


Fig.3 Spatial distributions of $\tau_{11}$ at y = 0.1. (a) DNS (b) NN model

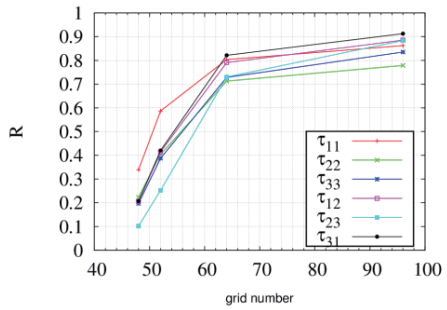


Fig.4 Correlation coefficients for different filter size

## References

[1] J.Smagorinsky, *Mon.Weath. Rev,* 91 (1963) 99-164.
[2] M. Germano, *J. Fluid Mech.*, 238 (1992) 325-36.
[3] H. Kobayashi, *Phys.Fluids*, 17 (2005) 045104.

# Numerical Simulation of 3-D Supercritical-fluid Flows using BCM and Meshless Method

Shibo Qi[1], Takashi Furusawa[1], Satoru Yamamoto[1]
[1]Dept. of Computer and Mathematical Sciences, Tohoku University.
6-6-01 Aramaki Aza Aoba, Aoba-ku, Sendai, Miyagi, 980-8579 Japan

**ABSTRACT**

The numerical simulation of three-dimensional supercritical-water flows is presented. In the present method, the Supercritical-fluids Simulator (SFS) is coupled with the Building-Cube Method (BCM), because of its simplicity and efficiency. A meshless method is further applied to the wall boundary treatment because of its flexibility. First, an experimental validation is conducted to show the effectiveness of the present method; then the mixings flows in T-shaped channels with circular and rectangular cross section shapes are calculated and compared.

## 1. Introduction

It is known that experimental researches of supercritical-fluid flows are rare because of the extreme conditions. Numerical simulation is likely to be a practical and promising tool. Our research group has developed Supercritical-Fluids Simulator (SFS) for numerical simulation of supercritical-fluid flows [1].

To treat the mesh generation for complex geometry, SFS has been coupled with Building-Cube Method (BCM) [2] for its simplicity. Further, a least-square meshless method has been introduced as wall boundary treatment for its flexibility in treating arbitrary geometry and complex physics.

In the paper, the hybrid method is applied to the numerical simulation of the supercritical hydrothermal synthesis (SCHS) process, which is a typical application of the supercritical water in nano-scale particle formation.

## 2. Numerical Method

### 2.1 Governing equation

The preconditioned three-dimensional compressible Navier-Stokes equations are used in the paper. The vector form equation set in the general curvilinear coordinates is written as

$$\Gamma\frac{\partial\hat{\boldsymbol{Q}}}{\partial t}+\frac{\partial\boldsymbol{F}_i}{\partial\xi_i}+\frac{\partial\boldsymbol{F}_{vi}}{\partial\xi_i}=0 \tag{1}$$

As spatial discretization, the preconditioned Roe scheme is used for inviscid-flux estimation, and the second-order MUSCL scheme is applied for the estimation of primitive variables. As time-integration process, the preconditioned implicit LU-SGS scheme is used.

### 2.2 Building-cube method

The Building-Cube method is used as the grid generation approach for CFD calculation in the paper. In BCM, blocks called ‘cubes’ are used as subdomains to adapt to local resolution length, and a uniform Cartesian mesh called ‘cells’ is generated in each cube as calculation grids, as shown in Fig. 1.

The wall boundary in BCM is defined in a staircase manner. How to define the location of solid wall surface is a critical issue for Cartesian mesh method.

Corresponding author: Shibo QI
*E-mail address*: qi@ caero.mech.tohoku.ac.jp

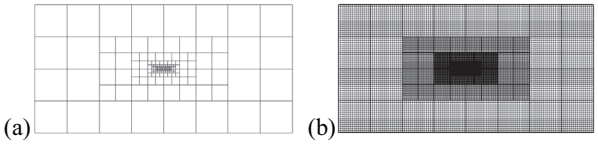


Fig. 1 Mesh configurations in BCM

### 2.3 Meshless method

The meshless method in the present study is based on the least-square approximation. The derivatives are defined by a linear approximation:

$$\frac{\partial\varphi}{\partial x}=\sum_{j=1}^{n}a_{ij}(\varphi_j-\varphi_i)\ ,\quad \frac{\partial\varphi}{\partial y}=\sum_{j=1}^{n}b_{ij}(\varphi_j-\varphi_i) \tag{2}$$

The coefficients are parameters related to the relative positions of the cloud points to its reference node.

In the meshless method, the governing equation is solved in the same way as in the Cartesian mesh method.

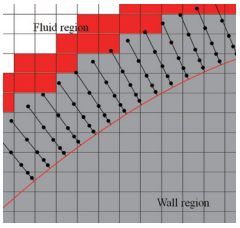


Fig. 2 Meshless nodes in the wall normal directions

In the hybrid method, there are basically three steps in the mesh generation process: background grid generation in BCM, meshless nodes generation in the meshless method and data communication point definition.

## 3. Results and Discussion

The supercritical hydrothermal synthesis (SCHS) is one of the innovative methods for fabricating nano-scale particles [3]. A T-junction reactor is a simple but typical design of the SCHS reactor.

The schematic of the T-junction reactor and the BCM mesh for the test case is shown in Fig. 3. The BCM mesh consists of 864 cubes and 8×8×8 cells in each cube, thus the total number of Cartesian mesh point is about 440,000; the surface point number in the meshless solver is about 30,000 and the total number of meshless point is about 200,000.

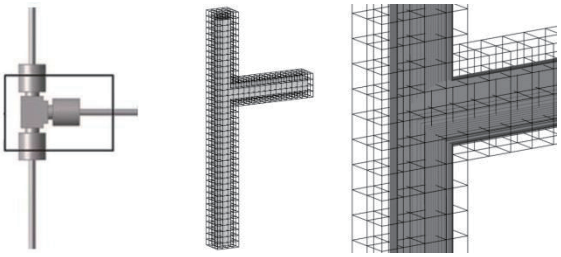

Fig. 3 Schematic and BCM mesh for the T-shape channel

### 3.1 Experimental validation

First, the validation based on experimental result was proposed. The basic settings of the test case are shown in Table 1.

Table 1 the basic settings of the experimental validation

| | Test case |
|---|---|
| Pressure [MPa] | 25.0 |
| T_SCF [K] | 663.00 |
| T_water [K] | 300.00 |
| Re_SCF | 2400 |
| Re_water | 25 |

Figure 4 shows the temperature distributions in comparison with the experimental results [4]. The significant backflow in the sub channel due to the natural convection effect is captured, and the numerical result is in good agreement with the experimental result.

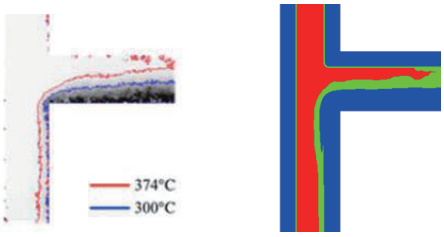


Fig. 4 Comparison of temperature distributions

### 3.2 Comparison of cross section shapes

Then, the comparison of T-junction reactors with rectangular and circular cross section shapes was proposed.The basic settings of the test case are shown in Table 2. The reference length was set to 0.6 mm (diameter of the circular one and width of the rectangular one).

Table 2 the basic settings of the test case

| | Test case |
|---|---|
| Pressure [MPa] | 30.0 |
| Fluid temperature in the main channel [K] | 700.00 |
| Fluid temperature in the sub channel [K] | 600.00 |
| Re_SCF | 500 |
| Re_water | 30 |

Figure 5 shows the 2-D temperature distributions of the test cases in the mid-section. The natural convection tends to be more significant in the rectangular one, and the mixing effect is more significant in the circular one.

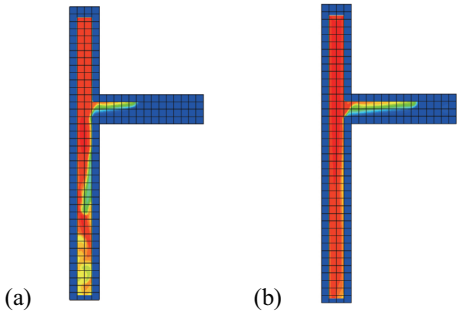


Fig. 5 Temperature distributions in the cross sections
(a) circular (b) rectangular

In addition, the isothermal surfaces in the circular and rectangular T-junction reactors are shown respectively in Fig. 6. The three dimensional structures are clearly captured, especially in the circular configuration.

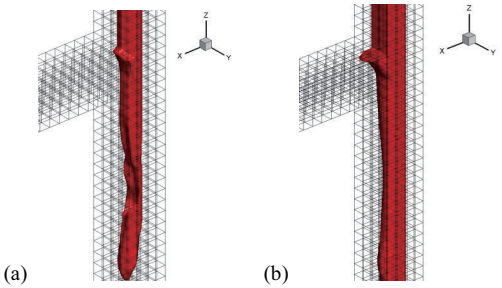


Fig. 6 Isothermal surfaces in the reactors
(a) circular (b) rectangular

## 4. Concluding Remarks

Numerical simulation of 3-D supercritical water flows was presented in this paper. The SFS was coupled with BCM for its simplicity, and a meshless method was further introduced as the wall boundary treatment for its flexibility. The test cases show that the present method is a promising tool for 3-D practical supercritical-fluid flow simulations.

For the future work, the turbulence model is to be added to solve the turbulent supercritical fluid flows in practical applications. A parallel implementation is also a critical issue for 3-D practical applications.

## References

[1] S. Yamamoto, *Journal of Computational Physics*, Vol. 207, No. 1 (2005), pp. 240-260.
[2] K. Nakahashi, L-S. Kim, *AIAA Paper*, Vol. 423, (2004).
[3] T. Adschiri, K. Kanazawa, K. Arai, *Journal of the American Ceramic Society*, Vol. 75, No. 9 (1992), pp. 2615-2618.
[4] K. Sugioka, K. Ozawa, T. Tsukada, et al. *AIChE Journal*, Vol. 60, No. 3 (2014), pp. 1168-1175.

Eleventh International Conference on Flow Dynamics
October 8-10, 2014, Sendai, Miyagi, Japan

# A Multi-step Aircraft Icing Simulation Method Based on Remesh Technology

Zhu Chunling[1], Zhu chengxiang[1], Liu Lei[2]
[1]Nanjing University of Aeronautics & Astronautics
Yudao Street, Nanjing, Jiangsu, 210016, China
[2]AVIV Cheng Du Aircraft Industrial(Group) CO.,LTD
Huang Tianba, Chengdu, Sichuan, 610000, China

**ABSTRACT**

A multi-step method based on remesh technology is introduced in this paper in order to improve the accuracy of aircraft icing simulation. Grid is generated by solving the elliptic PDEs. And sectorial partition grid reconstruction method is used to consider the dynamic effects of ice accretion on flow field, droplet trajectories and ice shape. In this way, the efficiency, quality and reliability of grids can be improved. The computational results which are agreed with the IRT results show that the method can improve the accuracy of simulation greatly.

## 1. Introduction

Aircraft icing seriously threat to flight safety, therefore, it must take reasonable protection methods to ensure flight safety. No matter which protection method is used, the predictions of icing region, icing volume and ice shape are precondition of efficient protection system design and arrangement. So far, computation and analysis of the ice accretion process on an aircraft and the resulting performance degradation have been undertaken by many researches.

Generally, the whole icing calculation should contain several separate program elements at least, they are:[1]

1) Grid generation and reconstruction;
2) Flow field calculation;
3) Droplet trajectory and impingement calculation;
4) Heat transfer process and ice growth calculation;

Aircraft icing is a dynamic process varying with time and the ice on the surface is gradually accumulated layer by layer. Ice accretion changes the aerodynamic shape, which affect the air flow filed and droplet trajectories and the ice shape ultimately. In this paper, grid reconstruction technology based on sector partition and high quality body fitted grid are used. Then a multi time step calculation method is achieved considering the dynamic effects of icing, and the accuracy of aircraft icing numerical simulation is improved.

## 2. Method

1) Grid generation and reconstruction

The grid module is designed to generate a perfect grid system automatically around the model and redefine the iced geometries. When the icing calculation is begun in the first time step, the boundary of airfoil is clean and keeps the streamline shape, so the geometry doesn't need to be dealt too much. During the grid generating system, this module can generate a discrete approximation to the surface as faithfully as possible for a given number of points. Points are clustered in the area of lead edge of the airfoil. In addition, the clustered points can ensure geometry fidelity for the iced airfoil surface. An elliptic grid generation method for finite difference computations about airfoil is used to obtain high quality single block grids .

In order to control the grid system better, the Laplace system is extended to a Poisson system.

The control source terms are described by Hilgenstock technique which can give a better control on the distribution of the grid system.

It is worth noting that ice-layer accretion on the geometry is simulated using the multiple time-step method so that the icing parameters can be updated in second after second.

The ice accretion always happens in the leading edge of geometry. Therefore, a best executive way for grid change is to use the multi-block gird method and put the grid reconstruction only in the leading edge of the airfoil. The whole calculation area sector partition can be divided into two sub zones, namely small sector near ice accretion (Zone I) and blank region (Zone II). The sub gird in each block is adjusted independently to satisfy the requirement for icing calculations. The illustration for multi-block grid method is given in Figure 1.

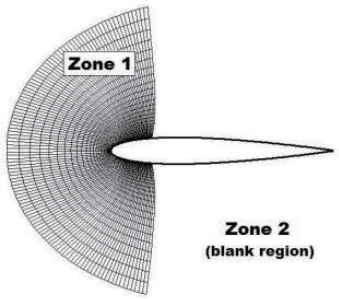


Fig.1 Grid partition for a single airfoil

In the icing calculation, the background grid is generated first (Zone II) and subsequent grid topology will no longer be changed. Grid of zone I is changed by time changed, and grid is reconstructed according to the ice shape. Grid interface of Zone I and II is a fan boundary changes due to ice only within the Zone I boundaries, and the rest of the boundary nodes on remains the same. Both sides of the position of the boundary are determined based on the frozen limitation, which ensure the ice accretion is located in the grid update region.

The scope of Poisson equation iteration is further narrow due to this method and the quality of grid is

Corresponding author: Zhu Chunling
*E-mail address*: clzhu@nuaa.edu.cn

greatly improved. In addition, the current time step flow field initialized values is derived from the former one time step after reaching convergence of the flow field information, so after the assignment the flow field can quickly reach convergence.

2) Flow field calculation

A two-dimensional Navier-Stokes algorithm is used to solve the stead or unsteady, uncompressible or compressible viscous airflow past an airfoil model. The flow solution is computationally expensive and time consuming in every time step because of the severe transients that the flow solver must dissipate.

3) Droplet impingement

The droplet trajectories can be obtained by adopting a Lagrangian approach, which bases on hypothesis of no interaction of the droplet motion on the airflow field.

4) Ice accretion

The growth of ice layer on the model surfaces refers to a complex fluid dynamics, heat transfer, and mass transfer process.

5) Geometry modification

In the icing computation, surface modeling and grid generation for iced airfoils are a very challenging job, and the change of the geometry boundary is unpredictable in each time step. Therefore, some functions like data probing, boundary smoothing, and structured grid refinement need to be done after every computational step of ice growth. The boundary smoothing function contains three steps, they are curve smoothing, discretization, and reshaping.

## 3. Results and Discussion

The numerical simulation of ice accretion on NACA 0012 is performed using the method above, under the geometric, aerodynamic, and meteorological conditions shown in Table 1, and the results are shown in Fig.2 and Fig.3.

Table 1. Input conditions

| Variable names | Value |
|---|---|
| Chord of airfoil | 0.5337m |
| Angle of attack | 4.0° |
| Free-stream velocity | 67.04m/s |
| Free-stream pressure | 101325(Pa) |
| Liquid water content | 1g/m$^3$ |
| Median Volume Diameter | 20.0 $\mu$ m |
| Static temperature | 268K |
| Time step | 60s |
| Total time of icing | 360s |

Fig.2 shows the results of the ice growth calculation, the total icing time is seven minutes, and the final type of ice shape is glaze ice because the environmental temperature is relative high. The growth of ice layer on the leading of airfoil is in the manner of time-step, which is set to be sixty seconds. Therefore, there are six ice layers to indicate the process of ice accretion. Analogously, solution data of all the modules must be updated after every time step during the icing computation.

The result (Fig.2) shows that computed ice shapes and the comparisons with the LEWICE result as well as experimental data. As it can be seen from the figure, when time-step is smaller than 30, the predicted ice shape is agreed very well with IRT data, while time-step is more than 60s, there are big errors between the predicted results and IRT data. Hence, in the icing numerical simulation, errors caused by dynamic ice accretion cannot be ignored.

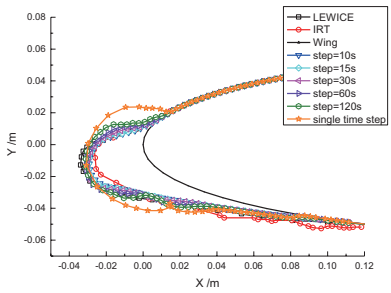


Fig.2 Ice shape calculated with single and multi-time step method compared with IRT and LEWICE computational data

Fig.3 shows the grid generator output for the iced airfoil, the orthogonality and node space are well controlled around the outer boundary of airfoil, especially in the region containing ice shape. It proved the validity of the method of grid reconstruction .

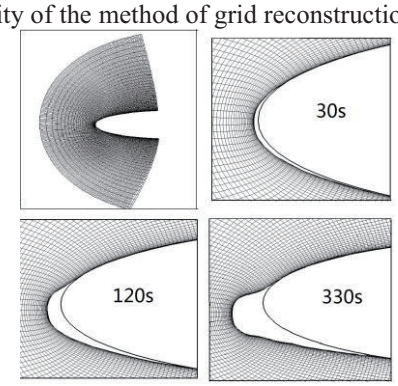


Fig. 3 Grid for NACA0012 airfoil with ice shape

## 4. Concluding Remarks

This paper provides a multi-step method based on remesh technology, which can be used for aircraft icing simulation. The computational results show that multi time-step is helpful to improve calculation accuracy in icing simulation. And partition grid reconstruction is contributed to the quality and efficiency of grid generation.

## References

[1] C.Ghenai and C.X.Lin. Verification and Validation of NASA LEWICE 2.2 Icing Software Code. *Journal of Aircraft*, (2006).

[2] David S.Thompson and Bharat K.Soni .Automated Geometric Modeling and Grid Generation for Airfoils with Ice Accretion". *AIAA 2002-0379*, Reno,Nevada, January (2002).

Eleventh International Conference on Flow Dynamics
October 8-10, 2014, Sendai, Miyagi, Japan

# High Resolution Implementation Of von Neumann-Richtmyer Typed Artificial Viscosity For Shock Capturing Scheme

Nobuyoshi Fujimatsu[1]
[1]TOYO University
2100, Kujirai, Kawagoe, Saitama, 350-8585, Japan

**ABSTRACT**

In the present paper, some problems of von Neumann-Richtmyer typed artificial viscosity used in the compressible flow analysis are discussed through the test problems to confirm the ability of this viscosity. We derived the equation which denoted the relationship between those gird points and the empirical parameter. The nonlinear function based on the strain of velocity is incorporated to control the intensity of artificial viscosity and the numerical results showed that the proposed method can more sharply capture the shockwave rather than the traditional method.

## 1. Introduction

In the compressible flow analysis and the fracture mechanics, the understandings of shockwave phenomena are one of main research topics. When we analyze the shockwave using the high order scheme, the numerical accuracy is reduced to suppress the numerical oscillation at the discontinuity of shock wave, the filtering treatment is applied as the post-processing and the artificial viscosity is used. Each methods are used to remove the numerical instability by applying the pseudo-viscosity at the region with sharp differences. In the present paper, we focused on the use of artificial viscosity.

The artificial viscosity is denoted as the equation so that the Rankine-Hugoniot's relations are satisfied with the exchange between the thermal energy and the kinetic energy at the shock wave. Von Neumann-Richtmyer's artificial viscosity[1] which is one of them is proposed in 1950 and is used in the wide variety of numerical simulation even now. However, there are some problems to treat it in the numerical analysis. N-R artificial viscosity is not able to take the differentiation for space variables because of not acting to the incompressible region and the effectiveness of that to the curvilinear coordinates are not validated.

In the present paper, we investigate some problems of artificial viscosity. The relationship of the artificial viscosity to the grid resolution for capturing the shock wave is revealed and the equation to automatically decide the coefficient of the artificial viscosity is proposed. Finally, we implement the appropriate form to apply the artificial viscosity to curvilinear coordinates.

## 2. Von Neumann-Richtmyer typed artificial viscosity

In the numerical simulation, the computational grids can not generate the finer computational grid than the thickness of the shockwave. One of ideas to resolve this problem is the numerical treatment to apply the artificial viscosity to the compression wave and we can capture the shock wave using the finite grid points. The representative example is von Neumann-Richtmyer artificial viscosity (N-R artificial viscosity).

Corresponding author: Nobuyoshi Fujimatsu
*E-mail address*: fujimatsu@toyo.jp

This approach does not need to detect the shock wave and can easily extend to the flow analysis even in the multi-dimensions. Therefore, we can save the increment of the numerical costs and do not need the complicated algorithm to the multi-dimensional problem. Von Neumann-Richtmyer proposed the following equation as the artificial viscosity[1]

$$q_1 = \rho(c\Delta x)^2 \left|\frac{du}{dx}\right| \frac{du}{dx} \tag{1}$$

$\Delta x$ is spacing of grids, $c$ is the compression parameter to control the artificial viscosity. $du/dx$ is velocity of strain and only acts to the compression region. In the multi-dimensional cases, the strain vector represents the sum of the diagonal term of strain velocity tensor, namely, volumetric rate. The use of strain vector as the function of artificial viscosity has the applicable characteristics because those terms increase in the shock wave and reduce to zero away from the compression region.

Eq. (1) is effective to the front of the shockwave, however, it is not suitable to the suppression of numerical instability after passing by the compression wave. Consequently, Landsoff et al.[2] proposed the linear function like Eq. (2).

$$q_2 = -\rho c \Delta x \frac{du}{dx} \tag{2}$$

In the almost cases, the artificial viscosity is treated as the combination of Eq. (1) with Eq. (2) like $q=q_1+q_2$. Yabe et al.[3] slightly modified the N-R artificial viscosity as Eq. (3). The coefficient $\alpha$ represents the strength of artificial viscosity and the range of $\alpha$ =0.6 to 1.0 is recommended in the numerical computation.

$$q = \begin{cases} \alpha\left[-\rho c_s\left(\frac{\partial u}{\partial x}\right)\lambda + \rho\frac{\gamma+1}{2}\left(\frac{\partial u}{\partial x}\right)^2\lambda^2\right] & if\ \frac{\partial u}{\partial x} < 0 \\ 0 & otherwise \end{cases} \tag{3}$$

## 3. Numerical method

In order to confirm the effect of the N-R artificial viscosity, we conducted some of numerical problems for the validation. In the present computation, the governing equations are one- and two-dimensional Euler equations. The perfect gas is assumed in this simulation and the ratio of specific heat is 1.4. The advection terms are solved using the CIP method and the

central difference scheme is adapted to the non-advection terms.

## 4. Numerical results and discussions

Here, we investigate the relationship between th thickness of the shockwave and the coefficient of $\alpha$. The one-dimensional steady Navier-Stokes equations can be written as following.

$$\rho u = \rho_0 u_0$$
$$p + \rho u^2 = p_0 + \rho_0 u_0^2 \qquad (3)$$
$$\rho u\left(h + \frac{1}{2}u^2\right) - \frac{4}{3}\chi u\frac{du}{dx} = \rho_0 u_0\left(h_0 + \frac{1}{2}u_0^2\right)$$

When we solve these equations for the thickness of shockwave $\Delta x_s$, we can approximately represent that term as Eq. (4).

$$\Delta x_s = n_s \Delta x = \frac{8}{\gamma+1}\frac{4}{3}\chi\frac{1}{\rho_0}\frac{1}{u_0 - u_1} \qquad (4)$$

$\gamma$ is specific heat. The subscript 0 and 1 are the physical value at the rear and the forward of shockwave, respectively. $n_s$ is the number of computational grids to capture the shockwave. Eq. (4) means that the artificial viscosity can control the resolution of the shockwave. Namely, the relation of the N-R viscosity to$\Delta x_s$ can be denoted as

$$\frac{4}{3}\chi = \rho_0\frac{\gamma+1}{8}\frac{1}{u_0 - u_1}\Delta x_s^2\left|\frac{\partial u}{\partial x}\right| \qquad (5).$$

From Eqs. (4) and (5), we found that the coefficient $\alpha$ was the function of grid points of shockwave.

$$\alpha = c^2 = \frac{\gamma+1}{8}n_s^2 \qquad (6)$$

In order to confirm the application of Eq. (6), we conducted the numerical simulation of the 1-D supersonic duct flow. Figures. (1)-(a) and -(b) show the pressure distribution with $\alpha$=1 and 3 and the number of mesh points to $\alpha$.

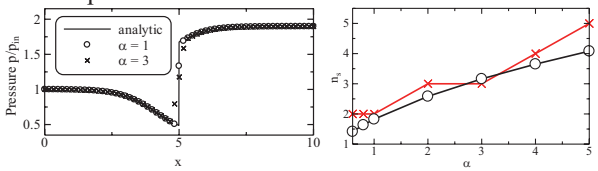


(a) Pressure distribution. (b) Number of mesh points in shockwave.

Fig. 1 One-dimensional supersonic duct-flow.

In order to improve the artificial viscosity, we propose the control function with variable of d$u$/d$x$ so that $\alpha$ increases at the location of shock wave and decreases in elsewhere.

$$\alpha = A\left(-\tanh\left(Bu_x + C\right)+1\right)/2 : \text{TYPE1} \qquad (7)$$
$$\alpha = A\left(-u_x + \sqrt{u_x^2 + \kappa^2}\right)/2 \quad : \text{TYPE2} \qquad (8)$$
$$\alpha = Au_x\left(u_x + |u_x|\right)/2 \qquad : \text{TYPE3} \qquad (9)$$

$A$, $B$, $C$, $\kappa$ are arbitrary constants. Figure 2-(a) show the characteristics of the control function Eqs. (7)-(8). The coefficient is varied by the control function to the compression parameters Fig. (2)-(a). Figure 2-(b) shows the numerical results of Sod's problem for the 1-D shock wave. The artificial viscosity with the control function only acts to the shock front and improve the resolution of the shock capturing rather than the traditional method.

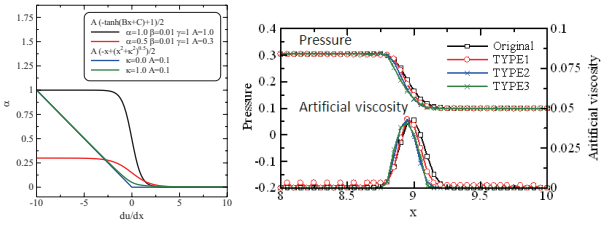


(a) Control function. (b) Effect of artificial viscosity to shockwave.

Fig. 2 Control function of artificial viscosity and those effect.

Figure 3 shows the density distribution of the 2-D incident shock wave problems. We modify the artificial viscosity to the non-linear function because the resolution of shock wave decreases in the multi-dimensional case even in the present method incorporated the control function. Figure 4 shows the comparison of the artificial viscosity at the location of shockwave. The proposed method can restrict the effect of the artificial viscosity to the narrow region of shockwave and clearly capture the shockwave rather than that of the traditional method.


Fig.3 Two-dimensional reflected shockwave (left: traditional, right:modified)

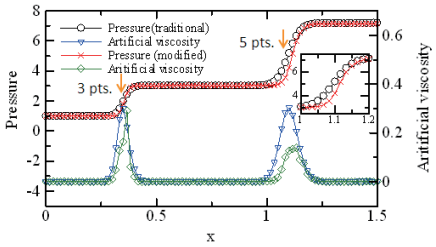


Fig. 4 Effect of the artificial viscosity to shockwave.

## 5. Concluding Remarks

We investigated some of problems on the NR-typed artificial viscosity. The relationship between the thickness of shockwave and the artificial viscosity was represented and the control function was proposed to decide the effect of artificial viscosity automatically. The numerical results showed that the proposed method was effective to the shock capturing problems.

## References


[1] Von Neumann J., Richtmyer R, D., A method for the calculation of hydrodynamic shock, *J. Appl. Phys.*, 21, (1950) 232-237.

[2] Landsoff, R., A numerical method for treating fluid flow in the presence of shocks, *J. Appl. Phys.*, 21, (1950) 281-303.

[3] Yabe, T., *Shock Waves*, 1(2), (1991) 187-195.

Eleventh International Conference on Flow Dynamics
October 8-10, 2014, Sendai, Miyagi, Japan

# Large-eddy Simulations of a Two-meter, Three-bladed Simple Wind Turbine Model Controlled by a Plasma Actuator

Hikaru Aono[1], Yoshiaki Abe[2], Kochi Okada[3], Makoto Sato[1], Aiko Yakeno[1], Taku Nonomura[1], Kozo Fujii[1]
[1]Japan Aerospace Exploration Agency
Yoshinodai 3-1-1, Chuo-ku, Sagamihara, Kanagawa, 252-5210, JAPAN
[2]The University of Tokyo
Yoshinodai 3-1-1, Chuo-ku, Sagamihara, Kanagawa, 252-5210, JAPAN
[3] IDAJ Co. Ltd.
Minatomirai 2-2-1-1, Nishi-ku, Yokohama, Kanagawa, 220-8137, JAPAN

**ABSTRACT**

Flow control using a DBD plasma actuator is applied to a three-bladed simple horizontal axis wind turbine model blades. Large-eddy simulations based on a high-order accurate and resolution computational method are performed using message passing interfaces and 18,800 cores of the K computer. The impacts of the DBD plasma actuator on flow fields around the blades and axial torque generation are discussed. Up to a 20% increase in revolution-averaged torque generation is attained. Effects of the DBD plasma actuator on the tip vortex is also presented.

## 1. Introduction

Recently, flow control using a dielectric barrier discharge (DBD) plasma actuator is applied to wind turbine blades with the aim of improving performance under near stall condition. Matsuda et al. [1] have constructed a small horizontal-axis wind turbine and demonstrated that an improvement of the wind turbine is realized in the low velocity region in the controlled cases for both yaw angle 15 and 30 degrees by wind tunnel tests. Mitsuo et al. [2] have developed a horizontal-axis wind turbine of simple experimental model and shown the improvement in torque by the flow control using the DBD plasma actuator through wind tunnel experiments. Aono et al. [3] have conducted numerical simulations of the wind turbine model constructed by Mitsuo et al. [2] and discussed effects of the DBD plasma actuator in terms of comparison of pressure distributions on the suction side of the blades. As a subsequent effort, this paper reports the effect of strength of excitation of DBD plasma actuator with the burst modulation on the aerodynamics of wind turbine model.

## 2. Problem Description

A simple horizontal axis wind turbine model is considered whereas a nacelle and a pole are not included in current simulations (see Fig. 1). A geometrical angle of attack is set to be 10 degrees with respect to the rotational plane. The blade rotates with a constant angular frequency (174 rpm). A position of the blade is represented by the azimuthal angle ($\phi$) and $\phi$=0 and 90 degrees correspond to the blade with 12 and 9 o'clock direction from the viewpoint of upstream. A tip-speed ratio is approximately 2. A chord ($c$)-and-freestream ($U_\infty$)-based Reynolds number of 133,333, a non-dimensional angular frequency of 0.058, and Mach number of 0.07 are considered based on the experiment [2]. A freestream is inclined at an angle of 40 degrees with respect to the rotational plane. An aspect ratio of the blade is 5 and a cross-sectional shape is NACA0012 (see Fig. 1). It should be noted that this flow condition may or may not often occur in practice. The effective angle of attack decreases when the azimuthal angle changes from 0 to 180 degrees.

Corresponding author: Hikaru Aono
*E-mail address*: aono@flab.isas.jaxa.jp

## 3. Methodologies

An in-house fluid analysis solver is employed. The Three-dimensional compressible spatially-filtered Navier-Stokes equations are employed as the governing equations. Six-order compact differencing is adopted for evaluating spatial derivative and Jacobian. Tenth order filtering is used with a coefficient of 0.4. These equations are solved in the generalized curvilinear coordinates. The computational time step is $3.5\times10^{-5}$ $c/U_\infty$ that corresponds to maximum Courant-Friedrichs-Lewy number of approximately 30. At the outflow boundary, all variables are extrapolated from one point in front of the outflow boundary. At the inflow boundary, the freestream velocity is assigned. For the airfoil surface, no-slip and adiabatic-wall conditions are adopted. For rotation of the blades all grids are rigidly rotated about the original of the coordinate as shown in Fig. 1. Coherent structure model is used as the sub-grid scale model. Parallel computation has been performed using message passing interfaces. All computations have been conducted using 2350 nodes of the K computer. Note that compact difference scheme-related subroutines in LANS3D have been well tuned for the K computer. Further computational methods in detail can be found in Aono et al. [3].

An overset grid technique [4] is used for dealing with the region of small body force and multiple turbine blades. As shown in Figure 1, the grid system requires four overset grids per blade to define the blade surface and the DBD plasma actuator. These grids consist of a main blade, blade-tip, and blade-root and the body force region. The body force distribution is calculated on the grid corresponding to the body force model region and then the body force is mapped to the DBD plasma

actuator grid beforehand. To complete the overset grid system, two background grids surround the blade volume grids. The length of outer boundary from the center of rotation is 50 of the chord. Total number of grid points is approximately seven hundred fifty million. The minimum grid size in the direction normal to the airfoil surface is 0.000137 of the chord that at least ten grid points are within the laminar boundary layer near the leading-edge. One computation without the DBD plasma actuator and two computations with the DBD plasma actuator with different strength (i.e. $Dc$=0.125 and 0.5) are conducted. Note that all parameters of controlled cases including the burst frequency ($F^+$=1) and burst ratio ($Br$=10%) have been determined based on previous experimental conditions [2].

## 4. Results and Discussion

Time histories of non-dimensional axial torque generated by each blade are plotted in Fig. 2. As expected, the axial torque varies as the azimuthal angle changes and time variation seems to be already periodic. All blades show similar time histories of the axial torque. This indicates nearly no interactions of flows around each blade. Effects of the DBD plasma actuator on axial torque generation can be seen during one blade revolution and the DBD plasma actuator improves torque generation. During $\phi$ between 360 and 480 degrees, its effect is clearly visible. Our previous study presented that for the no-control case, massive leading edge separation of blade has occurred and suppression of leading-edge separation has been observed by the DBD plasma actuator with $F^+$=1, $Dc$=0.5 and $F^+$=6 and $Dc$=0.5 [3].

Compared to the result of $F^+$=1, $Dc$=0.5, the result of $F^+$=1 and $Dc$=0.125 shows less improvement. Approximately 11% and 20% increase in revolution-averaged torque of each blade can be realized by the flow control in the two revolutions after the DBD plasma actuator switches on. Instantaneous iso-surfaces of second invariant velocity gradient tensor at $\phi$ of 400 degrees in the case of no-control and control of $F^+$=1 and $Dc$=0.5 are shown in Fig. 3. Tip and root vortices are generated for each blade. At $\phi$ of 400 degrees, many vortex shedding are observed in the suction side of "Blade 1". Such vortex shedding is also seen in the suction side of "Blade 2" and "Blade 3" but less. Looking at the tip vortex associated with "Blade 1", that of the no-control case does breakdown due to an interaction between shedding vortices from the leading edge and the tip vortex. This is secondary effect of flow control of DBD plasma actuator. This secondary influence might play a role in reduction of sound generation. Note that primary effect of the DBD plasma actuator considered in this study is suppression or delay of the leading edge separation of the turbine blade.

## 5. Concluding Remarks

Large-eddy simulations of the two-meter, three-bladed simple wind turbine model controlled by a plasma actuator have been conducted. Effects of the plasma actuator on massively separated flow around the wind turbine model blades have been studied.

Up to 20% increase in revolution-averaged torque is attained. Secondary effect of the DBD plasma actuator is observed and expected to reduce sound generation of wind turbine blades.


## Acknowledgements

This research used computational resources of the K computer provided by the AICS through the HPCI System Research Project (Project ID: hp130001, hp140207). H.A. would thank Dr. Mitsuo of JAXA for fruitful discussions and kind support.


## References


[1] H. Matsuda, M. Tanaka, S. Goshima, K. Amemori, M. Nomura, T. Osako, *AGGT2012-1058*, (2012).

[2] K. Mitsuo, S. Watanabe, T. Atobe, T. Ito, T. Shinohara, M. Tanaka, *JSME* S052023 (in Japanese)

[3] H. Aono, Y. Abe, M. Sato, A. Yakeno, K. Okada, T. Nonomura, K. Fujii, *Proc. 6th European Conference on Computational Fluid Dynamics*, (2014), 2935.

[4] K. Fujii, *J. Comp. Phys.*, 118 (1995) 92-108.


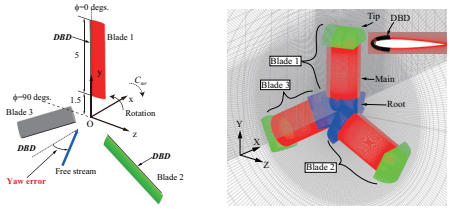


Fig. 1 Configuration of wind turbine models (left) and zonal grid system (right).

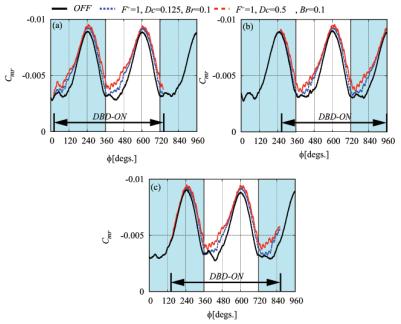


Fig. 2 Time histories of axial torque generated by each blade: (a) Blade 1; (b) Blade 2; and (c) Blade 3.

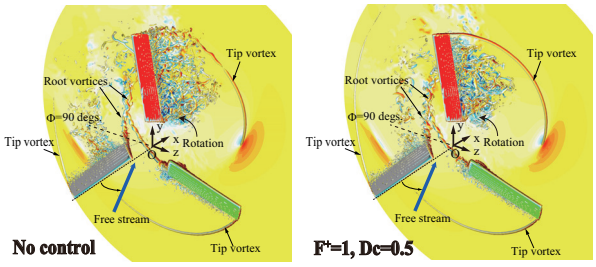


Fig. 3 Instantaneous iso-surfaces of second invariant velocity gradient tensor at $\phi$ of 400 degrees. Color indicates $x$-component of flow velocity.

Eleventh International Conference on Flow Dynamics
October 8-10, 2014, Sendai, Miyagi, Japan

# Effect of Wing Shape and Reynolds Number in Drag Reduction Method by Using Wing with Rotation Shaft

Kazushi Sato[1], Katsuyoshi Fukiba[1]
[1]Shizuoka University
3-5-1, Johoku, Naka, Hamamatsu, Shizuoka, 432-8011, Japan

**ABSTRACT**

We proposed a new drag reduction method for a cylinder in low Reynolds number. This method employed a pivoted airfoil which can rotate on the shaft freely so that it can head windward. We focused on the wing shape and Reynolds number and conducted 3-dimensional numerical calculation of aerodynamic force. As a result, we found that the movement of wing depends on the ratio of wing thickness to the chord. The effect of Reynolds number on the aerodynamic coefficient was small, which indicates that this reduction method is valid in wide Reynolds number range.

**Nomenclature**

| | | |
|---|---|---|
| $C$ | : | Chord of wing |
| $C_D$ | : | Drag coefficient |
| $C_M$ | : | Rotation moment coefficient |
| $D$ | : | Diameter of cylinder |
| Re | : | Reynolds number |
| $\alpha$ | : | Angle of attack |
| $\theta_c$ | : | Half vertex angle of wing |

## 1. Introduction

Because circular cylinder shape is used widely for many situations, many studies about aerodynamic drag reduction of it have been done. Among them, there are some examples for omnidirectional drag reduction methods. For instance, Ahmed et al[1] embed dimples on surface of cylinder. Nakamura et al[2] attached rings on middle of cylinder. However there is a problem that application range is restricted to high Reynolds number range because of its principle.

In our university the research about space elevator has been pushed forward with. Research and development of "stratosphere elevator", by using balloon which can climb to stratosphere is also conducted as a previous step of space elevator. In a design of stratosphere elevator, important technological problem is how to reduce aerodynamic force which works on a tether connecting balloon and ground by jet stream. The Re number calculated by the velocity and the diameter of the tether[3] at the altitude of 10 km, where the strongest jet stream flows, is about 3,000 – 30,000. The reduction method by new principle which is different from that of previous methods is required in this low Re number range.

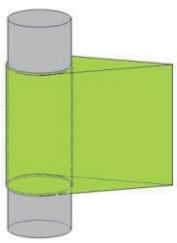

Fig.1 Wing device proposed in this study

Corresponding author: Kazushi Sato
*E-mail address*:f0330038@ipc.shizuoka.ac.jp

In this study we proposed a new drag reduction method by using wing with rotation shaft as shown in Fig.1. It can minimize drag worked on wing by jet stream which changes its velocity and direction. We conducted 3-dimensional calculation to prove effectiveness of this method.

## 2. Method

Dominant equations in this study are 3-dimensional Navier-Stokes Equations with compressibility. Wing shapes in this study are simple shapes composed of cylinder and plate as shown in Fig.2. This shape was determined in consideration of weight saving and the location of the center of pressure. We used two wing calculation grids whose ratio of wing thickness $D$ to the chord $C$ was 0.2 and 0.4, respectively. The reason why we use two kinds of grid is to investigate the difference of the aerodynamic coefficient attributed to the wing shapes. We call them 20 % wing and 40 % wing, respectively in this paper. The half vertex angle of wing $\theta_c$ is defined as shown in Fig.2. It is about 6.4 º in 20 % wing and about 14.5 º in 40 % wing. As an example, 20 % wing calculation grid is shown in Fig.3.

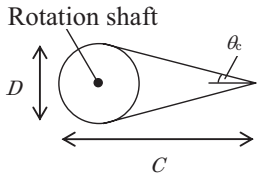


Fig.2 Cross section view of proposed wing

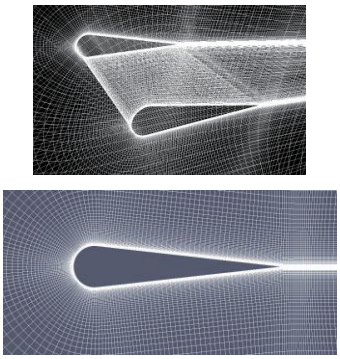

Fig.3 Calculation grid of 20% wing

As a calculation condition, Re number of flow is 10,000 in this study. We calculated drag coefficient $C_D$ and rotation moment coefficient around the shaft $C_M$ in each angle of attack.

## 3. Results and Discussion

### 3.1. Effect of wing shape

(a)40 % wing

Figure 4 shows variations of drag and moment coefficient in each angle of attack for 40 % wing. First, in regard to $C_D$, $C_D$ at $\alpha$=0 ° is 0.76. It is 64 % as compared to that of bare cylinder. $C_D$ at $\alpha$=10 ° is the local minimum value, which is 0.68. It is 56 % of that of bare cylinder, which means that 44% drag reduction was obtained with 40 % wing. Next, in regard to $C_M$, positive value turns into negative value at about $\alpha$=14-15 °, which is nearly equal to half vertex angle $\theta_c$ of 40 % wing. In other words, the direction of moment turns around. When $\alpha$ is smaller than 14 °, the rotation of the wing is promoted due to the aerodynamic moment acting on the wing. On the other hand, when $\alpha$ is larger than 14 °, the rotation of the wing is suppressed. As a result, wing becomes static stability condition and has non-zero stability point.

(b)20 % wing

Figure 5 shows variations of drag and moment coefficient in each angle of attack for 20 % wing. First, in regard to $C_D$, CD at α=0 ° is 0.64. It is 53% as compared to that of bare cylinder. $C_D$ increases monotonically with an increase in $\alpha$. There is no local minimal value like a result of 40% wing. Next, in regard to $C_M$, $C_M$ at a=0 ° is approximately zero. $C_M$ decreases monotonically with an increase in $\alpha$ and never turns into positive value.

Here we discuss the effect of wing shape on the movement of the wing. By comparison of 20 % and 40 % wings, we found that the parameter which determines whether wing has non-zero stability point or not is *D/C*. We also found that the boundary where the movement changed is located between *D/C*=0.2 and 0.4.

### 3.2. Effect of Re number

We also conducted the same calculation on 40 % grid in Re=2,000 in order to discuss the effect of Re number in this method. The aerodynamic coefficient at Re=2,000 was nearly equal to that at Re=10,000. Their difference is about 6 % at a maximum (at $\alpha$=10 °). Finally the effect of Re number on aerodynamic coefficient is very small, which indicates that this reduction method is valid in wide Re number range.

## 4. Conclusions

We conducted 3-dimensional calculation to investigate the effect of wing shape and Re number on a new drag reduction method.

Finally we got three conclusions as shown below.

(1) 40 % and 20 % wing reduces drag by up to 44 % and 47 %, respectively in Re=10,000 condition.

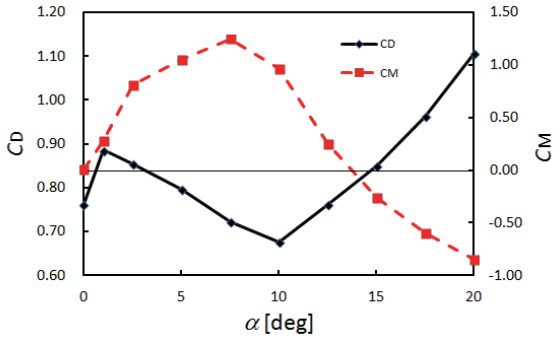


Fig.4 Variations of drag and moment coefficient in each angle of attack for 40 % wing

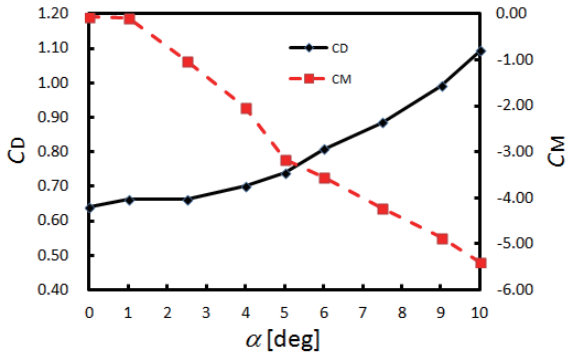


Fig.5 Variations of drag and moment coefficient in each angle of attack for 20 % wing

(2) The movement of the wing depends on *D/C* which is ratio of the thickness to the chord. The boundary where the movement changes is located between *D/C*=0.2 and 0.4.

(3) The effect of Re number on aerodynamic coefficient is very small, which indicates that this reduction method is valid in wide Re number range.


### Acknowledgement

We appreciate Cyber media center of Osaka University for using supercomputer system to calculate.


### References


[1]A.Ahmed , M.J.Khan , B.Bays-Muchmore , Experimental Investigation of a Three-Dimensional Bluff-Body Wake , *AIAA JORNAL* , Vol.31 , No.3( 1993-3).

[2]Hajime Nakamura,Tamotsu Igarashi, Omnidirectional Reduction of Drag and Fluctuating Forces of a Circular Cylinder by Attaching Rings, *Transactions of the JSME Series B* (in Japanese) , Vol.71, No.704(2005-4).

[3] Yoshiki Yamagiwa, Masafumi Nakata, Toru Miwa, Makoto Matsui, Feasibility Study of Stratopheric Elevator, *The 28th International Symposium on Space Technology and Science*, Okinawa 2011, 2011 g-28(2011).

# Numerical Simulation of Flow around a Body in Unsteady Motion

Hikaru Takano[1], Kota Fukuda[2]
[1]Graduate school of Engineering, Department of Aeronautics and Astronautics, Tokai University, Japan
4-1-1,Kitakaname, Hiratsuka, Kanagawa, 259-1292, Japan
[2]School of Engineering, Department of Aeronautics and Astronautics, Tokai University, Japan
4-1-1,Kitakaname, Hiratsuka, Kanagawa, 259-1292, Japan

**ABSTRACT**

In this study, unsteady aerodynamic effect of accelerated or decelerated 2D airfoil (NACA0012) was numerically examined using a vortex method. The flow characteristics and aerodynamic forces were compared among various accelerated or decelerated conditions. The results showed that large flow separation occurred under decelerated condition than accelerated condition and the lift-drag ratio decreased as the decelerated velocity became high and increased as the accelerated velocity became high.

## 1. Introduction

Vehicles like airplane do not usually move at a constant speed. On the other hand, most of the wind tunnel tests or numerical simulations via Computational Fluid Dynamics (CFD) have been carried out for steady states, even though it is well known that the aerodynamic characteristics at steady motion is different from the one at unsteady motion. In order to realize higher performance, the unsteady characteristics should be considered at the design stage.

Vortex methods are grid-free numerical schemes and it can easily be applied to moving geometries. So the methods are appropriate methods for prediction of unsteady aerodynamic characteristics of moving bodies.

On unsteady aerodynamic characteristics, some pioneering works have already been carried out, Maresca et al. [1] experimentally investigated oscillating airfoils, but unsteady force could not be obtained. Fukuta and Yokoi [2] numerically and experimentally examined flow around in-line oscillating airfoil. The results showed that flow separation was developed from the unsteady effect.

In this study, unsteady aerodynamic characteristics of accelerated or decelerated airfoil (NACA0012) were numerically examined using a grid-free vortex method.

## 2. Numerical Method

The basic equations of the vortex method in incompressible flow, is the continuity equation and the vorticity transport equation. vorticity transport equation in 2D incompressible flow and continuity equation are defined by the following equation.

$$\frac{d\boldsymbol{\omega}}{\mathrm{dt}} = \nu\nabla^2\boldsymbol{\omega} \tag{1}$$

$$\nabla\cdot\boldsymbol{u} = 0 \tag{2}$$

where $\boldsymbol{u}$ is a velocity vector and the vorticity $\boldsymbol{\omega}$ is defined as $\boldsymbol{\omega}$ = rot $\boldsymbol{u}$ . In the vortex methods, the time evolution of the flow is represented by the motion and evolution of vorticity strength of each element. In this study, the viscous term was expressed by the core spreading method proposed by Leonard [3]. The velocity filed was determined by the Biot-Savart law as explained by Wu and Thompson [4].

$$\boldsymbol{u} = \int_V \boldsymbol{\omega}_i\times\nabla_i G dV + \int_S\left[(\boldsymbol{n}_j\cdot\boldsymbol{u}_j)\cdot\nabla_j G - (\boldsymbol{n}_j\times\boldsymbol{u}_j)\times\nabla_j G\right]dS \tag{3}$$

Here, subscript "$i$" represents the physical amount at the position $r_i$ present in the region V and boundary surface S. And G is the fundamental solution of the scalar Laplace equation with the delta function. If $\boldsymbol{R} = |\boldsymbol{r} - \boldsymbol{r}_i|$, which is written for a 2D field as $G = -1/(2\pi)\log R$. In Eq. (3), the inner product $n_j \cdot u_j$ and the outer product $n_j \times u_j$ stand for normal velocity component and tangential velocity vector on the boundary surface. They correspond to the source distribution on the surface and the vortex distribution that has the rotating axis in parallel to the surface. The source and vortex corresponding to the second and third terms of right side of Eq. (3) are distributed on the boundary surface. On the other hand, with respect to pressure analysis, is used Eq. (4) pressure integral equations obtained from by introducing the $H = p/\rho + |\boldsymbol{u}|^2/2$ called Bernoulli function pressure Poisson equation.

$$\beta H + \int_S H\frac{\partial G}{\partial n}ds = -\int_V \nabla G\cdot(\mathbf{u}_i\times\boldsymbol{\omega}_i)dV - \nu\int_S \mathbf{n}_i\cdot(\nabla G\times\boldsymbol{\omega}_i)dS \tag{4}$$

It is possible to determine the pressure by applying the boundary element method to the Eq. (4) to calculate the value of $H$. Here, $\beta$=1 in the flow field and $\beta$=1/2 on the boundary $S$. The exact solution of the Navier-Stokes equation for a straight line vortex filament of infinite length, and the vortex core radius $\varepsilon$ radius the rotational speed is the maximum rate of change that time is represented as follows.

$$\frac{d\varepsilon}{dt} = \frac{c^2}{2\varepsilon},\ (c = 2.242) \tag{5}$$

Vorticity $\boldsymbol{\omega}_i(\boldsymbol{r})$ is expressed as follows by the $\Delta\Gamma_i$ the circulating volume representing the vortex element $i$, using the Gauss distribution vorticity distribution.

## 3. Calculation Conditions

In this study, firstly, flow around a 2D wing moving at a constant speed was calculated in order to understand aerodynamic characteristics at the steady motion. Secondly, flow around the wing moving under

Corresponding author: Kota Fukuda
*E-mail address*:fukuda@tokai-u.jp

accelerated condition was calculated in order to examine unsteady aerodynamic characteristics. The numerical model of the wing was expressed by 500 surface panels. Under constant velocity condition, the Reynolds number was set to be $\mathrm{Re}=V_0C/\nu = 4.0\times10^5$, here $V_0$ is the constant velocity and $C$ is the chord length. The attack angle was set to be 5.0°. The non-dimensional time step was $\Delta tV_0/C=0.0025$. Surface vortex panels were set on the surface of the body and the height was 0.004C based on the appropriate height proposed by Ota et al. [5]. For the accelerated condition, non-dimensional accelerated velocity was set to be $\alpha=\pm0.1$ and $\pm0.5$ respectively.

## 4. Results

Figures.1 shows the flow pattern around the trailing edge at the same time for each calculation cases. The color contour shows the vorticity strength of each vortex element. As compared with constant velocity case and accelerated case, larger vortex structure generated at the trailing edge under decelerated condition. As the non-dimensional decelerated velocity became high, the growth of the vortex structure became rapid. And in any case, the differences of flow were not occurred at the leading edge.

The analyzed fluid forces under each condition are shown in Figures 2. In the accelerated cases, the lift coefficient increased as time went on. On the other hand, in the decelerated cases, the lift coefficient decreased as time went on. The growth rate became high as the accelerated or decelerated velocity became high. About the drag coefficient, in the accelerated cases, the drag coefficient decreased as time went on, and in the decelerated cases, the drag coefficient increased as time went on. The growth rate became high as the accelerated or decelerated velocity became high. Furthermore, The lift-drag ratio decreased as the decelerated velocity became high and increased as the accelerated velocity became high.

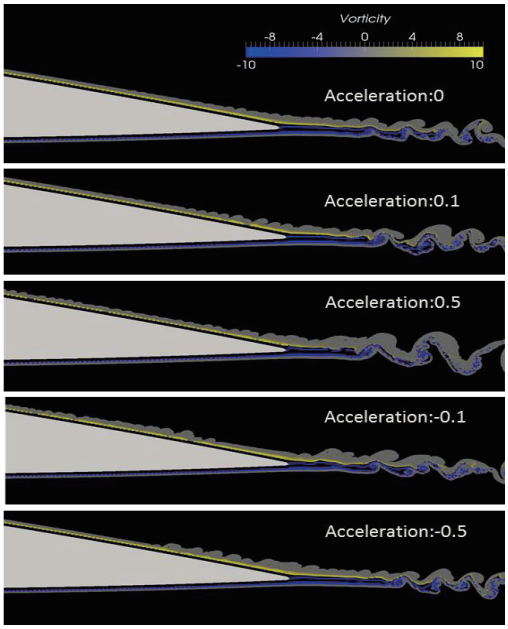


Fig. 1 Flow pattern around the trailing edge

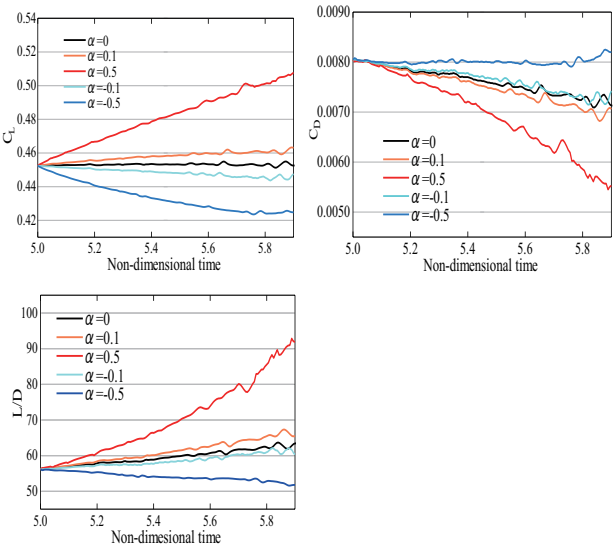


Fig. 2 Time history of aerodynamic coefficient

## 5. Conclusions

In this paper, unsteady aerodynamical effect of accelerated or decelerated 2D airfoil (NACA0012) was numerically examined using a grid-free vortex method. The results showed that larger vortex structure generated at the trailing edge under decelerated condition than under constant velocity condition and the growth of the vortex structure became rapid as the non-dimensional decelerated velocity became high. Furthermore, it was confirmed that the lift-drag ratio decreased as the decelerated velocity became high and increased as the accelerated velocity became high.

## References

[1] Maresca, C., Favier, & Rebont, J., *Experiments on an aerofoil at high angle of incidence in longitudinal oscillation*, *J.Fluid Mech,* Vol. 92-4, (1979), pp. 671-690.

[2] Fukuta, H. and Yokoi, Y., *Numerical Experiment of Flow Around an IN-Line Forced Oscillating Symmetrical Foil with Attack Angle of 5 degrees*, *TFEC8*, (2012).

[3] A. Leonard, *Vortex Methods for Flow Simulation*, *Journal of Computational Physics*, 37, (1980), 289.

[4] Wu, J. C., and Thompson, J. F., *Numerical Solutions of Time-Dependent Incompressible Navier-Stokes Equations Using an Integro-Differential Formulation*, *Computers and Fluids,* Vol.**1**, (1973), pp. 197–215.

[5] Ota, S. and Kamemoto, K., *A Study Improvement of Applicability of Vortex Method in Engineering*, *Transactions of the Japan Society of Mechanical Engineers Series B*, Vol.70, No. 698, (2004), pp. 2491-2498.

Eleventh International Conference on Flow Dynamics
October 8-10, 2014, Sendai, Miyagi, Japan

# Aerodynamic Performance Evaluation of Split-Tip Winglet

Ryo Kato[1], Wataru Yamazaki[1], Mitsuru Kurita[2], Mitsuhiro Murayama[2], Masataka Kohzai[2]
[1]Department of Mechanical Engineering, Nagaoka University of Technology
1603-1, Kamitomioka-machi, Nagaoka city, Niigata pref., 940-2188
[2]Japan Aerospace Exploration Agency, JAXA
7-44-1, Jindaiji Higashi-machi, Chofu city, Tokyo, 182-8522

**ABSTRACT**

Split-tip winglet configurations are discussed in this research to improve the aerodynamic performance of aircraft. The aerodynamic performance is evaluated by numerical simulations with a drag decomposition approach. By using this approach, the drag reduction mechanisms can be investigated in detail. The split-tip winglet configurations are defined by adding a small wing on a conventional winglet model. The aerodynamic drag reduction is observed in the split-tip winglets without increasing the bending moment of the main wing.

## 1. Introduction

Winglet is a wing tip device of an aircraft, which has the advantage to reduce aerodynamics drag. The winglets alleviate the formation of the wing tip vortex which causes induced drag and reduced lift force of aircraft. A drag reduction of 1% can lead to the reduction of the direct operational cost of about 0.2% for a large sized aircraft, which corresponds to 1.6 tons on the operating empty weight or 10 passengers [1]. Therefore, various numerical / experimental studies of wing tip devices are being performed even nowadays, from that some new wing tip devices have been proposed. As one of the newly proposed winglets, the split scimitar winglet in which a small wing is installed on the lower side of a conventional blended winglet is well-known recently [2]. To clarify the aerodynamics / drag reduction of such state-of-the-art winglet configuration, we examine the effect of small wing installed on a conventional winglet model by using computational fluid dynamics (CFD) approaches.

## 2. Numerical Methods

Three-dimensional transonic inviscid flows are analyzed by unstructured mesh CFD solver of TAS (Tohoku University Aerodynamic Simulation)-code. The governing equations are compressible Euler equations, that are solved via an unstructured mesh finite volume method. We use a drag decomposition method [3] in order to investigate the drag reduction effect in detail. The inviscid drag of aircraft can be decomposed into the induced drag and wave drag components by using this method.

Our considered aircraft model is the NASA-CRM wing-body configuration as Fig. 1 [4]. A conventional winglet model is attached on the NASA-CRM model. The cant angle of the designed winglet is 20[deg], which was designed by referring the aerodynamic design knowledge obtained in [5]. In this research, the drag reduction effect by adding a small wing on the main winglet is investigated. The small wing is a conventional unswept/untapered wing (its aspect ratio of 1.0), whose section thickness distribution is defined by that of 90% semi-span section of the NASA-CRM model (no camber airfoil, as shown in Fig. 2). The flow condition is set to the freestream Mach number of 0.85, and the angle of attack is adjusted in CFD simulations for the lift coefficient of 0.5.

Corresponding author: Ryo Kato
*E-mail address*: s113037@stn.nagaokaut.ac.jp


Fig. 1 NASA-CRM Model with Winglet

Fig. 2 Small Wing Cross Section

## 3. Results and Discussion

The small wing is attached on the lower/outer side of the main winglet to investigate the effects of the split-tip winglet. The chord length of the small wing is set to 75% of the chord length at the tip of the main winglet. The mid-chord position of the small wing is located on the mid-chord position of the main winglet. To evaluate the effect of the small wing, its attachment position is changed on the lower side of the main winglet as indicated in Fig. 3. The dihedral angle of the small wing is set to be orthogonal to the main winglet. These computational results are also summarized in Fig. 3. This figure indicates the variation of aerodynamic performance of the split-tip winglet configurations. The y-axis indicates the differences of aerodynamic performance from that of the conventional winglet configuration (without small wing). The plot of “ΔWave” is the variation of wave drag component related to the generation of shock waves. “ΔInduced” is the variation of induced drag component related to the wingtip vortex. “ΔPure” is the variation of the sum of the wave and induced drag components. “ΔBM” is the variation of the bending moment coefficient of the whole wing as well as the fuselage at the root position of the main wing. The variation of the bending moment is an important parameter to evaluate the structural penalty of the wingtip device (lower is better). The variation of the bending moment is indicated by its percentage while that of drag components are indicated by drag count (one drag count is 0.0001 in non-dimensional drag coefficient). It can be confirmed that the pure drag is reduced in the all cases mainly due to the reduction of the induced drag component. The best aerodynamic

performance is given at position 3 while the bending moment is slightly increased. At position 5, on the other hand, little bending moment penalty is observed with 0.6 counts total drag reduction. The visualizations are compared in Fig. 4, which indicates the induced drag strength on a near-wake surface of the winglet (color contours) as well as the generated shock wave surfaces (red surfaces). We can see the reduction of the induced drag strength by adding the small wing, compared with the case without the small wing.

Then, two small wings cases are also investigated in which the first small wing position is fixed to the position 5. The position of the second small wing is changed from the position 1 to 4. The wing tip model of a two small wing case (position 1 and 5) is shown in Fig. 5. The computational results are also summarized in Fig. 5. In this figure, the results shown at the position 5 are that of one small wing case (same as Fig. 3). Due to the flow interactions between the two small wings that are closely located, the aerodynamic performance of position 4 (and 5) is the worst in the all cases. The case of position 3 (and 5) is the best among the all cases, in which the drag is decreased more compared with the single wing cases. The visualizations of two small wing cases are shown in Fig. 6. The generations of additional shock waves can be observed in the case of position 4 (and 5).

## 4. Concluding Remarks

In this study, the aerodynamic performance evaluations of split-tip winglet configurations have been performed. The inviscid drag reduction by adding a small wing on the lower side of the main winglet has been confirmed. At the appropriate position of the small wing, the bending moment penalty was little, which indicates the aerodynamic promise of the split-tip winglet configurations. Additional inviscid drag reduction was achieved by adding two small wings, while the effect of the increase in the friction drag is not considered yet in this paper. As future works, the aerodynamic shape optimization of the split-tip winglet will be performed to clarify the relationships between the various shape parameters of the small wing as well as its attachment position.

## References


[1] Reneaux, J., *European Congress on Computational Methods in Applied Sciences and Engineering*, ECCOMAS, (2004).

[2] "Blended Winglets and Spiroid Technology", http://www.aviationpartners.com/future.html, 2014/07/16.

[3] Yamazaki, W., Matsushima, K., and Nakahashi, K., *International Journal for Numerical Methods in Fluids*, 57(4), (2008) 417-436.

[4] Ueno, M., Kohzai, M., Koga, S., Kato, H., Nakakita, K., and Sudani, N., *AIAA Paper* 2013-0493, (2013).

[5] Takenaka, K., Hatanaka, K., Yamazaki, W., and Nakahashi, K., *Journal of Aircraft*, 45(5), (2008) 1601-1611.


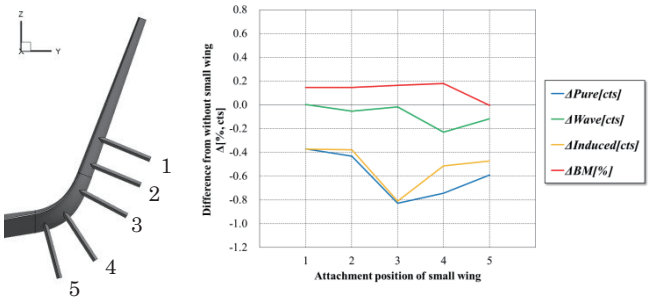


Fig. 3 (Left) Definition of Positions of Small Wing (Right) Calculated Results

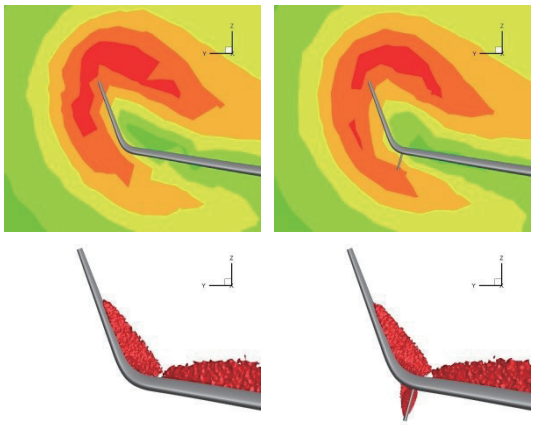

Fig. 4 Visualization of (Upper) Strength of Induced Drag and (Lower) Shock Wave Surfaces,
(Left) Only main winglet
(Right) With a small wing on position 5

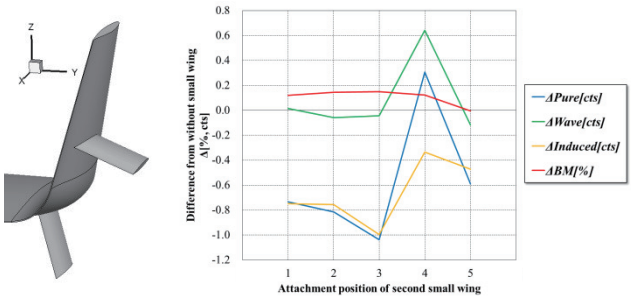


Fig. 5 (Left) A model of Two Small Wings on Winglet (Right) Calculated Results

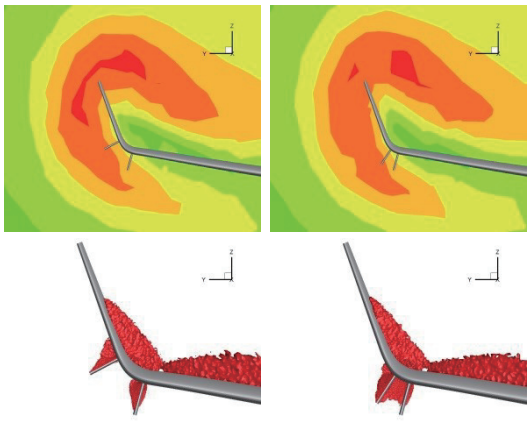

Fig. 6 Visualization of Two Small Wing Cases of (Left) Position 3 and 5 (Right) Position 4 and 5

Eleventh International Conference on Flow Dynamics
October 8-10, 2014, Sendai, Miyagi, Japan

# Experimental Investigation of Aspect Ratio Effect on the Pressure Oscillation in Supersonic Rectangular-Cavity Flows

Yusuke Kihara[1], Taro Handa[1], Shinji Maruyama[1]
[1]Kyushu University
6-1 Kasuga-Koen, Kasuga City, Fukuoka, 816-8580, Japan

**ABSTRACT**

In the present study, the effect of aspect ratio on the pressure oscillation induced by a rectangular cavity over which the gas flows at a supersonic speed is investigated experimentally. The temporal variations in pressure are measured on the wall changing the aspect ratio of the cavity and the power spectral densities are calculated for each aspect ratio. As a result, it is found that the transition between the transverse and longitudinal oscillations occurs between the aspect ratios ~1 and ~2.

## 1. Introduction

Supersonic flow over a rectangular cavity is known to oscillate at certain predominant frequencies. Cavity-induced pressure oscillations cause structural fatigue and sound noise. On the other hand, the oscillations are utilized to enhance supersonic mixing. According to linear stability analysis, the growth rate of the shear layer depends on the frequency of the disturbance imposed to the shear layer. Hence, it is important for supersonic mixing enhancement to estimate the frequency of cavity-induced pressure oscillation.

The predominant frequencies are presumed to depend on the aspect ratio (length-to-depth ratio) of the cavity. In the present study, the pressure oscillation frequencies are measured ranging aspect ratio between 0.50 and 3.0. The effect of the aspect ratio on the oscillation frequencies is discussed.

## 2. Experiments

Figure 1 shows the detailed structure of the test duct. Nitrogen gas flows into the test duct at a Mach number of 1.68. Detailed descriptions of the flow issuing from the nozzle are provided elsewhere; on the basis of the boundary layer thickness, the flow issuing from the nozzle results in a boundary layer thickness and a Reynolds number of 0.73 mm and $1.03 \times 10^4$, respectively [1]. The test duct has a rectangular cross section with a height and width of 10.5 mm and 28.0 mm, respectively. The cavity length $L$ is 14.0 mm, while the depth $D$ is adjustable. In the present experiments, $D$ is varied from 4.67 mm to 28.0 mm, which implies that the aspect ratio $L/D$ varies from 0.50 to 3.0.

The temporal variations in pressure are measured with semiconductor-type pressure transducers at locations *a* and *b* shown in Fig. 1. The power spectral densities are calculated from the temporal variation of the pressure signal. In the experiments, the pressure in the stagnation chamber is maintained at 101 kPa, and the chamber is at atmospheric temperature (this temperature is monitored during each experimental run).

Corresponding author: Yusuke Kihara
*E-mail address*: 2ES14176K@s.kyushu-u.ac.jp

## 3. Oscillation models

In each spectrum of the pressure oscillation measured in this study, several peaks are observed. Each peak could originate from a feedback mechanism for transverse or longitudinal oscillation. In the following paragraphs, feedback mechanisms for both oscillations are briefly explained.

On the basis of a shadowgraph visualization of the cavity flow, Rossiter [2] developed an oscillation model for the longitudinal oscillation. According to this model, a pressure wave is produced when a vortical structure impinges on the trailing edge of the cavity, and the wave then propagates upstream in the cavity. When the pressure wave reaches the leading edge of the cavity, another vortical structure is created, which is then convected downstream to the trailing edge of the cavity. The feedback loop is thus completed, and the pressure oscillation is sustained. Rossiter derived the following formula for the Strouhal number $St$,

$$St = \frac{fL}{U_\infty} = \frac{n - r}{M_\infty + \frac{1}{k}} \tag{1}$$

where $f$ is the oscillation frequency, $U_\infty$ is the free-stream velocity, $M_\infty$ is the free-stream Mach number, $n$ is the oscillation mode number, $r$ is the phase delay constant, and $k$ is the ratio of the convection velocity of a vortical structure $U_c$ to $U_\infty$. In the feedback mechanism expressed by Rossiter's model, the pressure wave propagates longitudinally. Hence, the oscillation expressed by Rossiter's model is called longitudinal oscillation.

Equation (1) is formulated on the basis of the assumption that the speed of sound inside the cavity is equal to that in a free stream. This assumption, however, leads to errors for high Mach-number flows, and so to overcome this difficulty, Heller et al. [3] assumed that the speed of sound inside the cavity $a_{\text{cavity}}$ was equal to that in a stagnating free stream and modified Eq. (1):

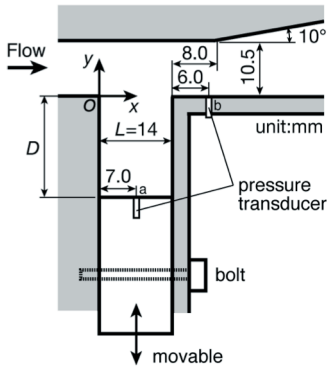


Fig. 1 Test duct

$$St = \frac{fL}{U_\infty} = \frac{n - r}{M_\infty \left(1 + \frac{\gamma - 1}{2} M_\infty^2\right)^{-1/2} + \frac{1}{k}} \quad (2)$$

Note that both Eqs. (1) and (2) do not include the wave reflection at the bottom wall of the cavity; i.e., the effect of the cavity depth is not accounted for by these equations. The constants $k$ and $r$ were empirically determined to be 0.57 and 0.25, respectively, by Rossiter.

The longitudinal oscillation (oscillation in shallow cavity flows) is expressed by the modified Rossiter formula in Eq. (2) for supersonic cavity flows. By using this formula, the predominant frequencies can be estimated rather accurately for shallow cavities, but the estimation fails for deep cavities because the effect of cavity depth is not included. Recently, Handa et al. [4] proposed the oscillation model to estimate the predominant frequencies of the transverse flow oscillation:

$$St = \frac{n - r - \Delta\phi / 2\pi}{\frac{M_\infty}{\alpha_I} \left(1 + \frac{\gamma - 1}{2} M_\infty^2\right)^{-1/2} + \frac{1}{k}} \quad (3)$$

$\Delta\phi$ in the above equation is expressed in detail elsewhere [4]. $\Delta\phi$ can be calculated by modeling the pressure wave propagation observed in a time sequence of the schlieren flow images captured by Handa et al. [1]: two pressure waves are considered; one wave is generated at the trailing edge of the cavity owing to the motion of the shear layer, and the other wave is generated as a result of the third reflection of the former wave at the cavity bottom. Because it was found from the schlieren images that the latter wave propagated transversely, a flow oscillation accounted for by Eq. (3) is considered to be a transverse oscillation. The constants $k$, $r$, and $\alpha_I$ are given as 0.76, 0.26, and 0.75, respectively.

## 4. Results and Discussion

The Strouhal numbers of detectable spectral peaks are plotted against $L/D$ in Fig. 2. Strouhal numbers calculated from Eqs. (2) and (3) are also shown in the figure by dashed and solid lines, respectively. The data corresponding to the spectral peaks resulting from amplitude modulation [5] are not plotted in the figure. As mentioned above, the oscillations accounted for by Eqs. (2) and (3) correspond to longitudinal and transverse oscillations, respectively. As shown in Fig. 2, the Strouhal numbers for $L/D$ <~ 1 are estimated well by Eq. (3), whereas, those for $L/D$ >~ 2 are estimated well by Eq. (2). Furthermore, the Strouhal numbers of the spectral peaks for 1 <~ $L/D$ <~ 2 are estimated by either of Eqs. (2) or (3). These findings imply that flows for 1 <~ $L/D$ <~ 2 oscillate not only transversely but also longitudinally; the transition from the transverse oscillation to longitudinal oscillation occurs between $L/D$ ~ 1 and ~2. Several spectral peaks that cannot be accounted for by Eqs. (2) and (3) appear for deeps cavities. It is expected that these peaks might result from the acoustic resonance. However, we have no strong evidence that these occur in the present flow.

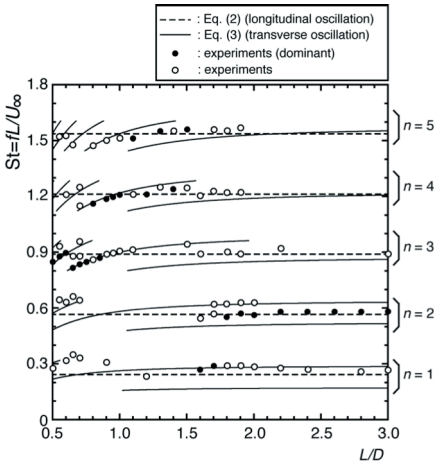


Fig. 2 Plot of Stouhal number $St$ vs. $L/D$

## 5. Concluding Remarks

The effect of aspect ratio on the frequencies of pressure oscillation induced by a rectangular cavity over which the gas flows at a supersonic speed was investigated experimentally. The temporal variations in pressure were measured on the wall changing the aspect ratio of the cavity and the power spectral densities were calculated for each aspect ratio. The results revealed that the predominant oscillation frequencies for aspect ratios lower than ~1 were accounted for by the model of the transverse oscillation and that the frequencies for the aspect ratios higher than ~2 were accounted for by the model of the longitudinal oscillation. The results also revealed that the transition between the transverse and longitudinal oscillations occurs between the aspect ratios ~1 and ~2.

## References

[1] T. Handa, H. Miyachi, H. Kakuno, T. Ozaki, *Exp. Fluids*, 53 (2012) 1855－1866.
[2] J.E. Rossiter, *ARC Rep. Memo.*, 3488 (1964).
[3] H.H. Heller, D.G. Holmes, E.E. Covert, *J. Sound & Vib.*, 18 (1971) 545－553.
[4] T. Handa, H. Miyachi, H. Kakuno, T. Ozaki, S. Maruyama, *AIAA J.*, (2014) published online.
[5] N. Delprat, *Phys. Fluids*, 18 (2006) 071703.

Eleventh International Conference on Flow Dynamics
October 8-10, 2014, Sendai, Miyagi, Japan

# Numerical Analysis on the Partial Admission of the Supersonic Impulse Turbine

Kenta Kato[1], Katsuyoshi Fukiba[1] , Kunio Hirata[1]
[1] Department of mechanical engineering, Shizuoka University
3-5-1 Johoku Naka-ku , Hamamatsu, Shizuoka, 432-8561, Japan

**ABSTRACT**

Currently, research of the heat recovery system using a steam turbine as a method for recovering and reusing exhaust heat of the vehicle has been performed. The steam turbine is expected to employ for automotive heat recovery system because of its small size and light weight. Previously this kind of turbine is adopted only for the limited use, and there are little research examples. In this study, we investigated the variation of the turbine efficiency attributed the difference in the wing leading edge distance from the outer wall and the rate of partial admission by CFD analysis.

**Nomenclature**

| | |
|---|---|
| $C$: | chord length |
| $H$: | blade height |
| $D$: | pitch diameter |
| $U$: | circumferential speed |
| $M_w$: | relative Mach number |
| $Re$: | Reynolds number |
| $Tw$: | Turbine power |
| $\eta$: | partial admission rate |
| $\eta_{full}$: | ratio of the power of the partial admission to that of the full admission |
| $\eta_{ad}$: | Admission efficiency |

## 1. Introduction

The present automobile is throwing away 60 % of energy as exhaust heat. Therefore, studies of the high efficiency vehicle using the heat recovery system with a steam turbine to recover and reuse the waste heat has been conducted in recent years [1]. Since the steam turbine for automobile is desired to be small size and a light weight, a small supersonic impulse turbine is suitable. However, the supersonic impulse turbine has been investigated in few study previously. Further, since the amount of steam entering the turbine is small, it is necessary to introduce steam flow not fully, but partially. Although the analysis of the turbine with about 50 % in the partial admission rate has performed in previous research, few analysis of the turbine with a low partial admission rate has been carried out [2]. The authors revealed in a previous study that an certain turbine rotor blade distance maximizes the whole output power in the condition of full admission [3]. In this research, at the fixed turbine blade distance ,partial admission rate and the distance from the leading edge of the blade and the outer wall were varied, and the turbine performance was investigated.

## 2. Definition of partial admission rate

Since inlet steam flow rate of the impulse turbine is small, the technology called partial admission is adopted. Partial admission is the mechanism to reduce the steam flow rate by means of introducing the flow partially to the rotor blades. The partial admission rate is defined as a ratio of steam inflow width to the turbine circumference. It is expressed as a ratio of a solid line to a dashed line (Fig1).

## 3. Method

This research was analyzed using steady ,two-dimensional calculations. The AUSM+UP scheme and LU-SGS implicit method was employed. The calculation grids used for the current analysis is shown in Fig. 2. The calculation grids consist of the inlet channel and the turbine cascades.

The calculation grid of an inlet channel consists of 71x100 =7,100 grid points. The calculation grids of a turbine cascades consist of 20 grids and each grid has 230x50=11,500 points. Since there are 20 cascade channel s, the total grids points are 7,100+11,500x20=237,100 points. The dimensions of the turbine blade is non-dimension alized by chord length, where C=is 1.0 and H=is 0.3. The distances between the rotor blades were fixed at 0.56C. A typical parameter of analysis conditions are shown in Table 1.

## 4. Results and Discussion

4.1 Effect of the partial admission rate

In order to take the movements of a rotor blades into consideration, Frozen Rotor analysis was employed [4]. Mach number contours at the partial admission rate of 25, 37.5 and 50 % are shown in Fig.3a)~c). The distance

. Table1. Analysis conditions

| | |
|---|---|
| D | 230[mm] |
| U | 240[m/s] |
| $M_w$ | 1.386 |
| $Re$ | 30000 |

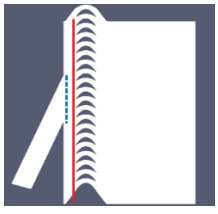

Fig.1 Rate diagram of Partial admission

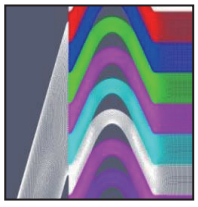

Fig.2 Calculation lattice

Corresponding author: Kenta Kato
*E-mail address*: f0330022@ipc.shizuoka.ac.jp

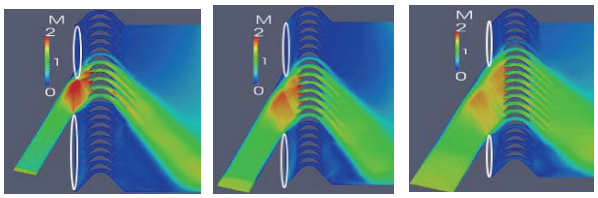


a) 25% b) 37.5% c) 50%

Fig.3 Mach number distribution

Table2. Rate conclusion of partial admission

| $\eta$[%] | $CL$ | $\eta_{full}$ [%] | $\eta_{ad}$[%] |
|---|---|---|---|
| 25 | 0.14 | 21.03 | 84.11 |
| 37.5 | 0.20 | 30.53 | 81.41 |
| 50 | 0.26 | 41.12 | 82.24 |
| 100 | 0.64 | | |

from the leading edge to the wall is 0.5c in each case. With the increase in the partial admission rate, the width of the steam which flows into a turbine cascade increases. Therefore, the moving blade number of sheets which works also increases. Next, a turbine output power at each grid is shown in Fig. 4. The partial admission rate is 25 % in Fig. 4. In Fig.3, the grid number of a lowermost part channel is 3, and a topmost channel is 22. From Fig. 4, six grids, the grid number 12 to 17, have contributed to power generating. At the grid 13, turbine power becomes larger than that of 100% in the partial admission rate. This is because the flow goes into the turbine cascade at supersonic speed and expands in the inlet of the rotor blades, is accelerated consequently. The turbine power of 25% in the partial admission rate achieved 21.03% as compared with that of full admission. Admission efficiency achieved about 84%. The result as regards the effects of partial admission rate (25%, 37.5%, 50%) is summarized in Table 2. With the increase in the partial admission rate, turbine power also increases. However, there is no significant difference in admission efficiency.

4.2 Effect of the distance from the leading edge to the outer wall

The turbine power at each grid with the variation of the distance from the leading edge to the outer wall is shown in figure 5a)~b) ,where the partial admission rate is 50 %. Here we focus on the grid 8 and 17. The turbine power of grid 8 in Fig. 5a is larger than that of Fig. 5b. The turbine power of grid 17 in Fig. 5b is larger than that of Fig. 5a. In the grid 17 of Fig. 5a, a flow does not arise from Mach number distribution, and I think that power also became small. With the variation of the distance from the leading edge to the outer wall, turbine power distribution to each channel also varies. However, the big difference for power did not arise as the whole turbine (Fig. 6). That is, the distance from the leading edge to the outer wall does not affect performance.

## 5. Concluding Remarks

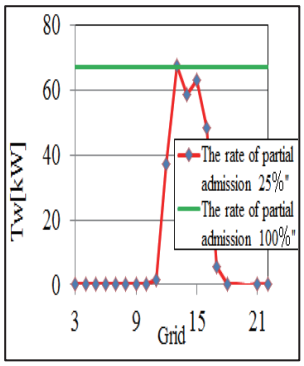


Fig.4 *Tw* (η=25%)

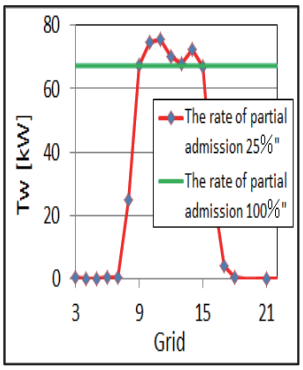


Fig.5a) *Tw* (0.1c)

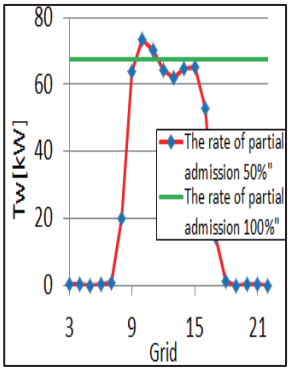


Fig.5b) *Tw* (0.5c)

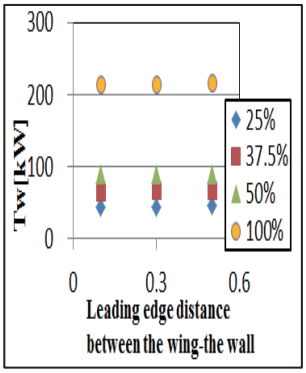


Fig.6 *Tw* by the leading edge distance between the wing-the wall

CFD analysis on impulse turbine blades was conducted, and The following conclusions were obtained as a result.

(1) Turbine power increases along with the increase in the partial admission rate.
(2) Admission efficiency is about 80 % in all cases of the partial admission rates. It varies only slightly.
(3) the distance from the leading edge to the outer wall does not affect turbine performance.

**References**

[1] K. Kawaziri, Y. Tsutsui, Research of the waste heat regeneration system for cars , The challenge by a Rankine cycle, *The Japan Society of Mechanical Engineers* ,Vol.110,(2007),66.

[2] Y.Tokuyama, K. Hunasaki, T.Kato, Z. Takida, Influence which the partial admission in the supersonic turbine for rocket engines has on an unsteady flow place, *An aviation motor and a space propulsion lecture meeting lecture collection(CD-ROM)*,Vol.53,(2013).

[3] K. Kato, K. Fukiba,K. Hirata, Numerical Analysis on the Partial Admission of the Supersonic Impulse Turbine, *Space transportation symposium*,(2013).

[4] H. Mashiko,K. Hunasaki, T. Kato, Z. Takida, Multiple-purpose form optimization and unsteady flow analysis in consideration of a wings load change of the turbine for rocket engines, *An aviation motor and a space propulsion lecture meeting lecture collection(CD-ROM),* Vol.53,(2013).

Eleventh International Conference on Flow Dynamics
October 8-10, 2014, Sendai, Miyagi, Japan

# Fundamental Experiments of Schlieren CT for Underexpanded Sonic Jets

Yuta Akita[1], Takefumi Usui[1], Daisuke Ono[1], and Yoshiaki Miyazato[1]
[1] The University of Kitakyushu
1-1, Hibikino, Wakamatsu-ku, Kitakyushu, 808-0135, Japan.

**ABSTRACT**

The rainbow schlieren deflectometry combined with computed tomography (schlieren CT) is applied to the underexpanded sonic jet issued from an axisymmetric convergent nozzle. Experiments have been conducted with the operating pressure ratio equal to 2.3 which corresponds to the range of underexpanded sonic jet. The jet density profiles reconstructed by the schlieren CT and Abel inversion are compared with each other.

## 1. Introduction

Clear understanding of the qualitative and quantitative properties of complex shock containing supersonic jet flows requires high-resolution, optical measurements across the whole flowfield. Schlieren methods [1] are widely used as optical tools to study the characteristics of compressible flows qualitatively.

However, there has been no practical application of the rainbow schlieren deflectometry for a quantitative three-dimensional density field measurement in a shock-containing jet. Therefore, in the present study, the rainbow schlieren deflectometry [2] combined with computed tomography (schlieren CT) is applied to the underexpanded sonic jet issued from an axisymmetric convergent nozzle.

## 2. Experimental Method

Experiments have been performed in a blow-down supersonic wind tunnel with the jet discharging in the quiescent laboratory air. A schematic diagram of the experimental apparatus with a schlieren optical system is shown in Fig. 1. The air supplied by a compressor that pressurizes the ambient air up to 1 MPa is filtered, dried and stored in a high-pressure reservoir consisting of two tanks with a total capacity of 2 $m^3$. The high-pressure dry air from the reservoir is stagnated in a plenum chamber and then discharged into the atmosphere through an axisymmetric convergent nozzle with 10 mm inner diameter at the exit plane. The total temperature in the plenum chamber is equal to the surrounding one, and the plenum pressure is controlled and maintained constant during the testing by a solenoid valve. The jet issued from the nozzle has been visualized by the rainbow schlieren deflectometry with a field of view of 100 mm diameter for a nozzle operating pressure ratio of 2.3, i.e., jet flow in moderately underexpanded condition for the present nozzle.

The rainbow schlieren system consists of rail-mounted optical components including a 50 μm diameter pinhole, two 100 mm diameter, 500 mm focal length achromatic lenses, a computer generated 35 mm wide slide with color gradation in a 1.4 mm wide strip, and a digital camera with variable focal length lens. A continuous 250 W metal halide light source connected to a 50 μm diameter fiber optic cable provides the light input at the pinhole through a 16.56 mm focal length objective lens. The camera output in the RGB format is digitized by a personal computer with 24 bit color frame grabber.

The convergent nozzle used in the present experiments is installed inside a GT pulley with a reduction gear ratio of 4 and it can be rotated about the center of the nozzle by a stepping motor with a reduction gear ratio of 36 connected through a GT belt. In the present experiment, rainbow schlieren pictures were acquired over a range of nozzle angular angles from 0 deg to −180 deg by rotating the nozzle about its longitudinal axis ($z$ axis) in equal angular intervals of −20 deg. These 10 schlieren pictures were used for reconstruction of the jet density fields by both the schlieren CT and Abel inversion. The jet density profiles obtained from their reconstruction methods are compared with each other.

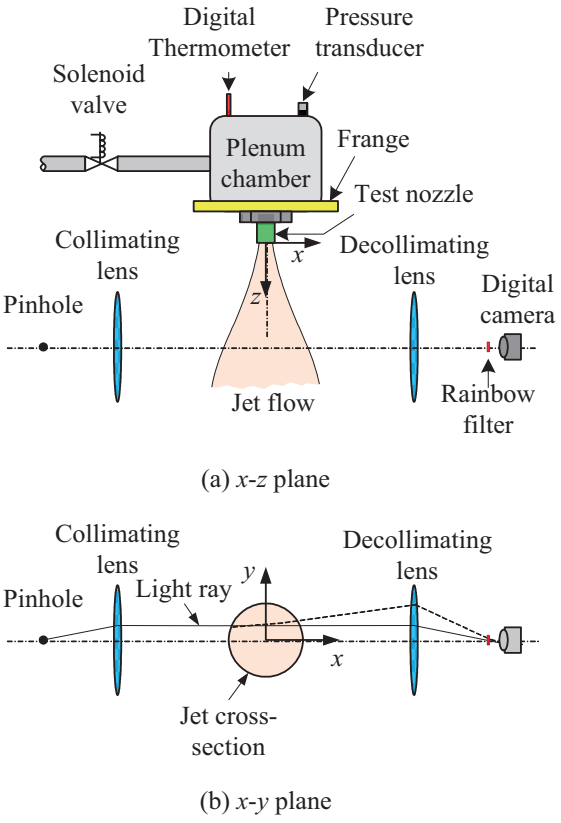


Fig. 1 Experimental set-up with optical system

Corresponding author: Yuta Akita
*E-mail address*: v4mba001@kitakyu-u.ac.jp

## 3. Results and Discussion

Figure 2 shows a rainbow schlieren picture with the flow from left to right where a rainbow filter is placed parallel to the $z$ axis in the schlieren cut-off plane. The filter orientation is shown on the upper right corner in the Fig. 2 and the location of the background hue is indicated as the dashed line on the filter. The schlieren picture has a high resolution of 55 pixels/mm. The ratio $p_{os}/p_b$ of the plenum pressure $p_{os}$ to back pressure $p_b$ ($p_b$ shows the atmospheric pressure) is held constant at 2.3 and the nozzle rotational angle is set to 0 deg. Figure 2 demonstrates the archetypal characteristics of shock cell structure appearing repeatedly in the flow field. The freestream Mach numbers at the nozzle exit plane are almost unity. Since the static pressure at the nozzle exit plane is slightly greater than the back pressure, Prandtl-Meyer expansion waves occur from the nozzle exit lip.

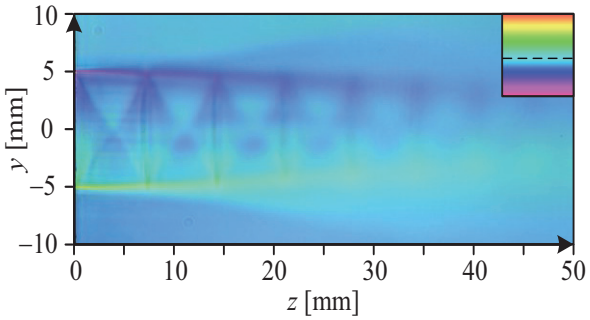


Fig. 2 Rainbow schlieren picture of underexpanded sonic jet for $p_{os}/p_b$ =2.3 and $\theta$ = 0 deg

The density contour plot for the flowfield of Fig. 2 is shown in Fig. 3. The contour plot was obtained by the schlieren CT using the horizontal rainbow schlieren images taken over 10 viewing angles from $\theta$ = 0 to −180 deg by rotating the nozzle about the $z$ axis in equal angular intervals of −20 deg and shows the densities on the cross-section including the jet centerline. Also, the results are presented with the color bar showing the density ranges from a maximum value of 2.5 kg/m$^3$ to a minimum value of 0.5 kg/m$^3$. The solid lines with a numeral in the contour show isopycnic. This contour plot indicates good qualitative and quantitative indications of the shape of the various features of the shock containing jet structure. The density contour exhibits nearly axial symmetry about the jet centerline. The density contour plot by the schlieren CT is valuable in gaining a quantitative knowledge of the shock containing flow.

A density contour plot can also be determined from the Abel inversion based on the assumption that the jet flow from the nozzle exit is axisymmetric. The density distributions along the jet centerline are indicated in Fig. 4 against the downstream distance from the nozzle exit plane. The red and blue lines show the densities reconstructed by the schlieren CT and averaged after estimated using the Abel inversion from the schlieren images recorded at nozzle rotational angles of $\theta$ = 0, −60 and −120 deg. The axial density distributions show the typical characteristics of shock cell structures appearing repeatedly in the flow field. Both the shock-cell intervals and density amplitudes agree extremely well over the full length of the shock-cell structure.

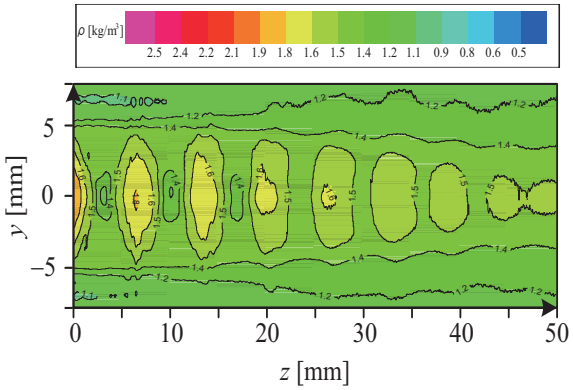


Fig. 3 Density contour plot of underexpanded sonic jet for $p_{os}/p_b$ =2.3 and $\theta$ = 0 deg

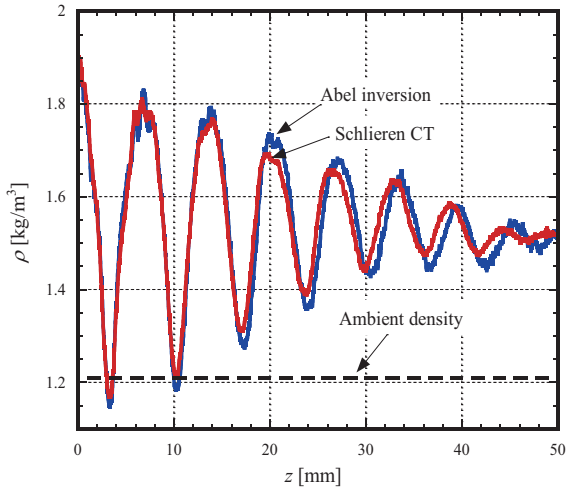


Fig. 4 Comparison of density distributions along jet axis

## 4. Concluding Remarks

The schlieren CT was applied to the underexpanded sonic jet issued from an axisymmetric convergent nozzle. As a result, excellent quantitative agreement is reached between the densities obtained from the schlieren CT and Abel inversion.


## Acknowledgement

This research is supported by the 2014 Grant for Specially Promoted Research of the Institute of Environmental Science and Technology, The University of Kitakyushu.


## References


[1] Settles,G.S., *Schlieren and Shadowgraph Techniques*, Springer, (2001).

[2] Al-Ammar, K., Agrawal, A.K., Gollahalli,S.R., and Griffin, D., *Experiments in Fluids*, 25(2), (1998) 89-95.

Eleventh International Conference on Flow Dynamics
October 8-10, 2014, Sendai, Miyagi, Japan

# Preliminary Studies of Underexpanded Moist Air Sonic Jets from Axisymmetric Convergent Nozzles

Ryotaro MINE[1], Daisuke ONO, and Yoshiaki MIYAZATO
[1] The University of Kitakyushu
1-1, Hibikino, Wakamatsu-ku, Kitakyushu, 808-0135, Japan

**ABSTRACT**

The structure of the moist air sonic jet issued from axisymmetric convergent nozzles has been experimentally investigated. Static pressures along the nozzle axis for relative humidity of $\phi$ = 43% and 70% have been measured by the through-tube system installed in the indraft supersonic wind tunnel. As a result, effects of the relative humidity on the centerline static pressures in the moist air sonic jets are clarified.

## 1. Introduction

Supersonic gas jets are widely used in various industrial, technological and scientific applications including a converter process in ironworks in which carbon-rich molten pig iron is made into steel, gas wiping in the continuous hot-dip galvanizing process to control the coating thickness of moving steel strip, gas-atomization process to obtain metal powders from molten steel, soot blower systems for removing the soot that is deposited on the furnace tubes of a boiler during combustion and so on. Most supersonic jets are not correctly expanded. In these jets, a quasi-periodic shock cell structure develops in the jet plume because of the static pressure mismatch at the nozzle exit. Therefore, a great deal of attention has been paid to study experimentally and theoretically shock-containing single-phase jets. However, a detailed understanding of shock containing multi-phase jets is lacking in the current literature.

Otobe et al. [1] have studied the flow characteristics of underexpanded moist air sonic jets issued from a convergent nozzle using the gray-scale schlieren method and numerical computations. They showed that the axial position of the Mach disk in an underexpanded moist air jet is almost the same as that in dry air jets and the Mach disk diameter increases slightly with increasing relative humidity. Also, the total pressure loss behind the Mach disk for moist air jet changed largely in comparison to that for dry air jet. Nevertheless, there are few available experimental data on the flow properties of shock containing moist air jets. The aim of the present study is to examine the effects of the relative humidity on the centerline static pressures in underexpanded moist air sonic jets.

## 2. Experimental Method

Experiments have been conducted in a continuous type indraft wind tunnel. The wind tunnel consists of a test section, settling chamber, two vacuum pumps, and silencer. The back pressure $p_b$ in the settling chamber is held constant at predetermined level by the vacuum pumps before starting the experiment. Atmospheric moist air with a stagnation pressure of $p_{os}$ is accelerated to sonic at a convergent nozzle and then is discharged into the settling chamber. The present experiments were performed for two different relative humidity of $\phi$ = 43% and 70% with a nozzle operating pressure ratio of $p_{os}/p_b$ = 2.34. The convergent nozzle used in the present experiment has 60 mm in diameter at the inlet and 20 mm in diameter at the exit with a curvature radius of 180 mm from the nozzle inlet to exit. The total temperature in the settling chamber was equal to the atmospheric one.

The static pressures along the nozzle center line were measured by a through-tube [2] inserted from far upstream of the convergent nozzle to the settling chamber. It consists of an inner tube and an outer tube. The inner tube with an outer diameter of 1.9 mm and an inner diameter of 1.7 mm is inserted into the outer tube with an outer diameter of 2.2 mm and an inner diameter of 2.0 mm. A static pressure hole with a diameter of 0.5 mm is vertically drilled on the prescribed place of the inner tube and a semi-conductor pressure transducer with an outer diameter of 1.65 mm is inserted just after the pressure hole. In the present experiments, the static pressure hole was moved along the nozzle axis in equal intervals of 1 mm. The pressure signal from the transducer was sampled at 1 kHz intervals with a 12 bit A/D converter after through an amplifier and then averaged over a 0.1 s period. Also, the experiments were repeated at least 5 times in time intervals of around 30 min to perform the uncertainty analysis. The percentage of the cross-sectional area (3.80 mm$^2$) of the outer tube to that (314 mm$^2$) of the nozzle exit is only 1.2 %, so that the effect on the flow by inserting the through-tube into the nozzle is negligible. The further detail of the configuration of the through-tube is described in Ref. [2].

## 3. Results and Discussion

Figure 1 shows the distributions of static pressures $p$ along the nozzle axis and their uncertainty $U_{95}$ for a 95% confidence estimate. Each abscissa in Fig. 1 represents the downstream distance $z$ from the center of the nozzle exit plane. The static pressure distributions as well as the uncertainty upstream of the nozzle exit plane for $\phi$ = 43% and 70% are almost the same values to each other. It was found that the values of their distributions agree very favorably with the calculated ones based upon the

Corresponding author: Ryotaro Mine
*E-mail address*: v4mba024@eng.kitakyu-u.ac.jp

assumption of the one-dimensional isentropic flow. On the other hand, the uncertainty for the centerline static pressures in the jet plume with $\phi$ = 70% indicates large fluctuations quantitatively when compared to that with $\phi$ = 43%.

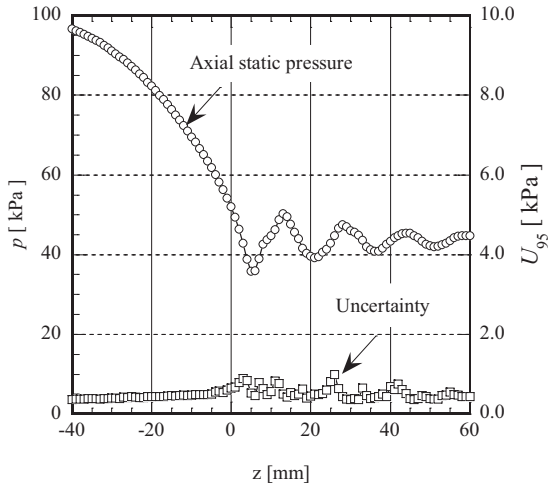


(a) $\phi$ = 43 %

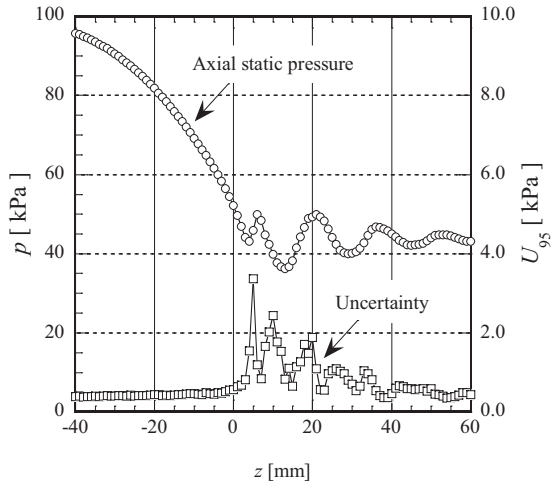


(b) $\phi$ = 70 %

Fig. 1 Static pressure and their uncertainties along nozzle centerline

The ratio of the difference between centerline static pressure and back pressure to back pressure is reproduced from the experimental values in Fig. 1 and the results are shown in Fig. 2 against normalized axial distance z where $D_e$ represents the inner diameter of the nozzle exit. The normalized static pressure distribution for $\phi$ = 43% exhibits some features similar to that of the single-phase underexpanded sonic jet in which the static pressure decreases abruptly due to the expansion waves from the nozzle lip before increasing soon by the compression waves reflected at the opposite jet boundaries and a similar static pressure variation is repeated over the downstream distance. While the static pressure distribution for $\phi$ = 70% demonstrates a notable feature when compared to that for $\phi$ = 43% in which the slight static pressure rise at $z/D_e$ = around 0.25 for $\phi$ = 70% results from the condensation. The static pressure rise in underexpanded moist air jet caused by the condensation is observed in the numerical results of Otobe et al. [1]. The most distinctive effect of the relative humidity on the underexpanded moist air sonic jet is that the static pressures for $\phi$ = 43% and 70% fluctuate in almost 180 degrees out of phase with each other. To the authors' knowledge, the existence or absence of such a phenomenon has never been reported so far.

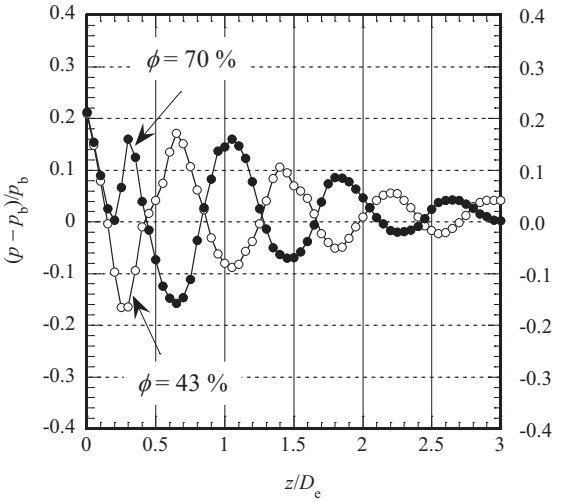


Fig. 2 Effect of relative humidity on underexpanded moist air sonic jet

## 4. Concluding Remarks

Moist air sonic jet structure from an axisymmetric convergent nozzle has been experimentally investigated. As a result, the relative humidity has no effect on the flow upstream of the nozzle exit plane, but a significant effect on the jet plume issued from the nozzle. The jet centerline static pressure distribution for $\phi$ = 70% fluctuate in almost 180 deg out of phase compared to that for $\phi$ = 43%.


## Acknowledgement

This research is supported in part by the 2014 Grant for Specially Promoted Research of the Institute of Environmental Science and Technology, The University of Kitakyushu.


## References


[1] Otobe, Y., Kashimura, H., Matsuo, S., Tanaka, M., and Setoguchi, T., Generation of Overpressure due to Condensation in Moist Air Jet, *J. Thermal Science*, Vol. 16, No. 2, (2007), pp. 145-148.

[2] Matuo, K., Mochizuki, H., Miyazato, Y., and Gohya, M., Oscillatory Characteristics of a Pseudo-Shock Wave in a Rectangular Straight Duct, *JSME International J.*, Series B, Vol. 36, No. 2, (1993), pp. 222-229.

Eleventh International Conference on Flow Dynamics
October 8-10, 2014, Sendai, Miyagi, Japan

# An Experimental Investigation on Aerodynamic Characteristics of External Nozzle in Hypersonic Propulsion System

Tatsushi Isono[1], Sadatake Tomioka[2], Hidemi Takahashi[2], Noboru Sakuranaka[2], Masato Ono[3], and Ryo Mikoshiba[3]
[1]Tohoku University
6-6, Aoba, Aramakiaza, Aoba-ku, Sendai, Miyagi, 980-8579, Japan
[2]Japan Aerospace Exploration Agency (JAXA)
1, Koganezawa, Kimigaya, Kakuda, 981-1525, Japan
[3]Keio University
3-14-1, Hiyoshi, Kohoku-ku, Yokohama, Kanagawa, 223-8522, Japan

**ABSTRACT**

An experimental study of a two-dimensional Single Expansion Ramp Nozzle (SERN), i.e. External Nozzle of TSTO-RLV-BS, was conducted to investigate how the nozzle flow is influenced by ambient or "back" pressure. The aerodynamic characteristics of External Nozzle were elucidated by measuring the ramp surface pressure distribution at various Nozzle Pressure Ratios (NPR) defined as the ratio between the internal nozzle total pressure and the ambient pressure. In order to focus on aerodynamic characteristics of the nozzle, cold gas experiments have been carried out.

## 1. Introduction

The vehicle which gain the both of the lift and the thrust, in hypersonic atmospheric flight condition, have a lifting body, what is called wave-rider (e.g. Fig. 1), so as to improve the aerodynamic and control performances. In addition, this type of vehicle requires efficient airframe propulsion integration due to preceding reason, especially reducing ram drag, since the propulsion system is equipped on the underbelly of the airframe. In this situation, after-body of the vehicle operates as the external nozzle[1]. This nozzle extracts more thrust from the exhaust flow of the internal nozzle, and then aims to improve the vehicle performance in terms of specific impulse. Performance estimation of the external nozzle, equipped on Two Stage To Orbit - Reusable Launch Vehicle – Booster Stage (TSTO-RLV-BS), was conducted by Tomioka et al.[2] at Japan Aerospace Exploration Agency (JAXA). This study showed that extension of external nozzle contribute the performance improvement, but the trade-off of nozzle size (or expansion ratio) and nozzle weight is extremely important, because the larger the nozzle size become, the heavier the nozzle weight become, however, this study made an assumption below.

(1) The flow expands isentropically in virtual stream tube which is fully enclosed by virtual solid wall, viz. extended side fences and cowl.
(2) The nozzle flow is quasi-one dimensional.
(3) Ramp surface pressure is set at ambient value if its value is less than the ambient one.

In a word, preceding estimation neglect the two or three dimensionality, but this aspects impact on a nozzle flow probably, since the jet boundary is formed at the bottom and lateral side of the nozzle. First, in order to focus on a two dimensionality of the nozzle flow, the cold gas experiments have been carried out in the situation that 2D type test nozzle is used for test piece and the lateral side of ramp flow is completely enclosed by side fences. Then, two dimensionality of the flow was discussed by analyzing the ramp surface pressure distribution. In addition, the difference of the ramp performance between two types of the ramp was discussed in order to collect the data to optimize the ramp shape (especially inclination angle and length).

Corresponding author: Tatsushi Isono
*E-mail address*: isono@scrj.mech.tohoku.ac.jp

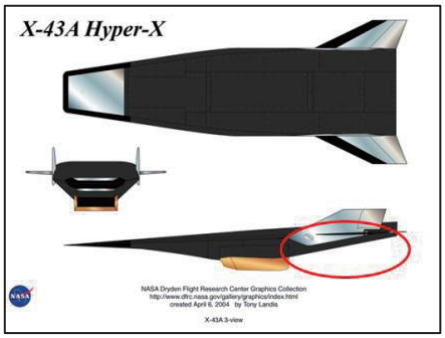


Fig. 1 Schematic image of typical wave-rider X-43 Hyper-X (Red circle part is external nozzle)

## 2. Experimental method

Fig.2 shows the experimental apparatus. As mentioned above, 2D type test nozzle simulate the internal nozzle of hypersonic propulsion system and the ramp simulate the external nozzle. Two types of ramp are used as test piece and the configurations of them are shown in Table 1. Nozzle Pressure Ratio (NPR) is shown in following expression (1),

$$\mathrm{NPR} = \frac{p_{0r}}{p_b} \tag{1}$$

where, $p_{0r}$ is internal nozzle total pressure and $p_b$ is ambient pressure. In this situation, each of them expresses test nozzle total pressure and test chamber pressure respectively. Optimum NPR is 76 for 2D type test nozzle. The condition that NPR value is larger than optimum one is called under-expanded condition, in contrast the condition that NPR is smaller than that is called over-expanded condition. Then, nozzle flow adopts various shapes so as to adjust each NPR value. In this experiment, $p_{0r}$ is varied to change the NPR widely with referring above features.

Table 1. Ramp configuration

| Ramp type | Inclination angle [deg.] | Total length [mm] | Expansion ratio |
|---|---|---|---|
| Ramp A | 20 | 200 | 4.42 |
| Ramp B | 10 | 400 | 4.47 |

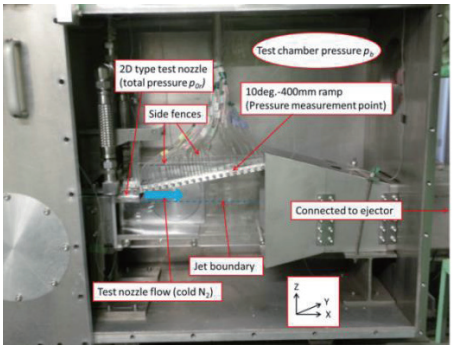


Fig. 2 Experimental apparatus

## 3. Results and Discussion

Fig. 3 and 4 shows the ramp surface pressure ($p_s$) distribution non-dimensionalized by test nozzle total pressure ($p_{0r}$). Comparison of $p_s/p_{0r}$ distributions on each ramp type in over-expanded condition (NPR=65, 70 respectively) is shown in Fig. 3 and in various NPR condition at ramp B is shown in Fig. 4.

Discussing Fig. 3 in the interval between 0mm and 200mm, each pressure distribution has some similarity, while at the interval between 0mm and 130mm, $p_s/p_{0r}$ value of ramp A is less than that of ramp B in spite of NPR of ramp A nearly equaling that of ramp B. This fact results from difference in inclination angle. Focusing on expansion ramp performance, namely pressure integral, ramp B more effectively work for the vehicle performance than ramp A in the case of over expanded condition, wherever the test chamber pressure (ambient pressure) is chosen, whereas to focus on ramp weight, ramp B is about twice heavier than ramp A. In addition to above discussion, isentropic expansion waves emerge from the top side of the test nozzle, on the other hand shock wave emerges from the bottom side of that in the case of over-expanded condition. This shock wave parameter is shown in Table 2, moreover schematic image of two dimensional waves model is shown in Fig. 5. In ramp A case, only reflected compression waves can reach the ramp surface but shock wave cannot. By contrast in ramp B case, both of the shock wave and reflected compression waves can reach the ramp surface. This difference made a superiority or inferiority between ramp A and B. Consequently, in this study case, shortening ramp length is much better for ramp performance rather than increasing inclination angle.

Meanwhile, taking a look at Fig. 4, expansion ramp generate a drag in under-expanded condition by virtue of the presence of rapid expansion corner and jet boundary of the bottom side. On the other hand in over-expanded condition, it makes an improvement of the ramp performance, due to high pressure region resulting from the incident of shock wave and reflected compression waves. According to the preceding discussion, the type of the incident wave (expansion, compression, or shock) impact on ramp performance. Hence, it is the best case for the ramp that only shock and compression wave enter the ramp surface but expansion wave doesn't.

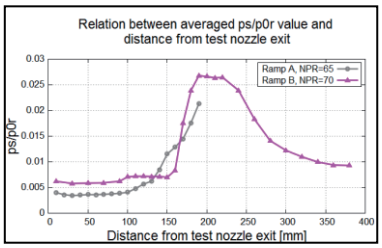


Fig. 3 Comparison of $p_s/p_{0r}$ distributions on each ramp type in over-expanded condition

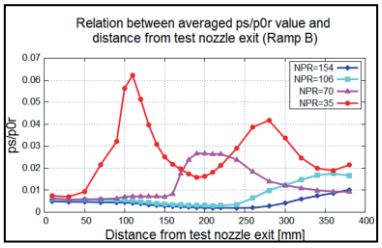


Fig. 4 Comparison of $p_s/p_{0r}$ distributions in various NPR condition at ramp B

Table 2. Shock wave parameters

| Ramp type | NPR | Turning angle [deg.] | Shock angle [deg.] |
|---|---|---|---|
| Ramp A | 65 | 1.8 | 17.8 |
| Ramp B | 70 | 1.0 | 17.2 |

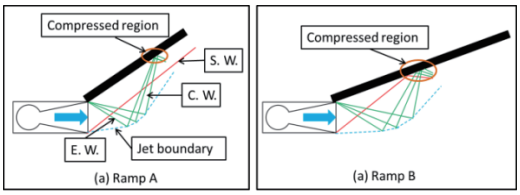


Fig. 5 Schematic image of two dimensional wave model

## 4. Conclusion Remarks

Cold gas experiments have been carried out in order to elucidate how the external nozzle flow is influenced by ambient pressure. Through this study, two characteristics of external nozzle flow, especially two dimensionality of the flow is gained. One is the fact that shortening ramp length is much better for ramp performance rather than increasing inclination angle, and the other is the fact that it is the best case for the ramp that only shock and compression wave enter the ramp surface but expansion wave doesn't.

## References


[1] Dalle, D. J., Torrez S. M., and Driscoll J. F., *Journal of Propulsion and Power*, 28, No. 3, (2012) 545-555.

[2] Tomioka S., Hiraiwa T., Saito T., Kato K., Kodera M., and Tani K., *ISTS*, (2013) 2013-a-36.

Eleventh International Conference on Flow Dynamics
October 8-10, 2014, Sendai, Miyagi, Japan

# Wind Tunnel Test on New Reaction Control System without High-Pressure Source

Yuta Ono[1], Katsuyoshi Fukiba[1], Yusuke Yamaguchi[1], Yusuke Maru[2]
[1]Department of mechanical engineering, Shizuoka University
3-5-1 Johoku, Naka-ku, Hamamatsu-city, 432-8561, Japan
[2]Japan Aerospace Exploration Agency
3-1-1 Yoshinodai, Chuo-ku, Sagamihara-city, 252-5210, Japan

**ABSTRACT**

This study is about new method of attitude control for supersonic experimental vehicle. In low air density at high altitude, Reaction Control System (RCS) is mainly used. However, the RCS components account for 20 % of the total experimental vehicle weight. In order to reduce weight, we propose a new RCS which takes in high-pressure air from external supersonic flow. We conducted a supersonic wind tunnel test using the models which adopted a new RCS. As a result, we could demonstrate the effectiveness of new RCS.

## 1. Introduction

The method of attitude control which emits lateral jet is called Reaction Control System (RCS). RCS has mainly three advantages over the method of attitude control by steering tail wings. They are high agility, simple mechanism and high thermal resistance. The most popular example using RCS is Space shuttle. When it flights in low air density at high altitude, it controls the attitude by RCS. This is because the control method by steering tail wings cannot generate enough control force.

Recently, the microgravity experiment using experimental vehicle (BOV) was held by JAXA [1]. In this experiment a balloon brings BOV to an attitude of 40km, and let it fall freely. During free-fall from high attitude, they succeeded maintaining the microgravity environment by RCS which equipped the vehicle [2]. Now, using technologies and experience obtained by these flight tests, the research and development of supersonic flight system have been conducted.

However, the RCS components such a high-pressure tanks account for 20 % of the total vehicle weight [2]. The RCS is overweight, considering the weight of experimental devices and components of vehicle. So it is the most important improvement to reduce weight of the RCS components as for the development of experimental vehicles in the future.

In this study we propose a new RCS which takes in high-pressure air from external supersonic flow in order to reduce weight. This new mechanism diverts high-pressure air from the stagnation point of the body top after the shock wave through a flow channel to sidewall of the body, where it is ejected. If this new RCS is realized, we do not have to equip, or can achieve downsizing the high-pressure tanks of vehicle. Hence we can reduce the vehicle weight substantially.

In this paper we report the results of the wind tunnel experiments intended to evaluate the effectiveness of the proposed RCS. We conducted a supersonic wind tunnel test using the models which adopted a new RCS. The effect of the jet was evaluated by measuring moment acting on the bodies. Specifically, (1) the effectiveness of new RCS, (2) comparison with theoretical value and test value, were investigated.

Corresponding author: Yuta Ono
*E-mail address*: f0330020@ipc.shizuoka.ac.jp

## 2. Method

First, we describe the method of the wind tunnel experiments. The experiments were conducted using the supersonic wind tunnel at JAXA Sagamihara campus. The wind tunnel model with a new RCS structure is shown in Fig. 1a). And inner structure of the model is shown in Fig. 1b). In this experiment high-pressure air is supplied from the stagnation point after the shock wave through a flow channel, and is held by a solenoid valve. After that, a high speed jet is ejected from sidewall of the body by operating a solenoid valve. The moments are measured with a six-component balance mounted inside the model. The index to evaluate the effect of the jet is a moment coefficient ($C_N$) as shown Eq. (1).

$$C_N = \frac{N}{\frac{1}{2}\rho v^2 \cdot D \cdot S} \quad [-] \tag{1}$$

In Eq. (1), a moment coefficient ($C_N$) is divided a measured moments ($N$) by dynamic pressure ($1/2\rho v^2$), diameter of the model ($D$) and projected area ($S$). Measured moments before and after jet injection were converted to moment coefficients. We evaluated the effect of the jet with the difference between these moment coefficients ( $\Delta C_N$). The test conditions are listed in Table 1.

Second, we describe the calculation method of the theoretical value. The theoretical thrust is calculated as shown Eq. (2)

$$F_t \cong A_e(\gamma p_e + p_e - p_\infty) \quad [\mathrm{N}] \tag{2}$$

where $A_e$ is an area of jet ejection tip, $\gamma$ is ratio of specific heat, $p_e$ is the static pressure which is calculated by stagnation point after the shock wave and $p_\infty$ is the static pressure of the wind tunnel main flow. Then, it converts the theoretical moment. The arm of moment is defined as the distance between the center of the balance and the center of the wind pressure. After that, we substitute the theoretical moment for Eq. (1), and calculate the theoretical moment coefficient. In addition, we assumed that the jet is ejected at Mach number $M$=1.

Table 1. Experimental conditions

| Items | Value | Unit |
|---|---|---|
| Mach number | 2.0 | - |
| Diameter of jet exit | 1.5/2.0 | mm |
| Total pressure | 180 | kPa |
| Angle of attack | 0 | degrees |

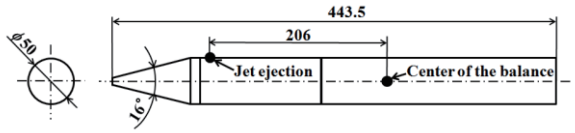


a) General view

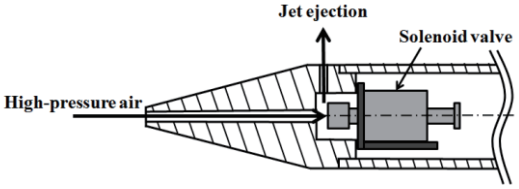


b) Inner structure

Fig.1 Model

## 3. Results and Discussion

First, we describe the effectiveness of new RCS. The Schlieren photographs that show before and after the jet ejection are shown in Fig. 2a) and Fig. 2b). After the jet ejection, we can recognize the jet plume clearly behind the expansion wave. And, the time variation of the measured moment around the center of the balance is shown in Fig. 3. After the jet ejection, we can recognize an increase of the measured moment definitely. Therefore, the new RCS, which supply high-pressure air from the stagnation point after the shock wave, is effective.

Second, we describe the comparison with theoretical value and test value. The theoretical moment and the measured moment are shown in Table 2. The theoretical value of 2.0-mm-diameter is 1.78 times larger than that of 1.5-mm-diameter. The test value of 2.0-mm-diameter is 1.69 times larger than that of 1.5-mm-diameter. These results can be thought that the test value and the theoretical value become the nearly same growth rates each other when the diameter of jet exit is enlarged. In addition, the test value of 1.5-mm-diameter is 48% of the theoretical value. The test value of 2.0-mm-diameter is 46% of the theoretical value. We consider that these results are caused by two things. One is the outbreak of the complex flow field near the body by the shock wave. Another is the pressure losses when high-pressure air is supplied through a flow channel. We are planning to carry out the experiments which improve our understanding.

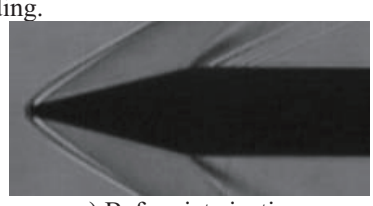

a) Before jet ejection

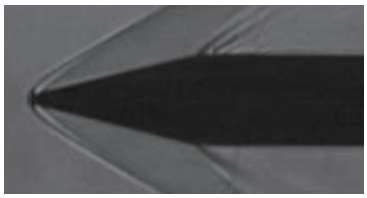

b) After jet ejection

Fig.2 Schlieren photographs

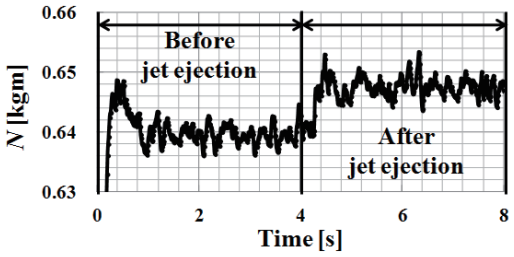


Fig.3 Time variation of measured moment

Table 2. Comparison between test and theory

| Jet diameters [mm] | $\Delta C_N$ [-] Test value | Theoretical value | Test/Theoretical |
|---|---|---|---|
| 1.5 | 0.00392 | 0.00815 | 0.48 |
| 2.0 | 0.00665 | 0.0145 | 0.46 |

## 4. Conclusions

The conclusions obtained in this study are listed below:

(1) We could demonstrate the effectiveness of new RCS which supply high-pressure air from the stagnation point of the body top.

(2) The theoretical value of 2.0-mm-diameter is 1.78 times larger than that of 1.5-mm-diameter. The test value of 2.0-mm-diameter is 1.69 times larger than that of 1.5-mm-diameter. In addition, the test value of 1.5-mm-diameter is 48% of the theoretical value. The test value of 2.0-mm-diameter is 46% of the theoretical value.

## References

[1] S. Sawai, T. Hashimoto, S.Sakai, N. Bando, H. Kobayashi, K. Fujita, T.Yoshimitsu, T. Ishikawa, Y. Inatomi, H.Fuke, Y. Kamata, S.Hoshino, K. Tajima, S. Kadooka, S. Uehara, T. Kojima, E. Ueno, K. Miyaji, N. Tsuboi, K. Hiraki, K. Suzuki, K. Matsushima, Y. Nakata, Development of Vehicle for Balloon-Based Microgravity Experiment and Its Flight Results, *Japan Society for Aeronautical and Space Sciences*, Vol.56, No.654, (2008) 339-346. (In Japanese)

[2] H. Kobayashi, S. Sawai, N. Bando, S. Sakai, K. Ishikawa, H. Inatomi, K. Fujita, Y. Maru, T. Hashimoto, Development of Cold Gas Thruster for Micro Gravity Experiment System with High Altitude Balloon, *JAXA Research and Development Report*, (2009), JAXA-RR-08-005. (In Japanese)

# Numerical Investigation of a Tantalum Block Subjected to Underwater Shock Wave Loading

Taketoshi Koita[1], Toshiya Gonai[2], Mingyu Sun[3], Shuji Owada[4], Takashi Nakamura[1]
[1]Institute of Multidisciplinary Research for Advanced Materials, Tohoku University
2-1-1 Katahira, Aoba-ku, Sendai, 980-8577, Japan
[2]Department of Aerospace Engineering, Graduate School of Engineering, Tohoku University
6-3 Aoba, Aramaki aza, Aoba-ku, Sendai, 980-8578, Japan
[3]Institute of Fluid Science, Tohoku University
2-1-1 Katahira, Aoba-ku, Sendai, 980-8577, Japan
[4]Faculty of Science and Engineering, Waseda University
3-4-1 Okubo, Shinjuku-ku, Tokyo, 169-8555, Japan

**ABSTRACT**

The pressure of a Ta block subjected to the underwater shock wave loading was analyzed numerically to discuss the separation of Ta from a Ta capacitor in the electrical disintegration. The simulation was performed by using ANSYS AUTODYN. The pressure of numerical results were compared with the theoretical results calculated by the extended Taylor's model. The underwater shock wave propagated into a Ta and reflected at the right surface of it as the expansion wave. The pressure on right surface of Ta was increased by the transmitted wave and decreased by the reflection wave.

## 1. Introduction

The electrical disintegration (ED) has been applied recently to the separation of the tantalum (Ta), the rare metal, from the Ta capacitor of the waste circuit board in the study of recycling technology for rare metals[1]. In the ED method, the discharge energy of high voltage pulse is released directly to materials in the water. The application of ED to the metal and rock disintegration has been studied [1, 2]. However, the mechanism of the separation of materials caused by ED has not been much researched. In order to study the mechanism of ED, it is important to investigate the pressure in the materials and water induced by the shock wave loading generated by the electric discharge. The displacement of a submerged plate subjected to the underwater shock loading have been studied theoretically by the extend Taylor's model [3]. In this model, the pressure generated by the shock wave propagating in the plate is not considered. Therefore, in this study, the pressure on the left and right surface of a Ta block put on a PMMA block subjected to the underwater shock wave loading was investigated numerically with considering the pressure inside the Ta in the simple model simulating the ED for a Ta capacitor. The pressure of numerical results were compared with that of theoretical results obtained by the Taylor's model.

## 2. Numerical Method

In this study, the pressure of a Ta block subjected to the underwater shock wave induced by the electric discharge with the discharge energy of 2.025 J and the energy per unit meter $E$ = 405 J/m was analyzed. The standoff distance between the discharge point and the Ta block $L$ was set to be 30 mm to compare the pressure of numerical results with theoretical results. The numerical simulation was performed using ANSYS® AUTODYN®. The analysis was carried out with the Multiple Material Euler solver in the two-dimensional (2D) model. Figure 1 shows the schematic diagram of the analysis model.

Corresponding author: Taketoshi Koita
*E-mail address*: koita@shock.ifs.tohoku.ac.jp

In order to calculate the pressure of the underwater shock wave, the circle region with the radius of 30 mm from the discharge point was modeled by using the 2D wedge model nearly identical to the one-dimensional circle model until 19.2 μs as shown in Fig. 1(a). The water with the radius of 0.1 mm from the discharge point was added with the energy $E$ and was given the internal energy per unit mass, $e_{wh0}$ = 12.89 MJ/kg. The uniform mesh size is 2 μm in this model. The wedge model was remapped into the 2D grid in the analysis region as presented in Fig. 1(b). The analysis region is 40 mm × 80 mm and the number of grids is 400 × 800. The width and high of Ta are 2 mm respectively. The initial pressure of water, Ta and PMMA were set up at 101.3 kPa. The time histories of pressure on the left surface of Ta at ($x$, $y$) = (30,0.5), (30,-0.5) and the right surface at ($x$, $y$) = (32,0) were calculated.

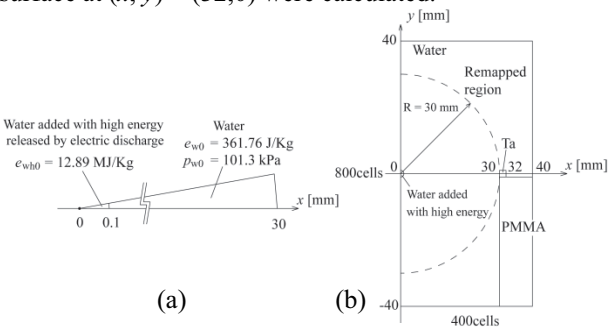


Fig. 1 Schematic diagrams of analysis models: (a) the wedge model for calculation of the propagating underwater shock wave, (b) the whole analysis model

These time histories of pressure of numerical results were compared with that of theoretical results analyzed by the extended Taylor's model for a freestanding water-backed plate (WBP) [3]. The pressure on the left and right surface of a Ta plate, $P_L(t)$ and $P_R(t)$, calculated by the WBP model are described as follow:

$$P_L(t) = 2P_{\max} e^{-t/\theta} - \rho_w c_w v_p(t) \quad (1)$$

$$P_R(t) = \rho_w c_w v_p(t) \quad (2)$$

where $P_{max}$ is the peak pressure of the underwater shock wave and $\theta$ is the decay time. $P_{max}$ and $\theta$ are calculated by the Cole empirical formula [4]. $\rho_w$ and $c_w$ are the density and the sound speed of water. $v_p(t)$ is the velocity of the plate displaced by the shock wave loading. $v_p(t)$ is calculated by theoretical method that takes into account the dynamic friction coefficient $\mu'$ between the Ta plate and PMMA based on the WBP model and is presented as

$$v_p(t) = \frac{2P_{\max}\theta}{m(1-\beta)}\left(e^{-\beta t/\theta} - e^{-t/\theta}\right) + \frac{\mu' g\theta}{\beta}\left(e^{-\beta t/\theta} - 1\right) \qquad (3)$$

where $m$ is the mass per unit area of the plate, $\beta = 2\rho_w c_w \theta / m$.

## 3. Results and Discussion

Figure 2 shows the pressure distribution of a Ta and a PMMA block subjected to the underwater shock wave loading. The underwater shock wave reflects at the left surface of these blocks. The shock wave also propagates inside the Ta and PMMA as the transmitted wave in Fig. 2(a), (b). As seen in Fig. 2(c), the transmitted wave reflects at the right surface of Ta as the expansion wave because the acoustic impedance of Ta is higher than that of the water. Figure 3 shows the numerical and theoretical results of the time histories of pressure on the left surface of Ta. In Fig. 3, the peak pressure of theoretical result is close to that of numerical result. This is because the $P_L(t)$ is calculated by the incident wave of the underwater shock wave and the reflection wave from the left surface of Ta in Eq. (1). The time histories of pressure on the right surface of Ta analyzed numerically and theoretically are presented in figure 4. The pressure of theoretical result is different from that of numerical result. In the numerical result, the pressure increases due to the prorogation of transmitted wave inside the Ta in the initial stage. The pressure decreases rapidly after reaching to the maximum value at $t$ = 20.2 μs in Fig. 4 because the transmitted wave reflects as the expansion wave at the right surface as seen in Fig. 2(c). After $t$ = 20.2 μs, the pressure fluctuation occurs due to the pressure rise and drop induced by the reflection wave from the surfaces of both side of Ta. It is considered from the numerical results in Fig.3 and Fig.4 that the displacement of Ta is caused by not only the pressure on the left surface but also that on the right surface of Ta. On the other hand, the pressure $P_R(t)$ calculated theoretically is considerably lower than the numerical result and does not fluctuate. This is because the pressure on the right surface of Ta induced by the propagating waves inside the Ta is not considered in Eq. (2) of the theoretical model.

## 4. Concluding Remarks

The pressure on the left and right surface of a Ta block subjected to the underwater shock loading were analyzed numerically. The pressure on the right surface fluctuated due to the interaction of the transmitted wave and reflection wave propagating in Ta with the surface. It is necessary to consider the pressure induced by these waves inside Ta when the displacement and the pressure on the right surface of Ta caused by the shock loading are analyzed with the Taylor's WBP model.

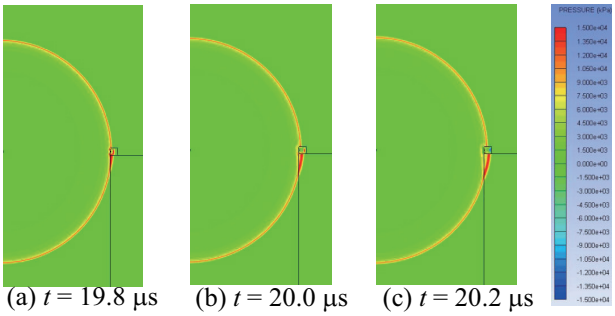

(a) $t$ = 19.8 μs (b) $t$ = 20.0 μs (c) $t$ = 20.2 μs

Fig. 2 Pressure distribution of a Ta and a PMMA block subjected to the underwater shock wave loading.

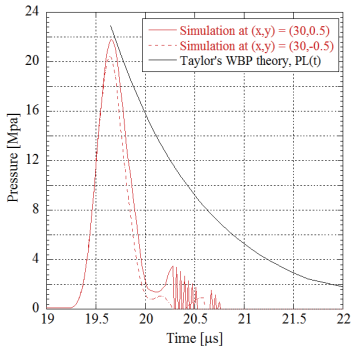


Fig. 3 Numerical and theoretical results of the time histories of pressure on the left surface of Ta.

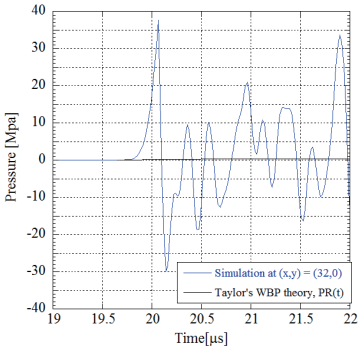


Fig. 4 Numerical and theoretical results of the time histories of pressure on the right surface of Ta.


## Acknowledgements

The present study was performed under the High Efficiency Rare Elements Extraction Technology Area in Tohoku Innovative Materials Technology Initiatives for Reconstruction.


## References


[1] S. Owada, T. Nakamura, et al., *Proceeding of International Workshop on Recycling Technology of Critical Elements,* (2013), 158－167.

[2] M. Ito, S. Owada, T. Nishimura, T. Ota, *Int. J. Miner. Process*, 92 (2009), 7－14.

[3] Z. Liu, Y. L. Young, *J. Appl. Mech.*, 75(4) (2008), 044504.

[4] R. H. Cole, Underwater Explosions, *Princeton Univ. Press*, (1948), 235－244.

# A Shock Wave Structure by Different Numerical Approaches

Ewgenij Malkov[1,2], Alexey Kokhanchik[1,2], Sergey Poleshkin[1,2], and Yevgeniy Bondar[1,2]
[1]Novosibirsk State University
Pirogova 2, Novosibirsk 630090, Russia
[2]Khristianovich Institute of Theoretical and Applied Mechanics SB RAS
Institutskaya 4/1, Novosibirsk 630090, Russia

**ABSTRACT**

A new deterministic method of solving the Boltzmann equation has been employed in numerical studies of plane shock wave structure. Results for various Mach numbers have been compared with predictions of the DSMC method. Particular attention in estimating the solution accuracy is paid to a fine structural effect: the presence of a total temperature peak exceeding the temperature value further downstream. The results of solving the Boltzmann equation for the shock wave structure are in excellent agreement with the DSMC predictions for various Mach numbers.

## 1. Introduction

Deterministic methods of the numerical solution of the nonlinear kinetic Boltzmann equation

$$\frac{\partial f}{\partial t} + v\frac{\partial f}{\partial r} = St(f)$$

for the one-particle distribution function $f$ are intensely developed at the moment, e.g. [1]. Application of these methods of solving the Boltzmann equation in practice is not very popular because such a solution is extremely computationally expensive. At the moment, the method used most often for rarefied flow studies is the Direct Simulation Monte Carlo (DSMC) method. As the performance of computational systems noticeably increased and massive computations became much less expensive, it became possible to develop software systems for computing rarefied gas flows on the basis of the deterministic numerical solution of the nonlinear kinetic Boltzmann equation. It should be noted that deterministic methods offer advantages over statistical methods in calculating slow and unsteady flows.

The theoretical analysis of convergence of numerical schemes of solving the Boltzmann equation is rather difficult. Therefore, it is important to validate the developed methods of solving the Boltzmann equation by means of solving benchmark test cases, i.e., classical problems of rarefied gas dynamics. A new method of solving the Boltzmann equation was developed and implemented in a code for computations on graphics processing units (GPUs). The results of the plane shock wave structure calculations by using this method are compared with the DSMC prediction which is considered as a reference solution.

One of the criteria of accuracy of the numerical solution is assumed to be the correspondence between the predicted streamwise temperature profile and the analytical relationship between the density of molecules and the streamwise temperature found by Yen [2].

Particular attention in estimating the solution accuracy is paid to a fine structural effect, i.e., the presence of a total temperature peak (overshoot) exceeding the temperature value further downstream, which corresponds to the Rankine-Hugoniot conditions.

Corresponding author: Yevgeniy Bondar
*E-mail address*: bond@itam.nsc.ru

## 2. Numerical Results

The proposed computational scheme of solving the Boltzmann equation was applied to calculate the structure of a strong shock wave in a hard sphere gas for various Mach numbers. Computation of the structure of a plane shock wave with a high Mach number required the use of a dense computational grid, which covers a large interval of velocities. Such a computation could be performed owing to the ensured speedup in collision integral computation due parallelization of algorithms on GPU. In numerical implementation of the deterministic method, we used a scheme with splitting over physical processes and with alternation of the calculation of homogeneous relaxation in each spatial cell and collisionless transfer in the physical space.

The formula obtained by Yen [2], which yields the relationship between the density and streamwise temperature and directly follows from the mass and momentum conservation laws. Thus, Yen's solution can be used as an indicator of the accuracy of the numerical solution. The calculated streamwise temperature profile is compared in Fig. 1 with the streamwise temperature profile obtained on the basis of the calculated density profile with the use of Yen's relation. The computations provide excellent agreement with Yen's solution.

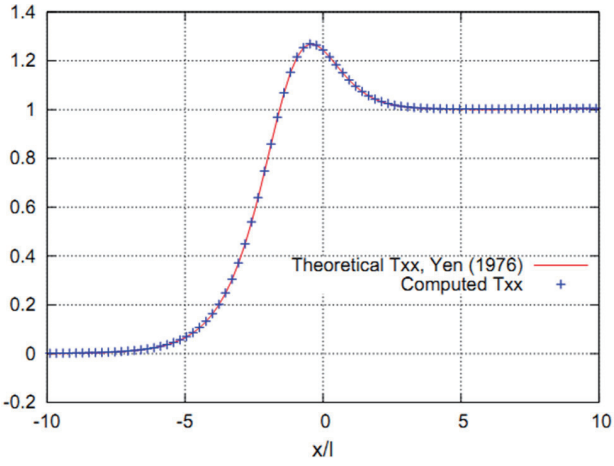


Fig. 1 Comparison of the streamwise temperature profile with Yen's solution, M=4.

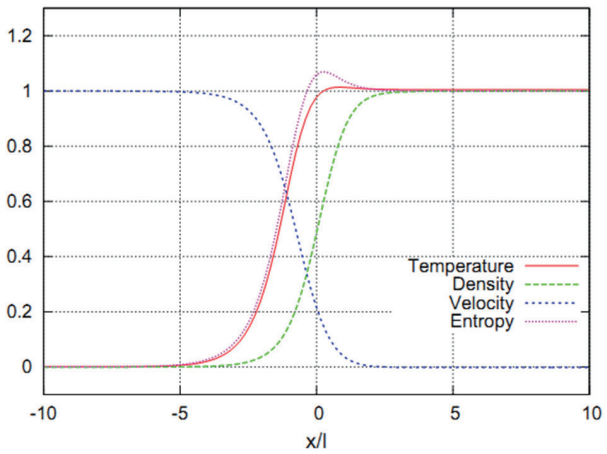


Fig. 2 Profiles of gas-dynamic quantities for M=8. The deterministic solution of the Boltzmann equation.

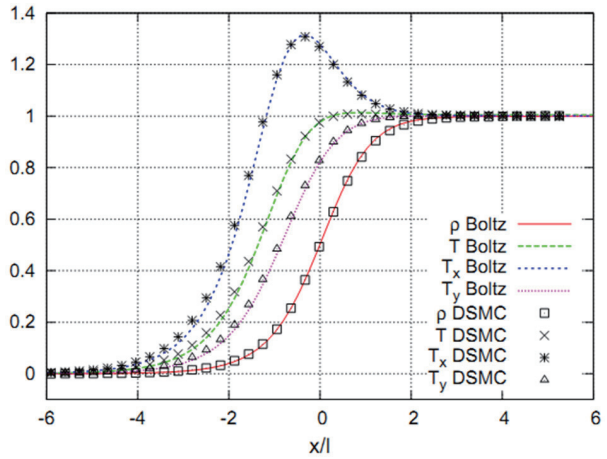


Fig. 3 Gas-dynamic quantities obtained on the basis of the deterministic solution of the Boltzmann equation and by the DSMC method for M=8.

Figure 2 shows the computed normalized profiles of gas-dynamic quantities: density, temperature, velocity, and entropy. In the shock wave front, the density monotonically increases, whereas the velocity monotonically decreases, and their product is constant because the mass flux in a steady flow is constant. The normalized temperature and entropy start to increase earlier than the density. It should be noted that the entropy inside the shock wave front has a clearly expressed maximum.

Figure 3 shows a comparison of the shock wave structure at the Mach number M=8, which was calculated by the deterministic method of the numerical solution of the Boltzmann equation and by the DSMC method. The DSMC computation was performed with SMILE software system [3]. Excellent agreement of the streamwise, transverse, and total temperature profiles obtained by both methods should be noted. It should also be mentioned that both methods predict a total temperature overshoot inside the shock, noticeable for the high Mach number case. The coincidence of the results obtained by principally different methods at the level of such fine details demonstrates that the proposed deterministic method of the numerical solution of the Boltzmann equation ensures high accuracy even at high Mach numbers, where the distribution function is rather far from the equilibrium function.

Figure 4 shows the zoomed neighborhood of the temperature peak for Mach numbers M=8 and M=4. For M=8, the overshoot is approximately 1%, and its value for M=4 is several times smaller. It should be noted that the results obtained in solving the Boltzmann equation are in excellent agreement with the DSMC predictions.

The obtained numerical results clearly demonstrate that the deterministic method ensures high acuracy even for highly nonequilibrium hypersonic flows at the level of fine features of the shock wave structure.

**Acknowledgements**

This work was supported by the Russian Government under the grant “Measures to Attract Leading Scientists to Russian Educational Institutions” (contract No. 14.Z50.31.0019), SB RAS Presidium (integration projects No. 39 and 47), and by the Russian Foundation for Basic Research (project No. 14-08-01252).

**References**

[1] V. Kolobov, R. Arslanbekov, V. Aristov, A. Frolova, S. Zabelok, *Journal of Computational Physics*, 223 (2007) 589-608.

[2] S.M. Yen, *Phys. Fluids*, 9 (1966) 1417-1418.

[3] Ivanov, M.S., Markelov, G.N., Gimelshein, S.F. *AIAA Paper 98-2669* (1998).

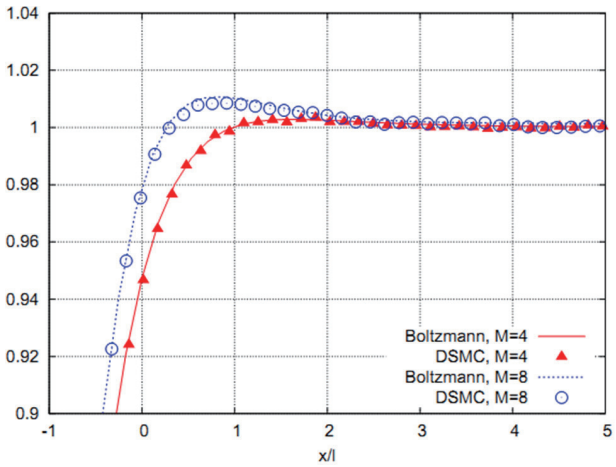


Fig. 4 Temperature obtained on the basis of the deterministic solution of the Boltzmann equation and by the DSMC method.

# Hypersonic Flow Modeling Using Parallel Direct Simulation Monte Carlo Code (PDSC$^{++}$)

Cheng-Chin Su[1], Ming-Chung Lo[1], Jong-Shinn Wu[1], Yen-Sen Chen[2]
[1]Department of Mechanical Engineering, National Chiao Tung University
1001 University Road, Hsinchu, 30010, TAIWAN
[2]National Space Organization, National Applied Research Laboratories
8F, 9 Prosperity 1st Road, Hsinchu Science Park, Hsinchu, 30078, TAIWAN

**ABSTRACT**

In this paper, a hypersonic flow modeling using parallel direct simulation Monte Carlo code (named PDSC$^{++}$) is developed and validated. The total collision energy (TCE) model [1] is implemented in PDSC$^{++}$. We consider a hypersonic flow over a cylinder w/wo the chemical reaction problem, including translational-rotational and translational-vibration energy exchange. Results show the calculations are in very close agreement with MONACO code's results [2].

## 1. Introduction

Hypersonic flow modeling has become an increasingly important research topics because of increasing suborbital or orbital space activities around the world. Detailed understanding of hypersonic aerothermodynamics (ATD), such as real-gas effects on shock-shock and shock-boundary layer interactions, micro aerothermodynamics and real-gas effects, is especially important for those reentry space vehicles and rockets with high-enthalpy flow fields because of high speed associated high total temperature. Even though there have been many ground wind tunnel experiments (e.g., HEG and LENS), it is not enough for efficiently optimizing the design of reentry vehicles. In addition, numerical modeling is considered to be the most attractive and affordable alternative in understanding these complex hypersonic ATD in detail, which would lead to a better design of the space vehicles. For studying hypersonic ATD in low-density flow, the direct simulation Monte Carlo (DSMC) method [1] has become the de facto tool for investigating complex multi-dimensional flows of rarefied hypersonic aerothermodynamics. In this paper, we would like to present our recent progress in developing a parallel DSMC cod using unstructured grid for modeling hypersonic reentry flows.

## 2. Parallel Direct Simulation Monte Carlo Code (PDSC$^{++}$)

In this study, a general-purpose parallel DSMC (PDSC$^{++}$) code based on the C++ language using a 2-D/2D-axis/3-D hybrid unstructured grid was developed and validated. Some important features of the PDSC++ include hybrid unstructured mesh, variable time-step (VTS) scheme [3], transient adaptive sub-cell (TAS) method [4], domain re-decomposition, convergence scheme, parallel computing technique, and chemical reaction based on TCE model [1]. Fig. 1 illustrates a simplified flow chart of the parallel DSMC method, including the initialization stage, particle moving, indexing, collision, and sampling. Here, the Message Passing Interface (MPI) protocol is used to synchronize and communicate among all MPI-processors. In addition, the two important functions of PDSC$^{++}$ are used through all DSMC simulations, which are VTS and TAS. Basic idea of the VTS scheme in the PDSC$^{++}$ is to enforce the flux conservation (mass, momentum and energy) of moving particles when crossing the interface between two neighboring cells. This strategy can greatly reduce both the number of iterations towards the steady state, and the required number of simulated particles for an acceptable statistical uncertainty. For the TAS method, a dynamically adaptive number of sub-cells, based on the number of simulation particles, is imposed in each cell to ensure the average collision distance is less than the local mean free path.

Corresponding author: Prof. Jong-Shinn Wu
*E-mail address*: chongsin@faculty.nctu.edu.tw


Fig. 1 Simplified flow chart of the parallel DSMC method for np processors.

## 3. Results and Discussion

The test case is a hypersonic flow over a cylinder of 2 m diameter which has been investigated numerically by Scanlon et al. [2]. PDSC$^{++}$ code is used to simulate the flow and compare with the results obtained using

MONACO [5]. Free-stream conditions for air include a Mach number of 24.85 and a temperature of 187 K. The nitrogen and oxygen number density in the free-stream region are $1.13\times10^{-20}$ and $3.031\times10^{-19}$ particles/m$^3$ respectively. The surface of the cylinder are modeled as fully diffusive walls at a temperature of 1000 K. Here, we consider the two test cases, including no chemical reaction and with chemical reaction. For all tests, the rotational and vibrational relaxation number are set as 5 and 50 respectively. In addition, the TCE model [1] is used to for chemical reactions in DSMC simulation. We consider 19 reaction channels with the 5 species as summarized in Table 1 of Ref. [2].

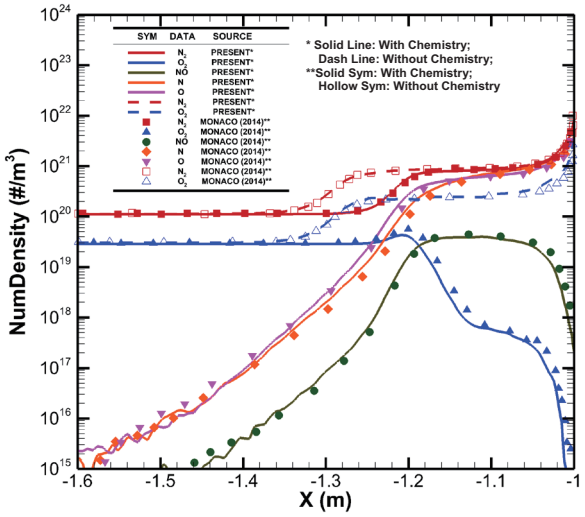


Fig. 2 Comparisons of number density profile along centerline ahead of the cylinder for non-reacting and reacting cases.

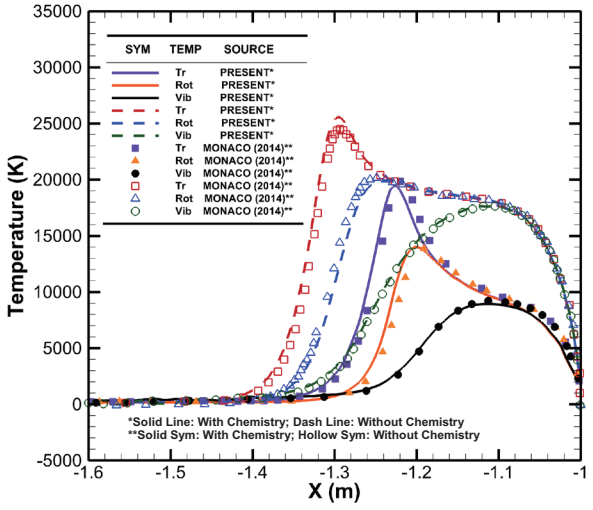


Fig. 3 Comparisons of temperature profile along center line to stagnation point ahead of the cylinder for non-reacting and reacting.

Figs. 2 and 3 show the comparison of the number density distributions of all species and temperatures along centerline ahead of the cylinder, respectively, between PDSC$^{++}$ and MONACO for both non-reacting and reacting cases. The PDSC$^{++}$ calculations are in good agreement with MONACO's results. Fig. 4 shows the comparison of pressure and heat flux along the surface of the cylinder between PDSC$^{++}$ and MONACO. The results of PDSC$^{++}$ also agree very well with those of MONACO. In addition, the heat fluxes along the surface of the cylinder in the non-reacting case is much higher than those of the reacting case, especially in stagnation point because the strongly dissociating flow greatly consumes flow enthalpy. However, the pressure distribution of both non-reacting and reacting cases are very close.

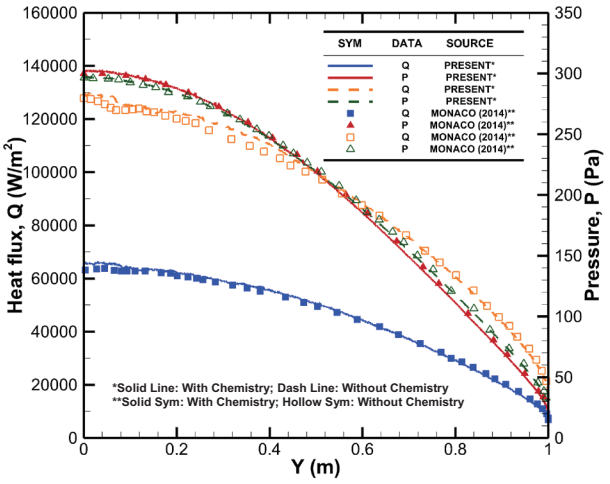


Fig. 4 Comparisons of pressure and heat transfer coefficient along the surface of the cylinder for non-reacting and reacting.

## 4. Concluding Remarks

In this paper, numerical modeling of hypersonic flows with and without chemical reactions using parallel direct simulation Monte Carlo code (PDSC$^{++}$) is developed and validated.


## Acknowledgments

Financial support of Minister of Science and Technology through Grant No. 102-2627-E-009-001 computing resources provided by National Center for High-Performance Computing (NCHC) of Taiwan is highly appreciated.


## References


[1] G.A. Bird, *Molecular Gas Dynamics and the Direct Simulation of Gas Flows*, Clarendon Press, Oxford, 1994.

[2] T.J. Scanlon1, C. White1, M.K. Borg, R.C. Palharini, E. Farbar, I.D. Boyd, J.M. Reese, R.E. Brown, *AIAA Journal* (2014), http://strathprints.strath.ac.uk/46619

[3] J.-S. Wu, K.-C. Tseng and F.-Y. Wu, *Comput. Phys. Comm.*, 162 (2004) 166-187.

[4] C.-C. Su, K.-C. Tseng, H.M. Cave, J.-S. Wu, Y.-Y. Lain, T.-C. Kuo and M.C. Jermy, *Comput. Fluids*, 39 (2010) 1136-1145.

[5] S. Dietrich, I.D. Boyd, *J. Comput. Phys.*, 126 (1996) 328-342.

# A Study of Micro/Nanoscale Gas Lubrication Based on Molecular Gas Dynamics

Shigeru Yonemura[1], Vladimir Saveliev[2], Masashi Yamaguchi[3], Susumu Isono[3], Yoshiaki Kawagoe[3], Takanori Takeno[3], Hiroyuki Miki[4], Toshiyuki Takagi[1]
[1]Institute of Fluid Science, Tohoku University
2-1-1 Katahira, Aoba-ku, Sendai 980-8577, Japan
[2]Institute of Ionosphere, NCSRT
Kamenskoe Plato, Almaty, 050020, Kazakhstan
[3]Graduate School of Engineering, Tohoku University
6-6-01 Aoba, Aramaki, Aoba-ku, Sendai 980-8579, Japan
[4]Frontier Research Institute for Interdisciplinary Sciences, Tohoku University
6-3 Aoba, Aramaki, Aoba-ku, Sendai 980-8578, Japan

**ABSTRACT**

It has been reported that laser textured surfaces have good tribological performance in the case of gas lubrication as well as the case of liquid lubrication. High gas pressure generation due to a micro/nanoscale surface structure in the case of liquid lubrication has been explained by considering formation of cavities in a liquid. But, cavities are not formed in the case of gas lubrication. In the present work, the mechanism of high gas pressure generation is clarified by the performance of numerical simulations and by theoretical analysis.

## 1. Introduction

Many studies on surface texturing have achieved improvements in tribological performance of sliding surfaces. Surface texturing is expected to act three roles. The first is a microhydrodynamic bearing by generating hydrodynamic pressure, the second is a micro reservoir for a lubricant, and the third is a micro trap for wear debris. In this work, the focus is only on the first role of surface texturing as a microhydrodynamic bearing.

In most studies of microhydrodynamic bearings, liquid is used as a lubricant. In cases where one surface moves relative to the other surface, the lubricant is drawn by the moving surface. The pressure becomes high over the region where the clearance converges and becomes low over the region where the clearance diverges. However, the pressure over the diverging region cannot be lower than the pressure at which cavities are formed in the liquid. Therefore, the pressure rise over the converging region is greater than the pressure drop over the diverging region, and then the pressure averaged over the whole surface becomes higher than the ambient pressure [1,2].

As well as liquid lubrication, gas lubrication has also been studied. Kligerman and Etsion performed numerical simulations of gas lubrication for the case where two non-contacting cylindrical surfaces with micro dimples rotate relative to each other [3]. They investigated the optimal conditions to improve sealing performance by changing the values of parameters, e.g., seal clearance, dimple area density, and dimple aspect ratio. Other parametric analyses have been conduced to investigate optimal conditions of gas lubrication with surface texturing [4,5]. However, a clear understanding of the mechanism that induces high gas pressure over a textured surface would help us to design the optimal configuration of the surface texture without trial and errors.

Corresponding author: Shigeru Yonemura
*E-mail address*: yonemura@ifs.tohoku.ac.jp

In the present work, in order to understand these phenomena clearly, we clarify the mechanism of high gas pressure generation induced by the micro surface structure theoretically with the assistance of numerical simulations.

## 2. Method

A micro/nanoscale gas flow treated here is in nonequilibrium due to a lack of intermolecular collisions and is governed not by the Navier-Stokes equations, but by the Boltzmann equation. Fukui and Kaneko derived the molecular gas film lubrication (MGL) equation [6] on the basis of the linearized Bhatnagar-Gross-Krook (BGK) model for the Boltzmann equation. On the other hand, the DSMC method [7] has been developed to analyze high Knudsen number flows like rarefied gas flows on the basis of the Boltzmann equation. Both the MGL equation and the DSMC method are herein used to analyze micro/nanoscale gas flows between two sliding surfaces.

A surface with an isosceles triangular dimple pattern shown in Fig. 1 is considered in the present work. This microscale dimple pattern is repeated periodically in the $x$ direction. The two-dimensional flow between the upper surface with dimples and the lower counter surface is analyzed by using the DSMC method and the MGL equation separately. The periodic boundary condition is applied for the inlet and the outlet of the computational domain in the $x$ direction. The lengths of the dimple region and the flat region of the upper surface are represented by $l_{\mathrm{d}}$ and $l_{\mathrm{f}}$, respectively. The total length $l_{\mathrm{T}}$ of the computational domain is given by $l_{\mathrm{T}} = l_{\mathrm{d}} + l_{\mathrm{f}}$. Dimple depth is denoted by $d$. The flat region of the upper surface is set to be parallel to the counter surface. The clearance between the two surfaces is denoted by $h$ and is set at its minimum value $h_0$ in the flat region. The counter surface moves at speed $U$ in the $x$ direction. The wall temperature is set at room temperature, $T_0 = 300\,\mathrm{K}$. The gas treated here is air. At the initial condition for DSMC simulations, the

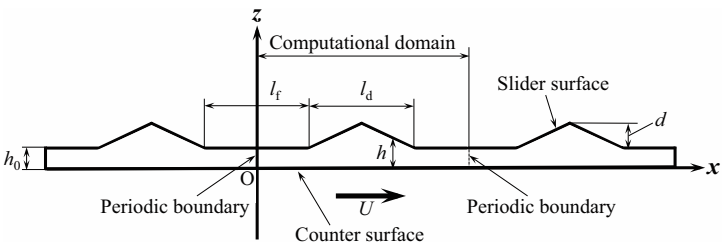


Fig. 1 Computational domain.

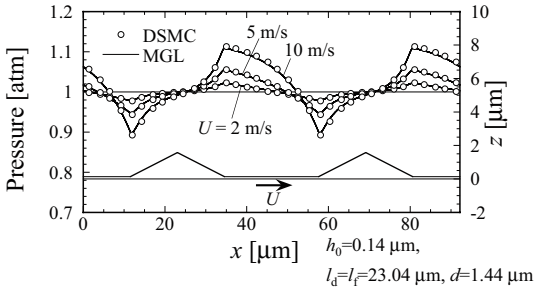


Fig. 3 Pressure distributions.

computational domain is filled with air molecules whose pressure and temperature are atmospheric pressure, $p_a = 1\,\mathrm{atm} = 101325\,\mathrm{Pa}$, and the room temperature, $T_0$, respectively. In the present work, we consider only the steady gas flow between sliding surfaces. Therefore, the clearance $h_0$ is fixed during the execution of each DSMC simulation.

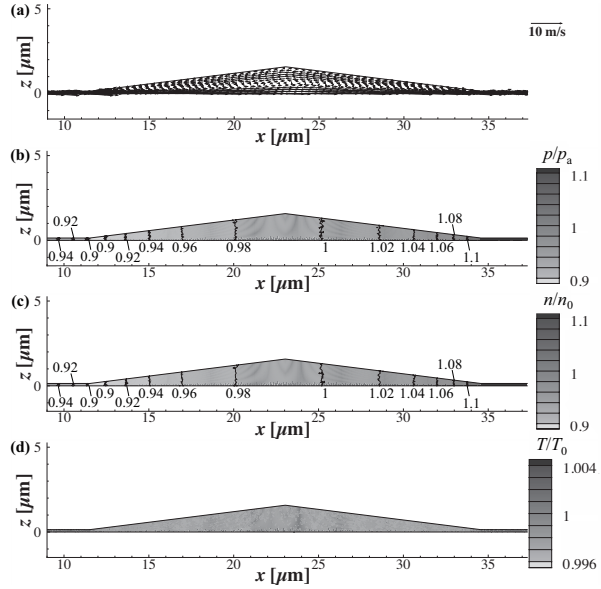


Fig. 2 Distributions of (a) gas velocity, (b) gas pressure, (c) molecular number density, and (d) gas temperature obtained in the DSMC simulation. ($l_d = l_f = 23.04\,\mu\mathrm{m}$, $d = 1.44\,\mu\mathrm{m}$, $U = 10\,\mathrm{m/s}$, $h_0 = 0.14\,\mu\mathrm{m}$).

## 3. Results and Discussion

Figure 2 shows typical distributions of the gas flow velocity, the gas pressure $p$, the molecular number density $n$, and the gas temperature $T$ obtained in the DSMC simulation for the case of $l_d = l_f = 23.04\,\mu\mathrm{m}$, $d = 1.44\,\mu\mathrm{m}$, $U = 10\,\mathrm{m/s}$, and $h_0 = 0.14\,\mu\mathrm{m}$, respectively. The rightward gas flow is induced by the rightward motion of the lower counter surface. However, the major portion of the gas flow induced in the dimple region cannot pass through the narrow channel in the flat region and is repelled at the converging part of the dimple. Therefore, a vortical flow appears in the dimple. Since some portion of gas flow can pass through the channel, the net gas flow at any $x$ is rightward. The gas pressure drops at the left edge of the dimple and rises at the right edge of the dimple, i.e., the gas pressure increases in the $x$ direction over the dimple region. The gas temperature is uniform because the gas flow channel is very narrow and surrounded by isothermal solid surfaces. Because of uniform temperature, the molecular number density distribution becomes similar to the gas pressure distribution, as shown in Fig. 2.

Figure 3 shows the distribution of the gas pressure exerted on the bottom surface of the slider for various sliding speeds $U$ under the condition of $l_d = l_f = 23.04\,\mu\mathrm{m}$, $d = 1.44\,\mu\mathrm{m}$, and $h_0 = 0.14\,\mu\mathrm{m}$. The line figure in the lower half of Fig. 3 shows the shape of the lubricated region. The arrow pointing right indicates the direction of the motion of the lower counter surface with speed $U$. Note that the shape of the lubricated region is enlarged in the $z$ direction.

## 4. Conclusion

It is found that the following two features of a pressure distribution play a key role in obtaining high average gas pressure.

(1) In the dimple region, gas pressure should increase in the direction of the counter surface's motion. This increase of gas pressure is induced by the presence of the dimple.
(2) The pressure distribution over the flat region should be convex upward. The combination of a gentler gradient at the inlet of the flat region and a steeper gradient at the outlet of the flat region is more beneficial for increasing the gas pressure averaged over the flat region.

The causes of these features are discussed at ICFD 2014. Readers can refer to Ref. 8 for more detail.

## References

[1] D. B. Hamilton et al., J. *Basic Eng. Trans. ASME*, 88 (1966) 177-185.
[2] X. Wang et al., *Tribol. Int.*, 36 (2003) 189-197.
[3] Y. Kligerman, I. Etsion, *Tribol. Trans.*, 44 (2001) 472-478.
[4] B. Raeymaekers et al., *Tribol. Lett.,* 28 (2007) 9-17.
[5] A. N. Murthy, I. Etsion, F. E. Talke, *Tribol. Lett.*, 28 (2007) 251-261.
[6] S. Fukui, R. Kaneko, J. Tribol. Trans. ASME, 110 (1988) 253-261.
[7] G. A. Bird, *Molecular Gas Dynamics and the Direct Simulation of Gas Flows,* Oxford University Press, New York (1994).
[8] S. Yonemura et al., *Tribol. Lett.,* (2014). doi:10.1007/s11249-014-0368-2

# The Study of Pressure Distribution in Microchannel Flow for Gas-MEMS Applications

Jia-Syuan Lee[1], Shaw-An Wan[1], Fang-Hsing Chou[1], Hsiang-Yu Wang[2], Chih-Yung Huang[1]*
[1] Department of Power Mechanical Engineering, National Tsing Hua University
Kuang-Fu Road, Hsinchu, 30013, Taiwan R.O.C.
[2] Department of Chemical Engineering, National Cheng Kung University
University Road, Tainan City, 701, Taiwan R.O.C.

**ABSTRACT**

This paper presents the investigation of pressure distribution in microchannel flow by applying pressure-sensitive paint technique. For gas-MEMS, the fluid becomes compressible as inlet/ outlet pressure ratio increases because of the small length scale. However, continuum model is not applicable and rarefaction effect dominates for large Knudsen number flow, resulting in the more linear pressure curve which is similar to the incompressible flow.

## 1. Introduction

Pressure-sensitive paint (PSP) technique has been developed since 1980s, which uses luminescence molecules to measure surface pressure distribution based on oxygen quenching mechanism [1]. In the past decades, PSP technique was commonly applied to macroscale measurements to obtain the surface pressure field of aerial vehicles and automobiles [2]. This technique depends on photo-chemical reaction of luminescence molecules as pressure sensors on the surface and it can provide global and high-resolution pressure distribution. PSP technique is applicable to microscale flow field measurements with its sub-micro size luminescence molecules. It has been used in MEMS research in 2002 and the interaction between compressibility effect and rarefaction effect for nonlinear pressure distribution has been found [3, 4]. In 2009, the feasibility of PSP technique for measurement in high Knudsen number flow in microchannels was discussed [5]. Considering the quenching capability of luminophore and oxygen permeability of binder, various PSP formulas were examined to find the preferable one for high Knudsen number flow field measurement, combined with nitride oxide-laser induced fluorescence (NO-LIF) technique to get global pressure distribution and the structure of flow field [6]. This study provides pressure maps to have a comprehensive discussion of compressibility effect and rarefaction effect in straight microchannels.

## 2. Method

For the investigation of pressure distribution inside the straight microchannels, various PSP sensors including pressure probes and binders were tested. Pt(II)meso–Tetra (Pentafluorophenyl) Porphine (PtTFPP)/PDMS was selected owing to its high sensitivity and more linear calibration curve within 1 kPa to 101 kPa pressure range compared to others. The rectangular straight PDMS microchannel with two reservoirs was fabricated by soft lithography. It is 0.5 cm long, 50 μm wide and 45 μm deep with a rectangular cross section.

Fig. 1 shows the schematic of PSP experimental setup. For improving spatial resolution, a 16 bit CCD camera was integrated with a microscopy system to capture fluorescence signal and an UV-LED was used as the excitation light source.

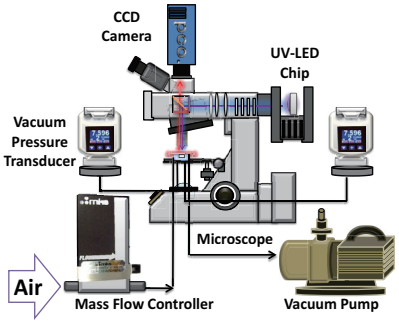


Fig. 1 Schematic of experimental setup

## 3. Results and Discussion

The PSP technique has been carried out to provide the 2-D pressure map inside the microchannel, as shown in Fig. 2. The pressure gradually decreases from channel inlet to the exit and almost uniform in the lateral direction. For the study of compressibility effect, the inlet pressure is controlled and the Knudsen number is fixed to isolate rarefaction effect. Experimental conditions are listed in Table 1. When the inlet/outlet pressure ratio in microchannel flow increases, the pressure and density in the flow field will change significantly. The fluid accelerates to resist wall friction while passing the channel and the fluid density is not constant. The dimensionless pressure deviation between incompressible flow and compressible flow are plotted in Fig.3. It can be noticed that if the Knudsen number is small (<0.001), the fluid remains continuum and compressibility effect dominates the flow field. It is noticed that the higher the pressure ratio, the larger the nonlinearity of pressure distribution. For the study of rarefaction effect, experimental conditions are listed in Table 2. If the characteristic length and mean free path of molecules reach the same order, the fluid becomes rarefied. From case R50-6 to R50-11, the outlet Knudsen number increases from 0.007 to 0.140, resulting in the decrease of dimensionless deviation, as shown in Fig. 4. It can be seen that at the location x/L =

Corresponding author: Chih-Yung Huang
*E-mail address*: cyhuang@pme.nthu.edu.tw

0.4~0.8 of the microchannel, the difference between pressure curve and linear profile almost remains the same. Furthermore, the pressure distribution becomes more linear as Knudsen number increases, and the flow regime now is approaching to incompressible and no-slip flow field.

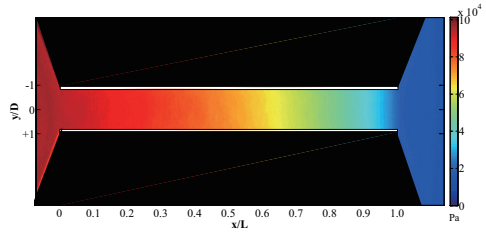


Fig. 2 The pressure map inside the microchannel for pressure ratio of 4.6.

| | C2-1 | C2-2 | C2-3 | C2-4 | C2-5 |
|---|---|---|---|---|---|
| Flow rate(sccm) | 13.5 | 22.5 | 26 | 28.5 | 30 |
| PSP inlet(kPa) | 101.3 | 96.6 | 96.3 | 96.1 | 93.8 |
| PSP outlet(kPa) | 79.1 | 54.4 | 44.9 | 35.4 | 20.5 |
| Pressure ratio | 1.3 | 1.8 | 2.2 | 2.7 | 4.6 |
| Mas flow rate Analytic (kg/s) | 2.75e-07 | 4.37e-07 | 4.98e-07 | 5.48e-07 | 5.8e-07 |
| Kn(inlet) | 0.001 | 0.001 | 0.001 | 0.001 | 0.001 |
| Kn(outlet) | 0.001 | 0.002 | 0.002 | 0.003 | 0.005 |
| Re | 2.10e+02 | 3.34e+02 | 3.80e+02 | 4.18e+02 | 4.40e+02 |

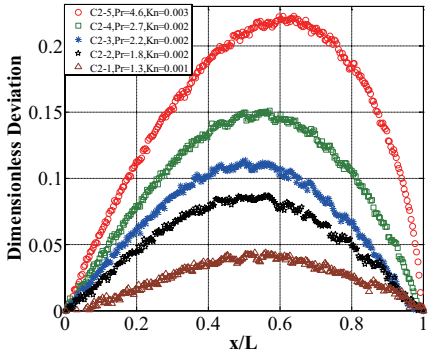


Fig. 3 The pressure deviation inside the microchannel due to compressibility effect.

Table 2 Experimental conditions in pressure measurement for discussion of rarefaction.

| | R50-6 | R50-7 | R50-8 | R50-9 | R50-10 | R50-11 |
|---|---|---|---|---|---|---|
| Flow rate(sccm) | 7.5 | 6 | 5.5 | 4 | 3.5 | 0.9 |
| PSP inlet(kPa) | 56.5 | 46.7 | 41.3 | 29.4 | 24.0 | 4.8 |
| PSP outlet(kPa) | 20.8 | 17.5 | 16.0 | 10.7 | 8.2 | 1.2 |
| Pressure ratio | 2.7 | 2.7 | 2.6 | 2.8 | 2.9 | 4 |
| Mas flow rate Analytic (kg/s) | 8.7e-08 | 6.0e-08 | 4.6e-08 | 2.4e-08 | 1.7e-08 | 8.4e-10 |
| Kn(inlet) | 0.003 | 0.003 | 0.004 | 0.005 | 0.006 | 0.034 |
| Kn(outlet) | 0.007 | 0.008 | 0.009 | 0.014 | 0.018 | 0.140 |
| Re | 8.49e+01 | 5.81e+01 | 4.49e+01 | 2.36e+01 | 1.63e+01 | 8.21e-01 |

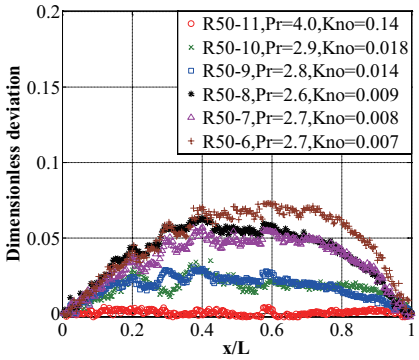


Fig. 4 The pressure deviation inside the microchannel for rarefaction effect.

## 4. Concluding Remarks

In this study, the investigation of internal pressure distribution under different inlet/outlet pressure ratios and Knudsen number conditions was successfully conducted by PSP technique. The flow becomes compressible due to the increase of pressure ratio inside the microchannel. As the flow rate and pressure keep decreasing, the increase of Knudsen number leads to the slip flow, and the rarefaction effect dominates the flow field. Accordingly, these two effects are against each other in microchannel flow, and the results from this study can be further employed to the gas-MEMS applications.

## References


[1] J. I. Peterson and R. V. Fitzgerald, "New technique of surface flow visualization based on oxygen quenching of fluorescence," *Review of Scientific Instruments*, 51 (1980) 670-671.

[2] M. Gouterman, "Oxygen quenching of luminescence of pressure sensitive paint for wind tunnel research," *Journal of Chemical Education*, vol. 74, (1997) 697.

[3] C.-Y. Huang, H. Sakaue, J. W. Gregory, and J. P. Sullivan, "Molecular sensors for MEMS," in *40th Aerospace Sciences Meeting & Exhibit*, (2002) 2002-256.

[4] X. Guo, C. Huang, A. Alexeenko, and J. Sullivan, "Numerical and experimental study of gas flows in 2D and 3D microchannels," *Journal of Micromechanics and Microengineering*, 18 (2008) 025034.

[5] Y. Matsuda, H. Mori, Y. Sakazaki, T. Uchida, S. Suzuki, H. Yamaguchi, and T. Niimi, "Extension and characterization of pressure-sensitive molecular film," *Journal of Experiments in Fluids*, 47 (2009) 1025-1032.

[6] H. Mori, T. Niimi, M. Hirako, and H. Uenishi, "Pressure sensitive paint suitable to high Knudsen number regime," *Measurement Science and Technology*, 17 (2006) 1242.

# The Development of Simultaneous Measurements of Velocity and Temperature in Microchannel Flow

Ying-Nuan Chen[1], Huan-Chieh Chen[1], Yu-Ting Chen[1], Tong-Miin Liou[1] and Chih-Yung Huang[1]*
[1]Department of Power Mechanical Engineering, National Tsing Hua University
Kuang-Fu Road, Hsinchu, 30013, Taiwan R.O.C.

**ABSTRACT**

This study aims to develop simultaneous measurements of velocity and temperature profiles in microchannel flow. Velocity and temperature measurements were successfully obtained by combining techniques of μ-Particle Image Velocimetry and lifetime-based Temperature-Sensitive Paint. The spatial resolution in the acquired experimental result was 5.3 μm/pixel and the temperature sensitivity was about -3 μs/℃.

## 1. Introduction

Simultaneous measurement of velocity and temperature has been important to reduce the experimental error while analyzing the heat transfer effect in thermally and hydrodynamically developing flow. The development of simultaneous measurements has been carried out using Digital Particle Image Velocimetry/Thermometry (DPIV/T) based on the foundation of thermotropic liquid crystal by Park et al. [1] and Praisner et al. [2]. In 1949, Pringsheim had presented that the decay time of fluorescent molecule is affected by temperature and sensor concentration, and the relation between temperature and decay time could be used to retrieve the temperature information [3]. Hu et al. successfully measured velocity and temperature variations of flow field behind a heated cylinder by combining Molecular Tagging Velocimetry (MTV) with Molecular Tagging Thermometry (MTT) [4]. Omrane et al. selected phosphorescence particles as the tracer particles of velocity and temperature using two lasers and two cameras [5]. Someya et al. prepared ceramic spheres covered with EuTTA as the tracer particles and used lifetime-based Temperature Sensitive Paint (TSP) and PIV to achieve simultaneous measurements with only one CCD camera [6]. The aim of this research is to obtain the whole field of velocity and temperature in microchannel flow by combining μ-PIV and lifetime-based TSP techniques.

## 2. Method

To facilitate simultaneous measurements of velocity and temperature profiles in microchannel flow, a silicon wafer was used as the mold for fabricating a polydimethylsiloxane (PDMS) microchannel using standard soft-lithography process. The microchannel is 10000 μm long, 385 μm wide, and 91 μm deep. Two reservoirs were located at the inlet and the outlet of the channel. The reservoir at the inlet was connected to a cold water bath in which the temperature maintained below 5℃ during the experiment. The channel outlet was connected to a syringe pump using a Teflon tube. The working fluid was drawn from the water bath and driven into the microchannel by the syringe pump. The microchannel device was heated by a heater through a slice of copper which was attached to the bottom of channel. Because of this design of microchannel and the low conductivity of PDMS, the side walls were considered as adiabatic in the experiment. To achieve simultaneous measurements of temperature and velocity, EuTTA was dissolved into ethanol to serve as the temperature-sensitive solution, and red fluorescent particles were added into the solution as the tracers. Two excitation sources, a green laser and UV LED arrays with different wave lengths, were used to excite red fluorescent particles and EuTTA separately because of their different excitation spectrum. A CCD camera is used to collect the fluorescence emitted from EuTTA and tracers. A 550 nm high pass filter was installed in front of CCD camera to remove the noise from environmental lights. Before measuring the temperature field, in-situ calibration was performed to acquire the relation between the temperature and the decay time. A schematic of experimental setup is shown in Fig. 1.

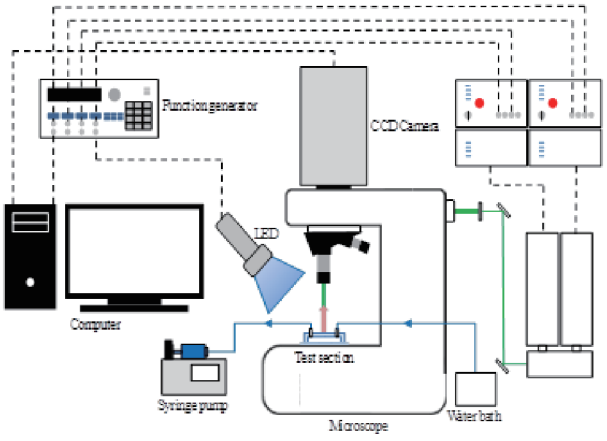


Fig. 1 Schematic of experimental setup

## 3. Results and Discussion

In the experiment, the Reynolds number was controlled as 15 and the temperature was 50℃ at the bottom of channel served as constant wall temperature condition. Fig. 2a and 2b are the raw images acquired at

Corresponding author: Chih-Yung Huang
*E-mail address*: cyhuang@pme.nthu.edu.tw

two gates in the lifetime decay of fluorescence and the region was focused at 2 mm downstream after the channel entrance. An image processing using average of 20 images has been carried to remove the fluorescence from tracers. The fluorescence decay from images recorded at two gates can be further translated to temperature distribution inside the microchannel, as shown in Fig. 3a and 3b. The movement of tracers in the microchannel flow is also calculated to obtain the velocity profile using commercial ED-PIV software. Due to the effect of the depth of correlation (DOC), the velocity distribution in the microchannel flow is the average through the depth. Figure 4 presents the velocity profile obtained in the experiment, and compared with theoretical analysis. In this study, the temperature sensitivity ranged from -2.7 to -3.2 μs/℃ and the spatial resolution was 5.3 μm/pixel.

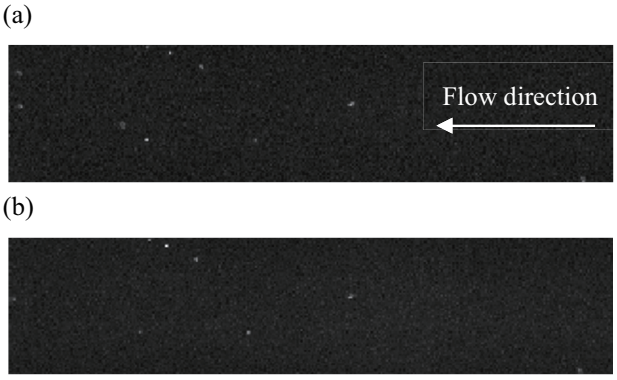


Fig. 2 (a) Raw image of first exposure in the lifetime decay (b) Raw image of second exposure.

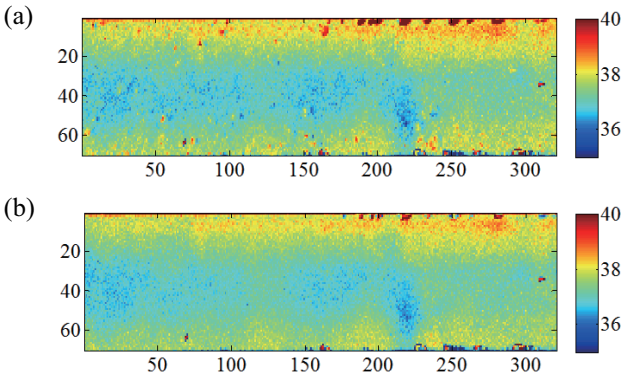


Fig. 3 (a) Temperature contour without image processing (b) Temperature contour with image processing

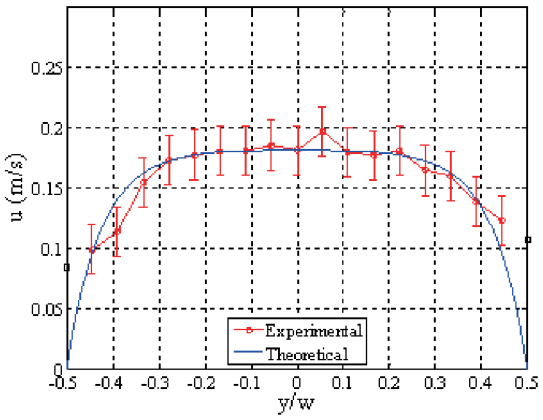


Fig. 4 Velocity profile inside the microchannel flow

## 4. Concluding remarks

In present study, simultaneous measurements in microchannel flow were successfully developed, and the spatial resolution in the experimental result was 5.3 μm/pixel. The velocity profile in the microchannel flow was successfully measured by μ-PIV and it agrees with the theoretical result. Temperature contour was measured by lifetime-based TSP, and the temperature sensitivity was about -3 μs/℃.


## Acknowledgements

This work is funded by the National Science Council of Taiwan via NSC 102-2311-B-006 -003 -MY3.


## References


[1] H. G. Park, D. Dabiri and M. Gharib, "Digital particle image velocimetry themometry and application to the wake of a heated circular cylinder," *Experiments in Fluids*, 30 (2001) 327-338.

[2] T. J. Praisner, D. R. Sabatino and C. R. Smith, "Simultaneously combined liquid crystal suface heat transfer and PIV flow-field measurement," *Experiments in Fluids*, 30 (2001) 1-10.

[3] P. Pringsheim, *Fluorescence and phosphorescence* : New York, Interscience, (1949).

[4] H. Hu and M. M. Koochesfahani, "Molecular tagging velocimetry and thermometry and its application to the wake of a heated circular cylinder," *Measurement Science and Technology*, 17 (2006) 1269-1281.

[5] A. Omrane, P. Petersson, M. Aldén and M. A. linne, "Simultaneous 2D flow velocity and gas temperature measurements using thermographic phosphors," *Applied Physics B*, 92 (2008) 99-102.

[6] S. Someya, S. Yoshida, Y. Li and K. Okamoto, "Combined measurement of velocity and temperature distributions in oil based on the luminescent lifetimes of seeded particles," *Measurement Science and Technology*, 20 (2009) 025403.

# Numerical Analysis of Microchannel Deformation Possibilities during Thermal Bonding

Ba Te[1], Yu Hao[2], Kang Chang-Wei[1], Tor Shu Beng[2]
[1] Institute of High Performance Computing, Agency for Science, Technology and Research
1 Fusionopolis Way, #16-16 Connexis, Singapore 138632
[2] School of Mechanical and Aerospace Engineering, Nanyang Technological University
50 Nanyang Avenue, Singapore 639798

**ABSTRACT**

In the present work, Thermal Stress Evolution model in Flow3D is coupled with other physics to simulate the filling, solidification and cooling during micro injection moulding. The effect of shear rate and temperature on the fluid viscosity has been included. The coupled FEA analysis revealed the region with high residual thermal stress where is the problematic location suffering deformation during the thermal bonding. The higher possibility of the deformation of horizontal channel comparing with transverse counterpart also could be predicted.

## 1. Introduction

Micro injection molding (μIM) has been widely used as the manufacturing technology to produce microfluidic devices from thermoplastics. Undesirable stresses such as flow-induced and thermal induced residual stresses may be created in the production process[1]. These residual stresses are a principal cause of the deformation of microchannels during direct thermal bonding, due to the bulk material reflow and warpage upon reheating above $T_g$[2]. The assessment of the local residual stress developed in the injection molding will help to control the fabrication process and mitigate the potential negative effects. Yu et al. [3]evaluated the microchannel irregularities as an indicator of the residual stresses and use design of experiment (DOE) analysis to address the molding parameters to be optimized. In the current paper, a coupled fluid dynamics and finite element analysis in Flow3D® is used to evaluate the local thermal-induced stresses in hardened (solidified) polymer components.

## 2. Method

Fluid flow and solid mechanics are computed at the same time and in the same domain. The fluid governing equations are computed on the rectangular Cartesian mesh while the solid stresses and deformations are calculated on a body-fitted FE mesh.

The microchannels of the device is fabricated to present two orientations: horizontal and transverse. It is achieved by installing the embossed micromixer BMG mold in the injection mold in two different orientations. Correspondingly two simplified cases were proposed to investigate the effect of the melt injection direction on the residual stress distribution, as shown in Fig.1. The mold dimension is 75×25×2mm and the mixer size is12×0.2×0.2mm. Due to the small size of the mixer in two dimensions, the resolution of the mesh is much finer in the mixer region , which is shown in Fig. 2.

The simulation consisted of two stages: the filling stage, which solves the Navier-Stokes equations only since the filling is so fast that the thermal stress is gnored; and the solidification stage, which also includes

Corresponding author: Ba Te
*E-mail address*: bat@ihpc.a-star.edu.sg

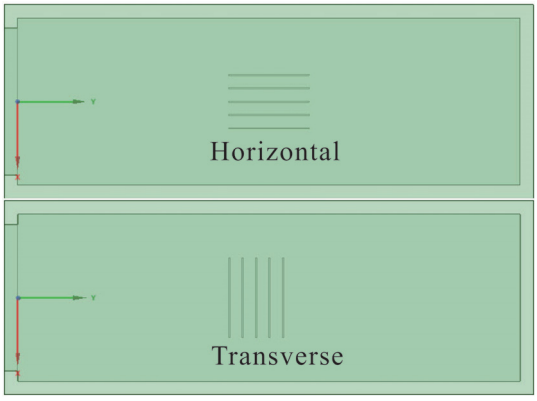


Fig. 1 Plane view of the mold with the micromixer BMG in two orientations.

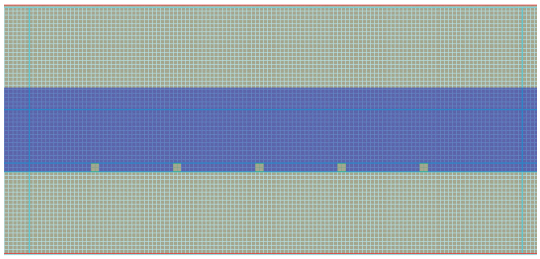

Fig. 2 The mesh grids in the mixer BMG region, which is finer than in the other regions.

the finite element analysis in the solidified fluid. Four cases are simulated for the two stages in the two alignment directions. The material injection flow rate is 1.9 L/min and the temperature is 270°C. The stainless steel mold initial temperature is 85°C.

The fluid is modeled as laminar flow and the molten PMMA polymer is considered as non-newtonian fluid which has shear-rate and temperature dependent viscosity.

The equations of momentum are the Navier-Stokes equations with some additional terms. For simplicity, the equation along *x* direction is as follow:

$$\frac{\partial u}{\partial t}+\frac{1}{V_F}\left(uA_x\frac{\partial u}{\partial x}+vA_yR\frac{\partial u}{\partial y}+wA_z\frac{\partial u}{\partial z}\right)-\varphi\frac{A_y v^2}{xV_F}=$$

$$-\frac{1}{\rho}\frac{\partial p}{\partial x} + f_x \quad (1)$$

where $f_x$ is the viscous accelerations, τ the viscous stress and the terms (*wsx*, *wsy*, *wsz*) are wall shear stresses.

The TSE model solves the standard equation of motion in the solidified fluid

$$\rho\frac{d^2x}{dt^2} = \nabla\cdot\sigma + \rho b \quad (2)$$

where ρ is the density of the solidified fluid, σ Cauchy stress tensor and *b* the body force vector.

.

## 3. Results and Discussion

The flow shear stress in the filling stage (0.117s) for the case with mixer in the transverse orientation is shown in Fig.3. The maximum value is 614465, which is very close to the value of 653688 for the case in the horizontal orientation. This flow-induced stress will be frozen in the solidified polymer but this value is very small comparing with the thermal stress induced in the solidification stage.

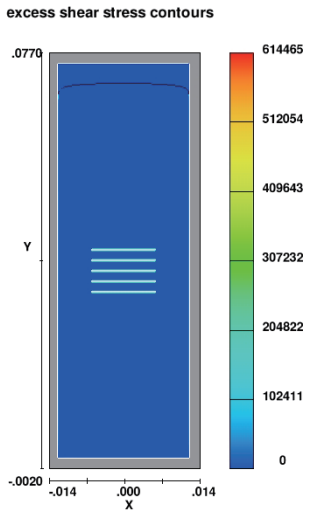


Fig. 3 Flow-induced stress at 0.117s for the case with the mixer in the transverse direction.

The Von Mises stress distribution in the vertical plane which cuts through the mixers perpendicularly is shown in Fig. 4, for the case with mixer aligned with the injection direction. High stress has been found near the mixer tips, which correspond to the microchannel bottom of the device. These region with high residual stress tend to deform during thermal bonding, which could be seen from the experimental observations as in Fig.5.

The stress contour in the horizontal plane close to mixer tips are shown in Fig. 6. The case with mixer in the transverse direction shows a much higher value, which may explains the problem that the produced corresponding device suffers a larger deformation.

## 4. Concluding Remarks

The coupled fluid dynamics and finite element analysis not only predicts the flow-induced stress but also the thermal stress during the solidification of the polymer. It predicts the mixer tip regions suffer the deformation problem, especially for the region with micromixer aligned in the transverse orientation.

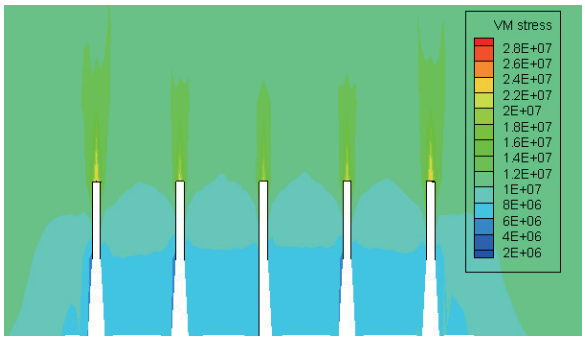


Fig. 4 Von Mises stress contour in the vertical (yz-) plane. High stress regions are around the mixer tips.

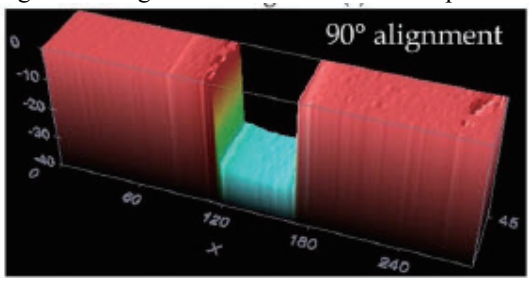


Fig. 5 The deformation of the microchannel after thermal bonding for the case with mixer in the transverse direction.

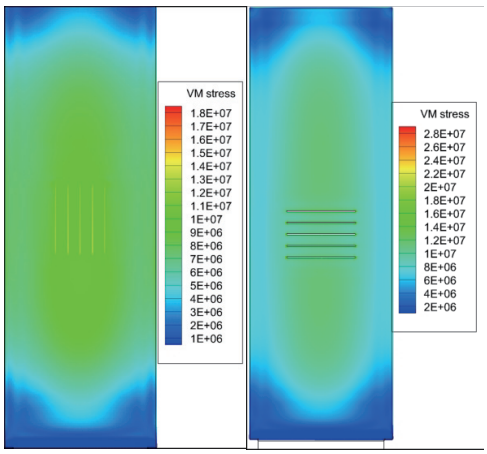


(a) Horizontal (b) Transverse

Fig. 6 Von Mises stress contour in the horizontal (xy-) plane. Higher value of thermal stress can be observed for the case with mixer in the transverse direction.

## References


[1] A.I. Isayev, G.D. Shyu, C.T. Li, *J. Polym. Sci. B Polym. Phys.* , 44 (2006), 622.

[2] D. Yao, S.-C. Chen, B.H. Kim, *Adv. Polym. Technol.* , 27 (2008), 233.

[3] H. Yu, S.B. Tor, N.H. Loh, A.K. *Asundi, J. Micromech. Microeng.* , 24 (2013), 015012.

Eleventh International Conference on Flow Dynamics
October 8-10, 2014, Sendai, Miyagi, Japan

# Experimental Study on AA-PSP Response to Change in High-Frequency Pressure Oscillation Using Cavity Flows

Koichiro Yamabe[1], Taro Handa[1], Keisuke Katsuta[1], Hirotaka Sakaue[2]
[1]Kyushu University
6-1 Kasuga-Koen, Kasuga City, Fukuoka, 816-8580, Japan
[2]Japan Aerospace and Exploration Agency
7-44-1 Jindaijihigashi-Machi, Chofu City, Tokyo, 182-8522, Japan

**ABSTRACT**

The response of anodized aluminum pressure sensitive paint (AA-PSP) to a periodic change in pressure is investigated. The periodic change is produced by mounting a rectangular cavity on the wall of the duct in which air flows at a Mach number of ~0.7. The pressure oscillation frequency is ranged between ~3 kHz and ~20 kHz by changing the length and depth of the cavity. The experimental results reveal that the attenuation in pressure oscillation amplitude becomes remarkable with increase in frequency and that the phase lag attains a maximum at a certain frequency.

## 1. Introduction

Pressure sensitive paint (PSP) has become a powerful tool for the surface pressure measurements in wind tunnel testing. This approach uses the luminescent molecules that emit luminescence whose intensity increases with decrease in the partial pressure of oxygen. By using PSP, we can measure the surface pressure with a high spatial resolution in wind tunnel testing.

In recent years, our attention is being paid to unsteady flows in which pressure oscillates at frequencies higher than ~10 kHz [1]. In order to apply the PSP technique to such unsteady flows, the frequency characteristics of PSP should be clarified for pressure oscillation frequencies higher than ~10 kHz. There are a few studies about the PSP response to a periodic change in pressure [2, 3]. However, as far as we know, there are no data of PSP frequency characteristics for pressure oscillation frequencies higher than ~10 kHz.

In the present study, the PSP response to a periodic change in pressure is investigated for the purpose of applying a PSP to the flows in which pressure oscillates at frequencies higher than ~10 kHz. The periodic change in pressure is provided by mounting a rectangular cavity on the duct in which air flows at a Mach number of ~0.7. Anodized aluminum pressure sensitive paint (AA-PSP) [4] is selected as a tested PSP because this PSP is expected to have a characteristic response time to resolve the pressure that oscillates at frequencies higher than ~10 kHz.

## 2. PSP Coating

The response of anodized aluminum pressure sensitive paint (AA-PSP) is investigated in the present study. The anodized aluminum is made by the same method as that of Sakaue and Sullivan [4]. An aluminum plate whose thickness is 0.3 mm is anodized in dilute sulfuric acid (1 mol/L) at a constant current of 0.10 A and at constant temperature of 5 °C. The applied voltage is 24 ± 0.7 V. The coting thickness is measured by the eddy-current thickness gage. As a result, the coting thickness is found to be 21.5 μm. Luminescent molecules of $H_2$TCPP are absorbed onto the anodized aluminum plate by dipping it into the solution in which luminescent molecules are dissolved.

Corresponding author: Koichiro Yamabe
*E-mail address*: 2ES14195W@s.kyushu-u.ac.jp

## 3. Experiments

Figure 1 shows the detailed structure of the test duct. A convergent nozzle is connected to this duct. The test duct has a rectangular cross section whose height and width have the same value of 20.0 mm. The leading edge of the cavity is located 50 mm downstream of the nozzle exit. The cavity length $L$ is adjustable. The cavity depth $D$ is set to 28.5 mm or 35.0 mm: the dominant oscillation frequency depends not only on the length $L$ but also on the depth $D$. Simultaneously with the luminescence detection, the temporal variation in pressure is measured with a semiconductor-type pressure transducer (Kulite, XCQ-062). The transducer is mounted on the rear face of the cavity and is located 2.0 mm below the trailing edge of the cavity. The oscillation frequency is controlled by changing the length and depth of the cavity.

In the PSP measurements, a mercury-xenon lamp (Hamamatsu, L5662-01) is used as an excitation light source. Light from this lamp passes through the optical filter (Sigma Koki, BLF-50S-390B) that cuts light with visible wavelengths. Light with ultraviolet wavelengths is then irradiated onto the AA-PSP. Luminescence from the AA-PSP is detected by the photomultiplier (Hamamatsu, R374) simultaneously with the pressure measurement. In order to restrict to the detection region, the plate having a square opening is placed at the location where luminescence is focused

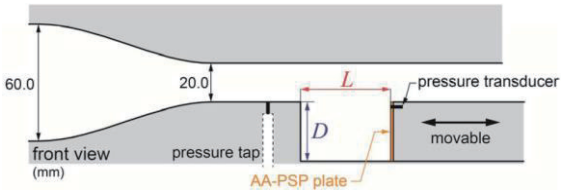


Fig. 1 Test duct

through the lens. The physical size of the detection region is 3 mm × 3 mm and this region surrounds the surface of the pressure transducer whose diameter is 1.7 mm.

The pressure signal is branched into two signals. One is input into the digital oscilloscope (Tektronix, TDS3034B). The other is filtered using a programmable filter (Stanford Research Systems, SR650) to extract the components whose frequencies are within $f_d \pm 0.5$ kHz ($f_d$: dominant oscillation frequency), and then is used as a source for triggering the oscilloscope. The luminescence intensity and unfiltered pressure signal are recorded into the oscilloscope simultaneously. The oscilloscope is triggered 256 times at the same phase in the filtered pressure signal. The 256 data sets of luminescence intensity and unfiltered pressure signal are averaged in the oscilloscope and recorded into the personal computer. The six experimental runs are conducted for each condition.

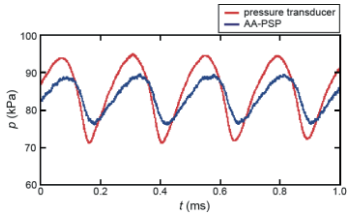

(a) $f_d = 4.2$ kHz

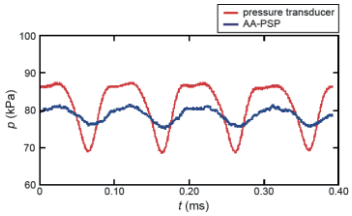

(b) $f_d = 10.2$ kHz

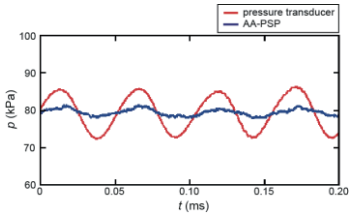

(c) $f_d = 19.2$ kHz

Fig. 2 Phase-averaged pressure histories

## 4. Results and Discussion

Figures 2(a)−(c) show representative phase-averaged pressure histories measured by the pressure transducer and AA-PSP for $f_d$ = 4.2kHz, 10.2 kHz, and 19.2 kHz. It is found from these figures that attenuation in PSP pressure-oscillation amplitude becomes remarkable with increase in oscillation frequency. It is also found that PSP pressure history lags behind the actual pressure history measured by the pressure transducer for all dominant frequencies.

The attenuation $\Delta p_{psp}/\Delta p_{actual}$ and phase lag $\Delta\phi$ in

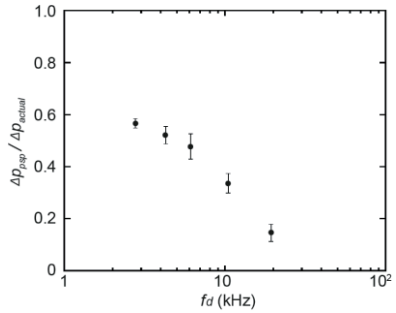

(a) $\Delta p_{psp}/\Delta p_{actual}$ vs frequency

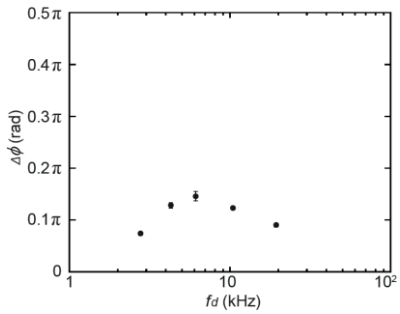

(b) $\Delta\phi$ vs $f_d$

Fig. 3 Plots of $\Delta p_{psp}/\Delta p_{actual}$ and $\Delta\phi$ vs frequency

PSP pressure oscillation are estimated from the pressure oscillation components within $f_d \pm 0.5$ kHz and plotted against the dominant frequency $f_d$ as shown in Figs. 3(a) and (b), respectively, where $\Delta p_{psp}$ and $\Delta p_{actual}$ are the pressure oscillation amplitudes measured by the AA-PSP and pressure transducer, respectively. It is clear from Fig. 3(a) that $\Delta p_{psp}/\Delta p_{actual}$ decreases with increase in $f_d$. On the other hand, $\Delta\phi$ attains a maximum at $f_d \sim 6$ kHz as shown in Fig. 3(b). We have no clear explanation on this maximum at present.

## 5. Concluding Remarks

The AA-PSP response to a periodic change in pressure was investigated experimentally. The periodic change was produced by mounting a rectangular cavity on the wall of the duct in which air flows at a Mach number of ~0.7. The pressure oscillation frequency was ranged between ~3 kHz and ~20 kHz by changing the length and depth of the cavity. The experimental results revealed that the attenuation in pressure oscillation amplitude became remarkable with increase in frequency and that the phase lag attained a maximum at a certain frequency.

## References

[1] T. Handa, H. Miyachi, H. Kakuno, T. Ozaki, *Exp. Fluids*, 53 (2012), 1855－1866.
[2] T. Sugimoto, S. Kitashima, D. Numata, H. Nagai, K. Asai, *AIAA Paper*, (2012), 2012-1185.
[3] J.W. Gregory, J.P. Sullivan, *AIAA Journal*, 44 (2006), 634－645.
[4] H. Sakaue, J.P. Sullivan, *AIAA Journal*, 39 (2001), 1944－1949.

Eleventh International Conference on Flow Dynamics
October 8-10, 2014, Sendai, Miyagi, Japan

# Characteristics of Unsteady Pressure-Sensitive Paint under Low Pressure Condition

Daisuke Sasaki[1], Daiju Numata[1], Keisuke Asai[1], Masayuki Anyoji[2]
1 Department of Aerospace Engineering, Graduate School of Engineering, Tohoku University
6-6-01 Aramaki Aza Aoba, Aoba-ku, Sendai, Miyagi, 980-8579 JAPAN
2 Japan Aerospace Exploration Agency,
7-44-1, Jindaiji Higashi-machi, Chofu, Tokyo182-8522, JAPAN

**ABSTRACT**

In this study, we studied static and dynamic characteristics of Pressure-Sensitive Paint (PSP) composed of polymer, luminophore and ceramic particle under low pressure condition to realize unsteady PSP measurement in Mars Wind Tunnel. We measured pressure and temperature sensitivity as static characteristic and frequency response as dynamic characteristic. The result of two calibrations showed that the PtTFPP and PdTFPP had good static characteristics under low pressure condition and PtTFPP could renponse to phenomena of around 4 kHz in 20 kPa, and more than 5 kHz in 100 and 50 kPa.

## 1. Introduction

In recent years, the study of an airplane that flies at low Reynolds number ($Re = O(10^4 - 10^5)$), such as mars exploration airplane, is proceeding. For conventional airfoils, laminarized boundary layer may easily induce massive separation at low Reynolds number, which significantly reduces the maximum lift-to-drag ratio. The steady pressure distribution measurements on whole wing with using Pressure-Sensitive Paint (PSP) have conventionally been conducted to reveal that phenomenon in Mars Wind Tunnel (MWT) at Tohoku University and have achieved a lot of results.

However, the recent studies show that unsteady flow behaviors are non-negligible at low Reynolds number in considering aerodynamic characteristics of an airfoil. According to the computational study conducted by Atobe, et al. [1], pressure fluctuation on the airfoil can be increased drastically. The technique of unsteady PSP measurement in MWT is expected as the experimental tool to reveal the unsteady phenomena. However, we still cannot realize the unsteady PSP measurement in MWT. It is mainly because the pressure fluctuation becomes small and dynamic characteristics are degraded under low pressure condition. In order to measure the unsteady phenomena in MWT test, the static characteristic of PSP must be superior to 1 %/kPa and -2 %/K and have the ability to response to phenomena of at least more than 1 kHz.

In this study, we focused on the static and dynamic characteristics of Polymer/Ceramic PSP (PC-PSP), one of the typical unsteady PSP, under low pressure environment similar to MWT condition to evaluate that the static and dynamic characteristics of PSP are suitable to measure the small and unsteady pressure fluctuation.

## 2. Experimental method

### 2.1 Pressure-Sensitive Paint (PSP)

PSP is an optical pressure measurement technique based on the photochemical process where the luminescent is quenched by oxygen. The rate of quenching is proportional to the local oxygen partial pressure, which is proportional to the absolute air pressure. Therefore, the luminescent intensity of PSP can be related to the absolute air pressure.

In this experiment, we used the Polymer/Ceramic PSP (PC-PSP) which is known as a binder of PSP for unsteady measurement with a porous binder.

### 2.2 Static Calibration (Sensitivity Measurement)

Both the pressure and temperature sensitivity was evaluated by using a calibration chamber. Luminescence from a PSP sample set in the chamber was acquired by using a CCD camera (ORCA II-BT1024). We used three luminophores often used for wind tunnel testing, PtTFPP, PdTFPP and RuDPP. The pressure were controlled from 1 kPa and 5 to 30 kPa every 5 kPa, and the temperature controlled from 5 K and 20 to 40 K every 10 K. Poly(TMSP)/PdTFPP being used in MWT was also measured for comparison.

### 2.3 Dynamic Calibration (Frequency Response)

#### 2.3.1 Experimental setup

Figure 1 shows the setup of the acoustic resonance tube [2] used to evaluate the frequency characteristic. The acoustic resonance tube consists of a closed tube with a speaker on one end. By inputting the sine voltage to the speaker, it can provide high pressure fluctuation at the resonance frequencies of the tube. We put an aluminum plate painted with PSP in the center of a cap placed on the other end of the tube. The excitation light, UV-laser, was irradiated to the PSP from the acrylic window and emission light from PSP was captured by a photomultiplier tube (PMT) with an optical band-pass filter (650±20). A high-frequency pressure transducer was placed also in the center of the cap to measure pressure fluctuation at the same time. PSP was evaluated in broad range frequency by changing speaker; one to provide high pressure fluctuation in low frequency (0.14 to 3 kHz) and another to provide high pressure fluctuation in high frequency (0.5 to 10 kHz). In this experiment, PtTFPP was used as the luminophore. The frequency responses were searched in 100, 50 and 20 kPa. Frequencies were changed from 0.15 to 5 kHz due to signal to noise ratio. The temperature of the sample was set at 273 K. In this study, we referred to the frequency at -3 dB as the response characteristic

#### 2.3.2 Data analysis

First, all measured signals were band pass filtered,

Corresponding author: Daisuke Sasaki
E-mail address: sasaki.daisuke@aero.mech.tohoku.ac.jp

the band width of the band-pass filter was ±100 Hz around the driving frequency of the speaker. Second, both pressure transducer and PSP time series datasets were respectively segmented on a wavelength to wavelength basis. Then that waves were averaged and the averaged data were fitted by the sinusoidal waveform for both pressure transducer and PSP. Finally, gain and phase characteristics were determined from the amplitude and phase of fitting equation.

## 3. Result and Discussion

### 3.1 Static Calibration

Figure 2 shows the pressure sensitivities of PC-PSP under low pressure condition. Each pressure sensitivity of PdTFPP, PtTFPP and RuDPP with PC-PSP was 3.15, 1.93 and 0.40 %/kPa respectively (the sensitivity of steady PSP for MWT test is 2.95 %/kPa). It can be seen from Fig. 2 that RuDPP prominently have inferior pressure sensitivity.

Figure 3 shows the temperature sensitivity of PC-PSP at low pressure environment. Each temperature sensitivity of PdTFPP, PtTFPP and RuDPP with PC-PSP was - 4.65, -1.56 and -1.14 %/K respectively. PdTFPP shows the highest temperature sensitivity and PtTFPP and RuDPP with PC-PSP have surperior temperature sensitivity to steady PSP for MWT.

These figures show the PC-PSP/PtTFPP has good static characteristics under the low pressure condition like MWT test.

### 3.2 Dynamic Calibration

Figure 4 shows the frequency response characteristic of PC-PSP/PtTFPP at 100, 50 and 20 kPa. This result shows that the dynamic characteristics gradually got worse as the surround pressure declined from 100 to 50 kPa, and drastically went down from 50 to 20 kPa. It can be also seen that the PC-PSP/PtTFPP has response characteristic of around 4 kHz in 20 kPa, and of more than 5 kHz in 100 and 50 kPa.

## 4. Concluding remarks

In this study, the characteristics of PC-PSP, that is a typical PSP for unsteady phenomena, under low pressure condition were studied. In the case of using the PtTFPP as luminophore, the PC-PSP had high pressure sensitivity surperior to 1 %/kPa and temperature sensitivity lower than -2.0 %/K. the dynamic characteristic became worse as the surrouding pressure decreased, especially at 20 kPa. The PC-PSP/PtTFPP had the ability to response to the phenomena which is lower than 4 kHz at 20 kPa and more than 5 kHz at 100 and 50 kPa. In the future, we will additionally measure the characteristics of other representative unsteady PSPs; Aluminium-Anodized PSP and TLC plate PSP with some luminophores. We will also apply these PSPs to unsteady PSP measurement in MWT and evaluate these avalability.

## Refferences


[1] T. Atobe, T. Ikeda, 27th Congress of International Council of the Aeronautical Sciences, (2010) ICAS2010-3.10.3

[2] T. Sugimoto, S. Kitashima, D. Numata, H. Nagai, K.. Asai, 50th AIAA Aerospace Sciences Meeting including the New Horizons Forum and Aerospace Exposition, (2012) AIAA 2012-1185


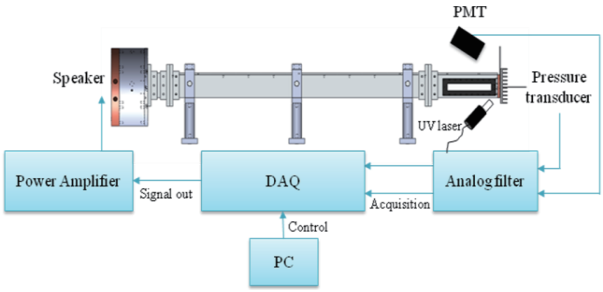


Fig. 1 Experimental Setup of Dynamic Calibration

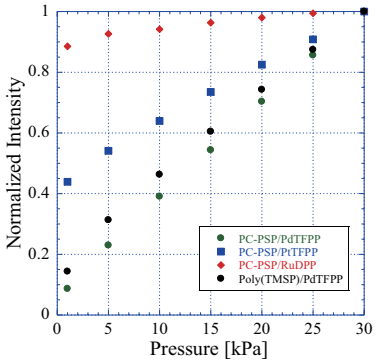


Fig. 2 Pressure Sensitivity

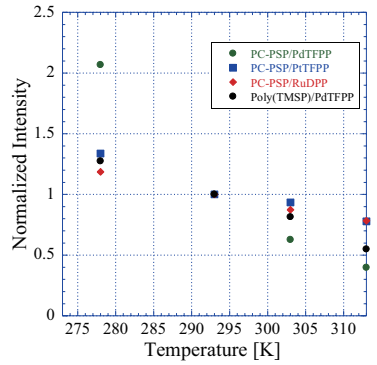


Fig. 3 Temperature Sensitivity

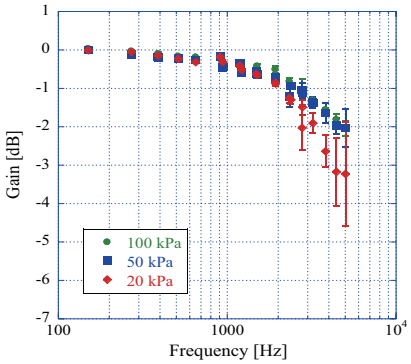


Fig. 4 Frequency Response Characteristic

# The Experimental and Numerical Analysis for the Micromixing Flow Generated by Surface Tension Effect on a Gas-Liquid Free Interface

Takashi Yamada[1], and Naoki Ono[1],
[1] Department of Engineering Science and Mechanics, Shibaura Institute of Technology
3-7-5 Toyosu, Koto-ku, Tokyo 135-8548, Japan

**ABSTRACT**

The micromixing flow caused by surface tension difference between the intermingled two fluids on a gas-liquid free interface has been observed in sub millimeter-scale capillary channel in our laboratory. We tried to measure the flow property by PIV system and simulate the similar situation by three-dimensional CFD analysis. As a result, it had same tendency of the oscillating flow but different cycle between the two results because of the some restriction for the calculation and a small different shape between the CFD model and the test channel used for the experiment.

## 1. Introduction

In micro scale, the flow property has almost laminar flow because of the very small reference length. Then the mixing acceleration has finally depended on molecular diffusion by the small reference length as diffusive distance because of the very small Reynolds number [1]. In this situation, some contributions in uniform mixing quality or accurate mixing management have been addressed because large heat or mass flax occurs between the two-phase interface due to the large value of "surface to volume ratio". Otherwise, it has also negative condition for the shortage of the reaction time because it depends on only the molecular diffusion and the retention time in the capillary channel [2]. Therefore, it is required to develop simple-structured new mixing device which can do fast and uniform mixing easily. In our laboratory, the micromixing flow caused by surface tension difference between the two fluids has been successfully observed on a gas-liquid free interface in capillary channel [3]. However, the improvement of the mixing performance, the suitable shape of the channel design has not been realized yet. In this study, we tried to measure the micromixing flow by Particle Image Velocimetly (PIV) system and simulate the similar situation used by three-dimensional computational fluid dynamics (CFD). We investigate the characteristic of the flow and the important factor for the suitable channel design compared with both results.

## 2. The Mechanism of the mixing device

The outline of the mixing process built in the elbow point of L-type micro channel is shown in Fig.1.

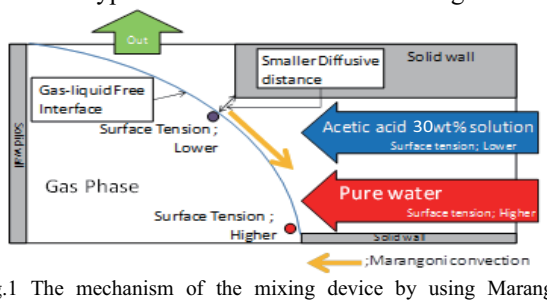


Fig.1 The mechanism of the mixing device by using Marangoni convection

When a gas-liquid free interface is put and made expanded in the elbow area, it makes narrow space between the interface and inner wall at that place. If the two fluids have different surface tension, the mixing at the local area between the interface and wall surface is developed. Therefore it can make the distribution of the surface tension value caused by concentration difference between the two fluids and it causes Marangoni convection as the source of the mixing device [3].

## 3. Method

Fig.2 shows the detail of the test channels for mixing experiments made by photo lithography [3]. The flow experiments used the two solutions. Namely, 30wt% of acetic acid aqueous solution at inlet 1 and pure water with 0.01wt% of tracer particle (diameter; 0.67μm) dissolved at inlet 2. Table1 shows Physical properties of the two solutions. Experimental setup was same as previous studies in our laboratory [3]. The movie for the experiment was taken by 1000 flames per seconds' (fps) high-speed video camera and analyzed by particle image velocimetly (PIV) software (Flow expert 2C2D, KATO KOKEN, co.Ltd). Volume flow rate of both test fluids are same value as 2.5μl/min in the mixing experiments.

Fig.3 shows the detail of the three-dimensional model for CFD analysis used by finite volume method as discretizing method and semi-implicit method as calculation algorithm. The model shape and flow condition are basically similar with the flow experiments. This analysis used one-phase flow calculation because the density of the acetic acid aqueous solution is approximately same with pure water as shown in Table 1. Unsteady calculation of 0.05[s] by the CFD model was carried out using the condition of stepping time; $\Delta t$ = 0.0005[s]. At the cells that Marangoni convection produces, the shear force estimated by the concentration difference between the next cells is increased in the governing equation as external force. Actual calculation used the commercial CFD software package PHOENICS. The calculation domain of x = 0.45mm (150cells), y = 0.3mm (300cells) and z = 0.12mm (25cells) were set on the Cartesian coordinate system. For the calculation, the fluid properties of pure water of 20 degrees Celsius were used. In the CFD model, $1.24\times10^{-9}$[$m^2$/s] as diffusivity of the acetic acid to pure water was adopted [3].

Corresponding author: Naoki Ono
*E-mail address*: naokiono@shibaura-it.ac.jp

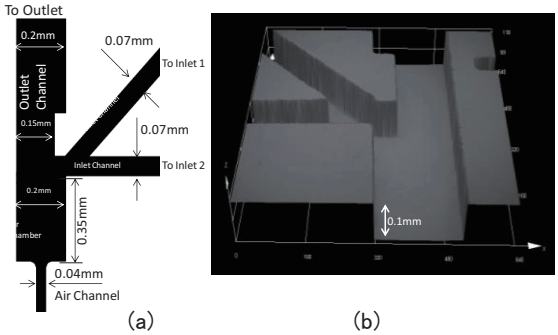


Fig. 2 The design of the test channel, (a) Detail of the mixing device including air-chamber and air-channel, (b) The image of the mixing device in a test channel.

Table 1 Physical properties of the test fluids in the experiments

| Test fluids | Density ($kg/m^3$) | Surface tension (mN/s) | Viscosity (mPa・s) |
|---|---|---|---|
| Pure water with 0.01wt% of tracer particles | 1012.0 | 69.0 | 0.96 |
| Acetic acid 30wt% solution | 1035.0 | 44.6 | 1.54 |

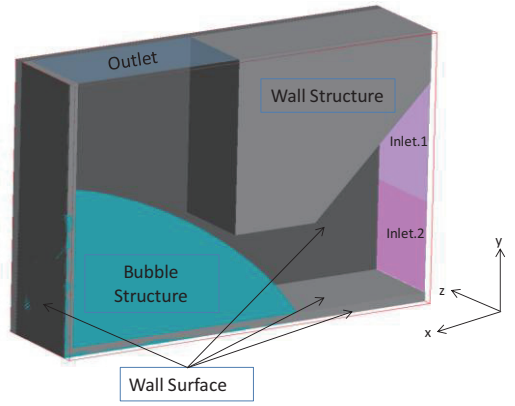


Fig. 3 The detail of the calculation model of the mixing device built in a commercial CFD software package PHOENICS

## 4. Results and Discussion

Fig.4 shows the result of PIV analysis for the flow experiment and Fig.5 shows the result of CFD analysis. Fig.4 and 5 shows that both experimental or CFD results caused the oscillating flow at the narrow space between the bubble surface and the wall surface in the mixing device. CFD analysis shows the oscillation flow was generated by the cyclic force acted in the opposite direction for the main-flow called as "Marangoni force" on the bubble surface. However, both results shows different cycle for the oscillating flow, the flow experiment shows about 0.03[s] but that of CFD analysis has about 0.01[s]. The result of the flow velocity at the circumference in the rotational flow has also quite large difference between the PIV analysis and the CFD result. The experimental result has about 7.0[mm/s] but the CFD analysis has over 20.0[mm/s]. There is about 3-times difference between the both results. The viscosity of the acetic acid aqueous solution varies in value from 1.01 [mPa・s] to 1.54 [mPa・s] by the the concentration value (0~30%). In the CFD model, the viscosity was fixed to be that of pure water as 1.01[mPa・s]. It is thought that the velocity difference influenced on the calculating result. However, both results has quite same tendency. These results suggested that the oscillating flow is the specific character of the micromixing flow affected by the viscosity coefficient. Then, It is thought that the influence of the wall surface must be considered to utilize the rotational flow in micromixing effectively.

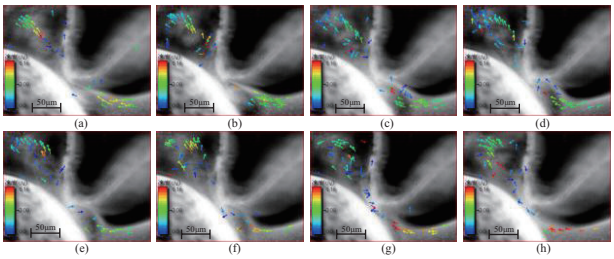


Fig. 4 The series of high speed photos with PIV analysis of flow velocity every 0.002[s] at the slice of channel plane from (a) to (h)

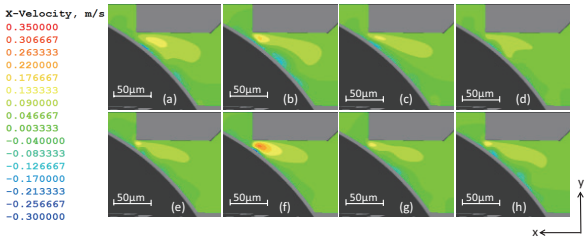


Fig. 5 The series of results of CFD analysis of flow velocity for x-direction every 0.001[s] at *x-y* plane ($z= 6.0\times10^{-5}$[m]) from (a) to (h)

## 5. Concluding Remarks

In this study, the flow property of the micromixing flow caused by the surface tension difference on a bubble surface in capillary channel was measured by PIV system and calculated by CFD analysis. The present investigation leads to the following conclusions.

(1) Both experiment and CFD results revealed the oscillating of the micromixing flow on the bubble surface generated by cyclic distribution of the Marangoni force acted in the opposite direction of the main-flow. The tendency of the flow behavior was in agreement between the both results.

(2) The CFD result of the frequency of the oscillating flow and of the flow velocity at the circumference in the rotational flow were 3-times larger than the experiment. It was thought that the treatment of the viscosity in the CFD model was different from the actual condition. It is suggested that the oscillating flow was greatly affected by the effect of the shear force in liquid phase.

## References

[1] W. Ehrfeld, V. Hessel, H. Lowe, “Microreactors”, WILEY-VCH, Weinhelm, Germany (2000) 1－82.
[2] V. Hessel, H. Lowe, F. Sohnfeld, *Chemical Engineering Science,* 60, (2005) 2464－2501.
[3] T. Yamada, N. Ono, *Transaction of the Japan Society of Mechanical Engineers, series B, vol.* 79, (2012) 888－899.

Eleventh International Conference on Flow Dynamics
October 8-10, 2014, Sendai, Miyagi, Japan

# Simulation of Transverse Liquid Jet to a Supersonic Gas Stream Based on Kinetic Theory of Granular Flow

Haixu Liu[1], Yincheng Guo[1], Wenyi Lin[1]
[1] Department of Engineering Mechanics, Tsinghua University
Beijing, 100084, China

**ABSTRACT**

The Eulerian approach based on kinetic theory of granular flow is introduced into the numerical investigation of transverse liquid jet into a supersonic gas stream. The well-posedness problem of the droplet governing equations is solved by appliying an equation of state in the kinetic theory. The numerical results of the jet penetration height show good agreement with the experiments, and characteristic flow structures of the jet plume is well described by the current Eulerian approach, indicating its adequacy in numerical modeling of compressible multiphase flow.

## 1. Introduction

The study of liquid jet into a supersonic crossflow has become an important research area as the development of liquid-fueled scramjet combustors. Extensive experimental studies have been carried out previously to investigate the liquid spray structures [1-3]. However, numerical studies have rarely been seen in the literature, due to the complexity of this problem. In the Eulerian approach for describing multiphase flow, the droplet phase governing equations system is found to be non-hyperbolic, which leads to an ill-posed problem and produces non-physical results [4,5]. In order to obtain a well-posed system, the kinetic theory of granular flow [6] is introduced in the current study. The particle kinetic theory built on the basis of kinetic theory of non-uniform dense gases [7], has been widely used in predicting granular flow, and it is implemented here in the simulation of liquid jet into a supersonic crossflow.

The scope of this paper is to construct a well-posed system for the droplet governing equations based on the kinetic theory, and carried out the numerical simulation of the liquid jet into a supersonic flow.

## 2. Method

The governing equations of the droplet phase can be expressed in conserved form in the Eulerian frame,

$$\frac{\partial \mathbf{W}_p}{\partial t}+\frac{\partial \mathbf{F}_p}{\partial x}+\frac{\partial \mathbf{G}_p}{\partial y}+\frac{\partial \mathbf{H}_p}{\partial z}=\frac{\partial \mathbf{F}_p^v}{\partial x}+\frac{\partial \mathbf{G}_p^v}{\partial y}+\frac{\partial \mathbf{H}_p^v}{\partial z}+\mathbf{S}_p \tag{1}$$

where the subscript "$p$" denotes the droplet phase, and the supscript "$v$" denotes the viscous terms. $\mathbf{W}_p$ is the conservation variables of the droplet phase, and the convection term are $\mathbf{F}_p$, $\mathbf{G}_p$, $\mathbf{H}_p$. Besides, $\mathbf{S}_p$ is the interaction term between the gas and droplet phases. The kinetic theory introduces the concept of granular temperature $\Theta$ in Equ. (1),

$$\begin{aligned}&\frac{\partial}{\partial t}\left(\alpha_p \rho_p \Theta\right)+\frac{\partial}{\partial x_j}\left(\alpha_p \rho_p v_p \Theta\right)_j \\ &=\frac{2}{3}\Pi_{i,j}\frac{\partial v_{pj}}{\partial x_i}+\frac{2}{3}\frac{\partial}{\partial x_j}\left(\Gamma_\Theta \frac{\partial \Theta}{\partial x_j}\right)-\frac{2}{3}\end{aligned} \tag{2}$$

where $\Gamma_\Theta$ and $\gamma$ are the transport coefficient and dissipation term of the granular temperature [8]. In kinetic theory, the pressure of the droplet phase can be described by an equation of state,

$$p_p=\alpha_p\rho_p\left[1+2(1+e)\alpha_p g_0\right]\Theta, \tag{3}$$

where $e$ and $g_0$ are the coefficient of restitution and radial distribution function, respectively.

Characteristics analysis is employed to investigate the well-posedness of the equation system. By applying the chain rule to the convection term $\mathbf{F}_p$ in the $x$ direction, the Jacobian matrix of the equation system is obtained,

$$\frac{\partial \mathbf{F}_p}{\partial \mathbf{W}_p}=\begin{bmatrix}0 & 1 & 0 & 0 & 0\\ -u_p^2 & 2u_p & 0 & 0 & R_p\\ -u_p v_p & v_p & u_p & 0 & 0\\ -u_p w_p & w_p & 0 & u_p & 0\\ -\Theta u_p & \theta & 0 & 0 & u_p\end{bmatrix}, \tag{4}$$

where $R_p=1+2(1+e)\phi_p g_0$. Through diagonalization of the Jacobian matrix, five real eigenvalues are obtained,

$$\lambda_1=u_p-\sqrt{p_p/(\phi_p\rho_p)},\quad \lambda_2=u_p+\sqrt{p_p/(\phi_p\rho_p)},$$
$$\lambda_3=\lambda_4=\lambda_5=u_p.$$

In the $y$ and $z$ directions, the same analysis can be used to get the eigenvalues, and similar results can be derived. Therefore, the set of the droplet phase equations is demonstrated to be hyperbolic, and a well-posed system is then established.

## 3. Results and Discussion

Simulation was conducted in conditions with respect to the experiment [9]. The inflow stagnation pressure in the experiment maintained at 4.5 atm ± 2%, and the stagnation temperature was close to the ambient air. The Mach number of the inflow air is 3.0. The jet-to-air momentum flux ratio $q=\rho_j v_j^2/\rho_\infty v_\infty^2$, where $\rho_j$ and $\rho_\infty$ are the density of the injected water and the inflow air. In this study, $q$ is set to be 6 in the computation corresponding to the experiment. The injected water flow rate was maintained at 90g/s ± 1.1%.

Fig. 1 shows the contours of Mach number of the gas phase. It is noted that the boundary layer detachment, the bow shock and the separation shock are well

Corresponding author: Yincheng Guo
*E-mail address*: guoyc@tsinghua.edu.cn

described by the simulation. As the jet penetrates into the cross flow, separation of the boundary layer is induced due to the adverse pressure gradient in front of the injection. The separation further results in the separation shock wave, which interacts with the bow shock wave above the liquid jet. The interaction between the separation shock and bow shock gives rise to alteration in pressure distribution, and in turn modifies the bow shock inclination, which is called the whipping phenomena [3].

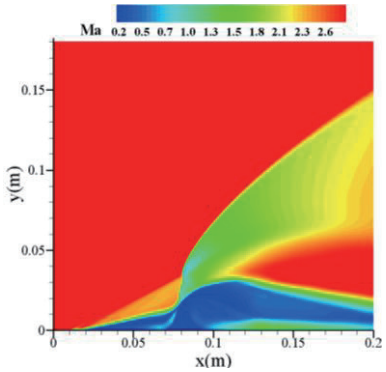


Fig. 1 Contours of the Mach number of the gas phase.

The comparison of the jet penetration height between the numerical results and the experiments is shown in Fig. 2. Curves of the experiments in Fig.2 are derived from the empirical correlations [3,9] of the liquid jet penetration in the experiments. The numerical penetration height is found to be well matched with the empirical correlations. The jet starts to incline at about $8d_0$ from the orifice, and the penetration height increases slowly after that.

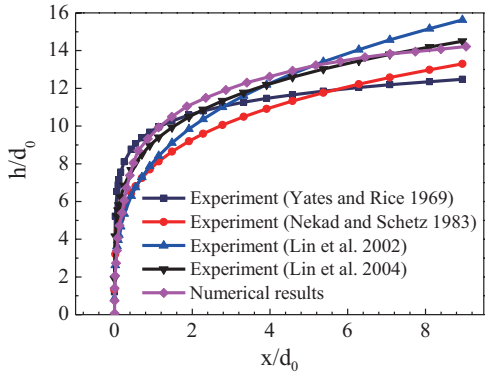


Fig. 2 Penetration height of the numerical results with predictions from the experimental correlations.

Fig. 3 shows the vector contour of the gas phase velocity. It is observed that a circulation zone is formed in front of the jet column. The flow velocity in this region will decrease to subsonic state, and the air upstream of the injection will enter this area due to the circular entrainment, which contributes to the mixing of the fuel with the air, and also benefits the flame stability in combustion. The direction of the inflow changes because of the separation shock and bow shock, and low-velocity zone also shows behind the jet.

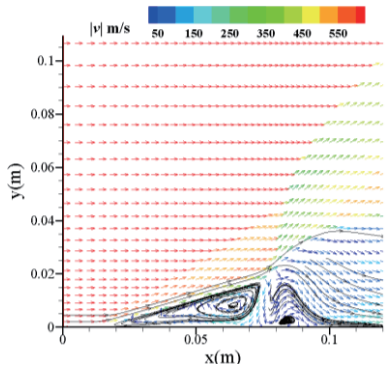


Fig. 3 Vector contours of the gas phase velocity.

## 4. Concluding Remarks

A transverse liquid jet into a supersonic gas stream is investigated numerically using the Eulerian approach. The kinetic theory of granular flow is introduced to simulate the droplet phase, and the hyperbolic nature of the equation set for the droplet phase is demonstrated. Therefore, a well-posed equation system is established. The penetration height of the numerical results is compared with empirical correlations from the experiments, and good agreements are achieved. Characteristic structures of the jet plume are predicted through the current simulation, indicating the Eulerian approach based on the kinetic theory is adequate in such compressible multiphase flow.


## Acknowledgment

This work was supported by the National Natural Science Foundation of China under Grant No. 51176099.


## References


[1] A.K. Edward, A.S. Joseph, *AIAA J.*, 11(1973), 1223-1224.

[2] J.A. Schetz, E.A. Kush, P.B. Joshi, *AIAA J.*, 18(1980), 774-778.

[3] J.B. Perurena, C.O. Asma, R. Theunissen, O. Chazot, *Exp. Fluids.*, 46(2009), 403-417.

[4] S.A. Slater, J.B. Young, *Int. J. Multiph. Flow*, 27(2001), 61-87.

[5] I. Toumi, A. Kumbaro, *J. Comput. Phys.*, 124(1996), 286-300.

[6] D. Gidaspow, Multiphase flow and fluidization: continuum and kinetic theory descriptions Academic Press, 1994.

[7] S. Chapman, T.G. Cowling, The Mathematical Theory of Non-Uniform Gases, 3rd ed., Cambridge University Press, 1970.

[8] C.K. Chan, Y.C. Guo, K.S. Lau, *Powder Technol.*, 150(2005), 42-55.

[9] R.H. Thomas, J.A. Schetz, *AIAA J.*, 23(1985), 1892-1901.

Eleventh International Conference on Flow Dynamics
October 8-10, 2014, Sendai, Miyagi, Japan

# Air-blast Atomizer of High Viscosity Liquids

S. I. Yang and T. C. Hsu
Department of Power Mechanical Engineering, National Formosa University
No.64, Wunhua Rd. Huwei Township, Yunlin County, 63202, Taiwan

**ABSTRACT**

In this study, we investigated the effects of gas-liquid ratios (GLRs) and viscosity on the flow field characteristics of an air-blast swirl atomizer. The results indicated that viscosity substantially influenced the breakup length of fluids. Additionally, the upstream area exhibited a higher momentum than did the downstream region. However, because of gravitational effects, a comparatively higher axial velocity is observed in the downstream area. GLRs exerted no considerable influence on the velocity distribution of droplets, but generated an effect on vorticity distribution.

## 1. Introduction

Liquid spray techniques have been continually applied in several technological applications, including spray drying, spray coating, spray cooling, and medical and printing applications [1]. Such techniques are also crucial in numerous industrial combustion applications. With the widespread use of liquid spray techniques, the viscosity requirements of liquids have become diverse. Therefore, the atomization characteristics of liquids with various viscosity coefficients are the key to developing advanced liquid spray techniques. The viscosity of a liquid influences the stress of the liquid. During a fluid flow and spray process, the interactive effects between a liquid and liquid, between a liquid and wall, and between a liquid and gas are related. These effects influence the spray characteristics of a fluid; specifically, the fluid phenomena (i.e., spray characteristics and transport phenomena) observed in a highly viscous liquid [2, 3] that result from the balance among viscous, gravitational, inertia-gravitational, and inertial forces.

Ochowiak [4] investigated the atomization characteristics of fluids with various viscosities; the results showed that the inertial force of fluids caused an increase in turbulence intensity, which increased the drag coefficient ($C_d$). However, an increased viscosity altered the surface tension of the fluids, causing the droplet's Sauter mean diameter (SMD) in the axial direction to increase. However, the radial SMD remained unchanged [5]. Li et al. [6] adopted an internal-mixing twin-fluid atomizer, investigating the effects of atomized gas pressure and gas-liquid ratios (GLRs) on an atomization process. Their results revealed that atomized gas pressure minimally influenced atomization characteristics; however, increasing GLR effectively reduced SMD. When fluid viscosity was reduced, the average spray cone angles increased; conversely, elevating fluid viscosity decreased the average spray cone angles, resulting in a decreased atomization performance [7]. Furthermore, the breakup length, frequency, and cone of liquid films are crucial factors that influence the spray performance of highly viscous fluids [8].

## 2. Experimental method

This study adopted silicon oil with various viscosities as the test fluid, which was introduced into an air-blast swirl atomizer (ABSA) at an angle of 45° from both sides of the atomizer. Atomized gas was used as air and was injected from the two sides of the ABSA at a horizontal plane. Subsequently, the air and silicon oil were mixed in the mixing chamber and then passed through an atomizer orifice, forming a spray. The droplet flow velocity at various positions (z-axis) was measured using the particle image velocemetry (PIV) system (Fig. 1). The parameters used for PIV image calculations were an interrogation area of 32x32 pixels and an overlap of 20%. The Nd:YAG laser was operated at 15 Hz with 54 μs as the time interval between each pulse.

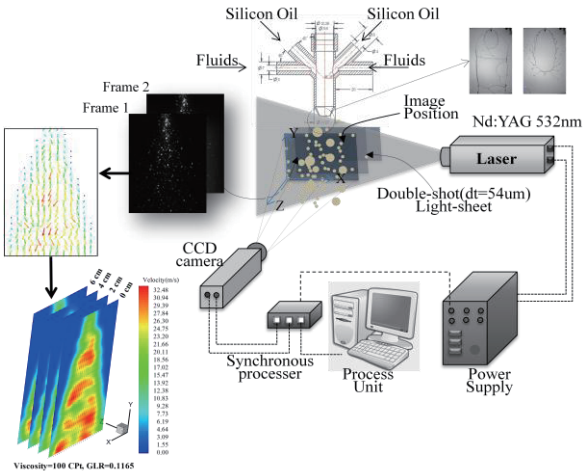


Fig. 1 Schematic of experimental setup.

## 3. Results and discussion

The experimental conditions are shown in Table 1. After passing through the ABSA, the silicon oil formed a layer of liquid film at the atomizer exit (upper right image of Fig. 1). This liquid film interacted with the atomizer gas, inducing the film to break up, atomizing the silicon oil into droplets. Subsequently, the two-dimensional flow velocity at various z-axis positions was measured using the PIV system (bottom left of Fig. 1). The obtained flow velocity fields were then analyzed to determine the effects of viscosity at various positions on the velocity and vorticity of the test fluid.

Table 1. Experimental conditions

| Fluid | Silicon Oil | | | | |
|---|---|---|---|---|---|
| Viscosity (cP) | 100 | 250 | 500 | 750 | 1000 |
| Gas-Liquid Ratio, GLR | 0.1165 | 0.1559 | 0.1952 | 0.2338 | |
| Z axis position (m) | 0 | 0.02 | 0.04 | 0.06 | |

- **The Effects of Viscosity on Axial Velocity**

The atomizer used in this study was an ABSA; the

Corresponding author: Shou-yin (Ian) Yang
*E-mail address*: shouyang@gamil.com

effects that the atomizer gas exerted on the bottom area of the nozzle were minimal. Figure 2 presents the velocity distribution along the y-axis when x-axis (central axis) was 0.0074 m, z-axis equaled 0 m, viscosity was 100 cP and 1000 cP, and GLR varied. Figures 2a present the radial (*u* component) and axial (*v* component) velocity distributions along the y-axis when the viscosity was low (100 cP). At the exit end of the atomizer, the effects of high tangential gas flow caused the droplet to exhibit a high *u*-velocity, which gradually diminished as the droplet moved downstream, while the *v*-velocity increased because of gravity. When the GLR increased, the upstream *u*-velocity and *v*-velocity accelerated, generating values that are larger than those produced when GLR was small. When the viscosity of the fluid increased to 1000 cP, the upstream *u*-velocity was higher than that at a low viscosity and accelerated further as GLR increased. These phenomena show that the ABSA used in this study effectively enhanced the radial velocity of the droplets and lengthened the residence time of the droplets.

- **The Effects of Viscosity and GLR**

Figures 3a–d present the vorticity distribution of the flow fields when GLR was fixed at 0.1165 and viscosity varied (100 cP, 500 cP, and 1000 cP). At a low viscosity (Fig. 3a), a high vorticity concentrated at the two sides of the spray cone angle; however, when this vorticity increased (Fig. 3b), only the upstream section of the cone exhibited a high vorticity. When viscosity increased to 1000 cP, a high vorticity was observed in the downstream section. Therefore, at a viscosity of 1000 cP and GLR of 0.1559, a high vorticity was identified in the midstream region; when the GLR further increased to 0.2338, the downstream region had a high vorticity. These results indicate that the balance between the fluid's stretch and inertial forces, which is influenced by fluid viscosity and atomized gas, determines the flow field characteristics of an atomization process.

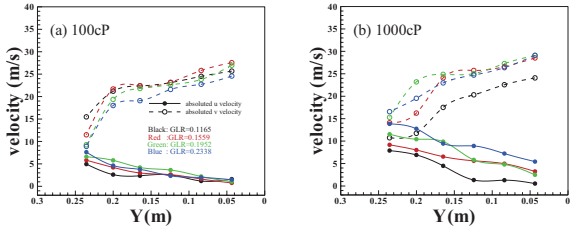


Figure 2. The *u*-velocity and *v*-velocity distributions at the central axis when the viscosity was 100 cP and 1000 cP and the GLR varied.

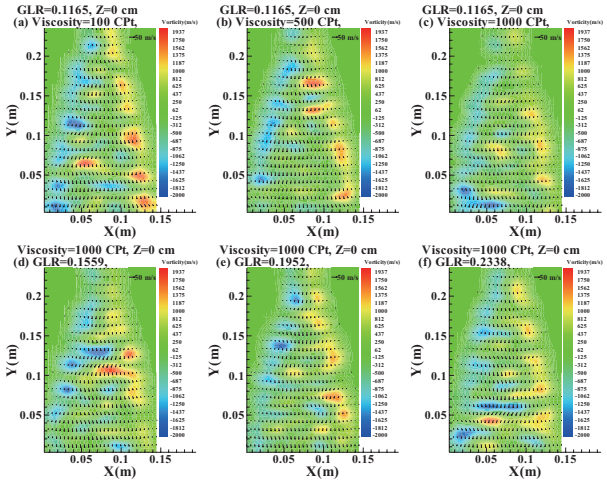


Fig. 3 The effects of GLR and viscosity on the velocity and vorticity distributions of a spray flow field.

## 4. Conclusion

This study experimentally investigated the atomization flow field characteristics of the ABSA when viscosity and GLR varied. The following results were obtained:

1. Because of the flow channel design of the atomizer and the high-speed stretching of gases, the test fluid forms a layer of liquid film at the exit end of the atomizer as it passes through the ABSA.
2. The liquid film breaks up into droplets because of the effects of gas stretch. The droplet yields a high u-velocity when GLR increases. Increasing the viscosity increases the breakup length of the liquid film, forming larger droplets. These droplets generate a comparatively higher momentum when influenced by GLR.


## Acknowledgements

The authors would like to thank National Science Council, Taiwan, for financially supporting this research under NSC 102-2221-E-150 -036, MOST 103-3113-E-008 -001 and MOST 103-2221-E-150 -056


## References


[1] A. Herczynski, C. Cernuschi, L. Mahadevan. *Physics Today*, Jun. (2011), 31.

[2] N. Kurti, H. Benckhard. *Scientific American*, Apr. (1994), 120.

[3] N.M. Ribe, M. Habibi, D. Bonn. *Annu. Rev. Fluid Mech*., 44 (2012), 249.

[4] M. Ochowiak, *Experimental Thermal and Fluid Science*, 50 (2013), 187.

[5] C.E. Ejim, M.A. Rahman, A. Amirfazli, B.A. Fleck, *Fuel*, 89 (2010), 1872.

[6] Z. Li, Y. Wu, H. Yang, C. Cai, H. Zhang, K. Hashiguchi, K. Takeno, J. Lu, *Fuel*, 103 (2013), 486.

[7] S. Yao, J. Zhang, T. Fang, *Experimental Thermal and Fluid Science*, 39 (2012), 158.

[8] Y. Fan, N. Hashimoto, H. Nishida, Y. Ozawa, *Fuel*, 121 (2014), 271.

Eleventh International Conference on Flow Dynamics
October 8-10, 2014, Sendai, Miyagi, Japan

# Numerical Analyses on Liquid-Metal MHD Flow in Sudden Expansion (Sudden Expansion in Direction of Applied Magnetic Field)

Hiroshige Kumamaru[1], Kazuhiro Itoh[1]
[1]University of Hyogo
Shosha 2167, Himeji, Hyogo 671-2280, Japan

**ABSTRACT**

Three-dimensional calculations have been performed on the MHD flow through a rectangular channel with sudden expansion. The sudden expansion is in the direction of the applied magnetic field. A large loss coefficient, i.e. a large MHD pressure drop for the sudden expansion, is calculated. The large loss coefficient is due to increase in the induced current in the region near to the sudden expansion. This result is in contrast to the sudden expansion in the direction perpendicular to the applied magnetic field, in which the loss coefficient is nearly zero.

## 1. Introduction

The authors have been performing three-dimensional numerical calculations on liquid-metal magneto-hydrodynamic (MHD) flow in order to apply analysis results to the cooling design of lithium-bearing blanket in a future fusion reactor power plant. Three-dimensional calculations are indispensable in order to predict exactly MHD channel flows with changes in flow direction, channel cross section, applied magnetic field and others. In this study, three-dimensional calculations are performed on the MHD flow through a rectangular channel with sudden expansion, particularly in order to estimate the pressure drop through the sudden expansion. The sudden expansion is in the direction of the applied magnetic field. The channel walls are assumed to be electrically-insulating.

## 2. Numerical Calculations

Figure 1 shows the calculation model, including the coordinate system, the main flow vector ($v$), the applied magnetic field ($B_0$) and the induced electric currents ($j$). Considering symmetry, the calculations are performed only for 1/4 of the channel cross-section. The applied magnetic field is imposed in the $z$ direction.

In the "small channel" upstream of the expansion and in the "large channel" downstream of the expansion, the fully-developed MHD flow appears except for the region near to the expansion. In the fully-developed MHD flow region, the induced electric current, which is produced by the vector product of flow velocity and applied magnetic field, flows in the negative $y$ direction in the fluid bulk region. The induced electric current returns in the positive $y$ direction by passing through region very near to the wall, within a $y$-$z$ plane at the same $x$, where the flow velocity is nearly zero. The induced electric current loop has a relatively large electrical resistance, since the electric current needs to flow in the thin regions very near to the walls. The Lorentz force, which is caused by the vector product of induced electric current and applied magnetic field, acts in the negative $x$ direction, and a large MHD pressure drop along the flow axis (i.e. $x$-axis) is produced.

Corresponding author: Hiroshige Kumamaru
*E-mail address*: kumamaru@eng.u-hyogo.ac.jp

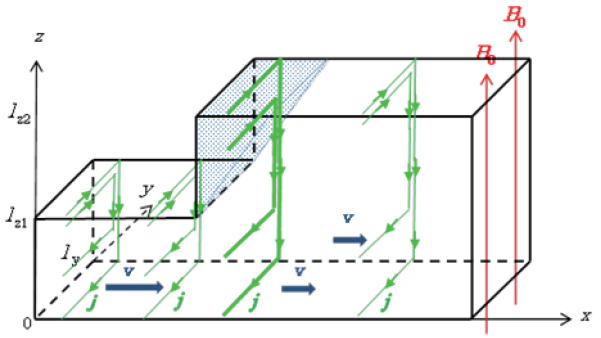


Fig. 1 Calculation model

On the other hand, the low-flow or reverse-flow region appears in the region just downstream of the expansion. (The low-flow or reverse-flow region is small comparing with that in non-MHD flow, i.e. flow under no magnetic field.) In this region, the induced electric current can return easily in the positive $y$ direction, since the region is large and its electric resistance is small. Thus, the induced electric current in the negative $y$ direction may become large in the region just downstream of the expansion, as shown in Fig. 1. The Lorentz force acting in the negative $x$ direction and thus the MHD pressure drop along the flow axis (i.e. $x$-axis) may become larger comparing with those in the fully-developed region.

The continuity equation, the momentum equation and the induction equation, which is derived from basic equations in electromagnetism, are solved numerically. The discretization of the equations is carried out by the finite difference method, and the solution procedure follows the MAC method.

## 3. Calculation Results

A base case calculation was carried out for $Ha$ (Hartmann number) =100, $Re$ (Reynolds number) =1000 and $Rm$ (magnetic Reynolds number) =0.001. These nondimensional parameters simulate typical "laboratory condition," i.e. a liquid-metal flow with a velocity of ~10 cm/s in a channel with ~1 cm width under an applied magnetic field of ~1 T. The other parameters are set as follows: $l_y$=1, $l_{z1}$=1, $l_{z2}$=2, $l_{x1}$=5 and $l_{x2}$=15 (i.e. an aspect ratio of 1 and an expansion ratio of 1).

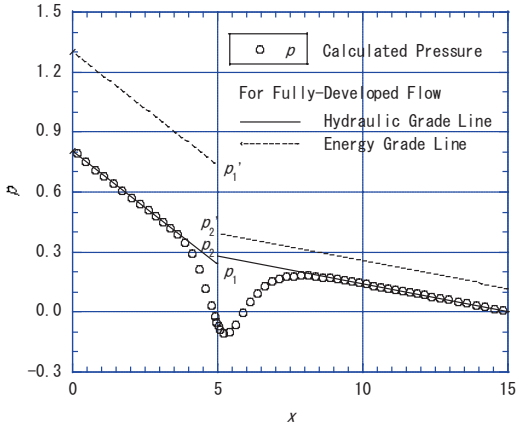


Fig. 2 Pressure along $x$-axis

Figure 2 show the pressure along the $x$ axis for the base case. The solid line indicates the hydraulic grade line (representing the static pressure energy). The pressure drops, i.e. the gradients of the hydraulic grade lines, for the fully-developed MHD flows in the small channel and in the large channel agree approximately with those obtained by the authors for fully developed MHD flows [1]. The dotted line indicates the energy grade line (representing the static pressure energy plus the kinematic energy). The difference in the energy grade lines at the expansion ($x=l_{x1}(=5)$), i.e. $p_1$'-$p_2$', corresponds to the energy loss due to the expansion. The loss coefficient ($\zeta$) obtained from Fig. 2 is 0.68. This value is much larger than that obtained by the authors for the expansion in the direction perpendicular to the applied magnetic field, i.e. $\zeta$=–0.08 [2].

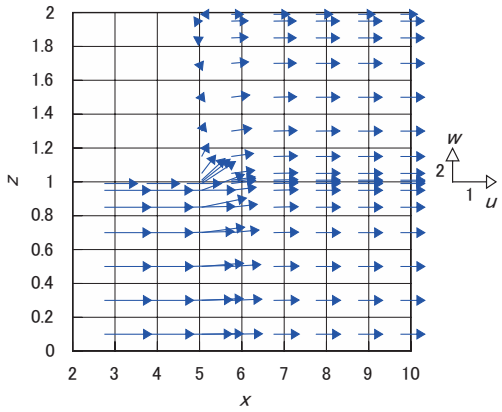


Fig. 3 Velocity ($u$,$w$) in $x$-$z$ plane at $y$=0.05

Figure 3 shows the velocity vector ($u$, $w$) distribution in the $x$-$z$ plane at $y$=0.05 for the range of $x$=2 to 10. Except for the region downstream of the expansion, a fully-develop flow velocity profile appears in both the small channel and the large channel. In the region just downstream of the expansion, i.e. 5<x<6, the low-flow or reverse-flow region appears.

Figures 4 and 5 show the induced electric current vector ($j_x$, $j_y$) distribution in the $x$-$y$ plane at $z$=0.05 and 1.875, respectively, for the range of $x$=2 to 10. In fully-develop flow regions except for the region near to the expansion, the electric induced currents are uniform along the $x$-axis and flow in negative $y$-direction in the fluid bulk region, as shown in Fig. 4. However, in the regions close to the expansion, the induced electric currents flow largely in negative $y$-direction in the fluid bulk region from $x$=3.5 to $x$=6, as shown in Fig. 4, and flow largely in positive $y$-direction in the low-flow or reverse-flow region from $x$=5 to $x$=7, as shown in Fig. 5. This increase in the induced electric current in the fluid bulk region from $x$=3.5 to $x$=6 results in increases in the Lorentz force and thus the MHD pressure drop.

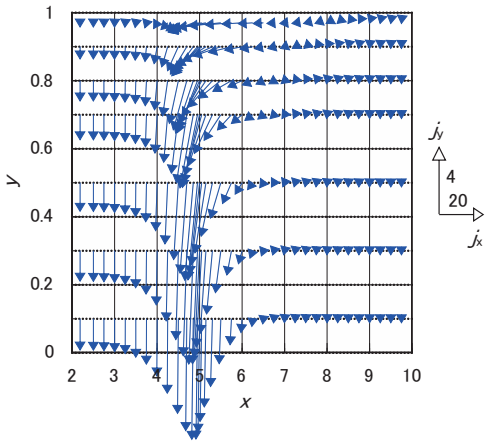


Fig. 4 Induced current ($j_x$,$j_y$) in $x$-$y$ plane at $z$=0.05

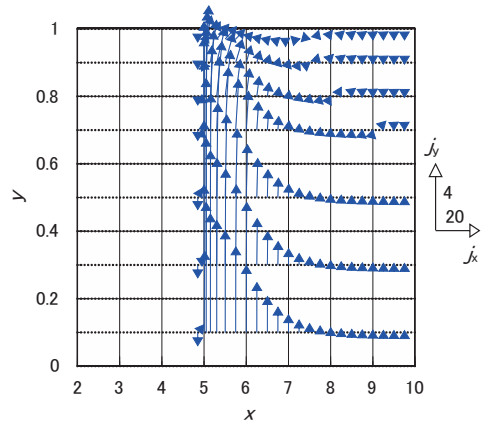


Fig. 5 Induced current ($j_x$,$j_y$) in $x$-$y$ plane at $z$=1.875

## 4. Conclusions

A large loss coefficient, i.e. a large MHD pressure drop, for the sudden expansion is calculated. The large loss coefficient is due to increase in the induced current in the region near to the sudden expansion. This result is in contrast to the sudden expansion in the direction perpendicular to the applied magnetic field, in which the loss coefficient is nearly zero.

## References

[1] H. Kumamaru, Y. Fujiwara, *Proc. JSME/ASME/ SFEN 7th Int. Conf. on Nuclear Engineering (ICONE-7)*, (1999), ICONE-7041.

[2] H. Kumamaru, K. Itoh, Y. Shimogonya, *Proc. The 24th Int. Symp. on Transport Phenomena (ISTP-24)*, (2013), (7 pages).

# OS1: The Second International Symposium on Innovative Energy Research Ⅰ
# Core Technology for Advanced Energy Devices

Eleventh International Conference on Flow Dynamics
October 8-10, 2014, Sendai, Miyagi, Japan

# Multiscale Si-based Materials for Photovoltaic Applications

Noritaka Usami, Isao Takahashi, Supawan Joonwichien, Satoru Matsushima, Yusuke Hoshi, and Kosuke Hara
Graduate School of Engineering, Nagoya University
Furocho, Chikusa-ku, Nagoya 464-8603, Japan

**ABSTRACT**

We review our recent research activities in multiscale Si-based materials for photovoltaic applications. The topic includes our attempt to realize high-quality multicrystalline Si ingot by originally developed floating cast method, integration of photonic nanostructures in crystalline Si solar cells for advanced light management, $BaSi_2$ as a novel material for Si-based thin film solar cells.

## 1. Introduction

Harvesting energy directly from sunlight using solar cells is recognized as an essential component for sustainable society. Various materials are being investigated for solar cells including Si, $CuInGaSe_2$, CdTe, III-V compound semiconductor, organic molecules, pervskites, and so on [1]. Although annual global production of solar cells reached more than 30GW, further increase of the production capacity is necessary since the accumulated installation above 1TW is required to provide power generation as one of the major energy sources. Therefore, materials for solar cells should be earth abundant. Since Si is the second abundant material in the earth's crust, Si, which is the dominant base material for solar cells, will be the mainstream also in the future. To accelerate the deployment of solar cells, innovations based on Si to lower costs/watt and/or increase the conversion efficiency are necessary.

In this contribution, we will introduce our recent research activities to develop various Si-based materials from bulk to nanomaterials for solar cell applications.

## 2. High-quality Multicrystalline Si Ingot

One of our attempts is to develop a novel crystal growth technique to permit realization of high-quality multicrystalline Si ingot, which is of equivalent quality with monocrystalline Si. The technique should have advantages in terms of production yield compared with Czochralski method. For this purpose, we have proposed "floating cast method [2]" and try to implement the technique to realize large-scale ingot to produce practical size wafers [3].

The concept of the floating cast method is to control the crystal growth and microstructures by utilizing dendrite crystals from the top of Si melt in a crucible with minimizing the contact of the ingot with the inner wall until the melt is entirely solidified. We can expect that the grain size will become larger by limiting the number of nucleation sites at the top center of the Si melt. In addition, grain boundary character can be controlled to suppress generation of dislocations by controlling the contact angle between adjacent dendrite crystals at the initial stage of the crystal growth. This can be achieved by introducing in-plane temperature gradient around the surface of the melt simply by modification of heat insulators [4]. Purposely designed double crucibles can be used to avoid the strong contact of the ingot with the bottom wall of the crucible at the final stage of solidification [5]. All these mechanisms are successfully applied to an industrial-scale furnace, and we realized large-scale multicrystalline Si ingot (Fig.1) to permit to obtain practical size wafers.

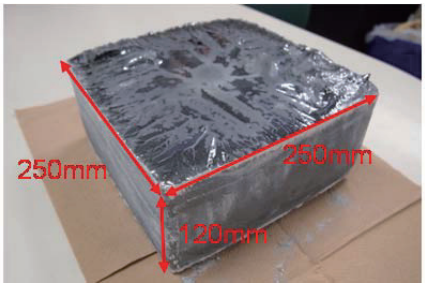


Fig. 1 A typical multicrystalline Si ingot grown by the floating cast method.

## 3. Photonic Nanocrystals Coupled with Quantum Dots

The conversion efficiency of crystalline silicon solar cells reached 25.6% with an advanced cell concept using back-contact heterojunction [6], which is almost the theoretical limit of single-junction solar cells. In order to drastically improve the performance of the solar cell, various novel concepts are proposed and extensively studied. As one of the concepts, we have recently proposed to integrate unique nanostructures to consist of photonic nanostructures coupled with Ge quantum dot multilayers in crystalline Si solar cells [7]. The unique nanostructures can be fabricated by combination of the bottom-up crystal growth and the top-down wet-etching as shown in Fig.2. Growth of Ge/Si multilayers results in self-organized formation of vertically aligned Ge quantum dots if appropriate growth conditions are chosen. In-plane modulation of strains and materials composition lead to self-modulated etching rate against a specific solution. Therefore, a simple maskless wet-etching of Ge/Si multilayers could result in formation of the unique nanostructures.

There are a number of advantages in the solar cell. By controlling geometry of the photonic nanostructures, we could control the surface reflection as well as internal reflection, which would lead to enhancement of optical absorption [8]. The interaction of the photonic

Corresponding author: Noritaka Usami
*E-mail address*: usa@numse.nagoya-u.ac.jp

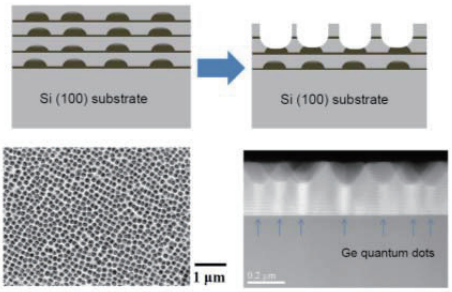


Fig. 2 (Upper row) Schematic illustration of our simple fabrication process (Lower row) A typical top-view SEM image and cross-sectional TEM image of photonic nanostructures coupled with Ge quantum dots

nanostructures with Ge quantum dots could improve the absorption of the near-infrared light, which is transparent to Si. Type-II Ge/Si heterointerfaces could separate photogenerated electrons and holes to reduce recombinations during transport. To fully take advantages, it is of crucial importance to establish a technology to control geometry of the photonic nanostructures and to implement the nanostructures in crystalline Si solar cells with minimized thermal budget.

For this purpose, we performed systematic study to investigate the impact of the structural parameters of the quantum dot multilayers [9], choice of the growth temperature [10], and etchant [11] on the geometry of the photonic nanostructures.

In addition, efforts to decrease thermal budget are underway to implement the photonic nanostructures in crystalline Si solar cells. For example, phosphorus thermal diffusion is carried out before growth of Ge/Si multilayers. Subsequently, growth of Ge/Si multilayers were performed at much lower temperature compared with the phosphorus thermal diffusion. Another attempt to apply heterojunctions with hydrogenated amorphous Si layers is also underway.

## 4. $BaSi_2$ as a novel earth-abundant absorber for thin film solar cells

We also attempt to develop a novel earth-abundant absorber $BaSi_2$ for thin film solar cells. $BaSi_2$ has a suitable band gap (1.3 eV [12]) for single-junction solar cells. The absorption coefficient at 1.5eV amounts to over $10^5 cm^{-1}$, which is more than two orders of magnitude larger than that of crystalline Si. In addition, we have recently shown that $BaSi_2$ films have a long bulk minority-carrier lifetime of 14 μs [13], which is enough long for solar cell applications. Both n- and p-type dopants [14-16] are already found. All these prove the potential of this material.

We are now trying to fabricate pn junction to demonstrate operation of the solar cell based on $BaSi_2$. In addition, an attempt is underway to establish a simple route to fabricate $BaSi_2$ thin film on large-area low-cost substrates, which is of crucial importance for practical applications.

This work was supported in part by the New Energy and Industrial Technology Development Organization (NEDO) of Japan, and Japan Science and Technology Agency (JST).

**References**

[1] M.A. Green, K, Emery, Y. Hishikawa, W. Warta, and E.D. Dunlop, *Prog. Photovolt: Res. Appl.,* 22 (2013) 1－9.
[2] Y. Nose, I. Takahashi, W. Pan, N. Usami, K. Fujiwara, and K. Nakajima, *J. Cryst. Growth,* 311 (2009) 228.
[3] N. Usami, I. Takahashi, K. Kutsukake, K. Fujiwara, and K. Nakajima, *J. Appl. Phys.,* 109 (2011) 083527.
[4] I. Takahashi, S. Joonwichien, S. Matsushima, and N. Usami, *Proceedings of the 23rd International Photovoltaic Science and Engineering Conference,* 1-P-54 (2013).
[5] S. Joonwichien, I. Takahashi, S. Matsushima, N. Usami, *Prog. Photovolt: Res. Appl.,* 113 (2013) 133503.
[6] http://panasonic.co.jp/corp/news/official.data/data.dir/2014/04/en140410-4/en140410-4.html
[7] N. Usami, W. Pan, T. Tayagaki, S. T. Chu, J. Li, T. Feng, Y. Hoshi, and T. Kiguchi, *Nanotechnology,* 23 (2012) 185401.
[8] T. Tayagaki, Y. Hoshi, Y. Kishimoto, and N. Usami, *Opt. Express,* 22, (2014) A225-A232.
[9] Y. Hoshi, W. Pan, T. Kiguchi, K. Ooi, T. Tayagaki, and N. Usami, *Jpn. J. Appl. Phys.,* 52 (2013) 080202.
[10] O. Aonuma, , Y. Hoshi1, Tayagaki, A. Novikov, D. Yurasov, and N. Usami (unpublished).
[11] Y.Hoshi, T.Tayagaki, T.Kiguchi, N.Usami, *Thin Solid Films,* 557 (2014) 338-341.
[12] K. Toh, T. Saito, and T. Suemasu, *Jpn. J. Appl. Phys.,* 50 (2011) 068001.
[13] K.O. Hara, N. Usmi, K. Nakamura, R. Takabe, M. Baba, K. Toko, and T. Suemasu, *Appl. Phys. Express*, 6 (2013) 112302.
[14] M. Kobayashi, Y. Matsumoto, Y. Ichikawa, D. Tsukada, and T. Suemasu, *Appl. Phys. Express,* 1 (2013) 051403.
[15] M. Ajmal Khan, K.O. Hara, W. Du, M. Baba, K. Nakamura, M. Suzuno, K. Toko, N. Usami, and T. Suemasu, *Appl. Phys. Lett.,* 102 (2013) 112107.
[16] M. Ajmal Khan, T. Saito, K. Nakamura, M. Baba, W. Du, K. Toh, K. Toko, and T. Suemasu, *Thin Solid Films,* 522 (2012) 95.

Eleventh International Conference on Flow Dynamics
October 8-10, 2014, Sendai, Miyagi, Japan

# Nanotechnology for Future Green Nanodevices

Seiji Samukawa[1,2,3]
[1] Institute of Fluid Science, Tohoku University, 2-1-1 Katahira, Aoba-ku, Sendai 980-8577, Japan
[2] WPI-AIMR, Tohoku University, Japan
[3] Japan Science and Technology Agency (JST), CREST, Japan

**ABSTRACT**

High density and regularly arranged 2-dimensional array of silicon nanodisk, a sub-10nm-silicon-nano-disk (Si-ND) structure, was fabricated using the bio-template (ϕ7-nm-etching-mask) and damage-free chlorine (Cl) neutral beam (NB) etching. In this structure, the controllable band gap energy (from 2.2eV to 1.4eV) and high photon absorption coefficient (>$10^5$ $cm^{-1}$) could be obtained at RT. This structure can be used to develop high efficiency and inexpensive silicon quantum dot solar cells.

## 1. Introduction

Recently, an all-silicon tandem solar cell comprising a quantum dot superlattice (QDSL) has attracted much attention due to its potential to breakthrough the Shockley-Queisser limit.[1,2] One of the advantages of the QDSL is that the required energy band gap for each cell can be engineered by changing the quantum dot size.[3] Reportedly, the maximum conversion efficiency can be improved up to 47.5% for three-cell tandem stacks.[4] However, not only the uniformity and control of QD size but also of the spacing between QDs are equivalently essential to generate the miniband in the QDSL for carrier transport.[5] The ideal spacing between QDs is approximately 2 nm or less in the $SiO_2$ matrix.[6] The technique widely used to fabricate the Si quantum dot superlattice is depositing alternately multiple layers of amorphous silicon-rich oxide ($SiO_x$, $x$<2) and stoichiometric silicon dioxide ($SiO_2$) by sputtering or plasma-enhanced chemical vapor deposition followed by annealing at a high temperature.[6] However, the results showed nonuniform dot size and dot spacing.

To address these problems, we have developed a sub-10nm-silicon-nano-disk (Si-ND) structure using the bio-template ($\phi$7-nm-etching-mask) and damage-free chlorine (Cl) neutral beam (NB) etching.[7] The fabricated ND had a quantum effect, i.e. Coulomb staircase, at room temperature (RT). Two geometrical parameters of thickness and diameter in Si-ND can be independently controlled. Interestingly, the quantum effect of a single Si-ND is strongly dependent on its thickness, while almost independent of its diameter.[7] In this study, a 2D Si ND array with a high-density and well-ordered arrangement could be fabricated by using bio-template and an etching process combined with nitrogen trifluoride ($NF_3$) gas/hydrogen radical treatment ($NF_3$ treatment) and Cl NB etching. In this structure, the controllable band gap energy (from 2.2eV to 1.4eV) and high photon absorption coefficient (>$10^5$ $cm^{-1}$) could be obtained at RT by controlling the Si-ND structure.

Corresponding author: Seiji Samukawa
*E-mail address*: samukawa@ifs.tohoku.ac.jp

## 2. Fabrication of High-density 2D Array of Si-ND

The fabrication of a 2D Si-ND array using the bio-template and damage-free NB etching [7] is schematically shown in Fig. 1(a). The steps are as follows: multilayer films of 1.4-nm $SiO_2$, several nm-thick poly-Si and 3-nm $SiO_2$ (the 3-nm $SiO_2$ was fabricated by our developed neutral beam oxidation at a low temperature of 300 ºC and is called NBO $SiO_2$ hereafter) were sequentially prepared on a Si wafer as shown in Figs. 1(1), (2), and (3), respectively; (4) a 2D array of ferritin molecules (protein including iron oxide core (Fe-core) in the cavity) was placed through directed self-organization on the surface of NBO $SiO_2$; (5) ferritin protein shells were removed by heat treatment in oxygen atmosphere to obtain 2D Fe-core as a template; (6) etching was carried out using a $NF_3$ treatment and Cl NB etching to remove NBO $SiO_2$ and poly-Si, respectively; (7) and finally 2D Fe core was removed by using hydrochloric solution. The sample underwent $NF_3$ treatment for 30 min to remove NBO $SiO_2$ and NB etching for 90 seconds to remove 4-nm poly-Si. Figure 2 shows a SEM image of the top view of the sample after etching. We can see that the 2D Si-ND array has a high-density (>$7 \times 10^{11}$ $cm^{-2}$) and well-ordered arrangement. The 2D array is what remained after etching, proving that a good-quality 2D Si-ND array was successfully fabricated using the bio-template and Cl NB etching with $NF_3$ treatment. We performed $NF_3$ treatment to investigate the controllability of the ND diameter, i.e. the spacing between NDs. When the $NF_3$ treatment times were 15 and 30 min, the average gaps were about 1 and 3 nm ($G_{ii}$ and $G_{iii}$), and the diameters were about 10 and 8 nm ($D_{ii}$ and $D_{iii}$), respectively . These results suggest that the spacing between adjacent NDs can be controlled by changing the $NF_3$ treatment time, which also indicates that the formation of miniband in a 2D Si-ND array can be controlled. Although the spacing control by $NF_3$ treatment is accompanied by inevitable changes in diameter, the diameter changes do not affect the quantum effect, which was proven in a previous work.[7]

## 3. Optical Properties of 2D Si-ND Array

The absorption properties of the structure were studied by measuring the transmission for samples by

UV-vis-NIR. The absorption coefficient has been calculated in accordance with the equation below

$$T = e^{-\alpha d} \quad (1)$$

$\alpha$ being the absorption coefficient, $d$ the total thickness of the ND thickness and surface oxide thickness (3-nm thick), and $T$ the transmittance of light passing through the structure. Figure 3(a) shows the results of an absorption coefficient of the structure as a function of ND thickness. We found that the absorption spectra strongly depend on the ND thickness and the absorption edge is blue-shifted when the ND thickness decreases due to the quantum size effect. Additionally, the absorption coefficient (>$10^5$ $cm^{-1}$) of 2D Si-ND array is extremely high, and therefore it is possible to obtain sufficient absorption if the NDs can be integrated into the 3rd dimension. To determine the optical band gap energy of the structure, the Tauc formula was used:

$$(\alpha\, h\, v)^{1/2} = A\,(h\, v - E_g)\,, \quad (2)$$

where $A$ is a constant, $h$ is Planck's constant, $v$ is frequency, $E_g$ is the band gap energy, and $n$ is 1/2 in the case of indirect allowed and forbidden electronic transitions. The Tauc formulation as a function of ND thickness is plotted in Fig. 3(b). As the ND thickness changes from 2 to 12 nm, the $E_g$ could be controlled from 2.2 to 1.4eV as shown in Fig. 4. From these results, we found that $E_g$ could be certainly controlled by simply changing ND thickness by thin-film deposition in our proposed fabrication. Based on the processes, all-Si tandem solar cells assembled with 3D ND array fabricated by stacking 2D Si-ND array as schematically shown in Fig. 5 could be constructed.

## 4. Conclusions

We created a 2D Si-ND array with a high-density and well-ordered arrangement using bio-template and an advanced etching process that included $NF_3$ treatment and damage-free Cl NB etching. The spacing between Si NDs can be controlled in the structure by changing $NF_3$ treatment time. The $E_g$ can be easily controlled by changing the ND thickness during thin film deposition. The absorption coefficient of single layer 2D Si-ND is comparable to that of 3D QDSL. Our proposed processes for 2D Si-ND array and stacked ND are very feasible for the all-Si tandem solar cells comprising QDSL.

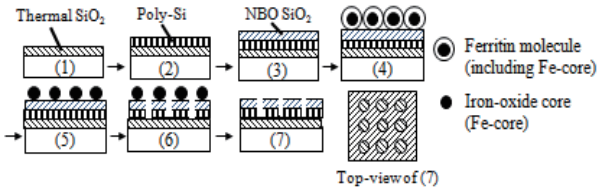


Fig. 1 Fabrication flow of 2 dimensional Si nano-disk array by bio-template and chlorine neutral beam etching.

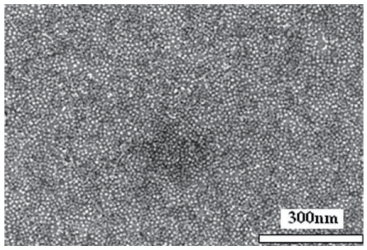


Fig. 2 SEM images of 2 dimensional Si nano-disk array fabricated by Cl neutral beam etching with bio-template.

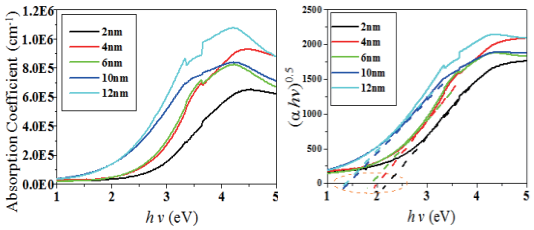


Fig. 3 (a) Absorption coefficient (b) Tauc plot of 2 dimensional Si nano-disk array with different nano-disk thicknesses from 2 nm to 12 nm.

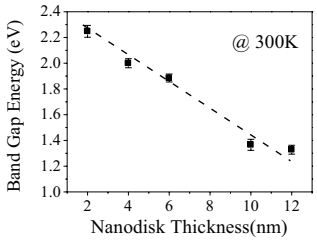


Fig. 4 Band gap energy ($E_g$) of nano-disk with different Si nano-disk thicknesses by using UV-vis-NIR.

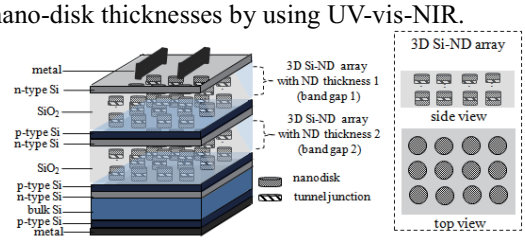


Fig. 5 Scheme of all-silicon tandem solar cell assembled with 3 dimensional Si nano-disk array.

## References


[1] W. Shockley and H. J. Queisser, *J. Appl. Phys.* 32 (1961) 510.

[2] M. A. Green, *20th EU-PVSEC (2005),* 1AP.1.1.

[3] A. Kongkanand, K. Tvrdy, K. Takechi, M. Kuno, and P. V. kamat, *J. Am. Chem. Soc.* 130 (2008) 4007.

[4] G. Conibeer, M. Green, E.-C. Cho, D. Konig, Y.-H. Cho, T. Fangsuwannarak, G. Scardera, E. Pink, Y. Huang, T. Puzzer, S. Huang, D. Song, C. Flynn, S. Park, X. Hao, D. Mansfield, *Thin Solid Films* 516 (2008) 6748.

[5] A. J. Nozik: *Physica* E 14 (2002) 115.

[6] Y. Kurokawa , S. Miyajima, A. Yamada, and M. Konagai, *Jpn. J. Appl. Phys.* 45 (2007) L1064.

[7] S. Samukawa, T. Kubota, C.-H. Huang, T. Hashimoto, M. Igarashi, K. Nishioka, M. Takeguchi, Y. Uraoka, T. Fuyuki, and I. Yamashita, *Appl. Phys. Express* 1 (2008) 074002.

Eleventh International Conference on Flow Dynamics
October 8-10, 2014, Sendai, Miyagi, Japan

# Optical Investigation of the Effect of Mini-band Formation on the Carrier Collection Mechanism in a Strain-balanced InGaAs/GaAsP MQW Solar Cell Structure

Tetsuo Ikari[1], Taketo Aihara[1], Masakazu Sugiyama[2], Yoshiaki Nakano[3] and Atsuhiko Fukuyama[1]
[1]DEAP, University of Miyazaki, 1-1 Gakuen-Kibanadai, Miyazaki 889-2192, Japan
[2]School of Engineering, The University of Tokyo, Bunkyo-ku, Tokyo 113-0032, Japan
[3]RCAST, The University of Tokyo, Bunkyo-ku, Tokyo 113-0032, Japan

**ABSTRACT**

Strain-balanced InGaAs/GaAsP multiple quantum well structure is useful for further increasing the solar cells conversion efficiency. Optical measurements were carried out and the miniband formation between the quantum wells was confirmed. We found that the rate equations for the carriers in the single quantum well might be applicable for understanding the carrier transport mechanism even when the band conduction through the miniband became dominant.

## 1. Introduction

Quantum effect is recently recognized as a new candidate for the solar cell structures. This increases drastically the photoelectric conversion efficiency more than the Shockley–Queisser limit. One typical example is a semiconductor quantum dot which leads to carrier confinement in the delta-function like density of states and the following miniband formation useful for the carrier transport. The tandem structure and the intermediate-band formation are materialized by using these structures. Another candidate is multi-junction solar cells. Decreasing the current mismatch problem inevitable in the conventional multi-junction structure such as InGaP/InGaAs/Ge, the insertion of a multiple quantum-well (MQW) structure into the absorbing layer of the solar cells is promising for further developing ultra-high-efficiency solar cells. This is because the MQW can extend the sunlight absorption region towards the longer-wavelength region and enhance the short circuit current. Furthermore, fabrication techniques such as molecular-beam epitaxy or atomic layer epitaxy are now remarkably developed and complex stacking structure made of high quality materials are more easily prepared than that for the quantum dots. However, MQW itself functions as carrier recombination centers for photo generated carriers at the same time, which degrades both the open-circuit voltage and the fill factor.

In this study, we report on the optical properties of strain-balanced InGaAs/GaAsP MQWs embedded in the GaAs solar cell [1] by using a piezoelectric photothermal (PPT) and photoreflectance (PR) spectroscopies. Since the PPT method is very useful to obtain an absorption spectrum of extremely thin film such as a single quantum well [2], we employed this to the present MQW structures. Effect of the miniband formation on the carrier transport, the mechanism of carrier releasing from the well, and the recombination within the well are studied for understanding the dynamics of the photo excited carriers in the QW solar cells.

Corresponding author: Tetsuo Ikari
*E-mail address*: ikari@cc.miyazaki-u.ac.jp

## 2. Experimental

Two kinds of *p-i-n* GaAs solar cell structure samples with different absorbing layers were grown on an *n*-type GaAs substrate using a metal-organic vapor phase epitaxy [3]. The absorbing layer of the first sample had 10 stacks of strain-balanced InGaAs/GaAsP MQWs composed of a 7.4-nm-thick $In_{0.23}Ga_{0.77}As$ wells and 10.8-nm-thick $GaAs_{0.61}P_{0.39}$ barriers. The second sample consisted of the absorbing layer with 50 stacks of super lattice (SL) structures composed of a 3.7-nm-thick $In_{0.23}Ga_{0.77}As$ wells and 5.4-nm-thick $GaAs_{0.61}P_{0.39}$ barriers. For investigating the miniband formation more systematically, we prepared additional samples with strain-balanced $In_{0.21}Ga_{0.79}As/GaAs_{0.59}P_{0.41}$ layer where the thickness of the barrier layers were changed from 5.3 to 1.9 nm.

For the PPT measurement, a lead-zirconium-titanate (PZT) disk as a detector was attached directly to the GaAs substrate surface with a coupling paste [4]. The frequency modulated probe light through a monochromator was illuminated the absorbing layer side of the sample. When the electrons are photo generated, they recombine through radiative or non-radiative transition. The PPT detects heat and elastic waves caused by this non-radiative recombination using the PZT detector. In the PR measurements, a 15-mW Ar+ laser was used as a modulation source. The modulated reflectivity signal was detected and calculated by using a Kramers–Kronig analysis. All measurements were carried out at room temperature.

## 3. Results and Discussion

PPT spectra of MQW and SL samples at room temperature are shown in Fig. 1. Since no signal below the band gap of GaAs, 1.42 eV, was observed for the sample without any QW, the observed peaks were due to the MQW and SL structure. The optical absorption region extended towards the longer-wavelength region which resulted in an increase of the PPT signals. For the MQW sample, a step-like spectrum accompanied by several peaks was observed. We concluded that the peaks at 1.238 and 1.336 eV are excitonic transitions between the localized levels in the well. For the SL sample, a broad peak around 1.333eV was observed and this may be explained by the presence of the miniband. Figure 1 also shows the PR modulus spectrum for the SL sample. Two

peaks at 1.326 and 1.345 eV were observed. These may be the energies at the bottom and the top of the miniband formed by decreasing the barrier thickness. We could, then, estimated the miniband widths as 19 meV. Simple Kronig–Penney model calculation was also carried out for evaluating the miniband width. It was 16 meV and was comparable to the experimental results.

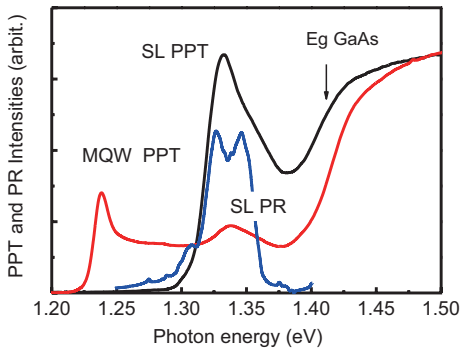


Fig. 1 PPT and PR spectra of MQW and SL samples.

Next we consider how the photo-generated carriers are collected to the electrode for generating photovoltaics. In the case of single quantum well without any interaction between the QW, three mechanisms might be considered for carrier relaxation. They are radiative and non-radiative recombination within the well, and the thermally escaping from the well. As we have reported, these phenomena are investigated by a photoluminescence (PL), a PPT and a surface photovoltage (SPV) spectroscopy, respectively [5]. Since the thermal activation for the confined carriers dominate the process, we have carried out the experiments for the temperature dependences of the PL, PPT and SPV signal intensities. The rate equations were then formularized and the activation energies were estimated by curve fitting procedures. Figure 2 shows the experimental results and the fitted curves by the proposed rate equation.

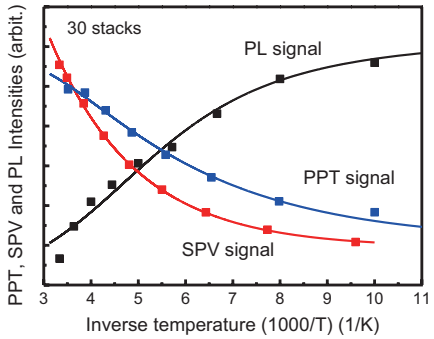


Fig.2 Temperature dependences of PL, PPT and SPV signal intensities. Curves are the best fitted results.

The estimated activation energy of 69 meV for carrier escaping from the well agreed with the energy difference between the quantized level and the top of the barrier. However, in the case of MQW and SL, the appearance of the carrier tunneling path and the formation of the miniband should be taken into account in the rate equation. When the band conduction occurs, this drastically enhances the carrier transport through QW and the carrier collection efficiency further increases.

## 4. Concluding Remarks

Miniband formation in the strain-balanced InGaAs/GaAsP quantum well solar cells are studied by using the PL, PPT, SPV and PR measurements. When the thickness of the barrier layer decreases, we observed the peak broadening in the PPT and the peak splitting in the PR spectra. This concluded the miniband formation in the present MQW and SL structure. The rate equations for the carrier transport in the single QW might be applicable even when the band conduction term becomes dominant.

## References

[1] M. Sugiyama, K. Sugita, Y. Wang, and Y. Nakano, *J. Cryst. Growth* 315 (2011) 1.
[2] M. Kondow, M. Uchiyama, M. Morifuji, S. Wu, H. Momose, S. Fukushima, A. Fukuyama, and T. Ikari, *Appl. Phys. Express* 2 (2009) 041003.
[3] H. Fujii, K. Watanabe, M. Sugiyama, and Y. Nakano, *Jpn. J. Appl. Phys*., 51 (2012) 10ND04.
[4] T. Ikari, S. Fukushima, Y. Ohta, A. Fukuyama, S. D. Wu, F. Ishikawa, and M. Kondow, *Phys. Rev.* B 77 (2008) 125311.
[5] T. Ikari, A. Fukuyama, H. Fujii, T. Aihara, Y. Yokoyama, M. Kojima, M. Sugiyama and Y. Nakano, *29th EU-PVSEC*, (2013) Paris France. 1AV.2.23

Eleventh International Conference on Flow Dynamics
October 8-10, 2014, Sendai, Miyagi, Japan

# Nanoscale Flow Phenomena of Materials in Polymer Electrolyte Fuel Cell

Takashi Tokumasu[1]
[1] Institute of Fluid Science, Tohoku University
2-1-1, Katahira, Aoba-ku, Sendai, Miyagi, 980-8577, Japan

**ABSTRACT**

In this paper, we analyzed nanoscale transport phenomena in a membrane electrode assembly (MEA) of polymer electrolyte fuel cell (PEFC) by large scale molecular dynamics (MD) simulations. Especially, the relation between the transport phenomena of proton and water and the structure of water cluster in polymer electrolyte membrane (PEM), oxygen permeability of ionomer in catalyst layer (CL), and transport phenomena of water droplet in a nano pore were simulated, and nanoscale transport characteristics were analyzed in detail to achieve the design of new concept of MEA for next generation PEFC.

## 1. Introduction

These days Polymer Electrolyte Fuel Cell (PEFC) is expected to be the next-generation power supply system. It is necessary to make the transport of proton, oxygen and water in PEFC faster to develop its performance and efficiency. Computational Fluid Dynamics (CFD) based on macroscopic transport equation is often used as a conventional numerical analysis. A Membrane Electrode Assembly (MEA) of PEFC, however, consists of Gas Diffusion Layer (GDL), Micro Porous Layer (MPL), Catalyst Layer (CL), and Polymer Electrolyte Membrane (PEM), which includes many nanoscale structures. Therefore the characteristics of flow phenomena in MEA cannot be analyzed at the macroscopic point of view. Molecular simulation is a powerful tool to analyze these phenomena.

In this study we have analyzed these nanoscale flow phenomena by large scale Molecular Dynamics (MD) method. Especially, the relation between the transport phenomena of proton and water and the structure of water cluster in PEM, oxygen permeability of ionomer in catalyst layer, and transport of water droplet in a nano pore were simulated, and the flow characteristics were analyzed in detail. In the analysis of proton transfer in PEM, we considered not only Vehicle mechanism but also Grotthus mechanism and the diffusivity of proton at various water contents was estimated. The structure of water molecule in a PEM was evaluated, and the results were compared with those data obtained by experiment. With regards to the oxygen permeability of ionomer, we estimated the dependence of water content or the kind of polymer on the oxygen permeability. With regards to the transport mechanism of water droplet in a nano pore, we focus on the difference of this mechanism from the macroscopic equations.

## 2. Proton Transfer in PEM

In this study, a revised empirical valence bond (EVB) model is developed based on the previous study of EVB model reported by Walbran et al.[1]. The new EVB model shows a proton diffusion coefficient of 0.57 Å$^2$/ps, which is comparable with the previous models of multistate EVB which is 0.72 ± 0.05 Å$^2$/ps. In addition, we have applied the new EVB model to Nafion system and performed an atomistic analysis of the transport of hydronium ions and water molecules in the nanostructure of hydrated Nafion membrane by systematically changing the hydration level using classical molecular dynamics simulations. After annealing procedure, the simulated density agreement with experiment is within 1.3 % for various water contents and the trends that density decreases with increasing hydration level are reproduced. The diffusion coefficients of hydronium ion against water content is shown in Fig. 1. Using this simulation method, the diffusivity and its relation with the structure of water cluster was analyzed in detail.

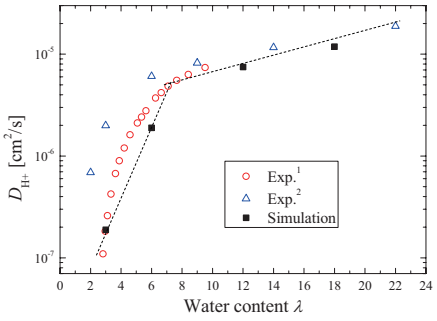


Fig. 1 The diffusion coefficient of hydronium ion in PEM against water content.

## 3. Oxygen Permeation in Ionomer

In this research, oxygen permeation of ionomer in CLs of the cathode side was simulated by molecular dynamics simulation. This system includes Pt wall, hydrocarbon or fluorocarbon membrane, water, hydronium ion and oxygen molecule. In this simulation, the platinum surface was placed at the bottom of simulation box and ionomer which was composed of hydrated hydrocarbon or fluorocarbon molecules were placed on the surface. The number of oxygen molecule was set so that the number corresponds to 10MPa in the gas space. The number of oxygen in the gas space was constant to keep the pressure in the gas space constant (10MPa) and permeated molecules were returned to gas space. By this procedure, we generated a constant oxygen mass flux in the ionomer. From these simulations we found that the hydrocarbon gathers toward the catalyst surface rather than fluorocarbon membrane. This phenomenon occurs because Pt strongly attracts the other molecules. Moreover, many

Corresponding author: Takashi Tokumasu
*E-mail address*: tokumasu@ifs.tohoku.ac.jp

water molecules distribute on high density hydrocarbon which are attracted by Pt. The density distribution of ionomer of fluorocarbon on Pt surface is shown in Fig. 2. Moreover, the oxygen permeability of ionomer decreases with the increase in water content, which is an opposite tendency of bulk membrane.

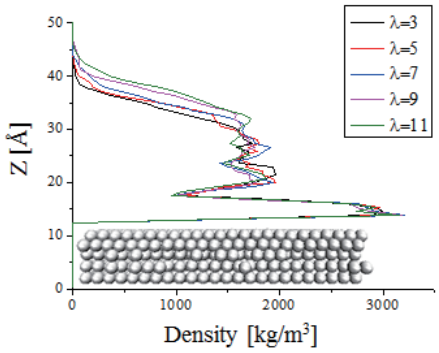


Fig. 2 Density distribution of ionomer on Pt surface.

## 4. Transport of Water Droplet in a Nano Pore

In this study, molecular dynamics simulations were performed to evaluate the shear stress acted on a nanoscale water droplet from solid walls, and the dependence of channel size on shear stress was clarified. Moreover, we also discussed the limit of macroscopic hydrodynamic models. From these results, we obtained basic knowledge about the transport properties of water droplets in micro-porous layer and gas diffusion layer.

Considering constant flow, the friction force between a water droplet and a solid wall can be described by a mechanical parameter as

$$F = 2\alpha W_x W_y V_{\text{slip}} + 2\sigma(\cos\theta_b - \cos\theta_a) \quad (1)$$

where $\alpha$ is a friction coefficient between a water droplet and a solid surface, $W_x$ and $W_y$ are the contact lengths in the $x$ and $y$ direction, $\theta_a$ and $\theta_b$ are the advancing and receding contact angles, $V_{\text{slip}}$ is the slip velocity of water on solid walls, $\sigma$ is the surface tension coefficient, respectively. The important point of this equation is the independence of channel width on shear stress. In order to evaluate the dependence of the channel width on shear stress, we carried out molecular dynamics simulations of different-sized micro channels. This model was composed of two alpha graphite-like slabs with honeycomb structure, and the distance between nearest atoms was set at 3.0 Å. This bond length was determined by adjusting the contact angle of the water droplet on the solid wall. The MPL material used in experiments is highly hydrophobic, and the contact angle is around 145 degree. The macroscopic contact angle derived by the surface tension coefficient between the water droplet and the wall is about 150 degree, which agrees with the experimental value. From the analysis, we found that the shear stress decreases with increasing the channel size, while it is almost constant in hydrodynamics. The results are shown in Fig. 3. This difference occurs due to the normal pressure generated by the surface tension, which is called "Laplace pressure". When the channel size is in a few nm, the pressure difference between liquid phase and vapor phase by the surface tension is in tens of MPa, since this difference is in a few Pa order in case of an mm channel. In the case of nm channel, it can be seen that the effect of the surface tension on the region far from the liquid-vapor interface cannot be ignored. By considering the Laplace pressure, we corrected the macroscopic equation shown in Eq. (1). The results are also shown in Fig. 3. As shown in this figure, the corrected equation can express the dependence of tangential force on channel size well.

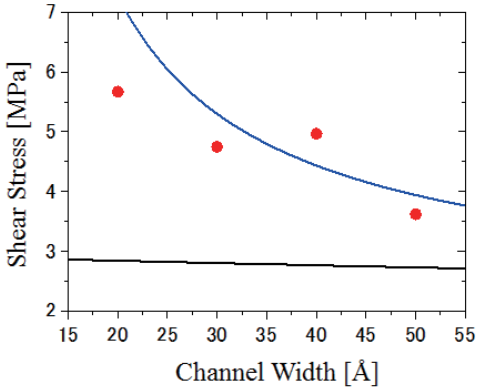


Fig. 3 The dependence of channel width on shear stress acted on a nanoscale water droplet. Dot: MD, Black: Eq. (1), Blue: corrected Eq. (1)

## 5. Concluding Remarks

We performed large scale molecular dynamics simulations to analyze the nanoscale transport phenomena of materials in MEA of PEFC. Especially, the relation between proton and water transport and water structure in polymer electrolyte membrane, oxygen permeation through ionomer in cathode catalyst layer, and transport mechanism of water droplet in a nano pore, all of which affects the efficiency of PEFC, were analyzed. From the results of this simulation we have obtained the knowledge about the nanoscale flow phenomena of proton, oxygen and water, which is difficult to analyze from the results by experiment. The knowledge helps us to design the new concept of MEA for higher efficiency and lower cost of PEFC in the future.


## Acknowledgements

This work was supported by the New Energy and Industrial Technology Development Organization (NEDO) of Japan and the simulations were mainly performed using the supercomputer of the Institute of Fluid Science (IFS) of Tohoku University.


## References


[1] S. Walbran, A.A. Kornyshev, *Journal of Chemical Physics*, 114 (2001) 10039-10048.

# Effective Reaction Area in Solid Oxygen Fuel Cell Cathodes

Koji Amezawa[1], Yoshinobu Fujimaki[2], Takashi Nakamura[1], Kiyoharu Nitta[3],
Yasuko Terada[3], Fumitada Iguchi[2], Hiroo Yugami[2], Keiji Yashiro[4], Tatsuya Kawada[4]
[1]Institute of Multidisciplinary Research for Advanced Materials (IMRAM), Tohoku University
Katahira 2-1-1, Aoba-ku, Sendai, Miyagi, 980-8577, Japan
[2]Graduate School of Engineering, Tohoku University
Aaramaki 6-6-01, Aoba-ku, Sendai, Miyagi, 980-8579, Japan
[3]Japan Synchrotron Radiation Research Institute (JASRI)
Kouto 1-1-1, Sayo-cho, Sayo-gun, Hyogo 679-5198, Japan
[4]Graduate School of Environmental Studies, Tohoku University
Aaramaki 6-6-01, Aoba-ku, Sendai, Miyagi, 980-8579, Japan

**ABSTRACT**

A novel *in situ* X-ray absorption spectroscopic technique, which enables us to measure X-ray absorption spectra with high special resolution of less than 1 μm while elevating temperature, controlling atmospheric conditions, and passing electrical current through the materials, were developed. This so-called *in situ* micro XAS technique was applied to observe the reaction distribution in the electrode of solid oxide fuel cells under operation. A model patterned electrode was proposed and fabricated with the help of MEMS. It was shown that *in situ* micro XAS measurements of the patterned electrode are useful for further quantitative discussion on SOFC electrode reactions.

## 1. Introduction

Solid oxide fuel cell (SOFC) is one of promising next-generation energy conversion devices, having many advantages such as high energy conversion efficiency, effective usage of exhaust heat and good fuel flexibility. In Japan, a 1 kW-class of SOFC systems have been commercialized since 2011, demonstrating excellent performance so far. However, it is pointed out that there exist some technological problems which have to be solved before their full-scale commercialization: *i.e*. improving durability and reliability, lowering operation temperature, reducing fabrication costs and so on. In order to meet these problems, improvement of the cell performance based on understanding of electrode reactions was highly required. For direct observation of reactions in SOFC, *in situ* analysis using spectroscopic technique is useful. However, it is not easy for conventional spectroscopic technique to be applied to the SOFC system working at high temperature under specific atmospheric conditions.

From the backgrounds mentioned above, in recent years, we have been developing in situ X-ray absorption spectroscopic techniques, which enable us to measure X-ray absorption spectra at elevating temperature under controlled atmospheres and polarization. In this work, the *in situ* micro X-ray absorption spectroscopy (XAS) was introduced. By means of this novel *in situ* spectroscopy, we tried to experimentally clarify the reaction distribution and the effective reaction area in SOFC cathodes (air electrodes). Such a novel analytical technique is expected to give us more direct and quantitative information on electrode reactions in SOFC.

Corresponding author: Koji Amezawa
*E-mail address*: amezawa@tagen.tohoku.ac.jp

## 2. Method

Figure 1 shows a picture of experimental setup for *in situ* micro XAS [1]. The experiments were carried out at the beam line BL37XU, SPring-8, JASRI, Japan. In this beam line, the incident X-ray from the synchrotron can be focused into micro or sub-micro meter size. The beam size used in this work was typically 0.8 x 0.5 μm. By using the focused X-ray beam, XAS measurements with the high special resolution of less than1 μm became possible.

In the center of the sample holder, a small electrochemical cell having three electrodes (working, reference, and counter electrodes) was placed together with small electrical furnace. The working electrode was a patterned $La_{0.6}Sr_{0.4}CoO_{3-\delta}$ (LSC) dense film. Porous platinum was used as the reference and counter electrodes. $Ce_{0.9}Gd_{0.1}O_{1.95}$ (GDC) was used as an electrolyte. The sample holder was covered by a Kapton film so that the atmosphere around the sample could be controlled by the gas flow. XAS measurements at the Co *K*-edge were performed in the temperature range of 873-973 K and the oxygen partial pressure $p(O_2)$ range of $10^{-4}$-1 bar under cathodic polarization of -0.1-0.25 V.

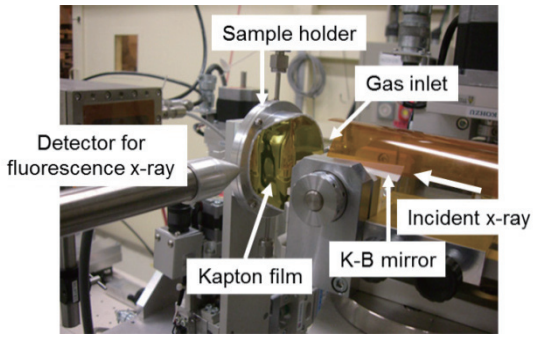


Fig. 1 Experimental setup for *in situ* micro X-ray absorption spectroscopy at BL37XU, SPring-8.

The patterned LSC electrode used in this work is schematically illustrated in Fig. 2. In this patterned electrode, an electrode/electrolyte interface with a width of 1.5 μm was fabricated with an interval of 300 μm. The incident X-ray was hit from the top of the electrode. XAS measurements were repeated under constant temperature, $p(O_2)$ and polarization conditions by changing the measurement position as a function of the distance from the interface. The position of the interface was determined from the results of X-ray fluorescence elementary mapping, which was performed in prior to each XAS measurement.

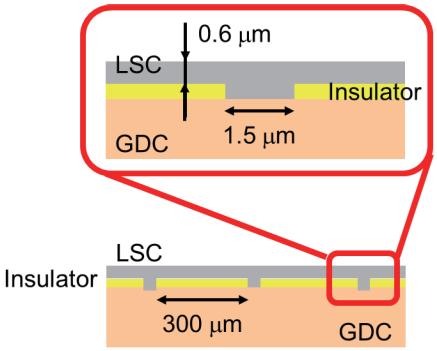


Fig. 2 Schematic illustration of the patterned LSC electrode for in situ micro XAS measurements.

## 3. Results and Discussion

Figure 3 shows Co *K*-edge XANES spectra observed at different positions in the LSC patterned electrode under cathodic polarization of -0.22 V at 973 K and $p(O_2)$ = 1 bar. The absorption edge was slightly shifted toward lower energy with decreasing the distance from the electrode/electrolyte interface. The shift of the absorption edge to lower energy reflected the partial reduction of Co ions in the oxide film. These results demonstrated the effectively low $p(O_2)$ condition, *i.e.* reducing situation, was achieved in the vicinity of the interface due to the cathodic polarization even in a constant ambient $p(O_2)$ atmosphere. As the distance from the interface increased, the absorption edge was gradually shifted to higher energy. And at the distance of longer than 20 μm, the absorption edge was almost equivalent to that observed under open circuit condition. The amount of the effective $p(O_2)$ change corresponded to how much reaction current we have. Thus, the results in Fig. 3 clearly showed us that electrode reaction preferentially takes place in the vicinity of the electrode/electrolyte interface, and no reaction at the positions far from the interface. It was found that the effective reaction area was approximately 20 mm in the case of the pattern LSC electrode under applied temperature, $p(O_2)$ and polarization conditions.

Throughout this work, it was concluded that the effective reaction area in SOFC electrode can be directly and quantitatively evaluated from *in situ* micro XAS measurements. The developed technique would be a powerful tool to clarify what kinds of factors determine the effective reaction area.

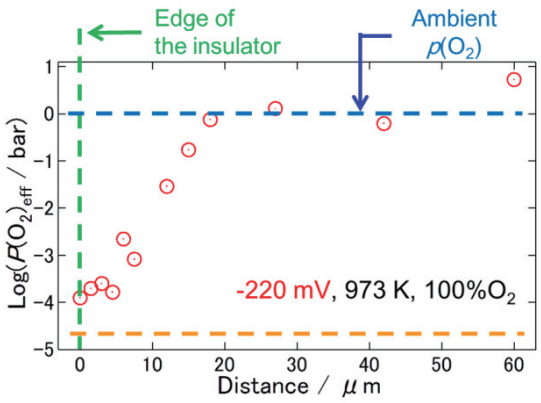


Fig. 3 In situ Co K-edge XANES spectra observed at different positions in the patterned $La_{0.6}Sr_{0.4}CoO_{3-\delta}$ dense film electrode under cathodic polarization of -0.22 V at 973 K and $p(O_2)$ = 1 bar.


## Acknowledgements

A part of this work was carried out under the financial support of CREST from the Japan Science and Technology Agency (JST) and Grant-in-Aid for Scientific Research of MEXT, Japan.


## References


[1] K. Amezawa, Y. Orikasa, T. Ina, A. Unemoto, M. Sase, H. Watanabe, T. Fukutsuka, T. Kawada, Y. Terada, Y. Uchimoto, *Electrochem. Soc. Trans.*, 13(26) (2008) 161-164.

[2] Y. Fujimaki, H. Watanabe, Y. Terada, T. Nakamura, K. Yashiro, S. Hashimoto, T. Kawada, K. Amezawa, *Electrochem. Soc. Trans.*, 57(1) (2013) 1925-1932.

Eleventh International Conference on Flow Dynamics
October 8-10, 2014, Sendai, Miyagi, Japan

# Multi-Objective Design Exploration Toward Intelligent Energy Management

Koji Shimoyama[1]
[1]Institute of Fluid Science, Tohoku University
2-1-1 Katahira, Aoba-ku, Sendai 980-8577, Japan

**ABSTRACT**

This paper describes a design approach named multi-objective design exploration (MODE) and a planned application of MODE to a smart home system that controls energy units economically and ecologically. Different from conventional design optimization, MODE aims to find various optimal solutions in a multi-objective sense, and visualize a structure of design space as a panorama. This application can be a trigger to step up on intelligent energy management, which will be based on the state-of-the-art energy technologies in future.

## 1. Introduction

Energy management includes planning and operation of energy-related production and consumption units. Objectives are resource conservation, climate protection, and cost savings while the users have permanent access to the energy they need. It is connected closely to environmental management, production management, logistics, and other established business functions. In addition, energy management is highly significant in disasters, which may risk a shortage or outage of electric power supply as seen in the Fukushima Daiichi nuclear disaster in March 2011.

A promising solution for energy management is a smart grid. It is an intelligent and modernized electrical grid that uses analog or digital information and communications technology to gather and act on information, such as information about the behaviors of suppliers and consumers, in an automated fashion to improve the efficiency, reliability, economics, and sustainability of the production and distribution of electricity.

Design of a smart grid can be considered as an optimization problem as follows. The design variables are how to construct the grid, how to combine energy units, how to control energy units in time, etc. The objective functions are to minimize the cost of energy consumption, to maximize the efficiency in energy production, etc. The constraints are to meet user demand, to observe the specification limits of energy units, to observe energy-related laws, etc.

Such an optimization problem containing multiple objective functions involves a set of compromising solutions, largely known as the *Pareto-optimal* or *non-dominated* solutions, while a single-objective problem involves a unique optimal solution. The non-dominated solutions reveal trade-off information among different objectives. They are optimal in the sense that no other solutions in the search space are superior to them when all objectives are taken into consideration.

Although design optimization is considered to aim to find a unique optimal solution, it is not satisfactory for real-world designers. They should always prepare various design candidates for the compatibility of various disciplines that may be conflicted with each other. Non-dominated solutions obtained from multi-objective optimization seem to be helpful for designers to solve multi-disciplinary compatibility issues.

Thus, the author's research group has been proposing a design approach named *multi-objective design exploration (MODE)* [1], which is different from conventional multi-objective design optimization. MODE aims to find various optimal solutions in a multi-objective sense (i.e., non-dominated solutions), and visualize a structure of design space as a panorama. The information about design space structure helps in understanding characteristic features (*e.g.*, tradeoffs between competing objectives), in discovering important design knowledge (*e.g.*, existence of design sweet spots), and in decision making on a design strategy (*e.g.*, selection of design candidates to be adopted). This paper describes the fundamentals of MODE, and a planned application of MODE to energy management.

## 2. MODE

Figure 1 shows a flowchart of MODE. The first step defines the problem of design optimization by formulating the design variables, objective functions, and constraint functions. Then, the second step collects the data of objective and constraint functions in the whole design space. Many sample points are generated in the design variable space, and then objective and constraint functions are evaluated at each sample point, which corresponds to a different combination of design variable values, by numerical simulations.

Using the sample dataset, the third step constructs surrogate models, which approximate the responses of objective functions to design variables in the form of simple algebraic functions. These algebraic functions are derived to interpolate the initial sample points with *real* values of the objective and constraint functions given by high-fidelity numerical simulations, and thus the surrogate models can promptly give an *estimate* of function values at other points with unknown values of the objective functions.

The fourth step searches for non-dominated solutions

Corresponding author: Koji Shimoyama
*E-mail address*: shimoyama@edge.ifs.tohoku.ac.jp

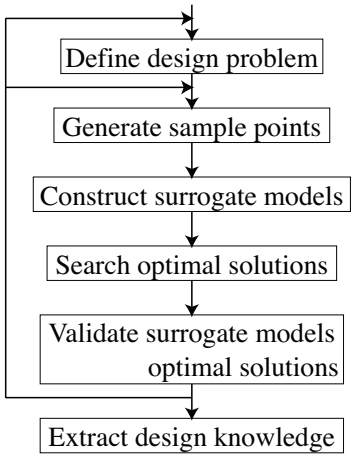

Fig. 1 Flowchart of MODE.

on the surrogate models through the multi-objective optimization using the genetic algorithm (GA) [2]. GA is a search heuristic that mimics the process of natural evolution. It deals with a population of multiple solutions to be searched for in parallel, and thus it can mostly reach for a global optimum in single-objective optimization. With regard to multi-objective optimization, GA can efficiently obtain a set of non-dominated solutions in a single optimization run.

The fifth step checks the accuracy of the surrogate models constructed in the third step. The surrogate accuracy also affects the quality of the non-dominated solutions obtained in the fourth step. If the surrogate models do not have sufficient accuracy, new sample points are generated and added to the current sample dataset. Using the updated sample dataset, the surrogate models are reconstructed and the multi-objective optimization is performed again (i.e., back to the second, third, and fourth steps). Iteration of this update strategy is expected to achieve the improvements in surrogate model accuracy as well as the exploration of global non-dominated solutions.

The final step analyzes the dataset of non-dominated solutions to extract design information. For two-dimensional or three-dimensional data, design information can be interpreted simply by plotting the data points. However, it becomes virtually impossible when the data have more than three dimensions. Therefore, MODE performs data mining [3] in the high-dimensional data that consist of many design variables, objective functions, and constraint functions. Data mining has its origins in the field of information science (pattern recognition, artificial intelligence, etc.). This can rewrite characteristic features in complex data into different formats, which are easy to understand (numerals, images, texts, etc.). To ensure reliability and variety of extracted design information, MODE adopts several different methods for data mining.

## 3. Application to Energy Management

Using MODE, the author is planning the energy management in a smart home system shown in Fig. 2. It contains various energy units (electric vehicle, photovoltaics, cogeneration, etc.). The objectives are to minimize total energy cost and to minimize $CO_2$ emission subject to the demand for heat, electricity, and hot water by temporally controlling the energy units through an entire day. In this application, MODE is expected to suggest to residents how to use and control energy units according to their various preferences balanced between economy and ecology.

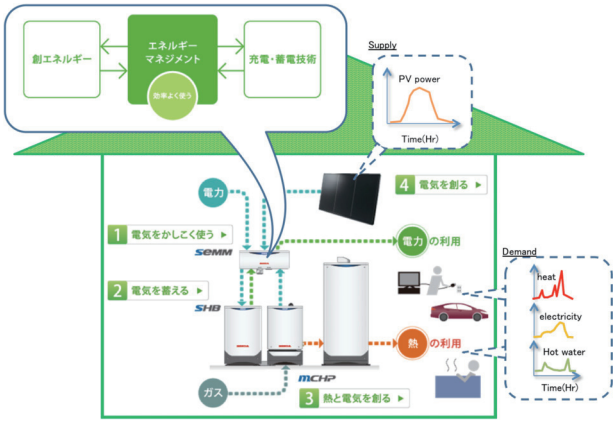

Fig. 2 Smart home system [4].

## 4. Summary

This paper stated the fundamentals of MODE and its planned application to a smart home system. This application can be a trigger to step up on intelligent energy management, which will be based on the state-of-the-art energy technologies (solar cell, secondary cell, fuel cell, etc.) in future. The author will give a talk that includes preliminary results of this application in the conference.

## References

[1] S. Obayashi, S. Jeong, K. Chiba, *AIAA Paper*, 2005–4666 (2005).

[2] K. Deb, *Multi-Objective Optimization using Evolutionary Algorithms* (2001).

[3] M. Kantardzic, *Data Mining: Concepts, Models, Methods and Algorithms* (2003).

[4] http://www.honda.co.jp/hshs/ (in Japanese).

Eleventh International Conference on Flow Dynamics
October 8-10, 2014, Sendai, Miyagi, Japan

# Solid State Lithium Ion Battery Devices for Mobile Applications

Itaru Honma
IMRAM, Tohoku University
Katahira 2-1-1, Aoba-ku, Sendai, Miyagi, 980-8577, Japan

**ABSTRACT**

Designing a lithium ion battery (LIB) with a three-dimensional device structure is crucial for increasing the practical energy storage density by avoiding unnecessary supporting parts of the cell modules. Here, we describe the superior secondary battery performance of the bulk all-solid-state LIB cell and a multilayered stacked bipolar cell with doubled cell potential of 6.5 V, for the first time.

## 1. Introduction

Large energy storage devices that can store electrical energy efficiently are essential for utilizing renewable energy. Lithium ion batteries (LIBs) with high energy density are an example of such devices and have attracted significant attention in recent times. LIBs are currently used not only for electronic devices but also for mobile applications such as electric and hybrid vehicles. Conventional LIBs use organic liquid electrolytes, and there is possibility of liquid leaks and flamable. Such problems must be resolved for practical and safe use of LIBs. The use of all-solid-state secondary batteries that use solid electrolytes, which are flame resistant and do not pose the risk of liquid leaks, can be cited as a possible solution to these problems. In addition, all-solid-state lithium secondary batteries make it possible to design bipolar layer-built cells fabricated by layering batteries within a single package. The energy density in such batteries is expected to be higher than that in LIBs with organic liquid electrolytes.

## 2. Method

In this work, we defined a quasi-solid-state electrolyte (QSE) [1-3] as the one that can be treated as a solid but that can maintain liquid-like high ionic conductivity. In cases when $SiO_2$ was used, it was possible to fabricate quasi-solid-state electrolytes by making composites of ionic liquid [Li (G4)] [TFSA] and oxide nanoparticles with $x$ = 75, where $x$ is the volume fraction of the composites as reported earlier [4]. Additionally, the other nanoparticles such as γ-$Al_2O_3$, α-$Al_2O_3$, and $ZrO_2$ have been studied and were found successful for QSE formation. Quasi-solidification was possible at $x$ = 75 with particle diameters of 10–30 nm for $CeO_2$ and 5 nm for γ-$Al_2O_3$. This is believed to be because when particle diameters are small, the specific surface area becomes greater and the interaction area between the oxide nanoparticle surfaces and [Li (G4)] [TFSA] liquids becomes larger. The quasi-solid electrolyte powder and free-standing film sheets fabricated using $CeO_2$ with particle diameters of 10–30 nm and using γ-$Al_2O_3$ with a particle diameter of 5 nm are shown in Fig. 1. The liquid and oxide nanoparticles in quasi-solid electrolytes as observed using TEM and the resultant images confirmed that Al (indicating γ-$Al_2O_3$) and F ([Li (G4)] [TFSA]) were evenly distributed. The ion conducting properties of quasi-solid-state electrolytes have been studied by AC impedance analysis.

Corresponding author: Itaru Honma
*E-mail address*: i.honma@tagen.tohoku.ac.jp

## 3. Results and Discussion

The results of the electrical conductivity measurement are shown in Fig. 1. Electrical conductivities of liquid [Li (G4)] [TFSA] and of quasi-solid-state electrolytes that are prepared using $SiO_2$, $CeO_2$, and γ-$Al_2O_3$ and that can be treated as solids when the volume fraction of the [Li (G4)] [TFSA] liquid is 75 vol%, are shown. The electrical conductivity of quasi-solid electrolytes of $CeO_2$ and γ-$Al_2O_3$ prepared in this study was lower than that of the [Li (G4)] [TFSA] liquid but was higher than that of the [Li (G4)] [TFSA]/$SiO_2$ quasi-solid-state

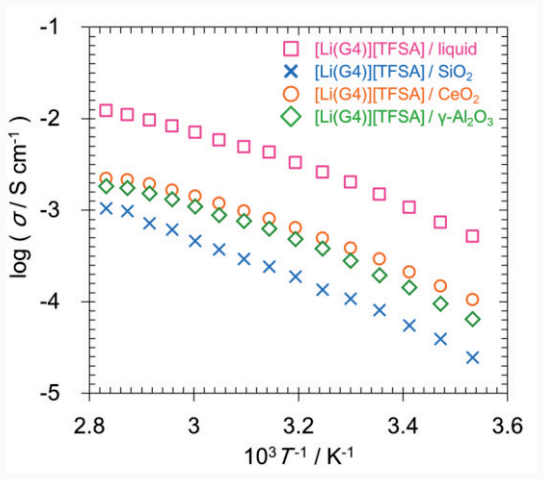


Fig. 1 Ion conducting properties of various quasi-solid state electrolytes employing ionic liquids Li(G4)/TFSA and nanoparticles of $SiO_2$, $CeO_2$ and γ-$Al_2O_3$, respectively.

electrolyte. $CeO_2$ interacts with cations and anions and has been reported to have significant effects on the transference number and electrical conductivity. Furthermore, it has also been reported that by adding an appropriate amount of γ-$Al_2O_3$ particles, the electrical conductivity of $Li^+$-conducting polymer electrolytes can be improved and favorable interfaces with Li metal can be realized. The SEM observation results for the cross sections of the fabricated all-solid-state battery using quasi-solid-state electrolyte prepared using γ-$Al_2O_3$ are shown in Fig. 2. Red and blue represent P and Al, respectively, and each of these elements is derived from $LiFePO_4$ in the cathode composite and γ-$Al_2O_3$ in the

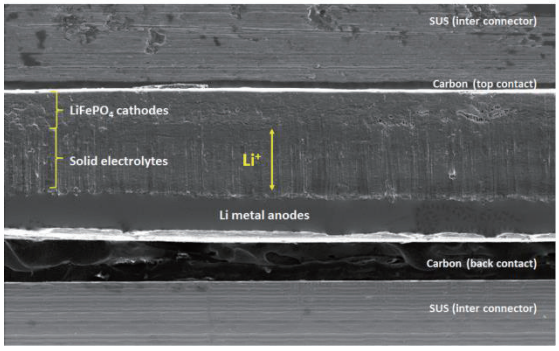


Fig. 2 Cross section SEM image of all solid state LIB, where Li metallic anode and quasi-solid state electrolyte and $LiFePO_4$ cathodes have been employed.

quasi-solid electrolyte. The cross-sectional SEM images confirmed that continuous dense interfaces were formed between the surface of the cathode composite and quasi-solid-state electrolyte.

The cycle characteristics of the single-layer all-solid-state lithium secondary battery at 1.0 C are shown in Fig. 3. No capacity degradation occurred up to 1,500 cycles and electric discharge capacity was maintained for all quasi-solid-state electrolytes composed of any oxide nanoparticles. The cathode utilization rate of devices that used [Li (G4)] [TFSA]/$SiO_2$, [Fi (G4)] [TFSA]/$CeO_2$, and [Li (G4)] [TFSA]/γ-$Al_2O_3$ was 74%, 47%, and 76%, respectively. Results indicating high conductivity for [Li (G4)] [TFSA]/$CeO_2$ quasi-solid-state electrolytes led us to anticipate an increase in the discharge capacity owing to the cathode utilization rate being higher than that for other systems. However, the actual results were different from those anticipated. The resistance of the interface between the cathode composite and the quasi-solid-state electrolyte is considered one of the reasons for this difference in results.

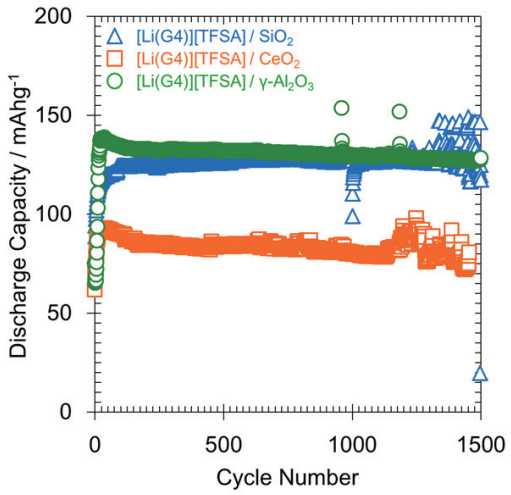


Fig. 3 Charge/discharge cycle performance of the various all solid state LIB while the three different kind of nanoparticles of $SiO_2$, $CeO_2$, and γ-$Al_2O_3$ were used for the quasi-solid electrolytes, respectively.

The electric charging and discharging profiles of the double-layer all-solid-state lithium secondary battery fabricated using [Li (G4)] [TFSA]/γ-$Al_2O_3$ quasi-solid-state electrolytes after 50 cycles are shown in Fig. 4. Current densities of 128, 101, 111, and 54 mAh $g^{-1}$ were used for rates of 0.1, 0.2, 0.4, and 1.0 C, respectively, with the coulombic efficiency being 96% or more in all cases. The plateau electrical potentials were observed to be double of those for the single-layer type, which is positioned around 3.3 V, indicating that the layered cell was operating well without any short- circuiting of the single cell inside the single package. The packaging energy densities of single and double cell are 122 mWh/kg- cell and 176 mWh/kg-cell, respectively. The bipolar stacked cell thus had a higher energy density. The electric discharge capacity at 1.0 C and 50 cycles was found to be 137 mAh $g^{-1}$ with the single-layer type, while that of the double-layer type was significantly lower at 54 mAh $g^{-1}$. The cycle characteristics of the double-layer all-solid-state lithium secondary battery at various C rates are and small capacity deterioration was observed at all C rates, even beyond 100 cycles.

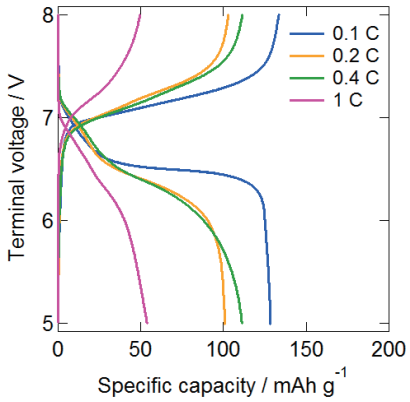


Fig. 4 Charge/discharge cycle performance of the double layer stacked bipolar solid state LIB after 50 cycles with various C-rate of 0.1, 0.2, 0.4 and 1.0, respectively.

## 4. Concluding Remarks

In this study, [Li (G4)] [TFSA] quasi-solid-state electrolytes were prepared using various oxide nanoparticles and electrochemical characteristic evaluations and device evaluations were conducted. Quasi-solid-state electrolytes using $CeO_2$ and γ-$Al_2O_3$ showed ion conducting properties at the practical level and single-layer all-solid-state lithium secondary batteries using such quasi-solid-state electrolytes discharged in a stable manner even after 1,000 cycles. Favorable operation was observed for the double-layer bipolar all-solid-state secondary batteries with the quasi-solid-state electrolytes prepared using γ-$Al_2O_3$.

## References

[1] Unemoto, A., Ogawa, H., Ito, S. & Honma, *J. Electrochem. Soc.* 160, (2013) A138–A147
[2] Yuki Hanyu, Itaru Honma, *Scientific Reports*, 2, (2012) 453
[3] Seitaro Ito, A. Unemoto, H. Ogawa, Takaaki Tomai, Itaru Honma, *J. Power Sources* 208, (2012) 271
[4] Takahiro Matsuo, Yoshiyuki Gambe, Yan Sun and Itaru Honma, *Scientific Reports*, 4, (2014) 6084

# Complex Hydrides for All-Solid-State Rechargeable Battery Electrolytes

Atsushi Unemoto[1], Motoaki Matsuo[2], Tamio Ikeshoji[1], Shin-ichi Orimo[1,2]
[1]WPI-Advanced Institute for Materials Research (WPI-AIMR), Tohoku University
2-1-1 Katahira, Aoba-ku, Sendai 980-8577, Japan
[2]Institute for Materials Research, Tohoku University
2-1-1 Katahira, Aoba-ku, Sendai 980-8577, Japan

**ABSTRACT**

In this study, a stable battery operation of a bulk-type all-solid-state lithium rechargeable battery was demonstrated by using the $LiBH_4$ electrolyte. The rechargeable battery, $TiS_2/LiBH_4$ | $LiBH_4$ | Li, could be stably operated at least for 50 discharge–charge cycles without any capacity fading over the battery operation. The results suggest that the complex hydride electrolyte is a promising candidate material for the next generation all-solid-state lithium rechargeable battery.

## 1. Introduction

Complex hydrides consisting of metal cations, and complex anions are represented by the general formula, $M(M'H_n)$. Here, examples of the metal cation, $M$, are $Li^+$, $Na^+$, $Mg^{2+}$, and so forth, and those of the complex anion, $(M'H_n)$, are $[BH_4]^-$, $[NH_2]^-$, $[AlH_4]^-$, and so on [1]. Despite of a classical application as a reducing agent in chemical processes, the energy storage-related functions including solid-state hydrogen storage [1,2], lithium storage [3,4], and fast ionic-conduction [5–7] attract attentions. In this paper, we focus on the all-solid-state rechargeable battery assembly on the basis of the fast Li-ionic conduction in the typical complex hydride, $LiBH_4$.

In the field of battery research, the enhancement of the energy density of the rechargeable device is one of the emerging technological challenges for large-scale applications including automotive applications and stationary uses for load leveling. Therefore, all-solid-state lithium rechargeable battery is considered as one of the next generation battery. This is because, the solid-state electrolytes allows a flexible battery design, i.e., a bi-polar stacking structure. As a result, the energy density is enhanced [8]. In addition, the solid-state electrolyte accepts the broader choice of the active materials that are used for the battery assembly compared to the conventional liquid electrolyte type battery. This also leads to the enhanced energy density. With this background, various solid-state electrolytes including the oxides and the sulfides have been developed so far, the materials that exhibit both the high lithium ionic conductivity ($> 10^{-3}$ S $cm^{-1}$) and the electrochemical stability in the voltage range for the battery operation are limited to a few cases [9]. Therefore, development of a new electrolyte family is highly desired.

In recent years, our research group has figured out that $LiBH_4$ possess high lithium ionic conductivity accompanied by the phase transition from orthorhombic to hexagonal systems at elevated temperatures and around 390 K [5]. At above 390 K, the $LiBH_4$ exhibits the fast lithium ionic conductivity that exceeds $2 \times 10^{-3}$ S $cm^{-1}$, and high electrochemical stabilities [6]. The fast Li-ionic conduction is realized by intrinsically induced mobile ionic defects, and subsequent Li-site percolation with low activation energy for Li migration [10–12]. The complex hydrides are expected to be the new solid-state electrolyte family for the rechargeable battery assembly [7]. In this study, a bulk-type all-solid-state lithium rechargeable battery was assembled to examine the validity to use the complex hydride electrolyte for a rechargeable battery assembly.

Corresponding author: Atsushi Unemoto
*E-mail address*: unemoto@imr.tohoku.ac.jp

## 2. Experimental

Commercially available powders of $TiS_2$ (99.9 %, Sigma-Aldrich) and $LiBH_4$ (≥ 95 %, Sigma-Aldrich) were used as the positive electrode active material and the solid-state electrolyte, respectively. The powders were mixed in a desired ratio, and then, used for a composite positive electrode. The powders of $LiBH_4$ and the composite positive electrode were placed in an 8-mm-diameter die, and uniaxially pressed to form a bi-layer compact. A lithium foil was used as a negative electrode, and placed on the opposite surface of the composite positive electrode. The resultant all-solid-state rechargeable battery was placed in a stainless-steel electrochemical cell as schematically illustrated in Fig. 1.

The microstructure of the composite positive electrode surface was observed by scanning electron microscopy (SEM, JSM-6009, JEOL Ltd.). The battery performance was evaluated at 393 K and 0.1 C in the cut-off voltage range of 1.6–2.7 V.

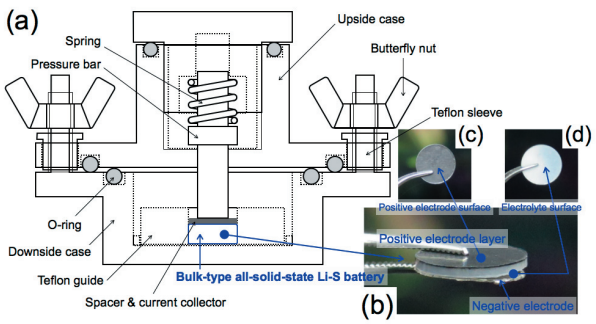


Fig. 1 (a) A schematic illustration of experimental setup for the battery test, and (b)–(d) photographs of the bulk-type all-solid-state rechargeable battery assembled in this study.

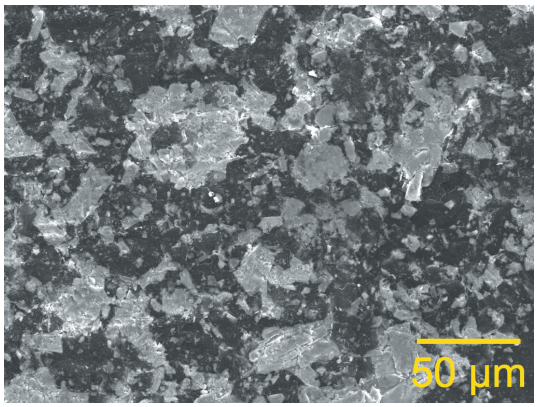

Fig. 2 Typical SEM image of a $TiS_2/LiBH_4$ composite positive electrode surface. Bright and dark parts represent $TiS_2$ and $LiBH_4$ phases, respectively.

## 3. Results and Discussion

One of the important factors that lead to a success of the stable battery operation of the all-solid-state lithium rechargeable battery relies if the tightly and closely attached interface is formed between the electrode active material and the electrolyte particles in the composite positive electrode layer. The complex hydrides, typically $LiBH_4$, are highly deformable. Therefore, a uniaxial pressing at room temperature is thought to be sufficient to induce the $TiS_2/LiBH_4$ interface that allows smooth electrochemical reaction in the composite positive electrode.

Figure 2 shows typical SEM image of the $TiS_2/LiBH_4$ composite positive electrode surface. As we expected, the good interface is formed between $TiS_2$ and $LiBH_4$ phases although the compact was prepared merely by uniaxial pressing at room temperature. The results implies that the use of the complex hydride electrolyte is advantageous for the introduction of the good electrode/electrolyte interface.

Electrochemical reduction and oxidation of $TiS_2$ proceed in accordance with the following reaction,

$$TiS_2 + xLi^+ + xe^- \underset{\leftarrow}{\overset{\rightarrow}{}} Li_xTiS_2 \qquad (1)$$

where $TiS_2$ is estimated to have a theoretical capacity of 239 mAh $g^{-1}$ when $x$ varies in the range of $0 \leq x \leq 1$ [13,14].

Our battery exhibited the discharge capacities of 200 mAh $g^{-1}$, corresponding to 85 % of a $TiS_2$ utilization ratio, over the battery test. Stable discharge–charge operations at least for 50 cycles were successfully demonstrated with nearly 100 % coulombic efficiency (ratio of charge to discharge capacities) as a result of the good interface formation between $TiS_2$ and $LiBH_4$ particles. The result suggests that the complex hydride electrolytes are promising candidate material of the bulk-type all-solid-state rechargeable battery assembly.

## 4. Conclusions

In this study, the stable battery operation of the bulk-type all-solid-state lithium rechargeable battery was successfully demonstrated by using $TiS_2$, $LiBH_4$, and Li as the positive electrode, the solid-state electrolyte, and negative electrode, respectively. Our cell realized the high $TiS_2$ utilization ratios with nearly 85 % without any capacity fading owing to the tight and close interface formation between $TiS_2$ and $LiBH_4$ particles in the composite positive electrode. The results suggest that the complex hydrides are promising candidate electrolyte materials for the bulk-type all-solid-state rechargeable battery assembly.

## Acknowledgements

Valuable collaboration and communication with G. Nogami, M. Tazawa, and Dr. M. Taniguchi of Mitsubishi Gas Chemicals Co., Ltd. are highly appreciated. This study was supported by the Target Project 4 of WPI-AIMR, Tohoku University; JSPS KAKENHI Grant Number 25220911; and the Advanced Low Carbon Technology Research and Development Program (ALCA) of the Japan Science and Technology Agency (JST).

## References

[1] S. Orimo, Y. Nakamori, J. R. Eliseo, A. Züttel, C. M. Jensen, *Chem. Rev.* 107 (2007) 4111.
[2] Y. Nakamori, K. Miwa, A. Ninomiya, H.–W. Li, N. Ohba, S. Towata, A. Züttel, S. Orimo, *Phys. Rev. B* 74 (2006) 045126.
[3] W. Zaidi, J.–P. Bonnet, J. Zhang, F. Cuevas, M. Latroche, S. Couillaud, J.–L. Bobet, M. T. Sougrati, J. C. Jumas, L. Aymard, *Int. J. Hydrogen Energ.* 38 (2013) 4706.
[4] J. Zhang, W. Zaidi, V. Paul-Boncour, K. Provost, A. Michalowicz, F. Cuevas, M. Latroche, S. Belin, J.–P. Bonnet, L. Aymard, *J. Mater. Chem. A* 1 (2013) 4706.
[5] M. Matsuo, Y. Nakamori, S. Orimo, H. Maekawa, H. Takamura, *Appl. Phys. Lett.* 91 (2007) 224103.
[6] M. Matsuo, S. Orimo, *Adv. Energ. Mater.* 1 (2011) 161.
[7] A. Unemoto, M. Matsuo, S. Orimo, *Adv. Funct. Mater.* 24 (2014) 2267; *ChemInform* 24 (2014) 29.
[8] Y. Kato, K. Kawamoto, R. Kanno, M. Hirayama, *Electrochemistry* 80 (2012) 749.
[9] N. Kamaya, K. Homma, Y. Yamakawa, M. Hirayama, R. Kanno, M. Yonemura, T. Kamiyama, Y. Kato, S. Hama, K. Kawamoto, A. Mitsui, *Nat. Mater.* 10 (2011) 682.
[10] T. Ikeshoji, E. Tsuchida, K. Ikeda, M. Matsuo, H.–W. Li, Y. Kawazoe, S. Orimo, *Appl. Phys. Lett.* 95 (2009) 221901.
[11] T. Ikeshoji, E. Tsuchida, T. Morishita, K. Ikeda, M. Matsuo, Y. Kawazoe, S. Orimo, *Phys. Rev. B* 83 (2011) 144301.
[12] J. S. G. Myrdal, D. Blanchard, D. Sveinbjörnsson, T. Vegge, *J. Phys. Chem. C* 117 (2013) 9084.
[13] M. S. Whittingham, *Science* 192 (1976) 1126.
[14] M. S. Whittingham, *Prog. Solid State Chem.* 12 (1978) 41.

# InGaN Quantum Nanodisks for High Efficiency Optoelectronic Devices by Combination of Bio-template and Neutral Beam Etching Processes

ChnagYong Lee[1,5], Akio Higo[2], Jitsuo Ohta[3], Ichiro Yamashita[4,5], Hiroshi Fujioka[3,5], and Seiji Samukawa[1,2,5]
[1]Institute of Fluid Science, Tohoku University
2-1-1 Katahira Aoba-ku, Sendai 980-8577, Miyagi, Japan
[2] WPI-Advanced Institute for Materials Research, Tohoku University
2-1-1 Katahira Aoba-ku, Sendai 980-8577, Miyagi, Japan
[3]Institute of Industrial Science, the University of Tokyo
4-6-1 Komaba, Meguro-ku, Tokyo 153-8505, Japan
[4]Nara Institute of Science and Technology
8916-5 Takayama, Ikoma, Nara 630-0192 Japan
[5]Japan Science and Technology Agency (JST), CREST
5 Sanbancho, Chiyoda, 102-0075, Tokyo, Japan

**ABSTRACT**

We developed a top-down method for fabricating InGaN quantum nanodisks (NDs) arrays by using bio-template and neutral beam etching (NBE) processes. Damage-free InGaN/GaN nano-pillar structures were successfully fabricated for the first time. The photoluminescence was measured and the emission originating from the NDs could be directly detected.

## 1. Introduction

Quantum Dots (QDs) using III-nitride semiconductors has attracted increasing attention as a quantum effective devices because of their theoretical improvement in performance compared to those of quantum wells and bulk. The QDs structures are usually formed by the bottom-up processes such as the metalorganic vapor phase epitaxy (MOVPE) selective area growth. However these methods have a limit of nanometer mask patterns by EB lithography. Large optical gain would be obtained for optoelectronic devices, when high-density, high-uniformity, and multiply-stacked QDs layers conditions were fulfilled but it is still a great challenge to achieve all of these conditions. Therefore, we have investigated a top-down approach for the fabrication of QDs by combining a bio-nano-process [1] and a damage-free neutral beam etching (NBE) process [2]. In this work, InGaN nanodisks (NDs) were successfully fabricated from an InGaN/GaN multiple quantum wells (MQWs) substrate.

## 2. Method

The neutral beam system consists of plasma and process chambers that are separated by an electrode with an aperture array. The electrode can effectively neutralize charged particles when the plasma particles pass through it and eliminate UV photons from the plasma. Thus, defect-free atomically flat sidewalls and anisotropic etching are observed after the neutral beam etching.

InGaN/GaN stacked layers samples were grown by pulsed sputtering deposition (PSD). A self-assembled monolayer (SAM) of ferritin proteins functionalized with polyethylene glycol (PEG-ferritin) was formed by spin-coating after conventional organic cleaning of the sample surface. The protein shell was then removed by the low temperature oxygen annealing in vacuum at 350 °C. A density of more than $1x10^{11}$ $cm^{-2}$ of iron core masks was achieved. Afterwards, the surface oxide layer was removed by the hydrogen radical treatment using an electron cyclotron resonance (ECR) radical gun. Subsequently, the sample temperature was set to room temperature, while hydrogen radicals were still flowing to the sample. Finally, etching by chlorine neutral beam was performed with optimized etching conditions. The shape (side profile and diameter) of the fabricated nano-pillar and the density were observed by scanning electron microscopy (SEM). Optical characteristic of NDs were measured by photoluminescence (PL).

Corresponding authors: Seiji Samukawa, ChangYong Lee
*E-mail address*: samukawa@ifs.tohoku.ac.jp, cylee@sammy.ifs.tohoku.ac.jp

## 3. Results and Discussion

After a 10 min etching, nano-pillars of ca. 95 nm-high, a minimum 11 nm in diameter were successfully realized with a high density of $1.0x10^{11}$ $cm^{-2}$. The PL emission of after 5 min of etching InGaN NDs was observed around 400 nm under 11 K. The emission energy of the NDs sample was blue-shifted by 30 nm compared with that of the deepest InGaN QW layers that were not etched during the process. The blue-shift is explained by taking into account the three-dimensional confinement of the wave function inside the NDs. Moreover, this demonstrates that the fabrication process of InGaAs NDs is a process that does not induce more defects.

Combining a bio-template and a neutral beam etching process has shown a great potential for the fabrication of III-nitride NDs. Moreover, the results show that, the fabricated NDs have great potential for realizing quantum level optoelectronic devices with controllable diameter and thickness.

## 4. Concluding Remarks

We fabricated a high-density nano-pillar structure

that includes InGaN NDs by using the bio-template and NBE processes. A high density (over $1.0x10^{11}$ $cm^{-2}$) and an anisotropic profile were achieved with our optimized etching conditions. The PL emission of InGaN NDs was blue-shifted compared to InGaN MQWs, establishing that NDs were defect-free. These results indicated that InGaN NDs for designable quantum energy levels were controllable with the developed approach.

**References**

[1] I. Yamashita, *Thin Solid Films*, 393 (2001) 12.
[2] S. Samukawa, *Jpn J. Appl. Phys*., 45 (2006) 2395.

# Neutral Beam Etching Of III-V Compounds For Laser Devices

Cedric Thomas[1,3], Chang Yong Lee[1,3], Yosuke Tamura[1,3], Kenichi Yoshikawa[1,3], Akio Higo[2], Ichiro Yamashita[3,4], and Seiji Samukawa[1,2,3]
[1]Institute of Fluid Science, Tohoku University
[2]WPI-AIMR, Tohoku University
2-1-1 Katahira, Aoba-ku, Sendai, 980-8577, Japan
[3]CREST Japan Science and Technology Agency
5 Sanbancho, Chiyoda-ku, Tokyo, 102-0076, Japan
[4]Nara Institute of Science and Technology
8916-5 Takayama, Ikoma, 630-0192, Japan

**ABSTRACT**

III-V compound semiconductor quantum dot (QD) optical devices have a great potential for the future of telecommunications and quantum cryptography. We developed a top-down approach for fabricating InGaAs (or GaAs) quantum nanodisks (NDs) array by combining a bio-template and a neutral beam etching process. InGaAs/GaAs (or GaAs/AlGaAs) nano-pillar structures embedding InGaAs (GaAs) NDs were successfully fabricated. Photoluminescence emission was detected from NDs after regrowth of barrier layers by metalorganic vapor phase epitaxy.

## 1. Introduction

Quantum dot (QD) lasers are one of the most promising light sources because of their theoretically improved performance compared to quantum well and bulk lasers [1]. Due to the change in the density of states caused by the three-dimensional confinement, QD lasers are expected to have high temperature stability [2], low threshold currents [3], and large modulation band width [4]. These QDs are usually formed from molecular beam epitaxy (MBE) methods. Namely, Stranski-Krastanov growth mode is used to form strained islands that develop into high-quality crystals without any process-induced damage. However this narrows the useful materials for making NDs as a lattice-mismatched system is required. For optoelectronic devices, it has been demonstrated that QD active layers can enhance the optical gain. When high-density, high-uniformity, and multiply-stacked QDs layers conditions were fulfilled, large optical gain would be obtained. But it is still a great challenge to achieve all these conditions. Therefore, we have investigated a top-down approach for the fabrication of QDs, by combining a bio-nano-process (BNP) [5] and a damage-free, neutral beam etching (NBE) process [6].

In this work, we report recent results obtained on the fabrication of InGaAs NDs embedded in a GaAs barrier layer and their optical characteristics.

## 2. Method

Multi-quantum well samples (MQW) were grown by metalorganic vapor phase epitaxy (MOVPE), as shown in Fig. 1(a). After conventional organic cleaning of the surface, a self-assembled monolayer of PEGylated ferritins (cage-liked proteins with an outer diameter of 13 nm and an inner diameter of 7 nm in which an iron oxide core of 7 nm can be introduced) was formed (Fig. 1(b)) [5]. Protein shells were then removed by low-temperature oxygen annealing in vacuum (LT-OAV) leaving the metal oxide cores on the surface as etching mask, Fig. 1(c). Afterwards, the surface oxide layer was removed by hydrogen radical treatment using an ECR gun at 350 °C and surface was passivated by flowing hydrogen radicals at room temperature. Chlorine neutral beam etching was subsequently carried out using a flow rate of 40 sccm and an ICP power of 800 W. Substrate temperature as well as beam energy effects on etching nanostructures were investigated. After NBE, hydrogen radical treatment was performed to passivate the surface.

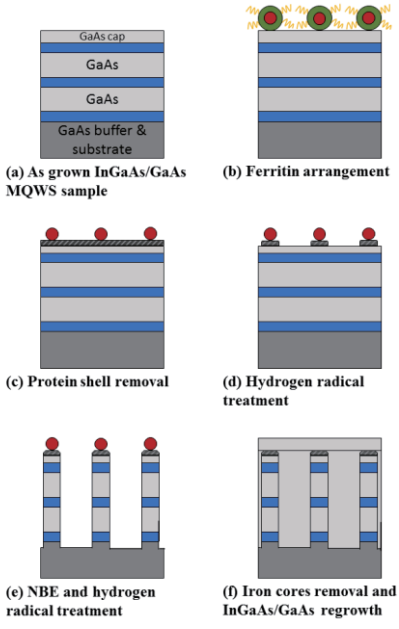


Fig. 1 Process flow of nanodisks fabrication. (a) MOVPE as-grown InGaAs/GaAs MQWs sample, (b) PEG-ferritin arrangement, (c) removal of protein shell by LT-OAV, (d) surface oxide removal by hydrogen radical, (e) etching by neutral beam and passivation by hydrogen, (f) removal of iron cores and regrowth of barrier

Corresponding authors: Seiji Samukawa, Cedric Thomas
*E-mail address*: samukawa@ifs.tohoku.ac.jp, thomas@sammy.ifs.tohoku.ac.jp

Afterwards, iron oxide cores were removed and barrier layer was regrown by MOVPE. Finally, photoluminescence spectra were measured to observe the quantum confinement effect of the fabricated NDs.

### 3. Results and Discussion

Figure 2 shows the effects of neutral beam energy on the nanopillar fabrication. By applying a bias to the bottom electrode [6], energy of neutrals impinging the surface can be controlled. At lower bias, nanopillars of ca. 54 nm high were fabricated, with a minimum diameter of 11 nm. However, due to the etching selectivity between InGaAs and GaAs layers, profile shape was not good. It is assumed that GaAs layers were etched faster than InGaAs layers. Increasing electrode bias resulted in better nanopillar shapes as the etching selectivity between InGaAs and GaAs became closer to one. However, when a too high bias was applied (such as 16 W, Fig. 2(c)), the etching selectivity between iron core masks and substrate would decrease resulting in the observed cone.

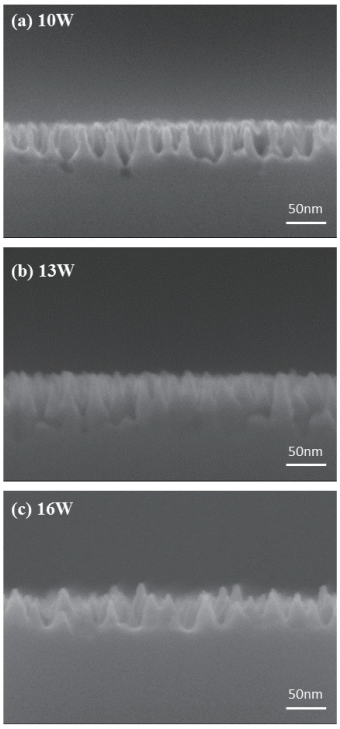


Fig. 2: effect of bias power on InGaAs/GaAs nanopillar fabrication. The substrate temperature was 50 °C, etching time fixed to 3 min and bias was (a) 10 W, (b) 13 W, and (c) 16 W.

Finally, after removal of iron cores and regrowth of barrier layer, PL emission was investigated. Results are shown in Fig. 3 where InGaAs NDs emission (blue curve) is compared to InGaAs MQWs of the same thickness as NDs. Clearly, InGaAs NDs emission peaked around 910 nm and thus, was blue-shifted from MQWs emission by about 70 nm. A shoulder also appeared on the spectrum and could be related to the deepest InGaAs QW layer that was not etched during the process. The blue-shift is explained by taking into account the three-dimensional confinement of the wave function inside the NDs. Moreover, this demonstrates that the fabrication process of InGaAs NDs is a process

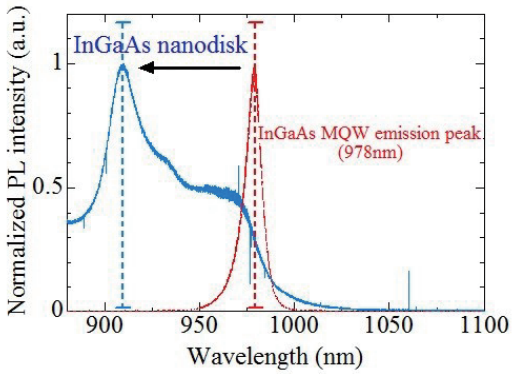


Fig. 3: PL spectra of InGaAs MQWs (red) and InGaAs NDs (blue).

that do not induce more defects.

### 4. Concluding Remarks

We fabricated a high density nano-pillar structure that includes InGaAs NDs by using the bio-template and NBE processes. Anisotropic profiles were achieved when using a substrate temperature of 50°C and an electrode bias of 13 W. The photoluminescence emission of InGaAs NDs was blue-shifted compared to InGaAs MQWs of the same thickness, establishing that NDs were damage-less nanostructures. These results demonstrate that fabrication of InGaAs NDs for designable quantum energy levels can be done with our approach. It is expected that such NDs embedded in LD active media would have great potential for high-performance semiconductor optical devices.

### References

[1] Y. Arakawa and H. Sakaki, *Appl. Phys. Lett.*, 40 (1982) 939.
[2] M. Asada, Y. Miyamoto and Suematsu Y., *IEEE J. Quantum Electron.*, 22 (1986) 1915.
[3] D. Bimberg, N. Kirstaedter, N.N. Ledentsov, Zh.I. Alferov.P.S. Kop'ev and V.M. Ustinov, *IEEE J. Sel. Top. Quant.*, 3 (1997) 196.
[4] R. Mirin, A. Gossin, and J. Bowers, *Electron. Lett.*, 32 (1996) 1732.
[5] I. Yamashita, *Thin Solid Films*, 393 (2001) 12.
[6] S. Samukawa, *Jpn. J. Appl. Phys. Lett.*, 45 (2006) 2395.

# Development Wind Turbine with Dynamic Varying Shape Surface Blades

Kussaiynov Kappas, Sakipova Saule, Kambarova Zhanar, Kussaiynova Assiya, Alibekova Assem
E.A.Buketov Karaganda State University
Universitetskaya Str. 28, Karaganda, 100026, Kazakhstan

**ABSTRACT**

We have developed a sail type wind turbine with dynamic varying shape surface blades working effectively at low wind speeds. The results of experimental study of aerodynamic characteristics of wind turbine are presented. Novelty of the design is the use as power elements of the wind turbine blades with dynamic varying shape surfaces, which made in the form of a triangular sail with flexible movable end. A sail type wind turbine was designed to be used in creating an autonomous wind power system.

## 1. Introduction

Renewable energy sources have attracted the last years, lots of attention due to the technology development, their nondependence on fossil fuels and their friendliness to the environment. Wind energy and consequently wind farms constitute one of the greatest renewable energy sources with rapid expansion all over world [1].

From the geographical and meteorological point of view, Kazakhstan is probably one of the best countries in the world to promote large-scale wind energy production. Prospective of wind power in Kazakhstan shows that about 2000MW of wind capacity can be used in Kazakhstan up to 2024 [2].

Exceptionally rich in wind resources, about 50% of Kazakhstan's territory has average wind speeds about 4-5 m/sec at a height of 30m. Windy sites are mostly located in the Caspian Sea area, and in central and southern Kazakhstan. A country wide-wind atlas is available [3].

Thus, the development and creation of wind turbine operating at low wind speeds and adapted to the climatic conditions, are relevant in Kazakhstan.

## 2. Method

Characteristics analysis of various wind-driven power plants showed that sail type wind turbines are suitable for low wind speeds. Sail type wind turbines match a wind direction and practically do not originate noise and vibration. Power generated by a sail type wind turbine is proportional to the third power of wind speed, i.e. when wind speed doubles, the power is increased by eight times [4].

The wind turbine consists of a wind wheel made of metal frame rods with six sail blades of triangular shape fixed on them. The sail blades are made of lightweight and durable material, one end of the blade is attached to the top of the frame by strong thread. The diameter of the sail wheel is 3 m. The wind turbine is fixedly attached to the mount by support rods. Sail type wind turbines have a unique feature, they work equally well for both small wind speeds and at high wind speeds on account of dynamic varying shape of work surface under the influence of wind flow.

Corresponding author: Kussaiynov Kappas
*E-mail address*: kappas090108@mail.ru

Wind turbine operates as follows: the triangular blade of the wind turbine angled to the direction of the wind flow, is subjected to the lateral pressure force and according to the laws of aerodynamics pushes the frame. This results in its rotational movement. This force is the traction force of blades that converts the wind energy into rotational motion of the wind turbine. When the wind direction changes to the opposite one, the direction of axis rotation of the wind turbine does not change (Fig.1).

Fig. 1 Sail type wind turbine

As shown on figure 2, when the wind direction changes the blade with dynamic varying shape surface bends to another side of the rotating frame of the wind turbine, thus ensuring the preservation of the original direction of axis rotation of the wind turbine. Figure 2 shows the following notation: 1 - wind turbine blade, 2 - flexible attachment of the movable end of the blade, made from a nylon, 3,4 - frame rods of wind turbine, 5 - rotation axis and a curved arrow - direction of axis rotation of the wind turbine, 6 - the arrows showing the direction of the wind.

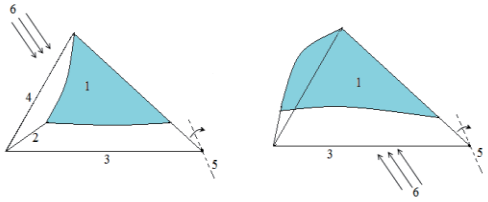


Fig.2 Wind turbine blade at forward and opposite wind flow directions

The dimensionless traction force coefficient $C_M$ and the similarity criterion - Reynolds numbers were computed from the measurements by the formulas:

$$C_M = \frac{2M}{\rho u^2 \cdot S \cdot l} \quad (1)$$

$$\mathrm{Re} = \frac{u \cdot L}{\nu} \quad (2)$$

where $M$ is the thrust moment, $\rho$, $\nu$ are the air density and viscosity , $u$ is the flow speed, $S$ is the characteristic area of midship section, $l$ is the length of the lever arm, $L$ is the characteristic size of the wind turbine.

### 3. Results and Discussion

As a result of the experiments we obtained dependences of changes in the traction force at various air flow speeds and different angles of attack. Figure 3 shows dependences of coefficient of traction force of the wind turbine on the Reynolds number at different wind flow directions. As shown on figure 3, coefficients of traction force in the forward and opposite directions coincide and approximately remain constant.

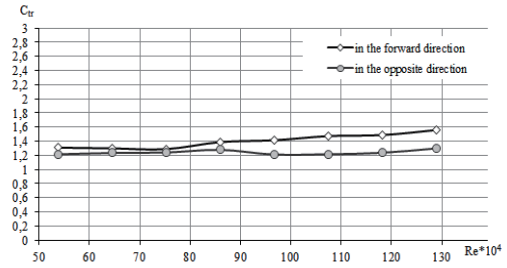


Fig.3 Dependences of coefficient of traction force of the wind turbine on the Reynolds number at different wind flow directions

Figure 4 shows dependences of traction force coefficient of the wind turbine on Reynolds number at various angles of attack of wind flow. The qualitative character of dependences on Reynolds number at various angles of attack of wind flow is almost alike. The highest value of the coefficient of traction force of wind turbine are observed in the forward direction of the wind flow $\alpha=0^0$.

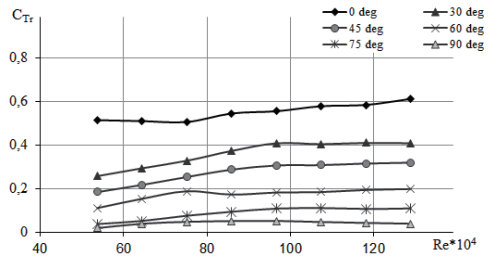


Fig. 4 Dependences of traction force coefficient of the wind turbine on Reynolds number at various angles of attack of wind flow

Figure 5 shows dependences of traction force coefficient of the wind turbine on the dimensionless angle of attack of wind flow at two different wind flow speeds: of 5m/s and 12 m/s. At a constant wind flow speed traction coefficient decreases with the change of attack angle. This is explained by a decrease in the area of the midship section of the wind wheel.

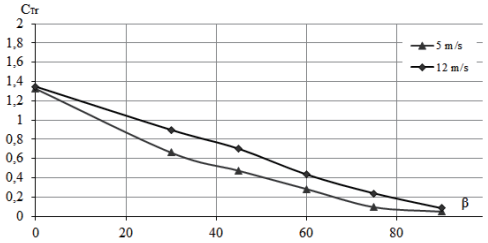


Fig.5 Dependences of traction force coefficient of the wind turbine on the dimensionless angle of attack

The experiments showed that the designed model of the sail type wind turbine has optimum aerodynamic characteristics due to a self-regulating surface shape of blades.

The wind turbine in the air flow acts as self-organized device, efficiently converting wind energy into the energy of rotational motion. The design flexibility with dynamic varying surface shape of blades provides the minimum aerodynamic resistance, and increases the utilization ratio of the wind.

The wind turbine maintains operability in a wide range of changes of wind direction that is a positive factor in operation. It was experimentally found that even when the direction of the airflow is reversed, the wind turbine continues to rotate in the previous direction.

### 4. Concluding Remarks

A sail type wind turbine with dynamic varying shape surface of the blades was designed and developed.

It was demonstrated that due to the self-regulated surface shape of blades of a sail type wind turbine, the latter can efficiently convert the energy of airflow even when the direction of airflow is reversed.

The results obtained will be used for engineering calculations in the development of sail type wind turbine, adapted to specific climatic conditions, i.e. operating at low wind speeds and generating a targeted amount of electricity.

### References


[1] L. Ekonomou, S. Lazarou, G.E. Chatzarakis, V. Vita, *Simulation Modelling Practice and Theory*, 21 (2012) 21–25.

[2] UNDP in Kazakhstan “Kazakhstan wind power market development initiative”. http://www.windenergy.kz/files/1213793646_file.pdf

[3] Kazakhstan Solar and Wind Power Markets 2014. Development opportunities. http://renewable-marketwatch.com/news-analysis/121-kazakhstan-solar-and-wind-power-markets-2014-development-opportunities

[4] S.E. Sakipova, Zh.T. Kambarova, M.M. Turgunov, E.K. Kussaiynov, A.K. Kussaiynova, *Eurasian Physical Technical Journal*, 20 (2013), 20-25.

# OS2: The Second International Symposium on Innovative Energy Research Ⅱ State-of-the-art Combustion Research

Eleventh International Conference on Flow Dynamics
October 8-10, 2014, Sendai, Miyagi, Japan

# Flame Speeds and Possible Self-Similar Propagation of Expanding Premixed Turbulent Flames at High Flow Reynolds Numbers up to 80,000

Shenqyang (Steven) Shy
Department of Mechanical Engineering, Center for Energy Research, National Central University
300 Jhong-da Road, Jhong-li City, Tao-yuan County, 32001, Taiwan

**ABSTRACT**

This note presents flame speeds and their scaling on high flow-Reynolds-number expanding turbulent premixed flames, propagating in statistically homogeneous isotropic turbulence in a large dual-chamber, fan-stirred explosion facility, using two different fuels with different Lewis numbers ($Le \approx 0.76$ and $Le \approx 1$). The effect of $Le$ on turbulent flame speeds and possible self-similar propagation are discussed and compared with a recent finding by Chaudhuri et al. (2012) using unity Lewis number expanding turbulent flames in a smaller dual-chamber, fan-stirred vessel.

## 1. Introduction

Law and his co-workers found that a constant-pressure, unity Lewis number expanding turbulent premixed flame of methane/air mixtures at the equivalence ratio $\phi$ = 0.9 has the self-similar propagation [1]. In it the normalized turbulent flame speed $[(1/S_L^b)d\langle R\rangle/dt]$ as a function of the average flame radius $\langle R\rangle$ scales as a flame turbulent Reynolds number, $Re_{T,flame} = u'\langle R\rangle/D_T < 2{,}500$, to the one-half power. $S_L^b$ is the laminar burning velocity on the burnt side before density correlation, $t$ is time, $u'$ is the r.m.s. turbulent fluctuation velocity, and $D_T$ is the thermal diffusivity. Here we add the subscript "flame" to distinguish it from the commonly-used flow turbulent Reynolds number ($Re_{T,flow} = u'L_I/\nu$), where $L_I$ is the integral length scale of turbulence. The finding of self-similar propagation of expanding turbulent premixed flames is very interesting [1], because all flame speeds at different pressures ($p$) varying from 1 atm to 5 atm and different values of $u'$ ranging from 1.34 m/s to 6 m/s can be represented by $[(1/S_L^b)d\langle R\rangle/dt] = 0.102Re_{T,flame}^{0.54}$, showing self-similar flame propagation. But such result was based on a rather small range of the average flame radius $\langle R\rangle$ about 10 mm to 25 mm to avoid the wall confinement effect due to the small dual-chamber, fan-stirred vessel used in Ref. [1], where the corresponding values of $Re_{T,flow} \approx 350 \sim 7{,}500$ and $Re_{T,flame} \approx 100 \sim 2{,}500$. This motivates the present study to address two important questions: Can the aforesaid self-similar propagation of expanding turbulent premixed flames be valid for $Re_{T,flame}$ up to 10,000 >> 2,500 at much higher $Re_{T,flow}$ up to 80,000 >> 7,500? Does the above self-similar relationship be valid for $Le$ < 1 flames?

## 2. Method

The setup was a large inner cruciform-shape burner constructed by three perpendicularly-aligned cylindrical pipes when it was viewed from all three directions having a near-spherical volume of a minimum diameter of about 300 mm, which was resided in a huge outer high-pressure vessel. At the two ends of the largest horizontal pipe, two identical counter-rotating fans each driven by a 10 HP motor together with a pair of perforated plates with a distance of about 420 mm were equipped to generate statistically intense isotropic turbulence in the central uniform region up to 150 x 150 x 150 $mm^3$. In it the r.m.s. turbulent fluctuation velocities in all three directions are about equal with negligible mean velocities and having -5/3 slopes of energy spectra. For details, the reader is directed to Ref. [2]. A high-speed Schlieren imaging technique with a view field of 120 x 120 $mm^2$ was used to measure $\langle R\rangle(t)$ of centrally-ignited, outwardly-propagating spherical premixed turbulent flames using both lean methane/air mixtures at $\phi = 0.9$ (same as [1] having $Le \approx 1$) and lean syngas ($35\%H_2/65\%CO$)/air mixtures at $\phi = 0.5$ having an effective $Le_{eff} \approx 0.76 << 1$ [3]. The experiments were performed at pressures of 1, 3, 5 atm and with $u'$ varying from 1.43 m/s to 6 m/s. The domain of experimentation was set at $0.17 \le \langle R\rangle/R_{min} \le 0.30$ to avoid ignition and wall effects, where the minimum wall confinement radius $R_{min} \approx 150$ mm. Thus, the present maximum $Re_{T,flow}$ and $Re_{T,flame}$ can be up to 80,000 and 10,000.

## 3. Results and Discussion

Figure 1 shows a typical set of Schlieren images for the case of methane, with different $p$ and $u'$ but at roughly the same $\langle R\rangle$. With increasing $u'$, the flame propagates faster, while with increasing $p$, the flame also propagates faster. The latter is more complicated than just due to the emergence of fine structures (reduction of the thickness of the laminar flamelets with increasing $p$ allowing flame surface wrinkling at progressively smaller scales). Actually, it is mainly influence by the increase of $Re_{T,flow}$ due to the decrease of $\nu$ at elevated pressure [4]. In it the average turbulent flame speed decreases similarly as laminar burning velocities with increasing $p$ in minus exponential manners when values of $Re_{T,flow}$ can be kept constant.

Figures 2 and 3 respectively show comparison between present and previous data for the same $CH_4$/air mixtures and comparison of syngas and methane data with different Lewis numbers. The former indicates that self-similar propagation of expanding turbulent premixed flames is valid even for $Re_{T,flame}$ up to 10,000, while the latter shows a strong influence of $Le$. Lean syngas flames with $Le << 1$ propagate roughly twice faster than methane flames with $Le \approx 1$.

Corresponding author: S. S. Shy
*E-mail address*: sshy@ncu.edu.tw

**References**

[1] S. Chaudhuri, F. Wu, D. Zhu, and C. K. Law, *Phys. Rev. Lett.*, 108 (2012) 044503-1 − 044503-5.

[2] C.C. Liu, S.S. Shy, H.C. Chen, M.W. Peng, *Proc. Combust. Inst.*, 33 (2011) 1293-1299.

[3] S.S. Shy, C.C. Liu, J.Y. Lin, L.L. Chen, A.N. Lipatnikov, S.I. Yang, To appear in *Proc. Combust. Inst.*, 35 (2014)

[4] C.C. Liu, S.S. Shy, M.W. Peng, C.W. Chiu, Y.C. Dong, *Combust. Flame*, 159 (2012) 2608-2619.

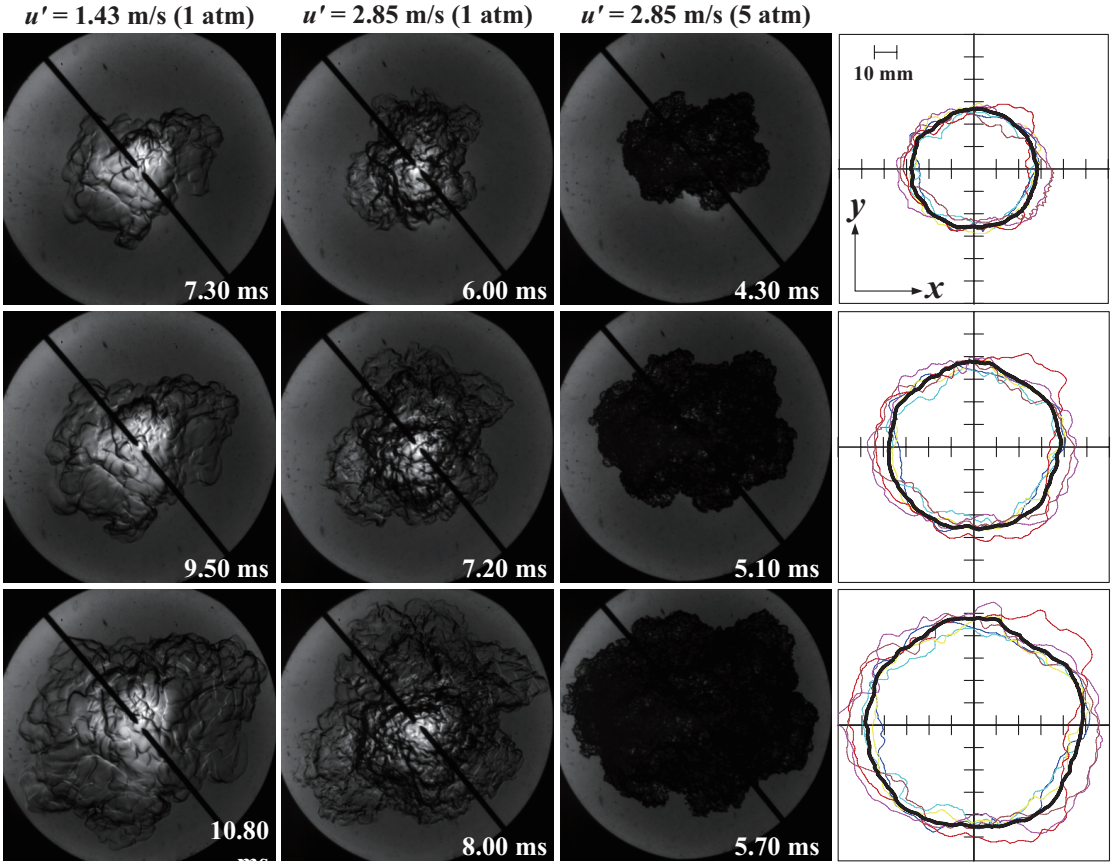


Fig. 1. The case of $CH_4$/air mixtures with $Le \approx 1$, showing Schlieren images with a view field of 120 mm x 120 mm at different $u'$ and $p$, but at nearly the same $<R>$. Similar to [1], the fourth column shows instantaneous flame fronts (thin lines) for the same $<R>$, at various conditions of $u'$ and $p$. The thick line shows an ensemble avaraging curve over the instantaneous flame fronts.

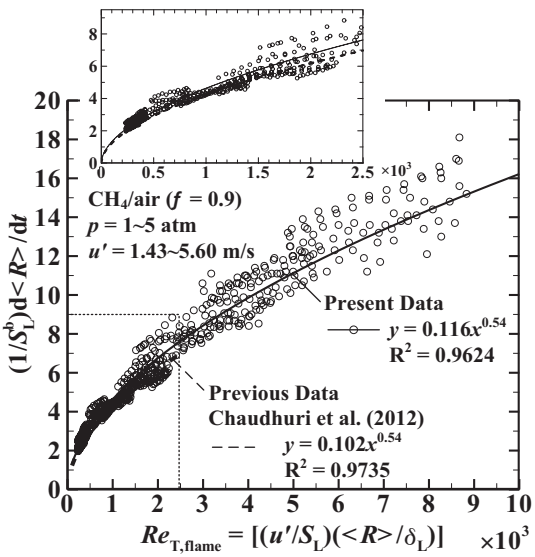


Fig. 2. Comparison between present data (solid line with symbol) and previous data (dash line only with $Re_{T,flame}$ < 2,500; see the inset) [1] for the same $CH_4$/air mixtures.

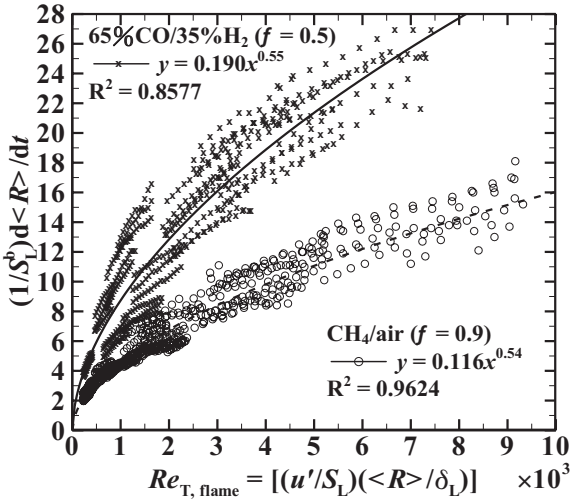


Fig. 3. Lean syngas/air mixtures with $Le_{eff} = 0.76 << 1$ *vs.* methane/air mixtures with $Le \approx 1$, showing the effect of $Le$ on turbulent flame speeds, where values of $[(1/S_L^b)d<R>/dt]$ in the former are almost twice than that in the latter at any given $Re_{T,flame}$.

Eleventh International Conference on Flow Dynamics
October 8-10, 2014, Sendai, Miyagi, Japan

# Plasma Activated Low Temperature Combustion

Yiguang Ju[1], Sang Hee Won[1], Joseph Lefkowitz[1], and Wenting Sun[2]
[1]Department of Mechanical and Aerospace Engineering, Princeton University, Princeton, 08544, USA
[2]School of Aerospace Engineering, Georgia Institute of Technology, Atlanta, 30332, USA

**ABSTRACT**

Plasma activated n-heptane and dimethyl ether cool flames were studied by using an *in situ* nanosecond pulsed discharge and a corona discharge ozone generator. The results showed that non-equilibrium plasma discharge can activate low temperature chemistry so that n-heptane and dimethyl ether cool flames can be established without $NO_x$ and soot emissions. Moreover, it was also found that plasma activated low temperature chemistry can result in a stretched *S*-curve without ignition/extinction limits.

## 1. Introduction

Advanced engine technologies such as Homogeneous Charge Compression Ignition (HCCI) engines, Partially Premixed Compression Ignition engines (PPCI), and the Reactivity Controlled Compression Ignition (RCCI) engines [1] use a higher compression ratio and lower combustion temperature to increase engine efficiency and reduce emissions. However, ignition timing in these engines is critical to engine performance. Failure of ignition control may lead to either excessive emissions or engine knocking. Therefore, there is a great need to develop new techniques capable of fast control of engine ignition.

Plasma, the fourth state of matter, provides an unprecedented opportunity for combustion and emission control. In last two decades, plasma has been demonstrated as a promising technique to enhance combustion, reduce emissions, and improve fuel reforming [2-7]. However, the impacts of plasma on low temperature ignition and cool flames have not been examined.

In this paper, we investigated the plasma activated low temperature combustion and cool flames of dimethyl ether (DME) and n-heptane mixtures in counterflow systems by using non-equilibrium plasma discharge. In the first experiment, *in situ* repetitive nanosecond discharge was employed. In the second experiment, to understand the kinetic mechanism of plasma activated low temperature combustion, ozone production by dielectric barrier discharge was used. The experimental results were compared with numerical modeling. The key reaction pathways for plasma activated cool flames were identified.

## 2. Experimental Methods

The first experimental setup [7,8] is shown in Fig. 1. A counterflow burner is located in a low pressure chamber. Both the fuel and oxidizer nozzles are made of stainless steel with a 25.4 mm inner diameter. The nozzle separation distance was kept at 16 mm. At both nozzle exits, porous metal plates (2 mm in thickness) were placed to provide uniform velocity profiles and to serve as the electrodes at the same time. The oxidizer- and fuel nozzle electrodes were connected to the positive and negative high voltage outputs of a nano-second repetitive pulse generator (FID, FPG 30-50MC4) [7,8], respectively. The discharge was generated between the two nozzle electrodes by high voltage (7.6 kV) pulses with pulse duration of 12 ns. The pulse energy supplied to the discharge was approximately 0.73 mJ/pulse. The pulse repetition frequency ($f$) was fixed at either 24 or 34 kHz during the experiments. Helium was used as the dilution gas for both the fuel (DME) and oxygen streams. The pressure was held constant at 72 Torr. OH and $CH_2O$ Planar Laser Induced Fluorescence (PLIF) were employed to characterize the progress of low and high temperature fuel oxidation chemistry.

In the second experiment, nitrogen diluted, prevaporized n-heptane (550 K) was used as the fuel stream [9]. A dielectric barrier discharge ozone generator was used to produce ozone directly in the oxygen stream. Depending on the flow rate of oxygen, 2 – 4 % of ozone in volume fraction within ± 0.2 % fluctuation was produced in the oxidizer stream at 300 K. All experiments were conducted at atmospheric pressure. Species profiles of cool diffusion flames were measured by gas sampling using a micro gas chromatography system coupled with a thermal conductivity detector (Inficon, 3000 micro-GC). Uncertainties of measured species concentrations were within ± 5 % in species mole fraction.

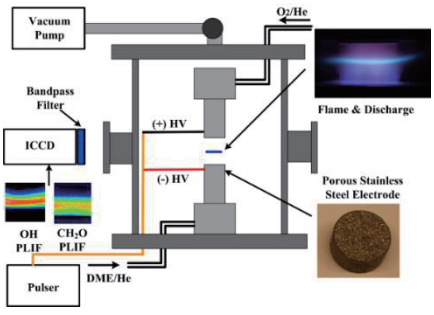


Fig. 1 Schematic of the low pressure experimental setup

## 3. Results and Discussion

The formation of $CH_2O$ in DME ignition and diffusion flame is an excellent marker of low temperature combustion kinetics. During the experiments, the strain rate (250 $s^{-1}$, with flow residence time of approximately 4 ms) [8]), the $O_2$ mole fraction at the oxidizer nozzle exit, $X_O$, and the discharge frequency ($f$ = 24 kHz) were held

Corresponding author: Yiguang Ju
*E-mail address*: yju@princeton.edu

constant, while the DME mole fraction from the fuel nozzle, $X_F$, was varied. The relationship between $CH_2O$ PLIF signal intensity and fuel mole fraction, $X_F$, is shown in Fig. 2 for $X_O$ = 0.6. As shown in Fig. 2, with the increase of the fuel mole fraction ($X_F$), the $CH_2O$ PLIF signal intensity increases significantly. This rapid increase of $CH_2O$ PLIF signal with undetectable OH level before ignition indicates the occurrence of plasma activated low temperature DME oxidation. When the DME mole fraction was larger than 6%, a sharp decrease of $CH_2O$ signal intensity occurred, indicating the occurrence of hot ignition. After hot ignition, the $CH_2O$ PLIF signal intensity became insensitive to the increase of DME mole fraction. This nonlinear change of $CH_2O$ concentration for DME flames was not observed for $CH_4$, which does not have low temperature chemistry. Simulations showed that the large amount of $CH_2O$ formation in DME was caused by plasma activated low temperature chemistry via,

$$e + O_2 = 2O + e \quad (1)$$

$$O+RH=R+OH \quad (2)$$

$$R+O_2=RO_2 \rightarrow QOOH \rightarrow Q_2OOH \rightarrow 3OH \quad (3)$$

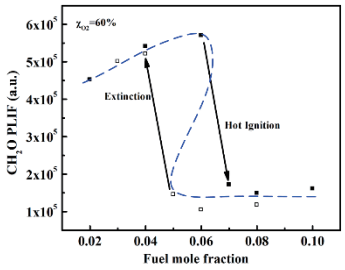


Fig. 2 Dependence of $CH_2O$ PLIF signal on fuel mole fraction $X_O$ = 0.6, P = 72 Torr, f = 24 kHz, a = 250 $s^{-1}$.

By increasing the plasma repetition rate (i.e. the energy input), unlike the *S*-curve in Fig.2, Fig.3 shows a direct transition from ignition to flame without ignition/extinction limit.

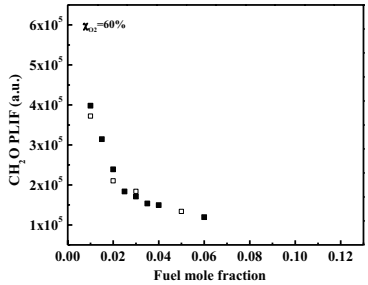


Fig. 3 Dependence of $CH_2O$ PLIF signal on fuel mole fraction $X_O$ = 0.6, P = 72 Torr, f = 34 kHz, a = 250 $s^{-1}$

The electron impact dissociation of molecular oxygen to form atomic O may be the main activator of low temperature chemistry by plasma. If so, ozone addition into the oxygen stream will play a similar role to activate cool flames, considering the moderately low temperature required to dissociate ozone.

Fig.4 shows direct images of hot and cool n-heptane/oxygen-ozone counterflow diffusion flames at 1 atm. It is clearly seen that with ozone addition, a cool flame, which is not possible to be observed at low pressure, can be self-sustained in a broad range of stretch rates [9]. The results demonstrated that non-equilibrium plasma or ozone with radical production can activate low temperature chemistry and cool flames without $NO_x$ and soot emissions. Species measurements in cool flames were also conducted. The results showed that the existing kinetic mechanism fails to predict the correct cool flame temperature and species distribution.

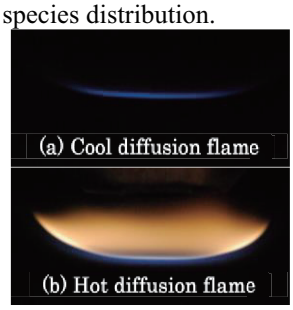


Fig. 4. Photos of cool (a) and hot (b) diffusion flames, observed at the same condition, $X_F$= 0.07, $a$ = 100 $s^{-1}$.

## 4. Concluding Remarks

Non-equilibrium plasma and ozone activated low temperature combustion and cool flames were observed for the first time. A stretched *S*-curve without ignition and extinction limits was found. Radical production in the plasma plays a key role in accelerating the low temperature chemistry and cool flames at low and atmospheric pressure.

## References


[1] Reitz, R.D., *Combustion and Flame*, Vol. 160, pp. 1-8, 2013.

[2] Starikovskiy, A., & Aleksandrov, N. (2013), *Progress in Energy and Combustion Science*, *39*(1), 61-110.

[3] Starikovskaia, S. M. (2006). Plasma assisted ignition and combustion. *Journal of Physics D: Applied Physics*, *39*(16), R265.

[4] Ombrello, T., Qin, X., Ju, Y., Gutsol, A., Fridman, A., & Carter, C. (2006). *AIAA journal*, *44*(1), 142-150.

[5] Lou, G., Bao, A., Nishihara, M., Keshav, S., Utkin, Y. G., Rich, J. W. Lempert, Adamovich, I. V. (2007). *Proceedings of the Combustion Institute*, *31*(2), 3327-3334.

[6] Takita, K., Uemoto, T., Sato, T., Ju, Y., Masuya, G., & Ohwaki, K. (2000). *Journal of Propulsion and Power*, *16*(2), 227-233.

[7] Sun, W., Uddi, M., Ombrello, T., Won, S. H., Carter, C., & Ju, Y. (2011). *Proceedings of the Combustion Institute*, *33*(2), 3211-3218.

[8 ] Sun, W., Won, S. H., & Ju, Y. (2014). Combustion and Flame, in press.

[9] Won, S. H., Jiang, B., Diévart, P., Ju, Y., & Sohn, C. H. (2014). Proceedings of *the Combustion Institute*, *35*. in press.

# Combustion-Synthesized Porous Materials. Methods Of Modifying The Porous Structure.

Anatoly S. Maznoy[1,2], Alexander I. Kirdyashkin[1,2], Alexander N. Guschin[1,2], Sergey S. Minaev[1].
[1] Far-Eastern Federal University
8 Sukhanova str, Vladivostok, 690950, Russia
[2] Tomsk scientific center SB RAS
10/4 Akademicheskiy Av, Tomsk, 634055, Russia

**ABSTRACT**

The effects of the particle size of powder components, the relative density of the reacting system, and the degree of dilution of the mixture by thermally inert components on the pore structure of combustion synthesized products were experimentally studied using the (Ti + 26% Si)-$Al_2O_3$ system.

## 1. Introduction

One practical application of combustion synthesis (CS) is the obtainment of finished or semi-finished products that do not require significant processing for further use. The key benefits and features of CS, such as the energy efficiency of the method, porosity of the synthesized products, obtainment of strong framework porous structures of the products, self-purification in the process of synthesis, etc. [1], are most fully implemented in the synthesis of porous permeable materials promising for use as gas burners, filters, implants, catalyst supports, etc. The formation of pore structures during synthesis is significantly affected by ultrafast chemical and structural transformations, such as melting, capillary spreading, coalescence, reaction diffusion, etc. Combustion synthesized porous permeable materials are characterized by a complex structure, namely, the possible gradient behavior, anisotropy, and periodicity of the pore space layers. The establishment of a relationship between the initial parameters of the reacting system (particle size of the reaction components, relative density of the sample, and mixture composition) and the porosity structure of the resulting CS product is an urgent problem.

## 2. Method

The initial reaction components were the PTEM titanium powder, KR-1 silicon powder, and a $Al_2O_3$ powder of chemical purity. The components were mixed in a ratio of (Ti +26% Si) + σ/(100% − σ) $Al_2O_3$ (σ is the weight percent of aluminum oxide in the reaction mixture). The powder cylindrical samples 20 mm in diameter and 30–40 mm in height were compressed in a mold by a compressing force of up to 80 kN. All component powders had the same fractional composition in certain sample. We used fractions of 40÷50 μm (average particle size $r$ = 45 μm), 63÷80 μm ($r$ = 71.5 μm), 80÷100 μm ($r$ = 90 μm), and 160÷200 μm ($r$ = 180 μm). The effect of the relative density of the sample (Δ) on the porous structure of CS products was determined using undiluted compositions ($\sigma$ = 0) whose components had a particle size of $r$ = 180 μm. The effect of the inert diluent on the porous structure of CS products was studied on samples of relative density Δ ≈ 0.59 with a particle size of all initial components $r$ = 45 μm. The effect of the particle size of the initial powdered reagents on the porous structure of CS products was studied using undiluted compositions ($\sigma$ = 0) compressed into samples to a relative density of Δ ≈ 0.59. The CS was performed under argon atmosphere at a pressure of $10^5$ Pa. The pore structure was studied from photographs of cross sections of the samples obtained by a Carl Zeiss Axiovert 200 M-Mat metallographic microscope and an ImageScope Color M automatic image analyzer. The porosity parameters were calculated using a metallographic method based on the simultaneous consideration of the geometric characteristics of the pore and the framework elements sections. The subgroup of closed pores includes those pores whose sections do not contain framework elements, and the rest are considered as open pores forming a network of connected transport channels in the material. The following parameters were calculated: the specific open porosity surface ($S_{surf}$), the average size of the framework elements ($D_{el}$), the size of the open porosity channel ($D_{ch}$), the average size of closed pores ($D_{por}$) and the portion of closed porosity in the total porosity of the material (ω).

Corresponding author: Anatoly Maznoy
*E-mail address*: maznoy_a@mail.ru

## 3. Results and Discussion

Figure 1 shows the dependences of the pore structure characteristics on the initial parameters of the reaction system. It is found that the average size of closed pores $D_p$ (curve 4) increases as the particle size grows, decreases as the relative density increases, and is practically independent of the dilution ratio. The pore channel size $D_{ch}$ (curve 3) decreases with increasing dilution ratio and relative density. For products with a density Δ ≈ 0.59, the channel size is approximately equal to the particle size of the initial powder mixture. Thus, the main factor that makes possible directional control of the gashydrodynamic permeability parameters of porous CS materials is a change in the particle size of the initial components. The use of powdered components with small particle size provides structures with a portion of closed porosity ω ≥ 50%, which are apparently translated from the structure of the original reaction system. This is explained by the fact that, as the powder particle size decreases, the pressing force required achieving the needed relative density increases, which leads to an increase in the portion of closed

porosity in the original sample. As the relative density grows above $\Delta \approx 0.59$, the parameter ω increases sharply to 90%. Upon dilution of the initial mixture by aluminum oxide, the structures of framework type with a small portion of closed porosity ($\omega \approx 10\%$) are obtained. It might be associated with a decrease of combustion temperature and the limitation of the coalescence completeness of the component particles due to an increase of viscosity in the combustion wave zone.

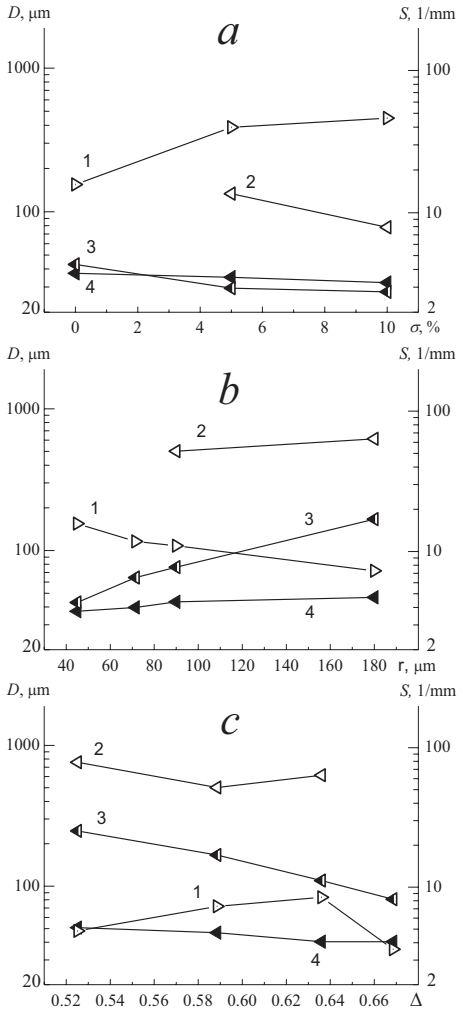


Fig. 1 Dependences of the specific surface of open porosity $S_{surf}$ (curves 1), the size of framework elements $D_{el}$ (curves 2), the size of transport channels $D_{ch}$ (curves 3), and the average size of closed pores $D_p$ (curves 4) on dilution ratio (a), particle size (b), and relative density of the sample (c) in the (Ti + 26% Si) + $Al_2O_3$ system; the values of $D_{el}$ are given for materials with $\omega < 50\%$.

With decreasing particle size of the reacting system, the portion of closed porosity in the synthesized products of the same relative density increases. With an increase in the portion of closed porosity above $\omega \approx 50\%$, the structure is characterized by the appearance of large closed pores, whose contribution to the closed porosity becomes higher as the particle size of the initial powder reagents increases.

The structural transformation rate of CS products is estimated using a parameter $\eta_s$ that characterizes the change in the specific surface of open porosity $S_{surf}$ of the synthesized product in comparison with the specific surface of the initial compressed powder sample:

$$\eta_S = \left(1 - \frac{S_{Sufr} \cdot r}{6 \cdot 10^3 \cdot \Delta}\right) * 100\% \qquad (1)$$

If $\eta_s \rightarrow 0$, the structure of the initial pressed sample is preserved during the CS process due to spot sintering of framework elements in the particle contact areas of the powder components. If $\eta_s \rightarrow 100\%$, the combusted product is sintered into a cast material ($\omega \rightarrow 100\%$). Thus, for the diluted systems of fine powders ($\sigma = 10\%$) we have $\eta_s \approx 41\%$, and for the low-density systems of large powders ($\Delta = 0.525$) we have $\eta_s \approx 72\%$ [2].

## 4. Concluding Remarks

The pore channel size of the synthesized products is determined by the particle size of the components and decreases with increasing relative density and dilution ratio of the initial reaction mixture.

Framework-type structures with a minimum portion of closed porosity ($\omega \approx 10$–$15\%$) are formed by the reaction in low-density powder mixtures and in the case of diluting the mixture with an inert substance. To describe the degree of structural transformation in the CS process (degree of coalescence of the substance in the combustion wave zone), the parameter $\eta_s$ characterizing the change in the specific surface of open porosity of the synthesized product in comparison with the specific surface of the initial powder sample was proposed. It was established that the synthesized products with a minimum value of $\eta_s$ is formed when the reacting system is diluted with an inert substance.

Thus, in the development of the technology of synthesis of porous permeable materials with a high specific surface of open porosity $S_{surf}$ and a small size of pore channels $D_{ch}$, it is necessary to use fine powders of reactants and also to lower the system energy by diluting the reaction mixture with the final reaction product or a thermally inert additive. The formation of small pore structures is also possible by shifting the mixture composition toward an excess of the most refractory component of the system. In this case, we obtain permeable porous materials with a structure similar to the structure of the initial powder sample.

The work was supported financially by the Ministry of education and science of Russian Federation (project 14.Y26.31.0003)

## References

[1] A. G. Merzhanov. *Adv. Mater. 4* (4), (1992) 294–295.
[2] A. S. Maznoi, A. I. Kirdyashkin. *Combustion, Explosion, and Shock Waves*, Volume 50, Issue 1, (2014) 60-67.

# Filtrational Combustion of Gaseous Hydrocarbons Inside Porous Ni-Al Materials.

Alexander I. Kirdyashkin[1,2], Alexander N. Guschin[1,2], Anatoly S. Maznoy[1,2], Sergey S. Minaev[1].
[1] Far-Eastern Federal University
8 Sukhanova str, Vladivostok, 690950, Russia
[2] Tomsk scientific center SB RAS
10/4 Akademicheskiy Av, Tomsk, 634055, Russia

**ABSTRACT**

An investigation is performed of the filtrational combustion of gaseous hydrocarbons inside a spherical nozzle manufactured from porous Ni-Al material. A combustion mode is demonstrated, wherein the combustion wave is localized inside the wall of the porous nozzle. Under this condition, up to 70 % of the total heat value of the fuel mixture is converted into IR flux radiated from the surface of the nozzle, with the maximum lying within the wavelength region 3–11 μm.

## 1. Introduction

The method of filtrational combustion is characterized by advanced ecological safety and can underlie the design of simple technological devices. It consists in the combustion of a mixture of air and gaseous fuel within a chemically inert porous environment [1]. In the course of combustion, the outer surface of the porous environment is heated to the temperatures about 1600 K, which gives rise to generation of an IR flux [2,3]. This method of conversion of the chemical energy of a fuel into the IR radiation requires the use of specially designed high-temperature materials. Intermetallic compounds of the Ni-Al system are of great interest due to their high melting temperature, corrosion resistance, thermal and electrical conductivity, and an extraordinary behavior of their yield stress as a function of temperature [4]. The purpose of this study is to investigate filtrational combustion of gas inside the porous Ni-Al materials manufactured by the combustion synthesis process.

## 2. Method

The energy and spectral characteristics of burners based on porous SHS materials were investigated using a spherical nozzle, made from porous Ni-Al material, with the outer diameter 78 mm and wall thickness 15 mm. Its chemical composition is $Ni_3Al$-NiAl, porosity –50%, and pore size – 1 mm. Figure 1 presents the scheme of porous burner testing. A homogenous fuel mixture (natural gas-to-air volume ratio – 1/11) was fed onto the inner surface of the spherical nozzle.

The natural gas with following composition was used: methane – 90.7%, ethane – 3.8%, propane – 1.7%, nitrogen 2.5%. The heat power of the gas was $q$ = 35270 kJ/m$^3$. The combustion rate of the natural gas-air mixture was controlled to the accuracy ± 1.5÷3.0 % using gas flow meters (SGBM-1.6 and SGMN-1M). The outer nozzle surface temperature $T_K$ and the exhaust gas temperatures $T_G$ were measured with a Cr-Al thermocouple having the fused junction diameter 0.8÷1.0 mm. The content of CO and $CO_2$ in the combustion products was determined using gas analyzers (GIAM-15 and GIAM-14). The content of $NO_X$ in the combustion products was measured using a Qointox KM 9006 gas analyzer.

Corresponding author: Alexander I. Kirdyashkin
*E-mail address*: kirdyashkin_a@mail.ru

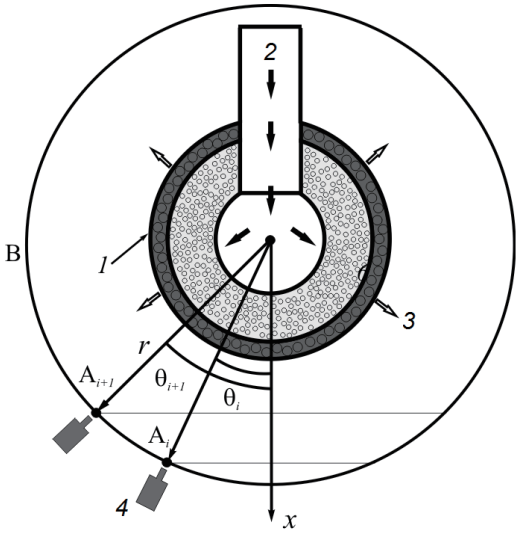


Fig. 1 Scheme of measurement of porous burner radiation characteristics. 1– spherical SHS nozzle, 2– fuel mixture feed, 3– combustion product outlet, 4 – power meter IMO-2N, B - guiding rig, $A_i$ – gage points.

In order to measure the energy and spectral characteristics of the burner radiation, an IMO-2N power meter (ETALON experimental plant, Volgograd, Russia) was placed in different points $A_i$ along the guiding rig B ($r$ = 540 mm from the center of the spherical nozzle). Distance $r$ corresponded to the conditions of radiation measurement in an assumption of a point source, which ruled out the effect of a convective flow of hot combustion products on the power meter readings. The directional radiation pattern was taken by placing the power meter at different angles $\theta_i$ with respect to the $x$ axis. The total radiation power into the sphere ($\theta$=±180°) was calculated using the following formula:

$$P_R \approx \sum_i^{N-1} (R_i + R_{i+1}) \cdot \pi \cdot r^2 \cdot \left| \cos\theta_i - \cos\theta_{i-1} \right|. \quad (1)$$

where $N$ is the number of angles, $R_i$ is the power meter irradiance (W/cm$^2$) at $\theta_i$.

The value of the radiative energy efficiency was estimated using the relationship

$$\eta = \frac{P_R}{P} \cdot 100\% . \quad (2)$$

where $P = Q_N \cdot q$ is the total heat efficiency of burner and $Q_N$ is the natural gas flow rate.

The spectral composition of radiation within the range 0.6÷50 μm was determined using light filters placed in front of the IMO-2M driving head. Use was made of light filters manufactured from crystalline materials (Ge, $CaF_2$, ZnSe), KRS-5 glass and interference narrow-band filters at the wavelengths 5.5, 9.8, and 10.6 μm, with the band pass half width being within 0.5÷0.6 μm.

### 3. Results and Discussion

Depending on the input power, the outer surface of the nozzle was heated to 1000÷1700 K, with a flow of nearly transparent reaction products being observed (flameless combustion mode). Radiation of the burner is controlled by the heat emitted by the porous burner ($P_K$) and the heat emitted by the combustion products ($P_G$). Our investigations have shown that an increase in the specific heat output *(W = P/S)* in the range $W$ = 10÷40 W/cm$^2$ results in a sharp increase in the nozzle temperature and burner radiation intensity. Beyond the upper bound of the above-mentioned range, quantities $T_K$ and $P_R$ vary only a little, with a transition from the flameless mode to a combustion mode with yellow flame above the nozzle surface. At $W \approx 30$ W/cm$^2$, the radiative energy efficiency observed is the highest $\eta \approx 60 \div 70\%$, the contribution from the gas phase into this energy being $\eta_G \approx 20 \div 30\%$ (Table 1). According to the measurements performed, radiation of the burners with a spherical nozzle is isotropic in all directions, with the maximum radiative energy yield of the burners lying within the wavelength range 3÷11 μm. As shown in [3], this is due to the radiation of the gas phase containing $CO_2$ and $H_2O$ molecules.

Table 1. Combustion parameters of burner under study

| Temperature of outer nozzle surface $T_K$ [K] | Total heat efficiency of burner, $P$ [W] | Total radiative power, $P_R$, [W] | Radiative energy efficiency, $\eta$ |
|---|---|---|---|
| 1210 | 4585 | 2761 | 60 |
| 1340 | 5604 | 3849 | 69 |
| 1470 | 7675 | 5273 | 69 |
| 1540 | 8827 | 6112 | 69 |

Accurate measurements with a thermocouple demonstrated that the temperature of the yielding combustion product $T_G$ is by 200÷300 K lower than that of the nozzle. The effect observed is hard to interpret in terms of the conduction-convection mechanism of heat exchange between the gas phase and the solid nozzle in the course of filtrational combustion of the fuel mixture. We might assume that in the course of transformation reaction there is a relatively intensive heat release of the gas phase in the pore space, which results in its fast cooling. Compared to the flare combustion, during filtrational combustion of natural gas the increased radiative energy efficiency of the reaction products is due to the following factors: **Gas layer thickness.** The radiative energy yield (W/cm$^3$) from gas onto the pore walls of the nozzle is inversely proportional to the effective gas-layer radius $R_G$. **Nonequilibrium excitation of radiation.** It is well known that during transformation reactions in hydrocarbon-fired flames the intermediate reaction products (OH, CH, $C_2$, etc.) undergo nonequilibrium chemical excitation up to the energies corresponding to extremely high translational, rotational and vibrational temperature of the molecules (≥ 5000÷10000 K), which is multiply higher than the adiabatic combustion temperature. **Nonequilibrium radiative energy exchange.** For small values of $R_G$, the heated pore walls radiate a continuous spectrum, whose absorption is limited to narrow spectral bands. In other words, the pore wall absorbs nearly all gas radiation, while the inverse process is complicated.

### 4. Concluding Remarks

We have shown that a burner made from porous intermetallic Ni-Al compound in the filtrational combustion mode provides a radiative energy efficiency of up to 70 % of the total fuel heat capacity. In addition, it is ecologically friendly – the NOx exhaust is within 33÷36 mg/m$^3$ only. We have found out that up to 30 % of the total radiative flux of the burner is accounted for by the gas-phase radiation, while the rest is made up by the thermal radiation from the porous material surface.

The work was supported financially by the Ministry of education and science of Russian Federation (project 14.Y26.31.0003)

### References

[1] J.R. Howell, M.J. Hall, J.L. Ellzey. *Progress in Energy and Combustion*. 22 (1996) 122-145.

[2] F.S. Palesskii, S.S. Minaev, R.V. Fursenko, V.K. Baev, A.I. Kirdyashkin, V.M. Orlovskii. *Combustion explosion and shock waves*. V.48, 1 (2012) 17-23.

[3] A.I. Kirdyashkin, V.M. Orlovskii, E.A. Sosnin, V.F. Tarasenko, A.N. Gushchin, V.A. Panarin. *Combustion explosion and shock waves*, V.46, 5 (2010) 523-527.

[4] S.C. Deevi, V.K. Sikka. *Intermatellics 4* (1996) 357-375.

Eleventh International Conference on Flow Dynamics
October 8-10, 2014, Sendai, Miyagi, Japan

# Simplified Numerical Model of the Combustion in a Porous Media

Fedir Sirotkin[1], Roman Fursenko[1,2], Sergey Minaev[2]
[1]Far Eastern Federal University
8, Sukhanova Str., Vladivostok 690950, Russia
[2]Khristianovich Institute of Theoretical and Applied Mechanics, SB RAS
4/1 Institutskaya str., Novosibirsk, 630090, Russia

**ABSTRACT**

A discrete quasi three-dimensional model of gas combustion in porous media is proposed. Our results imply that the flame propagation in the porous media can be considered as a collective process, when the actual combustion wave can be represented by a set of individual flame fronts propagating in the mutually connected micro-channels of the different diameter. Proposed model describes the flame anchoring phenomena when the combustion wave is stabilized inside of the porous media for a range of inlet velocities.:

## 1. Introduction

Filtration gas combustion in a porous media has attracted considerable interest due to a large number of applications such as lean mixtures burning, reduction of pollutants emission, methane to hydrogen conversion, power engineering. Heat feed-back from the high temperature combustion products by radiation and conduction through solid medium serves to preheat incoming mixture. This heat recirculation mechanism results in several features, namely higher burning velocities, super adiabatic temperature in the reaction zone [1], extension of the flammability limits [2], low emission of pollutants and the ability to burn low-caloric fuels.

## 2. Method

We use three-step numerical approach. On the first step, the porous media of the given porosity is generated by randomly placing solid grains. On the second step, the velocity field is calculated. At this step we use Smoothed Particle Hydrodynamics (SPH) method which is mesh-free Lagrangian particle method [3]. On the last step, the thermal-diffusion model is applied to model the flame propagation. The one-step irreversible Arrhenius type exothermic chemical reaction is applied. The gas density, thermal and molecular diffusion coefficients are constants. In order to include effects of the heat transfer within two-dimensional model of porous media we mimic third dimension assuming that the heat transfer between solid grains occurs through heat conducting artificial layer which connects all of them. The average height and diameter of cylinders are equal. The thickness of the plate is of the same order with the average diameter of solid grains.

The Newtonian heat exchange between this layer and solid grains is assumed. The heat transfer in the layer is assumed to be conventional thermal conductivity. In this way, the temperature of the layer, has the similar meaning as the temperature of the porous media in the continuum model.

Corresponding author: Fedir V. Sirotkin
*E-mail address*: sirotkin.f.v@gmail.com

## 3. Results and Discussion

Dependencies of filtration combustion wave propagation velocity on inlet gas velocity for different equivalence ratios and porosities is obtained and compared with continuous one-dimensional thermal-diffusion model.

Fig. 1 illustrates dependencies of combustion wave propagation velocity $U_f$ on the inlet velocity $U_0$ for different equivalence ratios and porosity $\epsilon = 0.7$. Solid and dashed lines with solid circles denote numerical results obtained with the proposed discrete model and continuous two-temperature model for the same parameters for the porous media. Dependencies for different equivalence ratio are illustrated with red ($\varphi = 0.6$), blue ($\varphi = 0.7$) and black ($\varphi = 0.8$) colors. If the combustion wave velocity is negative, the flame propagates in the upstream direction and in the downstream direction, otherwise. These dependencies have U-shape which is typical for the low-velocity combustion regime [4]. We distinguish three main combustion regimes for the given porosity and equivalence ratio: upstream regime ($U_f < 0$), downstream regime ($U_f > 0$), and the flame anchoring regime ($U_f = 0$).

The flame propagation is unsteady in upstream regime. The flame front consists of regions with pulsating and quasi-stationary regions. The location of these regions depends on the spatial distribution of solid grains in the flame front vicinity and spatial and temporal evolution of the combustion wave changes in the course of flame propagation. In the regions where the normal velocity of the flame front is close to the local gas velocity, the position of the flame front is quasi-stationary. If the local flame propagation velocity exceeds the local filtration velocity, this fragment of the flame front is propagating upstream. When the local flame front reaches the region where the local temperature of the porous media is low, the flame quenching occurs due to increasing heat losses. After that the fresh mixture moves downstream and fills the flame path. Once the fresh mixture reaches the solid with high temperature the flame is ignited again. This oscillating process repeats until the moment when the temperature of the porous media upstream is increased due to the heat

exchange between the solid and gaseous phases. The amplitude of these pulsations is close to the few characteristic pore size. The dynamical behavior of the local flame fronts resembles the flame repetitive ignition and extinction (FREI) phenomena [5]. When the inlet velocity increases, the pulsating part of the flame from becomes smaller.

In the downstream regime the flame wave propagation is quasi uniform and does not accompanied with pulsation of separate hot spots which was observed in the range of small filtration velocities. The flame front is much more distorted when compared with upstream regime. The finger-like high temperature regions behind the flame front are formed in the course of flame propagation. These regions are located along the streamlines with high velocity magnitude. Because of high gas velocity in these streamlines, combustion products pass a relatively long distance before cooling to equilibrium temperature due to heat loss to the porous media. The increasing of the flame front area results in a higher total heat release when compared with that predicted by continuous model.

In the flame anchoring regime the combustion wave is spatially stabilized for a range of inlet velocities. The results of computations in this regime are illustrated in Fig. 2. The position of the flame front depends on initial conditions while equilibrium temperature far behind the flame front depends on the inlet velocity. This result can be especially important taking into account the possible application of a porous burners for the domestic and industrial use when the existence of stable flame fronts is the key feature.

Our results imply that the flame propagation in the porous media can be considered as a collective process, when the actual combustion wave can be represented by a set of individual flame fronts propagating in mutually connected micro-channels of the different diameter. The flame propagation is accomplished with local pulsations which look like downstream/upstream motion within set of channels. These results suggest that the porous media structure on the scale of the solid grains play an important role in flame propagation.

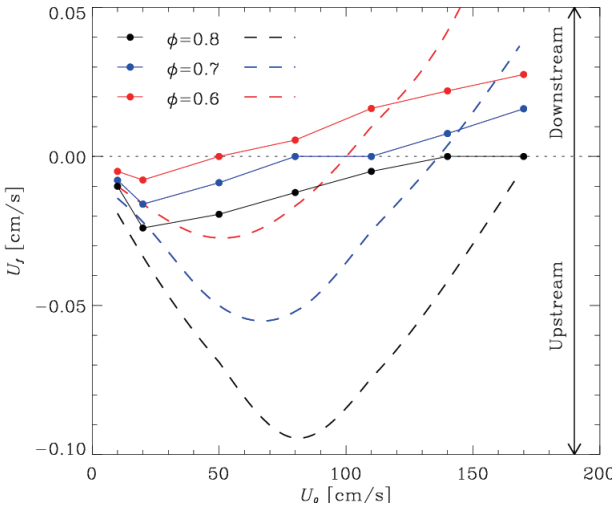


Fig. 1 Combustion wave velocity $U_f$ versus inlet velocity $U_0$ for different equivalence ratios.

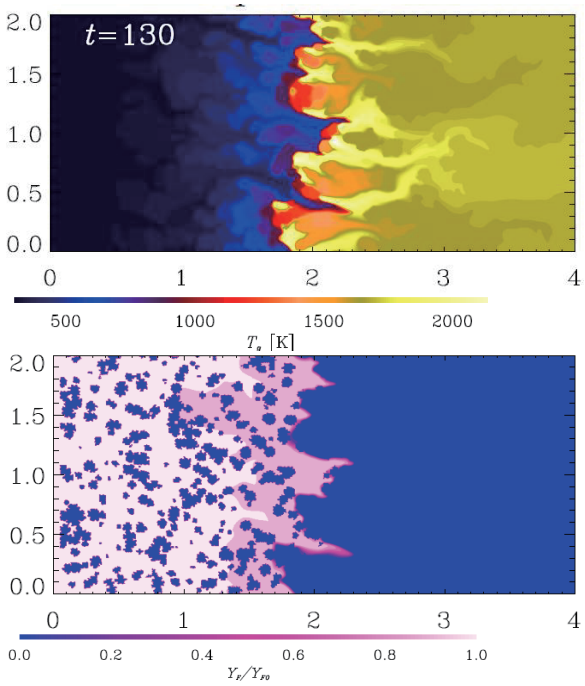


Fig. 2 Example illustrating the spatial distributions of the temperature and relative concentration in the flame anchoring regime.

**4. Acknowledgments**

The work was supported financially by the Ministry of education and science of Russian Federation (project 14.Y26.31.0003)).

**References**

[1] V.S. Babkin, V.I. Drobushevich, Y.M. Laevskii, S.I. Potytnyakov, *Expl. Shock Waves*, 19 (1983) 147-154.

[2] .P. Aldushin, *Combust. Flame*, 94 (1993) 308-320.

[3] F. Sirotkin, Jack J. Yoh, *Computers&Fluids*, 88 (2013) 418-429

[4] R. Fursenko, S. Minaev, K. Maruta, H. Nakamura, H. Yang, *Combustion Theory and Modelling*, 14 (2010) 571-581

[5] H.L. Yang, S. Minaev, E. Geynce, H. Nakamura, K. Maruta, , *Combust. Sci. Tech*., 181 (2009) 1-16

# Near-Blowoff Dynamics of Bluff-Body-Stabilized Premixed Flames in a Narrow Channel

Bok Jik Lee[1], Chun Sang Yoo[2], Hong G. Im[1]
[1]Clean Combustion Research Center, King Abdullah University of Science and Technology
Thuwal 23955-6900, Saudi Arabia
[2]School of Mechanical and Nuclear Engineering, Ulsan National Institute of Science and Technology
Ulsan 689-798, Korea

**ABSTRACT**

The dynamics of lean premixed hydrogen/air flames stabilized behind a square box in a two-dimensional meso-scale channel is investigated with high-fidelity numerical simulations by varying the mean inflow velocity. As the inlet velocity is increased, the initially stable steady flames undergo a transition to an unsteady asymmetric fluctuation until the flame is eventually blown off. A range of the mean inlet velocity is identified in which the flames exhibit local extinction and re-ignition repeatedly.

## 1. Introduction

Towards the development of combustion-based micro-device for power generation [1, 2], there have been efforts to understand the combustion characteristics of premixed flame in meso-scale combustors, in particular for the flame stability.

Recent studies reported that the blowoff limit of hydrogen/air premixed flames in a micro-combustor can be significantly extended using a bluff-body flame stabilizer [3-6]. Vortex shedding to the flow due to the presence of a bluff-body [7, 8] may affect the stability of flames anchored to it [9]. In the present study, high-fidelity numerical simulations are carried out to investigate the onset of instability of hydrogen/air premixed flames in a meso-scale channel with a square bluff-body. Through two-dimensional numerical simulations for a range of inflow velocities, flame dynamics and associated combustion characteristics are illustrated and discussed.

## 2. Method

Compressible, multi-species reacting Navier-Stokes equations are solved with a high-fidelity finite difference method using 8$^{th}$ order central difference and 4$^{th}$ order explicit Runge-Kutta time integration. For a lean hydrogen/air mixture of equivalence ratio 0.5, a detailed reaction mechanism [10] with 9 species and 19 reactions is used.

A two-dimensional computational domain (Fig.1) is set for a channel of 1 mm height and 10 mm length, with a square bluff-body of size 0.5 mm by 0.5 mm acting as a flame holder, whose center is located at 2.25 mm downstream of the inflow boundary. To fully resolve reaction layers, a uniform grid spacing of 5 microns is chosen.

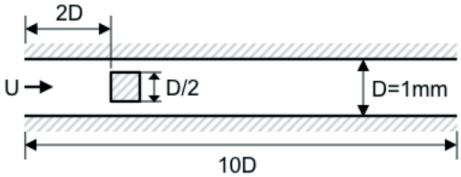


Fig. 1 Two-dimensional computational domain.

Corresponding author: Bok Jik Lee
*E-mail address*: bokjik.lee@kaust.edu.sa

No-slip, adiabatic conditions are applied to the channel walls and bluff-body surfaces. Non-reflecting characteristic boundary conditions are applied for both inflow and outflow boundaries [11, 12]. A fully developed channel flow velocity profile is imposed at the inflow boundary. Cases with a mean inflow velocity U ranging from 15 m/s to 25 m/s are investigated.

## 3. Results and Discussion

At the inflow velocities below U = 19 m/s, the flames anchored to the bluff-body remains stable and steady, suppressing the shedding of vortex, as shown in Fig. 2. At U = 19 m/s, however, a transition from steady to unsteady asymmetric flame starts to occur over time, as shown in Fig. 3. While the flame instability is gradually developed, the flame still remains anchored to the bluff-body. At U = 20 m/s, the flames show saw-tooth like dynamics (Fig. 4), coupled with the shedding of vortices, at this unstable regime.

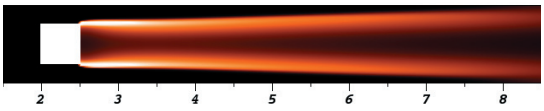


Fig. 2 Heat release rate at U = 15 m/s.

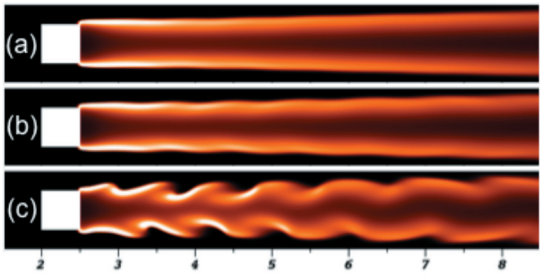


Fig. 3 Heat release rate at U = 19 m/s at times (a) 4.0 ms, (b) 4.2 ms, (c) 5.0 ms.

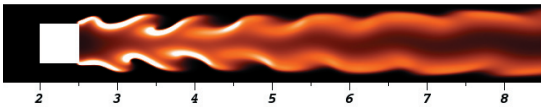


Fig. 4 Heat release rate at U = 20 m/s (t = 4 ms).

Critical flame dynamics near the blowoff limit is shown in Fig. 5 for the case U = 20.5 m/s, where periodic local extinction and recovery of flame occurs in the downstream. At U = 20.6 m/s (Fig. 6), the flame exhibits local extinction and recovery in a more intermittent and unstable manner than that in Fig. 5, and then eventually fails to recover, leading to the blowoff. Note that the blowoff of these flames is not caused by the flame detachment from the bluff-body, but by the local extinction which occurs at a certain distance downstream of the bluff-body. When the inflow velocity is further increased (U > 20.6 m/s), all the flames are eventually blown off.

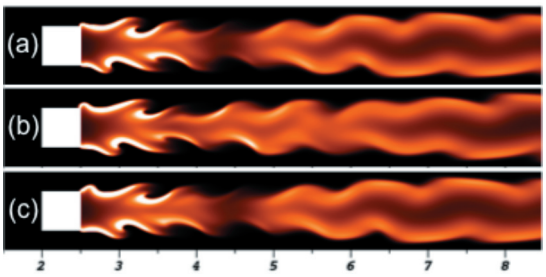


Fig. 5 Heat release rate at U = 20.5 m/s at times (a) 9.43 ms, (b) 9.47 ms, (c) 9.50 ms.

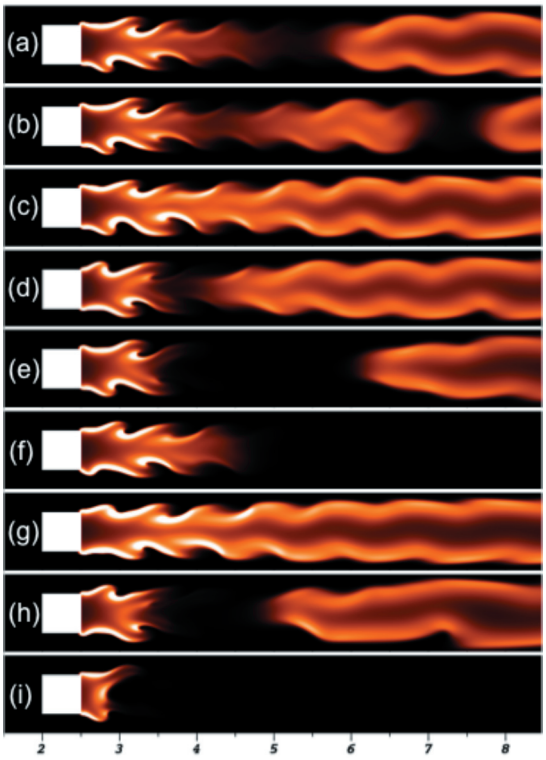


Fig. 6 Heat release rate at U = 20.6 m/s, at times (a) 2.60 ms, (b) 2.65 ms, (c) 2.75 ms, (d) 2.87 ms, (e) 2.96 ms, (f) 3.20 ms, (g) 3.30 ms, (h) 3.50 ms, (i) 3.70 ms.

The onset of local extinction generating holes in the flame, which leads to the blowoff of flame, has been observed experimentally at the near-blowoff limit of lean mixtures for larger scale flames [13-15]. It is found from the present simulations that the local extinction occurs near the downstream end of the recirculation area behind the bluff-body, where the heat supply from the recirculation is not maintained. A detailed analysis of the local extinction point is currently underway in order to provide further insights into the fundamental understanding of the blowoff mechanism.

## 4. Concluding Remarks

The present study presented highly unsteady dynamics of hydrogen/air lean premixed flame behind a bluff-body in a meso-scale channel by direct numerical simulations. When the local extinction of flame at near-blowoff conditions fails to be recovered, the detached bulk flame is blown-off, leading to the extinction of the anchored flame by losing the heat balance between the heat generation and loss. The detailed aerodynamic and chemical coupling that determines the limit conditions needs to be further analyzed.

## References

[1] K. Maruta, *P. Combust. Inst.*, 33 (2011) 125－150.
[2] N. S. Kaisare, D.G. Vlachos, *Prog. Energ. Combust.*, 38 (2012) 321－359.
[3] J. Wan, A. Fan, K. Maruta, H. Yao, W. Liu, *Int. J. Hydrogen Energ.,* 37 (2012) 19190－19197.
[4] A. Fan, J. Wan, Y. Liu, B. Pi, H. Yao, K. Maruta, W. Liu, *Int. J. Hydrogen Energ.*, 38 (2013) 11438－11445.
[5] A. Fan, J. Wan, Y. Liu, B. Pi, H. Yao, W. Liu, *Appl. Therm. Eng.*, 62 (2014) 13－19.
[6] G. Bagheri, S. E. Hosseini, M.A. Wahid, *Appl. Therm. Eng.*, 67 (2014) 266－272.
[7] H. Suzuki, Y. Inoue, T. Nishimura, K. Fukutani, K. Suzuki, *Int. J. Heat. Fluid Fl.*, 14 (1993) 2－9.
[8] K. Suzuki, H. Suzuki, *Int. J. Heat. Fluid Fl.*, 15 (1994) 426－437.
[9] J. Li, Z. Zhao, A. Kazakov, F.L. Dryer, *Int. J. Chem. Kinet.*, 36 (2004) 566－575.
[10] J. R. Hertzberg, I. G. Shepherd, L. Talbot, *Combust. Flame*, 86 (1991) 1－11
[11] C.S. Yoo, Y. Wang, A. Trouvé, H.G. Im, *Combust. Theory Model*. 9 (2005) 617－646.
[12] C.S. Yoo H.G. Im, *Combust. Theory Model*. 11 (2007) 259－286.
[13] S. Yamaguchi, N. Ohiwa, T. Hasegawa, *Combust. Flame*, 62 (1985) 31－41.
[14] S. Nair, T. C. Lieuwen, *J. Propul. Power*, 23 (2007) 421－427.
[15] S. Chaudhuri, S. Kostka, M. W. Renfro, B. M. Cetegen, *Combust. Flame*, 157 (2010) 790－802.

# Flame Propagation Through Smoothly Converging Microchannel

Taisia Miroshnichenko
Far Eastern Federal University
8 Sukhanova Str, Vladivostok, Primorsky Krai, 690950, Russia

**ABSTRACT**

Propagation of combustion wave through smoothly converging microchannel was simulated. Properties that influence on the flame propagation are analyzed. The flow velocities in which the flame is able to propagate beyond contraction, stays into contraction zone or it is quenched before contraction were found. Flame parameters are calculated depending on location of combustion wave. Comparison between smoothly and sudden converging microchannels are conducted.

## 1. Introduction

A phenomenon of propagation of combustion wave in a microchannel with converging zone is considered. It was assumed that narrowest part is located in the middle of channel's length and its diameter in 2 times less than the widest diameter which is situated on the ends (D = 6 mm, d = 3 mm) (see Fig. 1). Premixed methane and air mixture was inputted in the inlet boundary from the left side.

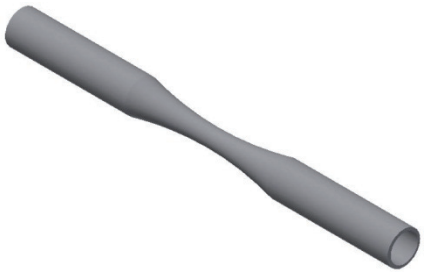

Fig. 1 The form of microchannel.

Not once in the works concerned to the studying of combustion in microchannels were mentioned about the importance of this studying. The main questions are the determining of flammability limits, forms and structures of combustion waves, determining of quenching diameter, flame velocity etc. See for example, [1-3].

The reason is why we started to consider the problem was the experiments conducted by prof. S. Kumar with colleagues from Indian Institute of Technology (Bombay). They were studying the flame propagation through the sudden converging microchannel. We supposed that the smoothly converging microchannel is more effective because the walls influence is less in this case. Moreover we plan to apply these results to study of combustion waves in porous media in the future. It can be proposed that porous medium is like the set of microchannels with such structure.

## 2. Method

The numerical study of the problem was conducted in two-dimensional formulation. The problem was solved in axisymmetric formulation because the tube is symmetric with respect to the horizontal plane. That is the upper half of microchannel was calculated only. The tube length was chosen so that the flame would have a time to take a run before it reaches the contraction. It was assumed that the combustion process goes on with heat losses, i.e. the temperature of microchannel walls is constant and equals 300 K. The mixture of methane and air was inputted to the inlet with different initial velocities and the fuel and oxidizer ratio. Atmospheric conditions were set in the outlet. The patch with higher temperature of 2400 K was assigned close to the outlet boundary for mixture ignition. Transient process was considered. The flow was assumed is laminar.

Corresponding author: Taisia Miroshnichenko
*E-mail address*: taisia.miroshnichenko@gmail.com

## 3. Results and Discussion

It was found that the inlet flow velocity plays critical role in the flame behavior in microchannel. All velocities, in which combustion takes place, can be divided in three parts: first is when the flame gets through the contraction, second is when the flame stays into it, third is when the flame gets quenching before it reaches the narrowest zone. The example of flame propagation through the smoothly converging microchannel is shown in Fig. 2 at different time steps (φ is equivalence ratio).

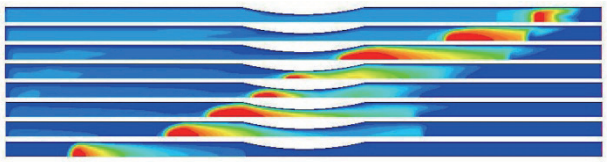

Fig. 2 Temperature contours at different time steps. v = 0.01 m/s, φ = 0.9.

Since the reaction zone of the flame can be defined as the region of heat release [4], it can be concluded that the temperature contours must follow the shape of the reaction zone. Also the maximum temperature which is reached in the channel was calculated depending on axial distance and time. The temperature gets higher than 2500 K at ignition moment but it becomes smaller when the flame comes up to the converging zone of the channel because of heat losses.

Simulation of sudden converging microchannel was made as well. Geometric parameters of such microchannel are almost the same as for smoothly converging microchannel (D, d, length of converging

zone). In this case flame also isn't able to propagate beyond the contraction for velocity of 0.02 m/s and more (see Fig. 3). When flame came to the step, temperature starts decreases faster and flame is extinguished. Note that such results were observed in experimental studying. But for smoothly converging microchannel, flame can come up closer to the middle of tube.

Fig. 3 Temperature contours at different time steps. v = 0.02 m/s, φ = 0.9.

**4. Concluding Remarks**

The problem of flame propagation in smoothly converging microchannel was studied numerically. It was found that the critical role in the flame propagation through it plays inlet flow velocity. Three regimes of flame propagation exist depending on the flame velocity. Heat losses due to influences of microchannel walls, temperature and velocity were analyzed. Comparison with sudden converging microchannel was conducted. It can be concluded that smoothly converging walls are more effective for flame propagation than sudden converging walls.

**Acknowledgements**

This work was supported by The Ministry of Education and Science of Russian Federation (grant №14.Y26.31.0003) and Far Eastern Federal University.

**References**

[1] Maruta K.,Parc J. K., Oh K. C., Fujimori T., Minaev S. S., Fursenko R. V. *Combustion, Explosion, and Shock Waves,* V. 40, (2004) 516-523.

[2] Kaoru Maruta, Takuya Kataoka, Nam Il Kim, Sergey Minaev, and Roman Fursenko. *Proceedings of the Combustion Institute*, 30(2), (2005) 2429 – 2436.

[3] Yiguang Ju and Kaoru Maruta. *Progress in Energy and Combustion Science*, 37(6), (2011) 669 –715.

[4] Irvin Glassman and Richard A. Yetter. *Combustion (Fourth Edition)*, (2008) 409 – 494.

# Efficiency of Thermoelectric Generator Combined with Small sized Countercurrent Microcombustor

Igor Terletskiy[1], Sergey Minaev[1], Sudarshan Kumar[2], Kaoru Maruta[1,3]
[1]FEFU, School of Engineering Sciences, Vladivostok, Russia
[2] Indian Institute of Technology, Bombay, Powai, Mumbai India 400 076
[3]Institute of Fluid Science, Tohoku University, Sendai, Japan

**ABSTRACT**

A new system for converting combustion heat into electric power was proposed on the basis of countercurrent burner with thermoelectric element embedded in a wall separating incoming fresh mixture and combustion products. The wall serves as heat exchanger between combustion products and the fresh mixture. Numerical simulations showed that almost whole combustion heat may be transferred through the thermoelectric element in such system and the total thermal efficiency attained a value close to the conversion efficiency of the thermoelectric device itself.

## 1. Introduction

Electric or mechanical power mostly obtained by converting thermal energy released by combustion hydrocarbon fuels. In some cases the heating value of very lean or low caloric gas premixture is not enough to provide self-sustaining combustion. Burning of very lean gas mixture or low caloric fuel can be provided in the system with heat regeneration. The effective heat regeneration may be realized in the countercurrent burner [1-3]. In a simple linear variant of such burner, the incoming reactant flows in one channel whereas the combustion products flow in another channel in opposite direction [4]. The channels are separated by heat conducting wall, which transfers heat from combustion products to unburned gas mixture. In this case, unburned mixture with elevated temperature enables to sustain combustion in combustion room even in the case of use of very lean gas premixtures. In this configuration of the burner, a temperature gradient forms both in the transverse and lateral cross sections of the separating wall. The transverse heat flux is used for heat regeneration, whereas the lateral heat flux along the separating wall is used for thermoelectric generation.

The main goal of this study is to estimate the total thermal efficiency of the system within a simple model taking into account the heat exchange and the thermoelectric generation.

## 2. Mathematical model

The scheme of burner with countercurrent heat exchanger and a thermoelectric converter is shown in Fig.1. The system is two channels with gas flows coming from the opposite directions and the thermoelectric element embedded into the heat conducting wall separating two channels. The unburned gas preheating by combustion products allows to burn very lean gas premixture. The unburned gas preheating occurs through the heat conducting wall separating combustion products and unburned mixture. The thermocouple embedded in the separating wall operates temperature difference at the wall ends.

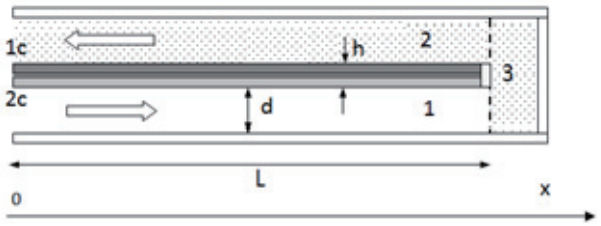


Fig. 1 Scheme of countercurrent burner with thermoelectric converter. 1, 2 – are thermocouples legs with electric insulation and electric junction at the hot end of separating wall; 3 – is combustion room, 1c, 2c – are electric junction connected with load. Dashed line marks the unburned mixture input and the combustion products exhaust from combustion room. White arrows show the direction of the gas flow in the microchannels.

The set of governing equations describing temperature distributions in the fresh mixture, combustion products and the separating wall can be written in the following form

$$m c_P d \frac{dT_1}{dx} = -\alpha(T_1 - \theta) \quad (1)$$

$$m c_P d \frac{dT_2}{dx} = \alpha(T_2 - \theta) \quad (2)$$

$$\lambda_S h \frac{d^2\theta}{dx^2} - \alpha(2\theta - T_1 - T_2) = 0 \quad (3)$$

Here $T_{1,2}$ is the scaled temperature in unburned mixture and combustion products; $\theta$ is wall temperature; m is the mass flow rate; α is the Newtonian heat exchange coefficient between solid and the gas; $h$ and $d$ are the wall width and the channel diameter, respectively. $c_P$ and $\lambda_S$ are the gas heat capacity and the solid wall heat conductivity, respectively.

Equations (1)-(3) are subjected by the following boundary conditions: at inlet (x=*0*): $T_1=\theta=T_0$; at x=$L$:

Corresponding author: Igor Terletskiy
*E-mail address*: minaevss@yahoo.com

$T_2$-$T_1$=$T_b$-$T_0$, $\lambda_S d\theta / dx = -Z(\theta_F - T_0)\theta_F / 8L$. Here the $\theta_F$ is the temperature of the hot end of the wall, Z is the thermocouple figure of merit; $T_b$ is adiabatic temperature of given premixture at initial temperature $T_0$; $L$ is the channel length.

The total thermal efficiency of the system $\eta$, which is defined as the ration of the electric power generated to the combustion heat, may be written in the form:

$$\eta = \frac{W_{el}}{W_{ch}} = \frac{\gamma Z(T_b - T_0)}{16}\left(\frac{\theta_F - T_0}{T_b - T_0}\right) \qquad (4)$$

where $\gamma = \lambda_S h / mc_P d\, L$ is nondimensional parameter. The solution of equations (1)-(3) can be found analytically and it yields the dependency of $\theta_F$ on parameters including length of the channel $L$. Note that the ideal efficiency of the thermocouple $\eta_0$ with the hot junction temperature $\theta_F$ and the cold junction temperature $T_0$ is defined by formula [5]:

$$\eta_0 = \frac{Z(\theta_F - T_0)}{16}$$

The maximal thermal efficiency of the system without heat regeneration is defined by formula

$$\eta_{0\max} = \frac{Z(T_b - T_0)}{64} \qquad (5)$$

and it attans in the case when the temperature of the hot junction is $\theta_F = (T_b + T_0)/2$.

## 3. Results and Discussion

Numerical simulations showed that the temperature of the hot junction $\theta_F$ is proportional to the channel length $L$. The increase of the channel length lead to the increase temperature of the combustion products and the temperature $\theta_F$. Formally, the simple model yields that temperature of the hot junction may reach any, even very large temperature, if the channel length is comparatively large. Inclusion in the model of the real heat losses and the detailed chemistry can change this conclusion. Inclusion in the consideration of the real heat losses and the detailed chemistry can change the conclusion. Nevertheless, the temperature of the hot junction may be very high and it can attain the melting temperature of the solid wall $\theta_M$. The model allows to estimate the channel length $L$ that is needed to reach the given maximal working temperature $\theta_M$. Knowing the length $L$ corresponding to the fixed value of $\theta_M$ one can estimate the thermal efficiency of the system by formula (4). The typical thermal efficiency $\eta$ dependencies on the inlet gas velocity $u$ is given in Fig.2. This results shows that for the maximum efficiency of energy conversion in a small-size device to be reached, the properties of thermoelectric materials, the device geometry, and other parameters have to be correlated with the gas combustion characteristics. It was shown that the efficiency of energy conversion in such system can be higher than in the system without heat regeneration. For example, the maximal efficiency corresponding to curve 1 in Fig.2 may be almost in four time larger than that calculated by formula (5)

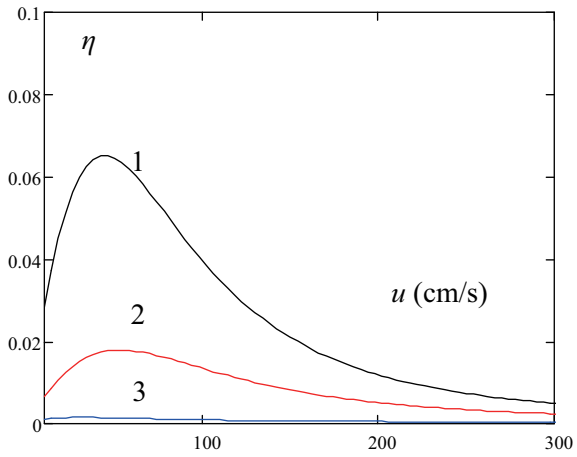


Fig. 2 The thermal efficiency $\eta$ dependencies on the inlet gas velocity $u$ evaluated for $T_b$-$T_0$=300K, Z=0.001, $d$=0.3 cm, Nusselt number $Nu$=4, $\lambda_S / \lambda_g = 5000$ and $h$=0.1 cm(1), 0.15cm(2), 0.2cm (3), $L$=5 cm (1), 40cm (2), 60cm (3), correspondingly.

describing ideal efficiency of the system without heat regeneration.

## 4. Concluding Remarks

The concept of countercurrent heat regenerating burner with thermoelectric element is proposed. The maximal efficiency of the proposed system can be close to the maximal efficiency of the applied thermoelement even in the case of operating with very lean gas premixture. Another advantage of the proposed system is the absence of special cooling system that is necessary to use in conventional system. The proposed system is perspective for conversion of lean gas mixture combustion heat into electricity by thermoelectric method.


## Acknowledgements

This work was partially supported by General Collaborative Research Project IFS, Tohoku University, by the Ministry of education and science of Russian Federation (project 14.Y26.31.0003), Far-Eastern Federal University and the RFBR project No. 14-08-92695.


## References


[1] P. D. Ronney, *Combust. Flame*, 135 (2003) 421-439.

[2] N. I. Kim, S. Kato, T. Kataoka, T. Yokomori, S.Maruyama, T. Fujimori and K.Maruta, *Combust. Flame*, 141 (2005) 229-240.

[3] S.A. Lloyd and F.J. Weinberg, *Nature*, 251 (1974) 47–49.

[4] R.V.Fursenko, S.S.Minaev and V.S.Babkin., *Explosion and Shock Waves*, 37, (2001) 493-500.

[5] S.S.Minaev and R.V.Fursenko, *Combustion, Explosion, and Shock Waves*, 43 (2007) 1–8.

Eleventh International Conference on Flow Dynamics
October 8-10, 2014, Sendai, Miyagi, Japan

# An Experimental Study on the Structural Characteristics of the Flame Formulated in a Mesoscale Fuel Mixing Layer

Min Jung Lee[1], Nam Il Kim[1*]
[1]Korea Advanced Institute of Science and Technology (KAIST)
Dept. of Mechanical Engineering, 291 Daehak-ro, Yuseong-gu, Daejeon, 305-701, Korea

**ABSTRACT**

The structural characteristics of the flame formulated in a mesoscale fuel mixing layer were investigated experimentally and theoretically. Various flame behaviors were observed. Due to the confined structure of the combustor in this study, diffusion flames and partially premixed flames at very narrow strain rates could be stabilized and their characteristics were investigated. There were three extinction modes corresponding to high strain rate (HSR), low strain rate (LSR) and fuel dilution ratio (FDR) limits for diffusion flame, additionally, flashback was observed for partially premixed flame.

## 1. Introduction

Recently, interest in combustion phenomena in a narrow space has been increased [1-3]. It is not only related to the development of micro-scale or meso-scale combustors for higher energy density of fossil fuel, but also concerned with the understanding on the interaction between gas combustion and burner configuration.

In the basic approach, various laminar flame characteristics have been investigated using opposed flow flames (hereafter OFFs) for premixed flames (PF), partially premixed flames (PPF), and non-premixed flames (or diffusion flame, DF) mostly in an open space [4-6]. However, OFFs have not been adopted sufficiently in the micro-combustion studies. Recently, an experimental study by Kim et al. [6] was conducted using an opposed fuel jet flow in a narrow coaxial air tube. In that study, a significant extension of flame stabilization conditions corresponding to very low strain rates could be obtained. A consecutive numerical study by Kim [7] on the same configuration showed more clearly that there are two distinctive flame stabilization limits: one at higher strain rates (HSRs) due to the flame stretch and the other at lower strain rates (LSRs) due to the thermal quenching.

Regarding to the LSR extinction of non-premixed flames, a limited number of papers has been reported. This is because a low strain rate experiment was difficult to realize mainly due to the buoyancy effect. To reduce the buoyancy effect, many experiments using opposed flow non-premixed flames (OFNPFs) have been conducted in micro-gravity conditions.

In this study, OFNPFs in a narrow channel were chosen as the basic model of flames in small-scale combustion spaces. Flame in a narrow channel was expected to have distinctive flame structures and behaviors mainly due to the restricted buoyancy effects and enhanced heat loss to the channel. Flame stabilization conditions are first investigated by changing simultaneously inlet flow velocities and fuel dilution ratios for various burner distances, burner width and channel gap for methane-air OFNPFs. The structures and characteristics of the partially premixed flames (PPF) at LSRs are also investigated in detail.

Corresponding author: Nam Il Kim
*E-mail address*: nikim@kaist.ac.kr

## 2. Method

A schematic of the experimental apparatus is shown in Fig. 1. The narrow channel of the burner consists of two quartz plates (400 mm×300 mm×3 mm), and it was set in the horizontal direction to minimize the buoyancy effect in the channel. Three cases of channel gaps ($h$= 5, 6, 8 mm) were examined. A pair of nozzle plates was installed in the opposite direction within the narrow channel. Flow straighteners were installed within each nozzle. The width of the nozzle, $^{w}$, in the transverse direction ($y$-direction) were 20 mm or 30 mm, and each nozzle had long burner rims. The nozzle distance, $^{d}$, in the axial direction ($x$-direction) was precisely varied using an optical traverse. A flame was ignited from the exit of the burner. Then, a pair of stainless steel poles was installed at the exit in order to help burner alignment and prevent the flame disturbances by the external flow.

The most representative parameter in the OFNPF study is a strain rate. In this study, therefore, the average inlet velocity from the both fuel and air nozzles, $V$, were controlled to be same, and the strain rate, $a$, was defined as follows for simplicity;

$$a = 2V / d \tag{1}$$

Another parameter for experiment is a fuel dilution ratio, $X_{N_2,F}$. Flow rates and concentrations of the mixtures were controlled by mass flow controllers. Methane (>99.995%), air (< 1% humidity), and nitrogen (>99.995%) were used. Air and fuel were introduced from the left and right nozzles, respectively. Flame images were captured with a camera (D80, Nikon) and a high speed camera (Hot Shot 1280, NAS) equipped with an intensifier (II18GD, Lambert).

## 3. Results and Discussion

The direct photos of diffusion flame (DF) near the LSR condition ($a$ < 20 $s^{-1}$) are shown in Fig 2. To decrease the strain rates, the nozzle distance were increased or the flow velocity were decreased. With an increase in nozzle distance, the flame moved to the stagnation surface at the center of the combustor. With a decrease in velocity, on the other hand, the flame front moved closer to the nozzle. One interesting phenomenon is that the flames could propagate even

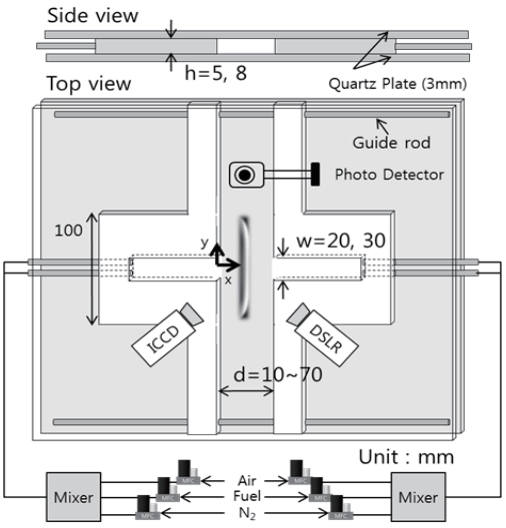


Fig. 1 Schematic diagram of counter flow burner and flow systems

into the nozzle with a further decrease in flow velocity. This implies that a stoichiometric condition could be departed far from the stagnation plane at LSRs.

To investigate the departure of the flame from the stagnation surface, methane and propane flames were compared for a larger nozzle distance ($d$ = 2cm) (not shown here). As a result, a propane flame could be located farther inside of the air nozzle. This flame departure can be explained by the deviation of the stoichiometric air composition. This large departure of a flame from the stagnation plane will be one representative mode at LSRs. With the increase in the nozzle distance, flames were formulated outside the nozzle, despite the large flame departure from the stagnation surface. Then the LSR-limits could be extended further lower conditions.

When the flames were formulated outside of the nozzle, the LSR-limits were not affected by nozzle distance. This means that there can be a unique mechanism for flame extinction at LSR. The flame oscillation near the LSR-limits was expected to provide some clues regarding to the flame extinction mechanism.

A representative behavior of the oscillating diffusion flame is shown in Fig 3. It can be broken down into two

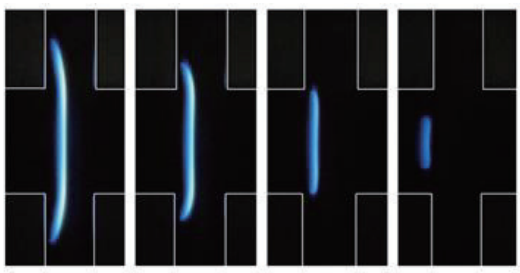

Fig. 2 Direct flame images of DF at LSR (w20h8d10, methane, without dilution).

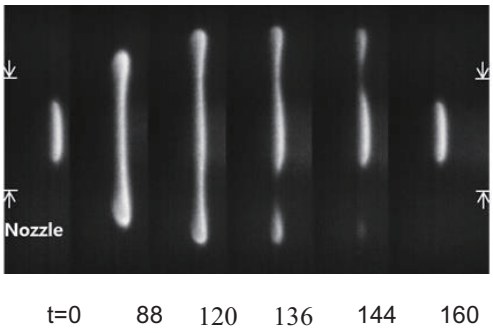


Fig. 3 Transient ICCD images for one period at the oscillation mode ($a$ =2.8 $s^{-1}$, methane)

regions: one is a core region where the flame shape is not varied and the other is a periodic oscillation region where a fragment of the flame propagates and extinguishes periodically in the $y$-direction. The diffusion flame edges had the propagation velocity in the stream wise direction from the view point of an edge flame, like a premixed flame. We can then explain this diffusion flame oscillation phenomenon with the previous premixed flame oscillation mechanism. Regarding to this phenomenon, a more detailed study is now in progress.

## 4. Concluding Remarks

An opposed flow burner in a narrow channel was suggested as an essential model of a small scale combustor. Flame structures and behaviors of diffusion flames and partially premixed flames were investigated. There were three extinction modes corresponding to high strain rate (HSR), low strain rate (LSR) and fuel dilution ratio (FDR) limits. In particular, the existence of LSRs is a typical characteristic of a small-scale combustion. Based on the significant dependency of the LSR-limits on the channel gap scale, conductive or convective heat loss from the flame was found to be the main cause. More detail explanations will be presented at the technical session.

## Acknowledgements

This work was supported by the National Research Foundation of Korea (NRF) grant funded by the Korea Government (MSIP) (NRF-2013R1A2A2A01015816).

## References

[1] K. Maruta, *Proc. Combust. Inst.* 33 (1) (2011) 125-150.
[2] Y. Ju, K. Maruta, *Prog. Energy Combust. Sci.* 37 (6) (2011) 669-715.
[3] M.J. Lee, N.I. Kim, *Combust. Flame* 157 (1) (2010) 201-203.
[4] H. Tsuji, *Prog. Energy Combust.* 8 (2) (1982) 93-119.
[5] J. Buckmaster, *Prog. Energy Combust.* 28 (5) (2002) 435-475.
[6] N.I. Kim, Y.M. Yun, M.J. Lee, *Int. J. Heat Fluid Flow* 31 (4) (2010) 680-688.
[7] N.I. Kim, *Combust. Flame* 159 (2011).

Eleventh International Conference on Flow Dynamics
October 8-10, 2014, Sendai, Miyagi, Japan

# Low-Lewis-Number Counterflow Flame Experiments Under Microgravity for a Comprehensive Combustion Limit Theory

Tomoya Kobayashi[1], Hisashi Nakamura[1], Takuya Tezuka[1], Susumu Hasegawa[1], Koichi Takase[1], Masato Katsuta[2], Masao Kikuchi[2], Kaoru Maruta[1]
[1]Institute of Fluid Science, Tohoku University
2-1-1, Katahira, Sendai, Aoba-ku, Miyagi, 980-8577, Japan
[2]Japan Aerospace Exploration Agency
2-1-1, Sengen, Tsukuba, Ibaraki, 305-8505, Japan

**ABSTRACT**

Relationship between propagating planar flames and flame balls was investigated for the purpose of constructing a comprehensive combustion limit theory. Numerical simulations of counterflow flames and flame balls, counterflow experiments under microgravity and normal gravity were conducted for $CH_4/O_2/CO_2$ and $CH_4/O_2/Xe$ mixtures. It was found that a wide variety of flame types is observed including ball-like flames, thus establishing a platform for future investigation on such theories.

## 1. Introduction

In light of today's demand for high efficiency combustors, an accurate and a comprehensive understanding of gaseous combustion limits is needed. Counterflow flames are one of the most common ways to investigate the combustion limits for a flame. At low flow velocities, flames can only be observed under microgravity and counterflow experiments with a droptower (JAMIC) has been conducted to obtain combustion limits[1]. Meanwhile, theoretical and experimental investigations revealed that spherical flames that do not propagate, flameballs, can exist below the planar flame limit for low-Lewis-number mixtures under microgravity[2]. Here, Lewis number is a non-dimensional parameter which can be described as the ratio of the diffusion coefficient and the heat diffusion coefficient. However, since the normal stretched flames and flameballs were investigated separately, there are only limited attempts to bridge these two flames[3]. For discussion on absolute combustion limits, a theory that encompasses these two types of flames is required. Therefore, the final goal of this research is to provide a comprehensive understanding on combustion limits and to provide a benchmark data connecting the counterflow flames and flameballs for further investigation.

## 2. Numerical and Experimental Method

1-D steady state computations of ideal counterflow premixed flames and flame balls were conducted to assess the possibility of transition from planar flames to flame balls and also to determine the experimental conditions. The employed mixtures are $CH_4/O_2/CO_2$ and $CH_4/O_2/Xe$ mixtures. $CO_2$ diluted mixtures are employed to assess the effect of radiative reabsorption on the combustion limit. Xe diluted mixtures are employed in order to obtain extremely low Lewis numbers. The ratio of oxygen to diluent mole fractions for $CO_2$ diluent and Xe diluent mixtures are set to 0.40 and 0.14 respectively. A 1-D steady state code modified from PREMIX was used for counterflow computations. The computed region was 10 cm and computations which consider radiative heat loss (OTM) was conducted. Since $CO_2$ is also a radiation absorbing species, computations that consider radiation reabsorption was also conducted (SNB) [3]. For computations using the SNB model, the arc-length continuation method was employed to reduce computation time [4]. A 1-D spherical steady state code modified from PREMIX was used for flame balls and the computed regions is 100 cm. The radiation model employed in this computation is the OTM. All computations were conducted under atmospheric pressure and the chemistry was taken from GRI-3.0 with reactions related to N removed while the parameters for Xe were inserted.

Counterflow experiments were conducted for a wide range of flow velocities. For high flow velocities where the gravity effect can be neglected, experiments were conducted on the ground whereas for low flow velocities, experiments were conducted under microgravity. Microgravity conditions were obtained onboard the MU-300 provided by Diamond Air Service Company located in Aichi, Japan. The burner diameter and the burner distance for experiments on the ground are 1.0 cm and 1.5 cm respectively, and the ones used on the airplane are both 3.0 cm. For flame observation, two HD cameras and a high-speed camera equipped with an image intensifier was used. To obtain transition from planar flames to flame balls, the flames were ignited at around equivalence ratio 0.7, and the equivalence ratio was gradually decreased while the stretch rate is kept constant.

## 3. Results and Discussion

Figure 1 shows computational results of counterflow flame temperature and flame ball temperature at different equivalence ratios for $CH_4/O_2/CO_2$ mixtures. For counterflow flames, flame temperature decreases with a decrease of equivalence ratio, resulting from a decrease in amount of fuel. In contrast, for flame balls, flame temperature increases with a decrease of equivalence ratio. This is because the decrease in

Corresponding author: Tomoya Kobayashi
*E-mail address*: t.kobayashi@edyn.ifs.tohoku.ac.jp

equivalence ratio causes the flame ball diameter to decrease, resulting in an intensification of the flame due to the Lewis number effect. This effect is seen at Lewis numbers lower than unity when flames experience stretch. In the region at low stretch rates and equivalence ratios, flame temperature of flame balls is higher than that of counterflow flames. Because of this stronger solution, it can be estimated that when the stretch rate is sufficiently low and the equivalence ratio is gradually decreased, a transition from planar flames to a flame ball may occur. Calculation results for Xe diluted mixtures showed the same tendency of flame temperature for counterflow flames and flame balls. However, for Xe diluted mixtures, the range of equivalence ratio where the flame ball temperature is higher than counterflow flame temperature was wider. This suggests that the region in equivalence-stretch rate plane that transition from planar flame to ball-like flame is expected to be observed may be wider than $CO_2$ diluted flames.

The observed flame types from microgravity experiments are shown in Fig. 2. Normal planar flames were observed in microgravity as shown in Fig. 2(a). For experiments on the ground, only planar flames were observed. In microgravity, cellular flames were also observed as shown in Fig. 2(b) which is a manifestation of instability intrinsic to low-Lewis-number flames. Furthermore, ball-like flames were observed in microgravity as shown in Fig. 2(c) demonstrating our hypothesis that transition from planar flames to flame balls may be observed by this method. In the transitional region from planar flames to flame balls, and for extremely low stretch rates around 1.0 $s^{-1}$, pulsating flames as shown in Fig. 2(d) were observed.

Figure 3 shows the combustion limit obtained from computations and experiments in the stretch rate-equivalence ratio plane for $CO_2$ diluted mixtures. The region surrounded by the plots is the region where the flames are able to exist. From counterflow computations, the so-called C-curve was obtained. For computations with the SNB model, a bifurcation that leads to the solution of the 1-D planar propagating flame can be observed at low stretch rates. Due to the radiation reabsorption effect, it was found that the combustion limit was extended to lower stretch rates and equivalence ratios. Computations with the SNB model are found to agree remarkably well with the experiment results in that the C-shaped curve is shown for relatively

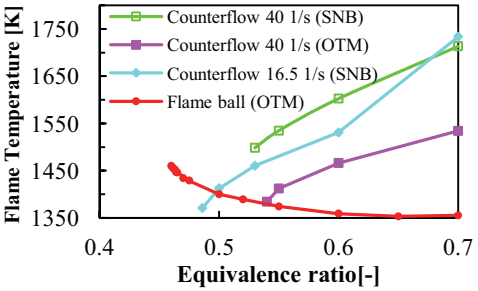


Fig. 1 Computational results of counterflow and flame ball temperature at different equivalence ratios for $CH_4/O_2/CO_2$ mixtures.

higher stretch rates. However, in the yellow triangular region, a break from the C-curve was seen and here, ball-like flames were observed. This shows that a combustion limit theory including the curved flames into consideration must be developed, since the conventional theory as shown in numerical simulations cannot express these types of phenomena. For Xe diluted mixtures, the break from the C-curve was found to be more prominent due to the lower Lewis number.

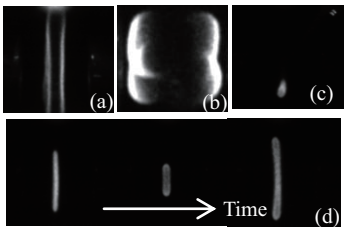


Fig. 2 Flame images seen in microgravity experiments. (a) Planar flames, (b) Cellular flames, (c) Ball-like flames, (d) Pulsating flames.

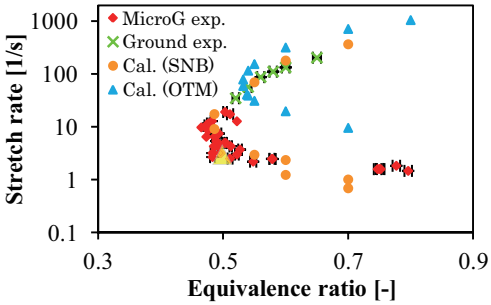


Fig. 3 Computational and experimental combustion limits of $CH_4/O_2/CO_2$ counterflow flames.

## 4. Conclusion

Numerical and experimental investigation of counterflow flames and flame ball for low-Lewis-number mixtures revealed results indicated below:

(1) Combustion limits for low-Lewis-number mixtures in a wide range of stretch rates were obtained numerically and experimentally.

(2) Both computations and experiments showed that the transition from planar flames to flame balls may be observed, and the transition to a ball-like flame was observed in microgravity experiments.

(3) A wide variety of flame types were observed in microgravity experiments.

## References

[1] K. Maruta, M. Yoshida, Y. Ju, T. Niioka, *Proc. Combust. Inst.*, 26 (1996) 1283－1289.

[2] P. D. Ronney, M. S. Wu, H. G. Pearlman, K. J. Weiland, *AIAA Journal*, 36, (1998) 1361－1368.

[3] K. Takase, X. Li, H. Nakamura, T. Tezuka, S. Hasegawa, M. Katsuta, M. Kikuchi, K. Maruta, *Combust. Flame*,160, (2013) 1235－1241.

[4] J. Wang, T. Niioka, *Combust. Theo. Model.*, 5 (2001) 385 - 398.

[5] Y. Ju, H. Guo, K. Maruta, F. Liu, *J. Fluid Mech.*, 342, (1997) 315－334.

Eleventh International Conference on Flow Dynamics
October 8-10, 2014, Sendai, Miyagi, Japan

# Development of Green Space Propulsion using Nitrous Oxide Based Propellants

Yen-Sen Chen[1], Jhe-Wei Lin[2], Tzu-Hao Chou[2], S. S. Wei[2], Jong-Shinn Wu[2], Luke Yang[1], Bill Wu[1]
[1] National Space Organization
8F, 9, Prosperity 1st Rd., Hsinchu Science Park, Hsinchu 30078, Taiwan
[2] Dept. of Mech. Engr., National Chiao Tung University
1001 University Road, Hsinchu 30010, Taiwan

**ABSTRACT**

In this study, a new method of using small pre-combustion chamber is proposed to easy the preheat requirement of the thruster system and provide good startup response and thrust performance for monopropellant, bi-propellant and hybrid rocket designs. A comprehensive computational method is employed in analyzing the design for the purpose of fine-tuning the flow path and to lower the inlet flow responses to combustion waves. This computational model includes conjugate heat transfer and finite-rate chemistry models with real-fluid properties in a turbulent flowfield.

## 1. Introduction

New trend in space propulsion system development include concepts and ideas of environmentally friendly green propellants. Nitrous oxide ($N_2O$), hydrogen peroxide ($H_2O_2$), ammonium dinitramide (AND), hydroxylammonium nitrate (HAN), hydrazinium nitroformate (HNF), etc. have been considered for potential space flight applications [1-9]. Among these propellants, nitrous oxide is one candidate that has easy storability, handling and with good performance when applied in monopropellant or in bipropellant designs. One important technical question regarding this propellant is the requirement of high initial catalyst bed temperature to start the decomposition process for quick thrust response.

Due to the high energy barrier in the decomposition of nitrous oxide, heated catalyst is usually required in the monopropellant applications. To make this decomposition process more effective, a small pre-combustion chamber can be employed to produce high-temperature combustion gas by decomposing nitrous oxide using a catalyst setup with small power input. This hot-gas stream is then used to cause more nitrous oxide decomposition in the main combustion chamber downstream where other propellants such as additional nitrous oxide and/or hydrocarbon fuel, either solid of liquid can be introduced.

In the case of monopropellant applications, the amount of additional oxidizer introduced in the main combustion chamber decides whether the overall combustion process can be completed as designed or not. Too much oxidizer flow rate added in the main combustion chamber may cause the hot gas from the pre-combustion chamber to quench. To determine the maximum oxidizer flow rate allowed in the main combustion chamber, numerical analysis using comprehensive computational models is a very cost-effective approach in the design cycles. Such model requires the computations of multi-components chemical reactions in complex turbulent flows.

For the monopropellant applications, the exothermic decomposition process of nitrous oxide results in the products of nitrogen and oxygen at 1915.6K. The ideal vacuum Isp is 192 sec in this case, which is lower than the 230 sec of hydrazine but higher than the 187 sec of hydrogen peroxide. Assuming the overall efficiency is about 97% in the design practice with finite nozzle area expansion, nominal monopropellant thrusters in space applications using nitrous oxide can reach 186.5 sec vacuum Isp.

With bipropellant designs using nitrous oxide and propane, the theoretical vacuum Isp can reach 312 sec. When athane is used instead of propane, 320 sec vacuum Isp can be obtained. It is also proposed that these hydrocarbon fuel can be premixed with nitrous oxide to produce high combustion efficiency in practical thruster designs. These nitrous oxide fuel blends (NOFBX) is theoretically safe to operate also due to the high energy barrier for the decomposition of nitrous oxide. Computational and experimental investigations are needed to produce a safety guideline for these novel propellant designs.

In this study, a new method of using small pre-combustion chamber is proposed to easy the preheat requirement of the thruster system and provide good startup response and thrust performance. This design is also applicable to bi-propellant and hybrid rocket designs. In case of bi-propellant applications, ethane or propane fuel is employed to boost the overall thrust performance. For hybrid rocket application, HTPB solid fuel is used to test the effectiveness of the present design. A comprehensive computational method is employed in analyzing the design for the purpose of fine-tuning the flow path and to lower the inlet flow responses to combustion waves. This computational model includes conjugate heat transfer and finite-rate chemistry models with real-fluid properties in a turbulent flowfield.

## 2. Method of Approach

The present numerical method solves a set of governing equations describing the conservation of mass, momentum (Navier-Stokes equations), energy, species concentration and turbulence quantities, for the flow variables of density, species mass fraction, mean velocities, total enthalpy, turbulence kinetic energy and its dissipation rate.

A finite-rate chemistry model with robust

Corresponding author: Yen-Sen Chen
*E-mail address*: yenchen@nspo.narl.org.tw

point-implicit approach is employed here [10,11]. The catalytic reaction mechanism is also incorporated in the region where the heated catalyst is located in the pre-combustion chamber. A porosity model is employed to model the fluid dynamics in the region of the catalyst material. An extended two-equation turbulence model is used that is suitable for transient and complex turbulent flows [12]. These numerical models are important for high fidelity simulations of combustion physics.

## 3. Pre-combustion Chamber with Heated Catalyst

The design of a pre-combustion chamber with effective catalytic ignition mechanism is the main goal of this study. The chemistry models considered herein are a nitrous oxide monopropellant system and a bi-propellant system that involves nitrous oxide and propane. The ignition source of these systems is the decomposition of the nitrous oxide. There is a wide variety of catalysts that can be used, including platinum, iridium, rhodium, tungsten carbide, copper, cobalt and gold. Heated platinum mesh is considered in this study. The first design of the pre-combustion chamber is 30 mm in length with 5 mm diameter. Simple injection of the propellants from the side wall near the head-end is arranged such that the injected fluid can have better contact with the catalyst material. The platinum mesh is installed in the head-end of the chamber with electric power for heating the platinum mesh.

## 4. Results and Discussion

The predicted temperature field in the chamber with $N_2O$-mono is shown in Fig. 1, which shows the maximum temperature is only about 580 K. This is far below the theoretical value and indicating that the platinum mesh design needs to be better improved. With the same pre-combustion chamber arrangement, propane or ethane is injected from the opposite side of the $N_2O$ in-flow in the second class of bi-propellant test cases. The O/F ratio is 8.6 for these cases. Figure 2 shows the predicted flowfield for a $N_2O$-$C_3H_8$ test case, which gives maximum flame temperature of 3462.8 K. However, the temperature striation is still obvious in the flowfield.

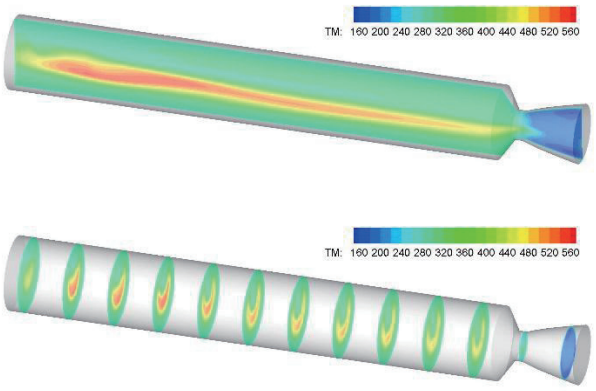


Fig. 1 Predicted temperature field in the pre-combustion chamber of a $N_2O$ monopropellant design case.

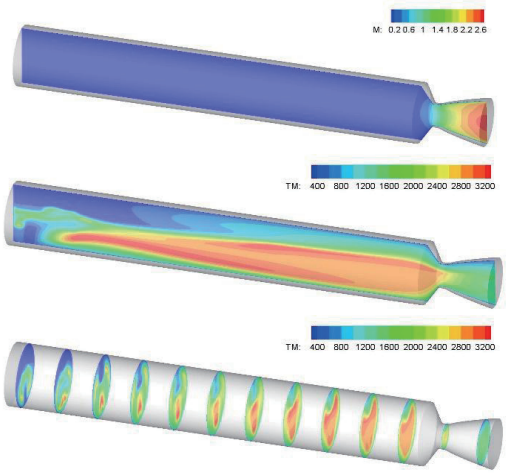


Fig. 2 Predicted temperature field in the pre-combustion chamber of a $N_2O$-propane bi-propellant design case.

## 5. Conclusions

A pre-combustion chamber design for $N_2O$ monopropellant and $N_2O$-hydrocarbon bi-propellant applications has been investigated numerically. Experimental hot-fire tests are to be conducted to anchor the numerical models. The heated platinum mesh is shown to have the effect of flame ignition. But, there is still rooms for improvement for an optimum design.

Acknowledgement

This work is supported by the Sounding Rocket Program of National Space Organization, National Applied Research Laboratory of Taiwan. The computational resources and services are provided by the National Center for High-performance Computing of the National Applied Research Laboratory of Taiwan.

## References

[1] C.D. Brown, *AIAA Book*, Washington DC, (1996), 203-213.
[2] G.P. Sutton, *Rocket Propulsion Elements*, 4th Edition, (1992), 233-257.
[3] V. Zakirov, M. Sweeting, V. Goeman, T. Lawrence, *14th AIAA/USU Conference on Small Sat.*, (2000).
[4] J.C. Whitehead, *1st Hydrogen Peroxide Propulsion Workshop, U. of Surrey*, (1998).
[5] V. Zakirov, T. Lawrence, J. Sellers, M. Sweeting, *5th Intl. Sym. On Small Sat. Sys. & Service*, (2000).
[6] V. Zakirov, M. Sweeting, T. Lawrence, J. Sellers, *51st Intl. Astro. Congress,* (2000).
[7] E. Keith, *1st Hydrogen Peroxide Propulsion Workshop, U. of Surrey,* (1998).
[8] J.C. Whitehead, *1st Hydrogen Peroxide Propulsion Workshop, U. of Surrey,* (1998).
[9] M.A. Vannice, A. Dandekar, *Applied Catalysis: Environment,* 22, (1999), 179.
[10] Y.S. Chen, T.H. Chou, J.S. Wu, G. Cheng, (2013), AIAA-2013-0714.
[11] Y.S. Chen, T.H. Chou, B.R. Gu, J.S. Wu, Bill Wu, Y.Y. Lian, L. Yang, *Computers & Fluids*, 45, (2011), 29.
[12] Y.S. Chen, S.W. Kim, (1987), NASA CR 179204.

# Realization of a Low-NOx Combustion System by Combinations of Burner and Furnaces

Kapuruge Don Kunkuma Amila Somarathne[1], Susumu Noda[2]
[1]Institute of Fluid Science, Tohoku University
2-1-1, Katahira, Aoba-ku, Sendai, Miyagi, 980-8577, Japan
[2]Department of Mechanical Engineering, Toyohashi University of Technology
1-1, Hibarigaoka, Tempaku, Toyohashi, Aichi, 441-8580, Japan

**ABSTRACT**

In confined flames, the recirculation vortex, which is generated between flame and the furnace wall, leads dilution of the combustion mixture. Therefore, the enhancement of the dilution should lead to a peak temperature reduction in the furnace and consequently, considerable thermal NOx abatement. The present study describes a numerical evaluation for characterizing the effect of self-dilution in confined flames, in terms of the furnace geometry and the global equivalence ratio, on the NOx emission properties, and the EINOx exhibits a liner reduction with the increase in the flame dilution.

## 1. Introduction

The several detrimental impacts of nitrogen oxides (NOx) on the environment and human health have led to the designing of an effective combustion system with minimum emission. Among the several combustion techniques, burnt gas recirculation has attracted a great deal of attention because of the unique ability to increase thermal efficiency, whereas simultaneously achieving low NOx emission. However, recirculation of burnt gases naturally takes place in a confined combustion system because of wall confinement. Accordingly, a small cylindrical furnace, which is proposed for placement in a large industrial furnace room, paves the way for combining the pre-heating and dilution phenomena. Hence, the present study describes a numerical evaluation for characterizing the effect of self-dilution in confined flames, in terms of the furnace geometry and the global equivalence ratio, on the NOx emission properties.

## 2. Numerical Models and Conditions

The flow calculation software Open FOAM is used as a finite-volume solver for RANS equations, and the $k$-$\omega$ SST model is used to model the turbulent flux terms. The turbulence-chemistry interaction is accounted with a partially-stirred-reactor model. An augmented reduced kinetic mechanism for the propane-air combustion [1], which includes 28-species, and 69-elementray steps, was selected and coupled with a NOx formation mechanism of GRI 2.11.

Furnaces consist of cylindrical combustion chambers, which are installed vertically, and a burner is installed at the center of the bottom of the combustion chamber [2]. The chambers have inner diameters, $D$, of 95 and 182 mm, and a height of 840 mm.

The numerical simulation was performed in three-dimensional grids using the axisymmetric condition. The calculation grids were concentrated in the flame region, and the smallest grid size was 0.2 mm. Propane was used as the main-fuel, whereas hydrogen was used as the pilot-fuel. The fuel inlet-velocities are listed in Table 1, in terms of the global equivalence ratio, $\phi$. The total airflow rate was fixed at 0.002 m$^3$/s, and thus, $\phi$ was determined based on the fuel flow rate. The high and low air velocities of the two air annular nozzles were 9.8 and 1.8 m/s, respectively. A turbulence intensity of 10% was set for both the fuel and air-inlet flows. The furnace walls were non-slip and adiabatic, and the outlet was specified by the continuity boundary condition. The origin of the coordinates was set at the center of the fuel nozzle exit, and the axial and radial coordinates are indicated by $z$ and $r$, respectively.

Table 1. Fuel-inlet-velocities

| Global equivalence ratio $\phi$ | 0.4 | 0.6 |
|---|---|---|
| Propane-inlet-velocity (m/s) | 10.4 | 15.5 |
| Hydrogen-inlet-velocity (m/s) | 4.0 | 6.0 |

## 3. Results and Discussion

### 3.1 Temperature and Flow-Field Characteristics

Figure 1 shows the radial temperature distributions in terms of $D$ and $\phi$. The present study reproduces the experimentally obtained temperature distributions to a considerable degree of accuracy. The increase in $\phi$ is related to the increase in the fuel rate, and so the reaction rate should be enhanced. Consequently, the flame temperature increases at $\phi$ =0.6, as shown in Fig.1.However, the increase in $D$ decreases the maximum temperature in the flame region. This should be caused by the strong dilution through the strengthened burnt gases entrainment to the flame in the larger cylindrical furnace.

Figure 2 shows the vector maps of the flow fields in the combustion chambers up to $z$ = 300 mm in terms of $D$ for $\phi$ = 0.4, and reveals a vortex, which has been generated between the jet and the wall. The arrows indicating the vectors are not to scale, and the colored bar indicates the magnitudes of the velocity vector. The vector maps illustrate that, in the case of $D$ = 95 mm, the recirculation vortex is limited to $z$ = 270 mm. On the other hand, in the case of $D$ = 182 mm, the recirculation extends beyond $z$ = 300 mm. The recirculation vortex cores for $D$ = 95 and 182 mm are located at axial distances of $z$ = 130 and 180 mm, respectively. This means the recirculation vortex becomes larger with the increase in $D$.

### 3.2 Entrainment and Dilution Characteristics

The recirculation flow characteristics are discussed by

Corresponding author: K.D.K.A.Somarathne
*E-mail address*: kunkuma@flame.ifs.tohoku.ac.jp

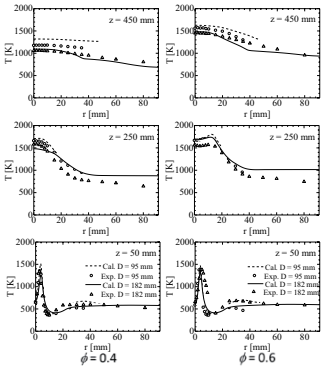


Fig. 1 Radial distributions of mean temperature

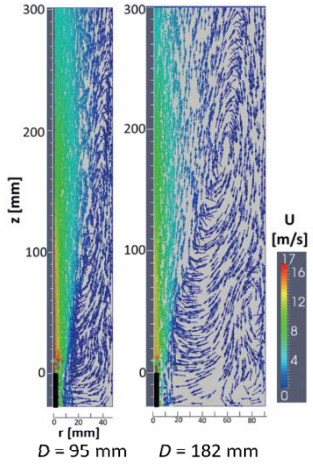


Fig. 2 Vector maps of combustion chambers

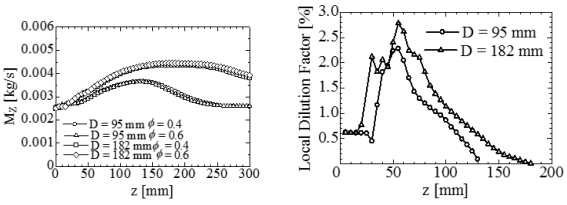


(a) (b)

Fig. 3 (a) Variation of $M_z$, in terms of $D$ and $\phi$ (b) Local dilution factor variation in terms of $D$ for $\phi$=0.4

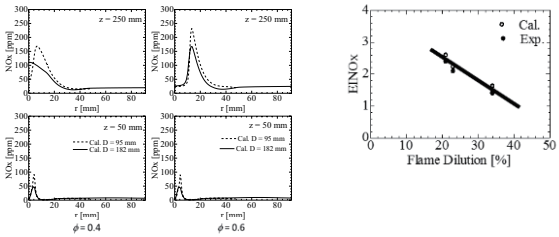


(a) (b)

Fig. 4 (a) Radial distributions of NOx in terms of $D$ and $\phi$ (b) EINOx with total flame dilution

examining the jet zone. In order to facilitate the discussion, a parameter, $M_z$, which represents the mass flow rate of the jet zone is introduced:

$$M_z = \int_0^R 2\pi r \bar{\rho} \tilde{U}_z dr \qquad (1)$$

where $R$ is the maximum radius of the jet zone at each cross section, and $\rho$ is the density of the combustion mixture. Figure 3(a) shows the variation of $M_z$ along the axial direction in terms of $D$ and $\phi$, and the value of $M_z$ increases in upstream of the recirculation vortex because of the entrainment process, and decreases in downstream of the vortex because of the discharge of gases from the jet zone to recirculation zone. Therefore, the peak is located on the cross section of the core of the recirculation vortex. In addition, Fig. 3(a) shows that the increase in $D$ significantly enhances the entrainment process and increases the peak value of $M_z$. However, the effect of fuel velocity, which is related to the $\phi$ on the entrainment is minimal compared to the effect of the inner diameter.

The local dilution factor (LDF) defined in the following equation characterized the entrained burnt and inert gases mass quantities into the flame at each cross section with respect to the jet zone mass flow rate;

$$\mathrm{LDF(z)} = \frac{\int_0^{\Delta z} \left[\frac{dM_z}{dz}\right] \times \left(\tilde{Y}_{CO2} + \tilde{Y}_{H2O} + \tilde{Y}_{N2}\right)_{Near\,wall} dz}{M_z} \times 100 \qquad (2)$$

Figure 3(b) shows the local dilution factor variation in terms of $D$, for $\phi$ =0.4, and the integration of local dilution factors along the axial direction derived total flame dilutions of 23% and 34% for $D$ = 95 and 182 mm, respectively, for $\phi$ = 0.4, whereas, in the case of $\phi$ = 0.6, the total dilutions are 21% and 34% for $D$ = 95 and 182 mm, respectively. Generally, the calculation verifies that confined flame dilution is enhanced by the increase in the inner diameter of the furnace. However, an increase in $\phi$ in small cylindrical furnaces leads to a decrease in flame dilution because the small diameter of the furnace limits burnt gas recirculation. On the other hand, an increase in $\phi$ in large cylindrical furnaces leads to either constant (or an increase) in flame dilution, because the large cylindrical furnace results in strong burnt gas recirculation, and an increase in $\phi$ results in a lower residual $O_2$ concentration in burnt gases. Both of these factors result in strong flame dilution in large cylinders.

### 3.3 NOx Emission Characteristics

Figure 4(a) shows radial distributions of NOx emission with respect to the $D$ and $\phi$. The increase in $D$ leads to a decrease in NOx at each axial position because of the strong flame dilution. The EINOx at the furnace exit was calculated by assuming continuity of the mass flow rate at the furnace exit, and the EINOx was then plotted with the total flame dilution, as shown in Fig. 4(b). The increase in flame dilution decreases the EINOx.

## 4. Conclusions

Strong entrainment leads to extensive flame dilution in large cylindrical furnaces, and, as such, decreases the flame temperature and NOx emission.

## References

[1] E.Djavdan, N.Darabiha, V.Glovangigli, S.M.Candel, *Combust.Sci.Tech*, 76 (1991) 287-309.

[2] S.Noda, J.Inohae, Z.S.Saldi, *Proc.Combust.Inst*, 31 (2007) 1625-1632.

# Special Features of Gas Combustion in Cyclone Vortex Burner

Konstantin Shtym[1], Tatiana Soloveva[1]
[1] Far Eastern Federal University
Sukhanova Street 8, Vladivostok, Primorsky kray, 690950, Russia

**ABSTRACT**

The present work demonstrates special features of air-cooled cyclone vortex burners construction and operation. Based on mathematical model, peculiarities of gas-and-air media mixing in the burner's combustion chamber are explained, conditions and locations for air and fuel inlets are proven.

## 1. Introduction

Working efficiency of burning devices has always been a vital issue in relation to their development, improvement, choice and operation. Department of Heat Power Engineering and Combustion Engineering, FESU, has developed and implemented at the Russian Far East heat generating sources cyclone vortex burner (CVB), a highly efficient device for burning gaseous fuels and residual fuel oils (please refer to fig.1).

The main special feature of gas and residual fuel oil CVB is presence of preliminary combustion chamber with combined inlet of air and gas, which allows to efficiently mix fuel and air in the situation of high combustion rate and high flow turbulence.

Design solution for organization of air and gas inlet into CVB, which is axial and tangential one, is based on optimal flame formation in the CVB combustion chamber and minimal aerodynamic resistance.

Tangential input of ≈75% of total air rate along volute provides for air outside cooling of CVB combustion chamber metal and inside brickwork. Construction of nozzle inlets allows creating wall-adjacent air curtain, which protects the brickwork from overheating and destruction. Axial air input of ≈25% of total air rate for CVB with swirl in the swirler creates an area of stable wall-adjacent burning and area of negative static pressures in the throat zone (diaphragm), so that to form optimal frame opening at the outlet to boiler furnace [1].

Tangential input of ≈70% of total gas rate in CVB through the tangential gas inlet nozzles allows to effectively mix gas with tangentially-input air.

Side input of ≈20% and axial input of 10% of fuel rate to axial and axial adjacent areas stabilize burning processes. Air input to combustion chamber through swirler allows arranging in the wall adjacent area of side gas input nozzles location a zone of minimal velocities, where stable burning is created. Axial gas input forms torch distribution in the axial area, which fact influences conditions of flame efflux to the boiler furnace. It is rational to sustain operation of CVB equipped boilers, at the load >40% of nominal load, with combined gas input into CVB along all three gas inlets. Starting of operation and warming-up of CVB and boiler is reasonable to do with gas supply through side and axial nozzles.

Corresponding author: Konstantin Shtym
*E-mail address*: kot_18@mail.ru

Residual fuel oil is burnt in the CVB combustion chamber through multi-nozzle swirl injector, located along the axis of combustion chamber.

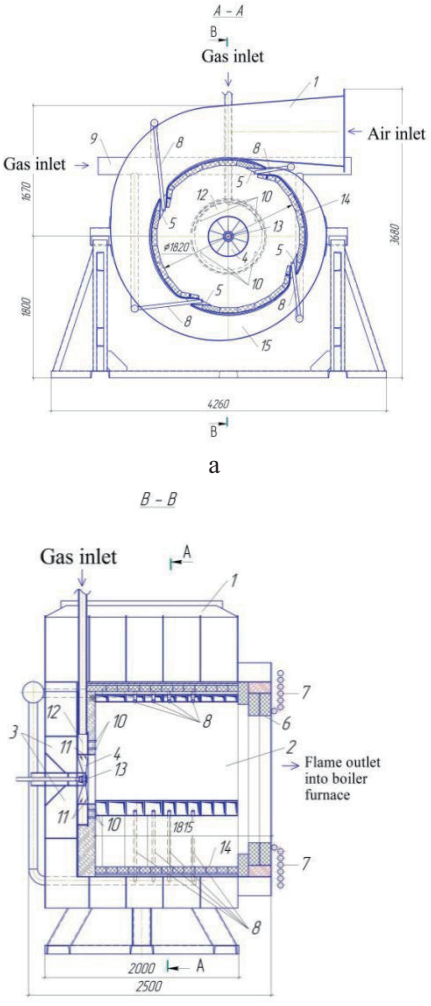


a

b

Fig. 1 Gas and residual fuel oil CVB with a capacity of 64 MW: (a) cross section; (b) longitudinal section; 1 – air distribution conduit; 2 – combustion chamber; 3 – side swirl chamber; 4 – axial swirler; 5 – tangential air inlet nozzles; 6 – throat area; 7 – boiler heating surfaces; 8 – tangential gas inlet nozzles; 9 – tangential gas collector; 10 – side gas inlet nozzles; 11 – axial gas inlet nozzles; 12 – side gas collector; 13 – multi-nozzle swirl injector; 14 – brickwork; 15 – "volute".

## 2. Method

Combined fuel and air distribution and mixing in CVB under consideration here is proven by many years of experience of their operation, as well as by results of mathematical modeling.

Mathematical model, similar to real life CVB construction, allows implementing fuel distribution options as follows:

Option 1 is gas supply through tangential, side and axial inlets;

Option 2 is gas supply through side and axial inlets;

Option 3 is gas supply through side inlet.

## 3. Results and Discussion

Results of calculations based on mathematical model with gas distribution per 1st option show that torch formation is optimal as regards geometry of CVB combustion chamber. Torch (fig. 2) is formed due to four-lateral tangential air and gar input. Fig. 2 shows calculated oxygen distribution in the longitudinal section of CVB combustion chamber with axial, side and tangential gas inlet. Air velocity at the entrance to CVB combustion chamber reaches 40 m/s, and gas velocity reaches 70 m/s. Tangential gas inlet nozzles (figure 8 fig. 1) are located angle wise towards tangential air flow (figure 5 fig. 1), which allows improving mixture with gas due to crossing of flows. Boiler work load range, with gas distribution in CVB per 1st option, is effective and rational from 40% to 100% of the nominal boiler capacity, which was also recorded and confirmed at the boilers in-situ testing and operation.

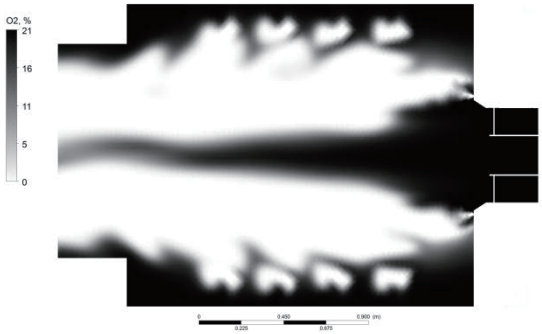


Fig. 2 Calculated oxygen distribution in longitudinal section of CVB combustion chamber (1st option).

According to the 2nd option, data of CVB combustion chamber processes modeling determine boiler operation within the range of 15-45% of the nominal capacity. When fuel is supplied through axis and side, a clearly defined cylinder shaped vortex core is formed. Fig. 3 shows calculated oxygen distribution along CVB combustion chamber longitudinal section with axial and side gas inlet. With such distribution torch has a prolate shape (fig. 3), which allows using effectively opposite arrangement of burners. Fuel distribution per 2nd option is used when warming up combustion chamber and also for boiler operation at the load up to 45% from nominal load. With power increase, torch central zone widening and its shift movement about axis is observed.

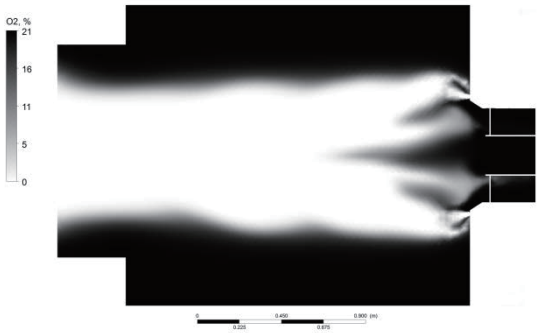


Fig. 3 Calculated oxygen distribution in CVB combustion chamber longitudinal section (2nd option).

3rd option with side fuel supply has been long time viewed in practice as the main variant to sustain medium and maximum boilers' loads. Measurements, visual researches and results of CVB model mathematical calculations showed that usage of chamber axial area in the 3rd option of gas supply to CVB was not effective. In the axial area almost along all the length of CVB combustion chamber fuel shortage is observed, together with large oxygen surplus (fig. 4).

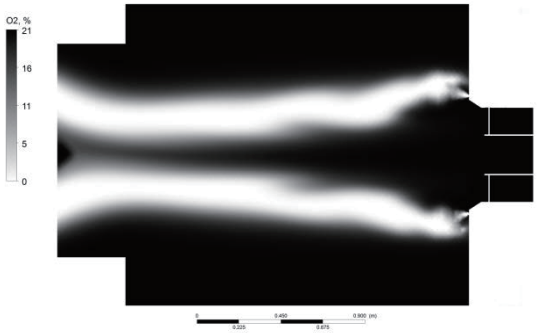


Fig. 4 Calculated oxygen distribution in CVB combustion chamber longitudinal section (3rd option).

## 4. Concluding Remarks

Based on results of testing in-situ and mathematical modeling, options of optimal gaseous fuel and air inlet into CVB have been developed and implemented. Different ways of gas input into CVB allow mixing it effectively with air and make it possible to form torch of any geometry at the CVB outlet.

## References

[1] A.N. Shtym, K.A. Shtym, Ye. Yu. Dorogov. *Boilers with cyclone burners* // Vladivostok. Far Eastern Federal University Publishing House. (2012) 421.

# Characteristics of Olefin Weak Flames in a Micro Flow Reactor with a Controlled Temperature Profile

Shogo Kikui[1], Hisashi Nakamura[1], Takuya Tezuka[1], Susumu Hasegawa[1], Kaoru Maruta[1,2].
[1]Institute of Fluid Science, Tohoku University
2-1-1 Katahira, Aoba-ku, Sendai, Miyagi 980-8577, Japan.
[2] ICE Lab., Far Eastern Federal University
8 Sukhanova Str., Vladivostok 690950, Russia.

**ABSTRACT**

Weak flames of ethylene, propylene and 1-butene were investigated using a micro flow reactor with a controlled temperature profile. Single luminous zone was observed for all three olefin at $p$ = 1 atm and the order of weak flame position was ethylene, 1-butene and propylene from the lower temperature side. Ethylene weak flame at higher pressure was examined and two luminous zones were observed at $p \geq 2$ atm. 1-D numerical simulation was conducted and computed results captured the experimental tendency.

## 1. Introduction

Numerical simulation of the combustion process is important in the development of practical combustors and an accurate reaction mechanism is essential. Olefin is a hydrocarbon which contains at least one carbon-carbon double bond and it is an key intermediate species in the oxidation of alkanes [1]. Therefore, understanding the oxidation process of olefin will lead to the improvement of reaction mechanisms. As a method to investigate oxidation process, a micro flow reactor with a controlled temperature profile is introduced [2]. In the micro flow reactor, oxidation process is separated into different temperature region and observed as stable multiple weak flames. In our previous studies, oxidation processes of dimethyl ether [3], *n*-heptane [4], gasoline and diesel primary reference fuels [5,6] and natural gas components [7] were examined using the micro flow reactor. These studies clearly indicated the possibility of the micro flow reactor to investigate oxidation processes.

In this study, three types of olefin (ethylene [$C_2H_4$], propylene [$C_3H_6$] and 1-butene [$C_4H_8$]) were applied to the micro flow reactor to investigate their weak flame responses. The effect of carbon number was investigated by comparing the three olefin weak flames. Pressure dependence of ethylene weak flame was also examined by conducting experiments up to 5 atm. 1-D numerical simulations were conducted to compare them with the experiment.

## 2. Experimental and computational methods

Figure 1 shows a schematic of the experimental setup. A quartz tube with an inner diameter of 1–2 mm was employed as a reactor and was heated using a $H_2$/air premixed burner to obtain a stationary temperature profile (300–1300 K) in the axial direction. A stoichiometric premixed *n*-butane/air mixture was supplied to the reactor with a mean flow velocity at the inlet of the reactor $u$ = 1–2 cm/s. The flame images were taken using a digital still camera with a optical band-pass filter. The pressure was controlled using a pressure regulator attached at the end of the reactor.

Corresponding author: Shogo Kikui
*E-mail address*: kikui@edyn.ifs.tohoku.ac.jp

To examine the experimental results, 1-D steady computations were conducted using the PREMIX-based code [2]. Heat convection term between the gas phase and the wall was added to the energy equation. The experimental wall-temperature profile was used in the computation. Natural Gas III [8] was employed as a reaction scheme. Same equivalence ratio, $\varphi$, and $U$ in the experiment were used in the computation.

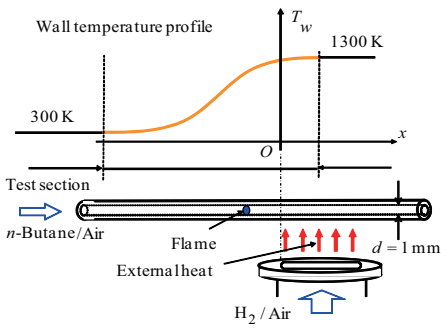


Fig. 1 Schematics of the experimental setup.

## 3. Results and Discussion

### 3.1 Weak flame response to carbon number

Three types of olefin, i.e. ethylene, propylene and 1-butene, were applied to the micro flow reactor. Figure 2 shows the weak flame images of each olefin at $u$ = 2 cm at $p$ = 1 atm. Only one luminous zone was observed indicating single-step oxidation for all of the olefin. Focusing on the flame position, the order of flame position for the three fuels was $C_2H_4$, $C_4H_8$ and $C_3H_6$ from the lower temperature side. These data were

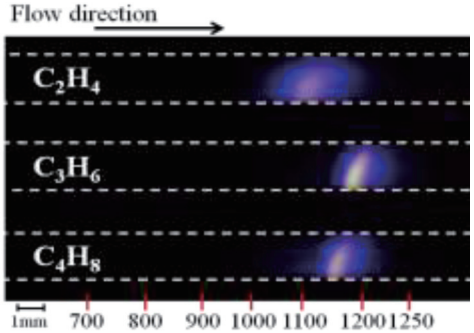


Fig. 2 Weak flame images of $C_2H_4$, $C_3H_6$ and $C_4H_8$ at $p$ = 1 atm, $u$ = 2 cm and $d$ = 2 mm.

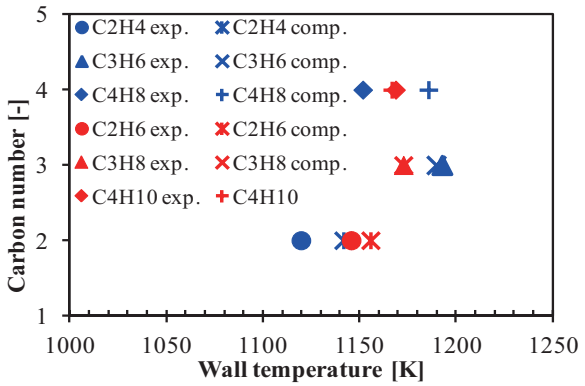


Fig. 3 Experimental and computational weak flame position of olefin and alkane at $p$ = 1 atm, $u$ = 2 cm and $d$ = 2 mm.

compared with computational results and with the past experimental and computational results obtained for alkanes with the same carbon number. Figure 3 shows the flame position for each olefin and alkane obtained by experiment and computation [7]. Comparing the experiment and computation results for the olefin, the order of the flame position among the three fuels in the experiment agree with that in computation. However, improvement of the reaction mechanism is required for quantitative agreement. The order of the flame position among the carbon numbers for the olefin agree with that for the alkanes.

### 3.2 Pressure dependence of ethylene weak flames

Experiments up to 5 atm was conducted to investigate the pressure dependence of ethylene weak flames. Figure 4 shows weak flame images of ethylene at $p$ = 1–5 atm $u$ = 1cm/s. When $p \geq 2$ atm, two luminous zones were observed which indicate two-stage oxidation. The two weak flames are known as the blue flame and hot flame respectively from the lower temperature side. Appearance of the blue flame becomes stronger as the pressure increases which indicates that the reactions occurring at the blue flame becomes stronger with the pressure increase. Focusing on the weak flame position, blue flame shifts towards the lower temperature side with the increase of pressure. Hot

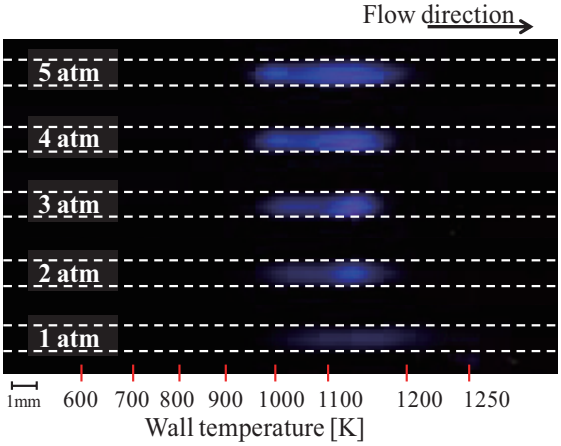


Fig. 4 Weak flame image of C2H4 at $p$ = 1–5 atm, $u$ = 1 cm/s and $d$ = 1 mm.

flame shifts towards the lower temperature side from 1-2 atm and then shifts to the higher temperature side from 2-5 atm. Figure 5 shows computational heat release rate profile at $p$ = 1–5 atm. The tendency that the blue flame becoming stronger with the pressure increase and the pressure dependence of the weak flame position agreed between the experiment and computation. The computation captured the experimental pressure dependence of ethylene weak flame.

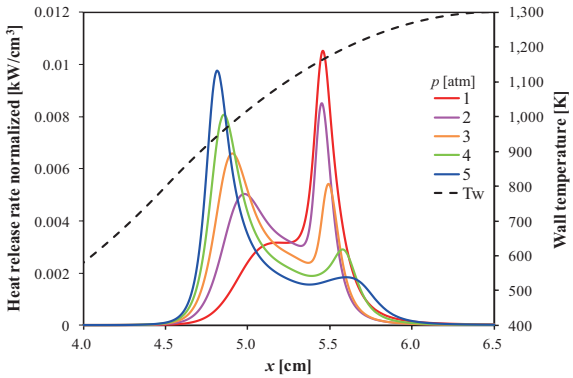


Fig. 5 Wall temperature at flame position in experiment and computation at $p$ = 1–5 atm, $u$ = 1 cm and $d$ = 1 mm.

## 4. Concluding remarks

Weak flames of ethylene, propylene and 1-butene were investigated using a micro flow reactor with a controlled temperature profile. Single luminous zone was observed for all three olefins at $p$ = 1 atm and the order of weak flame position was ethylene, 1-butene and propylene from the lower temperature side. Ethylene weak flame at higher pressure was examined and two luminous zones were observed when $p \geq 2$ atm. 1-D numerical simulation was conducted and captured the order of flame position and pressure dependence of ethylene weak flame.


## Acknowledgement

The part of the study was supported financially by the Ministry of education and science of Russian Federation (project 14.Y26.31.0003).


## References


[1] K. C. Salooja, *Combust. Flame* 11 (4) (1967) 370.
[2] K. Maruta et al., *Proc. Combust. Inst.* 30 (2005) 2429.
[3] H. Oshibe, et al., *Combust. Flame* 157 (8) (2010) 1572.
[4] A. Yamamoto, et al., *Combust. Inst.* 33 (2) (2011) 3259.
[5] M. Hori, et al., *Combust. Flame* 159 (3) (2011) 959.
[6] S. Suzuki, et al., *Proc. Combust. Inst.* 34 (2013) 3411.
[7] T. Kamada et al., *Combust. Flame* 161 (1) (2014) 37.
[8] Natural gas III, Combustion Chemistry Centre, National University of Ireland, Galway. http://c3.nuigalway.ie/naturalgas3.html.

Eleventh International Conference on Flow Dynamics
October 8-10, 2014, Sendai, Miyagi, Japan

# Experimental and Numerical Investigations of Laminar Burning Velocity of Ammonia/air Premixed Flames

Akihiro Hayakawa[1], Takashi Goto[1], Rentaro Mimoto[1], Taku Kudo[1], Hideaki Kobayashi[1]
[1]Institute of Fluid Science, Tohoku University
2-1-1 Katahira, Aoba-ku, Sendai, Miyagi 980-8577, Japan

**ABSTRACT**

Laminar flame characteristics were experimentally and numerically investigated. Experiments were carried out using a constant volume combustion chamber. Unstretched laminar burning velocity and Markstein length were evaluated from spherically propagating laminar flames. Numerical simulations were also performed using five detailed reaction mechanisms. As a results of numerical simulation, it was found that the reaction H + $O_2$ = OH + O has the largest sensitivity for laminar burning velocity.

## 1. Introduction

Ammonia is expected to be one of hydrogen energy carriers as well as carbon free fuels. Because of lower combustion intensities, such as lower burning velocity, narrower flammable range and so on, ammonia is not considered to be a fuel. Therefore, there are few studies have been conducted.

Takizawa et al.[1] and Pfahl et al.[2] clarified that the laminar burning velocity of ammonia/air premixed flames were very low compared to usual hydrocarbon fuels. However, the effects on flame stretch is not considered in the previous studies.

Reaction mechanisms which can be applicable for ammonia flames have been proposed. However, it is unclear whether the reaction mechanisms were appropriate for ammonia flames because the experimental results were insufficient.

In this study, the laminar burning velocity of annmonia/air premixed flames were experimentally and numerically investigated.

## 2. Experimental and Numerical Methods

Experiments were carried out using a constant volume combustion chamber. Ammonia was used as the fuel and dry air was used as the oxidizer. All experiments were conducted at the temperature of 298 K and initial mixture pressure, $P_i$, of 0.1 MPa, respectively. Equivalence ratio, $\phi$, was varied from 0.7 to 1.3. Mixture was prepared according to the partial pressure of ammonia and air. The volume of the chamber was approximately 23 L. Mixture was ignited at the nearly center of the chamber by two spark electrodes. A capacitor discharge ignition (CDI) circuit was adopted for spark ignition. The electrostatic energy was set to 2.8 J. Flame propagation was observed by a Schlieren technique with a high speed video camera and a continuous light source. Frame rate and resolution were set to 1000 fps and 768x768 pixel, respectively.

Numerical simulation was conducted using planer one-dimensional laminar flame model of CHEMKIN-PRO with detailed chemical kinetics proposed by Tian et al. [3], Miller et al. [4], Konnov [5], Lindstedt et al. [6] and GRI-Mech 3.0 [7]. Mixture temperature and pressure mixture was set to 298 K and 0.1 MPa, respectively.

Corresponding author: Akihiro Hayakawa
*Email address*: hayakawa@flame.ifs.tohoku.ac.jp

## 3. Analysis of Spherically Flames

Schlieren flame radius, $r_{sch}$, was determined as the radius of circle whose area is equivalent to the area of Schlieren image of spherically propagating flame. Laminar burning velocity during flame propagation, $S_N$, was evaluated by the following equation based on the continuous equation:

$$S_N = \frac{\rho_b}{\rho_u} \cdot \frac{\mathrm{d}r_{sch}}{\mathrm{d}t}. \quad (1)$$

where, $\rho_u$ and $\rho_b$ are the densities of unburned mixture and burned gas, respectively, and $t$ is time.

In the case of spherically propagating flames, the effects of stretch is occurred on the flame. The flame stretch rate, $\varepsilon$, can be evaluated by Eq. (2) for spherically propagating flames,

$$\varepsilon = \frac{1}{A} \cdot \frac{\mathrm{d}A}{\mathrm{d}t} = \frac{2}{r_{sch}} \cdot \frac{\mathrm{d}r_{sch}}{\mathrm{d}t}. \quad (2)$$

where, $A$ is flame front area. The laminar burning velocity of spherically propagating flames evaluated by Eq. (1) is the stretched laminar burning velocity.

According to the results of asymptotic analysis, the difference between unstretched laminar burning velocity to stretched one can be considered to be proportional to the flame stretch rate as shown in Eq. (3),

$$S_L - S_N = L \cdot \varepsilon. \quad (3)$$

where, $S_L$ is unstretched laminar burning velocity and the proportional constant, $L$, is Markstein length. The unstretched laminar burning velocity, $S_L$, was determined as $S_N$ at $\varepsilon = 0$ by the extrapolation by Eq. (3).

## 4. Results and Discussions

Flame did not propagates throughout the chamber at the equivalence ratios of 0.7 and 1.3. Figure 1 shows the relationship between unstretched laminar burning velocity, $S_L$, and equivalence ratio, $\phi$. The unstretched laminar burning velocities were lower than usual hydrocarbon fuels, such as methane or propane. The maximum value of unstretched laminar burning velocity was 6.92 cm/s at equivalence ratio of 1.0 within the examined conditions. Laminar burning velocities obtained by Takizawa et al. [1] and Phfal et al. [2] were also shown in Fig. 1. The unstretched laminar burning velocities obtained in this study were close to those obtained in the previous studies at equivalence ratio of 0.9, 1.0 and 1.1.

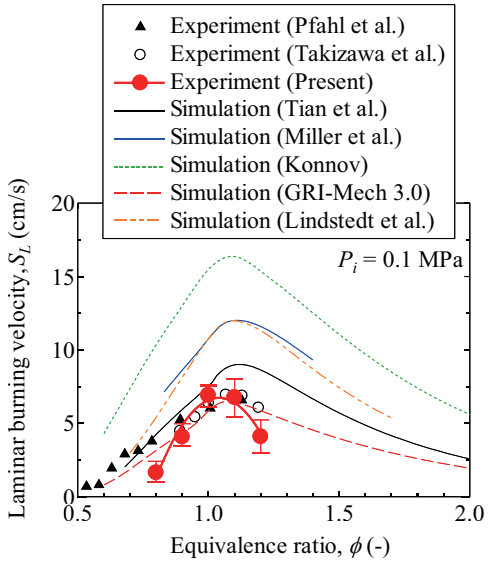


Fig. 1 Unstretched laminar burning velocity

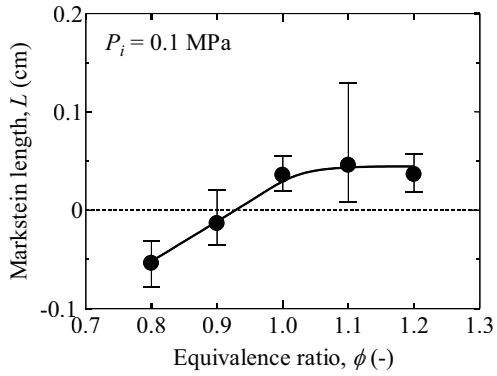


Fig. 2 Markstein length

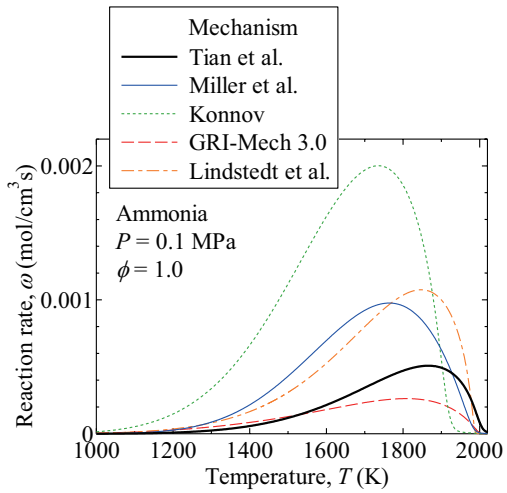


Fig. 3 Reaction rate of $H + O_2 = OH + O$

Figure 2 shows the variation of the Markstein length, $L$, with the equivalence ratio, $\phi$. The Markstein length increased with the increase in equivalence ratio. This variation was the same with those of hydrogen/air and methane/air flames. The Markstein length was negative at equivalence ratio of 0.8 and 0.9.

The laminar burning velocities calculated using detailed chemical kinetics were also shown in Fig. 1. As shown in the figure, the calculated laminar burning velocity was varied according to the detailed chemical kinetics. The laminar burning velocities calculated using Tian's mechanism or GRI-Mech 3.0 were close to those of experimental results. The sensitivity analysis of mass flow rate which correlates that of laminar burning velocity was conducted for each detailed reaction mechanism at equivalence ratio of 1.0. As a results, the sensitivity of following reaction was the largest for all detailed mechanisms:

$H + O_2 = OH + O.$ (R1)

Figure 3 shows the variation of the reaction rate of reaction R1 within the reaction zone. It was found that the peak values of the reaction rate or R1 were well correlate with the calculated laminar burning velocity, $S_L$, shown in Fig. 1 at $\phi$ = 1.0. Therefore, the maximum value of reaction rate of R1 might be influenced by the laminar burning velocity prediction. It implies that the appropriate prediction of the reaction R1 might be important for the prediction of unstreched laminar burning velocity of ammonia/air premixed flames.

## 4. Concluding Remarks

Laminar burning velocity of ammonia/air premixed flames were experimentally and numerically were investigated at various equivalence ratios. The maximum value of unstretched laminar burning velocity was 6.92 cm/s within the examined conditions. Markstein length increased with the increase in equivalence ratio. The calculated laminar burning velocities were different according to the detailed chemical kinetics. In order to predict the unstretched laminar burning velocity, the reaction $H + O_2 = OH + O$ might be important.

## Acknowledgement

This research was supported by Cross-ministerial Strategic Innovation Promotion Program (SIP) of the Japan Science and Technology Agency (JST).

## References

[1] K. Takizawa, A. Takahashi, K. Tokuhashi, S. Kondo, *J. Hazardous Material*, 155 (2008) 144-152.
[2] U.J. Pfahl, M.C. Ross, J.E. Shepherd, K.O. Pasamehmetoglu, C. Unal, *Combust. Flame*, 123 (2000) 140-158.
[3] Z. Tian, Y. Li, L. Zhang, P. Glarborg, F. Qi, *Combust. Flame*, 156 (2009) 1413-1426.
[4] J.A. Miller, M.D. Smooke, R.M. Green, R.J. Kee, *Combust. Sci. Tech.*, 34 (1983) 149-176.
[5] A.A. Konnov, *Combst. Flame*, 156 (2009) 2093-2105.
[6] R.P. Lindstedt, F.C. Lockwood, M.A. Selim, Combust. Sci. Tech., 99 (1994) 253-276.
[7] M. Frenklach, T. Bowman, S. Greg, (2000) available at <http://www.me.berkeley.edu/ gri-mech/index.html>.

# Sooting Behavior of Alkanes in a micro Flow Reactor with a Controlled Temperature Profile

Ajit Kumar Dubey, Takuya Tezuka, Susumu Hasegawa, Hisashi Nakamura, Kaoru Maruta
Institute of Fluid Science, Tohoku University
2-1-1 Katahira, Aoba-ku, Sendai, Miyagi, 980-8577, Japan

**ABSTRACT**

Sooting behavior of alkanes is studied using a micro flow reactor with a controlled temperature profile. Soot and flame response is observed for various conditions of equivalence ratio and mean inlet flow velocity for all fuels. Methane shows five different kind of flame responses namely flame, both soot and flame, soot, none and a low luminosity region prior to blow off in the region where both soot and flame are observed. All other fuels (Propane, *n*-heptane, *n*-octane, *iso*-octane and *n*-decane) show only the first three aforementioned responses.

## 1. Introduction

Soot emissions from combustion of hydrocarbon poses a major problem for environment and human health and also affects the performance of many combustion devices. Hence it is necessary to have better insight in the mechanism of soot formation and related processes. Soot formation depends on fuel structure as well as the flame configuration. Many fuels have been studied under premixed and diffusion flame configurations to determine relative sooting tendency among them [1,2]. Critical sooting equivalence ratio which is equivalence ratio at which first hint of soot appears is measured for premixed flames and correlated with number of C-C bonds. Micro flow reactor with a controlled temperature profile has been used to study sooting in acetylene flames in premixed flow configuration[3].

In this work sooting behavior of alkanes is studied using a micro flow reactor with controlled temperature profile. The fuels considered are methane, propane, *n*-heptane, *n*-octane, *iso*-octane and *n*-decane.

## 2. Experimental Method

The micro flow reactor (Fig. 1) employs a quartz tube whose inner diameter (2 mm) is less than ordinary quenching diameter for fuels. So, the tube is heated externally by a flat premixed flame hydrogen-air burner which generates a stationary temperature profile along the inner wall of quartz tube. The maximum temperature is 1300 K. The temperature is measured by a K-type thermocouple by inserting it from the end.

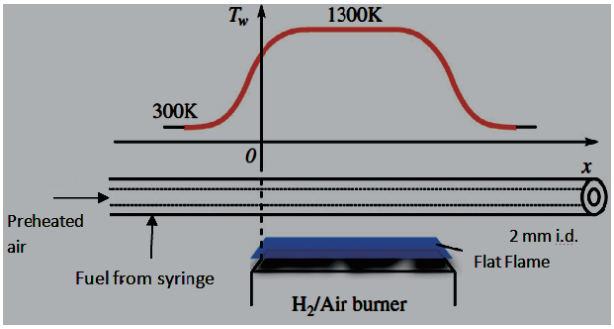


Fig. 1 Experimental setup.

Corresponding author: Ajit Kumar Dubey
*E-mail address*: ajit@edyn.ifs.tohoku.ac.jp

For the liquid alkanes a heater is used to preheat (not required for gaseous alkanes) the incoming air for vaporization of fuel. The preheat temperature is different for different fuel. The liquid fuel is fed in the micro flow reactor using a syringe whose motion is controlled using a programmed stepper motor.

## 3. Results and Discussion

Soot and flame response of all the considered fuels are observed by varying the equivalence ratio(1.5-4.5) and mean inlet flow velocity(10 cm/s-80 cm/s). For liquid fuels and Propane three kind of flame and soot responses are obtained namely, flame, soot and both soot and flame. Representative images are shown for different responses for *n*-heptane in Fig. 2. The experiments are performed for various conditions and the responses observed are plotted in a equivalence ratio-mean inlet flow velocity plane as is shown for *n*-octane in Fig. 3.

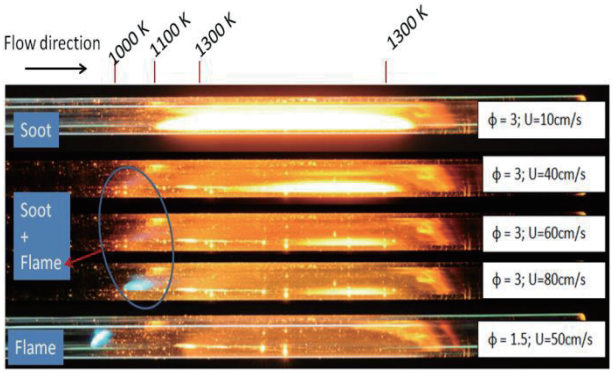


Fig. 2 Soot and flame response of *n*-heptane.

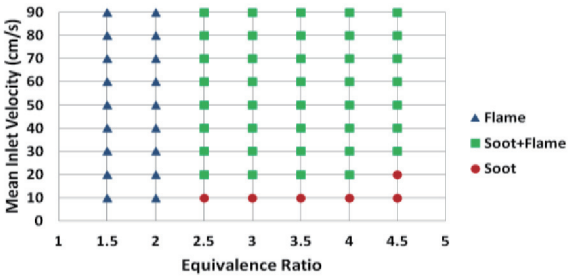


Fig. 3 Soot and flame response for *n*-octane on equivalence ratio - flow velocity plane.

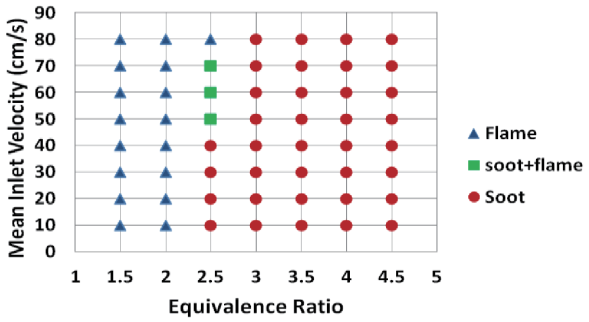


Fig. 4 Soot and flame response for *iso*-octane on equivalence ratio - flow velocity plane.

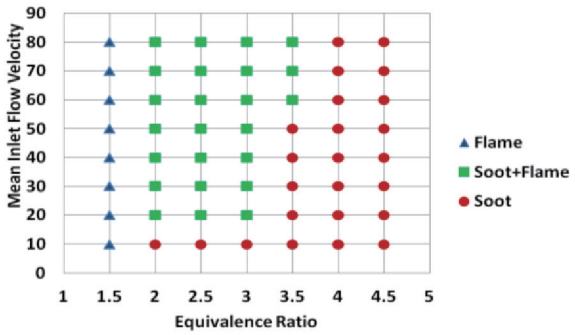


Fig. 5 Soot and flame response for propane on equivalence ratio - flow velocity plane.

The same diagram obtained for n-heptane and n-decane are very similar. Hence it is difficult to interpret about effect of carbon number. On the other hand iso-octane shows very different response as shown in Fig. 4. Also soot inception shifts downstream for iso-octane Soot inception begins at equivalence ratio greater than 2 for liquid alkanes which is very different than earlier predicted values of around 1.7-1.8 [2]. The difference may be due to temperature. In earlier work [2] measurements are reported at adiabatic flame temperatures of fuels whereas here the temperature is controlled and is much lower. Propane has wider sooting region as compared to liquid hydrocarbons as is seen in Fig. 5. Soot is observed at equivalence ratio 2 which is not seen in liquid hydrocarbons.

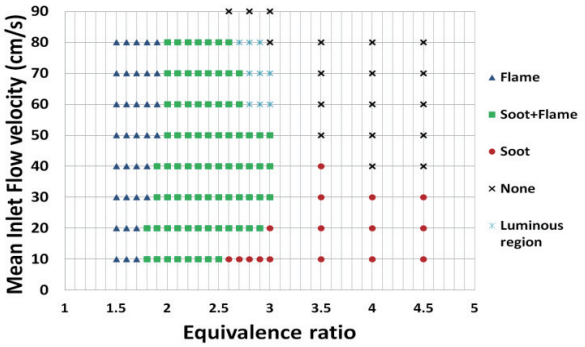


Fig. 6 Soot and flame response for methane on equivalence ratio - flow velocity plane.

Methane does not have C-C bond and it has very different sooting behavior compared to other higher hydrocarbons. Hence more detailed experiments are performed for methane to resolve various responses. For the aforesaid range of equivalence ratio and flow velocity it displays five kind of soot and flame response, namely flame, both soot and flame, soot, none and a low luminosity region prior to blow off in the region where both soot and flame is observed (Fig. 6). It has smaller sooting region compared to other hydrocarbons which means lower sooting tendency which is due to its higher H/C ratio and low carbon density which is also predicted in earlier works [2]. The soot first appears at equivalence ratio of 1.8. Soot formation depends both on equivalence ratio and flow velocity( or residence time). Soot formation for maximum velocity range happens close to equivalence ratio of 2. After that the range of velocity for soot formation decreases with equivalence ratio (Fig. 6). Soot inception point in obtained visual images also shifts downstream with increasing equivalence ratio at same inlet flow velocity for methane which is completely opposite to the behavior shown by higher hydrocarbons. This indicates that tendency to form soot decreases with increasing equivalence ratio for methane . Due to higher $H_2$ concentration the amount of soot formed is lower in Methane [4].Activated soot particles are formed with liberation of $H_2$.As the equivalence ratio increases $H_2$ mole fraction increases more, reducing the soot yield.

**4. Conclusions**

Sooting behavior of alkanes is studied using a micro flow reactor with a controlled temperature profile (Maximum temperature 1300 K). Soot and flame response is observed for all the considered fuels at different equivalence ratio and mean inlet flow velocity.

- Methane shows five different kind of soot and flame response for various equivalence ratio and flow velocity.
- The velocity range for soot formation goes on decreasing with equivalence ratio with maximum around equivalence ratio of 2.
- All other fuels show three different kind of soot and flame response.
- Propane shows broader sooting region compared to other hydrocarbons.
- *iso*-octane shows wider only soot region compared to straight chain alkanes which show wider both soot and flame region.

**References**

[1] I. Glassman, *Symposium (Int.) on Combustion* 22 (1988) 295-311.
[2] D.B. Olson, J.C. Pickens, *Combustion and Flame* 57 (1984) 199-208.
[3] H. Nakamura, R. Tanimoto, T. Tezuka, S. Hasegawa, K. Maruta, *Combustion and Flame* 161 ( 2014) 582-591.
[4] S. Senkan, M. Castaldi, *Combustion and Flame* 107 (1996) 141-150.

# Experimental Study on Flame Spread in Parallel Plates

TakuyaYamazaki[1], Tsuneyoshi Matsuoka[2], Yuji Nakamura[2], Susumu Noda[2]
[1]Graduate School of Engineering, Toyohashi University of Technology
1-1 Hibarigaoka, Tempaku-cho, Toyohashi, Aichi, 441-8580, JAPAN
[2]Department of Mechanical Engineering, Toyohashi University of Technology
1-1 Hibarigaoka, Tempaku-cho, Toyohashi, Aichi, 441-8580, JAPAN

**ABSTRACT**

An experimental system with adjustable gap was developed to examine the flame spread in parallel plates of PMMA. Although the spreading orientation was horizontal, symmetric flames spreading in 2-15 mm gap were observed as well as the spreading flame in the cylindrical gap. The spread rate increased with decreasing of the gap size. In further small gap, the spread rate turned to decrease. Although the trend was similar to that in the cylindrical gap, the critical gap size where the trend shifted was about 5 mm and it was larger than the cylinder.

## 1. Introduction

The flame spread is commonly recognized as the simplified/fundamental process of fire and has studied in the past few decades. A plate-shaped fuel has widely employed and has been burnt only the single side of the specimen under the controlled air flow. Blow-off is likely experienced when large opposed flow velocity adopted over the burning surface. Fernandez-Pello et al. indicated that the blow-off limit should be described by the critical Damköhler number (*Da*), defined as the ratio of the characteristic transport time to the characteristic chemical time [1]. In 2002, Hashimoto et al. [2] found the flame can be sustained in the cylindrical small gap of combustible tubes even when *Da* becomes smaller than the critical value; this combustion mode has been named “stable combustion mode”. Matsuoka et al. [3] revealed that the transition from the normal spreading mode to the stable combustion mode was determined by *Da* as well as the blow-off limit. However, it is not clear why the transition should occur. Our study aims to clarify the detailed mechanism of this transition phenomenon.

In previous studies, PMMA cylinders were used as fuel specimens [2,3]. However, it is difficult to observe the flame formed in the tube due to the highly-curved geometry. In this study, a new experimental system which has a parallel plates channel was developed to study the spreading flame in the gap. Hereafter, this rectangular gap composed of the parallel plates is called “plate gap.” Although the plate gap differs from the cylinder, it is expected to reproduce the stable combustion mode and provides to the better optical access to the flame easily. The objective of this study is to compare the flame shape and the spread rate between two cases; in cylindrical gap and plate gap and to summarize the effect of geometry and gap size or height on the spread rate.

## 2. Experimental Method

### 2.1. Designed Experimental System

A schematic diagram of designed experimental system and an assembly drawing of a test section are shown in Fig.1. The test section is a small wind tunnel made of stainless steels (SUS303/304). Width of the tunnel is 50 mm (fixed) and its length is 500 mm (fixed), whereas its height is adjustable from 1 mm up to 15 mm. The flow system, which can supply mixture gas as an oxidizer in wide range of the flow rate (1.5 ~ 300 L/min) and volumetric concentration of oxidizer (21 ~ 100 %), is connected to the tunnel. A sintered metal is installed at inlet of the tunnel for rectification of the flow. Mixture gas was sampled at the inlet and oxygen concentrations of the mixture gas were verified by the gas chromatography (Shimadzu GC-14-B) with 1 % repeatability standard error. The both flow rates are adjusted to the desired values by flowmeters to fulfill the condition with about 4 % repeatability standard error. In addition, main flow velocity profiles along the center and both sides 10 mm away from the center at the upstream tip of the solid fuel were measured by a pitot tube. Although large errors exist in the measurement, the nearly uniform velocity profiles were confirmed. Two PMMA plates of 10 mm thickness, 150 mm length, and 20 mm width, are embedded in top and lower plates and used as the fuel specimens in this study. Upstream edge of the specimens is positioned at 270 mm from the inlet so that the flow just in front of the fuel might not be

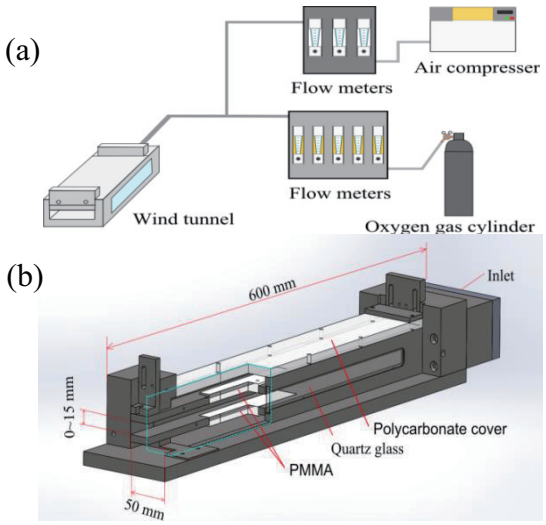


Fig.1 (a) Schematic diagram of the experimental system, (b) detail drawing of the wind tunnel.

Corresponding author: Tsuneyoshi Matsuoka
*E-mail address*: matsuoka@me.tut.ac.jp

fully developed depending on the condition applied. A quartz glass is installed on a side wall, whereas the upper part is covered with a polycarbonate plate to access the flame visually.

### 2.2. Experimental Conditions

The height of gap plate gap, *d,* studied in this work was 2-15 mm. The pure oxygen ($X_O$ = 1.0) and the mixture gas contained 30 vol% oxygen ($X_O$ = 0.3) were used as an oxidizer. The flame was recorded through the side window by a digital video camera (Canon iVIS HF G20) with a band-pass filter, which has the central wavelength of 430 nm and the half bandwidth of 10 nm. The visible leading edge of the flame was tracked by Spotlight software developed by NASA. This software records the pixel displacement of the detected edge and time history of the position is automatically corrected. The track data was fitted to the linear function by least squares method. The flame spread rate was determined by the slope of the fitted line with 98 % averaged coefficient of determination for each experiment.

## 3. Results and Discussion

Figure 2 shows the spreading flames in 4 mm cylindrical (vertically downward flame spread) and plate gap (horizontal flame spread). It is noted that the flame is formed circumferentially in the cylinder and exists even in the center. It prohibits detailed observation inside the cylinder. Considering the cross-sectional image of the flame, however, symmetric flames were observed irrespective of the orientation of samples. Although the quenching regions at the leading edge were clearly observed in both cases, inherent difficulty exists in observing the flame in detail due to the lens effect. It prevents measurement of the quenching distance. On the other hand, there was no such refraction within the specimen itself in case of parallel plates, it is possible to measure the quenching distance in resolution of the image processing system. The resolution adopted in the study was about 0.06 mm/pixel. The quenching distance seemed shorter than expected from the cylinder flame and the estimated value was about 0.6 mm on average between upper and lower flames.

Figure 3 shows the flame spread rate plotted against the gap size, *d*. The symbols of “upper” and “lower” in the figure represent the data obtained along the respective plate. With decreasing of gap size the flame spread rate increased. The simple theoretical analysis qualitatively demonstrated the experimental facts in large gap sizes [5]. Namely, the flame leading edge gets further and further away from the solid surface. Thus, the spread rate decreased with the quenching distance. In further small gap (about 5 mm), the spread rate turned to decrease as the plate gap became reduced in size. Although the similar trend was obtained in the cylindrical gap, the critical gap sizes in both cases were different. In plate gap, the shift of the trend was about 5 mm, whereas it was 2 mm in cylindrical gap. It is considered that the flame in the gap weakened due to heat loss to the surround solid. The extent of the heat loss should be different due to the geometry (curved or flat).

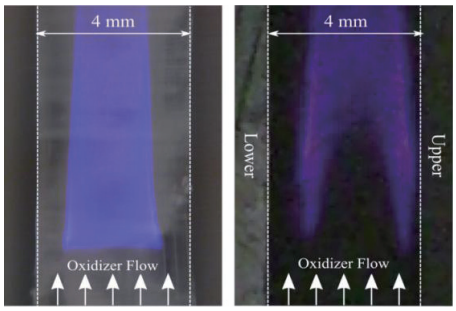


Fig.2 Flame photos (a) In 4 mm cylinder, (b) In 4 mm gap. Both conditions were $U_o$ = 0.9 m/s and $X_o$ = 1.0.

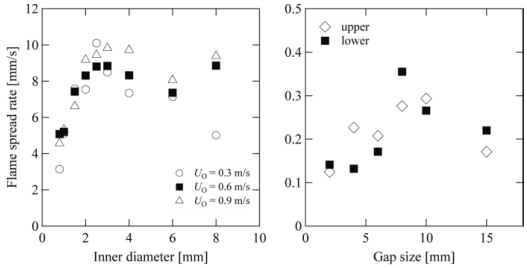


Fig.3 Flame spread rate vs. gap size. (a) $U_o$ = 0.3, 0.6, and 0.9 m/s and $X_o$ = 1.0 [4]. (b) $U_o$ = 1.5 m/s and $X_o$ = 0.3.

## 4. Conclusions

A new experimental system developed in this study and the flame spread in 2-15 mm plate gap was observed. The results are summarized as follows:

1. Symmetric flames were observed as well as the spreading flame in the cylindrical gap.
2. The spread rate increased with decrease of the gap size, while turning to decrease in smaller gap than 5 mm.
3. Although the trend was similar to that in the cylindrical gap, the critical gap size where the trend shifted was larger than the cylinder.


## Acknowledgements

This work was supported by Grant-in-Aid for Research Activity Start-up Number 24860002.


## References


[1] A.C. Fernandez-Pello, S.R. Ray, I. Glassman, *Eighteenth Symp. (Int.) Combust.*, 18 (1981) 579－589.

[2] N. Hashimoto, S. Watanabe, H. Nagata, T. Totani, *Proc. Combust. Inst.,* 29 (2002) 245－250.

[3] T. Matsuoka, S. Murakami, H. Nagata, *Combust. Flame,* 159 (2012) 2466－2473.

[4] T. Yamazaki, T. Matsuoka, Y. Nakamura, H. Nagata, S. Noda, *Proc. Symp. Japan Combust.,* 51 (2013) 244g.

[5] T. Matsuoka, Y. Nakamura, S. Noda, *Proc. Symp. Japan Heat Trans.,* 51 (2014) B343.

# OS3: The Second International Symposium on Innovative Energy Research Ⅲ
# Multiphase Energy Science and Risk Mitigation

# Decomposition Mechanism of PMMA-type Polymers by Hydrogen Radicals

Hideo Horibe
Department of Applied Chemistry and Bioengineering, Graduate School of Engineering, Osaka City University
3-3-138, Sugimoto, Sumiyoshi, Osaka 558-8585, Japan

**ABSTRACT**

The relationship between the chemical structure of PMMA-type polymers and the removal rate by hydrogen radicals was examined. Hydrogen radicals have superior reduction ability and can be generated by decomposing $H_2$ on hot-wire surfaces. PMMA-type polymers, which are widely used as base polymers for ArF resist. The removal rate of main chain scission type polymers was faster than that of main chain cross-linking type polymers. The removal rate was slow with benzene ring. The polymer with benzene ring was stable structure by resonance stabilization of benzene ring.

## 1. Introduction

Transistors are integrated on a silicon wafer substrate by repeating the several processes. In final process of lithography, the resist is removed. In here, the resist removal methods exist the major two methods as wet method and dry method. In the present resist removal, the wet method using solvents such as sulfuric acid hydrogen peroxide mixture and the dry method using the oxygen-plasma are used. However, these have problem, for example the chemicals is high costs and high environmental burdens in wet method [1], oxygen-plasma is oxidations-degradation of semiconductor substrate. In recent years, the new resist removal method that is chemical free, oxidation less, plasma less is strongly desired in industry. In order to break through the above-mentioned problems, we focused on hydrogen radical with excellent reduction ability. Therefore we work on the development of eco-friendly new resist removal method using hydrogen radical generated by Hot-wire method [2].

There is a need for shorter wavelength of the exposure wavelength of the resist with diversification of optoelectronic device and progress of miniaturization. Light sources which used by lithography are tend to become short wavelength such as i-line of 365 nm, KrF excimer laser of 248nm, ArF excimer laser of 193nm. Base polymer of resist has been changed to appropriate resist material against each exposure wavelength such as novolak resin (i-line), poly (vinyl phenol) (KrF) and poly (methyl methacrylate) (PMMA;ArF) according to becoming short wavelength of light sources.

Until now, many recent studies have focused on the removal of the resist by hydrogen radical [3-8]. However, there is no report on reactivity of hydrogen radical and polymers as basic structure in PMMA of base polymer for ArF resist (Referred to as “PMMA-type polymer”). In this study, the each removal rate was investigated by removing the PMMA-type polymer thin film which has different chemical structures by irradiation with hydrogen radical. From these result, we clarified the relationship between each chemical structure of polymer and the removal characteristics of these.

## 2. Method

Corresponding author: Hideo Horibe
*E-mail address:* hhoribe@a-chem.eng.osaka-cu.ac.jp

A resistively heated tungsten wire in hydrogen radical irradiation apparatus was used as a hot catalyst. Each polymer-coated Si substrate was put on the stage just below the catalyzer in fused-glass chamber. The distance between the catalyzer and the substrate was fixed at 100mm. The catalyzer was heated at 2020°C (current = 22A) using a direct current supply. $H_2/N_2$ mixed gas ($H_2$:$N_2$ = 10:90vol%, gas flow = 300sccm) was used as the working gas. The $H_2$ partial pressure was fixed at 2.13Pa, and the initial substrate temperatures were fixed at room temperature.

Figure 1 shows the basic structure of PMMA-type polymer, PMMA(a), poly(ethylmethacrylate)(PEMA)(b), poly(propylmethacrylate)(PPrMA)(f),poly(cyclohexylm ethacrylate) (PCHMA)(g). In the order of PMMA, PEMA, PPrMA PCHMA, the alkyl groups become bulky gruops. Poly(methylacrylate) (PMA)(c), poly(ethylacrylate) (PEA)(d), and poly(acrylacid) (PAA)(e) are polymers whose carbon of $\alpha$ position are hydrogen atom. Poly(phenylmethacrylate) (PPhMA)(h), and poly(benzylmethacrylate) (PBeMA)(i) are polymers with benzene ring.

Each polymers were spin-coated on Si wafer by using spin-coater at same rpm, for 20 sec. After the spin-coat, each polymer thin film sample was baked on hot-plate at 100 ºC, for 1min.

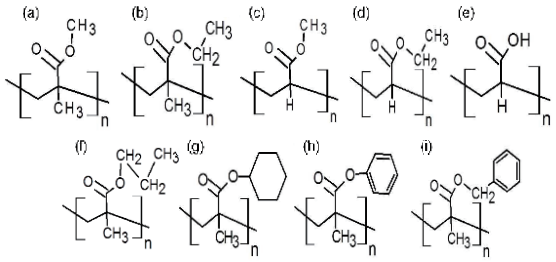


Fig.1 The PMMA-based polymer with different chemical structure of side chains. (a)PMMA, (b)PEMA, (c)PMA, (d)PEA, (e)PAA, (f)PPrMA, (g)PCHMA, (h)PPhMA, (i)PBeMA

We examined the removal rate of each PMMA-type polymers due to removing each polymer thin film sample by irradiation of hydrogen radical which were generated on hot-wire catalysis. When the polymer thin film had been removing by hydrogen radical irradiation, we checked the states of polymer thin film by seeing from outside the chamber.

## 3. Results and Discussion

Figure 2 shows the relationship between hydrogen radical irradiation time and polymer film thickness of PMMA, PEMA, PMA, PEA, and PAA. The removal rates of PMA, PEA and PAA were slow at 6-30% in comparison with PMMA, PEMA. The side chain of PMMA and PEMA is alkyl group (methyl, ethyl), but the carbon of $\alpha$ position of PMA, PEA and PAA is hydrogen atom. It is thought that this difference has a significant effect on the removal rate.

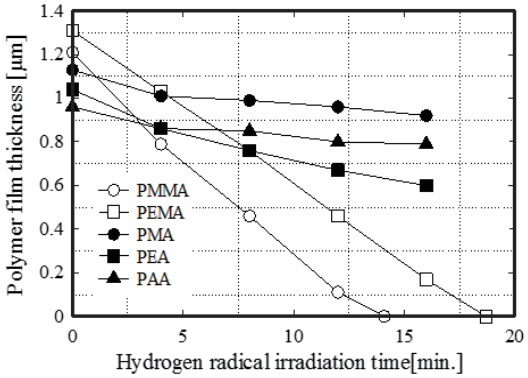


Fig.2 The relationship between polymer film thickness and hydrogen radical irradiation time for PMMA, PEMA, PMA, PEA, and PAA polymers.

Figure 3 shows the relationship between hydrogen radical irradiation time and polymer film thickness of PMMA, PEMA, PPrMA, PCHMA, PPhMA, and PBeMA. PPrMA and PCHMA could be removed by removal rate that was approximately similar to PMMA and PEMA. On the other hand, the removal rate of PPhMA and PBeMA were slow at 13-17% in comparison with these. It is thought that the difference of this removal rate is due to the presence of benzene ring in chemical structure.

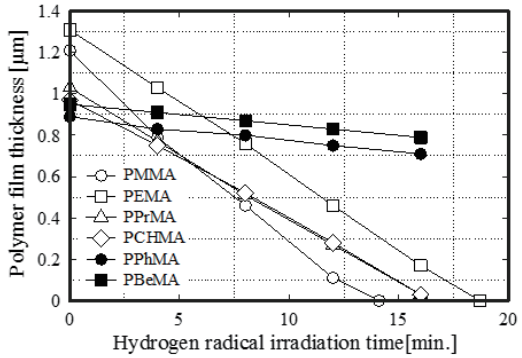


Fig.3 The relationship between polymer film thickness and hydrogen radical irradiation time for PMMA, PEMA, PPrMA, PCHMA, PPhMA, and PBeMA polymers.

In the vinyl polymers which don't have hydrogen atom at carbon of $\alpha$ position, main chain scission easily occurs (main chain scission type) by energy supply from outside (e.g., electron beam and gamma ray). On the other hand, if the carbon of $\alpha$ position is hydrogen atom, between main chains will occur the cross-links (main chain cross-linking type) [8]. We can classified be PMMA, PEMA, PPrMA, PCHMA, PPhMA, and PBeMA as main chain scission type polymers and also PMA, PEA and PAA can be classified as main chain cross-linking type polymer. The removal rate of the main chain cross-linking type polymer was slower than main chain scission type polymer. It considered that the removal rate of main chain cross-linking type polymer was reduced according to become lower the decomposition reaction rate into low molecule apparently, because the reduction decomposition by hydrogen radical and main chain cross-link in main chain cross-link occur simultaneously [5]. The removal rate of PPhMA and PBeMA with benzene ring as main chain scission type is less than 17% by comparison to the polymer without benzene ring.

Therefore, it can be said that the chemical property of benzene ring is more dominant against the removal rate than etching resistance in polymer of main chain scission type with benzene ring. In addition, we guessed that in the decomposition reaction of benzene ring, first, hydrogenation occur to benzene ring, next, the benzene ring decomposes due to changing the order of cyclohexadienyl (radical), cyclohexane, finally, such $CH_4$ and $H_2C{=}CH_2$ generated by ring cleavage of the benzene ring [9].

## 4. Conclusions

We concluded that the hot-wire method is useful as the removal method for ArF resist, because it can be relatively easily removed main chain scission type polymer without benzene ring.


## Acknowledgement

This work was supported by JSPS KAKENHI Grant Number 24560032.


## References


[1] M. Suyama ed., *Erekutoronikusu Senjo gijutsu,* Gijutsu Jouhou Kyokai, (2007)31-64. [in Japanese].

[2] M. Yamamoto, T. Maruoka, A. Kono, H. Horibe, H. Umemoto, *Appl Phys. Express*, 3(2) (2010), 026501.

[3] K. Hashimoto, A. Masuda, H. Matsumura, T. Ishibashi, and K. Takao, *Thin Solid Films*, 501 (2006), 326.

[4] M. Tanaka, K. Ogushi, Y. Yuba, Y. Akasaka, K. Tomioka, E. Soda, and N. Kobayashi, *Thin Solid Films*, 516 (2008), 847.

[5] M. Yamamoto, H. Horibe, H. Umemoto, K. Takao, E. Kusano, M. Kase, and S. Tagawa, *Jpn. J. Appl. Phys*., 48 (2009) 026503.

[6] M. Yamamoto, T. Maruoka, A. Kono, H. Horibe, and H. Umemoto, *Jpn. J. Appl. Phys*., 49 (2010) 016701.

[7] M. Yamamoto, T. Maruoka, Y. Goto, H. Horibe, M. Sakamoto, E. Kusano, H. Seki, and S. Tagawa, *J. Electrochem. Soc*., 157 (2010) H361-H370.

[8] A. Miller, E. J. Lawton, and J. S. Balwit, *J. Polym. Sc*i., 14 (1954) 503-504.

[9] P. Kim, J. H. Lee, R. J. Bonanno, and R. B. Timmons, *J. Chem. Phys*., 59 (1973) 4593-4601.

Eleventh International Conference on Flow Dynamics
October 8-10, 2014, Sendai, Miyagi, Japan

# Behavior of the Polymeric Material subjected to the Fire: Direct Numerical Simulation of Melting and Deforming Processes of Degrading Polymeric Material

Yuji Nakamura[1], Akter Hossain[1], Yangkyun Kim[2]
[1]Department of Mechanical Engineering, Toyohashi University of Technology
1-1 Hibarigaoka, Tempaku, Toyohashi 441-8580, Aichi, Japan
[2]School of The Building Environment, University of Ulster
Shore Road, Newtownabbey, BT37 0QB, U.K.

**ABSTRACT**

Direct numerical simulation of time-dependent polymer degradation process subjected by heat is presented. Melting followed by the gasification processes are traced numerically by adopting the enthalpy-porosity method as well as VOF method with surface gasification model based on Arrhenius law. An abrupt change of interface, such as pinched-off of the molten matter, is satisfactory simulated and following gasification enhances to form the mixture around the molten matter. Our model will be contributed to predict the precise process of fire dynamics and potential damages.

## 1. Introduction

Polymer becomes common material in these days since it has unique features; such as light-weight with sufficient strength. The weak points, on the other hands, are the less-stability (age degradation) and ignitability (easy to be degraded by thermal shock). Although the technology development would try to cover them through various ways, e.g., last-long coating is applied, flame retardant is doped in the polymer, there is no "perfect polymer" to date, namely, we should be careful in safety issue when the polymers are utilized. In this sense, more polymers are utilized in engineering purpose, more fire damage we should seriously considered. For this purpose, if we have acceptable universal (numerical) model to describe the thermal degradation, including the combustion (fire), is preferable. This is our basic motivation on this subject.

Once polymer is thermally degraded (subjected to the heat, for example), it first melts then gasify to release the gaseous fuel matter into the atmosphere. In most of past works in fire field, liquid phase is intentionally excluded to avoid any complexity so that the polymer can be recognized as the gas-producing-source. However, as we know, once the polymer is subjected to the heat, molten layer is frequently dripped off and firing point is no longer stay at the location where the original polymer is placed (e.g., Fig.1). This causes the increase of firing zone in vertical direction so that such fire scenario cannot be predicted/handled as long as the conventional model is considered. Hence, our target is to develop the complete model of polymer fire as the three-phase-involved-problem (solid-liquid-gas) and dynamic process of dripping off of molten polymer is simulated with gasification process. Since 2009, we have extensively developed the numerical scheme adopting the enthalpy-porosity method and VOF method and successfully reproduced the time-dependent dynamic behavior of molten polymer [1-4]. In this report, we have further upgraded the model including the gasification model based on the Arrhenius law to let the mixture forms in the gas phase over the molten matter.

(a) dripped off (b) pool fire formation

Fig.1 Direct photo of cable tray burning test. ((a) dripped-off molten polymer continuously burns as marked in red circle in the picture, then (b) eventually form the pool fire beneath of the original firing point)

Corresponding author: Yuji Nakamura
*E-mail address*: yuji@me.tut.ac.jp

## 2. Numerical model

Followings are governing equations to be solved in this study. Since the detail explanation of symbols are well-described in the past works [1-4], only the minimum information is given here.

$$\nabla\cdot(\mathbf{v}) = -\dot{m}\left(\frac{1}{\rho_v}-\frac{1}{\rho_l}\right)\ (\rho = const), \tag{1}$$

$$\frac{\partial(\rho\mathbf{v})}{\partial t}+\nabla\cdot(\rho\mathbf{v}\otimes\mathbf{v}) = -\nabla p+\nabla\cdot[\mu(\nabla\mathbf{v}+\nabla\mathbf{v}^T)]+\rho\mathbf{g} + \frac{\rho}{0.5(\rho_g+\rho_l)}[\sigma\kappa_c\mathbf{n}_\Sigma+(I-\mathbf{n}_\Sigma\otimes\mathbf{n}_\Sigma)\nabla_\Sigma\sigma^T]\delta_\Sigma - A_{mush}\frac{(1-\beta)^2}{(\beta^3+\varepsilon)}\vec{v}, \tag{2}$$

$$\rho\frac{\partial(h+\Delta H)}{\partial t}+\nabla\cdot[\rho\mathbf{v}(h+\Delta H)] = \nabla\cdot(\kappa\nabla T)+\dot{m}L_v, \tag{3}$$

$$here,\ \ \Delta H = \beta L$$

$$\frac{\partial(\alpha)}{\partial t}+\nabla\cdot(\mathbf{v}\alpha) = -\frac{\dot{m}}{\rho}, \tag{4}$$

$$\frac{\partial(\rho Y_F)}{\partial t}+\nabla\cdot(\rho Y_F\mathbf{v}) = \nabla\cdot[\rho D\nabla(Y_F)]+\dot{m}', \tag{5}$$

$$\dot{m} = Ae^{(-E/T)}\hat{n}. \tag{6}$$

Notable differences from the previous works are eqs. (5) and (6), where are necessary to consider the different mass species evolved from the surface by gasification. Gasification rate is modeled as eq.6, having the Arrhenius type of temperature dependency. The "n" appeared in eq.6 denotes the normal direction against the (curved) surface, ensuring that the gasification velocity directs always normal to the surface. It should be reminded that $\alpha$ and $\beta$ are phase-indicators to judge the corresponding cell is in which phase (gas/liquid/solid). $\alpha$ gives the boundary of gas/non-gas (either solid/liquid), whereas $\beta$ gives the boundary of liquid/solid and given as a function of temperature. Fluent is adopted for the simulation.

Considered numerical model in this study is shown in Fig.2. This is identical to what we have used in the most of previous works [1-4].

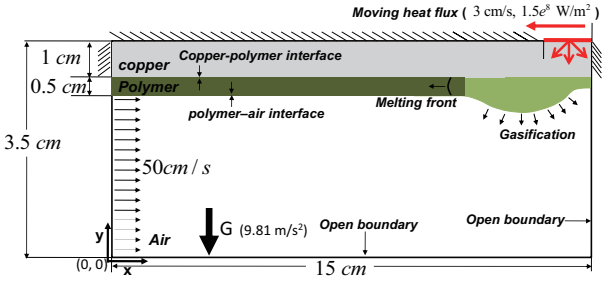


Fig. 2 Applied numerical model in this study

## 3. Results and Discussion

Represented numerical results are depicted in Fig.3, where the time-dependent change of the phase-indicator contours with streamlines (left) and fuel mass fraction (right) are shown. Note that the blue/green/red colors in the phase-indicator figure stands for solid/liquid/gas phase, respectively. Time zero is defined as the heating applied.

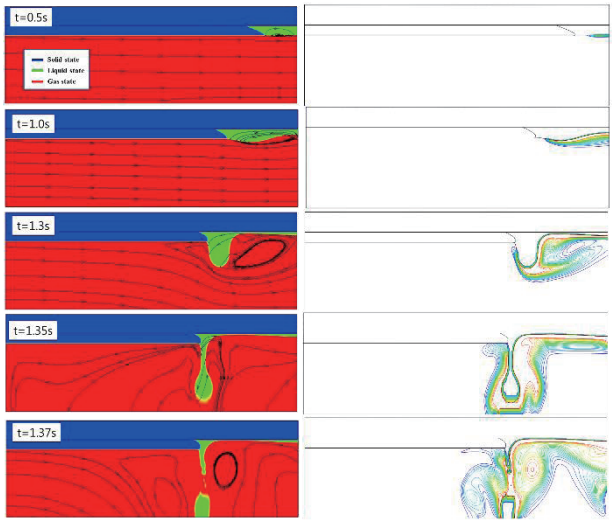


Fig.3 Time-dependent change of phase-indicator with streamlines (left) and fuel mass fraction (right)

As clearly shown in this figure, molten layer (green part) is abruptly deformed by the gravity drag and eventually pinched off. Such dynamic behavior is properly simulated in our model. Furthermore, during such non-linear dynamic events, releasing the fuel gas from the heated molten matter is properly simulated. Upon the dripping off, vortex is formed in downstream due to the blockage of deformed (suspended) molten matter. Magnified the flow patterns formed near the hanging molten matters are shown in Fig.4, showing that the evolved fuel gas species are transported by convection (from left to right) as well as pushed toward the ceiling due to the buoyancy-driven flow.

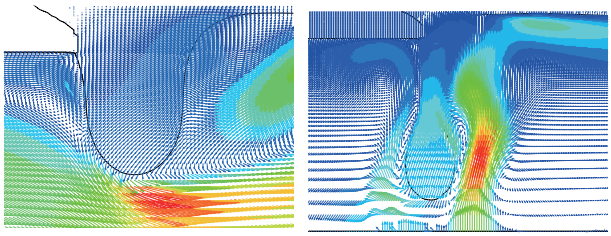

(a) t=1.3s (b) t=1.35 s

Fig.4 Velocity vectors formed at the vicinity of the surface of deformed molten matter.

Although not shown in figures listed here (due to the space limitation), mixture consists of the evloved fuel gas and ambient oxygen is formed over the molten surface. Although the current model is intentionally excluded the combustion model in gas phase, once it is developed and considered, ignition followed by the stable flame formation would be made. Now such upgrading is underway and will be reported in near future.

## 4. Concluding Remarks

We have successfully developed the numerical model to present the time-dependent melting and pinching off behavior of thermally-degraded polymer with gasification. Enthalpy-porosity method combined with VOF method works well for the present purpose. Inclusion of Arrhenius law for rate expression of gasification is found to be satisfactory without losing numerical stability. In future we are going to upgrade the model including combustion model in gas phase to simulate the complete process of the deformable polymer burning numerically.


## Acknowledgments

This work is supported by JNES (currently named NRA: Nuclear Regulation Authority in Japan) under the contracted work in Yr2013-2014.


## References


[1] Y. Kim, A. Hossain, S. Kim, S., and Y. Nakamura, *Two Phase Flow, Phase Change and Numerical Modeling (Chapt. 23)*, InTech Open Access Publisher, Croatia (2011.9) 523-540.

[2] Y. Kim, A. Hossain and Y. Nakamura, *Int. J. Heat Mass Transf.* 63 (2013) 101-112.

[3] Y. Kim, A. Hossain and Y. Nakamura, *J. Thermal Sci. Tech.* 8(1) (2013) 136-151.

[4] Y. Kim, A. Hossain and Y. Nakamura, *Proc. Combust. Inst.* 35, in print.

Eleventh International Conference on Flow Dynamics
October 8-10, 2014, Sendai, Miyagi, Japan

# Scale-model Experiments of Large-scale Fires

Kazunori Kuwana[1]
[1]Deparment of Chemistry and Chemical Engineering, Yamagata University
4-3-16 Jonan, Yonezawa, Yamagata 992-8510, Japan

**ABSTRACT**

Full scale experiment of a large-scale fire is generally difficult, and scale-model experiments are often conducted. When designing a scale-model experiment, important pi-numbers (dimensionless parameters) must be identified, and these pi-numbers of the scale-model must be set equal to those of the prototype. In this presentation, scale-model experiments of a fire whirl and a compartment fire are discussed. In both cases, scaling analysis is first conducted to identify important pi-numbers, and scale-model experiments are conducted to validate the proposed scaling laws.

## 1. Introduction

Because of difficulties in conducting large-scale fire experiments, scale-model experiments are often conducted. A scale-model experiment must be designed such that it reproduces the full-scale phenomenon (hereinafter called prototype). If one could design a scale-model experiment of which all pi numbers are equal to those of the prototype, the scale-model experiment would perfectly reproduce the prototype phenomenon. However, such a scale-model experiment is generally impossible owing to the large number of the pi numbers involved [1-3]. Therefore, one must seek relaxation of scaling laws (or partial modeling [4]). In other words, one must find important pi numbers and ignore marginal and nonessential ones.

In this presentation, two examples of scale-model experiments of fire phenomena are presented: fire whirl behind an L-shaped wall and a compartment fire. In the former example, experiments of different scales are compared to confirm the proposed scaling law, while in the latter, the proposed scaling law is validated by computational fluid dynamics (CFD) simulations (numerical scale-model experiments).

## 2. Fire Whirl behind an L-shaped Wall

A fire whirl is a phenomenon like a tornado of fire and occurs when a pool fire interacts with a vortex. Soma and Saito [5] surveyed the records of reported large-scale fire whirls and classified them according to their generation mechanisms. Many fire whirls are generated by the interaction between a mass fire and lateral wind. Sekimoto and coworkers [6] created a fire whirl of a different configuration, that is, a fire whirl behind an L-shaped wall. Under the presence of lateral wind, a recirculating flow is generated over a heptane pool fire, creating a fire whirl. As shown in Fig. 1, a tall fire column is created behind the L-shaped wall. Without the occurrence of fire whirl, the flame height is about 1 m; the flame height is increased by the factor of about 10. The measured wind velocity is about 2 m/s.

Because of the difficulty in conducting experiments of this scale, laboratory-scale experiments are also conducted using a wind tunnel. From the larger-scale experiment, it is found that an intense fire whirl occurs only when the wind velocity is within a certain range. Then, a question arises when designing the smaller-scale experiment: What is the wind velocity to create a fire whirl of the smaller scale? Dimensional analysis similar to Ref. [7] yields the following two pi numbers:

$$\frac{U^2}{gH}, \qquad \frac{UH}{\nu} \tag{1}$$

where $U$ is the wind velocity, $g$ the acceleration due to gravity, $H$ the flame height (before fire whirl is created), $\nu$ the kinematic viscosity. The first pi number is the Froude number, and the second is the Reynolds number.

It is almost impossible to make the both pi numbers equal between the scale model and the prototype. In general, the flow induced by a large fire is turbulent because of strong buoyancy effects. Therefore, it is expected that the Froude number is the dominant pi number and that the influence of Reynolds number is rather weak. Consequently, the wind velocity of the scale-model experiment is so adjusted that the resultant Froude number is equal to that of the prototype. Then, a similar fire whirl is reproduced as shown in Fig. 2.

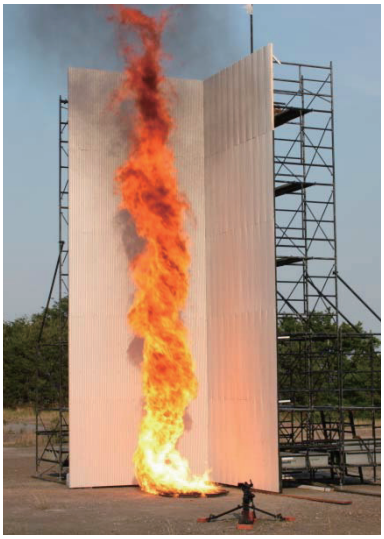

Fig. 1 A fire whirl created behind an L-shaped wall. The height of the wall is 9 m.

Corresponding author: Kazunori Kuwana
*E-mail address*: kuwana@yz.yamagata-u.ac.jp

Fig. 2 A fire whirl created behind an L-shaped wall using a 1/10th scale model.

## 3. Compartment Fire

The development of a fire inside a building involves such stages as ignition, flame spread, and flashover (a sudden event in fire growth that rapidly leads to full involvement of a room) [8]. Understanding fire behaviors, for example, the timing of flashover and the maximum heat release rate is important.

When we focus on a fire of a fixed scale, dimensional analysis yields the following relationship of total heat release rate:

$$\frac{\dot{Q}}{\rho_g c_g T_0 (gL^5)^{1/2}} = f\left(\left(\frac{g}{L}\right)^{1/2} t, \quad \frac{\dot{q}}{\rho_g c_g T_0 (gL^5)^{1/2}}\right) \tag{2}$$

where $\dot{Q}$ is the total heat release rate, $\rho_g$ the gas-phase density, $c_g$ the gas-phase specific heat, $T_0$ the ambient temperature, $L$ the characteristic length, $t$ the time from ignition, $\dot{q}$ the heat release rate of the ignition source, and $f$ denotes a certain function. To test the validity of Eq. (2), two different calculations are conducted with different intensities of ignition source. Then, the acceleration due to gravity is adjusted such that the second parameter on the right hand side of Eq. (2) remains unchanged. A CFD software package, Fire Dynamics Simulator (FDS) is used, and Fig. 3 shows a typical result. Figure 4 shows the relationships between (dimensionless) total heat release rate and (dimensionless) time. The agreement between the two different runs confirms the validity of the proposed scaling law, Eq. (2).

## 4. Concluding Remarks

Two examples of scale-model experiment of fire phenomenon are presented. In both cases, scaling laws are first proposed. The scaling laws are then validated by comparing results under different conditions.

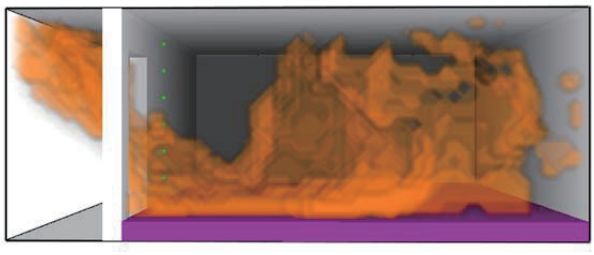

Fig. 3 A snapshot of a CFD simulation. Contour surface of the heat release rate is visualized.

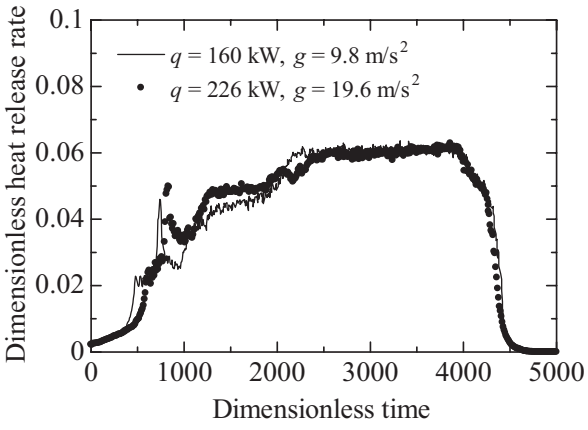


Fig. 4 Predicted heat release rate.


## Acknowledgments

The author thanks Prof. Kozo Saito and Mr. Kozo Sekimoto for their valuable advice on scale-model experiments. The author also thanks Mr. Yuta Kawagoe and Ms. Saori Nagasawa for their help in conducting the scale-model experiments presented.


## References


[1] I. Emori, K. Saito, K. Sekimoto, *Theory and Application of Scale-model Experiment (3rd ed.)*, Gihodo, (2000) (in Japanese).

[2] K. Saito ed., *Progress in Scale Modeling*, Springer, (2008).

[3] K. Saito, M.A. Finney, *J. Combust. Soc. Jpn.* 56 (2014).

[4] D.B. Spalding, *Proc. Combust. Inst.* 9 (1963) 833-843.

[5] S. Soma, K. Saito, *Combust. Flame* 86 (1991) 269-284.

[6] K. Sekimoto, K. Kuwana, *Proc. JAFSE Annual Symp.*, (2014) 252-253 (in Japanese).

[7] K. Kuwana, K. Sekimoto, K. Saito, *J. Chem. Eng. Jpn.*, 43 (2010) 952-955.

[8] J.G. Quintiere, *Principles of Fire Behavior*, Delmar, (1997).

Eleventh International Conference on Flow Dynamics
October 8-10, 2014, Sendai, Miyagi, Japan

# Numerical Simulation of Leaking Hydrogen in a Partially Open Space

Kazuo Matsuura[1]
[1]Graduate School of Science and Engineering, Ehime University
3 Bunkyo-cho, Matsuyama, Ehime, 790-8577, Japan

**ABSTRACT**

After reviewing recent progress of real-time sensing based risk mitigation of leaking hydrogen in enclosed spaces made by our group, I introduce a novel control algorithm for hydrogen ventilation that has a self-adjusting mechanism for the upper limit of exhaust flow rates. This upper limit is determined using a correlation between hydrogen concentrations sampled near a ceiling close to a leak source and the upper boundary of the region of acceptable exhaust flow rates for various leak flow rates. Effectiveness of the algorithm is examined by computations for various leak scenarios.

## 1. Introduction

For the wide use of hydrogen, the development of risk management strategies against hydrogen leakage and dispersion is necessary. This study investigates risk mitigation by ventilating leaking hydrogen in a highly enclosed space.

The authors have proposed a real-time sensing-based risk mitigation control of hydrogen dispersion in a partially open space with low-height openings using forced ventilation [1]. Based on the information of acceptable ventilation amounts to various leak amounts determined in advance to a partially open space, and information on hydrogen leakage acquired by sensing, we showed that we can successfully exhaust hydrogen within a short time. In the method, we plotted appropriate ranges of exhaust, i.e., an acceptable region, to various leak amounts by computational fluid dynamics (CFD). We control exhaust flow rates to be included in the appropriate region. When an exhaust amount is too small, hydrogen is not exhausted sufficiently. While, when the exhaust amount is too large, hydrogen accumulating near the ceiling is transported to the lower part of the space, and as a result, the space is filled with hydrogen. Although both upper and lower boundaries of the acceptable region depend on leak amounts, they are generally unknown from the viewpoint of sensing. Although the control algorithm proposed in [1] has a mechanism to make exhaust flow rates converge to the lower boarder of the acceptable region, it does not have a mechanism to regulate exhaust amounts below the upper limit according to leak amounts. In this study, we investigate the inclusion of a self-adjusting mechanism for the upper limit of exhaust flow rates by numerical computation. We propose a novel control algorithm of hydrogen ventilation possessing this mechanism.

## 2. Computational Model

The computational domain is a partially open rectangular space with a hydrogen inlet, roof vent and door vents (Fig. 1). The overall dimensions of the space are 2.9 m×1.22 m×0.74 m. At the hydrogen inlet, jet leakage of hydrogen occurs, and hydrogen-air mixture is exhausted mechanically from the roof vent.

Corresponding author: Kazuo Matsuura
*E-mail address*: matsuura.kazuo.mm@ehime-u.ac.jp

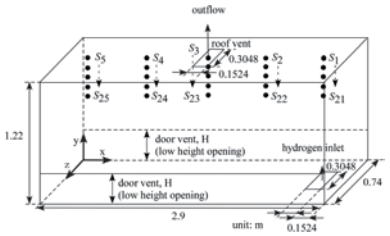


Fig. 1 Computational domain

During ventilation, air enters the space through the low-height openings on both sides of the constant $z$ planes marked as "door vents". In the space, twenty-five hydrogen sensors $S_1$, …, $S_{25}$ are distributed near the ceiling. As mentioned later, we control the exhaust flow rates $Q_{ex}$ at the roof vent using signals of hydrogen sensor. The upper limit of exhaust flow rates are determined using a correlation between hydrogen concentrations sampled near the ceiling close to a leak source and the upper boundary of the region of acceptable exhaust flow rates for various leak flow rates. It is unrealistic to use the values of sensors located immediately above the leak source on which plume from the source impinges directly. So, we define the sensor arrangement shown in Fig. 1 as arrangement A, and also take arrangement B into account defined as $S_{m,B} = S_{m+1,B}$, m=1,6,11,16,21. In both arrangements, hydrogen concentrations used for developing the above correlation are sampled at $S_{1,\chi}$, $\chi$=A, B. Computational details are described in [1,2].

## 3. New Control Algorithm Possessing a Self-adjusting Mechanism for the Upper Limit of Exhaust Flow Rates [2]

Exhaust flow rates $Q_{ex}$ is controlled by the instantaneous hydrogen amount accumulating near the ceiling $\Omega$, i.e., $Q_{accum}$, which is defined as follows:

$$Q_{accum}(t) \equiv \int_{\Omega} Y d\Omega \approx \sum_{i\in\{S_1,\cdots,S_m\}} Y_i(t)\Delta\Omega_i, m = 25 \quad (1)$$

Here, $Y_i$ is the volumetric concentration of hydrogen at sensor $i$, $\Delta V_i$ the volume element, the hydrogen concentration of which is represented by $Y_i$, and $T_p$ is the monitoring time period of the sensors. $Q_{ex}$ is updated every $T_p$ based on $T_p$ data. $T_p$ is set as 2.5 s. Let $I_n \equiv [(n\text{-}1)T_p, nT_p)$, $n \in \boldsymbol{N}$ be a single $T_p$ time interval, and $Q_{accum}(t)$ be evaluated at $t=t_1, t_2, \ldots, t_m$, where $t_1 \equiv (n\text{-}1)T_p$

and $t_m \equiv T_p$. From data sets $(t_i, Q_{accum}(t_i))(i=1,2,\ldots,m)$, we find a linear function $f^n(t) = a_0^n + a_1^n(t-t_1)(t \in I_n)$ such that the residual sum of the square $S_n$, which is defined below, becomes a minimum.

$$S \equiv \sum_{i=1}^{m} \{Q_{accum}(t_i) - f(t_i)\}^2. \quad (2)$$

Here, we define an average value and the variation of the average over successive time periods.

$$\bar{f}_n \equiv a_0^n + a_1^n(T_p/2), \quad \Delta\bar{f}^n \equiv \bar{f}^n - \bar{f}^{n-1}, \quad n \in N \quad (3)$$

$Q_{ex}(t)$ for $t \in I_{n+1}$ is given by the following two steps.

$(a)$ $Q_{ex}(t)=$

$$\begin{cases} \max(Q_{ex}(t-T_p) - \alpha S_{roof}, \beta_g) & \Delta\bar{f}^{n-1} \in I^{-\varepsilon} \cap \Delta\bar{f}^n \in I^{-\varepsilon}, \\ Q_{ex}(t-T_p) & \Delta\bar{f}^{n-1} \in I^{-\varepsilon} \cap \Delta\bar{f}^n \in I^0, \\ Q_{ex}(t-T_p) & \Delta\bar{f}^{n-1} \in I^{-\varepsilon} \cap \Delta\bar{f}^n \in I^{\varepsilon}, \\ \max(Q_{ex}(t-T_p) - \alpha S_{roof}, \beta_g) & \Delta\bar{f}^{n-1} \in I^0 \cap \Delta\bar{f}^n \in I^{-\varepsilon}, \\ Q_{ex}(t-T_p) & \Delta\bar{f}^{n-1} \in I^0 \cap \Delta\bar{f}^n \in I^0, \\ \min(Q_{ex}(t-T_p) + \alpha S_{roof}, c_0(t)) & \Delta\bar{f}^{n-1} \in I^0 \cap \Delta\bar{f}^n \in I^{\varepsilon}, \\ Q_{ex}(t-T_p) & \Delta\bar{f}^{n-1} \in I^{\varepsilon} \cap \Delta\bar{f}^n \in I^{-\varepsilon}, \\ Q_{ex}(t-T_p) & \Delta\bar{f}^{n-1} \in I^{\varepsilon} \cap \Delta\bar{f}^n \in I^0, \\ \min(Q_{ex}(t-T_p) + \alpha S_{roof}, c_0(t)) & \Delta\bar{f}^{n-1} \in I^{\varepsilon} \cap \Delta\bar{f}^n \in I^{\varepsilon}, \end{cases} \quad (4)$$

$(b)$ $Q_{ex}(t) = \min(Q_{ex}(t), c_0(t))$ (5)

Here,

$$\boldsymbol{R} = I^{-\varepsilon} \cup I^0 \cup I^{\varepsilon},$$
$$I^{-\varepsilon} \equiv \{x \in \boldsymbol{R}; x < -\varepsilon\}, \quad I^0 \equiv \{x \in \boldsymbol{R}; -\varepsilon \le x \le \varepsilon\}, \quad (6)$$
$$I^{\varepsilon} \equiv \{x \in \boldsymbol{R}; x > \varepsilon\}.$$

$S_{roof}$ is a roof vent area, $\alpha$=1 m/s, and $\varepsilon=1.0\times10^{-6}$. In Eq. (4), $c_0(t)$ is evaluated by the following equation.

$$c_0(t) = S_{roof}\left\lfloor (3.829\bar{Y}_c + 0.1530)/S_{roof} \right\rfloor \quad (7)$$

Here, $\bar{Y}_c$ is hydrogen volumetric concentration sampled at $S_1$ and time-averaged for every 10 s, and $\lfloor\ \rfloor$ means the round-off operation. $\beta_g$ is a value for preventing $Q_{ex}(t)$ from becoming too small, and $\beta_g/S_{roof}$=2 m/s [3].

## 4. Results and Discussion

Figures 2 and 3 show the results of ventilation simulations for arrangements A and B, respectively. In Case 1, the leak flow rate $Q_{leak}(t)=1.18\times10^{-4}$ m$^3$/s ($0 \le t < \infty$), and the control algorithm we proposed previously [1,3] is used. In Case 2, $Q_{leak}(t)=1.18\times10^{-4}$ m$^3$/s ($0 \le t < \infty$), and the present algorithm is used. In Case 3, time-dependent $Q_{leak}(t)=1.18\times10^{-4}$ m$^3$/s ($0 \le t < 20$ s), $4.72\times10^{-4}$ m$^3$/s (20 s$\le t \le$40 s), $9.44\times10^{-4}$ m$^3$/s(40 s$\le t < \infty$), and the present algorithm is used.

In Case 1, $Q_{ex}(t)$ becomes too large because $c_0(t)/S_{roof}$ is set as 6 m/s, which is due to the fact that $Q_{leak}$ is unknown on the viewpoint of sensing, in spite of that $c_0(t)/S_{roof}$ should be 4 m/s for the present $Q_{leak}$ as found

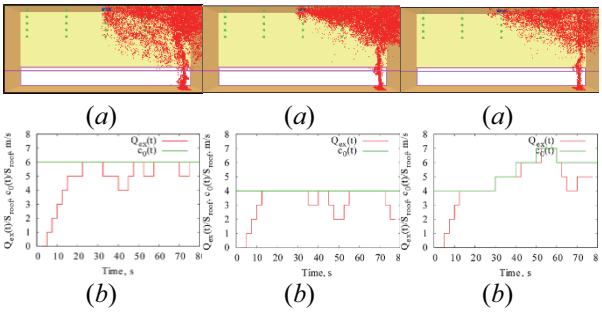


Fig. 2 Spatial distribution of hydrogen at $t$=80 s ($a$) and time histories of $Q_{ex}(t)$ and $c_0(t)$ ($b$) for Arrangement A (left: case 1, center: case 2, right: case 3)

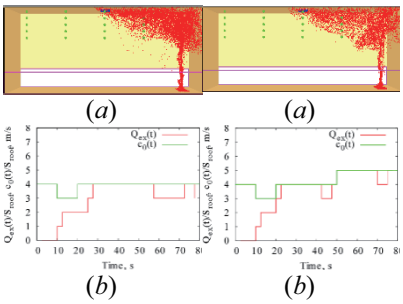


Fig. 3 Spatial distribution of hydrogen at $t$=80 s ($a$) and time histories of $Q_{ex}(t)$ and $c_0(t)$ ($b$) for Arrangement B (left: case 2, right: case 3)

from the acceptable region [1]. As a result, transportation of hydrogen accumulating near the ceiling to the lower part of the space occurs. While, in Cases 2 and 3 both in Figs. 2 and 3, $Q_{ex}(t)$ is regulated appropriately and hydrogen is stably exhausted. From these results, it is found the present control method works successfully.

## 5. Concluding Remarks

I introduced the novel algorithm that has the self-adjusting mechanism. I showed the effectiveness of this algorithm by applying it in numerical simulations of hydrogen ventilation assuming various leak flow rates and sensor arrangements.


## Acknowledgements

This research was supported by the Collaborative Research Project of the Institute of Fluid Science, Tohoku University. Computational resources are provided by the Advanced Fluid Information Research Center of the Institute of Fluid Science, Tohoku University.


## References


[1] K. Matsuura, M. Nakano, J. Ishimoto, *Int. J. Hydrogen Energy*, 37(2) (2012) 1972-1984.

[2] K. Matsuura, M. Nakano, J. Ishimoto, *Proc. of Eleventh Int. Conf. on Flow Dynamics* (2014), submitted.

[3] K. Matsuura, M. Nakano, J. Ishimoto, *Int. J. Hydrogen Energy*, 37(9) (2012) 7940-7949.

Eleventh International Conference on Flow Dynamics
October 8-10, 2014, Sendai, Miyagi, Japan

# Hazard Physical Modeling Challenge for Breach of Liquid Rocket Tank

Keiichiro Fujimoto[1], Yu Daimon[1], Nobuyuki Iizuka[1] and Koichi Okita[1]
[1]Japan Aerospace Exploration Agency,
3-1-1, Sengen, Tsukuba, Ibaraki 305-8505, Japan

**ABSTRACT**

Quantitative safety analysis method is proposed to evaluate the human space flight risk. High fidelity numerical simulation is used to evaluate evacuation success rate of launch abort system from the explosive hazards. Corresponding research needs especially on the fluid dynamics field are discussed for the uncertainty reduction.

## 1. Introduction

Safety analysis is essential and important to ensure public safety in case of the cargo transportation, and the crew safety in case of the human space transportation. Based on the safety analysis result, safety design requirement and the operational limitation are considered and decided to achieve high level of safety.

In case of the catastrophic failure of the cargo transportation vehicle, an acceptable criterion of safety distance and the trajectory is defined based on the safety analysis result. This safety analysis conventionally based on the high cost experimental results and the conservative semi-empirical engineering model.

Comprehensive research activity for human space flight is currently under the way at Japan Aerospace Exploration Agency (JAXA). In order to realize Japanese human space launch vehicle, an efficient system engineering methodology to maximize crew safety is essential. In this study, quantitative safety analysis (QSA) method is proposed, and the research needs in the fluid dynamics field are discussed to establish QSA technology.

## 2. Quantitative Safety Analysis Methodology

In order to achieve high-level of crew safety, technological effort should be made not only for launcher's reliability but for mission abort success rate. In order to improve vehicle's reliability, quantitative risk analysis technology is employed for the development of the new booster engine for next flag-ship rocket H-3[1].

In this development methodology, all of the failure modes are identified, failure mode probability is evaluated mainly by the high-fidelity numerical simulations, and uncertainty of the simulation model and the input parameters are quantified mainly based on the low cost experiments. If the failure mode probability is larger than the requirement, risk mitigation actions such as design change and the inspection requirement are taken. Proposed QSA-based development is mostly based on this quantitative risk analysis method [2]. QSA-based development process is overviewed in Fig. 1. In this study evacuation success rate has been evaluated in case of the explosive hazards. Since explosive yield is one of the sensitive parameters against evacuation success rate, its uncertainty should be reduced by the employment of high fidelity numerical simulations and by obtaining an additional experimental data.

Corresponding author: Keiichiro Fujimoto
*E-mail address*: fujimoto.keiichiro@jaxa.jp

Improvements in the numerical simulation accuracy can be directly contributes to the epistemic uncertainty reduction and the significant cost reduction in large scale experiments such as explosion tests.

## 3. Research Needs

Since explosive yield is largest in case of the pad-abort, near-pad destruction and the explosion process are focused as the numerical modeling research target in this study. In order to establish high fidelity numerical simulation of destruction and explosion process for liquid rockets, the following research should be carried out to understand its mechanism and to develop the numerical simulation model. Explosion process and the three research target numerical simulations are shown in Fig. 2. An Explosive yield is strongly depending on the volume of the mixture cloud of oxygen and hydrogen at the ignition timing. Therefore, all of the following explosion process should be modeled to evaluate explosive yield.

**A : Mechanical failure and cryogenic jet**

Cryogenic jet flow rate is strongly depending on the size of the mouth and the internal pressure increase due to the crash impact. Complicated tank breach should be modeled with flash evaporating cryogenic flow [3].

**B : Cryogenic jet in cross flow**

In-flight catastrophic failure case should be considered in the evacuation success rate evaluation. Cryogenic fuel and oxidizer distribution should be evaluated under the interaction of subsonic to supersonic free-stream [4].

**C : Flash evaporation of cryogenic jet**

Flash evaporation effect should be considered with including atmospheric temperature and pressure effect, explosive boiling effects [3].

**D : Bubble-collapse induced ignition**

Local shock wave due to GH2/GOX bubble collapse in LOX is considered as one of the ignition mechanism which can be resulting in the high explosive such as unconfined detonation [5].

**E : Explosive yield for vapor cloud explosion**

Existence of the droplet in the vapor cloud has strong influence on the explosive yield, therefore droplet distribution and the explosive yield for vapor cloud should be modeled [3].

## 4. Conclusion

In order to achieve challenging mission of space transportation system such as human space flight in Japan, quantitative safety analysis method was proposed in this

study. CFD research needs to establish QSA method was presented for the collaborative research with corresponding researchers.

## References


[1] Kumada, N., Nakajima, A., Ogawara, A., Manako, H., Taguchi, H., Fujimoto, K., Sunakawa, H. and Kobayashi, T., *Space propulsion,* (2014).

[2] Fujimoto, K., Tani, N. and Wada, E., *COMPSAFE,* (2014).

[3] Osipov, V., Muratov, C., Hafiychuk, H., Ponizovskya-Devine, E., Smelyanskiy, V., Mathias, D., Lawrence, S. and Werkheiser, M., *(arXiv:1012.5135v1),* (2011).

[4] Wu, P.-K., Kirkendall, K. A., Fuller, R. P. and Nejad, A. S., *Journal of Propulsion and Power,* (1997).

[5] Osipov, V. V., Muratov, C. B., Ponizovskaya-Devine, E., Foygel, M. and Smelyanskiy, V. N., *Applied physics letters,* 98, (2011) 134102.


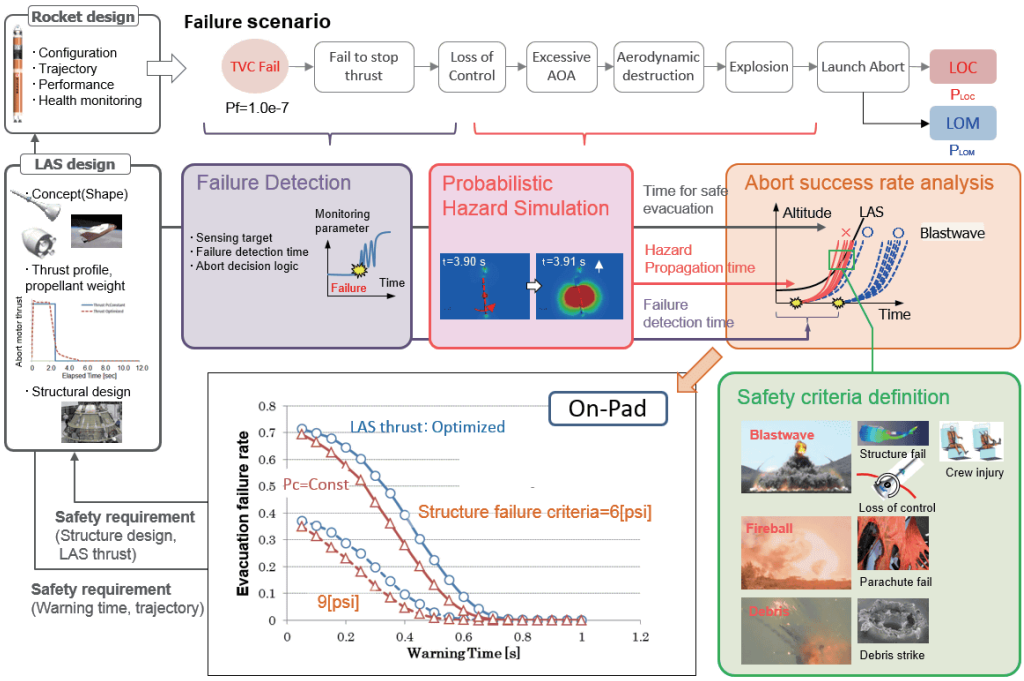


**Fig. 1 Process overview of quantitative crew safety analysis [2].**

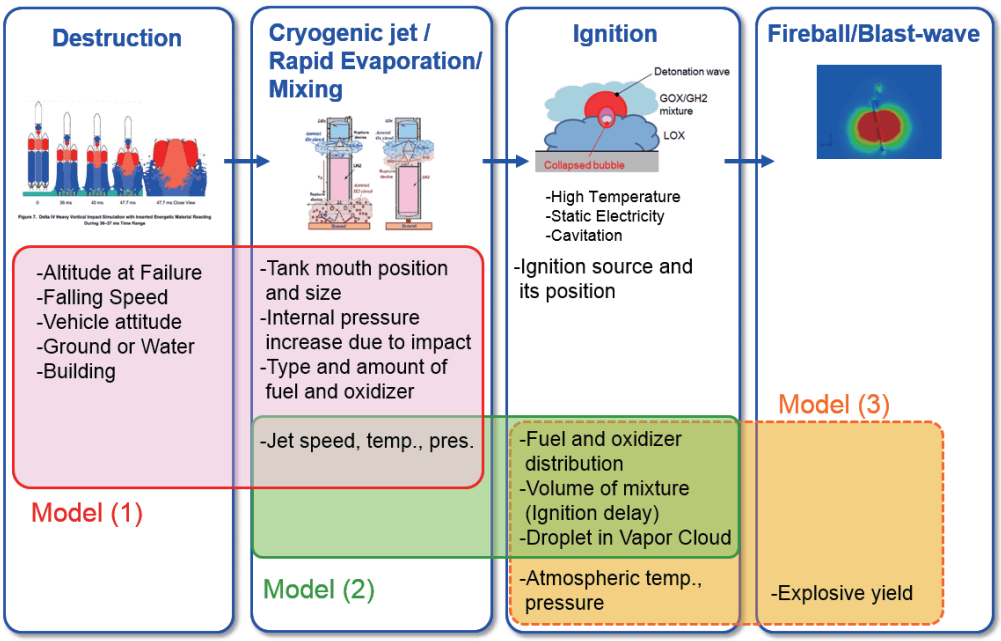


**Fig. 2 Explosion process modeling.**

# GPU-Accelerated Direct Numerical Simulation on Natural Convection Boundary layer of Helium near the Gas-Liquid Critical Point

Takahiro Okamura[1]
[1]Institute of Particle and Nuclear Studies KEK,
High Energy Accelerator Research Organization
1-1 Oho, Tsukuba, Ibaraki 305-0801, Japan

**ABSTRACT**

Direct numerical simulations by means of GPGPU (TESLA C2075) and CUDA 4.2 architecture were performed in order to clarify laminar-turbulent transition process, vortical structures in the boundary layer and characteristics of mean and fluctuation field in the supercritical helium near the gas-liquid critical point. Flow field structures were clarified by visualizing vortical structures. The existence of viscous sublayer and logarithmic layer is confirmed. The fluctuation field obtained from DNS obeys Kolmogorov K41 law.

## 1. Introduction

Supercritical helium is often used as a coolant for large scale superconducting magnet system such as accelerator and detector for particle physics. Forced convection cooling is mainly applied to the magnet system. But cooling channel has the several dead ends due to the geometrical problem. In such channel with the dead end we have to consider natural convection cooling because forced convection heat transfer does not occur in the dead end. Therefore it is necessary to understand heat and flow characteristics for natural convection of supercritical helium. Especially passive turbulent control is most effective way in order to improve cooling efficiency in a limited space. To perform this, turbulent transition process and vertical structure in the flow field should be clarified to generate turbulent transition intentionally. In addition, mean and fluctuation field should be clarified to confirm whether standard turbulent model are appropriate. In the case of helium especially near the critical point, thermal diffusivity and kinematic viscosity becomes very small compared to other fluid. Therefore minimum scale of flow structure tends to become very small. So the direct numerical simulation is best way to clarify the flow field structures with various sizes which obey K41.

In this study, direct numerical simulations were performed for natural convection heat transfer of helium near the critical point in a rectangular channel in order to clarify heat transfer characteristics and boundary layer structure. Especially mean field and fluctuation profile of velocity and temperature with respect to normal direction are confirmed. Not only heat transfer characteristics but also transition process, vertical structures and statistical characteristics for fluctuation components such as energy spectrum are clarified from DNS results.

## 2. Method

Numerical simulations were performed by employing mass conservation, momentum conservation, energy conservation and thermal equation of state of helium. In this study, low Mach number approximation is applied to reduce the numerical calculation load. Figure 1 shows the vertical channel system. Table 1 shows the channel dimension and thermo physical condition of supercritical helium. In the case of ordinary natural convection, laminar-turbulent transition point is described as follows.

$$x_c \sim \left(\frac{Ra_{xc}\nu D_T}{g\beta_T \Delta T}\right)^{\frac{1}{3}}$$

$Ra_{xc}$ is local Rayleigh number at transition point, $x_c$. In this study, total channel length,$L_x$ is larger than $x_c$. Therefore laminar-turbulent transition process can be obtained from DNS.

In order to reduce calculation time, TESLA C2075 GPGPUs (General Purpose of Graphical Processing Unit) which is manufactured by NVIDIA are employed in this study. Own calculation code was established by employing CUDA-4.2 architecture.

Table 1. Channel dimension and thermo physical conditions

| Parameter | Value |
|---|---|
| Channel length, $L_x$ | 0.177 m |
| Channel span length, $L_y$ | 0.019 m |
| Channel normal length, $L_z$ | 0.01 m |
| Heated surface temperature, $T_w$ | 5.29 K |
| Initial bath temperature, $T_b$ | 5.25 K |
| Minimum mesh number, $dx_3\_min$ | $1 \times 10^{-6}$ m |

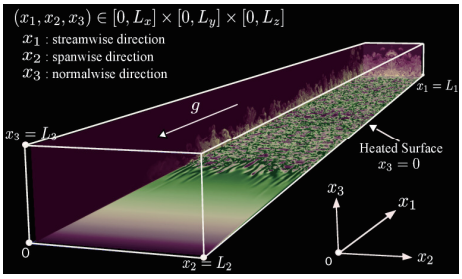


Fig.1 Schematic view of analytical system

## 3. Results and Discussion

Figure 2 shows vortical structures in the subdomain at 1.35 sec and 2.0 sec. Vortical structures are obtained from positive value of second invariant of velocity

Corresponding author: Takahiro Okamura
*E-mail address*: takahiro.okamura@kek.jp

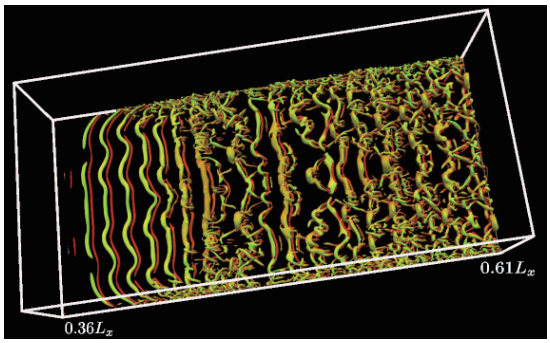


Fig.2-(a) Vortical structure at $t = 1.35$ sec

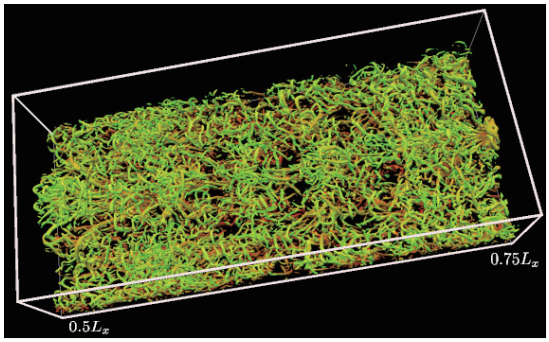


Fig.2-(b) Vortical structure at $t = 2.0$ sec.

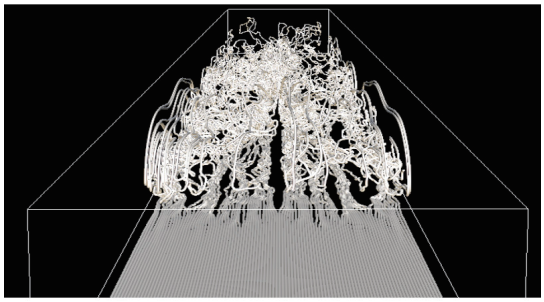

Fig.3 Quasi streamline at $t = 2.0$ sec

gradient tensor, $\partial_j u_i$ [1]. Turbulent boundary layer is generated following two steps.

1) Primary instability: Kelvin-Helmholtz instability occurs at the interface between high temperature domain and low temperature one. This interface is generated due to low thermal diffusivity near the critical point. KH instability induces a lot of horizontal vortex tube with length of span width of channel.
2) Secondary instability: Horizontal vortex itself becomes unstable. As a result, aspect of the horizontal vortex tube becomes change from straight to wavy shape as shown in the figure 2-(a)

After the two kinds of instability, fully developed turbulent boundary layer shown in the figure 2-(b) is generated. Quasi streamline at $t$=2.0 sec becomes fractal-like structure as shown in the figure 3.

Figure 4 shows the mean temperature profile at various positions, $x_1 \in [0, L_x]$. In the case of $x_1 < x_c$, mean temperature field obeys universality law of viscous sublayer, $T^+ = \langle Pr \rangle y^+$. On the contrary, in the case of high local Rayleigh number, not only viscous

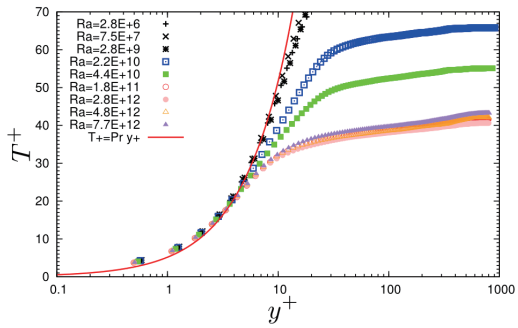


Fig.4 Mean temperature profile in wall units at various local Rayleigh number.

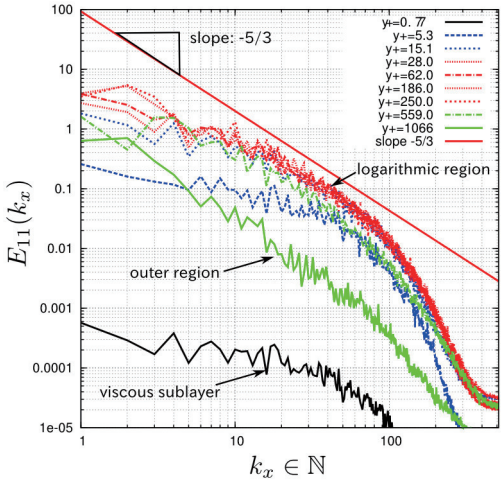


Fig.5 One dimensional energy spectra, $E_{11}$ at various $y^+$.

sublayer $y^+ < 5$ but also logarithmic layer, $y^+ > 5$, appear in the boundary layer.

Figure 5 shows the one dimensional energy spectra with respect to the velocity fluctuation, $\delta v_1 = v_1 - \langle v_1 \rangle$. As shown in the figure, energy spectra obeys Kolmogorov K41 law with the slope of $-5/3$ at $y^+ > 20 \sim 30$.

These results are obtained in the case of open system which means isobaric system. But in the case of isochoric system, piston effect appears in the system due to high compressibility. In such case flow and heat transfer characteristics are different from isobaric system [2].

## 4. Concluding Remarks

Direct numerical simulations were performed to clarify the heat and flow characteristics of supercritical helium. Not only mean field but also fluctuation one are obtained from DNS. The mean fields in the case of isobaric system are consistent with ordinary law of natural convection. Fluctuation components in the $y^+ > 20 \sim 30$ obey Kolmogorov K41 law.

## References

[1] Hunt, J.C.R., Wray, A.A. and Moin, *P., Center for Turbulent Research* CTR-S88, (1988) 193-208.
[2]A. Onuki, *Phase transition dynamics, Cambridge University Press*, (2002).

# Dynamic Simulation of Snowblower in Consideration of Snow Characteristic

Yosuke Yamamoto[1], Jun Ishimoto[2], Naoya Ochiai[2]
[1]Honda R&D Co., Ltd.
3-15-1 Senzui, Asaka-shi, Saitama 351-0024, Japan
[2]Institute of Fluid Science, Tohoku University
2-1-1 Katahira, Aoba-ku, Sendai 980-8577, Japan

**ABSTRACT**

Snow characteristics are influenced by climate or region. For the efficient development of a snowblower, stable and quantitative performance evaluation method is required. We tried to reproduce the snow removal work using Discrete Element Method (DEM) in this study. In addition to conventional DEM, we developed potential model for reproducing the compaction of snow and air drag model to consider the characteristics of actual snow. We found that simulation result is qualitatively consistent with the experimental result.

## 1. Introduction

A high efficient snowblower is required because of reduction in time required for snow removal or improvement of fuel efficiency. Performance of snowblower is mostly measured by working with an actual machine in heavy snowfall area. We need stable and quantitative evaluation method for efficient development of snowblower.

In this study, we developed simulation method using the DEM (Discrete Element Method) to reproduce snow removal. The DEM is widely used as an effective method in granular flow, powder mechanics and rock mechanics. [1] However, it is difficult for the DEM to reproduce unique behavior of snow such as compaction or snow cover. Therefore, we develop characteristic model of snow and reproduce snow behavior in the simulation.

## 2. Snowblower

Figure 1 shows the appearance of snowblower. This snowblower is called a two-stage type, which moves snow by two mechanisms: an auger feeds snow to a blower which rotates at high speed and blows snow out of the machine. Discharge direction and height of snow can be changed by operating a chuter.


Fig. 1 Snowblower

Corresponding author: Yosuke Yamamoto
*E-mail address*: yosuke.yamamoto@h.rd.honda.co.jp

## 3. Calculation Method

### 3-1. Discrete Element Method

The DEM is applied to granular flow, powder mechanism, rock mechanism, and snow. [2, 3] In the DEM, target materials are expressed as particles. Their connections are expressed using springs and dampers as shown in Fig. 2. Particles have equations of motion for translational and rotational degrees of freedom as shown in Eq. (1) and (2).

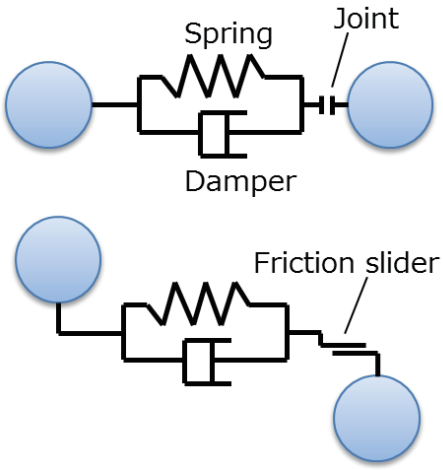


Fig. 2 Discrete Element Method

$$m\frac{d^2u}{dt^2}+\eta\frac{du}{dt}+Ku=0 \qquad (1)$$

$$I\frac{d^2\psi}{dt}+\eta\frac{d\psi}{dt}+K(\frac{D}{2})^2\psi=0 \qquad (2)$$

### 3-2. Reproduction of Snow Compaction

Microscopically, snow is comprised of multiple elements, such as ice, water and air. Its properties change depending on the ratio and geometrical configuration of such elements. In this study, we constructed snow compaction behavior using Lenard-Jones potential model [4] which is used in molecular dynamics as shown in Eq. (3). The influence range of potential force is limited in order to avoid excessive shrink.

$$U(r) = \begin{cases} 4\epsilon\left[\left(\frac{\sigma}{r}\right)^{12} - \left(\frac{\sigma}{r}\right)^{6}\right] & (0 < r \le r_{eff}) \\ 0 & (r > r_{eff}) \end{cases} \quad (3)$$

### 3-3. Air Drag for Lump of Snow

In this study, surrounding air flow is not calculated and we give air drag as function of velocity to snow particles. Single snow particle and a lump of snow will be mixed while calculation progresses, but their influence of air drag is difference. We assumed air drag only acting on surface particles of a lump, which are extracted by calculating the gradient of the particle number density.

### 3-4. Constraint of Degrees of Freedom of Motion

Snow is expressed as particles in this study. A lump of particles as block shape on the ground cannot be kept initial shape with the gravity because a particle shape is spherical and easy to roll down. But, fallen snow can be kept initial shape. It is because ice shape in actual snow is different from sphere and difficult to roll down. And tangential motion is constrained by surface tension of water or sintering.

Therefore, we constrain tangential and rotational degrees of freedom. Constraint of rotational motion means that Eq. (2) is ignored. Constraint of tangential motion means that friction slider between elements in Fig. 2 is ignored.

## 4. Results and Discussion

At first, we confirmed the effect of snow characteristic model by simulation in which snow particles collide wall. Case 1 does not include snow property, Case 2 include snow property as shown in Table 1. In Case 2, particles aggregate and become lumps by colliding wall in comparison with Case 1. (Fig. 3)

Next, we made experimental apparatus which is half size of an actual snowblower, and the experimental results were compared with simulation results. We evaluated snow velocity at chuter inlet and outlet section by experiment and simulation.

Figure 4 shows comparison of snow velocity at inlet and outlet section. Particle diameter is 5 mm, about 1,800 particles are used for simulation. Calculation condition is shown in Table 1. In Case 1, snow velocity is 9.5 m/s at chuter inlet, 7.5 m/s at outlet. In Case 2, snow velocity is 8.5 m/s at chuter inlet, 4.5 m/s at outlet. Case 2 is closer to the experimental result than Case 1.

Table 1 Calculation condition

| | Case 1 | Case 2 |
|---|---|---|
| | without snow property model | with snow property model |
| ε [J] Depth of potential well | 0 | 0.0001 |
| σ [m] Distance at which potential is zero | 0 | 0.005 |

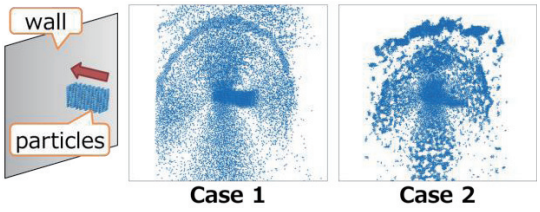


Fig. 3 Effect of property model for snow

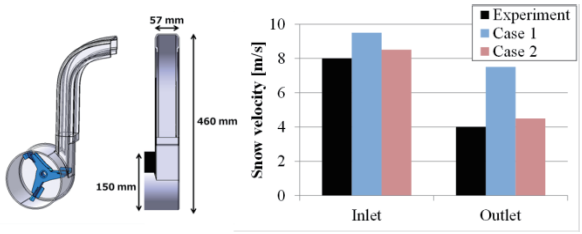


Fig. 4 Experimental and simulation results

## 5. Concluding Remarks

Detailed Snow behavior in relation to snowblower was reproduced by simulation using the DEM. Experiment and simulation results are compared and a qualitatively good correspondence can be obtained by considering snow property model. In the future, we will reproduce a phenomenon which assumes actual snow removal.

### Nomenclature

| | |
|---|---|
| $D$ : particle diameter | [m] |
| $I$ : moment of inertia | [kg · $m^2$] |
| $K$ : elastic coefficient | [N/m] |
| $m$ : particle mass | [kg] |
| $r$ : distance between particles | [m] |
| $r_{eff}$ : threshold for potential force | [m] |
| $U$ : potential energy | [J] |
| $u$ : displacement | [m] |

**Greek letters**

| | |
|---|---|
| $\epsilon$ : depth of potential well | [J] |
| $\eta$ : viscosity coefficient | [Pa · s] |
| $\sigma$ : distance at which potential is zero | [m] |
| $\psi$ : angle of rotation | [rad] |

### References


[1] The Society of Powder Technology, JAPAN ed., *Introduction of powder simulation (in Japanese)*, Sangyo-tosho (1998) 29-82.

[2] Abe, M., Ariga, N., Furukawa, S., *Journal of Snow Engineering 20(5)*, 2004-11-01 (2004) 67-68.

[3] Abe, M., Saito, F., Nishijima, K., *Journal of Snow Engineering 23(4)*, 2007-07-01 (2007) 55-56.

[4] Kotake, S., *Molecular dynamics for thermal fluids (in Japanese)*, Maruzen Company, Limited (1998) 133-134.

Eleventh International Conference on Flow Dynamics
October 8-10, 2014, Sendai, Miyagi, Japan

# Numerical Investigation of Two Interacting Bubbles Behavior in a Megasonic Field

Naoya Ochiai[1] and Jun Ishimoto[1].
[1]Institute of Fluid Science, Tohoku University
2-1-1 Katahira, Aoba-ku, Sendai, 980-8577, Japan

**ABSTRACT**

The clarification of the mechanism of the bubble behavior in a megasonic field is necessary to establish the megasonic cleaning without damage. In the present study, two interacting bubbles in a megasonic field are numerically analyzed using a locally homogeneous model of a gas-liquid two-phase medium to clarify the multiple bubble dynamics. It is confirmed that the direction of the interaction force is dependent on the initial bubble radius. The direction is also dependent on the phase difference, and the reversal of the direction occurs due to the variation of the phase difference.

## 1. Introduction

Megasonic cleaning which uses acoustic wave of higher frequency than 1MHz have been studied [1] for wafer cleaning without damage in semiconductor manufacturing. Cavitation bubble collapse which is induced by a megasonic wave can cause damage to nano devices. Therefore, the clarification of the mechanism of the bubble behavior in a megasonic field is necessary to establish the megasonic cleaning without damage. The authors performed the numerical analysis of the single bubble behavior in a megasonic field [2]. The multiple bubbles dynamics is also important because many bubbles interact in actual megasonic field. In the present study, two interacting bubbles in a megasonic field are numerically analyzed, and the effects of the initial bubble radius and the distance between the bubbles on the interaction between the bubbles are discussed for the first step to clarify the multiple bubble dynamics.

## 2. Numerical Method

A locally homogeneous model of a gas-liquid two-phase medium [3] is used. The governing equations which are the continuity, the momentum, the total energy equations of a compressible two-phase medium, and the continuity equations of the mixture gas and noncondensable gas, are expressed as follows:

$$\frac{\partial \boldsymbol{Q}}{\partial t} + \frac{\partial (\boldsymbol{E}_j - \boldsymbol{E}_{\mathrm{v}j})}{\partial x_j} = \boldsymbol{S} \tag{1}$$

$$\boldsymbol{Q}=\begin{bmatrix} \rho \\ \rho u_i \\ e \\ \rho Y \\ \rho Y D_{\mathrm{a}} \end{bmatrix}, \boldsymbol{E}_j=\begin{bmatrix} \rho u_j \\ \rho u_i u_j + \delta_{ij} p \\ \rho u_j H \\ \rho u_j Y \\ \rho u_j Y D_{\mathrm{a}} \end{bmatrix}, \boldsymbol{E}_{\mathrm{v}j}=\begin{bmatrix} 0 \\ \tau_{ij} \\ -q_j + \tau_{jk} u_k \\ 0 \\ 0 \end{bmatrix}, \tag{2}$$

where $Y$ and $D_{\mathrm{a}}$ are the mass fraction of a gas and the density ratio of noncondensable gas, respectively. The source terms $\boldsymbol{S} = [0 \ -\kappa\sigma_{\mathrm{st}} n_i \ 0 \ \dot{m} \ 0]^t$ where $\dot{m}$ is the evaporation and condensation rate [2].

## 3. Calculation Condition

In the present study, two interacting bubbles in a megasonic field are numerically analyzed. Figure 1 shows the calculation area. The water surface is 1.3 mm above the moving wall. The initial liquid pressure and temperature are 100 kPa and 293.15 K, respectively. The following boundary condition for the velocity component perpendicular to the wall is applied at the moving wall:

$$v = \begin{cases} A_{\mathrm{am}} \sin(2\pi f t), & (t < 2h_{\mathrm{w}}/C) \\ A_{\mathrm{am}} \sin(2\pi f t) & \\ \quad + A_{\mathrm{am}} \sin(2\pi f (t - 2h_{\mathrm{w}}/C)), & (t \geq 2h_{\mathrm{w}}/C) \end{cases} \tag{3}$$

where $A_{\mathrm{am}}$ and $f$ are the velocity amplitude and frequency, respectively. $A_{\mathrm{am}} = 0.02$ m/s and $f = 1$ MHz are used. $h_{\mathrm{w}}$ is the height of the water surface from the moving wall. $C$ is the speed of sound. $\partial u_i/\partial n = 0$, and constant pressure and temperature are applied at the upper boundary. Bubble2 is further than Bubble1 from the vibrating wall. The initial radius and the initial position of Bubble1 are $R_{10}$ and $h_1$ and these of Bubble2 are $R_{20}$ and $h_2$.

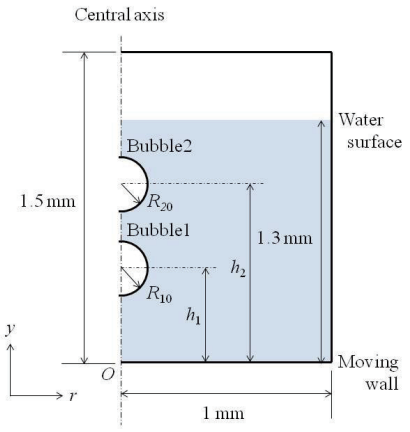


Fig. 1 Calculation area

## 4. Results and Discussion

Figure 2 shows the typical two interacting bubbles behaviors. Figure 2(1) shows the result of the cases of $R_{10} = 2.0$ $\mu$m and $R_{20} = 3.0$ $\mu$m. In the single bubble case, the bubble of $R_0 = 2.0$ $\mu$m moves toward the pressure antinode [2]. It is the upward motion from the initial position of Fig. 2(1). However, in the present case, Bubble1 whose initial radius is 2.0 $\mu$m moves toward the pressure node (downward) due to the repulsive force between Bubble1 and Bubble2 which moves downward. Figure 2(2) shows the result of the cases of $R_{10} = R_{20} = 3.0$

Corresponding author: Naoya Ochiai
*E-mail address*: ochiai@alba.ifs.tohoku.ac.jp

$\mu$m and the bubbles coalesce due to the attractive force between the bubbles. Figure 2(3) shows the result of the cases of $R_{10}$ = 3.4 $\mu$m and $R_{20}$ = 3.0 $\mu$m. The interaction force between the bubbles changes from attractive to repulsive and the variation of the distance between the bubbles is small from $t$ = 34 $\mu$s to $t$ = 50 $\mu$s.

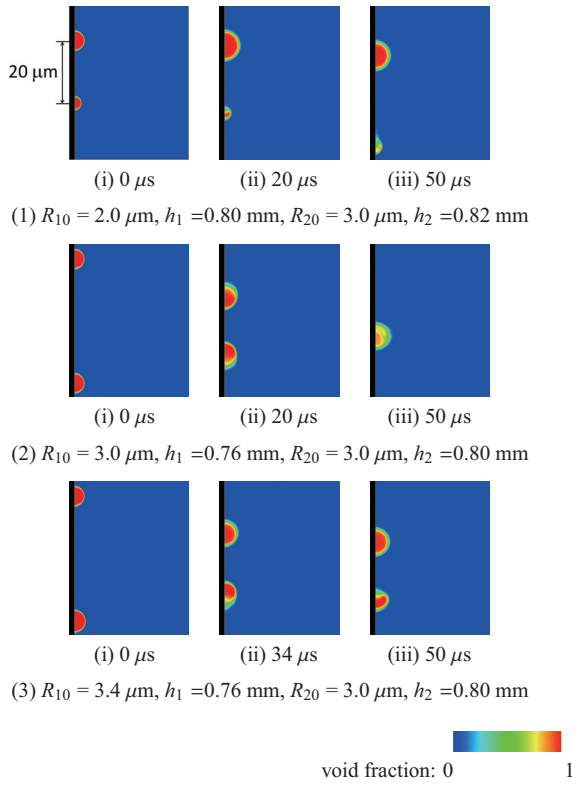


Fig. 2 Time evolution of void fraction distribution.

Figure 3 shows the time histories of the distance between bubbles $l_b$ in the case of several $R_{10}$. And $R_{20}$ = 3.0 $\mu$m, $h_1$ = 0.76 mm and $h_2$ = 0.80 mm are constants. The interaction force and the bubble behavior are found to be largely dependent on the initial bubble radius although the range of $R_{10}$ is small (2.6 $\mu$m $\leq$ $R_{10}$ $\leq$ 5.0 $\mu$m). In the case of $R_{10}$ = 2.6 $\mu$m which is smaller than $R_{20}$, the interaction force changes from attractive to repulsive, and the variation of $l_b$ is small. In the case of $R_{10}$ = $R_{20}$ = 3.0 $\mu$m, the attractive force acts on the bubbles, and the bubbles coalesce at about 27 $\mu$s. In the case of $R_{10}$ = 3.1 $\mu$m which is slightly larger than $R_{20}$, the bubbles coalesce after $l_b$ repeats increase and decrease several times. When $R_{10}$ becomes more larger, $l_b$ keeps repeating increase and decrease ($R_{10}$ = 3.2 $\mu$m) and $l_b$ is almost constant after $l_b$ decreases at a certain value ($R_{10}$ = 3.4 $\mu$m and $R_{10}$ = 5.0 $\mu$m). Figure 4 shows the time histories of radius of Bubble1 and Bubble2 in the case of $R_{10}$ = 3.2 $\mu$m in Fig. 3. The time is 32 $\mu$s $\leq$ $t$ $\leq$ 56 $\mu$s which corresponds to the one cycle of the increase and decrease of $l_b$. Considering the oscillation phase of the two bubbles in Fig. 4, the phase difference is found to decrease when $l_b$ increases (until about 45 $\mu$s). Conversely, the phase difference increases when $l_b$ decreases. The direction of the interaction force is dependent on the phase difference. Therefore, in the present calculation, the reversal of the direction of the interaction force is thought to repeat due to the variation of the phase difference.

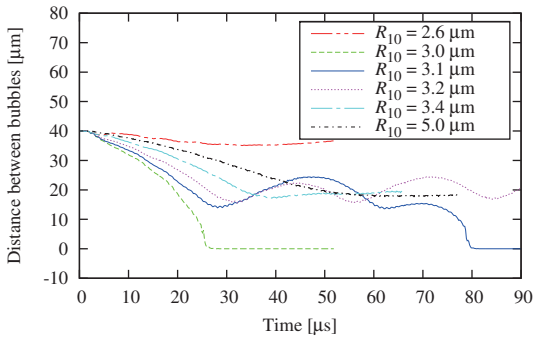


Fig. 3 Time history of distance between bubbles ($R_{20}$ = 3.0 $\mu$m, $h_1$ = 0.76 mm and $h_2$ = 0.80 mm)

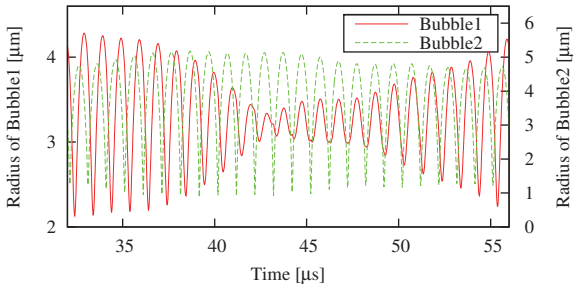


Fig. 4 Time history of bubble radius ($R_{10}$ = 3.2 $\mu$m, $R_{20}$ = 3.0 $\mu$m, $h_1$ = 0.76 mm and $h_2$ = 0.80 mm)

## 5. Conclusions

Two interacting bubbles in a megasonic field are numerically analyzed, and it is confirmed that the direction of the interaction force is dependent on the initial bubble radius. The direction is also dependent on the phase difference, and the reversal of the direction occurs due to the variation of the phase difference.


## Acknowledgements

The part of this work was supported by JSPS Grant-in-Aid for Young Scientists B (26820038) and FRIS Supported Research of Frontier Research Institute for Interdisciplinary Science, Tohoku University.


## References


[1] B.-K. Kang, J.-H. Jeong, M.-S. Kim, H.-S. Sohn, A. A. Busnaina and J.-G. Park, *Solid State Phenomena*, 195 (2013) 169-172.

[2] N. Ochiai and J. Ishimoto, *ECS J. Solid State and Tech.*, 3-1 (2014) N3112-N3117.

[3] N. Ochiai, Y. Iga, M. Nohmi and T. Ikohagi, *J. Fluid Science and Tech.*, 5-3 (2010) 416-431.

# OS4: International Symposium on Smart Layered Materials and Structures for Energy Saving (Joint Symposium)

# Evaluation of Residual Strain in the Structural Materials of Nuclear Power Plants

Tetsuya UCHIMOTO[1], Toshiyuki TAKAGI[1], Zhenmao CHEN[2], Kensuke YOSHIHARA[3] and Gerd Dobmann[4]
[1] Institute of Fluid Science, Tohoku University
Katahira 2-1-1, Aoba-ku, Sendai Miyagi 980-8577, Japan
[2] State Key Laboratory for Strength and Vibration of Mechanical Structures, Xi'an Jiaotong University, China
[3] Nuclear Power Division, The Kansai Electric Power Co., Inc., Japan
[4] Saarland University, Germany

**ABSTRACT**

Residual strain measurements are required for structural integrity evaluation of components in nuclear power plants after seismic loading. In this study, various electromagnetic nondestructive testing methods are applied to estimate small residual strain in austenitic stainless steels and carbon steels that are representative structural materials of nuclear power plants. In view of practical application performance of nondestructive testing methods are evaluated and compared using identical set of specimens with residual strain.

## 1. Introduction

When a large seismic load is exerted on components of a nuclear power plant such as during the Great East Japan Earthquake, it is necessary to evaluate the structural integrity of the components. In Japan, the evaluation of structural integrity following large earthquakes comprises two steps [1]. The first step involves visual and leak testing together with analysis of the response to seismic loads, and critical components are screened. In the second step, additional inspections are made to detect cracks and deformation. Since residual strain more than 10 % may decrease low cycle fatigue strength [2], it should be quantitatively evaluated after the first screening.

In view of the practical application of residual strain measurement in nuclear power plants after seismic loading, the electromagnetic nondestructive methods are extensively investigated in this study. The target materials here are type 304 austenitic stainless steels and carbon steels, which are representative structural materials in nuclear power plants. To compare various techniques, the identical set of tensile test specimens was employed for experiments. Here, we focus on the performance of strain evaluation in the low strain region under 10 %.

## 2. Tensile Test Specimens

Specimens were cut out by machining from plates with thickness of 5 mm for austenitic stainless steels and 4mm for carbon steels. Figure 1 shows the schematic drawing of tensile specimens. Tensile test was carried out using INSTRON5582 and prepared specimens with residual strains ranging from 1 % to 15 %.

## 3. Evaluation of Residual Strain in Austenitic Stainless Steels

Although type-304 austenitic stainless steels are originally paramagnetic, they become magnetic through a strain-induced martensite transformation. Electro-magnetic nondestructive techniques are required to evaluate a small change in permeability for evaluation of small residual strain in type-304 austenitic stainless steels. In this study, various types of eddy-current testing methods and the natural magnetization method were applied[3, 4]. Figure 2 compares results obtained using the two methods. For each method, the as-received specimen is used as reference, and the signals are normalized by that of specimen with 15 % strain.

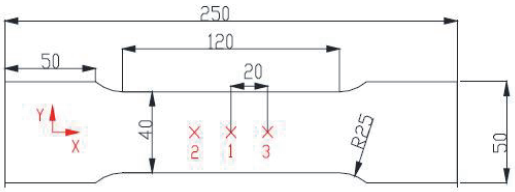


Fig. 1 Schematic drawing of tensile specimens.

### 3.1. Conventional Eddy Current Testing

As a reference, eddy current testing (ECT) was carried out using a simple pancake coil probe with an outer and inner diameter of 5.0 and 2.0 mm, and a height of 3.0 mm. The test frequency is 50 kHz. As shown in Fig. 2, though there is some correlation between EC signals and residual strain, the dispersion is large. In subtracting the initial signals before the tensile tests, the dispersion of the signals decreased, which means the dispersion is due to the variation in initial condition of as-received materials.

### 3.2. TR type ECT

Transmitter-receiver (TR) type probe was applied to residual strain measurement. The parameters of transmitter and receiver coils are identical except numbers of turn; the outer and inner diameters, and the height are 10 mm, 5 mm and 5 mm, respectively. Here, distance between transmitter and receiver coils, and test frequency are systematically investigated. When the coil distance and test frequency are 40 mm and 10 kHz, respectively, quite high correlation was obtained, as shown in Fig. 1. Since larger coil distance with lower frequency gives better correlation, the present probe works like remote field ECT probe.

Corresponding author: Tetsuya Uchimoto
*E-mail address*: uchimoto@ifs.tohoku.ac.jp

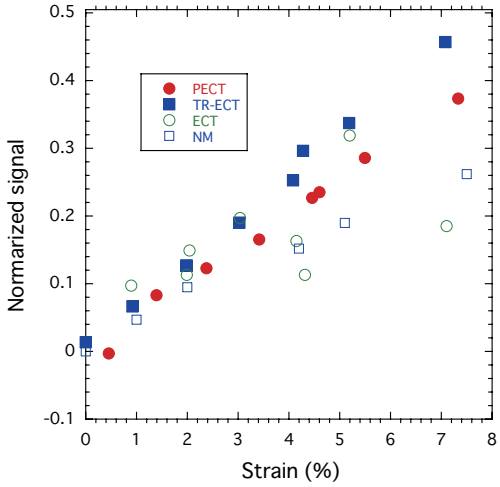


Fig. 2 Results obtained with electromagnetic non-destructive techniques for the evaluation of residual strain in type 304 austenitic stainless steels.

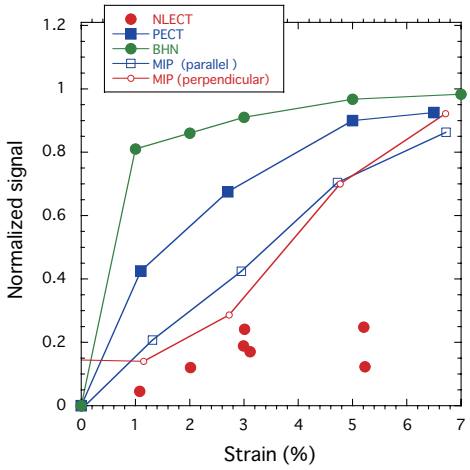


Fig. 3 Results obtained with electromagnetic non-destructive techniques for the evaluation of residual strain in carbon steels.

## 4. Evaluation of Residual Strain in Carbon Steels

Carbon steels JIS SS400 are discussed as a target material. Since the carbon steel is ferromagnetic, magnetic properties are sensitive to structure change due to residual strain. Here, magnetic nondestructive testing methods are applied, such as Barkhausen noise method, magnetic incremental permeability method, and so on. Figure 3 compares results obtained using the two methods. For each method, the as-received specimen is used as reference and the signals are normalized by that of specimen with 16 % strain.

### 4.1. Barkhausen Noise Method

Barkhausen noise (BN) method was applied using the probe consisting of an exciting coil with a magnetic yoke and pickup coil with a ferrite core. Exciting frequency is 1 Hz. The frequency range of BN signals is mainly from 1 kHz to 150 kHz. Two types of featured parameters are compared: the energy of BN signals and the root mean square of signals (RMS). The energy and RMS of BN signals fall rapidly at low level of plastic strain, when plastic strain exceed 2%, the signals decrease slowly till saturation, which imply the signals are affected by the microscopic residual stress on the interface between ferrite and perlite phases. The energy of BN signals gives better results in view of dispersion of signals. BN signals are affected by many factors such as rolling direction of specimens, heat treatment for stress relieve.

### 4.2. Magnetic Incremental Permeability Method

Magnetic incremental permeability (MIP) method measures the incremental permeability $\mu_\Delta = \Delta B / \Delta H$ during the magnetization process. The incremental permeability is equivalent to voltage measured by eddy current testing probe, and evaluated by the eddy current probe in this study. Here, the probe for MIP measurement consists of a magnetic yoke with an exciting coil for magnetization and a pancake coil and a Hall element between the yoke legs. The specimens are magnetized at the frequency of 0.5 Hz and the probe voltage was measured at the test frequency of 50 kHz using an EC instrument. If the probe voltage is plotted as function of tangential magnetic field measured by the Hall element, its waveform shows butterfly shape having two peaks. This waveform includes large amount of information reflecting the magnetic properties. For the simplicity, the peak-to-peak distance, which has a correlation with the coercivity, is plotted as function of residual strain in Fig. 2.

## 4. Summary

In this study, the electromagnetic nondestructive methods are extensively investigated in view of structural integrity evaluation of nuclear power plants. Performance of various methods are compared and evaluated through the experiments using the identical set of tensile test specimens.


## Acknowledgement

This work was partly supported by the JSPS Core-to-Core Program, Advanced Research Networks, “International Research Core on Smart Layered Materials and Structures for Energy Saving”.


## References


[1] *Guidelines for Structural Integrity Assessment for Nuclear Power Components Experienced Earthquake*, JANTI-SANE-G1, JANTI-SANE-G2, Japan Nuclear Safety Institute (2012) (in Japanese).

[2] Y. Takagi, H. Torii, T. Ogawa, J. Komotori, M. Nakane, S. Kanno, M. Itatani, T. Saito, *Journal of JSNDI*, 59 (2010), 267－270 (in Japanese).

[3] S. Xie, Z. Chen, H.E Chen, S. Sato, T. Uchimoto, T. Takagi, and Y. Yoshida, *Int. J. Appl. Electromagn. Mech.* (2014) in press.

[4] H. Li, Z. Chen, Y. Li, T. Takagi, T. Uchimoto, N. Chigusa and Y.Yoshida, *Int. J. Appl. Electromagn. Mech.* 38, (2012) 17-26.

# Assessment of Mechanical Reliability for Development of Electrochemical Devices

Kazuhisa Sato[1], Nacer Azeggagh[2] , Toshiyuki Hashida
[1]Tohoku University, Fracture and Reliability Research Institute
6-6-11-708, Aza-Aoba, Aramaki, Aobaku, Sendai 980-8579, Japan
[2] LaMCoS/MATEIS- INSA Lyon
18-20, rue des Sciences, France

**ABSTRACT**

Deformation and mechanical damage measurements were developed in order to investigate the degradation process of SOFC cell/stack under SOFC operation. In this study, the deformation and mechanical damage test was applied to simulated cell/stack. The observation method determined location of signal and mechanism of the deformation and microcrack in the SOFC. By using this method, it was possible to show the possibility that the detailed deterioration process can be evaluated, visually, and in real-time, even when applied to cell/stack at the actual equipment level.

## 1. Introduction

It is a pre-requiste to ensure the reliability and durability of SOFCs for their realization and commercialization. Especially, mechanical damage is one of the most important issues that may cause a serious damage on the cell and stack [1, 2]. On the other hand, their main component material is mechanically brittle ceramic with low fracture toughness, and they may also contain materials which have the property of expanding or shrinking in oxidizing/reducing conditions. Therefore, under the SOFC operation, not only thermal stresses but also chemically or electrochemically induced expansion or contraction may potentially cause a stress/strain induced fracture. For this reason, the evaluation of the reliability of the SOFC under the operating condition is extremely important. In order to address the above issues, we had previously developed a technique for monitoring the mechanical damage of SOFCs using the acoustic emission (AE) method, and succeeded in observing the fracture process at the single cell level [3]. However, the stack and modules in actual equipment are comprised of single cells with hundreds of layers in a unit, and in order to obtain detailed damage information, many sensors are necessary. The primary objective of the research presented in this paper was to use AE and displacement gauge to determine the location and mechanism of the deformation and microcrack associated with the development of mechanical damage in the SOFC cell/stack. This report describes progress so far in the current research.

## 2. Experimental

The data acquisition system employed in this study is described in our previous report [4]. Figure 1 shows a schematic of the deformation and micro fracture measurement system for electrochemical devices under operations. AE measurement was done using resonant sensor and wideband piezoelectric transducer (NF circuit block or Physical Acoustic Corporation).

Corresponding author: Kazuhisa Sato
*E-mail address*: kazuhisa@rift.mech.tohoku.ac.jp

Electric signals from the transducer were amplified with a handmade amp (variable: 0 dB - 40 dB, multichannel: 1 - several dozen), and then digitized by handmade analyzer.

Analysis and imaging of the obtained data were done by improving information technique, which are one of the techniques for wavelet analysis and location analysis. In order to show the effectiveness of those analyses, the AE method and optical displacement meter were used to measure deformation and fracture of a simple, simulated single cell/stack which occurs when the cell temperature and atmosphere changes.

The arrival times and direction of first motion of waves detected at each transducer were automatically picked. Arrival times could be measured with an accuracy of better than 0.1 $\mu$ sec. The location of the event was determined by assuming a velocity model for the sample and using an iterative method to minimize the travel time error computed for raypaths from the estimated source location to each sensor. Source mechanism was determined by analyzing the first motion of an event detected by all the sensors.AE sensors locations are shown on example schematic Fig. 2. A location system modified to enable control of the temperature and oxygen partial pressure conditions were used to measure the change of AE propagation velocity. Testing temperatures were 300 K - 1023 K.

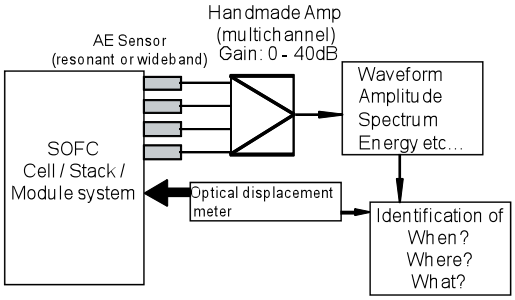


Fig. 1 Schematic layout of the deformation and micro crack evaluation system for electrochemical devices.

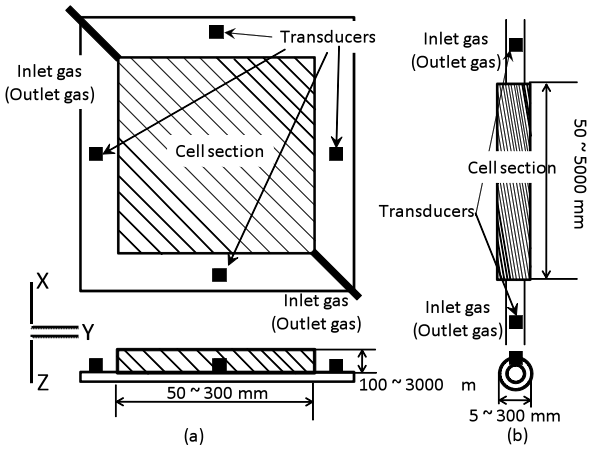


Fig. 2 Schematic image of sample showing the locations of the AE sensors on a simulated SOFC single cell. (a) Plate type, (b) Tube type

## 3. Results

AE signals observed during the tests can be classified into three groups, types A, B, and C. This classification is made on the basis of the difference in frequency and wave shape of the AE signal. This suggests that the type A may correspond to the deformation of the cell/stack and the type B to the friction or delamination in the power collector. The type C is expected to correspond to the mechanical damage in the cell/stack.

The temperature dependences of AE propagation velocity of simulated plate type cell at several temperatures are shown in Fig. 3. The AE propagation velocity gradually decreased from 300 to 1023 K.

Figure 4 shows the Acoustic event locations identification by false signal at 1023K. (a) is the before adjustment for AE propagation velocity, (b) is the after adjustment basis of the Fig.3. These locations could measure to an accuracy of several mm at 300K - 1273K. Thus, it is important to calibrate the velocity as a function of the temperature.

Monitoring AE activity was shown to be useful to detect and laser displacement gauge observations indicated that possibly identify the deformation and damage process of the SOFC cell/stack (Plate type, Tube type).

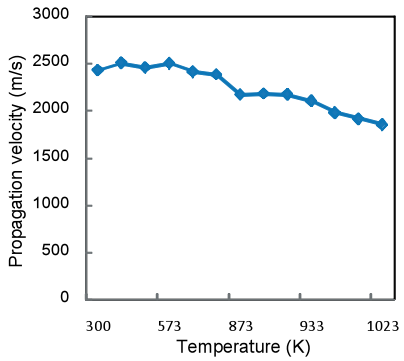


Fig. 3 Temperature dependences of AE propagation velocity of simulated plate type cell measured under atmospheric condition.

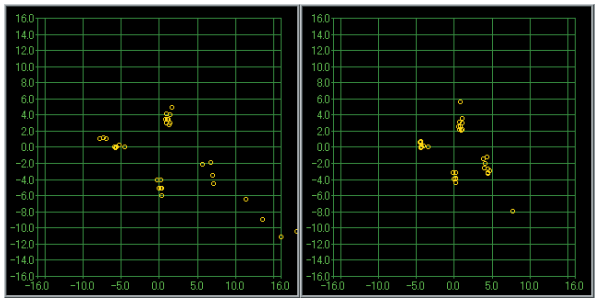

(a) (b)

Fig. 4 Acoustic event locations identification by false signal at 1023K.
(a) before adjustment for AE propagation velocity, (b) after adjustment for AE propagation velocity

## 4. Conclusion

In this research, a technique for automatically classifying and visualizing SOFCs deformation and damage were successfully developed by information technique, which is wavelet analysis and location analysis. AE signals detected in this study could be classified, based on their time lag, frequency, and wave form. It was possible to discuss the correlation between the classified AE signals and the deformation and fracture process confirmed by the optical displacement meter, suggesting the significance of AE monitoring in simulated testing of SOFCs. Also, it was found that the fracture process at each time can be visually observed by indicating the course of the AE signal at each time. By using this method, it was possible to show the possibility that the detailed degradation process can be evaluated, visually, and in real-time, even when applied to modules at the actual equipment level. Future efforts will focus on development of techniques for efficiently processing the huge volume of data, and investigating methods for automatic extraction of the period and features of valid signals, without setting threshold values beforehand.


## Acknowledgments

This work was partly supported by the JSPS Core-to-Core Program, A. Advanced Research Networks, "International research core on smart layered materials and structures for energy saving" and a Grant-in-Aid for Scientific Research A (No. 24686017) from the MEXT.


## References


[1] A. Atkinson, *Solid State Ionics*, 95, 249 (1997).
[2] R. Krishnamurthy and B.W. Sheldon, *Acta Materialia*, 52, 1807 (2004).
[3] T. Kawada, *et al.*, *ECS Transactions*,25(2) 467-472(2009)
[4] K. Sato *et al.*, *Journal of Power Sources*, 195, 5481–5486 (2010)
[5] K. Sato et al., *Journal of Testing and Evaluation*, Volume 34, No.3, 246 (2006).

Eleventh International Conference on Flow Dynamics
October 8-10, 2014, Sendai, Miyagi, Japan

# Impact Force Identification and Damage Monitoring of Laminated Structures

Satoshi Atobe[1], Hisao Fukunaga[1]
[1]Department of Aerospace Engineering, Tohoku University
6-6-01 Aramaki-aza-Aoba Aoba-ku, Sendai, Miyagi, 980-8579, Japan

**ABSTRACT**

This paper examines a method for monitoring impact damages induced in composite pressure vessels. The location and occurrence of the damage are predicted from the impact location and force history which are identified using the strain responses measured with built-in sensors. Here, the impact force is identified by a method based on experimental transfer matrices which relate the impact force to the strain responses. The validity of the method is verified experimentally by monitoring impact damages induced by drop-weight impact tests.

## 1. Introduction

Development of a structural health monitoring system, which is a technique for monitoring damages and assessing the structural integrity in real time using the data from a built-in sensor network, could enhance the safety and maintainability of structures. In the case of composite structures, such as laminated panels and filament wound pressure vessels, damages induced by impact forces are crucial since they significantly degrade the structural stiffness. Thus far, several methods for monitoring damages based on impact force identification has been reported for CFRP laminates [1,2].

In this study, impact force identification and damage monitoring of FRP pressure vessels are discussed. Drop weight impact tests are conducted and the location and force history of the impact are determined from the measured strain responses by an identification method based on experimental transfer matrices. Subsequently, the location and occurrence of the damage are estimated from the identified force to monitor the induced damage.

## 2. Method for Identifying the Impact Force

Figure 1 depicts a FRP pressure vessel subjected to an impact force. The time history of the strain measured with the $i$-th sensor $\{\boldsymbol{\varepsilon}_i\}$ ($i$=1,...,$M$) can be related to the force history $\{\boldsymbol{f}\}$ in the following equation:

$$\{\boldsymbol{\varepsilon}_i\} = [G_i(x_F, y_F)]\{\boldsymbol{f}\}. \tag{1}$$

Here, $[G_i(x_F,y_F)]$ is a transfer matrix whose components are determined experimentally using the measured data obtained from impact tests which are conducted without inducing damages to the structure [1,2]. The experimental transfer matrix is defined by a function of the impact location($x_F$,$y_F$), and is not dependent on the force history.

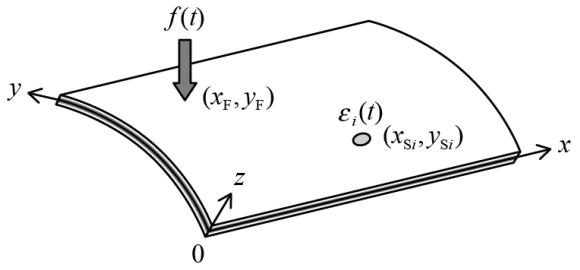


Fig. 1 FRP pressure vessel subjected to impact force.

When the impact location is determined, the force history is identified by minimizing the deviation between the measured strains and the strains estimated from Eq.(1) with the preliminarily-constructed experimental transfer matrices.

$$\min_{\{f\}} \sum_{i=1}^{M} \left\| \{\boldsymbol{\varepsilon}_i\} - [G_i(x_F, y_F)]\{\boldsymbol{f}\} \right\|^2 \tag{2}$$

subject to $f(t) \geq 0$.

In the impact force identification, the impact location is first approximated at an adequate location ($x_e$,$y_e$) and the estimated force history $\{\boldsymbol{f}_e\}$ is calculated at the location by employing Eq.(2). Then, the accurate impact location is obtained from the following minimization problem.

$$\min_{x_F, y_F} \sum_{i=1}^{M} \left\| \{\boldsymbol{\varepsilon}_i\} - [G_i(x_F, y_F)]\{\boldsymbol{f}_e\} \right\|^2 \tag{3}$$

The estimated impact location ($x_e$,$y_e$) is updated with the location obtained from Eq.(3), and the same process is repeated until the impact location converges to a certain location. Lastly, force history identification is performed at the identified location.

## 3. Results and Discussion

The schematic of the experimental apparatus is shown in Fig. 2. The specimen is a FRP pressure vessel (Torey Industries SÉCURE CF TC8515) which consists of an aluminum liner, a carbon FRP layer, a glass FRP layer and a resin layer. The length, outer diameter and thickness of the pressure vessel are 473mm, 173.5mm and 5.5mm, respectively. The impact force is applied with an impulse hammer in the preparatory tests in which the experimental transfer matrices are constructed, while a drop weight impact tester is used for the demonstration of damage monitoring. Four biaxial strain gauges are bonded on the surface of the structure, and the measured strains are used for the impact force identification. The force is also measured in order to construct the transfer matrices and to examine the accuracy of the identification results. The acquired data is sent to a computer to perform the impact force identification and the damage monitoring.

Corresponding author: Satoshi Atobe
*E-mail address*: atobe@ssl.mech.tohoku.ac.jp

The identification region is 80mm×80mm and it is divided into grid areas as shown in Fig. 2. The experimental transfer matrices are constructed for each grid node. Inside each grid area, the transfer matrices are interpolated with shape functions similar to those used in finite element analyses.

Figure 3 shows a result of impact force identification for a drop weight impact test in which damage was not induced. The impact energy was 2J, and the specimen was inspected with a thermographic NDT system (Thermal Wave Imaging Echo Therm) after the test to confirm that no damage was induced. The error of the identified impact location, i.e. the distance from the measured location, was 8.0mm. As can be seen from Fig. 3, the identified force is in good agreement with the measured one, and its shape is similar to a sine pulse when no damage is induced by the impact.

Figure 4 shows an identification result for a case in which impact damage was induced in the structure. The impact energy was 7J, and the error of the identified location was 6.1mm. When damages are induced, a sharp drop and small fluctuations due to the damage occurrence and propagation can be seen in both the measured force and the identified force. The deviation in the magnitude of the force between the measured and the identified is due to the reduction of the structural stiffness which is not considered in the present impact force identification.

Considering the results of impact force identification, the location of the damage can be predicted from the accurately-identified impact location. Seventeen drop weight impact tests, i.e. 10 non-damaged cases and 7 damaged cases, were conducted in total and the average error of the identified location was 5.5mm. As to the judgment of damage occurrence, the peak value of the identified force history is chosen as the criterion. From the measured force histories, it was revealed that the damage is induced when the peak force exceeds 4.2kN. Therefore the occurrence of damage can be judged referring to the peak value of the identified force even though the force is overestimated in the damaged cases. In addition, the shape of force history could be also used to predict the occurrence of damage since it changed remarkably between the non-damaged cases and the damaged cases.

## 4. Conclusions

A method for monitoring damages induced in FRP pressure vessels based on impact force identification has been proposed and its validity has been verified experimentally. The results revealed that the impact force is identified with sufficient accuracy regardless of impact damage. Moreover, damage monitoring has been performed by predicting the location and occurrence of the damage from the location and peak force of the identified impact force.

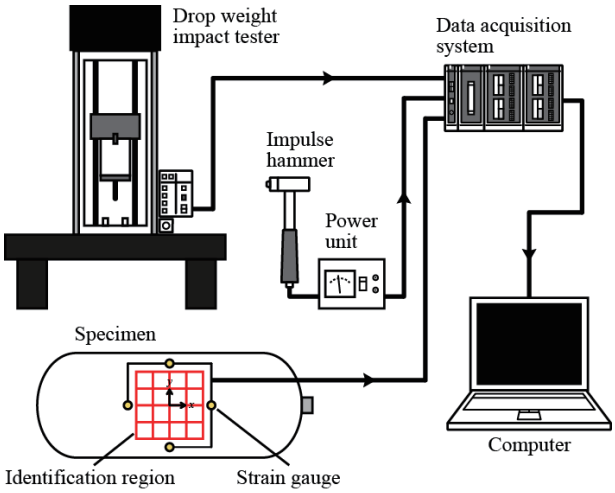


Fig. 2 Experimental apparatus.

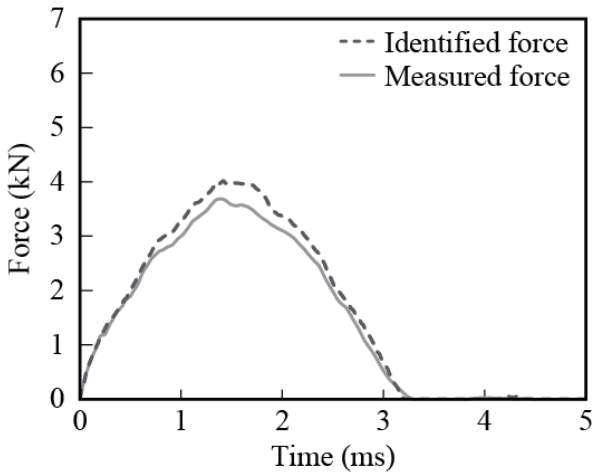


Fig. 3 Identification result of force history (No-damage).

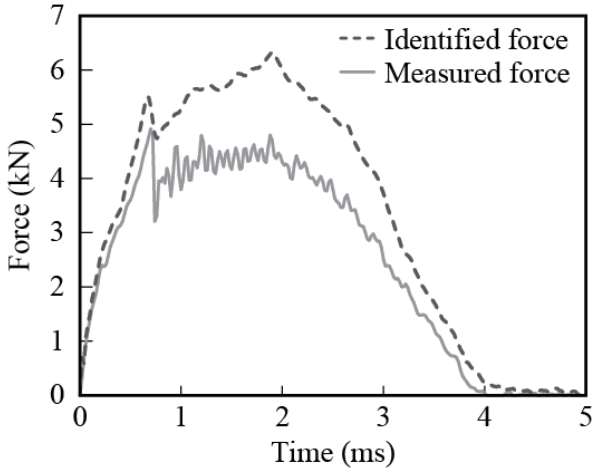


Fig. 4 Identification result of force history (Damaged).

## References

[1] H. Fukunaga, Y. Miura, M. Tajima, N. Hu, *Proc. US-Japan Conf. Compos. Mater. 2008*, (2008), SHM-4.

[2] S. Atobe, H. Fukunaga, N. Hu, *Computers, Materials & Continua*, 26 (2011), 67-90.

# Damage Evaluation of Cu-Alloy Combustion Chamber of Liquid Rocket Using ECT

Mitsuharu Shiwa, Donfeng He, Masao Hayakawa[1], Sinich Moriya, Teiu Kobayashi[2]
[1]National Institute for Materials Science
Sengen 1-2-1, Tsukuba, Japan
[2]Japan Aerospace Exploration Agency
Yoshinodai 3-1-1, Chuo-ku, Sagamihara, Kanagawa, Japan

**ABSTRACT**

The simulated creep fatigue damage in a small scale combustion chamber mockup, which is made of Cu-Cr-Zr alloy, can be detected by multi-frequency ECT technique with AMR probe. Also the low cycle fatigue damage progression such as plastic deformation and crack propagation of copper alloy specimens could be evaluated by using multi-frequency ECT technique with single coil probe.

## 1. Introduction

The combustion chamber of liquid fuel rocket is made of Cu-Cr-Zr copper alloy. Inside of the combustion chamber is the ultra high temperature gas of about 3000 K. Cooling grooves are made in the wall of the combustion chamber and liquid hydrogen (20 K) flow in them for the cooling. Due to the big thermal gradient and cyclic operation testing before the launch, creep fatigue damage occurs in the wall of the combustion chamber. For the recycling and safety checking of the combustion chamber of rocket engine, it is necessary to develop nondestructive techniques to evaluate the damage before and after using.

We have two purposes in the research project using eddy current testing (ECT) method. One is the small crack detection in the combustion chamber; and another is lifetime estimation of copper alloy. We once developed high sensitive AMR (anisotropic magneto resistive) sensor and used it in ECT system [1]. With the single frequency and multi-frequency AMR-based ECT system, we successfully detected EDM notch in plate type specimens [2-4].

In this report, we will illustrate the experimental results of multi-frequency ECT system for small crack detection of combustion cumber mockup and fatigue damage evaluation of copper alloy specimens.

## 2. Crack Detection of Combustion Camber

Figure 1 shows the schematic block diagram of dual frequency ECT system with AMR sensor for the crack detection. AMR sensor of HMC1001 was used. Two lock-in amplifiers and two frequencies were used in this ECT system. For high frequency f2 (20 kHz), the penetration depth is small, surface condition and lift-off information were detected. For low frequency f1 (2 kHz), the penetration depth is big. Both the inside and surface properties of the material can be detected. By subtracting the two output signals, the lift off related noise can be successfully reduced.

A chamber type specimen made of copper alloy was fabricated to simulate the combustion chamber of liquid rocket as shown in Fig. 2. Grooves were made on it to simulate the cooling grooves of the combustion chamber. From the bottom of the grooves, the wall thickness was about 1 mm. 9 EDM notches (artificial slits) with different length and depth were made under the bottom of some grooves to simulate the defects. The width of the notch was about 0.2 mm. The lengths were 2 mm, 5 mm, and 10 mm; and the left thickness of the wall at the positions of the notches were 0.2 mm, 0.4 mm, and 0.6 mm.

All defects were successfully detected. Figure 3 shows the signal amplitudes for the defects with different depths and lengths. For the smallest defect with the depth of 0.2 mm and the length of 2 mm, the signal to noise ratio is bigger than 2. After improvement, the detection limit of defect can be depth of 0.2 mm and length of 1 mm.

Corresponding author: Mitsuharu Shiwa
*E-mail address*: SHIWA.Mitsuharu@nims.go.jp

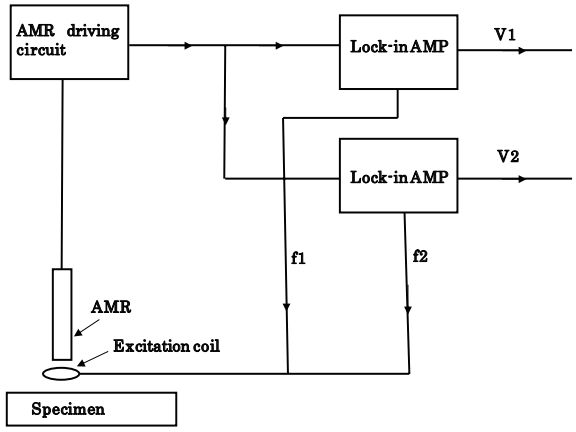


Fig. 1 Schematic ECT block diagram with AMR sensor.

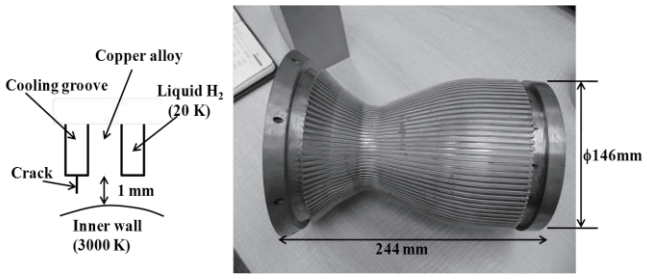


Fig. 2 Chamber type specimen to simulate the combustion chamber of liquid rocket.

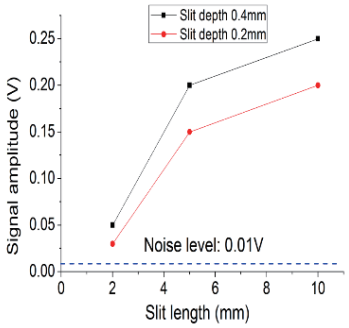


Fig. 3 Scanning results for the slits with the slit depth of 0.4 mm and 0.6 mm.

### 3. Evaluation of Fatigue Damage Progression

Figure 4 shows the schematic block diagram of multi-frequency ECT system with saw-tooth wave excitation. The exciting frequency was 2 kHz. The diameter of probe coil was 7 mm with 50 turns. The maximum fatigue strain from -1.5% to +1.5%. Fig. 5 and 6 shows stress versus cycle number and hysteresis courses of fatigue testing.

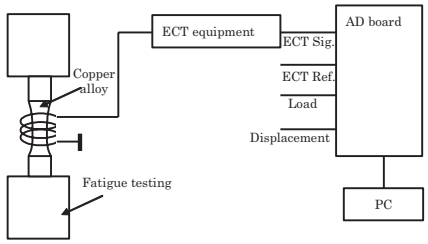


Fig. 4 Schematic ECT block diagram of fatigue testing.

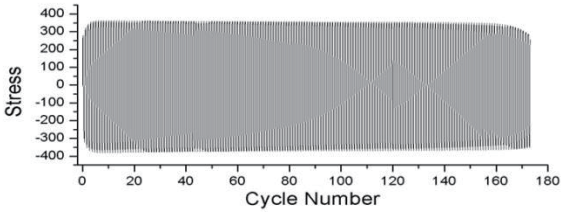


Fig. 5 Stress versus cycle number of fatigue testing.

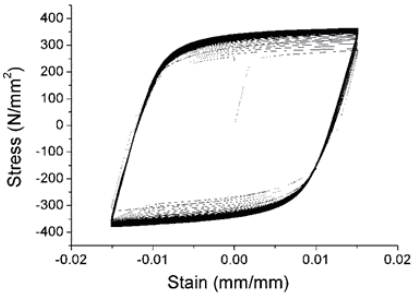


Fig. 6 Hysteresis curves during fatigue testing.

Figure 7 shows the ECT-Y signal during fatigue testing. As the ECT-Y signal had a vibration related to the applied strain, the ECT-Y signal was subtracted from the strain signal as shown in Fig. 7. The subtracted signal had good relationship between hardening from plastic deformation and macro crack propagation phenomena during fatigue testing as shown in Fig. 8 and Fig. 9.

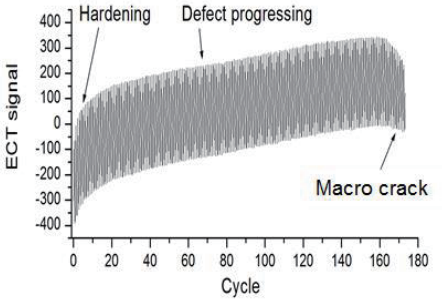


Fig. 7 ECT-Y signal of fatigue testing.

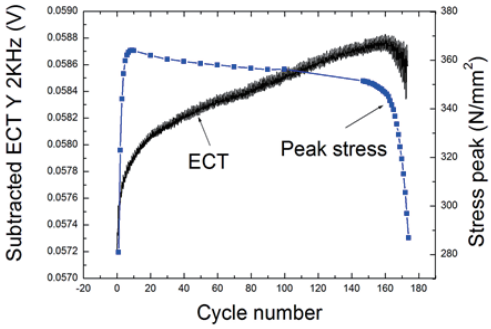


Fig. 8 Subtracted signal and peak stress.

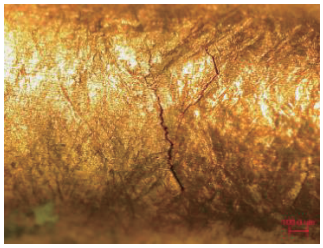

Fig. 9 Macro crack after the fatigue testing.

### 4. Concluding remarks

Using multi-frequency ECT system, we successfully detected a small size notch in the combustion chamber mockup. We also evaluated damage progression during fatigue testing such as hardening from plastic deformation and macro crack propagation at room temperature. We are planning to evaluate residual life prediction during high temperature creep fatigue damage of copper alloy.

### References

[1] D.F. He, M. Tachiki, and H. Itozaki, *Rev. Sci. Instru.*, 80 (2009) 036102.

[2] D.F. He, M. Shiwa, H. Yamawaki, M. Tachiki, H. Itozaki, S. Moriya, T. Masuoka I. Uetake, *Journal of JSNDI*, **59** (2010) 510.

[3] D.F. He, M. Shiwa, J.P.Jia, *NDT & E International*, 44 (2011) 438.

[4] M. Shiwa, D.F. He, H. Yamawaki, L. Xinbao, H. Sunakawa, A. Kurosu, K. Okita, *Electromagnetic Nondestructive Evaluation XV*, (2012) 211.

Eleventh International Conference on Flow Dynamics
October 8-10, 2014, Sendai, Miyagi, Japan

# Physically Based Fatigue Monitoring of Metals

Dietmar Eifler, Marek Smaga, Marcus Klein
Institute of Materials Science and Engineering, University of Kaiserslautern
P.B. 3049, Kaiserslautern, Rhineland-Palatinate, D-67653, Germany

**ABSTRACT**

The fatigue behavior of metals was investigated in the high cycle (HCF) and in the very high cycle fatigue (VHCF) regime. To describe the cyclic deformation behavior load increase tests (LIT) as well as single step tests (SST) were performed with servo hydraulic and ultrasonic test systems and described via process parameters like electrical resistance, specimen temperature, generator power and electromagnetic ultrasonic signals indicating that irreversible changes occur in the microstructure. SEM and TEM investigations were used to identify slip bands and micro cracks.

## 1. Introduction

Reliable fatigue life calculations of metallic materials require a systematic investigation of their cyclic deformation behavior and a comprehensive understanding of the fatigue mechanisms. In general, material response to cyclic loading is characterized by the plastic strain amplitude. Additionally, temperature, electrical resistance magnetic and acoustic measurements were performed for a detailed characterization of the cyclic deformation behavior of steels, cast iron and light metal alloys with particular attention to deformation-induced changes of the microstructure. E. g. the electrical resistance depends on the resistivity, which is strongly influenced by the load- and cycle-dependent defect structure and defect density of each individual material, such as dislocation arrangement and density, pores, micro-cracks and macro-cracks. For the early detection of fatigue in the metastable austenitic steel AISI 347 electromagnetic acoustic transducers (EMAT) were used to describe the cyclic deformation behavior on the basis of time of flight of sound. All results were interpreted by scanning- and transmission-electron-microscopy as well as x-ray. The physically based fatigue life calculation "PHYBAL" [1] requires only one load increase and two single step tests for the calculation of S,$N_f$ -curves in excellent accordance with conventionally determined ones.

## 2. Method

Stress-controlled load increase tests as well as stress and strain controlled constant amplitude tests were carried out with a frequency of 5 Hz on servohydraulic testing systems. Additionally fatigue tests at 20 kHz were realized with an ultrasonic test system. The cyclic deformation behavior was characterized by mechanical hysteresis measurements, changes in the defor-mation-induced temperature $\Delta T$ as well as changes in electrical resistance $\Delta R$ due to changes of the defect structure of the regarded materials. The physical values $\varepsilon_{a,p}$, $\Delta T$ and $\Delta R$ can be equally used for a precise fatigue life calculation on the basis of Morrow and Basquin equations in generalized formulation. In addition electromagnetic nondestructive testing methods using EMAT and a Feritescope® sensor to identify phase transformation, were used to measure strain-stress hysteresis to allow a microstructure-related description of the cyclic deformation behavior of metastable austenitic steels.

Corresponding author: Dietmar Eifler
*E-mail address*: Eifler@mv.uni-kl.de

## 3. Results and Discussion

The "PHYBAL" concept allows reliable fatigue life calculations by using cyclic 'deformation' data of only one load increase test (LIT) and two single step tests (SST). Figure 1 shows a LIT of a quenched and tempered SAE 4140 (42CrMo4). The test started at a stress amplitude of $\sigma_{a,start}$ = 100 MPa with a stepwise increase of $\Delta\sigma_a$ = 20 MPa each $\Delta N = 9 \cdot 10^3$ cycles to estimate the endurance limit. In Fig. 1a), the stress amplitude $\sigma_a$ and the change of the electrical resistance $\Delta R$ are plotted versus the number of cycles N. The transition from linear to exponential slope of the $\Delta R$, N-curve occurs at $\sigma_{a,LIT}$ = 480 MPa and failure at $\sigma_a$ = 680 MPa. The stress amplitude $\sigma_{a,LIT}$ can be used to estimate the endurance limit. In addition two SST were performed at the stress amplitudes 500 and 640 MPa. In Fig. 1b) the cyclic deformation curves of both SST are plotted. The $\Delta R$,N-curves are characterised by continuous cyclic softening until failure what is typical for quenched and tempered steels.

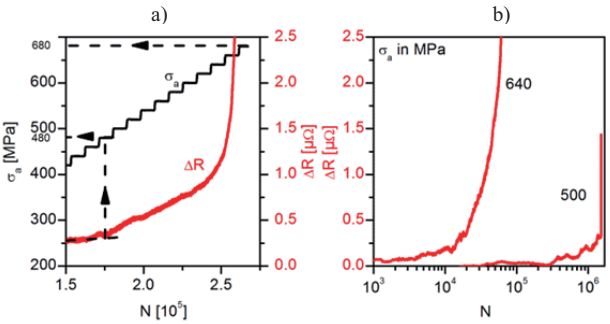


Fig. 1 Development of the electrical resistance in a load increase test (a) and in single step tests (b)

Using a generalised Morrow equation (Eq. 1) it is possible to describe the relation between the stress amplitude $\sigma_a$ and the measured values M(N) = $\varepsilon_{a,p}$ (N), $\Delta T$ (N) or $\Delta R$ (N) values in SST at defined numbers of cycles.

$$\sigma_a = K' \cdot \left(\varepsilon_{a,p}\right)^{n'} \quad \mapsto \quad \sigma_a = a(M) \cdot \left(M\left(N\right)\right)^{b(M)} \qquad (1)$$

Figure 2 shows that the experimentally determined S,$N_f$ -curve based on 23 single step tests (●) and the S,$N_f$ -curves calculated on the basis of the plastic strain amplitude, the change of the temperature and electrical resistance of three experiments agree very good.

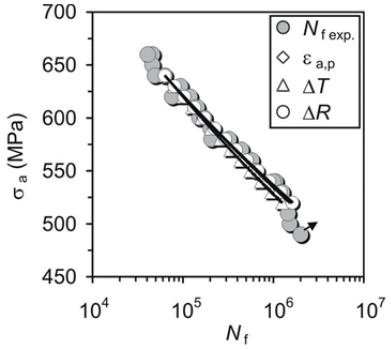


Fig. 2 S,$N_f$ -curves calculated on the basis of $\varepsilon_{a,p}$ (◇), $\Delta T$ ($\Delta$) and $\Delta R$ (○) from one LIT and two SSTs

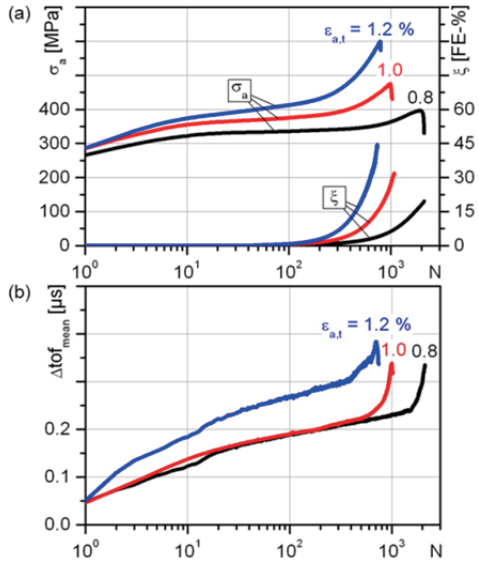


Fig. 3 Stress amplitude $\sigma_a$ and ferromagnetic martensite fraction $\xi$ (a) and change in $\Delta tof_{mean}$ (b)

Figure 3 shows the development of the stress amplitude $\sigma_a$ and ferromagnetic martensite fraction $\xi$ (Fig. 3a) and the change in the mean value of time of flight $\Delta tof_{mean}$ (Fig. 3b) versus the number of cycles N of the metastable austenite AISI 347 (X6CrNiNb1810) in fatigue tests at ambient temperature. The cyclic deformation behavior is predominantly determined by the deformation induced austenite-martensite transformation. After a load dependent number of cycles, the formation of $\alpha'$-martensite starts and increases continuously with increasing number of cycles until specimen failure. The $\sigma_a$, N-curves illustrate the cyclic hardening processes, which lead for $\varepsilon_{a,t}$ = 1.2 % to a maximum stress amplitude in the range of the tensile strength $\sigma_f$ = 569 MPa of the solution-annealed austenite.

Results of single step tests with Ti6Al4V performed at a frequency of 20 kHz are summarized in Figure 4. The multi slope S,$N_f$ -curve can be separated in four ranges according to the concept of Nishijima and Kanazawa [2]. Some specimens reached $10^{10}$ cycles without failure. An important result is the change in the failure mechanisms at the transition from the HCF to the VHCF regime. At stress amplitudes above 645 MPa surface crack initiation was observed, below 645 MPa subsurface cracks dominate.

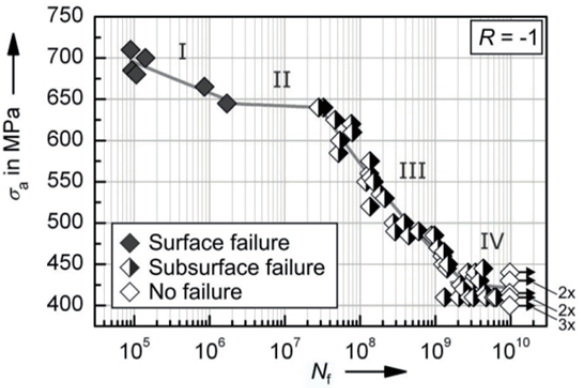


Fig. 4 Multi slope S,$N_f$ -curve for Ti6Al4V

## 4. Concluding Remarks

Plastic strain amplitude, temperature and electrical resistance measurements can be equivalently used for the detailed characterization of the cyclic deformation behavior and a precise fatigue life calculation of metallic materials. All measured physical quantities represent the actual fatigue state. Temperature and resistance measurements are proportional to cyclic plastic deformation corresponding to the deformation work and can be applied also on components. By means of cyclic deformation data of one load increase and two single step tests, S,$N_f$ -curves were calculated in excellent accordance with conventionally determined ones. The physically based fatigue life calculation "PHYBAL" allows an enormous saving of time and costs compared to the common determination of S,$N_f$ -curves. An ultrasonic testing facility was used to perform fatigue experiments with Ti6Al4V in the VHCF regime. The S,$N_f$ -curve indicates a significant decrease of the tolerable stress amplitude if $10^7$ cycles are exceeded and a change in the failure mode from surface to subsurface cracks. At the crack initiation sites inhomogeneities in the α- and β-phase distribution were identified as a possible reason for crack initiation. In SEM investigations fatigue markers like twinning and crack clusters were found also in the volume of run outs at $10^{10}$ cycles.

## References

[1] P. Starke, F. Walther and Eifler: *Int. J. Fatigue* Vol. 28 (2006) 1028-120.
[2] S. Nishijima, K. Kanazawa, *Fatigue Fract. Eng. Mater. Struct.* 22 (1999) 601-607.

Eleventh International Conference on Flow Dynamics
October 8-10, 2014, Sendai, Miyagi, Japan

# Nondestructive Evaluation of Plastic Deformation in Biaxial Specimen using Pulsed ECT Method

Shejuan Xie[1], Zhenmao Chen[1], Toshiyuki Takagi[2], Tetsuya Uchimoto[2], and Kensuke Yoshihara[3]
[1]State Key Laboratory for Strength and Vibration of Mechanical Structures, Xi'an Jiaotong University, Xi'an 710049, China
[2]Institute of Fluid Science, Tohoku University, Aoba-ku, Sendai 980-8577, Japan
[3]The Kansai Electric Power Co., Fukui-ken, 919-1141, Japan

**ABSTRACT**

Plastic deformation, as a type of micro-damage caused by external loads such as earthquake, is necessary to be evaluated using an efficient non-destructive evaluation technique in order to guarantee the structural safety. In this study, the feasibility of pulsed eddy current testing method for evaluating the biaxial plastic deformation in austenitic stainless steel has been studied. Moreover, the optimal coil distance of TR probe for PECT method has also been analyzed.

## 1. Introduction

Plastic deformation is a type of micro-damages in structures arising during manufacturing process, or caused by external loads such as a large-scale earthquake, welding or cold machining etc. [1, 2]. Plastic deformation is a severe threat to the safety of important mechanical structures. Therefore, the quantitative non-destructive evaluation (QNDE) of the plastic deformation in mechanical structures is quite important to assess the early damage and to ensure the structural integrity.

For the ferromagnetic material, magnetic effective methods (e.g. Barkhausen noise method, magnetic incremental permeability method etc.) are studied by researchers [3]. Except this, AISI304 is a typical austenitic stainless steel material widely used in NPPs structures. Concerning the NDT of plastic deformation in nonmagnetic stainless steel, pulsed eddy current testing (PECT) method has been validated as an efficient way for the uniaxial specimen [4, 5]. For the specimen with biaxial plastic deformation, the efficient NDT method has not been reported.

Based on the backgrounds above, the feasibility of QNDE for biaxial plastic deformation in stainless steel using PECT method is investigated in this study.

## 2. Investigation of Coil Distance (TR Probe) for Residual Strain Evaluation using PECT Method

In this section, austenitic stainless steel 304 specimens with various residual strains are employed for the investigation of coil distance (TR probe) using PECT method. The schematic of TR probe on the specimen is shown in Fig. 1. The pulsed excitation current is applied to the excitation coil where the magnitude is 1.7A, the period is 0.01s and the duty is set as 50%.

The distance of TR coil is set as 10, 20, 30, 40, 50, 60, 70, 80mm respectively for investigation of the optimal distance. Figure 2 shows the rate of change of signal of 5% strain specimen compared to 0% strain specimen for various coil distance. From the above result, we can see that the coil distance of 40mm and 50mm can give better evaluation effect for plastic deformation.

Corresponding author: Shejuan Xie
*E-mail address*: xiesj2014@mail.xjtu.edu.cn

## 3. Feasibility Investigation of NDE for Plastic Deformation in Biaxial Specimen

To investigate the feasibility of NDE for plastic deformation in biaxial specimen using PECT method, the biaxial specimens of AISI304 with various residual strains are fabricated. Figure 3 shows the figure of biaxial specimen. Six samples are prepared, and the residual strain for each sample is: No1: the original state; No2: X direction (1.06%) and Y direction (0.96%); No3: X direction (1.60%) and Y direction (1.64%); No4: X direction (2.96%) and Y direction (2.62%); No5: X direction (3.82%) and Y direction (3.80%); No6: X direction (4.00%) and Y direction (4.00%). The thickness is 2.875 mm, 2.850 mm, 2.845 mm, 2.770 mm, 2.760 mm, 2.755 mm, respectively.

Due to the small area of the center part of the biaxial specimen, the coil distance of TR probe is set as 40mm to decrease the slit effect for the evaluation. TR probe is put in four different ways which are along X direction (shown in Fig. 4), along Y direction, along 45 degree direction and along -45 degree direction respectively.

Figure 5 gives the PECT signals for biaxial specimen of four inspection ways, from where we can see that all the four inspection ways can give similar promising evaluation results. The PECT signal is monotonically increasing with residual strain which is smaller than 5%. This can tell that it is feasible for plastic deformation evaluation in biaxial specimen using PECT method with help of TR probe.

In addition, the comparison of the evaluation effect for the uniaxial specimen and biaxial specimen has also been carried out and the result is shown in Fig. 6. It shows that the inspection sensitivity of TR probe for biaxial plastic deformation is similar with the uniaxial ones, therefore we can deduce that the developed methods for uniaxial residual strain are also promising for the application to biaxial ones.

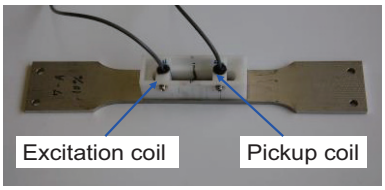


Fig. 1 The schematic of TR probe on the specimen

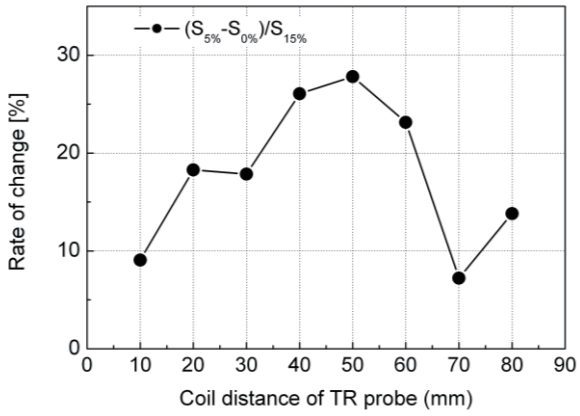


Fig. 2 Rate of change of signal of 5% strain specimen compared to 0% strain specimen for various coil distance

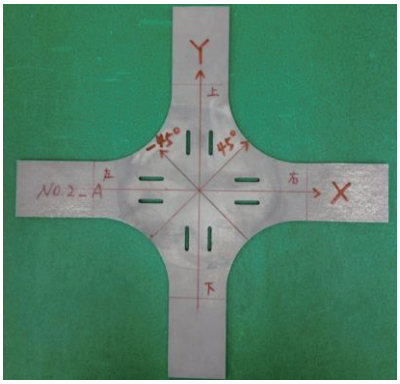

Fig. 3 Biaxial specimen of SUS304

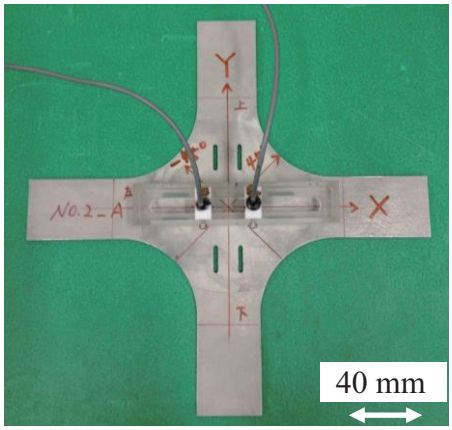


Fig. 4 TR probe put along X direction

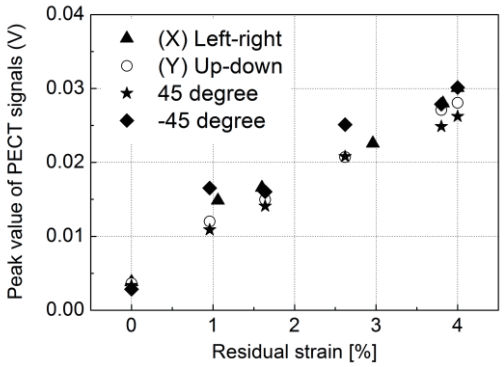


Fig. 5 PECT signals for biaxial specimen of four inspection ways

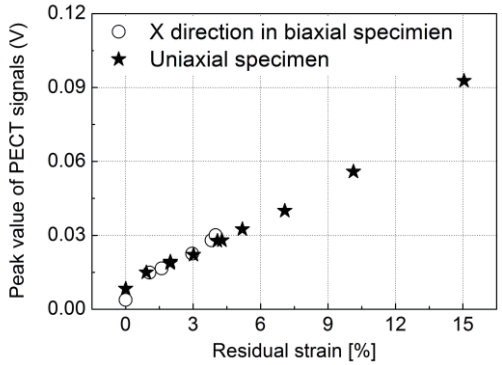


Fig. 6 Comparison of the evaluation effect for the uniaxial and biaxial specimen

**References**

[1] F. D. Backer, V. Schoss, G. Maussner, *Nuclear Engineering and Design*, 206 (2001) 201–219.

[2] R. Andreescu, B. Spellman, E.P. Furlani, *International Journal of Applied Electromagnetics and Mechanics*, 32 (2010) 183–193.

[3] G. Dobmann, *Electromagnetic Nondestructive Evaluation (XI)*, IOS press, (2008) 18–25.

[4] G. Y. Tian and A. Sophian, *NDT & E International*, 38 (2005) 77–82.

[5] S. Xie, Z. Chen, H. Chen, S. Sato, T. Uchimoto, T. Takagi and Y. Yoshida, *International Journal of Applied Electromagnetics and Mechanics*, 45 (2014) 755–761.

**Acknowledgements**

This work is supported by the JSPS core to core program, “International research core on smart layered materials and structures for energy saving”. The authors would also like to thank the National Magnetic Confinement Fusion Program of China (No. 2013GB113005), the Natural Science Foundation of China (No. 51277139, 11321062, 11342014) and the National Basic Research Program of China (No. 2011CB610303) for funding this study.

# Development of Guided Wave Testing System Using Electromagnetic Acoustic Transducer Array

Akinori Furusawa[1], Atsushi Morikawa[1], Fumio Kojima[1]
[1]Department of Systems Science, Graduate School of System and Informatics, Kobe University
1-1 Rokkodai-cho, Nada-ku, Kobe-shi, Hyogo Pref., 657-0013, Japan

**ABSTRACT**

This paper demonstrates the way to develop the ultrasonic guided wave testing system using electromagnetic acoustic transducer (EMAT) for inner corrosion of pipe and the applicability of the system. First, three dimensional guided wave simulator in cylindrical coordinate is developed to calculate the guided wave propagation in steel pipe. Second, guided wave testing system is developed. EMATs array are used for the guided wave transmitter and receiver and each EMAT is arranged in circumferential direction at regular intervals. Finally, simulation and experimental results are discussed.

## 1. Introduction

Guided wave is a kind of ultrasonic which is able to propagate long distance along longitudinal direction of the pipe or plate like structure. By the virtue of characteristic above, ultrasonic guided wave is said to have the great potential of rapid, long range, and safety non-destructive testing. In recent years, as the number of aged nuclear power plants increases, guided wave testing becomes more important.

Conventional guided wave testing system is classified into two categories: ones using piezoelectric transducer and ones using magnetostrictive sensor (MsS) [1]. Piezoelectric transducer needs a kind of gel to help ultrasonic penetrate the medium. These gels are so weak against for heat that the systems are not used in high temperature environment or for heated objects. On the other hand, MsS does not need the gel to be tolerant of heat however, it has less controllability because of the characteristic that its excitation power is worked uniformly in circumferential direction.

Electromagnetic Acoustic Transducer (EMAT) is a transducer for non-contact ultrasonic excitation and reception, which does not need couplant to be heat-tolerant. Each EMAT can be actuated individually to have controllability equivalent to piezoelectric transducers. In addition to that, EMAT is simple mechanism, durable, and inexpensive. Therefore, EMAT guided wave testing system has many advantages compared to conventional testing systems.

In this paper, we demonstrate that the EMAT guided wave testing system is applicable for pipe evaluation. First of all, we reviewed conventional transducers for guided wave testing systems and the advantage of EMAT. In the next section, numerical scheme for guided wave propagation in straight pipe and EMAT guided wave testing system are delivered. Finally, the applicability is shown numerically and experimentally.

## 2. Numerical Scheme and Models for EMAT Guided Wave Testing System

We modeled the EMAT guided wave testing system as shown in Fig. 1. Straight steel pipe with a inner corrosion and EMAT arrays for transmitter and receiver are considered.

Corresponding author: Akinori Furusawa
*E-mail address*: akinori.furusawa@kojimalab.com

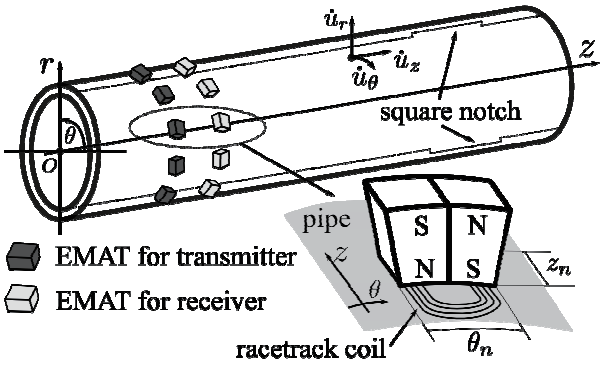


Fig. 1 The Guided wave testing model: coordinate setting, the layout method and the design of EMAT and shape of the corrosion for simulation and laboratory experiment.

Guided wave propagation is calculated by solving Newton's equation of motion and Hooke's Low in cylindrical coordinates:

$$\rho\frac{\partial}{\partial t}\dot{\mathbf{U}}=\begin{bmatrix}\frac{1}{r}+\frac{\partial}{\partial r} & -\frac{1}{r} & 0 & 0 & \frac{\partial}{\partial z} & \frac{1}{r}\frac{\partial}{\partial\theta}\\ 0 & \frac{1}{r}\frac{\partial}{\partial\theta} & 0 & \frac{\partial}{\partial z} & 0 & \frac{2}{r}+\frac{\partial}{\partial r}\\ 0 & 0 & \frac{\partial}{\partial z} & \frac{1}{r}\frac{\partial}{\partial\theta} & \frac{1}{r}+\frac{\partial}{\partial r} & 0\end{bmatrix}\mathbf{T}+\mathbf{F} \quad , (1)$$

$$\frac{\partial}{\partial t}\mathbf{T}=[c]\begin{bmatrix}\frac{\partial}{\partial r} & \frac{1}{r} & 0 & 0 & \frac{\partial}{\partial z} & \frac{1}{r}\frac{\partial}{\partial\theta}\\ 0 & \frac{1}{r}\frac{\partial}{\partial\theta} & 0 & \frac{\partial}{\partial z} & 0 & \frac{\partial}{\partial r}-\frac{1}{r}\\ 0 & 0 & \frac{\partial}{\partial z} & \frac{1}{r}\frac{\partial}{\partial\theta} & \frac{\partial}{\partial r} & 0\end{bmatrix}^T\dot{\mathbf{U}}, \quad (2)$$

where $\dot{\mathbf{U}}$, $\mathbf{T}$, $[c]$, and $\rho$, are particle velocity vector, stress vector, stiffness tensor, and density respectively. Free boundary condition is given as follows:

$$\mathbf{T}\cdot\mathbf{n}=\mathbf{0}, \quad (3)$$

where $\mathbf{n}$ is normal vector to each surface. In this study, we discretize eq. (1) – eq. (3) with Finite Difference Time Domain (FDTD) Method[1] because of its easiness of implementation, low computational cost, and high accuracy.

Wave excitation force of typical EMAT is numerically and experimentally investigated in our previous work [2]. The work shows that the excitation force of EMAT

shown in Fig.1 acts only in tangential direction of the medium when it is ferromagnetic and permanent magnets are coupled to give tangential bias field. The Schematic illustration is shown in Fig. 2. In this case, Lorentz force and magnetization force cancel each other out to become totally almost zero.

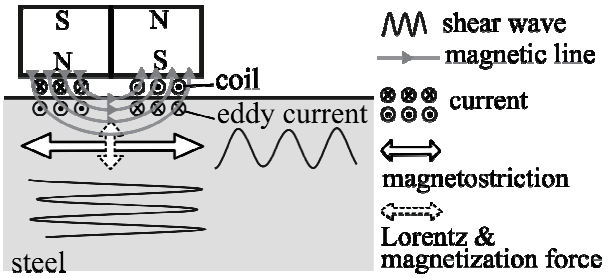


Fig. 2 The basic principle of EMAT and direction of the excitation force.

Therefore, we modeled the excitation force of the EMAT as follows:

$$\mathbf{F}(t)=\begin{cases}[0 \quad W(t)\cdot\sin(2\pi ft) \quad 0]^{\mathrm{T}} & \left(r=r_{\mathrm{out}},-\frac{\theta_n}{2}<\theta<\frac{\theta_n}{2},-\frac{z_n}{2}<z<\frac{z_n}{2}\right)\\ \mathbf{0} & (\text{others})\end{cases},(4)$$

where $f$ , $r_{\mathrm{out}}$ , $\theta_n$ , $z_n$ are exciting frequency, outer surface of the pipe, coordinate values of EMAT respectively. The index $n$ means nth EMAT. $W(t)$ is a window function. Received signals are modeled as circumferential component of the particle velocity $u_\theta$ at receiving points.

### 3. Experimental Setup for EMAT Guided Wave Testing System, the Results and Discussion.

EMAT guided wave testing system is comprised as shown in Fig. 3. Eight EMATs are used for transmitter and receiver, arranged in circumferential direction in regular interval. EMAT array for transmitter are series connected and for receiver are parallel connected to enhance the signal intensity[3]. Key parameters for the simulation and the experiment are listed in Table 1.

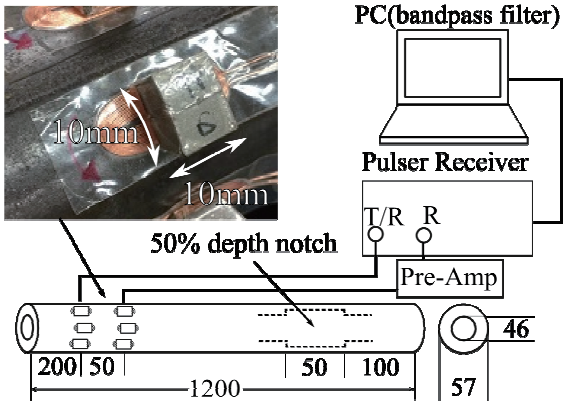


Fig. 3 Schematic illustration of EMAT guided wave system and the dimensions.

Simulation and experimental results are shown in Fig. 4. Solid line and dashed line are simulation and experimental results, respectively.

Table 1. List of key parameters for the simulation and laboratory experiment.

| | |
|---|---|
| excitation frequency | 100[kHz] |
| voltage | 300[V] |
| turns of the trans. coil | 15 |
| turns of the rec. coil | 30 |
| magnet type | samarium-cobalt |
| pipe medium | SS400 (steel) |
| mesh size (simulation) | dr=dz=1[mm], dθ =0.0327 [rad.] |

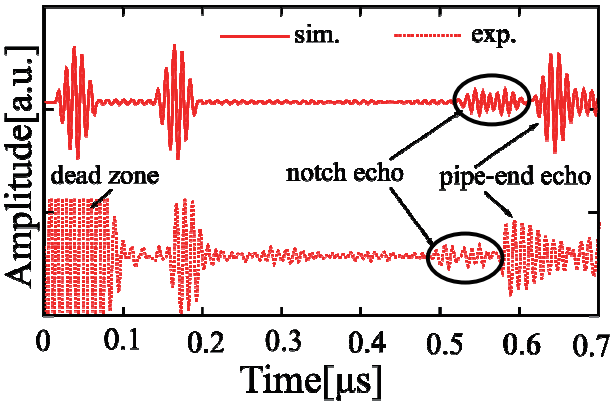


Fig. 4 Comparison of the simulation result and laboratory experiment result: solid line is the simulation result and dashed line is experimental. Each result is normalized to ease profile comparison.

These results are good agreements in time of flight and signal profile. The Circled signals in Fig. 4 are reflect signals from the front and back edge of the inner notch. In this paper, we demonstrate the followings:

1) Numerical scheme for EMAT guided wave testing system and its availability.
2) EMAT guided wave testing system is applicable to nondestructive evaluation of the pipe.

Future work is to develop multichannel control system realize multimode excitation using EMAT array.

**Acknowledgement**

This work was partly supported by the JSPS Core-to-Core Program, A. Advanced Research Networks," International research core on smart layered materials and structures for energy saving" .

**References**

[1]Yanna H. and Masahiro S., *SIMULATION*, JSST, vol.20, no.2, (2001), 162-170.

[2] F. Kojima and T. Ito, *Studies in Applied Electromagnetics and Mechanics*, IOS Press, (2014) (to be submitted)

[3]R. Murayama, K. Imai, and N. Sonoda, *The 22nd MAGDA Conference*,(2013), 385-390.

# Cavitation Induced Damage: FEM Inverse Modeling of the Flow Aggressiveness

Samir Chandra Roy[1], Marc Fivel[1], Jean-Pierre Franc[2], Christian Pellone[2]
[1]Univ. Grenoble Alpes / CNRS, SIMaP-GPM2, F-38000 Grenoble, France
[2]Univ. Grenoble Alpes / CNRS, LEGI, F-38000 Grenoble, France

**ABSTRACT**

An inverse method is proposed to identify the pressure fields that could generate individual pits as observed experimentally in eroded samples made of three different materials. Assuming each pit was generated by a single bubble collapse, the pressure load is defined by two parameters, the peak pressure and its radial extent. An inverse method based on finite element modeling is proposed. The method gives access to the load distributions relevant to the aggressiveness of the cavitation test which is found to be consistent with the three materials responses.

## 1. Introduction

In order to predict erosion damage, it is essential to know the loading conditions generated by the bubble collapses. However, the determination of the loading conditions due to bubble collapses remains a major issue in cavitating flows. The pressure pulses may be directly measured experimentally inside the cavitation facilities for example by using pressure transducers flush mounted in the region of the bubble collapses [1-3]. However this method gives the impact loads in Newtons but the determination of the pressure field in term of stress amplitude (in MPa) is difficult because the loaded surface area is unknown and usually much smaller than the transducer sensitive surface.

Alternatively, CFD simulations could be used but generally these simulations assume that the impacted materials is a rigid surface which is a strong assumption leading to overestimations of the applied pressure.

In order to overcome these measurement difficulties, another option may be used based on an inverse modeling approach. The idea is that each pit is the signature of a single bubble collapse. Then, it can reasonably be expected that the loading conditions be derived from the geometry of the pit and the material properties.

In the present work, such a technique is proposed for deriving the loading conditions from pitting tests conducted during the incubation period. It is based on FEM (Finite Element Method) computations of the response of the material to a representative pressure pulse. An inverse procedure is then proposed to derive the distribution of the pressure profiles from the depth and diameter of pits observed experimentally.

## 2. Method

### 2.1 Material characterization

Prior to any simulation, the material behavior needs to be identified. This has been done using spherical nanoindentation tests performed on three tested materials: an Aluminum alloy Al 7075 (Al), a stainless steel A2205 (SS) and a Bronze (NAB). Using Tabor's equation, the tensile equivalent loading curves have been identified as the dashed curves plotted in Fig.1.

Corresponding author: Marc Fivel
*E-mail address*: Marc.Fivel@simap.grenoble-inp.fr

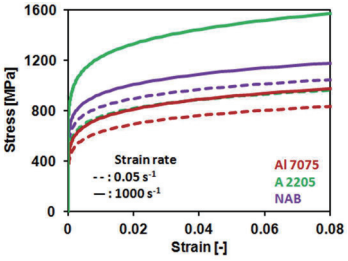


Fig. 1 Material characterization using nanoindentation data and Johnson-Cook extrapolations to high strain rate.

Since a bubble collapse takes place in a very short period of time (typically less than one microsecond), the stress-strain curve has been corrected in order to account for high strain rates. The stress is modified using the Johnson Cook model

$$\sigma_0(\dot{\varepsilon}) = \sigma_0\left(1 + C\ln\frac{\dot{\varepsilon}}{\dot{\varepsilon}_0}\right)$$

for which parameter C has been taken from literature (Al: C=0.017 ; SS: C=0.011; NAB: C=0.06). The strain rate effect on the stress-strain curve is shown in Fig.1.

### 2.1 Cavitation erosion data

Cavitation erosion tests have been performed on the same three materials using the device described in details in [4]. Pits produced at upstream pressure of 10 and 40 bars for exposure times up to 15 minutes have been considered for the current analysis. Sample surfaces after pitting test have been analyzed using a conventional contact profilometer with microprobe of radius 2 µm.

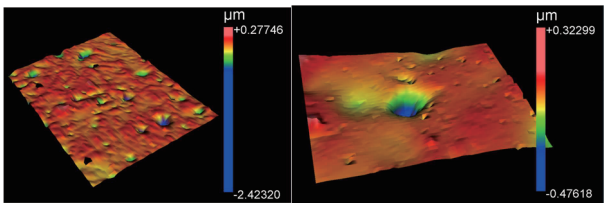


Fig. 2 Typical eroded surface of Al sample. (a) 2x3mm scan of the surface with multiple impacts (b) zoom on a 10x10µm zone surrounding a typical pit.

For each material, image analysis of the measures gave 200 characterizations of isolated pits as the one shown in Fig.2b. Each pit is characterized by its diameter and depth.

### 2.2 Finite Element Modeling

For sake of simplicity, the modeling is restricted to a 2D axisymmetric investigation. The applied load consists of a pressure distribution with a Gaussian shape applied on the top surface defined by the hydrodynamic pressure $\sigma_H$ and its extent radius $r_H$.

$$\sigma = \sigma_H \exp\left(-\left(\frac{r}{r_H}\right)^2\right)$$

The mesh is locally refined in the vicinity of the maximum loaded zone. Finite Element simulations are conducted using software ABAQUS© and 8100 CAX4R elements surrounded by a layer of CINAX4 infinite elements in the bottom-right sides of the simulation cell.

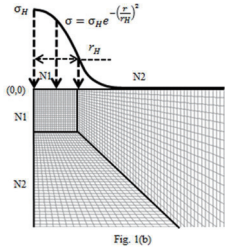


Fig. 3 Typical FEM mesh used in the simulations (N1=20 N2=30 elements). The figure only shows a magnified view of the loaded zone.

The material behavior is taken as elastic-plastic with the reference curves defined at the strain rate of $1000s^{-1}$ (continuous curves in Fig.1).

### 3. Results and Discussion

An inverse method is conducted in a view to find the best set of parameters ($\sigma_H$,$r_H$) that generates a given experimental pit profile. Results are reported in Fig.4. As expected the higher upstream pressure leads to higher hydrodynamic stresses.

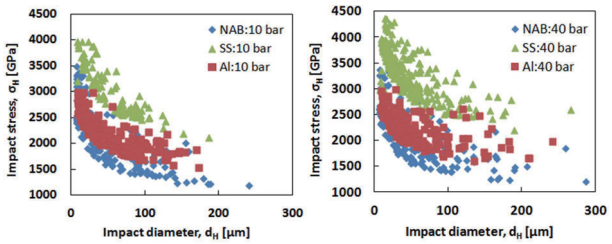


Fig. 4 Results of the inverse method for the two test conditions (10 and 40 bars).

In order to quantify the flow aggressiveness, we chose to plot the number of impacts per area and per unit of time. It appears that the points calculated from the three materials do not fall on a given master curve. This indicates that such a plot is not relevant of the flow characteristics. One way to solve this problem is to plot the impact frequency for a given range of $r_H$ or $\sigma_H$. This better addresses the bubble distribution in term of pressures and sizes. This has been done in Fig.5 where the impact frequency is now plotted as a function of the impact stress $\sigma_H$, but for a given range of applied pressure radius $r_H$. One can clearly see that the three materials get aligned on a given unique curve.

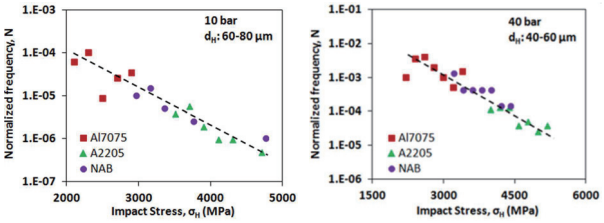


Fig. 5 Impact frequency as a function of the pressure stress $\sigma_H$ for a given range of pressure extent $r_H=d_H/2$.

Figure 6 gives the 2D distribution of the impact frequency.

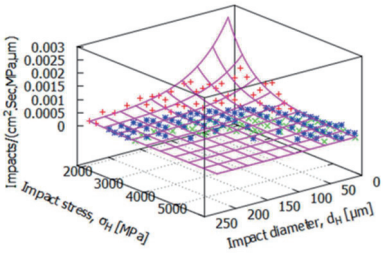


Fig. 6 2D distribution of impact frequency. Data obtained for the upstream pressure of 40bars.

A 3D fit of the surface passing through all the data points give the following analytical expression of the frequency of impacts in function of $\sigma_H$ and $d_H$.

$$N = N^* \exp\left(-\left(\frac{\sigma_H}{\sigma_H^*}\right)\right)\exp\left(-\left(\frac{d_H}{d_H^*}\right)\right)$$

This expression is the signature of the flow aggressiveness.

### 4. Concluding Remarks

The inverse FEM approach presented here gives an analytical expression of the impact frequency for a given cavitation condition. This expression is material independent and quantifies the flow aggressiveness. Since each material reacts differently to a pressure pulse, they filter the impacts left at the surface so that the material can be viewed as a sensor of the cavitation conditions.

### References


[1] Franc, J.-P., M. Riondet, A. Karimi and G. L. Chahine, *Journal of Fluids Engineering* 133(12) (2011) 121301-121308.

[2] Hattori, S., H. Mori and T. Okada, *Journal of Fluids Engineering* 120(1) (1998) 179-185.

[3] Soyama, H., A. Lichtarowicz, T. Momma and E. J. Williams, *Journal of Fluids Engineering* 120(4) (1998) 712-718.

[4] J.-P. Franc, *Journal of Fluids Engineering* 131(2) (2009) 021303.

# Development of Ultra High Molecular Weight Polyethylene Coatings by Cold Spray

Kesavan Ravi[1], Kazuhiro Ogawa[1], J Y Cavaille[2], Tiana Deplancke[2]
[1]Tohoku University,
6-6-01, Aoba, Aramaki, Aoba-ku, Sendai 980-8579, Japan
[2]Université de Lyon
CNRS, INSA-Lyon, MATEIS, UMR5510, F-69621, Villeurbanne, France

**ABSTRACT**

The cold spray deposition of ultra high molecular weight polyethylene (UHMWPE) powder was attempted on two different substrates polypropylene (PP), aluminum (Al). UHMWPE particles were mixed with fumed nano alumina. Deposition occurred readily on to polypropylene substrates at 170$^0$C gas temperature and on to Al and $Al_2O_3$ at 350$^0$C gas temperature. Deposits were formed at temperatures substantially below the melting point of the polymer. Melting of the polymer particles did not occur. Porosities in the coatings were observed.

## 1. Introduction

The process known as cold spraying (CS) was developed in the 1980s by Dr. Papyrin and co-workers and involves the impact of metallic particles on to a target at very high speeds (500 to 1500 m/s) to form coatings or solid components [1]. The accelerating gas may be heated, mainly to achieve higher particle velocities. Fig.1 represents a schematic diagram of a cold spray system where the powder particles are accelerated to supersonic velocities through a De Laval nozzle and deposited onto a suitable substrate material.

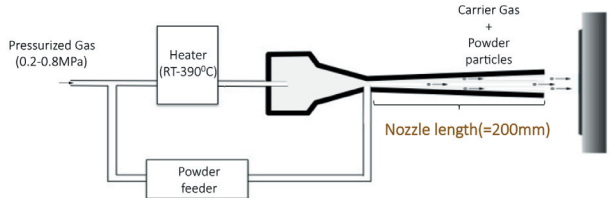


Fig.1 Schematic of a cold spray apparatus.

Main idea behind this research work is the development of Ultra high molecular weight polyethylene coatings with functional properties like wear resistance, impact resistance and cavitation erosion resistance.

## 2. Experimental

UHMWPE powder was hand mixed with 3.8% (by weight) fumed nano alumina particles before the cold spray. The powder mixture was deposited on each of the substrates using low-pressure cold spray technique. Pressurized gas (air) from 0.2MPa to 0.8MPa was supplied from a compressor, which meets the powder particles at the nozzle region. The gas temperature was varied from room temperature to 500$^0$C. The powder particles were then fed through a vibrated powder feeder at a steady controllable rate. The air stream containing the polymer particles was then passed through a de Laval nozzle of length 200mm to deposit onto Aluminium (Al) and Polypropylene (PP) substrates.

Corresponding author: Kesavan Ravi
*E-mail address*: kesavan_ravi@rift.mech.tohoku.ac.jp

## 3. Results and Discussion

### *3.1. Effect of nozzle length*

The metallic particles, when cold-sprayed, bonds with the substrate due to energy released by excessive plastic deformation and active surface creation [2]. But the UHMWPE particles behaved differently when it was subjected to the high strain rate conditions. The particles were observed to crack at the base (Fig.2), which suggests that the energy released is consumed in crack formations instead of plastic deformation.

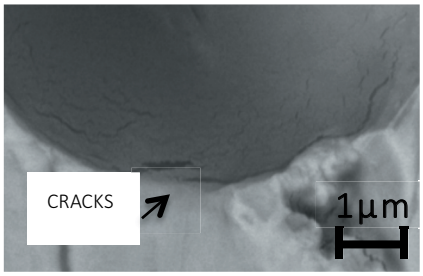


Fig.2 SEM image of a UHMWPE particle on Al surface.

Increasing the nozzle length from 100mm to 200mm solved this problem. The increase in the length rendered an increase in the travel time for the polymeric particles with the carrier gas aiding a better and more uniform softening and plastic deformation of the particles.

### *3.2. Effect of gas temperature/pressure*

It was observed that deposition of the polymer-nanocomposite mixture occurred when the temperature of the gas was close to 350$^0$C and gas pressure between 0.3-0.4MPa in the case of Al substrate.

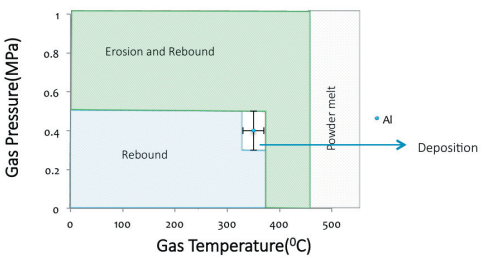


(a)

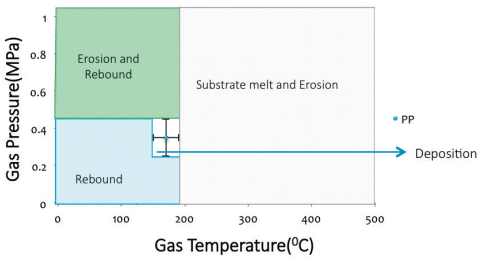


(b)

Fig.3 Deposition behavior of the UHMWPE- fumed nano alumina mixture at different gas temperature and pressure on
(a) Al
(b) PP.

On PP substrate, the deposition was observed at $170^0$C gas temperature and 0.3-0.4MPa gas pressure. Figures 3 (a) and (b) represent the deposition behavior of the UHMWPE-nano alumina mixture at different gas temperature and pressure on Al and PP respectively.

*3.3. Coating Characteristics*

After a careful tuning of the cold spray parameters, a coating thickness of 3-4mm and 1mm thicknesses was obtained on Al and PP substrates.

Fumed nano alumina particles acted as a bridge bond between the polymeric grains. Such a behavior can be attributed to the presence of the fumed nano alumina particles on the grain surface increasing its surface energy by creating a network of finely dispersed particles, which strongly bonded to the polymer surfaces. Fig.4 (a) and (b) show the cross-sectional SEM/EDX images of the coating on Al and PP substrates respectively.

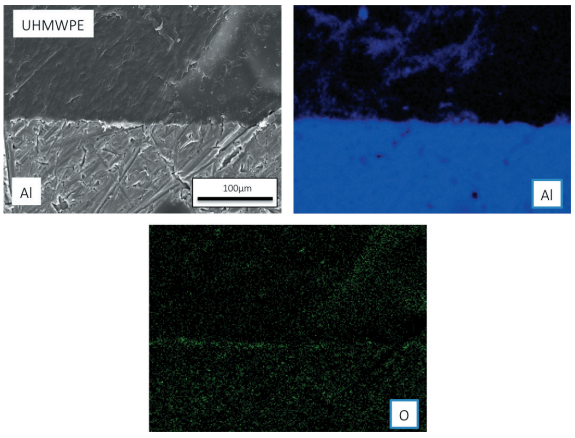


(a)

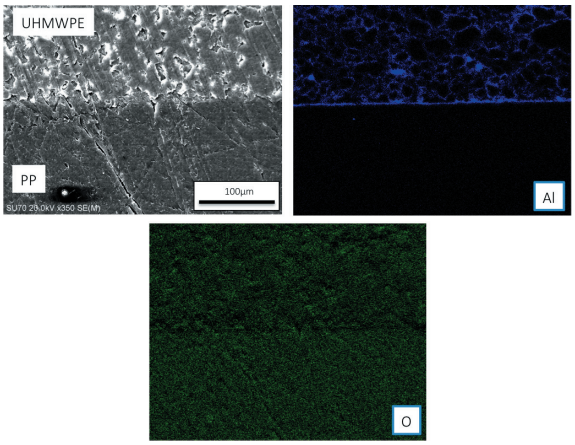


(b)

Fig.4 Cross sectional SEM/EDX images of the coating on
(a) Al
(b) PP.

## 4. Concluding Remarks

This study dealt with polymer coating by cold spray technique. The following can be concluded from the investigation,

1. UHMWPE coating of 4mm and 1mm thickness was achieved on Al and PP substrates respectively.
2. UHMWPE particles tend to crack instead of plastic deformation at high impact velocities.
3. Interaction of gas temperature on the softening of the polymeric particles was increased by increasing the nozzle length.
4. Nano particles creates a network of finely dispersed particles which are strongly bonded to the polymers.
5. Surface properties of the nano additives like surface charge and surface impurities clearly affect the coating quality.

## Acknowledgements

Authors would like to thank JTSS internship program for financing and supporting the internship, carried out at Iwate Industrial Research Institute. This work was partly supported by the JSPS Core-to-Core Program, A. Advanced Research Networks, “International research core on smart layered materials and structures for energy saving”.

## References

[1] McCune, R. C., W. R. Donlon, E. L. Cartwright, A. N.Papyrin, E.F.Rybicki and J.R.Shadley. *Proceedings of the 1996 National Thermal Spray Conference*, (1996) 7-11.

[2] Assadi, Hamid, Frank Gärtner, Thorsten Stoltenhoff, and Heinrich Kreye. *Acta Materialia* 51, 15 (2003) 4379-4394.

Eleventh International Conference on Flow Dynamics
October 8-10, 2014, Sendai, Miyagi, Japan

# Analysis of High Reynolds Number Flow Behind a Square Cylinder by Hybrid Wind Tunnel (Improvement of Critical Gain of Instability for Pressure Feedback)

Jumpei Okutani[1], Toshiyuki Hayase[2], Kosuke Inoue[2], Shusaku Sone[3], Kenichi Funamoto[2]
[1]Graduate School of Engineering, Tohoku University
6-6-01 Aramaki Aza Aoba, Aoba-ku, Sendai, Miyagi, 980-8579, Japan
[2]Institute of Fluid Science, Tohoku University
2-1-1 Katahira, Aoba-ku, Sendai, Miyagi, 980-8577, Japan
[3]Graduate School of Biomedical Engineering, Tohoku University
6-6-01 Aramaki Aza Aoba, Aoba-ku, Sendai, Miyagi, 980-8579, Japan

**ABSTRACT**

This study dealt with the improvement of critical feedback gain of instability of MI simulation in the hybrid wind tunnel with pressure feedback. By linearization of the feedback signal in the source term of the pressure equation, the critical gain increased from 6 to 30, resulting in better reproduction of pressure fluctuation on the cylinder wall.

## 1. Introduction

Experiment and numerical simulation are essential tools in flow analysis, which is used in various fields of engineering and industry. In experiment, limited information in the real phenomenon is provided within the measurement precision. On the other hand, numerical simulation provides a detailed information of the flow field. However, it is difficult to give exact initial condition and boundary condition. In order to overcome these difficulties, flow analysis methods that integrate experimental measurement and numerical simulation have been proposed. Among them, measurement integrated simulation (MI simulation) is used to analyze various flow fields.

Hybrid wind tunnel is an application of MI simulation to a wind tunnel experiment. Previous studies of MI simulation for the Karman vortex street behind a square cylinder using pressure measurement on the cylinder wall [1] and PIV measurement around the cylinder [2] showed the effectiveness of the hybrid wind tunnel. However, they are limited in relatively low Reynolds number ($Re$ = 1200). Verification in high Reynolds number flow is required for practical applications.

This study aims for analysis of high Reynolds number flow including turbulent flow by MI simulation with the pressure feedback in the hybrid wind tunnel.

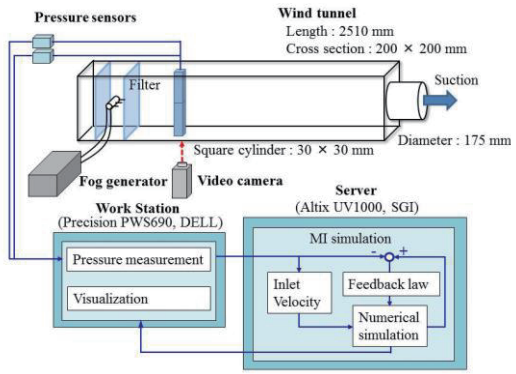


Fig. 1 Configuration of the hybrid wind tunnel

Corresponding author: Jumpei Okutani
*E-mail address*: okutani@reynolds.ifs.tohoku.ac.jp

For analysis of flow in high frequency domain, increased feedback gain is needed. However, divergence phenomenon occurs at the critical gain so far. So this study intends to improve the critical gain of instability for MI simulation with pressure feedback. [3]

## 2. Method

Figure 1 shows a hybrid wind tunnel which consists of a wind tunnel, a square cylinder, pressure sensors (SSK, DP8A-2, 20 Pa, 260 Hz), a work station (DELL, Precision PWS690) and a server (SGI, Altix UV1000). Figure 2 shows a schematic of the wind tunnel. The wind tunnel measures 2510 mm in length and 200 × 200 mm in cross section. The square cylinder (acrylic, 30 × 30 × 200 mm) was placed 515 mm downstream from the entrance. A visualization acrylic nozzle was placed 145 mm downstream from the entrance and smoke provided by a fog generator (Kanomax, Model 8304) was introduced. Two filters (Bridgestone, Everlight SR HR-13, 30 mm thickness) were placed 125 mm and 195 mm from the entrance. The suction flow of the blower was controlled by an inverter. To incorporate the real flow information in the numerical simulation, pressure on the square cylinder surface was measured (Fig. 2). The differential pressure between the center of each side wall and that of the front side was measured through an A/D converter (VMIC, VMIPCI-3322, 1000 Hz, 16 bit) and a digital low pass filter (20 Hz).

Based on the pressure measurement results

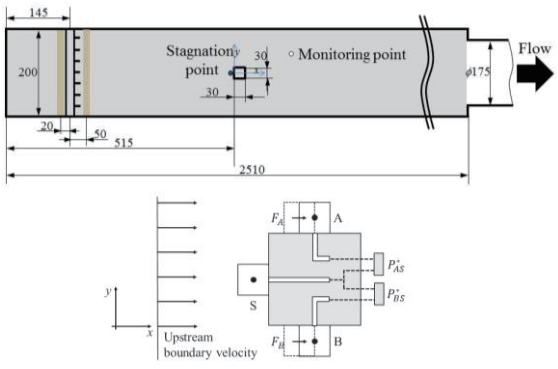


Fig. 2 Geometry of the wind tunnel and the square cylinder

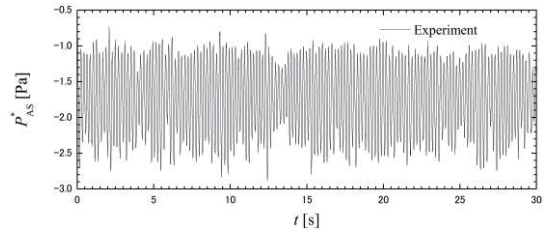


(a) Experiment

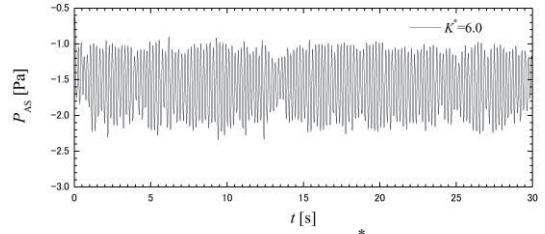


(b) MI simulation ($K^*$ = 6)

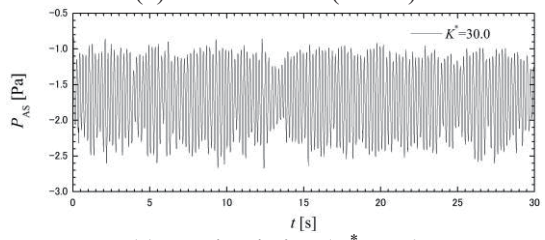


(c) MI simulation ($K^*$ = 30)

Fig. 3 Differential pressure on the cylinder

two-dimensional MI simulation was performed. The computational domain was a two-dimensional area of the mid-plane of the wind tunnel and the fluid was assumed as incompressible viscous fluid. Governing equations are Navier-Stokes equations and pressure equation. These governing equations are discretized with the finite volume method, and are solved with the SIMPLER-based method. Feedback points are set in both sides of square cylinder (Fig. 2). The body force in the mainstream direction proportional to the difference between the calculation results of the differential pressure $P_{AS}$ ( $= P_A - P_S$ ), $P_{BS}$ and corresponding measurement results $P^*_{AS}$, $P^*_{BS}$ were added to control volumes on the left side of A and B. Upstream boundary condition is parallel uniform flow and the velocity is given by Pitot tube law and the first-order low-pass filter. The computational domain is the entire area of the wind tunnel and computational grid is a staggered orthogonal grid system of 248 × 21 points with the grid space of $\Delta x = \Delta y = 10$ mm.

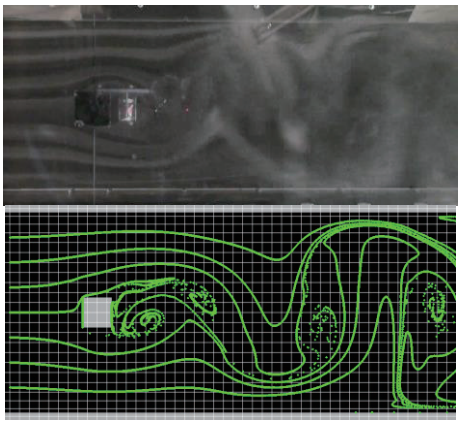

Fig. 4 Comparison of streak lines between experiment and MI simulation with $K^*$ = 30 (t = 6.0s)

As to improvement of the critical gain of instability, the feedback signal in the source term of the pressure equation was linearized to improve the stability of the numerical scheme. [4]

The flow was set corresponding to the Reynolds number Re = 2000 with the shedding frequency of Karman vortex street of 5.1 Hz. The smoke was provided when the flow became stable. After that, video recording and pressure measurement were done for 30 seconds. Pressure measurement results were incorporated to the calculation server, and 2D MI simulations was performed. For analysis condition, the velocity coefficient $K_e = 0.619$ and the time constant $T_c = 0.3$ [s], the computation time step $\Delta t = 0.01$. The analysis was performed by gradually increasing the feedback gain until the computation diverged.

## 3. Results and Discussion

The MI simulation was performed with increasing feedback gain from $K^* = 0$. In the former algorithm, the calculation diverged over $K^* = 6$. In the present algorithm, the calculation was stable until $K^* = 30$ and diverged at $K^* = 31$.

Figure 3 shows variations of the differential pressure $P_{AS}$ ( $= P_A - P_S$ ) for the experiment and the MI simulation results at $K^* = 6$ and $K^* = 30$. Both the MI simulation results properly reproduce the oscillation in the experiment, but the amplitude of MI simulation result for $K^* = 6$ is smaller than that of the experiment. The errors of the average and RMS values of $P_{AS}$ at $K^* = 6$ were 8.2% and 23.8%, while the errors at $K^* = 30$ were 1.8% and 6.1%.

Figure 4 compares streaklines between experiment and MI simulation with $K^* = 30$. Both results agree very well.

## 4. Conclusions

This study dealt with the improvement of critical feedback gain of instability of MI simulation in the hybrid wind tunnel with pressure feedback. By linearization of the feedback signal in the source term of the pressure equation, the critical gain increased from 6 to 30, resulting in better reproduction of pressure fluctuation on the cylinder wall.

## References

[1] Nisugi, K., Hayase, T., Atsushi, S., *JSME. Int. J. Ser. B*, 47 (2004), 593-604.
[2] Yamagata, T., Shibata, H., Hayase, T., Smit, T., *J. Fluid Sci. Tech.*, 3 (2008), 477-487.
[3] Okutani, J., Hayase, T., Inoue, K., Sone, S., Funamoto, K., *Proc. 49th JSME Tohoku Annual Meeting*, (2014) 15-16 (In Japanese).
[4] Patanker, S.V., *Numerical Heat Transfer and Fluid Flow*, Taylor & Francis (1980).

Eleventh International Conference on Flow Dynamics
October 8-10, 2014, Sendai, Miyagi, Japan

# Short Range and Long Range Magnetic Order in Zig-Zag Chain Compound $Bi_2Fe(SeO_3)_2OCl_3$

Peter S. Berdonosov[1], Ekaterina S. Kuznetsova[1], Valery A. Dolgikh[1], Alexey V. Sobolev[1], Igor A. Presniakov[1], Andrei V. Olenev[2], Badiur Rahaman[3], Tanusri Saha-Dasgupta[3], Konstantin V. Zakharov[4], Elena A. Zvereva[4], Olga S. Volkova[4], Alexander N. Vasiliev[4]

[1]Lomonosov Moscow State University, Faculty of Chemistry, Moscow 119991, Russia
[2]University of California Davis, Department of Chemistry, CA 95616, USA
[3]S.N. Bose National Centre for Basic Sciences, Kolkata 700098, India
[4]Lomonosov Moscow State University, Faculty of Physics, Moscow 119991, Russia

**ABSTRACT**

We present synthesis and characterization of a new bismuth iron selenite oxochloride $Bi_2Fe(SeO_3)_2OCl_3$. The main feature of its crystal structure is the presence of reasonably isolated set of spin S = 5/2 zigzag chains of corner sharing $FeO_6$ octahedra. At cooling, the magnetization passes through the broad maximum at $T_{max} \sim 130$ K which indicates the formation of the magnetic short-range correlations regime. At $T_N = 13$ K, $Bi_2Fe(SeO_3)_2OCl_3$ exhibits transition into antiferromagnetically ordered state evidenced in the magnetization, specific heat and Mössbauer spectra.

## 1. Introduction

Magnetism in quasi-one-dimensional magnetic systems, which are quantum in nature, is currently a hot topic due to the diversity of exciting physical phenomena exhibited by them. To mention a few; we note the observation of the spin-Peierls transition in $CuGeO_3$ [1] the charge-driven and orbital-driven spin-Peierls-like transitions in $NaV_2O_5$ [2] and $NaTiSi_2O_6$ [3] the Bose-Einstein condensation of magnons in $TlCuCl_3$ [4] the spiral spin structures in $LiCuVO_4$ [5,6] and $LiCu_2O_2$ [7-9] All these compounds are based on the ions with low spin value, i.e. S = 1/2, where the quantum effects on physical properties are most pronounced.

Less studied are classical quasi-one-dimensional magnetic systems based on the ions with high spin values, e.g. S = 5/2. The low dimensional behavior in classical magnetic systems was found in particular in $FeOHSO_4$ [10], $N_2H_6FeF_5$ [11] and $SrMn_2V_2O_8$ [12], however no evidence of reduced dimensionality was seen in the sawtooth chain $Rb_2Fe_2O(AsO_4)_2$ [13]. All these compounds undergo three-dimensional ordering at low temperatures resulting from the interchain coupling. The more isolated are the chains in a given compound, the quantum aspect in properties is expected to be more pronounced. In case of S = 5/2 compound, $Mn_2(OD)_2(C_4O_4)$, the inelastic neutron scattering measurements have revealed the characteristic behavior of a spin liquid coexisting with a valence bond solid. The departure from the classical behavior observed in the high spin value systems, is generally assumed to be originating from low-dimensionality and geometrical frustration [14].

In the present study, we report the synthesis, crystal structure determination of new quasi-one-dimensional compound, bismuth iron selenite oxochloride $Bi_2Fe(SeO_3)_2OCl_3$, and its characterization through magnetization, specific heat, electron spin resonance and 57Fe Mössbauer spectroscopy measurements.

Corresponding author: Olga Volkova
*E-mail address*: volkova@mig.phys.msu.ru

Significant quantum reduction of spin-only value of the iron magnetic moment is found through the analysis of the low-temperature Mössbauer spectra. The electronic and magnetic structures of $Bi_2Fe(SeO_3)_2OCl_3$ are obtained through the first principles calculations. The calculated parameters of nearest-neighbor intrachain $J_{\parallel}$ and next-nearest-neighbor intrachain $J_{\parallel}'$ exchange interacations, as well as interchain $J_{\perp}$ exchange interaction agree with experimental data, supporting quasi one-dimensional nature of the compound.

## 2. Experimental Details

The compound was obtained from mixture of chemically pure $Bi_2O_3$ 0.4792 g (1.028 mmol), $SeO_2$ 0.229 g (2.064 mmol) and 0.165 g $FeCl_3$ (1.017 mmol) at 300°C for 60 hrs. The electron spin resonance (ESR) study was carried out using using an X-band ESR spectrometer CMS 8400 (ADANI) (frequency≈ 9.4 GHz, B ≤ 0.7 T) equipped with a low-temperature mount, operating in the range 6 - 470 K. Thermodynamic properties of $Bi_2Fe(SeO_3)_2OCl_3$ ceramic sample, i.e. magnetization and specific heat, were measured by "Quantum Design" Physical Property Measurement System PPMS – 9T. The $^{57}Fe$ Mössbauer spectra were recorded at 4.6 – 300K temperature range using a conventional constant-acceleration spectrometer. First-principles calculation in a plane wave basis, as implemented in VASP was used to arrive at a self-consistent description of electronic structure of $Bi_2Fe(SeO_3)_2OCl_3$ compound within the framework of density functional theory (DFT).

## 3. Results and Discussion

Polyhedral representation of $Bi_2Fe(SeO_3)_2OCl_3$ crystal structure is shown in Fig. 1. $FeO_6$ octahedra are connected into zigzag chains by common O3 vertexes. $FeO_6$ octahedron share O1 – O3 edges with $Bi1O_4Cl_3$ polyhedron and O2 vertexes with $Bi2O_3Cl_3$ polyhedron. These Bi polyhedrons are connected by common Cl1 and Cl2 vertexes. $FeO_6$ octahedrons share O2 and O1 vertexes with $Se1O_3$ and $Se2O_3$ groups. The third

oxygen atom of Se1 and Se2 groups, i.e. O4 and O5, are shared with Bi1 and Bi2 polyhedrons. Therefore, $SeO_3$ groups additionally stitch Fe–Bi–O chains.

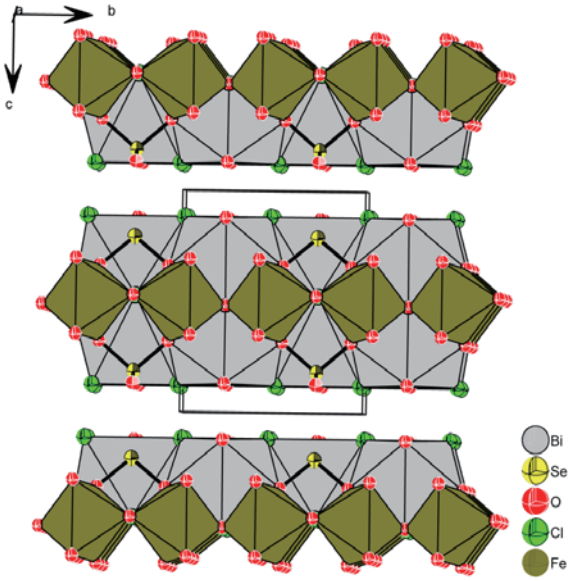


Fig. 1 Polyhedrons of Bi1, Bi2 and Fe atoms in $Bi_2Fe(SeO_3)_2OCl_3$ crystal structure a axis. Bi1 polyhedrons are drawn as light gray. SeO3 groups stitch FeO6 octahedrons and $BiO_4Cl_3$ polyhedrons.

The temperature dependence of magnetic susceptibility $\chi$ of $Bi_2Fe(SeO_3)_2OCl_3$ taken in the field-cooled regime at B = 0.1 T is shown in Fig. 2. At elevated temperatures, the field-cooled and zero-field-cooled curves coincide, but slightly deviate from each other at low temperatures. This divergency is ascribed routinely to defects and/or impurities we neglect it in further discussion. However, the increase of magnetic susceptibility at lowest temperatures can be of intrinsic origin. In zig-zag chains of $FeO_6$ octahedra the Dzyaloshinskii-Moriya interaction results in canting of magnetic moments seen as the rise of magnetic susceptibility at low temperatures [15]. At cooling, the magnetic susceptibility passes through broad maximum at about Tmax ~ 130 K. Well below this maximum, $\chi$ demonstrates Curie-like upturn interrupted by sharp anomaly at $T_N$ = 13 K. This anomaly is seen also in specific heat, as shown in the Inset to Fig. 2, despite the fact that it is rather weak. Overall, the temperature dependence of $\chi$ in $Bi_2Fe(SeO_3)_2OCl_3$ can be treated as formation of the short-range correlation regime at elevated temperatures with subsequent three-dimensional long-range order at Neel temperature. Note, that $T_{max}$ and $T_N$ differ by order of magnitude signifying quasi-low-dimensional nature of magnetism in $Bi_2Fe(SeO_3)_2OCl_3$.

## 4. Concluding Remarks

From the first principles calculations the values of J's using the super-exchange formula, and taking Hubbard U value of 8 eV, turned out to be J|| ≈ 21 K, J||' ≈ 4.6 K and J⊥ ≈ 0.6 K, which shows the dominance of the nearest-neighbor intrachain Fe–Fe interaction, proving the quasi-one-dimensional nature of the underlying spin model of the compound.

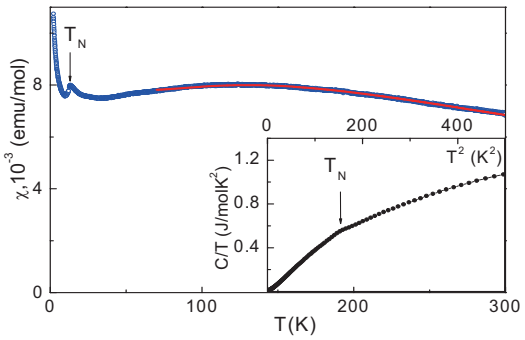


Fig. 2 The temperature dependences of magnetic susceptibility in $Bi_2Fe(SeO_3)_2OCl_3$. Solid line represents the fit in Heisenberg S = 5/2 antiferromagnetic chain model. The inset represents the temperature dependence of specific heat in C/T vs. $T^2$ scale.

## References


[1] M.Hase, I. Terasaki, K. Uchinokura *Phys. Rev. Lett.* 70 (1993) 3651-3654.

[2] M. Isobe, Y. Ueda *J. Phys. Soc. Jpn.* 65 (1996) 1178-1181.

[3] E. Ninomiya, M. Isobe, A.N. Vasil'ev, Y. Ueda, *J. Phys. Soc. Jpn.* 71 (2002) 1423-1426.

[4] T. Nikuni, M. Oshikawa, A. Oosawa, H. Tanaka, *Phys. Rev. Lett.* 84 (2000) 5868-5871.

[5] A.N. Vasil'ev, L.A. Ponomarenko, H. Manaka, I. Yamada, M. Isobe, Y. Ueda *Phys. Rev. B* 64 (2001) 024419.

[6] M. Enderle, C. Mukherjee, B. Fåk, R.K. Kremer, J.-M. Broto, H. Rosner, S.-L. Drechsler, J. Richter, J. Malek, A. Prokofiev, W. Assmus, S. Pujol, J.-L. Raggazzoni, H. Rakoto, M. Rheinstädter, H.M. Rønnow, *Europhys. Lett.* 70 (2005) 237-243.

[7] A.A. Gippius, E.N. Morozova, A.S. Moskvin, A.V. Zalessky, A.A. Bush, M. Baenitz, H. Rosner, S.-L. Drechsler *Phys. Rev. B* 70 (2004) 020406(R).

[8] T. Masuda, A. Zheludev, A. Bush, M. Markina, A. Vasiliev, *Phys. Rev. Lett.* 92 (2004) 177201.

[9] M. Chen, C.D. Hu *J. Phys. Soc. Jpn.* 83 (2014) 014702.

[10] B.D. Rumbold, G.V.H. Wilson *J. Phys. Chem. Solids* 35 (1974) 241-248.

[11] D. Hanzel, A. Tressaud, J.-M. Dance, P. Hagenmuller *Sol. St. Comm.* 22 (1977) 215-218.

[12] S.K. Niesen, O. Heyer, T.T. Lorenz, M. Valldor *J. Magn. Magn. Mater.* 323 (2011) 2575-2578.

[13] R.A. Mole, J.A. Stride, T. Unruh, P.T. Wood *J. Phys.: Condens. Matter* 21 (2009) 076003.

[14] V.O. Garlea, L.D. Sanjeewa, M.A. McGuire, P. Kumar, D.H.J. Sulejmanovic, S.-J. Hwu *Phys. Rev. B* 89 (2014) 014426;

[15] E.E. Kaul, H. Rosner, V. Yushankhai, J. Sichelschmidt, R.V. Shpanchenko, C. Geibel *Phys. Rev. B* 67 (2003) 174417.

# Experimental Study on $BaTiO_3$/Ionic Polymer Metal Composite

Xiong Ke, Bian Kan, Zhu Kongjun, Liu Hongguang
State Key Laboratory of Mechanics and Control of Mechanical Structures, Nanjing University of Aeronautics and Astronautics
No.29, Yudao Street, Nanjing, Jiangsu, 210016, China

**ABSTRACT**

Nafion and $BaTiO_3$, with different mass distribution ratios, were uniformly mixed by the ultrasonic dispersion method, $BaTiO_3$/Nafion ion-exchange membrane (IEM) and Pt-IPMC were prepared by using the solvent casting method and chemical deposition method respectively. The IEM and Pt-IPMC sample testing results demonstrated that the elasticity modulus of Pt-IPMC with $BaTiO_3$ increased by 68%, tensile strength limitation by 15.2% and driving force by 227% than those parameters of samples without $BaTiO_3$. $BaTiO_3$ can speed Pt-IPMC responding.

## 1. Introduction

As an electrically actuated functional material, Ionic Polymer Metal Composites (IPMC) possess the similar properties as biological muscle[1]. Therefore, IPMC, called as the artificial muscle[2], is provided with potential applications in many fields[3].

$BaTiO_3$, a kind of ferro-electrical material with high dielectric constant and low dielectric loss, is one of the most important inorganic phrases with high dielectric constant for composites. In some researches, $BaTiO_3$ was used as the filler for composite polymers in order to improve the dielectric characteristics[4].

In this research, Nano-$BaTiO_3$ powders were used as the reinforced additive for basement membrane to enhance the IPMC mechanical properties as well as improve the electrical properties and actuating ability.

## 2. Preparation of IPMC

### 2.1 Nafion solution concentration

5% Nafion solution was concentrated to 25% in vacuum and at temperature 50℃. Dimethyl sulfoxide (volume ratio: DMSO : Nafion≈1:40) was added into the concentration solution to make the casting solution. Bubble in the casting solution was removed by ultrasonic oscillation for 20min approximately.

### 2.2 $BaTiO_3$ dispersion

The casting solution (Nafion solute) was mixed up with $BaTiO_3$ by mass ratio 100:5 before molding.

### 2.3 Ion exchange membrane curing

The mold was kept in a oven of 50℃. When the surface was dried, the temperature was raise to 100℃ for 1 hour and 300℃ for 3 hours, then the sample was naturally cooling to the room temperature.

### 2.4 Pt-IPMC sample preparation

Pt-IPMC was produced by two-step reduction method[3]. The reaction mechanism is as follows:

Step1: $Pt^{+}+NaBH_4+4OH^{-}\rightarrow 4Pt+2H_2+B(OH)_4^{-}+Na^{+}$

Step2: $Pt^{+}+2N_2H_4\rightarrow Pt+2NH_4^{+}+4NH_3+N_2\uparrow$

Fig.1 shows the results of the EDX analyses of Pt-IPMC samples. Inner electrode is important to the conductivity and moisture retention of IPMC, and ion exchange ability of IEM. Outer electrode mainly plays the role of maintaining a continuous surface of IPMC. The inner electrode thickness of Pt-IPMC with $BaTiO_3$ increased by 34.6%, and the outer electrode was denser than those without $BaTiO_3$, as shown in Table 1.

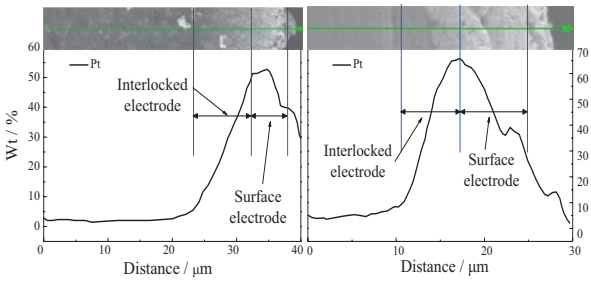


(a) With $BaTiO_3$ (b) Without $BaTiO_3$

Fig. 1 The SEM photos and EDX analyses of Pt-IPMC samples' cross section

Table 1. The electrode thickness of Pt-IPMC samples

| Pt-IPMC Sample | Electrode thickness / μm | |
|---|---|---|
| | Interlocked | Surface |
| with $BaTiO_3$ | 8.90 | 4.93 |
| without $BaTiO_3$ | 6.61 | 7.50 |

## 3. Experimental Results and Discussion

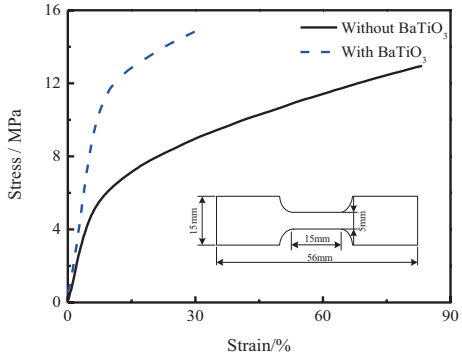


Fig. 2 Tensile stress-strain curves of Pt-IPMC samples

Mechanical properties of IPMC can be obviously affected by $BaTiO_3$ additives. In Fig. 2, Pt-IPMC

Corresponding author: Xiong Ke
*E-mail address*: kxiong@nuaa.edu.cn

exhibited typical polymer elastic-plastic properties in tensile testing, and trends of tensile stress-strain curve didn't changed. But the elastic modulus of IPMC was improved from 97.70MPa to 164.75MPa (68%), the strength limitation was increased from 12.96MPa to 14.93MPa (15.2%), IPMC's maximum elongation was reduced from 83.4% to 30.7%, as shown in Table 2.

Table 2. Mechanics parameters of Pt-IPMC samples

| Sample | E / MPa | $\sigma_b$/ MPa | $\varepsilon_b$ / % |
|---|---|---|---|
| Without $BaTiO_3$ | 97.70 | 12.96 | 83.4 |
| With $BaTiO_3$ | 164.75 | 14.93 | 30.7 |

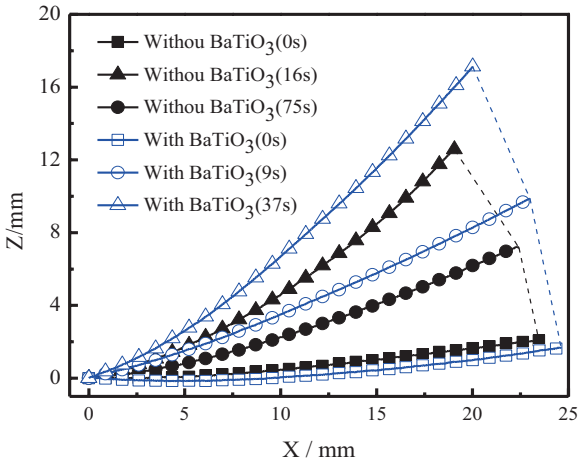


Fig.3 Deflections of Pt-IPMC samples under 5V applied

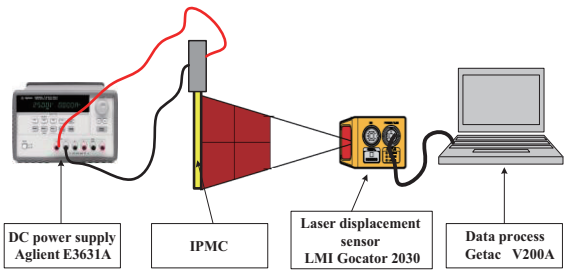


（a）testing for the deflection of IPMC

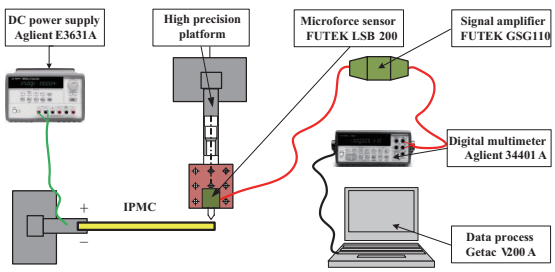


（b）testing for the output force of IPMC

Fig.4 A schematic diagram set-up for IPMC experiments：（a）for deflection；（b）for output force

Driving ability and responding of Pt-IPMC can be evidently enhanced by $BaTiO_3$. Deflections of Pt-IPMC and Pt-IPMC with 5% $BaTiO_3$ were shown in Fig. 3, and the transformation ability of IPMC with $BaTiO_3$ was improved under same excited conditions. The responding speed of IPMC was doubled as the time for returning to balance reduced from 73s to 37s. The transformation testing system was shown in Fig. 4(a).

Table 3. Output forces of Pt-IPMC samples under 5V applied

| Sample | Force/N |
|---|---|
| Without $BaTiO_3$ | 1.75×10-3 |
| With $BaTiO_3$ | 6.59×10-3 |

$BaTiO_3$ enhances the strength and stiffness of IPMC so that output forces, at the end of a Pt-IPMC cantilever beam, were increased. Table 3. showed the output forces of Pt-IPMC with 5% $BaTiO_3$ was about 4 times than that of pure Pt-IPMC. The output force testing system was shown in Fig. 4(b).

## 4. Concluding Remark

The experimental researches on Pt-IPMC tensile and cantilever beam specimens presented Young's modulus, stress at break, output forces and responding speed under bending transformation can be effectively improved by $BaTiO_3$ additives. $BaTiO_3$ heightens the transformation ability of IPMC.

## References

[1] Mohsen Shahinpoor, Kwang J Kim. Smart Materials and Structures, (2001)10: 819-833.
[2] Wataru Aoyagi, Masaki Omiya. Smart Materials and structures, (2013)22: 055028(10)
[3] Bian Kan, Xiong Ke, Liu Gang, Chen Qi, Wang Bangfeng. Acta Material Compositae Sinica, (2011)28(3): 115-120.
[4] Hanemann T, Gesswein H, Schumacher B. Microsyst Technol, (2011)17: 195-201.

# Effects of Delamination in Strength of Drilled CFRP Laminates

Chongcong Tao[1], Jinhao Qiu[1], Tomonaga Okabe[2], Hongli Ji[1], Toshiyuki Takagi[2]
[1]State Key Laboratory of Mechanics and Control of Mechanical Structures,
Nanjing University of Aeronautics and Astronautics, Nanjing, 210016, China
[2]Tohoku University
Sendai, Miyagi, 980-8577, Japan

**ABSTRACT**

Delamination is one of the major damages in drilled laminates and may reduce the laminates performance drastically. This work employs a continuum damage model and cohesive elements to investigate the final strength of drilled laminates with different levels of delamination. A smeared crack model is used to avoid mesh dependence meanwhile elastic stiffness of cohesive elements is properly defined to assure the accuracy of the propagation of delamination.

## 1. Introduction

Composite materials are commonly used these days for their excellent mechanical properties. Generally composite parts are produced to a near-net shape however additional manufacture is often required for easy assemble. Drilling is one of the most used machine processes, which creates a hole in order to place bolts or rivets. The delamination is one of the major damages induced by drilling and often takes place around the hole's entry and exit. The performance of carbon fiber reinforced plastics (CFRPs) can be affected by delamination drastically. Some excellent work has been done to investigate the drilling process experimentally and mechanics of damage propagation numerically but little has focused on the performance like strength of a drilled CFRP laminates with delamination caused by the drilling process.

This work employs a continuum damage model (CDM) and cohesive elements to investigate the final strength of drilled laminates with different levels of delamination.

## 2. Method

There are two most important parts of a CDM model: the definitions of the failure criteria and damage variables. Pinho et al. [1] proposed an energy-regularized CDM model with physically meaningful failure criteria to determine the ultimate failure of CFRP laminates. Maimí et al. [2] used a combination of linear and exponential damage evolution laws to calculate the damage variables. Good results were obtained by both models. The CDM model used by this work is based on Pinho's numerical model and implemented with Abaqus/Explicit codes.

Four different failure criteria are used for each failure mode. For fiber tensile failure, a simple maximum stress criterion is used.

$$F_{\mathrm{ft}} = \frac{\sigma_{11}}{X_T} = 1 \tag{1}$$

where $X_T$ is the fiber tensile strength.

For matrix compressive failure, Puck and Schürmann proposed the following criterion which considers the fact that the angle of fracture surface with the through-the-thickness direction under pure compression loading is generally 53±2° for most technical composite materials.

$$F_{\mathrm{mc}} = \left(\frac{\tau_T}{S_T - \mu_T \sigma_n}\right)^2 + \left(\frac{\tau_L}{S_L - \mu_L \sigma_n}\right)^2 = 1 \tag{2}$$

The tractions are calculated from the stress tensors and the fracture surface angle α:

$$\begin{aligned} \sigma_n &= \frac{\sigma_{22}+\sigma_{33}}{2} + \frac{\sigma_{22}-\sigma_{33}}{2}\cos(2\alpha) + \tau_{23}\sin(2\alpha) \\ \tau_T &= -\frac{\sigma_{22}-\sigma_{33}}{2}\sin(2\alpha) + \tau_{23}\cos(2\alpha) \\ \tau_L &= \tau_{12}\cos(\alpha) + \tau_{31}\sin(\alpha) \end{aligned} \tag{3}$$

The friction-like parameters $\mu_L, \mu_T$ and the transverse shear strength $S_T$ can be determined using the fiber compressive strength $Y_C$, the longitudinal shear strength $S_L$ and the fracture plane angle $\alpha_0$ under pure compression loading by the Mohr-Coulomb criterions:

$$\tan(2\alpha_0) = -\frac{1}{\mu_T}, \quad S_T = \frac{Y_C}{\tan(2\alpha_0)}, \quad \frac{\mu_L}{S_L} = \frac{\mu_T}{S_T} \tag{4}$$

In FE implementation the fracture plane angle is taken either 53° or 0° for simplicity.

For matrix tensile failure, a quadratic interaction between tractions on fracture plane is used. The angle of the fracture plane is 0°.

$$F_{\mathrm{t}} = \left(\frac{\sigma_n}{Y_T}\right) + \left(\frac{\tau_T}{S_T}\right) + \left(\frac{\tau_L}{S_L}\right) = 1 \tag{5}$$

In fiber compressive direction, fiber kink phenomenon is assumed to be caused by initial fiber misalignments and following matrix failure. A 2D fiber kinking model is used to predict the onset of the fiber compressive failure. It's necessary to transform the stress tensor into the misaligned coordinate frame before checking the matrix failure criterion:

$$\begin{aligned} \sigma_{11}^m &= \frac{\sigma_{11}+\sigma_{22}}{2} + \frac{\sigma_{11}-\sigma_{22}}{2}\cos(\theta_C) + \tau_{12}\sin(2\theta_C) \\ \sigma_{22}^m &= \frac{\sigma_{11}+\sigma_{22}}{2} - \frac{\sigma_{11}-\sigma_{22}}{2}\cos(\theta_C) - \tau_{12}\sin(2\theta_C) \\ \tau_{12}^m &= -\frac{\sigma_{11}-\sigma_{22}}{2}\sin(2\theta_C) + \tau_{12}\cos(2\theta_C) \end{aligned} \tag{6}$$

where $\theta_C$ is assumed to be a constant misalignment angle as the sum of initial misalignment and the rotation due to loading and can be calculated as:

Corresponding author: Jinhao Qiu
*E-mail address*: qiu@nuaa.edu.cn

$$\theta_C = \arctan\left(\frac{1-\sqrt{1-4\left(\frac{S_L}{X_C}+\mu_L\right)\frac{S_L}{X_C}}}{2\left(\frac{S_L}{X_C}+\mu_L\right)}\right) \quad (7)$$

With the transformed stresses, matrix failure criteria can be checked depending on the sign of $\sigma_{22}^m$. It should be noted that shear nonlinearity is not taken into consideration in this work.

The damage variables $d_n$ are quantitative notions of damage and relate the applied stress to the effective stress. In Pinho's numerical model, the damage variables are defined to linearly degrade the relevant stress to zero. The instantaneous value of the damage variable is therefore defined as:

$$d = \max\left\{0, \min\left\{1, \varepsilon^f \frac{\varepsilon-\varepsilon^0}{\varepsilon\left(\varepsilon^f-\varepsilon^0\right)}\right\}\right\} \quad (8)$$

where $\varepsilon^0$ is the equivalent strain of damage onset and $\varepsilon^f$ is the equivalent strain of final failure. The onset strain $\varepsilon^0$ is defined by appropriate failure criteria. The final strain is calculated by Eq. (9) to ensure that the absorbed energy calculated equates the fracture toughness.

$$\varepsilon^f = \frac{2G}{\sigma^0 L_C} \quad (9)$$

where $L_C$ is the characteristic length of mesh elements introduced to avoid mesh dependence.

Cohesive elements are used to model the interface of laminates, the elastic stiffness of the cohesive elements are defined according to Turon et al. [3] using Eq. (10)

$$K_{ss} = K_{tt} = K_{nn}\frac{G_{IC}}{G_{IIC}}\left(\frac{S}{N}\right)^2 \quad (10)$$

The above mentioned CDM model and cohesive elements are used to investigate the effects of delamination in strength of drilled laminates. The geometric model is shown in Fig.1 and the lay-up sequence is $(0/\pm45/90)_s$. The delamination factor can characterize the level of damage caused by drilling. The conventional delamination factor is defined as the ratio of the maximum diameter of the delamination zone ($d_{max}$) to the drilled hole diameter ($d_0$). Also the adjusted delamination factor can be calculated as Eq. (11) according to Paulo Davim et al. [4].

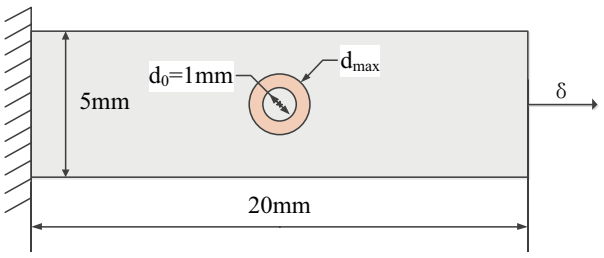


Fig.1 geometric model (annulus represents the delamination area induced by drilling)

$$F_{da} = \frac{d_{\max}}{d_0} + \frac{A_d}{A_{\max}-A_0}\left[\left(\frac{d_{\max}}{d_0}\right)^2 - \frac{d_{\max}}{d_0}\right] \quad (11)$$

where $A_{max}$ is the area related to the maximum diameter of the delamination zone, $A_0$ is the area of the drilled hole and $A_d$ is the damage area.

## 3. Results and Discussion

Four conditions with different levels of delamination are simulated. Condition 1 is simulated without initial delamination and used as a reference. Condition 2 and 3 are set with initial delamination in only 0/45 interfaces (drill entry and exit). Condition 4 has the same delamination factor for all interface layers. Details are listed in Table. 1.

Table1. Model details and calculated strength

| Condition | Delamination factors | | Predicted |
|---|---|---|---|
| | Conventional | Adjusted | strength(Mpa) |
| 1 | / | / | 494.3 |
| 2 | 1.5 | 2.25 | 455.1 |
| 3 | 2 | 4 | 375.5 |
| 4 | 1.5 | 2.25 | 395.8 |

It can be seen from the results that the delamination induced by drilling reduced the strength of laminates severely. Condition 3 with the conventional delamination factor at 2 reduced the final strength about 24%. A smaller delamination area of the conventional delamination factor at 1.5 reduced the strength about 8% for condition 2 and 20% for condition 4.

## 4. Concluding Remarks

This work shows that the delamination induced by drilling reduced the strength of laminates drastically. It's necessary to take the delamination into account when assessing the performance of drilled laminates.

Furthermore it's promising to combine the non-destructive testing (NDT) techniques and CDM model to give a precise prediction of strength of drilled laminates and this would be the author's main objective in future research.


## 5. Acknowledgements

This work was supported by PAPD, the NUAA Fundamental Research Funds (NS2013008), JSPS Core-to-Core Program, "Inter. research core on smart layered materials and structures for energy saving".


## References


[1] S. T. Pinho, L. Iannucci, P. Robinson, *Composites Part A,* 37.1 (2006) 63-73.

[2] P. Maimí, P. P. Camanho, J. A. Mayugo, C. G. Dávila, *Mechanics of Materials,* 39.10 (2007) 897-908.

[3] A. Turon, P. P. Camanho, J. Costa, J. Renart, *Composite Structures,* 92.8 (2010) 1857-1864.

[4] J. Paulo Davim, J. Campos Rubio, A. M. Abrao, *Composites Science and Tech.,* 67.9 (2007) 1939-1945.

# Smart Energy-Harvesting from Various Vibrations with Digital Regulation Approach

Yuta Yamamoto[1], Kenji Yoshimizu[1] and Kanjuro Makihara[1]
[1] Department of Aerospace Engineering, Tohoku University
6-6-01 Aramaki-Aza-Aoba, Sendai, Miyagi 980-8579, Japan

**ABSTRACT**

This study presents a new method of vibration energy-harvesting that manages various vibrations including noise-mixed vibrations, multi-modal vibrations and random vibrations. The point that we make much of is developing an efficient and independent energy harvester. A low-power digital processor is utilized in the developed harvester, which regulates selector switches and induces effective power generation. Experimental results show that this approach possesses great availability of harvesting and a large amount of electric power is actually obtained from structural vibrations.

## 1. Introduction

The technology of energy harvesting collects a lot of attention as a clean power generation. It is also expected to become a substitute of primary batteries, which makes low-power electric devices prevented from battery exchanging. This study deals with the energy-harvesting from structural vibrations (Vibration-based Energy Harvesting). The objective structures are automobiles, airplanes, bridges, artificial satellites and so on. A stack piezoelectric transducer is used for the energy transduction from vibrational energy to electrical energy. A standard harvester is a conventional style for vibration-based energy-harvesting. A circuit which consists of a rectifier and a storage-capacitor is connected to a piezoelectric transducer. Electricity generated by the transducer will be rectified and stored in the storage capacitor. Following this standard harvester, various styles of harvesting circuits have been proposed for improving the generation performance. In particular, the techniques that use an electrical resonance phenomenon by switch regulation are remarkable. Because they increase the generated voltage and they are adjustable to wide vibrational frequency. By extending the synchronized switch damping technique in vibration suppression field, Gyomar *et al.* proposed Synchronized Switch Harvesting on Inductor (SSHI) [1]. Makihara *et al.* proposed a harvesting system that drives in self-powered with the use of a digital-processor. The vibration harvester is completely independent from the outside in spite of performing complex digital control [2].

In this paper we employ a self-powered digital processor in order to deal with multimodal vibrations. The harvester separates the measured displacement data into modal values with the Kalman-filter, and it regulates selector switches in the circuit based on LQR control theory. Some experiments were conducted to reveal the generation ability of the switching harvester comparing with the standard harvester. Under the condition of various input waveforms that include 1st and 2nd mode waves, the proposed harvester shows the high generation capability.

Corresponding author: Yuta Yamamoto
*E-mail address*: yamamoto@ssl.mech.tohoku.ac.jp

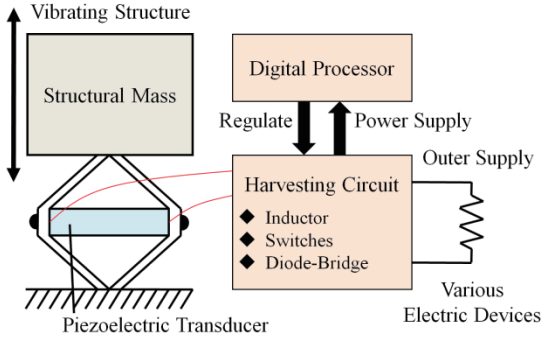


Fig. 1 Smart energy harvester with self-powered digital processor

## 2. Method of Proposing Energy Harvesting

Figure 1 shows the system configuration of our smart energy harvester. A piezoelectric transducer is embedded in the vibrating structure that the harvester wrests the energy from. The harvester circuit is connected to the transducer's electrodes. At first, when the vibration occurs in the structure, the transducer generates voltage at the electrodes. Subsequently, the circuit rectifies the electrical current from the transducer and stores the energy in a storage capacitor, which is similar to the standard harvester mechanism. After enough voltage is stored in the capacitor, a DC/DC converter starts to supply the energy to the digital processor. The digital processor receives displacement data from a piezoelectric sensor. The sensor is a small piezoelectric element that is stuck on the structure. The processor calculates modal value from the sensor data, which is a process of Kalman-filter, and it sends output signal to regulate switches in the circuit. The switching timing is decided based on LQR control theory. According to the switch regulation, voltage inversion at the piezoelectric transducer, we call energy-recycling, occurs, and the voltage increases. The harvester can supply the residual energy in the storage capacitor for outer various electric devices.

## 3. Experimental Results and Discussion

We conducted some harvesting experiments with standard harvester and proposed switching-harvester. The experimental structure that the harvesters will be installed in is a 2DOF spring-mass system. The structure is forced to oscillate by a vibration shaker. Input voltage waveform for the shaker is made by mixing 1st and 2nd

wave modes of the structure. The structure has a first-modal frequency of 20.02 Hz and a second-modal frequency of 36.01 Hz. The input modal ratio is summarized in Table 1.

Figure 2 shows a comparison of generated voltage at the storage capacitor in each harvester. The voltage is divided by RMS of structural displacement, because the vibration amplitude is unsettled in this experimental condition. In this figure, the switching harvester generated higher voltage than the standard harvester in all input mode condition.

Figure 3 shows the time history of piezoelectric voltage and the stored voltage at the switching harvester. Here input waveform number 4 is applied. The switches in the harvester circuit are regulated by the self-powered digital processor, which is shown in the figure as voltage inversions that the variation from plus to minus or *vice varsa*. The switch timing is decided by the processor based on LQR control theory. Every time when piezoelectric voltage exceeds capacitor voltage, generated electricity is repeatedly stored in the storage capacitor.

Figure 4 shows the result of the experiment supplying harvested energy to various load resistors. The standard harvester has a peak voltage of 28.7 mW at 22 kΩ, and switching harvester has a peak voltage of 37.2 mW at 40 kΩ. The switching harvester has superior performance within high resistance area. This tendency can be seen in other input conditions.

## 4. Concluding Remarks

This paper presented a method of vibration energy-harvesting that manages various vibrations. We conducted harvesting experiments with a 2DOF spring-mass system. Comparing with the standard harvester, the proposed switching harvester obtained higher voltage, and it supplied larger electrical power at the optimal load resonance.


## Acknowledgment

This work was partly supported by the JSPS Core-to-Core Program. Advanced Research Networks, "International research core on smart layered materials and structures for energy saving". This research was supported by the Grant-in-Aid for Challenging Exploratory Research (No. 25630436) from the Japan Society for the Promotion of Science.


## References


[1] Guyomar, D., Badel, A., Lefeuvre, E. and Richard, C., *IEEE Transactions on Ultrasonics, Ferroelectrics and Frequency Control*, 52 (2005) 584-95.

[2] Makihara, K., Takeuchi, S., Shimose, S. and Onoda, J., *Transactions of the JSASS Aerospace Technology Japan*, 10, 28 (2012) 13-18.


Table 1. Waveform composed of various modal ratios

| Input number | Mode 1 : Mode 2 |
|---|---|
| 1 | 1 : 0 |
| 2 | 0 : 1 |
| 3 | 1 : 1 |
| 4 | 2 : 1 |
| 5 | 1 : 2 |

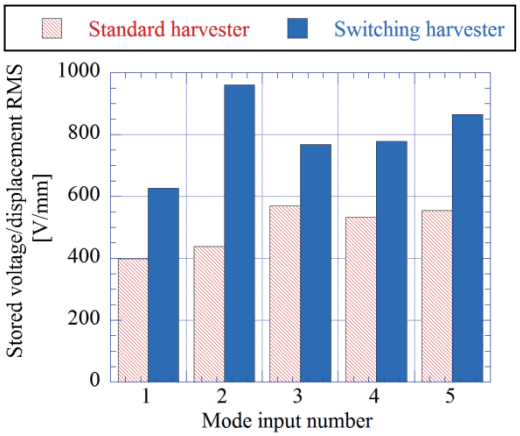


Fig. 2 Comparison of stored voltage par displacement

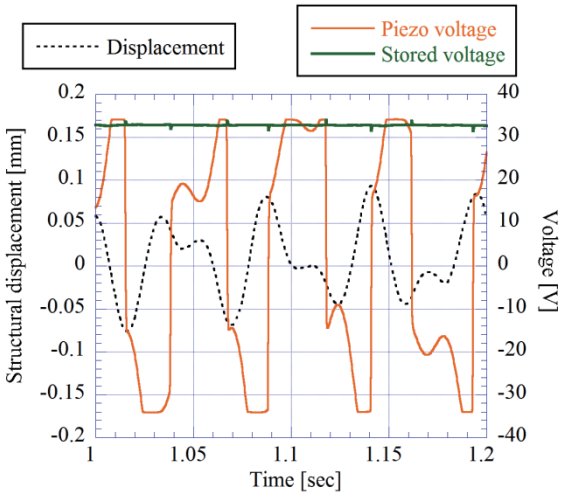


Fig. 3 Time history of piezoelectric voltage and stored voltage with switching harvester

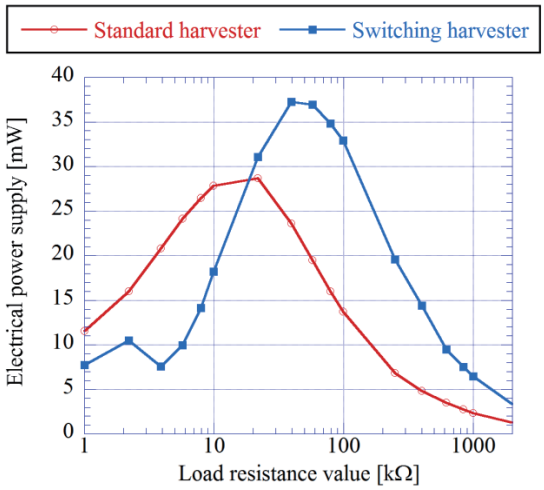


Fig. 4 Electrical power supply by each harvester

Eleventh International Conference on Flow Dynamics
October 8-10, 2014, Sendai, Miyagi, Japan

# Development of Energy Harvesting Devices based on Magnetic Shape Memory Alloy Thin Films

Marcel Gueltig[1], Makoto Ohtsuka[2], Hiroyuki Miki[3], Toshiyuki Takagi[4], and Manfred Kohl[1]
[1]Karlsruhe Institute of Technology (KIT), Institute of Microstructure Technology
Hermann-von-Helmholtz-Platz 1, 76344 Eggenstein-Leopoldshafen, Germany
[2]Tohoku University, Institute of Multidisciplinary Research for Advanced Materials, Sendai, Japan
[3]Tohoku University, Frontier Research Institute for Interdisciplinary Sciences, Sendai, Japan
[4]Tohoku University, Institute of Fluid Science, Sendai, Japan

**ABSTRACT**

In this work we show the feasibility of thermal energy harvesting by using the multifunctional properties of ferromagnetic and metamagnetic shape memory alloy thin films. Two novel thermal energy harvesting principles are shown, using the thermally induced change of magnetic and mechanical properties due to a first order phase transformation. By up-conversion of low thermal to high mechanical oscillation frequencies up to 200 Hz, first demonstrator devices generate power densities in the order of 1 μW/cm$^3$.

## 1. Introduction

Sensors and sensor networks will gain increasing importance in future industry and everyday life. Especially new miniature sensors at hardly accessible places as, e.g., in building infrastructure, will need alternatives to batteries, as battery change would be very expensive or even impossible [1]. Energy conversion of thermal energy, especially by micro energy harvesting promises new convenient solutions for future wireless sensor networks, portable devices, as well as implantable microsystems in the medical field.

Research and applications of thermal energy harvesting was until now focused mainly on thermoelectric generators. Disadvantages are, for instance, the need for cooling beyond natural convection and high temperature differences ΔT [2]. Smart materials, as for example magnetic shape memory alloys (SMA), offer new promising solutions for thermal energy harvesting. They exhibit abrupt changes in lattice parameters up to 10% and large changes of their magnetic properties at small temperature changes ΔT, due to a diffusionless first order phase transformation [3,4]. The large surface-to-volume ratio inherent to thin films enables short heat transfer times. Here, we present two novel thermal energy harvesting principles, using the large change of magnetic properties and actuation capability of magnetic SMA thin films at the same time.

## 2. Material properties and design

Two magnetic SMA thin films, based on the ternary and quaternary Heusler alloys Ni-Mn-Ga and Ni-Co-Mn-In have been investigated. The films are sputtered by (dual) magnetron sputtering in order to tailor their chemical composition [5]. The RF sputtering power is 200 W using Ni-Mn-Ga and Ni-Mn-In targets. In the case of Ni-Co-Mn-In thin films, the DC sputtering power for the Co target is 8 W. After substrate release, the freestanding films are heat treated at 900 °C for 1 h. The chemical composition is measured by the inductive coupled plasma method (ICP) to be $Ni_{52.5}Mn_{22}Ga_{25.5}$ and $Ni_{50.4}Co_{3.7}Mn_{32.8}In_{13.1}$, respectively.

Corresponding author: Marcel Gueltig
*E-mail address*: marcel.gueltig@kit.edu

Thermomagnetic measurements, as well as differential scanning calorimetry and electrical resistance measurements, are performed in order to characterize the material properties such as temperature dependent magnetization and transformation temperatures.

Design concept 1 is shown in Fig. 1. Active components are a Ni-Mn-Ga film cantilever and tip, which are ferromagnetic below the transition temperature $T_C$ of approximately 100 °C. The martensitic transformation temperature $T_0$ is tailored by material composition to be close to $T_C$.

Fig. 1 Design concept 1: The set-up consists of the

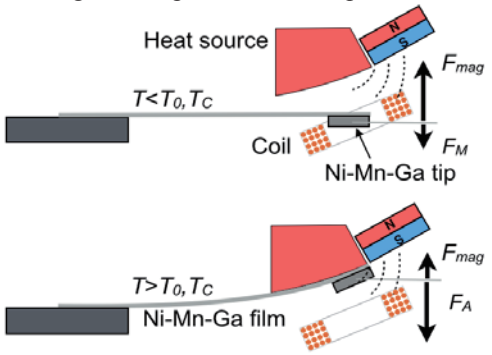


magnetic SMA film cantilever, magnetic SMA tip, heat source and miniature magnet placed above the cantilever tip. In non-deflected state the tip dips into a pick-up coil. Legend: $T_0$, $T_C$ – transformation and transition temperatures, $F_{mag}$ – magnetic attraction force, $F_M/F_A$ reset forces in martensitic/austenitic state.

In non-deflected, cold state, the magnetostatic force $F_{mag}$ exceeds the low restoring force in the martensitic cantilever $F_M$ and the tip is deflected towards heat source and magnet. On heating above $T_0$ and $T_C$, the magnetic force vanishes and the shape recovery effect produces a strong restoring force $F_A$. This bidirectional actuation is used for energy harvesting. While moving away from the heat source, the cantilever oscillates at resonance frequency. This frequency up-conversion effect allows for efficient induction of current in the pick-up coil according to Faraday's law [6]. The forced heat convection during oscillation allows for rapid cooling of the cantilever.

Design concept 2 makes use of the strong change of magnetization ΔM during first order phase transformation in a Ni-Co-Mn-In film. The film is antiferromagnetic below and ferromagnetic above $T_0$. The design again consists of a movable cantilever, see Fig. 2. In this case, an elastic polyimide (PI) foil carries a stack of Ni-Co-Mn-In films at the tip and a pick-up coil. The heat source is placed below the tip.

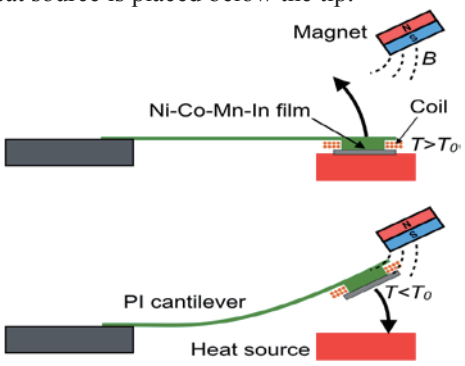


Fig. 2 Design concept 2: The setup consists of a polyimide (PI) cantilever with a pick-up coil and a stack of Ni-Co-Mn-In films. A heat source and a magnet are placed below and above the cantilever tip, respectively. A current according to Faraday's law is induced in the coil, which is electrically contacted to the substrate.

While being in contact to the heat source, the tip heats above $T_0$ and deflects due to the magnetic attraction force between magnetic film and permanent magnet. Resetting to the initial position at the heat source occurs below $T_0$ by the elastic PI cantilever. Again, a resonant oscillatory motion of the cantilever tip is excited by frequency up-conversion. In this case, a current is induced by the magnetization change and the motion of the pick-up coil in the magnetic field gradient according to Faraday's law [7]. Rapid cooling of the cantilever occurs due to forced heat convection.

## 3. Results

A series of time-dependent displacement measurements has been made using both design concepts. As an example, Fig. 3 shows the dependence of oscillation frequency on the heat source temperature as well as the oscillation amplitude for a heat source temperature of 130 °C using design concept 1. The data are derived by image tracking. The results show the broad operational temperature range as well as the frequency up-conversion of the relatively slow heating/cooling cycle of about 2 Hz to mechanical oscillations beyond 80 Hz. Further information on thermography measurements, tensile tests and magnetization measurements can be found in [6,7]. In order to define the electrical output, current measurements with an electrical load of 100 Ω are performed. The results show an average power density of almost 1 μW/cm$^3$ for design concept 1.

The mechanical characterization of design concept 2 reveals oscillation frequencies of up to 200 Hz. This leads to induced current peaks of more then 10 μA.

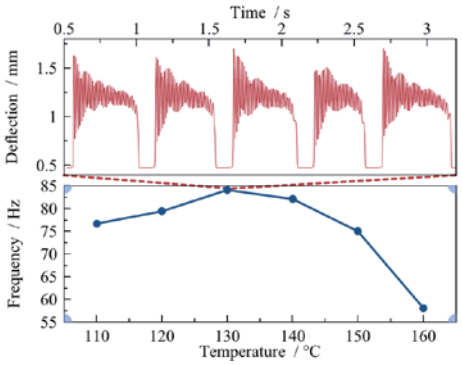


Fig. 3 Operation frequencies for different heat source temperatures using design concept 1. Operation is possible over a large temperature range. For a heat source temperature of 130 °C, the time-dependent deflection is shown in the upper graph.

The periodic thermomagnetic actuation thereby produces an average power density of over 3 μW/cm$^3$. Infrared thermography reveals that the average temperature change of the Ni-Co-Mn-In tip is less than 10 K allowing for energy harvesting at small temperature differences.

## 4. Conclusions

Novel energy harvesting principles are developed by making use of tailored multifunctional thermo-magneto-mechanical properties of magnetic SMA thin films exhibiting large ΔM at small ΔT. Design concepts for film-based devices are presented that show promising power output in the order of 1 μW/cm$^3$.


## Acknowledgement

This work was partly supported by the JSPS Core-to-Core Program, A. Advanced Research Networks, "International research core on smart layered materials and structures for energy saving".


## References


[1] R. Vullers, R. Schaijk, H. Visser, J. Penders, and C. Hoof, *IEEE Solid-State Circuits Mag.*, 2 (2010) 2938.

[2] J.L. Bierschenk, in: *Energy harvesting technologies*, S. Priya and D.J. Inman Eds., Springer, New York (2009) 337.

[3] V. Srivastava, Y. Song, K. Bhatti, and R. D. James, *Adv. Ener. Mat.*, 1 (2011) 97 104.

[4] R. Kainuma, Y. Imano, W. Ito, Y. Sutou, H. Morito, S. Okamoto, O. Kitakami, K. Oikawa, A. Fujita, T. Kanomata, K. Ishida, *Nature*, 439 (2006) 957.

[5] M. Ohtsuka and K. Itagaki, *Int. J. Appl. Electromagnet Mech*, 12 (2000) 49.

[6] M. Gueltig, B. Haefner, M. Ohtsuka, M. Kohl, *Proceedings IEEE Transducers & Eurosensors*, 17 (2013) 2803.

[7] M. Gueltig, H. Ossmer, M. Ohtsuka, H. Miki, K. Tsuchiya, T. Takagi and M. Kohl, *Adv. Ener. Mat.*, in press.

Eleventh International Conference on Flow Dynamics
October 8-10, 2014, Sendai, Miyagi, Japan

# Fabrication of Lead-based Relaxor Piezoelectric Ceramics with High Performance

Kongjun Zhu[1], Jianzhou Du[1], Jinhao Qiu[1]
[1]State Key Laboratory of Mechanics and Control of Mechanical Structure, Nanjing University of Aeronautics and Astronautics
No. 29# Yudao Street, Nanjing 210016, China

**ABSTRACT**

The Fe-doped 0.45Pb($Zr_{0.3}Ti_{0.7}$)$O_3$-0.55Pb($Ni_{1/3}Nb_{2/3}$)$O_3$-$x$$Fe_2O_3$ (PZT- $x$PFNN, $x$=0.0, 0.4%, 0.6%, 0.8%) relaxor-type piezoelectric ceramics have been fabricated by a conventional solid-state reaction process. The effects of $Fe^{3+}$ addition on phase structure, microstructure and electrical properties of PZT-PFNN ceramics were studied. The results show that Fe doping leads to a remarkable improvement of the piezoelectric and ferroelectric properties of PNN-PZT. The excellent electrical properties of $d_{33}$~956 pC/N, $k$p~74%, $\varepsilon_r$~6095 were obtained for the sample with $x$=0.6%.

## 1. Introduction

Lead zirconate titanate (PZT)-based piezoelectric ceramics have been widely used in various electronic devices, such as actuators, transducers, sensors, capacitors and resonators, owing to their excellent electrical properties close to morphotropic phase boundary (MPB) between rhombohedral and tetragonal phase[1-2]. The solid solution of PNN with PZT is one of most famous relaxor-type ferroelectrics, which has drawn much interest in recently years for its high piezoelectric constant and relatively low sintering temperature [3-4]. In previous reports, the proper element additive is an effective approach to enhance material properties for special application. The donor dopants such as $La^{3+}$, $Cd^{2+}$, $Bi^{3+}$ (occupy A-site) or the acceptor dopants such as $Fe^{3+}$, $Mg^{2+}$, $Ni^{2+}$, $Cu^{2}$+, $Zn^{2+}$, $In^{3+}$ (occupy B-site) can improve electrical properties of the PZT-based ceramics in the previous works.

In this work, a transitional element of iron has been used as dopant to modify the electrical properties of 0.55PNN-0.45PZT ceramics. Especially, the effects of $Fe_2O_3$ content on the microstructure, phase transition, and electrical response have been studied investigated in detail.

## 2. Experimental procedure

Reagent-grade powders of PbO, NiO, $Nb_2O_5$, $ZrO_2$, $TiO_2$, and $Fe_2O_3$ were utilized as the raw materials, the 0.45Pb($Zr_{0.3}Ti_{0.7}$)$O_3$-0.55Pb($Ni_{1/3}Nb_{2/3}$)$O_3$-$x$$Fe_2O_3$ ($x$=0.0, 0.4%, 0.6%, 0.8%) ceramics were synthesized by a conventional ceramic technique. After removal of the PVA binder at 800°C for 5 h, the green pellets were sintered at 1200°C for 2 h.

The microstructure and crystal structure of samples were analyzed by a scanning electron microscopy (SEM, JMS-5610LV, Tokyo, Japan) and an X-ray diffraction (XRD, Bruker D8 Advance, Karlsruhe, Germany) using Cu $K\alpha$ radiation. The piezoelectric constant $d_{33}$ of these ceramics was measured by a quasi-static $d_{33}$ meter (ZJ-3A, Institute of Acoustics, Chinese Academy of Sciences, China). The ferroelectric hysteresis loops (P-E) was measured at 10 Hz using a ferroelectric analyzer system (TF2000, aixACCT Systems GmbH, Aachen, Germany). The temperature-dependent dielectric behavior was obtained by a HP4294A impedance analyzer with an automated temperature controller system.

Corresponding author: Jinhao Qiu
*E-mail address*: Qiu@nuaa.edu.cn

## 3. Results and Discussion

Figure 1 show the XRD patterns of PZT-$x$PFNN ceramics with 0.0≤$x$≤0.8% sintered at 1200 °C for 2 h. All ceramics exhibit a pure perovskite phase with no obvious secondary phase were observed in the range investigated. This result indicates that the $Fe^{3+}$ ions had diffused in to PNN-PZT lattice to form solid solution. To clearly analyze the phase structure, the enlarged XRD patterns in the range of 44-46° for all ceramics were shown in Fig. 1(b). It could be seen that the diffraction peaks of (200) shift to higher diffraction angles with increasing $Fe_2O_3$ content, indicating that the perovskite lattice will shrink due to the ionic radius of $Fe^{3+}$ (0.645Å) is smaller than those of $Ni^{2+}$ (0.69 Å) , $Zr^{4+}$ (0.72 Å) and $Ti^{4+}$ (0.605 Å).

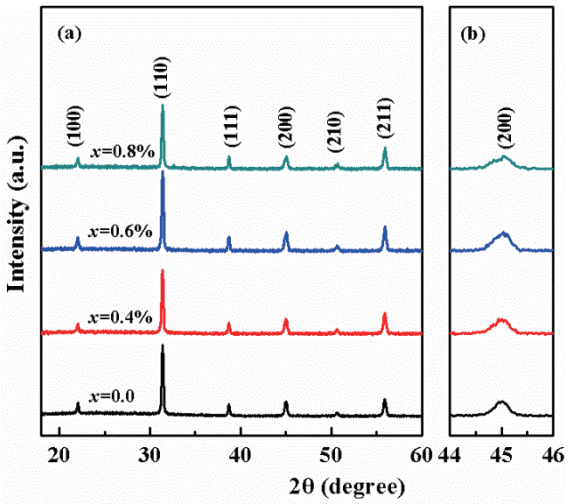


Fig. 1 XRD patterns of the PZT-$x$PFNN ceramics sintered at 1200 °C for 2 h.

Figure 2 show the SEM images of PZT-$x$PFNN ceramics with different $Fe_2O_3$ content. All the sintered ceramics have very dense microstructure with well-grown grains, no distinct pores and clear gain boundary, which also confirm the high relative density in the range 95-96%.

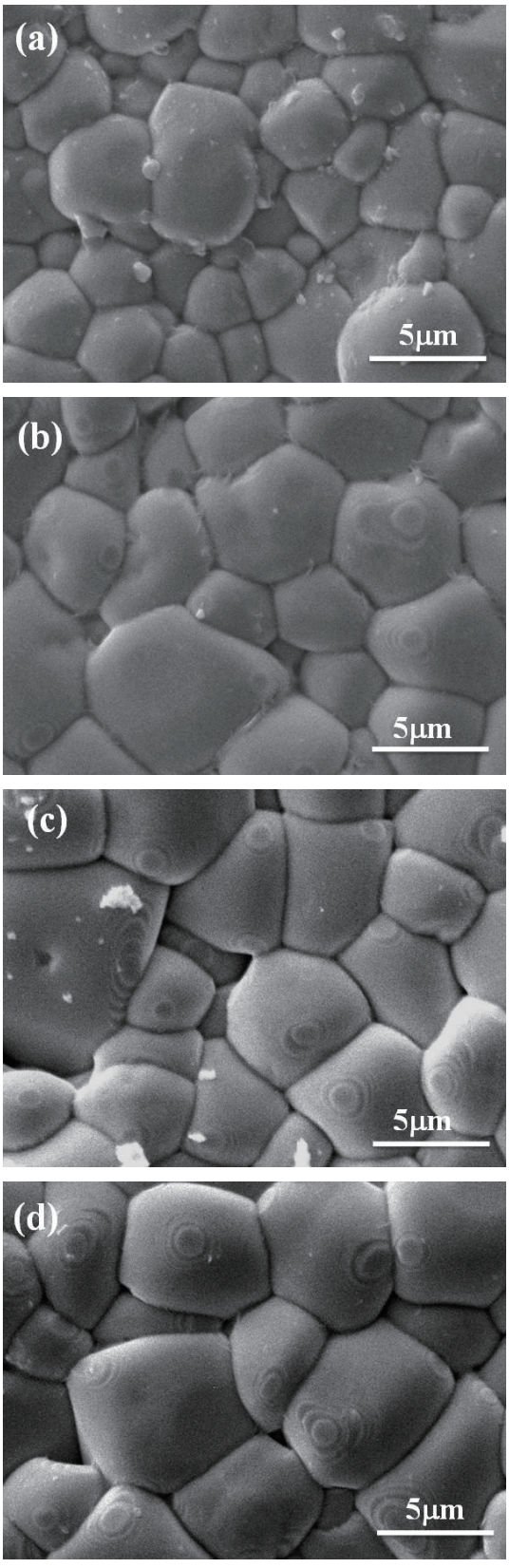


Fig. 2 SEM of PZT-*x*PFNN ceramics with (a) *x*=0.0, (b) (a) *x*=0.4%, (a) *x*=0.6%, (a) *x*=0.8%,.

With the increase of $Fe_2O_3$ content (*x*), the bulk density of PZT-*x*PFNN samples increases initially and reaches a maximum value of 7.97 g/cm$^3$ (around 96% of the theoretical value) at *x*=0.6%, then decreases slightly, as shown in Fig.3.

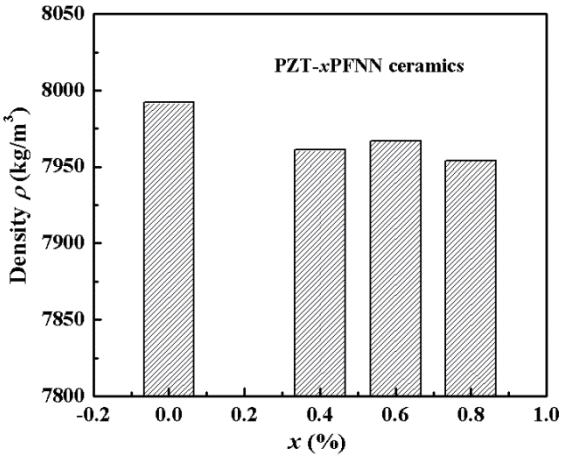


Fig. 3 The densities of PZT-*x*PFNN ceramics as a function of *x*.

The piezoelectric constants ($d_{33}$), electromechanical coupling coefficient ($k_p$), and dielectric constants ($\varepsilon_r$) are summarized in Table 1. The variation of $d_{33}$ are in agreement with the trend of $k_p$, the maximum values of $d_{33}$~956 pC/N and $k_p$~0.74 are achieved in the sample with *x*=0.6%, which is significantly improved compared with the pure 0.55PNN-0.45PZT ceramics with $d_{33}$~802 pC/N and $k_p$~0.68. The *tan*δ of all samples are very low (<3%), the sample with *x*=1.2 mol% shows the lowest value of 2.6%. The variation of the electrical properties is due to the complex effects of phase evolution, grain size, and oxygen vacancy caused by the addition of $Fe_2O_3$.

Table 1. Electrical properties of PZT-*x*PFNN ceramics.

| *x* (wt) | $E_c$(kV/cm ) | $d_{33}$(pC/N) | $k_p$ | $\varepsilon_r$ | *tan*δ |
|---|---|---|---|---|---|
| 0.0 | 3.89 | 802 | 0.68 | 5362 | 2.9% |
| 0.4% | 4.08 | 873 | 0.70 | 5691 | 2.8% |
| 0.6 % | 4.30 | 956 | 0.74 | 6095 | 2.6% |
| 0.85 % | 4.51 | 941 | 0.71 | 6834 | 2.8% |

**4. Concludions**

This work investigated the effects of small amount $Fe^{3+}$ ions addition on the microstructures and electrical properties of $0.45Pb(Zr_{0.3}Ti_{0.7})O_3$- $0.55Pb(Ni_{1/3}Nb_{2/3})O_3$ -*x*$Fe_2O_3$ ceramics. The optimized amount of $Fe_2O_3$ is *x*=0.6 %, the values of $d_{33}$, $k_p$, $\varepsilon_r$ and *tan*δ are 956 pC/N, 0.74, 6095, 2.6%, respectively.

**References**

[1] Saito Y, Takao H, Tani T, Nanoyama T, Takatori K, Homma T, Nagaya T, Nakamura M. *Nature* (2004) 43284-87.
[2] Guo R, Cross LE, Park SE, Noheda B, Cox DE, Shirane G. *Phys Rev Lett* 84(23), (2000) 5423-26.
[3] Vittayakorn N, Rujijanagul G, Tan X, Marquardt M A, Cann D P. *J Appl Phys* 96, (2004) 5103-9.
[4] Cao R, Li G, Zeng J, Zhao S, Zheng L, Yin Q. *J Am Ceram Soc* 93, (2010) 737-41.

# Development of Smart Fatigue Sensor using Metal-containing Amorphous Carbon Coatings

Hiroyuki Kosukegawa[1], Mami Takahashi[2], Julien Fontaine[3], Takanori Takeno[2], Hiroyuki Miki[4], Toshiyuki Takagi[1]
[1]Institute of Fluid Science, Tohoku University, 2-1-1 Katahira Aoba-ku, Sendai, Miyagi, 980-8577, Japan
[2]Graduate School of Engineering, Tohoku University, 6-6 Aramaki aza Aoba, Aoba-ku, Sendai, Miyagi, 980-8579, Japan
[3]Laboratoire de Tribologie et Dynamique des Systèmes, CNRS UMR 5513, École Centrale de Lyon, 36 Avenue Guy de Collongue, 69134 Ecully Cedex, France
[4]Frontier Research Institute for Interdisciplinary Sciences, Tohoku University, 6-3 Aramaki aza Aoba, Aoba-ku, Sendai, 980-8578, Japan

**ABSTRACT**

We propose a metal-containing diamond-like carbon (Metal DLC) film for corrosion-resistant fatigue sensor. Metal DLC including molybdenum was prepared by hybrid technique combining chemical vapor deposition and DC sputtering technique. After applying high cycle bending vibrations on Metal DLC with molybdenum, an increase of electrical resistance of Metal DLC film is observed. The phenomenon would be attributed to the change of binding condition of amorphous carbon matrix. These results indicate that Metal DLC can be a smart fatigue sensor.

## 1. Introduction

Fatigue sensor is required for health monitoring and residual life prediction for structural materials used in huge complex system such as power plant. Previously some fatigue sensors were proposed following different approaches [1], all based on metallic materials. However, such metallic sensors are not tolerable in corrosive environments.

Recently, we have developed metal-containing diamond-like carbon coating (Metal DLC), which has high chemical resistance and good shape deformation response, for the use of strain sensor [2]. In this study, we propose Metal DLC for corrosion-resistant fatigue sensor and attempt to discuss its effectiveness by performing alternative current impedance test, morphological observation and Raman spectroscopy.

## 2. Method

We employed commercial elastic ceramic plate (Ceraflex®–A) purchased at Japan Fine Ceramics Co., Ltd., for deposition of DLC. The ceramic plate, made of zirconia, has high resistivity and enough bending strength to tolerate cyclic bending test with the maximum bending strain of 500 με. The dimensions of rectangular ceramic substrate is $7 \times 4 \times 0.1$ ($mm^3$).

In this study, we prepared two types of DLC films: a-C:H containing molybdenum clusters (Mo-DLC) and pure a-C:H DLC (DLC w/o Me). Mo-DLC film was deposited by using hybrid technique combining plasma-enhanced chemical vapor deposition (PECVD) and DC magnetron sputtering. PECVD apparatus is a setup with capacitively coupled plasma generated by RF power source with 13.56 MHz frequencies. The self-bias voltage of RF electrode was controlled at -400 V by using a capacitance-matching box. Methane ($CH_4$) gas, the carbon source for PECVD, and Ar gas for sputtering were flown into the reaction chamber. The flow rates of $CH_4$ and Ar were controlled with mass flow meters set at 6.0 sccm and 7.5 sccm respectively. DC sputtering was simultaneously performed when PECVD worked to obtain Mo-DLC. The power of DC sputtering was controlled at 200 W. All specimens in this study were prepared at the pressure of $1.0 \times 10^{-2}$ Torr for 30 min.

On the other hand, DLC w/o Me film was prepared by using a PECVD only with $CH_4$ gas. The flow rate of $CH_4$ was 10.0 sccm, and the process gas pressure was set to $1.0 \times 10^{-1}$ Torr. The processing time was 25 min. Self-bias voltage was -600 V.

After deposition, four Cu terminals were deposited on Mo-DLC film for the measurement of resistivity of Mo-DLC by four-terminal method. The gab of between each Cu terminal was 1.5 mm. A typical specimen of Mo-DLC is shown in Fig. 1.

Mo-DLC and DLC w/o Me specimens were glued near the fixed end of a carbon steel beam with the dimension of $10 \times 150 \times 1$ $mm^3$ by using cyanoacrylate adhesive agent. The distance between fixed end and free end of the beam was 100 mm. The beam was vibrated at resonance frequency (60 ~ 80 Hz) by using an electromagnetic coil. The strain amplitude of DLC films was 500 με, and the stress was about 500 MPa. The vibration was continuously generated up to $10^8$ cycles.

The influence of fatigue on Mo-DLC was evaluated in terms of electrical resistance change, film morphology, and amorphous carbon structures. The resistance of Mo-DLC was measured with alternative current impedance method after cyclic bending stress. The morphology of Mo-DLC film was observed by scanning electron microscopy (SEM) and transmission electron microscopy (TEM). The binding condition of amorphous carbon in Mo-DLC film was evaluated by using Raman spectroscopy (NRS-5100, JASCO Co.). According to the method proposed by Robertson [3], the Raman spectra of Mo-DLC were analyzed by fitting the combination of Lorenz function and Breit-Wigner-Faro (BWF) function. The intensity ratio of the peak of disorder, I(D), and that of graphite, I(G), was calculated after fitting the above functions.

## 3. Results and Discussion

With alternative current impedance measurement,

Corresponding author: Hiroyuki Kosukegawa
*E-mail address*: kosukegawa@wert.ifs.tohoku.ac.jp

the electrical resistance of Mo-DLC increases with the numbers of bending vibration cycles (Fig. 2). This result means the Mo-DLC is sensitive to fatigue.

SEM observation of Mo-DLC film exhibits no cracks and no delamination after cycles of bending. Therefore, an increase of resistance of Mo-DLC is not attributed to macroscopic variation of the film. TEM observation shows that Mo-DLC before bending vibration has granular structure with molybdenum clusters with a diameter of three nanometers in amorphous carbon matrix. It also shows that the dispersion and diameter of molybdenum clusters in amorphous carbon matrix is not affected by bending vibration. Conductivity in Metal DLC film can be dominated by "tunneling conduction" and "hopping conduction". "Tunneling conduction" in Metal DLC is determined by diameter of clusters and distance between metal clusters. These microscopic images indicate that the change of resistance of Mo-DLC is not attributed to the structural variation of metal clusters.

On the other hand, the results of Raman spectroscopy suggest that binding condition in amorphous carbon matrix could induce the increase of electrical resistance of Mo-DLC. Fig. 3 shows indeed the I(D)/I(G) ratio in Raman spectra of Mo-DLC, which are obtained by fitting a combination of Lorentz and BWF functions. The I(D)/I(G) ratio of DLC w/o Me is not changed whereas the Mo-DLC one decreases after high cycles of bending. These results indicate that Mo-DLC can be sensitive for fatigue of materials.

We may explain the mechanism of electrical resistance change of Mo-DLC in terms of microscopic alteration. Cyclic bending vibration would induce the change of carbon bonding status in amorphous carbon matrix of Mo-DLC. According to Ferrari et al. [4], the reduction of I(D)/I(G) ratio means an increase of the $sp^3$ binding rate in amorphous carbon matrix. In addition, Wood et al. [5] describes that graphitic sites of amorphous carbon matrix, which consist of $sp^2$ bonds, contribute to "hopping conduction" of charge. These two reports suggest that the increase of $sp^3$ binding rate in the carbon matrix of Mo-DLC may then induce an increase of the activation energy for charge hopping, resulting in an increase of the electrical resistance of Mo-DLC. To validate this explanation, we need more detailed investigation focusing on carbon bonding status of Mo-DLC.

## 4. Concluding Remarks

Repeated bending stresses affect the electrical resistance of DLC film containing molybdenum clusters. The bending stress would induce the microscopic alteration in amorphous carbon matrix of Mo-DLC, resulting in the change of electrical resistance of the film. From these results and discussion, we suggest the possibility to use Mo-DLC as fatigue sensor.


## Acknowledgement

This work was partly supported by a Grant-in-Aid for Scientific Research (A) (23240638) and the JSPS Core-to-Core Program, A. Advanced Research Networks, "International research core on smart layered materials and structures for energy saving".


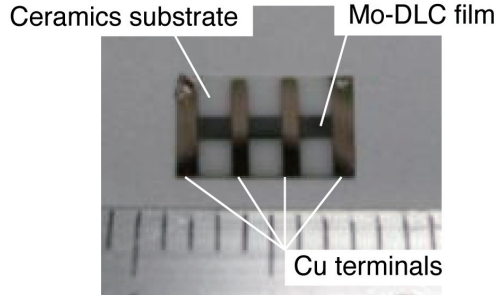


Fig. 1 Mo-DLC specimen coated with Cu terminals for alternative current impedance testing.

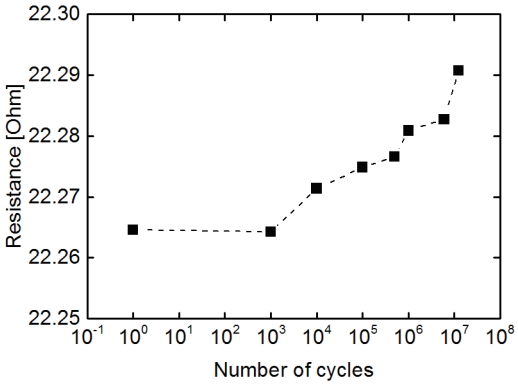


Fig. 2 Variation of resistance of Mo-DLC according to the numbers of bending cycles.

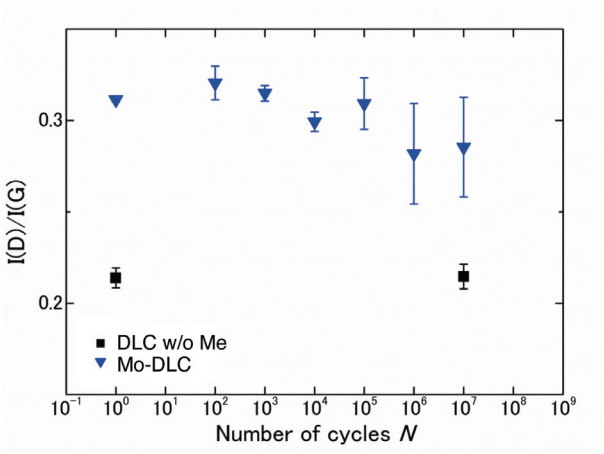


Fig. 3 I(D)/I(G) variation of Mo-DLC and a-C:H DLC w/o Me according to bending cycles.

## References


[1] P. Wang, T. Takagi, T. Takeno, H. Miki, *Sensors and Actuators A-Physical*, 198 (2013) 46-60.

[2] T. Ohno, T. Takeno, H. Miki, T. Takagi, *Diam Relat Mater*, 20 (2011) 651-654.

[3] J. Robertson, *Material Science and Engineering R*, 37 (2002) 129-281.

[4] AC. Ferrari, J. Robertson, *Physical Review B*, 61 (2000) 14095-14107.

[5] P. Wood, T. Wydeven, O. Tsuji, *Thin Solid Films*, 258 (1995) 151-158.

# Ferrimagnetism in Kagome – Type Antiferromagnet $Ni(NO_3)_2$

Olga S. Volkova,[1,2] Vladimir V. Mazurenko,[2] Igor V. Solovyev,[2,3] Evgenya B. Deeva,[4] Igor V. Morozov,[4] Jiunn-Yuan Lin,[5] Chih-Kuang Wen,[5] Jinming Chen,[6] Mahmoud Abdel-Hafiez,[7,8] and Alexander N. Vasiliev[1,2]
[1]Physics Faculty, M.V. Lomonosov Moscow State University, Moscow 119991, Russia
[2]Ural Federal University, Ekaterinburg 620002, Russia
[3]National Institute for Materials Science, 1-2-1 Sengen, Tsukuba, Ibaraki 305-0047, Japan
[4]Chemistry Faculty, M.V. Lomonosov Moscow State University, Moscow 119991, Russia
[5]Physics Department, National Chiao-Tung University, Hsinchu 30076, Taiwan
[6]National Synchrotron Radiation Research Center, Hsinchu 30076, Taiwan
[7]Department of Physics, Liege University, Liege B-4000 Sart Tilman, Belgium
[8]Physics Department, Faculty of Science, Fayoum University, 63514 - Fayoum, Egypt

**ABSTRACT**

Both spin - liquid and magnetically ordered phases of both half-integer and integer low-spin quantum magnets are of interest since the magnetic structures found in latter case usually have no classical counterparts. It is what was found in combined experimental and theoretical study of the integer spin system $Ni(NO_3)_2$. We show that a consistent description of the available data for this compound is possible within a non-collinear ferrimagnetic ground state model for which both intra- and inter-layer magnetic interactions should be antiferromagnetic.

## 1. Introduction

Attractiveness of antiferromagnetic kagomé lattices is supported by unique triangular motive in two–dimensional arrangement of magnetic ions. For the spin-1/2 case, numerous treatments point to a disordered spin–liquid ground state with appreciably small spin gap compared to the exchange parameter [1-3]. Significantly less studied spin-1 kagomé lattices are assumed to possess hexagonal singlet solid state [4-6]. Experimental studies of spin-1 kagomé lattices revealed either the absence of long range order [7,8] or antiferromagnetic/glassy state [9-13] typical for the systems with competing exchange interactions. On the other hand, the existence of ferromagnetism in kagomé compounds has been intensively discussed *theoretically*, albeit with the presence of antiferromagnetic exchange. The kinetic origin of ferromagnetism for partially–filled kagomé lattice was discussed. The dipolar interactions were shown to support the non-uniform ferromagnetic state in kagomé lattices. Besides, large single–ion anisotropy in comparison with exchange interaction might inspire the x-y ferromagnetic state into spin-1 kagomé antiferromagnets. The entropy gain due to the phase transition into magnetoordered state with spontaneous moment in finite "weathervane loops" separated in kagomé spin-1 anisotropic antiferromagnetic lattices was also discussed. Here, we suggest a non-collinear ferrimagnetic ground state model for $Ni(NO_3)_2$ where both intra- and inter-layer magnetic interactions are assumingly antiferromagnetic.

## 2. Experimental Details

The polycrystalline samples of $Ni(NO_3)_2$ were prepared by crystallization from nitric acid solution in presence of adsorbent–dessicant [14]. Thermodynamic properties were measured by PPMS–9T of "Quantum Design" with the sample mounting done in the nitrogen atmosphere. The X-ray absorption spectroscopy (XAS) experiments were performed at the H-SGM beam line at the National Synchrotron Radiation Research Center in Taiwan.X-ray absorption spectroscopy (XAS) was recorded in total electron yield in ultra high vacuum ($\sim 10^{-10}$ mbar) chamber.

Corresponding author: Alexander Vasiliev
*E-mail address*: vasil@mig.phys.msu.ru

## 3. Results and Discussion

As shown in Fig. 1, the $NiO_6$ octahedra share all corners with the $NO_3$ groups to form the framework structure. In the *ab*-plane, the Ni(1) ions linked through $N(1)O_3$ triangles form structurally perfect kagomé layers with Ni(2) ions occupying the hexagons. Within this plane, the Ni(2) ions are linked to Ni(1) ions through non-symmetrical $N(2)O_3$ units. The same $N(2)O_3$ nitrate groups link successive layers along *c*-axis. With respect to this axis the successive layers are shifted by quarter of periods along *a* and *b* axes.

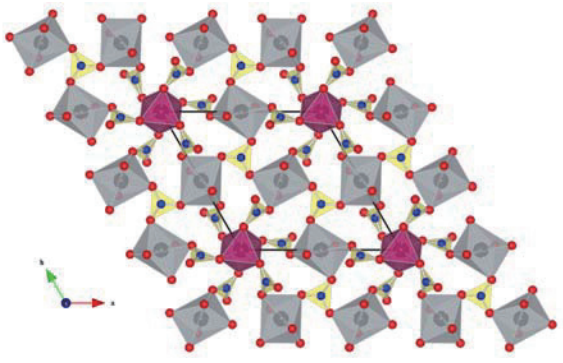

Fig. 1 The crystal structure of $Ni(NO_3)_2$ in the *ab* – plane. The $Ni_1$ and $Ni_2$ ions are shown in octahedral oxygen environment, the nitrate groups are shown by triangles. The $Ni_1$ form kagomé – type layers while $Ni_2$ ions occupy the hexagonal cavities.

The temperature dependence of dc-magnetic susceptibility $\chi = M/B$ taken at $B = 0.1T$ in $Ni(NO_3)_2$ is

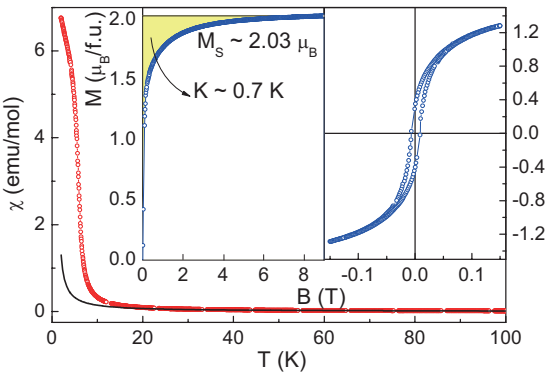


Fig. 2 The temperature dependence of magnetic susceptibility in $Ni(NO_3)_2$ taken at B = 0.1T (symbols), the solid line represents the high temperature fit of experimental data. The field dependence of magnetization and the hysteresis loop taken at T = 2K are shown in left and right insets, respectively.

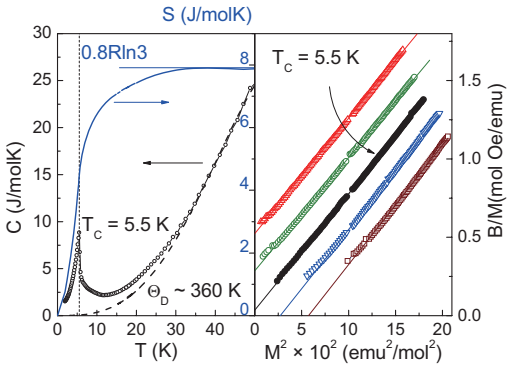


Fig. 3 The temperature dependences of specific heat (symbols) and magnetic entropy (solid line) in $Ni(NO_3)_2$. The dashed line represents the lattice contribution to the specific heat (left panel). The Arrott's plot in $Ni(NO_3)_2$ (right panel).

shown in Fig. 2. At high temperatures, the magnetic susceptibility follows the Curie–Weiss law with addition of temperature independent term $\chi = \chi_0 + C/(T-\Theta)$, where $\chi_0 = 2.3\times10^{-4}$emu/mol, Curie constant C equals 1.3Kemu/mol and negligibly small Weiss temperature $\Theta$ is about ±1K. The value of the temperature independent term corresponds to summation of negative Pascal's constants of $Ni^{2+}$ ions and $(NO_3)^-$ groups $\chi_{dia}$=–$0.5\times10^{-4}$emu/mol [14] and positive van-Vleck term of $Ni^{2+}$ ions $\chi = 2.8\times10^{-4}$emu/mol [15]. At cooling, the $\chi(T)$ dependence sharply deviate upward signaling formation of magnetically ordered state in the system. At low temperatures, the hysteretic behavior of magnetization, shown in the right inset to Fig. 2, is that of a soft magnet with the remnant magnetization $0.3\mu_B$, a coercive force $B_C$ = 5.4kA/m, and the saturation

Further evidence for the phase transition into magnetically ordered state was obtained in specific heat measurements. As shown in the left panel of Fig. 3, the $C_p$ vs. T curve demonstrates sharp λ–type anomaly at $T_C$ = 5.5K, which indicates a second-order phase transition from paramagnetic state to magnetically ordered state. The magnetic entropy released below $T_C$ amounts $S_{mag}$ ~ 4.5J/molK which constitutes about one half of the expected value Rln3 for $Ni^{2+}$ high-spin state S=1. At T >> $T_C$, the specific heat possesses the lattice contribution only which can be approximated by the cubic term $C_p = \beta T^3$with $\beta=3.75\times10^{-4}$ J/molK$^4$. This value allows estimating the Debye temperature $\Theta_D$ in $Ni(NO_3)_2$ as about 360K.

## 4. Concluding Remarks

To study the spin state of nickel ions, the XAS at nickel $L_{2,3}$ edge was employed for $Ni(NO_3)_2$ and a NiO as a reference. These studies confirmed the presence of $Ni^{2+}$ ions in the structure. noncollinear Hartree-Fock The ground state obtained from the calculations can be presented by umbrella-type magnetic structure along z axis. The ground state of the $Ni(NO_3)_2$ is degenerate, the axis of the umbrella is arbitrary and can be controlled by the external magnetic field.

## References


[1] P. Sindzingre, G. Misguich, C. Lhuillier, B. Bernu, L. Pierre, Ch. Waldtmann, H.-U. Everts *Phys. Rev. Lett.* 84 (2000) 2953.

[2] C. Waldtmann, H.-U. Everts, B. Bernu, C. Lhuillier, P. Sindzingre, P. Lecheminant, L. Pierre *Eur. Phys. J. B* 2 (1998) 501.

[3] Y. Okamoto, H. Yoshida, Z. Hiroi *J. Phys. Soc. Jpn.* 78 (2009) 033701.

[4] K. Hida *J. Phys. Soc. Jpn.* 69 (2000) 4003.

[5] N. Wada, T. Kobayashi, H. Yano, T. Okuno, A. Yamaguchi, K. Awaga *J. Phys. Soc. Jpn.* 66 (1997) 961.

[6] H. Kato, M. Kato, K. Yoshimura, K. Kosuge *J. Phys. Soc. Jpn.* 70 (2001) 1404.

[7] S. Hara, H. Sato, Y. Narumi *J. Phys. Soc. Jpn.* 81 (2012) 073707.

[8] W. Miiller, M. Christensen, A. Khan, N. Sharma, R.B. Macquart, M. Avdeev, G.J. McIntyre, R.O. Piltz, C.D. Ling *Chem. Mater.* 23 (2011) 1315.

[9] M. Kato, T. Hori, N. Oba, K. Yoshimura, T. Goto *Physica B* 329-333 (2003) 1042.

[10] J. Behera, C.N. Rao *J. Am. Chem. Soc.* 128 (2006) 9334.

[11] D.E. Freedman, R. Chisnell, T.M. McQueen, Y.S. Lee, C. Payen, D.G. Nocera *Chem. Commun.* 48 (2012) 64.

[12] G. Lawes, M.Kenzelmann, N. Rogado, K. H. Kim, G.A. Jorge, R.J. Cava, A. Aharony, O. Entin-Wohlman, A.B. Harris, T. Yildirim, Q.Z. Huang, S. Park, C. Broholm, A.P. Ramirez *Phys. Rev. Lett* 93 (2004) 247201.

[13] G.A. Tikhomirov K.O. Znamenkov E. Kemnitzand, S.I. Troyanov *Z. Anorg. Allg Chem.* 628 (2002) 269.

[14] G.A. Bain, J.F. Berry *J. Chem. Educ.* 85 (2008) 532.

[15] Y. Yamaguchi, N. Sakamoto *J. Phys. Soc. Jpn.* 27 (1969) 1444.

# $MoS_2$-DLC Nanocomposite Coating for Low Friction Systems

Takanori Takeno, Kazuki Ikoma, Toshiyuki Takagi, Koshi Adachi
[1]Graduate School of Engineering, Tohoku University
6-6-01, Aramaki, Aoba, Aoba-ku, Sendai 980-8579, Japan
[2]Institute of Fluid Science, Tohoku University
2-1-1, Katahira, Aoba-ku, Sendai 980-8577, Japan

**ABSTRACT**

The purpose of this study is to develop coating solid lubricant for vacuum environment. The results on friction experiments indicate that friction coefficient decreases with increase of $MoS_2$ concentration, and developed nanocomposite coating showed lower friction compared with sputtered $MoS_2$ coating. When the lowest friction was observed, very thin, ~ 60 nm, transfer layer was obtained. Auger electron spectroscopy revealed that selectrived transfer of $MoS_2$ nanocluster occurred during friction.

## 1. Introduction

Molybdenum-disulfide ($MoS_2$) is well known material as a solid lubricant. It is used in various engineering field. Especially, for spacecraft, $MoS_2$ is now standard material. $MoS_2$ has special crystallographic structure, that $MoS_2$ monolayers are aligned along c-axis that is perpendicular to friction direction, and it shows very low friction thanks to weak van der Waals force between sulfur atoms. However, there are some disadvantages. One of the biggest disadvantages is that $MoS_2$ coatings do not show low friction under humid condition[1] . Oxygen in air migrates into $MoS_2$ layer and chemical reaction between oxygen and molybdenum occurs [2]. Finally, molybdenum oxides ($MoO_x$) is formed, which prevents the formation of $MoS_2$ lamellar structure. So, components of the spacecraft are stored in dry nitrogen condition just before launch, which costs a lot.

Trial to avoid oxidation in atmospheric condition has been made by combining diamond-like carbon coatings (DLCs) in this study. One of key feature is to work as a gas barrier coating [3]. Permeability of gases is well studied up to now, and such DLCs have been already used on inner wall of polyethylene terephthalate (PET) bottles, especially for hot drinks. Therefore, if $MoS_2$ was packed in DLC matrix, fresh $MoS_2$ can be maintained even in air-condition and shows low friction in vacuum.

We have shown microstructure and friction properties of $MoS_2$-DLC nanocomposite coatings [4]. With increase in $MoS_2$ concentration in the coatings, friction became lower [5]. In the conference, recent progress on this research project is presented.

## 2. Experimental

The investigated coatings were deposited using r.f. plasma chemical vapor deposition and DC magnetron co-sputtering of a $MoS_2$ target (99.9 purity). A schematic of the deposition apparatus is shown in fig. 1. The cathode connected to r.f. source though capacitor is located bottom of the deposition chamber, and substrate is placed on it. There is DC magnetron device at the top of the chamber. Deposition process is basically same as ones done in our previous works [4]. In this study, DC power was changed to 200 W. Concentration of $MoS_2$ was changed by changing $CH_4$/Ar ratio. Working pressure was fixed at 1.0 Pa, and deposition time was 10 minutes, resulting in that 0.5 μm in thickness was achieved.

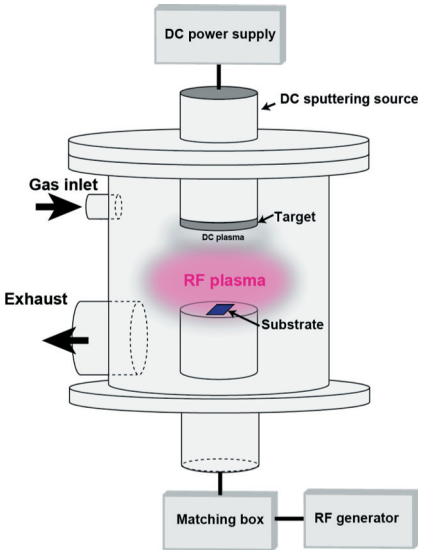


Fig. 1 Schematic illustration of deposition chamber

Ball-on-disk type tribometer was employed in this study. Silicon carbide (SiC) ball and disk were used. Coatings were prepared on disk specimens. Ball and disk were installed into vacuum chamber and evacuated up to $10^{-5}$ Pa. Load and speed for the tests were fixed at 2 N and 60 rpm, respectively.

## 3. Results and Discussions

Fig. 2 shows evolution of friction coefficient of $MoS_2$-DLC coatings with different $MoS_2$ concentration. Results on SiC disk, a CVD-growth DLC and sputtered MoS2 were also shown in this figure as references. A SiC and DLC-coated disks were observed from the beginning. Friction became lower with increase in $MoS_2$ concentration, and the lowest friction could be observed in 86 % $MoS_2$ specimen. What is surprise was that the lowest friction achieved by $MoS_2$-DLC coating even compared with sputtered $MoS_2$ coating.

Corresponding author: Takanori Takeno
*E-mail address:* takeno@tribo.mech.tohoku.ac.jp

Optical images of the ball after the friction test were shown in fig. 3 [5]. One can see very clear difference between $MoS_2$ and $MoS_2$-DLC (86 %) coatings. Cross-sectional transmission electron micrograph, that is not shown in this paper, revealed that thicknesses of transfer layers from $MoS_2$ and $MoS_2$-DLC are ~200 nm and ~60 nm, respectively [5]. High-resolution image indicated the formation of a lamellar structure of $MoS_2$. The monolayer of $MoS_2$ plane is aligned parallel to sliding direction [5], which caused low friction.

Elemental distribution of the wear track of $MoS_2$-DLC (86 %) is shown in fig. 4. On the map, C, Mo and S were detected. The SEM image showed some part of the coating was delaminated, which was also identified by higher intensity of C signal from the SiC substrate and very low Mo and S signals from the coating. On smoothen surface, higher C intensity and lower Mo and S intensity compared with outside wear track were observed, indicating lack of Mo and S elements after robbing the surface. It seems that Mo and S were selectively transferred to the ball during the friction. And thickness of observed carbon layer on the wear track is at least 2 nm that is analytical depth of AES.

Finally, possible mechanism of low friction in $MoS_2$-DLC is discussed. Let us consider phenomena at steady-state friction regime. According to fig. 4, carbon rich layer could be observed on wear track. When counter material came, firstly carbon layer was robbed. Then, $MoS_2$ nanoparticle inside the coating appear. The particles are selectively transferred to the counter material due to adhesion, and empty region, that is a kind of hole, was created. Actually, due to adhesion between transferred MoS2 and carbon in the coating, MoS2 transfer may not be grown. Therefore, in case of pure MoS2, there's very thick MoS2 transferred film was formed, and thin MoS2 layer with carbon. Since the growth and remove of MoS2 film or layer occurred in a same time, when the coating is optimized in term of such phenomena, thinner layer of MoS2 may be formed and further low friction can be achieved.

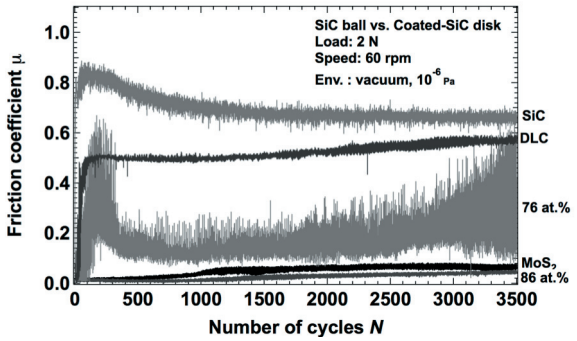

Fig. 2 Evolution of friction coefficient of MoS2-DLC, MoS2, DLC and SiC in vacuum

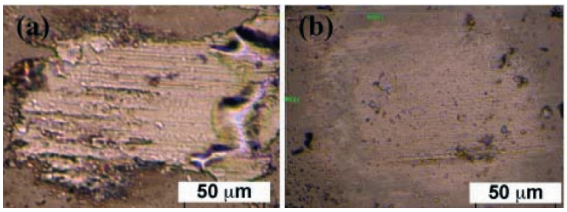

Fig. 3 Optical images on wear scar on the ball

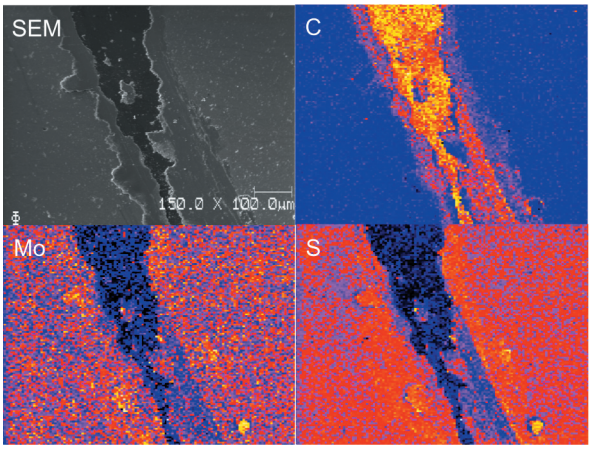

Fig. 4 Auger map on wear track of MoS2-DLC (86 % $MoS_2$).

## 4. Conclusion

In this study, $MoS_2$-DLC coatings with various $MoS_2$ concentration were investigated. The lowest friction could be obtained by $MoS_2$-DLC (86 % MoS2) among all specimens including sputtered $MoS_2$. When the lowest friction was achieved, very thin $MoS_2$ transfer layer on the ball was formed. Transmission electron micrograph and Auger electron spectroscopy revealed that $MoS_2$ particle was selectively transferred to the ball during friction, and thinner $MoS_2$ transfer was formed when lower friction was achieved.


## Acknowledgement

This work was partly supported by the JSPS Core-to-Core program, A. Advanced Research Networks, "International research core on smart layered materials and structures for energy saving".


## References


[1] A.J. Haltner, C.S. Oliver, *Industrial & Engineering Chemistry Fundamentals* 5 (1966) 348-355.

[2] P.D. Fleischauer, J.R. Lince, *Tribology International* 32 (1999) 627-636.

[3] S. Vasquez-Borucki, W. Jacob, C.A. Achete, *Diamond and Related Materials* 9 (2000) 1971-1978.

[4] T. Takeno, S. Abe, K. Adachi, H. Miki, T. Takagi, *Diamond and Related Materials* 19 (2010) 548-552.

[5] T. Takeno, S. Yoshida, K. Nishigaki, H. Miki, T. Takagi, K. Adachi, *Proceedings of World Tribology Congress* (2013) 1004.

# OS5: Biomedical Flow Dynamics

Eleventh International Conference on Flow Dynamics
October 8-10, 2014, Sendai, Miyagi, Japan

# Hemodynamic Features of Cerebral Aneurysms that Influence to Rupture

Yi Qian
The Australian School of Advanced Medicine, Macquarie University
2 Technology Place, Sydney, 2109, Australia

**ABSTRACT**

Computational fluid dynamic (CFD) technology has been utilized to understand difference of hemodynamic condition between stable unruptured aneurysms and ruptured aneurysms. The hemodynamic characteristics; energy losses (EL), were calculated under 100 aneurysms and the results indicated that there are more than five times difference from ruptured and unruptured aneurysms. These results indicate that EL may be a useful parameter to quantitatively estimate the risks of ruptured of cerebral aneurysm.

## 1. Introduction

Cerebral aneurysms are pathological dilations of the arterial wall that frequently occur near arterial bifurcations. The most serious consequence is their rupture and intracranial bleeding into the subarachnoid space, with an associate high mortality and morbidity rate [1]. Cerebrovascular diseases are one of the three major high mortalities. However, currently the prognosis methods for subarachnoid hemorrhages (SAHs) are still not developed enough. The mechanism of cerebral aneurysm's genesis, growing, and rupture are not competitively understood. Although the evolution of cerebral aneurysms are affected by variety reasons; such as pathological, hemodynamic and other factors, a better understanding of the blood patterns pass through the aneurysm and physically analysis the progression of aneurysms vessel wall will provide to aneurysm surgery a lot of valuable references to understand relationship between the pathophysiological aspects and aneurysms progression depending on its geometry and local hemodynamics. It will be critically support aneurysm surgery to understanding aneurysm growth, preparing treatment, and predicting the risk of its regrowth after treatment.

The hemodynamic analysis of cerebral aneurysms have been developed using numerical and experimental methods [2]. The relationship between flow patterns and diseases development, particularly the WSS, have been motivated in several of the researches in recent years. However, most of the studies have focused on particularly wall shear stress (WSS), has been proposed for flow characterization of cerebral aneurysms. All these findings as an addition have no quantitative expression and are difficult for use in predicting rupture. Therefore, the challenge for aneurysm's hemodynamic analysis using the computational numerical methods are; validation with large numbers and specific geometries of aneurysms from clinical records, specification the blood flow boundary conditions at performing vessel domain, and availability to create a predicting criterion to recognize the risk of cerebral aneurysm before rupture.

Our studies are to develop an efficient transfer system to convent the clinical image data into computational available vessel shape geometries, to computationally validate blood flow patterns, and as well to analyse flow characteristics.

Corresponding author: Yi Qian
*E-mail address*: yi.qian@mq.edu.au

## 2. Method

Patient specific image data was segmented by using image DICOM format clinical image into three dimensional vessel surface format data. Image segmentation software was developed based on Insight Toolkit (ITK) and open source software 3DSlicer. The segmentation process was validated by using our in-vitro mock circulation system [3]. The STL format geometry was transferred into mesh generation software ICEM (ANSYS®) to generate volume mesh for fluid simulation.

The flows in this study was assumed as an incompressibility, Newtonian and laminar flows. Navier-Stocks governing equations solved basing on Finite Volume Method (FVM), was introduced as a main solver. All simulations were performed under a personal computer. The simulated results were validated by PIV measurements.

The energy (E) was calculated follow equation.

$$E = \left( P_i + \rho \frac{1}{2} v_i^2 + \rho g h_i \right) Q_i - \left( P_o + \rho \frac{1}{2} v_o^2 + \rho g h_o \right) Q_o \quad (1)$$

Where, using Bernoulli's equation, E [W] is energy calculated from total pressure in the artery domain inlet and outlet at the average of heart pulse.

The energy loss (EL) was calculated from the energy difference between with and without aneurysm. The simulations of the non-aneurysm cases were carried out with the same flow conditions as that of the with-aneurysm cases. In order to avoid the influence from aneurysm size. The EL was divided by aneurysm volume;

$$EL = (E_{with} - E_{without}) / V \quad (2)$$

Where, V is the volume of aneurysm.

## 3. Results and Discussion

In Fig. 1, a high speed recirculation and flow attachment on the bleb can be observed around the bleb edge. In generally, the bleb on aneurysm is judged as

one of highest risk at cerebral aneurysm clinical diagnose. From observations of the flows within aneurysms, the flow pattern appeared very complex, with the occurrence of jet flows, swirling and separating flows, and flow attachment. This haemodynamic energy transfer is assumed to be one of the major factors in the development, growth and final rupture of aneurysms. The EL for ruptured aneurysms was around 5 times ($P < 0.001$, N=100) higher than for unruptured. (Fig. 2). The energy loss might be transferred into physical stimulus, force and stress, to load on the pathological aneurysm surfaces.

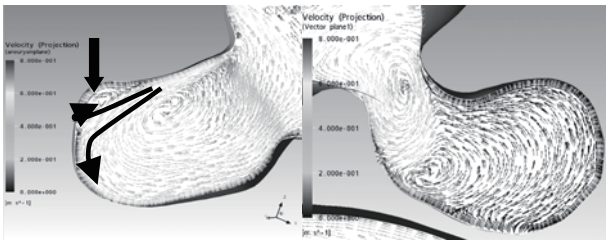

Fig. 1 Blood flows aneurysm
(ruptured left, unruptured right)

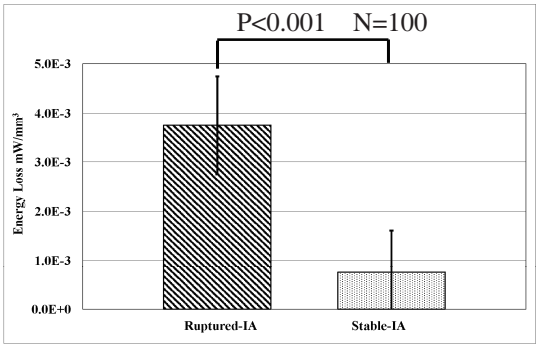


Fig. 2 Energy loss

**Energy loss with respect to the morphology infects of bifurcation aneurysms**

Aneurysm growth was simulated by increasing the aneurysm size (H) from 5 to 12 mm in the idealized model (all model calculation were performed for aspect ratio (AR) of 1.25, 1.5, 1.75, 2, 2.25, and 3. From the fluid dynamic aspect, in the bifurcation without aneurysm, the flow from the parent artery impacts at the apex of the bifurcation, resulting in the formation of a stagnation zone and creating higher variation of wall shear stress around the apex. The power of collision is considered as a possible reason causing damage to endothelial cells. From the fluid mechanics point of view, a small space created at the apex would reduce the speed of jet flow and the collision pressure. However, blood flow in the parent artery of the MCA bifurcation was separated proximal to the aneurysm where the size of the separation region reduces with increase in aneurysm size due to reduction of the pressure difference. To define critical area that might increase the risk of rupture for small and large aneurysms, the EL was examined in idealized and patient-specific models.

Figure 3 demonstrates the effect of the sac diameter on EL of ideal aneurysm models for different aspect ratios. Comparing the aneurysms with the same aspect ratios and different sac diameters showed that the EL in aneurysms with a small sac diameter is higher than that with a large sac diameter for all three bifurcation angles (122 Pa/cm3 and 29 Pa/cm3, AR:1.25, sac diameter equals to 5mm and 12 mm respectively). These results highlight the important role of the sac diameter on flow pattern and energy loss at similar ARs. This has not been considered in explicit terms by previous investigations. The EL curve also shows that increasing AR is associated with decreasing magnitude of EL. Only one ruptured aneurysm's EL was higher than the ideal aneurysm's EL curves and other EL of unruptured aneurysms were under or close to the EL curves. This implies that the safe limits of EL for large AR reduce, hence confirming the higher risk of rupture in large aneurysms. EL curves tend to flatten for ARs greater than 1.6. The result agrees with the patient's statistic results which indicated aneurysm are at higher risk of rupture as AR becomes larger than 1.6.

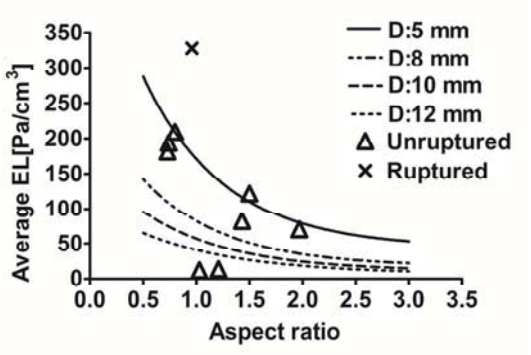


Fig. 3 Average EL for different sac diameter sizes (D) as a function of aspect ratios (AR).

**4. Concluding Remarks**

Using EL concept to estimate the risk of aneurysm rupture was performed by hemodynamic simulation. Flow energy loss in aneurysms was significantly different between ruptured aneurysm and unruptured aneurysm.

**References**

[1] H. R. Winn, JA Sr Jane, J Taylor, D Kaiser, GW Britz, *J Neurosurg,* 96, (2002) 43-49.
[2] Y. Qian, H. Takao, M. Umezu and Y. Murayama, *AJNR Am J Neuroradiol*, 32(10), (2011) 1948-55.
[3] Yuka Sen, Yi Qian, Alberto Avolio, and Michael Morgan, *Journal of Biomechanics*, 47(5) (2014) 1014–9.

Eleventh International Conference on Flow Dynamics
October 8-10, 2014, Sendai, Miyagi, Japan

# Investigation of Aneurysm Development and Rupture using Fluid-Structure Interaction (FSI) Methods

Chang-Joon Lee[1], Hiroyuki Takao[2], Yuichi Murayama[2], Yi Qian[1]
[1]Australian School of Advanced Medicine, Macquarie University
2 Technology Place, Sydney, 2109, Australia
[2]Department of Neurosurgery, Jikei University
3-25-8 Nishi-Shimbashi, Tokyo, 105-8461, Japan

**ABSTRACT**

Fluid-structure interaction (FSI) simulations using five patient-specific aneurysm geometries were carried out to investigate the difference between ruptured and unruptured aneurysms. Two different blood pressure conditions were tested. Ruptured aneurysms (RA) generally displayed larger displacement at the dome, lower area-average wall shear stress, and higher von Mises stress than unruptured aneurysms (URA). The difference in these expansion patterns may be one of the keys to explaining aneurysm rupture.

## 1. Introduction

Cerebral aneurysms are pathological dilations found around the circle of Willis and its sudden rupture is one of the main causes of stroke [1,2], which has a mortality rate of 40 – 50% [3]. The cause of aneurysm rupture still remains unexplained, although it is generally thought that it is based on the interaction between arterial hemodynamics and vascular wall biomechanics. This study aims to investigate the difference in the interaction between hemodynamics and wall biomechanics for ruptured and unruptured aneurysms using fluid-structure interaction simulation method, with the focus on the wall deformation, wall shear stress (WSS) and von Mises stress (VMS).

## 2. Method

Five sidewall aneurysms, two ruptured aneurysms (RA1 and RA2) and three unruptured aneurysms (URA1, URA2, and URA3), were tested. Their general dimensions are shown in Table 1. The aspect ratio (AR), which is defined as a ratio between the dome height and the neck width, is 1.83 and 1.11 for RA and URA, respectively.

Table 1. Dimensions of RA and URA (units in mm).

| | RA | URA |
|---|---|---|
| Height | 6.61 | 5.12 |
| Neck Width | 3.61 | 4.62 |
| Aspect Ratio | 1.83 | 1.11 |

The patient data was obtained using a three-dimensional (3D) computed tomography angiography (CTA) in Jikei University Hospital, obtained during a period of five months. Medical visualization software RealINTAGE was used to transfer and extract DICOM formatted clinical CT images into 3D angiography, and the final reconstructed aneurysm models were exported in stereolithography (STL) file format to ICEM CFD 13.0 (ANSYS, Inc, Cannonsburg, PA, USA) for computational meshing. Approximately 370,000 tetrahedral elements were employed for fluid domain, and 43,000 elements for solid domain. A uniform wall thickness of 0.3 mm was assumed for both arterial and aneurismal wall based on other previous FSI studies [4,5].

The blood flow is governed by the Navier-Stokes equations of incompressible flow for a moving domain. The Arbitrary Lagrnagian-Eulerian (ALE) formulation was used in this study. The blood properties were assumed as incompressible, laminar, and Newtonian flow with a constant density of 1050 kg/m$^3$ and a constant dynamic viscosity of 0.0035 Pa s. A pulsatile mass flow and pressure waveform from a study by Ford et al. [6] were imposed at the inlet and the outlet, respectively, for a period of 0.882 s. The average time-dependent mass flow rate at the inlet was approximately 0.0041 kg/s. The range of pressure was approximately 80 – 130 mmHg for normotensive blood pressure (NBP) and 120 – 170 mmHg for hypotensive blood pressure (HBP). A no-slip boundary condition was applied at the arterial and the aneurismal walls.

The solid model was assumed isotropic, incompressible, homogenous, and linearly elastic solid with the density of 1100 kg/m$^3$ and Poisson's ratio of 0.49 [4,7]. The arterial wall dynamics through a linear elastic model was governed by the momentum conservation equation. The value of elastic modulus was set to 1 MPa. The elastic parent artery was constrained by specifying zero-displacements in all directions at its ends and no rotation about all axes.

ANSYS CFX and ANSYS Mechanical solvers were used to iteratively solve the governing equations for fluid and solid domains, respectively, and coupled using ANSYS Workbench 13.0. The simulation was performed using a uniform coupled time step of 0.002 s for a total of two cardiac cycles (total time of 1.77 s).

## 3. Results and Discussion

The largest maximum total displacement of the aneurysm at the peak systole (t = 0.11s) was found in RA HBP model, with a displacement of approximately 4.4 mm, whereas the smallest maximum displacement was found in URA NBP model, with approximately 2.52

Corresponding author: Chang-Joon Lee
*E-mail address*: chang-joon.lee@mq.edu.au

mm displacement (Fig.1). HBP was found to yield larger displacement than their counterparts. The cross-sectional area changes at the aneurysm neck and dome region were also measured for all models, based on the change in the cross-sectional area at the peak systole relative to diastole state. Regardless of the blood pressure, wall expansion of RA was characterized by relatively larger expansion at the dome region than URA (18% and 9%, respectively), whereas the expansion of URA was characterized by relatively larger expansion at the neck region than RA (26% and 5%, respectively).

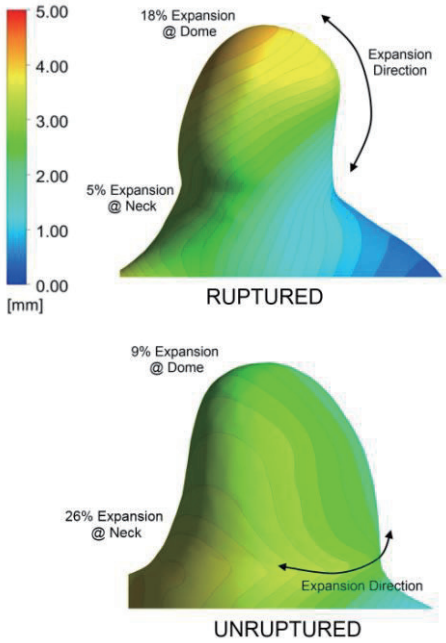


Fig. 1 Aneurysm wall displacement for ruptured (top) and unruptured aneurysm (bottom) under hypertension condition.

URA NBP resulted in highest area-averaged WSS of 3.67 Pa, while RA HBP had the lowest WSS of 1.46 Pa. Both aneurysms had low WSS region at the dome, and HBP condition resulted in lower WSS regardless of aneurysm type. In terms of flow patterns, RA had more longitudinal flow pattern compared to the lateral swirling flow pattern of URA. This flow pattern remained unchanged in both NBP and HBP conditions.

A comparison of RA and URA showed that RA experiences relatively higher VMS at the bleb and the dome region than URA. In addition, HBP further increased the stress magnitudes from its NBP state.

The results have shown that RA experiences a relatively larger expansion and higher VMS at the dome region, which has been reported as the most common rupture site [8,9], than URA. RA also had a larger region of low WSS (> 2 Pa) than URA, especially at the dome, which is known to lead to biological wall deterioration. The results fit the hypothesis that the large continuous wall expansion in conjunction to the low WSS experienced by RA at the dome region may be significantly contributing to the weakening of the aneurysm dome. Biologically, low WSS damages endothelial cells (EC), which modulates local vessel wall remodeling, and this damage consequently degrades and dilates the arterial wall and effectively reduces the wall strength. Simultaneously, the arterial wall undergoes continuous stretching/deformation by an oscillatory internal pressure, which further weakens the aneurysm wall structure. Eventually, aneurysm rupture will occur when the wall tension (VMS) exceed the wall strength, and the continuous biological and mechanical wall weakening at the dome likely increases the possibility of rupture for RA than URA. Based on these findings, this study suggests that RA could be inherently more prone to the hypothesized rupture mechanism than URA.

Hypertension is found twice as often in patients with aneurysms than in patients without, and considered as one of the key risk factors for aneurysm rupture [10]. The results of this study seems to support the notion that hypertension is a risk factor but does not necessarily indicate that it is one of the causes of aneurysm rupture, since the effect of hypertension is found in both RA and URA. Rather than being the cause, it seems that hypertension contributes to the aneurysm rupture by amplifying the associated hemodynamic and mechanical responses.

## 4. Concluding Remarks

RA has shown to exhibit relatively larger wall displacement, lower WSS and higher VMS than URA, and under HBP condition, these characteristics were further enhanced. The expansion pattern for RA and URA were found to be quite different to each other, which could potentially be used as an indicator for clinicians to predict the probability of aneurysm rupture.

## References

[1] J.D. Humphrey, C.A. Taylor, *Annu. Rev. Biomed. Eng*., 10 (2008) 221-246.
[2] W.I. Schievink, *New Engl. J. Med*., 336 (1997) 28-40.
[3] L.L. Teunissen, G.J.E. Rinkel, A. Algra, J. van Gijn, *Stroke*, 27 (1996) 544-549.
[4] R. Torii, M. Oshima, T. Kobayashi, K. Takagi, T.E. Tezduyar, *Comput. Mech*., 43 (2008) 151-159.
[5] Y. Bazilevs, M.C. Hsu, Y. Zhang, W. Wang, X. Liang, T. Kvamsdal, R. Brekken, J.G. Isaksen, *Comput. Mech*., 46 (2010) 3-16.
[6] M.D. Ford, N. Alperin, S.H. Lee, D.W. Holdsworth, D.A. Steinman, *Physiol. Meas*., 26 (2005) 477-488.
[7] A. Valencia, D. Ledermann, R. Rivera, E. Bravo, M. Galvez, *Int. J. Numer. Meth. Fl.*, 58 (2008) 1091-1100.
[8] B. Weir, R.L. Macdonald, *Neurosurgery*, 2nd ed. McGraw-Hill, New York (1996) 2191-2213.
[9] J.G. Isaksen, Y. Bazilevs, T. Kvamsdal, Y. Zhang, J.H. Kaspersen, K. Waterloo, B. Romner, T. Ingebrigtsen, *Stroke*, 39 (2008) 3172-3178.
[10] S. Juvela, *Stroke*, 34 (2003) 1852-1857.

# Fundamental Study of Interaction between Erythrocyte and Endothelial Cell under Inclined Centrifugal Force (Reproduction of Friction Characteristics by Numerical Analysis Using Simple Interaction Model)

Akira Yatsuyanagi[1], Toshiyuki Hayase[2], Kenichi Funamoto[2], Kosuke Inoue[2], Atsushi Shirai[2]
[1]Graduate School of Engineering, Tohoku University
6-6-01 Aramaki Aza Aoba, Aoba-ku, Sendai, 980-8579 Japan
[2]Institute of Fluid Science, Tohoku University
2-1-1 Katahira, Aoba-ku, Sendai, 980-8577 Japan

**ABSTRACT**

In order to elucidate the interaction between erythrocyte and endothelial cell, we performed numerical analysis for the erythrocyte moving in plasma on a plate under the effect of inclined centrifugal force with a simple model of the interaction, in which shear stress inversely proportional to the distance between the cell and the plate applied was to the erythrocyte. As the result, the computational results with the model parameter of 25.2 Pa·μm properly reproduced the frictional characteristics of the experiment on an endothelia-cultured plate.

## 1. Introduction

Blood flow in microcirculation plays an important role in supply of nutrients and oxygen to cells and collection of waste from them. Erythrocytes, or red blood cells, flow in blood capillaries interacting with the vascular endothelial surface layer. Therefore, elucidation of the mechanical interaction between an erythrocyte and an endothelial cell is an important issue that may lead to clarification of mechanisms and development of new treatments of cardiovascular diseases [1].

To elucidate the interaction, Hayase et al developed an inclined centrifuge microscope in Fig. 1, and measured the frictional characteristics of erythrocytes moving on a glass plates surface of which was plain, coated with bio-compatible materials, or covered with endothelial cells under the effect of inclined centrifugal force in plasma [2]. As a result, the friction force on the endothelia-cultured plate was much larger than that on the other plain or material-coated plates. The authors performed a 3D flow analysis around a rigid erythrocyte model, obtaining the result which was qualitatively consistent with those on the plain and material-coated glass plates [3]. However, mechanism in the frictional characteristics of erythrocyte on the endothelia-cultured plate has not been clarified yet.

This study, focusing on the endothelial glycocalyx layer (EGL), intends to acquire fundamental knowledge on the mechanical interaction between erythrocytes and endothelial cells. Numerical analysis is performed for the erythrocyte moving on a plate under the effect of the inclined centrifugal force with a simple model of the interaction between erythrocyte and EGL to reproduce the frictional characteristics of erythrocyte on the endothelia-cultured plate [4].

## 2. Method

In this study, we consider an erythrocyte that moves in plasma on a plate with a constant velocity $U$, the angle of attack α, and the minimum gap width $h_1$ as shown in Fig. 2. In equilibrium state, forces of inclined centrifugal force with components $F_N$ and $F_T$, flow force with components $F_L$ and $F_D$, and shear force $F_\tau$ due to the interaction between erythrocyte and EGL, and their moments should balance. This paper proposes a model of interaction in which the shear stress $f_\tau$ inversely proportional to the distance $h$ between the plate and the bottom surface of the erythrocyte acts on the flat bottom surface of the erythrocyte.

$$f_\tau = b/h \tag{1}$$

where $b$ is an unknown coefficient. It is noted that moment around the point A in Fig. 2 due to this shear stress is null. The effect of vertical component of the shear stress was ignored since the angle of attack α is usually small.

In order to derive the equilibrium state of erythrocyte, 3D flow analysis was performed [4]. Computational model and grid were generated by GAMBIT2.4 (ANSYS, Inc., USA), and flow analysis was performed by FLUENT6.3 (ANSYS, Inc., USA). Computational domain and conditions of the 3D flow analysis are

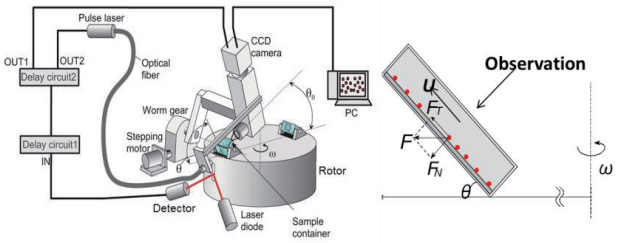


Fig. 1 Inclined centrifuge microscope

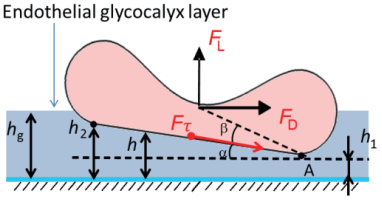


Fig. 2 Erythrocyte moving on endothelial glycocalyx layer

Corresponding author: Akira Yatsuyanagi
*E-mail address*: yatsuyanagi@reynolds.ifs.tohoku.ac.jp

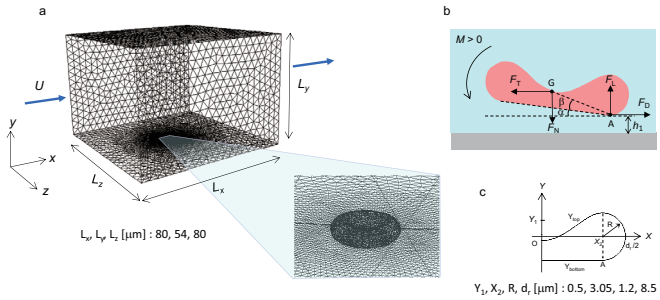


Fig. 3 Numerical analysis condition

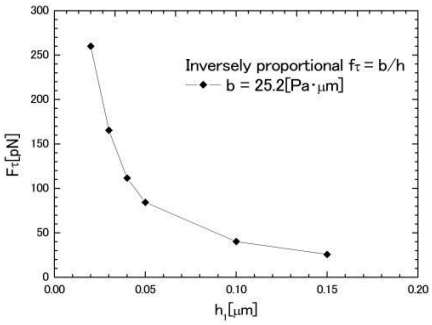


Fig.5 Shear force acing on the erythrocyte from endothelial glycocalyx layer as a function of the minimum gap width

shown in Fig. 3.

The erythrocyte moves at a velocity $U = 50$ μm/s on endothelial cells by the effect of inclined centrifugal force. The erythrocyte was assumed to be rigid with a deformed shape of a flat bottom surface. The density ρ and viscosity μ of the plasma around the erythrocyte was defined as 1025 kg/m$^3$ and 0.0012 Pa · s, respectively. Tetrahedral elements were used with grid size of 0.05 μm around the erythrocyte and 2.0 μm otherwise. The number of elements was about 2.6 million. Three-dimensional flow analysis was performed to obtain the equilibrium angle of attack α, and corresponding inclined centrifugal force $F_N$ and $F_T$ in the range of the plasma layer thickness of 0.02 μm ≤ $h_1$ ≤ 0.15 μm [4].

Integrating the shear stress in Eq. (1) over the flat bottom surface of the erythrocyte with approximation that the value of α is small, the shear force $F_\tau$ applying on the erythrocyte from EGL is obtained as

$$F_\tau = \frac{\pi b}{2} \frac{L^2}{h_1 + \frac{\alpha L}{2} + \sqrt{{h_1}^2 + \alpha L h_1}}, \qquad (2)$$

where $L$ is the diameter of a circular flat bottom surface of the erythrocyte model. By changing the value of the parameter $b$, we obtained the frictional characteristic which best agrees with the experimental result on the endothelia-cultured plate.

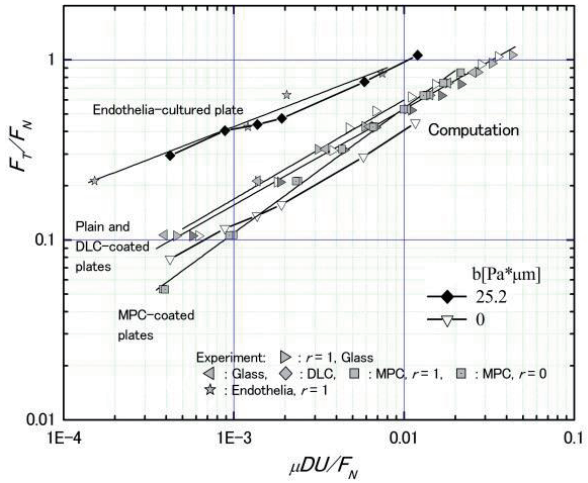


Fig. 4 Nondimensional frictional characteristics of an erythrocyte on plates under the inclined centrifugal force

## 3. Results and Discussion

Figure 4 shows the computational results in comparison with the frictional characteristics of experimental results. The figure shows the nondimensional friction force $F_T/F_N$ as a function of the nondimensional cell velocity $\mu DU/F_N$. The computational results agree with the experimental results on the plain and material-coated glass plates.

Next, we consider the frictional characteristics obtained by adding the shear force due to the present interaction model to the computational results. By applying the results of the computation to Eq. (2), and changing the value of $b$, the frictional characteristics that properly reproduces the experimental results on the endothelia-cultured plate was obtained with $b = 25.2$ Pa·μm as shown in Fig. 4. Figure 5 shows the relationship between the shear force $F_\tau$ and the minimum gap width $h_1$ in this condition. In the present condition, the shear force due to EGL changed in the range between 20 - 260 pN.

## 4. Conclusions

In order to elucidate the interaction between erythrocyte and endothelial cell, we performed numerical analysis for the erythrocyte moving in plasma on a plate under the effect of inclined centrifugal force with a simple model of the interaction, in which shear stress inversely proportional to the distance between the cell and the plate was applied to the erythrocyte. As the result, the computational results with the model parameter of 25.2 Pa·μm properly reproduced the frictional characteristics of the experiment on an endothelia-cultured plate.

## References

[1] S. Weinbaum, Y. Duan, M. M. Thi, L. You, *Cell. Mol. Bioeng.*, 4 (2011) 510-537.

[2] T. Hayase, K. Inoue, K. Funamoto, A. Shirai, *Proc. 8th Int. Conf. Multiphase Flow (ICMF 2013)*, (2013) 1-8.

[3] T. Oshibe, T. Hayase, K. Funamoto, A. Shirai, *Proc. 9th Int. Conf. Flow Dynamics (ICFD2012)*, (2012) 756-757.

[4] A. Yatsuyanagi, T. Hayase, K. Inoue, K. Funamoto, A. Shirai, *Proc. 49th JSME Tohoku Annual Meeting*, (2014) 133-134, (in Japanese)

# Evaluation of Lymph Node Metastasis by Interstitial Fluid Pressure

Kazu Takeda[1], Tomoki Ouchi[2] Tetsuya Kodama[2]
[1] Department of Information and Intelligent Systems, School of Engineering, Tohoku University
4-1 Seiryo Aoba, Snedai Miyagi, 980-8575, Japan
[2] Graduate School of Biomedical Engineering, Tohoku University
4-1 Seiryo Aoba, Snedai Miyagi, 980-8575, Japan

**ABSTRACT**

Interstitial fluid pressure (IFP) increases in metastasized lymph nodes (LNs) and become higher than that of normal LN tissue. Here we show that a correlation between the IFP and number of tumor cells in the LN. We used lymph node metastasis mice model, MXH10/Mo-*lpr/lpr* mice which exhibit remarkable systemic lymphadenopathy. We injected tumor cells into the subliac LN (SiLN) to induce metastasis to the proper axillary LN (PALN). IFP was measured in the SiLN and PALN. We found that IFP has potential to diagnose LN metastasis at the early stages.

## 1. Introduction

Cancer is the most common cause of death in modern society. Especially, LN metastasis plays an important role of distance metastasis [1].Therefore it is needed to develop a diagnostic method of LN metastasis at the early stages. Some methods have been developed for LN metastasis evaluation, however, there is still no methods to diagnose metastasis quantitatively. Normally, IFP of tumor tissue becomes much higher than normal tissue [2, 3]. If IFP is measured quantitatively, LNs can be evaluated less invasively. The aim of the present study is to obtain the correlation between IFP in metastasized LN and number of metastasized tumor cells. We found there is a correlation between elevated IFP and number of tumor cells, and there is a possibility of a clinical application of IFP.

## 2. Method

All *in vivo* studies were done in accordance with the ethical guidelines of Tohoku University.

### Cell line

KM-Luc/GFP cells, which stably express a fusion of the luciferase (Luc) and enhanced-green fluorescent protein (EGFP) genes, were prepared by transfection of MRL/MpTn-*gld/gld* malignant fibrous histiocytoma-like (MRL/N-1) cells (obtained from M. Ono, Tohoku University, on January 24, 2007)[4].

### Animal model

We used MXH10/Mo-*lpr/lpr* (MXH10/Mo/lpr) mice in this study. This animal model develops systemic lymphadenopathy enlarged to a size similar to human LN [5]. The lymphatic vessel from the SiLN to the PALN is the metastatic route depicted in Fig.1.

### Induction of metastasis

Tumor development in mice was induced by injection of $1.0\times10^6$ cells/mL, suspended in 20 μL of PBS and 40 μL of 400 mg/mL Matrigel (Collaborative Biomedical Products) in the into the SiLN under guidance of a high-frequency ultrasound imaging system (VEVO770; VisualSonics) with a 25 MHz transducer (RMV-710B). Metastasis to PALN from the SiLN was assessed using an *in vivo* luminescence imaging system (IVIS; Xenogen,). 200 μL of 15 mg/mL luciferin (Promega) was injected intraperitoneally under anesthesia (2% isoflurane in oxygen). After 10 min, luciferase bioluminescence was measured for 60 s using IVIS. This procedure was carried out on day 0, 3, and 6.

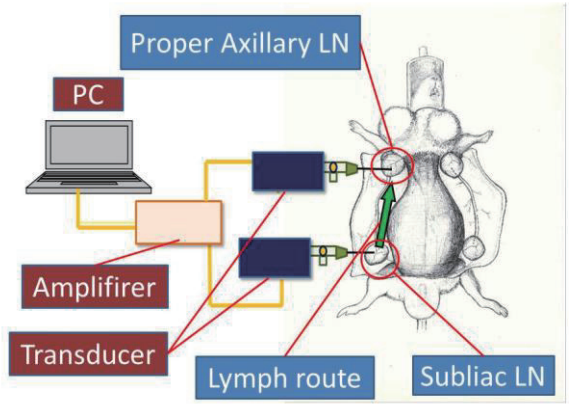


Fig. 1 MXH10/Mo/lpr mouse. LNs are enlarged and the size is as large as human. The SiLN is connected by single lymphatic vessels to the PALN. Tumor cells injected into the SiLN reaches the PALN via the lymphatic vessel. We inserted a needle connected to a pressure transduce to the central region of either the SiLN or PALN to measure IFP.

### Measurement of IFP

After measuring of bioluminescence, we measure the IFP in the SiLN and PALN. A 21G needle was connected to a pressure transducer (BLPR; World Precision Instruments), this transducer was connected to DC amplifier system (Bridge8; World Precision Instruments) and we analyzed dumped date using computer software (Labscribe2; iWorx System). Opening the abdomen to make lymph node visibly, we inserted the tip of needle central region of the PALN and SiLN for 5 min. The sampling rate was 0.02 s, and obtained IFP as a mean value.

Corresponding author: Kazu Takeda
*E-mail address*: kazu.takeda@bme.tohoku.ac.jp

## 3. Result and Discussion

Figure 2 shows the luciferase activity of KM-Luc/GFP cells in the SiLN and PALN (Fig.2A was control, Fig.2B was on day 3 and Fig.2C was on day 6). The luciferase activities increased in both lymph nodes over time, and metastasis was detected on day 6. And Figure 3 shows changes of IFP in SiLN and PALN, where PBS injection was used as control. IFP of SiLN was higher than that of PALN. IFP in the both LNs also increased over time. These results indicate that there is a relation between the elevated IFP and increased cell number.

## 4. Concluding Remarks

We demonstrated that IFP increase in the lymph nodes in the early stages of metastasis. IFP will be used for diagnosis of LN metastasis in clinical settings.

## Reference


[1] Hanahan, D. & Weinberg, R. A. *Cell 100*, (2000) 57-70.

[2] Jain, R. K. & Stylianopoulos, T. *Nature reviews. Clinical oncology 7*, (2010) 139.

[3] Padera TP, Kadambi A, di Tomaso E, Carreira CM, Brown EB, Boucher Y, Choi NC, Mathisen D, Wain J, Mark EJ, Munn LL, Jain RK. *Science 296*, (2002) 1883-1886.

[4] Li L, Mori S, Sakamoto M, Takahashi S, Kodama T. *PloS one 8*, (2013) 0055797.

[5] Shao, L, Mori S, Yagishita Y, Okuno T, Hatakeyama Y, Sato T, Kodama T. *Journal of immunological methods 389,* (2013) 69-78.


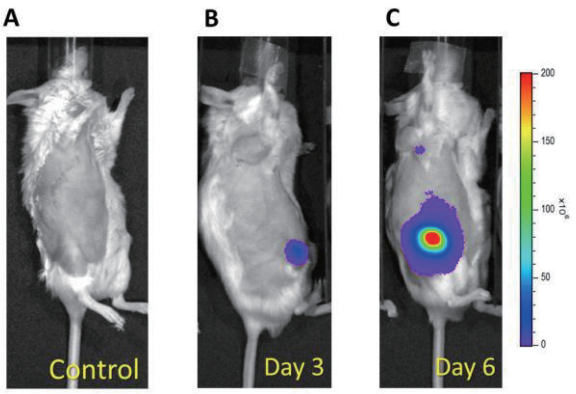


Fig. 2 Changing of Luciferase activities in LNs. There is almost no luciferase activities in control group, A. Metastasis to PALN was detected on day 6. The luciferase activities increased in both LNs, but SiLN was higher than PALN.

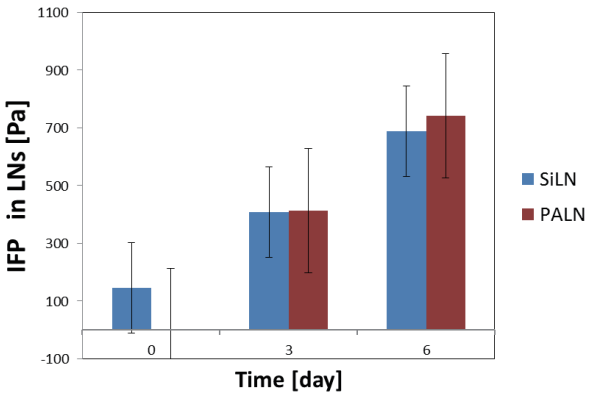


Fig. 3 IFP measurement in the SiLN and PALN. IFP value in the both lymph node increased over time. IFP was elevated in the PALN before metastasis was detected on day 3.

Eleventh International Conference on Flow Dynamics
October 8-10, 2014, Sendai, Miyagi, Japan

# EPTFE Valve Dynamics in the Pulmonary Mock Circulatory System

Yasuyuki Shiraishi[1], Yusuke Tsuboko[1], Ichiro Suzuki[2], Satoshi Matsuo[3], Yoshikatsu Saiki[3], Tomoyuki Yambe[1], Masaaki Yamagishi[4], Yi Qian[5]
[1]Department of Medical Engineering and Cardiology, Institute of Development, Aging and Cancer, Tohoku University
4-1 Seiryo-machi, Aoba-ku, Sendai 980-8575, Japan
[2]Sendai Open Hospital
5-22-1 Tsurugaya, Miyagino-ku, Sendai 983-0824, Japan
[3]Department of Cardiovascular Surgery, Graduate School of Medicine, Tohoku University
2-1 Seiryo-machi, Aoba-ku, Sendai 980-8575, Japan
[4]Department of Cardiovascular Surgery, Kyoto Prefectural University of Medicine
Kajii-cho, Kawaramachi-Hirokoji, Kamigyo-ku, Kyoto 602-8566, Japan
[5]Australian School of Advanced Medicine, Macquarie University
2 Technology Place, Sydney, NSW 2109, Australia

**ABSTRACT**

An expanded polytetrafluoroethylene (ePTFE) pulmonary arterial heart valve is clinical available. The valve design was anatomically identical and it consisted of the fan-shaped trileaflet valve with bulging sinuses on the ePTFE conduit. In this paper, the authors examined the ePTFE valve motion as well as hemodynamics in the mechanical pulmonary circulatory system. Consequently, it was indicated that the mechanical and fluid dynamics interactive relations between the leaflet and wall shapes in the vicinity of valve might be effective parameters for the improvement of valve function.

## 1. Introduction

Recently, an artificial right ventricular outflow tract reconstruction (RVOTr) has been one of the common surgical treatment of the patients with severe right heart failure (Fig. 1). An expanded polytetrafluoroethylene (ePTFE) valve (Fig. 2) exhibited excellent clinical outcomes in Japan with low ratio of freedom from reoperation in the long-term follow-up study [1]. The special features of the valve were as follows: a) an anatomically identical trileaflet valve, and b) bulging sinuses structure on the ePTFE conduit. The leaflet was cut off from an ePTFE pericardial sheet and formed to be fan-shape. The leaflets were to be sutured along with the bulging bottom lines as in the natural Valsalva structure of the pulmonary valve. It was anticipated that the important design parameters providing good valvular functions were the shapes of leaflet and the size of bulging sinuses because of the different elastic characteristics in the polymer materials from the native pulmonary valve. In this study, we focused on the leaflet motions along with the bulging sinus structure as well as fluid dynamic properties in the vicinity of the valve under the pulsatile flow condition which could be simulated in the mechanical pulmonary circulatory system. As the valves are commonly applied for the reconstruction of congenital heart failure, we set the driving conditions of the circulatory system as to be small sized patients' hemodynamics. We also calculated the internal pressure distributions in the bulging structure based on the scanned data by the CT, and compared the hemodynamic effects by the bulging structure in the ePTFE valve on the leaflet dynamic motions during systole and closing phase of the valve.

Corresponding author: Yasuyuki Shiraishi
*E-mail address*: shiraishi@idac.tohoku.ac.jp

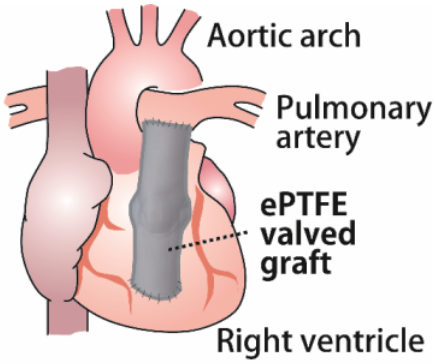


Fig. 1 Schematic illustration of the right ventricular outflow tract reconstruction (RVOTr) with the extracaradiac conduit shown as an ePTFE (expanded polytetrafluoroethylene) valved graft. The surgical bypass from the right ventricle and the main trunk of pulmonary artery can supply blood flow in the patients with heart failure caused by stenosis or malformation at the pulmonary valve portion.

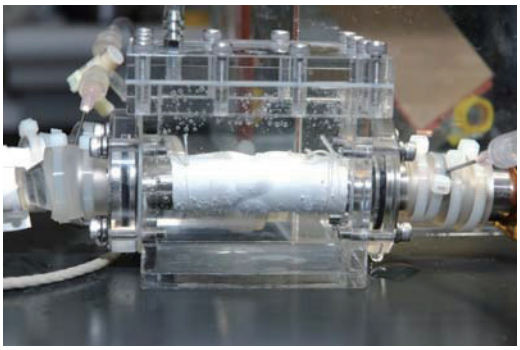

Fig. 2 The ePTFE pulmonary valve with bulging sinuses connected to the mechanical pulmonary circulatory system

## 2. Method

(1) Mechanical pulmonary circulatory system for valve testing

As the pulmonary valvular surgical treatments were generally performed from the small sized children, the specifications on the mechanical circulatory system was set to be capable of simulating pediatric patients' hemodynamic condition [2]. Special features of the system were as follows: a) a pneumatic driven right ventricle made of silicone rubber, b) a valve visualization port with connectors, and c) a pulmonary resistive unit, as shown in Fig. 3. The inflow portion of the right ventricular model was connected to the right atrium model with a polymer bileaflet valve, and the outflow portion could be pulmonary valve unit in which we could install the ePTFE valve.

(2) Comparison of the flow characteristics by the effects of bulging sinuses

Transvalvular pressure and flow could be measured simultaneously and digitally recorded at the sampling rate of 1 kHz. Two different types of the valves, the standard fan-shaped ePTFE valve with bulging sinuses and the ePTFF valve in the straight conduit which was to be a control, were used in the hemodynamic study. Root mean square flow was measured and the effective orifice area was calculated in each valve under the pediatric pulmonary flow condition at 0.9 L/min at the pump rate of 60 and 120 bpms. Then we compared the characteristics of the valves from the fluid dynamic point of view.

(3) Computational analyses for the changes in shapes of conduit wall

As the effect of shapes of bulging sinuses on the conduit wall on hemodynamic and fluid dynamics in the vicinity of valve leaflet, we performed the computational analyses of the ePTFE valve by ANSYS. Prior to the calculation, we obtained the structural data of the ePTFE valved conduit by the microfocus X-lay CT (ScanXmate, Comscan Techno, Japan). Then the wall share stress or pressure gradient distributions were obtained based on the 3-D data.

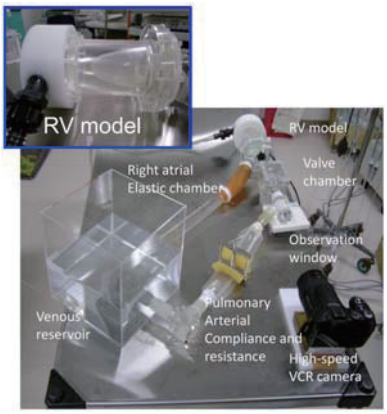


Fig. 3 Whole view of the mechanical pulmonary circulatory model for testing the ePTFE valves

## 3. Results and Discussion

Figure 4 shows the relationships between the Reynolds number (Re) and the effective orifice area calculated from the transvalvular pressure and flow with the different root mean square flow at the systole. The changes in Re at the straight conduit valve was smaller than those obtained at the valve with bulging sinuses, and the values at low flow of the straight conduit was higher than that with the bulging valve. Effective orifice areas might provide the information of valvular leaflet motion during systole, and it was suggested that the bigger opening and lower resistive motions could be achieved at the valve with bulging sinuses. Moreover, the result from numerical analyses indicated that the higher share rate could be observed after a backward regions at the bulging sinuses (Fig. 5). Therefore, it was indicated that the shape of bulging sinuses should be taken into consideration as well as the sophisticated design of the valve leaflet including coaptation zones.

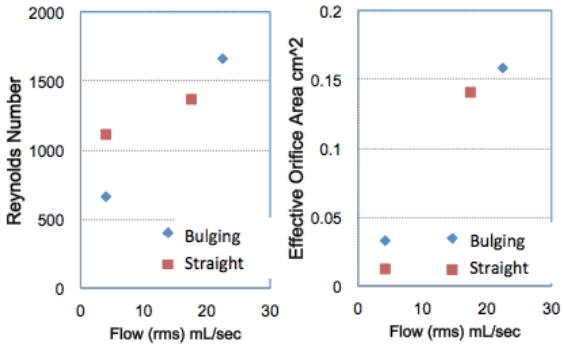


Fig. 4 Relationships between the Re and flow (left) and the effective orifice area and flow (right) obtained at the two different types conduit valves.

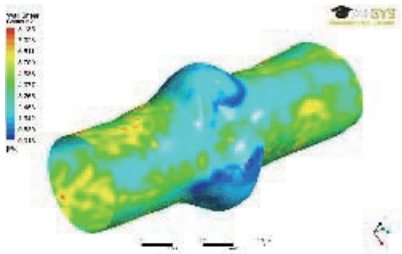

Fig. 5 An example of the wall share stress calculated from the shape with bulging sinuses derived from the CT measurement. Colour distribution indicated the wall stress and the large stress (shown as warm colour) could be investigated on the conduit wall along with the bulging sinuses at the outflow portion of the valve.

## References

[1] Miyazaki T, Yamagishi M, Maeda Y, Yamamoto Y, Taniguchi S, Sasaki Y, Yaku H. *JTCS*, 142(5) (2011) 1122－1129.

[2] Suzuki I, Shiraishi Y, Tsuboko Y, Sugai TK, Kameyama T, Saijo Y, Umezu M, Feng Z, Miyazaki T, Yamagishi M, Yambe T. *J Artif Organs*, 15(1) (2012) 49－56.

# Nanoparticle Mediated Laser Irradiation of Pig Lung as a Function of Respiration

Rupesh Singh[1], Subhash C. Mishra[1]
[1]Department of Mechanical Engineering, Indian Institute of Technology Guwahati,
Guwahati, Assam, 781039, India

**ABSTRACT**

Hyperthermia treatment of lung cancer is modeled and studied. Gold silica nanoshells infusion is used for enhancing absorption of lung tissue as well as for selective targeting. Because of varying optical properties, lung volumes during different cycles of respiration are considered. Effect of continuous wave laser irradiation on cylindrical lung with nanoshell infused tumor on temperature evolution is analyzed.

## 1. Introduction

Lung cancer is an emerging health concern for developing nations. Research and innovation in lung cancer treatment has increased over the past decade. Laser induced hyperthermia treatment of lung cancer is as emerging and promising method of treatment. In the present study, a lung with tumor is modelled for laser induced hyperthermia. Respiratory lung volumes are considered for accurate modelling. Gold-silica nanoshells infusion in tumor is studied for selective targeting of tumor.

## 2. Method

A 2-D axisymmetric cylindrical tissue-tumor geometry is considered for simulation (Fig. 1). Laser of wavelength 632.8 nm is irradiated at the top surface of cylindrical tissue. Pennes bioheat transfer equation is used for modelling heat transfer in biological tissue. For 2-D axisymmetric cylindrical tissue, Pennes bioheat equation is given by:

$$\rho c_p \frac{\partial T}{\partial t} = k\left[\frac{1}{r}\frac{\partial}{\partial r}\left(r\frac{\partial T}{\partial r}\right)+\frac{\partial^2 T}{\partial z^2}\right]+\eta_b \rho_b c_{pb}\left(T_a - T\right) + Q_m - \nabla \cdot q_r \quad (1)$$

where $\rho_b$ is the density, $c_b$ is the specific heat of the blood, $T_a$ is the arterial blood temperature and $Q_m$ is the metabolic heat generation rate. In Eq.1, $\rho, c_p$ and $k$ are the density, the specific heat, and the thermal conductivity of the tissue, , respectively, and $T$ is the tissue temperature.

The radiative source term appearing as divergence of radiative heat flux in Eq.1 is calculated by solving the radiative transfer equation, which is given by [1,2]:

$$\frac{\partial I}{\partial s} = -\beta I + \kappa_a I_b + \frac{\sigma_s}{4\pi}\int_{\Omega'=4\pi} I(\Omega')\, p\left(\Omega,\Omega'\right) d\Omega' \quad (2)$$

where $s$ is the distance in the direction $\hat{s}$, $\kappa_a$ is the absorption coefficient, $\sigma_s$ is the scattering coefficient, and $p$ is the scattering phase function.

The finite volume method is used for solving Eq. 1 and the discrete ordinate method is used for solving Eq. 2.

Corresponding author: Subhash C. Mishra
*E-mail address*: scm_iitg@yahoo.com

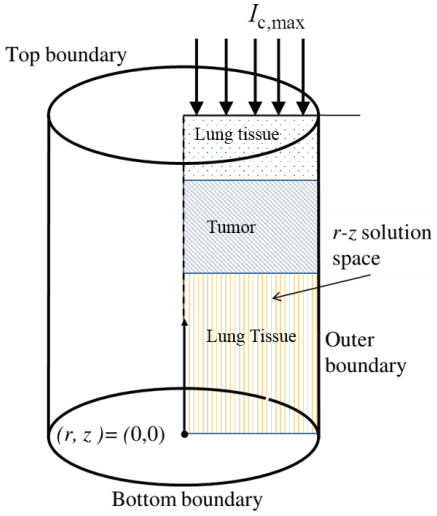


Fig. 1 Schematic of a 2-D axisymmetric cylindrical tissue tumor geometry.

## 3. Results and Discussion

For a radius of 3 mm and tissue height of 8 mm (with tumor height of 2 mm), for laser irradiation of wavelength 632.8 nm, tissue temperature was calculated by solving Eq. 1. The laser exposure time of 2 s was selected for continuous wave laser with beam radius of 1 mm. A laser power of 4 W was used. Nanoshell infusion with volume fraction $10^{-7}$ was used and the enhanced optical properties viz. absorption coefficient and scattering coefficient were calculated using Eq. 3 and Eq. 4, respectively [3,4].

$$\kappa_a = \kappa_{a,t} + 0.75 f_v \frac{Q_a}{a} \quad (3)$$

$$\sigma_s = \sigma_{s,t} + 0.75 f_v \frac{Q_s}{a} \quad (4)$$

where $Q_a$ and $Q_s$ are the dimensionless efficiency factors of for single particle, $f_v$ is the specific volume fraction of the tissue-nanoshell and $a$ is the radius of the nanoshell. The absorption coefficient and scattering coefficient using Eq. 3 and Eq. 4 come out to be 9.533 and 0.7871, respectively.

Using the thermophysical and optical properties of

Table 1 and Table 2, and optical properties of nanoshell infused tumor from above, the centerline temperature distribution is obtained for lung tissue-tumor cylindrical geometry. For laser exposure time of 2 s, temperature evolution for different stages of respiratory volume are presented in Fig. 2.

Table 1. Thermophysical properties of lung tissue and tumor.

| Properties | Lung | Tumor |
|---|---|---|
| $k\left(\mathrm{W/m\cdot K}\right)$ | 0.51 | 0.558 |
| $\rho_{tissue}\left(\mathrm{kg/m^3}\right)$ | 1085 | 1030 |
| $c_p\left(\mathrm{J/kg\cdot K}\right)$ | 3800 | 3582 |
| $Q_m\left(\mathrm{W/m^3}\right)$ | 684.2 | 9000 |

Table 2. Optical properties of pig lung tissue

| Lung volume (ml) | $\kappa_a\,(1/\mathrm{mm})$ | $\omega$ |
|---|---|---|
| 25 | 30.0134 | 0.9995 |
| 50 | 32.5005 | 0.9998 |
| 100 | 25.2002 | 0.9999 |
| 150 | 21.2018 | 0.9959 |

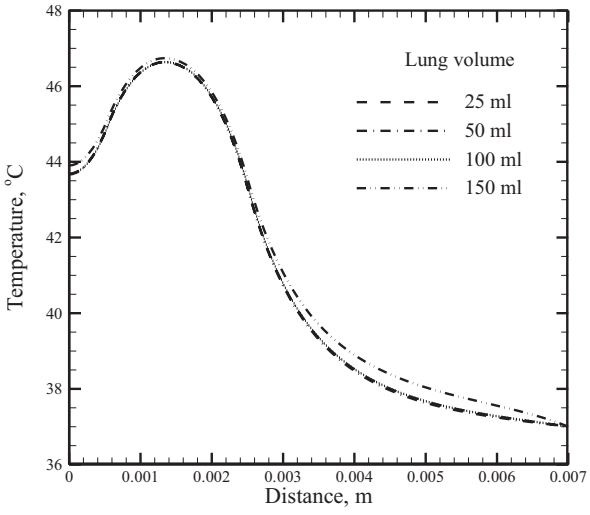


Fig. 2 Centerline temperature distribution of lung tissue with nanoshell infused tumor at time 2 s, for different lung volumes; Laser power = 4 W, beam radius = 1 mm.

For two lung volumes of 25 ml and 150 ml, 2-D temperature contours are shown in Fig. 3 (a) and Fig. 3 (b), respectively. Temperature rise in the tumor is observed to be higher than other tissue regions. While centerline temperature plot doesn't show much variation for different lung volumes, the difference is visible in 2-D Contour plots.

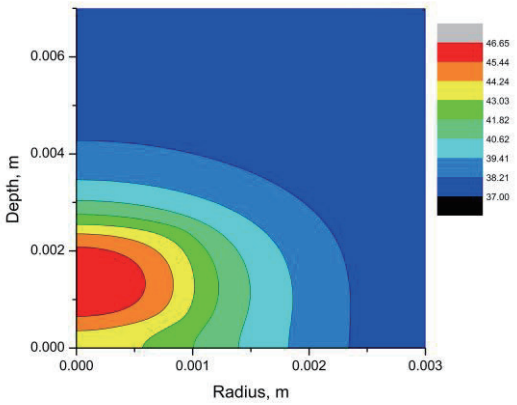


(a)

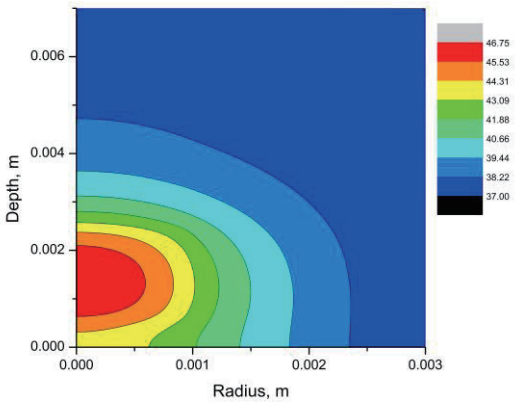


(b)

Fig. 3 2-D temperature contour of laser irradiated lung tissue with tumor at exposure time 2 s, for lung volume (a) 25 ml and (b) 150 ml.

## 4. Concluding Remarks

Temperature evolution during laser irradiation on pig's lung with nanoshell infused tumor was studied for different stages of respiratory lung volumes. High temperature in tumor region is observed for lung volume of 150 ml.

## References


[1] S.C. Mishra, R. Singh, P. Agarwal, C. Krishna, *Numerical Heat Transfer, Part A: Applications,* 66 (2014), 884-903.

[2] A. Bhowmik, R. Repaka, S.C. Mishra, K. Mitra, *International Journal of Heat and Mass Transfer,* 68(2014), 278-294.

[3] J. F. Beekyx, H. J. van Staverenz, P. Posthumusy, H. J. C. M. Sterenborgy, M. J. C. van Gemerty, *Physics in Medicine and Biology*, 42(1997), 2263–2272.

[4] L. A. Dombrovsky, V. Timchenko, M. Jackson, *International Journal of Heat and Mass Transfer*, 55(2012), 4688–4700.

Eleventh International Conference on Flow Dynamics
October 8-10, 2014, Sendai, Miyagi, Japan

# Patient specific simulation on focused ultrasound ablation of liver tumor

Maxim A. Solovchuk [1], Tony W.H. Sheu [1], Marc Thiriet[2].
[1] Center of Advanced Study in Theoretical Sciences (CASTS), National Taiwan University
No. 1, Sec. 4, Roosevelt Road, Taipei, Taiwan 10617, Republic of China
[2] Sorbonne Universities, UPMC Univ Paris 06, UMR 7598
Laboratoire Jacques-Louis Lions, F-75005, Paris, France

**ABSTRACT**

The present study is aimed at predicting the temperature during a high-intensity focused ultrasound (HIFU) thermal ablation in a patient-specific liver geometry. The model comprises the nonlinear Westervelt equation with relaxation effects being taken into account and bioheat equations in liver and blood vessels. The nonlinear hemodynamic equations are also considered with the convected cooling and acoustic streaming effects being taken into account. The results presented in the current work can be further used to construct a surgical planning platform.

## 1. Introduction

Liver cancer is the second leading cause of cancer death in men [1,2] and the sixth leading cause among women in the world. In 2008 around 748 300 patients suffered liver disease in the world [2]. At an early stage liver cancer can be successfully treated with surgery or liver transplantation. For a patient diagnosed at an advanced stage of disease fewer surgical options exist. High intensity focused ultrasound (HIFU) is a promising method for the tumor ablation and it can be used when other methods cannot be applied. Temperature 56 $^0$C for one second heating causes irreversible tissue damage [3] and this fact is the explanation for the ablation of tumor.

Ultrasound beam should be properly focused to heat the tumor and avoid the damage of the healthy tissues. The primary problem in the thermal ablation therapy of liver tumor is due to a heat sink resulting from the blood flow in large blood vessels; therefore more energy is necessary for the ablation of tumor close to blood vessel. This can lead to the use of redundant ultrasound powers and undesirable damage of healthy tissues. Special care should be taken to avoid destruction of vessel walls by a high temperature. Recently, three-dimensional acoustic-thermal-hydrodynamic coupling model has been proposed [4].

The model can be used to predict liver tumor temperature in a patient specific liver geometry. Computational model can play an important role in the planning and optimization of the treatment based on the patient's image.

## 2. Method

The three-dimensional (3D) acoustic-thermal-hydrodynamic coupling model is proposed to compute the pressure, temperature, and blood flow velocity.

Acoustic field generated by a HIFU source was modeled using the nonlinear Westervelt equation (1). In the above, $p$ is the sound pressure, $\beta$ is the coefficient of nonlinearity, and $\delta$ is the diffusivity of sound resulting from viscosity and heat conduction, $\tau_n$ is the relaxation time and $c_n$ is the small signal sound speed increment for the $n$-th relaxation process. The first two terms describe the linear lossless wave propagating at a small-signal sound speed. The third term denotes the loss due to thermal conduction and fluid viscosity, and the fourth term accounts for the relaxation processes. The last term accounts for acoustic nonlinearity which may considerably affect thermal and mechanical changes within the tissue.

$$\nabla^2 p - \frac{1}{c_0^{\,2}}\frac{\partial^2 p}{\partial t^2} + \left[\frac{\delta}{c_0^{\,4}} + \frac{2}{c_0^{\,3}}\sum_{i=1}^{2}\frac{c_i\tau_i}{1+\tau_i\dfrac{\partial}{\partial t}}\right]\frac{\partial^3 p}{\partial t^3} + \frac{\beta}{\rho_0 c_0^{\,4}}\frac{\partial^2 p^2}{\partial t^2} = 0. \quad (1)$$

In the current simulation of thermal field the physical domain has been split into the domains for the perfused tissue and the flowing blood.

In a region free of large blood vessels, the diffusion-type Pennes bioheat equation given below will be employed to model the transfer of heat in the perfused tissue region

$$\rho_t c_t \frac{\partial T}{\partial t} = k_t \nabla^2 T - w_b c_b (T - T_\infty) + \mathbf{q}. \quad (2)$$

In the above bioheat equation proposed for modeling the time-varying temperature in the tissue domain, ρ, $c$, $k$ denote the density, specific heat, and thermal conductivity, respectively, with the subscripts $t$ and $b$ referring to the tissue and blood domains. The notation $T_\infty$ is denoted as the temperature at a remote location. The perfusion rate for the tissue cooling in capillary flow is $w_b = 0$. The above bioheat equation for $T$ is coupled with the Westervelt equation (1) for the acoustic pressure through a power deposition term $q$.

In the region containing large vessels, within which the blood flow can convect heat, the biologically

Corresponding author: Maxim A. Solovchuk
*E-mail address*: solovchuk@gmail.com

relevant heat source, which is $q$, and the heat sink, which is $\rho_b c_b \vec{\mathbf{u}} \cdot \nabla T$, are added to the conventional diffusion-type heat equation. The resulting energy equation given below avoids dealing with the high recurrence situation stemming from the tumor cell survival next to large vessels

$$\rho_b c_b \frac{\partial T}{\partial t} = k_b \nabla^2 T - \rho_b c_b \vec{\mathbf{u}} \cdot \nabla T + \mathbf{q}. \quad (3)$$

To simulate blood flow velocity inside the blood vessel nonlinear hemodynamic equations was considered

$$\frac{\partial \vec{u}}{\partial t} + (\vec{u} \cdot \nabla)\vec{u} = \frac{\mu}{\rho}\nabla^2 \vec{u} - \frac{1}{\rho}\nabla P + \frac{\mathbf{1}}{\boldsymbol{\rho}}\vec{\mathbf{F}} \quad (4)$$

In the above, P is the static pressure, μ(= 0.0035 kg/m s) the shear viscosity of blood flow, and ρ the blood density. In Eq. (16), the force vector ***F*** acting on the blood fluid due to ultrasound is assumed to act along the acoustic axis n. The resulting nonzero component in ***F*** takes the following form

$$\vec{\mathbf{F}} \cdot \vec{n} = \frac{1}{c_0}\sum_n 2\alpha(nf) I_n \quad (5)$$

### 3. Results and Discussion

Nonlinear Westervelt equation (1) for acoustic pressure is solved using finite difference method [4]. The acoustic pressure was calculated only once for a given set of transducer parameters. Afterward ultrasound power deposition and acoustic streaming force were determined and stored. Blood flow velocity was computed from Eq. (4) at every time step with the acoustic streaming effect being taken into account and then substituted to the bioheat equation (3). With the known blood flow velocities and power deposition terms, temperatures in blood flow domain and in liver were calculated. A detailed description of the solution procedures can be found in our previous articles [4-6].

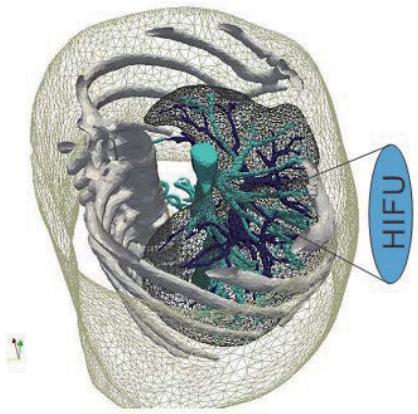


Fig. 1 Patient specific 3D geometry reconstructed from CT images

In this study the single element HIFU transducer is used with an aperture of 12 cm and a focal length of 12 cm, frequency 1 MHz. The solid tumor was assumed to be exposed to a 0.4 s ultrasound. The present numerical experiments are carried out in a patient specific liver model reconstructed from CT images. A reconstructed surface mesh for the hepatic vein, portal vein and liver is presented in Fig. 1.

The simulated temperature contours in tumor and in the portal vein at the cutting plane *z=0.16* are presented in Fig. 2 at time t=0.4 s (end of sonication). The temperature 56 $^0$C can be achieved on the blood vessel wall, therefore tumor close to blood vessel can be ablated. There is a very sharp temperature gradient near the blood vessel wall. The temperature inside the blood vessel remains almost unchanged except in the boundary layer close to the focal point. Therefore focused ultrasound can be a safe therapy to ablate tumors close to blood vessel wall.

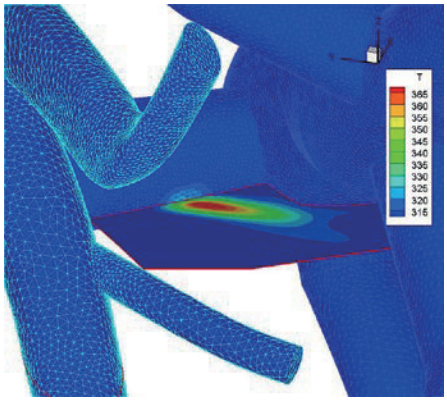


Fig. 2 Temperature contours in tumor and in portal vein at the selected cutting plane *z = 0.16* m.

### 4. Concluding Remarks

The proposed three dimensional physical model for HIFU study was conducted in an image-based liver geometry. It was shown that tumors near the blood vessel wall can be ablated without damaging blood vessel wall. These results can be further used to construct a surgical planning platform for the non-invasive HIFU tumor ablating therapy in real liver geometry and can lead in the future to a substantial improvement of the focused ultrasound ablation of liver tumor. The presented model can be used in planning tools for the thermal ablation of tumor in other organs.

### References

[1] J.S. Huang, D.A. Gervais, P.R. Mueller, *Chinese J. Radiology*, 26 (2001) 119-134.
[2] American Cancer Society. Global cancer facts and figures. Atlanta, GA: 2nd edition. American Cancer Society; 2011.
[3] N.T. Wright, J.D. Humphrey, *Annu. Rev. Biomed. Eng.*, 4 (2002) 109-128.
[4] M.A. Solovchuk, T.W.H. Sheu, M. Thiriet, *J. Acoust. Soc. Am.*, 134 (2013) 3931-3942.
[5] M.A. Solovchuk, T.W.H. Sheu, M. Thiriet, W.L. Lin, *Applied Thermal Engineering*, 56 (2013) 62-76.
[6] M.A. Solovchuk, S.C. Hwang, H. Chang, H., M. Thiriet, T.W.H. Sheu, Medical physics, 41 (2014) 052903.

# The Effect of Contact Force on Electrode Temperature and Internal Tissue Temperature during Ablation with a Vibrating Catheter

Kaihong Yu[1], Tetsui Yamashita[2], Shigeaki Shingyochi[3], Makoto Ohta[4]
[1] Graduate School of Biomedical Engineering, Tohoku University
6-6-12, Aoba, Aramaki, Aoba-ku, Sendai, 980-8578, Japan
[2] JMS CO., LTD.
1-13-5, Minamiohi, Shinagawa, Tokyo, 140-0013, Japan
[3] R&D CENTER, NIDEC COPAL ELECTRONICS CORP.
2188, Akami, Sano, Tochigi, 327-0104, Japan
[4] Institute of Fluid Science, Tohoku University
2-1-1, Katahira, Aoba, Sendai, 980-8577, Japan

**ABSTRACT**

The electrode-tissue interface overheating may cause serious complications such as thrombus. The authors have proposed a new method for preventing the overheating by making the catheter vibrating. In this study, we looked into the effect of contact force during ablation with vibration by temperature measurement using an in-vitro system. Increasing the contact force from 2 gf to 10 gf may keep the effect of electrode cooling and tissue heating during ablation with vibration. More experiments with the heavier contact force are necessary for the future study.

## 1. Introduction

Radiofrequency (RF) catheter ablation is a highly effective treatment for many cardiac tachycardias. During catheter ablation, a catheter with an electrode on the tip is inserted into the heart through blood vessels and placed at the target place which causing the heart rhythm disorder. Then RF current generated by a RF generator is delivered to the target cardiac tissue through the electrode on the catheter. The cardiac tissue is heated by the Joule heat and thermal conduction. A tissue temperature ≥50°C causes irreversible loss of cellular excitability and forms a lesion [1]. Consequently, the abnormal heart tissue is destroyed by RF energy.

Deeper lesion is necessary for postinfarction ventricular tachycardia because the target tissue can be located deep to the endocardium [2]. Lesion size can only be increased by using higher power. However, high power delivery causes the electrode-tissue interface overheating (interface temperature ≥80°C) which may lead to serious complications such as thrombus. Therefore, allowing higher power delivery to cardiac tissue with overheating becomes a key issue for postinfarction ventricular tachycardia.

Currently, temperature-control, larger electrode and active electrode cooling by open irrigation, these three strategies have been generally accepted to prevent the overheating at electrode-tissue interface during high power delivery. In temperature-control approach, a thermistor and a feedback system are used to deliver the maximum power which maintains the electrode temperature at a target value (55°C or 60°C). The interface overheating is limited by the maintained electrode temperature. The electrode temperature is a result of heating from the contacted tissue and cooling from surrounding blood flow. Under temperature-control, high power delivery is ineffective in low blood flow, because the cooling from blood flow decreases, the output power also decreases to maintain the electrode temperature at the target value. Larger electrode (8 mm or 12 mm length) has larger electrode surface which increase the convective cooling from blood. However, the convective cooling increase is effective only under temperature-control. The effect of larger electrode is also limited in low blood flow. In open irrigation, the saline in room temperature is flushing from the holes arranged in the electrode. The saline cools electrode, surrounding blood and tissue surface. This active cooling by irrigation allows high power delivery to cardiac tissue with significantly low incidence of thrombus formation even in low blood flow. However, about 1500 ml saline infusion during open irrigation can aggravate heart failure or pulmonary edema.

For the low blood flow situations when open irrigation cannot be used, a new method for the overheating prevention may be needed. We think active electrode cooling can be increased without using cooling fluid. And we proposed a new active electrode cooling by making the catheter vibrating to increase the convective cooling from blood flow. In our previous work, we looked into the effect of vibration frequency on electrode temperature using an in-vitro system with PVA-H as ablated tissue and saline flow in an open channel. RF ablation with vibration shows a decrease on electrode temperature, and the higher frequency shows the lower electrode temperature. It proves that ablation with vibration can increase the effect of electrode cooling, and the higher frequency increase electrode cooling more. We also observed the flow around the catheter by Particle Image Velocimetry (PIV) method to look into the mechanism of the cooling effect by vibration. From PIV analysis, the vibrations disturbed the flow around the catheter, and the flow velocity around the catheter is higher with the higher frequency. The vibration decrease the electrode temperature may result form that the vibration could increase the flow velocity around the catheter.

Besides vibration frequency, contact force between

Corresponding author: Kaihong Yu
*E-mail*: kaihongmr_yu@biofluid.ifs.tohoku.ac.jp

electrode-tissue is also a major factor which may affect the electrode cooling by vibration. The purpose of this study is to investigate the effect of contact force on electrode cooling and tissue heating during ablation with vibration. By using an in-vitro system developed for vibrating catheter, we measured electrode temperature and internal tissue temperature under different contact forces and various vibration frequencies without flow condition.

## 2. Method

Instead of using animal myocardium which used in many previous researches, we used PVA-H as ablated tissue for the following advantages: The high transparency makes PVA-H is easily to insert thermocouple accurately; PVA-H also has dynamic viscoelasticity similar to biological soft tissue; And the catheter can contact with the PVA-H surface in a manner similar to its mode of contact with heart tissue [3]. The in vitro ablation system is shown in Fig. 1. The open channel (built by acrylic boards, 500 × 50 × 20 mm) was filled with 0.9% saline. A K-type thermocouple (Hayashi Denko Co., Ltd.) with the diameter of 0.5 mm was located at a depth 2 mm from the surface to measure the internal PVA-H temperature. A 7 Fr catheter (Ablaze Single Directional Type, Japan Lifeline Co., Ltd.) with a 4-mm ablation electrode was set perpendicular to the PVA-H surface. The contact force between the electrode-tissues was measured by the electronic balance. The 2.2 gf and 10 gf were used as the light and normal contact. A RF current was introduced into the system at the room temperature. The output power was set at 8W, and the perform duration was 60s. Vibrations with amplitude of 0.5 mm and frequencies of 0, 31 Hz and 63 Hz were used in each contact force.

## 3. Results and Discussion

The electrode temperatures at 60 s under different contact force with various vibrations are shown in Fig. 2. With no vibration (0 Hz), the electrode temperature shows no difference between 2 gf and 10 gf. After the contact force increased, the contact area is the only parameter may be changed to affect tissue heating thus affect electrode temperature. The result of no difference between 2 gf and 10 gf suggests that increasing contact force from 2 gf to 10 gf may be not enough to increase the contact area of electrode and PVA-H surface. With 31 Hz and 63 Hz vibrations, the electrode temperatures also show no difference between 2 gf and 10 gf and the temperature decreases with increasing vibration frequency. After the contact force increased, the friction force between electrode and PVA-H may be increased during vibration. And the vibration frequency may be decreased by the increased friction force, and then the effect of electrode cooling may decrease. The result of no difference between 2 gf and 10 gf during vibrations suggests that increasing contact force from 2 gf to 10 gf may not affect the electrode cooling by vibration.

The internal 2 mm depth temperatures at 60 s under different contact force with various vibrations are shown in Fig. 3. For each contact force, the temperature decreases with the increasing vibration frequency. These decreases may result from the constant energy is delivered to a larger ablated area expanded by vibration. The temperature with 10 gf is slightly higher than with 2 gf at each frequency. And the increased temperature from 2 gf to 10 gf at each frequency is same. The same electrode temperature with no vibration already suggests that no difference in tissue heating with these two contact force. These same slight increases may result from the depth from the inserted thermocouple to electrode tip has been slightly reduced by the increased contact force. And the internal temperature is higher at the lower depth.

## 4. Concluding Remarks

Increasing the contact force from 2 gf to 10 gf may keep the effect of electrode cooling and tissue heating during ablation with vibration. More experiments with the heavier contact force are necessary for the future study.

## References


[1] Nath S, Lynch C, Whayne JG, Haines DE. *Circulation*, (1993) 88:1826–31.

[2] Svenson RH, Littmann L, Gallagher JJ, Selle JG, Zimmern SH, Fedor JM, Colavita PG. *J Am Coll Cardiol*., (1990) 15:163–70.

[3] Yu K, Yamashita T, Ohta M. *Ninth Int. Conf. Flow Dyn*., (2012) 616–7.


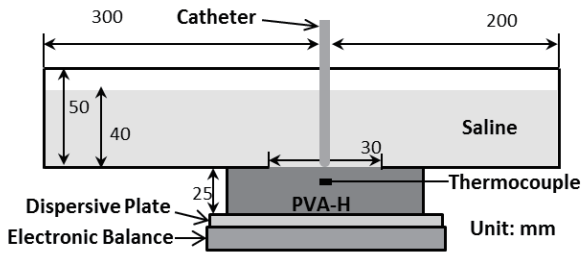


Fig. 1 Schematic diagram of the in vitro ablation system.

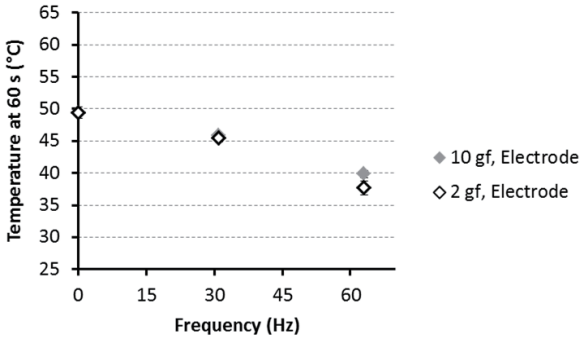


Fig. 2 Electrode temperatures at 60 s.

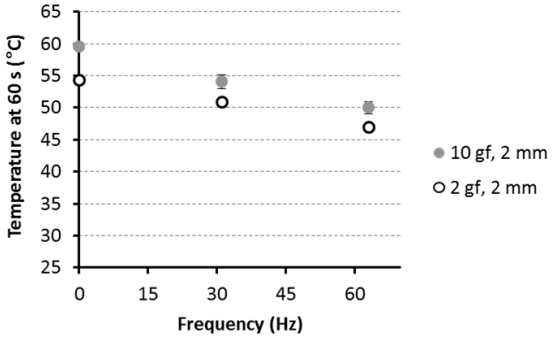


Fig. 3 Internal 2 mm depth temperature at 60 s.

# Wall Shear Stress Fluctuations in Disturbed Blood Flow: Calculation and Classification

Yuji Shimogonya[1], Kristian Valen-Sendstad[2], David A. Steinman[2]
[1]Frontier Research Institute for Interdisciplinary Sciences, Tohoku University
6-3 Aoba, Sendai, Miyagi, 980-8578, Japan
[2]Department of Mechanical & Industrial Engineering, University of Toronto
5 King's College Road, Toronto, Ontario, M5S 3G8, Canada

**ABSTRACT**

We propose a framework for classifying Wall Shear Stress (WSS) phenotypes in arterial disturbed blood flow, which consists of a permutation of WSS magnitude change, WSS angle change, and Time-Averaged WSS (TAWSS); a total of 9. The proposed framework is shown to be capable of distinguishing the phenotypically different WSS patterns.

## 1. Introduction

Recent High-Resolution (HR) Computational Fluid Dynamics (CFD) simulations have revealed that flow instabilities with high-frequency fluctuations can occur at relatively low Reynolds numbers in arterial blood flow [1]. Current indices designed to quantify disturbed Wall Shear Stress (WSS), such as Oscillatory Shear Index (OSI) [2] and transverse wall shear stress (transWSS) [3], sometimes fail to distinguish different types of highly disturbed WSS. Here we propose a framework for quantifying and distinguishing the WSS fluctuations adequately and demonstrate its capability.

## 2. Method

**CFD modeling**: Pulsatile CFD simulation was performed for an Internal Carotid Artery (ICA) model using an energy conservative and minimally dissipative second order accurate schemes with 30,000 time steps per cardiac cycle and quadratic tetrahedral meshes equivalent of 26 million linear elements.

**WSS Phenotype**: Fluctuations in instantaneous WSS vector at each node $x$ were decomposed into WSS magnitude and angle changes, with the angle $\phi$ defined relative to the Time-Averaged WSS (TAWSS) direction, integrated over the cardiac cycle, respectively. Then the proposed classification of WSS Phenotype consists of the following permutation of WSS_mag, WSS_ang, and TAWSS; a total of 9.

Table 1. Classification of the WSS Phenotype.

| Phenotype | WSS_mag | WSS_ang | TAWSS |
|---|---|---|---|
| **1** | L | L | L |
| **2** | L | L | M |
| **3** | L | L | H |
| **4** | Other than | | L |
| **5** | L-L and H-H | | M |
| **6** | combinations | | H |
| **7** | H | H | L |
| **8** | H | H | M |
| **9** | H | H | H |

L : Lower than respective 20th percentile value
M: Medium
H : Higher than respective 80th percentile value

Corresponding author: Yuji Shimogonya
*E-mail address*: yujish@pfsl.mech.tohoku.ac.jp

In Table 1, WSS_mag and WSS_ang are defined as follows.

$$WSS\_mag(\boldsymbol{x}) = \int_0^T \left| \frac{\partial |\boldsymbol{\tau}_w(\boldsymbol{x},t)|}{\partial t} \right| dt \quad (1)$$

$$WSS\_ang(\boldsymbol{x}) = \int_0^T \left| \frac{\partial \phi(\boldsymbol{x},t)}{\partial t} \right| dt \quad (2)$$

## 3. Results and Discussion

The polar plots in Figs. 1 and 2 show the temporal evolution of the WSS, i.e., the magnitude radially (plotted logarithmically) and the angle of the instantaneous WSS relative to the TAWSS direction. These temporal evolutions of the WSS represent actual signals predicted by the CFD model on the vessel wall that endothelial cells (ECs) may sense. The results show that many different signals can give rise to the identical numerical values for OSI and transWSS.

On the other hand, the WSS Phenotype classification

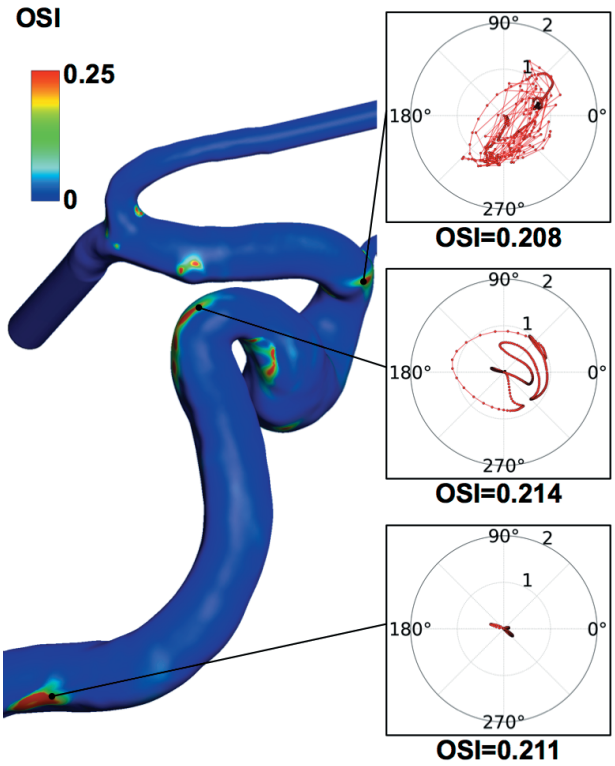


Fig. 1 Surface map of OSI and three selected WSS polar plots having almost the same value of OSI.

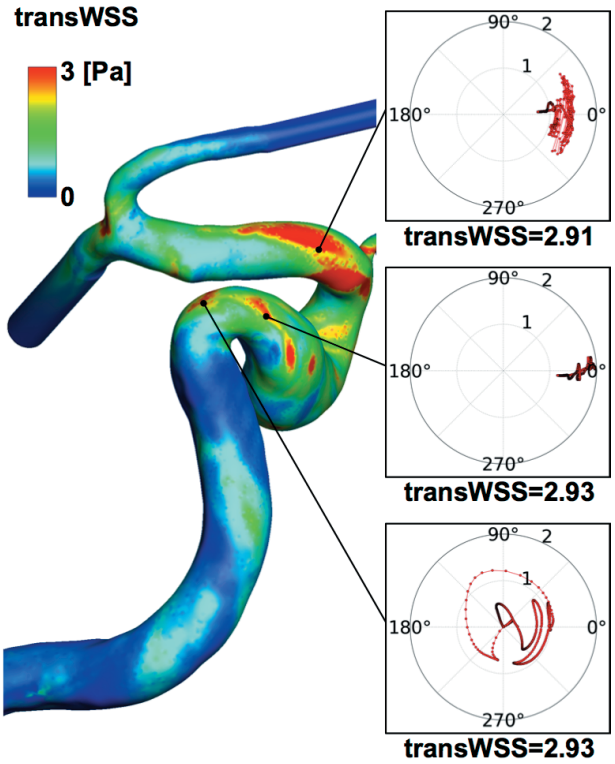


Fig. 2 Surface map of transWSS and three selected WSS polar plots having almost the same value of transWSS.

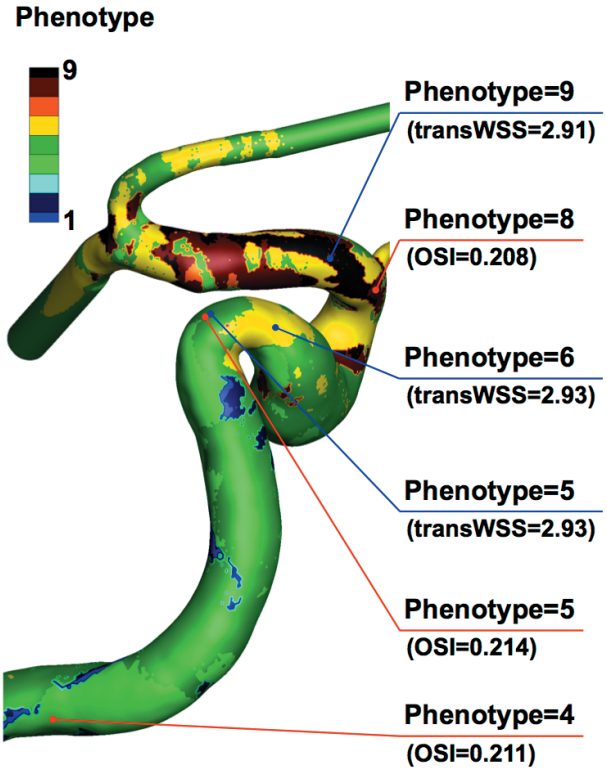


Fig. 3 Surface map of Phenotype and its local values at the six points selected in Figs. 1 and 2.

shown in Fig. 3 is capable of discriminating between the visually different cellular stimuli revealed by the polar plots. For example, flow visualizations showed relatively stable flow proximal to the siphon, destabilizing only towards the distal end of the siphon. This spatial evolution of flow complexity is evident in the Phenotype plot, but not the OSI plot. Spatial evolution of flow is seen for transWSS, but with non-specific hotspots at the upstream end of the siphon.

Several previous studies [4-6] have indicated that the dynamic character of biomechanical stimuli induced by blood flow has a vital role in the mechanotransduction and possible pathophysiological changes of arterial ECs. The results presented here demonstrated that Phenotype would be more sensitive to dynamic temporal fluctuations in WSS than OSI alone or transWSS alone, suggesting that the proposed classification of WSS phenotypes could be one of the useful ways to predict the character of the complex biomechanical stimuli to which the arterial ECs may be exposed.

The choice of thresholds for WSS magnitude change, WSS angle change, and TAWSS affects the Phenotype (data not shown). Since we still do not have a objective way to determine their thresholds, we set the lower and upper thresholds to their 20th and 80th percentile values, respectively. It will be needed, at least, to have a population of cases from which to determine the thresholds more objectively and to check the sensitivity.

## 4. Concluding Remarks

We have proposed a framework for quantifying and distinguishing the WSS fluctuations adequately and demonstrated its capability. The proposed framework will help us to investigate the roles of the phenotypically different blood flow-induced stimuli in the mechanotransduction and possible pathophysiological changes of the ECs for various vascular territories, in which wide variety of time-varying flows can coexist.

## Acknowledgements

This work was supported by a grant from the Heart & Stroke Foundation of Canada. DAS also acknowledges salary support from a Heart & Stroke Foundation Mid-Career Investigator award.

## References

[1] K. Valen-Sendstad, M. Piccinelli, D.A. Steinman, *J. Biomech.*, In Press.
[2] X. He, D.N. Ku, *J. Biomech. Eng.*, 118 (1996) 74-82.
[3] V. Peiffer, S.J. Sherwin, P.D. Weinberg, *J. Biomech.*, 46 (2013) 2651-2658.
[4] A.R. Brooks, P.I. Lelkes, G.M. Rubanyi, *Physiol. Genomics*, 9 (2002) 27-41.
[5] G. Garcia-Cardeña, J. Comander, K.R. Anderson, B.R. Blackman, M.A. Gimbrone, Jr., *PNAS.*, 98 (2001) 4478-4485.
[6] C.M. Prado, S.G. Ramos, J.C. Alves-Filho, J. Elias Jr., F.Q. Cunha, M.A. Rossi, *J. Hypertens.*, 24 (2006) 503-515.

# Enhancing Cell Free Layer Thickness by Bypass Channels in a Wall

Maryam Saadatmand[1], Takami Yamaguchi[2] and Takuji Ishikawa[1, 2]
[1]Department of Bioengineering & Robotics, Tohoku University
Aramaki Aza Aoba 6-6-01, Sendai 980-8579, Japan
[2]Department of Biomedical Engineering, Tohoku University
Aramaki Aza Aoba 6-6-01, Sendai 980-8579, Japan

**ABSTRACT**

When blood flows in microchannels, a cell free layer (CFL) is formed adjacent to the wall. This CFL is affected by the geometry of the microchannel, flow rate and hematocrit (Hct). It was shown in the previous study, that a stenosis in the channel could artificially enhance the CFL thickness. In this study, we propose to add bypass channels in a channel wall to increase the CFL thickness. Testing the bypass geometry with 5%Hct blood flow showed 1.3 times increase in CFL thickness compared to a case without the bypass. We believe that thicker CFL can be useful for plasma separation.

## 1. Introduction

Blood flow in microchannels shows several interesting phenomena, such as natural tendency of red blood cells (RBCs) to move away from the boundaries and form the cell free layer adjacent to the boundary [1]. During the last decade, this phenomenon has been applied to develop microfluidic systems for plasma separation and analysis [2,3]. Faivre et al. by varying the width and length of a constriction showed an enhancement of CFL downstream of the constriction region [4]. Fujiwara et al. also investigated the motion of RBCs in a microchannel with stenosis and showed an increase in CFL after the stenosis [5]. Here, we propose bypass channels in a channel wall to enhance CFL. Such a technology should be useful in biomedical engineering, because it can prevent adhesion of RBCs on medical devices and be utilized for the cell separation, etc.

## 2. Materials and Methods

The working fluid used in this study was dextran40 with 5% human RBCs.

The microfluidic device was made by polydimethyl-siloxane (PDMS) using conventional soft-lithography technique. It was sealed with glass cover after treatment of both surfaces with oxygen plasma (PIB-20, Vacuum Device, Japan). The geometry of the device is shown in Fig. 1. As shown, we made two microchannels in one device, one has two stenosis and bypass channels in the wall and the other only has two stenosis. The width of each microchannelis 680 $\mu$m and the device height is 20 $\mu$m.

The experimental set-up used in our experiment consists of an inverted microscope (IX71, Olympus, Japan) with an objective lens with a magnification of 20X (the same as previous study [5]). A syringe pump (KD Scientific Inc.) with 100 $\mu L$ syringe (Hamilton) was used to control the flow rate of blood at 1 $\mu$L/min. The images of the flowing blood were captured using a high-speed camera (phantom v7.1, USA). A thermo plate controller (Tokai Hit, Japan) was set to 37 ℃.

Corresponding author: Maryam Saadatmand
*E-mail address*: m.saadatmand@pfsl.mech.tohoku.ac.jp

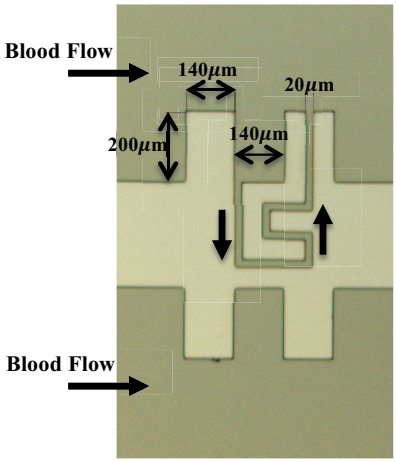


Fig. 1 The 2-dimensional geometry and dimensions of the microfluidic device.

Recorded images at the central plane of microchannels at a rate of 125 frames/s were evaluated with Image J (NIH) software. First, the captured video was converted to a sequence of static images. Using Z project function, an average image was obtained, in which each pixel showed the average intensity of all the sequence images [6]. Hence, a region of RBCs core is darker than the background (Fig. 2(a)). To measure the CFL thickness, the gray scale image was converted to binary image with a certain threshold. For an example, the CFL could be seen clearly in the binary image obtained after image processing, as in Fig. 2(b).

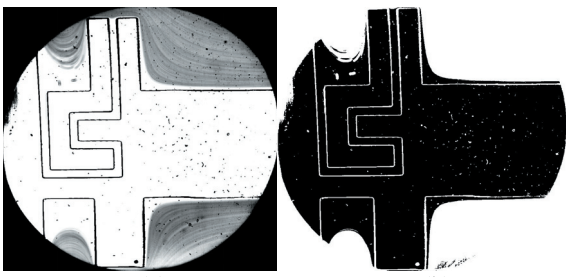

(a) (b)

Fig. 2 Images of RBCs; (a) The gray scale projected image, (b) The binary image obtained from the gray scale image

## 3. Results and Discussion

In this section, we show the blood flow pattern in the microfluidic device and evaluate the effect of bypass channels on the CFL thickness. Figure 3 shows a halogen -illuminated image of RBCs flowing in the device downstream the stenosis in both sides (with bypass and without bypass). As can be seen, the cell free layer thickness between the two stenosis is thick. Because of this as well as large viscous drag of the bypass channel (cross section of 20x20 $\mu$m, and the length of 1100 $\mu$m), the RBCs do not flow into the bypass, but only dextran40 flows into it.

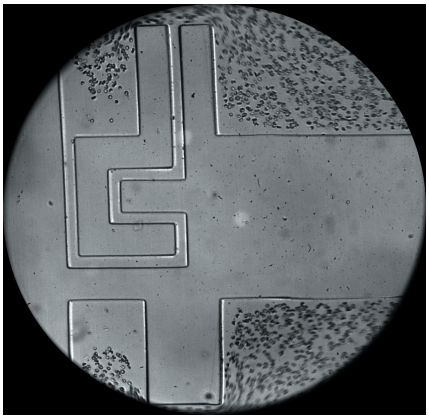

Fig. 3 A sample image of flowing RBCs in the microfluidic device.

By using the image analysis technique as described before, we automatically measured the CFL thickness after the stenosis in both sides. We did this analysis for four independent experiments. The CFL thickness is shown in Fig. 4, where x-axis is taken from the end of the stenosis in the flow direction.

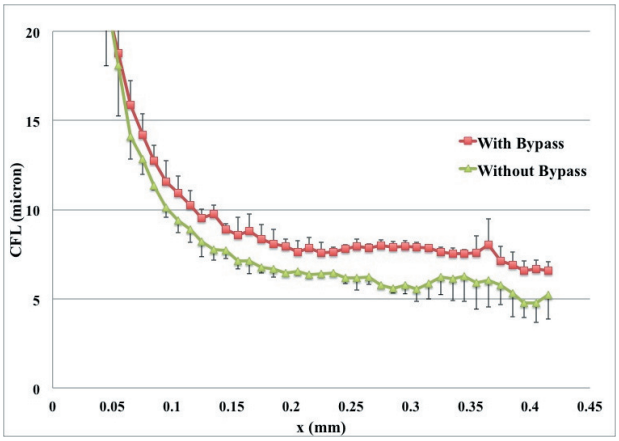


Fig. 4 CFL thickness after the stenosis in both sides (with bypass and without bypass). The error bars indicate the standard deviations of four independent experiments.

In both sides, due to the interaction between the deformable RBCs and the stenosis, RBCs located near the wall before the stenosis tended to move away from the wall after the stenosis, as reported in our previous study [5]. Besides, the results shown in Fig. 4 clearly demonstrate that the bypass channels made in the channel wall could increase the CFL thickness. This result can be explained as follow: only dextran40 flows into the bypass microchannels, which reduces the cell CFL thickness between the two stenosis. The RBCs again experience drift at the second stenosis. Moreover, the outflow of dextran at the second stenosis push RBCs further away from the wall. As a consequence, the CFL thickness increases by adding the bypass channels.

The thicker cell free layer can be useful for plasma separation and also preventing adhesion of RBCs on medical devices. In addition, it may affect the microscale flow field near the wall, and consequently mass transport of large molecules and platelets in biomedical microdevices.

## 4. Conclusion

In this study, we reported experiments on the flow of RBCs in stenosed microchannels with bypass in the wall. We showed that bypass channels in the wall could enhance the cell free layer thickness downstream of the stenosis. The basic knowledge obtained in this study is useful in designing microfluidic devices dealing with RBCs.

## References


[1] S. Kim, P.K. Ong, O. Yalcin, M. Intaglietta, P.C. Johnson, *Biorheology*, 46 (2009) 181-189.

[2] E. Sollier, M. Cubizolles, Y. Fouillet, J. Achard, *Biomedical Microdevices*, 12 (2010) 485-97.

[3] A. Aota, S. Takahashi, K. Mawatari, Y.Tanaka, Y. Sugii, T. Kitamori, *Analytical Sciences*, 27 (2011) 1173-1178.

[4] M. Faivre, M. Abkarian, K. Bickraj, H.A. Stone, *Biorheology*, 43, (2006) 147–159.

[5] H. Fujiwara, T. Ishikawa, R. Lima, N. Matsuki, Y. Imai, H. Kaji, M. Nishizawa, T. Yamaguchi, *Journal of Biomechanics*, 42, (2009) 838-842.

[6] B. Namgung, P.K. Ong, Y.H. Wong, D. Lim, K.J. Chun, S. Kim, *Physiological Measurment*, 31 (2010) N61-N70.

# Numerical Analysis of the Effect of Hematocrit on the Hemodynamic Characteristics at AAA

Ji Tae Kim[1], Kun Hyuk Sung[1], Hong Sun Ryou[1]
[1] Department of Mechanical Engineering, Chung-ang University
84, Heukseok-ro, Seoul, 156-756, Korea

**ABSTRACT**

Hematocrit which is volume percentage of red blood cells in blood has important influence on blood viscosity. Numerical study perform for investigate to effect of hematocrit with multiphase blood model at abdominal aortic aneurysm. The hematocrit at aorta inlet changed 30%, 45% and 60%. When the hematocrit varies from 30%, 45% 60%, the area of high wall shear stress increases 43% and 56% respectively. Consequently, the variation of hematocrit should be considered the analysis of the hemodynamic characteristics at AAA.

## 1. Introduction

Hemodynamic characteristics such as wall shear stress and oscillatory shear index are important to analyze development of abdominal aortic aneurysm (AAA) pathology. Researches on atherosclerosis showed that the extremely low(less than 1Pa) and high (over 7Pa) wall shear stress cause endothelial cell injury [1]. Also, Glor et al.[2] proposed OSI index which over 0.2 value associated damage to endothelial cells.

These hemodynamic characteristics determined by viscosity and shear rate. In addition, many researches on blood viscosity indicated that hematocrit has important influence on blood viscosity. Hematocrit is the volume percentage of red blood cells in blood. To consider variation of local blood viscosity, effect of hematocrit should be considered. However, previous researches on AAA had a difficulty to considering the variation of local hematocrit.

Thus, we used multiphase blood model suggested by Jung, Jonghwun[3] for considering the effect of hematocrit.

To investigate the effect of hematocrit on hemodynamic characteristics at AAA, numerical study performed on three different cases. The hematocrit of each case at AAA changed 30%, 45% and 60%.

## 2. Method

Figure 1 showed boundary conditions of AAA. Geometry of an AAA is obtained from CT. The boundary condition of aorta inlet is given from ultra sonography. The boundary conditions of aorta outlet 1 and 2 are assumed zero gage pressure as shown in Fig. 1. Blood vessel wall is assumed rigid body for reducing computational resource. The no-slip wall condition was applied. Initial velocity was set zero. Initial hematocrit of each case are set 30% 45% and 60% respectively.

The material property of human red blood cells is $d_p = 8.2\mu m$, $\rho = 1.10 kg/m^3$. Also, material property of Plasma is $\rho = 1.02 kg/m^3$, $\mu$=0.002kg/m·s in this study, commercial CFD software Fluent v14.5 was used. The computational grid shape was tetra cells generated by ICEM 14.5 The total number of grid are 219,313 nodes selected from grid independence test.

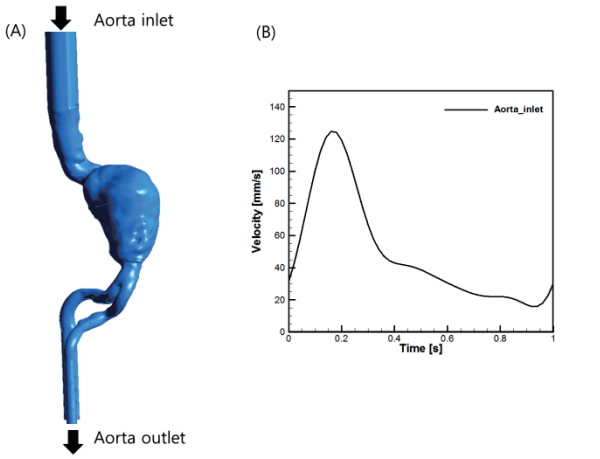


Fig. 1 (A): Boundary conditions of AAA, length of aorta inlet and aorta outlet are extended 150mm for fully development flow. (B): Velocity profile at aorta inlet

## 3. Results and Discussion

Adel M malek et al., showed that extremely high (over 7Pa) and low (less than 1Pa) wall shear stress cause endothelial cell injury [1].

Figure 2 shows the high wall shear stress (HWSS) region when peak systole velocity. The HWSS region appears at bifurcation. Table 1 shows area of high wall shear stress region. The area of high wall shear stress region of over 7Pa in case 2 increased by 43% from that in case 1. Also, the area of high wall shear stress region of over 7Pa in case 3 increased by 56% from that in case 2. As a mentioned earlier, wall shear stress is determined by viscosity and shear rate. The distributions of shear rate, viscosity, and hematocrit at bifurcation are shown in Figure. 3. In dimensionless radius 0, the HWSS of case 1, case 2 and case 3 are 79Pa, 90Pa and 141Pa. The difference of shear rate at dimensionless radius 0 is about 6% between case 1 to case 3 as shown in Figure 3 (B). Because difference of velocity gradient at

Corresponding author: Hong Sun Ryou
*E-mail address*: cfdmec@cau.ac.kr

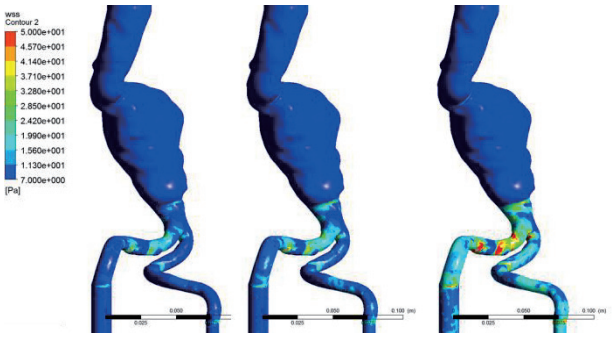


Fig. 2 High wall shear stress region over 7 Pa [1]

dimensionless radius 0 is about 7% between case 1 to case 3 as shown in Figure 3 (F). In addition, the difference of viscosity at dimensionless radius 0 is about 368% between case 1 to case 3 as shown in Figure 3 (D). These results indicate that variation of viscosity affects HWSS mainly more than shear rate.

In this multiphase blood model, viscosity is determined by shear rate and hematocrit. The shear rates at highest wall shear stress region (dimensionless radius 0) are almost similar to all cases as shown in Figure 3 (B). Because velocity gradient is similar to all case (F). It means that variation of viscosity is primarily affected by hematocrit. Hence, effect of hematocrit is important to hemodynamic characteristics at AAA. Future more, we hope this numerical study of hemodynamic characteristics give more insight to understand pathology of AAA.

## 4. Concluding Remarks

In this study, the effect of hematocrit on hemodynamic characteristics at AAA was analyzed by numerical simulation using a multiphase blood model. When the hematocrit varies from 30%, 45% 60%, the area of HWSS increases 43% and 56% respectively. Consequently, the variation of hematocrit should be considered analysis of the hemodynamic characteristics at AAA.

| Case Hct | Case 1 (Hct 30%) | Case 2 (Hct 45%) | Case 3 (Hct 60%) |
|---|---|---|---|
| HWSS area | 0.00367852 | 0.00851653 | 0.015045 |

Table 1. Area of high wall shear stress.

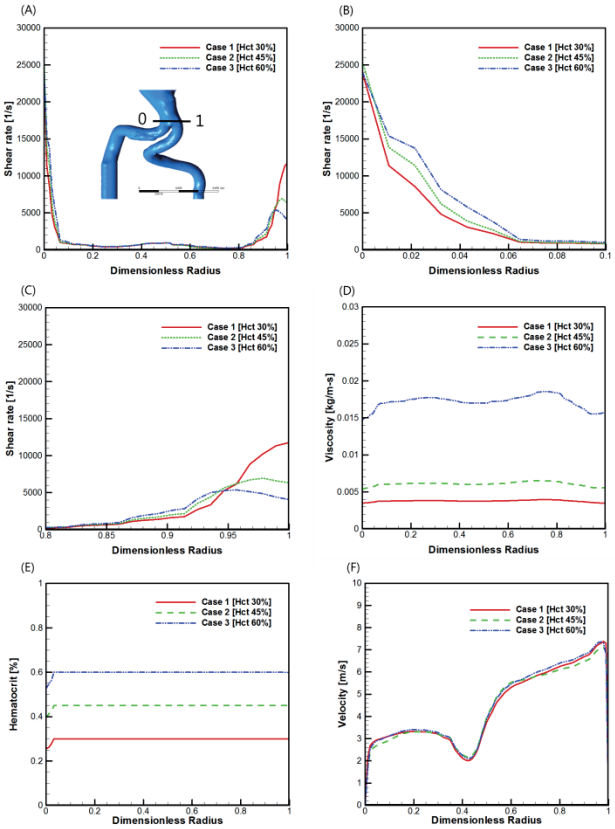


Fig. 3 (A) (B) (C): Shear rate at dimensionless radius 0 to 1, 0 to 0.1, 0.8 to 1 respectively. (D): Viscosity at dimensionless radius. (E): Hematocrit at dimensionless radius 0 to 1.(F)Velocity at dimensionless radius 0 to 1

## References

[1] Malek, Adel M., Seth L. Alper, and Seigo Izumo, *Jama* 282.21 (1999) 2035-2042.

[2] Glor, F. P., Q. Long, A. Hughes and A. Augst, *Annals of Biomedical Engineering* 31.2 (2003) 142-151.

[3] Jung, Jonghwun, and Ahmed Hassanein, *Medical engineering & physics* 30.1 (2008): 91-103.

# A Development of Manufacture-oriented Optimization Strategy for Flow Diverter Stent based on Cylindrical Spirals

Mingzi Zhang[1], Hitomi Anzai[2], Bastien Chopard[3], Makoto Ohta[2]
[1]Graduate School of Engineering, Tohoku University
2-1-1 Katahira Aoba-ku Sendai Miyagi, 980-8577, Japan
[2]Institute of Fluid Science, Tohoku University
2-1-1 Katahira Aoba-ku Sendai Miyagi, 980-8577, Japan
[3]Computer Science Department, University of Geneva
7 route de Drize, 1227 Carouge, Switzerland

**ABSTRACT**

The Flow Diverter (FD) placement as a modern endovascular treatment is designed to decrease the aneurysmal flow to prevent its rupture by rebuilding the local hemodynamics of the parent artery with its aneurysm. The shape and structure of the FD device determines the flow diversion efficiency which varies from one patient to another. This study introduced a manufacture-oriented optimization strategy for FD device based on a group of cylindrical spirals, which could automatically find the optimal solution with better flow diversion efficiency for a certain aneurysm configuration.

## 1. Introduction

Intracranial Aneurysm is a vascular disorder which could result in subarachnoid hemorrhage due to its rupture and severely threaten patients' life quality. Modern endovascular treatment such as Flow Diverter (FD) stent placement has been proved to be an effective and non-invasive method to reduce the rupture risk by rebuilding the local hemodynamics.

The FD stents currently existed usually have a homogeneous woven wire structure which were widely applied to treat various shape of aneurysms. Many researches have been performed to examine either the structure or the materials of the stent to improve the prognosis of stent placement therapy. Our previous research also presented the automated strut optimization to reduce the aneurysmal flow which suggested that the flow diversion efficiency could be evidently improved by interrupting the bundle of inflow (BOI) zone [1]. To make out a patient-specific stent which has the best flow reduction (FR) rate correspondence to the particular patient's aneurysm, the cheapest way is to perform pre-operation case study and optimal stent design by computational fluid dynamics (CFD) simulation.

This study presented a FD stent optimization strategy based on the structure of a set of cylindrical spirals following the design concept of widely employed braided FD stent such as Pipeline, Silk, etc. This strategy was designed to automatically find out the optimal set of wires arrangement which has the best performance in reducing the aneurysmal flow by a sequence of pre-operative CFD simulations.

## 2. Method

*1. Vascular and FD stent Model.* A straight pipe with a side-wall sphere was employed following Imai et al [2] as the side-wall aneurysm geometry in this study, which had an aneurysmal diameter (D) of 4.8mm with a neck diameter (N) of 2.8mm and arterial diameter (d) of 3.5mm. To verify the proposed optimization process in the realistic case, a 3D reconstructed human internal carotid artery (ICA) with side wall aneurysm was also applied. The mathematical definition of FD device was generated as a set of helixes adhering to the wall of parent artery along the centerline. Each stent was designed with 8 helixes: 4 clockwise and 4 counter-clockwise.

*2. Stent Modification.* At each stage of the random modification, one of the helixes was arbitrarily chosen and then a tiny stochastic variation was added to its starting phase, which finally resulted in a slight displacement $\Delta x \in (-\delta, \delta)$ of the selected wire. The optimization started with the widely employed homogeneous wire arrangements and each stage's modification was performed based on the previous stage (Fig. 1).

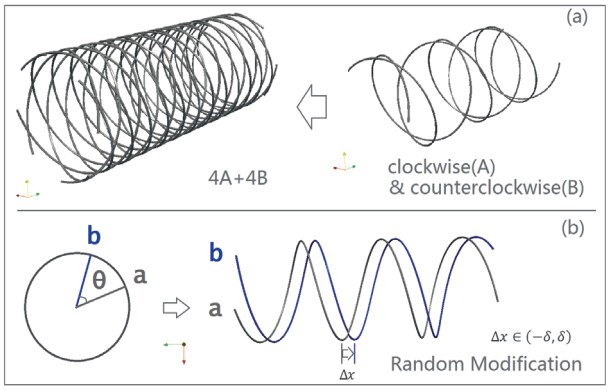


Fig. 1 The spirals-like FD stent generation (a) and the schematic of random modification (b).

*3. Optimization Method.* Simulated Annealing (SA) was considered as the optimization method to control the random process running towards the optimal solution within a certain range of temperature in accordance with our previous study [1]. We considered the average velocity inside the aneurysm to be the objective function.

*4. Hemodynamic Model.* The open library Palabos v1.4 based on Lattice Boltzmann (LB) method was

Corresponding author: Mingzi Zhang
*E-mail address*: mingzi.zhang@biofluid.ifs.tohoku.ac.jp

utilized as the CFD solver. The LB method for hydrodynamics is a mesoscopic approach in which the fluid is described in terms of the density distribution $f_i(r,t)$ of idealized fluid particles moving and colliding on a regular lattice. These collision-propagation dynamics could be written as

$$f_i(r+\Delta t v_i, t+\Delta t) = f_i(r,t) + \frac{1}{\tau}(f_i^{eq} - f_i) \quad (1)$$

where $f^{eq}$ and $\tau$ are the so-called local equilibrium distribution and relaxation time, respectively. The stent structure was directly defined as bounce-back lattice in the beginning of each simulation, which enabled the optimization process fully automated. The fluid was assumed to be Newtonian and incompressible. To reach the Reynolds Number (Re) of 200, the blood flow was set up to have the constant velocity of 0.23m/s, 0.21m/s and defined as parabolic profiles at the inlets, respectively. At the outlet, a constant pressure boundary was imposed. Constant density and kinematic viscosity were assumed to be 1040 kg/m$^3$ and 4.0e-6 m$^2$/s, respectively. The kinetic viscosity of the lattice ($\nu_{LB}$) was chosen as 0.012, giving the relaxation time $\tau$ of $(6\nu_{LB}+1)/2$ = 0.536.

## 3. Results

To quantitatively measure the stent placement effect of various strut structures, the index of flow reduction rate $R_f$ was defined

$$R_f = \frac{V_{w/o} - V_{current}}{V_{w/o}} \quad (2)$$

to evaluate the stent efficiency. The $V_{w/o}$ is the average velocity inside an aneurysm without stent placement and the $V_{current}$ is the average aneurysmal velocity at the current stage. Higher $R_f$ indicates the correspondence stent shape has a better performance. The parallel computing technique is utilized in this research to speed up the optimization process. We use 160 cores (SGI UV2000) for each model. The idealized and the realistic model usually cost more than 30min and 150min to reach a stable state of one stent configuration, respectively.

After more than 500 steps' SA process, an optimal solution for the pipe model with a better $R_f$ = 95.41% is obtained compared with the initial $R_f$ = 90.48%. The flow pattern depicted in Fig. 2 shows that the optimized wire struts have the tendency to cover the inflow zone and interrupt the BOI area, which shows the agreement with our previous research. Also, after 200 steps' SA process, an optimal solution for the human ICA model with a better $R_f$ = 93.47% is obtained compared with the initial $R_f$ = 66.7%. The simulation results were depicted in Fig. 3.

## 4. Discussion

The intersection angle of arbitrary two wires does not change after modification here but this strategy also works even if the angle plays as an optimization parameter. The method associated with its optimization process can be directly blended to the stent manufacture strategy as it shares the same concept with the real stent design and either modern braided or laser-cut production technology could possibly make out the optimal configuration.

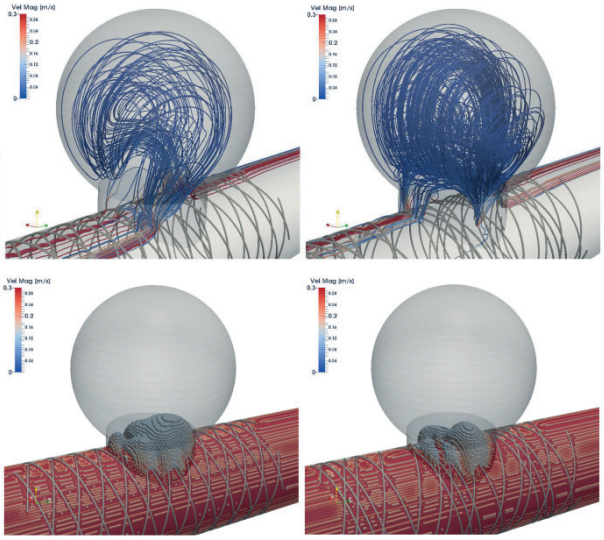

Fig. 2 The streamlines (up) and ISO surfaces (down) of initial stented aneurysm (left) and optimal stented aneurysm (right), respectively. (Idealized geometry)

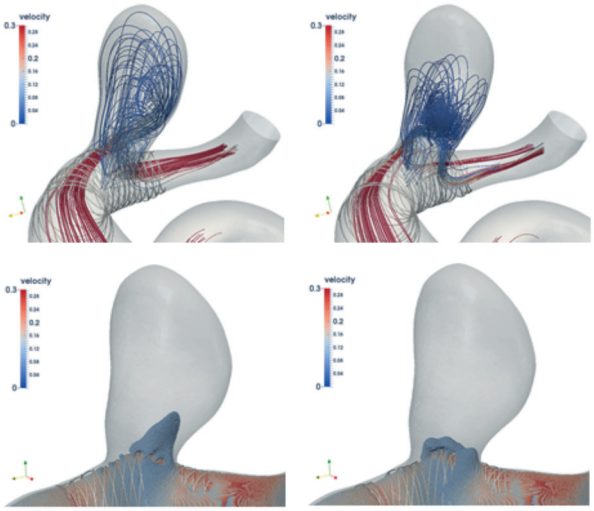

Fig. 3 The streamlines (up) and ISO surfaces (down) of initial stented aneurysm (left) and optimal stented aneurysm (right), respectively. (Realistic geometry)


## 5. Acknowledgement

This study was supported by the Grant-in-Aid for Scientific Research (B), MEXT, 2013-2015 (25282140, Makoto Ohta).


## References


[1] H. Anzai, B. Chopard, J. Falcone M. Ohta, *Journal of Biomechanical Engineering,* (2014)16:061066, pp. 1-7.

[2] Y. Imai, K. Sato, T. Ishikawa, T. Yamaguchi, Annals of Biomedical Engineering, (2008)36-9, pp. 1489–1495.

# OS6: Advanced Physical Stimuli and Biological Responses

Eleventh International Conference on Flow Dynamics
October 8-10, 2014, Sendai, Miyagi, Japan

# Cold Atmospheric Plasma Treatment on Eukaryotic and Prokaryotic Cells

Tetsuji Shimizu, Julia L. Zimmermann, Gregor E. Morfill
terraplasma GmbH
Lichtenbergstr. 8, Garching, 85748, Germany
Max-Planck Institute for extraterrestrial physics
Giessenbachstr., Garching, 85748, Germany

**ABSTRACT**

Cold atmospheric plasma can be a new treatment option in medicine because it produces relevant reactive species for biological reactions. In this contribution, we demonstrate some of our in vivo clinical studies from 2005 to 2013. The results show that the plasma treatment can offer several beneficial effects, e.g. wound disinfection and healing. This technique could open new horizons in medicine.

## 1. Introduction

Cold atmospheric plasma discharges have been applied in biomedical applications because they can produce relevant reactive nitrogen and oxygen species for biological reactions [1]. A contact-free treatment is possible with no thermal damage. It has been reported that they can inactivate a wide range of pathogenic bacteria without thermal damage. Since the plasma treatment is mainly due to the gaseous reactive species, the treatment is feasible on rough surfaces down to even micrometer-scale. Moreover, it is possible that the plasma gas has not only a bactericidal property but also a "healing" effect, e.g. a cell regeneration effect.

In a joint effort between Max-Planck Institute for extraterrestrial physics and the Department of Dermatology, Allergology and Environmental Medicine in Hospital Munich Schwabing, several clinical studies were carried out from 2005 till 2013. The used device is MicroPlaSter where all the functional units including a microwave plasma torch, a power supply, etc., are incooperated (Fig. 1). This device was developed in cooperation with Adtec Plasma Technology. The plasma torch consists of 6 stainless steel electrodes placed inside an aluminum cylinder of 135 mm in length [2]. The centers of the 6 electrodes, whose surfaces are serrated, are distributed equally at a distance of 6 mm from the inner surface of the cylinder. The size of the torch's opening is 35 mm in diameter. Argon of 4-5 slm is applied from the base of the electrodes through a shower plate which regulates gas flow around the electrodes. Microwave power at 2.45 GHz is applied to the electrodes through coaxial cables via an auto tuner. The input power was 80 W. Six plasmas are produced between each of the electrode's tips and the inner surface of the cylinder.

Before starting a phase II study (clinical study), a phase I study was carried out. The focus of this study is to show safety parameters and the optimum bactericidal dose for relevant bacteria, satisfying the safety requirements of the medical device directive and the ethics committee. In the phase I study, in addition to the plasma characterization, bactericidal effects on relevant bacteria to chronic wounds were shown. And skin histology showed that there was almost no change by the plasma treatment. This clinical study had the approval of the Bavarian State Association for Medical Issues. In this contribution, the results from our several clinical studies are summarized.

Corresponding author: Tetsuji Shimizu
*E-mail address*: shimizu@terraplasma.de

Fig. 1 Plasma device, MicroPlaSter. At the end of a flexible arm, there is a microwave plasma torch.

## 2. Results from the Clinical Studies

### 2.1. Chronic Wound Disinfection

The development of antibiotic resistance by microorganisms and the decrease in number of antibiotics released in the market are a large concern in medicine. It is required to have a technique to minimize the use of antibiotics. The plasma treatments have an advantage that the plasma can inactivate bacteria including antibiotic-resistant strains without building up the resistance.

Using the MicroPlaSter device, twenty four patients with chronic infected wounds were treated in vivo for two mintes [3,4]. The applied plasma treatments were an "add-on" therapy, i.e. the patients were treated by the plasma in addition to standard wound care.

On wounds, there were several bacteria detected, e.g. *Pseudomanas aeruginosa*, *Staphylococcus aureus*, *Enterococcus*, MRSA, etc. From the results with larger than 200 treatments, the plasma treatments showed that a highly significant reduction in bacterial load. It is important to note that no side-effects were reported and all the plasma treatment was well tolerated in all cases.

### 2.2. Plasma Treatments on Skin Graft Donor Sites

As shown before, the plasma treatment has a bactericidal property even on wounds. Here the topic is whether the plasma treatments can improve wound healing. To assess the impact of the plasma treatments, forty patients with skin graft donor sites were treated [5]. Wound infection did not occur in any of the cases.

The wound sites were divided into two areas with a same size. One side was treated by the plasma and the other was by only argon gas (placebo). Both treatment time was two minutes. The healing process in the donor sites was evaluated by two blinded dermatologists.

From the second treatment day, donor site treated by the plasma showed significantly improved healing compared with placebo-treated areas. There were positive effects observed, improved reepithelialization, less fibrin layers and blood crusts. No side-effects occurred and the treatment was well tolerated.

### 2.3. Treatment of Lesions in Hailey-Hailey Disease

Hailey-Hailey disease is an autosomal dominant condition as a result of mutations in the *ATP2C1* gene. A limited number of treatment options is available because this disease is rare. Here a part of our case report is presented.

A 56-yesr-old patient with a 25-year history of Hailey-Hailey disease was treated by the cold atmospheric plasma [6]. There were erosive lesions in the axillae, groin, and neck region. The patient reported aggravation of symptoms and the lesions were associated with stinging, burning and sometimes pruritus.

A five-minute plasma treatment is applied to the axilla and the groin in addition to treatment with topical fusidic acid/ betamethasone. A number of treatments for the axilla was eight and that for the groin was four. After four times of the plasma treatments, the skin lesions in the axilla healed with relief of the stinging sensations. With the plasma treatments, the groin area was also improved with symptomatic relief. But some minor erosions persisted.

### 2.4. Treatment on Herpes Zoster

Herpes zoster is an acute painful infectious skin condition due to the reactivation of varicella zoster virus. Thirty-seven inpatients with herpes zoster were treated in a randomized placebo-controlled clinical study with five-minute of the plasma in addition to standard treatment[7]. Pain was assessed by visual analogue scale before and after application. The lesions were photographed and the taken images were evaluated independently by three blinded clinicians.

The analysis on the data showed that there was a significantly greater reduction in pain in the plasma treated patients. Moreover, the plasma treatment led to significantly faster healing in the first 1-2 days. No side-effects were reported and the plasma treatment was well tolerated in all cases.

## 3. Summary

Here, we demonstrate some of our clinical studies. The results show that a new technique with cold atmospheric plasma can show several beneficial effects in vivo. The plasma treatment has been shown to be safe and painless. It is not yet fully understood how the plasma treatment give several effects. A further investigation is required to understand and optimize all the processes. However, this innovative technique may offer an option in several treatments in medicine.

## References


[1] M. Kong, G. Kroesen, G. E. Morfill, T. Nosenko, T. Shimizu, J. van Dijk, and J. L. Zimmermann*, New J. Phys.*, 11 (2009) 115012.

[2] T. Shimizu, B. Steffes, R. Pompl, F. Jamitzky, W. Bunk, K. Ramrath, M. Georgi, W. Stolz, H.-U. Schmidt, T. Urayama, S. Fujii, and G. E. Morfill, *Plasma Process. Polym.*, 5 (2008) 577.

[3] G. Isbary, G. E. Morfill, H.-U. Schmidt, M. Georgi, K. Ramrath, J. Heinlin, S. Karrer, M. Landthaler, T. Shimizu, B. Steffes, W. Bunk, R. Monetti, J. L. Zimmermann, R. Pompl, and W. Stolz, *Br. J. Dermatol.*, 163 (2010) 78.

[4] G. Isbary, J. Heinlin, T. Shimizu, J. L. Zimmermann, G. Morfill, H-U. Schmidt, R. Monetti, B. Steffes, W. Bunk, Y. Li, T. Klaempfl, S. Karrer, M. Landthaler, and W. Stolz, *Br. J. Deratol*., 167 (2012) 404.

[5] J. Heinlin, J. L. Zimmermann, F. Zeman, W. Bunk, G. Isbary, M. Landthaler, T. Maisch, R. Monetti, G. Morfill, T. Shimizu, J. Steinbauer, W. Stolz, and S. Karrer, *Wound Rep. Reg*., 21 (2013) 800.

[6] G. Isbary, G. Morfil, J. Zimmermann, T. Shimizu, and W. Stolz, *Arch. Dermatol*., 147 (2011) 388.

[7] G. Isbary, T. Shimizu, J. L . Zimmermann, J. Heinlin, S. Al-Zaabi, M. Rachfeld, G. Morfill, S. Karrer, and W. Stolz, *Clinical Plasma Medicine*, accepted.

Eleventh International Conference on Flow Dynamics
October 8-10, 2014, Sendai, Miyagi, Japan

# Biological Flow Generated by Cilia and Flagella

Takuji Ishikawa[1]
[1]Department of Bioengineering & Robotics, Tohoku University
6-6-01, Aoba, Aoba-ku, Sendai 980-8579, Japan

**ABSTRACT**

Cilia and flagella generate flow at the cellular scale, which is utilized for locomotion and mass transport. The generated flow sometimes shows complex flow structures, though the mechanism is still largely unknown. In this study, we review some of our recent attempts to clarify biological flow generated by cilia and flagella. Especially, we focus on flagella bundling of a bacterium, pattern formation of swimming cells, and ciliary flow on the surface of the tracheal lumen. The results reveal the importance of fluid mechanics in understanding the biological functions.

## 1. Introduction

Cilia and flagella generate flow at the cellular scale, which is utilized for locomotion and mass transport. The generated flow sometimes shows complex flow structures, though the mechanism is still largely unknown. In this study, we review some of our recent attempts to clarify biological flow generated by cilia and flagella.

The first topic is about flagella bundling of a swimming bacterium. When flagella of *E. coli* bacteria rotate in the counter-clockwise (CCW) direction, they form a bundle and propel the cell. When the flagella rotate in the clockwise (CW) direction, on the other hand, they are unbundled and the cell tumbles. Since mechanism of the bundle formation is unclear, we investigate it by a numerical analysis [1].

The second topic is about pattern formation of swimming cells. Former studies reported that pushers, like bacteria, form coherent structures in a concentrated suspension, whereas pullers do not. We numerically investigate the mechanism of the pattern formation of pushers and pullers. A microorganism is modeled as a squirmer with different swimming modes.

The last topic is about ciliary flow in the airway. Dusts and viruses are trapped on the surface of the tracheal lumen and transported towards the larynx by cilia-generated flow. The transport phenomena are affected not only by the time- and space-average flow field but also by the fluctuation of the flow. We experimentally investigate it and discuss efficiency in the clearance function [2].

## 2. Flagella Bundling [1]

In this section, swimming motion of bacteria with multiple flagella is investigated numerically by a boundary element method. The cell body is modeled as a rigid ellipsoid, and the flagella are modeled as rigid helices suspended on flexible hooks. Because of the small scale of bacteria, the flow around it can be assumed as Stokes flow, which is solved by the boundary element method. Motors apply constant torque to the hooks, rotating the flagella either clockwise or counterclockwise.

When all three flagella rotate in the CCW direction, they form a bundle regardless of their initial configuration, as shown in Fig. 1. When two flagella rotate in the CW direction, on the other hand, the cell tumbles regardless of the initial configuration, as shown in Fig. 2. The interactions between individual flagella are induced only by hydrodynamic forces. Thus, we can conclude that the flagella bundling and unbundling can be controlled by the rotational direction at the flexible hooks.

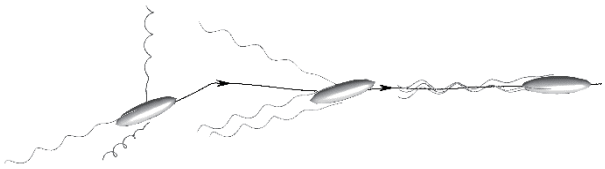

Fig. 1 Flagella bundling when all flagella rotate in the CCW direction. The arrow indicates trajectory of body center motion [1].

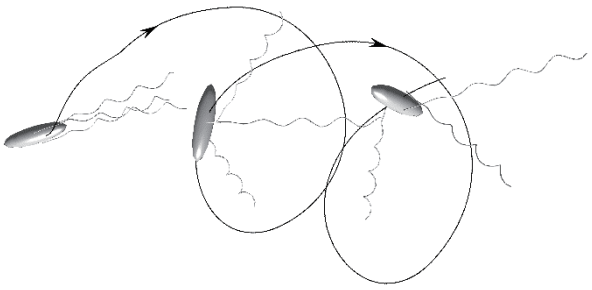

Fig. 2 Tumbling of bacteria when two flagella rotate in the CW direction. The arrow indicates trajectory of body center motion [1].

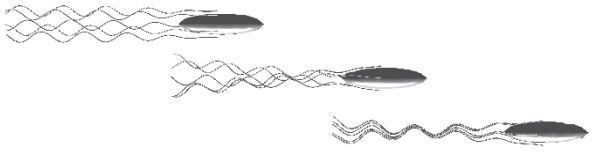

Fig. 3 Synchronization of five flagella initially out of phase. Three bacterial images indicate flagella configuration at $t$ = 0 (left), $t$ = 750 (center), and $t$ = 1500 (right) [1].

In a setup of two parallel rigid flagella with their axes fixed in space and driven by the same torque, no phase synchronization occurs. However, by adding another degree of freedom at the flexible hooks, flagella tend to synchronize by hydrodynamic interactions, as shown in Fig. 3. Once the synchronization occurs, flagella rotate faster and the swimming speed of the cell increases.

### 3. Collective Swimming

We solve both far- and near-field fluid dynamics precisely and investigate the collective motions of hydrodynamically interacting microorganisms. The model microorganism is assumed to be spherical or ellipsoidal and propels itself by generating tangential velocities on its surface, i.e. a squirmer. Three types of microorganisms were modeled by varying the surface velocity; (i) a puller that has the thrust-generating apparatus in front of the body, (ii) a pusher that has the thrust behind the body, and (iii) a neutral swimmer. We employed the boundary element method based on the double-layer representation. The method is suitable for parallel computing.

We analyze interactions of 100 squirmers with various swimming mode and aspect ratio in a mono-layer. The results showed that neutral swimmers with spherical shape tended to orient in one direction and formed an ordered structure. The order was destroyed slightly by increasing the aspect ratio, which induced chaotic fluctuations of the ordered directions. It is found that pullers tended to aggregate and form clusters, whereas pushers tended to avoid to each other and vortex like structures appeared. Further analysis revealed that the near-field fluid dynamics plays a major role in the development of the collective motions.

### 4. Ciliary Flow in the Airway [2]

Although we inhale air that contains many harmful substances, including, for example, dust and viruses, these small particles are trapped on the surface of the tracheal lumen and transported towards the larynx by cilia-generated flow. The transport phenomena are affected not only by the time- and space-average flow field but also by the fluctuation of the flow. Because flow fluctuation has received little attention, we investigated it experimentally in mice.

To understand the origin of flow fluctuation, we first measured the distribution of ciliated cells in the trachea and individual ciliary motions. The results indicated that the spatial distribution as well as the beat direction of ciliated cells were inhomogeneous.

Next, we measured the in-plane flow field at different heights using a confocal micro-PTV system, as shown in Fig. 4. Strong flow fluctuations were observed, caused by the reciprocal motion of the ciliary beat and the spatial inhomogeneity of ciliated cells. The spreading of particles relative to the bulk motion became diffusive if the time scale was sufficiently larger than the beat period. Finally, we quantified the effect of flow fluctuation on bulk flow by evaluating the Peclet number of the system. The results illustrated that ciliated cells could generate directional transport despite the large fluctuations caused by the reciprocal motion of the ciliary beat and the spatial inhomogeneity of ciliated cells. Pe = 7.5, indicating that the directional transport is one order of magnitude larger than the isotropic diffusion. These results are important for understanding the transport phenomena of airways on the cellular scale.

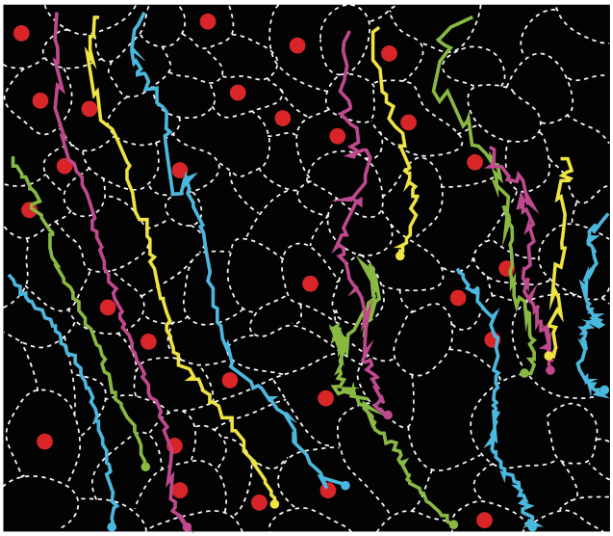

Fig. 4 Trajectories of tracer particles. Borders of epithelial cells are shown by white dashed lines, and ciliated cells are indicated by red circles. Particle trajectories are shown by colored lines. Particles moved from the lungs side (bottom of the figure) to the larynx side (top of the figure), on average.

### 5. Concluding Remarks

In this study, we reviewed some of our recent researches on flagella bundling of a bacterium, pattern formation of swimming cells, and ciliary flow on the surface of the tracheal lumen. The results revealed the importance of fluid mechanics in understanding the biological functions.


### Acknowledgement

The researches were conducted in collaboration with Prof. Y. Imai, Prof. H. Ueno, Dr. T. Omori, Mr. P. Kanehl, Mr. K. Kyoya, Mr. K. Kiyota and my lab members. The study was supported by Grants-in-Aid for Scientific Research (A), and the NEXT program of JSPS.


### References


[1] P. Kanehl and T. Ishikawa, *Phys. Rev. E*, 89 (2014) 042704.

[2] K. Kiyota, H. Ueno, K. Numayama-Tsuruta, T. Haga, Y. Imai, T. Yamaguchi and T. Ishikawa, *Amer. J. Phys. - Lung Cell. Mol. Phys*., 306 (2014) L144-L151.

Eleventh International Conference on Flow Dynamics
October 8-10, 2014, Sendai, Miyagi, Japan

# Thermal Transport in Lipid Bilayers

Taku Ohara[1], Takeo Nakano[1], Gota Kikugawa[1]
[1]Institute of Fluid Science, Tohoku University
2-1-1 Katahira, Aoba-ku, Sendai, 980-8577, Japan

**ABSTRACT**

Lipid bilayers that are formed in water in a self-organized manner have peculiar static and dynamic structures. The authors have performed molecular dynamics simulations and analysis of the molecular-scale mechanism of the thermal transport recently, and the results are summarized in this paper. Thermal conductivity of the lipid bilayer membranes has been determined, in which remarkable anisotropy was found; thermal conductivity in the cross-plane direction is five times higher than that in the in-plane direction. The mechanism of this phenomenon is discussed here.

## 1. Introduction

Amphiphilic phospholipid molecules in water form bilayer structures with their polar head groups pointing outside to contact ambient water and their apolar tail groups pointing toward the counterpart monolayer. This bilayer structure is a model of cell membranes and its characteristics have been extensively studied, which includes mainly vesiculation [1], fusion of vesicles [2,3], pore formation [4], mass transport such as in-membrane lateral diffusion [5] and water permeation [6], and response to friction in bio-lubrication [7,8].

The lipid bilayer membrane (LBM) have been attracting attentions also in engineering. Various systems of LBM with a solid support have been investigated [9−12] to provide bio-MEMS platforms for sensors and various observation fields.

From another point of view, LBM is a sort of the soft matters, which are promising engineering materials. They are structured by polymer molecules with a self-organization manner. They offer a wide variety of properties and functions depending on features of polymers, which can be designed by selecting and modifying the molecules. It should be noted that the soft matters can play a major role to form nanoscale structures, just like solids in macroscale. The soft matters worthy to be noted in engineering include polymer brushes [13−17], polymer nanosheets [18,19], and multilayer thin films produced by the layer-by-layer technique.[20,21] These soft matters have peculiar structures which can be designed for specific purposes.

Thermophysical properties such as thermal conductivity have not been reported for most of the soft matters. The influences of the peculiar structures of the soft matters on thermophysical properties have not been known, and it should be clarified and accumulated as a basic data for the design of soft matters. For that purpose, the conventional method of thermophysical properties, i.e., measurement, is not sufficient because it does not give the mechanism to explain how the thermophysical properties appear.

Molecular dynamics (MD) simulations give all the data of individual molecules that are attending to the thermal and fluid phenomena. Although it is new to this engineering field, and despite of the difficulty to extract useful information from the huge amount of molecular data, MD is now working as a powerful tool to “analyze” thermophysical properties.[22]

In the present paper, thermal transport in molecularly structured soft matters is discussed in the next section. Heat conduction in lipid bilayer membranes, as a typical soft matter, is analyzed in section 3.

Corresponding author: Taku Ohara
E-mail address: ohara@ifs.tohoku.ac.jp

## 2. Thermal energy Transport in polymer structure

To elucidate the elementary process of thermal energy transport in polymer materials, heat conduction in polymer liquids have been analyzed.[23] Heat conduction flux under a temperature gradient reproduced by MD simulations was decomposed to the contributing energy transfers based on the molecular dynamics expression of heat flux proposed by the authors.[24-26] The results are shown in Fig. 1 for several n-alkane saturated liquids, which are made of simple long-chain molecules, at the same reduced temperature. The heat conduction flux is decomposed to: (1) Transport of potential and kinetic energy of molecules due to migration of molecules, (2a) Transport of energy due to work done by intermolecular forces, (2b) Transport of energy by intramolecular interactions. It is observed in the figure that as the molecular length increases, the contribution of intramolecular energy transfer, a mode of energy transfer along the stiff covalent bonds within the chain molecules, becomes dominant. This finding implies that if chain polymer molecules are aligned in a

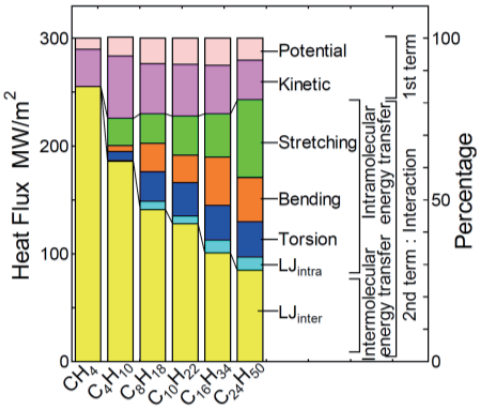


Fig. 1 Contribution of inter- and intramolecular energy transfer to heat conduction flux in n-alkane saturated liquids at the same reduced temperature. Reprinted with permission from ref. [23]. Copyright 2011, AIP Publishing LLC.

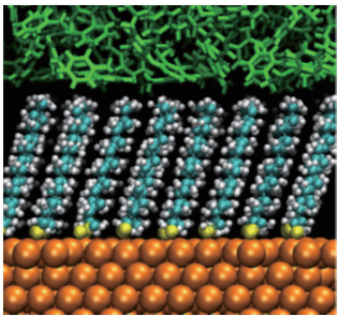

Fig. 2 Alkanethiol SAM on a gold substrate with liquid toluene.[27]

certain direction, the intramolecular energy transfer works only in the direction, which produces enhanced anisotropic thermal energy transport. We can see a good example in which ordered structures of polymers will exhibit high thermal conductivity in the direction of molecular alignment of the polymers in the case of SAM (self-assembled monolayer) [27], a typical polymer brush as shown in Fig. 2 where alkanethiol molecules are grafted to a solid substrate with a uniform orientation. It has been found that thermal conductivity of the SAM layer is much higher than that of bulk liquid of the same alkane molecules.[28] This effect is expected also in the case of LBM where lipid molecules are aligned to form a highly ordered structure as shown in Fig. 3.

### 3. Thermal transport in lipid bilayer membrane

Heat conduction in LBM have been analyzed by the authors for DPPC [29], DLPC and SMPC [30]. Stable bilayers of these lipid molecules in water were reproduced by MD simulations and heat flux was applied in the direction normal to the membrane plane (cross-plane heat conduction) or parallel to the plane (in-plane heat conduction). Temperature distribution resulted in the case of cross-plane heat conduction is shown in Fig. 4. The highest thermal resistance, indicated by the largest temperature gradient, lies at the center of the system where the apolar long chain tail groups belonging to the two lipid monolayers are facing each other. This thermal resistance between two monolayers reduces the overall cross-plane thermal conductivity over the bilayer. The cross-plane thermal conductivity of the bilayer was determined to be 0.25

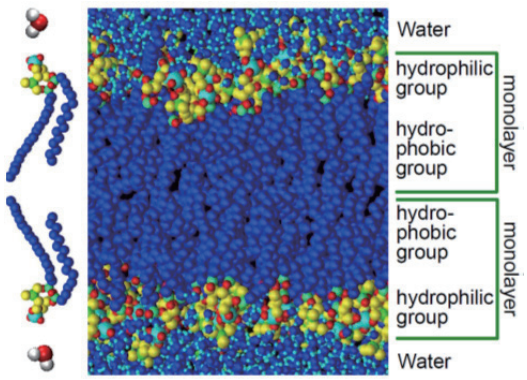


Fig. 3 DPPC Lipid bilayer membrane in water [29]

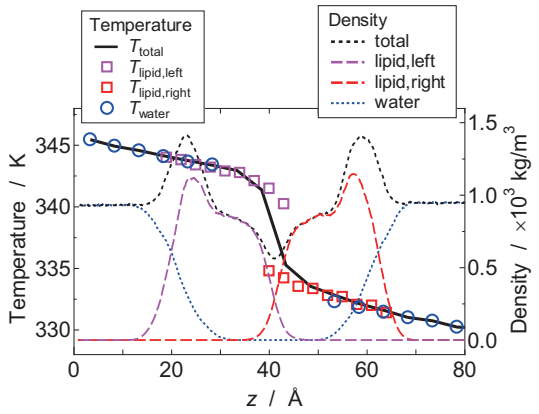


Fig. 4 Temperature distributions in the case of cross-plane heat conduction in DPPC lipid bilayer. Reprinted with permission from ref. [29]. Copyright 2010, AIP Publishing LLC.

W/(m·K), while that of the monolayer is 0.48 W/(m·K). The in-plane thermal conductivity is 0.10 W/(m·K), which is much lower than the cross-plane ones. It can be seen that the tail chains aligned in an almost uniform manner enhance the cross-plane heat conduction. This molecular-scale structure produces the asymmetric thermal conductivity of LBM.

### References


[1] B. J. Reynwar, et al, *Nature*, 447 (2007), 461−464. [2] L. Yang and H. W. Huang, *Science*, 297 (2002), 1877−1879. [3] E. H. Chen and E. N. Olson, *Science*, 308 (2005), 369−373. [4] A. A. Gurtovenko and I. Vattulainen, *J. Am. Chem. Soc.*, 127 (2005), 17570−17571. [5] G. R. Kneller, et al., *J. Chem. Phys.*, 135 (2011), 141105. [6] T. Sugii, et al., *J. Chem. Phys.*, 123 (2005), 184714. [7] P. D. Blood, et al., *J. Phys. Chem. B*, 109 (2005), 18673−18679. [8] A.-M. Trunfio-Sfarghiu, et al., *Langmuir*, 24 (2008), 8765−8771. [9] J. T. Groves, et al., *Science*, 275 (1997), 651−653. [10] M. A. Holden, et al., *J. Am. Chem. Soc.*, 126 (2004), 6512−6513. [11] H. Nabika, et al., *J. Am. Chem. Soc.*, 127 (2005), 16786−16787. [12] C. M. Hartshorn, et al., *Langmuir*, 26 (2010), 2609−2617. [13] C. Yoshikawa, et al., *Macromolecues*, 39 (2006), 2284−2290. [14] S. S. Sheiko, et al., *Progress Polymer Sci.*, 33 (2008), 759−785. [15] D. F, Moyano and V. M. Rotello, *Langmuir*, 27 (2011), 10376−10385. [16] R. C. Van Lehn and A. Alexander-Katz, *J. Chem. Phys.*, 135 (2011), 141106. [17] L. Cheng and D. Cao, *J. Chem. Phys.*, 135 (2011), 124703. [18] M. Mitsuishi, et al., *Polymer J.*, 38 (2006), 877−896. [19] H. Endo, et al., *J. Materials Chem.*, 18 (2008), 1302−1308. [20] P. A. Chiarelli, et al., *Advanced Materials*, 13 (2001), 1167−1171. [21] K. Ariga, et al., *Phys. Chem. Chem. Phys.*, 9 (2007), 2319−2340. [22] Handbook of Nano- and Micro-Thermophysical Properties, ed. Y. Nagasaka and K. Miyazaki, 2014, Yokendo, Japan. [23] T. Ohara, et al., *J. Chem. Phys.*, 135 (2011), 034507. [24] T. Ohara, *J. Chem. Phys.*, 111 (1999), 6492−6550. [25] T. Ohara, *J. Chem. Phys.*, 111 (1999), 9667−9672. [26] D. Torii, et al., *J. Chem. Phys.*, 128 (2008), 044504. [27] G. Kikugawa, et al., *J. Chem. Phys.*, 130 (2009), 074706. [28] G. Kikugawa, et al., *Int. J. Heat Mass Transfer*, in print. [29] T. Nakano et al., *J. Chem. Phys.*, 133 (2010), 154705. [30] T. Nakano et al., *J. Heat Transfer*, 135 (2013), 061301.

Eleventh International Conference on Flow Dynamics
October 8-10, 2014, Sendai, Miyagi, Japan

# Characterization of an Argon Atmospheric-Pressure Plasma Jet and Its Application in Sterilization

Zhi-Hua Lin[1], Chen-Yon Tobias Tschang[1], Yin-Min Xu[1], Chih-Tong Liu[1], Yi-Wei Yang[1], Jong-Shinn Wu[1]
[1]Department of Mechanical Engineering, National Chiao-Tung University
1001 Ta-Hsueh Rd., Hsinchu, 30010, Taiwan

**ABSTRACT**

In this paper, we have developed an argon atmospheric-pressure plasma jet (APPJ), which was carefully characterized and applied to sterilize the Escherichia coli and Bacillus subtilis. The results show that the APPJ produces a high level of OH radical emission in the post-discharge region with a maximal jet length of 20 mm and a gas temperature of roughly the human skin temperature. The sterilization experiments show that it can effectively inactivate both bacteria within 5 seconds with linearly increasing inactivation area with increasing time.

## 1. Introduction

Low temperature atmospheric-pressure plasma jets (APPJs) have been demonstrated to be very efficient and flexible in biomedical applications as compared to the use of, e.g., conventional wet chemical methods [1]. Most APPJs employ helium as the discharge gas, which has pros and cons. It is generally well-known that it is relatively easy to sustain helium discharge due to penning ionization caused by the metastable molecular helium excimer; however, it is very costly and much lighter than air that may not be difficult/suitable for several applications. In contrast, argon is relatively cheap and heavier than air; however, it is generally more difficult to sustain an argon discharge. In addition, some specific sterilization effect on bacteria by argon APPJ as compared to helium one was demonstrated [2]. Nevertheless, the difficult sustainment of argon APPJ can be overcome through a proper design of the electrode arrangement.

In the current study, we have developed a new type of argon round APPJ. We have carefully characterized the APPJ by measuring its electrical properties, optical emission spectroscopy (OES) and gas temperature, to name a few. At the end, we also applied this APPJ to sterilize some bacteria such as Escherichia coli and Bacillus subtilis to demonstrate its potential application in sterilization.

## 2. Experimental Methods

Figure 1 shows the argon round APPJ system along with some instruments for characterization. It consists of a powered electrode, a grounded electrode, and an inner floating electrode which are made of copper. The dielectric tube is made of quartz. The argon gas flows into the quartz tube. The plasma jet is driven by a sinusoidal power source with a frequency of 20 kHz and an amplitude of 7 kV. The downstream temperature is measured by an alcohol thermometer that can avoid the arcing phenomenon. The relative excited OH radical intensity is measured by the OES system (Model SP 2500, Princeton Instruments) with an ICCD (Princeton Instruments).

E. coli and B. subtilis were used for sterilization experiments using the newly developed APPJ. Other types often found in dental and wound healing clinics will be used in the near future. The cultures were diluted 1/10 in 100 mL of LB Broth repeatedly for 3 h to 6 h at 37.5 °C until the optical density (OD) reaching the required concentration level ($1.5\times10^7$ CFU/mL).

The OD value was calibrated before bacteria culture preparation. Then, added 100 ml solution to a sterile Petri dish (diameter: 80 mm), in which 20 mL of LB Agar was coated. We used glass balls to spread solution uniformly. The Petri dishes were exposed to the APPJ with a treating distance of 5 mm. The test condition is as shown later. After plasma jet treatment for different times, the dishes were incubated at 37.5 °C for 8 h, and we measured the inactivation area by the NIH Image software, which can easily calculate the area based on gray level and pixel counting.

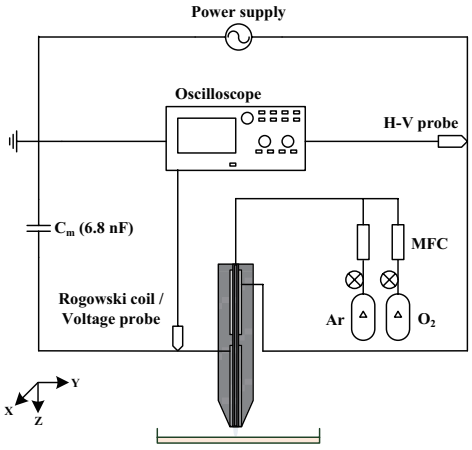


Fig. 1 Schematic diagram of the new argon round APPJ system.

## 3. Results and Discussion

Figure 2 shows the plasma jet images taken at various argon mass flow rates. The results show that the jet length increases with increasing mass flow rate with a maximal length of 20 mm when the argon mass flow rate is 5 slm. Figure 3 shows the corresponding temporal

Corresponding author: Jong-Shinn Wu
*E-mail address*: chongsin@faculty.nctu.edu.tw

gas temperature of the plasma jet measured at a downstream distance of 5 mm, at which sterilization will be applied later. The results show that the temperatures become steady approximately after 5 minutes of power on, except the case of the mass flow rate of 1 slm. In addition, the gas temperature decreases from 35 °C to 31 °C when the mass flow rate increases from 2 slm to 5 slm. These steady gas temperatures were either well below or close to human skin temperature, which are highly potential for direct contact with human body.

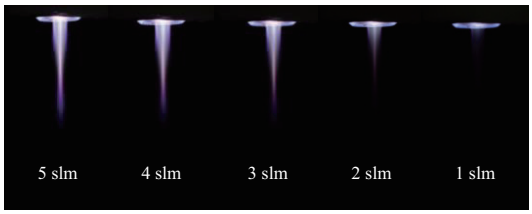


Fig. 2 Images of plasma jet with different gas flow rates.

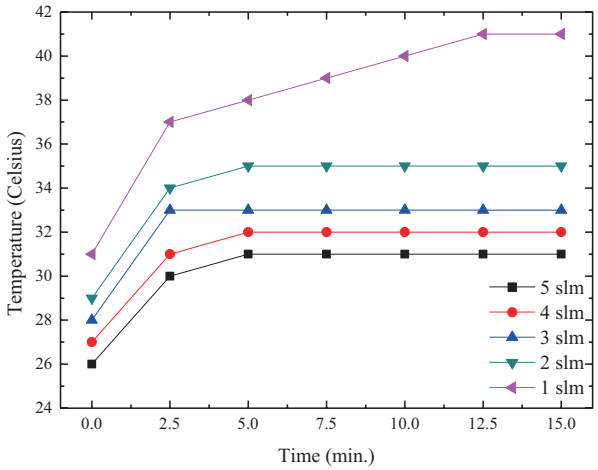


Fig. 3 Temporal gas temperatures with different gas flow rates.

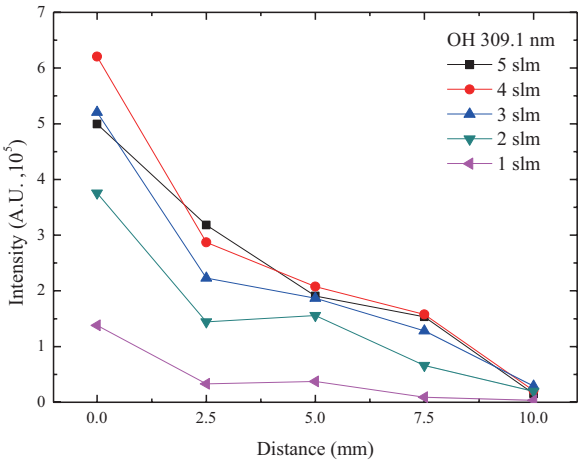


Fig. 4 Centerline distributions of OES intensity of excited OH (309.1 nm) with different argon mass flow rates in post-discharge region.

Figure 4 shows the measured relative OES intensities of excited OH radical as a function of downstream distance from the jet exit with various argon mass flow rates. The results show that the OES intensity decreases with increasing downstream distance due to quenching effect of ambient air. Specifically, the OES intensity of OH radical drops 2.5 times from the exit to the distance of 5 mm when the argon mass flow rate is 5 slm.

Figure 5 shows the images of bacteria growth after argon APPJ treatment with various times. The plasma jet is focus on the center of inactivation area for 5, 10, and 15 seconds, respectively. The treatment distance is fixed at 5 mm. The results show that the new argon APPJ can effectively sterilize both bacteria within 5 seconds. In addition, the inactivation area increases almost linearly with increasing treatment time. More data such as detailed temporal spatial distribution of OH OES intensity, sterilization efficacy on other kinds of bacteria and their cause of inactivation will be presented in the upcoming meeting.

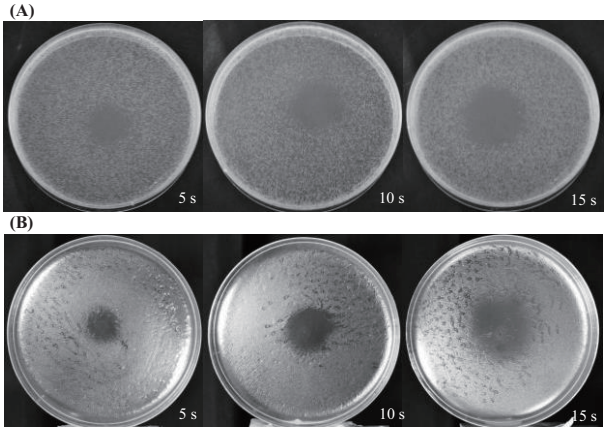


Fig. 5 Bacteria growth images after argon plasma jet treatments with different times (from left to right: 5s, 10s, and 15s) (A) E. coli, (B) B. subtilis.

## 4. Concluding Remarks

A new type of argon round APPJ system was developed and characterized carefully. Jet length can reach up to 20 mm at a mass flow rate of 5 slm with gas temperature below human body temperature at a distance of 5 mm with a high level of excited OH radical. The APPJ was used to effectively inactivate E. coli and B. subtilis within 5 seconds of treatment time.

## Acknowledgements

Financial support of the Ministry of Science and Technology through Grant No. 102-2811-E-009 -010 is highly appreciated.

## References

[1] M. Laroussi, et al., *Plasma Medicine: Applications of Low-Temperature Gas Plasmas in Medicine and Biology*, Cambridge University Press, UK, (2012).

[2] Young Sik Seo, et al., *Comparative Studies of Atmospheric Pressure Plasma Characteristics Between He and Ar Working Gases for Sterilization*, (2010).

# Vascularization of Endothelial Cells with Microgroove Structure

Toshiro Ohashi[1], Shaoyi Chen[1], Irza Sukmana[2]
[1]Faculty of Engineering, Hokkaido University
Kita 13, Nishi 8, Kita-ku, Sapporo 0608628, Hokkaido, Japan
[2]Department of Biomechanics and Biomedical Materials, Universiti Teknologi Malaysia (Present: Institute of Technology Bandung, Indonesia)
UTM Skudai, 81310 Johor Bahru, Malaysia

**ABSTRACT**

This study was performed to test promotional effects of topographic features on *in vitro* vascularization. Endothelial cells were cultured in a 3D environment within fibrin gel on a polydimethalsiloxane (PDMS) microgroove substrate. The widths of the microgrooves were designed from 50 μm to 200 μm. It was confirmed that cells showed morphologies within the gel which related to vascularization, particularly cell circle structures with lumens inside. The results showed that microgrooves with the width of 100 μm were an optimal condition for vascularization.

## 1. Introduction

Vascularization is a phenomenon of de novo blood vessel formation of endothelial cells, playing an important role in many biological and pathological processes, such as embryogenesis, wound healing and tumor development [1]. To understand the mechanism of vascularization, a number of *in vivo* and *in vitro* studies have been performed. Among them, there are reports about the promotional effect of substrate topography on angiogenesis. Sukmana and Vermette cultured endothelial cells *in vitro* with paralleled fibers made from polyethylene terephthalate (PET) for stimulating vascularization [2]. It was demonstrated that the PET fibers served as a geometrical guidance for cell behaviors towards the formation of tube-like structure between adjacent fibers. It was also concluded that in the range of 50 μm to 200 μm, fibers spaced at a distance of 100 μm was the best condition for tube-like structure formation. In another study of them, Sukmana and Vermette cultured endothelial cells in the same device in the presence of vascular endothelial growth factor in culture medium [3]. It was proved that VEGF has a promotional effect on tube-like structure formation and the effect was dose dependent with the best VEGF concentration of 2 ng/ml.

Based on these results, this study patterned PDMS substrate with microgrooves by MEMS techniques (Fig. 1a and Fig. 1b). The microgrooves were separated from each other with 100-μm-wide rectangular ridges, which served as a mimic of PET fibers used in the studies of Sukmana and Vermette [2, 3]. The widths of these microgrooves changed from 50 μm to 200 μm, which are in good comparison with spacing distances between PET fibers. The purpose of this study was to investigate the promotional effect of topographic features on microvascularization as a geometrical guidance. Also, the promotional effect of VEGF on microvacularization was tested. The promotional effect was evaluated by cell morphologies which cells did not show in a 2D environment.

## 2. Method

*The new experimental system* - It consists of two components (Fig. 1c): a PDMS substrate patterned with microgrooves and a fibrin gel embedded with endothelial cells. Fabricated in a square region (14 mm × 14 mm) in the PDMS membrane, the microgrooves have a rectangular profile, with the width of 50, 100, 150 and 200 μm, and the depth of 100 μm. The surface of PDMS substrate was treated with plasma to become hydrophilic and was coated with Pronectin F, which helps cell adhesion. The fibrin gel with embedded cells was made by incubating a mixture of fibrinogen solution, thrombin solution and cell suspension. The gel and PDMS substrate were bound following a surface treatment with air plasma.

*Cell culture* – Bovine aortic endothelial cells (BAECs) under passage 10 were cultured in a 3D environment within fibrin gel for 4 days with DMEM + 10% FBS on the top (Fig. 1c). To test the promotional effect of VEGF on structure formation, VEGF was supplemented into culture medium with a concentration of 2 ng/ml.

*Cell morphology analysis* – After 4 days of incubation, BAECs were immunofluorescently stained with rhodamine phalloidin for actin filaments and Hoechst for cell nuclei. Fluorescence images of cells were obtained with a microscope and three types of cell morphologies that related to vascularization were observed: cord-like cells, sprouting cells and cell circles. The total number of each specific cell structure was counted in 10 images and the number of structure per unit area was calculated using Image J software (Fig. 2).

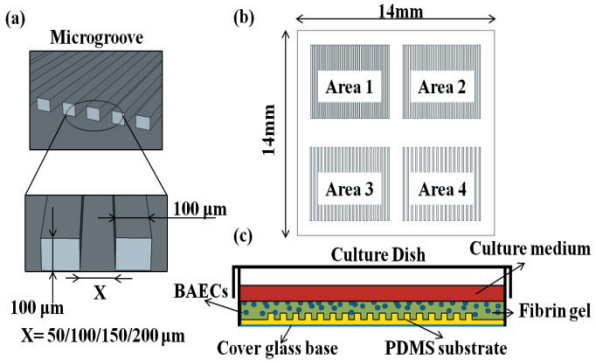


Fig. 1 Schematics of (a) geometries of microgrooves with different widths, (b) microgroove-patterned PDMS substrate and (c) 3D cell culture system.

Corresponding author: Toshiro Ohashi
*E-mail address: ohashi@eng.hokudai.ac.jp*

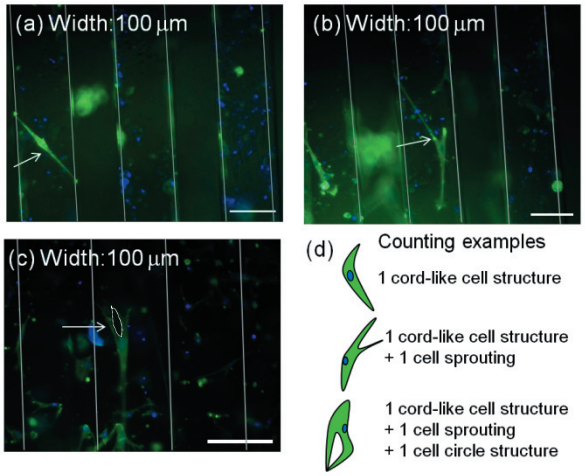


Fig. 2 Representative fluorescence images of (a) cord-like cells, (b) sprouting cells and (c) cell circle. Scale bars: 100 μm. (d) Counting method of cell structures.

## 3. Results

*Effect of topographic features*– Cord-like cells were found in all microgrooves. The number of sprouting cells was much less in microgrooves with the width of 50 μm than in the other three patterns. Cell circle structures were mainly found in microgrooves with width of 100 μm (Fig. 3).

*Effect of VEGF*– After adding 2 ng/ml VEGF into cell culture medium, a larger number of all types of structures were found in microgrooves (Fig. 4). Effects of VEGF supplementation were statistically significant in the most cases.

## 4. Discussion

We have developed a new experimental system to test *in vitro* vascularization of endothelial cells. This new system was able to drive endothelial cells to form morphologies that relate to *in vitro* vascularization: cord-like cells, sprouting cells and cell circles. The three types of cell morphologies can be explained by a sequential change in cell shapes. Round endothelial cells elongated into cord-like cells. Cord-like cells sprouted branches and formed sprouting cells. The cell branches connected with each other and formed cell circles with lumens inside. These cell morphologies were not found when endothelial cells were cultured in a 2D environment in a normal culture dish or on a PDMS microgroove pattern without fibrin gel. The 3D environment was advantageous to structure formation. Our experimental results also demonstrated that microgroove with the width of 100 μm was an optimal structure among the four conditions examined for cell structure formation, which was consistent with the previous study performed by Sukmana and Vermette [2, 3]. In addition, VEGF promoted structure formation, which is in agreement with the finding that endothelial cells change their shapes during vasculogenesis through actin filaments remodeling in response to VEGF [4]. With VEGF, microgroove with the width of 100 μm was still an optimal condition, suggesting that VEGF and

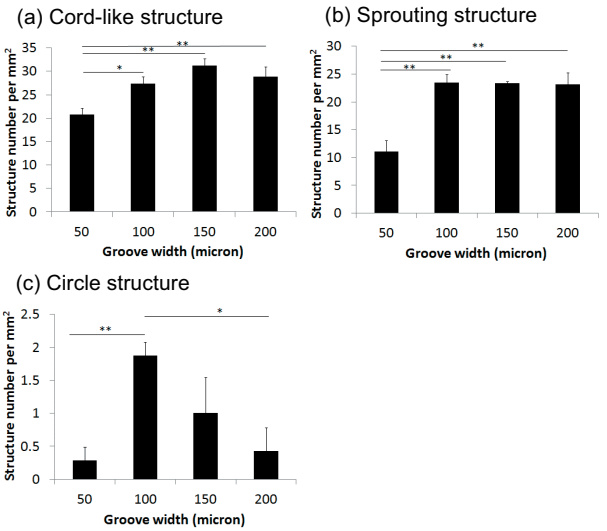


Fig. 3 Effect of microgroove width on the formation of (a) cord-like cell structures, (b) sprouting structures and (c) cell circle structures. * $p<0.05$, ** $p<0.01$.

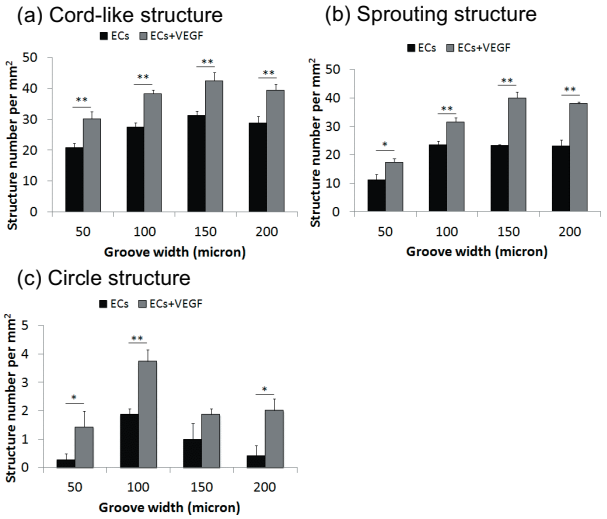


Fig. 4 Effect of VEGF on the formation of (a) cord-like cell structures, (b) sprouting structures and (c) cell circle structures. * $p<0.05$, ** $p<0.01$.

microgroove topography synergestically influence endothelial cell vascularization.


## Acknowledgements

Open Facility, Hokkaido University Sosei Hall for microfabrication. China Scholarship Council (CSC): sholarship to Mr. Shaoyi Chen. Dr. Eijiro Maeda: preparation of the proceeding.


## References


[1] F. Arnold and D.C. West, *Pharma Ther*, 52 (1991) 407-422.

[2] I. Sukmana and P. Vermette, *J Biomed Mater Res*, 92 (2010) 1587-1597.

[3] I. Sukmana and P. Vermette, *Biometer*, 31 (2010) 5091-5099.

[4] R.M.H. Merks, S.V. Brodsky, M.S. Goligorksy, M.S. Newman and J.A. Glazier, *Dev Bio*, 289 (2006) 44 – 54.

Eleventh International Conference on Flow Dynamics
October 8-10, 2014, Sendai, Miyagi, Japan

# Molecular Basis of Cellular Responses to Nanosecond Pulsed Electric Fields - Signal Transduction, Stress Response, and Cell Death -

Ken-ichi Yano and Keiko Morotomi-Yano
Department of Bioelectrics, Institute of Pulsed Power Science, Kumamoto University
2-39-1 Kurokami, Kumamoto-shi, Kumamoto 860-8555, Japan

**ABSTRACT**

Nanosecond pulsed electric fields (nsPEFs) have received considerable attention as a novel means for life sciences, although their mechanism of action remains to be fully elucidated. Employing experimental approaches in molecular biology, we have demonstrated that nsPEFs induce various cellular responses, including signal transduction and cell death. Notably, human cells recognize sublethal nsPEFs as a novel form of cellular stress. These findings show the therapeutic potential of nsPEFs and provide important mechanistic insights into actions of other physical stimuli.

## 1. Introduction

Pulsed electric fields (PEFs) are widely used for various applications in life sciences, because different biological effects can be achieved depending on the duration of electric pulses. Milli-to-microsecond PEFs are widely used for DNA electroporation because these PEFs primarily act on the cell membrane. In contrast, ultrashort PEFs in the range of nanoseconds (nanosecond PEFs, nsPEFs) have a distinct mode of action and directly reach intracellular components without membrane destruction. Importantly, intense nsPEFs are known to kill tumor cells efficiently *in vitro* as well as *in vivo*. Thus, nsPEFs are increasingly recognized as a novel potential means for cancer therapy, although the molecular mechanisms of their biological actions should be fully understood prior to clinical applications of nsPEFs to human patients. We have investigated intracellular responses to nsPEFs by employing various experimental approaches in molecular biology and have successfully demonstrated that nsPEFs elicit multiple cellular responses, which vary depending on the nsPEF intensity.

## 2. Method

Cultured human and mouse cells were suspended in regular cell culture medium. The cell suspension was placed in an electroporation cuvette (Thermo Fisher) and exposed to nsPEFs at 1 Hz. nsPEFs were generated using a pulsed power modulator, which has been developed in Kumamoto University and is now commercially available (Suematsu Electronics, MPC3000S). Under our standard experimental conditions, the pulse width at half maximum was estimated to be approximately 80 ns [1]. After the exposure to nsPEFs, cell suspension was diluted 5-fold and incubated at 37°C for appropriate periods. Cell viability was measured by the MTT method [1]. For analyses of protein status and gene expression, cells were subjected to western blotting and quantitative real-time PCR, respectively [1-6]. Rates of protein synthesis were calculated by measuring the incorporation of radioactive amino acids into protein fractions [3].

Corresponding author: Ken-ichi Yano
*E-mail address*: yanoken@kumamoto-u.ac.jp

## 3. Results and Discussion

### 3.1. Dependency on nsPEF intensity

Human cells respond differently to nsPEFs, dependently on nsPEF intensity (Fig. 1). Intracellular signaling can be activated by relatively mild nsPEFs [1, 2, 4]. When the intensity of nsPEFs is increased to sublethal levels, these nsPEFs act as a novel form of cellular stress [3]. Intense nsPEFs induce either apoptotic or necrotic cell death in a cell type-dependent manner [5, 6].

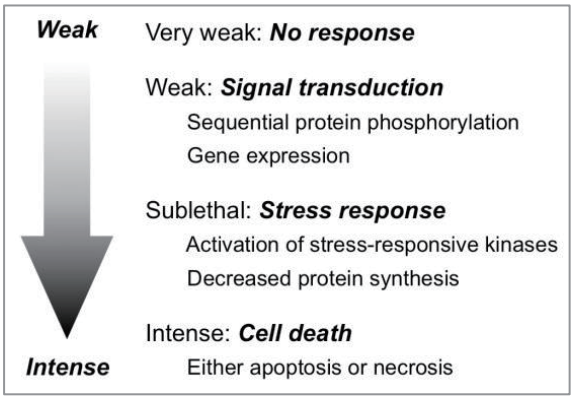


Fig. 1 Intensity-dependent cellular responses to nsPEFs.

### 3.2. Intracellular Signal Transduction

Relatively mild nsPEFs do not cause morphological changes observable under microscope or cell death. However, cells rapidly respond to such stimuli by activating multiple intracellular signal pathways, including MAPK pathways [1, 2] and AMPK pathway [4]. The intracellular signaling is mediated by sequential phosphorylation of proteins in these pathways and leads to the expression of genes that are located downstream of these pathways (Fig. 2). The relationship among proteins and genes affected by nsPEFs can be verified using inhibitors of specific proteins in these pathways (Fig. 2).

### 3.2. Induction of Stress Responses

Human cells can respond to various adverse physiological conditions, which are collectively called cellular stress. Four stress-responsive protein kinases exist in human cells and play critical roles in cellular

stress responses, including phosphorylation of the translation regulator eIF2α and subsequent suppression of protein synthesis. Relatively intense nsPEFs, which cause slight growth retardation, induce the activation of two stress-responsive kinases, eIF2α phosphorylation, and transient suppression of global protein synthesis (Fig. 3). This observation means that human cells recognize nsPEFs as cellular stress.

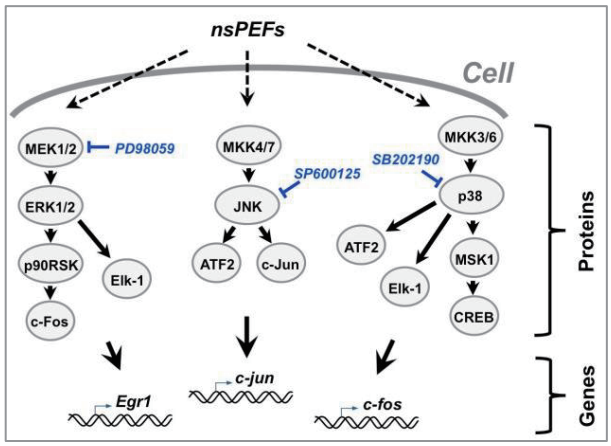


Fig. 2 nsPEFs activate MAPK pathways. Exposure of human cells to nsPEFs elicits sequential activation of protein components in the MAPK pathways and results in expression of genes located downstream of these pathways. Specific inhibitors (shown in blue) are commercially available and can be used to verify the relationship between upstream and downstream events in each pathway.

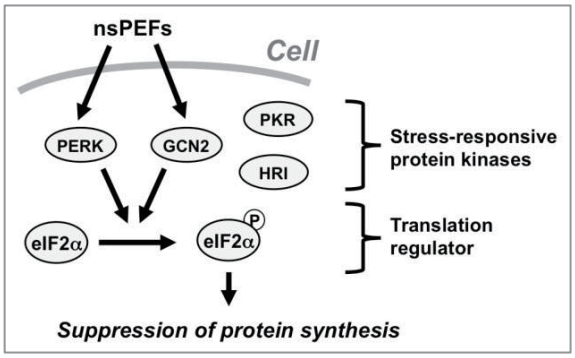


Fig. 3 Stress responses induced by nsPEFs. Human cells have four stress-responsive protein kinases, and two of them (PERK and GCN2) are activated by nsPEFs and subsequently phosphorylate eIF2α, leading to suppression of protein synthesis.

### 3.3. Induction of Cell Death

Apoptosis and necrosis are major modes of programmed cell death. For a long time, necrosis has been regarded to be passive uncontrolled cell death, but recent studies have clearly demonstrated that necrosis is also programmed cell death.

Exposure of human cells to intense nsPEFs leads to significant reduction in cell viability, indicating that nsPEFs induce cell death. In HeLa S3 cells, nsPEFs induce necrosis, instead of apoptosis (Fig. 4) [5]. Interestingly, the presence and absence of extracellular calcium determine the mode of cell death in nsPEF-exposed HeLa S3 cells [6]. In the absence of extracellular calcium, HeLa S3 cells become less susceptible to nsPEFs and exhibit apoptotic phenotypes.

Furthermore, the modes of cell death induced by nsPEFs are cell-type dependent. Jurkat and HL-60 cells exposed to nsPEFs undergo apoptosis, whereas HeLa S3, K562, HEK293 exhibit necrotic phenotypes after nsPEF exposure [6], demonstrating that the cellular context is critical for the choice of cell death modes.

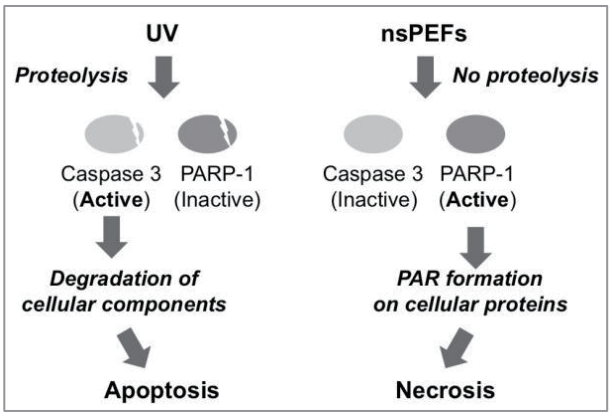


Fig. 4 UV and nsPEFs induce apoptosis and necrosis, respectively, in HeLa S3 cells. Status of Caspase 3 and PARP-1 can be used to discriminate apoptotic and necrotic cell death. nsPEFs do not induce apoptosis-related proteolysis of these proteins but activate protein modification with poly ADP-ribose (PAR), which is associated with necrosis.

### 4. Concluding Remarks

Our studies employing experimental approaches in molecular biology have revealed the multiple intracellular responses to nsPEFs. These studies support the therapeutic potential of nsPEFs and provide important mechanistic insights into actions of other physical stimuli.


### Acknowledgements

This work was supported by Grants-in-Aid for Scientific Research from Japan Society for the Promotion of Science.


### References


[1] K. Morotomi-Yano, Y. Uemura, S. Katsuki, H. Akiyama, K. Yano, *Biochem. Biophys. Res. Comm.*, 408 (2011) 471-476.

[2] K. Morotomi-Yano, H. Akiyama, K. Yano, *Arch. Biochem. Biophys.,* 515 (2011) 99-106.

[3] K. Morotomi-Yano, S. Oyadomari, H. Akiyama, K. Yano, *Exp. Cell Res.*, 318 (2012) 1733-1744.

[4] K. Morotomi-Yano, H. Akiyama, K. Yano, *Biochem. Biophys. Res. Comm.*, 428 (2012) 371-376.

[5] K. Morotomi-Yano, H. Akiyama, K. Yano, *Biochem. Biophys. Res. Comm.*, 438 (2013) 557-562.

[6] K. Morotomi-Yano, H. Akiyama, K. Yano, *Arch. Biochem. Biophys.*, 555-556 (2014) 47-54.

# Atmospheric Pressure Plasma Induced Alterations in Cellular Responses

Bomi Gweon[1], Kijung Kim[2], Jin Seung Choung[3], Wonho Choe[2], Jennifer H. Shin[3]
[1]Department of Public Health, Harvard University,
664 Huntington Ave, Boston, MA, 02115, USA
[2]Department of Physics, KAIST
291 Daehak Ro, Yuseong Gu, Daejeon, 305-701, Republic of Korea
[3]Department of Mechanical Engineering, KAIST
291 Daehak Ro, Yuseong Gu, Daejeon, 305-701, Republic of Korea

**ABSTRACT**

Atmospheric pressure plasma (APP) was shown to be effective in selective killing of cancer cells and altering the physiology of a number of different cell types. Among numerous effectors of the APP, increase in intracellular ROS has been identified as a predominant key factor that regulates cellular functions. However, our recent studies on stromal cell types such as fibroblasts and endothelial cells, exhibited distinct behaviors which potentially are regulated by ROS independent pathway, suggesting that the APP-cell interactions are cell-type specific.

## 1. Introduction

Recently, the uses of atmospheric pressure plasma (APP) on mammalian cells and tissues have been reported as promising tools in potential clinical applications. A number of attempts have been made on the APP-based skin therapy to enhance wound healing or to treat skin cancers [1-3]. In particular, APP has been used to remove cancer cells by causing apoptosis and necrosis. However, the effect of APP on the neighboring tissues of tumors remains unknown. Tumor is structurally very complex, made of many different cell types. In tumor progression, two very important processes occur, namely epithelial-mesenchymal transition (EMT) and angiogenesis [4]. For the efficacy of APP for the cancer treatment, its effects on other cell types must be investigated. However, cells of different origin and cells of different disease state have been shown to respond differently to the APP treatment. In this study, we applied APP on human dermal fibroblasts (HDF) and human aortic endothelial cells (HAECs) in a moderate plasma condition, and observed their distinct responses that are inconsistent with typical ROS induced responses. These observations suggest that APP treatment must involve distinct mechanism that regulates the cellular physiology apart from the well-accepted ROS dependent pathway, and the APP-cell interactions are very much cell type specific.

## 2. Method

2.1 Cell preparation

HAECs (Lonza #CC-2535, passage 7 - 9) and HDFs were cultures in endothelial cell growth medium-2 (EGM-2, Lonza #CC-3162) and Dulbecco's modified Eagle's medium (DMEM) supplemented with 10% fetal bovine serum and 1% penicillin/streptomycin, respectively, in a humidified atmosphere of 5% $CO_2$ air at 37°C. Cells grown to 90% confluency on a fibronectin coated glass-bottom dish were placed 15 mm below a plasma applicator (Fig. 1). A culture medium thickness of 3 mm was sufficient to prevent the plasma plume from coming into direct contact with the cells.

Corresponding author: Jennifer H. Shin
*E-mail address*: j_shin@kaist.ac.kr

2.2 Real time PCR

Total RNA was isolated from HAECs and HDFs using NucleoSpin RNAII kit (MN, Düren, Germany) and cDNA was prepared with iScriptTM cDNA synthesis kit (Bio-Rad Laboratories, Hercules, CA, USA). Real time PCR was performed on a Bio-Rad CFX96 using iQ SYBR Green supermix (Bio-Rad Laboratories). The reaction conditions were set at 95 °C for 3 min followed by 40 cycles at 95 °C for 15 sec and 60 °C for 20 sec. Reactions were done in triplicate and the genes of our interests were normalized by GAPDH.

2.3 Immunofluorescence

Cells were washed with pre-warmed PBS and fixed for 20 min in 3.7% formaldehyde (Sigma, St Louis, MO). Cells were then permeabilized for 15 min in 0.2% Triton X-100 (Sigma) and blocked for 60 min in 3% bovine serum albumin (BSA, Gibco). After washing, they were incubated overnight with primary antibodies against vimentin (1:200; Biosciences) in blocking buffer. After washing the cells with PBS, cells were incubated for 12 h with rabbit Alexa Fluor 488-conjugated secondary antibodies (1:200) in blocking buffer. Alexa 568-phalloidin (1:50) in blocking buffer was used to counter stain F-actin. The nuclei were stained by 4', 6-diamidino-2-phenylindole diluted in PBS (1:50000) for 5 min.

## 3. Results and Discussion

3.1 Human aortic endothelial cells

Following the 20 mins of exposure to APP, the treated HAECs were cultured for 24 - 72 hours in the incubator to allow response time for cellular changes. Dramatic reduction of the cell proliferation along with alterations in cell cycle related gene expressions were observed which indicates the cellular cyclic arrest. The morphology of the APP treated HAECs became more symmetric and rounded with thinner and shorter actin stress fibers compared to that of the untreated cells. In addition to the decrease in the 2D migration speed, tube assay for the APP treated HAECs showed the decrease in the total tube length of the complete loops when

compared to that of the untreated cells. Since the elevated new vessel formation (angiogenesis) is one of the major problems in tumor growth, our results support the potential use of APP in controlling the proliferation, migration, and tube formation of the endothelial cells for anti-angiogenic therapies.

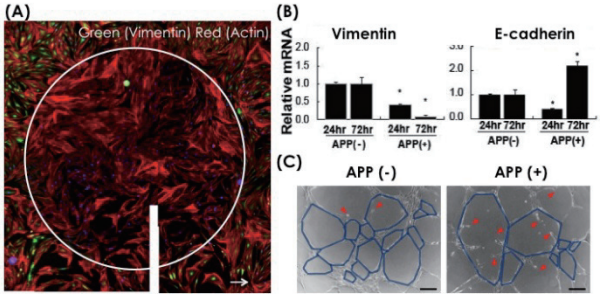


Fig. 1 (A) Immuno-fluorescent images of APP treated (encircled by a white line) HDFs showing distinct regions of different morphologies, (B) APP treatment suppresses mesenchymal marker vimentin while promotes epithelial marker e-cadherin, (C) APP treated HAEC show disrupted integrity (marked by red arrows) in network structures via suppression of angiogenic capability.

3.2 Human dermal fibroblasts

When the APP treated HDFs were incubated for 24 h, we noticed a striking change in cellular morphology featuring rounded polygonal shapes with cortically arranged actin whereas the untreated control cells were in elongated spindle shapes with pronounced intracellular actin stress fibers. This morphological change is considered the landmark feature of a MET (mesenchymal-epithelial transition)-like process. The changes in morphology were accompanied by a dramatic reduction in the level of vimentin and α-smooth muscle actin (α-SMA) expressions, suggesting the loss of characteristic of the mesenchymal cells. Strikingly however, the observed phenotypic changes were opposite to what was expected for the ROS-induced cellular responses. Our study confirmed that the intracellular ROS level was indeed decreased by the APP treatment through the elevated anti-oxidant activities.

Plasma is difficult to characterize and the plasma-induced chemical and physical effects are very complex. Among numerous effectors of the APP, ROS has been identified as a predominant key factor that regulates cellular functions. Especially, the majority of the research performed on cells of the epithelial has shown significant increase in intracellular ROS (reactive oxygen species) by APP treatment, which then led to various ROS dependent responses including apoptosis. However, our recent studies on stromal cell types such as fibroblasts and endothelial cells, exhibited distinct behaviors that are inconsistent with typical ROS induced responses. Our studies support strongly that cells of different types not only have different level of ROS to begin with, but also have different level of ROS handing capacity (ROS scavenging effects).

**Acknowledgment**

This research was supported by the National Fusion Research Institute of Korea (NFRI) and the Korea Research Council of Fundamental Science & Technology (N04130012), and supported in part by National Research Foundation of Korea (NRF) (2011-0025465).

**References**

[1] G. Fridman, G. Friedman, A. Gutsol, A.B. Shekhter, V.N. Vasilets, and A. Fridman, *Plasma Process. Polym.*, 5 (2008) 503-533.

[2] K.-D. Weltmann, M. Polak, K. Masur, T. von Woedtke, J. Winter, and S. Reuter, *Contrib. to Plasma Phys*., 52 (2012) 644-654.

[3] O. Volotskova, T.S. Hawley, M. a Stepp, and M. Keidar*, Sci. Rep*., 2 (2012) 636.

[4] M. O'Hayer, C. L. Salanga, T. M. Handel, and S. J. Allen, *Biochemical J. (*2008), 409, 635-649.

[5] D. B. Graves, *J. Phys D*., 45 (2012) 263001.

Eleventh International Conference on Flow Dynamics
October 8-10, 2014, Sendai, Miyagi, Japan

# Control of Cell Viability Treated by Neutral Oxygen Species

Takayuki Ohta[1], Masafumi Ito[1], Hiroshi Hashizume[2], Keigo Takeda[2], Kenji Ishikawa[2], Masaru Hori[2]
[1] Faculty of Science and Technology, Meijo University
1-501 Shiogamaguchi, Tempaku, Nagoya, 468-8502, Japan
[2] Department of Electrical Engineering and Computer Science, Nagoya University
Furo-cho, Chikusa, Nagoya, 464-8603, Japan

**ABSTRACT**

We have measured the densities of ground-state atomic oxygen O($^3P_j$) and singlet oxygen molecule [$O_2(^1\Delta_g)$] produced from the oxygen radical source. The O($^3P_j$) density was between 1.4 x $10^{14}$ and 1.5 x $10^{15}$ $cm^{-3}$. $O_2(^1\Delta_g)$ density was monotonically increased up to $1.2\times10^{15}$ $cm^{-3}$ with increasing $O_2/(Ar+O_2)$ flow rate ratio. O ($^3P_j$) density decreased with increasing exposure distance, while $O_2(^1\Delta_g)$ density was constant. We conclude that O ($^3P_j$) is one of the dominant species responsible for inactivating microorganisms.

## 1. Introduction

Recently, non-equilibrium plasma has been much attention for applications in biology, medicine, agriculture and so on. There are many reports that microorganisms such as fungi, yeast, bacteria, cancer cell, and so on, were inactivated using cold plasmas. The cold plasma simultaneously produces various factors, such as reactive oxygen species (ROS) including ground-state atomic oxygen (O($^3P_j$)), hydroxyl radical (•OH), singlet oxygen molecule ($O_2(^1\Delta_g)$), superoxide anion ($\bullet O_2^-$), and ozone ($O_3$), ultraviolet (VUV) and UV-C emissions, neutral and charged species, and electric fields, which may synergistically affect to inactivate microorganisms. Several studies suggested that ROS may be the dominant factor on the inactivation of the microorganisms by plasmas. The bactericidal effect of plasma differs depending on microorganisms owing to the resistance against the bactericidal factor. It is essential to study the resistance against the bactericidal factor produced by the plasma based on the quantitative diagnostics of the plasma. We have focused on inactivating the spores of *Penicillium digitatum* using non-equilibrium atmospheric pressure plasma (NEAPP) in gas phase. We reported that the contributions of UV radiation and ozone were not dominant for inactivating spores of *P. digitatum* by NEAPP.[1] By measuring the radical densities of ground-state atomic oxygen [O($^3P_j$=0,1,2)] with an atmospheric-pressure oxygen radical source, which only supplies neutral oxygen radicals, we quantitatively elucidated that O($^3P_j$) is one of the effective factors responsible for inactivating *P. digitatum* spore.[2]

In this study, we have measured the densities of ground-state atomic oxygen O($^3P_j$) and singlet oxygen molecule [$O_2(^1\Delta_g)$] by vacuum ultraviolet absorption spectroscopy(VUVAS), which are produced from the oxygen radical source. We have exposed the radicals to *P. digitatum* spores to evaluate the bactericidal effects.

## 2. Experimental

A schematic diagram of the experimental setup containing an oxygen-radical source employing a non-equilibrium atmospheric pressure $O_2$/Ar plasma with a vacuum ultraviolet absorption spectroscopy optical system is described in elsewhere.[2] The radical source is based on an atmospheric-pressure high-density $O_2$/Ar plasma, which produces a high electron density of about $10^{16}$ $cm^{-3}$.[3, 4] Charged species and optical radiation from the $O_2$/Ar plasma were blocked using electrodes and the structural shape of the exit aperture so that only neutral species were supplied to the samples. The chamber containing the radical source was purged with Ar gas to eliminate the influence of atmospheric gases. Measurements and exposures of radicals to spores were performed at 10 mm, 15 mm or 20 mm downstream from the radical head. Flow rate ratio $O_2/(O_2+Ar)$ was 0.6 % at total flow rate of 5 slm.

The absolute densities of O($^3P_j$) and $O_2(^1\Delta_g)$ were measured by VUVAS using a microdischarge hollow-cathode lamp (MHCL) and a deutrium lamp, respectively. VUV light from the light source passed though the $MgF_2$ window and was introduced into the chamber. VUV light passing through the absorption region was focused on the slit of a VUV monochromator with the $MgF_2$ lens and detected by a photomultiplier tube. The measurements were performed 10, 15, and 20mm downstream from the exit of the radical source. The method for calculating the O($^3P_j$) density has been described in detail elsewhere[5]. The $O_2(^1\Delta_g)$ density was calculated based on the absorption intensities at 128.5 and 134.0 nm, using a reported method involving the solution of simultaneous equations[6].

## 3. Results and Discussion

Fig. 1 shows O($^3P_j$) and $O_2(^1\Delta_g)$ densities, and D values, which are inversely proportional to the inactivation rate, dependent on exposure distance. The O($^3P_j$) density decreased according to extending the exposure distance, while the $O_2(^1\Delta_g)$ was constant. The life time of O ($^3P_j$) was estimated to be 0.47 ms from the gradient of the data. On the other hand, the D values were increasing together with the extending. These results suggests that the O($^3P_j$) radical is the exclusively effective to the inactivation of *P. digitatum* spores.

We have investigated the change of intracellular nanostructure in the spores treated with oxygen radicals

Corresponding author: Takayuki Ohta
*E-mail address*: tohta@meijo-u.ac.jp

on the inactivation process using a transmission electron microscopy (TEM). Figures 2(a)-(f) show TEM images of cross sections of the control spore and the spores of *P. digitatum* with radical treatment for 1.5, 3, 5, 7, and 10 min, respectively. The control spore clearly shows the intracellular structure and organelles such as a nucleus and mitochondria, as shown in Fig. 2(a). Those membrane structures in the spores with $O(^3P_j)$ dose of $2.1\times10^{19}$ and $4.2\times10^{19}$ $cm^{-2}$ were relatively maintained, as shown in Figs. 2(b) and (c), respectively. On the other hand, the intracellular structure was degraded over $O(^3P_j)$ dose of $7.0\times10^{19}$ $cm^{-2}$, as shown in Figs. 2(d), (e), and (f). Cerioni et al. also reported that excess oxidative stress with hydrogen peroxide caused the severe damage in the intracellular structure of *P. digitatum* spore with a TEM observation[7]. These results indicated that oxygen radicals gradually caused decomposition of intracellular membrane structure with an increase of $O(^3P_j)$ dose.

## 4. Concluding Remarks

We successfully inactivated *P. digitatum* spores using an oxygen radical source employing a non-equilibrium atmospheric-pressure remote $O_2$/Ar plasma. The ground- state oxygen radical O ($^3P_j$) and singlet oxygen molecule [$O_2(^1\Delta_g)$] densities were measured using VUV absorption spectroscopy. The $O(^3P_j)$ density was between 1.4 x $10^{14}$ and 1.5 x $10^{15}$ $cm^{-3}$. $O_2(^1\Delta_g)$ density was monotonically increased up to $1.2\times10^{15}$ $cm^{-3}$ with increasing $O_2/(Ar+O_2)$ flow rate ratio. O ($^3P_j$) density decreased with increasing exposure distance, while $O_2(^1\Delta_g)$ density was constant. Based on these results obtained by quantitative analysis of the gas phase, we conclude that O ($^3P_j$) is one of the dominant species responsible for inactivating microorganisms.

## References


[1] S. Iseki, T. Ohta, A. Aomatsu, M. Ito, H. Kano, Y. Higashiyama and M. Hori, *Appl. Phys. Lett.*, 96 (2010) 153704.

[2] S. Iseki, H. Hashizume, F. Jia, K. Takeda, K. Ishikawa, T. Ohta, M. Ito and M. Hori, *Appl. Phys. Express*, 4 (2011) 116201.

[3] M. Iwasaki, H. Inui, Y. Matsudaira, H. Kano, N. Yoshida, M. Ito and M. Hori, *Appl. Phys. Lett.*, 92 (2008) 081503.

[4] H. Inui, K. Takeda, H. Kondo, K. Ishikawa, M. Sekine, H. Kano, N. Yoshida and M. Hori, *Appl. Phys. Express*, 3 (2010) 126101.

[5] H. Nagai, M. Hiramatsu, M. Hori, and T. Goto, *Rev. Sci. Instrum.*, 74, (2003) 3453.

[6] G. Gousset, P. Panafieu, M. Touzeau, and M. Vialle, *Plasma Chemistry and Plasma Processing*, 7 (1987) 409.

[7] L. Cerioni, S. I. Volentini, F. E. Prado, V. A. Rapisarda, and L. Rodríguez-Montelongo, *J. Appl. Microbiol.*, 109 (2010) 1441.


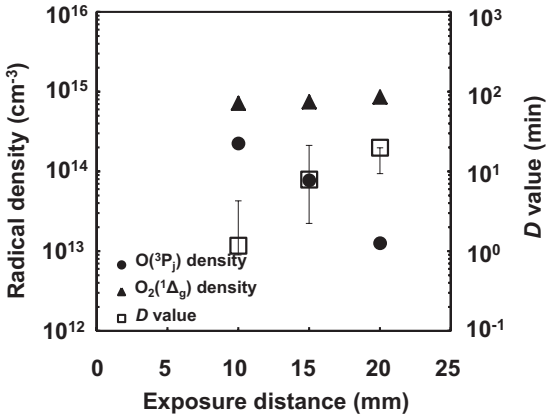


Fig. 1 $O(^3P_j)$ and $O_2(^1\Delta_g)$ densities, and D values as a function of exposure distance.

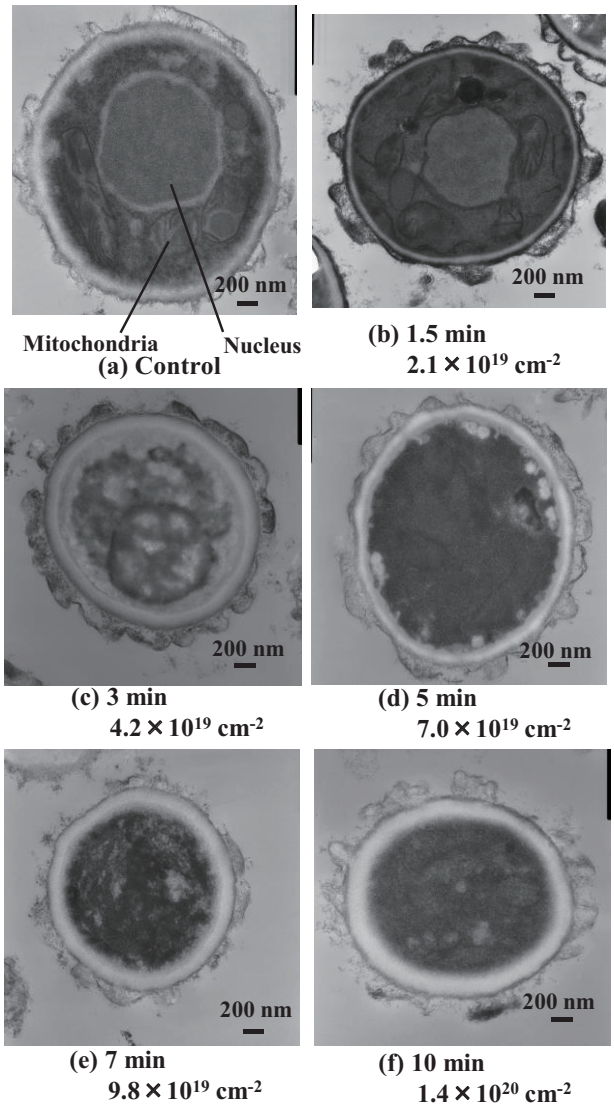


Fig. 2 TEM images of cross sections of *P. digitatum* spores: (a) a control spore, and (b)-(f) spores with oxygen radical treatment for 1.5, 3, 5, 7, and 10 min, respectively. The doses of $O(^3P_j)$ for each treatment time are also expressed under the flux of $2.3\times10^{17}$ $cm^{-2}s^{-1}$.

# Study on Shock Wave Propagation Phenomena in Simulated Materials for Understanding Mechanism of the Primary Blast Induced Traumatic Injury

Kiyonobu Ohtani[1], Atsuhiro Nakagawa[2], Keisuke Goda[3], Daiju Numata[4]
[1]Insititute of Fluid Science, Tohoku University, 2-1-1, Katahira, Aoba, Sendai, 980-8577, Japan
[2]Dept. of Neurosurgery, Tohoku University Graduate School of Medicine, 1-1, Seiryo, Aoba, Sendai, 980-8574, Japan
[3]Graduate school of Science, The University of Tokyo, 7-3-1, Hongo, Bunkyo, Tokyo 113-8686, Japan
[4]Graduate school of Engineering, Tohoku University, 6-6-01, Aza Aoba, Aramaki, Aoba, Sendai, 980-8579, Japan

**ABSTRACT**

This paper reports an experimental result of shock wave propagation in simulated biomedical materials for understanding mechanism of the primary blast induced traumatic injury. Shock wave generated by detonating of a micro explosive, was interacted with a brain model. The process of shock wave interaction with a brain model was visualized by shadowgraph method and recorded by a high-speed video camera. The sequential shadowgraph images shows the transmitted waves were propagated, reflected in gelatin layer of the brain model, and reflected wave; expansion wave was focused and bubble was generated at the opposite side from shock wave entry in the brain model.:

## 1. Introduction

The prominent role of the improvised explosive device in the current conflicts in Iraq and Afghanistan has dramatically increased the number of troops suffering from traumatic brain injury (TBI) [1], especially the blast injury [2]. However, the mechanism of the contra-cup injury in the primary blast-induced traumatic brain injury (bTBI) caused by the pressure wave has not been revealed yet.

Underwater shock wave and expansion wave propagation related to cavitation bubble generation are an important research issue for shock wave medical and biomedical application. Especially, expansion wave was generated by underwater shock wave reflecting from water surface, because of shock wave was reflected as expansion wave propagates by reflection with lower acoustic impedance. Acoustic impedance is defined as $z = \rho c$ where $\rho$ is density of material, $c$ is the speed of sound. The shock wave interaction phenomena with the interface of different materials in acoustic impedance have to be evaluated, because it is important to understand of the mechanism of the primary bTBI [3].

In this study, the experiment of shock wave propagation in the brain model made of simulated biomedical materials was performed for understanding the mechanism of primary blast-induced brain injury. The process of micro-explosive induced shock wave interaction with a brain model was visualized by shadowgraph method and recorded by a high-speed video camera.

## 2. Experimental Setup

Figure 1 shows the experimental setup for shock wave interaction with the brain model. In this study, the brain model is the simple cylindrical shape (diameter of 24 mm, length of 49 mm) for evaluating of two-dimensional shock wave interaction phenomena made of an acrylic tube (thickness of 1.5 mm) with 20 wt% gelatin. A shock wave was generated by exploding of a micro explosive pellet (silver azide; $AgN_3$, Showa Kinzoku Kogyo Co., Ltd., weight of 10mg, diameter of 1.5 mm, length of 1.5mm) with pulse Nd: YAG laser beam irradiation on it. A silver azide pellet is glued at the tip of a quartz optical fiber (G.C.600/750, Fujikura Ltd.) and placed at about $h$ = 1.0 mm from the edge of the acrylic tube. A pulsed Nd: YAG laser beam (SAGA220, 7ns pulse duration) guided through this optical fiber then ignites the micro explosive. Figure 2 shows the schematic setup of the optical arrangement for shadowgraph method by using a parabolic mirror (focal length of 1000 mm, diameter of 190 mm) and a flash lamp was used as a light source. The process of shock wave interaction with the brain model was

Corresponding author: Kiyonobu Ohtani
*E-mail address*: ohtani@ifs.tohoku.ac.jp

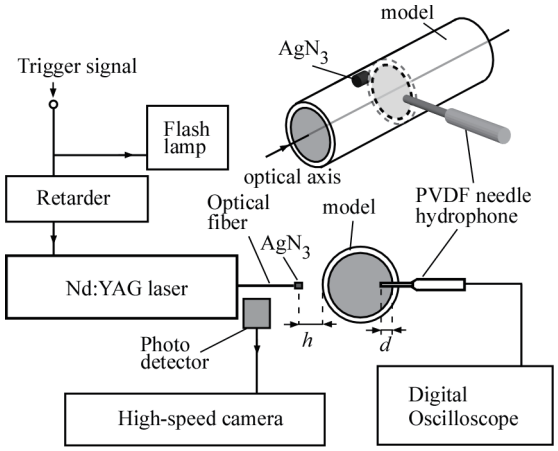


Fig. 1 Schematic diagram of an experimental setup for shock wave interaction with the brain model.

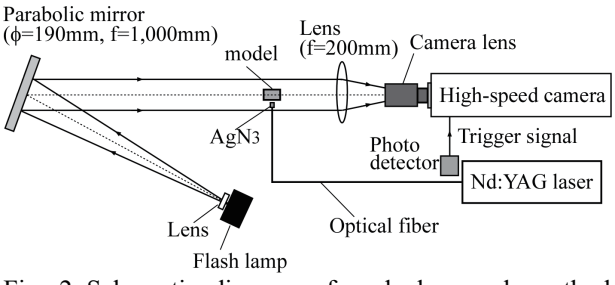


Fig. 2 Schematic diagram of a shadowgraph method optical setup.

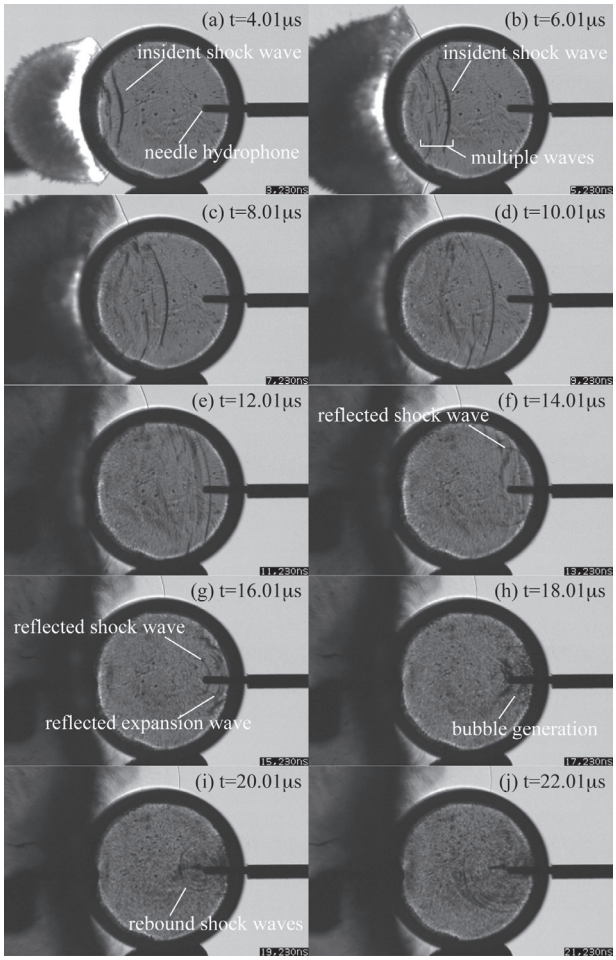


Fig. 3 Sequential shadowgraph images of micro-explosive induced shock wave interaction with the brain model. (*h*=1mm, Interframe time 200ns, exposure time 110ns)

visualized by this shadowgraph method optical setup and recorded by a high-speed camera (HPV-X, Shimadzu Corp.). The pressure distribution in the brain model was measured simultaneously by the PVDF needle hydrophone (Platte Needle Probe, Muller Instruments).

## 3. Results and Discussion

Figure 3 shows sequential shadowgraph images of micro-explosive induced shock wave interaction with the brain model. The observation was performed at Interframe time of 200 ns and exposure time of 110 ns.

The micro explosive induced shock wave in air was interacted with the outside of the acrylic tube and transmitted into the inside of an acrylic tube and a gelatin layer. The several wave were generated by propagating repeatedly in an acrylic tube and propagated toward the opposite side from shock wave entry. Transmitted wave was reflected form the interface of a gelatin and an acrylic tube, at first, the interface of an acrylic tube and air, secondary. These reflected waves were the compressive wave and the expansion wave by the interface of acoustic impedance mismatching.

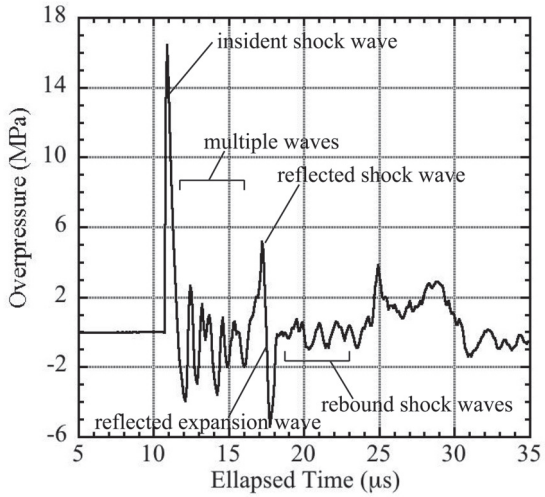


Fig. 4 Pressure history in the brain model (*d*=5 mm).

Reflected waves were focusing at near the PVDF sensor head and rebounded, and then bubble generation.

Figure 4 shows the pressure distribution in the brain model. The transmitted waves in gelatin layer were reached the tip of the needle hydrophone, and then the pressure was raised sharply and reduced by the compressive wave and the expansion wave. The shock wave and expansion wave pressure at 3 mm from the opposite inner wall of acrylic tube, the maximum peak pressure is about 16.5 MPa (at 10.9 μs after exploding), and minimum pressure is about -5.4 MPa (at 17.5 μs).

## 4. Concluding Remarks

We performed an experiment of the micro-explosive induced shock wave interaction with the brain model made of simulated biomedical materials considering acoustic impedance. The expansion wave and bubble were generated at the part of the opposite side from shock wave entry in the brain model. The results explain that the primary bTBI, especially the contra-coup injury is affected by these phenomena at the part of the opposite side.


## Acknowledgement

This work was supported by MEXT KAKENHI Grant Numbers 26420100, Japan Industrial Explosives Technology Grant and Toray Science and Technology Grant.


## References


[1] R.A. Armonda, R.S. Bell, A.H. Vo, G. Ling, T.J. DeGraba, B. Crandall, J. Eclund, W.W. Campbell, *Neurosurgery*, 59 (2006) 1215-1225.

[2] R.A. Bauman, G. Ling, L. Tong, A. Janszkiewicz, D. Agoston, N. Delanerolle, Y. Kim, D. Ritzel, R. Bell, J. Eclund, R. Armonda, F. Bandak, S. Parks, *J. Neutorauma*, 26 (2009) 841-860.

[3] A. Nakagawa, G.T Manley, A.D. Gean, K. Ohtani, R. A. Armonda, A. Tsukamoto, H. Yamamoto, K. Takayama, T. Tominaga, *J. Neurotrauma*, 28, (2011) 1101-1119.

# Optical Observations and Theoretical Models of DNA Flow at Nanoscale

Satoshi Uehara[1] and Satoyuki Kawano[2]
[1]Institute of Fluid Science,Tohoku University
2-1-1 Katahira, Aoba-ku, Sendai 980-8577, Japan
[2]Osaka University
Machikaneyama 1-3, Toyonaka, Osaka 560-8531, Japan

**ABSTRACT**

Control of DNA flow in nanoscale structures such as nanochannels and nanopores has recently become important in developing next-generation high-speed DNA sequencers. In this paper, we study a flow dynamics of DNA at nanoscale both experimentally and theoretically. Dynamical behaviors of double-stranded and single-stranded DNAs are measured by using fluorescent imaging techniques in nanochannel and near solid surface, respectively. The effects of restriction due to the nanoscale structure on the behaviors are evaluated from the viewpoint of the mobilities.

## 1. Introduction

Recently, nano-biodevices such as DNA sequencers are attracted significant attention. Electrical measuring methods of DNA base using single-stranded DNA molecule in the nanopore with nanoscale electrodes are proposed for the novel sequencing [1].

A development of precise fabrication technique based on micro electro mechanical systems (MEMS) accelerated an advancement of DNA sequencers. Then, flow dynamics of a single DNA in such a nanoscale structure have become important for the devices.

However, the electrokinetic flow of DNA in nanoscale structures must be different from those in bulk or microscale structure due to the effects of the solid walls on the flow dynamics of DNA. The detail of the flow is still unclear, although it is one of the most important phenomena to design nano-biodevices [2].

In order to clarify the effect of nanoscale structure on DNA flow, the fluorescent measurement of DNA at nanoscale is conducted. Double-stranded DNA (dsDNA) and single-stranded DNA (ssDNA) are observed in nanoscale domain such as in a nanochannel [3] and near a cover glass surface [4], respectively. In particular, in this paper, we review these researches from the view point of flow restriction at nanoscale. It is found that the mobility of DNA decreases and that the tendency should be due to nanoscale effects.

## 2. Experimental

Two types of experiments are conducted to measure mobility of DNA at nanoscale. Figure 1 shows schematic concept of the experiment. Electorophoresis of dsDNA in nano-slit like channel (hereinafter referred to as nanochannel) is measured by high-speed camera (Fig. 1 (a)) and diffusion of ssDNA near a solid surface is measured by using a total internal reflection fluorescent (TIRF) microscope (Fig. 1(b)). Detailed discussion is described as follows.

### 2.1. Double-stranded DNA in Nanochannel

The nanochannel is originally designed and fabricated using basic MEMS methods. The heights of nanochannels are controlled by changing the thickness of Si thin film which corresponds to the nanochannel wall. We successfully fabricate the nanochannels with the height of 330, 430 and 650 nm, where the heights are measured from SEM images and the inaccuracy is in nanometer order. All the nanochannels are shallower than the characteristic length of λDNA.

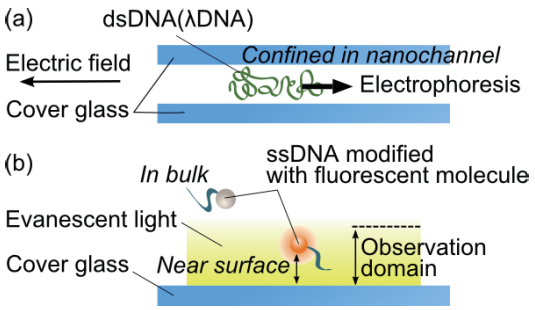


Fig.1. Schematic of experiments in order to clarify the effect of cover glass surface on the dynamics of DNA. (a) Electrophoresis of dsDNA confined in nanochannel. (b) Diffusion of ssDNA near cover glass surface measured by TIRF microscope.

We focus on electrokinetic flows of λDNA under confinement by nanochannel walls. The electrokinetic flow of λDNA and surrounding liquid are observed using a fluorescent measurement system. Negative and positive electrodes are set in the reservoirs which set on the inlet and outlet of the nanochannel in order to apply a controlled electric field.

### 2.2. Single-stranded DNA near Solid Surface

From the view point of the application of nanobiodevices such as next-generation DNA sequencers, ssDNA is treated to sequence base pairs of DNA. Therefore, it is important to measure ssDNA in single molecular level.

We observed 24 mer ssDNA and the one 5 prime end is tagged with tetramethyl-6-carboxyrhodamine (TAMRA). Total internal reflection fluorescent (TIRF) microscope is used in order to obtain weak fluorescence from TAMRA for sure. It is possible to observe ssDNA

Corresponding author: Satoshi Uehara
*E-mail address*: uehara@paris.ifs.tohoku.ac.jp

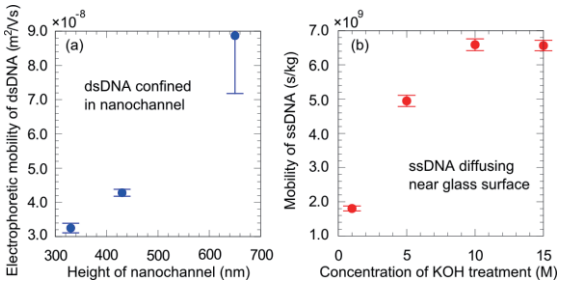


Fig.2 (a) Electrophoretic mobility of dsDNA in nanochannel is increasing with respect to height of nanochannel. (b) Mobility of ssDNA diffusing near solid surface is increasing with respect to the concentration of KOH treatment.

diffusing in 240 nm domain from the glass surface due to the reduction property of evanescent light worked as excitation light [4]. The effect of TAMRA can be negligible since a molecular mass of TAMRA and 24-mer ssDNA are about 500 and about 7000, respectively. The concentration of KOH solution for rince a surface of cover glass is changed in order to observe the effect of surface condition of cover glass[4].

## 3. Results and Discussion

First, we explain about the results of dsDNA measurement which is mentioned in the section 2.1.

The configuration of λDNA is found to be globular shape and weakly aggregated in nanochannel from the images obtained by fluorescent microscope. The displacement of dsDNA is obtained from the sequential images in three types of nanochannels with different height. The displacements appear to increase linearly with time. This result indicates that the velocity of λDNA reaches the terminal velocity immediately.

In nanochannel, electroosmotic flow (EOF) arises due to ions which gathered near the nanochannel wall with the ζ potential by the Coulomb force. In order to evaluate the effect of the EOF on the terminal velocity of λDNA, we measure the velocity of the continuous phase by particle image velocimetry using two types of polystyrene fluorescent particles [3]. The relative velocity $u_{\mathrm{DNA}}$ is estimated by taking into account the EOF. Then, electrophoretic mobility $\mu_{\mathrm{dsDNA}}$ is obtained as below.

$$\mu_{dsDNA} = u_{DNA} / E \,, \tag{1}$$

where $E$ denotes the strength of electric field applied in nanochannel.

Figure 2 (a) shows the electrophoretic mobility of dsDNA moving in the nanochannel. The terminal velocity of λDNA is proportional to the strength of the electric field and the mobility is found to decrease as the channel height decreases. This result indicates that the effect of nanoscale confinement on the flow of DNA is successfully observed and it is varied with respect to the height of channel. When the confinement becomes strong, i.e., nanochannel height decreases, the flow is restrained and the electrophoretic mobility decreases.

A simple theoretical model explaining the decreasing in the mobility is developed with taking into account the shear stress due to small clearances between the interface of λDNA and the walls of nanochannels. The validity of the model is confirmed by reasonable agreement between the theoretical and experimental results. The theoretical details is described in [3]

Next, we explain about the results of ssDNA measurement which mentioned in the section 2.2.

Diffusion coefficient $D$ of ssDNA is obtained by analyzing displacements of bright spot of tetramethyl-rhodamin from high-speed images. The result contains the nanoscale effect [4] of the cover glass surface interaction on the diffusion of ssDNA, since only the DNA flowing near the cover glass surface can be observed by TIRF microscope.

When we assume that equilibrium statistical mechanics can be applied to the translational motion of mass center of DNA, a mobility of DNA, $\beta_{\mathrm{ssDNA}}$, is written from the Einstein relation as below.

$$\beta_{ssDNA} = D / k_B T \,, \tag{2}$$

where $k_{\mathrm{B}}$ and $T$ denote Boltzmann constant and temperature which assumed as 300 K, respectively.

Figure 2 (b) shows the mobility of ssDNA diffusing near the solid surface obtained in our experiment. The result indicates that the mobility is varied with respect to surface conditions. A decreasing of the KOH concentration for pretreatment is equal to an increase of adsorbability of a cover glass surface for ssDNA mainly due to the OH group and Coulomb force [4]. Therefore, the result indicates the restriction of mobility due to the cover glass surface interaction at nanoscale.

It is difficult to discuss quantitatively about the mobility with comparing Fig. 2 to Fig. 3 since Fig. 2 shows the electrophoretic mobility which is considering the effect of negative electric charge of dsDNA. However, from these experiments, it is found that mobility of DNA is restrained at nanoscale. This fact is significantly important for DNA sequencer since an electric signal is a function of time which is related to the mobility of flowing DNA. And also it may be possible to control a flow of DNA with changing mobility of DNA by using a nanoscale structures.

## 4. Concluding Remarks

The flow dynamics of dsDNA and ssDNA at nanoscale are successfully measured by using fluorescent observation method. It is found that the mobility of DNA is different from the bulk state due to the effect of nanoscale.

## References

[1] S. Uehara, M. Tsutsui, K. Doi, M. Taniguchi, S. Kawano, T. Kawai, *JBSE*, 8 (2013) 244-256.

[2] Y. He, M. Tsutsui, R. H. Scheicher, F. Bai, M. Taniguchi., T. Kawai, *ACS NANO*, 7(1) (2013) 538-546.

[3] S. Uehara, H. Shintaku, S. Kawano, *J. Fluids Eng., ASME*, 133 (2011) (121203-1)–(121203-8).

[4] S. Uehara, I. Hanasaki, Y. Arai, T. Nagai, S. Kawano, *Micro & Nano Letters*, 9 (2014) 257-260.

# OS7: Cutting Edge of Thermal Science and Engineering

# Improvement of Defrosting Method for Cryogenic Heat Exchanger Using Impingement of Alumina Particles

Nobuki Sonobe[1], Katsuyoshi Fukiba[1], Sota Sato[1]
[1]Graduate School of Engineering, Shizuoka University
3-5-1, Johoku Nakaku, Hamamatsu, Shizuoka, 432-8561, Japan

**ABSTRACT**

This study was conducted to conquer the frost formation problem on a cryogenic heat exchanger for the hypersonic airplane developed by Japan aerospace exploration agency. In previous study, the defrosting method using impingement of air jet was presented for the heat exchanger[1]. In this study, we developed new defrosting method using impingement of air jet and alumina particles. This defrosting method is suitable for iterative use for long duration.

## 1. Introduction

A precooled turbojet engine for Mach 5 class hypersonic airplane has been developed by Japan aerospace exploration agency (JAXA)[2]. Figure 1 illustrates a precooled turbojet engine. This engine has a cryogenic heat exchanger which is called precooler before a compressor. When a plane flies at hypersonic speed, deceleration of the air flow at the air intake increases the air temperature. Heated breathed air decreases the engine power and causes damage to the engine. Therefore, precooled turbojet engine cools breathed air using the precooler to solve these problems.

Developing of precooler has some problems. In these problems frost formation seems to be one of the most serious problems. Because the cooling tubes in the precooler are cryogenically cooled, moisture causes frost formation on them. The frost causes pressure loss and decreases the amount of heat exchanged. These problems have serious influences for the engine. Therefore, an effective defrosting method for precooler is needed. In previous study, some defrosting methods including methanol spray into the breathed air were presented[3]. However, defrosting method using liquid is improper for airplane because of its weight. Air jet defrosting is a method without liquid. This method uses air jet impingement on cooling tubes. This method has an advantage in weight saving but not sufficiently effective in sever conditions.

In this study we present a new defrosting method using impingement of air jet and alumina particles. In this method, alumina particles are accelerated by compressed air and impinge on cooling tubes to defrost. Our previous study revealed that piccolo tube is proper for the jet nozzle. In this study, we found the defrosting method using alumina particles and a piccolo tube is very effective.

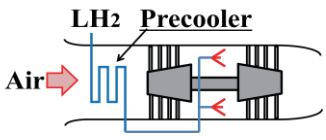


Fig. 1 Precooled turbojet engine

Corresponding author: Nobuki Sonobe
*E-mail address*: f0330053@ipc.shizuoka.ac.jp

## 2. Experimental Setup

The test section duct and heat exchanger used for the experiments are shown in Fig. 2. Air conditioned by a thermo-hygrostat flows to the duct through a booster fan, a honeycomb and an orifice flowmeter. Main flow temperature is 20 °C and humidity is 50 %. The cross-section shape of the duct is 60 mm × 60 mm square. The test section duct is set vertically. The heat exchanger which has 5 cooling tubes in parallel is installed in the duct. The duct is partitioned by two metallic meshes (metallic mesh A and B) before and after the heat exchanger. Alumina particles are encased between two metallic meshes. Because the metallic mesh A is V-shaped, alumina particles accumulate to the center. The piccolo tube shown in Fig. 3 is installed just below the metallic mesh A. When we use this defrosting system, alumina particles are accelerated by air jet from the piccolo tube and impinge on cooling tubes. Because the metallic mesh B stems the particles, they circulate between the two metallic meshes. We measured pressure and temperature of main flow before and after the heat exchanger to calculate the pressure loss coefficient and the amount of heat exchanged. The coolant provided to the heat exchanger is liquid nitrogen. Main flow speed is 2.7 m/sec and jet pressure is 0.5 MPa at all cases. The experimental cases were following:

1) With defrosting / Without defrosting
2) With particle jet defrosting / With air jet defrosting

In the case with defrosting, jet impinges two times (300 sec and 600 sec). In the case with air jet defrosting, only air jet from the piccolo tubes impinges. In the case without defrosting, the piccolo tube, the metallic meshes and the alumina particles are installed in the duct but we do not use them. Test duration is 600 sec at all cases.

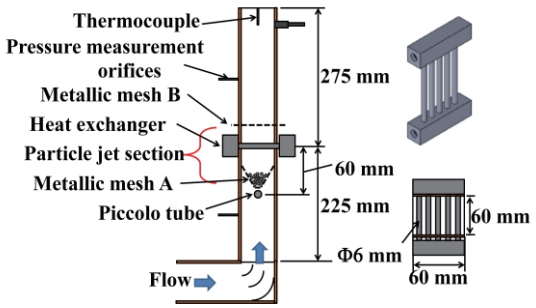


Fig. 2 Test section duct and heat exchanger

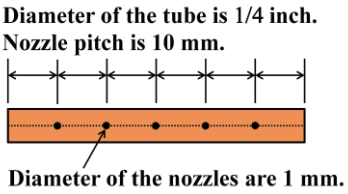


Fig. 3 Piccolo tube

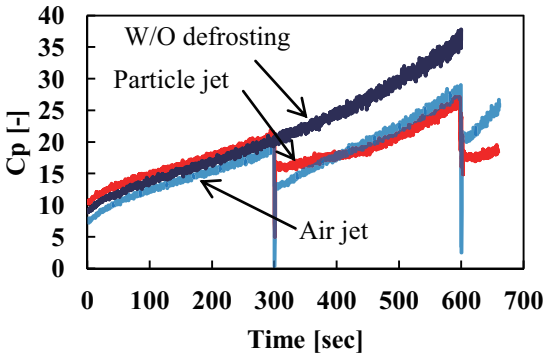


Fig. 4 Variation of the pressure loss coefficient

## 3. Results

Figure 4 shows variation of pressure loss coefficient (Cp). In the case without defrosting, pressure loss coefficient at 600 sec after the test started was 36. In the case with defrosting, it was considerably decreased by first and second defrosting. The pressure loss coefficient at 600 sec after the test started was 21 when we used air jet defrosting. It was 18 when we used particle jet defrosting. Note that the pressure loss coefficient at 300 sec just after the first particle jet defrosting is 16. The pressure loss coefficient at 600 sec just after the second particle jet defrosting is 18, which is the similar value as that of the first particle jet defrosting. The pressure loss coefficient with air jet defrosting was smaller than that with particle jet defrosting before 400 sec. However, the coefficient with air jet increases rapidly after first jet defrosting. As a result, the pressure loss coefficient becomes larger than that with particle jet after 400 sec. Particle jet defrosting could decrease pressure loss coefficient by the second defrosting to the same level as the first defrosting. Therefore, particle jet defrosting is proper for heat exchanger running for a long period of time. Figure 5 shows variation of the amount of heat exchanged (Q). It decreased rapidly after the test started and be improved considerably by defrosting. Amount of improvement by the particle jet defrosting was larger than that by air jet defrosting. In the both cases, amount of heat exchanged was same level at 200-300 sec and 500-600 sec, where the effect of the defrosting is no more shown. Figure 6 shows the pictures of the cooling tubes at first defrosting (300sec after the test started). The frost was removed almost perfectly at all areas of the cooling tubes by particle jet defrosting. On the other hand, partial frost wasn't removed when we used air jet defrosting. Efficiency of air jet defrosting was not enough under the condition in this study.

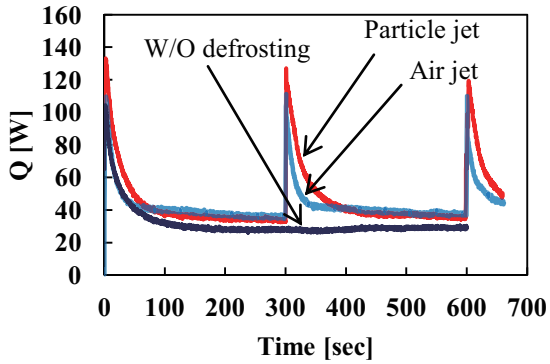


Fig. 5 Variation of the amount of heat exchanged

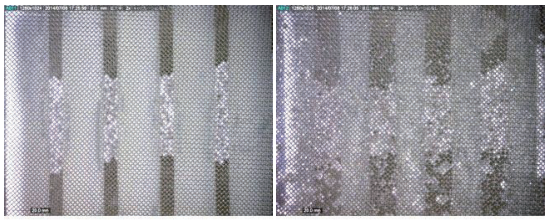

(a) Particle jet defrosting at 300sec

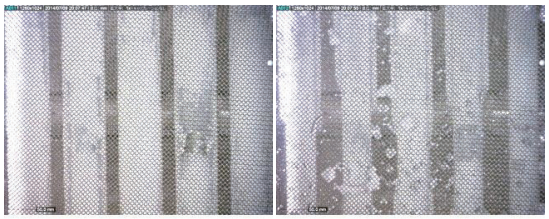

(a) Air jet defrosting at 300sec

Fig. 6 Effect of jet defrosting (L: Before R: After)

## 4. Conclusions

In this study, we developed the new defrosting method using impingement of air jet and alumina particles. This method is improved version of air jet defrosting. The heat exchanger performance after the second particle jet defrosting is the same level as that after the first defrosting. Therefore, we concluded that particle jet defrosting is suitable for iterative use for long duration.

## References

[1]K. Fukiba, S. Inoue, H. Ohkubo, T. Sato, *Journal of Thermophysics and Heat Transfer*, 23, 3, (2009) 533-542.

[2]T. Sato, H. Taguchi, H. Kobayashi, T. Kojima, K. Fukiba, D. Masaki, K. Okai, K. Fujita, M. Hongo, S. Sawai, *Acta Astronautica*, 66, (2010) 1169- 1176.

[3]T. Kimura and T. Sato, *Journal of the Japan Society for Aeronautical and Space Sciences*, 51, 598, (2003) 597-605.

Eleventh International Conference on Flow Dynamics
October 8-10, 2014, Sendai, Miyagi, Japan

# Studies on Redistribution of Inlet Temperature Distribution in a Turbine using High-Order LES Approach

Debasish Biswas[1]
[1]Toshiba Corporation
1, Komukai Toshiba-Cho, Saiwai-Ku, Kawasaki, 212-8582, Japan

**ABSTRACT**

In advanced gas turbine the implementation of cooling method requires a clear understanding of the aerodynamics involved. Both qualitative and quantitative assessments of the redistribution of inlet temperature distortions can be used to considerable advantage by the turbine designer. The main purpose of this study is to test the performance of a high-order LES model in terms of predicting this type of highly complicated unsteady flow and heat transfer phenomena.

## 1. Introduction

Today's gas turbine operates at very high temperature to meet the demand of an increase in the cycle performance by creating severe heat loads in the first turbine stage As a result the mean flow temperature usually well exceeds the limit supported by the surrounding material. Therefore usually it is necessary to cool both end-walls and the blades of the first stage. Consequently, mid-span streaks of hot gas pass through the first stator row and become hot jets of fluid. Additionally, the flow from a gas turbine combustor exit entering a turbine stage can have a wide variation in temperature. Both spatial and temporal variation of flow temperature may occur under such flow environment. A clear understanding of the aerodynamics involved under such conditions is required for the implementation of above mentioned cooling method. Hence the turbine designer can use both qualitative and quantitative assessment of the redistribution of inlet temperature distortions with considerable advantage. The measured characteristics of the streamline patterns in the rotor row resulted from the secondary flow effect and consequently from the inlet temperature distortion effect is also presented by Butler (1). Their results led to an understanding that the existence of a local hot spot on the pressure side of the rotor is caused by the migration of the hot gas to its pressure side and the cooler gases to its suction side. An important physical behavior related to temperature redistribution that there exists more flow of fluid from the hot streak towards the hub and tip end walls on the pressure side of the channel is also understood by their results. In our study emphasis is put to predict the unsteady turbulence characteristics and to study the effect of the stator-rotor blade ratio used in the experiment. In this work 3-D unsteady Navier-Stokes analysis of a turbine stage (satisfying the experimental stator-rotor blade ratio) is carried out to study the above mentioned phenomena. A high-order LES turbulent model developed by the author and tested by carrying out a detail study regarding its performance on various types of turbulent flow problem and DNS data is used. From computational point of view, one major difficulty in simulating flows induced by rotor-stator interaction arises because of the relative motion of the rotor and stator airfoils. A single grid that wraps around both the rotor and stator would have to distort considerably to accommodate the motion of the rotor and could result in inaccurate calculations. For small values of axial gap between the rotor and stator airfoils such an approach may even be altogether impractical. The obvious solution to this problem is to use several grids that move relative to each other. Typically, one would use a set of stationary grids to envelope the stator airfoils and a set of moving grids (stationary w.r.t stator) to envelop the rotor airfoils. Information is then transferred between the several grids used with the help of special boundary conditions.

*Corresponding author: Debasish Biswas*
*E-mail address*: debasish.biswas@toshiba.co.jp

## 2. Method

Since the Mach number of the flow (inlet Mach number 0.07) considered here is very small (where the variation of flow density with respect to pressure is negligibly small), the basic equations are unsteady three-dimensional continuity, momentum equations for incompressible flows and the energy equation to obtain the temperature variation. In this case of incompressible flow since it is not possible to obtain pressure from the solution of density and internal energy equations, a Poisson type equation for pressure derived from the momentum equations is solved to obtain the pressure field. The dependent variables have been non-dimensionalized by a characteristic velocity, temperature and reference length scale. All the equations are written in generalized coordinate to have sufficient grid resolutions in the near wall boundary layer region and to generate grids to fit the body configuration. Accurate spatial discretization is crucial in LES. In LES, numerical diffusion however small it is, can easily overwhelm physical diffusion. Also, one of the problems encountered in LES of turbulent flow is the control of aliasing error. Use of schemes, which do not have a mechanism of controlling aliasing error can result in decay of the turbulence in a given flow field or an unbounded growth of the solution. In the present work, this problem is overcome by using a spatially high order accurate, upwind-biased WENO (Weighted Essentially Non-Oscillatory) finite difference scheme developed for incompressible N-S equations in three-dimensions. In this method a fifth order upwind differencing technique is used for convective terms and fourth order central differencing technique is used for viscous diffusion terms. All these equations are solved using an efficient high order finite difference scheme of second order accuracy in time. In this approach, fully implicit finite difference equations are solved performing several iterations at each time step to make the differencing errors zero. In the present work a high-order LES model developed by the author is used to predict this turbulence mixing characteristics. In this high order LES concept, in a dynamic eddy viscosity model, transfer of information between the sub-grid and large scale eddies are improved by solving an additional transport equation for turbulent kinetic energy in the grid scale level. Here the sub-grid scale turbulent stresses are closed using a dynamic turbulent kinetic energy transport model. The sub-grid scale length scale is represented by the minimum of universal length scale and the grid scale. A test filter is used for the dynamic procedure, which will be applicable to stretched grid near the body surface.

The advantages of such model include resolution of interesting scales, simultaneous modeling of high shear region and large scale unsteadiness, and use of stretched grids. In the turbulent kinetic energy transport equation the dissipation of turbulent kinetic energy is defined on the basis of time scale.

### 3. Results and Discussion

Patched grids are used to discretize the regions surrounding the rotor-stator configuration. Since overlaid grid calculations are difficult to make conservative at the overlay boundaries. The airfoil geometry used in the current study is the same as that used in the experimental investigation of Dring (2). The geometry consists of 22 stator and 28 rotor airfoils. In order to perform an accurate computation of temporal behavior in the flow passage, eleven stator airfoils and 14 rotor airfoils are used to satisfy the experimental stator/rotor blade ratio. Fig.1(a) and (b) show the rotor-stator geometry of Dring(2) at mid-span and the computational model, respectively. The multi-zone grid used to discretize the region consists of 39 zones. Eleven zonal grids representing eleven stator passages, fourteen zonal grids representing fourteen rotor passages, and 14 zonal grids to cover the region of tip clearance are used. All the zones are discretized with H-grid. Exit of the stator zones are patched together with inlet of rotor zones.

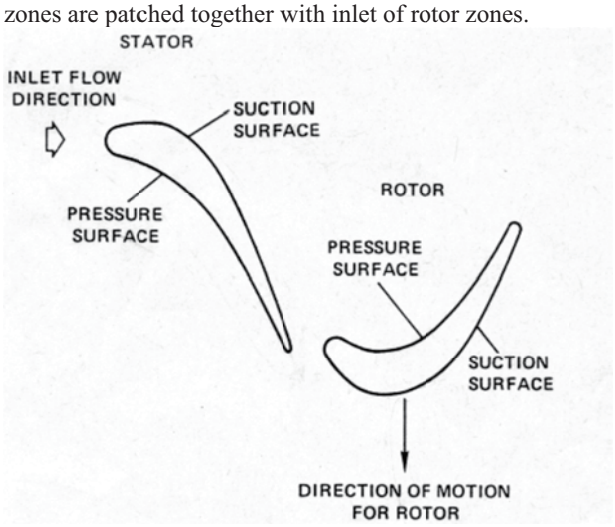


Fig. 1(a) Schematic view of stator-rotor of Dring

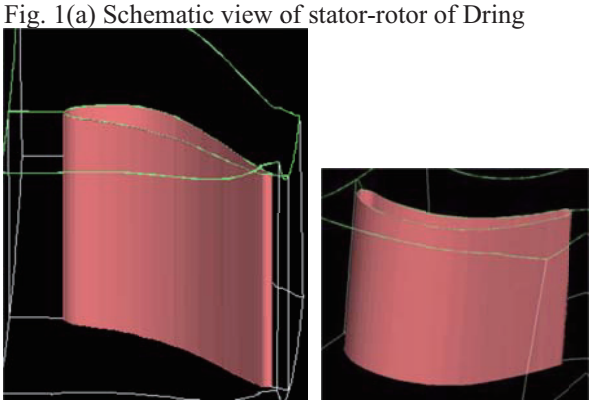

Fig. 1(b) Computational model of stator-rotor

In each stator zone 181X141X201 grid points in the radial ($x$), pitch-wise ($y$), and axial ($z$) directions are used. In each rotor zones 171X111X211 grid points in the radial ($x$), pitch-wise ($y$), and axial ($z$) directions are used. In the tip clearance region 11X11X121 grid points in the radial ($x$), pitch-wise ($y$), and axial ($z$) directions are used. Near wall $y^+$, $x^+$ and $z^+$ are kept nearly equal to 0.1.

In Fig.2 is presented the time-averaged temperature coefficient distribution on the rotor which is defined as follows;

$$C_T = \frac{T - T_\infty}{T_{av} - T_\infty} \quad (1)$$

Where, $T$, $T_{av}$ and $T_\infty$ are local temperature, time-averaged temperature and surrounding gas temperature, respectively. In Fig.2 zero-point in the abscissa represents the leading edge of the rotor and the negative and positive sides correspond to the suction and pressure surface, respectively. Since the rotor passes through the hot streak in every cycle, its surface temperature is expected to vary about the average inlet temperature ($C_T$=1.0). This fact is clearly demonstrated by the results presented in Fig.2. In Fig.2 is presented the surface temperature variation simulated on the basis of measured results. Both the measured and predicted results showed the occurrence of a temperature peak on the pressure surface at about 45% chord from the leading edge which is about 85% higher than the average inlet ($C_T$). This indicates that the local time averaged temperatures on the rotor pressure side can be expected to be well above the average inlet temperature. Over the rest 30% of the chord, there occur a sharp temperature drop to the average inlet temperature. In the region near the trailing edge of the pressure side temperature drops to about 75% of the average inlet temperature. The suction side shows a minimum at about 30% of the chord and the temperature also drops to much lower values than the average inlet temperature toward the trailing edge on the suction side. All these experimentally observed facts are predicted quite well by the present physics based turbulent model.

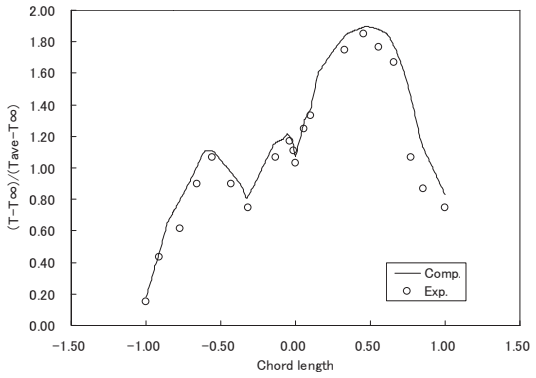


Fig.2 Time-averaged temperature distribution on the rotor

### 4. Concluding Remarks

The present computation method along with the physics-based turbulent model could predict the complicated 3-D unsteady stator-rotor interaction phenomenon in practical gas-turbine environment. The results revealed that the introduction of upstream total temperature distortion significantly affects the rotor flow fields.

### References

[1] Butler, T.L., Sharma, O.P., Joslyn, H.D., and Dring, H.P., *AIAA Paper,(1986)* 86-1468.

[2] Dring, R.P., Joslyn, H.D., Hardin, L.W., and Wanger, J.H. *Journal of Engineering for Power,* Vol.104, (1982 Oct) 729-742.

Eleventh International Conference on Flow Dynamics
October 8-10, 2014, Sendai, Miyagi, Japan

# Density Measurement of Supersonic Air Flow Inside a Bumped Micro-channel using Interferometer

Yuya Takahashi[1], Junnosuke Okajima[2], Yuka Iga[2], Atsuki Komiya[2], Shigenao Maruyama[2]
[1]Graduate School of Engineering, Tohoku University
6-6-1, Aramaki, Aoba-ku, Sendai, Miyagi, 980-8579, Japan
[2]Insitute of Fluid Science, Tohoku University
2-1-1, Katahira, Aoba-ku, Sendai, Miyagi, 980-8577, Japan

**ABSTRACT**

In this study, the density distribution of a supersonic air flow inside a micro-channel which has a bumped shape as a convergent-divergent section was measured by using phase-shifting interferometer to evaluate the density distribution inside the channel. The micro-channel was fabricated on Si plate by an MEMS process. The channel size was about 200 μm in width, 500 μm in depth, and 6000 μm in length. The density distribution was determined from the measured refractive index distribution. The density distribution was compared with the calculation results.

## 1. Introduction

In recent years, power density of integrated circuit such CPUs comes up to 1 MW/m$^2$ with increasing of components per chip. Thus, the energy consumption to cool datacenters and its cost were becoming big issue [1]. However, conventional on-chip cooling devices are not enough to cool CPUs in the present state.

In the previous study [2], it is revealed that the supersonic air flow inside a micro-channel has great cooling ability due to the relatively lower working energy of air and low temperature flow generated by an adiabatic expansion. In addition, throat was designed as simple bumped shape. However, it was investigated only from the results of numerical simulations. Thus, experimental evaluation of the supersonic air flow inside the micro-channel is required to understand the details.

There are many experimental methods for the measurement of the flow field, such as the background oriented schlieren method and the temperature sensitive paint method [3]. The Mach-Zehnder interferometry has been widely used because of its non-intrusive and quantitative nature. Generally, it is difficult to measure the flow inside the micro-channel because it is hard to take enough length of optical path, and its low spatial resolution for the conventional interferometer. However, the measurement of density distribution of sub/supersonic flow inside a micro-channel was succeeded in the previous study [2].

In order to develop an effective air cooling device, it is required to understand the phenomenon of the temperature decrease of the supersonic flow under the expansion inside the micro-channel with a throat at the channel inlet. The objective of this study is the measurement of the density distribution of supersonic flow inside the bumped micro-channel using the phase-shifting interferometer to evaluate the temperature decrease due to the bumped section.

## 2. Experimental apparatus

To visualize the density distribution of supersonic air flow inside a micro-channel, the phase-shifting technique was applied to conventional Mach-Zehnder interferometer [4]. The phase-shifting technique is an image processing technique, which calculates and conflates brightness of the interferograms at three different polarization angles. Then, all pixel of a CCD camera detects phase difference values using the phase-shifting interferometer every 1/10 s by synchronism with a frame rate of the CCD camera. This is in contrast to the conventional interferometer, which can only obtain values in the brightest and darkest points on the fringe. As a light source, a He-Ne laser of 632.8 nm in wavelength was used. The estimated appearing fringe number and the number of the data points can be calculated using Gladstone-Dale relation [5]. From this estimation, it was expected that the channel depth of more than 500 μm is enough for the phase-shifting interferometer.

The micro-channel was fabricated by an MEMS process in this study. However, it is difficult to make a deep micro-channel. Hence, channel depth was decided on the trade-off between the optical path length and the limitation of the fabrication by the Deep Reactive Ion Etching (D-RIE).

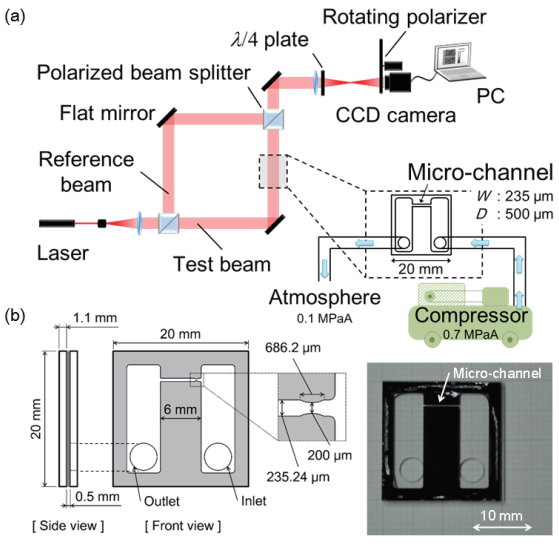


Fig. 1 Schematic diagrams of the experimental apparatus. (a) Detail of phase-shifting interferometer. (b) Details of bumped micro-channel.

Corresponding author: Yuya Takahashi
*E-mail address*: yuya@pixy.ifs.tohoku.ac.jp

Figure 1 shows the schematic diagrams of the experimental apparatus. The air was compressed to 0.7 MPaA at the inlet and through the micro-channel to the outlet reservoir of 0.1 MPaA. The detail of the bumped channel was shown in Fig. 1(b). The length, width, and depth of the channel were 6000 μm, 235 μm, and 500 μm, respectively. The cross-section ratio of the channel to the throat was set to about 1.18, which is determined from the designed Mach number of 1.50.

## 3. Results and Discussion

The measured phase-shifted data and the density distributions for each pixel on/around the centerline of the channel were shown in Fig. 2(a) and (b), respectively. For the density evaluation, Gladstone-Dale relation and the pressure boundary conditions were used. Then, the working fluid and the temperature were assumed as air and at room temperature of 300 K, respectively. The spatial and the time averaged values were used for the evaluation in order to confirm the one-dimensional phenomenon and the steady state of the flow. Here, the 5 pixels around the centerline of the channel and the data for 3 seconds were used for the spatial and temporal average of the density distributions, respectively.

As seen in Fig. 2(a), the refractive index distribution was visualized by phase-shifted data. The density distributions of each averaged values showed good agreement, as shown in Fig. 2(b). This indicates that the flow can be treated as one-dimensional and steady state. The large change at the inlet and the outlet of the channel was observed. The rapid decrease of density at the inlet was caused by the adiabatic expansion due to the bumped section.

In order to validate the experimental result, the measured density distributions were also compared with the result of the numerical simulation, which was performed using ANSYS FLUENT 13 software. Compressible governing equations were calculated using Roe's Flux Difference Splitting (Roe-FDS) method for flux estimation. The calculation was performed with assumptions of steady state, two-dimensional, laminar flow, and adiabatic wall. The Reynolds number inside the channel was about 20000 in maximum. The measured density distribution shows good agreement with the calculated one. Therefore, this measurement could detect density distribution of the supersonic air flow inside the bumped micro-channel. In addition, the temperature inside the channel can be estimated as the result of calculation. The calculated density distribution was gradually increased toward the channel end. The reasons of the difference caused by the three dimensional effect, disregard of the isothermal condition of the room temperature, and the accuracy of the channel shape and roughness of the channel wall, which were caused by the MEMS fabrication process.

## 4. Conclusions

In order to understand the phenomenon of the supersonic air flow inside the bumped micro-channel, visualization of density distribution were performed by using phase-shifting interferometer. The distribution of density was compared with the calculated result to validate this measurement method. The main results are summarized as follows.

1. From the comparison, the proposal measurement system could detect the details of the density distribution of supersonic air flow inside the bumped micro-channel.
2. From the comparison between the measurement and numerical simulation, the calculated result can be used for estimation of the temperature distribution inside the channel, which could not measure.

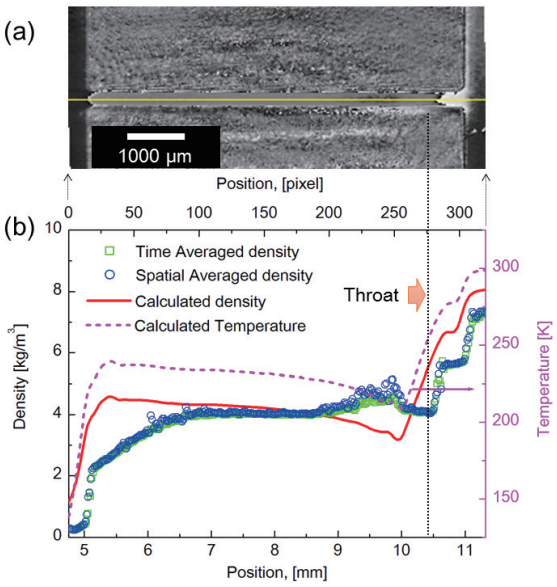


Fig. 2 Experimental results. (a) Measured refractive index distribution as phase-shifted data, (b) Evaluated density distributions on the centerline of the channel and comparison with the result of numerical simulation.

## 5. Acknowledgements

This work was supported by JSPS Grant-in-Aid for Challenging Exploratory Research Number 25630060, JSPS Grant-in-Aid for JSPS Fellows Number H4267353, Tohoku University IIARE, Center for Integrated Nanotechnology Center at Tohoku University, and also by Nanotechnology Network Project of the MEXT of the Japanese Government.

## References

[1] J. B. Marcinichen, J. A. Olivier, V. Oliveira, and J. R. Thome, *Applied Energy*, 92, (2012) 147–161.
[2] Y. Takahashi, J. Okajima, Y. Iga, A. Komiya, and S. Maruyama, *Proceedings of the 51th National Heat Transfer Symposyum*, (2014) Paper No. E233.
[3] Y. Matsuda, T. Uchida, S. Suzuki, R. Misaki, H. Yamaguchi, and T. Niimi, *Microfluid Nanofluid*, 10, (2011) 165–171.
[4] S. Maruyama, T. Shibata, and K. Tsukamoto, *Experimental Thermal and Fluid Science*, 19, (1999) 34–48.
[5] W. C. Gardiner. Jr, Y. Hidaka, T. Tanzawa, *Combustion and Flame*, 40, (1981) 213–219.

# Thermal Investigation of Human Breast and Utilization of Curve Fitting Technique in Inverse Estimation of Tumor Characteristics

Koushik Das and Subhash C. Mishra
Dept. of Mechanical Engineering, Indian Institute of Technology Guwahati
India – 781039

**ABSTRACT**

Pennes' bioheat equation is numerically solved for a 3-D model of breast. With a tumor inside, the skin surface temperature distribution of the breast is Gaussian in nature. Considering various parameters of the Gaussian profile, an inverse algorithm is proposed to estimate the size and the location of the tumor. To obtain the skin surface temperature distribution, finite element method is used in the numerical discretization the computational space.

## 1. Introduction

Cancer is a disease characterized by uncontrollable growth of cells and tissues. Globally, it has affected many lives. Cancer of lung in male and breast in female, shows the highest rate of mortality all over the globe. As per GLOBOCAN-2012, breast cancer accounts for 14.7% of cancer related deaths in women, and the rate is increasing every year. In the year 2012, USA alone witnessed an incidence of 2,32,714 new cases of breast cancer, with 43,909 deaths. The same for India were 1,44,937 and 70,218 [1], respectively.

For any cancer, an early diagnosis helps in better treatment, and many a times, proves to be a life saver. Being a thermal system, a human body shows a change of thermal behavior due to alteration of its properties. Measurement and analysis of any altered thermal signal may lead to characterization of any abnormality inside the tissue. In the present work, an effort has been made to estimate the size and location of a tumor in a 3-D model of breast using the measured skin surface temperature distribution. Numerical study has been performed by solving Pennes bioheat equation (PBHE) using finite element method (FEM); and the size and the location of malignancy, if present, have been estimated utilizing a newly proposed curve fitting technique.

## 2. Formulation

A human breast can be demonstrated in the form of a hemisphere (Fig. 1). Consideration is given to a 3-D hemispherical model of breast of radius $R$, embedded with a spherical tumor of radius $r_t$ (Fig. 1), located at a radius $r_o$ of the hemisphere. The skin surface of the breast is exposed to an environment of temperature $T_f$ with convective heat transfer coefficient $h$; and the base of the tissue is maintained at an adiabatic condition. The location of the tumor inside the breast can be characterized by the radial distance $r$, and the polar angle $\theta$ and the azimuthal angle $\phi$ (Fig. 1).

In a living issue, heat transfer takes place mainly by conduction, which is also affected by the flow of blood and the metabolic heat generation in the tissue. Mathematically, it can be expressed using the PBHE, given by,

$$\rho C_p \frac{\partial T}{\partial t} = k\nabla^2 T + \eta_b \rho_b C_{pb}(T_a - T) + Q_m \qquad (1)$$

where $t, T, k, \rho, c_p, \rho_b, c_{pb}, \eta_b, Q_m$ and $T_a$ are the time, the temperature, the thermal conductivity, the density of tissue, the specific heat of the tissue, the density of blood, the specific heat of the blood, the blood perfusion rate, the metabolic heat generation rate of the tissue and the temperature of the artery, respectively. COMSOL 4.3a has been used for FEM discretization of the PBHE (Eq. 1). Prior to the estimation of the size and location of a tumor, for the considered geometry, the solver is validated with the experimental data given in [2].

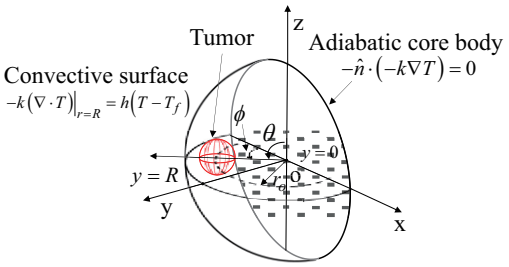


Fig.1: Schematic of the 3-D model of breast

With a tumor, the skin surface temperature profile of a breast shows a unique Gaussian nature. This uniqueness corresponds to a particular attribute of the tumor. Using this uniqueness as the basis, an inverse algorithm is proposed [3] to estimate size and the location of a tumor utilizing the skin surface temperature of the breast.

## 3. Results and Discussion

Numerical modelling of a 3-D breast to estimate the size and the location of a malignant tumor is the aim of the present work. The PBHE has been solved numerically to obtain the temperature field. The model has been validated using the experimental results of Gautherie [2]. In order to accommodate large variation of sizes, a breast of radius $(R)$ 9 cm is considered embedded with a spherical tumor of 1.15 cm radius $(r_t)$ at a depth of 2 cm. For a breast, with $k = 0.42$ W/m·K, $\rho = 920 kg/m^3$, $c_p = 3000$ J/kg·K,

Corresponding author: Subhash C. Mishra
*E-mail address*: scm_iitg@yahoo.com

and $T_a = 37\,^oC$, for a normal tissue, the value of $Q_m$ and $\eta_b$ are $450\,\mathrm{W\cdot m^{-3}}$ and $0.00018\,\mathrm{s^{-1}}$; while in cancerous condition, these values are $29000\,\mathrm{W\cdot m^{-3}}$ and $0.009\,\mathrm{s^{-1}}$, respectively [4]. With the known thermophysical properties and the considered boundary conditions, numerical solution of Eq. 1, yields the temperature field for the computational domain (Fig. 1). Figure 2 shows the steady-state temperature distribution along the radial direction $(0 \le r \le R \quad \theta = \pi/2, \phi = \pi/2)$ of the breast through the center of the tumor. With an overestimation of 0.0451°C and 0.525°C at the skin surface $(r = R)$, the numerical results shows a similarity in the profile for normal and malignant tissues (Fig. 2).

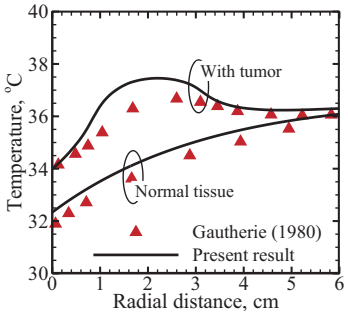


Fig. 2: Validation of the 3-D hemispherical model of breast with experimental results of Gautherie [2].

Following validation, with the known boundary conditions and thermophysical properties of the normal and malignant tissues, the effect of tumor size and location on the skin surface temperature profile have been studied. With a tumor of radius $(r_t)$ 1.5 cm located at a depth $(r - y)$ of 2.25 cm, 3.25 cm, 3.75 cm and 4.25 cm, Fig. 3a shows the steady-state skin temperature distribution of the breast. The effect of size is observed for tumor radii 1 cm, 2 cm and 3 cm, located at a depth of 3.25 cm in Fig. 3b. For a healthy tissue, the temperature variation on the skin surface is found uniform. Whereas it has been found that, closer is the tumor to the skin surface and bigger is its size, higher is the rise in temperature of the skin. It is due to higher value of metabolic heat generation of the tumor which could not be compensated by high rate of blood perfusion, and this manifests on the skin surface of the breast in the form of rise of temperature.

Having observed the uniqueness in the Gaussian skin surface temperature profile of the breast for different attributes of the tumor, the skin surface temperature profiles can be represented by,

$$y = y_o + Ae^{-(x-x_c)^2/2w^2} \qquad (2)$$

where $y_o, x_c, A$ and $w$ are the offset, the center, the amplitude and the width of the profile, respectively.

For any case of malignancy in the breast with a tumor inside, a high precision measurement technique will provide the maximum temperature of the skin surface. With the location of the maximum temperature, line joining the point and the center of the hemisphere assures the $\theta$ – location of the tumor. Consideration of a semicircle passing through the point of maximum surface temperature subtended on the *x*- axis (Fig. 1), the analysis is reduced to a 2-D semicircular geometry. Following the procedure outlined in [3], Table 1 shows the estimated values of size and location of the tumor inside the breast. With an exact estimation of the size, the location of the tumor is estimated with a maximum error of 7%. All the values are well within desired limit. The method has been found exceedingly fast due to non-requirement of iterative solution of the PBHE.

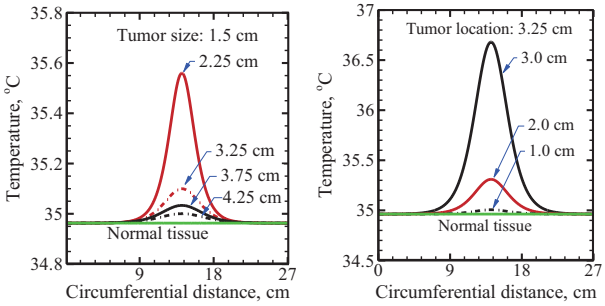


Fig. 3: Steady state skin surface temperature distribution of breast showing the effect of (a) size and (b) location.

Table 1. Estimated value of size and location of tumor

| Actual | | | | Estimated | | | |
|---|---|---|---|---|---|---|---|
| Size | r | θ | φ | Size | r | θ | φ |
| 1.5 | 5.25 | 0.00 | 90.00 | 1.5 | 5.25 | 0.25 | 90.00 |
| 1.5 | 6.05 | 29.74 | 90.00 | 1.5 | 6.00 | 30.13 | 90.02 |
| 1.5 | 6.37 | 29.74 | 69.15 | 1.5 | 6.33 | 30.13 | 71.64 |
| 2.5 | 5.77 | 33.69 | 66.04 | 2.5 | 5.76 | 35.18 | 69.67 |
| 2.0 | 5.77 | 23.96 | 123.69 | 2.0 | 5.76 | 24.36 | 121.34 |
| 1.0 | 7.14 | 11.31 | 45.0 | 1.0 | 6.82 | 11.00 | 44.98 |

## 4. Conclusions

A 3-D realistic model of breast is simulated numerically using PBHE to analyze the effect of size and location of a tumor. Higher rate of metabolism of the tumor was found responsible for rise of the temperature of the breast even after having higher rate of blood perfusion. At a particular location, a tumor yields a unique Gaussian temperature profile at the skin. Having known this fact, the newly proposed curve fitting technique was used to estimate the size and location of the tumor inside the breast. The estimated results were within the acceptable accuracy, method was computationally very fast.

## References


[1] GLOBOCAN, *http://globocan.iarc.fr*

[2] M. Gautherie, *Ann. N. Y. Acad. Sci.*, 335 (1980) 383–415D.

[3] K. Das, S.C. Mishra, *Int. Commun. Heat Mass Transf*, 56 (2014) 63-70.

[4] D.A. Mankoff, L.K. Dunnwald, J.R Gralow, G.K Ellis, A. Charlop, T.J Lawton, E.K Schubert, J. Tseng, R.B Livingston, *J. Nucl. Med*, 43 (2002) 500–509.

Eleventh International Conference on Flow Dynamics
October 8-10, 2014, Sendai, Miyagi, Japan

# Preliminary Study of Self-heated Thermistor Probe for Non-invasive Medical Diagnosis

Takahiro Okabe[1], Junnosuke Okajima[2], Atsuki Komiya[2], Shigenao Maruyama[2]
[1]Graduate School of Engineering, Tohoku University
6-6 Aoba, Aramaki-aza, Aoba-ku, Sendai, Miyagi, 980-8579, Japan
[2]Institute of Fluid Science, Tohoku University
2-1-1 Katahira, Aoba-ku, Sendai, Miyagi, 980-8577, Japan

**ABSTRACT**

This paper describes the possibility of non-invasive and faster medical diagnosis for the malignant melanoma by using the self-heated thermistor probe. In order to evaluate the possibility, the 2D axisymmetric numerical calculation was done. The calculation result indicated that there was an obvious difference of thermal response both during and after heating between the case with and without the malignant melanoma. Moreover, the sensitivity analysis was conducted to evaluate the sensitivities of thermal conductivity and blood perfusion rate, and indicated that the thermal conductivity is dominant in this calculation.

## 1. Introduction

The malignant melanoma is a form of cancerous skin lesion, and has highest death rate in a disease of the skin. According to a medical report [1], if the lesion area was appropriately removed by a surgical operation, a 5-year survival rate would be approximately 100%. Therefore, the early detection and treatment are quite important for the melanoma patients. However, it is still difficult for even a medical doctor to accurately determine the malignant potential of pigmented lesions in human skin and to discriminate a melanoma from normal moles, because it requires the substantial experience to detect it. Thus, new effective diagnosis techniques for the malignant melanoma at an early stage are being required in the medical field.

Çetingül et al. have developed the imaging technique using an infrared camera that allows for accurate measurement of temperature differences on the skin surface for the diagnosis of an early-stage lesion [2]. In this method, a cold air was disbursed to cool the skin for 60 seconds. After the cooling, the skin is re-warmed within 3-4 minutes while being exposed room temperature. During the cooling and re-warming phases, the surface temperature was measured. As the result, the thermal responses after the cooling were obviously different between the lesion and healthy skin due to the difference of thermophysical properties of malignant melanoma such as the thermal conductivity or blood perfusion rate.

In this study, we have proposed a new rapid diagnosis for the malignant melanoma by the measurement of effective thermal conductivity of tissue. We used a pulse-power integrated-decay technique for the measurement of thermal conductivity proposed by Kharalkar et al. [3], having advantages in the practical use such as a fast and point contact measurement. The objective of this study is to investigate whether the measurement of thermal conductivity can be applied for the diagnosis of the malignant melanoma by using the numerical simulation.

## 2. Calculation Model

Figure 1 shows the 2D axisymmetric calculation model consisting of five layers viewed from the surface: epidermis, papillary dermis, reticular dermis, fat layer, and muscle layer. There is a thermistor ($d$ = 0.8mm) with constant heat generation contacting with the skin surface, and a malignant lesion in the dermis layer. The thermophysical properties of tissues are tabulated in Table 1. The bioheat equation by Pennes [4] is used to describe the temperature distribution in each tissue as:

$$\rho c\frac{\partial T}{\partial t}=\frac{1}{r}\frac{\partial}{\partial r}\left(kr\frac{\partial T}{\partial r}\right)+\frac{\partial}{\partial z}\left(k\frac{\partial T}{\partial z}\right)+\rho_b c_b \omega_b\left(T_a-T\right)+q_{met}, \quad (1)$$

where $\rho$, $c$, $T$, $t$, $k$, $\omega_b$, $T_a$, and $q_{met}$ denote density [kg/m$^3$], specific heat [J/(kg·K)], temperature [$^o$C], time [s], thermal conductivity [W/(m·K)], blood perfusion rate [1/s], arterial temperature [$^o$C] and metabolic heat generation per unit volume [W/m$^3$], respectively. Subscript $b$ means the blood.

In this calculation, the initial temperature distribution in the tissue at the steady-state was calculated at first. After that, the transient calculation was done. As for the heating protocol, a thermistor was heated by making constant power equal to 10 mW for 3 seconds. After the heating, the temperature decay of a thermistor was calculated for 12 seconds. In this study, we investigated the thermal responses of a thermistor in the case with and without the malignant melanoma when an above heating protocol is applied.

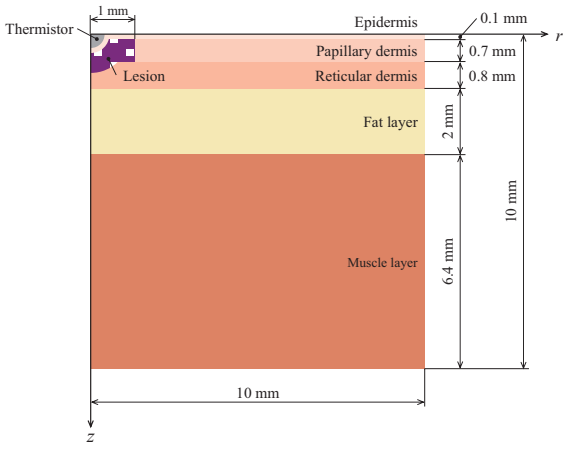


Fig. 1 2D axisymmetric calculation model

## 3. Results and Discussions

Figure 2 shows the time variations with the temperature difference of a thermistor from the temperature before heating. The black line shows the case with the malignant

Corresponding author: Takahiro Okabe
*E-mail address*: okabe@pixy.ifs.tohoku.ac.jp

Table 1. Thermophysical properties of tissues selected based on [2]

| | $c$ J/(kg·K) | $k$ W/(m·K) | $\rho$ kg/m$^3$ | $\omega_b$ 1/s | $q_{met}$ W/m$^3$ |
|---|---|---|---|---|---|
| Epidermis | 3589 | 0.235 | 1200 | 0 | 0 |
| Papillary dermis | 3300 | 0.445 | 1200 | 0.0002 | 368.1 |
| Reticular dermis | 3300 | 0.445 | 1200 | 0.0013 | 368.1 |
| Fat | 2674 | 0.185 | 1000 | 0.0001 | 368.3 |
| Muscle | 3800 | 0.51 | 1085 | 0.0027 | 684.2 |
| Lesion | 3852 | 0.558 | 1030 | 0.0315 | 3680 |

melanoma while the red line shows the case of the healthy tissue. As seen in figure, there is an obvious difference between the case with and without the malignant melanoma in both heating and cooling phase. The largest temperature difference is about 0.5 °C after 3 seconds which is detectable enough. This difference causes a change of approximately 12% in the effective thermal conductivity estimated by a pulse-power integrated-decay technique. Thus, it was revealed that the melanoma can be detected by the measurement of effective thermal conductivity using a pulse-power integrated-decay technique.

In order to evaluate the sensitivities of thermal conductivity and blood perfusion rate to the temperature difference in this calculation, the sensitivity analysis was conducted using the dimensionless sensitivity coefficient when the change rate of parameters is 10%. Figure 3 shows the time variations with dimensionless sensitivity coefficient to the temperature difference of a thermistor. As seen this figure, the dimensionless sensitivity coefficient of thermal conductivity is much higher than that of blood perfusion rate. It means that the thermal conductivity is dominant in a thermal response both during and after heating.

On the other hand, Fig. 4 shows the time variations with surface temperature of a thermistor. In this figure, the temperature before the heating is different between the case with and without the melanoma. This difference is caused by the different initial temperature distribution in the tissue. The dimensionless sensitivity coefficient of blood perfusion rate to the temperature before heating is ten times as large as that of thermal conductivity, which means that the blood perfusion rate affects only the temperature before heating significantly.

## 4. Concluding Remarks

In order to investigate whether the measurement of thermal conductivity can be applied to the diagnosis of the malignant melanoma, the numerical simulation was done.

1. Calculation results indicated that there was an obvious difference in the thermal responses between the case with and without the malignant melanoma.
2. The thermal conductivity is dominant in the change in thermal response both during and after heating.
3. If the thermal conductivity of melanoma was different from that of healthy skin, our method would be effective for the diagnosis of malignant melanoma.

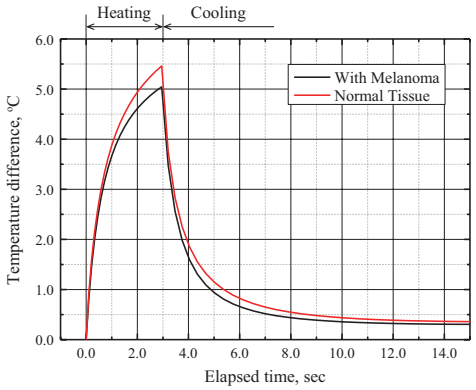


Fig. 2 Time variations with temperature difference of thermistor

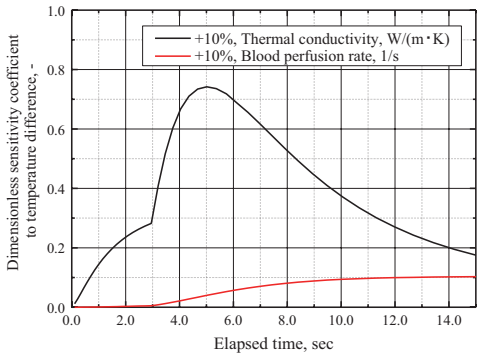


Fig. 3 Time variations with dimensionless sensitivity coefficient to temperature difference of thermistor

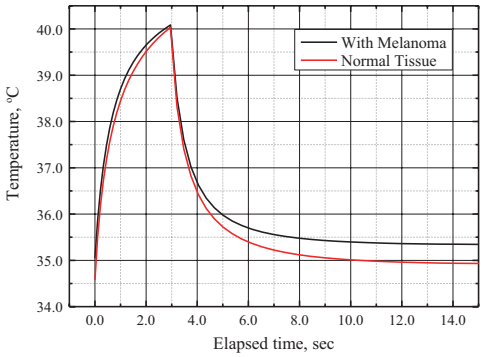


Fig. 4 Time variations with surface temperature of thermistor


## Acknowledgements

Takahiro Okabe was supported by Grant-in-Aid for JSPS Fellows 13J08342.


## References


[1] G. Hildenbrand, L. Hildenbrand, K. Bradford, S. Cavin, *Altern. Ther. Health Med.*, 1 (4) (1995) 29-37.

[2] M. Pirtini Çetingül, C. Herman, *Int. J. Ther. Sci.*, 50 (2011) 421-431.

[3] N. M. Kharalkar, L. J. Hayes, J. W. Valvano, *Meas. Sci. Technol.*, 19 (2008) 075104.

[4] H. H. Pennes, *J. Appl. Physiol.*, 1 (1948) 93-122.

Eleventh International Conference on Flow Dynamics
October 8-10, 2014, Sendai, Miyagi, Japan

# Evaluation on Endothermic Effect of Dissociation in Methane Hydrate Reservoir

Hiroki Gonome[1], Richard Arnold[2], Junnosuke Okajima[1], Atsuki Komiya[1], Shigenao Maruyama[1, 3]
[1]Institute of Fluid Science, Tohoku University
2-1-1 Katahira, Aoba-ku, Sendai, Miyagi 980-8577, Japan
[2]Graduate School of Engineering, Tohoku University
6-6 Aoba, Aramaki-aza, Aoba-ku, Sendai, Miyagi 980-8579, Japan
[3]CREST, JST
4-1-8 Honcho, Kawaguchi, Saitama, 332-0023, Japan

**ABSTRACT**

One of the solutions for the exhaustion of fossil fuels is the effective utilization of Methane Hydrate (MH). Three methods, a depressurization method, a thermal stimulation method, and an inhibitor injection method are general to utilize MH. This study verifies the possibility of the depressurization method by thermal analysis. Terminal temperature after dissociating all MH by depressurization showed lower than the temperature of freezing point of water. When the initial temperature was up to 15 °C, the percentage of dissociating MH was up to 80%.

## 1. Introduction

Conventional thermal power generation systems have faced significant issues recently. One of the issues is the exhaustion of fossil fuels. The global energy demand has continued to increase, but the remains of fossil fuels have decreased. One of the solutions to the problem is the effective utilization of Methane Hydrate (MH) [1].

The MH has a chemical structure that the methane gas traps inside cage-like crystal structures made up of water molecules, and its chemical formula can be written as $CH_4 \bullet 5.75H_2O$. The MH can be utilized as a primary energy source by dissociating MH to methane gas and water as expressed as following equation;

$$CH_4 \cdot 5.75H_2O \rightarrow CH_4 + 5.75H_2O - 56.9 \text{ kJ/mol.} \quad (1)$$

This equation shows the endothermic reaction. This is one of the difficulties of practical utilization of MH.

Three methods, depressurization method, thermal stimulation method and inhibitor injection method are general to utilize MH [2]. A depressurization method entails the pressure decrease in a free gas zone adjacent to a MH stability layer. A thermal stimulation method entails increasing the temperature of a MH layer by injecting hot water or steam into the layer.

A thermal stimulation method needs the external energy to prepare the hot injected water. Depressurization method does not need a lot of external energy; therefore, it is considered as the most effective method for utilizing MH. However, the reaction stops because of the endothermic effect. As the reaction runs, the temperature of the reservoir decreases. Therefore, self-preservation of MH might be promoted by generated ice and the depressurization method cannot be applied.

This study verifies the possibility of the depressurization method by thermal analysis. In the analysis, the effect of the mud layer was estimated. Terminal temperature after dissociating all MH and the percentage of dissociating MH were calculated.

Corresponding author: Hiroki Gonome
*E-mail address*: hiroki1006@pixy.ifs.tohoku.ac.jp

## 2. Method

To estimate the temperature of the reservoir after dissociating MH, thermal analysis was conducted. Actually, the heat conduction and the mass transfer occur in MH reservoir. Then, the MH dissociation becomes complex. In this study, it was assumed that the endothermic occurred homogeneously in the MH concentrated zones and the rate of MH dissociation was constant. Equation of the energy conservation in the MH concentrated zones is expressed as follow;

$$C_{mix} = f[\phi\left(\rho_g S_g c_{p,g} + \rho_w S_w c_{p,w} + \rho_h S_h c_{p,h}\right) + \left(1-\phi\right)\rho_s c_{p,s}] + \left(1-f\right)\rho_{mud} c_{p,mud}, \quad (2)$$

$$C_{mix}\left(T_{ini} - T_{term}\right) = f\phi\rho_h S_h \Delta H_D, \quad (3)$$

where $C_{mix}$ is mixed heat capacity, $f$ is Net Gloss (NG) ratio, $\phi$ is porosity, $\rho$ is density, $S$ is saturation, $c_p$ is specific heat capacity, $T$ is temperature and $\Delta H_D$ is latent heat. Subscript $g$, $w$, $h$, $s$, *mud*, *ini* and *term* are gas, water, methane hydrate, sand, mud, initial and terminal, respectively. NG ratio means the ratio of the sand layer against the total volume. Porosity means the ratio of void against sand in sand layer. $\Delta H_D$ can be calculated as follow [3];

$$\Delta H_D = 446.12 \times 10^3 - 132.64 \times T_{ini}. \quad (4)$$

Temperature of freezing point of water $T_{fp}$ was also calculated as follow;

$$T_{fp} = 273.16 \times \sqrt[9]{1 - \frac{p_{ini}}{395.2}}, \quad (5)$$

where $p_{ini}$ is initial pressure.

Table 1 shows the constant values for calculation [4-7] and initial saturation. $\rho_g$, $c_{p,g}$ and $c_{p,m}$ are dependent on the temperature and/or the pressure. $\rho_g$ was calculated using the ideal gas law. $c_{p,g}$ and $c_{p,m}$ are quoted from the database [8]. Table 2 shows examples of values which are dependent on temperature and/or pressure when temperature is 10 °C and the pressure are 5, 10 and 15 MPa. In Table 2, the density of the methane gas is variable in the initial pressure. In this study, the variation of the initial temperature against the final temperature and the percentage of dissociating MH were shown.

Table 1. Constant values and initial saturation [4-7]

| Symbol [Unit] | Value | | | | |
|---|---|---|---|---|---|
| | gas | water | MH | sand | mud |
| $f$ [-] | 0.37 | | | | |
| $\phi$ [-] | 0.4 | | | | |
| $S$[-] | 0.2 | 0.2 | 0.6 | – | – |
| $\rho$ [kg·m$^{-3}$] | 998 | – | 910 | 1750 | 1950 |
| $c_p$ [J·kg$^{-1}$·K$^{-1}$] | 4180 | – | – | 820 | 770 |

Table 2. Examples of values which are dependent on temperature and/or pressure [8]

| Symbol [Unit] | Value | | |
|---|---|---|---|
| $p_{ini}$ [MPa] | 5 | 10 | 15 |
| $T_{ini}$ [°C] | 10 | | |
| $\rho_g$ [kg·m$^{-3}$] | 36.56 | 73.12 | 109.66 |
| $c_{p,g}$ [J·kg$^{-1}$·K$^{-1}$] | 2175.80 | 2175.84 | 2175.89 |
| $c_{p,m}$ [J·kg$^{-1}$·K$^{-1}$] | 2103.18 | 2103.37 | 2103.56 |

## 3. Results and Discussion

Terminal temperature after dissociating all MH was calculated. Figure 1 shows the variation of the terminal temperature with the initial temperature and the temperature of freezing point when initial pressure $p_{ini}$ is 5, 10 and 15 MPa. In Fig. 1, the terminal temperature was lower than the temperature of freezing point in the initial temperature from 1 to 19 °C. There is a possibility that the self-preservation of MH is promoted by generated ice and the dissociation of MH stops. The initial pressure had no effect on the terminal temperature. The initial temperature was the most effective on the terminal temperature. To select a mining zone, the survey of the temperature in the seabed is important.

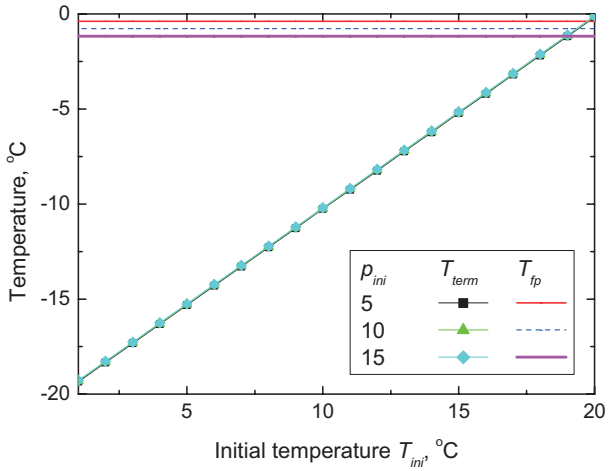


Fig. 1 Variation of the terminal temperature $T_{term}$ with the initial temperature $T_{ini}$ and the temperature of freezing point when initial pressure $p_{ini}$ is 5, 10 and 15 MPa

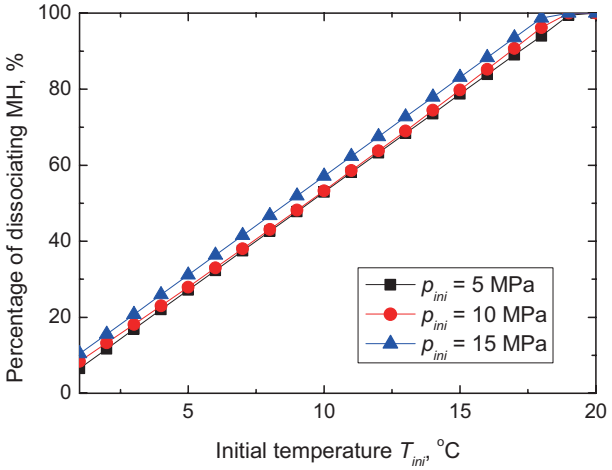


Fig. 2 Percentage of dissociating MH for $T_{final} = T_{fp}$

Percentage of dissociating MH for $T_{term} = T_{fp}$ was calculated. Figure 2 shows the calculated result. When the initial temperature was up to 15 °C, the percentage of dissociating MH was up to 80%. When the initial temperature was over 19 °C, all MH could be dissociated. As same as the terminal temperature, the initial pressure did not have much effect on the percentage of dissociating MH. The initial temperature was the more effective than the initial pressure.

## 4. Concluding Remarks

The possibility of the depressurization method was verified by thermal analysis.

1. Final temperature after dissociating all MH was lower than the temperature of freezing point.
2. There is a possibility that the self-preservation of MH is promoted and the dissociation of MH stops.
3. When the initial temperature was up to 15 °C, the percentage of dissociating MH was up to 80%.

## References


[1] S. Maruyama, K. Deguchi, M. Chisaki, J. Okajima, A. Komiya, R. Shirakashi, *Energy*, 47, (2012) 340-347.

[2] K. A. Kvenvolden, *Reviews of Geophysics*, 31 (1993), 173–187.

[3] M.S. Selim, E.D. Sloan, *AIChE journal*, 35 (1989) 1049–1052.

[4] E.D. Sloan, *Clathrate Hydrates of Natural Gases*, (1998).

[5] H. Narita, *Journal of the JIE*, 90 (2011) 492–498.

[6] Research Consortium for Methane Hydrate Resources in Japan.

[7] M.H. Yousif, H.H. Abass, M.S. Selim, E.D. Sloan, *SPE Reservoir Engineering*, 6 (1991), 69–76.

[8] R.P. Warzinski, I.K. Gamwo, E.J. Rosenbaum, E.M. Myshakin, H. Jiang, K.D. Jordan, N.J. English, D.W. Shaw, *Proceedings of ICGH 2008*, (2008).

Eleventh International Conference on Flow Dynamics
October 8-10, 2014, Sendai, Miyagi, Japan

# Local Consumption Speed of Turbulent Premixed V-shaped Flames of Methane-Air

Sina Kheirkhah, Ömer L. Gülder
University of Toronto Institute for Aerospace Studies (UTIAS)
4925 Dufferin Street, Toronto Ontario M3H 5T6 Canada

**ABSTRACT**

Local consumption speed of turbulent premixed V-shaped flames was investigated experimentally. The experiments were performed for relatively weak, moderate, and intense turbulence conditions. The results show that, for the range of turbulence conditions tested, the values of the local consumption speed normalized by the un-stretched laminar flame speed vary from unity to 1.5. The local consumption speed normalized by the root-mean-square of the streamwise velocity is shown to follow a power-law correlation with the Karlovitz stretch factor.

## 1. Introduction

Turbulent premixed combustion is the mode of operation in several engineering equipment, e.g., gas turbines, lean premixed and prevaporized jet engines, and spark ignition engines [1-3]. In order to investigate turbulent premixed combustion characteristics, several flame configurations, e.g., V-shaped, Bunsen-type, and stagnation flames have been developed in the past decades, see for example, [3-5]. In the studies associated with these flame configurations, the local consumption speed ($S_{\mathrm{LC}}$) has been of significant importance. $S_{\mathrm{LC}}$ is the speed at which the reactants mixture is consumed at the flame surfaces, and is obtained from the following equation.

$$S_{\mathrm{LC}} = S_{\mathrm{L0}} I_0 \int_{-\infty}^{+\infty} \Sigma \mathrm{d}\eta, \quad (1)$$

where $S_{\mathrm{L0}}$, $I_0$, and $\Sigma$ are the un-stretched laminar flame speed, the stretch factor, and the flame surface density, respectively. $\eta$ is the coordinate system that is locally perpendicular to the mean-progress-variable contours.

In the studies associated with turbulent premixed V-shaped flames, the local consumption speed has been mainly investigated for relatively small and moderate values of turbulence intensity ($u'/U \lesssim 0.1$), see [4-7]. However, most practical combustion devices operate under relatively intense turbulent conditions. Thus, the present study aims at experimentally investigating the local consumption speed of turbulent premixed V-shaped flames for relatively intense turbulence conditions. For comparison purposes, experiments are also performed for relatively weak and moderate turbulence conditions.

## 2. Experimental Methodology

A burner setup has been utilized to produce the V-shaped flames. Schematic of the burner nozzle section along with photograph of a turbulent premixed V-shaped flame is presented in Fig. 1. The burner is composed of an expansion section, a settling chamber, a contraction section, and a nozzle. The nozzle section has a diameter of 48.4 mm. A flame-holder is placed at the exit of the burner. The centerline of the flame-holder is located 4 mm above the exit of the burner. The flame-holder is cylindrical and has a diameter of 2 mm. Further details associated with the burner setup can be found at [8].

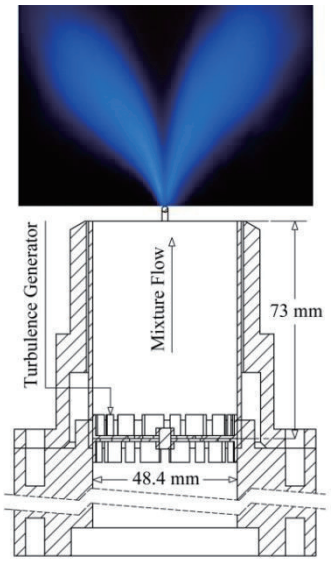


Fig. 1. Schematics of the burner nozzle section along with photograph of a V-shaped flame.

Mie scattering and Particle Image Velocimetry (PIV) techniques were utilized in the present study. The Mie scattering technique was used to obtain the flame front contours, with detailed algorithm provided in [8]. The PIV technique was used to estimate characteristics of the turbulent flow field. Specifically, the turbulence intensity ($u'/U$), where $u'$ and $U$ are the RMS and mean streamwise velocity, as well as the integral length scale associated with the streamwise velocity ($\Lambda$) were estimated as turbulent flow characteristics.

Three turbulence generating mechanisms were used in the present study. The first mechanism is associated with the turbulence generated by mesh screens inside the settling chamber. The turbulence intensity pertaining to this mechanism is $u'/U = 0.02$. The second and third turbulence generating mechanisms are associated with one perforated plate and combination of two perforated plates attached back to back, respectively.

Corresponding author: Ö. L. Gülder
*E-mail address*: ogulder@utias.utoronto.ca.

The turbulence intensities associated with the second and third turbulence generating mechanisms are $u'/U = 0.06$ and 0.17, respectively. The integral length scale associated with the first, second and third turbulence generating mechanisms are approximately $\Lambda \approx 2.5$, 4.0, and 6 mm, respectively. These turbulence characteristics correspond to Reynolds numbers ($Re_\Lambda = u'\Lambda/\nu$) ranging from about 13 to 501, with $\nu$ being the reactants kinematic viscosity.

Methane-air was used as the reactants mixture in the experiments. For each turbulence generating mechanism, three mean bulk flow velocities of $U$ = 4.0, 6.2, and 8.3 m/s were examined. For each mean bulk flow velocity, two fuel-air equivalence ratios of $\varphi$ = 0.6 and 0.7 were tested. For $\varphi$ = 0.6 and 0.7, the un-stretched laminar flame speed were estimated as 0.13 and 0.2 m/s, respectively, and the laminar flame thickness ($\delta_L$) were estimated as 0.17 and 0.11 mm, respectively. The experimental conditions are such that $u'/S_{L0}$ ranges from 0.4 to 11; and $\Lambda/\delta_L$ varies from 15 to 55.

## 3. Results

The local consumption speed ($S_{LC}$) was estimated using Eq. (1). Values of the local consumption speed depend on the vertical distance from the flame-holder. For this reason, $S_{LC}$ was averaged at several vertical distances above the flame-holder for each experimental condition tested. The averaged local consumption speed results are presented in Fig. 2. In the figure, the circular, square, and triangular data points correspond to the first, the second, and the third turbulence generating mechanisms, respectively. $S_{LC}$ is normalized by the RMS of the streamwise velocity. In Fig. 2, the results are presented against the Karlovitz stretch factor ($K$), given by the following equation [9].

$$K = 0.157\left(\frac{u'}{S_{L0}}\right)^2 Re_\Lambda^{-0.5}. \quad (2)$$

Also shown in Fig. 2 are the experimental results of Shepherd [6] and Sattler et al. [7]. The uncertainty associated with the estimation of the $S_{LC}/u'$ and $u'/S_{L0}$ depends on the experimental conditions tested. The maximum uncertainty is presented by the error bars in Fig. 2. The results show that the normalized local consumption speed follows a power-law correlation with the Karlovitz stretch factor, given by:

$$\frac{S_{LC}}{u'} \approx 0.1K^{-0.66}. \quad (3)$$

Substituting Eq. (2) into Eq. (3) and using the definition of the laminar flame thickness ($\delta_L \propto \nu/S_{L0}$), it can be shown that:

$$\frac{S_{LC}}{S_{L0}} \approx 0.4\left(\frac{\Lambda}{\delta_L}\right)^{0.33}. \quad (4)$$

Considering that the values of the ratio $\Lambda/\delta_L$ vary from 15 to 55, Eq. (4) indicates that the local consumption speed normalized by the un-stretched laminar flame speed varies from 1 to 1.5 for the data shown in Fig. 2.

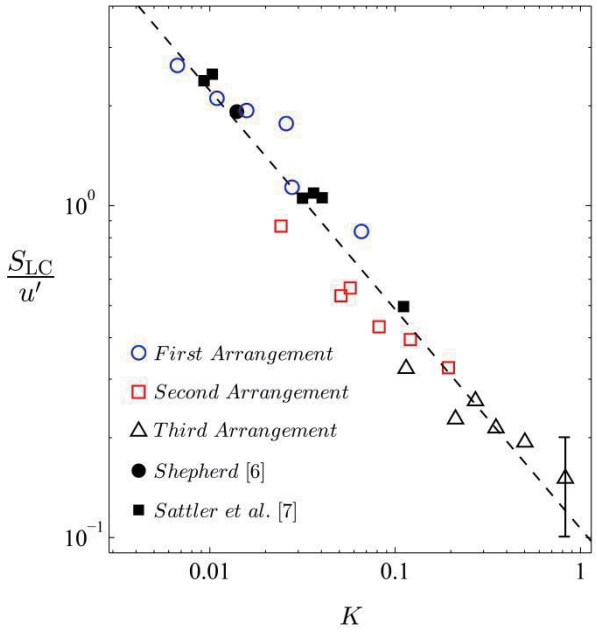


Fig. 2. Variation of the normalized local consumption speed with the Karlovitz stretch factor.

## 4. Concluding Remarks

Local consumption speed of turbulent premixed V-shaped flames was investigated for relatively small, moderate, and large values of turbulence intensities, corresponding to $u'/U$ = 0.02, 0.06, and 0.17, respectively. The experiments were performed for mean bulk flow velocities of $U$ = 4.0, 6.2, and 8.3 m/s along with two fuel-air equivalence ratios of $\varphi$ = 0.6 and 0.7.

The results show that, for the range of turbulence conditions tested, the values of the local consumption speed normalized by the un-stretched laminar flame speed varies between unity and 1.5. Also, the local consumption speed normalized by RMS of the streamwise velocity follows a power-law correlation with the Karlovitz stretch factor.

## References


[1] N. Peters, *Turbulent Combustion, 1st ed., Cambridge University Press*, (2000).

[2] I. Glassman, R.A. Yetter, *Combustion 4th ed., Elsevier Inc.*, (2008).

[3] P. Clavin, *Prog. Energy Combust. Sci.*, 11 (1985) 1-59.

[4] A. N. Lipatnikov, J. Chomiak, *Prog. Energy Combust. Sci.*, 28 (2002) 1-78.

[5] J.F. Driscoll, *Prog. Energy Combust. Sci.*, 34 (2008) 91-134.

[6] I.G. Shepherd, *Proc. Combust. Inst.*, 26 (1996) 373-379.

[7] S.S. Sattler, D.A. Knaus, F.C. Gouldin, *Proc. Combust. Inst.*, 29 (2002) 1785-1792.

[8] S. Kheirkhah, Ö.L. Gülder, *Phys. Fluids*, 25 (2003) 055107.

[9] R.G. Abdel-Gayed, D. Bradley, M. Lawes, *Proc. R. Soc. Lond. A.*, 414 (1987) 389-413.

Eleventh International Conference on Flow Dynamics
October 8-10, 2014, Sendai, Miyagi, Japan

# Analysis of Liquid Petroleum Gas Combustion in a Porous Radiant Burner

Snehasish Panigrahy and Subhash C. Mishra
Dept. of Mechanical Engineering, Indian Institute of Technology Guwahati
India – 781039

**ABSTRACT**

This work deals with the analysis of combustion of liquid petroleum gas–air mixture in a 1-D porous radiant burner. Gas- and solid-phase energy equations, chemical species transport equations are simultaneously solved. Combustion is modelled by a multistep kinetics mechanism. Axial distributions of gas temperature, solid temperature and species mole fractions are studied.

## 1. Introduction

The combustion of liquid as well as gaseous fuels in conventional combustion devices such as burners, furnaces, etc., take place in the free-flame mode, and therefore, their thermal efficiencies are low, and emission of CO and NOx are high. However, if these fuels are made to combust in an inert porous matrix that is highly conducting and radiating, thermal efficiencies go up and emissions come down. Sathe et al. [1] did both numerical and experimental investigations. The methane-air oxidation was modeled using a one-step irreversible reaction. It was found that the stable combustion could be maintained in two spatial domains, one in the upstream half of the porous segment, and another at the downstream edge of the segment.

In the field of modelling porous radiant burner (PRB), Rumminger et al. [2] considered a 1-D bi-layered reticulated ceramic PRB. For the combustion process, they solved the chemical species transport equations simultaneously with two separate energy equations for gas and solid phases. Volumetric radiative information was accounted in the solid phase energy equation. Khanna et al. [3] did experiments with pre-mixed methane and air, and showed that the concentration of NOx increased with flame speed, due to the increase in peak temperature, while the concentration remained relatively constant for a given equivalence ratio. They also showed that CO increased with the flame speed.

In the recent past, a good number of experimental and computational studies on combustion in porous media have been reported. However, the study on a liquid petroleum gas (LPG) fuelled PRB has not been reported. The ongoing development of a LPG cooking stove with PRB in mind, the present work deals with the heat transfer analysis of combustion of LPG in a PRB.

## 2. Formulation

The burner geometry (Fig. 1) examined in this study is the same one used by Diamantis et al. [4] and Bidi et al. [5]. A premixed LPG-air mixture passes through the SiC porous matrix of thickness $L$ contained in the adiabatic axi-symmetric duct (Fig. 1). The flame may be located anywhere inside the porous matrix. Conservation of mass, gas energy, solid energy, and species, for a multicomponent mixture give rise to four coupled partial differential equations.

Corresponding author: Subhash C. Mishra
*E-mail address*: scm_iitg@yahoo.com

Continuity equation:

$$\frac{\partial(\phi\rho_g)}{\partial t}+\frac{\partial(\phi\rho_g u)}{\partial x}=0 \tag{1}$$

Gas phase energy equation:

$$\begin{aligned}&\phi\rho_g C_g\left(\frac{\partial T_g}{\partial t}+u\frac{\partial T_g}{\partial x}\right)+(1-\phi)h_V(T_g-T_s)\\&+\phi\sum_{i=1}^{n}\rho_g Y_i C_{g,i}V_i\frac{\partial T_g}{\partial x}+\phi\sum_{i=1}^{n}\dot{\omega}_i h_i W_i-\phi\frac{\partial}{\partial x}\left(\lambda_g\frac{\partial T_g}{\partial x}\right)=0\end{aligned} \tag{2}$$

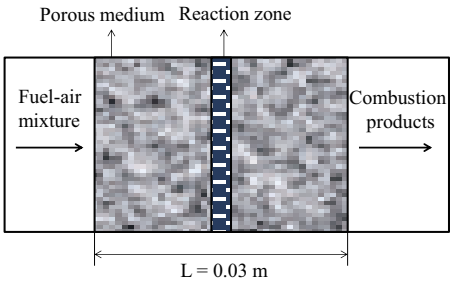


Fig. 1: Schematic diagram of the porous radiant burner.

Solid phase energy equation:

$$\begin{aligned}&(1-\phi)\rho_s C_s\frac{\partial T_s}{\partial t}-(1-\phi)h_V(T_g-T_s)\\&-(1-\phi)\lambda_s\frac{\partial^2 T_s}{\partial x^2}+\nabla\cdot q=0\end{aligned} \tag{3}$$

Species conservation equation is expressed as:

$$\phi\rho_g\left(\frac{\partial Y_i}{\partial t}+u\frac{\partial Y_i}{\partial x}\right)+\frac{\partial}{\partial x}\left(\phi\rho_g V_i Y_i\right)-\phi\dot{\omega}_i W_i=0 \tag{4}$$

where $\rho$ is the density, $\phi$ is the porosity, $u$ is the velocity, $C$ is the specific heat, $T$ is the temperature, $n$ is the number of species, $Y$ is the mass fraction, $\omega$ is the species production rate, $h$ is the enthalpy, $W$ is the molecular weight, $\lambda$ is the thermal conductivity, $h_V$ is the volumetric heat transfer coefficient, $q$ is the radiative heat flux, $V$ is the diffusion velocity. In the solid phase energy equation, the radiative information $\nabla\cdot q$ is computed using the two-flux method.

$$\nabla\cdot q=4\kappa(1-\Omega)\left(\sigma T_s^4-\frac{q^+ + q^-}{2}\right) \tag{5}$$

## 3. Results and Discussion

For conservation of mass, a fixed inlet velocity is selected as the inlet condition. For conservation of energy in the gas phase, a fixed inlet gas temperature and a zero gradient exit gas temperature are taken as the boundary conditions. The thermophysical properties used for 8 PPC SiC PRB are: solid thermal conductivity 10 W/m·K, pore diameter 1.1 mm, porosity 0.9, radiative extinction coefficient 270.0 $m^{-1}$, and radiative scattering albedo = 0.8.

The open source software package Cantera was used for combustion simulations. For the LPG–air combustion, chemical kinetics and transport properties were obtained from USC mech 2.0. The LPG comprised of 60% $C_4H_{10}$ and 40% $C_3H_8$ by volume.

Before presenting results for LPG, with methane as the fuel, the solver was validated by comparing the results from the present work with that of Diamantis et al. [4] and Bidi et al. [5]. Fig. 2 shows comparison of the axial temperature variation of the gas and the solid phase with that reported in [4]. In Fig. 3, species profiles are compared with the results given in [5]. Both temperature distributions and species profiles from the present work are found to compare exceedingly well with those reported in the literature [4,5].

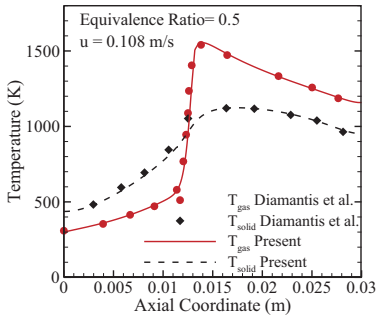


Fig. 2: Comparison to numerical data for temperature distributions at equivalence ratio = 0.5.

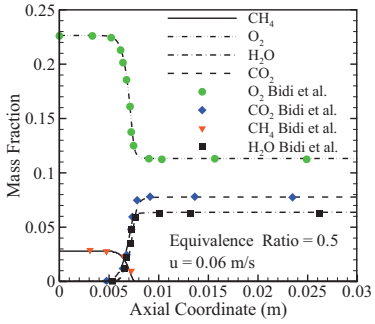


Fig. 3: Major species profiles in flame front for the reference case.

Having validated the present formulation, next the results are presented for LPG-air mixture. The variation of the solid and gas temperatures for two different locations, $u$ = 0.08 and 0.15 m/s for LPG-air mixture are shown in Fig. 4. The LPG-air flames behaves in a similar fashion as that of the methane flame. Figure 5 gives the profiles of species $C_3H_8$, $C_4H_{10}$, CO, $CO_2$, $O_2$ and $H_2O$ along the axial direction of the PRB for the fuel-air mixture velocity u = 0.15 m/s. It is observed that that the combustion process starts within the porous medium, since $C_3H_8$, $C_4H_{10}$ are almost completely consumed at flame front. The CO profile also follows the expected trend, forming quickly in the flame front and then being consumed by the excess oxygen in the reaction zone.

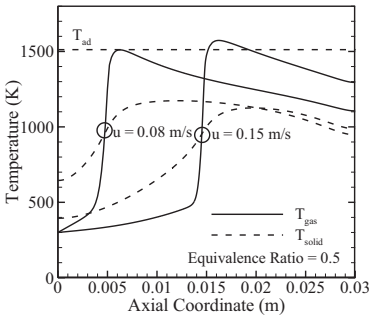


Fig. 4: Temperature distributions at equivalence ratio = 0.5 for two flow velocities.

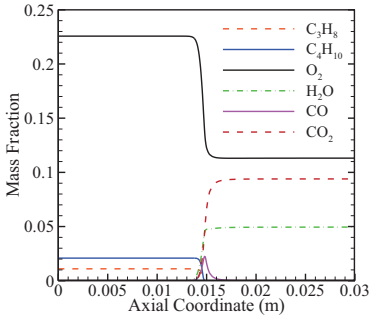


Fig. 5: Profiles of the species mass fractions along axial direction of porous burner for u = 0.15 m/s.

## 4. Conclusions

With methane as the fuel, first the formulation was validated by comparing with results available in the literature. Next, premixed combustion of LPG-air mixture in a 1-D PRB was studied. Multi-step kinetic mechanism was used to simulate LPG-air combustion. Solid and gas temperature profiles were studied. Profiles of mass fraction of major species like $C_3H_8$, $C_4H_{10}$, CO, $CO_2$, $O_2$ and $H_2O$ were also studied.

## References


[1] S.B. Sathe, M.R. Kulkarni, R.E. Peck, and T.W. Tong, *International Symposium on Combustion,* 34 (1990) 1011-1018.

[2] M.D. Rumminger, R.W. Dibble, N.H. Heberle, *International Symposium on Combustion*, 26 (1996) 1755-1762.

[3] V. Khanna, R. Goel, and J. L. Ellzey, *Combustion Science and Technology,* 99 (1994) 133-142.

[4] D.J. Diamantis, E. Mastrakos, D.A. Goussis, *Combustion Theory and Modelling,* 6 (2002) 383-411.

[5] M. Bidi, M.R.H. Nobari, M. Saffar Avval, *Energy,* 35 (2010) 3483-3500.

# Combined Mode Conduction and Radiation Heat Transfer in a 2-D Porous Medium and Simultaneous Estimation of its Optical Properties

Vijay K. Mishra, Subhash C. Mishra and Dipankar N. Basu
Dept. of Mechanical Engineering, Indian Institute of Technology Guwahati
India – 781039

**ABSTRACT**

Analysis of combined mode conduction and radiation heat transfer in a porous medium, and simultaneous estimation of optical properties of the 2-D porous matrix are reported. Simultaneous solution of the gas-phase and the solid-phase energy equations takes care for the local thermal non-equilibrium. For a given set of boundary conditions and operating parameters, the computed solid phase temperature distribution serves as the exact temperature profile needed in the estimation of parameters. The objective function is minimized using the genetic algorithm.

## 1. Introduction

Compared to burners based on free-flame combustion, porous radiant burners (PRB) in which the combustion takes place in the inert porous cavity, offers several advantages such as high thermal efficiency and low pollutant emissions [1]. The performance of PRBs is strongly dependent on relevant thermo-physical and optical properties, matrix dimensions and porosity. Effective utilization of a PRB can be ensured only with the use of optimum values of associated parameters. For a given wattage of the burner, with a given fuel, inverse analysis is a means to estimate some or all of the needed thermophysical and optical properties of the porous matrix employed. Known through some experiments or other way, an inverse analysis utilizes [2,3] temperature and/or heat flux distribution, and minimizes the objective function.

In the present work, a combined mode conduction and radiation heat transfer in a 2-D rectangular porous matrix is analyzed, and simultaneous estimation of two parameters, such as emissivity and scattering albedo, is reported. A centrally located uniform volumetric heat generation source mimics the combustion. With volumetric radiative information needed in the solid-phase energy equation computed using the finite volume method (FVM), the gas phase and the solid phase energy equations are also simultaneously solved using the FVM [4]. Steady-state solid-phase temperature distribution is utilized to frame the objective function, and the genetic algorithm (GA) is used to minimize the objective function.

## 2. Formulation

The geometry under consideration is shown schematically in Fig. 1. Air-fuel mixture flows through a 2-D rectangular porous matrix. A heat generation zone $0.45L_x < x \le 0.55L_x$ is situated at the center of the porous matrix. The solid is radiatively absorbing, emitting and isotropically scattering, while gas is radiatively non-participating. Separate energy equations for the two phases accounts for the thermal non-equilibrium between them. The gas and the solid thermally interacts with each other by convection, so convective coupling term is used to couple the two energy equations. The steady-state energy equations for the two phases in non-dimensional form are:

$$\phi P_1 \frac{\partial \theta_g}{\partial \eta_x} + (1-\phi) P_2 (\theta_g - \theta_s) = \phi \delta(\eta_x) + \phi P_3 \left( \frac{\partial^2 \theta_g}{\partial \eta_x^2} + \frac{\partial^2 \theta_g}{\partial \eta_y^2} \right) \quad (1)$$

Solid phase

$$(1-\phi) P_2 (\theta_g - \theta_s) + (1-\phi) P_4 \left( \frac{\partial^2 \theta_s}{\partial \eta_x^2} + \frac{\partial^2 \theta_s}{\partial \eta_y^2} \right) - \nabla \cdot \Psi_R = 0 \quad (2)$$

With $T, A, h, \dot{Q}, k,\ q_R, \rho, c, \phi$ and $u$ as temperature, pore surface area per unit volume, heat transfer coefficient, volumetric heat generation rate, thermal conductivity, radiative flux, density, specific heat, porosity and flow velocity, respectively, in Eqs. (1) and (2), the various terms are defined as $\theta = \frac{T - T_i}{T_i}$, $\eta_x = \frac{x}{L_x}$, $\eta_y = \frac{y}{L_x}$, $\Psi_R = \frac{q_R}{\dot{Q} L_x}$, $P_1 = \frac{\rho_g c_g u T_i}{\dot{Q} L_x}$, $P_2 = \frac{hAT_i}{\dot{Q}}$, $P_3 = \frac{k_g T_i}{\dot{Q} L_x^2}$, $P_4 = \frac{k_s T_i}{\dot{Q} L_x^2}$ and $P_5 = \frac{h L_x}{k}$. In Eqs. (1) and (2), suffix $g$ stands for gas and $s$ stands for solid. The boundary conditions for the gas-phase and the solid-phase energy equations are the followings.

$$\theta_g = 0 \text{ at } \eta_x = \eta_{x,e}, \frac{\partial \theta_g}{\partial \eta_x} = 0 \text{ at } \eta_x = \eta_{x,e}, \quad \frac{\partial \theta_g}{\partial \eta_y} = 0 \text{ at } \eta_y = 0, \frac{\partial \theta_g}{\partial \eta_y} = 0 \text{ at } \eta_y = \eta_{Ly}, \quad (3)$$

$$-\frac{\partial \theta_s}{\partial \eta_x} = P_5 (\theta_g - \theta_s) \text{ at } \eta_x = 0, \frac{\partial \theta_s}{\partial \eta_x} = P_5 (\theta_g - \theta_s) \text{ at } \eta_x = 1, \quad \frac{\partial \theta_s}{\partial \eta_y} = 0 \text{ at } \eta_y = 0, \quad \frac{\partial \theta_s}{\partial \eta_y} = 0 \text{ at } \eta_y = \eta_{Ly}, \quad (4)$$

For a diffuse-gray boundary having temperature $\theta_b$ and emissivity $\varepsilon_b$, the boundary intensity is computed from

$$I_b^* = \varepsilon_b \frac{\Phi (1+\theta_b)^4}{\pi} + \frac{1-\varepsilon_b}{\pi} \sum_{k=1}^{M_\mu} \sum_{l=1}^{M_\lambda/2} I^{*,m} \sin \lambda_l^m \cos \lambda_l^m \sin \Delta \lambda_l^m \Delta \mu_k^m \quad (5)$$

Corresponding author: Subhash C. Mishra
*E-mail address*: scm_iitg@yahoo.com

where in Eq. (5), $I^* = \dfrac{I}{\dot{Q}L_x}$ is the non-dimensional intensity.

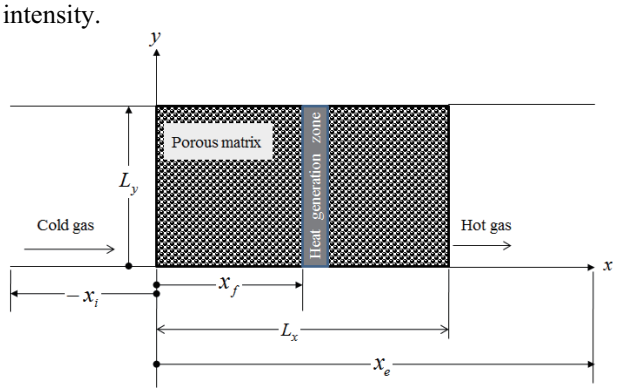


Fig.1: Schematic of the porous matrix.

## 3. Results and Discussion

Solid temperature distribution is the known variable in the simultaneous estimation of two optical properties of the porous matrix. In the present case, the solid temperature distribution is numerically computed by simultaneously solving Eqs. (1) and (2), subjected to boundary conditions stated in Eqs. (3)-(5). Present problem is solved using 300×20 control volumes for solid energy equation in the computational domain $0 \le \eta_x \le 1$ and $0 \le \eta_y \le \eta_{Ly}$ and 32 number of intensities. For solving gas energy equation 900×20 control volumes in the computational domain $-1 \le \eta_x \le 2$ were taken.

The optical properties of porous matrix which are simultaneously estimated in the present problem are the scattering albedo $\omega$ and the emissivity $\varepsilon$. In the inverse analysis for the estimation of parameters, the objective function is minimized using GA. The objective function for the present problem is constructed as follows

$$J = \sum_{i=1}^{N} \left( \tilde{\theta}_{s,i} - \theta_{s,i} \right)^2 \qquad (6)$$

where $\tilde{\theta}_{s,i}$ and $\theta_{s,i}$ are the exact and unknown solid temperatures, respectively.

For high aspect ratio $\dfrac{L_y}{L_x}$ =10, the present problem reduces to a 1-D planar one, and for this case, gas and solid temperatures distributions obtained are compared against the results of Tong and Sathe [5] in Fig. 2 for extinction coefficient $\beta = 1.0$ and a very strong convective coupling $P_2 = 500.0$. The values of different parameters used in the comparison are: $P_1$ = 0.01, $P_3$ =2.5×10$^{-4}$, $P_4$ =0.02, $P_5$ =5, $\omega$ =0.5, $\varepsilon$ =1.0, and $\Phi_i = \Phi_e$ =2.98×10$^{-5}$. A good comparison is observed.

We next provide results of simultaneous estimation of two parameters $(\omega, \varepsilon_e)$. The exact values for these parameters are: (0.5,0.9). With four different combinations of crossover probability $P_c$ and mutation probability $P_m$, results are shown in Table1. Reasonably accurate estimation has been obtained.

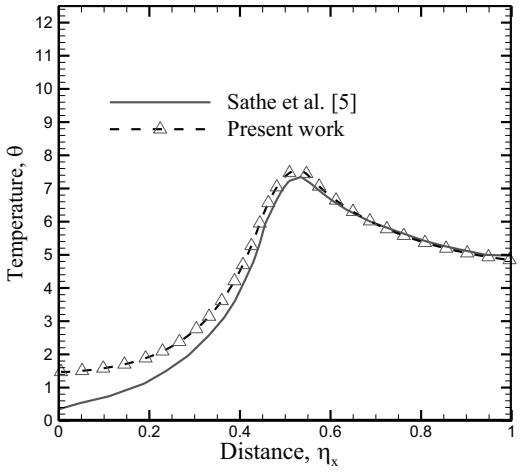


Fig. 2: Comparison of temperature $\theta\left(\theta_s = \theta_g\right)$ with Tong and Sathe [5]; $P_2$ = 500 and β = 1.0.

Table 1. Effect of crossover probability $P_c$ and mutation probability $P_m$ for exact value of ($\varepsilon_e$, $\omega$) = (0.9, 0.5); number of generations = 40, population size = 40.

| $P_c$ | $P_m$ | Fitness | Time (s) | $\omega$ | $\varepsilon_e$ |
|---|---|---|---|---|---|
| 0.3 | 0.3 | 0.002185 | 8457.71 | 0.509 | 0.857 |
| 0.3 | 0.03 | 0.005723 | 8186.95 | 0.489 | 0.956 |
| 0.8 | 0.3 | 0.002306 | 8333.03 | 0.499 | 0.869 |
| 0.8 | 0.03 | 0.011588 | 8383.25 | 0.518 | 0.847 |

## 4. Concluding Remarks

Combined mode conduction and radiation heat transfer in 2-D rectangular geometry was analyzed, and two parameters $(\omega, \varepsilon_e)$ were simultaneously estimated. With radiative information needed in the solid-phase energy equation computed using the FVM, the solid and the gas phase energy equations were simultaneously solved using the FVM. The GA was used to minimize the objective function. A very good estimations were obtained.

## References


[1] P. Talukdar, S. C. Mishra, D. Trimis, F. Durst, *J. Quant. Spectrosc. Radiat. Transfer*, 84(2004) 527-537.

[2] V.K. Mishra, S.C. Mishra, D.N. Basu, *Proc. 22nd National and 11th International ISHMT-ASME Heat and Mass Transfer Conference*, 2013, Paper No. HMTC1300078.

[3] R. Das, S. C. Mishra, R. Uppaluri, *Numer. Heat Transfer A*, 54(2008) 983-998.

[4] S.C. Mishra, H.K. Roy, N. Misra, *J. Quant. Spectrosc. Radiat. Transfer*, 101(2006) 249-262.

[5] T. W. Tong, S. B. Sathe, *J. Heat Transfer*, 113(1991) 423-428.

# OS8: Flow Dynamics and Combustion in Hybrid Rockets

Eleventh International Conference on Flow Dynamics
October 8-10, 2014, Sendai, Miyagi, Japan

# Status Summary of FY 2013 Hybrid Rocket Research Working Group

Toru Shimada
Japan Aerospace Exploration Agency, Sagamihara, Kanagawa, 252-5210, Japan

**ABSTRACT**

In this report, the status summaries of Hybrid Rocket research Working Group (HRrWG) activities of the fiscal year of 2013, especially about the fabrication and tests of Hybrid Test Engine (HTE-5-1) and basic technology R&D, are described.

## 1. Introduction

The status of Hybrid Rocket research Working Group (HRrWG) activities in the fiscal year of 2013 is described. With the approval of the Space Engineering Steering Committee of ISAS/JAXA, HRrWG is working for R&D of next-generation hybrid rockets (HR) as an inter-university research activity in Japan.

## 2. Static Firing Tests of Hybrid Test Engine (HTE-5-1)

As the first step to demonstrate technologies for next-generation hybrid rockets, we have been working on HTE-5-1 since FY 2011 [1,2]. In FY 2013, series of static firing tests were successfully conducted using a swirling- oxidizer- flow-type HTE-5-1 test engine. The first static firing was for 20s with averaged thrust of 1.5kN, the second static firing was for 2s with that of 4.5kN, and the third was for 5s with the same level of thrust. The success of these firing tests is thought to lead to achievement of the sub-goal No.1, that is to achieve 5kN thrust for more than 10s with GOX at above 95% C* efficiency with average regression rate of 3mm/s.

## 3. Study of Low-cost 100kg-Satellite Launcher Using Hybrid Rocket Engines [3]

A conceptual study of low-cost, 100 kg-satellite launcher using hybrid rocket engines is conducted. Mission requirements such as ground launch, dedicated launch, maximum total payload weight of 100kg, and target orbit of 500km Sun-synchronous orbit are considered. Constraints such as minimum environmental impact, reassuring and safe mission, and low price of launch are imposed on the mission. As a system requirement, a three-staged launch vehicle with a third-stage propulsion system capable of two firings is considered.

An assessment of propulsion subsystem's conformity to mission and system requirements is conducted and liquid, solid, hybrid propulsions are assessed from the viewpoint of performance, safety, environmental impact, quality assurance and quality control (QA/QC) efficiency, cost reduction potential, and technical maturity.

On top of its relative simplicity, because of high safety and thanks to the indifference of fuel cracks to the propulsion performance, hybrid rockets can utilize industrial-level raw materials, production methods and inspection methods. Also, QA/QC can be done efficiently, which reduces the production cost. Furthermore, because even a fully loaded launch system can be treated as "inert", safeguard actions in launch operations can be reasonably reduced, so can be the inspection actions, both of which reduce the operational cost.

The assessment results give a strong rationale for using a hybrid propulsion system to achieve the present mission and system requirements.

Basic concept of development with a keyword of "low cost" is described with a development scenario and clustering unit-engine concept. Then, Kanazaki, Chiba, et al. [4] have conducted a multi-objective optimization to get an optimized launcher with engine clustering. A concept of a unit engine development is described with identifying important element technologies, such as swirling-oxidizer-flow- type hybrid rocket engine with LOX pre-vaporization, throttling with optimal mixture ratio, and re-ignition in vacuum.

It is determined that the goal of HRrWG is to make proposal of a project to certify the flight-proven unit engine by a flight test. In the flight, propulsion characteristics under specified acceleration and oxidizer mass flow rate should be monitored and evaluated. The flight path should be checked with the predicted one. Also, stop and restart of the unit-engine should be tested under micro-gravity and low atmospheric pressure.

## 4. Technology R&D

Aso et al. [5] have studied multi-section swirl injection hybrid rockets in which swirling oxidizer flows are generated at several cross-sections in the cavity of the fuel grain. They have conducted firing tests, for both paraffin and high-density polyethylene, for several grain types to clarify influences of difference in the number and diameter of injector ports on the regression rate.

Nagata et al. [6] investigated a scaling rule about the fuel gasification rates of their CAMUI-type hybrid rockets in order to reduce number of costly full-scale static firing tests. This scaling rule comes from their previous findings that similarity conditions based on convective heat transfer are valid for most burning surfaces. The validity of the scaling rule, static firing tests with two motors having geometrically- similar fuel grain with a scale ratio of 2.05 were conducted. Temporal variation of fuel gasification rates gave close agreement with the scaling rule. Weight loss of both fuel grains, consisting of nine fuel blocks, also obeyed the scaling rule.

Corresponding author: Toru Shimada
*E-mail address*: shimada.toru@jaxa.jp

Wada, et al. [7] have been developing lab-scale hybrid rockets using low melting point thermoplastics (LT) as a fuel. The LT developed by Katazen Corporation have the higher regression rate comparing with Hydroxyl-Terminated-PolyButadiene (HTPB) and excellent mechanical properties. A small hybrid rocket motor of the LT was prepared using $N_2O$ as oxidizer. They investigated C* function by static firing tests using several types of baffle plate and several shapes of aft combustion chamber and confirmed large increasing of C* under the small L*.

Takayama, Kitagawa, and Shimada [8] studied on multi-parallelized swirling flow inside a circular pipe by discrete-vortex numerical simulations. They compared the effects of mixing capability between multi-parallelized swirling flows and a single swirl flow. From the results the mixing enhancement is clearly observed by parallelized swirling flows.

Funami and Shimada [9] have been developing a numerical prediction method to the internal ballistics. A quasi-one-dimensional model describes the flow, using source terms for the mass and energy addition due to fuel gasification and combustion. The amount of fuel gasification is evaluated from the energy-flux balance equation at the solid fuel surface. In FY2013, in addition to convective heat transfer, radiation heat transfer is included in the model. The calculation results are compared with the experimental data in an open literature to confirm that the calculations with radiation predict the regression rate dependency on oxidizer mass flux more precisely than those without radiation.

Yamanaka and Shimada [10] have developed a systematical method for the reduction of chemistry model of hydro-carbon oxygen/air reaction in order to compute the ignition process of boundary layer combustion with a proposed dynamic load balance strategy for the parallel computation of unsteady non-equilibrium chemically reacting flows. As a result, computational costs have reduced dramatically by one or two order of magnitude.

Motoe and Shimada [11] have developed a large-eddy-simulation computer program to simulate chemically reacting flows in a swirling-oxidizer-flow-type (SOFT) hybrid rocket. Comparing solutions with experimental data of a swirling burner validated the code. A simulation for a SOFT hybrid rocket successfully revealed the structure of flow and flame, distributions of physical quantities and chemical species, and state of turbulent eddy. The flame structure has shown similar structure as to that of experimental visualization.

Ozawa [12] and Shimada have extended an exiting method of combustion stability analysis in axial injection hybrid rocket to vortex injection systems. They have validated the accuracy of the quasi-steady boundary layer combustion model by comparing regression rates with experiments. Then, a stability analysis was conducted coupling the unsteady boundary combustion model with the thermal time lags model in solid fuels.

Besides the above described, there are several other activities conducted but not reported here.

## 5. Summary

Major activities of Hybrid Rocket research Working Group of FY 2013 are described. We would like to continue these activities toward the establishment of next-generation rocket technologies that meet the future social demands.

**Acknowledgments**

The author would like to thank for the support of the members of Hybrid Rocket research Working Group.

**References**

[1] T. Shimada, *Proceedings of Ninth International conference on Flow Dynamics*. (2012) 288-289.
[2] T. Shimada, *Proceedings of Tenth International conference on Flow Dynamics*. (2013) 204-205.
[3] T. Shimada, K. Kitagawa, M. Kanazaki, S. Yuasa, T. Sakurai, I. Nakagawa, K. Chiba, M. Nakamiya, and K. Ozawa, *2014 Space Propulsion Proceedings*. (2014).
[4] F. Kanamori, M. Nakamiya, K. Kitagawa, M. Kanazaki, and T. Shimada, *57th Conference on Space Science and Technology*. (2013).
[5] K. Araki, Y. Hirata, S. Ohyama, K. Ohe, S. Aso, Y. Tani, and T. Shimada, *AIAA 2013-3634*. (2013), also S. Ohyama, Y. Hirata, K. Araki, S. Aso, Y. Tani, and T. Shimada, *AIAA 2013-4040*. (2013).
[6] H. Nagata, T. Ishiyama, Y. Inaba, R. Kanai, M. Wakita, T. Totani, and T. Uematsu, *AIAA 2013-4048*. (2013).
[7] Y. Wada, Y. Kawabata, K. Shinnakazaki, R. Kato, N. Kato, and K. Hori, *Transactions of JSASS, Aerospace Technology Japan*, 12(2014) 9-14.
[8] A. Takayama, K. Kitagawa, and T. Shimada, *AJCPP2014-162*. (2014).
[9] Y. Funami and T. Shimada, *Transactions of JSASS, Aerospace Technology Japan*, 12(2014) 21-30.
[10] S. Yamanaka and T. Shimada, *IAC-13-C4.2.11*. (2013).
[11] M. Motoe and T. Shimada, *AIAA 2014-0310*. (2014).
[12] K. Ozawa, *ISTS 2013-s-53-a*. (2013).

Eleventh International Conference on Flow Dynamics
October 8-10, 2014, Sendai, Miyagi, Japan

# Regression Characteristics of CAMUI-type Fuel Grain at Hign Reynolds Numbers

Harunori Nagata[1], Tatsuya Ishiyama[2], Yasuhiko Inaba[2], Yuji Saito[2], Ryuichiro Kanai[2], Masashi Wakita[1], Tsuyoshi Totani[1]
[1]Faculty of Engineering, Hokkaido University
Kita 13 Nishi 8, Sapporo, 060-8628, Japan
[2]Graduate School of Engineering, Hokkaido University
Kita 13 Nishi 8, Sapporo, 060-8628, Japan

**ABSTRACT**

In a CAMUI type motor, two regions showing different heat transfer mechanisms of stagnation point and wall jet are completely mixed in a burning surface. Because of the difference in the *Re* exponent *m* in *Nu* formulas, the dominant heat transfer mechanism may change from that of stagnation points (m = 0.5) to the wall jets (m = 0.8) with increasing *Re*. To confirm this, the authors conducted static firing tests with a larger motor covering *Re* range up to 500,000. Experimental results show that the exponent *m* stays below 0.8, showing that the above understanding is appropriate.

## 1. Introduction

The authors have developed CAMUI type hybrid rockets to realize a nontoxic propellant sounding rocket system [1]. Figure 1 shows the key idea, a distinctive fuel grain design to accelerate gasification rates of solid fuels. To design initial fuel shape appropriately, regression formulas for burning surfaces are necessary. Because main burning surfaces in a CAMUI-type grain are forward end faces of fuel blocks, regression formulas in a jet impinging flow field is important. Generally, Eq. (1) expresses Nusselt number in a jet impinging flow field [2]:

$$Nu = c\,Pr^{l}\,Re^{m}\left(\frac{H}{D}\right)^{n} \tag{1}$$

$$Re = \frac{G_p D}{\mu} \Leftrightarrow G_p = \frac{\mu}{D} Re \tag{2}$$

where $H$, $D$, and $G_p$ are impingement distance, upstream port diameter, and mass flow density in the upstream port, respectively, and $l$, $m$, and $n$ are empirical constants. Based on these formulas, we obtained Eq. (3) as a regression formula for forward end faces:

$$\dot{L}_f = a G_p^{m}\left(\frac{H}{D}\right)^{n} \tag{3}$$

When we developed the first CAMUI motor of 500 N thrust class, the empirical exponent of *m* was 0.53 [3], being very close to the theoretical value of 0.5 for a stagnation heat transfer [4]. However, for the next 900 N-class motor, *m* was obtained to be 0.65, and for the following 2500 N-class motor, *m* farther increased to be 0.8 [3]. Accordingly, the exponent *m* increased with increasing the motor scale. This is not a good situation because we have to obtain a new empirical exponent *m* every time when we develop a new motor, taking much cost and efforts.

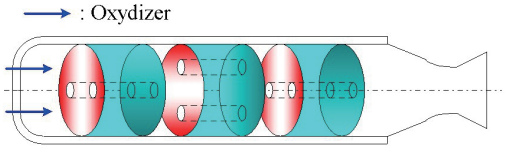


Fig. 1 Basic concept of CAMUI fuel grain.

Corresponding author: Harunori Nagata
*E-mail address*: nagata@eng.hokudai.ac.

The empirical exponent *m* of 0.8 for the 2500N-class motor is rather close to the value for the boundary layer wall jet heat transfer [4]. To sketch the transition, Fig. 2 shows the exponent depending on Reynolds number *Re*

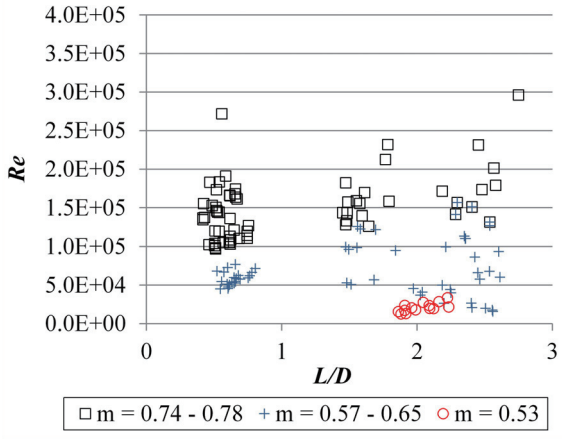


Fig. 2 Variation of the empirical exponent *m* depending on *Re* and *L*/*D*.

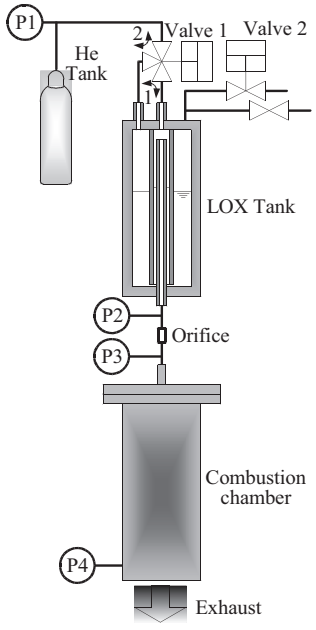


Fig. 3 Schematic view of the test motors.

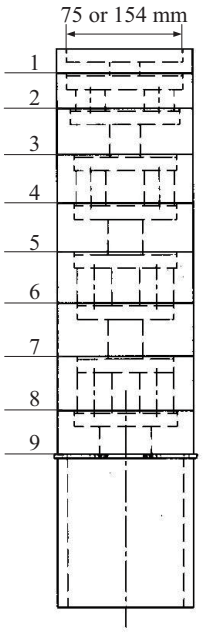


Fig. 4 A CAMUI-type fuel grain.

and *L*/*D* (port axis length divided by port diameter). It clearly shows that the exponent gradually changes from 0.5 to 0.8 as *Re* increases, indicating that the dominant heat transfer mechanism changes from the stagnation heat transfer to the wall jet heat transfer. If this understanding is correct, the exponent *m* remains at 0.8 with a further increase in *Re*, meaning that experiments to obtain the empirical constant for a larger motor are not necessary. Therefore, in this research, we examined whether the above understanding is correct or not by obtaining the exponent *m* experimentally at high *Re* being greater than 200,000.

## 2. Experimental Method

We employed two scales, 2.5 kN and 10 kN thrust class motors, for static firing experiments. These two motors are similar in shape with the homothetic ratio of 2.05. By using an appropriate firing duration for each test, *L*/*D* and fuel geometry after firing coincides with different scales (Table 1). Figure 3 shows a sketch of the experimental setup. Both motors employ high density polyethylene and liquid oxygen (LOX) as propellants. A fuel grain consists of nine stages of fuel blocks, as Fig. 4 shows. Main measurement items are the helium tank pressure, the upstream and downstream pressures of the orifice to obtain LOX flow rate, combustion chamber pressures at downstream of the LOX injector and upstream of the exhaust nozzle, and mean fuel regression rates obtained by total regression distance divided by burning duration.

## 3. Results and Discussion

Figure 5 shows experimental results, together with the previous results Fig. 2 shows. In this figure, "2.5 kN Hi" and "2.5 kN Lo" represent the 2.5 kN motor results for below and above 100,000 of *Re*, respectively. The empirical exponent *m* for 2.5 kN Lo was 0.62, falling within the range of 0.57 to 0.65 previously obtained for this *Re* region. The most important result is that the exponent *m* at high *Re*, up to 600,000, stays just below 0.8 (0.78). Accordingly, it is commonly true at high-*Re* that wall jet heat transfer mechanism is dominant with a weak contribution of impinging jet heat transfer. Although the CAMUI-design intends to take advantage of the jet-impinging heat transfer, each heating surface is a mixture of stagnation region and wall jet region. This is because of the mutual interference between two jets, the confined flow field between fuel blocks, and the complicated flow field. Considering that the Nusselt number in the wall jet region increases more rapidly than that in the stagnation region with increasing *Re*, it is likely that the heat transfer in the wall jet region becomes dominant at high *Re*.

## 4. Concluding Remarks

In a CAMUI type motor, two regions showing different heat transfer mechanism of stagnation point and boundary layer wall jet are completely mixed in the flow field. Because of this, the *Re* exponent *m* in the forward-end face regression formulas are 0.5 for a stagnation region and 0.8 for a wall jet region. With the increase in *Re*, *Nu* in a wall jet region increases more rapidly than that in a stagnation region because of the larger exponent *m*. This leads to a hypothesis that the exponent *m* stays below 0.8 with a further increase in *Re*. To confirm this, the authors developed a 10 kN thrust class motor to conduct static firing test with larger *Re*. This motor covers *Re* range reaching 500,000. Experimental results show that the exponent *m* stays below 0.8, showing that the above hypothesis is appropriate.

Table 1. Experimental conditions.

| | 2.5 kN motor | 10 kN motor |
|---|---|---|
| *Re* | 66,000 - 300,000 | 150,000 - 600,000 |
| Burning duration [s] | 2.2 - 3.2 | 4.8 - 6.9 |
| L/D | 0.68 - 0.81 | 0.70 – 0.82 |


## Acknowledgements

This research is supported by the Ministry of Education, Science, Sports and Culture, Grant-in-Aid for Scientific Research (A), 40281787, 2012.

This research is supported by the Hybrid Rocket Research Working Group (HRrWG) of Institute of Space and Astronautical Science, Japan Aerospace Exploration Agency. The authors thank members of HRrWG for their helpful discussion.


## References


[1] H. Nagata, M. Ito, T. Maeda, M. Watanabe, T. Uematsu, T. Totani, I. Kudo, *Acta Astronautica*, Vol. 59/1-5 (2006) 253-258.

[2] R. Viskanta, *Experimental Thermal and Fluid Science*, Vol.6/2 February (1993) 111-134.

[3] H. Nagata S. Hagiwara Y. Kaneko M. Wakita, T. Totani, T. Uematsu, *46th Joint Propulsion Conference & Exhibit*, (2010) AIAA 2010-7117.

[4] C. D. Donaldson, R. S. Snedeker, D. P. Margolis, *Journal of Fluid Mechanics*, Vol.45/3 (1971) 477-512.


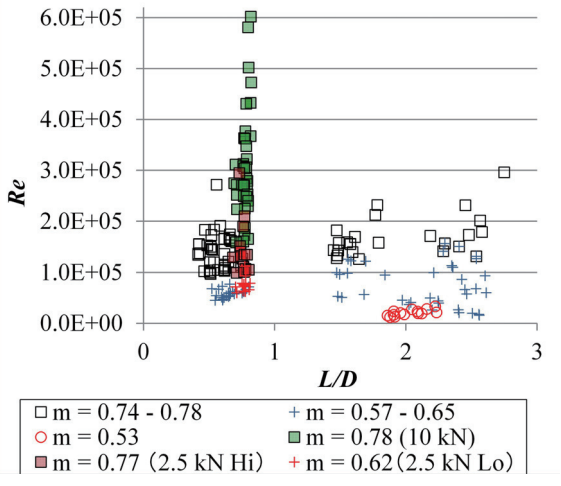


Fig. 5 Variation of the pressure exponent *m* depending on *Re* and *L*/*D*.

# Safety Issues with Nitrous Oxide

Arif Karabeyoglu
KOC University
Rumeli Feneri Yolu, Istanbul, 34450, Turkey

## Abstract

Even though $N_2O$ is a widely used energetic material, the number of decomposition related accidents are quite limited due to its abnormally slow decomposition kinetics. However hazards do exist especially in propulsion systems where large quantities of $N_2O$ is stored at room temperature in thin walled vessels. The results of a model developed earlier to predict the pressure rise in a closed vessel subject to decomposition is summarized to demonstrate the significant hazard that exists in the $N_2O$ tank. A list of safety related recommendations unique to $N_2O$ operations have been included.

## 1. Introduction

Nitrous oxide and liquid oxygen are the most commonly used oxidizers in hybrid rocket systems. This is primarily due to their cost, safety, availability and handling advantages compared to the other liquid oxidizers that can be used in propulsion applications. Despite its moderate Isp performance and poor impulse density at room temperature, $N_2O$ has been the choice for small motors for which the systems and operational simplicity are the dominant driving forces. This fact explains the extensive use of $N_2O$ in amateur rocketry and in many sounding rocket programs. A good example of a $N_2O$ based hybrid sounding rockets is the currently ongoing NASA/Stanford/SPG Peregrine [1] effort.

The most impressive demonstration of a $N_2O$ hybrid to date is the X-Prize winning SpaceShipOne system. The larger follow on SpaceShipTwo vehicle, which is designed to carry tourists into space on a sub-orbital flight, is also baselined for a $N_2O$ hybrid propulsion system. If successful, this will be the first operational large scale hybrid rocket in commercial or military use. Unfortunately, the recent fatal accident at the Mojave Airport during a cold flow test of the SpaceShipTwo propulsion system has raised some safety concerns with the use of $N_2O$ as an oxidizer. The primary hazard associated with $N_2O$ is related to its energetic nature, namely its release of thermal energy by molecular decomposition. Although this exothermic behavior presents significant benefits in terms of the theoretical Isp performance and motor stability/efficiency characteristics, it also introduces a chemical explosion hazard in the various components of the rocket system including the oxidizer tank and the feed lines. Even though the hazard itself has been known well before the Scaled accident, the understanding of the decomposition process in practical systems has been lacking. The deficiency in the understanding, modeling and testing of the decomposition chemistry of $N_2O$ is highly problematic, since it introduces unknown risks in the development of large scale $N_2O$ propulsion systems.

Corresponding author: Arif Karabeyoglu
*E-mail address*: akarabeyoglu@ku.edu.tr

## 2. $N_2O$ Decomposition in the Oxidizer Tank

Arguably the most important mode of decomposition hazard is associated with the oxidizer tank. Due to the large quantities of $N_2O$ in the tank ullage, a decomposition process in the tank could potentially produce large explosions. This is especially a problem for propulsion systems with closely coupled oxidizer tank and combustion chamber. For such systems, at the end of the liquid burn, the hot injector could potentially heat the nitrous vapor in its vicinity and start a deflagration wave that would propagate freely in the tank. Such a situation is illustrated in Figure 1.

Note that for pure nitrous oxide in a closed vessel at 300 K, complete decomposition will result in a 20 fold increase in the tank pressure (a number much larger than the safety factor of all flight and run tanks used in propulsion) [2]. In fact this indicates that even a partial decomposition could lead to a structural tank failure and loss of mission. Unfortunately the decomposition hazard increases with increasing system scale due the unfavorable surface to volume ratio scaling.

The two methods that can be implemented to mitigate this great hazard are 1) Dilution of the ullage with an inert gas such as helium (supercharging) and 2) Incorporation of a properly designed burst disk to limit the overpressurization in the case of ignition in the ullage.

## 3. Recommendations

The following are the safety related recommendations for $N_2O$ based propulsion systems.

- Nitrous oxide is an energetic material and it must be respected! When $N_2O$ is used in any risky testing or other operations, all personnel should be at a safe distance and/or in a protected area. A comprehensive hazard analysis is recommended, especially for large scale operations and testing.

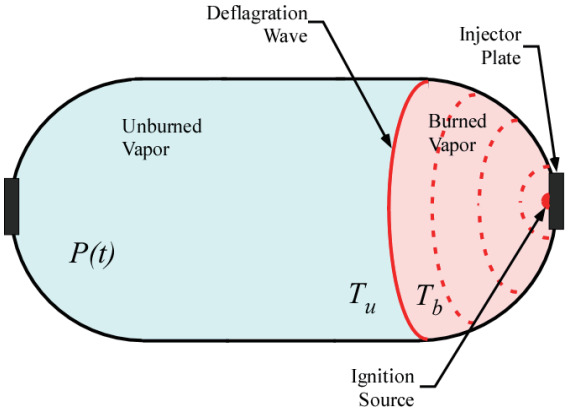

Fig. 1 Decomposition wave propagation in oxidizer tank. (From Ref. 2)

- In manned systems, a properly designed pressure relief system must be installed on the flight tank. This system should be tested at full scale.
- The dilution of $N_2O$ in the tank ullage by supercharging is highly recommended. Blow down $N_2O$ systems, especially the ones that are allowed to burn in the vapor phase are inherently hazardous. Some of the possible diluents that can be used with $N_2O$ systems are helium, molecular nitrogen and molecular oxygen.
- For small scale motor testing, the oxidizer tanks should be run in the vertical configuration such that a liquid layer of $N_2O$ always separates the vapor in the tank ullage from the combustion chamber.
- In order to prevent accumulation of $N_2O$ in the combustion chamber, the $N_2O$ flow should always lag the igniter action.
- One should follow strict oxygen cleaning procedures for $N_2O$. Note that very small concentrations of fuels in $N_2O$ might change the entire decomposition dynamics, making most of the findings with uncontaminated $N_2O$ irrelevant. Also note that the lean flammability limit for $N_2O$ is zero, resulting in high sensitivity at very low concentrations of fuel.
- Nitrous oxide is a reasonably effective solvent for a number of hydrocarbons including a lot of common polymers. Any polymeric or nonpolymeric materials that will be used in the $N_2O$ system should be carefully tested for compatibility. This includes the valve seals, o-rings or gaskets.
- One should avoid using catalytic materials in $N_2O$ systems.
- All past experience indicates that it is impossible to ignite and sustain a decomposition wave (detonation or deflagration) in liquid $N_2O$ [2]. Note that fuel contamination in the liquid changes this situation, potentially resulting in very dangerous conditions.
- One must understand that it is almost impossible to eliminate all of the ignition sources in a practical system. A system should be designed to mitigate a potential decomposition event. The famous quote by Trevor Kletz is worth remembering in the design and operation of $N_2O$ based propulsion systems [3].

"Ignition source is always free"

Despite its decomposition hazard, nitrous oxide is still a much safer material compared to the other monopropellants used in the industry including $H_2O_2$. In our opinion, if handled properly, nitrous oxide (or other $N_2O$ containing oxidizers) is one of the safest oxidizers used in chemical propulsion systems.

**References**

[1] Zilliac G., Waxman, B., Evans B., Karabeyoglu, A. and Cantwell, B., *AIAA Propulsion and Energy Conference*, Cleveland Ohio, July (2014).

[2] M. A. Karabeyoglu, J. Dyer, J. Stevens and B. Cantwell, 44th AIAA/ASME/SAE/ASEE Joint Propulsion Conference and Exhibit, Hartford, CT, July 21-23, (2008), AIAA-2008-4933.

[3] Willey, R. J., Hu S. and Moses J. M., "Reactivity Investigation of Mixtures of Propane and Nitrous Oxide", *Process Safety Progress*, Vol. 24, No 4, pp. 303-309,(2005).

Eleventh International Conference on Flow Dynamics
October 8-10, 2014, Sendai, Miyagi, Japan

# Numerical Simulation on Unsteady Compressible Low-Speed Shear Flow in Hybrid Rocket Combustion Chamber Using Preconditioned Method : Effects of Preconditioned Method Including Multi-Species Mass Conservation Equations

Nobuyuki Tsuboi
Department of Mechanical and Control Engineering, Kyushu Institute of Technology
1-1 Sensui-chou, Tobata-ku, Kitakyushu, Fukuoka, 804-8550, Japan

**ABSTRACT**

Hydrogen/oxygen low-speed shear flow is simulated by using the time-dependent preconditioned compressible full Navier-Stokes equations with multi-species equations. Four preconditioning matrices $\Gamma$ are adopted in order to estimate the convergence histories in the pseudo-time domain. The preconditioning matrices with off-diagonal components have better convergence. The preconditioned scheme starts the generation of vortices earlier than the scheme without preconditioned technique.

## 1. Introduction

The hybrid rocket engine uses a solid fuel and gas oxidizer to become more safety and less expensive than the solid rocket engine because the fuel and oxidizer are separated and solid fuel is typically made of polymer materials. Therefore the hybrid rocket is a candidate for the transportation of the manned space mission.

Although the numerical simulations are necessary for the design of the hybrid rocket motor, common compressible flow solvers are "density-based" schemes, which are difficult to solve incompressible flow lower than free-stream Mach number of 0.1 due to small time step and slow converging rate. This causes a stiffness problem in which the ratio of maximum eigen value to minimum one in inviscid flux is of the order of hundred. This stiffness problem also arises in the simulations with chemical reaction. The preconditioned Euler or Navier-Stokes equations [1] , which is control the eigenvalues without stiffness, can be solved for such the low speed as well as the supersonic flow. However, few researches applied the preconditioning technique on the combustion problems because the preconditioning matrix is arbitrary and becomes complex.

We have recently developed the time-dependent preconditioning Navier-Stokes code to solve such the high $Re$ number and low speed flow in order to understand the flow mechanism in the hybrid rocket combustion chamber. In the present research, the unsteady preconditioning method is applied to the full Navier-Stokes code with species mass conservation equations[2] in order to simulate the combustion flow under the low-speed and high-Reynolds number effectively. The present paper reports the results of the unsteady hydrogen/oxygen low-speed shear flow in order to estimate the various preconditioning matrices.

## 2. Numerical Method and Simulation Conditions

The unsteady three-dimensional compressible Navier-Stokes equations including the preconditioning matrix are used:

$$\frac{\partial \boldsymbol{Q}}{\partial t}+\Gamma\frac{\partial \boldsymbol{W}}{\partial \tau}+\frac{\partial \boldsymbol{E}}{\partial x}+\frac{\partial \boldsymbol{F}}{\partial y}+\frac{\partial \boldsymbol{G}}{\partial z}=\frac{\partial \boldsymbol{E}_v}{\partial x}+\frac{\partial \boldsymbol{F}_v}{\partial y}+\frac{\partial \boldsymbol{G}_v}{\partial z} \quad (1)$$

where $t$ is real time and $\tau$ is pseudo time, respectively. The time accuracy assumes second-order and $i$ is the number of sub-iteration, then

$$\left[\Gamma+\frac{3\Delta\tau}{2\Delta t}\frac{\partial \boldsymbol{Q}}{\partial \boldsymbol{W}}\right]\Delta \boldsymbol{W}^{(i)} = -\Delta\tau\left[RHS^{(i-1)}+\frac{3\boldsymbol{Q}^{(i-1)}-4\boldsymbol{Q}^{n}+\boldsymbol{Q}^{n-1}}{2\Delta t}\right] \quad (2)$$

where $\boldsymbol{Q}=[\rho,\rho u,\rho v,\rho w,e,\rho_i]^T$ are the conservation variables, $\boldsymbol{E},\boldsymbol{F},\boldsymbol{G}$ are the inviscid fluxes, and $\boldsymbol{E}_v,\boldsymbol{F}_v,\boldsymbol{G}_v$ are the viscous fluxes, respectively. The above equations are transformed by using the method proposed by Weiss and Smith[1]. Instead of the consevation variables $\boldsymbol{Q}$, the primitive variables $\boldsymbol{W}=[p,u,v,w,T,Y_i]^T$ and the preconditioning matrix $\Gamma$ are applied to the above equations. There are three sets of primitive variables including the species mass fractions: $\boldsymbol{W}_T=[p,u,v,w,T,Y_i]^T$(pressure-temperature type), $\boldsymbol{W}_{\overline{h}}=[p,u,v,w,\overline{h},Y_i]^T$(pressure-enthalpy type), and $\boldsymbol{W}_{p_i}=[p_i,u,v,w,T]^T$(partial pressure-temperature type). Merkle et al.[3] and Yang et al.[4] adopt $\boldsymbol{W}_T$. Chen et al.[5], Olsen et al.[6], and Yang et al.[7] adopt $\boldsymbol{W}_{\overline{h}}$. Edwards et al.[8] use $\boldsymbol{W}_{p_i}=[p_i,u,v,w,T]^T$. The present study uses first and second sets of the primitive variables. Then the preconditioning matrix $\Gamma$ is

Table 1. Various preconditioning matrices $\Gamma$.

| Type | Primitive variable | Off-diagonal components for species |
|---|---|---|
| $\mathrm{prec}_{T0}(\Gamma_{T_0})$ | $T$ | 0 |
| $\mathrm{prec}_{T}(\Gamma_{T})$ | $T$ | cal. |
| $\mathrm{prec}_{h0}(\Gamma_{\overline{h}_0})$ | $\overline{h}$ | 0 |
| $\mathrm{prec}_{h}(\Gamma_{\overline{h}})$ | $\overline{h}$ | cal. |

defined by using the primitive variables $\boldsymbol{W}_T$ and $\boldsymbol{W}_{\overline{h}}$. Four preconditioning matrices, which depend on the treatment of $\partial/\partial Y_i$, can be derived. If $Y_i$ is a variable independent of the conservative variables and $\partial/\partial Y_i$ sets zero(for example, $\partial\rho/\partial Y_i=0$), the preconditioning matrix becomes simple one. However, the preconditioning matrix has a complex off-diagonal components

Corresponding author: Nobuyuki Tsuboi
*E-mail address*: tsuboi@mech.kyutech.ac.jp

as $Y_i$ is a variable dependent on the conservative variables and $\partial/\partial Y_i \neq 0$. An example of the simple preconditioning matrix by using $\boldsymbol{W}_T$ is shown as follows:

$$\Gamma_{T_0} = \begin{pmatrix} \Theta & 0 & 0 & 0 & \rho_T & 0 & \cdots & 0 \\ \Theta u & \rho & 0 & 0 & \rho_T u & 0 & \cdots & 0 \\ \Theta v & 0 & \rho & 0 & \rho_T v & 0 & \cdots & 0 \\ \Theta w & 0 & 0 & \rho & \rho_T w & 0 & \cdots & 0 \\ \Theta H - 1 & \rho u & \rho v & \rho w & X & 0 & \cdots & 0 \\ \Theta Y_1 & 0 & 0 & 0 & \rho_T Y_1 & \rho & 0 & 0 \\ \vdots & \vdots & \vdots & \vdots & \vdots & 0 & \ddots & 0 \\ \Theta Y_N & 0 & 0 & 0 & \rho_T Y_N & 0 & 0 & \rho \end{pmatrix} \tag{3}$$

where $e = \rho H - p$, $H = \overline{h} + (u^2 + v^2 + w^2)/2$, $h_i = \int C_{p_i} dT$, $\overline{h} = \sum_{i=1}^{N} Y_i h_i$, $\Theta = 1/U_r^2 - 1/c^2 + \rho_p$, $U_r^2 = \min[c^2, \max(|V|^2, K|V_\infty|^2)$, $K = 0.25$, and

$$X = e_T = \rho_T \sum_{i=1}^{N} Y_i h_i + \rho \sum_{i=1}^{N} Y_i C_{p_i} + \frac{1}{2}\rho_T \left(u^2 + v^2 + w^2\right). \tag{4}$$

Table 1 shows the various preconditioning matrices $\Gamma$.

The inviscid flux adopts the preconditioning AUSMDV(pAUSMDV)[8]. The second-order MUSCL without limiter is used. The viscous term is second-order central difference. Time integration uses preconditioned Eulier explicit method because the computational cost for third-order preconditioned TVD Runge-Kutta method is three times more than that for preconditioned Euler explicit method.

Inflow conditions are as follows: upper gas is oxygen, $\rho_{O_2} = 1.29$ kg/m$^3$, $p_{O_2}$ =0.1 MPa, $T_{O_2}$ =300 K, $u_{O_2}$ = 10 m/s, and $M_{O_2} = 0.03$; lower gas is hydrogen, $\rho_{H_2}$ = 0.082 kg/m$^3$, $p_{H_2}$ = 0.1 MPa, $T_{H_2}$ = 300 K, $u_{H_2}$ =30 m/s, and $M_{H_2} = 0.027$, respectively. $Re_{H_2}$ = 2.75 x $10^5$ /m. The present computational grid is orthogonal system with 301 x 5 x 93. The inflow velocities for both flows are Blasius profile assuming $Re = 10^5$ /m.

## 3. Results and Discussions

Figure 1 shows the effects of preconditioned method on the istantaneous Mach number contours. The unsteady formation of the vorticies appears due to the Kelvin-Helmholtz instability for both cases. However, the results for the preconditioned scheme start the generation of vortices earlier than those without preconditioned scheme. Figure 2 shows the comparison of RMS histories during sub-iterations at N=35000 for various preconditioning matrix $\Gamma$. RMS for $\Gamma_{\overline{h}}$ and $\Gamma_T$ decreases the three orders magnutude from the initial sub-iteration. Therefore, the complex off-diagonal components in the preconditioning matrix $\Gamma$ require to simulate the unsteady simulations efficiently.

## 4. Conclusions

Hydrogen/oxygen low-speed shear flow is simulated by using the time-dependent preconditioned compressible Navier-Stokes equations with multi-species equations. The preconditioned scheme starts the generation of vortices earlier than the scheme without preconditioned technique. The preconditioning matrices with the complex off-diagonal components such as $\Gamma_{\overline{h}}$ and $\Gamma_T$ can simulate an efficient unsteady flow. Further simulations such as a hydrogen/oxygen diffusion flame will be carried out in the future.

**Acknowledgements**

This research is conducted as a contribution to the Hybrid Rocket Research Working Group (HRrWG) with the approval of the Space Engineering Steering Committee of Institute of Space and Astronautical Science, Japan Aerospace Exploration Agency. This research has also been supported by the Ministry of Education, Science, Sports and Culture, Grant-in-Aid for Scientific Research (B) (No.23360380). The present numerical simulations are collaborated with Cybermedia Center in Osaka University.

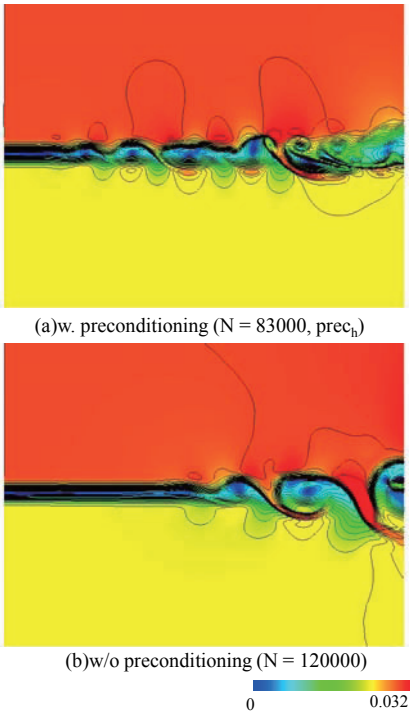


Fig. 1 Comparison of instantaneous Mach number contours.

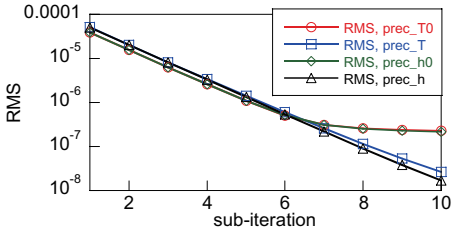


Fig. 2 Comparison of RMS histories during sub-iterations at N=35000 for various preconditioning matrices $\Gamma$.

## References

[1] J.M. Weiss and W.A. Smith, AIAA J., 33, 11, (1995)2050.
[2] N. Tsuboi, T. Ito, H. Miyajima, Transactions of The Japan Society for Aeronautical and Space Sciences, 51, 172, (2008)86-92.
[3] S. Venkateswaran, M. Deshpande, C.L. Merkle, AIAA paper, (1995)95-1673.
[4] N.Zong, V. Yang, Int. J. Computational Fluid Dynamics, 21, 5-6, (2007)217-230.
[5] J.S. Shuen, K.H. Chen, Y. Choi, J. Computational Physics, 106, (1993)306-318.
[6] V. Sankaran, M. Olsen, AIAA paper (2003)2003-3543.
[7] H. Meng, V. Yang, J. Computational Physics, 189, (2003)233-304.
[8] J.R. Edwards and M.-S. Liou, AIAA J., 36, 9, (1998)1610.

Eleventh International Conference on Flow Dynamics
October 8-10, 2014, Sendai, Miyagi, Japan

# Numerical Investigation of Regression Rate Enhanced by Various Surface Patterns on Solid Fuel

Ryosuke Takahashi, Yousuke Ogino, and Keisuke Sawada
Department of Aerospace Engineering, Tohoku University,
Sendai 980-0579, Japan

**ABSTRACT**

Flows over various surface patterns on solid fuel grain for hybrid rocket engine are computed numerically for the purpose of improving fuel regression rate. The Navier-Stokes equations with a chemically equilibrium assumption are solved by the second order accurate discontinuous Galerkin CFD solver which is loosely coupled with a regression model of fuel surface. In the preliminary computations, distinct flow patterns are obtained for a bump or groove on the surface of fuel grain.

## 1. Introduction

In recent years, a hybrid rocket engine has attracted attention as a rocket engine that combines the advantages of both solid rocket motor and liquid rocket engine. Hybrid rocket engine has excellent properties, such as safety, simple structure, low-cost and so on. But, so far, has not been put into practical use because of the drawback that the regression rate of solid fuel in hybrid rocket engine is substantially lower than that for solid motor, thus resulting in lower thrust. In order to improve the regression rate, various methods, such as swirling oxidizer injection [1,2] and improved fuels, have been proposed.

In order to improve regression rate, an experimental study to examine grooved fuel surface was carried out by Hatagaki et al. [3]. Various combinations of width and depth of grooves were examined, which actually created concave-convex surface grain shapes. It was shown that concave-convex surface grains were quite effective in enhancing the surface regression rate up to about 1.7 and 2.0 times of the original regression rate with and without swirling oxidizer injection, respectively, at the same oxygen mass flux condition. It was also shown that a deeper concave depth was more effective in enhancing regression rate than a narrower width, although a deeper depth degraded $C^*$ efficiency.

We note that use of 3D-printer will enable us to devise a fuel grain with complicated surface patterns for accomplishing a larger regression rate. It is therefore necessary to determine which patterns will be effective for improving regression rate. The ultimate purpose of the present study is to optimize the surface pattern of fuel grain. As a preliminary study for that purpose, we examine the regression rate of relatively simple surface patterns on a flat plate fuel grain.

## 2. Numerical Methods

The governing equations are the Navier-Stokes equations with the mass conservation equations for fuel and oxidizer gases. We employ the Discontinuous Galerkin (DG) finite element method [4]. The DG method can achieve a formal spatial accuracy even on unstructured meshes, though the computational cost becomes much higher than that for conventional finite volume methods. The convective numerical flux is given by SLAU [5], and the viscous and diffusion terms by BR2 formulation. We employ the cellwise relaxation implicit scheme developed by Yasue et al [6] in time integration for achieving a faster convergence.

We consider HTPB as solid fuel and GOX as oxidizer in this study. In particular, 1,3-butadiene ($C_4H_6$) that is the monomer of HTPB is assumed for fuel in gas phase. The equilibrium compositions and thermodynamic properties of gas mixture are determined by utilizing NASA CEA [7]. An equilibrium state of a mixture of fuel and oxidizer gases are obtained for 9 chemical species of CO, $CO_2$, H, $H_2$, $H_2O$, O, $O_2$, OH and $C_4H_6$ by employing the table lookup method. In the look-up table, total density and mass fraction of fuel gas are input data to determine coefficients of fitting curves for other thermodynamic state quantities, transport coefficients and equilibrium chemical composition as functions of temperature. The range of the total density is assumed from 0.1 to 100 kg/m$^3$ which is divided into 25 data points equally spaced in logarithmic scale. On the other hand, mass fraction of fuel gas is considered from 0 to 100% divided into 21 data points equally spaced in linear scale. The temperature range is then divided into two different ranges from 200-900 K and 900-5,000 K, to give two fitting curves,

$$q_1(T) = c_{11}T^{-1} + c_{12} + c_{13}\ln T + c_{14}T + c_{15}T^2 \quad (1)$$

$$q_2(T) = c_{21}T^{-1} + c_{22} + c_{23}\ln T + c_{24}T + c_{25}T^2 \quad (2)$$

where coefficients $c_{ij}$ are determined by least square fitting. Then these fitted curves $q_1(T)$ and $q_2(T)$ are combined into a single curve by the following mixing formula,

$$q(T) = q_2(T) + \frac{q_1(T) - q_2(T)}{1 + \exp\left((T - T_0)/\Delta T\right)} \quad (3)$$

where $T_0$ is 900 K and $\Delta$ is 10 K, respectively.

The surface regression rate is given by a pyrolysis law in Arrhenius form as,

$$\dot{r} = A \exp\left(-\frac{E_a}{RT_s}\right) \quad (4)$$

where $A$ is the pre-exponential factor, $E_a$ is the pyrolysis activation energy, $R$ is the universal gas constant and $T_s$ is the temperature of fuel surface. Those constants of $A$ and $E_a$ for pure HTPB are determined by experimental study of Chiaverini et al [8].

Corresponding author: Ryosuke Takahashi
*E-mail address*: takahashi@cfd.mech.tohoku.ac.jp

The surface temperature is determined by solving the heat balance equation on the fuel surface.

The CFD code is parallelized using the MPI library where the computational mesh is partitioned by METIS.

## 3. Computed Cases in This Preliminary Study

The schematic illustration of computational domain is shown in Fig. 1. We consider a slab geometry fuel grain, which is a simplified model of inner part of combustion chamber. For the inflow gas, a gaseous oxygen of $p_{\mathrm{inflow}} = 1.0$ MPa, $T_{\mathrm{inflow}} = 293$ K and $M_{\mathrm{inflow}} = 0.2$ are assumed as the typical conditions in the combustion chamber.

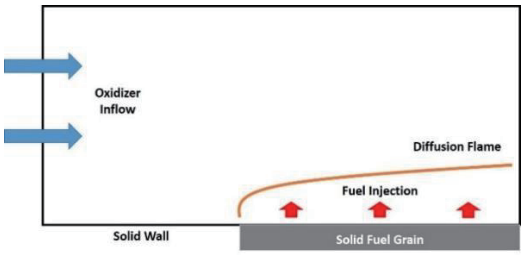


Fig. 1 Schematic of the computational domain.

We first obtain a steady flowfield without surface regression, then a loosely coupled calculation is started to account for surface regression. Figure 2 shows typical examples of hybrid unstructured meshes to discretize the computational domain with a bump or a groove on the fuel surface. Computational meshes in the periodic boundary plane are depicted.

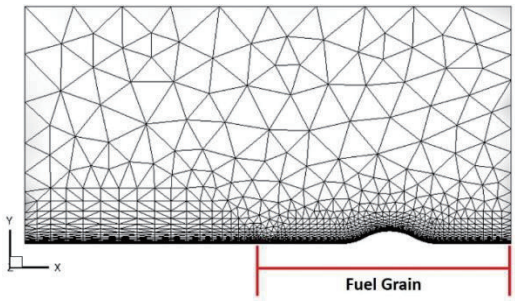


(a) bump

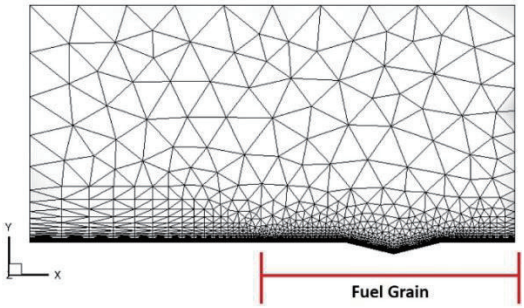


(b) groove

Fig. 2 Examples of computation meshes.

## 4. Results and Discussions

Preliminary computations are carried out for the fuel grain with a bump or a groove. Surface regression is not accounted for. The computed temperature profiles on a periodic boundary plane are shown in Fig. 3. For the bump geometry, the high temperature regions appear both the upstream and downstream side of the bump. A separated flow region seems to develop in upstream side of the bump. On the other hand, for the groove geometry, the high temperature region appears only at the upstream edge of the groove. When surface regression is accounted for, the surface geometry will be changed according to local heat flux. The shape of the resulting surface patterns will be shown in the presentation.

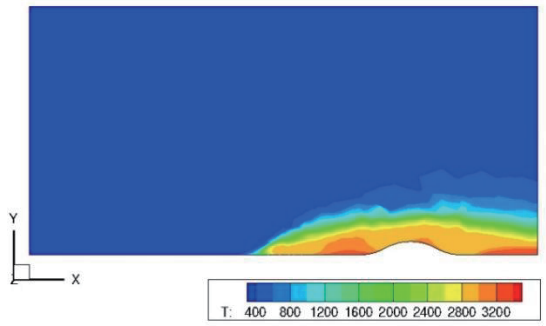


(a)

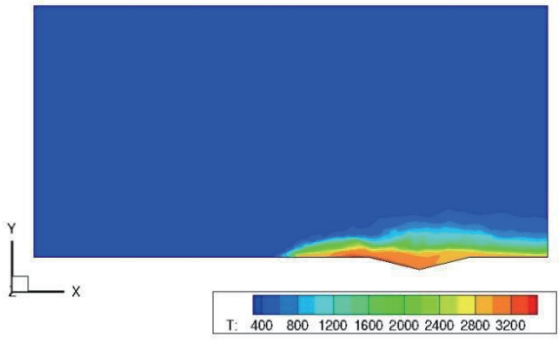


(b)

Fig. 3 Computed temperature contours.

## 5. Conclusion

In this study, regression rate of solid fuel grain with various surface patterns is examined numerically. A preliminary results show different flow patterns over the bump and groove on the fuel surface.

## References


[1] W. H. Knuth, M. J. Chiaverini, D. J. Gramer and J. A.Sauer, *AIAA paper*, (1998) 98-3348.

[2] S. Yuasa, O, Shimada, T. Imamura, T. Tamura and K. Yamamoto, *AIAA paper*, (1999) 99-2322.

[3] S. Hatagaki, S. Yuasa, K. Hirata and T. Sakurai, *AIAA paper*, (2012) 2012-4107.

[4] B. Cockburn and C-W. Shu, *J. Comput. Phys.*, 141(1989) 199-244.

[5] K. Kitamura and E. Shima, *AIAA paper*, (2009) 2009-136.

[6] K. Yasue, M. Furudate, N. Onishi and K. Sawada, *CiCP*, 7, (2010) 510-533.

[7] S. Gordon and B. J. McBride, *NASA Reference Publication*, (1996) 1311.

[8] M. J. Chiaverini, G.C. Lu, K. K. Kuo, A. Perez, S. Jones, B. Wygle and J. P. Arves, *J. Prop. and Power.*, 15, (1999) 888-895.

Eleventh International Conference on Flow Dynamics
October 8-10, 2014, Sendai, Miyagi, Japan

# Investigation of Dual-Vortical-Flow Hybrid Rocket Engine Propulsion

Yen-Sen Chen[1], S. S. Wei[2], Alfred Lai[2], Jhe-Wei Lin[2], Tzu-Hao Chou[2], Jong-Shinn Wu[2]
[1] National Space Organization
8F, 9, Prosperity 1st Rd., Hsinchu Science Park, Hsinchu 30078, Taiwan
[2] Dept. of Mech. Engr., National Chiao Tung University
1001 University Road, Hsinchu 30010, Taiwan

**ABSTRACT**

One main physical feature of hybrid rocket combustion is its diffusion flame nature that has required excessively long combustion chamber which leads to undesirable large slenderness of a rocket configuration. The diffusion flame also results in generally low combustion efficiency of hybrid rockets. In the present study, a compact hybrid rocket motor design is investigated to provide a form factor with small slenderness that delivers high efficiency. This design concept features in multiple vortical flow structures such that much enhanced combustion efficiency can be obtained.

## 1. Introduction

Hybrid rocket combustion research has received renewed attention in recent years due to its safety feature implied low development costs and relatively benign environmental impacts. This has lead to the space tourism business development in the US and around the world with SpaceShipTwo of Virgin Galactic among others. However, there are still some important technical issues regarding hybrid rocket propulsion that need to be addressed in order for this technology to be more competitive in the mainstream where liquid and solid rockets are dominating.

Besides the safety features, overall thrust performance, operational robustness and reliability are key factors for a propulsion technology to be viable for business operations. Some research efforts have been dedicated in the area of boosting the thrust performance of hybrid rocket performance [1-10]. These include multi-port grain designs [1,2], high-regression-rate liquefying fuel grains [3,4], energetic material for the solid grain additives [5], performance boosting blended oxidizers [6], mixing enhancement chamber designs [7-10], etc. With these new design concepts and propellant formulas, the conventional fuel regression rate relations with the oxidizer mass fluxes and port geometry, developed based on the classical model, need to be further modified in order to benefit the design optimization processes for the hybrid rocket propulsion.

Although it is well know that the theoretical performance of hybrid propulsion systems can be higher than the conventional composite solid propellant rocket systems, the traditional hybrid systems fall short of their potential theoretical performance. This is mainly attributed to the low combustion efficiency and varying mixture ratio of the hybrid system. This study addresses the combustion efficiency aspect of the issues by introducing an innovative dual-vortical flow structure in the combustion chamber such that the overall mixing and combustion efficiency can be pushed towards the theoretical performance and the slenderness of the chamber can be drastically reduced.

Corresponding author: Yen-Sen Chen
*E-mail address*: yenchen@nspo.narl.org.tw

In the designs of rocket combustion chambers, there were various propellant injection schemes using swirling and vortex flows [7,8] to increase the residence time and mixing effects in the chamber. However, this has often lead to lowered pressure near the chamber axis where the vortex core resides, which presents negative effects to the overall thrust of the rocket engine. Certain amount of energy is also wasted in the swirling flow pattern which is retained all the way through the nozzle and in the plume. To overcome these drawbacks and to further enhance the mixing effectiveness inside the chamber, a dual-vortical-flow chamber was initially proposed by Chen et al. [9] and also ended up with a much reduced slenderness of the combustion chamber for hybrid rockets. The main feature of this design is in the counter-rotating vortical-flow patterns created by the proposed oxidizer injection schemes. This has resulted in increased center port pressure due to swirling cancelation and energy recovery. The propellant mixing and combustion efficiency is also enhanced in this process. The combined effect of this counter-rotating vortical-flow design is higher overall thrust performance.

To reach the goals of this research, a comprehensive computational model is developed in the present study to predict the complex three-dimensional flowfield inside the combustion chamber with innovative chamber geometry design and oxidizer injection method. Turbulent reacting flow modeling with finite-rate chemistry and radiative transfer effects is employed herein to numerically reveal the flow physics that is attributed to the mixing enhancement effects of the propellants inside the combustion chamber. The hybrid systems of $N_2O$ or $H_2O_2$ as oxidizer with HTPB as solid fuel are considered in the present study.

## 2. Numerical Approach

The present numerical method solves a set of governing equations describing the conservation of mass, momentum (Navier-Stokes equations), energy, species concentration and turbulence quantities, for the flow variables of density, species mass fraction, mean velocities, total enthalpy, turbulence kinetic energy and its dissipation rate.

A finite-rate chemistry model with robust

point-implicit approach is employed here [10]. An extended two-equation turbulence model is used that is suitable for transient and complex turbulent flows [11]. These numerical models are important for high fidelity simulations of combustion physics.

## 3. Multiple Vortical Flow Hybrid Propulsion

The design of the present combustion system is aiming at high-altitude upper-stage rocket applications, which involves propellants of $N_2O$ or $H_2O_2$ oxidizer and HTPB solid fuel. With the firing of a pyro grain, installed downstream of the injectors, to serve as an ignition heat source for the hybrid rocket engine, the combustion flame is established upon the injection of the oxidizer almost tangentially (about 15 degrees inward) from multiple injectors on the outer radius of the disk-shaped combustion chambers which are stacked side-by-side and divided with a short single-port HTPB grain placed in between.

These counter rotating flows are developing independently inside each chamber until the flows exit the disk-shaped chambers and enter the center port. In addition, there are bluff struts with triangular cross-sectional shape installed downstream of the injectors. These bluff bodies serve as effective flame holders in the combustion chambers. The sizes of these flame holders are determined through numerical experimentation.

## 4. Results and Discussion

The predicted flowfield of the dual-vortical-flow combustion chamber is shown in Figs 1 to 3. The temperature solution gives uniformly high temperature before the convergent section of the nozzle. Counter-rotating vortical flow patterns are clearly shown in each disk-shaped chamber in Fig. 2. Stream traces show the strong mixing effects in the center port region. The overall thrust performance of the present design is compared in Table 1.

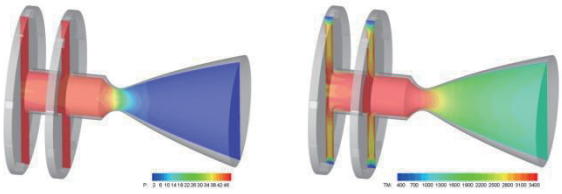

Fig. 1 Predicted center-plane pressure (left) and temperature (right) contours of a dual-vortical-flow chamber design.

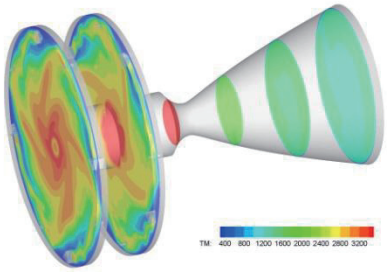

Fig. 2 Predicted temperature contours on YZ-planes of a dual-vortical-flow chamber design.

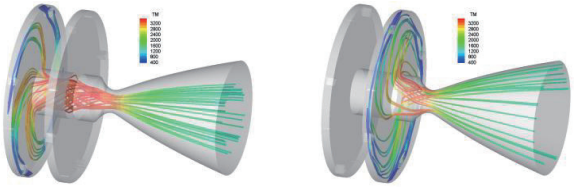

Fig. 3 Predicted stream traces colored by temperature of a dual-vortical-flow chamber design.

Table 1. Predicted thrust performance of the original dual-vortical-flow chamber design.

| Thrust (N) | $\dot{m}_{N_2O}$ (kg/s) | $\dot{m}_{HTPB}$ (kg/s) | O/F | Vacuum Isp (sec) |
|---|---|---|---|---|
| 7096.9 | 2.2646 | 0.2217 | 10.2 | 291.3 |
| 10,706.2 | 3.4258 | 0.3143 | 10.9 | 292.1 |
| 44,754.5 | 14.3977 | 1.2739 | 11.3 | 291.4 |

## 5. Conclusions

The present numerical solutions have shown interesting counter-rotating vortical flowfield in the combustion chamber that serves to boost the mixing and combustion efficiency of the hybrid rocket system through greatly increased shear stresses in the center port of the combustion chamber. The predicted quasi steady-state specific impulses are shown to be close to their theoretical ideal values. The predicted overall combustion efficiency is around 0.956.

Acknowledgement

This work is supported by the Sounding Rocket Program of National Space Organization, National Applied Research Laboratory of Taiwan. The computational resources and services are provided by the National Center for High-performance Computing of the National Applied Research Laboratory of Taiwan.

## References

[1] M.D. Bradford, R.J. Kniffen, B.C. McKinney, (1996), U.S. Patent 5582001.
[2] G. Story, T. Zoladz, J. Arves, D. Kearney, T. Abel, O. Park, (2003), AIAA-2003-5198.
[3] M.A. Karabeyoglu, G. Zilliac, J. Cantwell, S. DeZilwa, P. Castellucci, *Journal of Propulsion & Power*, (2004), 1037.
[4] M.A. Karabeyoglu, G. Zilliac, (2006), AIAA-2006-4674.
[5] M. Calabro, 7th ICFD Conference, (2010).
[6] M. Arif Karabeyoglu, *Journal of Propulsion and Power*, (2014), 30-3, 696.
[7] S. Yuasa, K. Yamamoto, H. Hachiya, K. Kitagawa, Y. Oowada, (2001), AIAA-2001-3537.
[8] W.H. Knuth, M.J. Chiaverini, D.J. Gramer, J.A. Sauer, (1998), AIAA 98-3351.
[9] Y.S. Chen, T.H. Chou, J.S. Wu, G. Cheng, (2013), AIAA-2013-0714.
[10] Y.S. Chen, T.H. Chou, B.R. Gu, J.S. Wu, Bill Wu, Y.Y. Lian, L. Yang, *Computers & Fluids*, (2011), 45, 29.
[11] Y.S. Chen, S.W. Kim, (1987), *NASA CR 179204*.

# Flight Performance Estimation for Swirling-Oxidizer-Flow-Type Hybrid Rocket with Swirling Control

Tomoaki Usuki[1], Kohei Ozawa[1], Shimada Toru[2]
[1]The University of Tokyo
Sagamihara, Kanagawa, 252-5210, Japan
[2]ISAS/JAXA
Sagamihara, Kanagawa, 252-5210, Japan

**ABSTRACT**

Swirling-Oxidizer-Flow-Type Hybrid Rocket with dual pipelines can control both thrust level and O/F independently by swirling control in principle. Therefore, this system enables hybrid rocket motor to drive with high combustion efficiency and high regression rate. This report estimates the effect of swirling control on the aspect of flight performance by using 6DOF flight simulation. In this study, swirling and throttling histories are treated as design variables, and are optimized by genetic algorithms to obtain the maximum flight performance.

## 1. Introduction

A hybrid rocket, by ordinary, is a rocket with solid fuel and liquid oxidizer. In hybrid rocket, thrust level can be controlled by changing the mass flow rate of oxidizer. However, if the mass flow rate changes, oxidizer/fuel mixture ratio (O/F) also changes. In addition to this, O/F also changes because the port diameter changes as the regression of solid fuel proceeds. This problem is known as O/F shift. The hybrid rocket has difficulty to obtain ideal performance because of it. If the hybrid rockets are brought out the ideal performance, they have launch capability comparable to LOX-Kerosene liquid rockets, moreover, the hybrid rocket can reduce operational cost drastically because of its safety derived from its inert characteristics.

Swirling-Oxidizer-Flow-Type (SOFT) hybrid rocket can control O/F by adjusting effective swirl numbers. It has been proposed that the SOFT hybrid with active swirl control can improve the performance of rocket system [1]. By controlling swirling flow valve and axial flow valve independently, the effective swirling number can be controlled active. Additionally, swirling effect improves regression rate. Thus, SOFT hybrid rocket has higher thrust density than conventional hybrid rocket and can reduce the gravity-loss. The purpose of this study is to qualify the effect of active swirling control of SOFT hybrid rocket on the aspect of flight performance.

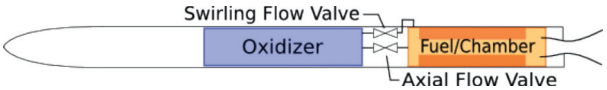


Fig. 1 Swirling controlled SOFT hybrid rocket

## 2. Method

Accurate performance estimation needs the environment profile for the motor model throughout a flight. For example, acceleration, dynamic pressure, roll rate are important because they must constraint flight operations. If these environments are out of operating range of rocket system, the estimation will not make sense.

Therefore, flight dynamics simulation that includes attitude motion is necessary for the purpose of accurate performance estimation.

In addition, the SOFT Hybrid Rockets include "Single Hardware, Multiple Operation" concept. In other words, they involve the design problems for operation. Under an initial stage of flight, high thrust density is effective from a point of view of the gravity-loss. On the other hand, under a final stage of flight, low thrust density and high specific impulse are effective to reduce maximum acceleration and to obtain momentum. Therefore, optimizing how to drive the motors is necessary for estimating the performance of hybrid rockets. In this study, three cases of SOFT hybrid rocket systems are assumed. First, single pipeline with regulated mass flow rate of oxidizer (conventional SOFT hybrid rocket). Second, single pipeline with variable mass flow rate. Third, dual pipelines with variable mass flow rates. These hybrid rockets must be compared after optimizing motor operations for each.

### 2. 1. Flight Dynamics

The flight of rocket is based on rigid body dynamics [2]. If assumed to be a rigid body, the six degrees of freedom motion of rocket is represented with dynamical state variables, position, velocity, attitude, angular velocity and the mass of rocket.

$$x = \begin{bmatrix} r & v & q & \omega & m \end{bmatrix}^T \tag{1}$$

The variable q is a quaternion, which represents the attitude of the rocket from the Earth Centered Inertial Coordinate ( Σ ECI).

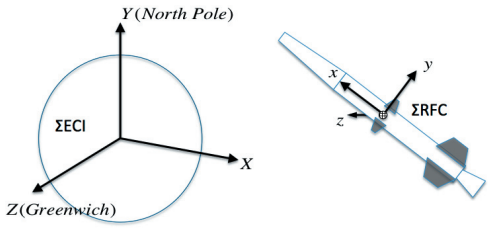


Fig. 2 Coordinate systems

Corresponding author: Tomoaki Usuki
*E-mail address*: usuki.tomoaki@ac.jaxa.jp

On an inertial coordinates, the equation of translational motion is written on the Σ ECI as below.

$$m\frac{dv}{dt} = F_{gravity} + F_{thrust} + F_{aerodynamics}. \quad (2)$$

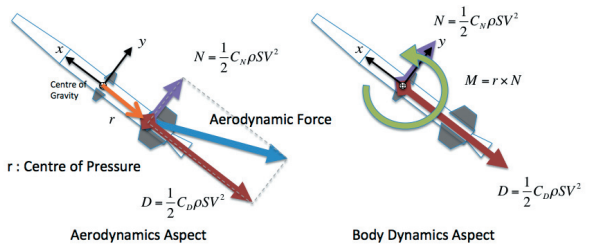


Fig. 3 Aerodynamics act on the rocket body

Rotational motion is computed on the Rocket Fixed Coordinate ( Σ RFC), a movable coordinate system on the center of gravity.

$$\frac{d(I_{RFC}\omega_{RFC})}{dt} + \omega_{RFC} \times (I_{RFC}\omega_{RFC}) = M_{thrust} + M_{aerodynamics}. \quad (3)$$

The variable I is the inertial tensor, and subscript RFC means it is defined on Σ RFC.

This simulation uses the SOFT hybrid motor model constructed on prior research. On the assumption that the rocket is fin stabilized and aerodynamic moment act as restitution force, however, the direction the rocket exactly point is the result of rotational dynamics. Air pressure, density and Mach number is provided by US Standard Atmosphere model [3].

### 2. 2. Design Problems

Throttling and Swirling histories are parameterized and they are treated as design variables, because the highest performance of swirling controlled SOFT hybrid rocket is obtained from the solutions of optimization problem for Throttling and Swirling histories. In this optimization problem, primary variables are mass flow rate of each pipeline, because each pipeline corresponds to axial and tangential flow injector, and thrust level and swirl number is the result of fluid dynamics. A step function, Fourier series, and polynomial expression can be used for represent mass flow rate curves with some parameters.

The method I use for this optimization is genetic algorithms. The individuals those who violate the operational range of rocket system are terminated, such as an individual who experiences too much dynamic pressure or acceleration.

The angle of elevation on launch complex is fixed, and the flight performance is mainly evaluated as the highest altitude the rocket reaches.

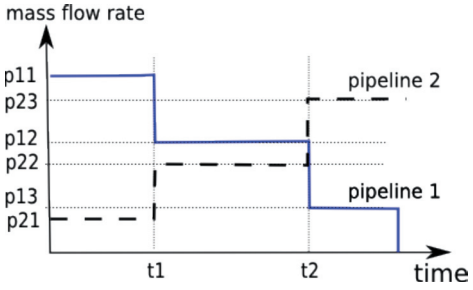


Fig. 4 Simple parameterize for throttling and swirling history with step function.

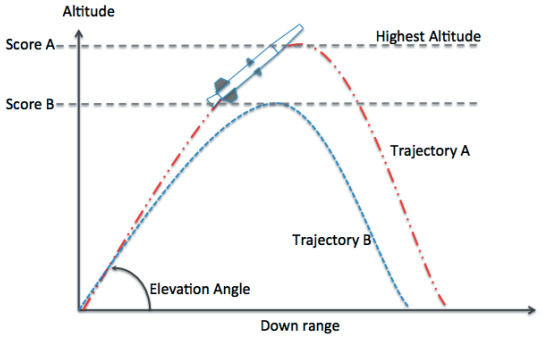


Fig. 5 Evaluation method for optimization problem

To compare the effect of swirling control, three cases of hybrid rocket system is simulated:

---

Case 1: constant throttle without swirling control
Case 2: optimized throttle without swirling control
Case 3: optimized throttle with swirling control

---

Case 1 is a basic type of hybrid rocket. The system has single pipeline and its mass flow rate is regulated, and the swirl number is depend on the injector design. Thus, the design variables are combustible duration and default swirling number.

Case 2 is a throttle controlled hybrid rocket with a default swirling number. The system has single pipeline and its mass flow is controllable. The design variables are axial mass flow rate history and default swirling number.

Case 3 is a throttle controlled hybrid rocket with swirling control. This system has dual pipelines, and its mass flow rate is both controllable. The design variables are mass flow rate histories of both pipelines...

After optimizing each case of SOFT hybrid rocket, flight performance is estimated by comparing flight profile of case 1 to 3. For example, highest altitude, down range, highest roll rate and highest acceleration can be the performance indicators.

### References


[1] K. Ozawa, T. Shimada, *Proc. Space Transportation Symposium*, (2014).
[2] D. Baraff, Carnegie Mellon University, *An Introduction to Physically Based Modeling*, (1977).
[3] NOAA, NASA, and US Air Force, U.S. Standard Atmosphere 1976, (1976).

Eleventh International Conference on Flow Dynamics
October 8-10, 2014, Sendai, Miyagi, Japan

# A Theoretical Study on Individual and Optimized Control of Thrust and Mixture Ratio of Swirling-Oxidizer-Flow-Type Hybrid Rocket

Kohei Ozawa[1], Toru Shimada[2]
[1]Department of Aeronautics and Astronoutics, Graduate School of The University of Tokyo
3-1-1 Yoshinodai, Chuo-ku, Sagamihara city, Kanagawa, 252-5210, Japan
[2]Institute of Space and Astronautics Science, Japan Aerospace Exploration Agency
3-1-1 Yoshinodai, Chuo-ku, Sagamihara city, Kanagawa, 252-5210, Japan

**ABSTRACT**

This paper shows characteristics of shifts of mixture ratio in hybrid rocket motors in long time burning and throttling and theoretical considerations on optimal thrust and mixture ratio control by oxidizer mass flow rate and swirl intensity control. It is clarified that oxidizer swirl injection decreases this shift and optimal geometric swirl intensity in cases of fuel port increment and throttling is specified.

## 1. Introduction

In hybrid rocket engines, in long time burning and throttling situations, mixture ratio shifts from a reference point by changes of oxidizer mass flux and surface area of fuel ports [1]. In this paper, these changes of mixture ratio are called "O/F shift". These shifts make time averaged specific impulse decrease worse than potential one.

In order to improve this performance decrement, one more independent variable of oxidizer mass flow rate to control fuel regression rates is needed. Recently, as this kind of variables, geometric swirl intensity of swirl oxidizer flow hybrid rocket engines (SOFT-HREs), and a practical injection method to control this parameter are proposed by Ozawa et al. [1] SOFT-HRE is a type of hybrid rocket engines aiming to increase fuel regression rates by adding circumferential velocity component of oxidizer mass flux. Regression rates of SOFT-HREs depend on swirl intensity besides oxidizer mass flux. In this paper, after O/F shift without swirl intensity control is theoretically evaluated with solid fuel regression rates modeled from experimental results, a control theory of geometric swirl intensity to keep mixture ratio constant is derived.

## 2. Assumptions and Regression Rates Model

Before evaluating O/F shifts, assumptions on propellant and flow of boundary layer combustion are set to simplify the evaluation of regression rates and mixture ratio.

In this paper, regression rates and mixture ratio are considered under the following assumptions or conditions. Oxidizer is gas phase and solid fuels are decomposed and gasified instantly once receiving heat flux from boundary layer. There is no additive particle in solid fuels. Convective heat transfer is dominant in heat flux into solid fuels. This is because radiative heat transfer from flame can be neglected and this assumption is well fit under the condition of $Re_x > 10^6$($Re_x$:local axial Reynolds number). The effect of swirl intensity on regression rates is uniform toward axial direction and independent of oxidizer mass flux. Fuel port radius is uniform toward axial direction. Propellants of these are PMMA and GOX.

From these assumptions, the evaluation of regression rates by Marxman et al. [2] is adopted as

$$\dot{r}(x,t) = aG(x,t)^n x^{n-1} \quad (1)$$

where $a$ is independent of axial position and time but depends on swirl intensity and chemical species of propellants, $G$ is total mass flux and $n$ is a constant exponent. $a$ is fit from combustion tests on SOFT-HREs by Yuasa et al. [3,4] $a$ is approximated as

$$a = \left\{1 + \eta_1 {S_g}^{n_3}\right\}^{n_2} a_0 \quad (2)$$

where $S_g$ is geometric swirl intensity only determined by the geometry of swirl injector [5] and $S_g$ is assumed to be equal to initial swirl intensity $S$ [6] under the condition that radius of swirl injector is the same as one of fuel port, $\eta_1 = 0.2638$, $n_3 = 0.6902$, and $n_2 = 0.7854$. $a_0$ is $a$ in $S = 0$. When fuel port radius is different from one of swirl injector, $S_g$ is replaced by $\frac{r_p}{r_o} S_g$. $r_p$ is fuel port radius and $r_o$ is radius of swirl injector outlet. This correction is based on axial mass conservation law, angular momentum conservation law, and the definition of swirl intensity.

## 3. Evaluation of O/F Shift

$G(x)$ and $F/O$(inverse of O/F) is calculated as

$$G(x) = \frac{\dot{m}_o + 2\pi\rho_f \int_0^x \dot{r}(x) r dx}{\pi r^2} = \frac{\dot{m}_o}{\pi r^2}\left(1 + \frac{F}{O}(x)\right) \quad (3)$$

$$\frac{F}{O}(x) = \frac{2\pi\rho_f \int_0^x \dot{r}(x) r(x) x^{n-1} dx}{\dot{m}_o} \quad (4)$$

Substituting Eq. (3) and Eq. (4) into Eq. (1) and integrating it from head and to tail end of fuel port yield

$$\frac{F}{O}(L) = \frac{F}{O} = \left\{1 + \left(\frac{F}{O}\right)_0\right\}^{\frac{1}{1-n}} - 1 \approx \alpha\left(\frac{F}{O}\right)_0^2 + \beta\left(\frac{F}{O}\right)_0 \quad (5)$$

where $\left(\frac{F}{O}\right)_0 = 2a\frac{(1-n)}{n}\rho_f \left(\frac{\pi}{\dot{m}_o}\right)^{1-n} r^{1-2n} L^n$ is $F/O$ excluding the effect of fuel mass flux on regression rates, and $(\alpha, \beta) = (0.4761, 0.9845)$ is set. From Eq. (5), normalized O/F shift, $\overline{\triangle O/F} \equiv (F/O)^{-1}/\{(F/$

Corresponding author: Kohei Ozawa
*E-mail address*: kohei.ozawa@ac.jaxa.jp

$O)^*\}^{-1} - 1$, can be calculated. "*" means a referential operational point.

Figure 1 and Figure 2 show O/F shifts under the condition of $\frac{r_p}{r_o}S_g = 0$ and 20, respectively. $(F/O)^* = 0.67$ is set. The gradational curves are the contours of normalized O/F shift. From both figures, you can know that the tendency of O/F shift differs depending on swirl intensity. This difference is caused by the corrected geometric intensity $\frac{r_p}{r_o}S_g$. The increase of swirl intensity by increment of fuel port radius decreases O/F shift. The higher geometric swirl intensity is, the stronger this decrease effect is.

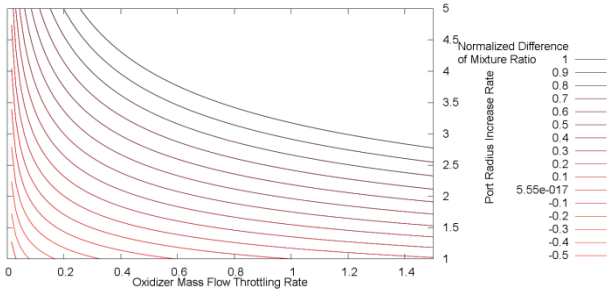


Fig. 1 The normalized O/F shift in $S_g = 0$.

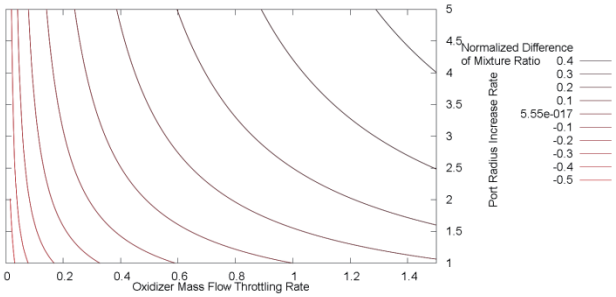


Fig. 2 The normalized O/F shift in $S_g = 20$.

## 4. Swirl Intensity Control Theory

The optimal swirl intensity is calculated from the condition of $\frac{F}{O} = \left(\frac{F}{O}\right)^*$ and Eq. (5) as

$$S_g = \left[\frac{\left\{1+\eta_1\left(\frac{r_p r^*}{r^* r_o}S_g^*\right)^{n_3}\right\}\overline{\dot{m}_o}^{\frac{1-n}{n_2}}\left(\frac{r_p}{r^*}\frac{r^*}{r_o}\right)^{\frac{2n-1}{n_2}} - 1}{\eta_1}\right]^{\frac{1}{n_3}}\left(\frac{r_p}{r^*}\frac{r^*}{r_o}\right)^{-1} \quad (6)$$

Figure 3 and Figure 4 show the optimal geometric swirl intensity to keep mixture ratio constant. Figure 3 is the contour of optimal geometric swirl intensity under port radius increment by long time burning and constant oxidizer mass flow rate to keep constant thrust. In this figure, $r^* = r_0$ is assumed. The horizontal axis is $(r^*/r_o)S_g^*$ and vertical axis is fuel port radius normalized by $r_0$. The gradational curves mean the contour of optimal geometric swirl intensity. For example, $S_g$ should be set about 12 in $(r^*/r_o)S_g^* = 20$ and $r_p = 3r_0$. Figure 4 is the contour of under fixed port radius $r_p = r^*$ and variable oxidizer mass flow rate for thrust control. The horizontal axis is $(r^*/r_o)S_g^*$ and vertical axis is oxidizer mass flow rate normalized by the reference one. For example, $S_g$ should be set about 16 in $(r^*/r_o)S_g^* = 20$ and 50% throttling.

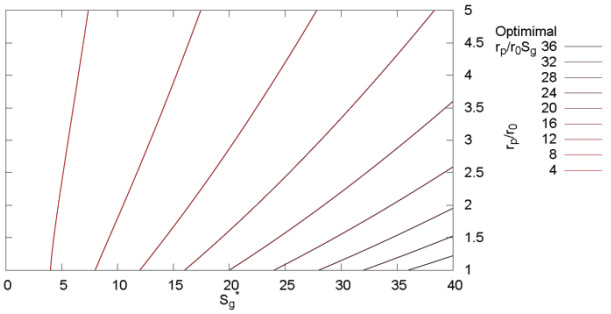


Fig. 3 The optimal geometric swirl intensity under constant oxidizer mass flow rate and port radius increment.

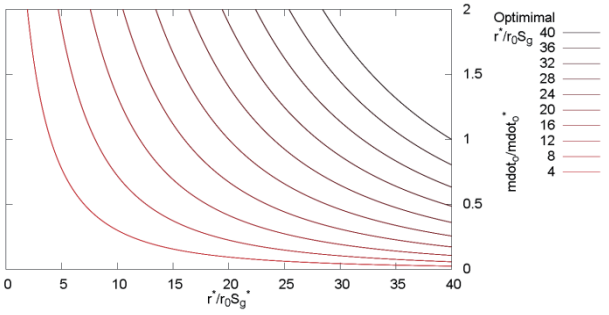


Fig. 4 The optimal corrected geometric swirl intensity under constant port radius and throttling.

## 5. Concluding Remarks

In this paper, using Marxman's evaluation of regression rates and the relation of swirl intensity and regression rates derived by combustion tests, mixture ratio of SOFT-HREs is analytically expressed. With this expression, O/F shifts in hybrid rocket motors under long time burning and throttling conditions and optimal thrust and mixture ratio control by oxidizer mass flow rate and swirl intensity control are theoretically considered. It is clarified that swirl injection of oxidizers decreases this shift and optimal geometric swirl intensity charts in cases of fuel port increment and throttling are plotted.

## References


[1] K. Ozawa, T. Shimada, *Space Transportation Symposium FY2013*, (2014), STCP-2013-043.(Japanese)

[2] M. J. Chiaverini, K. K. Kuo, *Fundamentals of Hybrid Rocket Combustion and Propulsion*, (2007), 37-126.

[3] T. Tamura, S. Yuasa, K. Yamamoto, *35th JPC*, (1999), AIAA 1999-2323.

[4] S. Yuasa, K. Yamamoto, H. Hachiya, K. Kitagawa, *37th JPC*, (2001), AIAA 2001-3537.

[5] S. Yuasa, O. Shimada, T. Imamura, T. Tamura, K. Yamamoto, *35th JPC*, (1999), AIAA 1999-2322.

[6] W. Steenbergen, *Ph. D. Dissertation of University Eindhoven of Technology*, (1995), 15.

# Design Optimization of Launch Vehicle Concept Using Cluster Hybrid Rocket Engine for Future Space Transportation

Shoma Ito[1], Fumio Kanamori[1], Masaki Nakamiya[2], Koki Kitagawa[3],
Masahiro Kanazaki[1] and Toru Shimada[3]
[1]Tokyo Metropolitan University, 6-6 Asahigaoka, Hino-shi, Tokyo, Japan
[2]Kyoto University, Gokasho, Uji-shi, Kyoto, Japan
[3]Institute of Space and Astronautical Science/Japan Aerospace Exploration Agency, 3-1-1 Yoshinodai,Chuo-ku, Sagamihara-shi, Kanagawa, Japan

**ABSTRACT**

This paper considers the conceptual design of the three-stage launch vehicle with the clustered hybrid rocket engine (HRE) by a multi-disciplinary design optimization. In this study, three cases are compared: In the first case, HREs are optimized for each stage. In second case, HREs are optimized for 1st and 2nd stages and 3rd stage (namely, the same design is used in 1st and 2nd stages). In the third case, HREs are optimized for each stage. According to the optimization result, it is found that the design case which use same HREs in all stages is 40% reduced compared with the design case which use optimized HREs for each stage.

## 1. Introduction

A hybrid rocket engine (HRE) has the advantages of being safe, cost effective, and environmentally friendly. Thus, a launch vehicle (LV) with HREs is expected to be used for next-generation space transport. In our previous study[1], we developed a conceptual design methodology based on a multi-objective genetic algorithm (MOGA) for a three-stage hybrid rocket, including thrust evaluation, vehicle sizing, and trajectory analysis. Several solutions achieved good performance that was suitable for space transport. However, the performance, such as the maximum payload, was limited because only one HRE was installed for each stage.

In this study, an LV with clustered HREs is considered, as illustrated in Fig. 1. A cluster rocket is expected to have a lower development cost, if the same engine designs can be used for all stages. To investigate this possibility, we compared three design cases regarding the combination of optimum engines for each stage.

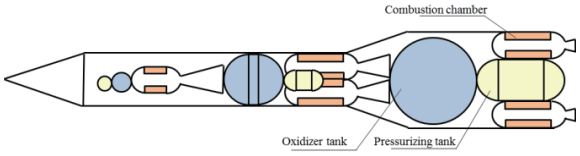


Fig. 1 Conceptual illustration of cluster hybrid rocket

## 2. Overview of Design Method

### 2.1. Evaluation of LV Performance

The hybrid rocket of this study is comprised of a nozzle, chamber, pressurized tank, oxidizer tank, and an exterior wall for each stage (Fig. 1), in addition to a payload. The evaluation procedure is shown in Fig. 2.

A single-port fuel grain is considered here. The regression rate $\dot{r}_{port}(t)$ of the fuel is expressed as follows:

$$\dot{r}_{port}(t) = \beta a [G_o(t)]^n \quad (1)$$

$G_o$ is the mass flux of the oxidizer which go through the port of the fuel. The coefficient $a$ and the exponent $n$ are empirical parameters, and the values used in this study are given in Table 1[2]. $\beta$ is a design variable that is used to simulate the swirling effect of the oxidizer, which can increase the regression rate. From $\dot{r}_{port}(t)$ and the burning time $t_b$, which is also a design variable, the rocket size can be calculated.

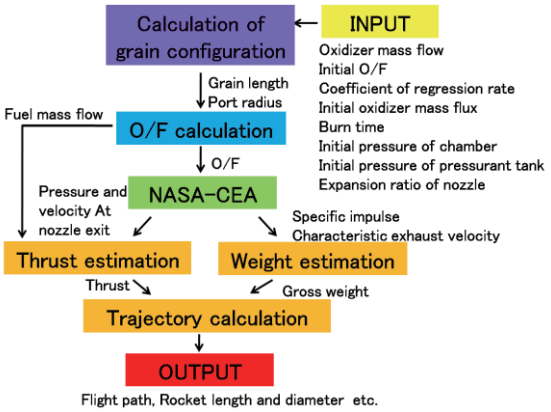


Fig. 2 Flow chart of design and evaluation

### 2.2. Layout of Components for Cluster Rocket

In this study, eight HREs are installed in the first stage, and two HREs are installed in the second stage. The arrangement of these components for each stage is illustrated in Fig. 3. The third stage contains only one HRE, and the associated pressurized tank, oxidizer tank, combustion chamber, and nozzle are placed sequentially as shown in Fig. 1.

Corresponding author: Masahiro Kanazaki
*E-mail address*: kana@tmu.ac.jp

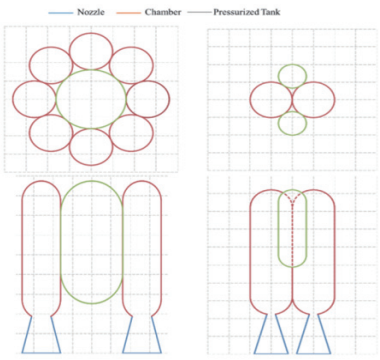


(a) (b)

Fig. 3 Component layouts for first and second stages.

## 3. Results

In this study, an LV is considered that can deliver a payload to Earth orbit at 800 km. As mentioned earlier, three cases are compared: In Case1, the HREs are optimized separately for each stage. In Case2, the first and second stages share an engine design, while the third stage is optimized separately. In Case3, all stages share the same engine design. We applied an MOGA called the non-dominated sorting genetic algorithm-II (NSGA-II) to each case, with a total generation number of 100 and population size of 50 for each generation. The objective functions are the minimization of the total mass ($M_{tot}$) and the maximization of the payload to total mass ratio ($M_{pay}/M_{tot}$)

### 3. 1. Design Exploration Results

Figure 4 shows a comparison of the non-dominated solutions for each case. The result for the single engine rocket is taken from the previous study[1]. This figure allows the trade-off between the objective functions to be found. Case1 can reach a greater value of $M_{pay}/M_{tot}$ at a lower $M_{tot}$ than either Case2 or Case3, because all the stages have an optimized engine.

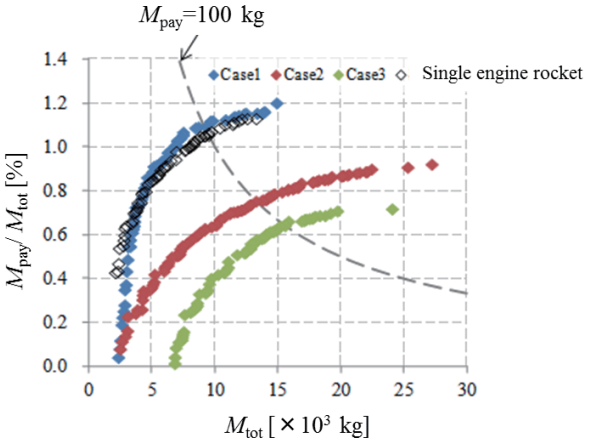


Fig. 4 Comparison of non-dominated solutions.

### 3. 2. Comparison of Design Results

Rocket designs that can deliver a payload of 100 kg are compared. Table 1 shows the values of $M_{tot}$ and $M_{pay}/M_{tot}$, found from where the design curves intersect the dashed line in Fig. 4. The value of $M_{pay}/M_{tot}$ for Case3 is only 60% of that for Case1, because the engines are not optimized for each stage in Case3. Figure 5 shows a visual comparison of the design results, for each case and also for the single engine rocket. As can be seen from Fig. 5, the diameters of the first stage of Case2 and Case3 are larger than that of Case1. Because the first stage is independently designed in Case1, the resulting engine is narrow. However, when the engine designs are shared, the width constraint from second stage causes the first stage to have a large diameter.

Table. 1 Comparison of performance of the designed LVs, which can deliver a 100 kg payload.

| | $M_{tot}$ [×10³ kg] | $M_{pay}/M_{tot}$ [%] |
|---|---|---|
| Case1 | 9.31 | 1.10 |
| Case2 | 13.3 | 0.75 |
| Case3 | 15.5 | 0.64 |

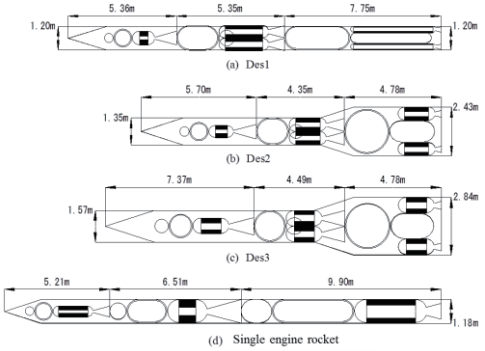


Fig. 5 Comparison of rockets designed to carry 100 kg payload.

## 4. Conclusion

In this study, we considered the conceptual design of a multi-stage launch vehicle with a clustered hybrid rocket engine. Three optimization cases were considered. The results suggest that an LV that uses the same engines for each stage can only achieve 60% of the payload mass ratio, compared with an LV that has engines optimized separately for each stage. In addition, an LV that uses same engines for each stage has a lower aspect ratio than an LV with an optimized engine for each stage. These findings are significant for LV development and manufacturing.


### Acknowledgments

We thank members of the hybrid rocket research working group in ISAS/JAXA for giving their experimental data and their valuable advices. This paper and presentation was supported ISAS/JAXA.


### References


[1] Y. Kitagawa, K. Kitagawa, M. Nakamiya, M. Kanazaki and T. Shimada, *T JSASS*, 55 (2012).

[2] I. Nakagawa, *Proc AJCPP*, (2010).

# Experimental Study on Regression Rate of Solid Combustibles by Double Impinging Jets

Kyohei Kamei[1], Tsuneyoshi Matsuoka[2], Susumu Noda[2], Harunori Nagata[3]
[1]Graduate school of Engineering, Toyohashi University of Technology
1-1 Hibarigaoka, Tenpaku-cho, Toyohashi, Aichi, 441-8580, JAPAN
[2]Department of Mechanical Engineering, Toyohashi University of Technology
1-1 Hibarigaoka, Tenpaku-cho, Toyohashi, Aichi, 441-8580, JAPAN
[3]Division of Mechanical and space Engineering, Hokkaido University
Kita 13, Nishi 8, Kita-ku, Sapporo, Hokkaido, 060-8628, JAPAN

**ABSTRACT**

The regression rate of solid combustibles by double impinging jets was experimentally investigated. Two jets were merged before the primary impingement for 4 mm of jet-to-jet spacing, whereas they independently impinged on the solid surface and the secondary impingement occurred at the center for 18 mm spacing. In the secondary impingement region, the flame was enhanced and sustained even in blow-off regime. The non-dimensional regression rate can be evaluated in similar manner to the heat transfer characteristic of the non-reactive flow.

## 1. Introduction

Expecting high heat transfer characteristics at the stagnation region, using an impinging oxidizer jet is proposed as an effective method to combust solid combustibles. For example, CAMUI hybrid rocket motor [1] uses double oxidizer jets impinging to polyethylene and achieved higher regression rate than traditional ones. Although the practical combustors generally employ the multiple jets, most studies about solid combustion with impinging jet have treated the single jet. In case of non-reactive flow, however, it is known that the heat transfer characteristics by multiple jets differs from the single jet, since interaction between jets causes secondary stagnation and fountain flow between jets [2]. Thus, the solid combustion by multiple oxidizer jets may also differ from the single jet. To optimize design of the practical combustors, it is necessary to predict the regression rate precisely.

The object of this study is to investigate the regression rate of solid combustion of multiple impinging jets. A nozzle consisting of the double slits was employed to simplify the phenomenon. The experiments with different jet-to-jet spacing nozzles were conducted in wide range of Reynolds number (*Re*) and various oxygen concentrations. Furthermore, the results are compared with the heat transfer characteristics of non-reactive flow.

## 2. Experimental Method

Figure 1 shows a schematic diagram of the experimental apparatus. The double slits nozzle was connected to a gas supply system. Width and length of the slits were 3 mm and 30 mm, respectively. The double plane oxidizer jets were fed from the slits and impinged into the PMMA slab (H20 x W60 x D20 mm) as a fuel positioned 24 mm below the nozzle. Jet-to-jet spacing, *S*, used in this study was 4 or 18 mm. Pure oxygen ($X_O$ = 1) and a mixture gas containing 50 vol% oxygen ($X_O$ = 0.5) were used as an oxidizer. Oxygen concentration of the mixture gas was confirmed by a gas chromatography. The flow rate was adjusted to desired values by flow meters. Reynolds number, *Re*, of the oxidizer jet based on the slits width was varied in wide range about 300 to 2500. Combustion was initiated by a hot wire placed on the fuel surface. Each test was recorded by a digital video camera with a 430 nm band-pass filter with 10 nm FWHM during the event. After combustion, the fuel surface profile was measured by a laser displacement meter. The regression rate was derived by dividing the obtained surface regression depth with the combustion duration.

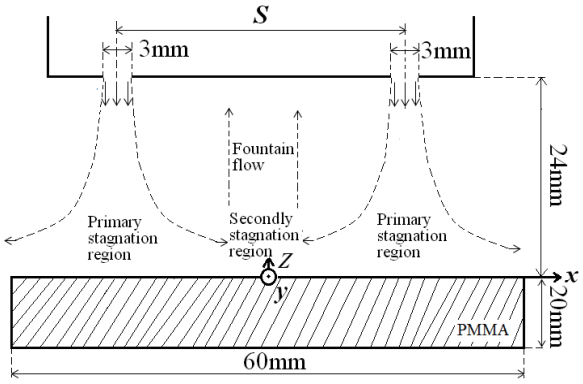


Fig. 1 Schematic diagram of the experimental apparatus

## 3. Results and Discussion

### 3.1. Regression Rate Profile

Figure 2 shows regression rate profiles along the *x*-axis for *S* = 4 mm and 18 mm. It should be noted that the surface regression in *y* direction was not entirely uniform and the results shown here were obtained along the center (*y* = 0). In addition, there was uncertainty in measurement of fuel regression in some extent. Data obtained here was interpreted in qualitative way.

The horizontal axis, *x*, was non-dimensionalized with the half of jet-to-jet spacing (*P* = *S* / 2). Introducing the characteristic velocity of the flow $(2a\nu)^{1/2}$ [3], where *a* [$s^{-1}$] is the velocity gradient of the flow and $\nu$ [$m^2/s$] is the kinematic viscosity of the oxidizer, and dividing the regression rate by this velocity, the regression rates

Corresponding author: Tsuneyoshi Matsuoka
*E-mail address*: matsuoka@me.tut.ac.jp

obtained in various flow conditions were organized. In some experiments at $X_O$ = 0.5 and high *Re*, the non-dimensional regression rate in the stagnation region was very small. It is considered that local extinction occurs in these conditions. For $S$ = 18 mm, two peaks clearly appeared. It implies that each free jet independently impinged on the PMMA surface. Then, the secondary impingement must occur at the midpoint of the two jets and the upward fountain flows were formed. They may push the free jet outwardly and the points of the local maximum of regression rate shifted as shown in Fig. 2 C and D of low *Re*. For $S$ = 4 mm, on the other hand, a wide broadened peak appeared. This suggests that two independent jets merged and impinged into the fuel bed as the single jet.

3.2. Comparison with Non-reactive Flow

The regression rate plotted against *Re* at $x / P = 0$ and 1 are shown in Fig. 3. The data was fitted to exponential lines by the least square method. It is known that, for a non-reactive impinging jet, Nusselts number depends on *Re* with the exponent of 0.5 in a stagnation region and 0.8 in a wall-jet region [4]. The exponent values were close to those of the non-reactive flow, though it is difficult to quantitatively compare with non-reactive flow due to the uncertainty in regression rate. It suggests that the regression rates by double impinging jets might be evaluated in similar manner to the heat transfer characteristics of non-reactive flow.

When $X_O$ = 0.5, the regression rate decreased sharply at high *Re* for $S$ = 4 mm due to flame extinction. On the other hand, the regression rate still increased approximately in proportion to *Re* to the power of 0.5 at the center of $S$ = 18 mm. The flame was compressed due to the wall jets from both sides. Therefore, the flame in the secondary region might be enhanced and not extinguished even in blow-off regime.

## 4. Concluding Remarks

The regression rate of solid combustibles by double impinging jets was investigated experimentally. The regression rates were organized introducing the characteristic velocity, $(2a\nu)^{1/2}$. Although the distributions of non-dimensional regression rate depended on jet-to-jet spacing, they can be evaluated in similar manner to the heat transfer characteristic of a non-reactive flow. Two jets were merged before the primary impingement for $S$ = 4 mm, whereas they independently impinged on the solid for $S$ = 18 mm and the secondary impingement occurred at the center. The flame in the secondary region should be enhanced, and thus the flame does not extinguish even in blow-off regime.


## Acknowledgements

This work was partially supported by Grant-in-Aid for Research Activity Start-up No. 24860002. It was also supported by The Naito Research Grant and Tatematsu-Foundation.


## References


[1] H. Nagata, M. Ito, T. Maeda, M. Watanabe, T. Uematsu, T. Totani, I. Kudo, *Acta Astronaut.*, 59 (2006) 253-258.

[2] J.Y. San, J.J. Chen, *Int. J. Heat Mass Tran.*, 71 (2014) 8-17.

[3] K. Matsui, A. Koyama, K. Uehara, *Combust. Flame*, 25 (1975) 57-66.

[4] M. Kumada, T. Nakatogawa, M. Hirata, *J. Jpn. Soc. Mech. Eng.*, 76 (1973) 822-830 (in Japanese).


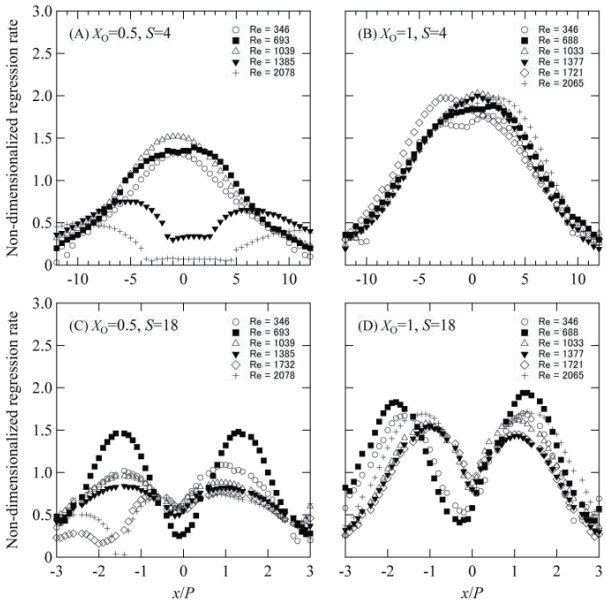


Fig. 2 Non-dimensional regression rate profile.

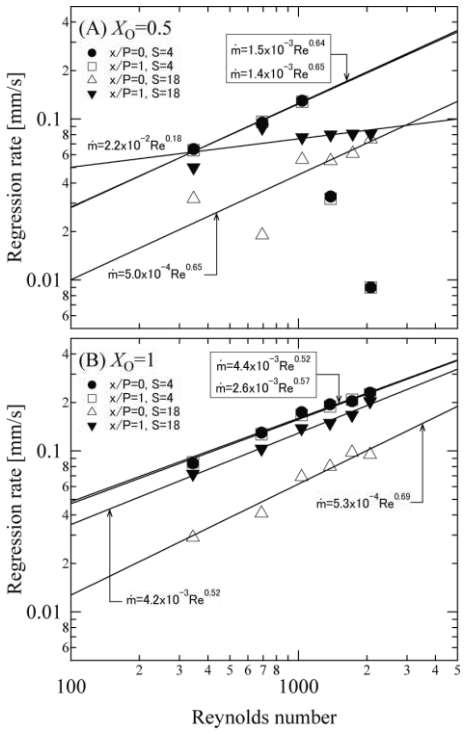


Fig. 3 Dependence of regression rate on *Re* (upper) for $X_O$ = 0.5, (lower) for $X_O$ = 1.

Eleventh International Conference on Flow Dynamics
October 8-10, 2014, Sendai, Miyagi, Japan

# Investigation of Fuel Regression Rate Characteristics of the 5 kN-thrust Swirling-Oxidizer-Flow-Type Hybrid Rocket Engine

Takashi Sakurai[1], Hideyuki Ando[1], Saburo Yuasa[1], Shun Takahashi[1], Tsutomu Tomizawa[1], Daiki Hayashi[1], Koki Kitagawa[2], Akimasa Takayama[3], Ryosuke Yui[3], Toru Shimada[2]
[1]Tokyo Metropolitan University, 6-6 Asahigaoka, Hino, Tokyo, 191-0065, Japan
[2]ISAS JAXA, 3-1-1 Yoshinodai, Chuo-ku, Sagamihara, Kanagawa, Japan
[3]The University of Tokyo, 7-3-1 Hongo, Bunkyo-ku, Tokyo, Japan

**ABSTRACT**

To verify the engine design and to obtain the combustion characteristics, a 5 kN-thrust swirling-oxidizer-flow-type hybrid rocket engine was developed. The burning test at the design condition was carried out by using the GOx/PP propellant. Time-averaged thrust of 4.4 kN was attained during 5 s burning test. The local fuel regression rate as well as engine performance was evaluated. It was found that the local fuel regression rate at the grain leading edge correlated well with the controlling parameter whereas that at the grain rear region showed lower regression rate than predicted value.

## 1. Introduction

To actualize technologies of practical hybrid rocket engines, a 5 kN-thrust hybrid rocket engine was manufactured as a project of Hybrid Rocket research Working Group (HRrWG) of ISAS/JAXA. In the design of the 5 kN-thrust engine, the swirling-oxidizer-flow-type was adopted and the fundamental burning properties of the engine were predicted by considering the fuel regression behavior [1-3]. The combustion test of the engine have been carried out at the 5 kN-thrust conditions. In this paper, the results of the burning tests and the local fuel regression rate are presented.

## 2. Experimental Apparatus and Conditions

Figure 1 shows the schematic of 5kN-thrust swirling-oxidizer-flow-type hybrid rocket engine called HTE-5-1. This engine was designed to be matched with the system of the Akiruno facility of ISAS/JAXA and the detail is described elsewhere [4]. The oxidizer is GOx and the fuel is polypropylene. The engine consisted of a commercial miniature rocket-type igniter, a swirler-type injector with *Sg*=19.4, a fuel grain and a graphite nozzle.

To verify the engine design and to obtain the combustion characteristics, the burning tests were carried out in the Akiruno facility. The burning conditions are 1.5 kN-thrust tests of #3-1(10 s duration), #3-2(20 s) and 5 kN-thrust tests of #4-1(2 s), #4-3(5 s). The #4-1 and #4-3 burning tests were carried out by using the same fuel grain.

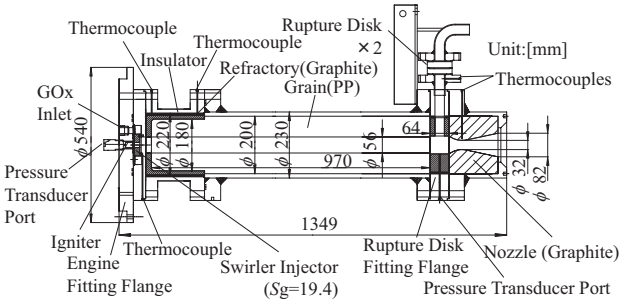


Fig.1 Schematic of the 5kN-thrust swirling-oxidizer-flow-type hybrid rocket engine, HTE-5-1

Corresponding author: Takashi Sakurai
*E-mail address*: tsakurai@tmu.ac.jp

## 3. Experimental Results and Discussion

Typical time histories of the thrust, combustion chamber pressure and oxidizer mass flow rate in the burning test (#4-3) is shown in Fig.2. The ignition was smooth and stable combustion was attained. The oxidizer mass flow rate was almost constant during the test, whereas the combustion chamber pressure gradually decreased. This was due to nozzle erosion. In spite of chamber pressure decrease, the increases of fuel mass flow rate and throat diameter against time resulted in constant thrust time history. Although the oxidizer flowed at the estimated mass flow rate for the 5 kN-thrust, the thrust did not reach to 5 kN.

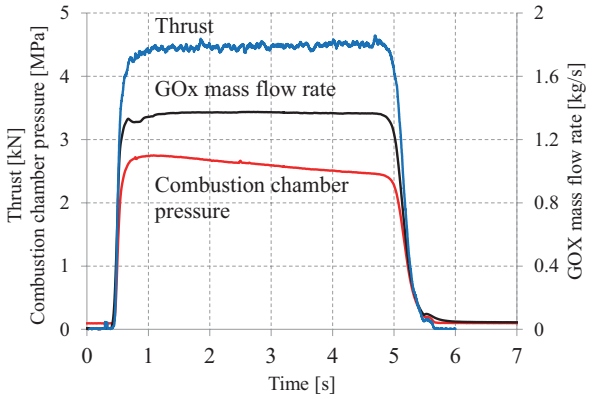


Fig.2 Typical time history of engine performance (#4-3)

To clarify the reason of lower thrust under the designed burning condition, the engine performance of the burning tests are summarized in Table 1. In #3-1 and #3-2 burning tests, the obtained chamber pressure, equivalence ratio, and regression rate agreed well with the performance prediction [1,2] and the C* efficiency were quite high. In #4-1 and #4-3, although the C* efficiency was high, but the equivalence ratio was lower than the target value of 1.4. This means that the fuel regression rate was lower than the predicted value.

Table 1 Engine performance of the burning tests

| Run No. | | #3-1 | #3-2 | #4-1 | #4-3 |
|---|---|---|---|---|---|
| Measured Values (Avg.) | $F$ [N] | 1400 | 1300 | 4152 | 4438 |
| | $P_{cr}$ [MPa] | 1.43 | 1.26 | 2.76 | 2.59 |
| | $m_0$ [g/s] | 459 | 417 | 1228 | 1357 |
| Estimated Values | $\varphi$ | 1.50 | 1.70 | 1.16 | 1.12 |
| | $G_{oave}$ [kg/(m$^2$・s)] | 134.9 | 93.4 | 438.8 | 322.7 |
| | $r_{ave}$ [mm/s] | 1.12 | 0.99 | 2.52 | 2.18 |
| | $\eta_{C^*}$ | 1.00 | 1.02 | 0.97 | 0.96 |
| | $\eta_{Isp}$ | 0.86 | 0.88 | 0.95 | 0.94 |

The local fuel regression rate along the grain axial direction was measured and the result is shown in Fig.3. The distribution of local regression rate showed same tendency for the different burning conditions. In #4-1 and #4-3, the local regression rate increased due to the increase of oxidizer mass flow rate comparing with those of #3-1 and #3-2. Using this data, the relation between axial-averaged local regression rate ( $\dot{r}_{f,x}$ , $\dot{r}_{r,x}$ ) and controlling parameters was examined as shown in Fig.4. At the grain leading edge region in Fig.4(a), $\dot{r}_{f,x}$ of #3-1, 3-2, and 4-1,3 correlated well with the controlling parameter. On the other hand, at the grain rear region in Fig.4(b) $\dot{r}_{r,x}$ of #3-1 and #3-2 were slightly lower than the correlation line and $\dot{r}_{r,x}$ of #4-1,3 decreased more. Hence, it is found that the decrease in local regression rate at rear region in #4-1,3 caused the decrease of fuel mass flow rate and thus the thrust did not reach to 5 kN. Since the controlling parameter at the rear region means the oxidizer mass flux, combustion at the rear region might become reaction rate limited process by the increased mass flux in #4-1,3.

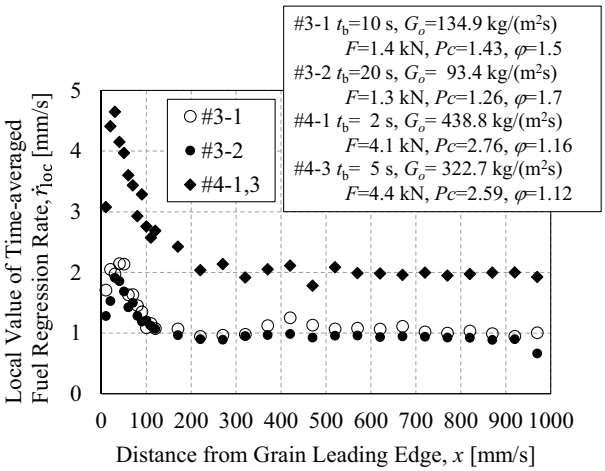

Fig.3 Variations of local fuel regression rate

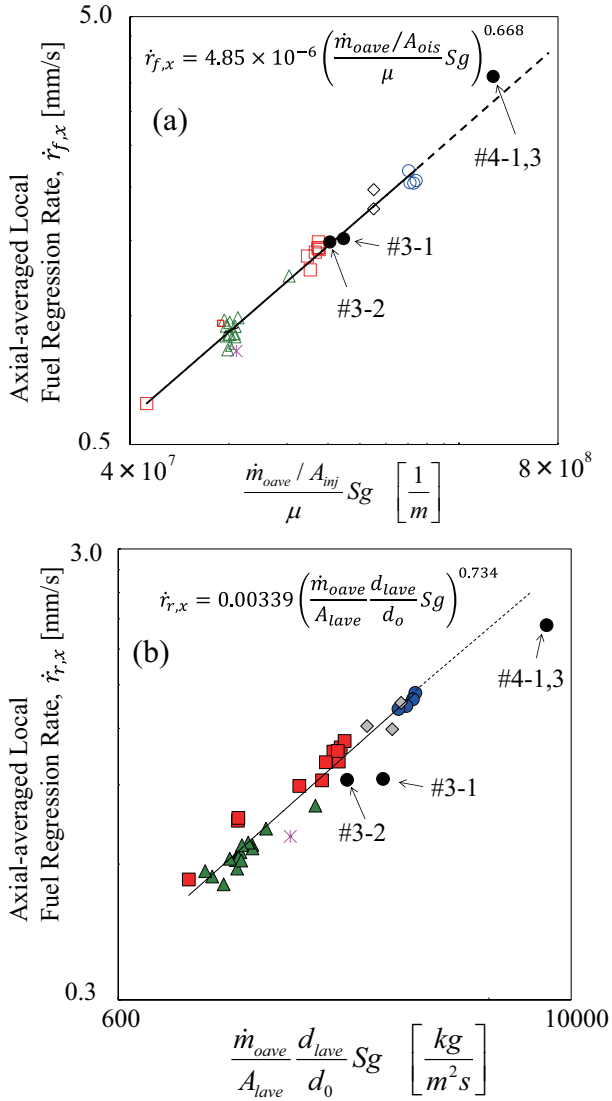

Fig.4 Relation between axial-averaged local fuel regression rate and controlling parameters

## 4. Concluding Remarks

- The burning tests up to 4.4 kN was carried out by using HTE5-1 using GOx/PP propellant. Stable combustion was attained and engine performance was obtained.
- Local fuel regression rates at grain leading edge region and rear region were evaluated. $\dot{r}_{r,x}$ showed lower regression rate than the prediction.


## Acknowledgments

This research is supported by the Hybrid Rocket Research Working Group (HRrWG) of Institute of Space and Astronautical Science, Japan Aerospace Exploration Agency. The authors thank Irie, G., Ozawa, K., Suzuki, N., and Yasuda, S. for their cooperation in conducting this study.


## References


[1] S. Yuasa., et al., *Proc. 57th Space Sciences and Technology Conference*, (2013) JSASS-2013-4515. (in Japanese)

[2] H. Ando., et al., *Proc. Asian Joint Conf. on Propul. and Power*, (2014) AJCPP-2014-164.

[3] S. Yuasa., et al., *Proc.48th AIAA Joint Propul. Conf.*, (2012) AIAA Paper 2012- 4106.

[4] K. Kitagawa., et al., *10th Inter. Sympo. on Special Topics in Chemical Propulsion*, (2014) Log#66.

# Development of High Performance Hybrid Rocket Engine with Multi-Section Swirl Injection Method through Combustion Visualization and Various Injection Modification

Shigeru Aso[1], Yasuhiro Tani[1], Kengo Ohe[1], Hiroshi Tada[1], Masato Mizuchi[1], Masato Yamashita[1] and Toru Shimada[2]
[1]Department of Aeronautics and Astronautics, Kyushu University, Fukuoka 819-0395, Japan
[2]ISAS, JAXA, Sagamihara 252-5210, Japan

**ABSTRACT**

In order to improve fuel regression rate of hybrid rockets, a new method with multi-section swirl injection has been proposed. The new method is to introduce swirling flow within fuel port through multi-section swirl injection holes, which are placed at several locations along the fuel grain. The method is applied for paraffin fuel (FT-0070) with pressurized gaseous oxygen. In order to clarify combustion phenomena of hybrid rocket engines with multi-section swirl injection method, visualization tests of combustion flames has been conducted.

## 1. Introduction

Recently, hybrid rocket engine becomes one of the promising space propulsion systems. The advantages of hybrid rocket engines are safety, low cost, throttling of thrust, re-ignition, nontoxic and nonhazardous propellant. However, hybrid rocket engines have low fuel regression rate and low combustion efficiency. In order to overcome those disadvantages, there are several research activities [1-6].

In the present study the new method that can improve the fuel regression rate more than that of conventional methods is proposed. The method is multi-section swirl injection method. In the previous, though the proposed method showed excellent increase of fuel regression rate [7-8]. In the present study, in order to clarify combustion phenomena of hybrid rocket engines with multi-section swirl injection method, visualization tests of combustion flames has been conducted.

## 2. Experimental Method

Figure 1 shows the schematic diagram of multi-section swirl injection method. The injection of the oxidizer through a number of injector holes that are set in the fuel grain causes swirling flow.

Figure 2 shows the schematic diagram of combustion chamber. The new combustion chamber for visualization was newly designed and built. The combustion chamber has quartz glass in front end of combustion chamber.

Paraffin fuel is used for the present study. Figure 3 shows the schematic diagram of each fuel grain shape. The fuel had a single port with an inner diameter of 35 mm and a length of 80 mm. Diameter of the injector holes, which inject the oxidizer, are 2 mm. Case 1 is standard grain shape of multi-section swirl injection method. Case 2 is intended to observe changes due to different number of injector ports in each cross-section. Case 3 and Case 4 are intended to observe changes due to different distance between each cross-section.

Figure 4 and Table 1 shows camera setup and settings. We use video camera and digital single-lens reflex camera.

Corresponding author: Shigeru Aso
*E-mail address*: aso@aero.kyushu-u.ac.jp

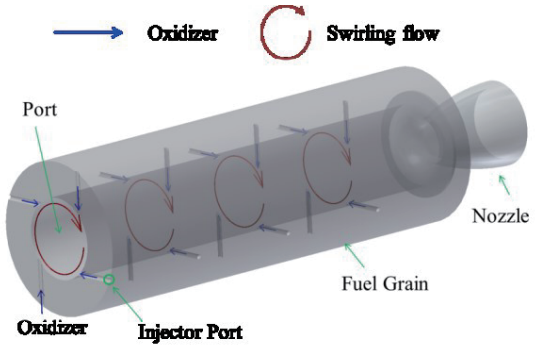


Fig. 1 Schematic diagram of multi-section swirl injection method

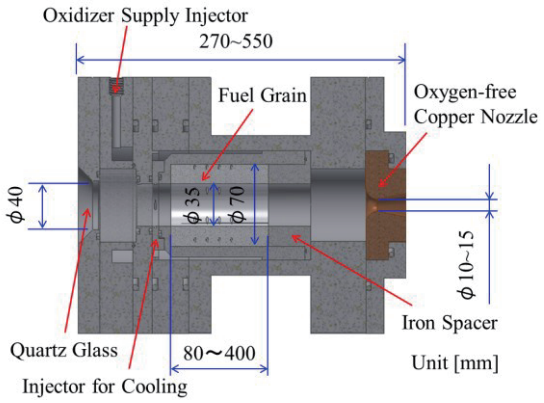


Fig. 2 Schematic diagram of combustion chamber

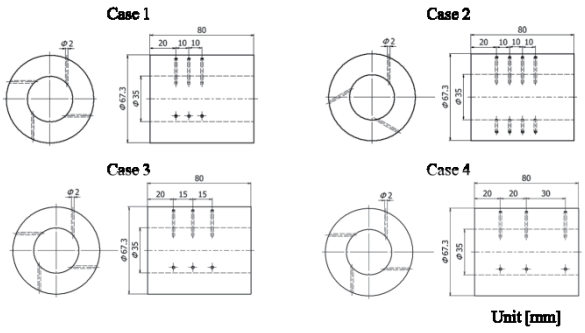


Fig. 3 Schematic diagram of each fuel grain shape

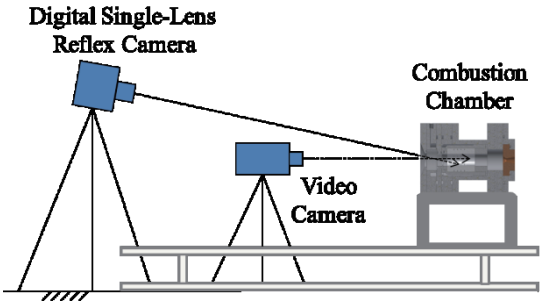


Fig. 4 Setup of cameras

Table 1. Camera settings

| | Video Camera | SLR Camera |
|---|---|---|
| Shatter Speed [s] | 1/2 - 1/1000 | 1/1600 |
| F-stop | F1.8 - 2.2 | F16 |
| Filter | ND 200 | ND 200 |

## 3. Results and Discussions

Table 2 shows results of each combustion test.

Table 2. Results of each combustion test

| | case 1 | case 2 | case 3 | case 4 |
|---|---|---|---|---|
| Fuel | Paraffin | | | |
| $p_c$ [MPa] | 0.97 | 0.96 | 0.93 | 0.92 |
| $t$ [s] | 2 | | | |
| $\overline{G_{ox}}$ [kg/m2·s] | 46.2 | 45.6 | 45.0 | 43.5 |
| $\dot{r}$ [mm/s] | 3.5 | 3.6 | 4.0 | 3.5 |
| $\overline{O/F}$ | 1.9 | 1.8 | 1.7 | 1.8 |
| c* effiency | 0.97 | 0.95 | 0.91 | 0.96 |

### 3.1 Comparison with different port placement in each cross-section

Figure 5 shows typical pictures of Case 1 and Case 2. Swirling turbulent flow and bright gaseous material was observed in whole of combustion chamber. There was dark region around injector ports in all cases with swirling injection. From results in Table 2 and Figure 5, the number of ports per section had marginal effect on regression rate with the paraffin fuel. This result contribute to reduce number of injector holes with keeping the same combustion performance.

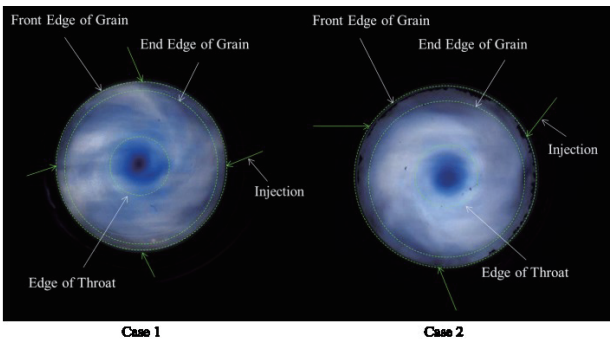


Fig. 5 Typical pictures of combustion chamber in Case 1 and Case 2

### 3.2 Effects of location of cross-sections on combustion performance

Figure 6 shows typical pictures of Case 1, 3 and 4. From those pictures, some common phenomena is observed. However, there are also some different combustion phenomena in pictures of in Figure 6. The color of combustion had changed from blue to red as the distance between cross-sections becomes longer. And Case 3 had a highest regression rate. This result indicates there might be the most suitable length between cross-sections. It is necessary to conduct more experiments in order to clarify the optimum distance between cross-sections and in order to improve engine performance.

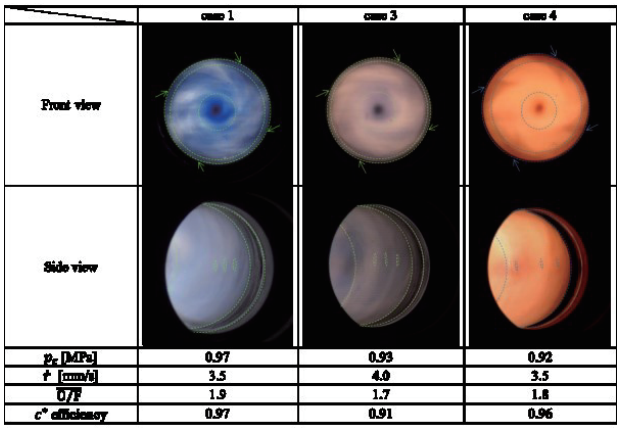


Fig. 6 Typical pictures of combustion chamber in Case 1, Case3 and Case 4

## 4. Conclusions

1) Swirling turbulent flow and bright gaseous material are observed in whole of combustion chamber.
2) There was dark region around injector ports in all cases with swirling injection.
3) The number of ports per section had marginal effect on regression rate with the paraffin fuel.
4) The color of combustion had changed from blue to red as distance between cross-sections becomes longer.

## References

[1] Nagata, H. et al.: Acta Astronautica, 59 (1-5) (2006), 253-258.
[2] Tamura, T. et. al.: AIAA paper 99-2323 (1999).
[3] William, H. et. al.: AIAA paper 99-2318 (1999).
[4] Aso, S. et. al.: AIAA paper 2011-5907 (2011).
[5] Sutton, G.P.: Rocket Propulsion Elements, John Willey & Sons, New York, 6th Edition (1992).
[6] Karabeyoglu, A. et. al.: Journal of Propulsion and Power, 20, No. 6 (2004), 1037-1045.
[7] Ohyama, S. et. al.: AIAA-2013-4040(2013)
[8] Araki, K. et. al.: AIAA-2013-3634(2013)

Eleventh International Conference on Flow Dynamics
October 8-10, 2014, Sendai, Miyagi, Japan

# Numerical and Experimental Investigation of Propulsion Performance of Single-Port Hybrid Motors with Thrusts of > 1,000 kgf

Tzu-Hao Chou[1], Guan-Rung Lai[1], Shih-Sin Wei[1], Jhe-Wei Lin[1], Jong-Shinn Wu[1], Yen-Sen Chen[2]
[1]Department of Mechanical Engineering, National Chiao Tung University
1001 University Road, Hsinchu, 30010, TAIWAN
[2]National Space Organization, National Applied Research Laboratories
8F, 9 Prosperity 1st Road, Hsinchu Science Park, Hsinchu, 30078, TAIWAN

**ABSTRACT**

In this paper we have presented CFD simulations and planned static-burn tests of several hybrid $N_2O$-HTPB motor designs with 2 stages of mixing enhancer with a thrust level of ~1000 and 3,500 kgf with and without a diaphragm. The simulation results show that with proper geometrical arrangement these motors can produce the required thrust levels with 250-270 s of vacuum ISP, depending upon whether a diaphragm is added in the post-combustion chamber. Several ground tests are in progress to verify these simulations.

## 1. Introduction

Hybrid rocket propulsion represents a potentially useful alternative technology as compared to solid and liquid ones and thus has received much attention recently because of its simplicity, safety, and throttling capability. In our group, we have been developing a two-stage sounding rocket system which can reach up to 100 km in altitude for carrying out ionospheric plasma measurement by the end of 2014 [1]. The scientific mission requires thrusts of ~3,500 kgf (12 s) and ~1,000 kgf (45 s), respectively, for the first and second stage. For simplicity, we have adopted a patented single-port hybrid combustor with 2-stage mixing enhancer using $N_2O$ and HTPB (hydroxyl-terminated polybutadiene) as oxidizer and fuel respectively [2]. Based on these requirements, we have initiated a series of CFD simulations and static burn tests aiming at verifying the designs. In this paper, we would like to report our progress in achieving this goal.

## 2. Numerical Method

In the CFD code, we have solved the continuity equation, the momentum equations (Navier-Stokes equations), the energy equation, the species continuity equations and the extended k-ε turbulence modeling equations using the finite-volume method with unstructured grid. In addition, a radiation heat transfer model and a finite-rate chemistry model with real-fluid modeling for mimicking two-phase nitrous oxide in the reacting process are also included. More details can be found in [3]. Parallel computing is realized through domain decomposition using message passing interface (MPI).

Diffusion-flame combustion is established when $N_2O$ is injected into a single-port combustion chamber and ignited to react with HTPB grain. Heat originated from the combustion decompose the $N_2O$ and HTPB through the influence of radiation and convection heat transfer process. In the reaction, the decomposition rate of HTPB is modeled using empirical correlations for energy balance through the pyrolysis process that presumably produces $C_4H_6$ (70%) and some $C_2H_4$ (30%) on the solid grain surface. The $C_4H_6$ and $C_2H_4$ are further decomposed into CO and $H_2$ as irreversible global reactions as part of the gas reaction mechanisms. The gas reaction steps mainly involve the $N_2O$ decomposition and the wet-CO mechanisms. In total, there are 16 species and 28 reaction channels considered in the chemical kinetics [4].

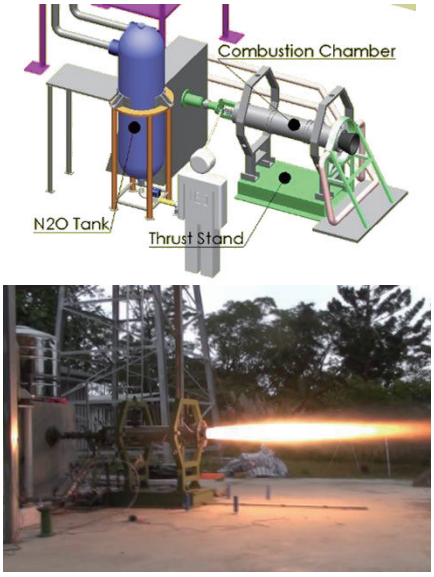


Fig. 1 Schematic diagram of the static-burn test facility (top) and snapshot of a test with a thrust level of 1,000 kgf (bottom).

## 3. Experimental Method

For verifying the design of hybrid motor proposed in the current study, several static-burn tests are planned using the test facility as shown in Figure 1. Time-dependent thrust, pressures and temperatures are measured during the tests, in addition to high-speed videotaping of the flame plume at a rate of 600 fps. The bottom image of Figure 1 shows the typical snapshot of static-burn test of 1,000-kgf hybrid $N_2O$-HTPB motor during 20 s of burn time.

Corresponding author: Jong-Shinn Wu
*E-mail address*: chongsin@faculty.nctu.edu.tw

## 4. Results and Discussion

CFD Simulations

Figure 2 show the typical temperature distribution of the hybrid motor with a thrust of ~1,000 kgf. The combustion chamber pressure is 28.1 bars with a total inlet pressure of 45 bars and corresponding O/F ratio is 8.13 that is still slightly fuel rich. The resulting thrust is 1,124 kgf with a vacuum ISP of 256 s, which is reasonably good for a single-port design. The results show that combustion efficiency is extremely high with very high and uniform temperature distribution after the 2nd stage of mixing enhancer. Without the addition of mixing enhancers, the vacuum ISP could be as low as 200-210 s.

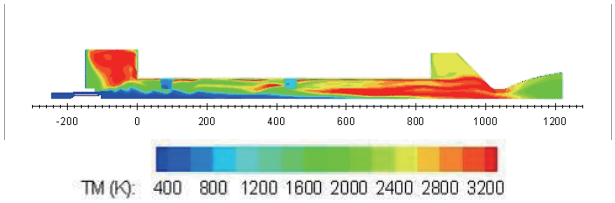


Fig. 2 Typical temperature distribution of hybrid motor with a thrust of 1,124 kgf.

For the case of 3,500 kgf hybrid motor, we have performed CFD simulations without and with a diagram with 8 through holes in the post-combustion chamber for comparison purpose. Figure 3 show the typical temperature distribution (> 3,000K) and molar fraction of oxygen (> 0.02) of the hybrid motor (~3,500 kgf) without the addition of a diagram. The combustion chamber pressure is 23.6 bars and corresponding O/F ratio is 12.71, which is highly fuel lean. The resulting thrust is 3,363 kgf with a vacuum ISP of 249 s that is not impressive. The combustion efficiency is not high since there is much oxygen leaving the chamber unburned as can be clearly seen in Figure 3. The unburned oxygen is highly corrosive (oxidative) to the graphite when it is used as the throat material.

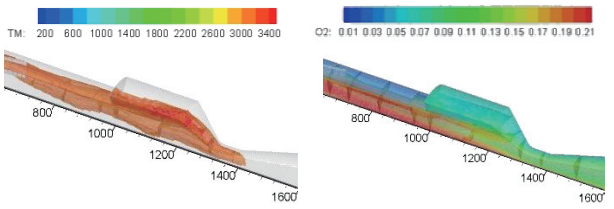


Fig. 3 Typical temperature distribution (> 3,000K) (left) and molar fraction of oxygen (> 0.02) (right) of the hybrid motor (~3,500 kgf) without the addition of a diagram.

Figure 4 shows that the typical temperature distribution (> 3,000K) and molar fraction of oxygen (> 0.02) of the hybrid motor (~3,500 kgf) with the addition of a diagram in the post-combustion chamber. The results show that the high-temperature region in the post combustion chamber becomes wider, which represents a better combustion efficiency that results in a much better propulsion performance (vacuum ISP: 272 s; thrust: 3,607 kgf; chamber pressure: 27.68 bars). In addition, almost all oxygen is depleted before reaching the nozzle throat since the O/F ratio (9.61) is very close to the stoichiometric value. This is very important for long-time combustion using graphite as the throat material, which we would like to verify from the planned near-future static-burn tests. However, the use of the diaphragm does have some drawbacks such as increase of the pressure drop from the port region into the post-combustion chamber at the cost of 2-3 bars and structure integrity, which is still worthwhile in general.

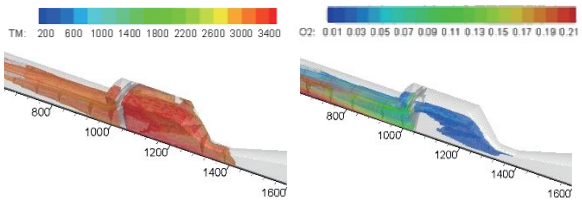


Fig. 4 Typical temperature distribution (> 3,000K) (left) and molar fraction of oxygen (> 0.02) (right) of the hybrid motor (~3,500 kgf) with the addition of a diagram.

## 5. Concluding Remarks

In this paper, a series of CFD simulations of 1,000-kgf and 3,500-kgf levels of hybrid $N_2O$-HTPB motors are presented along with limited static-burn tests (1,000-kgf). More detailed static-burn test data of the 3,500-kgf hybrid motor will be presented in the meeting.


## Acknowledgments

Financial support of Minister of Science and Technology through Grant No. 102-2627-E-009-001 computing resources provided by National Center for High-Performance Computing (NCHC) of Taiwan is highly appreciated.


## References


[1] J.-S. Wu, T.-H. Chou, Y.-S. Chen, H.-W. Hu, M.-T. Ho, H.-P. Lin, T.-L. Chen, Mathew R. Smith, Bill Wu, Y.-Y. Lin, *28th ISTS* (2011).

[2] U.S Patent, 2011/0203256 (2011).

[3] Wang & Chen, *J. of Prop. & Power*, 9:5 (1993).

[4] Y.-S. Chen, T. H. Chou, B. R. Gu, J.-S. Wu, Bill Wu, Y. Y. Lian, Luke Yang, *Computers & Fluids*, 45:29, (2011).

Eleventh International Conference on Flow Dynamics
October 8-10, 2014, Sendai, Miyagi, Japan

# Technological Issues of Hybrid Propulsion System Required for Practical Use

Koki Kitagawa[1], Toru Shimada[1]
[1]Japan Aerospace Exploration Agency
3-1-1, Yoshinodai, Chou, Sagamihara, Kanagawa, 252-5210, Japan

**ABSTRACT**

In Hybrid Rocket research Working Group, a three-stage clustering rocket which has unit hybrid rocket engines is suggested for a 100 kg-payload launcher. Key technologies to develop the unit hybrid rocket engine for the 100 kg-payload launcher are LOX-vaporization technology, scale-up technology, re-ignition technology and thrust control technology with optimal mixture ratio. Issue and experimental activities for these key technologies were introduced.

## 1. Introduction

Recently, demand for a low-cost launcher dedicated for nano/micro satellites is growing. In Hybrid Rocket research Working Group (HRrWG), a conceptual design of a low-cost three-staged launcher dedicated for 100 kg-payload has been conducted, with propulsion system assessment concerning the conformity to mission and system requirements and constraints [1]. As the result of this, a strong rational is obtained for using a cluster of unitary (unit) hybrid rocket engines for three stages and an example of design specification of a unit hybrid rocket engine is obtained utilizing a multi-objective optimization technology. Also, a 7-step development scenario is described from conceptual design to operation of the launcher. In the scenario, firstly one unique engine (unit engine) will be developed and flight-tested followed by a cluster engine systems development and flight test. Finally, the whole system will be developed and flight tested. The goals of current HRrWG are formulating the project plan to prove the unit engine with flight test, as well as developing element technologies sufficient to achieve the project.

In Table 1, a typical example of design specification of the unit engine obtained for a launcher capable of Sun synchronous transfer orbit (250x800 km, or equivalent energy level of 500 km SSO) is shown. The regression rate, here, is given by multiplying a magnification factor to the regression rate of the baseline fuel.

As described in Ref. [1], the third-stage engine should be capable of the second firing for apogee kick and this can be done by taking advantage of thrust control capability of hybrid propulsion systems.

In this paper, current situations, issues and experimental activities about technologies required to develop the unit engine are described.

## 2. Current Situations and Issues

Now, in order to demonstrate our hybrid propulsion technology obtained in HRrWG, a 5 kN hybrid rocket test engine program (HTE-5-1) is being conducted. The final goal (Goal III) of HTE-5-1 is that the oxidizer is liquid oxygen (LOX), the average thrust is more than 5 kN, the burning duration is more than 30 s, the average regression rate is more than 3 mm/s, and the average C* efficiency is more than 95%. Before this, we set two primary goals. Goal I is that the oxidizer is gaseous oxygen (GOX), the average thrust is more than 5 kN, the burning duration is more than 10 s, the average regression rate is more than 3 mm/s, the average C* efficiency is more than 95%. Goal II is that the oxidizer is LOX, the LOX flow rate is 1.5 kg/s, LOX is heated to more than 160 K and vaporized for more than 30 s.

Table 1. Specification of unit engine obtained via MOGA

| | 1st stage | 2nd stage | 3rd stage |
|---|---|---|---|
| Number of unit engines | 8 | 2 | 1 |
| Oxidizer | LOX | | |
| Baseline fuel | Wax(FT-0070) | | |
| Fuel mass [kg] | 377 | | |
| Fuel grain length [m] | 1.78 | | |
| Fuel grain outer diameter [m] | 0.764 | | |
| Fuel grain inner diameter [m] | 0.317 | | |
| Oxidizer mass flow rate [kg/s] | 23.2 | 9.29 | 6.73 |
| Regression rate magnification factor | 7.3 | 3.4 | 3.4 |
| Fuel regression rate (initial)[mm/s] | 10.5 | 3.42 | 3.02 |
| Fuel regression rate (burnout)[mm/s] | 5.20 | 1.69 | 1.49 |
| Oxidizer mass flux(initial)[kg/m$^2$-s] | 293 | 117 | 85.1 |
| Oxidizer mass flux(burnout)[kg/m$^2$-s] | 48.8 | 19.3 | 13.9 |
| Combustion pressure (initial)[MPa] | 1.56 | 0.84 | 0.52 |
| Thrust (initial) [kN] | 74.3 | 29.9 | 28 |
| Burning duration [s] | 33.5 | 104.4 | 118.3 |

In Table 1, the regression rate magnification factors are from 3.4 to 7.4. It means that the regression rate must be enhanced by some technic. Therefore, swirling-oxidizer-flow-type (SOFT) [2] is adopted. The 5 kN-thrust SOFT hybrid rocket engine using the GOX/PP propellant has been designed and manufactured as the demonstrator. Several combustion tests have been carried out and the average thrust of 4.4 kN for 5 s has been achieved, so far. Goal I will be achieved in this year. In SOFT hybrid rocket engine which is adopted in HRrWG, the oxygen to which swirl is applied should be in a gaseous state to increase the engine performance. Therefore, to achieve Goal II and III, it is necessary to acquire LOX-vaporization technology.

The thrust of the unit engine is about ten times higher than that of the demonstrator and the combustion duration of the unit engine is much longer. To design the unit engine, it is necessary to create the technology to scale-up.

Corresponding author: Koki Kitagawa
*E-mail address*: kitagawa.koki@jaxa.jp

In the third stage of the 100 kg-satellite launcher, after the launcher enters 250 x 800 km altitude Sun-synchronous transfer orbit, the third stage is quenched, and then the third stage is re-ignited at apogee. Therefore, functions of re-ignition and reliable ignition at vacuum condition are required of the unit engine. In the hybrid propulsion system, the combustion mechanism is boundary-layer combustion by diffusion flame near the fuel grain wall. Therefore, at the time of ignition, it is necessary to supply the oxidizer to the fuel grain wall. However, it is difficult to supply the oxidizer to the fuel grain wall at the condition of very low combustion chamber pressure because of rapid diffusion. It is necessary to confirm whether the fuel is ignited or not under the low pressure condition. If not, the ignition technology under the low pressure condition must be developed.

After re-igniting of the 3rd stage at apogee, low thrust must be kept in order to enter the payload to proper orbit. However, it is difficult to keep high specific impulse, because of the shift of the mixture ratio. Because the fuel regression rate of hybrid propulsion depend on oxidizer mass flux, combustion in optimal mixture ratio cannot be kept, when the oxidizer mass flow rate is changed or the inner diameter of fuel grain is changed. Therefore, it is necessary to develop the thrust control technology with optimal mixture ratio.

## 3. Experimental Activities

### 3.1. LOX-vaporization Technology

Some methods were proposed to vaporize liquid oxygen in HRrWG. One is a regenerative-cooling LOX-vaporization nozzle [3]. As the results of burning vaporization experiments, it was confirmed that LOX increased in temperature and sufficiently vaporized while passing through the nozzle. The engine performances were also increased due to the vaporized oxygen. There was no essential problem in vaporizing LOX with the nozzle. However, the cost of manufacturing this nozzle system is quite high, so far.

One is a combustion chamber type like a hybrid rocket engine. The other is a torch type [3], which burns a small amount of fuel in a large amount of LOX. These are being studied and developed. Furthermore, method of the vaporization by heat of decomposition of $N_2O$ or $H_2O_2$ by a catalyst is under consideration.

At first, trade-off analysis of the LOX-vaporization systems for the unit engine will be conducted from viewpoint of cost, performance, weight and so on to choose the proper LOX-vaporization system. Then, one of them will be constructed and vaporization tests will be conducted to demonstrate the LOX-vaporization technology.

### 3.2. Scale-up Technology

To scale-up, a prediction method of fuel regression rates must be created. After achieving Goal III, combustion tests with changing the oxygen mass flow rates and combustion duration parametric in the possible range with the HTE-5-1 demonstrator. Then, the regression rates of the unit engine will be predicted by numerical simulation with the combustion tests data.

### 3.3. Re-ignition Technology

We are trying to develop a plasma jet torch [1] to ignite the unit engine twice or more times. Argon gas is used for the plasma jet torch. Lab-scale ignition tests with the plasma jet torch have been conducted and ignition to some fuels were succeeded.

At the next step, lab-scale ignition tests with the plasma jet torch in a vacuum chamber will be conducted in order to obtain the reliable ignition technic at vacuum condition.

## 4. Thrust Control Technology with Optimal Mixture Ratio

In order to improve this problem, we focus on the technique of SOFT hybrid rocket engine. The increase of the fuel regression rate depends on the geometric swirl intensity of injector [2]. Therefore, if geometric swirl intensity is independently controllable [1],[4] during the operation, the fuel regression rate, in other words, the mixture ratio can be controlled. This means that hybrid rockets have an operational flexibility in operational range as liquid rockets. As a swirl intensity controllable injector, dual injection system is suggested [1],[4]. In this system have two injectors. One is axial-flow type. The other is swirling-flow type. Each line has oxidizer mass flow control valve independently. This system can control mass flow rate and swirl intensity simultaneously.

At first, in order to confirm the feasibility of this system, dual injection system without oxidize mass flow control valves will be constructed and the combustion tests will be conducted with constant swirl intensity during burning. Orifices will be used to keep the oxidizer mass flow rates instead of the control valves. Then, the full system will be designed and manufactured and the combustion tests will be conducted with controlling the mass flow rates and the swirl intensity.

## 5. Summary

Key technologies to develop the unit hybrid rocket engine for the 100 kg-satellite launcher are LOX-vaporization technology, scale-up technology, re-ignition technology and thrust control technology with optimal mixture ratio. Issues and experimental activities for these key technologies were introduced.

## References


[1] Shimada, T. et al., *Space Propulsion 2014*, (2014) 2980899.

[2] Yuasa, S., et al., *35th AIAA/ASME/SAE/ASEE Joint Propulsion Conference & Exhibit*, (1999) AIAA 99-2323.

[3] Yuasa, S., et al., *International Journal of Energetic Materials and Chemical Propulsion*, 10(2) (2011) 155 – 168.

[4] Ozawa, K. et al, *Space Transportation Symposium 2013*, (2013) STCP-2013-043. (Japanese)

# OS9: Advanced Control of Smart Fluids and Fluid Flows

# Development of a Novel Multi-Layer MRE Isolator

Jian Yang[1], Shuaishuai Sun[1], Weihua Li[1], and Masami Nakano[2]
[1]School of Mechanical, Materials and Mechatronic Engineering, University of Wollongong, Wollongong, NSW 2522, Australia
[2]Intelligent Fluid Control Systems Laboratory, Institute of Fluid Science, Tohoku University, 2-1-1 Katahira, Aoba-ku, Sendai, 980-8577, Japan

**ABSTRACT**

This paper presents the development of a novel MRE isolator that its stiffness was reduced when the applied current was increased. This innovative work was accomplished by applying a hybrid magnet (electromagnet and permanent magnets) onto a multilayered MRE structure. Its performance in terms of the effective stiffness and natural frequency was experimentally evaluated. The vibration suppression effectiveness was experimentally investigated.

## 1. Introduction

As a solution to dealing with the unwanted vibrations, the development of a magnetorheological elastomer (MRE)-based isolator has become a promising choice [1, 2]. The main idea of incorporating the MRE isolator in an isolation system is to shift the natural frequency of the primary structure as far away as possible from the excitation frequency, and when a multi-layered MRE is considered, the isolator will satisfy the required vertical load capacity while maintaining horizontal flexibility.

Due to its high efficiency and facility, a great deal of effort has been expended on developing the MRE isolator [3, 4]. A successful development and experimental evaluation of a MRE isolator was presented in [5]. Experimental results demonstrated that the force of the MRE isolator increased up to 1579% and the stiffness increased up to 1730%.

In this paper, a novel multi-layer MRE isolator which can achieve negative changing stiffness has been designed, fabricated, and evaluated. The testing results characterize the negative changing stiffness property of the MRE isolator and the vibration isolation experiment verifies the potential of the MRE isolator for isolation applications.

## 2. Design and Fabrication

One of the novel designs that had to be developed for this study was an adjustable hybrid magnet system with permanent magnets and electromagnetic coil, as shown in Figure 1. By incorporating the permanent magnets, a stable magnetic field (yellow circuit shown in Figure 1) could be applied to the multi-layer MRE structures at all times without any power consumption. Then the electromagnetic field (blue circuit shown in Figure 1) was responsible for either strengthening or weakening the nominal magnetic field through adjusting the direction and magnitude of the applied current. The stiffness of the MRE isolator was controlled by the superposition of the hybrid magnetic system. When a positive current was applied, the electromagnetic field was opposed to the permanent magnetic field, as shown in Figure 1, which means the superposition of the hybrid magnetic system was reduced such that the stiffness of the MRE isolator decreased. Otherwise, the hybrid magnetic system was strengthened, which means the stiffness of the MRE isolator increased. Figure 2 shows the prototype of the novel MRE isolator.

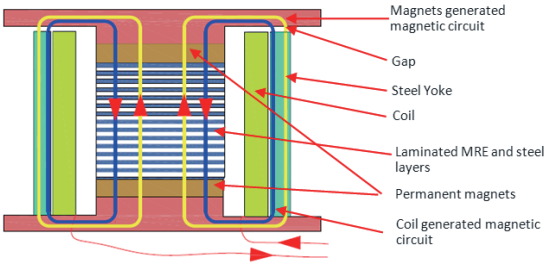


Fig. 1 Structure of the hybrid magnetic system.

Fig. 2 Prototype for the MRE isolator.

## 3. Testing Results

Figure 3 shows the experimental setup for testing the MRE isolator which was mounted on shaking table. Figure 4 shows the force-displacement relationships under different levels of applied current but same frequency and amplitude. It is clearly observed that the effective stiffness (slope of force-displacement loop) decreases when the applied current increases.

In order to further verify the negative changing stiffness of the MRE isolator, the transmissibility was provided in Figure 5. It is seen that the natural frequency shifted to the left when the current increased.

Corresponding author: Weihua Li
*E-mail address*: weihuali@uow.edu.au

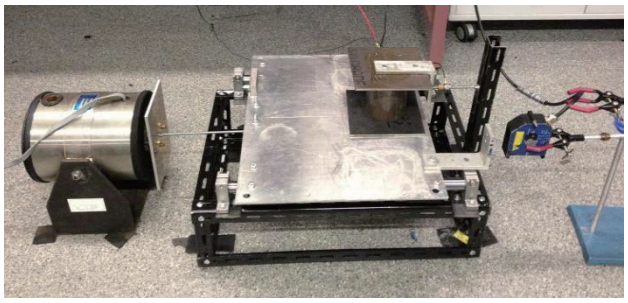

Fig. 3 Experimental Setup for testing the MRE isolator.

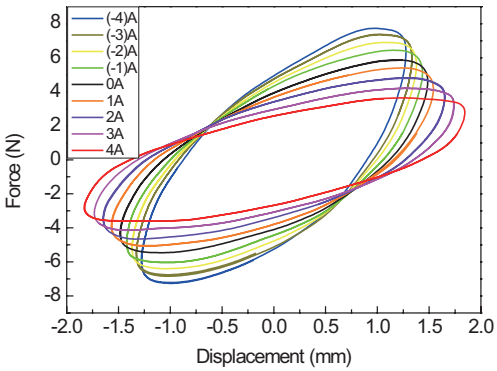


Fig. 4 Force versus displacement with various currents.

For the purpose of evaluating the effectiveness of the MRE isolator as an isolation device, the vibration isolation experiment was conducted. In the case, a mass was attached on the isolator serving as the primary system. The whole system can be represented by a single-degree-of-freedom system. The dynamic equation for the system is governed by:

$$m_p\ddot{x_p} + c_s(I)\left(\dot{x_p} - \dot{x_{in}}\right) + k_s(I)\left(x_p - x_{in}\right) = 0 \quad (1)$$

where $m_p$ represents the mass, $c_s(I)$ and $k_s(I)$ represent the controllable damping coefficient and lateral stiffness, respectively; and the control logic used is the ON-OFF control logic which is expressed as:

$$I = \begin{cases} 0, & if\,(x_p - x_{in})(\dot{x_p} - \dot{x_{in}}) > 0 \\ I_{MAX}, & if\,(x_p - x_{in})(\dot{x_p} - \dot{x_{in}}) < 0 \end{cases} \quad (2)$$

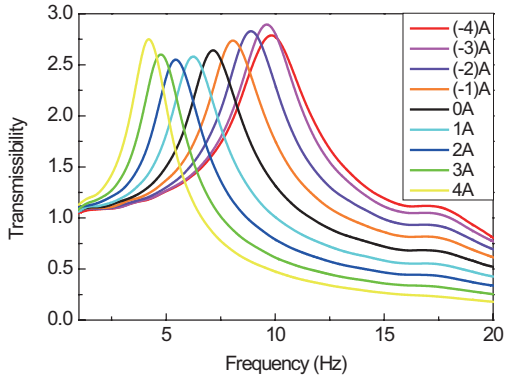


Fig. 5 Transmissibility versus frequency

Figure 6 shows the acceleration responses under ON-OFF control when the isolation system was subjected to a sinusoidal excitation with 5.55Hz which is the natural frequency of the system. It is seen that the acceleration is obviously reduced during the period when the ON-OFF control was working (10-15s). Figure 7 shows that the acceleration of the primary system was effectively reduced under ON-OFF control when the isolation system was excited by a sweep sinusoidal signal. Both of these figures demonstrated the feasibility of the proposed MRE isolator as an isolation device.

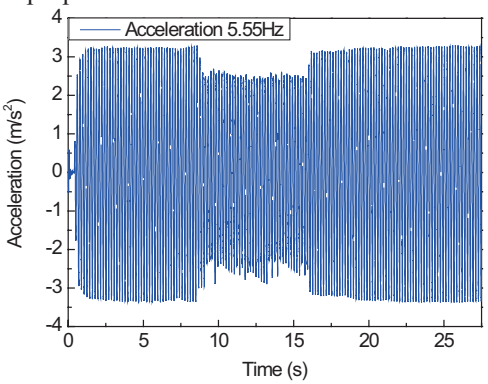


Fig. 6 Acceleration responses

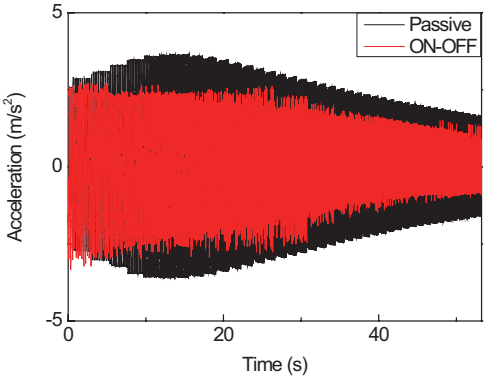


Fig. 7 Acceleration response under sweep sinusoidal

## 4. Concluding remarks

In this study, a novel MRE isolator that includes a hybrid magnetic system was presented. The force-displacement relationship and the natural frequency performances verified the property of negative changing stiffness of the MRE isolator. The acceleration responses under ON-OFF control logic demonstrated that the proposed MRE isolator is effective in isolating vibrations.

## References

[1] G Liao, X Gong, S Xuan, C Kang, L Zong, *J. Intell. Mater. Syst. Struct.*, 23 (2012) 25-33.

[2] J Li, Y Li, W Li, B Samali, *Proc. SPIE on Sensors and Smart Structures Technologies for Civil, Mechanical, and Aerospace Systems*, (2013), 8692.

[3] M Behrooz, X Wang, F Gordaninejad, *Smart Mater. Struct.*, 23 (2014) 045014.

[4] Y Li, J Li, W Li, B Samali, *Smart Mater. Struct*. 22 035005.

[5] Y Li, J Li, T Tian, W Li, *Smart Mater. Struct*. 22 095020.

Eleventh International Conference on Flow Dynamics
October 8-10, 2014, Sendai, Miyagi, Japan

# Creep and Recovery Behaviours of MR Shear Thickening Fluids

Tongfei Tian[1], Gangrou Peng[1], Weihua Li[1], and Masami Nakano[2]
[1]School of Mechanical, Materials and Mechatronic Engineering, University of Wollongong, Wollongong, NSW 2522, Australia
[2]Intelligent Fluid Control Systems Laboratory, Institute of Fluid Science, Tohoku University, 2-1-1 Katahira, Aoba-ku, Sendai, 980-8577, Japan

**ABSTRACT**

This paper presents experimental and modeling study of creep and recovery behavior of the novel liquid material Magneto-rheological Shear Thickening Fluid (MRSTF) under constant stresses. Experiments are carried out on a stress controlled rheometer with parallel plate configuration. The resultant strains are recorded as varied constant shear stresses are applied to the MRSTF, which demonstrate the viscoelastic properties of the fluid. On top of this, the experimental facts are predicted mathematically through a four-parameter model proposed with fair precision.

## 1. Introduction

The Magneto-rheological fluids (MRFs) as well as Shear Thickening Fluid (STFs) have separately attracted considerable interest due to their fast reversible response to either external magnetic field or rapid shear loading[1,2]. Unfortunately, however, many defects concerning both materials have been mentioned by many researchers: the sedimentation problems concerning the magneto-rheological fluids (MRFs), the shear thinning feature of MRFs upon abrupt deformation applied, and the passive formation of hydro-clusters which deliver the shear thickening phenomenon, just to mention a few [3-5]. According to the study of Brown *et al*. [6], attractive magnetization dipolar force could be applied to mask or control the onset of the shear thickening behavior as additional yield stress was triggered due to magneto-rheology. Besides, due to the fact that the fumed silica, which is a widely used particle in shear thickening study, is consider an adequate stabilizer to resolve the sedimentation problem of magneto-rheological fluids. Thus, the author proposed to include both properties in a combined manner by dispersing iron particles to base shear thickening medium of mixture of fumed silica and ethylene glycol, and the novel fluidic material is referred in context as Magneto-rheological Shear Thickening Fluid (MRSTF).

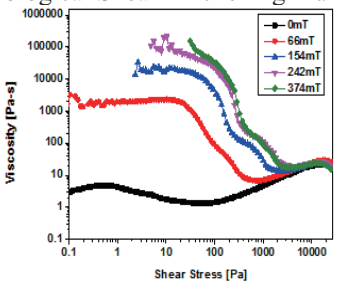


Fig.1 Stress Sweep of MRSTF under varied external field conditions

From Fig.1, MRSTF's steady property is presented. It is seen that through adding iron particles, the onset of shear thickening phenomenon point, as the shear stress point, where obvious viscosity increase is observed, shifts possesses wide controllability till magnetic saturat-ion right with the increase of external magnetic field.

In this paper, the creep and recovery behavior of the combined phase is illustrated with varied shearing conditions and quantified through mathematical method.

## 2. Method

The Shear Thickening Fluid was used as base material, where it is composed of hydrophilic fumed silica (S5505, from Sigma-Aldrich used as received) of a primary size of 14 nm and carrier fluid of ethylene glycol [$HOCH_2CH_2OH$] (102466, ReagentPlus, from Sigma-Aldrich). In this case 25% wt fraction sample was selected for study. Carbonyl iron particles (C3518, from Sigma-Aldrich) with 5 μm mean particle size were added to the prepared STF base to generate target Magneto-rheological Shear Thickening Fluid (MRSTF) samples, the sample fraction generated is 10% [7].

Creep is the time-dependent increase in strain (γ) of viscoelastic material under sustained stress ($\tau_0$). When the stress is removed, it enters recovery stage. In recovery stage, part of the time-dependent deformation is recoverable with time after the removal of stress. The schematic of the experiment as well as creep and recovery curve of a typical viscoelastic material at a constant temperature is shown in Fig. 2.

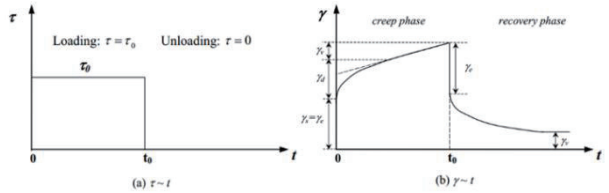


Fig.2 Creep and recovery behavior to applied constant stress for linear viscoelastic materials (a) τ-t (b) γ-t

In creep phase, the creep strain of viscoelastic material is expressed in following Eq.1:

$$\gamma_C(t) = \gamma_s + \gamma_d(t) + \gamma_v(t) \quad (1)$$

where $\gamma_s$ is the instantaneous strain, it is reversible elastic in nature. And it disappears immediately after stress removal and is usually represented to as $\gamma_e$. $\gamma_d(t)$ is the retardation strain. It is also elastic and can be recovered gradually with time elapse, thus it is also referred to as delayed elastic strain. $\gamma_v(t)$ is viscous flow, which is an irreversible component of strain.

For linear viscoelastic materials, the instantaneous strain $\gamma_s$ is sole elastic component, and is entirely recovered on unloading. However, when the applied

Corresponding author: Weihua Li
*E-mail address:* weihuali@uow.edu.au

stress increases beyond linear range, the irreversible plastic component $\gamma_p$ begins to grow, as shown in Fig.3. In this case the instantaneous strain is presented by Eq.2

$$\gamma_s = \gamma_e + \gamma_p \quad (2)$$

## 3. Results and Discussion

Constant stress level is an important factor on the creep and recovery behavior of viscoelastic materials. Thus, series of tests of different constant stresses are conducted with and without external magnetic field, as details given in Fig.4 and Fig.5.

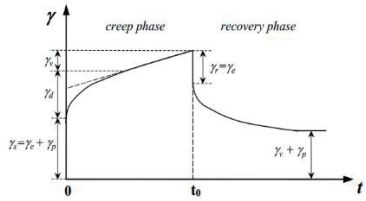


Fig.3 Creep and recovery behavior of nonlinear viscoelastic materials

In Fig.4, we can see that the strain is increasing considerably and proportional with the increase of creep time when the external magnetic field is absent, which signals the tested fluid has started to flow at quite small amount of shear stress as Newtonian liquid. And at this occasion the discussion concerning creep and recovery behavior is invalid.

The creep and recovery experiment result with the application of magnetic field is given in Fig.5. The standard figures of creep recovery like what is given in Fig.2 and 3 can be shown as represented in Fig.5. When the external shear stress is small, for instance 50 Pa, the instantaneous deformation at the application of constant stress is equal to the instantaneous strain recovery at the removal of constant stress, this means that the MRSTF at this stage performs within linear viscoelastic range.

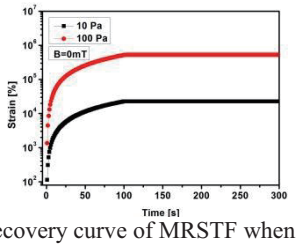


Fig.4 Creep and recovery curve of MRSTF when external magnetic field is absent

As the external shear stress increases, the creep strain increases. The instantaneous recovery deformation is, however no longer the same with the instantaneous strain, this phenomenon demonstrates that the irreversible plastic component of the strain grows. Unlike typical MR fluids [8], the MRSTF still exhibits observable strain recovery when relatively large applied shear stresses are removed. This signals the interaction of iron particle and shear thickening medium fluid.

From the description of the experimental results, it is clear to see that the creep and recovery property is an efficient tool to scale the transient property of viscoelastic material. Also the elastic, plastic and viscous component of the fluid behavior can be quantitatively defined. To this end, a four-parameter model is proposed to simulate the creep behaviour of MRSTF, the schematic diagram is given in Fig.6. The plastic-elastic parameter $K_p$ and $K_e$ is used to represent the instantaneous strain consisting of plastic strain and elastic strain. The retardation strain is attributable to the Voigt element. Therefore, the time dependent strain can be represented in Eq.3

$$\gamma = \frac{\tau_0}{K_p} + \frac{\tau_0}{K_e} + \frac{\tau_0}{K_1}\left(1 - e^{-t/\tau_R}\right) \quad (3)$$

where $t$ is the time elapsed during the experiment, $K_p$ is defined as 'plastic modulus' and $\tau_R = C_1 / K_1$

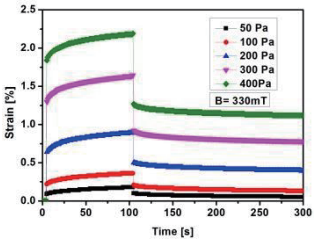


Fig.5 (a) Creep and recovery curve of MRSTF (stress less than 500 Pa), B=330mT

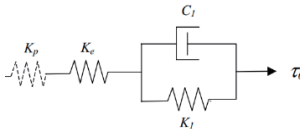


Fig.6 A schematic of four-parameter model to simulate the creep behavior of MRSTF

The comparison between the model prediction and actual experimental result is thus given in Fig.7, where the creep stages of MRSTF experiencing 50Pa and 100Pa shear stress are exemplified.

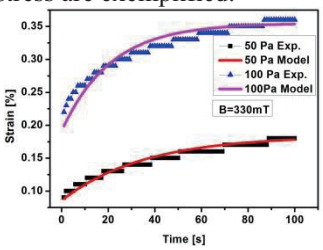


Fig.7 Comparison of model prediction and experimental data

## 4. Concluding Remarks

In this paper, the creep and recovery property of MR Shear Thickening Fluids under constant shear stress is investigated experimentally. Also, modelling approach is also adopted in reconstructing the experimental behavior of the MRSTF fluid being studied in the context though a proposed 4 parameter model, where the strain deformation contributions are clearly defined.

## References


[1] J. de Vincente, D. J. Klingenberg, R. Hidalgo-Alvarez, *Soft matter,* 7 (2010).

[2] Fischer, C., Braun, S.A., Bourban, P.E., Michaud, V., Plummer, C.J.G. and Manson, J.A.E., *Smart Mater. Struct.* 15(2006).

[3] Gong, X.L., Xu, Y.G., Xuan, S.H., Guo, C.Y. and Zong, L.Z., *J.Rheol*, 56 (2012).

[4] Neagu, R.C., Bourban, P.E. and Manson, J.A.E., *Composites Science and Technology*, 69 (2009).

[5] Bender, J.W., Wagner, N.J., *Journal of Colloid and Interface Science*, 172 (1995).

[6] Brown, E. et al., *Nature Materials*, 9 (2010).

[7] X. Z. Zhang, W. H. Li and X. L.Gong, *Smart Mater. Struct.* , 17 (2008).

[8] Li W H, Du H, Chen G, Yeo S H. *Materials Science and Engineering A*, 333(2002).

# Water Flow Produced by the Oscillation of Magnetic Fluid Adsorbed on a Permanent Magnet in Alternating Magnetic Field

Masahide Ito[1], Seiichi Sudo[1] and Hideya Nishiyama[2]
[1]Faculty of Systems Science and Technology, Akita Prefectural University
Ebinokuchi 84-4, Yurihonjo 015-005, Japan
[2]Institute of Fluid Science, Tohoku University
Katahira 2-1-1,Aoba-ku, Sendai 980-8577, Japan

**ABSTRACT**

This paper is concerned with the development of micro magnetic fluid devices driven by the alternating magnetic field. Water flows produced by the oscillating surface of magnetic fluid adsorbed on a permanent magnet in alternating magnetic field were examined by using a high-speed video camera system. The displacements of surface oscillations were measured by the image analysis system. The velocity of water flow produced from the magnetic fluid surface were observed and measured. The vortex pattern in water flow was observed at the front of four flows.

## 1. Introduction

With the development of micro electromechanical systems, the importance of the development of micro mechanisms and micro actuators well recognized. Therefore, extensive investigations on the micro devices have been conducted and reported. Authors also proposed novel micro electromechanical actuators using permanent magnet and magnetic fluid [1-4].

On the other hand, horizontally oriented labyrinthine pattern of magnetic fluid between closely spaced parallel plates subject to uniform magnetic fluid was established [5]. Theory for onset of the instability has been developed by Cebers and Maiorov for flat interface [6], drop [7], and bubble [8]. Authors also proposed the dynamic behavior of magnetic fluid adsorbed on the disk-shaped permanent magnet placed in the confined space between two parallel plates subject to alternating magnet field [9]. However, the water flows around the magnetic fluid subject to external magnetic fields have not been studied. There are many points which must be clarified.

In this paper, the micro water flows produced by the oscillation of magnetic fluid adsorbed on the disk-shaped permanent magnet placed in the confined water channel subject to alternating magnet field were studied experimentally.

## 2. Test Device

In this experiment, the micro device composed of magnetic fluid and a disk-shaped permanent magnet placed in the closely spaced parallel plates was examined. Test device is shown in Fig. 1. In this device, excellent $Nd_2Fe_{14}B$ permanent magnet was used. The permanent magnet was sandwiched between two acrylic plastic plates. Dimensions of the permanent magnet were 5mm in diameter and 5mm in height. Magnetic fluid was adsorbed on the magnet by the magnetic body force. The direction of the magnetic field of the magnet was parallel to the surface of the flat plate. The magnetic flux density of the magnet was 450mT at the surface. The sample magnetic fluid was kerosene-based

Corresponding author: Seiichi Sudo
*E-mail address*: sudo@akita-pu.ac.jp

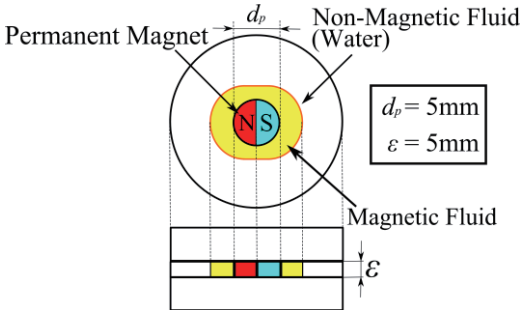


Fig. 1 Test magnetic fluid device.

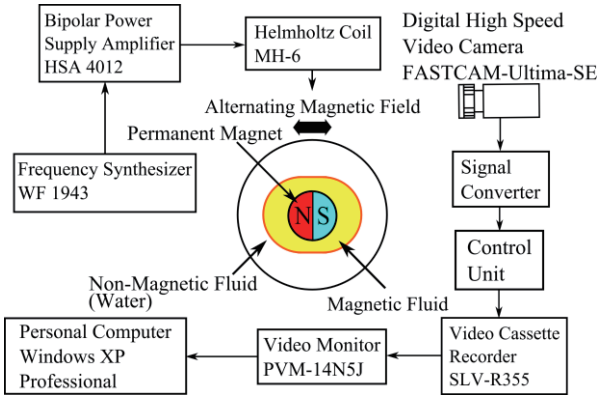


Fig. 2 Block diagram of experimental apparatus.

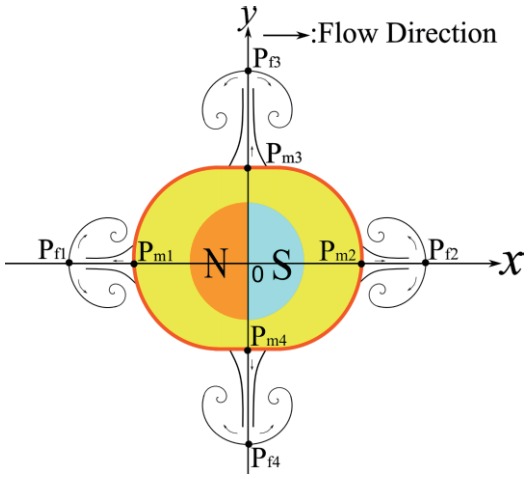


Fig. 3 Definition of coordinate system.

magnetic fluid. Test fluid as non-magnetic fluid in Fig. 1 was distilled water.

## 3. Experimental Apparatus and Procedures

A block diagram of the experimental apparatus is shown in Fig. 2. The experimental apparatus consists of the test magnetic fluid device, alternating magnetic field generation system, and optical measurement system. The alternating field was generated by applying alternating voltage to the Helmholtz coil. The alternating voltage signal was supplied from the frequency synthesizer. The directions of the alternating magnetic field were parallel and anti-parallel to the magnetic field produced by the permanent magnet. The optical measurement system was composed of a high-speed video camera system and personal computer. The motion of magnetic fluid was recorded with the high-speed video camera and analyzed by the personal computer. In the experiment, the applied voltage was given in the sinusoidal form. The magnetic field was generated at a constant voltage $E_0$. The experiment performed under the condition of room temperature.

## 4. Experimental Results and Discussion

*4.1 Oscillating response of magnetic fluid drop*

The response of magnetic fluid in the water subject to external alternating magnetic field was studied in the first stage. When alternating magnetic field was applied to the magnetic fluid adsorbed on the permanent magnet, the oscillation with small amplitude was generated on the magnetic fluid surface. In the analysis, the coordinate system was given as shown in Fig. 3. Figure 4 shows the surface oscillation of magnetic fluid at $P_{m2}$ in Fig. 3. It can be seen from Fig. 4 that response frequency of surface oscillation at $P_{m2}$ was precisely same that of the external alternating magnetic field.

*4.2 Micro water flow*

Four micro water flows were produced from the magnetic fluid surface by the oscillating magnetic fluid surface. Figure 5 shows the photograph of the flow pattern produced by the surface oscillation of magnetic fluid. It can be seen from Fig. 5 that four micro streams flow four directions such as, up, down, right, and left. The vortex pattern is recognized at four flow tips.

Figure 6 shows the position change of flow tip at $P_{f2}$ defined in Fig. 3. The time $t$ was defined by $t = 0$ at the moment of start of excitation external magnetic field. The velocity of water flow is $v_w = 6.67$ mm/s at the initial stage ($t < 0.1$ s). In the next stage ($t \geq 0.6$ s), velocity of flow shows the constant value ($v_w = 0.94$ mm/s).

## 5. Concluding Remarks

The water flows produced by the oscillation of magnetic fluid adsorbed on a permanent magnet in alternating magnetic field were observed and the flow velocity was measured. It was found that the flows with four different directions were generated from the surface of magnetic fluid with the start of alternating magnetic field. The vortex pattern in each flow tip was observed.

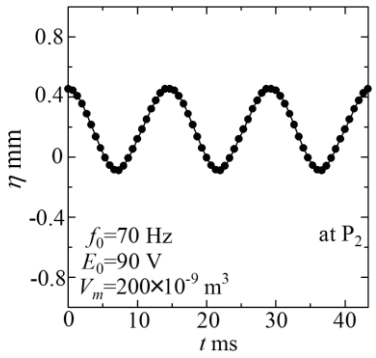


Fig. 4 Responses of magnetic fluid surface.

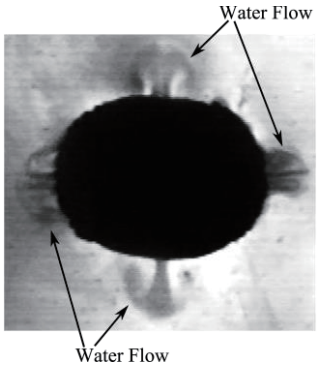


Fig. 5 Water flow of magnetic fluid drop in AC field.

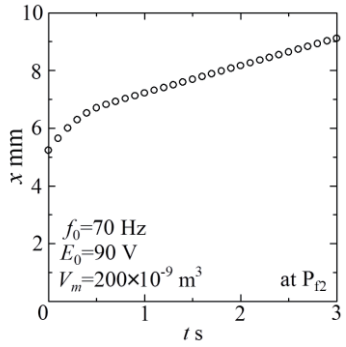


Fig. 6 Responses of water flow.

## References


[1] S. Sudo, Y. Takaki, Y. Hashiguchi, and H. Nishiyama, *JSME Int. J.*, 48(2005) 464.

[2] S. Sudo, T. Yano, M. Okabe, and T. Komatsu, *Int. J. Appl. Electromagn. Mech*., 25(2007) 95.

[3] S. Sudo, T. Goto, T. Yano, M. Futamura, H. Takana and H. Nishiyama, *J. Solid Mech. Mater. Engn*., 6(2012) 555.

[4] S. Sudo, D. Asano, H. Takana, and H. Nishiyama *J. Magn. Magn. Mater*., 323(2011) 1314.

[5] R. Rosensweig, M. Zahn, and R. Shumovich, *J. Magn. Magn. Mater*, 39(1983) 127.

[6] A.O. Cebers and M.M. Maiorov, *Magnetohydrodynamics*, 2 (1980) 22.

[7] A.O. Cebers and M.M. Maiorov, *Magnetohydrodynamics*, 1(1980) 27.

[8] A.O. Cebers and M.M.Maiorov, *Magnetohydrodynamics*, 3(1980) 15.

[9] M. Ito, S. Sudo and H. Nishiyama, *Proc. 13th Int. Symp. Adv. Fluid Info*., (2013) 70.

Eleventh International Conference on Flow Dynamics
October 8-10, 2014, Sendai, Miyagi, Japan

# Application of Electrorheology to Improve Energy Production

Rongjia Tao
Department of Physics, Temple University
1900 N 13th Street, Philadelphia, PA 19122, USA

**ABSTRACT**

Recently, we developed a new green technology, utilizing eletrorheology to make the viscosity of crude oil inside a pipeline anisotropic: along the flow direction the viscosity is significantly reduced, while in the directions perpendicular to the flow it is substantially increased. In such a way, the turbulence inside the pipeline is suppressed and the flow output along the pipeline is greatly enhanced. Our recent field tests fully confirm the theoretical prediction, showing that the required pump power is substantially reduced. This technology will have great impact on energy production.

## 1. Introduction

At present, most of our energy comes from liquid fuels. The viscosity plays a very important role in liquid fuel production. For example, to improve transportation of crude oil via pipeline, we need to reduce the oil's viscosity along the flow direction and suppress turbulence inside the pipeline. These are especially important for the off-shore crude oil production, requiring transportation via deep water pipeline at a very low temperature. Currently, the dominant method to reduce viscosity is to raise the oil temperature, which not only requires much energy, but also impacts the environment. Moreover, raising temperature does not suppress turbulence. As the Reynolds number goes up with temperature, the turbulence is, in fact, getting worse.

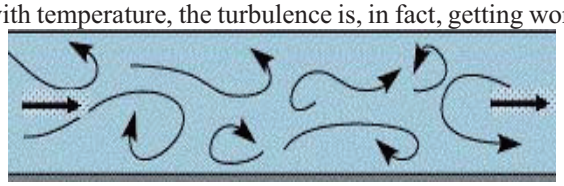

Fig.1 Turbulent flow inside a pipeline.

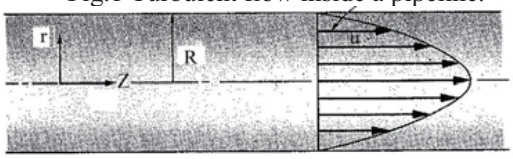


Fig.2 Laminar flow inside the pipeline

Shown in Fig.1 is a turbulent flow inside a pipeline when the Reynolds number > 2300. To enhance the flow output, we need to reduce the viscosity along the flow direction. Meanwhile, in order to suppress turbulence, we need to prevent the fluid's motions in the directions perpendicular to the flow direction as all vortices in turbulence must have the fluid moving in the directions transversal to the pipeline axis. This can be achieved if we raise the oil's viscosity in the directions perpendicular to the pipeline axis. In such a way, the rotational symmetry is broken and the fluid must have anisotropic viscosity. Such a fluid will then only move along the pipeline axis to become laminar even if the Reynolds number is much higher than 2300 (Fig.2).

Recently, based on the basic physics of viscosity, we developed a new green technology, which utilizes electrorheology to change the rheology of complex fluid and make the fluid viscosity anisotropic [1]. Along the flow direction, the viscosity is significantly reduced; while in the direction perpendicular to the flow direction, the viscosity is substantially increased. In this way, the turbulence is suppressed, the flow output is enhanced, and the required power to pump the flow is significantly reduced. The technology is friendly to the environment, energy-efficient, universal, and applicable to all complex fluids with suspended particles in nano-meters, sub-micrometers, or micrometers. We have applied this technology to crude oil. The results are very significant.

Corresponding author: Rongjia Tao
*E-mail address:* rtao@temple.edu.

## 2. Method

Einstein [2] first studied a dilute liquid suspension of non-interacting uniform spheres in a base liquid of viscosity $\eta_0$ and found the effective viscosity $\eta = \eta_0(1+2.5\phi)$, which is good for a very small particle volume fraction $\phi$. For high $\phi$, we must consider the maximum volume fraction $\phi_m$ available for adding particles. Let us consider adding $d\phi$ spheres to a liquid suspension of volume fraction $\phi$. As the net available volume fraction to add spheres is only $1-\phi/\phi_m$ now, the increase of viscosity would be $d\eta/\eta = 2.5d\phi/(1-\phi/\phi_m)$. Integrating this equation gives $\eta/\eta_0 = (1-\phi/\phi_m)^{-2.5\phi_m}$, applicable for high. $\phi$, too. Krieger-Dougherty introduced the intrinsic viscosity $[\eta]$ for particles of different shapes [3],

$$\eta/\eta_0 = (1-\phi/\phi_m)^{-[\eta]\phi_m} \quad (1)$$

which enables us to estimate the viscosity for particles of any shape by choosing a suitable $[\eta]$. It should also be noted that $[\eta]$ can have different value along different direction. In this way, Equation (1) enables us to calculate anisotropic viscosity.

Crude oil is a liquid suspension. The base liquid of crude oil, gasoline, has very low viscosity. The oil's high viscosity is due to randomly suspended paraffin, asphalt, and other particles in the base liquid. Our technology is illustrated in Fig.3: a strong electric field is applied along the flow direction in a small section of the pipeline. Because the suspended particles and the base liquid have different dielectric constants, the suspended particles are polarized once the electric field is applied. As the dipolar interaction is strong enough, the particles aggregate along the field direction to form short chains

or ellipsoids. Hence, the symmetry is broken. Similar to a flow of nematic liquid crystal with its molecule alignment in one direction, the viscosity is no longer isotropic [4]. Based on the neutron scattering information [5], we can approximate the short chain by a prolate spheroid with its rotational z-axis along the flow direction (Fig.4),

$$(x^2 + y^2)/b^2 + z^2/a^2 = 1 \qquad (2)$$

For such spheroid, the intrinsic viscosity $[\eta]$ along the z- axis, is much smaller than that of the intrinsic viscosity along the other direction,. If *(a-b)/a=0.9,* for example, we have $[\eta]_z = 2.01$ while $[\eta]_\perp = 4.48$ [6].

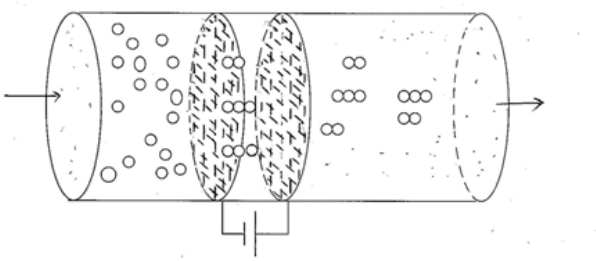

Fig.3 As the flow passes a strong electric field, the suspended particles aggregate along the field direction and the effective viscosity becomes anisotropic.

Fig.4 The aggregated short chain.

Fig.5 The new device on pipeline.

In application of Eq.(2), we also note that recent work finds that $\phi_m$ strongly depends on the particle shape. For spheres, $\phi_{sphere} = 0.64$ and for spheroids $\phi_{spheroid} \geq 0.72$, higher than that for spheres [7]. If $\phi = 0.5$, the original viscosity is $\eta/\eta_0 = 11.38$; after the electric field is applied, the viscosity along the flow direction is reduced to $\eta_z/\eta_0 = 5.56$, down 51.1%, while the viscosity perpendicular to the flow is increased to $\eta_\perp/\eta_0 = 45.80$, up 302%. As the viscosity in the directions other than the flow direction is increased substantially, the turbulence is suppressed. Meanwhile, the reduced viscosity along the axial direction enhances the flow output.

**3. Results and Discussion**

Recently we conducted a field test at crude oil pipeline with our viscosity reduction device (Fig.5). The crude oil is asphalt based and has viscosity $\eta = 214.1$ cp at $25^0$C. The pipeline has diameter D=88.9cm. Before our device was turned on, the flow rate was 2345 $m^3$/h and the pump power was 1800 kW. After the device was turned on, the oil viscosity along the flow direction was reduced to 110cp. While the flow rate was unchanged, the pump power consumption was down with time and eventually stayed at about 398KW, reduced by 77.9%.

Before the electric field was applied, the Reynolds number $N_R = \rho v D/\eta = 4061$, where $v$ is the flow velocity and the oil density $\rho = 0.932 g/cm^3$. As the friction factor $f_T = 0.314/(N_R)^{0.25} = 0.039635$ for the turbulent flow, $Pwi = \pi\rho v^3 D L f_T/8$ is the required pump power if other pressure loss was ignored. Here $L$ is the pipeline length. After the electric field was turned on, while $N_R$ was increased to 7904 due to the reduced viscosity along the flow direction, the turbulence was suppressed in the section of pipeline occupies by treated oil. The friction factor $f_L = 64/N_R = 0.0080967$ is for the laminar flow. The pump power for $0 \leq t \leq L/v$ is

$$Pw(t) = \pi\rho v^3 D[vtf_L + (L - vt)f_T]/8. \qquad (3)$$

After $t \geq L/v$, the pump power is $Pwf = \pi\rho v^3 D L f_L/8$.

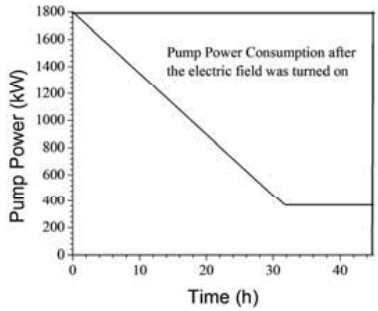


Fig.6 The observed pump power after the electric field was turned on.

Ignoring any other power loss, we could estimate that the final pump power $Pwf=(f_L/f_T)Pwi=367.7$kW. In our test, the pump power was eventually kept about 398 kW, very close to our estimation. The energy saving is very significant.

**4. Concluding Remarks**

The above finding fully confirms that application of electrorheology can reduce the viscosity and suppress turbulence for crude oil in pipeline. The new technology will have great impact on energy production. The basic physics here is general, applicable to other fluids as well.

This work was supported in part by STWA

**References**

[1] R. Tao and X. Xu, *Energy & Fuels*, 20 (2006) 2046.
[2]A. Einstein, *Ann. Physik* , 17(1905) 549-560; *Ann Physik* 19(1906) 289-306.
[3] I. M. Krieger & T. J. Dougherty, *Tans. Soc. Rheol*. 3 (1959) 137.
[4] M. Miesowicz, *Nature* ,158 (1946) 27.
[5] R. Tao, *et al*, *Fuel* , 134 (2014) 493-498.
[6] G. B. Jefferry, *Proceedings of the Royal Society of London Series A,* V.102, Issue 715 (1922) 161.
[7] W. Man, *et al*, *Phys Rev Lett*, 94 (2005) 198001 1-4.

Eleventh International Conference on Flow Dynamics
October 8-10, 2014, Sendai, Miyagi, Japan

# Electro-Rheological Behavior and Microstructure of Nano-Suspensions based on Titanium Dioxide Nano-Particles

Katsufumi Tanaka[1], Haruki Kobayashi[1], and Masami Nakano[2]
[1]Department of Macromolecular Science and Engineering, Kyoto Institute of Technology,
Matsugasaki, Kyoto 606-8585, Japan
[2]Institute of Fluid Science, Tohoku University,
Katahira, Sendai 980-8577, Japan

**ABSTRACT**

Flow behavior and microstructure were discussed for electro-rheological (ER) nano-suspensions based on titanium dioxide nano-particles with particle diameter on the order of 100 nm. The ER effect was also discussed in relation to the microstructure developed between parallel plates of the rheometer.

## 1. Introduction

A suspension composed of micro-particles and insulating oil is known to show the electro-rheological (ER) effect [1]. The flow of the ER micro-suspension under no electric fields is generally assumed to be the Newtonian flow. Under an electric field, the flow is well assumed to be the Bingham flow. In such a micro-suspension, a chain-like microstructure along the electric field is induced, the ground state of which was found to be a body-centered tetragonal (bct) lattice [2]. A ring-like microstructure was also observed under shear and electric fields [3]. Because a characteristic response time of the ER micro-suspension is on the order of milliseconds [4, 5], there are expectations for applications [6], such as dampers, clutches, valves, robotics, force display devices, and so on.

For practical applications, however, there are still demands for the ER fluid to be improved. Although a much higher yield stress has been a major demand, stability in the ER effect would also be a demand. Recently, a suspension based on rutile titanium dioxide ($TiO_2$) nano-particles with diameter of primary particles around 15 nm has been reported [7]. The suspended secondary particles were remarkably stable against sedimentation and electrical breakdown. The nano-suspension showed a good fluidity within a narrow gap, while it showed a plateau stress at the lower shear rates under no electric fields.

In a previous paper, the flow behavior and microstructure were reported for nano-suspensions based on nano-particles of $TiO_2$ with particle diameter around 400 nm suspended in chemically-modified silicone oils with viscosities of 0.1 and 0.04 Pa·s. The ER effect was also reported [8]. The nano-suspensions based on the modified silicone oil of 0.04 Pa·s showed lower stresses than those of 0.1 Pa·s under no electric fields and comparable stresses under the electric field.

In the present paper, the flow behavior and microstructure will be reported for nano-suspensions based on nano-particles of rutile $TiO_2$ with particle diameter around 400 nm suspended in the chemically-modified silicone oil of 0.04 Pa·s. The effects of particle volume fraction will be reported for the nano-suspensions. The ER effect will also be reported. Furthermore, the effect of shear rate and time on the shear stress and flow behavior in the presence of the dc electric field will be reported.

Corresponding author: Katsufumi Tanaka
*E-mail address*: ktanaka@kit.ac.jp

## 2. Experimental

Nano-particles of rutile $TiO_2$ with particle diameter ($2a$) around 400 nm were suspended in a chemically-modified silicone oil with a viscosity of 0.04 Pa·s. The volume fractions of the particles ($\phi$) were from 1.2 to 25 vol%. The rheological measurements were performed at room temperature using a rotational rheometer [7-10]. Particle behavior was observed using an optical microscope equipped with a CCD camera. The effect of shear rate and time on the shear stress and flow behavior in the presence of the dc electric field was also investigated using a specially designed rheometer at Tohoku University, with increasing and decreasing the shear rate from 0.1 to 1000 $s^{-1}$.

## 3. Results and Discussion

Figure 1 shows the shear stress under no electric fields plotted logarithmically against the shear rate for the nano-suspensions based on the modified silicone oil of 0.04 Pa·s. The particle volume fractions were 8.8, 12, 20 and 25 vol%. In Fig. 1, the modified silicone oil based samples of 20 and 25 vol% show plateau stresses at the lower shear rates, the plateau stresses of which are lower than the reference value of the silicone oil based sample of 8.8 vol% around 10 Pa [7].

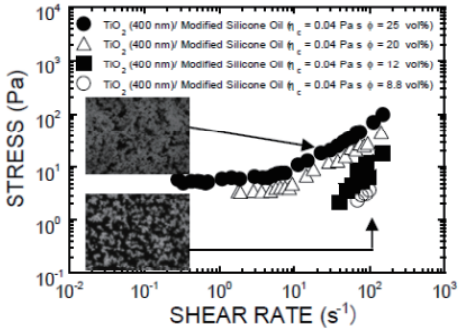


Fig. 1 Stress plotted logarithmically against shear rate for nano-suspensions with $\eta_c$ = 0.04 Pa·s under no electric fields. The particle volume fractions were 8.8, 12, 20, and 25 vol%.

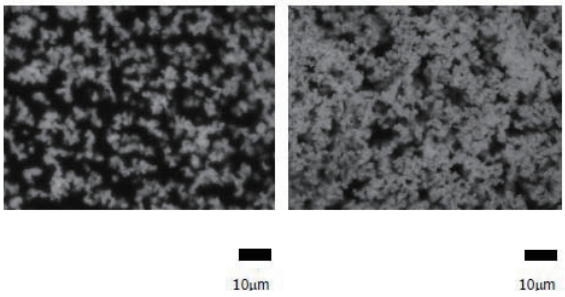


Fig. 2 Optical micrographs for the nano-suspensions of 8.8 vol% (left) and 25 vol% (right) shown in Fig.1.

These results are closely related to microstructures of the nano-particles developed in the samples.

Figure 2 shows typical optical micrographs taken in the quiescent state for the sample based on the modified silicone oil with particle volume fractions of 8.8 vol% (left) and that of 25 vol% (right). In the micrographs, the white portions represent secondary particles (or particle rich phase), while the black portions represent the oil (or oil rich phase). For the sample based on the modified silicone oil with $\phi$ = 25 vol% (right), the microstructure of secondary particles is slightly more densely developed across the imaging field of view than that of the sample of 8.8 vol% (left).

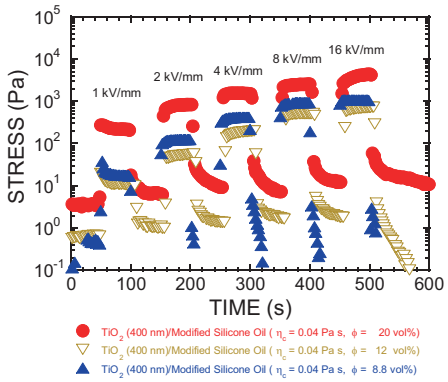


Fig. 3 ER responses for the nano-suspensions based on the modified silicone oil of 0.04 Pa·s. The particle volume fractions were 8.8, 12 and 20 vol%. The shear rate was 1.88 $s^{-1}$.

Figure 3 shows ER responses for the samples based on the modified silicone oil of 0.04 Pa·s. The particle volume fractions were 8.8, 12 and 20 vol%. The shear rate was 1.88 $s^{-1}$. The dc electric field, the strength of which is shown in the figure, was applied and then removed. Correspondingly, the increase and recovery of the stress is seen in the figure. In Fig. 3, the stresses under the electric field for the sample based on the modified silicone oil with $\phi$ = 20 vol% (and also 25 vol%) are comparable to those of the normal silicone oil based sample with $\phi$ = 12 vol%.

The effect of shear rate and time on the shear stress and flow behavior in the presence of the dc electric field was also investigated. In the measurements, the shear deformations and the electric field were applied at the same time. The shear rate was increased, and then decreased. The flow pattern was also recorded simultaneously. Unexpectedly, the sample based on the modified silicone oil with $\phi$ = 20 vol% showed lower stresses under the electric field. In the shear rate dependence of the shear stress, shear thinning behavior and significant hysteresis were observed, especially at higher shear rates and strengths of the electric field. From the simultaneous observations of flow behavior, circular or ark shaped defect similar to the MR suspension [11] was observed, and macroscopic void was developed.

## 4. Conclusions

Flow behavior and microstructure were discussed for the ER nano-suspensions. The plateau stresses under no electric fields for the sample based on the modified silicone oil of 0.04 Pa·s and particle volume fractions of 20 and 25 vol% were much lower than the plateau stress of the silicone oil based sample. The ER responses were comparable. In the measurements of shear rate sweep, the sample of 0.04 Pas and 20 vol% showed the shear thinning behavior and hysteresis in the presence of the dc electric field. These results were closely related to the flow behavior observed simultaneously with rheology.

## Acknowledgement

This work was partially supported by the Cooperative Research Program of the Institute of Fluid Science, Tohoku University.

## References

[1] W. M. Winslow, *J. Appl. Phys.*, 20 (1949) 1137.
[2] R. Tao, and J. M. Sun, *Phys. Rev. Lett.*, 67 (1991) 398.
[3] S. Henley, and F. E. Filisko, *J. Rheol.*, 43 (1999) 1323.
[4] A. Hosseini-Sianaki, W. A. Bullough, R. Firoozian, J. Makin, and R. C. Tozer, *Int. J. Mod. Phys. B*, 6 (1992) 2667.
[5]K. Tanaka, A. Sahashi, R. Akiyama, and K. Koyama, *Phys. Rev. E*, 52 (1995) R3325.
[6] M. Nakano, and K. Koyama (eds.), *Proc. of 6th Int. Conf. on ER Fluids, MR Suspensions and Their Applications* (1998).
[7]K. Tanaka, T. Wakayasu, A. Kubono, and R. Akiyama, *Sensors and Actuators A*, 112 (2004) 376.
[8] K. Tanaka, S. Robson, W. Nakano, H. Kobayashi, R. Akiyama, M. Nakano, and A. Totsuka, *Proc. of the 13th International Symposium on Advanced Fluid Information*, (2013) 142.
[9] K. Tanaka, T. Hira, R. Fukui, N. Nakagawa, R. Akiyama, M. Nakano, K. Yoshida, and T. Tsujita, *Colloid Polym. Sci.*, 289 (2011) 855.
[10] K. Tanaka, T. Hira, R. Fukui, H. Kobayashi, R. Akiyama, M. Nakano, S. Enami, and A. Totsuka, *Colloid Polym. Sci.*, 291 (2013) 1279.
[11] M. Nakano, A. Satou, Y. Sugamata, and H. Nishiyama, *JSME International Journal, ser B*, 48 (2005) 494.

# Control Problems for the MHD Equations under Inhomogeneous Mixed Boundary Conditions

Roman Brizitskii[1,2]
[1]Institute of Applied Mathematics FEB RAS
7, Radio St., Vladivostok, 690041, Russia
[2]Far Eastern Federal University
8, Sukhanova St., Vladivostok, 690950, Russia

**ABSTRACT**

The global solvability of the boundary value problem for the stationary magnetohydrodynamics equations under nonhomogeneous boundary conditions for the magnetic field was proved. The new control problems with effective mechanisms of hydrodynamic control for this model are considered firstly.

## 1. Introduction. The Statement of the Boundary Value Problem

Let Omega be a bounded domain of space $\mathbf{R}^3$ with boundary $\partial\Omega$ consisting of two parts $\Gamma_N$ and $\Gamma_T$. We consider the following boundary value problem for stationary magnetohydrodynamic equations of viscous incompressible fluid:

$$-\nu\,\Delta\mathbf{u}+(\mathbf{u}\cdot\nabla)\mathbf{u}+\nabla p-\kappa\,\mathrm{rot}\,\mathbf{H}\times\mathbf{H}=\mathbf{f},\ \ \mathrm{div}\,\mathbf{u}=0,\ (1)$$

$$\nu_1\,\mathrm{rot}\,\mathbf{H}-\rho_0^{-1}\,\mathbf{E}+\kappa\,\mathbf{H}\times\mathbf{u}=\upsilon_1\mathbf{j},\ \mathrm{div}\,\mathbf{H}=0,\ \mathrm{rot}\,\mathbf{H}=\mathbf{0},\ (2)$$

$$\mathbf{u}=\mathbf{g}\ \text{on}\ \Gamma,\ \ \mathbf{H}\cdot\mathbf{n}=q\ \text{on}\ \Gamma_N,\ \mathbf{H}\times\mathbf{n}=\mathbf{q}\ \text{on}\ \Gamma_T\,.$$

$$\text{and}\ \ \mathbf{E}\times\mathbf{n}=\mathbf{k}\ \ \text{on}\ \ \Gamma_N\ (3)$$

Here**u** is the velocity vector; **H** and**E** are magnetic and electric field intensity vectors, respectively; $p=P/\rho_0$where P is the pressure, $\rho_0$=const is a fluid density, **f** is a volume density of external forces, **j** is the exterior current density, $\kappa=\mu/\rho_0$, $\nu_1=1/\rho_0$, $\sigma=\kappa\nu_m$,$\nu$ and $\nu_m$ are constant kinematic and magnetic viscosity coefficients,$\sigma$ is a constant conductivity, $\mu$ is a constant magnetic permeability, **n** is the outer normal to $\partial\Omega$.

In the remainder of the paper we will refer to problem (1)-(3) for given functions **f**,**j, g,** q, **q**и**k** as Problem 1.We note that all the quantities in (1)–(3) are dimensional and theirphysical dimensions are defined in terms of SI units.Physically the homogeneous case of the boundary conditions for the electromagnetic field in (3) correspond to the situation when the part $\Gamma_N$ of theboundary $\partial\Omega$ is a perfect conductor and other part $\Gamma_T\subset\partial\Omega$ is a perfect insulator.

Beginning with the pioneering paper by Solonnikov [1] the solvability of boundary value problems for stationary magnetohydrodynamic equations was studied in a number of papers. Among them we mention [2-7] devoted to study of the solvability of the boundary value and controlproblems for stationary MHD equations under Dirichlet condition for the velocityand [8-10] where the MHD equations are considered undermixed boundary conditions for the velocity.As to boundary conditions for magnetic field we note that two main typesof conditions were used in cited papers. The first type corresponds to relations $\mathbf{H}\cdot\mathbf{n}=0$ and $\mathbf{E}\times\mathbf{n}=\mathbf{0}$ on $\partial\Omega$ describing the boundary conditions on perfectly type is described by the condition $\mathbf{H}\times\mathbf{n}=\mathbf{0}$ on $\partial\Omega$ [8]

Corresponding author: Roman Brizitskii
*E-mail address*: mlnwizard@mail.ru

boundary (see, e.g., [1,4,5,7,9]. The second corresponding to a perfectly insulating boundary.

It should be noted that when studying flows of conductive fluids in real-life devices the necessity can arise in modeling of flows of conductive fluids in domains with boundaries consisting of parts with different electrical conductivity properties. Mathematical modelling of conductive flows in such type domainsgives rise to studying boundary value problems for MHD equations under mixed boundary conditions for magnetic field.

In author knowledge respective mixed boundary value problems for magnetohydrodynamic equations have not been yet considered in the mathematical literaturebefore the release of paper[11]. In [11] the global solvability of the boundary value problem for the equations (1), (2) under homogeneous boundary conditions of the form (3) was proved. In this paper we summarize the results of [1] for the case of the inhomogeneous boundary conditions (3). In other words, we have proved the global solvability of the inhomogeneous mixed boundary value (1)-(3).

As the same time there are some papers in literature devoted to study of solvabilityof corresponding boundary value problems for static Maxwell equations.Among them we mention [12-14] where the solvability of div-curl system and static Maxwell equations with mixed boundary conditions is studied.

We note one important feature of the Problem 1.

In [5] the global solvability of the boundary value problem for the equation (1), (2) was proved under following boundary conditions:

$$\mathbf{u}=\mathbf{g},\ \ \mathbf{H}\cdot\mathbf{n}=q,\ \mathbf{k}\times\mathbf{n}=\mathbf{k}\ \text{on}\ \Gamma\,.\qquad(4)$$

There is a caveat. The global solvability of the boundary value problem (1), (2), (4) was proved under condition $\mathbf{g}\cdot\mathbf{n}=0$ on $\Gamma$. In the case of $\mathbf{g}\cdot\mathbf{n}\neq0$ on $\Gamma$ we have only local solvability of the boundary value problem (1), (2), (4) (solvability under smallness conditions of initial date of problem (1), (2), (4)) or open difficult mathematical problem. The condition $\mathbf{g}\cdot\mathbf{n}=0$ on $\Gamma$is so-called not called flow conditions. Obviously, we cannot upload or pumped fluid from the $\Omega$ under this condition. This fact significantly reduces the possibility of “hydrodynamic” control.

In our paper we proved the global solvability of Problem 1in the case of $\mathbf{g}\cdot\mathbf{n}\neq0$ on $\Gamma_T$. From the practical point of view, this means that we can pump out and

pump fluid at least across a part $\Gamma_T$of boundary $\partial\Omega$. The control problems are presented in the next section.

Note one more feature of the mixed boundary value problem (1)-(3). The inhomogeneous mixed boundary conditions for the magnetic fields

$$\mathbf{H}\cdot\mathbf{n} = q \text{ on } \Gamma_N, \ \mathbf{H}\times\mathbf{n} = \mathbf{q} \text{ on } \Gamma_T$$

are defined only on disjoint part $\Gamma_N^i \subset \Gamma_N$, $\Gamma_T^j \subset \Gamma_T$ .

## 2. Control Problems

The mathematical statement of the optimal control problem is as follows: find a pair $(\mathbf{x},\mathbf{g})$, where $\mathbf{x}=(\mathbf{u},H,p)\in X$, and $\mathbf{g}\in K$ such that

$$J(\mathbf{x},\mathbf{g}) = I_i(\mathbf{u},p) + \frac{\mu_1}{2}\|\mathbf{g}\|^2_{1/2,\Gamma} \to \inf .$$
$$F(\mathbf{x},\mathbf{g}) = 0, \ \mathbf{x}\in X, \mathbf{g}\in K \qquad (5)$$

Here $F(x,\mathbf{g})=0$ is the operators form of the weak formulation of Problem 1; $\mu_1$ is nonnegative parameter, $I_i(\boldsymbol{u},p)$ is a cost functional. The possible cost functionals are usually defined as

$$I_1(\mathbf{v}) = \|\mathbf{v}-\mathbf{v_d}\|^2_Q, \ \ I_2(\mathbf{v}) = \|\mathbf{v}-\mathbf{v_d}\|^2_{1,Q}$$
$$I_3(\mathbf{v}) = \|\mathrm{rot}\,\mathbf{v}-\eta_\mathbf{d}\|^2_Q, \ \ I_4(p) = \|p-p_\mathbf{d}\|^2_Q \qquad (6)$$

Here Q is a some subset of domain $\Omega$, $\mathbf{v}_d\in\mathbf{L^2}(Q)$ (or $\mathbf{v}_d\in\mathbf{H}^1(Q)$) is function, which simulates a given distribution of the velocity field in Q. Functions $\eta_d\in\mathbf{L^2}(Q)$ and $p_d\in L^2(Q)$ have a similar sense. On the results and research methods such tasks see [15,16].

We show further the stability estimates of solutions of concrete control problem:

$$J(\mathbf{v},\mathbf{g}) \equiv \frac{\mu_0}{2}\|\mathbf{v}-\mathbf{v}_d\|^2_Q + \frac{\mu_1}{2}\|\mathbf{g}\|^2_{1/2,\Gamma} \to \inf,$$
$$F(\mathbf{x},\mathbf{g},\mathbf{j}) = 0, \ \mathbf{x}\in X, \mathbf{g}\in K, \qquad (7)$$

corresponding to the cost functional $I_1(\mathbf{v})$. Let us assume below that the is the exterior current density$\mathbf{j}$ in (6) can change in some bounded set $J\subset\mathbf{L}^2(\Omega)$. Denote by $(\mathbf{x}_1,\mathbf{g}_1)\equiv(\mathbf{u}_1,\mathbf{H}_1,p_1,\mathbf{g}_1)$ a solution to problem (7) that corresponds to given functions $\mathbf{v}_d \equiv \mathbf{u}_d^{(1)} \in \mathbf{L}^2(Q)$ and $\mathbf{j}=\mathbf{j}_1\in J$. By $(\mathbf{x}_2,\mathbf{g}_2)\equiv(\mathbf{u}_2,\mathbf{H}_2,p_2,\mathbf{g}_2)$ we denote a solution to problem (7) that corresponds to perturbed functions $\mathbf{v}_d \equiv \mathbf{u}_d^{(2)} \in \mathbf{L}^2(Q)$ and $\mathbf{j}=\mathbf{j}_2\in J$.

Denote by

$$\Delta \equiv \left\|\mathbf{u}_d^{(1)} - \mathbf{u}_d^{(2)}\right\|_Q + (a\|\mathbf{j}_1-\mathbf{j}_2\| + b\|\mathbf{j}_1-\mathbf{j}_2\|^2)^{1/2}.$$

We obtained local stability estimates for the solutions of problem (7):

$$\|\mathbf{u}_1-\mathbf{u}_2\|_{\mathbf{H}^1(\Omega)} \le M_\mathbf{u}\Delta, \ \ \|\mathbf{H}_1-\mathbf{H}_2\|_{\mathbf{H}^1(\Omega)} \le M_\mathbf{H}\Delta,$$
$$\|p_1-p_2\| \le M_p\Delta, \ \ \|\mathbf{g}_1-\mathbf{g}_2\|_{1/2,\Gamma} \le M_\mathbf{g}\Delta, \qquad (8)$$

where a, b, $M_\mathbf{u}$, $M_\mathbf{H}$, $M_p$ and $M_\mathbf{g}$ are not decreasing functions of norms of the initial data of Problem 1.

The control of the normal component of the magnetic field on the part $\Gamma_N$ of boundary $\Gamma$ is also very interesting from the point of view of applications. Because it is one of the few technically feasible control mechanisms.

Indeed, we can create a magnetic field directed perpendicular to the part $\Gamma_N$. For this purpose the wires with electrical current can be placed in parallel $\Gamma_N$.

Using the control q on $\Gamma_N$ we can minimize "hydrodynamic" functionals (5). Such control problems are called the mixed-type control problems. For example we consider the following control problem:

$$J(\mathbf{v},q) \equiv \frac{\mu_0}{2}\|\mathbf{v}-\mathbf{v}_d\|^2_Q + \frac{\mu_1}{2}\|q\|^2_{1/2,\Gamma_N} \to \inf,$$
$$F(\mathbf{x},q) = 0, \ \mathbf{x}\in X, q\in K \qquad (9)$$

and

$$J(\mathbf{v},q) \equiv \frac{\mu_0}{2}\|p-p_d\|^2_Q + \frac{\mu_1}{2}\|q\|^2_{1/2,\Gamma_N} \to \inf,$$
$$F(\mathbf{x},q) = 0, \ \mathbf{x}\in X, \mathrm{q}\in K \qquad (10)$$

We note that the study of the problems (9), (10) is a difficult from a mathematical point of view. In [17] the uniqueness of solutions of the control problems (9) and (10) are proved in the first.

**Acknowledgments**

This work was supported financially by the Ministry of education and science of Russian Federation (project 14.Y26.31.0003), Russian Foundation for Basic Research (projects no. 13-01-00313-a).

**References**

[1] V. Solonnikov, *Trudy Mat. Inst. Steklov*, 59(1960) 174-187 (in Russian).
[2] M.D. Gunzburger, A.J. Meir, J.S. Peterson, *Math. Comp.*, 56(1991) 523-563.
[3] A.J. Meir, L.S. Hou, *Appl. Math. Optim.*, 32(1995)143-162.
[4] G. Alekseev, *J. Appl. Mech. Phys*., 44(2003) 890-898.
[5] G. Alekseev, *Siberian Math. J.*, 45 (2004) 197-213.
[6] D. Schotzau, *Numer. Math*. 96(2004) 771-800.
[7] L. Consiglieri, S. Necasova, J. Sokolowski, *Control and Cybernetics*, 38(2009) 1193-1215.
[8] G. Alekseev, R. Brizitskii, *Daln. Math. J,.*3(2002) 285-301 (in Russian).
[9] R. Brizitskii, D. Tereshko, *Diff. Eq.*, 43(2007) 6-258.
[10] A.J. Meir, *Comp. Math. Applic.*, 25(1993) 13-29.
[11] G. Alekseev, R. Brizitskii, *Applied Mathematics Letters*, 32(2014) 13-18.
[12] P. Fernandes, G. Gilardi, *Math. Mod.Meth. Appl. Sci.*, 7(1997) 957-991.
[13] G. Auchmuty, Math. Modeling and Methods in Applied Sciences, 14(2004) 79-103.
[14] G. Auchmuty, J.S. Alexander, *Quarterly of Applied Mathematics*, 64(2006) 335-357.
[15] G. Alekseev, R. Brizitskii, *Differential Equations*, 46(2010) 1-13.
[16] G. Alekseev, R. Brizitskii, *Differential Equations*, 48(2012) 397-409.
[17] G. Alekseev, R. Brizitskii, *Differential Equations*, 49(2013) 963-974.

Eleventh International Conference on Flow Dynamics
October 8-10, 2014, Sendai, Miyagi, Japan

# Fluid Control Analysis of Piston Typed Valve Core in the Pilot-Control Globe Valve

Qian Jin-yuan[1,2], Jin Zhi-jiang[1,*] Gao Xiao-fei[1], Liu Bu-zhan[1]
[1] Institute of Process Equipment, Zhejiang University
Zheda Street 38, Hangzhou, 310027, China
[2] Institute of Thermal, Environmental and Natural Materials Process Engineering, TU Bergakademie Freiberg
Leipziger Street 28, Freiberg, 09599, Germany

**ABSTRACT**

The pilot-control globe valve (PCGV) can utilize pressure difference before and after itself to control its open or close status. PCGV has simple structures and low driving energy consumption. Piston typed valve core is adopted in PCGV. In this paper, fluid control by piston typed valve core is analyzed. It indicates that the piston typed valve core takes the place of the huge driving device in traditional globe valve and changes its seals type to metal-to-metal seal. In addition, another structure of PCGV which can adapt to vertical piping in introduced.

## 1. Introduction

Globe valve is widely used in petroleum engineering, chemical engineering, marine engineering and so forth. Its main function is to control fluid flow in piping systems, such as diversion and preventing backflow. To realize these controls, globe valve relies on the movement of the valve core to change the size of the flow channel, driving by different kinds of driving device. However, with the further development of industries, the automation level and the energy consumption level of globe valves are put forward to higher requirements. Especially for large sized globe valves, long reaction time and high energy consumption of the large drive device are very sharp problems.

Based on these situations, we invent a novel globe valve, which can utilize the pressure difference to control its open or close status [1]. It is realized by opening or closing the smaller valve (pilot-control valve) to control the larger valve (main valve), so we name this novel globe valve as pilot-control globe valve (PCGV). Figure 1 shows the main structure of PCGV. Compared to traditional globe valve, piston typed valve core is adopted in PCGV, which is the main difference.

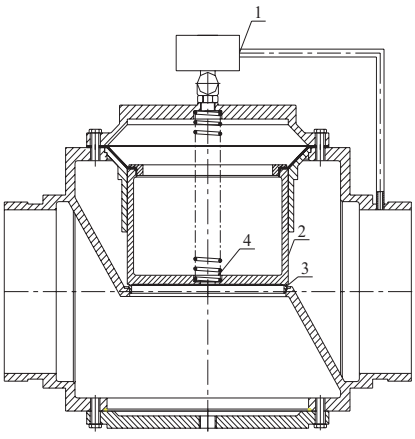


Fig. 1 The main structure of PCGV
1- Pilot-control valve; 2- Piston typed valve core;
3- Valve seat; 4- Hole in bottom surface of valve core;

Corresponding author: Jin Zhi-jiang
*E-mail address*: jzj@zju.edu.cn

## 2. Fluid Control Process Analysis

PCGV is the collection of two valves: Pilot-control valve and main valve. Pilot-control valve can control the obstructed or unobstructed status of the pilot tube. The status decides the pressure difference before and after the main valve [2]. Meanwhile, the pressure difference can push piston typed valve core up and down to control the opening or closing status of the main valve.

Due to the replacement from controlling the larger valve (main valve) to the smaller valve (pilot-control valve), PCGV owns less driving energy consumption. The detail working process is as follows in Table 1.

Table 1. Control Process of PCGV
PV- Pilot-control valve; MV- Main Valve;
VC- Piston typed valve core; S- Valve seat;

| PV State | VC State | MV State |
|---|---|---|
| Closed | At S | Closed |
| Open to Closed | Away from S | Open to Closed |
| Open | Stay up S | Open |
| Closed to Open | Back to S | Closed to Open |

Here, we assume the initial status of the pilot-control valve is closed. Thus, the pilot tube is obstructed. Because the upper chamber (up the valve core) is connected with the cavity (under the valve core) with the hole in the bottom surface of the valve core, the pressures up and down the bottom surface of piston typed valve core are uniform. As a result, the valve core is in the closed to the valve seat by gravity and the force of the spring.

When we open the pilot-control valve, the fluid in the upper chamber flows through the pilot tube. Therefore, the equilibrium of forces is broken and there turns out a pressure difference up and down the bottom surface of piston typed valve core, which pushes the valve core away from the valve seat. Then, the main valve is open and fluid can flow directly to the outlet.

According to the Bernoulli equation, the pressure in the chamber changes with the flow rate. At the same time, the spring force on the valve core changes with the displacement of the valve core. The valve core will keep in a static place when reaching the new equilibrium.

When we close the pilot-control valve, the pilot tube

will be obstructed again but the fluid will keep flowing into the chamber, so that the former equilibrium will be broken again. Meanwhile, the fluid in the chamber pushes the piston typed valve core to the valve seat with the help of gravity and the force of the spring. As a result, the main valve turns out to be closed again.

As is shown in Figure 2, compared to traditional globe valve, piston typed valve core and valve seat are metal-to-metal seal in PCGV. This seal can avoid great applied torque on the valve core and seal surface of the valve seat, and prolongs the service life of the valve.

In addition, we make a comparison of the energy consumption. In PCGV, we use a much smaller valve to control the main valve instead of controlling the main valve directly, which of course is much easier and energy saving. In other words, when the size of the valve is larger, the advantage of PCGV is more obvious.

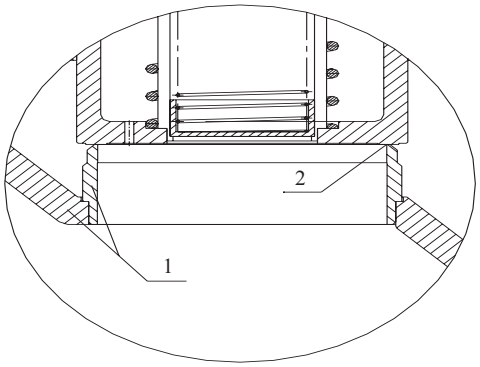


Fig. 2 The detail structure of the seal part in PCGV
1- Valve seat; 2- Metal-to-metal seal;

## 3. Further Design in Vertical Pipelines

As is mentioned before, during the control process of PCGV, the gravity is very useful especially when turning to close. However, when this kind of valve is applied in vertical pipeline, the force of the spring alone cannot push the piston typed valve core to the valve seat successfully to complete the close process of PCGV [3]. In other words, PCGV in Figure 1 can only be used in horizontal pipelines.

In order to solve this problem, we design another structure of PCGV, which is shown in Figure 3. In the optimization design, the valve body is divided into three parts, and piston typed valve core and guide sleeve are totally inside the valve body and linked to the middle parts of the valve body with ribbed plates [4]. When the pilot-control valve is closed, due to the gravity and the force of the spring, piston typed valve core shall stay at the valve seat, assembled as the metal-to-metal seal. When the pilot-control valve is opened, the fluid can pass to the outlet, which turning out the decrease of the pressure in the chamber up the valve core. Therefore, the piston typed valve core will be pushed to a higher place and the fluid can flow through the ribbed plates to outlet. What's more, the valve seat can change the angle to the valve body, which means this variable structure can also be used in different angles pipelines.

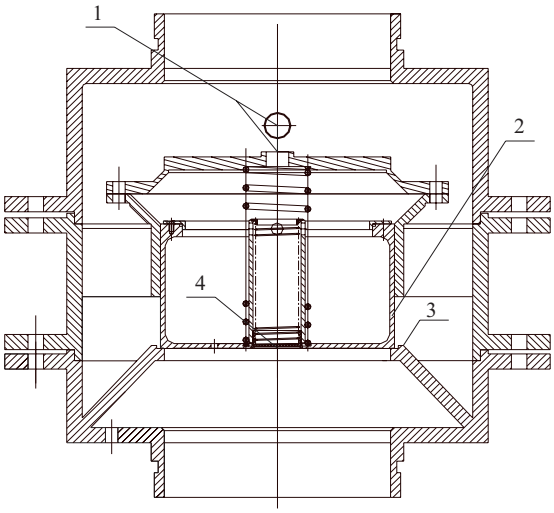


Fig. 3 The main structure of PCGV in vertical pipeline
1- Pilot-control valve with the pilot tube (inside valve);
2- Piston typed valve core; 3- Valve seat;
4- Hole in bottom surface of valve core;

## 4. Conclusions

PCGV can utilize the pressure difference before and after itself to control its open or close status by pushing the piston typed valve core up and down.

Piston typed valve core is the key element of PCGV which can control the fluid with the operation of the pilot-control valve. Piston typed valve core takes the place of the huge driving device in traditional globe valve and changes its seals type as metal-to-metal seal. Compared to traditional globe valve, PCGV with piston typed valve core has much simpler structures and low driving energy consumption.

The optimization structure of PCGV can be used in vertical pipelines by dividing the valve body into three parts with piston typed valve core and guide sleeve inside the valve body. Besides, by changing the angle of the valve seat to the valve body, the variable structures can also be used in different angles pipelines.

## Acknowledgements

This work is supported by the National Natural Science Foundation of China (NSFC) through Grant No.51175454, the Science and Technology Department of Zhejiang Province through Grant No.2012C11018-1 and No. 2012C11002, and China Scholarship Council.

## References

[1] J.K. Wang, Z.J. Jin, J.Y. Kuang, H. Zhang, *Valve*, 3(2009)10-11.
[2] H. Zhang, J.Y. Kuang, J.K. Wang, J.Y. Qian, Z.J. Jin, *Light Industry Machinery*, 2(2011)10-13.
[3] J.Y. Qian, H. Zhang, J.K. Wang, A.L. Lu, Z.J. Jin, *Applied Mechanics and Materials*, 331(2013) 65-69.
[4] A.L. Lu, J.Y. Qian, H. Zhang, J.K. Wang, Z.J. Jin, *Light Industry Machinery*, 5(2013), 15-19.

Eleventh International Conference on Flow Dynamics
October 8-10, 2014, Sendai, Miyagi, Japan

# Novel Electroactive Polymer for Micro-Motor Development

Miklos Zrinyi[1], Masami Nakano[2]
[1] Department of Biophysics and Radiation Biology, Faculty of Medicine, Semmelweis University
Nagyvarad ter 4, Budapest, H-1089, Hungary
[2]Intelligent Fluid Control Systems Laboratory, Institute of Fluid Science, Tohoku University
2-1-1 Katahira, Aoba-ku, Sendai, 980-8577, Japan

**ABSTRACT**

Epoxy based polymer has been developed for novel electric micro-motor construction. Polymer disks and hollow cylinders were prepared in few micrometer dimensions as rotors. Electrorotation of these micro tools was studied under uniform DC electric field. The effect of shape, size and thickness were investigated. The novel epoxy based micro devices show intensive spinning in uniform DC electric field. The rotational speed of micron-sized polymer rotors can be conveniently tuned in wide range (between 300-2000 rpm) by the electric field intensity.

## 1. Introduction

Electroactive polymers (EAP) exhibit a change in size and shape when stimulated by electric field. Controllable rotation of EAP polymer is of relevance for a range of practical applications, for example in micro-motors or in microfluidics. It is therefore an important task to find proper materials with controllable shape and size in order to perform reliable measurements as well as to use them for developing micro-motors. The main purpose of this research is to find electroactive polymer as possible candidate of rotor of micro-sized electro-motors.

Electrorotation is the circular movement of an electrically polarized micron-sized particle or material [1, 2]. In our previous work, the development of novel electroactive polymer composites has been reported [3, 4]. As a direct continuation of this research work, our intention is to replace polymer composites to pure polymers that can be fabricated by photolithography instead of polymer composites.

## 2. Materials and Method

Epoxy based polymer has been developed for novel electric micro-motor construction. The polymer hardens in a pre-defined 3D shape upon illumination with focused laser light. Disks, hollow cylinders and gearwheels as rotors, were prepared with variable diameter and thickness. The diameter was varied between 100 to 500 microns with heights of 20 - 40 microns. Figure 1 shows the photo of three main rotor forms.

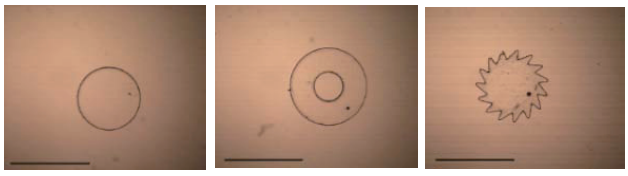

(a)Polymer disk (b)Hollow cylinder (c)Gearwheel

Fig. 1 Polymer rotor made of epoxy based polymer. The bar indicates 500 microns. The dot close to the edge of the micro rotors was used to determine the speed of rotation.

Corresponding author: Miklos Zrinyi
*E-mail address*: mikloszrinyi@gmail.com

Electrorotation was studied in oil mixture containing substantial amount of triglicerid of oleic-, palmitic-, and linoleic acids, with conductivity of $\sigma_1 = 9.56 \cdot 10^{-10}$ S/m and relative permittivity of $\varepsilon_1 = 3.32$, respectively. We have studied the influence of DC electric field intensity on the speed of rotation.

Figure 2 shows an experimental device to apply electric field to the disk shaped polymer rotor. The gap distance between the electrodes was 3 mm. The space between the electrodes was filled up with special oil. The electric field was supplied by a high voltage DC power supply (TREC, USA). We have increased the electric field intensity step by step up to 2.2 kV/mm. Uniform DC electric field was applied perpendicularly to the axis of the disk. The rotation was followed by an optical microscope (OLYMPUS, Japan) equipped by a high speed camera (Photron, Japan). In order to visualize the rotation and to determine the angular frequency, a visible sign close to the edge of the disk was used. The angular frequency of the rotation was determined by recording the spinning motion of the disk.

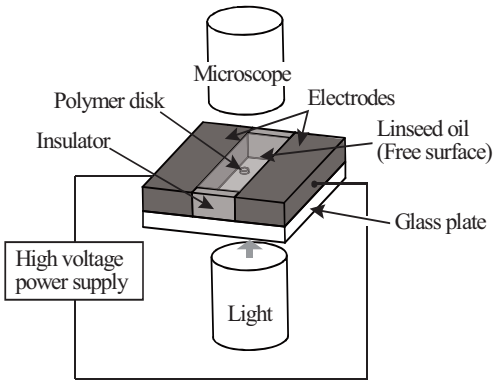


Fig. 2 Experimental device to apply electric field to the disk shaped polymer rotor and to monitor the electrorotation of a polymer rotor.

## 3. Results and Discussion

We have presented the direct observation of DC electric field induced rotation of epoxy based chemically crosslinked polymer rotors. Polymer disks,

hollow cylinders as well as gearwheels of different size perform very intensive rotation in uniform DC electric field. We have studied the influence of disk diameter as well as the disk thickness on the speed of rotation.

Figure 3 shows the dependence of rotational speed on the electric field intensity for three disk-shaped polymer rotors. In DC electric field above a critical value of electric field intensity which was found to be 0.6 kV/mm, the polymer rotors perform spinning at a constant rate. This rate is sensitive to the electric field intensity. It was found that within the experimental accuracy the dependence of speed of rotation linearly depends on the DC electric field for every polymer rotors. And there is a significant size effect on the speed of rotation. At the same electric field intensity, the smallest disk (100μm) performs the most intensive rotation.

Figure 4 shows the influence of disk thickness on the speed of rotation. At the same electric field intensity, the thicker disk (38 μm) performs more intensive rotary motion. On the basis of Fig. 4, one can establish that the thickness of the polymer disk plays an essential role.

We have also studied the rotation behavior of hollow disks and gearwheels. Figure 5 and 6 show these results.

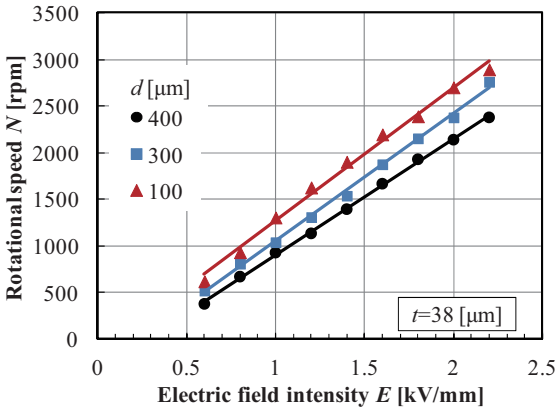


Fig. 3 Dependence of rotational speed $N$ of polymer rotor on the electric field intensity $E$ for three disk rotors having different diameter $d$.

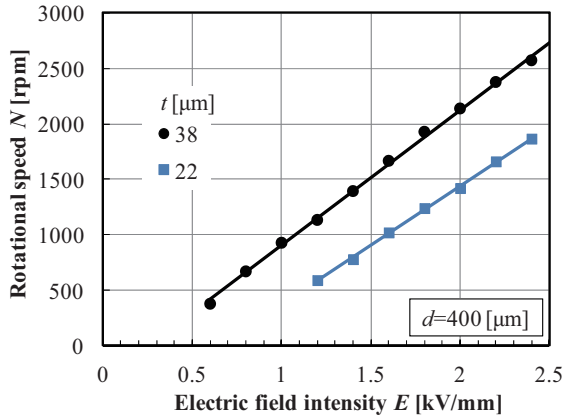


Fig. 4 Dependence of rotational speed $N$ of polymer rotor on the electric field intensity $E$ for two disk rotors having different thickness $t$.

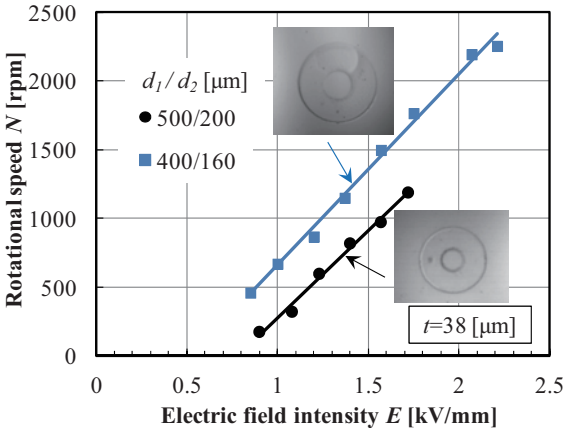


Fig. 5 Dependence of rotation speed $N$ of hollow cylinder on the electric filed intensity $E$ for two different cylinders. The internal- and outer diameters ($d_2$, $d_1$) are shown in the figure.

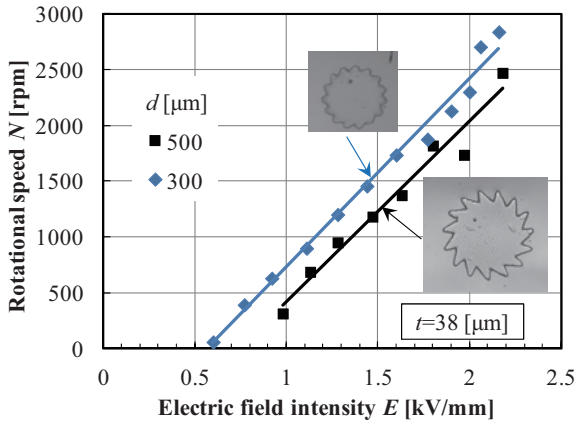


Fig. 6 Dependence of rotation speed $N$ of gearwheel rotors on the electric filed intensity $E$.

All these measurements provide fundamental information on micro-motor characteristics which is important for further micro-engineering development.

**Acknowledgements**

This research was performed under the Collaborative Research Project of Institute of Fluid Science, Tohoku University and in the frame of Cooperation Agreement between Institute of Fluid Science, Tohoku University and, Department of Biophysics and Radiation Biology, Semmelweis University. The financial support of OTKA Foundation (Grant No. NK101704 ) and JSPS Grant-in-Aid for Challenging Exploratory Research (Grant No. 26630084, 2014-2015) are gratefully acknowledged.

**References**

[1] G. Quincke, *Ann. Phys. Chem.*, 59 (1896) 417-486.
[2] T.B. Jones, Electromechanics of Particles, Cambridge University Press, New York, (1995).
[3] M. Antal, G. Filipcsei, M. Zrínyi, *Composites Science and Technology*, 67-13 (2007) 2884-2885.
[4] M. Zrinyi, M. Nakano, T. Tsujita, *Smart Mater. Struct.* 21, Paper No. 065022 (2012) 1-6.

Eleventh International Conference on Flow Dynamics
October 8-10, 2014, Sendai, Miyagi, Japan

# Micro-Motor Consisting of Electro-Active Polymer Composite Rotor in Dielectric Liquid

Masami Nakano[1], Takayuki Okumura[1], Miklos Zrinyi[2]
[1] Intelligent Fluid Control Systems Laboratory, Institute of Fluid Science, Tohoku University
2-1-1 Katahira, Aoba-ku, Sendai, 980-8577, Japan
[2] Department of Biophysics and Radiation Biology, Faculty of Medicine, Semmelweis University
Nagyvarad ter 4, Budapest, H-1089, Hungary

**ABSTRACT**

For the purpose of developing a micro motor utilizing the Quincke rotation, polymer composites have been developed as materials for a micro motor rotor with micro-fabrication possibilities, and the motor characteristics of disk shaped rotor of polymer composites are investigated as a function of electric field intensity and the diameter and thickness of the rotor using a high speed video camera. The induced torque of micro motors decreases with increasing the rotational speed, and increases with increasing the electric intensity and both diameter and thickness of the rotor.

## 1. Introduction

Recent trend in science and technologies is in the direction of micro- and nano dimension due to their extraordinary properties. In order to construct a novel type of micro-motors, we have intended to exploit Quincke rotation phenomenon [1], which is the rotation of non-conducting objects immersed in dielectric liquids and subjected to a strong homogenous DC electric field. We have proposed a micro motor utilizing the Quincke rotation. The micro motor has several advantages. As only two electrodes are used, the size and weight of the micro motor can be reduced, and the rotational speed of the motor can be simply controlled by only DC electric field applied by DC power supply. In our previous work, the development of novel electroactive polymer composites for micro-motor rotors has been reported [2, 3].

In this study, for the purpose of developing the micro motor utilizing the Quincke rotation, a polymer composite which is contained non-conducting particles in a gelatin has been developed as materials for the micro motor rotor with micro-fabrication possibilities, and the motor characteristics of several disk-shaped polymer composite rotors have been investigated as a function of electric field intensity and the diameter $d$ and thickness $t$ of the rotors.

## 2. Fabrication of Rotors and Experiments

The disk-shaped rotors of polymer composite was fabricated with variable diameter and thickness as follows [3, 4]; FeO(OH) particles were dispersed into the gelatin solution at 70 ℃ such a way, that the mass ratio $m$ of the filling material to the dried polymer was varied between 1.00 and 4.00 in order to find an ideal composition for the rotor. The mixture was poured into cylindrical mold made of a brass plate and then it was dried carefully at 70 ℃in a vacuum.

Electrorotation was studied in oil mixture (salad oil) containing substantial amount of triglicerid of oleic-, palmitic-, and linoleic acids, with conductivity of $\sigma_1 = 9.56 \cdot 10^{-10}$ S/m and relative permittivity of $\varepsilon_1 = 3.32$, respectively.

Corresponding author: Masami Nakano
*E-mail address*: m-nakano@fmail.ifs.tohoku.ac.jp

As the motor characteristics of the polymer composite rotor, the rotational speed $N$ vs. applied electric field intensity $E$ without load and the torque $T$ vs. rotational speed $N$ under constant electric field intensity were measured and evaluated. When measuring the electrorotation without load, the polymer composite rotor was immersed in the salad oil which was filled up between two parallel electrodes. The electric field was supplied by a high voltage DC power supply (TREC, USA), and was increased step by step up to 2.0 kV/mm. Uniform DC electric field was applied perpendicularly to the axis of the disk. The rotation was followed by an optical microscope (OLYMPUS, Japan) equipped by a high speed camera (Photron, Japan).

Figure 1 shows an experimental device to measure the torque vs. rotational speed of the polymer composite rotor. A shaft of nylon fiber was fixed perpendicular to the center of the rotors. When a DC motor rotated the polymer composite rotor immersed in the salad oil between two electrodes under DC electric field, a torsional angle between two nylon fibers (a distance between two fibers is 10mm) adhered perpendicular to the shaft was measured by recording on a high speed camera. The rotor torque is calculated from a calibrated relationship between the applied torque and the torsional angle of the nylon shaft.

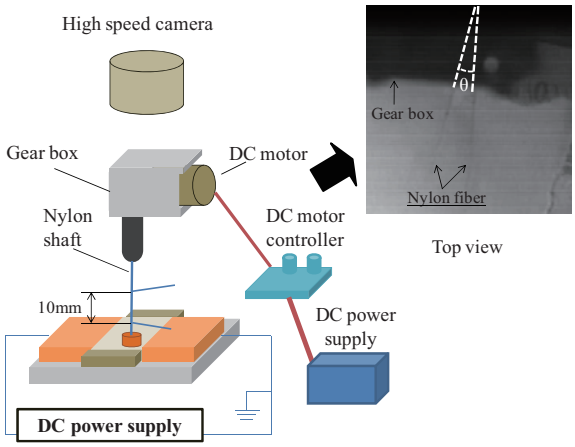


Fig. 1 Experimental apparatus for measuring torque vs. rotational speed of polymer composite rotor

## 3. Results and Discussion

### *3.1 Rotational Speed without Load*

Above a threshold value of the electric field, the polymer composite rotor rotates itself around an axis perpendicular to the DC electric field. Figure 2 shows experimental relationships between the applied electric field intensity $E$ and the rotational speed $N$ without load, depending on the diameter of the rotor. The rotational speed of the rotor without load increases with increasing the electric intensity not significantly depending on both the diameter and the thickness (not shown here), and also the threshold value of the electric field is close to 1 kV/mm. The maximum rotational speed is about 1300 rpm at $E$= 2.00 kV/mm.

### *3.2 Torque vs. Rotational Speed*

Figure 3 shows the characteristics of torque vs. rotational speed of the micro motor depending on applied electric field intensity. It can be seen in Fig. 3 that the generated torque of the micro motor decreases with increasing the rotational speed and also increases with increasing the applied electric field intensity. The disk rotor generates the maximum torque of 5.9 μNm when the electric field intensity of 2.00kV/mm is applied. In the operating conditions denoted by a circle in Fig. 3, 4, and 5, the fluctuation of the torque occurs. It means that it might be difficult to control the rotor rotation in a stable condition in the range of the relatively low rotational speed less than about 250 rpm. In the experiments for measuring torque, no-load (at $T$=0) rotational speed of about 700 rpm at $E$=2.00 kV/mm in Fig. 3 remarkably decreases, compared with about 1300 rpm in the experiments without load in Fig. 2. The reason might be why the rotor is glued with the nylon fiber to measure the torque.

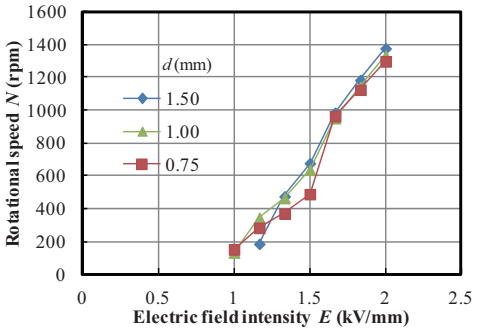


Fig. 2 Relationships between electric field intensity $E$ and rotational speed $N$ without load ($t$=0.6mm, $m$=2.67)

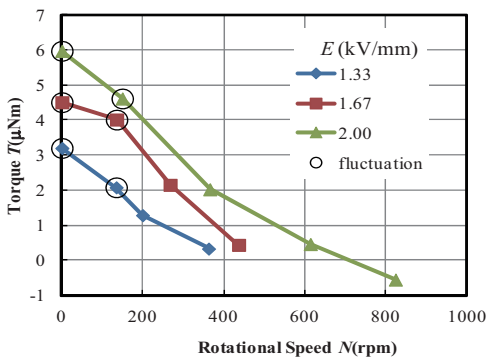


Fig. 3 Motor characteristics of torque $T$ vs. rotational speed $N$ of micro motor depending on applied electric field intensity $E$ ($d$=2.0 mm, $t$=1.0 mm, $m$=4).

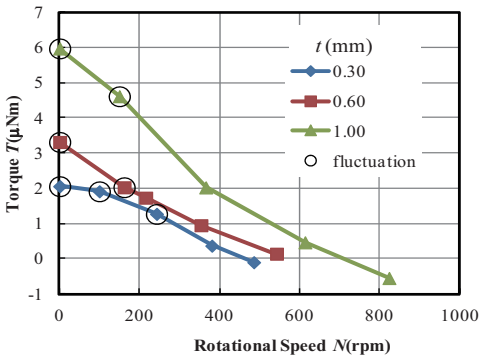


Fig. 4 Changes of torque $T$ vs. rotational speed $N$ with rotor thickness $t$ ($d$=2.0mm, $E$=2.0 kV/mm, $m$=4).

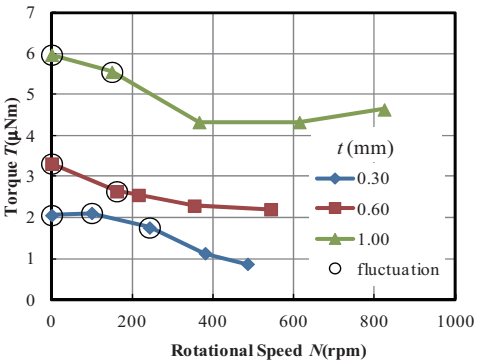


Fig. 5 Changes of electric torque $T_E$ vs. rotational speed with rotor thickness $t$ ($d$=2.0mm, $E$=2.0kV/mm, $m$=4).

As shown in Fig. 4, the torque decreases with increasing the rotational speed, and increases with increasing the rotor thickness $t$ as well as the rotor diameter $d$ (not shown here). Figure 5 shows the influence of rotor thickness on the characteristics of electric torque $T_E$ vs. rotational speed. The electric torque was obtained by adding viscous resistive torque $T_v$ to the measured torque $T$, where the viscous torque $T_v$ was measured as the torque without electric field and was directly proportional to the rotational speed $N$. It can be seen from Fig. 5 that the decreasing rate of the electric torque to the rotational speed becomes small remarkably, compared with that of the measured torque in Fig. 4. It means that the remarkable decrease of the measured torque $T$ with $N$ is mainly caused by the viscous resistive torque $T_v$ due to the dielectric oil.


## Acknowledgements

This work was partially supported by JSPS Grant-in-Aid for Challenging Exploratory Research (Grant No. 26630084, 2014-2015) and the Collaborative Research Program of IFS, Tohoku University.


## References


[1] G. Quincke, *Ann. Phys. Chem.*, 59 (1896) 417-486.

[2] M. Antal, G. Filipcsei, M. Zrínyi, *Composites Science and Technology*, 67-13 (2007) 2884-2885.

[3] M. Zrinyi, M. Nakano, T. Tsujita, *Smart Mater. Struct.* 21, Paper No. 065022 (2012) 1-6.

# Active Flow Control by Multi-electrode Microplasma Actuator

Yoshinori Mizuno[1], Marius Blajan[2], Hitoki Yoneda[3], Kazuo Shimizu[1, 2]
[1]Graduate School of Engineering, Shizuoka University.
3-5-1 Johoku, Hamamatsu, Shizuoka, 432-8561, Japan.
[2]Organization for Innovation and Social Collaboration, Shizuoka University.
3-5-1 Johoku, Hamamatsu, Shizuoka, 432-8561, Japan.
[3]Insutitute for Laser Science, The University of Electro-Communications.
1-5-1, Chofugaoka, Chofu, Tokyo, 182-8585, Japan.

**ABSTRACT**

In the field of fluids flows, atmospheric non-thermal plasma has attracted much attention. In this study, multi-electrode microplasma actuator was developed and investigated. Air flow induced by plasma was visualized by Particle Image Velocimetry (PIV). Each electrode could be driven independently, to control the air flow direction without changing electrode geometry. Two types of flows were observed, 1) parallel to a plane, 2) perpendicular to a plane. When discharge voltage was 1.3 kV, 15 kHz, about 0.1 ~ 0.5 m/s flow velocity was obtained.

## 1. Introduction

Flexible flow control has been required in various industry applications for improvement of the efficiency of systems or reduction to the environmental load. Atmospheric non-thermal plasma for active air flow has been investigated by many groups due to the advantages, 1) No-moving parts, 2) Simple construction 3) Thickness under 1 mm [1]. Figure 1 shows a typical plasma actuator. Horizontal component is the main term in this plasma actuator. Principle of air flow caused by plasma is momentum transfer from accelerated ions to neutral molecules [2].

In this paper, a multi-electrode microplasma actuator was developed and investigated. Due to the very small discharge gap of 25 μm, plasma in atmospheric air could be generated at around 1 kV, respectively low voltage. It contributes to the miniaturization of the power system and allows the parallel operation of the electrodes. By driving the each electrode selectively, air flow direction could be controlled without changing electrode geometry. Two types of flows were obtained, 1) parallel to a plane, 2) perpendicular to a plane.

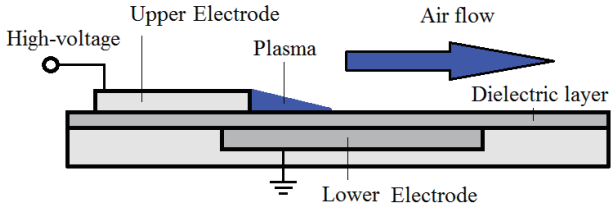


Fig. 1 Principle of plasma actuator.

## 2. Method

Multi-electrode microplasma actuator is shown in Figure 2. Two electrodes were on both side of a thin dielectric layer. Lower electrode was connected to the ground. Upper electrode consists of 4 independent electrodes. Each upper electrode could be switched to ground or to high-voltage.

Corresponding author: Kazuo Shimizu
*E-mail address*: Shimizu@cjr.shizuoka.ac.jp

By supplying high-voltage to the upper electrode, plasma was generated at the surface of the upper electrode. Lower electrode was insulated to prevent to the discharge at lower side.

Figure 3 shows the experimental setup for visualization the air flow. Power consumption of microplasma actuator was measured by a digital oscilloscope and calculated using the Lissajous Figureure. Air flow was visualized by the Particle Image Velocimetry (PIV). Sub-micron incense smoke was used for tracer particle. Nd $YVO_4$ 532 nm laser was utilized to visualize. Phenomenon of the microplasma actuator was measured by a high-speed camera.

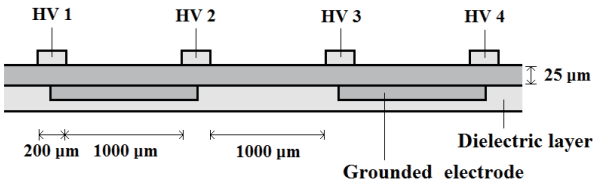


Fig. 2 Geometry of microscale and multi-electrode plasma actuator.

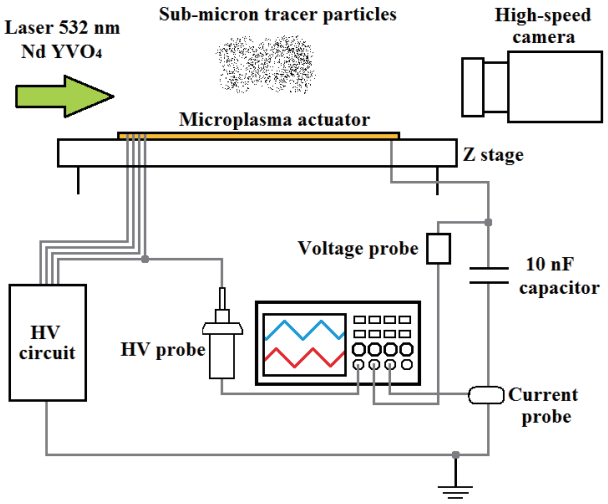


Fig. 3 Experimental setup for the visualization of the air flow.

## 3. Results and discussions

Upper electrodes were energized at 1.3 kV, 15 kHz sinusoidal high-voltage. Discharge power by one electrode was 1.5 W measured by the Lissajous Figureure. When two electrodes were energized, power consumption was 3.0 W.

Air flow induced by plasma flows is principally from upper electrode to lower one. Thus, by driving the HV 1 and HV 3, right-ward flow could be generated. Figure 4 shows the visualized right-ward air flow, when HV1 and 3 were energized by a sinusoidal wave of 1.3 kV, 15 kHz. Flow velocity was about 0.5 m/s at right edge of the plasma actuator, 0.5 mm height. Schematic image of right-ward flow depicts in Figure 5.

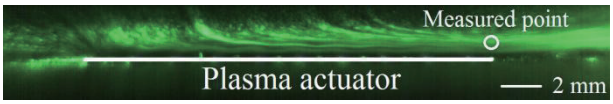


Fig. 4 Right-ward flow was occurred by driving the HV 1 and HV 3 by sinusoidal wave 1.3 kV and 15 kHz.

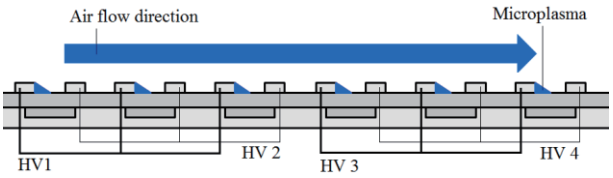


Fig. 5 Schematic image of right-ward flow by energized HV1 and HV 3.

When HV 2 and HV 4 were driven, opposite left-ward air flow was generated. Visualized left-ward flow is shown in Figure 6. Flow velocity was about 0.5 m/s at left edge of the plasma actuator, 0.5 mm height. Schematic image of left-ward flow depicts in Figure 7.

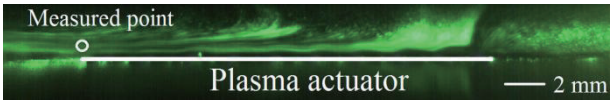


Fig. 6 Left-ward flow was occurred by driving the HV 2 and HV 4 by sinusoidal wave 1.3 kV and 15 kHz.

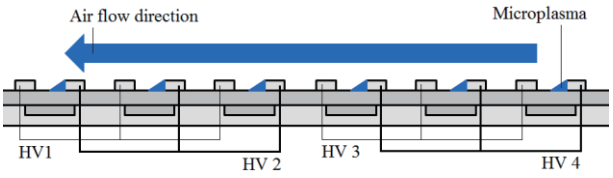


Fig. 7 Schematic image of left-ward flow by energized HV2 and HV 4.

By driving HV 1 and HV 4, flow direction is from both edges to center. At center, two flows conflicted and up-ward flow was generated. Figure 8 shows visualized up-ward flow. Flow velocity was about 0.5 m/s at center of the plasma actuator, 1 mm height. Schematic image of up-ward flow depicts in Figure 9.

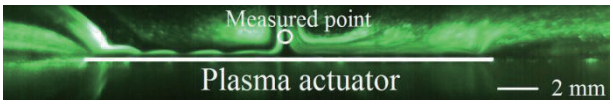


Fig. 8 Left-ward flow was occurred by driving the HV 1 and HV 4 by sinusoidal wave 1.3 kV and 15 kHz.

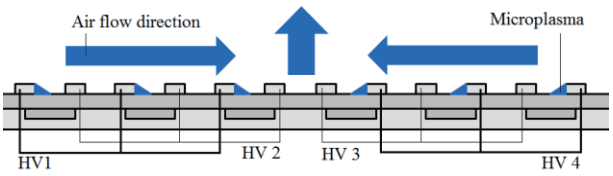


Fig. 9 Schematic image of up-ward flow by energized HV1 and HV 4.

When HV 2 and HV 3 were driven, flow direction is from center to both edges. At center, down flow was generated to satisfy the equation of continuity. Visualized down-ward flow is shown in Figure 10. Flow velocity was about 0.1 m/s at center of the plasma actuator, 1 mm height. Schematic image of down-ward flow depicts in Figure 11.

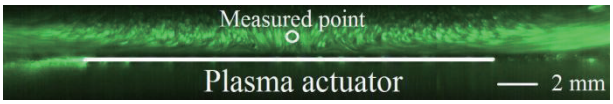


Fig. 10 Down-ward flow was occurred by driving the HV 2 and 3 by sinusoidal wave 1.3 kV and 15 kHz.

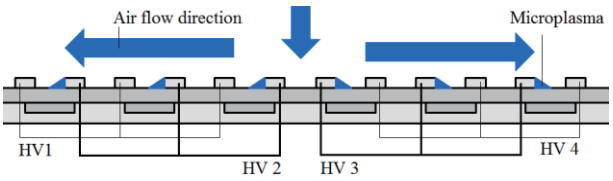


Fig. 11 Schematic image of down-ward flow by energized HV2 and HV 3.

## 4. Conclusion

In this study, multi-electrode microplasma actuator was investigated. By driving four HV electrodes independently, four types of flows were generated, Right-ward, left-ward, up-ward and down ward. Before two are horizontal flow, after two are perpendicular flow. Flow velocity was on the order of 0.1 m/s.

## References

[1] K. P. Singh, S. Roy, J. *Appl. Phys*. 103, (2008) 013305.

[2] J. R. Roth, X. Din, *Proc. 44th AIAA Aerospace Sciences Meeting and Exhibit*, (2006) 14604-14631.

# A Spiral-tube-type Valveless Piezoelectric Pump With Gyroscopic Effect

Jianhui Zhang
State Key Laboratory of Mechanics and Control of Mechanical Structures, Nanjing University of Aeronautics and Astronautics
Nanjing, 210016, China

**ABSTRACT**

The valveless piezoelectric pump integrates driving and transmitting into one operating element, and characterizes easy micro-miniaturization. But there is the original sin of low pressure and low flow. Thus, it must be avoid weakness to choose applications field. This paper analyzes the flow characteristics in the rotary spiral-tube, which will cause the Coriolis force, and subsequently influence the fluid moving. The principle of the pump is deduced and the spiral-tube-type valveless piezoelectric pump is invented.

## 1. Introduction

The last two decades has seen considerable progress and development in theoretical studies regarding to the valveless piezoelectric pump. However, few reports have been found in practical application. It is highly possible that there exists original sin of low pressure and low flow despite of many advantages of the valveless piezoelectric pump. So the pump which is in need of miniaturization and demands no pressure and flow can be chosen. So far, no researches and reports have been found to extend its advantages and inhibit its shortcomings [1-5].

In 1974, Ito H found the direction of the Coriolis force caused by rotation is related to the direction of the rotational angular velocity [1]. In 1990, Zhang FuXue proposed the piezoelectric fluidic gyro, in which the airflow beam deflected by the Coriolis force can cause peripheral circuit voltage changes to sense angular velocity [2]. In 2001, Zhang JianHui proposed that using the Coriolis force caused by flow moving in spiral tube can implement the principle of the pump [3].

In this article, we report the phenomenon that flow in a spiral tube valveless piezoelectric pump is sensitive to the pump position, and apply this phenomenon to a new pump with gyroscopic effect. In the spiral tube, when the fluid flows clockwise or counterclockwise, the Coriolis force will alter the flow resistance.

## 2. Principle

In an effort to investigate the phenomenon of flow in a spiral tube, a rotating reference system shown in Figure 1 is selected. Assuming that the fluid is inviscid, incompressible, homogeneous, and steady state, that is only the average flow considered. The mathematical model of spiral flow tube is Archimedes spiral: $r = a\theta$ .Here a is a parameter. We consider the element of fluid M moving in the spiral tube, which is equivalent to the original inertial reference system $(r_I, \theta_I)$ rotates around an axis perpendicular to the plate in which spiral flow tube is. Thus, a rotating coordinate system $(r_R, \theta_R)$ which rotates in angular velocity $\Omega$ is involved. Here, the subscript I indicates the inertial reference system, and the subscript R indicates the rotating coordinate system, as shown in the Figure 1 (a).

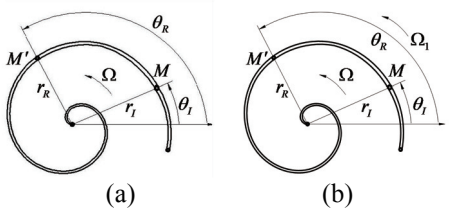


Fig. 1 The reference system diagram of flow in the spiral tube (a) and (b) with additional $\Omega_1$.

The Coriolis acceleration comes from the Coriolis force, which is generated by the particle do the circular motion and also do the radial movement. And this Coriolis force will be caused by the rotation of reference system, which is a non-inertial reference system. In the spiral tube, when the fluid flows clockwise or counterclockwise, the Coriolis force will be caused and change the flow resistance. Thus, the macro-phenomenon is that clockwise flow will be different from the counterpart.

When the original inertial reference system $(r_I, \theta_I)$ rotates in angular velocity $\Omega_1$ , thus, a rotating coordinate system $(r_R, \theta_R)$ ,which rotates in angular velocity $\Omega + \Omega_1$ around an axis perpendicular to the spiral tube plate, is involved, as shown in Figure 1(b). The element of M moves in the spiral tube on the condition of the angular velocity being $\Omega + \Omega_1$ , the angular velocity $\Omega$ and the angular velocity $\Omega + \Omega_1$ on the contribution to the Coriolis acceleration is clearly not the same, so the flow resistance in spiral tube is changed. Due to the existence of new $\Omega_1$ , the macro-phenomenon of clockwise flow being different from counterclockwise flow will also change accordingly.

## 3.Experiments

The pressure differential between pump inlet and outlet increases with the increase of rotary speed of plate.

Corresponding author: Jianhui Zhang
*E-mail address*: zhangjh@nuaa.edu.cn

Especially when the rotary speed of plate significantly increases, the pressure differential also increases significantly. It proves that the gyroscopic effect is more suitable for measuring the change of attitude that has a large angular velocity(Figure 2).

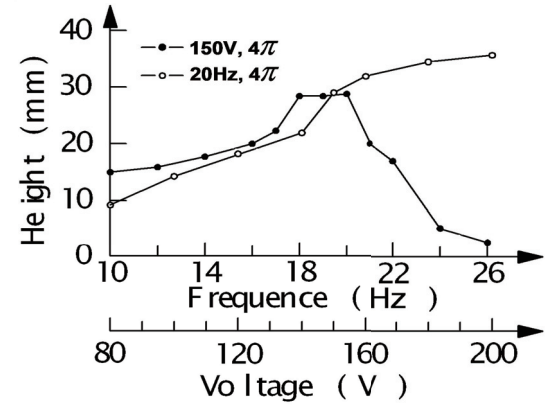


(a)

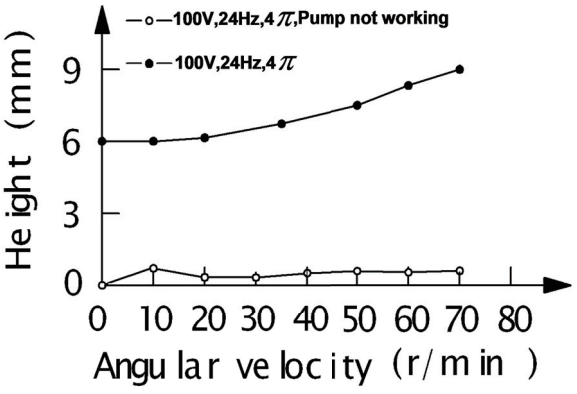


(b)

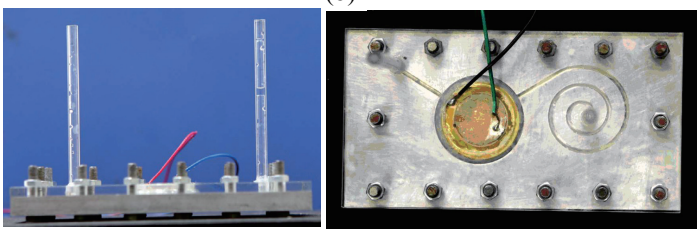

(c)

Fig. 2 (a):The curve of the piezoelectric vibrator frequency, driving voltage and the pump pressure differential. (b):The curve of the pump attitude and the pressure differential.(c):Photographs of the spiral-tube-type valveless piezoelectric pump.

**4. Summary**

When the rotary speed is 0, the pressure differential is 6 mm H2O. This pressure is generated by the simple pump motion driven by the piezoelectric vibrator. The fluid moves in the spiral tube, feel the Coriolis force caused by the spiral rotation. When the piezoelectric vibrator does not work, the pressure differential is very tiny and changes in non-obvious rule even if the plate is rotating in high speed. While the piezoelectric vibrator is working, the pressure differential is a superposition of 6mm above and clearly reflects the speed change of the rotary table. This indicates that the Coriolis force caused only by plate rotation is hardly to measure. In this study, the important of the pump is to drive flow in spiral tube to induce the Coriolis force, and in the meanwhile, the pump flow reciprocating in the tube also has a discharge effect of attitude measurement saturation.

The principle of flow in a spiral tube element can feel the Coriolis force change and is utilized to invent a valveless piezoelectric pump with gyroscopic effect. This pump has not only the function of sensing the attitude change, but also the function of driving fluid transmitting. This brings the integrated applications of valveless piezoelectric pump into a new field. Experimental results show that the spiral-tube-type valveless piezoelectric pump can convert the attitude change to a form of pressure differential output. This article offers a new possibility for a new low cost and miniature gyro, and promises the future development of civil gyroscope.

**References**

[1] Ito H, Motai T. *High Speed Mech,* 29(1974)33-57.
[2] Zhang F X, Tian W J. *J Chin Inert Technol,* (1990) 60-66.
[3] Zhang J H. *Japan Patent,* P2001-221166A.
[4] Bolinder C J, SundÉn B. *Int J Heat Mass Transfer*, 39(1996)3101-3115
[5] Kapur P C, Meloy T P. *Powder Technol*, 102(1999) 244-252

# Examination of Discretization Schemes for the Numerical Simulation of Ion Transport around a Plasma Actuator

Kohei Matsumoto[1], Koji Fukagata[1]
[1]Keio University
Hiyoshi 3-14-1, Kohoku-ku, Yokohama 223-8522, Japan

**ABSTRACT**

We perform numerical simulations of ion transport around a dielectric-barrier discharge plasma actuator. A special focus is laid upon the difference in the numerical schemes used for the advection term of plasma fluid model, and we examine how the numerical schemes affect the ion transport and the resultant ion distribution. The positive ion density distribution is found to be slightly different in the case with a high-resolution scheme (Kurganov and Tadmor (KT) central scheme) from that in the case with the first-order upwind scheme.

## 1. Introduction

Active flow control methods have been extensively investigated in order to reduce energy loss and environmental load. Recently, a dielectric-barrier discharge plasma actuator (DBD-PA, hereafter simply referred to as PA) has attracted increasing attention to be used for such an active flow control [1, 2].

A PA induces a body force around its upper electrode. Although the detailed physics on the body force generation mechanism is not completely understood, it is generally believed that the body force is generated by acceleration of ions and their collision with neutral molecules [3].

In numerical simulation of ions and electron transport around a PA, it is important to resolve an ion sheath that has a high ion density region and discontinuous regions. Therefore, it might be important for a numerical simulation to well resolve such an ion sheath. In the present study, we investigate the effect of difference in the discretization schemes used for the advection term in the plasma fluid model.

## 2. Method

### A. Governing equation and calculation condition

Atmospheric pressure plasma is generally considered as a continuum. Hence, the plasma around the PA is considered as fluid, and the plasma fluid model is used in this simulation.

Three types of charged particles are considered: a generic monovalent type of positive ions (index $p$ is in the equations below), a generic monovalent type of negative ions (index $n$) and an electron (index $e$). The transport equations for the number of densities of ions and electron are written, respectively, as

$$\frac{\partial \mathrm{n_p}}{\partial t} + \nabla \cdot \left(\mathrm{n_p}\mu_p \mathbf{E} - D_p \nabla n_p\right) = \alpha n_e \mu_e |\mathbf{E}| - r_{pe} n_p n_e - r_{pn} n_p n_n \quad (1)$$

$$\frac{\partial \mathrm{n_n}}{\partial t} + \nabla \cdot \left(-\mathrm{n_n}\mu_n \mathbf{E} - D_n \nabla n_n\right) = \beta n_e \mu_e |\mathbf{E}| - r_{pn} n_p n_n \quad (2)$$

$$\frac{\partial \mathrm{n_e}}{\partial t} + \nabla \cdot \left(-\mathrm{n_e}\mu_e \mathbf{E} - D_e \nabla n_e\right) = (\alpha - \beta) n_e \mu_e |\mathbf{E}| - r_{pe} n_p n_e \quad (3)$$

where $\mu$, $D$, $\alpha$, $\beta$, and $r$ represent the mobility, the diffusion coefficient, the impact ionization coefficient, the attachment ionization coefficient, and the recombination coefficient.

Equation (1)-(3) above must be coupled to Poisson's equation for the electric potential and the definition of the electric field, which are written as,

$$\nabla \cdot (-\varepsilon_d \nabla \phi) = \frac{c\left(n_p - n_n - n_e\right)}{\varepsilon_0 \varepsilon_d} \quad (4)$$

$$\mathbf{E} = -\nabla \phi \quad (5)$$

where $\varepsilon_d$ and $\varepsilon_0$ are the relative permittivity and the permittivity of a vacuum, $c$ is the elementary charge, $\phi$ is the electric potential, and $\mathbf{E}$ is the electric field vector.

The computational domain is shown in Fig. 1. A sinusoidal AC voltage signal is applied to the upper electrode. The driving frequency $f$ and the peak-to-peak voltage $V_{pp}$ are $f = 5$ kHz and $V_{pp} = 16$ kV, respectively. The grid spacing in $x$ direction is 100 μm. The grid spacing in y direction is 10 μm in the region of $0 \le \mathrm{y} \le 400$ μm. The number of computational cells is 290×110.

### B. Discretization schemes for the advection term

The first-order upwind scheme (UW1) and a high-resolution scheme, i.e., KT central scheme [4] (KT2), are used for the advection term. The KT central

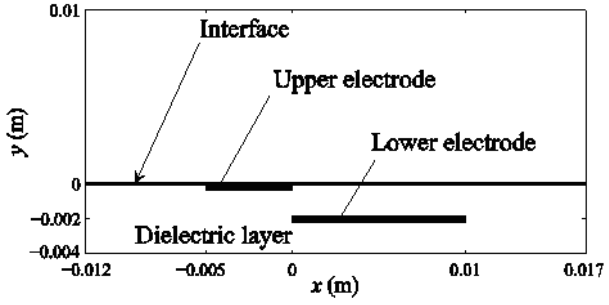


Fig. 1 Computational domain

Corresponding author: Koji Fukagata
*E-mail address*: fukagata@mech.keio.ac.jp

scheme is a Riemann-solver-free second-order scheme, and it is effective for resolving sharp gradient phenomena.

## 3. Results

Figure 2 shows the positive ion density distributions around the upper electrode at $t/T = 0.03$ with UW1 and KT2 schemes, where $T$ denotes the period of voltage signal. In order to investigate the difference more quantitatively, the positive ion density distributions at a constant value of $y$ is shown in Fig. 3.

At $t/T = 0.03$, obvious differences of positive ion density distributions are observed near the upper electrode. At $t/T = 0.03$, the shape of the high positive ion density distribution area obtained using UW1 scheme is akin to a half-ellipse and is located on the upper electrode, but that using KT2 scheme is more triangular and is located above the upper electrode. The height of the high Positive ion density distribution area of KT2 scheme is about twice larger than that of UW1. These differences suggest that difference between UW1 and KT2 schemes makes a difference in a shift of positive ion density.

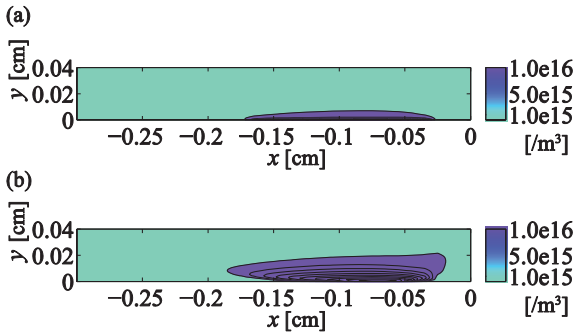


Fig. 2 Positive ion density distribution near the upper electrode at $t/T = 0.03$: (a) with first order upwind scheme; (b) KT scheme.

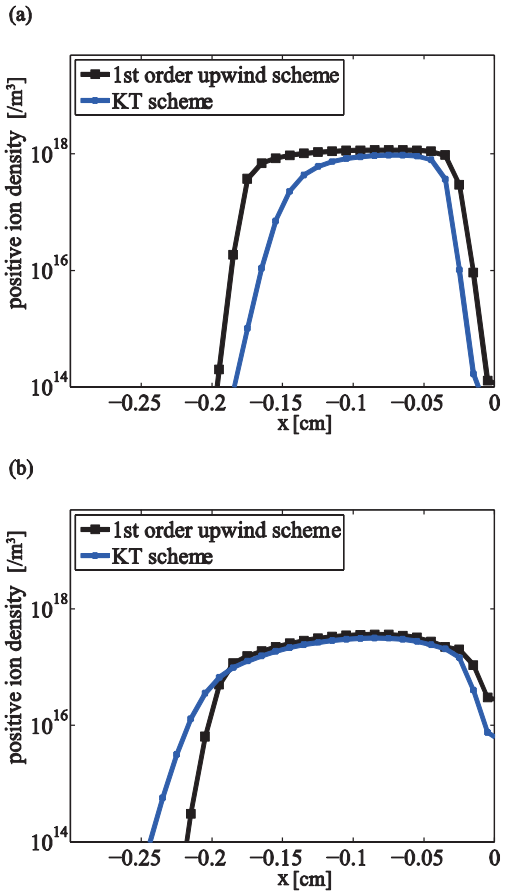


Fig. 3 Positive ion density distribution at $t/T = 0.03$: (a) at $y = 20$ μm, (b) at $y = 100$ μm.

When KT2 scheme is used, the length of the high positive ion sheath area, over $10^{16}$ m$^{-3}$, at $y = 20$ μm is 300 μm smaller than that in UW1 case, as shown in Fig. 3(a). At $y = 100$ μm, the length of the high positive ion sheath area of KT2 scheme is nearly equal to that of UW1, as shown in Fig. 3(b). In both Figs. 3(a) and (b), the gradient in $x$ direction is smaller with KT2 scheme than with UW1 scheme. In general, KT2 scheme is more suitable to resolve a sharp gradient in transport than UW1 scheme; from the present results, however, it appears that a higher gradient of positive ion density exists when UW1 scheme is used. A possible reason for this is that the equations of plasma fluid model have many different terms in addition to the advection term, and these terms should strongly affect the positive ion density distribution.

## 4. Conclusions

We performed two-dimensional numerical simulations of ion transport around a plasma actuator with the first-order upwind scheme and the Kurganov-Tadmor (KT) high resolution scheme in order to investigate the effect of the numerical schemes.

It is found that the difference in the schemes makes difference of shapes of the high ions density area. This phenomenon suggests the difference of schemes makes a difference in the motion of ions density. However, against our initial expectation, the use of KT scheme resulted in a smaller gradient of the high positive ion density distribution area in $x$ direction as compared to the case of the first-order upwind scheme.

Since the plasma fluid model includes terms other than the advection term, the effect of numerical scheme may be more complicated than that in a simple advection problem. For a complete understanding, there is still a need to investigate how these terms affect the ion distribution.

## References

[1] J. R. Roth, D. M. Sherman, and S. P. Wilkinson, *Proceedings of the AIAA 36th Aerospace Sciences Meeting and Exhibit*, *AIAA Paper*, (1998) 98–0328.

[2] T. C. Corke, C. L. Enloe, and S. P. Wilkinson, *Annu. Rev. Fluid Mech*. 42, (2010) 505.

[3] J. P. Boeuf, Y. Lagmich, T. Unfer, T. Callegari, and L. C. Pitchford, *J. Phys. D* 40, (2007) 652.

[4] A. Kurganov and E. Tadmor, *J. Comput. Phys.*, 160, (2000) 214–282.

# Optimal Control Approach for Solving Inverse Heat Convection Problems

Gennady Alekseev[1,2], Dmitry Tereshko[1,2]
[1]Institute of Applied Mathematics FEB RAS
7, Radio St., Vladivostok, 690041, Russia
[2]Far Eastern Federal University
8, Sukhanova St., Vladivostok, 690950, Russia

**ABSTRACT**

This work is concerned with a numerical solution of inverse extremum problem for the nonstationary heat convection equations. In this problem we need to estimate the temperature value on some part of the boundary using the velocity vector measured in a flow domain. Optimal control approach reduces this problem to the minimization of a cost functional depending on the velocity. We propose numerical algorithm for solution of boundary control problem and discuss some results of numerical experiments.

## 1. Introduction

One of the important problems of thermal convection is the estimation of the temperature boundary values using the data of measurements. The interest to these problems is connected with a large number of applications in science and engineering. Because we don't know the boundary values but have some information about the state, we can consider these problems as inverse problems. From a mathematical point of view inverse problems are usually ill-posed therefore regularization methods and special algorithms are required for the numerical solution of these problems. In our work we reduce inverse problems to corresponding minimization problems by choosing a suitable cost functional that adequately describes the given data. Then inverse problems can be analyzed and solved by applying a unified approach based on the constrained optimization theory in Hilbert or Banach spaces [1-4].

Let $\Omega$ be a bounded domain in the space $\boldsymbol{R}^m$, $m=2, 3$ with Lipschitz boundary $\Gamma$. As a mathematical model we consider the initial boundary value problem for the Oberbeck-Boussinesq equations

$$\mathbf{u}_t - \nu\Delta\mathbf{u} + (\mathbf{u}\cdot\nabla)\mathbf{u} + \nabla p = -\beta T\mathbf{G} \ \text{in}\,\Omega\times(0,t_1), \quad (1)$$

$$\operatorname{div}\mathbf{u} = 0 \ \text{in} \ \Omega\times(0,t_1), \quad \mathbf{u} = \mathbf{g} \ \text{on} \ \Gamma\times(0,t_1), \quad (2)$$

$$T_t - \lambda\Delta T + \mathbf{u}\cdot\nabla T = f \ \text{in} \ \Omega\times(0,t_1), \quad (3)$$

$$T = 0 \ \text{on}\ \Gamma_D\times(0,t_1), \quad T = \psi \ \text{on}\ \Gamma_C\times(0,t_1), \quad (4)$$

$$\mathbf{u}\big|_{t=0} = \mathbf{u}_0 \ \text{in}\ \Omega, \quad T\big|_{t=0} = T_0 \ \text{in} \ \Omega \quad (5)$$

which describes the flow of viscous incompressible heat-conducting fluid in the domain $\Omega$ on the time interval $(0,t_1)$. Here $\mathbf{u}$, $p$ and $T$ denote the velocity, pressure and temperature fields respectively, $\nu$ is the kinematic viscosity coefficient, $\mathbf{G}$ is the gravitational acceleration vector, $\beta$ is the volumetric thermal expansion coefficient, $\lambda$ is the thermal diffusivity coefficient, $\mathbf{g}$ is a given vector-function on $\Gamma$, $\Gamma=\Gamma_D\cup\Gamma_N$. In the optimal control problem the boundary function $\psi$ will be the control on the part $\Gamma_C$ of $\Gamma$.

Corresponding author: Gennady Alekseev
*E-mail address*: alekseev@iam.dvo.ru

## 2. Constrained Minimization Problems

Our goal is the numerical study of the inverse extremum problems for the model under consideration. The problems consist in minimization of certain cost functional depending on the velocity and control. We assume that the temperature boundary value $\psi$ vary in some closed convex set $K$. The mathematical statement of the constrained minimization problem is as follows: find $(\mathbf{u},p,T,\psi)$ such that $F(\mathbf{u},p,T,\psi)=0$ and

$$J(\mathbf{u},\psi) = J_i(\mathbf{u}) + \frac{\mu}{2}\int_0^{t_1}\int_{\Gamma_C}\psi^2 d\Gamma\, dt \to \inf \ . \quad (6)$$

Here $F(\mathbf{u},p,T,\psi)=0$ is the operator constraint in the form of the weak formulation of problem (1)-(5); $\mu$ is a positive constant, $J_i(\mathbf{u})$ is a cost functional. In the considered temperature estimation problem the possible cost functionals are defined as

$$J_1(\mathbf{u}) = \frac{1}{2}\int_0^{t_1}\int_{\Omega_d}|\mathbf{u}-\mathbf{u}_d|^2 d\Omega\, dt,$$

$$J_2(\mathbf{u}) = \frac{1}{2}\int_0^{t_1}\int_{\Gamma_d}|\mathbf{u}-\mathbf{u}_d|^2 d\Gamma\, dt$$

in the cases where the velocity field data $\mathbf{u}_d$ in some subdomain $\Omega_d$ or on some curve $\Gamma_d$ are given.

## 3. Numerical Experiments

We propose a numerical algorithm based on main idea of the paper [5] where an optimal boundary control problem for the stationary Navier-Stokes equations was solved. At the beginning we split the time interval $(0,t_1)$ into $N$ parts $(t_{n-1},t_n)$, $n=1,2,\ldots,N$. Then we assume that unknown boundary function $\psi$ at time $t=t_n$ can be written as

$$\psi^n = \sum_{i=1}^{M} k_i^n \psi_i \quad (7)$$

where $\psi_i$, $i=1,2,\ldots,M$ are the given basis functions and $k_i^n$ are the unknown coefficients. Using the linearized implicit scheme for approximation of problem (1)-(5) we find at time $t=t_n$ solution $(\mathbf{u}^n,p^n,T^n)$ corresponding to the boundary function $\psi^n$ in (7). After that we can approximate the value of the functional $J(\mathbf{u},\psi)$ with $J_i=J_1$ at time $t=t_n$ as follows

$$I(\mathbf{u}^n,\psi^n)=\frac{1}{2}\left\|\sum_{i=1}^{M}k_i^n\mathbf{u}_i-\mathbf{u}_d\right\|_{\Omega_d}^2+\frac{\mu}{2}\left\|\sum_{i=1}^{M}k_i^n\psi_i\right\|_{\Gamma_C}^2=$$
$$\frac{1}{2}\sum_{i=1}^{M}\sum_{j=1}^{M}a_{ij}k_i^n\,k_j^n-\sum_{j=1}^{M}b_jk_j^n+\frac{c}{2}$$

where $a_{ij}=(\mathbf{u}_i,\mathbf{u}_j)_{\Omega_d}+\mu(\psi_i,\psi_j)_{\Gamma_C}$, $b_j=(\mathbf{u}_d,\mathbf{u}_j)_{\Omega_d}$, $c=\|\mathbf{u}_d\|_{\Omega_d}^2$ and $\mathbf{u}_i$ is the solution corresponding to the basis function $\psi_i$. So we obtain the finite minimization problem. Solution of this problem can be find by solving the following system of linear algebraic equations

$$\sum_{i=1}^{M}a_{ij}\,k_i^n=b_j,\ \ j=1,2,\dots,M.$$

Substituting the coefficients $k_i^n$ in the formula (7) we find the boundary function $\psi$ at time $t=t_n$. Then we calculate $(\mathbf{u}^n,p^n,T^n)$ and go to the next time step.

Let us note that this algorithm does not use the first order necessary optimality conditions (see [1-4]) and more simple to implement. Besides that the regularization parameter $\mu$ can be chosen equal to zero.

The open source software freeFEM++ (www.freefem.org) was used for the discretization and solution of initial boundary value problems by the finite element method.

The main goal of the computational experiments is to determine the dependence of the solution accuracy on the choice of the problem parameters. For example, the number of the basis functions $M$ and the regularization parameter $\mu$ have a great influence on the accuracy of numerical solutions.

Following example is connected with the 2D viscous heat-conducting fluid flow in the square cavity

$$\Omega=\{(x,y):\ -1<x,y<1\}$$

with the heated internal boundary

$$\Gamma_C=\{(x,y):\ x^2+y^2=0.25\}.$$

In inverse problem we don't know the temperature values on boundary $\Gamma_C$ and reconstruct these values using the velocity vector data in the flow domain $\Omega$. In our numerical experiments these velocity data $\mathbf{u}_d$ are obtained as a solution of the Oberbeck-Boussinesq equations on time interval $(0,1)$ with no-slip boundary conditions $\mathbf{u}=\mathbf{0}$ for the velocity on $\Gamma$, the homogeneous Dirichlet boundary condition $T=0$ for temperature on the external boundaries $\Gamma_D$ and the Dirichlet boundary condition $T=\psi_d$ on the internal boundary $\Gamma_C$. We assume that distributed heat source $f=0$ and the original temperature boundary value $\psi_d$ on $\Gamma_C$ is defined by the formula $\psi_d=t(2-t)$, $t\in(0,1)$.

The problem (1)-(5) with $\psi=\psi_d$ is solved in dimensionless form for the Prandtl number Pr=7 and Raleigh number $\mathrm{Ra}=10^4$. The numerical solution to this initial boundary value problem is denoted as $(\mathbf{u}_d,p_d,T_d)$. Then we use the velocity field data $\mathbf{u}_d$ for numerical estimation of the corresponding temperature boundary value $\psi$ on the part of boundary $\Gamma_C$. Velocity vector $\mathbf{u}_d$ and temperature field $T_d$ at $t=1$ are shown in Fig. 1.

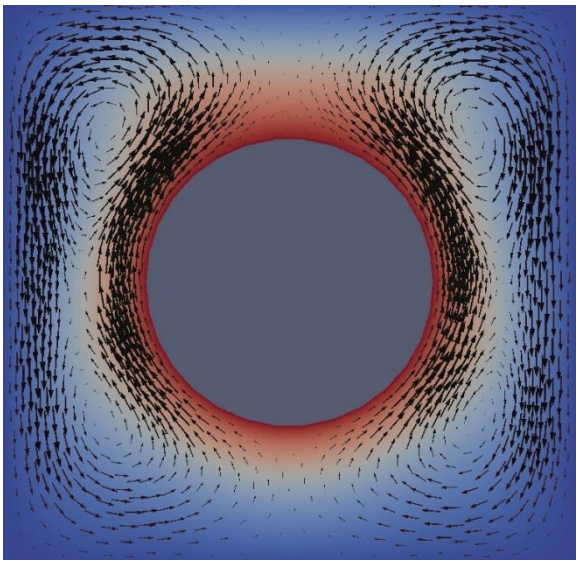

Fig. 1 Velocity and temperature fields for the viscous heat-conducting fluid flow around the heated circular cylinder in a cavity with cold external walls.

In our numerical experiments we choose different ways to specify the given velocity data $\mathbf{u}_d$. For example, in the case of the cost functional $J_1(\mathbf{u})$ the observation domain $\Omega_d$ can be equal to the whole flow domain $\Omega$ or can be some subdomain. In the case of the cost functional $J_2(\mathbf{u})$ we can choose different curves $\Gamma_d$. The more data are given, the more accurate solution is obtained. But the location of the observation domain can be also very important. Another important parameter affecting the accuracy of the solution is the number of basis functions $M$. In order to minimize the computational cost we want to choose this number as small as possible but the accuracy should be sufficiently high. Based on the analysis of computational results we can choose optimal values of important parameters and develop some recommendations for future applications.

**Acknowledgments**

This work was supported by the Russian Foundation for Basic Research (project no. 13-01-00313-a), the Russian Science Foundation (project no. 14-11-00079) and the Ministry of Education and Science of Russia (project no. 14.Y26.31.0003).

**References**

[1] M.D. Gunzburger, *Perspectives in flow control and optimization*, 2003, 261 p.

[2] G.V. Alekseev, D.A. Tereshko, *Analysis and optimization in hydrodynamics of viscous fluid*, 2008, 365 p.

[3] G.V. Alekseev, D.A. Tereshko, *J. Appl. Mech. Tech. Phys.*, 51(2010) 510-520.

[4] G.V. Alekseev, D.A. Tereshko, *Comp. Math. Math Phys.*, 51(2011) 1539-1557.

[5] G.V. Alekseev, V.V. Malikin, *Comp. Fluid Dynamics J.*, 3(1994) 1-26.

# Low-Reynolds-Number Aerodynamic Characteristics of Various Airfoils

Shogo Kondo, Ryo Nozawa, Jiro Funaki, Katsuya Hirata
Department of Mechanical Engineering, Doshisha University
Kyoto, 610-0321, Japan

**ABSTRACT**

The aerodynamic characteristics of airfoils have been researched in higher Reynolds-number ranges more than $10^6$, in a historic context closely related with the developments of airplanes and fluid machineries in the last century. However, our knowledge is not enough in low and middle Reynolds-number ranges. So, in the present study, we investigate three kinds of high-performance airfoils proposed for low Reynolds numbers; namely, an iNACA0015, a FPBi and a FPBN, in comparison with such basic airfoils as NACA0015 and flat plate at a low Reynolds number $Re = 1.0\times10^2$.

## 1. Introduction

Airfoil is one of the most elemental devices to control flow and its reacting force. However, most of aerodynamic characteristics of airfoils have been measured at Reynolds numbers *Re's* more than about $1.0\times10^6$, where *Re* is defined using a chord length *c* as a characteristic length scale [1] – [4].

On the other hand, we have been requiring more precise knowledge about the aerodynamic characteristics of airfoils especially at low and middle *Re* ranges at $Re < 10^6$, because of the recently-increasing importance in such applications as unmanned aerial vehicles known as UAVs, micro air vehicles known as MAVs, insect/bird flight dynamics, small-scale machines like micro fluid machineries and micro combustion engines and so on.

Concerning the aerodynamic characteristics at low values of *Re*, there have been several studies [5] – [13]. However, in such a lower range of *Re*, our knowledge has not been enough yet, due to non-negligible and complicated *Re* effects related with the laminar-to-turbulent transition whose strong non-linearity brings us some technical difficulties in the accuracies of analyses, computations and experiments.

In the present study, referring to our previous findings [13], we propose three kinds of two-dimensional airfoils with high efficiency at low *Re*; namely, an iNACA0015, a FPBi and a FPBN (for their definitions, see later). And, we investigate them at $Re = 1.0\times10^2$ in comparison with such basic airfoils as a NACA0015 and a flat plate by two- and three-dimensional computations.

## 2. Method

### 2.1 Model

Figure 1 shows the present models. They are three kinds of two-dimensional airfoils with high efficiency at low *Re*; namely, an iNACA0015 (the NACA0015 placed back to front), a FPBi (a flat plate blended with iNACA0015 as its upper half) and a FPBN (a flat plate blended with NACA0015 as its upper half), together with two kinds of fundamental airfoils such as a NACA0015 and a flat plate. The iNACA0015 and the FPBi are similar to the optimum shapes for drag minimisation [14] and for lift maximisation [15], respectively.

Corresponding author: Shogo Kondo
*E-mail address*: duo0538@mail4.doshisha.ac.jp

### 2.2 Computation

In many actual situations, most of the flow at $Re < 10^6$ could be usually regarded as incompressible and viscous. So, we consider the incompressible full Navier-Stokes equations for the present numerical analyses. We approximately solve the equations using the MAC method in a finite-difference disccritisation, a third-order-upwind difference scheme in spatial discretisation of convective terms, a second-order-central difference scheme in spatial discretisation of the other terms, and the Euler explicit scheme in a time marching. The boundary condition on the airfoil surface is viscid. On the outer boundaries of the computational domain, we suppose the Dirichlet condition as $u = U_\infty$, $v = 0$ and $w = 0$.

## 3. Results and Discussion

Figure 2 shows a sample of three-dimensional computations. We can see that the flow is fully two-dimensional.

Figure 3 shows a typical example of the aerodynamic characteristics $C_L/C_D$ of five airfoils at $Re = 1.0\times10^2$ plotted against attack angle $\alpha$. To correct the camber effects as seen in Fig. 2(*a*), we show Fig. 2(*b*) whose abscissa $\alpha'$ is modified instead of $\alpha$ in Fig. 2(*a*).

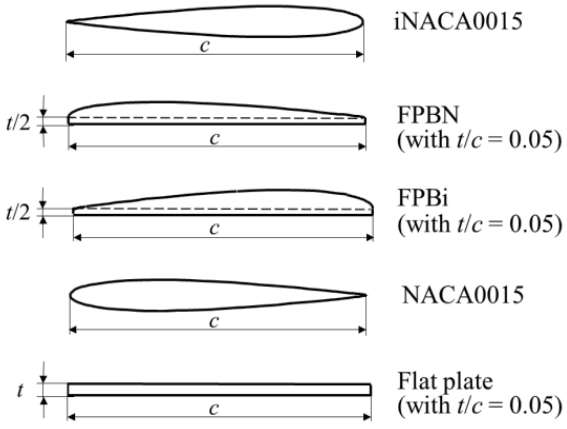


Fig. 1 Model: two-dimensional airfoils.

## 4. Concluding Remarks

We have proposed three kinds of two-dimensional airfoils with high efficiency at low *Re*; namely, the iNACA0015 and the FPBi and the FPBN. And, we have investigated them in comparison with such basic airfoils as a NACA0015 and a flat plate, by two- and three-dimensional computations, at $Re = 1.0\times10^2$.

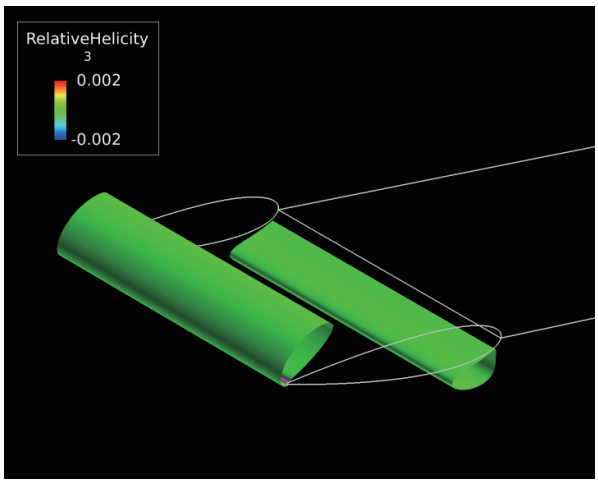


Fig. 2 three-dimensional computation for iNACA0015 at $Re = 1.0\times10^2$ and $\alpha = 18$ deg. visualized using iso-Q surfaces with normalized $Q = 3$.

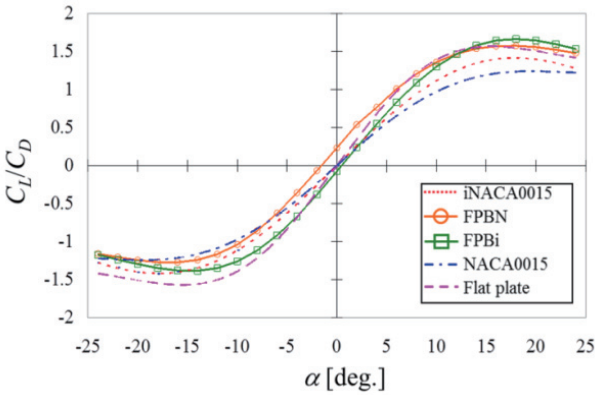


($a$) $C_L/C_D$

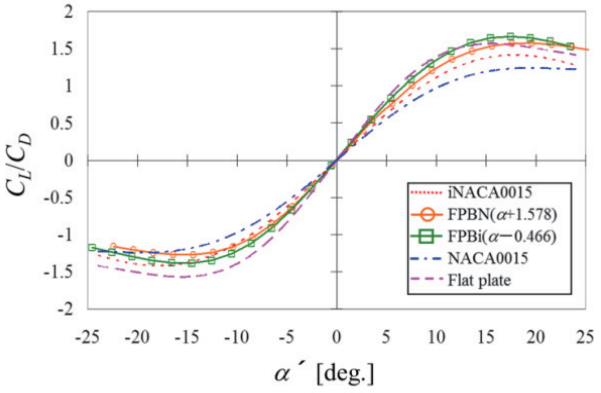


($b$) $C_L/C_D$ with corrected attack angle $\alpha'$

Fig. 3 Aerodynamic characteristics versus at $\alpha$ at $Re = 1.0 \times 10^2$

As a result, the flow is completely two-dimensional, even at large attack angle $\alpha$. We have revealed the effects of $\alpha$ upon various aerodynamic characteristics such as $C_L$, $C_D$ and $C_L/C_D$. In summary, at such a low *Re* as $1.0\times10^2$, the aerodynamic characteristics of all the five airfoils are qualitatively almost similar with one another. At $|\alpha| \lesssim 10$ deg., those of the FPBi are quantitatively almost the same as those of the flat plate, and superior to those of the other three airfoils. The maximum $C_L/C_D$ is attained by the FPBi at $\alpha = 17$ deg. and the minimum is attained by the flat plate at $\alpha = -15$deg.

In addition, concerning the controllability, the NACA0015 is superior among the five airfoils especially at $|\alpha| \gtrsim 10$ deg., due to the lack of a remarkable stall feature on $C_L/C_D$. Besides, we have visualised the flow around the airfoils by streamlines and pressure/vorticity distributions around the airfoils at various $\alpha$'s.

## References


[1] Jacobs, E. N. and Sherman, A., *NACA Technical Report*, No. 586 (1937), 227－267.

[2] Abbott, I. H. and Doenhoff, A. E. von., *Theory of Wing Sections* (1958), Dover, New York, 462－463.

[3] Riegels, F. W., *Aerofoil Sections* (1961), Butterworths, London.

[4] Eppler, R., *Airfoil Design and Data* (1990), Springer-Verlag, Berlin.

[5] McMasters, J. H. and Henderson M. L., *Tech. Soaring, Vol. 6* (1980), 1－21.

[6] Okamoto, M., Yasuda, K. and Azuma, A., *Journal of Experimental Biology, Vol. 199* (1996), 281－294.

[7] Sunada, S., Sakaguchi, A. and Kawachi, K., Transactions ASME, *Journal of Fluids Engineering, Vol. 119* (1997), 129－135.

[8] Motohashi, T., Proc. *39th Aircraft Symposium JSASS, 3D6* (2001), 1－4 (in Japanese).

[9] Nakane, N., Tanaka, T. and Motohashi, T., Proc. *35th Fluid Dynamics Conference, JSASS* (2003), 179－182 (in Japanese).

[10] Sun, Q. and Boyd, I. D., *Journal of Fluid Mechanics, Vol. 502* (2004), 199－206.

[11] Ohtake, T., Nakae, Y. and Motohashi, T., *Journal of the Japan Society for Aeronautical and Space Sciences, Vol. 55* (2007), 439－445 (in Japanene).

[12] Taira, T and Colonius, T, *Journal of Fluid Mechanics, Vol. 623* (2009), 187－207.

[13] Hirata, K., Kawakita, M., Iijima, T., Koga, M., Kihira, M. and Funaki J., *Journal of Fluid Science and Technology, Vol. 5* (2010), 447－463.

[14] Yagi, H. and Kawahara, M., *Computer Methods in Applied Mechanics and Engineering, Vol. 196* (2007), 5084-5091.

[15] Katamine, E., Nishihashi, N. and Azegami, H., *Transactions of the Japan Society of Mechanical Engineers, Series B, Vol. 74* (2008), 2426-2433.

Eleventh International Conference on Flow Dynamics
October 8-10, 2014, Sendai, Miyagi, Japan

# Drag Reduction of a High Reynolds Number Spatially Developing Boundary Layer Using a Uniform Blowing or Suction

Daigo Noguchi[1], Koji Fukagata[1], Naoko Tokugawa[2]
[1]Department of Mechanical Engineering, Keio University
3-14-1 Hiyoshi, Kohoku-ku, Yokohama, Kanagawa, 223-8522, Japan
[2]Institute of Aeronautical Technology, Japan Aerospace Exploration Agency
6-13-11 Oosawa, Mitaka, Tokyo 181-0015, Japan

**ABSTRACT**

To investigate the effect of friction drag reduction in a spatially developing boundary layer using a combined uniform blowing and suction, Reynolds-Averaged Navier-Stokes simulation was performed. The Reynolds number based on the distance from the inlet was up to $Re_x = 3\times10^6$. A uniform suction and blowing at 0.1% of freestream velocity was applied to the wall and calculated. The local friction coefficient was found to decrease about 20% regardless of the distance from inlet and regardless whether the flow is turbulence or laminar.

## 1. Introduction

Uniform suction or blowing from the wall is one of the methods to reduce the friction drag. The uniform suction improves the stability of laminar boundary layer: the transition will be delayed and the overall friction drag will be reduced due to the extended laminar region. In contrast, the uniform blowing is known to reduce the drag in the fully-turbulent regime, as studied, e.g., by Kametani & Fukagata [1]. Therefore, a combination of suction and blowing is expected to be effective for the flow with transition, such as the flow around an airfoil, by delaying the transition near the trailing edge and by reducing the turbulent drag in the past-transition (i.e., turbulent) region. In particular, if such a control is devised to the natural laminar flow wing of the silent supersonic transport being developed by JAXA [2], its fuel consumption can further be reduced.

However, there are few studies on the effect of such a combined uniform suction and blowing. Therefore, it is necessary to investigate the effect of the blowing/suction amplitude or the Reynolds number dependency in order to consider its feasibility. However, it is difficult to compute the friction drag in a high Reynolds number flow including transition such as the flow around the wing because of the necessity of a large amount of computational grids.

The purposes of this study are to develop a computational code of a low computational cost and to investigate the effect of a uniform suction or blowing separately. In this study, a spatially developing boundary layer flow was calculated to validate the computational code and to investigate the fundamental effect of suction or blowing.

## 2. Method

Two-dimensional unsteady Reynolds Averaged Navier-Stokes simulation (URANS) was performed. For the turbulence model, the Spalart-Allmaras model [3] was used. This model is a one-equation eddy viscosity model and suits for the transition or separation.

An incompressible flow is assumed. The governing equations are the continuity equation, the momentum equation, and the transport equation for an external quantity related to the eddy viscosity:

$$\nabla \cdot \mathbf{u} = 0 \tag{1}$$

$$\frac{D\mathbf{u}}{Dt} = -\nabla p + \frac{1}{Re}\nabla \cdot \left((1+\nu_t)(\nabla \mathbf{u} + (\nabla \mathbf{u})^T)\right) \tag{2}$$

$$\begin{aligned}\frac{D\chi}{Dt} &= C_{b1}\left(S + \frac{1}{Re}\frac{\chi}{\kappa^2 d^2} f_{v2}\right)\chi \\ &+ \frac{1}{Re}\frac{1}{\sigma}\left[\nabla\cdot((1+\chi)\nabla\chi) + C_{b2}(\nabla\chi)^2\right] \\ &- \frac{1}{Re}\left[C_{w1} f_w - \frac{C_{b1}}{\kappa^2} f_{t2}\right]\left[\frac{\chi}{d}\right]^2\end{aligned} \tag{3}$$

Here, all quantities are made dimensionless by using inlet velocity $U_\infty$ and the wing chord length $c$; $\nu_t = \chi f_{v1}$ in Eq. (2) is the eddy viscosity, and $f$ denotes the wall function, $d$ is the distance from the wall, $S$ is the vorticity, and $C$, $\sigma$ and $\kappa$ are constants.

The second-order central difference scheme is used for the spatial discretization. To suppress the dispersion error, the TVD scheme [4] is used for the advection scheme. The time integration is done by using the low-storage third-order Runge-Kutta/Crank-Nicolson scheme.

Two computational domains are used. A computational domain of ($L_x$, $L_y$) = (30, 4) is used to validate the present simulation code in a fully developed turbulent boundary layer. The Reynolds number based on the distance from inlet is up to $Re_x = 3\times10^6$. Another computational domain, ($L_x$, $L_y$) = (4, 4), which resolves the transition point, is used to study the effect of uniform blowing or suction In this case, the Reynolds number is up to $Re_x = 4\times10^5$. In both domains, the numbers of grid points are ($N_x$, $N_y$) = (256, 100). The grid is uniform in the streamwise direction and nonuniform in the wall-normal direction.

Boundary conditions used are the uniform inlet condition, the convective outlet condition, the no-slip condition on the lower wall and the free-slip condition on the upper wall. With the uniform blowing or suction, a wall-normal velocity of $v = \pm 0.001 U_\infty$ is applied to the lower wall.

Corresponding author: Daigo Noguchi
*E-mail address*: noguchi@fukagata.mech.keio.ac.jp

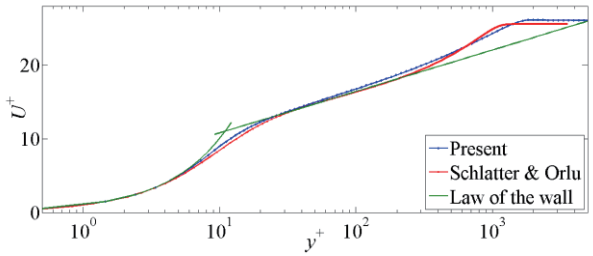

Fig. 1 Mean streamwise velocity profiles at $Re_\theta = 3{,}660$.

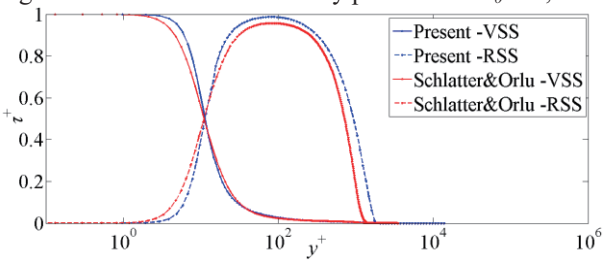

Fig. 2 Shear stress distributions at $Re_\theta = 3{,}660$.

Hereafter, the superscript of $^+$ denotes the wall unit based on the local friction velocity $u_\tau$ of the case without blowing or suction.

## 3. Results and Discussion

Figure 1 shows the streamwise velocity profiles at $Re_\theta = 3{,}660$. Figure 2 shows the shear stress distribution at the same position. In both figures, the DNS data [5] at $Re_\theta = 3{,}626$ is plotted for comparison. It is found that $U^+$ is slightly higher than the DNS data at $y^+ = 10$ and $100 < y^+ < 500$. The contribution of viscous stress is higher in $y^+ < 10$ and Reynolds stress is higher in $y^+ > 10$. Despite these differences, the present RANS results are in fair agreement with the DNS data.

Figure 3 shows the distributions of the local friction coefficient $c_f = \frac{\tau_w}{1/2\rho U_\infty^2}$ with a uniform suction or blowing, where $\tau_w$ is the wall shear stress and $\rho$ is the density of the fluid. The friction coeffient $c_f$ in the case without blowing/suction (denoted as "No control") decreases from the inlet to $Re_x = 0.7\times10^5$; then, increases drastically. It suggests that the transition occurs at this position. In this study, the transition point is defined as the inflection point. The computed $c_f$ in the past-transition region is in excellent agreement with the power-law theory. In the uniform suction case, $c_f$ increases about 30% at any streamwise position. Although a delay of transition was expected, such an effect was not observed in the present study. In the uniform blowing case, $c_f$ is decreased about 20%. The friction drag reduction effect is observed in both laminar and turbulent regions.

Figure 4 shows the velocity distribution with blowing/suction at $Re_\theta = 470$. In the viscous sublayer, the velocity gradient is increased with the suction and decreased with blowing. In the blowing case, the velocity profile is kept lower throughout the boundary layer.

Figure 5 shows the shear stress distribution at $Re_\theta = 470$. Below $y^+ = 10$, the viscous stress was increased with suction and decreased with blowing. The Reynolds stress was decreased with suction and increased with blowing. These modifications are essentially the same as those observed the DNS at a lower Reynolds number by Kametani & Fukagata [1].

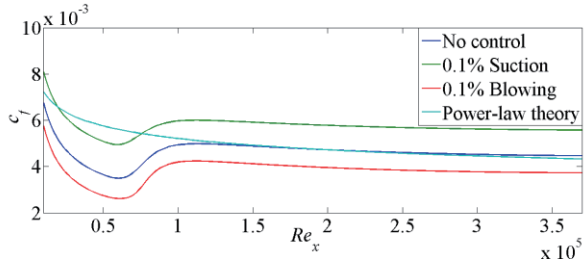

Fig. 3 Local friction coefficient.

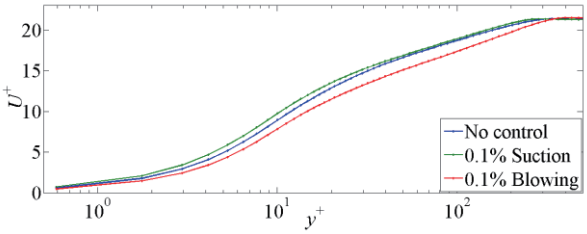

Fig. 4 Mean streamwise velocity profiles with uniform suction or blowing.

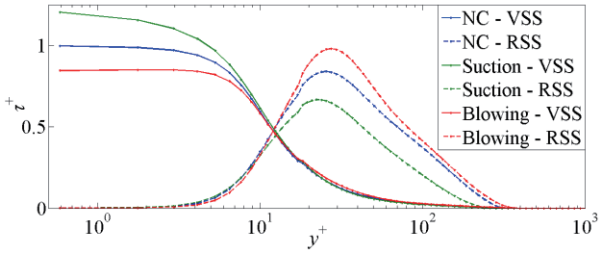

Fig. 5 Shear stress distributions with uniform suction or blowing.

## 4. Conclusions

A low-computational-cost computation code using a turbulent model was developed, and a spatially developing boundary layer flow with a uniform suction or blowing, of which amplitude was 0.1% of the freestream velocity, was simulated. A good agreement with DNS was confirmed in the base flow, i.e., without blowing/suction. With a uniform blowing, the local friction coefficient $c_f$ was decreased about 20% within the region below $Re_x = 4\times10^5$. With a uniform suction control, a delay of transition was not observed against the initial expectation.

## References

[1] Y. Kametani, K. Fukagata, *J. Fluid Mech.,* 681 (2011) 154-172.
[2] N. Tokugawa, D.-Y. Kwak, K. Yoshida, Proc. 25th Int. Congr. Aeronaut. Sci. (2006).
[3] P.R. Spalart, S.R. Allmaras, *La Recherche Aerospatiale,* 1 (1994) 5-21.
[4] A. Harten, *SIAM J. Numer. Anal.,* 21 (1984) 1.
[5] P. Schlatter, R. Örlü, *J. Fluid Mech.,* 659 (2010) 116-126.

# Flow Measurement and Flow Visualisation around a Flat Plate on the Moving Belt System for Wind Tunnel

Tatsuya Inoue[1], Satoshi Maeno[1], Hiroaki Mihara[2], Katsuya Hirata[1]
[1]Department of Mechanical Engineering, Doshisha University
1-3 Tataramiyakodani, Kyotanabeshi, Kyoto 610-0321, Japan
[2]General Building Research Corporation of Japan
5-8-1 Fuzishirodai, Suitashi, Osaka 565-0873, Japan

**ABSTRACT**

In the present study, we develop a moving-belt system for fundamental and accurate wind-tunnel experiments concerning the ground effect, and show its basic performance such as the profiles of time-mean flow velocity and turbulence intensity above the moving belt of the system using a hot-wire anemometer. And in order to show the effectivity of the moving-belt system, we put a thin flat plate above the moving-belt and visualisation the flow to find out the ground effect.

## 1. Introduction

So called "the ground effect" for a moving object in stationary fluids above/on a stationary ground surface or for stationary object above/on a moving wall together with mainstream is typical interesting topic from both theoretical and practical points of view[1,2]. In the present study, we deal with one of the most fundamental and common topics related with the ground effect: that is, a sliding flat plate just above the stationary ground surface. Specifically speaking, by using the developed moving-belt system, we investigate the ground effect in such the most simple model. Namely, we put a thin flat plate above the belt in a wind-tunnel test section, and conduct flow visualisations together with flow-velocity measurements using a HWA.

## 2. Method

### 2.1 Wind Tunnel and Model

We use a closed-return (Göttingen-type) low-speed wind tunnel at Doshisha University. The wind tunnel has a test section with a square cross section of 1000 mm by 1000 mm. The range of the mean velocity $U_\infty$ of a uniform mainstream is 0.5 m/s – 40 m/s. The main experiments are conducted at $U_\infty$ = 3.0 m/s, where turbulence intensity is less than 0.5 %. The moving belt system located in the test section. There is a BLCS (Boudary layer control system) upper the moving belt system.

Figure 1 shows schematic diagram of a flat plate and end plates. A belt moves as a moving ground together with the uniform flow above it, with a belt speed $V_b$. Of course, $V_b$ coincides with the uniform flow velocity $U_\infty$. We install a two-dimensional flat plate, which does not move but is stationary, above the belt at its height $h$. The height $h$ varies from 5 mm to 100 mm. The attack angles of the flat plate is fixed to zero. Then, the flat plate is parallel to both the uniform flow and the ground. The geometry of the flat-plate cross section is an elongated rectangle with a chord $c$ = 50 mm and a thickness $t$ = 1.0 mm. And, the flat plate has a span $s$ = 500 mm. Figure 1 also shows the present coordinate system. We should note that the original Cartesian coordinate system is defined for the moving-belt system. Then, we introduce auxiliary Cartesian coordinate system O′-$x'y'z'$ in order to discuss the ground effect efficiently. The origin O′ is at the centre and on the base (namely, a downstream side face) of the flat plate. In the main experiments, $U_\infty$ and $V_b$ are also fixed to 3.0 m/s.

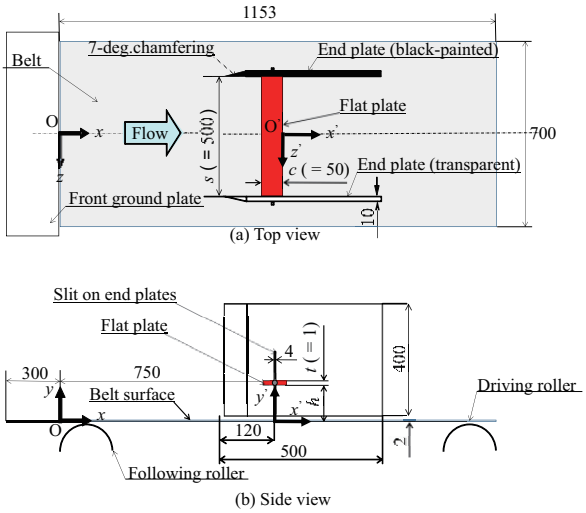


Fig. 1 Schematic diagram of a flat plate and end plates.

### 2.2 Flow Measurement and Flow Visualisation

We used HWA to measure flow around a flat plate. The measurement points are $x'/c$ = 0.02, $z$ = 0, $h/c$ = 2.0, 1.0, 0.5, 0.2, 0.15, 0.1. Figure 2 shows the experimental apparatus for flow visualisation. Air flow is visualised by the smoke which is issued from a heated smoke wire above the belt. The smoke is illminated by a laser sheat and recorded by a high-speed video camera. The measurement points are $z$ = 0, $h/c$ = 2.0, 1.0, 0.2, 0.1.

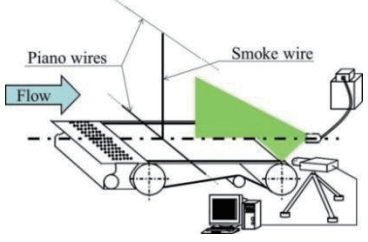


Fig. 2 Experimental apparatus for flow visualisation.

Corresponding author: Tatsuya Inoue
*E-mail address*: euo1503@mail4.doshisha.ac.jp

## 3. Results and Discussion

### 3.1 Flow Velocity

Figure 3 show examples of mean-velocity and turbulence-intensity profiles just behind a flat plate for $h/c$ = 1.0. More specifically, the profiles are at $x'/c$ = 0.02 (at $x$ = 801 mm) and $z/c$ = 0 ($z$ = 0 mm) and $Re$ = $1.1 \times 10^4$ ($U_\infty$ = 3.0 m/s). As is noted earlier, $x'$ denotes the streamwise distance from the base surface of the flat plate. In each Figure 3(a) and Figure 3(b), coloured (red) symbols represent with a flat plate, and black symbols represent in the no-flat-plate condition. And, open and solid symbols represent above the MB and above the SB, respectively.

In advance of main discussion, we consider the profiles in the no-flat-plate condition. At first, we see Figure 3(a). The mean-velocity profile above the moving belt MB is almost uniform, while the profile above the stationary belt SB shows a well-developed boundary layer. Next, we see Figure 3(b). The turbulence-intensity profile above the MB shows very-low turbulence level everywhere, while the profile above the SB indicates the existence of non-negligible turbulence inside the boundary layer in Figure 3(a).

Then, we consider the profiles with a flat plate. We can see that both the mean-velocity and turbulence-intensity profiles almost coincide with those in the no-flat-plate condition, except for a narrow wake of the flat plate especially for the mean-velocity profile. (Of course, we can confirm the narrow wake even for the turbulence-intensity profile. However, the corresponding increment in turbulence intensity is not remarkable, due to the coarse special resolution in the present measurements.) In other words, the influences of the flat-plate existence upon the flow above the MB/SB are the approximately negligible, and are independently restricted in a narrow space of the flat-plate wake especially for the mean-velocity profile.

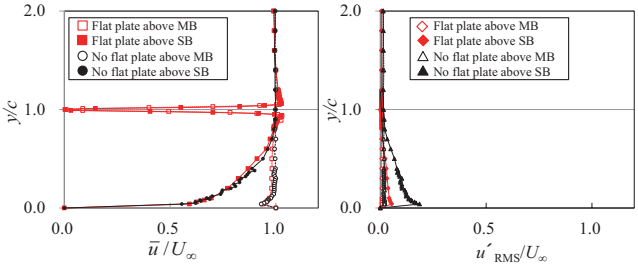


(a) Mean-velocity profile (b) Turbulence-intensity profile

Fig. 3 Mean-velocity and turbulence-intensity profiles just behind a flat plate for $h/b$ = 1.0.

### 3.2 Shedding-Vortex Frequency

Figure 4 shows Strouhal number $St$ plotted against the reduced height $h/c$, at $x'/c$ = 1.0 and at 0.06$c$ downward from the flat-plate centre. We cannot detect any dominant frequencies above the SB for $h/c$ < 1.0. We can see that $St$ above the MB attains the maximum at $h/c$ = 0.2. This fact suggest that the flow could critically change at $h/c$ = 0.2. The critical change at $h/c$ = 0.2 is more influential to fluctuating properties than time-mean velocity.

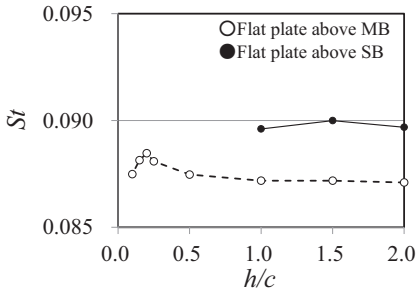


Fig. 4 Strouhal number $St$ against reduced height $h/c$.

### 3.3 Flow Visualisation

Figure 5 shows conventional visualised photographs of the wakes of the flat plate for $h/c$ = 1.0,0.2. When we see the results MB for $h/c$ = 1.0, the wake is almost anitisymmetric about the flat-plate centre. Next, we see the results MB for $h/c$ = 0.2, the interval between neighboring vortices seems shorter than MB for $h/c$ = 1.0. This fact corresponds to the increasing $St$ for $h/c$ = 0.2 in Figure 4.

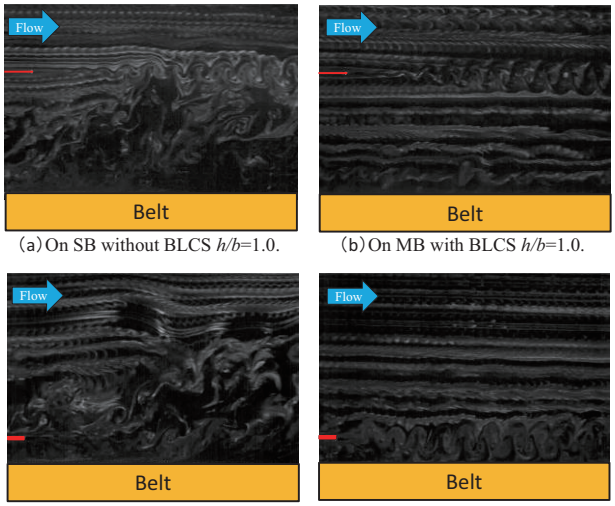


(a) On SB without BLCS $h/b$=1.0. (b) On MB with BLCS $h/b$=1.0.

(a) On SB without BLCS $h/b$=0.2. (b) On MB with BLCS $h/b$=0.2.

Fig. 5 Visualised photograph of the wakes of a flat plate above a moving/stationary belt for $h/b$ = 1.0, 0.2.

## 4. Concluding Remarks

In the present study, we investigate the ground effect in the most basic and simple model, by using this moving-belt system. That is to say, we put a two-dimensional thin flat plate above a moving belt in wind-tunnel test section, and conduct flow visualisations, together with flow-velocity measurements using a HWA. As a result, we have confirmed a critical change in the ground effect at $h/c$ = 0.2.

## References

[1] K. Hirooka, H. Takahashi, *Journal of the Japan Society for Aeronautical and Space Sciences Vol19*., 206 (1971)16-21.

[2] Y. Yoshida, T. Imaizumi, M. Muto, *Transactions of the Society of Automotive Engineers of Japan Sciences Vol7*., 7 (1985)285-288.

# Effects of a Tailpipe on Hole Tone Phenomena

Kazuo Matsuura[1], Masami Nakano[2]
[1]Graduate School of Science and Engineering, Ehime University
3 Bunkyo-cho, Matsuyama, Ehime, 790-8577, Japan
[2]Institute of Fluid Science, Tohoku University
2-1-1 Katahira, Aoba-ku, Sendai, Miyagi, 980-8577, Japan

**ABSTRACT**

Interaction of a hole tone system with a tailpipe is investigated experimentally and computationally. When jet speed is increased, experimental results show transition from an original hole tone state to a locked-in state. From laser-smoke visualization, we observe a flapping motion of jet shear layers at the lock-in condition due to the interaction of the hole tone system with the tailpipe. The present computation predicts similar phenomena, and therefore it surely reproduces the interaction of the hole tone system with the tailpipe in spite of the stiffness of the present computation.

## 1. Introduction

The sound produced when a jet, issued from a circular nozzle or hole in a plate, goes through a second plate with a hole of the same diameter as the jet is referred to as a hole tone. The tone becomes noise and vibration sources in many practical situations such as solid propellant rocket motors, automobile intake-&exhaust-systems, ventilation systems, gas distribution systems, etc. Although hole tone research has a long history [1,2], systematic analyses including the interaction of the hole tone with other resonators have not been necessarily reported. In this paper, we investigate interaction of the hole tone with a tailpipe experimentally and computationally.

## 2. Hole Tone System with a Tailpipe and Its Computational Model

Figure 1 shows the hole tone system with a tailpipe. The diameters of the nozzle and the end plate hole are both $d_0$=51 mm. The length of the tailpipe $L_t$ is 1562 mm. The impingement length between the nozzle and the end plate $L_{im}$ is 50 mm. The nozzle exit plate is rectangular with a dimension of 300 mm×300 mm. The thickness of the end plate is 10 mm. At 20°C, this corresponds to a Reynolds number $\mathrm{Re}=u_0 d_0/\nu \approx 4.1\times10^4$. In the computation, field equations are solved including the interior space inside the tailpipe and its exterior environment. The overall computational domain consists of 6 zones, and cylindrical-coordinate grids of the O-type topology are generated in each zone.

## 3. Numerical Method

The governing equations are the unsteady three-dimensional compressible Navier-Stokes equations. To close the system the perfect gas law is assumed. The equations are solved by the finite-difference method. Spatial derivatives that appear in metrics, convective and viscous terms are basically evaluated by the 6th-order tridiagonal compact scheme [3]. Time-accurate solutions to the governing equations are obtained by the 3rd-order Runge-Kutta scheme.

Corresponding author: Kazuo Matsuura
*E-mail address*: matsuura.kazuo.mm@ehime-u.ac.jp

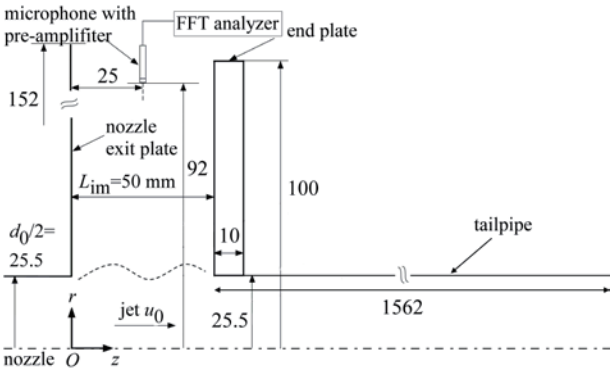


Fig. 1 Hole tone system with a tailpipe

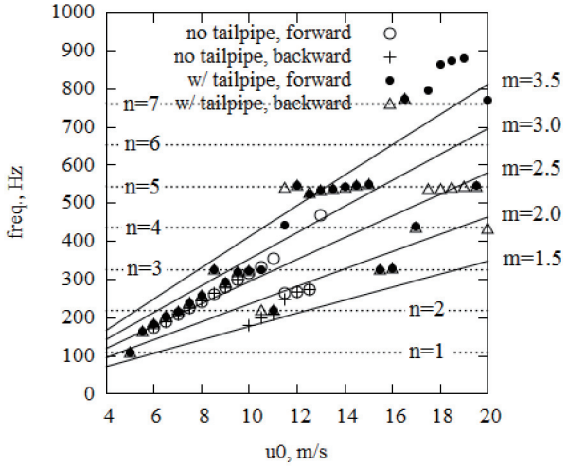


Fig. 2 Variation of the most dominant peak tone frequency with jet speed $u_0$; solid line: Rossiter's equation $m/f=L_{im}/u_c+L_{im}/c_0$, $u_c=0.6c_0$, dotted line: $n$th eigenfrequency of plane wave modes in the tailpipe $f_n=nc/(2L_t)$

In addition to the above-mentioned spatial discretization and time integration, a 10th-order implicit filtering [4] is introduced to suppress instabilities of the computations. The parameter that appears in the left-hand side of the filtering formulation is set to be 0.492 in interior grid points. The details of the present numerical method are shown in [5]. The present computation is very stiff because fluids need to flow through the long tailpipe before flow states become equilibrium.

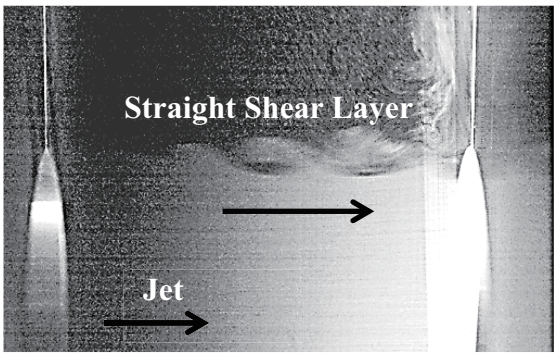


(a) When the shear layers impinge on the hole edge

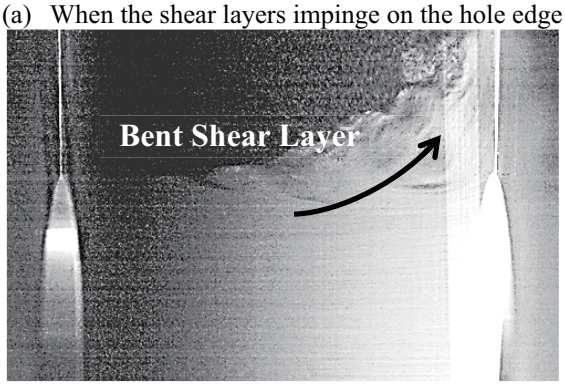


(b) When the shear layers bend outward

Fig. 3 Flapping motion of jet shear layers visualized by the laser-smoke method in the hole tone system with the tailpipe ($u_0$=12 m/s)

## 4. Results and Discussion

Figure 2 shows the measured variation of the most dominant peak tone frequency with jet speed $u_0$. In the figure, the results are shown both for a pure hole tone system, i.e., without the tailpipe, and for the hole tone system with the tailpipe. Because the systems exhibit hystereses, the results both when $u_0$ is increased monotonically and when $u_0$ is decreased monotonically are shown. Also, in the figure, line series determined by Rossiter's equation and eigenfrequencies of plane wave modes in the tailpipe are shown for reference. The results of all the cases collapse when $u_0$ is less than about 11 m/s. While the peak tone frequencies then drop to lower frequencies for larger $u_0$ in the case of the pure hole tone, transition to lock-in phenomena is observed for the system with the tailpipe for larger $u_0$.

Figure 3 shows jet shear layers visualized by the laser-smoke method as the result of analyzing time-series snapshots when $u_0$=12 m/s. We observe a so-called flapping motion of the shear layers. When the shear layers bend outward, vortices do not go through the end plate hole.

Figure 4 shows the computed results in terms of vorticity magnitude when $u_0$=12 m/s. The flapping motion mentioned above is also observed in the computation. Although quantitative agreement between computation and experiment remains as a future subject at present, the evident feature of the interaction between hole tone phenomena and the tailpipe is reproduced in the present computation in spite of the stiffness of the present computation.

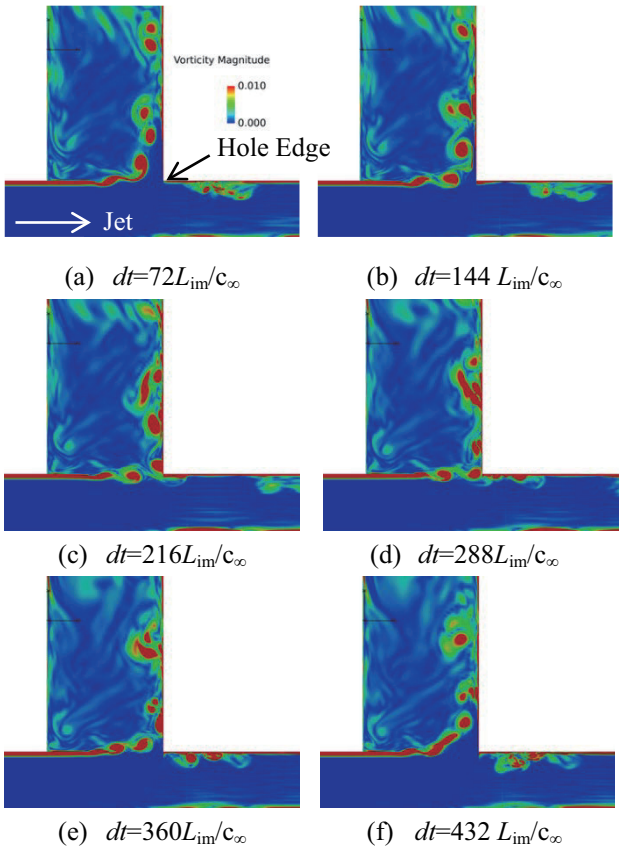


(a) $dt$=72$L_{im}$/$c_\infty$ (b) $dt$=144 $L_{im}$/$c_\infty$

(c) $dt$=216$L_{im}$/$c_\infty$ (d) $dt$=288$L_{im}$/$c_\infty$

(e) $dt$=360$L_{im}$/$c_\infty$ (f) $dt$=432 $L_{im}$/$c_\infty$

Fig. 4 Computed shear layers visualized in terms of vorticity magnitude ($u_0$=12 m/s)

## 5. Concluding Remarks

Effects of the tailpipe on the hole tone system are investigated experimentally and computationally. When jet speed is increased, experimental results show transition from an original hole tone state to a locked-in state. The flapping motion of jet shear layers are observed both in the experiment and computation.

## Acknowledgements

This research was supported both by the Collaborative Research Project of the Institute of Fluid Science, Tohoku University. Computational resources were provided by the Advanced Fluid Information Research Center of the Institute of Fluid Science, Tohoku University.

## References

[1] M. S. Howe, *Acoustics of Fluid-Structure Interactions*, Cambridge Univ.press. (1998).
[2] Lord, Rayleigh, *Theory of Sound*, Dover, 2 (1945).
[3] S. K. Lele, *J. Compt Phys.*, 103(1) (1992) 16-42.
[4] D. V. Gaitonde, M. R. Visbal, *AIAA J.*, 38(11) (2000) 2103-2112.
[5] K. Matsuura, M. Nakano, *J. Fluid Mech.*, 710 (2010) 569-605.

Eleventh International Conference on Flow Dynamics
October 8-10, 2014, Sendai, Miyagi, Japan

# Interaction between Self-Sustained Flow Oscillations and Acoustic Resonance in a Cavity-Pipe System

Mikael A. Langthjem[1], Masami Nakano[2]
[1]Graduate School of Science and Engineering, Yamagata University
4-3-16 Jonan, Yonezawa, Yamagata 992-8510, Japan
[2]Institute of Fluid Science, Tohoku University
2-1-1 Katahira, Aoba-ku, Sendai, Miyagi 980-8577, Japan

**ABSTRACT**

This work is concerned with the mathematical modeling of fluid dynamics and acoustics in a coupled cavity-pipe system. Special attention is paid to the coupling between the self-sustained flow oscillations in the cavity and acoustic resonances in the pipe. The present paper describes a simplified one-dimensional acoustic model based on the Webster horn equation. Work on a more precise model, where solutions for the sub-systems are appropriately coupled, is in progress.

## 1. Introduction

Expansion chambers are often used in connection with silencers in engine exhaust systems, with the aim of attenuating the energy flow. The gas flow through the chamber may however generate self-excited oscillations, thus becoming a sound generator rather than a sound attenuator. Similar geometries and thus similar problems may be found in, for example, solid propellant rocket motors and heat exchangers.

The present work is concerned with a mathematical model of a simple axisymmetric silencer model consisting of an expansion chamber followed by a tailpipe. The aim is to contribute to the understanding of the interaction between oscillations of the flow field and the acoustic field.

By oscillations of the flow field we mean the self-sustained oscillations of the jet shear layer. It is unstable and rolls up into a large, coherent vortex (a 'smoke-ring') which is convected downstream with the flow. It cannot pass through the hole in the downstream plate but hits the plate, where it creates a pressure disturbance. The disturbance is thrown back (with the speed of sound) to the upstream plate, where it disturbs the shear layer. This initiates the roll-up of a new coherent vortex. In this way an acoustic feedback loop is formed, making up one type of flow-acoustic interaction.

These so-called hole-tone feedback oscillations may interact with the acoustic axial and radial eigen-oscillations of the cavity and the tailpipe, making up another type of flow-acoustic interaction.

It is these interactions that we seek to understand.

## 2. Flow Model

The unstable shear layer is modeled via a discrete vortex approach [1], based on axisymmetric vortex rings. The solid surfaces are represented by 'fixed' vortex rings, as illustrated by Fig. 1. A detailing description of the model can be found in the earlier papers [2, 3].

Corresponding author: Mikael A. Langthjem
*E-mail address*: mikael@yz.yamagata-u.ac.jp

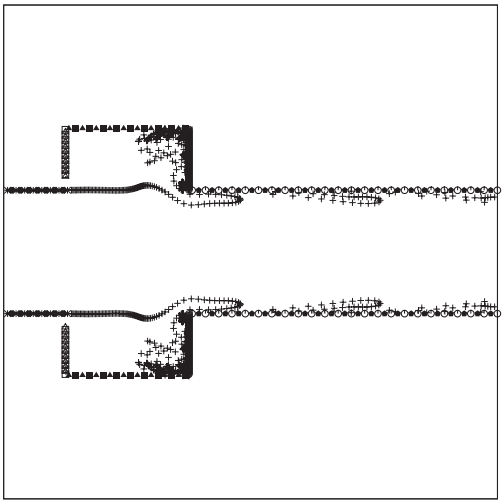

Fig. 1 Discrete vortex ring representation of a cavity-tailpipe system. The flow is from left to right.

## 3. Aeroacoustic Model

The aeroacoustic model is based on the Powell-Howe theory of vortex sound [4, 5]. The starting point is thus taken in Howe's equation for vortex sound at low Mach numbers [4, 5]. Let $\mathbf{u}$ denote the flow velocity, $\boldsymbol{\omega} = \nabla \times \mathbf{u}$ the vorticity, $c_0$ the speed of sound, and $\rho$ the the fluid density. The sound pressure $p(\mathbf{x}, t)$ at the position $\mathbf{x} = (r, z)$ and time $t$ is related to the vortex force (Lamb vector) $\mathfrak{L}(\mathbf{x}, t) = \boldsymbol{\omega}(\mathbf{x}, t) \times \mathbf{u}(\mathbf{x}, t)$ via the non-homogeneous wave equation

$$\left( \frac{1}{c_0^2} \frac{\partial^2}{\partial t^2} - \nabla^2 \right) p = \rho \nabla \cdot \mathfrak{L}, \tag{1}$$

with boundary conditions $\frac{\partial p}{\partial n} = \nabla p \cdot \mathbf{n} = 0$ on the surfaces ($\mathbf{n}$ = normal vector), and $p \to 0$ for $|\mathbf{x}| \to \infty$.

## 4. A Simple One-Dimensional Solution

A very simple solution of (1) can be obtained by assuming one-dimensional wave propagation. [Of course, the acoustic field in the cavity is not one-dimensional (or even nearly so), but that in the pipe nearly is.] A further simplification of the analysis can be obtained by taking the area variation of the cavity-pipe system into account via application of the Webster acoustic horn equation.

This may seem as going well beyond the limits of applicability of this equation; and in a way we are guilty of doing this. But recently, Mercier and Maurel [6] presented an improvement of the Webster equation, and compared this improved equation with the original (Webster) one for a variety of (2D) geometries, including a duct with a sudden variation in the height. A surprising result was that the original Webster equation, in fact, isn't performing that badly in such a situation. This is the motivation behind trying to apply it to the present case.

Thus we rewrite (1) to the form

$$\frac{1}{c_0^2}\frac{\partial^2 p}{\partial t^2} - \frac{1}{A(x)}\frac{\partial}{\partial x}\left(A(x)\frac{\partial p}{\partial x}\right)p = \rho\frac{\partial \mathfrak{L}_x}{\partial x}. \qquad (2)$$

We expand the solution $p(x,t)$ in terms of acoustic eigenmodes for an open-open pipe, as follows

$$p(x,t) = \sum_k a_k(t) f_k(x),\ f_k(x) = \sin k\pi\frac{x}{L}, \qquad (3)$$

where $L$ is the full length of the cavity-pipe system. The time functions $a_k(t)$ are determined by applying the Galerkin method. The Galerkin weak form of (2) is

$$\sum_{k=1}^{K}\int_0^L \left[\frac{1}{c_0^2}A(x)f_j(x)f_k(x)\ddot{a}_k(t) \qquad (4)\right.$$
$$\left. -f_j(x)\frac{\partial}{\partial x}\left(A(x)\frac{\partial f_k(x)}{\partial x}\right)a_k(t)\right]dx$$
$$= \rho\int_0^L A(x)f_j(x)\frac{\partial \mathfrak{L}_x}{\partial x}dx.$$

These $K$ coupled o.d.e.'s in time $t$ are integrated by using the trapezoidal rule.

The acoustic particle velocity $v(x)$ within the cavity-pipe system can be evaluated 'exactly', at least within the approximation of one-dimensionality. This acoustic velocity field is added to the free vortex rings in the cavity, thus playing the role of an acoustic feedback.

## 5. Numerical Example

Computations were preformed for a jet of diameter $d_0 = 50\,\text{mm}$ with mean flow speed $u_0 = 10\,\text{m/s}$. The length of the cavity is also $d_0$, while the diameter is $2d_0$. The frequency of the self-sustained flow oscillations within the cavity is $f_0 \approx 160\,\text{Hz}$. The length of the tailpipe is $\ell = 19.4d_0$, which gives a resonance frequency of $f_1 \approx 175\,\text{Hz}$ for the first mode (corresponding to one half-wave) and $f_2 \approx 350\,\text{Hz}$ for the second mode (corresponding to one full wave).

Figure 2 shows the sound pressure spectrum at the position $x_p = 7\ell/8$ where $x = 0$ is the pipe entrance and $x = \ell$ the pipe exit. $K = 40$ was used in (4) for this result. It is seen that the second resonance frequency $f_2 \approx 350\,\text{Hz}$ comes out strongly.

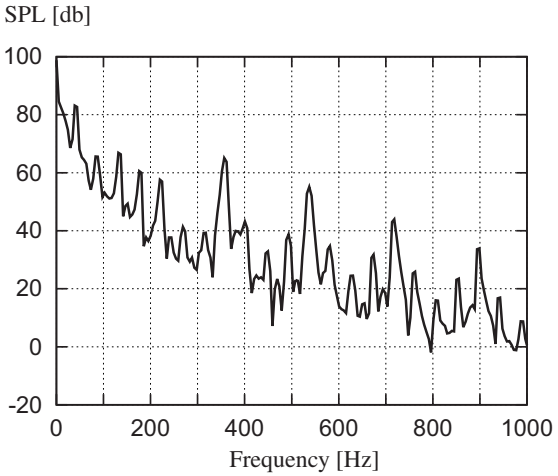


Fig. 2 Sound pressure spectrum inside the tailpipe, near the pipe exit.

## 6. Summary and Concluding Remarks

Clearly a more rigoristic approach needs to be considered as well, at least in order to verify the one-dimensional approach. Such work is ongoing (and will be presented at the lecture). It is concerned with coupling of the solutions for the cavity- and the pipe-part via the method of matched asymptotic expansions. A two-dimensional frequency domain-solution has been given in [7]. The present work involves, in a sense, a generalization of this paper to an axisymmetric geometry in the time domain. Also, open-end conditions are being considered at the pipe-exit, along the lines given in Part II of [7].


## Acknowledgements

The support of the present project by Institute of Fluid Science, Tohoku University, via a 'Collaborative Research Project 2014' (project code J14031) is gratefully acknowledged.


## References


[1] G.-H. Cottet, P. D. Koumoutsakos, *Vortex Methods: Theory and Practice*, Cambridge University Press, Cambridge, 2000.

[2] M.A. Langthjem, M. Nakano, *J. Sound Vibr.*, 288 (2005), 133-176.

[3] M.A. Langthjem, M. Nakano, *Fluid Dyn. Res.*, 42 (2010), 1-26.

[4] M. S. Howe, *Acoustics of Fluid-Structure Interactions*, Cambridge University Press, Cambridge, 1998.

[5] M. S. Howe, *Theory of Vortex Sound*, Cambridge University Press, Cambridge, 2003.

[6] J.-F. Mercier, A. Maurel. Acoustic propagation in non-uniform waveguides: revisiting Webster equation using evanescent boundary modes. *Proc. Roy. Soc. Lond. A*. 469 (2013), 20130186.

[7] M.B. Lesser, J.A. Lewis. Application of matched asymptotic expansion methods to acoustics. Parts I and II. *J. Acoust. Soc. Amer.* 51 (1972), 1664-1669 and 52 (1972), 1406-1410.

Eleventh International Conference on Flow Dynamics
October 8-10, 2014, Sendai, Miyagi, Japan

# Three-dimensional Wavelet Transform of a Dune Wake

Yan Zheng and Akira Rinoshika
Department of Mechanical Systems Engineering
Graduate School of Science and Engineering
Yamagata University
4-3-16 Jonan, Yonezawa-shi, Yamagata 992-8510, Japan

**ABSTRACT**

The three-dimensional orthogonal wavelet multi-resolution technique is applied to analyze flow structures behind a dune model. The instantaneous velocity, vorticity, were decomposed into the large-, intermediate- and small-scale components by three-dimensional wavelet multi-resolution technique. It is found that large-scale structure determine the formation of separation bubble and its vortcity makes main contribution, some intermediate-scale and small-scale streamwise vortices cause the upwelling of vortical structures, and they tends to be more active at the downstream.

## 1. Introduction

The barchan dune, as the simplest and most studied type of dune, is formed when the wind mainly blows from one direction with a restricted sediment supply [1]. Since the first pioneer works by Bagnold [2], the investigation of dune morphology and dynamics has been much studied by experimental measurement as well as numerical simulation.

Up to now, large eddy simulation (LES) have become rather common for numerical simulations and provides good agreement with both the time-averaged velocities as well as the turbulent fluctuations measured experimentally. Yue et al. [3] performed LES with 2D dune and concentrated on the coherent structures behind the dune crest. Maddux et al. [4] measure the structure of mean flow and turbulence over the fixed, artificial, asymmetric, three-dimensional dunes with unidirectional turbulent open channel flow. However, little attention has been paid to the analysis of the complex three-dimensional multi-scale turbulent structures of wake flow, to give further understanding of fluid dynamics over dune, the detailed information on three-dimensional as well as multi-scale turbulent structures of dune wake should be acquired. This is of fundamental significance and has not been previously investigated, thus motivating the present work.

For a deeper understanding of turbulent wake of dune, it is an effective way to perform multi-scale analysis of turbulent structures. The purpose of this study is to provide a new method to reveal the 3D multi-scale turbulent structures. Three-dimensional wavelet analysis was used to provide both quantitative and qualitative information on the unsteady flow structures of dune wake. The velocity, vorticity, data based on LES are decomposed into large-, intermediate- and small-scale structures.

## 2. Details of numerical simulation

The commercial CFD software, Fluent 6.3 was used to compute unsteady 3D incompressible unsteady flow around the dune. The LES turbulence model was used for numerical simulation at the Reynolds number of 5534. The computational domain, as shown in Fig.1, the inlet flow locates at 80mm (4h) upstream of dune, and the outlet flow locates at 400mm (20h) downstream of dune. The height and width of computational domain is 100mm (5h), 180mm (9h) respectively.

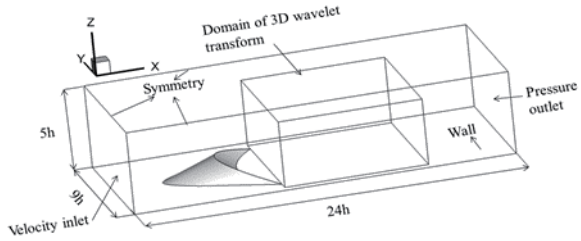


Fig.1 Computational domain and boundary conditions

## 3. Results and Discussion

### 3.1 Scale Characteristics of Wavelet Components

As shown in Fig.1, a 3d wavelet transform domain, with the volume of 8h×8h×4h, is divided into a mesh of 128×128×64. The turbulent structures in this domain were decomposed into large-scale, intermediate-scale and small-scale structures.

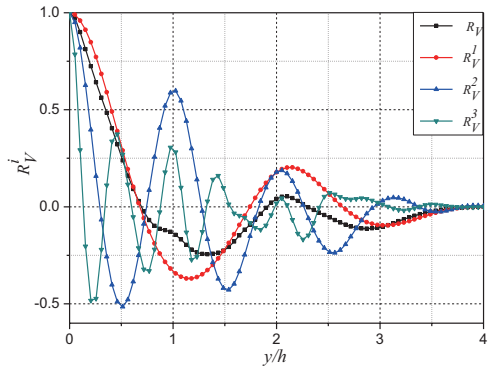


Fig.2 Two-point autocorrelation of spanwise velocity and wavelet components

To determine the scale length of wavelet components, we computed correlation function for each wavelet component of different scales. Figure 2 presents correlation function of spanwise velocity and its wavelet components at the location of x/h=2.6 and z/h=0.3 along spanwise direction. It is evident that and reduce to

Corresponding author: Yan Zheng
*E-mail address:* zy30003333@163.com

the first minimum and continue oscillating before they become zero at y/h ≈ 3.7, the length scales of y/h ≈ 2.1, 2.15, 1, and 0.48 are observed by $R_V$ , $R_V^1$, $R_V^2$ and $R_V^3$ respectively. We define that large-scale structure has the central scale of 43mm(y/h=2.15), intermediate-scale structure has the central scale of 20mm(y/h=1), small-scale structure has the central scale of 9.6mm(y/h=0.48).

### 3.2 Multi-scale instantaneous vortical structure

The instantaneous streamlines and vorticity $\omega_x$ of LES and $\omega_x^i$ of wavelet components in (y, z) plane from the location of x/h=2.7 to x/h=9.6 are shown in Fig.3. A pair of large-scale vortex clearly observed in the separation bubble (Fig.3a and Fig.3b), as the effect of dune surface, the vortex pair stretches to the side boundary and move up along at the downstream of separation bubble. Some relatively smaller streamwise vortices are observed around the large-scale vortices (Fig.3a), these vortices seem to induce the generation and upwelling of vortical structure at the downstream. As shown in Fig.3c and Fig.3d, some vortical structures which are unidentifiable by large-scale structure, are clearly identified by intermediate-scale and small-scale structures, besides, the small-scale structures (Fig.3d), seems to become active at the downstream, this may because of the upwelling of vortical structure which lead to large-scale vortical structure break into small-scale vortices.

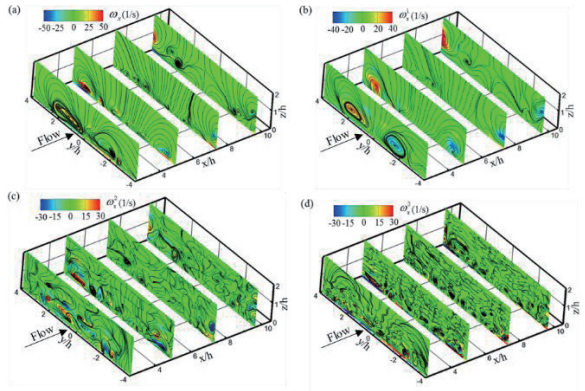


Fig.3 Instantaneous streamlines and vorticity contours $\omega_x$ and $\omega_x^i$ (a) LES, (b) Large-scale, (c) Intermediate-scale, (d) Small-scale

### 3.3 3D pressure distribution

Figure 4 presents instantaneous pressure iso-surfaces of LES and wavelet components, the high pressure and low pressure areas are colored by green and yellow respectively. It is evident that the separation bubble-like boundary with adverse pressure gradient is distinctly distinguished by LES (Fig.4a) and large-scale structure (Fig.4b), indicating that the distribution of pressure is mainly characterized by large-scale structures, the spanwise rollers are induced by the adverse pressure gradient of large-scale and cause flow separation. Near the two side boundary, two “legs” with low pressure are also clearly identified, they are considered to induce the large-scale streamwise vortical structures mentioned in Fig.3a. At the downstream, two low pressure regions are observed in Fig.4a and Fig.4b respectively, which may lead to the second time upwelling of vortical structures. The intermediate-scale structures, as shown in Fig.12c, they distributed disorderly in and around large-scale structures, which may leads to the generation of intermediate vortical structures. At the downstream, small-scale structures (Fig.4d) are observed at the two side boundary, which may be interfered as the reason why large-scale vortical structures break into small-sale vortices.

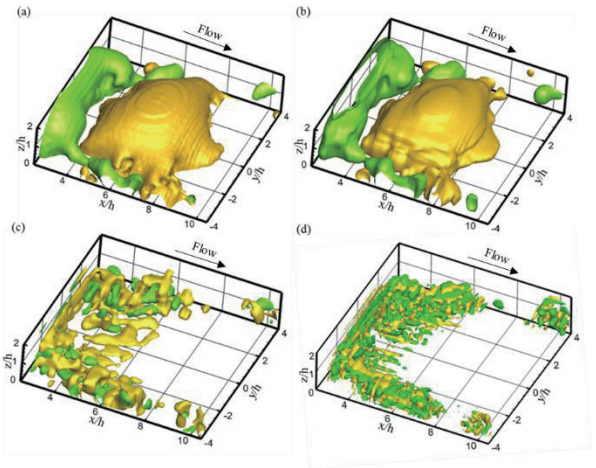


Fig. 4 Instantaneous iso-surfaces of pressure (a) LES, (b) Large-scale, (c) Intermediate-scale, (d) Small-scale

## 4. Concluding Remarks

1. Three-dimensional velocity, vorticity and pressure fields of the LES are decomposed into three wavelet components having large-, intermediate- and relatively small-scale, the scale of each wavelet component is quantified by two-point autocorrelation function.
2. Several intermediate-scale vortices, which cannot be observed by LES, are clearly identifiable, inducing the upwelling of vortical structures. Besides, the intermediate-scale as well as the small-scale ones, tend to become more active after flow separation.
3. The iso-surfaces of pressure are mainly characterized by large-scale structures, displaying a distinct adverse pressure gradient field around the separation bubble. The distribution of small-scale structures may explain why large-scale vortical structures break into small-sale vortices.

## References

[1] N. Lancaster, *Routledge: London,* (1995) 1-10.
[2] R.A. Bagnold, *London,* (1941), 265.
[3] W. Yue, C. L. Lin, and Patel, V. C., *J. Fluids Eng.,* 127(5), (2005) 858–864.
[4] T. B. Maddux, J. M. Nelson, and S. R. McLean, *Journal of Geophysical Research,* 108(F1) (2003) 6009.

# OS10: The Tenth International Students / Young Birds Seminar on Multi-scale Flow Dynamics

# Multi-objective Optimization for Intake and Vent Grilles of Tank

Kaiping WEN[1], Chenguang LAI[1], Hao SUN[1] and Chao MAN[1]
[1]Chongqing University of Technology, Chongqing, 400054, China

**ABSTRACT**

To improve the protective and aerodynamic performances of tank grilles simultaneously, the minimal shrapnel incidence angle and the maximum cooling air flow rate are proposed as optimization objectives. Based on the Kriging approximate model, the multi-objective genetic algorithm is applied to optimize the intake and vent grilles. The Self-Organizing Map is used to explore the trade-off relations between objective functions and correlations among design variables and objective function.

## 1. Introduction

The requirements for mobile ability and combat performance of modern tanks are extremely demanding. It is needed that a more powerful engine and a relatively lighter tank body. This makes the power bulk ratio of tank engine cabin high and the thermal environment severe. The cooling of high-power tank engine is one of the key factors to constrain the development of tank engine. Grille is an important part in cooling system, especially for armored vehicles. It not only ensures enough flux of cooling air, but also protects the engine cabin against bullet, shrapnel, stone, shrub, and so on. Therefore, the protective performance and the cooling performance of tank engine cabin are two significant aspects in grill design. In general, the two aspects are trade-off relation . The objectives of this research are to find the optimal solution and explore the design space by data mining techniques.

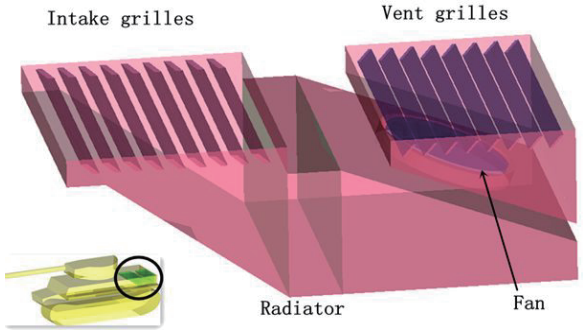


Fig. 1 The simplified tank engine cabin

## 2. Numerical Model

To describe the shape and the position of grills, the thickness, length, bank angle and the interval between grills and the end plane are considered as variable parameters (see Fig. 2). The total length, total width and the distance between grilles are constant. Both intake grilles and vent grilles have the same four parameters. In total, eight parameters are considered as design variables.

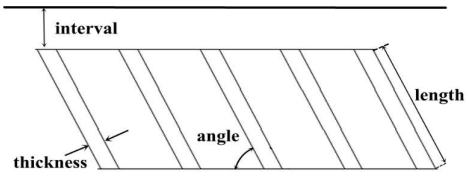


Fig. 2 Grille parameters

The aerodynamic and protective performances are two important aspects in grille design. The cooling air flow rate ( $q_m$ ) of engine cabin and the shrapnel incidence angle (ψ) are proposed to evaluate the aerodynamic performance and the protective performance, respectively (see Fig. 3) [1]. The smaller shrapnel incidence angle, the better protective performance. The higher cooling air flow rate, the better cooling performance.

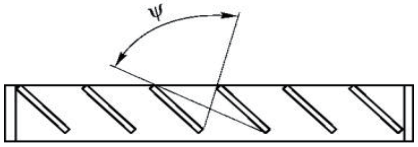


Fig. 3 Shrapnel incidence angle

## 3. Optimization Method

The optimization method based on CFD and approximate model is performed in the study. Fig. 4 shows the basic processes of the optimization. The Latin Hypercube Sampling is applied to obtain evenly distributed initial sample points so that more accurate result can be got with smaller amount of samples. To reduce the times of computation, the approximate model is built by Kriging model technique to replace the CFD

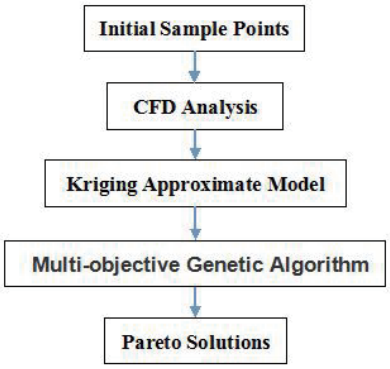


Fig. 4 Optimization processes

Corresponding author: Kaiping WEN
*E-mail address*: 603375138@qq.com

solver. Then, multi-objective genetic algorithm is used to calculate the Pareto solutions on the Kriging approximate model.

## 4. Result and Discussion

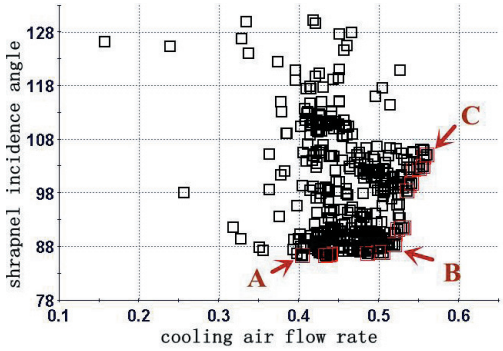


Fig. 5 Optimization result with convergence history

Fig. 5 shows 501 points based on the Kriging approximate model and 30 Pareto solutions that are signed by red squares. The average errors of shrapnel incidence angle and cooling air flow rate are 1% and 11%, respectively.

There are three typical Pareto solutions, in which solution A with the lowest shrapnel incidence angle, and solution C with the highest cooling air flow rate. For solution B, the cooling air flow rate is slightly less than that of solution C, but with a large reduction on shrapnel incidence angle.

SOM (Self-Organizing Map), as one of the most popular unsupervised neural networks techniques, nonlinearly projects high dimensional data in an ordered vector quantization graph and gives a visual insights into the properties of the data such as its shape, typical values and correlations between vector component. It is used to explore the trade-off relations between objective functions and correlations among design variables and objective function [2].

As shown in Fig. 6, when shrapnel incidence angle is small, the cooling air flow rate is large in the same position. Similarly, when cooling air flow rate is small, the corresponding shrapnel incidence angle is large. It indicates that the two objective functions are severe trade off relation.

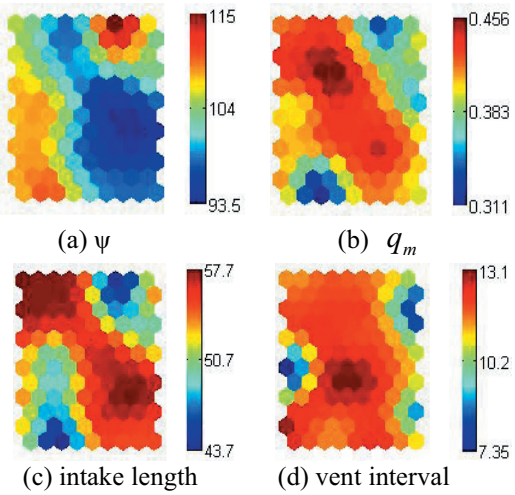


(a) ψ (b) $q_m$

(c) intake length (d) vent interval

Fig. 6 Component maps

The color pattern of intake length is almost completely opposite to that of ψ and similar to that of $q_m$. It implies that the ψ is sensitive and negatively related to intake length. Similarly, $q_m$ is sensitive and positive related to intake length. In the red region of the vent interval, the $q_m$ is basically red in the same region. It suggests that the vent interval and $q_m$ are positive correlation.

The SOM-based scatterplot is different from traditional scatterplot. The points on it are color-coded with their soordinates in the component maps. So, the scatterplots and component maps are linked. The same results can be get from scatterplots (see Fig. 7).

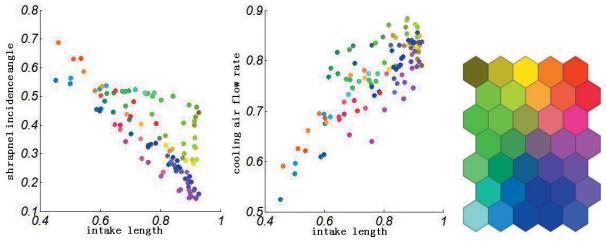


Intake length & ψ Intake length & $q_m$ Color-coding

Fig. 7 SOM-based scatterplots

## 5. Concluding Remarks

The multi-objective genetic algorithm based on Kriging approximate model is time saving and efficient to optimize the intake and vent grilles. The optimum result can be obtained near solution B because of the chief status of protective performance. The shrapnel incidence angle and the cooling air flow rate of solution B is improved 12% and 29%, respectively. By the analysis of SOM-based data mining, the severe trade off relation between shrapnel incidence angle and cooling air flow rate is visualized. The intake length is found to have significant effects on the two objective functions.


## Acknowledgement

Project 51305477 supported by NSFC. This research is also supported by Natural Science Foundation Project of CQ CSTC (CSTC, 2011BB6113). Part of the work was carried out under the Collaborative Research Project of the Institute of Fluid Science, Tohoku University, Japan.


## References


[1] Y.L. LI, C.L. ZHAO, F.J. ZHANG, X. LI, X.Q. WANG, *ACTA ARMAMENTAR,* 33 ,2(2012)

[2] Y.J. SONG, Z.D. GUO, L.M. SONG, J. LI, Z.P. FENG, *Turbine technical conference and exposition,* GT2014-25492

# Experimental Study on Intermittent Air-Water Replacement during Water Draining from a Closed Tank

Eiji Sakamoto[1], Takumu Tamaki[1] and Tameo Nakanishi[1]
[1]Graduate School of Science and Engineering, Yamagata University
4-3-16 Jonan, Yonezawa-shi, Yamagata-ken, 952-8510, Japan

**ABSTRACT**

Experiments were made for intermittent air-water replacement during water draining from a closed tank. The flow undergoes a slight change with descending water head. Bubble enters from bottom hole without breaking at a large water head. Bubble enters and breaks into pieces at a small water head. There also observed instant swirling flow in some cases. It was found that the discharge rate, the bubble volume, and the bubble entering period were related to the water head and the hole diameter. Specifically, the flow rate is proportional to the cube of the hole diameter. The discharge rate increases slightly as to decreasing water head.

## 1. Introduction

The leak of liquid from a closed chemical storage tank can bring various unfavorable influence and damages to the environment. The bubble-liquid flow related to the intermittent air-liquid replacement during liquid draining from a closed tank is important in disaster prevention engineering. The most important feature of this flow is that the average discharge velocity is almost independent of the water head (h) as compared with the open-top single-phase flow where the flow velocity is proportional to $\sqrt{2gh}$. Figure 1 shows the schematics of the flows in (a) the open-top case and (b) the closed-top case. In the open-top case, single-phase flow occurs. The theoretical value of the flow velocity from the bottom hole becomes $u = \sqrt{2gh}$ . In the closed-top case, the flow of intermittent air-liquid replacement occurs. The flow velocity u is approximately constant at all water head [1]. The study on the similar flow situation was conducted in the past [1, 2]. The purpose of this study was to clarity the characteristics of the intermittent bubble-liquid flow from a closed tank.

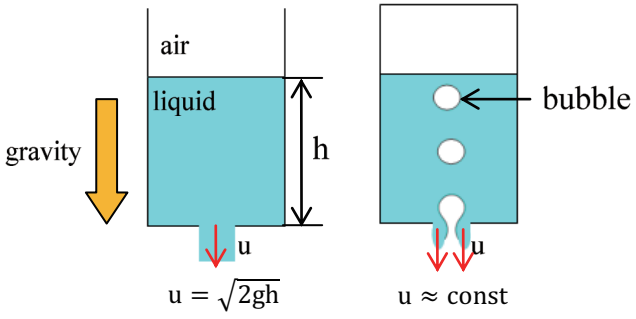


(a) Open-top (b) Closed-top

Fig. 1 Schematics of liquid flows draining from open and closed containers

## 2. Method

A cylindrical tank was made of acrylic to elucidate the mechanisms of the flow from the closed tank. Figure 2 shows an experimental setup. The top of the tank is sealed by openable lid. The cylindrical tank is 1000mm in height and its inner diameter D is 190mm. The heights from the bottom of the tank are marked every 50mm on the tank surface. The liquid volume per one scale is

$$\Delta V = \frac{\pi}{4} D^2 \Delta H \tag{1}$$

A stainless plate of diameter $D = 190\,\mathrm{mm}$ and thickness of 1mm with a center hole of diameter d is placed at the bottom of the tank which is supported by a hollow acrylic plate. The experiment was conducted for hole diameters of 10, 12, 13, 14, 15, 20mm.

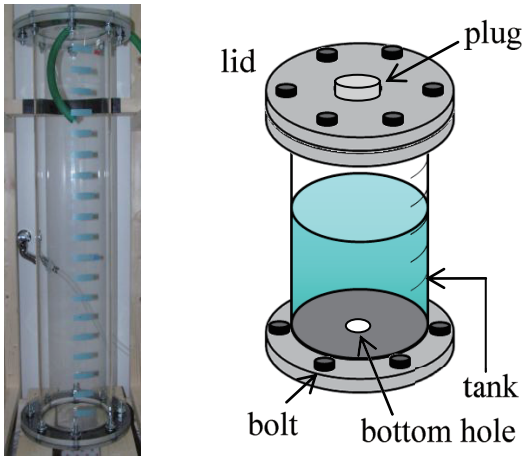


Fig. 2 Experimental setup

$$T_b = \Delta T / n \tag{2}$$

$$V_b = \Delta V / n \tag{3}$$

$$Q = \Delta V / \Delta T \tag{4}$$

To start the experiment, the tank is firstly fulfilled with water up to H=1000mm. The top lid of the tank is then sealed by a plug. After sufficient rest time, the intermittent bubble-liquid flow is started by opening the bottom hole. The bubble-liquid flow is filmed by a video camera. Measuring the number (n) of bubbles entering into the tank from the hole and the time (ΔT) elapsed as water descending one scale from the water head of ΔH, the mean bubble entering period ($T_b$), the mean bubble volume ($V_b$) and the discharge rate (Q) are calculated by

Corresponding author: Eiji Sakamoto
*E-mail address*: thy40086@st.yamagata-u.ac.jp

Eqs.(2)-(4). The experiments are carried out five times and take average.

### 3. Results and Discussions

Figure 3 shows the typical bubble flow patterns entering into the tank for d=15mm. The flow patterns can be classified into three types; (a) bubbles enter from the bottom hole without breaking, (b) bubble enters and breaks into pieces, and (c) the flow becomes instant swirling flow. Type (a) occurs at a large water head. Type (b) occurs at a small water head. The resonance of water inside the tank is seen as the water head approaches the same order of the inner diameter of the tank.

Figure 4 shows the mean bubble entering period versus water head. The mean bubble entering period increases as to decreasing water head. Moreover, the mean bubble entering period decreases as to increasing hole diameter.

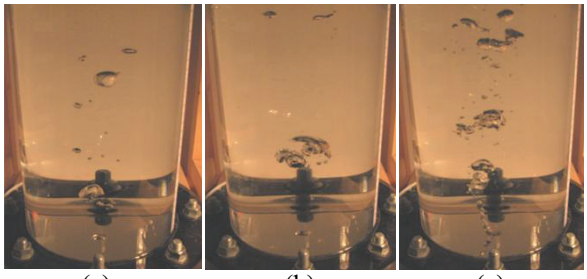

(a) (b) (c)

Fig. 3 Typical flow patterns

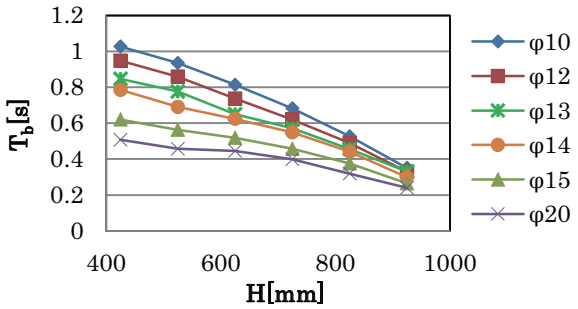


Fig. 4 Mean bubble entering period versus water head

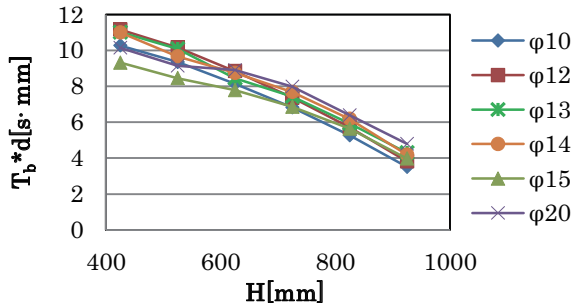


Fig. 5 $T_b$*d versus water head

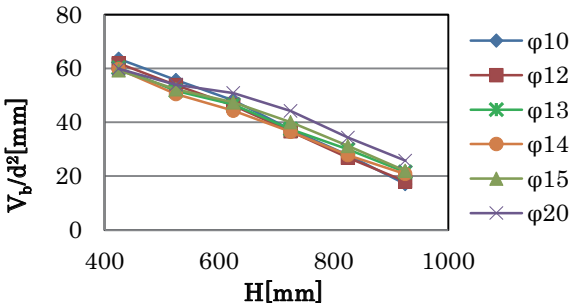


Fig. 6 $V_b/d^2$ versus water head

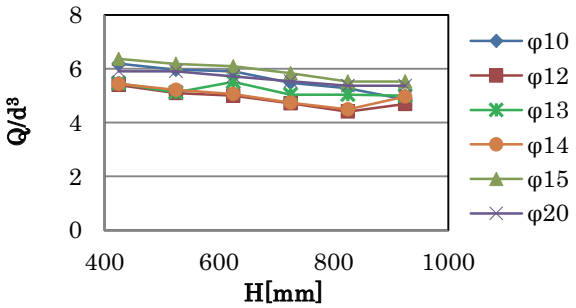


Fig. 7 $Q/d^3$ versus water head

Figure 5 shows $T_b$*d versus water head. After adequate scaling, the results can be made nearly independent of the hole diameter.

Figure 6 shows $V_b/d^2$ versus water head. The mean bubble volume increases as to decreasing water head. All data for different diameters almost fall on the same line. Thus, it is found that the mean bubble volume is proportional to $d^2$.

Figure 7 shows $Q/d^3$ versus water head. The discharge rate increases slightly as to decreasing water head. The discharge rate is proportional to the cube of the hole diameter.

Assuming that a hemisphere of an air pocket of the height of $h = d/2$ is about to enter the bottom hole of the tank, we have $u \approx \sqrt{2gh} = \sqrt{gd}$. We can obtain a theoretical estimation for these cases that $Q \propto \sqrt{d} \cdot d^2 = d^{2.5}$. However, the experimental data show that Q is propositional to $d^3$ other than $d^{2.5}$.

### 4. Concluding remarks

The bubble-liquid flow related to the intermittent air-water replacement during water draining from a closed tank was investigated. The flow patterns can be classified into three types. The characteristics of bubble entering period, the bubble volume and the discharge rate as to the water head and the hole diameter were clarified.

### References

[1] T.Tamaki, et al. , Proc. 10th International Conference on Flow Dynamics (ICFD), November 25-27, 622-623, 2013, Sendai.

[2] M.I.Kohira, et al. , American J. Physics 75, 10, (2007) , 893-895.

Eleventh International Conference on Flow Dynamics
October 8-10, 2014, Sendai, Miyagi, Japan

# Identification of Local Turbulent Regions in a Transitional Boundary Layer Using Wavelet Transformation

Joe Yoshikawa[1], Yu Nishio[1], Seiichiro Izawa[1], Yu Fukunishi[1]
[1]Mechanical Systems and Design, Tohoku University
6-6-01 Aramaki-Aoba, Aoba-ku, Sendai, Miyagi, 980-8579, Japan

**ABSTRACT**

Destabilization process of a laminar boundary layer due to a short duration jet is simulated, and the identification of local turbulent regions from the flow field is attempted using a wavelet analysis. It is shown that local turbulent regions can be identified using the wavelet analysis.

## 1. Introduction

The transition process of boundary layers is affected by the intensity of Free Stream Turbulence (FST). When the FST is higher than 1% of the free stream velocity, the bypass transition takes place instead of the transition initiated by the viscous type instability via Tollmien-Schlichting waves. In the bypass transition, first, high and low speed regions alternately aligned in the spanwise direction appear in the boundary layer. These streamwise structures are called streaky structures. Next, localized turbulent regions, i.e. turbulent spots, are randomly generated in the downstream region. And finally, when they fill the boundary layer, the bypass transition is completed.

In general, a very strong input such as a strong jet ejection [1] or a spark [2] is required to artificially generate a turbulent spot in the boundary layer. However, they appear one after another without such strong inputs in a natural condition. This fact implies that it is possible to generate a turbulent spot by much weaker stimulations if the environmental condition is correct. The goal of this research is to obtain the better understanding of bypass transition by finding such a condition. In this study, identification of turbulent regions using a wavelet transformation is attempted. The turbulent regions are artificially excited in a laminar boundary layer by ejecting a jet from a hole in the wall into the low-speed streak region.

## 2. Computational Methods

Governing equations are the 3-D incompressible Navier-Stokes equations and the continuity equation.

$$\frac{\partial \boldsymbol{u}}{\partial t} + (\boldsymbol{u}\cdot\nabla)\boldsymbol{u} = -\nabla p + \frac{1}{Re}\nabla^2\boldsymbol{u}$$

$$\nabla\cdot\boldsymbol{u} = 0$$

Each variable is non-dimensionalized by the uniform flow velocity $U$ and the displacement thickness at inlet $\delta_0^*$. The MAC method is used. The multi-directional difference scheme is used to the spatial derivatives of the velocity. The convection term and the other terms are discretized by the 3rd-order upwind difference scheme and the 2nd-order central difference scheme. The 2nd-order Crank-Nicolson method is used for the time integration.

In the computation, only the velocity difference from the Blasius profile is computed to handle the velocity fluctuation with a higher degree of accuracy. The Red-Black SOR method is used to solve the system of equations.

Figure 1 shows the computational domain. The coordinate origin is placed at the center of the inlet, where $x$, $y$, and $z$ axes denote the streamwise, wall-normal, and spanwise directions, respectively. The Reynolds number defined as $\mathrm{Re}_{\delta^*} = U\delta_0^*/\nu$ is 530. The computational region is $400\delta_0^* \times 30\delta_0^* \times 40\delta_0^*$. Total grid number is $2001\times101\times201$, where the grids are concentrated near the wall.

The simulation is performed in two steps. At the first step, the preliminary computation is carried out to obtain a flow field of steady streaky structures by placing small bumps of $1\times1\times2$ at $x$ = 50, which are regularly arranged every 10 unit length in the spanwise direction. The height of the bumps is approximately one third of the local boundary layer thickness. In the second step, the jet is intermittently ejected through a square hole of $2\times2$, 50 unit length downstream of the bump at $z$ = 0, into the steady low speed streak region obtained by the preliminary computation. The duration of jet ejection is 15 ($t$ = 0~15), and the jet velocity $v_{\mathrm{jet}}$ is 30% of the free stream velocity.

In the preliminary computation, the Blasius profile is given as the base flow and the inlet velocity profile (at $x$ = 0) is fixed to the Blasius profile. On the other hand, the velocity distribution of streaky structures obtained in the preliminary computation is used as the inlet boundary condition (at $x$ = 60) in the main computation. The non-slip condition is used at the wall, and the Neumann condition is imposed at the outlet and far boundaries. As for the pressure boundary condition, Neumann condition is used at all boundaries. The periodic boundary condition is imposed in the spanwise direction.

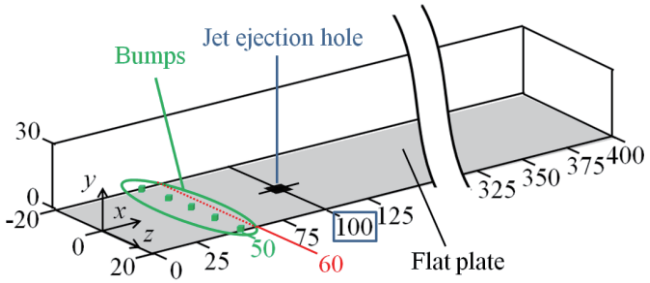


Fig. 1 Computational domain

Corresponding author: Joe Yoshikawa
*E-mail address*: yoshikawa@fluid.mech.tohoku.ac.jp

## 3. Results and Discussion

Figure 2 shows the computed vortex structures visualized by $Q$ iso-surfaces ($Q$=0.025) colored by the value of streamwise vorticity $\omega_x$. At $t$=50, two hairpin vortices exist and there is no sign of turbulence. However, at $t$ = 300, though they are entangled with a large number of streamwise vortices. Apparently, the flow field is turbulent in some areas.

Figure 3 shows the spatial variation of velocity fluctuation $u'$ in the streamwise direction at $y$=3 and $z$=0. Both data are filtered by a high-pass filter with cut-off wave number of 0.1. The results of their wavelet analyses are shown in Fig.4. In Fig. 4(a), the hairpin vortex appears as a high amplitude spot in the wavelet spectrum. The spot is small in both the wavenumber-wise scale and the streamwise scale. On the other hand, in Fig. 4(b), the isolated turbulent region appears more wide spread in the wavenumber-wise scale. It is shown that wavelet analysis is capable of identifying local turbulent regions from the flow field.

## 4. Concluding Remarks

Wavelet analysis was applied to the identification of isolated turbulent region in a transitional boundary layer. As a result, it was found that the wavelet analysis could identify local turbulent regions from a transitional flow field.

## References


[1] H. Makita and A. Nishizawa, *Journal of Turbulence*, Vol.2 (2001), pp.1-14.

[2] I. Wygnanski, M. Sokolov and D. Friedman, *Journal of Fluid Mechanics*, Vol.78 (1976), pp.785-819.


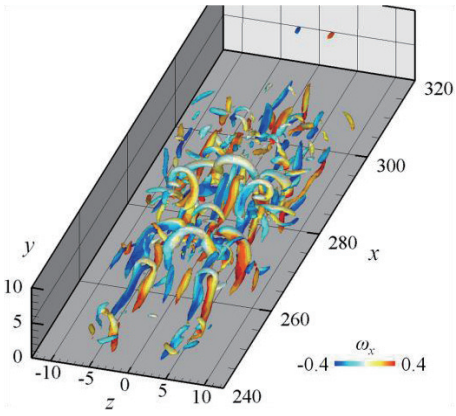


(b) $t$ = 300

Fig. 2 Visualized vortex structures

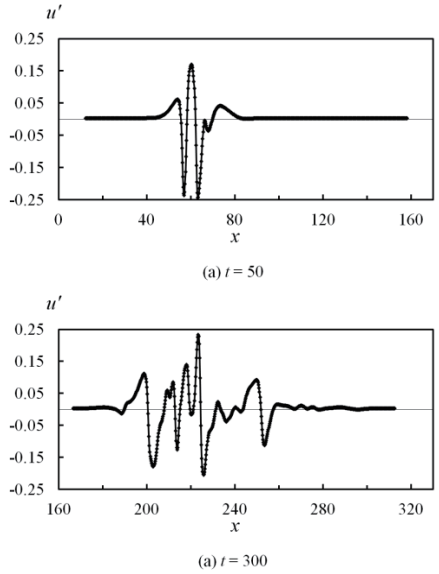


Fig. 3 Spatial variation of $u'$ at $y$=3 and $z$=0

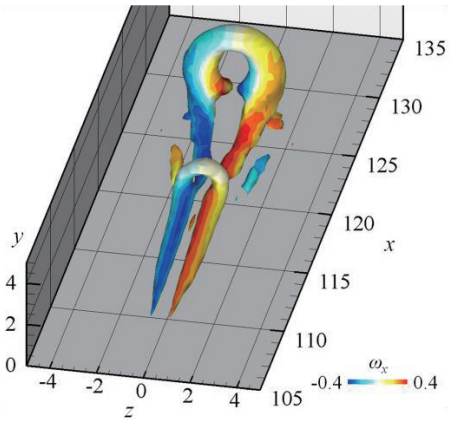


(a) $t$ = 50

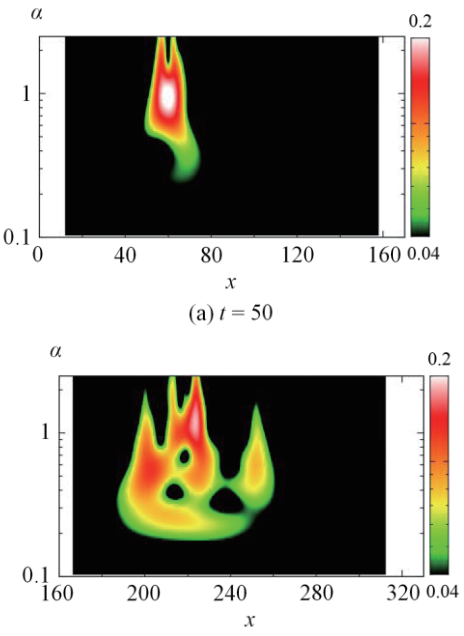


Fig. 4 Wavelet analysis of $u'$ in Fig. 3

# Outflow Boundary Condition for the Simplified Marker and Cell Method on a Staggered Grid in the Finite Volume Method

Tatsuya Soma[1], Tomoyuki Katayama[1], Yasuhiro Saito[1], Yohsuke Matsushita[1], Hideyuki Aoki[1]
[1] Department of Chemical Engineering, Graduate School of Engineering, Tohoku University, 6-6-07 Aoba, Aramaki, Aoba-ku, Sendai, Miyagi 980-8579 Japan

**ABSTRACT**

This paper applies the outflow boundary condition for unsteady-state and incompressible fluid flow computations to SMAC method in finite volume method, on the staggered grid. The concept is to satisfy the mass flow rate between the inflow and the outflow boundary conditions and the summation of the transient term of the computational domain. The mass conservativeness and the stability of the calculation are compared with the original SMAC method, and the condition achieves convergence performance comparable to conventional method.

## 1. Introduction

Boundary conditions are significant in computational fluid dynamics. In general, the velocity distribution at inflow boundary can be known, but the distribution at outflow boundary may be unknown. Thus, effort has been devoted to propose a well-posed free outflow boundary condition. Zero-gradient condition does not guarantee flow continuity during iterative calculation, which causes decrease of convergence rate. In the Simplified Marker and Cell (SMAC) method [1], tentative velocity field with zero-gradient condition is modified by pressure correction. Matsushita has proposed an outflow boundary condition in Finite Volume Method, FVM, for unsteady-state, variable density, incompressible fluid flow, which ensures the mass conservation exactly between inflow and outflow boundaries [2]. The concept of the outflow boundary condition is to apply Neumann condition not to the velocity or the momentum but to the mass flux as a part of Semi-Implicit Method for Pressure-Linked Equations (SIMPLE) algorithm. Till date, the applicability of this condition to other pressure-velocity coupling algorithms has not been investigated. In this study, the boundary condition is applied to the SMAC method, and the mass conservation and the stability of the calculation are compared with the original SMAC method.

## 2. The Velocity Field at Outflow Boundary

### 2.1 Boundary condition of the SMAC Method

A tentative velocity field is calculated by solving discretized momentum equation with arbitrary pressure field. The boundary velocity obtained using zero-gradient condition for tentative velocity is corrected by pressure corrections. This allows fluid to flow out the computational domain at its own chosen rate.

$$u_{\mathrm{o}} = \acute{u}_{\mathrm{o}} - \frac{\Delta t}{\rho}\frac{\partial p'}{\partial x}\bigg|_{\mathrm{o}}, \qquad (1)$$

where $\acute{u}_{\mathrm{o}}$ is the velocity at outflow boundary obtained by solving the discretized momentum equation, which does not necessarily satisfy the discretized continuity equation. $p'$ is pressure correction, and the value outside outflow boundary $p'_{\mathrm{O}}$ shown in Figure 1 is set to zero.

Corresponding author: Tatsuya Soma
*E-mail address*: soma@tranpo.che.tohoku.ac.jp

### 2.2 The Outflow Boundary Condition by Matsushita

Inflow, outflow and the increment of mass are balanced in computational domain. Assuming that fluid density is constant, the amount of fluid mass in computational domain hardly changes at all. Therefore, imbalance between inflow and tentative outflow calculated from tentative velocity field is eliminated by the following equation:

$$u_{\mathrm{o}} = \acute{u}_{\mathrm{o}} + \frac{F_{\mathrm{I}} - F_{\mathrm{o}}}{\sum \rho A|_{\mathrm{o}}}, \qquad (2)$$

where $F_{\mathrm{I}}$ and $F_{\mathrm{O}}$ are the mass flow rate through the inflow and outflow boundary, respectively. The second term on the right-hand side is correction amount for the imbalance, and when the convergence is obtained, the value approaches zero. For the unsteady-state flow with variable density, the amount of fluid mass in computational domain can increase or decrease. Consequently, the velocity-correction formula is obtained as:

$$u_{\mathrm{o}} = \acute{u}_{\mathrm{o}} + \frac{F_{\mathrm{I}} - F_{\mathrm{o}} - \sum \frac{\rho_{\mathrm{p}}^{\mathrm{n+1}} - \rho_{\mathrm{p}}^{\mathrm{n}}}{\Delta t}\Delta V_{\mathrm{p}}}{\sum \rho A|_{\mathrm{o}}} \qquad (3)$$

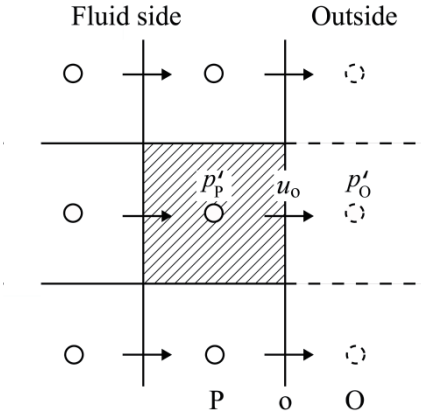


Fig. 1 Grid arrangement near the outflow boundary and the notations

## 3. Method

To evaluate the two boundary conditions, the

backward-facing step flow was considered. The layout of the analytical object is shown in Figure 2. The supply flow rate on the inflow boundary is constant, and the above algorithms were applied for outflow boundary conditions. The no-slip boundary condition was applied to the wall. The flow was assumed to be incompressible, viscous and laminar, and the Reynolds number was set to 1095. The fluid flow is governed by the momentum equation and continuity equation. The governing equations were discretized via the finite volume method. The convection term of the momentum equation was discretized by using the quadratic upstream interpolation for convective kinetics (QUICK) scheme. The diffusion term was discretized with the second-order central difference scheme. The simplified marker and cell (SMAC) method was applied for pressure-velocity coupling. The pressure correction equation was solved by using the algebraic multigrid solver (AMGS) [3] as the matrix solver.

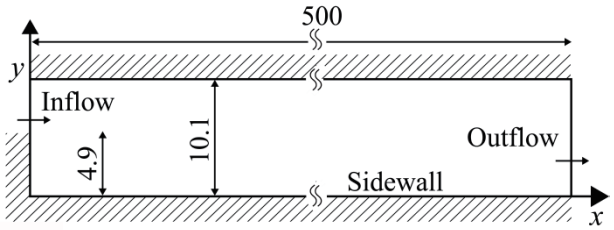


Fig. 2 Layout and geometry of the analytical object ($500 \times 40$ grid meshes)

## 3. Results and Discussion

The residual histories of continuity equation for the iterations at the tenth time step are shown in Figure 3 as a typical example. The residual is normalized by the inflow mass flow rate. The residual with Eq. (2) rapidly decreases, and then the calculated velocity field satisfies the mass conservation within tolerance error. For every time step to reach steady-state, the same accuracy is achieved. Figure 4 provides the mass flow rate on each time step. Since the density is assumed to be constant in this computation, as is obvious, the mass flow rate does not change at all. Thus, the proposed outflow boundary condition is applicable not to only SIMPLE but also to SMAC. The boundary condition compares favorably with the condition of the original SMAC method using Eq. (1) in terms of convergence performance.

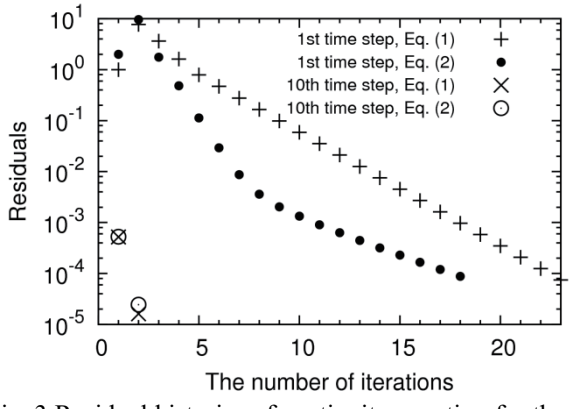


Fig. 3 Residual histories of continuity equation for the iterations at the tenth time step

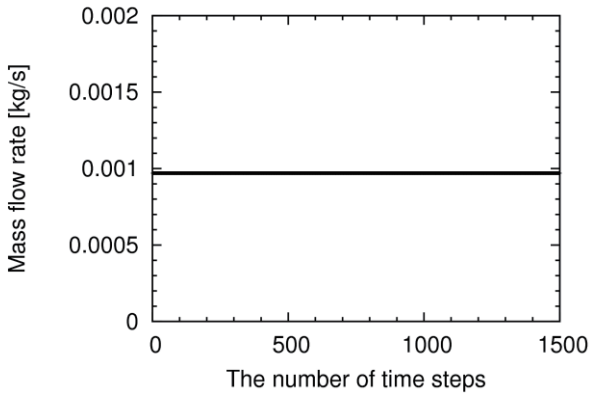


Fig. 4 The history of mass flow rate with proposed outflow boundary condition

One of major differences between these methods is the treatment of pressure correction outside outflow boundary. In the original SMAC method, since the value is zero, the pressure on the position is treated as constant pressure. This method is innately the constant pressure boundary condition, which does not determine boundary velocity directly. On the other hand, in the proposed condition, pressure correction is non-defined outside boundary, and the boundary velocity is configured to balance inflow and outflow. Thus, these methods can differ in convergence performance at first time step, and can be selected as a situation demand.

## 4. Concluding Remarks

In this study, the outflow boundary, developed for unsteady-state, variable density and incompressible fluid flow computation as a part of SIMPLE algorithm in Finite Volume Method, is applied to the SMAC method on a staggered grid. The proposed condition is applicable to SMAC. It indicates good convergence performance as free outflow boundary condition.

## Nomenclature

| | | |
|---|---|---|
| $F$ | mass flow rate | [kg/s] |
| $u$ | velocity component | [m/s] |
| $x$ | coordinate | [m] |
| $\rho$ | fluid density | [kg/m$^3$] |
| $\Delta t$ | time step | [s] |
| $\Delta V$ | cell volume | [m$^3$] |
| | Subscript / Super script | |
| I | inflow boundary | |
| O | outside | |
| o | outflow boundary | |
| P | present cell | |
| n | time level | |

## References


[1] A. A. Amsden, *Los Alamos Scientific Laboratory*, Report LA-4370 (1970)

[2] Y. Matsushita, *Computational Thermal Sciences*, **3** (2011) 531-537

[3] High Performance Computing Laboratory, 2010. available at: <http://hpcl.info.kogakuin.ac.jp/olab>. Last accessed: August 2013

# Experimental Study on Swirling Flow with an Air-Core during Water Draining from a Cylindrical Tank

Yoshihiro Aoki[1], Eiji Sakamoto[1], and Tameo Nakanishi[1]
[1]Graduate School of Science and Engineering, Yamagata University
4-3-16 Jonan, Yonezawa, Yamagata, 992-8510, Japan

**ABSTRACT**

When water drains from the bottom hole of a tank, the swirling flow with an air-core forms toward the hole from the water surface. This flow may be further classified into two types considering the open-top and the closed-top situations. In the former case, the air flows downward dragged by the descending water. In the latter case, the air flows upward in order to replace the volume of the drained water. The discharge rate, the discharge coefficient, and the discharge angle as to the water head and the hole diameter were investigated.

## 1. Introduction

When water drains from the bottom hole of a tank, the swirling flow with an air-core forms toward the hole from the water surface [1]. A water bell is generated just out of the hole due to centrifugal force. This flow may be further classified into two types considering the open-top and the closed-top situations. Figure 1 shows different type of swirling flows. In the open-top case, the air inside the air-core is dragged by the descending water, and thus flows downward. In the close-top case, an equivalent amount of air is to replace the drained water, air flows upwards. The appearance of intense vortices with an air core in fluid machine, such as pump and hydroelectric generator, is undesirable as energy loss increases [2, 3].

A lot of experiments and numerical simulations have been done for the open-top case [1-4]. However, there is few researches for closed-top cases. The purpose of the present study is to clarify the characteristics of these swirling flows.

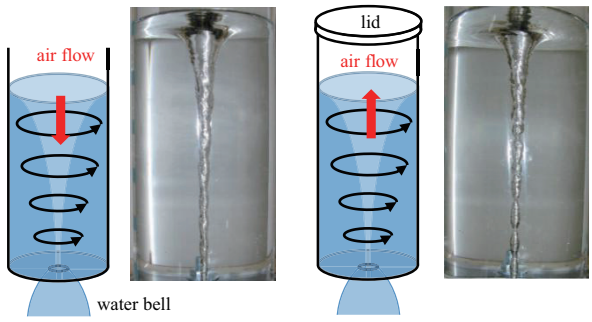


(a) open-top case (b) closed-top case

Fig. 1 different type of swirling flows

## 2. Experimental Method

Figure 2 shows a schematic of the experimental setup. An acrylic cylindrical tank of height of h=1000mm and inner diameter of D=190mm is used. The bottom part of the tank is designed that circular stainless steel plate of diameter of D=190mm and thickness of 1mm with a center hole of diameter d is supported by a hollow acrylic plate. The top lid can be removed, so that two kinds of experiments are possible, the open-top case and the closed top case.

The drainage hole is firstly plugged by a cork. To start the experiment, water is filled at a constant flow rate in the peripheral direction to a given water level by a hose attached to the inner surface of the tank near the top side. The initial angular momentum L inside the tank is estimated as:

$$L = 2\pi\rho \int_0^H \int_0^R r^2 v_\theta(r,z)\, dr dz \qquad (1)$$

where $\rho$ is density of water, H is water head, and $v_\theta$ is the average velocity from the hose.

The angular momentum cannot flow out during water draining since the axis of rotation is through the drainage hole. The mass of water decreases while the angular momentum remains nearly constant, leading to acceleration of rotation speed. The air-core develops in depth and finally reaches the draining hole.

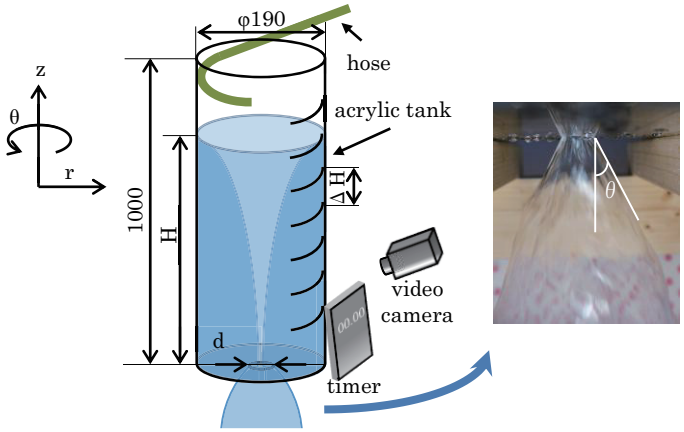


Fig. 2 Experimental setup and the water bell just out of the hole

The experiment is started by open the drainage hole and is recorded by a video camera and the recorded data are processed afterward.

The discharge rate Q, the discharge velocity $V_z$, and the discharge coefficient C are calculated by:

$$Q = \frac{1}{4}\pi D^2 \frac{\Delta H}{\Delta T}, \qquad (2)$$

$$V_z = Q/A, \qquad (3)$$

$$C = V_z/\sqrt{2gH}. \qquad (4)$$

Here, $\Delta T$ is the time elapsed as water descending

Corresponding author: Yoshihiro Aoki
*E-mail address*: tar11524@st.yamagata-u.ac.jp

one scale (ΔH), A is the area of the drainage hole, and g is gravitational acceleration.

The photos of the water bell out of the drainage hole are taken by a digital camera and the spread angles are measured by an image-analysis software.

## 3. Results and Discussion

In the open-top case, the air is dragged by the descending water and thus flows downward. In the closed-top case, the air flows upward in order to replace the volume of the drained water. The counter flow experiences a greater friction. The air-core of the closed-top case is found more unstable than that of the open-top case as seen in Fig. 1. This tendency is more significant at a higher water head.

Figure 3 shows discharge velocity versus water head plots (φ20). The result of single-phase flow (SPF) is also included for comparison. Firstly, the discharge velocity decrease as to decreasing water head in each case. Secondly, the discharge velocity of the open-top swirling flow is lower than that of the SPF case. This is because a part of potential energy has been transformed into the energy of swirling motion and eventually dissipated. Thirdly, the difference of the average discharge velocity of open-top swirling flow and closed-top swirling flow decrease as to decreasing water head. This tendency was seen despite of the size of the hole diameter.

Figure 4 shows discharge coefficient versus water head plots for the cases with different hole diameters. In the open-top case (Fig. 4(a)), the discharge coefficient is almost a constant independent of the hole diameter when the water head is high. The discharge coefficient deviates from this value as the water head decreases. The value increases in the small hole diameter cases and decreases in large hole diameter cases as to decreasing water head. This is because that the angular momentum inside the tank is easier to discharge through a larger hole. In the closed-top case (Fig. 4(b)), the discharge coefficient is almost independent of the water head and hole diameter.

Figure 5 shows the graph of the discharge angle ( $\theta$ ) of the water bell versus water head plots for the open-top case. The definition of $\theta$ is denoted in Fig. 2. The discharge angle decreases in the small hole diameter cases and increases in the large hole diameter cases as to decreasing water head. Comparing Fig. 4(a) and Fig. 5, the tendency is similar to each other. It turned out that the discharge angle is related to the discharge coefficient.

## 4. Concluding Remarks

Two different types of swirling flows with an air-core were investigated. Lower discharge rate and discharge coefficient are measured for the closed-top case as compared to the open-top case. The characteristics of the discharge velocity, the discharge coefficient, and the discharge angle as to the water head and the drainage hole diameter were disclosed.

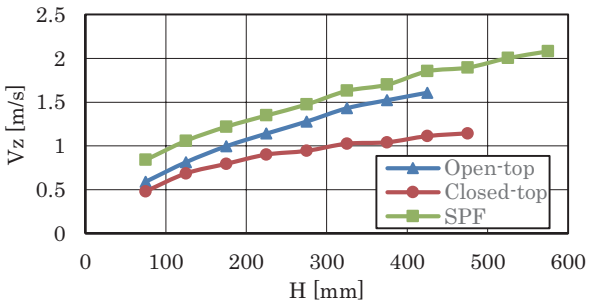


Fig. 3 Discharge velocity versus water head (drainage hole diameter= $\phi$ 20)

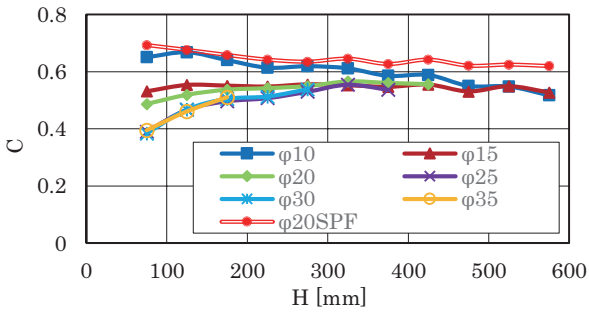


(a) Open-top cases

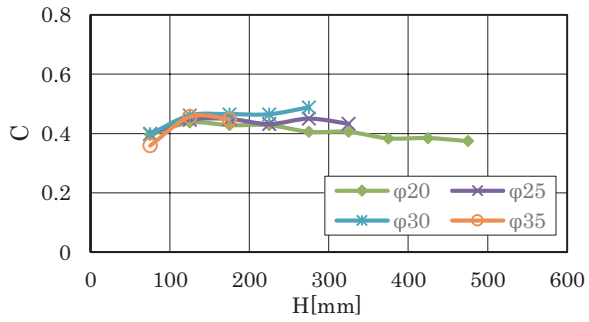


(b) Closed-top cases

Fig. 4 Discharge coefficient versus water head

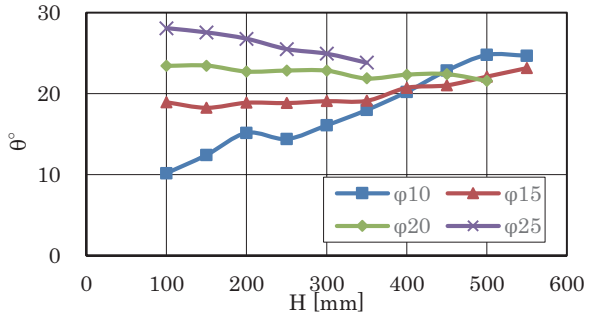


Fig. 5 Discharge angle versus water head (open-top cases)

## References


[1] A. Andersen, et al., Physical Review Letters, 2003, Vol.91, No.10, 104502-1-4.

[2] S. Sakai, et al., Trans. JSME (in Japanese). Ser. B, 1998, Vol. 63, No. 614, 23-30.

[3] A. Stepanyants, H. Yeoh, J. Fluid Mech., 2008, Vol.604, 77-98.

[4] P. Basu, et al., International Journal of Fluid Mechanics Research, 2013, Vol. 40, No. 1, 27-41.

Eleventh International Conference on Flow Dynamics
October 8-10, 2014, Sendai, Miyagi, Japan

# Visualization of Flow Phenomena Induced by Necklace Vortex in Front of a Circular Cylinder

Yuki Mino[1], Takafumi Abe[1], Ayumu Inagaki[1], Hidemi Yamada[1]
[1]Department of Mechanical and Energy Systems Engineering, Oita University
Dannohal 700, Oita, Oita, 870-1192, Japan

**ABSTRACT**

In this paper the effect of the laminar boundary layer on the flow phenomena in front of a circular cylinder have been investigated by visualization and measurement of surface pressure. The relative boundary layer thickness δ/d is varied from δ/d=0.26 to 0.82. Reynolds number is Re=3000 for measurement of pressure, and Re=500 or 1000 at visualization. Only in the case of thick boundary layer, pressure coefficient increase in vicinity of end wall, and corner vortex might be formed.

## 1. Introduction

It is known that the flow around a circular cylinder is affected by the aspect ratio and the blockage ratio[1,2]. But many of studies verifying the effect of aspect ratio and blockage ratio did not comprehend the condition of the end of the cylinder, therefore results of these studies are sometimes different. Accordingly, it is important that the effect of the end condition was comprehended in the experiment. If the boundary layer is thick, the secondary flows behind the circular cylinder are stronger, and the base suction coefficient is smaller than the case of thin boundary layer[3]. But the cause why secondary flow occurs still has not been found.

The aim of this investigation is to clarify the effect of laminar boundary layer on the flow structure in front of a circular cylinder. Especially, flow phenomena induced by necklace vortex in front of a circular cylinder was investigated by visualization of flow and measurement of surface pressure.

## 2. Method

In the experiments, a blow down wind tunnel was used for measurement of surface pressure, and a circulating type water channel was used for visualization of flow phenomena.

The outlet cross section of the wind tunnel was 400mm high and 400mm wide, as shown as Fig.1. A circular cylinder was supported by two end walls whose leading edge was transformed into a long semi-elliptical shape (Long: Short = 4: 1). The aspect ratio was fixed L/d=20, and test section does not have side walls to take away the influence of test section blockage. The diameter of the circular cylinder and pressure hole was d=6mm and $d_p$=0.25mm, respectively. The position of the circular cylinder was varied from $X_L$=50mm to 500mm ($X_L$ is the distance from the leading edge to cylinder position). On that occasion, relative boundary layer thickness was varied from δ/d=0.26 to 0.82. Reynolds number was Re=3000.

Figure 2 shows the circulating type water channel with a test section 300mm high and 300mm. The end wall used for the flow visualization was transformed into a long semi-elliptical shape, and set in the position 50mm away from the test section floor. The diameter of the circular cylinder was d=32mm, and the position of the cylinder was varied from $X_L$=56mm to 560mm. Relative boundary layer thickness and Reynolds number were δ/d=0.26, Re=1000 and δ/d=0.82, Re=500.

Corresponding author: Yuki Mino
*E-mail address*: v13e1029@oita-u.ac.jp

## 3. Results and Discussion

Figure 3 shows the spanwise distribution of pressure coefficient on stagnation point and Fig.4 shows the flow visualization of x-z plane at y/d=0 for two different relative boundary layer thickness δ/d=0.26 and 0.82.

In the case of thin boundary layer, δ/d=0.26, the surface pressure coefficient exhibits the minimum value Cp≒0.92 at z/d=0, and increases gradually toward the mid-span of a cylinder. The surface pressure coefficient continues to increase across the outer end of the boundary layer z/d=0.26, and takes Cp=1.0 at z/d≒0.6. As be seen Fig. 4, the flow approaching to the cylinder lean to down near the end wall. In addition, in the very close to end wall, the flow in front of the cylinder go to down and flow back, then the necklace vortex is formed in front of the circular cylinder. The region which flow

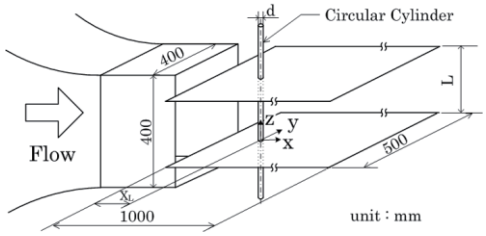


Fig. 1 Experimental apparatus and coordinate system of wind tunnel

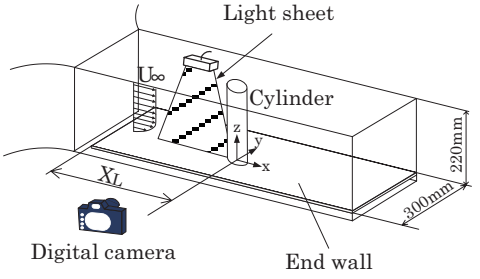


Fig. 2 Experimental apparatus and coordinate system of water channel

goes down or leans to down almost coincide with the region which pressure coefficient is Cp<1.0.

In the case of thick boundary layer, δ/d=0.82, the surface pressure coefficient exhibit different distribution from the case of thin boundary layer. The pressure coefficient increases gradually after decreasing the region 0<z/d<0.18. The pressure coefficient increases across the outer end of the boundary layer z/d=0.82, as shown in the case of δ/d=0.26. The pressure decrease in the range 0<z/d<0.18 was not seen in the case of δ/d=0.26, and it is suggested the corner vortex exists in the case of thick boundary layer.

Figure 5 shows the flow visualization in the x-z plane at y/d=-0.3. The inclination of the flow approaching the cylinder is small, and the flow passes the side of the cylinder with keeping the inclination in the very close to end wall. On the other hand, Fig. 6 shows the distribution of pressure gradient around the separation point of the cylinder. The point where pressure gradient takes peak shift rear of the cylinder as measurement point reaches end wall. It suggests that the separation point shift rear of cylinder in and around in boundary layer. It is guessed that the cause of this is the flow passing the cylinder leans to down near end wall as seen in Fig. 5.

## 4. Concluding Remarks

The phenomena induced by necklace vortex in front of the circular cylinder were studied by the flow visualization and measurement of surface pressure.

Both cases of thin and thick laminar boundary layer, pressure coefficient on stagnation point near end wall is lower than Cp=1.0 in a range over the outer end of the boundary layer, and it is almost same with the region flow in front of a cylinder go down or lean to down. In addition, only in the case of thick boundary layer, pressure coefficient increase in the range 0<z/d<0.18. It is considered corner vortex is formed in a case of thick boundary layer.

In and around in boundary layer, the separation point shift rear of cylinder because the flow passes the side of the cylinder with keeping the inclination.

## References


[1] G.S. West, C. J. Apelt, *Journal of Fluid Mechanics*, (1982), Vol.114, 361-377.

[2] S. Szepessy, and P. W. Bearman, *Journal of Fluid Mechanics*, (1992), Vol.234, 191-217.

[3] A. Inagaki, Y. Mino, M. Iwamoto, H. Yamada, *16th ISFV,* (2014), 1092.


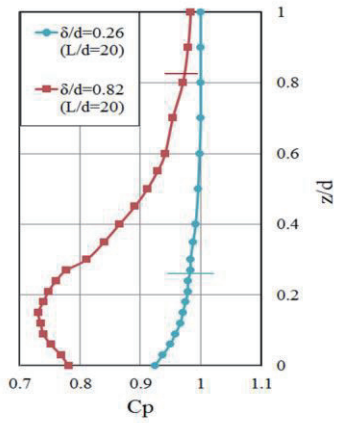


Fig.3 spanwise distribution of surface pressure coefficient on stagnation point

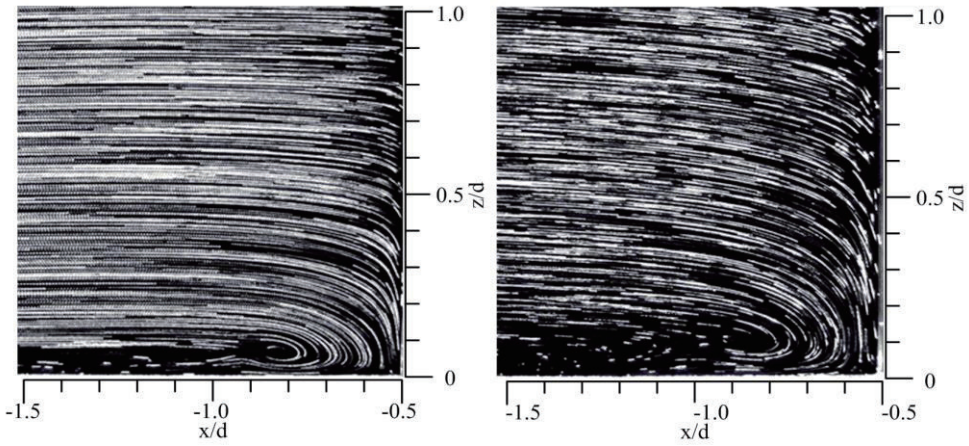


(a) δ/d=0.26 (b) δ/d=0.82

Fig.4 Flow visualization of x-z plane at y/d=0

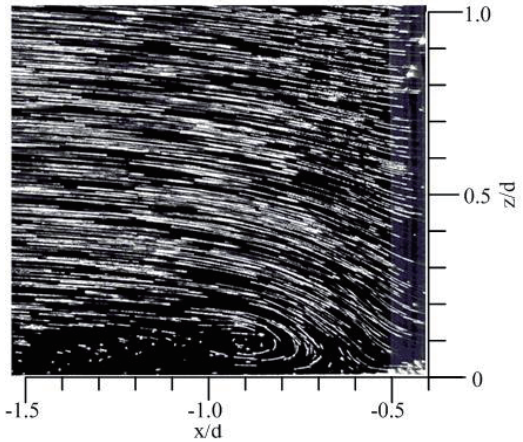


Fig.5 Flow visualization of x-z plane at y/d=-0.3 (δ/d=0.82)

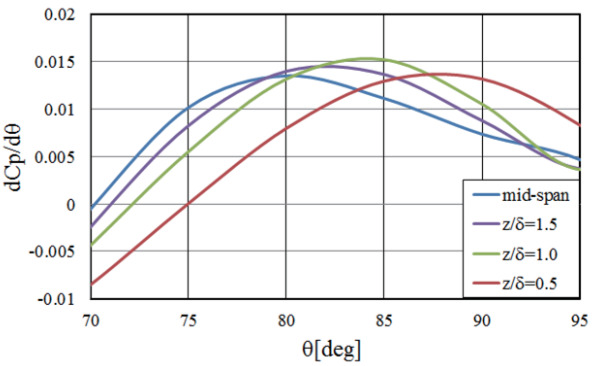


Fig.6 Distribution of pressure gradient in δ/d=0.82

Eleventh International Conference on Flow Dynamics
October 8-10, 2014, Sendai, Miyagi, Japan

# Effect of Single-phase Turbulence Model on 3-D Structure of Cavitation inside a Nozzle

Anh.D. Le [1], Yuki Yamagchi [1], Motohiko Nohmi [2], Yuka Iga [3]
[1]Graduate School of Engineering, Tohoku University
[2]Ebara Corporation
[3]Institute of Fluid Science, Tohoku University

**ABSTRACT**

This study deals with the numerical analysis of the cavitation inside an abrupt reduction nozzle by commercial CFD program FLUENT 14.0 with three types of availability single-phase turbulence models such as RNG k-ε turbulence model, Menter's Shear Stress Transport (SST) turbulence k-ω model and Large-Eddy Simulation (LES) turbulence model. The results show that different turbulence models provided different cavity structures. In comparison with our previous experimental data, the SST k-ω turbulence model showed better results than the two other.

## 1. Introduction

In the liquid flow, due to pressure reduction by acceleration, vapor bubbles are formed when the local pressure becomes lower than saturation vapor pressure, which is cavitation. Since atomization nozzle normally has a small size and works with high velocity, cavitation easily occurs in the abrupt reduction corner. Cavitation is hated for the material damage, at the same time that promotes the atomization. Still now, non exact turbulence model is developed for cavitating flow. Instead of that, single-phase turbulence models are often used to simulate cavitating flow. In general, one does not really know which turbulence model will work well for the cavitating flow. In this study, we use the commercial CFD program FLUENT to analyze the cavitation in 3-D abrupt reduction nozzle. Three types of single-phase turbulence models are applied to the calculation, which are RNG k-ε model, Menter's Shear Stress Transport (SST) turbulence k-ω model from RANS (Reynolds Averaged Navier-Stokes Simulation) model and LES (Large-Eddy Simulation) turbulence model [2, 3]. The availability of the single - phase turbulence models is investigated focusing on the cavity structure through the comparison with our previous experimental result in which the characteristics of cavity structure depends on the Reynolds number of the flow field.

## 2. Numerical Method

### 2.1 Cavitation model

Gas-liquid two-phase model is used in this study. By neglecting the effect of slip velocity between vapor and liquid interface, this model has same concept of homogeneous equilibrium model, in that the vapor - liquid two - fluid medium is modeled as pseudo-single fluid medium [4]. Two types of cavitation model were used to model the cavitating flow: Singhal's full cavitation model and Schneer and Sauer model which are based on Rayleigh – Plesset's equation [1, 4].

### 2.2 Turbulence models

Three types of single-phase turbulence model are applied in this study to cavitating flow, which are RNG k-ε turbulence model with enhanced wall function, SST k-ω turbulence model and LES turbulence model with Smagorinsky-Lilly's model for subscale modeling [2,3].

### 2.3 Numerical Scheme

Implicit finite - volume method was used. The pressure base solve algorithm PISO was chosen as the velocity–pressure–coupling algorithm [4]. For RANS turbulence model, the PRESTO! scheme was used to discrete the convection term in the pressure equation. Other equations, the QUICK discretisation scheme were used for convection term, while the Bounded Central Differencing scheme was applied to discrete momentum equation for LES model [2, 3, 5]. The Singhal's full cavitation model was used for RANS turbulence models, while Schneer and Sauer's model was used for LES model due to Singhal's cavitation model is unstable and is not compatible with the LES turbulence model [4]. No-slip boundary condition was applied at the wall.

## 3. Results and Discussion

### 3.1 Calculation conditions

Three dimensional abrupt reduction nozzle with throat geometry of 4 mm in height, 1 mm in width and 16 mm in length is used to analyze the effect of Reynolds number on the structure of cavity. The geometry of the nozzle, upstream and downstream is same as our previous experiment [6]. For boundary condition, constant pressure $p_{up}$ is imposed similar to experimental condition at upstream boundary as shown in the Table 1. For downstream boundary, pressure is specified to reproduce the same cavity length in the experiment which is shown in Fig.1 [6]. In the experiment, the cavity lengths are same in the three cases but the aspects are completely different. According to increase of Reynolds number, the cavity surface is disturbed and small bubble is released from the surface.

Table1. Calculation cases

| Case | $p_{up}$ [MPa] |
|---|---|
| Case1 | 0.040 |
| Case2 | 0.046 |
| Case3 | 0.150 |

### 3.2 Results and discussion

Instantaneous aspects of the cavitation in each RANS model in each calculation case are shown in Fig.2. The calculation is converged and the cavity become quasi-steady. In all calculations, sheet cavitation appears

Corresponding author: Yuka Iga
*E-mail address*: iga@ifs.tohoku.ac.jp

and the length is adjusted to the outlet in order to realize same cavity length as experimental results. In RNG k-ε turbulence model in Fig. 2 (a), the surface of the cavity looks smooth in case 2 and case 3 but that become somewhat be disturbed in case 1. These are opposite tendency to that in experiment. Also, the cavity is occurred on the wall of nozzle with almost no separate region.

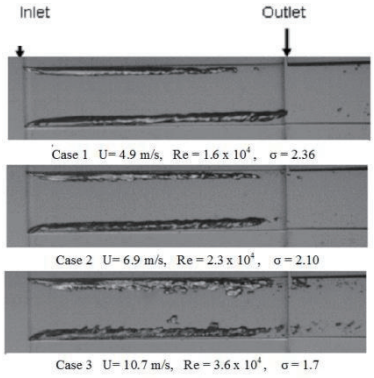


Fig. 1 Cavitation aspects in nozzle experiment [6]

In SST k-ω turbulence model in Fig.2(b), the cavity surface is also smooth and has same thickness as with the RNG k-ε turbulence model. However, cavity appears on wall just in the region near the front edge of sheet cavity, and separates from the wall in the downstream region. And the aspect of cavity surface seems to be disturbed in case 3. From these figures, the difference can be seen in the aspect of sheet cavity between two RANS models.

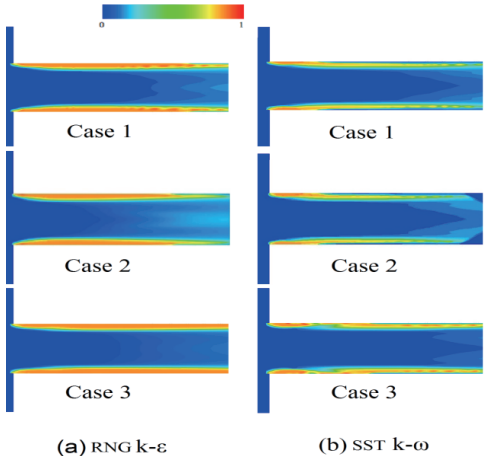


Fig. 2 Numerical results of void fraction distribution: (a) RNG k-ε turbulence models, (b) SST k-ω turbulence model

The aspect of cavity surface can be seen clearly in Fig.3, which shows the iso-surface at 30% void fraction of both RNG k-ε turbulence model and SST k-ω turbulence model. In the RNG k-ε turbulence model, the cavity surface nearly looks smooth in all regions for all cases. On the other hand, in the SST k-ω turbulence model, the surface looks smooth at the region near the front edge of sheet cavity and becomes disturbed configuration at downstream region, which agrees with experiment qualitatively.

Figure 4 shows the result with LES mode in case 3. The aspect of cavity is different from both RANS turbulence model and experimental results. The region in which void fraction is over 0.9 is short and locates in the vicinity of front edge of the cavity. The sheet cavity with void fraction around 0.3 appears behind this region and develops to reaching the outlet. These void fraction distribution are considered to correspond to short sheet cavity and bubble cavity downstream of the sheet cavity, although the bubble structure cannot be resolved by the present homogeneous model.

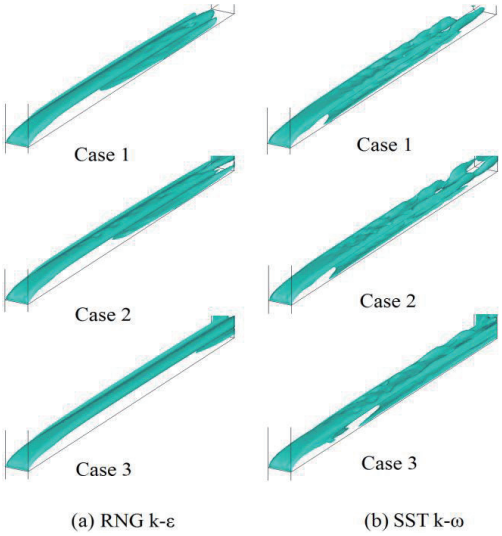


Fig. 3 Iso-surface of void fraction at 30%: (a)RNG k-ε turbulence model, (b) SST k-ω turbulence model

Fig. 4 Numerical result of void fraction in Case 3 by LES

## 4. Conclusion

In our work, availability of three kinds of single-phase turbulence models was investigated in cavitating flow in a 3-D abrupt reduction nozzle. Through the numerical simulation, it shows that the aspect of cavity is different with each other depending on the turbulence models,. The aspect of cavity with SST k-ω turbulence model gives better result than two other models.

## References


**[1]** Brennen C.E: Cavitation and Bubble Dynamic. Oxford University Press 1995.

**[2]** Wilcox D. C.: Turbulence modeling for CFD 1994 by DCW Industry, Inc. ISBN 0-9636051-0-0

**[3]** Georgiadis. J. N, Rizzetta. P. D, Fureby. C. 47th AIAA Aerospace Sciences Meeting, January 2009, Orlando, Florida.

**[4]** Fluent 14.0 theory guide.

**[5]** Matevz. D, Bachert, Stoffel, Sirok. Eur.j.mech. B, Fluids, 2005, vol. 24, pp, 1176-1184

**[6]** Yamaguchi, Y., Anh. D. Le., Nohmi, M., Iga. Y. Visualization Symposium Japan 2014.

Eleventh International Conference on Flow Dynamics
October 8-10, 2014, Sendai, Miyagi, Japan

# Effects of Laminar Boundary Layer and Aspect Ratio on Surface Pressure around a Circular Cylinder

Takafumi Abe[1], Yuki Mino[1], Ayumu Inagaki[1], Hidemi Ymada[1]
[1]Department of Mechanical and Energy Systems Engineering, Oita University
Dannoharu 700, Oita, Oita, 870-1192, Japan

**ABSTRACT**

The effects of laminar boundary layer and aspect ratios on the surface pressure around a circular cylinder supported by two large end walls were examined experimentally at Reynolds number 3000. The relative laminar boundary layer thickness was altered between 0.26 and 0.82, and the aspect ratio was varied from 20 to 55. Consequentially, the base pressure coefficient approaches the constant value $C_{pb}$=-0.8, as the boundary layer thickness is small and aspect ratio is large. Then two dimensionality flow is ensured at midspan of the cylinder.

## 1. Introduction

It is well known that the aerodynamics of a circular cylinder is strongly affected by the aspect ratio which defined the ratio of the cylinder diameter to the distance between end walls. Szepessy and Bearman investigated the effect of the aspect ratio on vortex shedding on a wide range of Reynolds numbers [1]. Furthermore, Norberg carefully carried out his experiments to examine effects of the aspect ratio on the Strouhal number and base pressure coefficient at the midspan [2]. He proposed a significant idea for "the required aspect ratio" defined as the smallest aspect ratio needed to obtain aerodynamic features of a quasi-infinite cylinder. He came to the conclusion that aspect ratios as large as L/d=60-70 were needed for the range $Re=4\times10^3$-$10^4$.

On the other hand, flow around a circular cylinder is affected by the end condition of the cylinder. The surface pressure distribution is different for transitional boundary layer thickness δ/d [3] (boundary layer thickness defined as the ratio of the boundary layer thickness δ to the cylinder diameter d). Above the experiment was carried out the experimental for only transitional boundary layer. The studies about the conditions of ensuring two dimensionality flow at the midspan of the cylinder, considering aspect ratio L/d and boundary layer thickness δ/d at the same time is not enough. Therefore, the aim of this investigation is to clarify the conditions of ensuring a two dimensionality flow around a circular cylinder at the midspan by searching the effects of aspect ratio L/d and laminar boundary layer thickness δ/d on the base pressure coefficient.

## 2. Method

In the measurement of the surface pressure on a circular cylinder, a blow down wind tunnel with outlet cross section 400 mm high and 400 mm wide was used. The turbulence intensity in the free stream was less than 0.5%. A circular cylinder with a pressure tapping hole was supported by two end walls as shown in Fig.1. The diameters of the cylinder and the pressure hole were d=4mm with $d_p$=0.20mm and d=6mm with $d_p$=0.25mm. The end walls were the 10 mm thickness acrylic plate whose leading edges were transformed into the long semielliptical shape (long: short = 4:1). The test section does not have side walls to take away the influence of the test section blockage. The aspect ratio L/d was altered between 10 and 55 by moving two end walls. The relative boundary layer thickness δ/d was altered between 0.26 and 0.82 by varying distance $X_L$ from the leading edge to the cylinder position. The Reynolds number based on the cylinder diameter d and the uniform flow velocity $U_\infty$ was kept at about 3000. Then the velocity of the uniform flow was 7.5 m/s or 12 m/s.

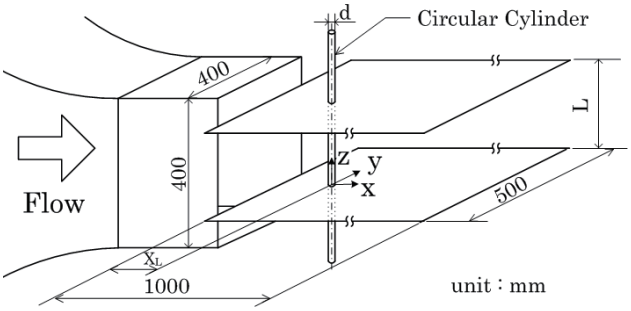


Fig. 1 Experimental apparatus and coordinate system of the wind tunnel

## 3. Results and Discussion

### 3.1 Spanwise Distribution of Base Pressure

Figure 2 (a), (b) shows the spanwise distribution of the base pressure coefficient for two different relative the laminar boundary layer thickness δ/d measuring used by the cylinder diameter of 4 mm in the case of varied aspect ratio at Reynolds number 3000.

In the case of δ/d=0.26 which the laminar boundary layer is relatively thin, the base pressure coefficient is constant value over the whole area of the cylinder. The value of the base pressure coefficient for varied aspect ratio L/d do not change at $C_{pb}$=-0.80. Therefore, the base pressure coefficient is hardly affected by aspect ratio in the case of thin boundary layer.

In the case of δ/d=0.82 which the laminar boundary layer is relatively thick, the base pressure coefficient is different from the case of δ/d=0.26. The base pressure coefficient varies greatly over the large spanwise range from the cylinder end. The pressure coefficient increases rapidly after decreasing the region 0<z/d<1.0. On the

Corresponding author: Takafumi Abe
*E-mail address*:v14e1004@oita-u.ac.jp

other hand, in the region z/d>3.0, the value of the pressure coefficient is constant. The value taking constant in the region z/d>3.0 is largely different for the varied aspect ratio L/d. The gap of the value of pressure coefficient becomes the smaller, the aspect ratio is the larger. According to the above results, the base pressure coefficient is affected by aspect ratio more strongly in the case of the thick boundary layer.

Similarly, it was noticed that the effect of the boundary layer is greater in case of small aspect ratio.

### 3.2 Base Pressure Coefficient at Midspan Position

The base pressure coefficient is greatly influenced by end walls distance L and laminar boundary layer thickness δ. A new parameter called "span coefficient" L/2δ was defined. Fig.3 shows the base pressure coefficient at the midspan position versus L/2δ at Reynolds number Re=3000. If the span coefficient L/2δ is same, the pressure coefficient is almost constant value, even if aspect ratio L/d and boundary layer thickness δ/d is different value. The variation of the pressure coefficient is the smaller, as the span coefficient L/2δ becomes large. In the range of L/2δ>55, the base pressure coefficient is nearly constant value $C_{pb}$=-0.80. That is to say, two dimensionality flow of a circular cylinder at the midspan coefficient is required, and enough value of the span coefficient is larger than approximately 55.

## 4. Concluding Remarks

The effects of the laminar boundary layer and aspect ratio on surface pressure around a circular cylinder were studied at the Reynolds number 3000. The experimental result reveals the following.

The base pressure coefficient is hardly affected by aspect ratio in the case of the thin boundary layer, and the pressure coefficient is affected more strongly in the case of the thick boundary layer.

The variation of the pressure coefficient is the smaller, as the span coefficient L/2δ becomes large. In the range of L/2δ>55, the base pressure coefficient is nearly constant value $C_{pb}$=-0.80.

## References


[1] Szepessy, S. and Bearman, P. W., *Journal of Fluid Mechanics*, 234, (1992) 191-217.

[2] Norberg, C., *Journal of Fluid Mechanics*, 258, (1994), 287-316.

[3] Inagaki A., Mino Y., Iwamoto M. and Yamada H., *4th International Conference on Jets, Wakes and Separated Flows*, Nagoya, Japan, (2013), 1196.


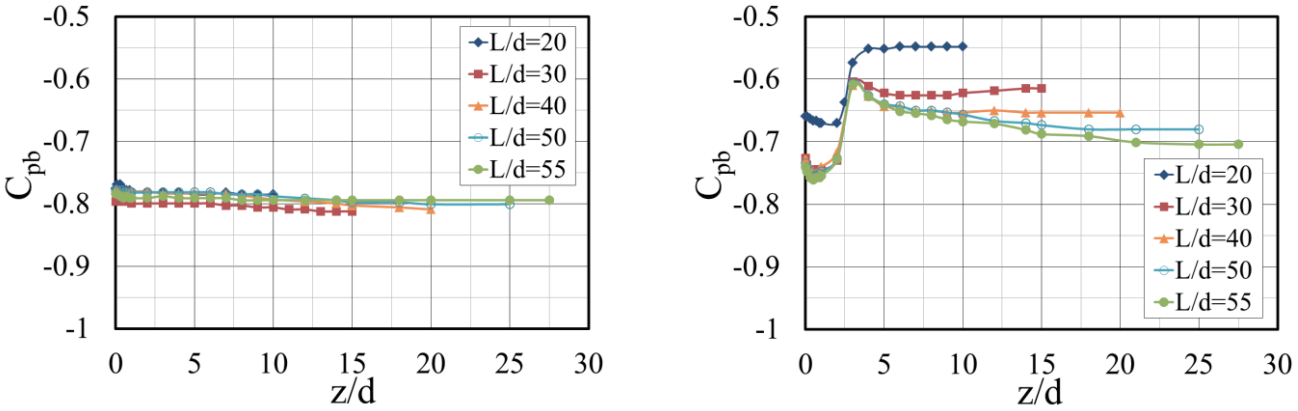


(a) δ/d=0.26 (b) δ/d=0.82

Fig. 2 Spanwise distribution of the base pressure

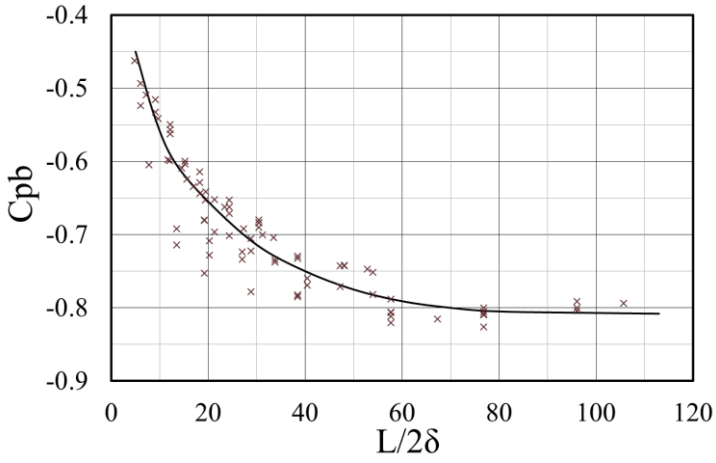


Fig. 3 Base pressure coefficient at the midspan of the cylinder

# A Study on Nanoscale Gas Transport in Porous Media

Yoshiaki Kawagoe[1], Tomoya Oshima[1], Sigeru Yonemura[2], Takashi Tokumasu[2]
[1] Graduate School of Engineering, Tohoku University
6-6-01, Aoba, Aramaki, Aoba-ku, Sendai, 980-8579, Japan
[2] Institute of Fluid Science, Tohoku University
2-1-1, Katahira, Aoba-ku, Sendai, 980-8577, Japan

**ABSTRACT**

Porous media are used in various engineering devices such as catalytic converters and fuel cells. It is important to understand transport phenomena in porous media for improvement of performance of such devices. In this study, we analyze nanoscale gas flows in porous media by performing DSMC simulations and propose the model to predict the velocity of gas flow in porous media.

## 1. Introduction

Gas flow in porous media can be seen in various engineering devices such as catalytic converters and fuel cells. In order to improve performance of such devices, it is important to understand transport phenomena in porous media. In porous media with pores as large as a mean free path of gas molecules, it is difficult to measure the structure and the flow inside them. Furthermore, the gas flow cannot be treated as a continuum and governed by the Boltzmann equation because the Knudsen number Kn is in the order of unity. Therefore, to simulate the flow, we use the direct simulation Monte Carlo (DSMC) method [1], which is the stochastic solution of the Boltzmann equation. We propose the model of the nanoscale gas transport in porous media theoretically and compare it with results of the DSMC simulations.

## 2. DSMC method

In this study, the porous media are created by arranging solid spherical particles which interpenetrate with each other randomly, as shown Fig. 1. Gas flows due to the pressure gradient in the $y$ direction. The lengths of the computational domain in the $x$, $y$, and $z$ directions are set at 3, 30, and 3 times as long as the diameter of solid particle, respectively.

The DSMC method is the stochastic solution of the Boltzmann equation. The computational domain is divided into cells of which length is smaller than the mean free path of gas molecules. The motion and collision of molecules are calculated separately. We calculate gas flow without surface reactions using hard sphere model. When a molecule collides with the surface of solid particles, it is reflected according to the diffusive reflection model. Intermolecular collisions in the same cell are calculated stochastically by using the maximum collision number method. The gas treated here is $H_2$. The gaseous temperatures at the inlet and the outlet are set at 293 K, and the temperature of solid surfaces is also set at 293 K. The gaseous pressure at the inlet is set at 101325 Pa, and the lower gaseous pressure is given at the outlet to generate the negative pressure gradient. The time step is set at smaller than mean free time of gas molecules. Boundaries in the $x$ and $z$ directions are periodic.

Corresponding author: Yoshiaki Kawagoe
*E-mail address*: kawagoe@chapman.ifs.tohoku.ac.jp

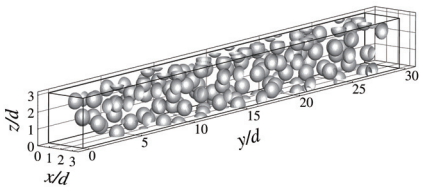


Fig. 1 The computational domain.

## 3 Knudsen diffusion in porous media

In the conventional researches, the flow channel in porous media is treated as a bundle of capillary tubes of uniform diameter. In the case of diameter smaller than the mean free path of gas molecules, the Knudsen number Kn becomes in the order of 10 or lager. In such high Knudsen number region, gas molecules collide with the pore walls much more frequently than with other molecules, and then they diffuse gradually. This phenomenon is called "Knudsen diffusion." The Knudsen diffusion coefficient $D^{\mathrm{K}}_{\mathrm{cylinder}}$ is given by

$$D^{\mathrm{K}}_{\mathrm{cylinder}} = \frac{2}{3} R\bar{v}\,, \tag{1}$$

where $R$ is the radius of capillary tubes, $\bar{v}$ is the mean molecular velocity and given by

$$\bar{v} = \sqrt{\frac{8kT}{\pi m}}\,, \tag{2}$$

where $k$ is Boltzmann constant, $T$ is the gas temperature and $m$ is the mass of gas molecules. The molecular number flux $J_{\mathrm{cylinder}}$ due to the Knudsen diffusion under the pressure gradient is given by

$$J_{\mathrm{cylinder}} = -D^{\mathrm{K}}_{\mathrm{cylinder}} \frac{1}{kT} \nabla p\,. \tag{3}$$

where $p$ is the gas pressure. The molecular mean velocity in porous media is given by

$$U_{\mathrm{cylinder}} = -D^{\mathrm{K}}_{\mathrm{cylinder}} \frac{1}{nkT} \nabla p\,, \tag{4}$$

where $n$ is the number density of gas. Whereas the flow in the cylindrical tube is governed by the Poiseuille flow in the low Knudsen number region, in the middle region the flow is governed by both the Knudsen diffusion and .

the Poiseuille flow.

It is difficult to determine the diameter of capillary tubes in Eq. (1). In the present work, we pay attention to the importance of molecule-wall collisions and use the mean free path for such collisions in place of the diameter of capillary tubes as follows:

$$D^{\mathrm{K}}_{\mathrm{cylinder}} = \frac{1}{3}\lambda_{\mathrm{wall}}\bar{v}\,. \tag{5}$$

Considering the tortuosity due to the structure of porous media, let us correct the Knudsen diffusivity as follows:

$$D^{\mathrm{K}}_{\mathrm{porous}} = \varepsilon^{\alpha} D^{\mathrm{K}}_{\mathrm{cylinder}}\,, \tag{6}$$

where $\varepsilon$ is the porosity of porous media. The mean molecular velocity in the porous media is given by

$$U_{\mathrm{porous}} = -\frac{1}{3}\lambda_{\mathrm{wall}}\bar{v}\varepsilon^{\alpha}\frac{1}{nkT}\nabla p\,. \tag{7}$$

## 4. Results and Discussion

Let us compare the mean molecular velocity obtained in the models with that obtained in the DSMC simulation. In Eq. (7), we used $\lambda_{\mathrm{wall}}$ calculated from the collision frequency between molecules and pore walls in the DSMC simulations. Figures 2 and 3 show mean molecular velocities obtained by three empirical models [2-4] derived from the continuum theory, that obtained by the present model for $\alpha$=4/3 in Eq. (7), and that obtained DSMC simulations. The calculated condition is that the porosity $\varepsilon$ is 0.6, the pressure gradient $dp/dy$ is 0.3378 Pa and diameter of solid particles $d_{\mathrm{p}}$ is 10, 50, 100, 500, 1000 μm. The pressure at inlet $p_{\mathrm{in}}$ are 1 and 4 atm in the Figs. 2 and 3, respectively.

In Fig. 2, the results of Eq. (7) coincide with the results of DSMC simulations. In the case of other empirical models, however, the results for the smaller $d_{\mathrm{p}}$ were deviated from the results of DSMC simulations more largely. This is because in the case of smaller $d_{\mathrm{p}}$, Knudsen number becomes large and the continuum approximation becomes invalid. Therefore, in such Knudsen number regions, the empirical models are not adequate.

In Fig. 3, the results of Eq. (7) also coincide with the DSMC results in the case of small $d_{\mathrm{p}}$. However, when $d_{\mathrm{p}}$ becomes larger to $d_{\mathrm{p}}$=500 and 1000 nm, it deviates from the DSMC result. This is because that in the case of $d_{\mathrm{p}}$=500 and 1000 nm, Knudsen number becomes low and the effect of the continuum flow becomes large. On the other hand, in the case of $d_{\mathrm{p}}$=1000 nm, the results of the empirical models coincide with the DSMC result. Since the Knudsen number is proportional to the pressure, the Knudsen numbers in Fig. 3 are four times as large as those for the corresponding cases in Fig. 2. Therefore, in Fig. 3 the DSMC results agree with the results obtained from the empirical model in the case of large spherical particles.

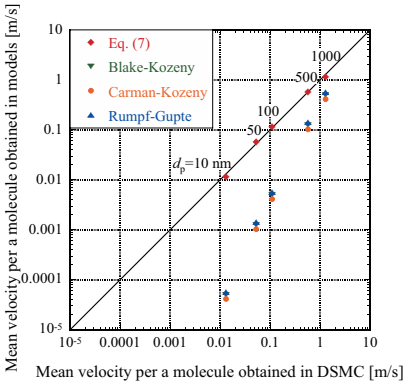


Fig. 2 Comparison between the mean velocity per a Molecule obtained in DSMC simulations and that for the models ($\varepsilon$=0.6, $dp/dy$=-0.3378 Pa/nm, $p_{\mathrm{in}}$=1 atm, $\alpha$ = 4/3).

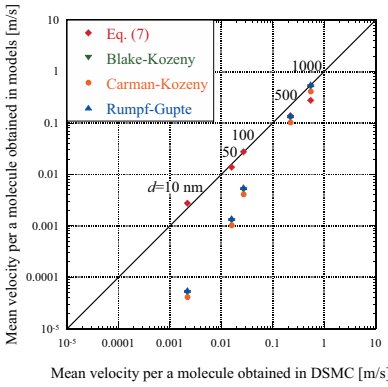


Fig. 3 Comparison between the mean velocity per a Molecule obtained in DSMC simulations and that for the models ($\varepsilon$=0.6, $dp/dy$=-0.3378 Pa/nm, $p_{\mathrm{in}}$=4 atm, $\alpha$ = 4/3).

## 5. Conclusion and remarks

We proposed the model to estimate the mean molecular velocity in porous media. By comparing results obtained from the present model and DSMC simulations, it is found that the present model is valid in high Knudsen number region, while the contribution due to continuum flow should be considered in low Knudsen number region.

## References


[1] G.A. Bird, *Molecular Gas Dynamics and the Direct Simulation of Gas Flows*, (1994), Clarendon, Oxford.

[2] R.B. Bird et al., *Transport Phenomena 2nd ed.*, (2002), Wiley.

[3] B. Jacob, *Dynamics of Fluids in Porous Media*, (1972), American Elsevier.

[4] F.A.L. Dullien, *Porous Media Fluid Transport and Pore Structure*, (1979), Academic press.

Eleventh International Conference on Flow Dynamics
October 8-10, 2014, Sendai, Miyagi, Japan

# Effects of Liquid Properties on Airblast Atomization in a High Pressure Environment

Soichiro Suzuki[1], Kodai Kato[1], Taku Kudo[1], Soichiro Kato[2], Mitsunori Ito[2], Masahiro Uchida[2]
Akihiro Hayakawa[1], Hideaki Kobayashi[1]
[1]Institute of Fluid Science, Tohoku University, 2-1-1 Katahira, Aoba-ku, Sendai,
Miyagi 980-8577, Japan
[2]IHI Corporation, 1 Shin-nakahara-cho, Isogo-ku, Yokohama,
Kanagawa 235-8501, Japan

**ABSTRACT**

The purpose of this study is to clarify the effects of liquid properties on airblast atomization in a high pressure environment. In order to investigate the breakup of liquid sheet carefully in primary atomization region, a two-dimensional atomizer was introduced. The images of the liquid sheet were taken by a high-speed camera. Furthermore, particle diameter of the droplets in secondary atomization region were measured by PDPA. The results showed that the liquid properties affected the particle diameter and the length of liquid ligament.

## 1. Introduction

The environmental issues, such as a drain on resources and the increase in green gas emissions, have been deteriorating. In addition, the demand of air transportation is increasing rapidly worldwide. Thus, further efforts for the reduction of fuel consumption is required. In order to achieve them, improvement of combustion in a gas turbine combustor for aircraft is necessary. A spray combustion is adopted for the most of gas turbine combustor of an aircraft. Therefore, the atomization characteristics of fuel affects combustion performance and hence a fuel injector having excellent atomization performance is required to achieve higher efficiency of gas turbine combustor.

Airblast atomizer has been widely used as the fuel injector for gas turbines of aircraft. This atomizer has several advantages including high degree of homogeneity, relatively little change in performance over the wide operation range and rapid mixing of fuel and air [1]. However, the atomization mechanism of airblast atomizer in a high pressure environment is insufficiently understood. In addition, it is known that liquid properties effect the mechanism of atomization [2]. The objective of this study is to clarify the mechanism of atomization in high pressure environment by experiments using a two-dimensional atomizer, Phase Doppler Particle Analyzer(PDPA), and back light high-speed images. The effects on atomization mechanism were also investigated using five types test liquids which have different liquid properties for airblast atomization.

## 2. Method

The two-dimensional atomizer was used to observe the liquid sheet breakup process. Figure 1 shows a schematics of two-dimensional atomizer which simulates the spray port of the airblast atomizer two-dimensionally. Liquid sheet was ejected between two co-flowing airstreams at the nozzle edge and broken into droplets.

The PDPA was applied to measure the particle diameter of droplets. In addition, high-speed back light imaging was used to observe the behavior of the liquid sheet breakup. Frame rate was set to 75000 fps.

Five kinds of liquids having different liquid properties were used as the test liquids to evaluate the effects of liquid properties on airblast atomization. The liquid viscosity, μ, and surface tension, σ, were shown in Table 1. Air flow velocity, $U_A$, was set to 70 m/s. The ambient pressure in the chamber, $P_C$, was set to 0.1, 0.3, 0.5, and 0.7 MPa.

Table 1. Liquid properties of the test liquids

| | water | simulation liq. A | simulation liq. B | simulation liq. C | simulation liq. D |
|---|---|---|---|---|---|
| μ [mPa・s] | 1.002 | 2.450 | 4.4 | 10.5 | 1.002 |
| σ [N/m] | 0.07274 | 0.0292 | 0.0292 | 0.0292 | 0.0292 |

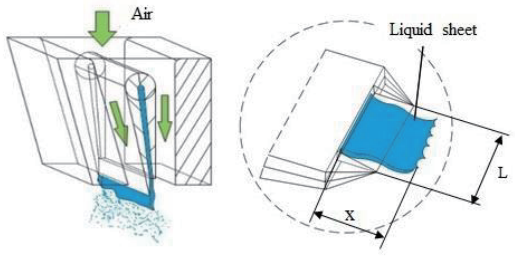


Fig. 1 Schematics of two-dimensional atomizer

## 3. Results and Discussion

### 3. 1 Effects of liquid viscosity on liquid sheet breakup

The high-speed back light images were shown in Figs. 2 and 3. The mass flow rate, $Q_L$, was set to 76 ml/min. The length of liquid ligament and the path widths of the atomizer were defined as x and L, respectively. The variations of x/L with ambient pressure were shown in Fig. 4. The values of x/L decreased with the increase in ambient pressure for all test liquids. As the viscosity of test liquids increased, the longer the liquid ligament were observed. As ambient pressure increased, air density and air flow momentum increased. It causes the increase in an impulse to the liquid sheet. As a result, the decrease in the length of liquid ligament with the increase in ambient pressure.

Corresponding author: Soichiro Suzuki
*E-mail address*: s.suzuki@flame.ifs.tohoku.ac.jp

The length of ligament of water which has the lowest viscosity at $P_C$ = 0.7 MPa was 70 % smaller than that at $P_C$ = 0.1 MPa. On the other hand, the length of ligament of simulation liq. B at $P_C$ = 0.7 MPa was 34 % smaller than that at $P_C$ = 0.1 MPa. The increase in liquid viscosity decreases in velocity gradient between air flow and the ligament. Therefore, it causes that the shear force acting on liquid ligament becomes weaker, and thus the ligament becomes hard to be broken.

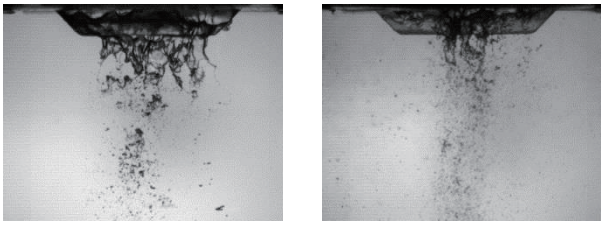

(a) Pc = 0.1 MPa (b) Pc = 0.7 MPa

Fig. 2 High-speed back light images (water, $Q_L$ = 76 ml/min)

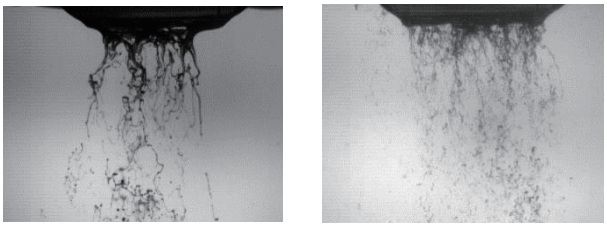

(a) Pc = 0.1 MPa (b) Pc = 0.7 MPa

Fig. 3 High-speed back light images (simulation liq. A, $Q_L$ = 76 ml/min)

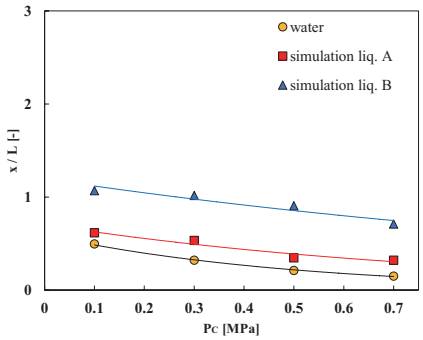


Fig. 4 Pressure dependence of the length of the ligament ($U_A$ = 70 m/s, $Q_L$ = 76 ml/min)

3.2 Effects of liquid properties on particle diameters

Figures 5 and 6 showed the variation of arithmetic diameter, $D_{mean}$, and Sauter Mean Diameter, SMD, with ambient pressure. Air / liquid mass flow ratio (ALR) was set to 40. As shown in Fig. 5, the value of $D_{mean}$ became larger with the increase in the ambient pressure for all the test liquids. It was considered that the spread of liquid in vertical direction to liquid sheet is suppressed by the increase in ambient pressure. The value of $D_{mean}$ for all test liquids are almost the same quantitatively.

As shown in Fig. 6, SMD is not strongly affected by the difference of liquid surface tension. However, the difference of liquid viscosity has an influence on SMD. As shown in Fig. 6, although the value of $D_{mean}$ did not depend on the liquid properties, higher viscosity significantly caused the large value of SMD. These results corresponded that small number of droplets which have large particle size appeared at the case of high viscosity liquid. This is because the velocity gradient in the liquid flow boundary layer decreased with the increase in liquid viscosity and the shear force acting on liquid ligament became weaker.

As shown in Fig. 6, the value of SMD of the lowest viscosity liquids (water and liq. D) becomes larger with the increase in ambient pressure. On the other hand, the value SMD of the largest viscosity liquid (liq. C) decreases with the increase in ambient pressure. This result indicates that the change in the atomization behavior with the increase in liquid viscosity affects the value of SMD.

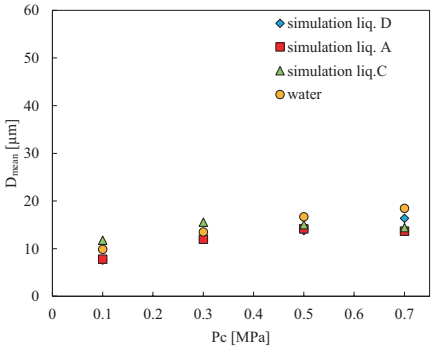


Fig. 5 Pressure dependence of $D_{mean}$ ($U_A$ = 70 m/s, ALR = 40)

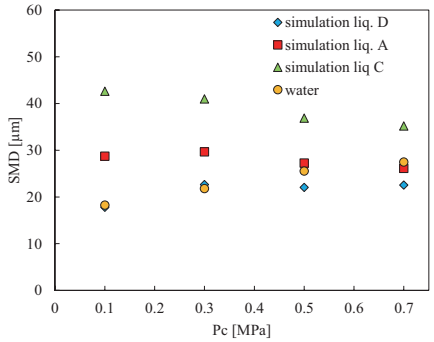


Fig. 6 Pressure dependence of SMD ($U_A$ = 70 m/s, ALR = 40)

## 4. Concluding Remarks

1. As the liquid viscosity increased, the velocity gradient in the liquid flow boundary layer decreased. It caused that the shear force acting on liquid ligament became weaker, and thus the liquid ligament became hard to be broken.
2. Relatively small number of droplets which had large particle size appeared, and also the atomization behavior was changed as liquid viscosity increased.

## References

[1]U. Bhayaraju, C. Hassa, *Atomization and Sprays*, 19 (2009), 1147-1169.

[2]V. Dorfner, J. Domnic, F. Durst, R. Kohler, *Atomization and Sprays*, 267 (1995), 261-285.

# A Study on a Floating Drop on a Liquid Surface

Shota Suzuki[1], Tomoya Oda[1], Shigeru Yonemura[2]
[1] Graduate School of Engineering, Tohoku University
6-6-01 Aoba, Aramaki, Aoba-ku, Sendai, 980-8579, Japan
[2] Institute of Fluid Science, Tohoku University
2-1-1 Katahira, Aoba-ku, Sendai, 980-8577, Japan

**ABSTRACT**

It is sometimes seen that a liquid drop is floating on a pool surface of the same liquid without coalescing. Considered physically, it is a surprising phenomenon..The objective of this study is to investigate the mechanism of the drop floating phenomenon by performing numerical simulations of collisions between a drop and a bath surface solving the drop motion and the gas film flow simultaneously.

## 1. Introduction

A phenomenon that a water drop dripping on a water pool does not coalesce with the surface and floats on the pool was pointed out by Reynolds [1]. This phenomenon is shown in Fig. 1. If the drop and the pool consist of the same liquid, it is predicted that they immediately coalesce with each other by surface tension. Non-coalescence is a surprising phenomenon physically and intuitively.

Walker [2] performed an experiment in which a liquid drop was dripped on a liquid surface having the standing wave. In this experiment, the drop was floating on the surface for a few minutes. Nahmias [3] performed an experiment in which droplests were slightly put in contact with a rotating liquid surface of the same liquid. The droplets go into the vortex and coalesce, but the resulting drop stayed in equilibrium in this position. Dell'Aversana et al. [4] investigated the effect of the temperature difference between a drop and a pool in his experiment.. It was observed that the drop was floating on the pool stably for long time. Furthermore, Savino et al. [5] performed numerical simulations and concluded that the reason of non-coalescence is because the temperature difference induces a thermo-capillary convection on liquid surfaces and generate high gas pressure between both surfaces. However, in our experience, the temperature deference is not a necessary condition of this phenomenon because the non-coalescence shown in Fig. 1 is realized in the case of no temperature difference between both surfaces. In the present study, we investigate the mechanism of this phenomenon by simulating the motion of a drop and a gas flow between the drop and a vibrating pool surface.

The clearance between the drop and the pool surface may be close to the mean free path of anbient molecules just before the drop coalesces with the pool. Therefore, the flow in the gas film is calculated by using molecular gas film lubrication (MGL) equation [6] derived from the Boltzmann equation.

Corresponding author: Shota Suzuki
*E-mail address*: suzuki@chapman.ifs.tohoku.ac.jp

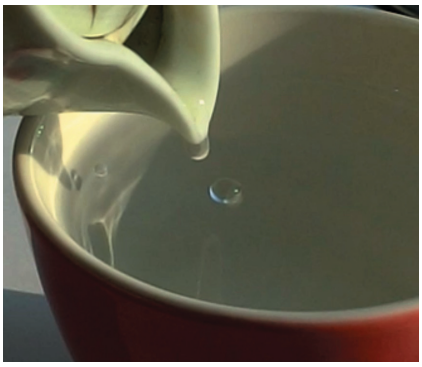

Fig. 1 Non-coalescence of a water drop and a water pool.

## 2. Method

The model of a drop and a liquid pool is shown in Fig. 2. The upper circular plate imitates the drop. The pool surface is imitated by an infinitely wide plate. Let us call the position of the pool surface $z_p$ in the laboratory coordinate system, $O-XYZ$. We consider the coordinate system $(r,z)$ with their origin on the vibrating pool surface $Z=z_p$ ..For simplicity, The liquid velocities on both surfaces are considered as zero. Let us assume that the flow is axisymmetric with respect to the $z$-axis, where the $z$-axis penetrates the center of the drop and the gravity is oriented in the $-z$ direction. $h$ is the clearance between the drop and the pool surface, and $h$ is assumed to be constant with respect to $r$ although it changes temporally depending on the drop motion. The gas pressure at the edge of the upper plate i.e., the drop, is equals to the ambient pressure $p_a$. The drop moves in the vertical direction due to the gravity and the pressure difference between the gas film and the atmosphere. The gas film will be compressed and expanded due to the movement of the drop. The gas flow at the edge of the drop varies from inflow to outflow depending on the pressure of the gas film.

In this study, the floating phenomenon of the drop is analyzed by tracing the pressure of the gas film and the movement of the drop. The equation of motion of the drop is given by

$$m\frac{d^2h}{dt^2} = F_p - mg + F_{\mathrm{I}}, \tag{1}$$

where $t$ is time, $m$ is mass of the drop. $g$ is the gravity, $F_{\mathrm{I}}$ is the inertia force on the drop due to the acceleration of the origin, $F_p$ is the force due to the pressure difference between the gas film and the ambient air. Note that the clearance $h$ represents the position of the upper plate, i.e., the lower surface of the drop, relative to the pool surface. The inertia force $F_{\mathrm{I}}$ is given by

$$F_{\mathrm{I}} = -m\alpha_{\mathrm{P}}, \tag{2}$$

where $\alpha_{\mathrm{P}}$ is the acceleration of pool surface vibration in the laboratory coordinate system, $\mathrm{O}-XYZ$. The positive directions for $F_p$ and $F_{\mathrm{I}}$ are the $z$ direction, and that for $\alpha_{\mathrm{P}}$ is the $Z$ direction. The force $F_p$ is given by

$$F_p = 2\pi\int_0^R r(p-p_a)dr, \tag{3}$$

where $R$ is the radius of the upper plate. The MGL equation in the axisymmetric coordinate system is

$$12\mu\frac{\partial(ph)}{\partial t} + 6\mu\frac{1}{r}\frac{\partial}{\partial}(rphU) - \frac{1}{r}\frac{\partial}{\partial r}\left(rph^3Q\frac{dp}{dr}\right) = 0, \tag{4}$$

where $\mu$ is the viscosity of the gas, $U$ is the velocity of the liquid surface and $Q$ is the dimensionless flow rate coefficient for the Poiseuille flow depending on the inverse Knudsen number $D(=\sqrt{\pi}/(2\mathrm{Kn}))$. In this study, the velocity of the liquid surface $U$ is assumed to be 0. The MGL equation is solved by the finite difference method. The drop motion is traced by the velocity Verlet algorithm.

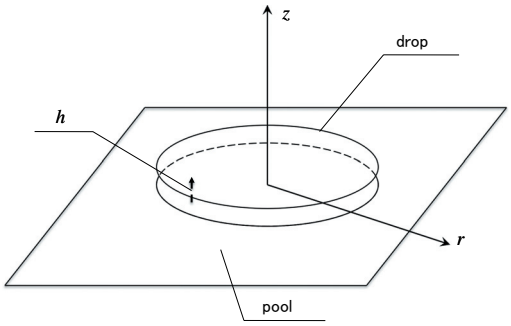


Fig. 2 The model of a drop and a liquid pool.

## 3. Results and Discussion

We simulate the motion of the drop when it drops onto the vibrating liquid surface from the constant height. The radius of the drop is $r_{\mathrm{D}} = 1$ mm. The amplitude of the liquid surface vibration is $A = 1$ mm. The frequency of vibration of the pool surface is $\omega/2\pi = 100$ Hz. The initial height of the drop is $h_0 = 10$ mm. The pool surface position is given by

$$z_p = A\sin\left(\omega t + \frac{\pi}{5}i\right), \qquad i = 0,1,2,\cdots,9 \tag{5}$$

in the $\mathrm{O}-XYZ$ coordinate system.

Figures 3(a) and (b) show the temporal change of the position of the drop and the pool surface, and the clearance $h$. When $h$ becomes shorter than 10μm, the drop suddenly decelerates and the velocity of the drop becomes nearly equal to that of the pool surface. Let us call this a "collision". Paying attention to temporal change of $h$ in the case of Fig. 3(a), both surfaces gradually approach and soon will contact each other. In the case of Fig. 3(b), it is found that the colliding velocity of the drop gradually decreases and the minimum distance increases. Therefore, the drop can keep on floating on the vibrating pool surface stably.

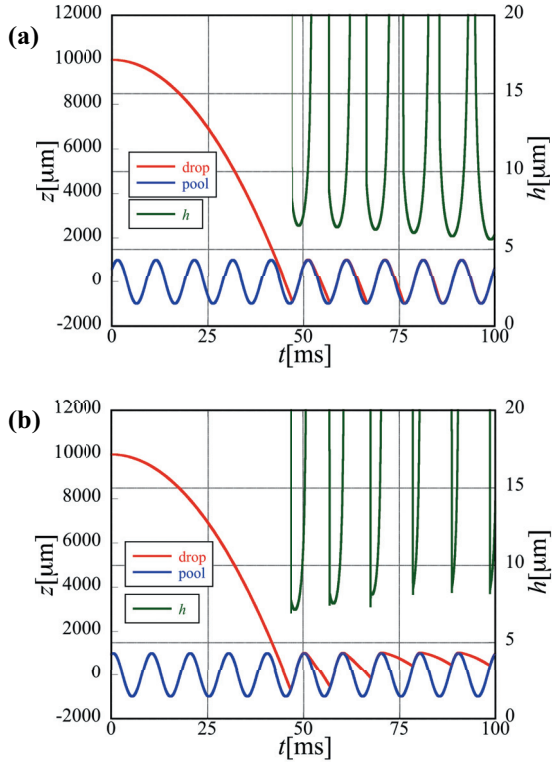


Fig.3 Temporal change of the positions of the drop and the pool surface, and the clearance $h$ between them for the cases (a) $i = 1$ and (b) $i = 2$ in Eq. (5).

## 4. Summary

We reproduced coalescence and non-coalescence in numerical simulations. Let us discuss the difference between both phenomena at ICFD 2014.,

## References


[1] O. Reynolds, *Chem. News*, 44 (1881), 211－212.
[2] J. Walker, *Scientific American*, 238, (1978), 123-129.
[3] J. Nahmis, *J. Colloid Interface Sci.*, 190 (1997), 497-498.
[4] P. Dell 'Aversana, J. R. Banavar, J. Koplik, *Phys. Fluids*, 8 (1996), 15－28.
[5] R. Savino, D. Paterna, and M. Lappa, *J. Fluid Mech.*, 479 (2003), 307－326.
[6] S. Fukui and R. Kaneko, *ASME J. Tribol.* 110 (1988), 253–261.

Eleventh International Conference on Flow Dynamics
October 8-10, 2014, Sendai, Miyagi, Japan

# Study on spray characteristics of high temperature and high pressure water jet flow

Narumi hiramoto[1], Hiroki ishii[1], Rikio Watanabe[1]
[1]Tokyo City University
Department of Mechanical Systems Engineering
1-28-1 Tamazutumi, Setagaya, Tokyo, 158-8557, Japan

**ABSTRACT**

Experimental studies on spray characteristics of atomized water jet under high temperature and pressure are conducted by a simple visualization utilizing a video camera. This is intended for clarifying a propellant mixing observed in a Water/liquid nitrogen rocket which was developed in our lab. We observed spray jet patterns using an atomizing spray nozzle and a single-hole nozzle for overheated water. It is found that the spray patterns are classified in five patterns according to their temperature and pressure setting and it is strongly affected by bubble generation inside a tube.

## 1. Introduction

Water/liquid nitrogen rocket engine (WNE engine) is a non-combustion rocket engine that uses cryogenic liquid nitrogen and heated water [1]. Because it does not have combustion process, risk of explosive combustion is lower compared to conventional combustion type rocket engines. In this engine, generating higher pressure in a mixing chamber is crucial for better rocket performance. The pressure generation is enhanced when the heat exchange from heated water to liquid nitrogen is completely attained. Thus, we used a pair of spray nozzle injectors to prompt the heat exchange by reducing spray particle size [2]. As a result, we attained 95 [%] efficiency in characteristic exhaust velocity ($C^*$). However, modeling and controlling the pressure generation process is difficult because there are many issues to be considered [3]. Typical parameters which would affect the pressure generation process are (1) injector type (spray pattern and velocity distribution, spray particle diameter and distribution), (2) supply pressure of propellants, (3) supply temperature of water, (4) injector layout (distance, collision angel) etc [4]. Also, we need to understand the spray jet property itself without propellant collision. In this paper, we are aiming at claying the characteristics of heated water jet flow with and without using a spray nozzle. Parameters tested are temperature and pressure of water and a tube diameter.

## 2. Experimental method and conditions

### 2.1 Propellant injection

In the WNE engine, a pair of spray nozzles are used for injection of water and liquid nitrogen in order to enhance the heat exchange between propellants by reducing the jet particle diameter. However, the dispersed jet flow generated by a spray nozzle has complicated nature especially when water is injected under overheated condition which our engine uses. A spray nozzle is characterized by how flow inside the nozzle is atomized. Typical parameters are the particle diameter and the velocity distribution and the injection pressure. We also tested the case of simple nozzle flow without using spray nozzle for comparison and understanding the effect of parameters on spray characteristic because of simplification. We used two types of spray nozzles whose specification is shown in Table 1. They are from H.Ikeuchi & Co.,LTD.

Table 1 Spray nozzles specification [5].

| | Screw size | Sauter mean diameter $d_{32}$[μm] |
|---|---|---|
| 1 | 1/8M | 380 |
| 2 | 1/2M | 850 |

Table 2 shows experimental condition. The temperature of the water was changed from 373~433 [K]. This temperature is the temperature used during operation of the WNE engine. The injection pressure is also varied from 0.3 to 1.0 [MPa] where they correspond to the pressure difference between the propellant injection pressure and mixing chamber pressure in the engine during operation.

Table 2 Experimental condition.

| The diameter changed by single-hole nozzle[mm] | | | |
|---|---|---|---|
| 4.8 | 7.1 | 9.7 | 10.4 |
| Water temperature [K] | | Injection pressure [MPa] | |
| 373～433 | | 0.3～1.0 | |

### 2.2 Experimental setup

Figure 1 illustrates schematic of experimental apparatus. Water is heated in the tank by a band heater and supplied by nitrogen gas.

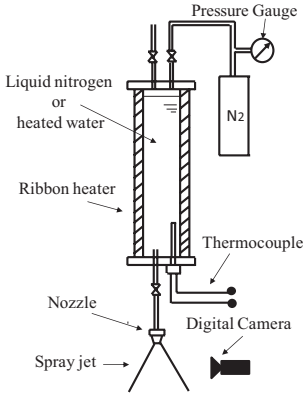


Fig. 1 Schematic of experimental apparatus.

Corresponding author: Narumi Hiramoto
*E-mail address*: g1381225@tcu.ac.jp

## 3. Results and Discussion

Figure 2 shows the results of simple jet injection with a diameter of 9.7 [mm] under the supply pressure of 1.0 [MPa].

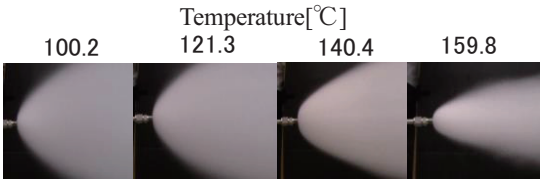


Fig. 2 Effect of injection temperature on water spray jet.

The spray patterns are identical when the water temperature is below 140.4 [°C], but in the case of 159.8 [°C] injection, the spray width becomes narrower compared to the previous ones. In the case of higher temperature cases, the liquid bubble diameter increases inside the tube and the void fraction becomes high [6]. The bubbles retards the jet flow spreading and thus the jet width becomes narrower and the spray angle becomes lower.

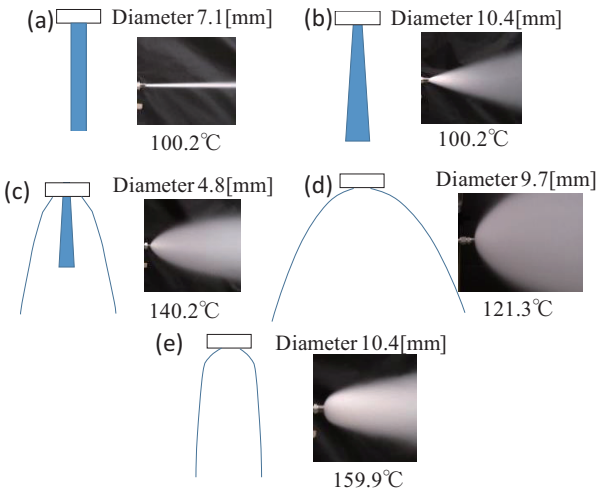


Fig. 3 The spray pattern of high-temperature water.

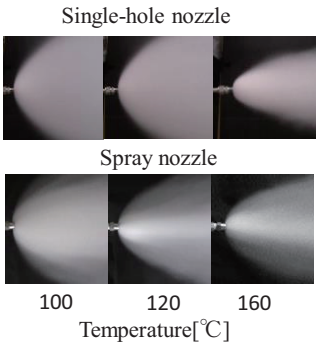


Fig. 4 Spray patterns of simple pipe and spray nozzle.

Spray patterns obtained in the present experiments are categorized in five patterns as shown in Figure 3. The spray angle becomes larger as the diameter increases by comparing (a) and (b). In the case of large diameter tube, the bubble generation is enhanced because the liquid in the tube makes much contact with the tube wall [6]. The pressure inside the bubbles is released when water injected and thus the injection angle is expanded. Another consideration for different spray angles between (a) and (b) is that heat loss happens by entrainment phenomenon, and is relatively small for rapid boiling flow rate [7]. As a result, high temperature steam is produced and expands which is observed in Fig. 3(b) as a mist corner grow. In Fig. 3(c), a jet core which consists of atomized water particle is observed. The jet angle is also expanded in Fig. 3(d) because it has a larger diameter, but it has enough temperature that forms a bell shaped jet flow. The jet angle is much larger compared to Fig. 3(c) because of the high temperature effect as seen in the case of 140.2 [°C] of Fig. 2. In Fig. 3(e), the diameter is larger and the temperature is higher compared to other cases. Then, no jet core is observed and high intensity of spray injection is observed. This is because much part of the flow contains atomized water particle which has enough momentum to show straight like spray injection.

The comparison of spray pattern between the simple nozzle injection and the spray nozzle injection is given in Fig. 4. It seems there is no significant difference of injection patterns between them except for the case of 160 [°C] injection where the jet flow is much dispersed and spreaded.

## 4. Conclusion

We conducted experimental investigations on spray patterns of heated and pressurized water jet flow from a simple injector and a spray nozzle injector. We found that the spray mode changes according to the reduced pressure boiling phenomena and thus bubble generation inside a tube. The effect of temperature is not obvious below 160 [°C] injection. The spray mode is categorized in five patterns according to the change of the diameter and temperature. In both the single-hole nozzle and spray nozzle, the spray angle is reduced as the water temperature increases considering that heat loss due to entrainment. The spray patterns of single injection are almost the same as the case of spray nozzle injection.

## References

[1] R.Nagashima, Proceedings of the Science and technology Conference (in Japanese), No.2B14 (2002-10), pp. 604-609.

[2] R. Watanabe, Journal of Space Engineering, Vol.3, No.1 (2010).

[3] H. Suzuki, STCP-20120-071(2010).

[4] The Japan Society of Mechanical Engineers, Handbook of Gas-Liquid Two-phase flow technology, CORONA PUBLISHING (2006), pp.483-491.

[5] H.Ikeuchi & Co.,LTD, Catalog on Hydraulic Spray Nozzles(2013), pp.15-18.

[6] K. Sato, Transaction of JSME,Vol.50,No.455(1984).

[7] ILASS-Japan, Atomization Technology, MORIKITA PUBLISHING (2001), p.145.

Eleventh International Conference on Flow Dynamics
October 8-10, 2014, Sendai, Miyagi, Japan

# Effects of a cold plasma flow on HeLa cells viability

Kazuki Okazaki[1], Takehiko Sato[2], Daisuke Yoshino[2]
[1]Graduate School of Engineering, Tohoku University
6-6-01 Aramaki-Aoba, Aoba, Sendai, 980-8579, Japan
[2]Institute of Fluid Science, Tohoku University
2-1-1 Katahira, Aoba, Sendai, 980-8577, Japan

**ABSTRACT**

Cold plasma has been remarked for medical applications because it could inactivate cancer cells and bacteria. Inactivating methods require lower cost and harmless to living body. In this study, we developed a device of a low temperature plasma flow without gas feeding, and its characteristics ware investigated. Inactivated regions of HeLa cells were localized by exposure to the plasma flow. The localization may be caused by the effect of chemical species transported by the plasma flow.

## 1. Introduction

The plasma discharge can easily generate heat, electric field, radiation of UV and reactive chemical species, thus plasma has been remarked for medical applications. It has been reported that the plasma can inactivate cancer cell and bacterium effectively [1-3]. For many practical applications it is important that the inactivation effect is harmless to living body. In practical application, a surface micro discharge (SMD) and a plasma jet are often used because they generate low-temperature plasma, resulting in less thermal damages. However, non-direct plasma for SMD and the cost for the plasma jet are disadvantage. Therefore, the direct plasma generation method and lower cost are important.

In this study, we aimed at developing a low temperature plasma jet and investigating plasma characteristics. In addition, an effect of exposure to the plasma jet on HeLa cells viability was investigated.

## 2. Development of a cold plasma flow

Schematic of an electrode configuration is shown in Fig. 1 (a), consisted of a needle electrode and a cylindrical grounded electrode. The needle electrode of 0.5 mm in diameter was made of platinum. The cylindrical aluminum electrode was surrounded a glass tube where outer and inner diameters are 5.2 and 3.6 mm, respectively.

Schematic of the experimental setup is shown in Fig. 1 (b). The square voltage of +7.5 $kV_{0p}$ was applied to the needle electrode with a frequency of 5.0 kHz and duty ratio of 50%. The discharge voltage and current were measured by using an oscilloscope. The concentration of $O_3$, $H_2O_2$, $HNO_2$ and $HNO_3$ in water were examined by using a DIGITAL PACKTEST (Kyoritsu Chemical-Check Lab., Corp) for the pure water of 1.5 mL exposure to the plasma flow. A flow field generated by the discharge was visualized by the Schlieren method. This method can be used to visualize a density variation in the flow of the fluid. The thermocouple was used for the temperature measurement.

Corresponding author: Kazuki Okazaki
*E-mail address*: okazaki@plasma.ifs.tohoku.ac.jp

The electrical power consumption calculated by Lissajous figure was 1.6 W. The concentration of each chemical species generated by the discharge is increased in proportion to the discharge time. Therefore, there is a possibility of controlling the production of chemical species by the discharge time. The flow field generated by discharge is shown in Fig. 2. It is shown that the discharge can generate an air flow without using a gas supply apparatus. The temperature rise at the point located 5 mm below the electrode tip was about 5 $^{o}$C, thus it is considered as the influence on living cells is small.

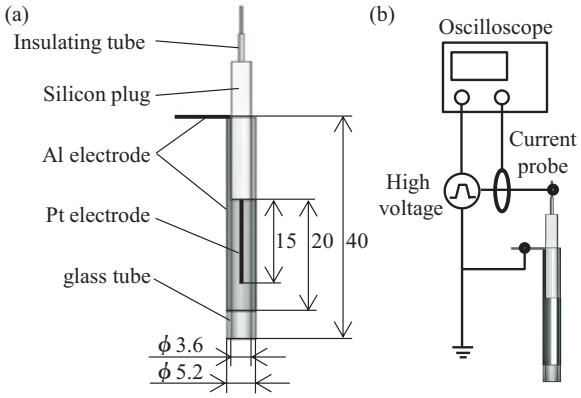


Fig. 1 Schematic of (a) the electrode configuration and (b) the experimental set up.

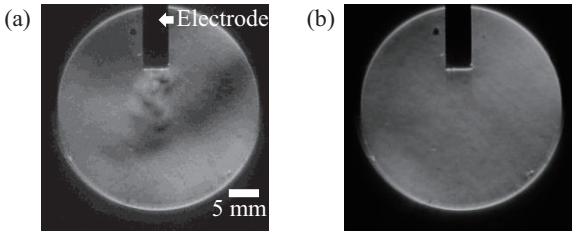


Fig. 2 Schlieren images of (a) the plasma discharge and (b) the control (without plasma discharge).

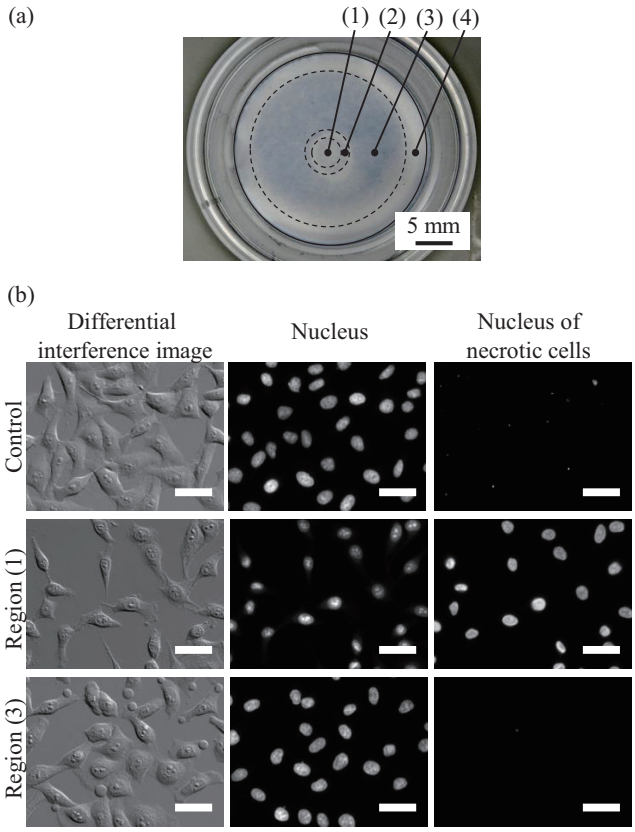


Fig. 3 (a) Distribution of the inactivated/survival HeLa cells 24 hours after exposure to the plasma flow. (b) Representative cell images of the regions (1) and (3), and control (without exposure to plasma flow), bar = 50 μm.

## 3. HeLa cells exposed to plasma flow

### 3.1 Methods

The HeLa cells (obtained from Tohoku Univ.) were used in this study. The culture medium to cultivate cells was the DMEM (Gibco) contained the 10% fetal bovine serum (Gibco) and 0.1 % penicillin-streptomycin (Gibco). The cells were disseminated onto ϕ35 glass base dishes (IWAKI), then the dishes were incubated at 37 $^{o}$C with 5 % $CO_2$ up to a confluent state. The discharge target was the cells removed the medium and gap length between electrode and cells was 5 mm. The time of plasma treatment was 2 minutes. After treatment, the dishes are washed by the DMEM twice in order to remove chemical species which stay behind, dropped the DMEM of 2 mL and incubated. The nucleus of the all cells and the necrotic cells is stained by Hoechst 33342 (PromoKine) and Ethidium Homodimer III (PromoKine) respectively 24 hours after exposure. After staining, the cells are fixed by 4 % paraformaldehyde phosphate buffer solution (Wako Pure Chemical Industries, Ltd.) and observed by using a fluorescence microscope (Carl Zeiss).

### 3.2 Results

Distribution of inactivated/survival HeLa cells 24 hours after exposure to the plasma flow is shown in Fig. 3 (a). The cells are stained by a trypan blue (Life technologies) in order to make the position of cells easy to see. The cell images of the region (1) and the region (3) are shown in Fig. 3 (b): differential interference image and fluorescence images. Therefore, the four regions were observed after exposure: region (1) where the cells were dead sticking to the dish, region (2) where the cells were concentrically removed, region (3) where the cells were not influenced by exposure and region (4) where the cells were concentrically removed.

### 3.3 Discussion

In the case of region (1) in Fig. 3, the cells were damaged because the cells were located just below the tube. It could be caused by an etching of chemical species which react to the cell membrane although the surface of cells should be wet.

In the case of region (2) in Fig. 3, the cells were removed. It could be caused by chemical species generated by the discharge. In this study, reactive oxygen species, such as $O_3$, $H_2O_2$, $HNO_2$ and $HNO_3$, were generated in water and these species especially, $H_2O_2$, are known as a harmful factor for HeLa cells [3]. Therefore, it seems that the cells were damaged because of generation of reactive oxygen species in the medium which cover the cell.

In the case of region (3) in Fig. 3, the cells were not influenced by the discharge. It could be because the air flow generated by the discharge prevented chemical species from staying the region. Therefore the cells located in region (3) were not damaged.

In the case of region (4) in Fig. 3, the cells were removed because the cells were located near the step of the dish. It could be caused by chemical species generated by the discharge. Chemical species were transported to bottom of dish by air flow, finally the flow run into a wall of dish. It seems that the concentration of chemical species in medium is increased there, therefore the cells was damaged and removed.

## 4. Conclusions

For practical application, we developed a device of the cold plasma flow without gas feeding. When HeLa cells were exposed to the plasma flow, the regional inactivation of cell viability was observed because the flow induced by the plasma affected to the transport of chemical species.

## References

[1] T. Sato, O. Furuya, K. Ikeda and T. Nakatani, *Plasma Process. Polym.*, 5 (2008) 606 - 614.
[2] V. Scholtz, J. Julák and V. Kříha, *Plasma Process. Polym.*, 7 (2010) 237 - 243.
[3] T. Sato, M. Yokoyama and K. Johkura, *J. Phys. D: Appl. Phys.*, 44 (2011) 372001.

Eleventh International Conference on Flow Dynamics
October 8-10, 2014, Sendai, Miyagi, Japan

# Sonic Boom Analysis of Low-Wave-Drag Concept SST Model

Naohiko Ban[1], Wataru Yamazaki[1], Kazuhiro Kusunose[2]
[1]Nagaoka University of Technology
Department of Mechanical Engineering, Nagaoka University of Technology
1603-1, Kamitomioka-machi, Nagaoka-shi, Niigata Pref., 940-2188
[2]Japan Aerospace Exploration Agency (JAXA)
7-44-1, Jindaiji Higashi-machi, Chofu-shi, Tokyo, 182-8522

**ABSTRACT**

The generation of shock waves is inevitable in supersonic cruise which results in the generation of wave drag as well as sonic boom on the ground. Some innovative concepts as supersonic biplane concept and supersonic twin-body fuselage concept have been proposed in recent to reduce the supersonic wave drag dramatically. In this study, the sonic boom performance of the innovative SST wing-body configurations is discussed by numerical approaches. The effect of fairing at the joint part of the wing/fuselage is also discussed in this paper.

## 1. Introduction

Concorde has ended its operations in 2003, mainly due to its poor fuel efficiency as well as sonic boom problem. However, the realization of next-generation supersonic transport (SST) is highly anticipated. To propose low-drag / low-boom SST configurations, many research activities related to next-generation SST are being performed.

A reduction method of the shock strength due to the lifted wing has been discussed in Ref.[1] by introducing a supersonic biplane wing concept. In this concept, the strength of wave drag has been successfully reduced by the interference of shock waves between the biplanes. According to Ref.[1], the wave drag at zero lift of the biplane airfoil was reduced by nearly 90% compared to an equal volume diamond-wedge airfoil in two dimensional inviscid simulations. A twin-body fuselage concept [2] has also been proposed by the present authors to reduce the wave drag due to the fuselage volume of aircraft. According to Ref.[2], over 20% total drag reduction was achieved by an optimized twin-body fuselage compared with the Sears-Haack (S.H.) single-body fuselage under the constraint of fixed fuselage volume. The S.H. body is well-known as the supersonic single-body configuration that has the lowest wave drag for specified volume and length.

The fusion of the two advanced concepts yields an innovative SST configuration which is a biplane wing / twin-body fuselage configuration. It was proved that the innovative wing-body SST configuration was aerodynamically effective for the reduction of wave drag with a large-sized twin-body (about for 400 passengers) [3]. In this study, the biplane wing / twin-body fuselage configurations are designed with its half-sized body, and then those aerodynamic / sonic boom performance is investigated.

## 2. Computational Methodologies

Three-dimensional supersonic inviscid flows are analyzed by an unstructured mesh CFD solver of TAS (Tohoku University Aerodynamic Simulation)-code [4]. Compressible Euler equations are solved by a finite-volume cell-vertex scheme.

The sonic booms on the ground are predicted by a nonlinear acoustic propagation solver of Xnoise [5] which has been developed by JAXA. Initial (input) pressure distributions are extracted from CFD solutions on the lower side of SST configurations (typically two fuselage lengths below). Then the propagation of the pressure distribution to the ground is solved by an augmented Burgers equation.

## 3. Results and Discussion

The section airfoil thickness ratios of the Busemann biplane are set to 5% of the chord length in both the upper and lower wings. For comparison purpose, an unswept tapered conventional wing configuration is also designed whose section shape is a diamond-wedge airfoil. The thickness ratio is set to 10%, which has the same volume as the biplane wing configuration. The following combinations are investigated in this research:
-S.H. twin-body (twice volume compared with other fuselages) with diamond-wedge wing
-S.H. twin-body with diamond-wedge wing
-S.H. twin-body with Busemann biplane wing
-S.H. single-body with Busemann biplane wing
-S.H. twin-body with Busemann biplane wing, installing a fairing at the wing/body junction
The pressure contours around the SST configurations at $M_\infty$ of 1.7 are visualized in Fig.1.

The sonic boom performance of the proposed SST configurations is investigated at $M_\infty$ of 1.7 and $C_L$ of 0.15. In the sonic boom propagation analyses, standard atmosphere temperature/humidity profiles are utilized. The fuselage length and the cruise altitude are respectively set to 62[m] and 18,000[m], that are given from the conditions of Concorde. The pressure distributions extracted at two fuselage lengths lower from the SST configurations are compared in Fig.2. The pressure distributions on the ground are compared in Fig.3. The aerodynamic / sonic boom performance at $M_\infty$ of 1.7 and $C_L$ of 0.15 is summarized in Table 1. The symbols of $\alpha$, V, $C_{DP}$, $C_{DF}$, $C_D$, and $\Delta P$ are respectively angle of attack (for $C_L$ of 0.15), half aircraft volume, inviscid drag coefficient, friction drag coefficient (estimated from wetted areas of the objects), total drag

Corresponding author: Naohiko Ban
*E-mail address*: s101065@stn.nagaokaut.ac.jp

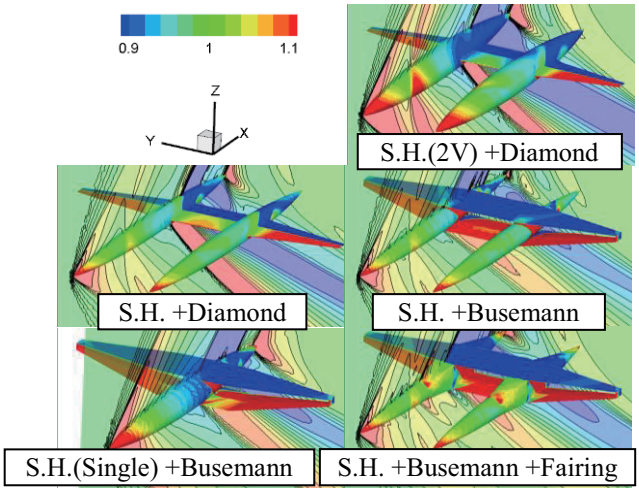

Fig.1 Pressure Distributions around Considered SST Configurations

coefficient and maximum pressure rise of the sonic boom waveform.

The largest pressure variation at the first peak is observed with"S.H.(2V)+Diamond" in Fig.2. This is due to its larger (twice) fuselage volume, which results in the largest ΔP in Fig.3.

With respect to the pressure variation at the second peak in Fig.2, it can be primarily classified by the wing configurations. Larger pressure variations can be observed in the diamond wedge wing configurations at the second peak location. Consequently, the sonic boom performance became better by the adoption of the biplane wing configurations.

However, the drag performance of "S.H. +Busemann" is worse than "S.H.(single)+Busemann" at the present (half-sized) fuselage volume. This issue is due to unnecessary wave interactions at the junction regions of the twin-body and biplane wing (that make long thin spaces), which yields additional parasite wave drag penalties. To overcome this issue, the installation of a wing/body fairing is considered. Its drag coefficient is almost comparable with the single-body / biplane wing configuration while the aircraft volume is increased about 20%.

## 4. Concluding Remarks

The aerodynamic / sonic boom performance of innovative SST configurations was investigated in this research. It was confirmed that the adoption of the Busemann biplane has the possibility to improve sonic boom performance and the installation of a wing/body fairing is promising to reduce parasite wave drag originated from wing/body junction. We will optimize the fairing shape to propose more efficient low-boom / low-drag SST configuration.

## Acknowledgements

The authors are very grateful to numerical simulation research group of JAXA for providing us their nonlinear acoustic propagation solver of Xnoise, as well as for their helpful advices.

Table 1 Aerodynamic / Sonic Boom Performance of SST Configurations at $M_\infty$ of 1.7 and $C_L$ of 0.15

| | α [deg] | V [m³] | $C_{DP}$ [cts] | $C_{DF}$ [cts] | $C_D$ [cts] | ΔP [Pa] |
|---|---|---|---|---|---|---|
| S.H.(2V) +Diamond | 2.57 | 1055 | 430 | 89 | 519 | 48.9 |
| S.H. +Diamond | 2.78 | 564 | 345 | 74 | 419 | 46.4 |
| S.H. +Busemann | 2.34 | 584 | 217 | 124 | 340 | 39.0 |
| S.H.(Single) +Busemann | 2.53 | 576 | 177 | 105 | 282 | 38.3 |
| S.H. +Busemann +Fairing | 2.41 | 692 | 181 | 117 | 297 | 41.4 |

(Drag coefficients in drag count, 1drag count = 0.0001)

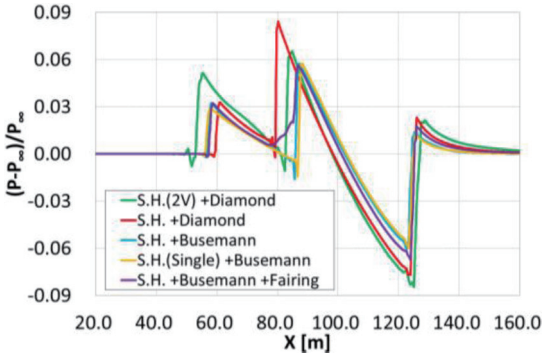

Fig.2 Pressure Distributions at Two Fuselage Lengths Lower from the SST Configurations

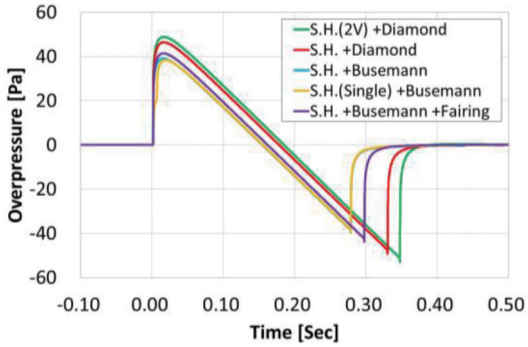

Fig.3 Pressure Distributions at Ground

## References

[1] K. Kusunose, K. Matsushima, and D. Maruyama, Progress in Aerospace Sciences, Vol.47, pp.53-87, 2011.

[2] W. Yamazaki and K. Kusunose, Transactions of the Japan Society for Aeronautical and Space Sciences, Vol.56, No.4, pp.229-236, 2013.

[3] W. Yamazaki and K. Kusunose, Journal of Aircraft, reviewing.

[4] W. Yamazaki, K. Matsushima, and K. Nakahashi, International Journal for Numerical Methods in Fluids, Vol.57, No.4, pp.417-436, 2008.

[5] M. Yamamoto, AIP Conference Proceedings, Nonlinear Acoustics, pp.339-342, 2012.

# Preliminary Evaluation of Multiphase Flow in Artificial Sand Sediment for Gas Production from Methane Hydrate Reservoir

Jun Sasaki[1], Hiroki Gonome[2], Junnosuke Okajima[2], Atsuki Komiya[2], Shigenao Maruyama[2, 3]
[1]Graduate School of Engineering, Tohoku University
6-6 Aoba, Aramaki-aza, Aoba-ku, Sendai, Miyagi 980-8579, Japan
[2]Institute of Fluid Science, Tohoku University
2-1-1 Katahira, Aoba-ku, Sendai, Miyagi 980-8577, Japan
[3]CREST, JST
4-1-8 Honcho, Kawaguchi, Saitama, 332-0023, Japan

**ABSTRACT**

Clarification of characteristics of flow in sand sediment is this study objective. Because, four phase flow is occur in methane hydrate reservoir in the case of thermal stimulation method of hot water injection. Single-phase flow and multi-phase flow in artificial sand sediment were examined through fluid flow experiments and theoretical calculation to verify the characteristic of them in sand sediment. Experiment and calculation result show that characteristics of them were different and permeability for single-phase water flow is higher than that for air-water mixed flow.

## 1. Introduction

In Japan, methane hydrate has been attracted a lot of attention as a future energy resource because of exhaustion of fossil fuels, increasing of energy demand and existing in large quantity in the sea around Japan [1]. Thermal stimulation method, which is one of the dissociation methods of methane hydrate, is expected to produce the methane gas from methane hydrate reservoir with high efficiency compared with other method because of high energy input. Maruyama et al. proposed power generation system utilizing oceanic methane hydrate [2]. In this case, four phase complex thermal hydraulics phenomenon occur which consist of methane gas generated from methane hydrate, matrix rock, water and undissociated methane hydrate as shown in Fig. 1. In order to predict the amount of methane gas production from methane hydrate reservoir, it is important to understand characteristics of at the view point of small scale structure multi-phase flow in methane hydrate reservoir.

The objective of this study is to verify the characteristics of multi-phase flow in sand sediment, since methane hydrate is formed in sand sediment reservoir under seafloor.

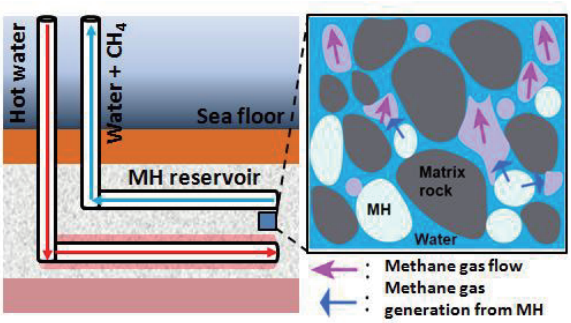


Fig. 1 Concept of power generation system utilizing methane hydrate

## 2. Experimental apparatus and procedure

Figure 2 shows the schematic diagram of experimental apparatus. This apparatus was made of wooden frames of 10 mm in thickness, transparent acryl plates of 5 mm in thickness, copper injection and production wells Toyoura sand, which typical diameter is 200 μm, was used to imitate Nankai Trough sand sediment in which off shore production test was conducted on March, 2013. Four slit were distributed around the copper wells. Mesh sheet was rolled around the wells to prevent sand clogging. Figure 3 show a schematic diagram of experimental setup. This apparatus consisted of a water pump, a mass flow meter, a compressor, a pressure gauge, a balance and a movie recorder.

The visualization cell was filled with Toyoura sand and water. After that water and air were injected from the injection well and drained from the production well through the artificial sand sediment while recording the flow. In this experiment, colored water was used to visualize the flow.

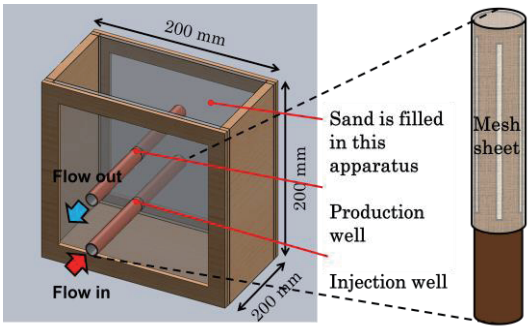


Fig. 2 The schematic diagrams of visualization cell

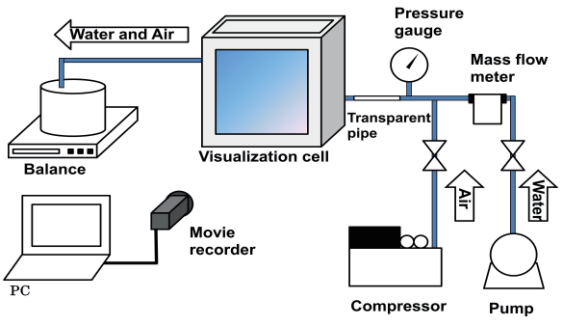


Fig. 3 The schematic diagram of experimental setup

Corresponding author: Jun Sasaki
*E-mail address*: sasaki@pixy.ifs.tohoku.ac.jp

## 3. Results and Discussion

Figure 4 shows the visualization result of single-phase water flow and air-water mixed flow in artificial sand sediment. In case of single-phase water flow, the penetration area size was gradually spreading with time. On the other hand, in case of air-water mixed flow, the chamber size was not spreading. Thus, flow pattern difference was observed between single-phase water flow and air-water mixed flow. In both experiment, injection flow rate was constant and it was same as drained flow rate of water. Therefore it was considered that the cause of this difference was permeability. To confirm the permeability, theoretical calculation was carried out by assuming that air-water mixed flow is flowing into the porous structure of representative cross-section area and representative length. By using these assumptions, Darcy's law is applicable to this phenomenon [3]. It is expressed as follow.

$$Q = \frac{K\Delta pA}{\mu L}, \tag{1}$$

where $Q$ [ml/min] is the flow rate, $K$ [m$^2$] is the permeability of sand sediment, $\Delta p$ [MPa] is the pressure loss in sediment, $\mu$ [Pa・s] is the fluid viscosity, $A$ [m$^2$] is the cross section, $L$ [m] is the length. In this calculation, representative length was defined as distance between injection well and production well. Cross section was defined as product of diameter of well and length of well in sand sediment. Flow rate of air was estimated by movie air-water mixed flow in transparent pipe as shown in Fig. 3. Flow rate of air-water mixed flow was defined as the sum of water flow rate and air flow rate. In this experiment, pressure loss difference was measured as shown in Fig. 5. Hence, pressure loss was defined as the difference between average of injection pressure and initial pressure. Viscosity of air-water mixed flow was defined by following equation [4].

$$\mu_{\mathrm{mix}} = \alpha\mu_{\mathrm{air}} + (1-\alpha)\mu_{\mathrm{water}}. \tag{2}$$

where $\alpha$ is void fraction of air-water mixed flow, $\mu_{\mathrm{air}}$ is viscosity of air, $\mu_{\mathrm{water}}$ is viscosity of water. Void fraction was estimated by movie of air-water mixed flow in transparent pipe as shown in Fig. 3. $\mu_{mix}$ is substituted for $\mu$ of equation (1). Table 1 shows the values for calculation. Table 2 shows the calculation result.

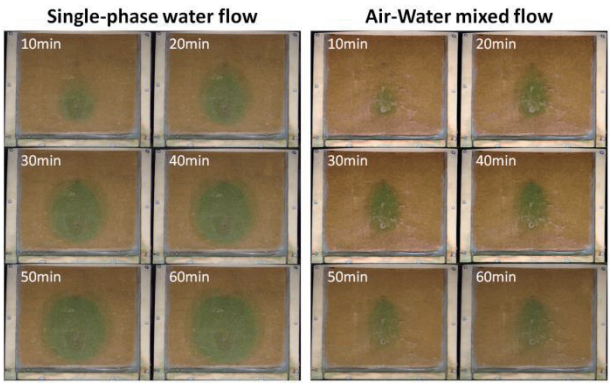


Fig. 4 Visualization result of single-phase water flow and air-water mixed flow

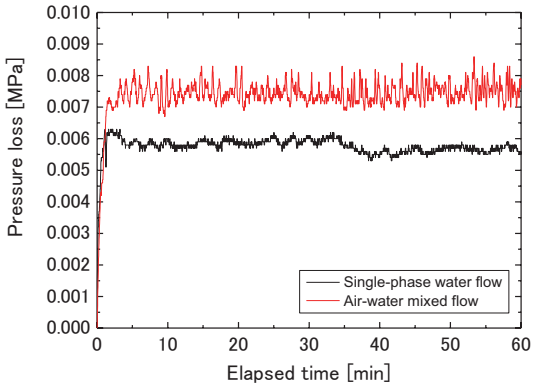


Fig. 5 Pressure loss of single-phase water flow and air-water mixed flow

Table 1. Value for calculation

| | |
|---|---|
| Flow rate of water | 50 ml/min |
| Flow rate of air | 50 ml/min |
| Flow rate of air-water mixed flow | 100 ml/min |
| Viscosity of water | 0.00089 Pa・s |
| Viscosity of air | 0.000018 Pa・s |
| Viscosity of air-water mixed flow | 0.00045 Pa・s |
| Void fraction of air-water mixed flow | 0.5 |
| Length | 0.08 m |
| Cross section | 0.001 m$^2$ |
| Pressure loss of single-phase water flow | 0.0058 MPa |
| Pressure loss of air-water mixed flow | 0.0074 MPa |

Table 2. Calculation result

| | Single-phase water flow | Air-water mixed flow |
|---|---|---|
| Permeability of sand sediment | 1.0E-5 m$^2$ | 8.2E-6 m$^2$ |

As shown in Table 2, the permeability for single-phase water flow is higher than permeability for air-water mixed flow. This result show that single-phase water flow is easily penetrated compared with air-water mixed flow. Therefore, permeability must influence the characteristic of flow in sand sediment.

## 4. Concluding Remarks

Characteristics of air-water mixed flow in artificial sand sediment were examined.

1. Permeability for single-phase water flow is higher than permeability for air-water mixed flow.
2. Permeability must influence the characteristic of flow in sand sediment.

## References


[1] H. Narita, *Journal of the Japan Institute of Energy*, 90 (2011), 492-498

[2] S. Maruyama et al., *Energy*, 47 (2012) , 340–347,

[3] Craig M, Bethke, *Geologiche Rundschau*, 78/1 (1989), 129-154

[4] H. Enwald, *International Journal of Multiphase Flow,* 22 (1996), 26-66

Eleventh International Conference on Flow Dynamics
October 8-10, 2014, Sendai, Miyagi, Japan

# Topology Optimization of Flow Channels Using a Surrogate-Based Genetic Algorithm

Mitsuo Yoshimura[1], Takashi Misaka[1], Koji Shimoyama[1], Shigeru Obayashi[1]
[1]Institute of Fluid Science, Tohoku University
2-1-1 Katahira, Aoba-ku, Sendai, 980-8577, Japan

**ABSTRACT**

This research presents a topology optimization method applied to flow problems, which involve nonlinearity in governing equations and require expensive computation for performance evaluation. A genetic algorithm assisted by the Kriging surrogate model is employed for efficient global optimization. The objective function is to minimize the pressure loss of flow channels in the present optimization. These optimization results agree with the analytical results obtained in the previous study qualitatively. Thus the proposed method shows its capability to explore global optima in flow topology optimization problems.

## 1. Introduction

Shape optimization has been attracting much attention in flow problems, which define the boundary between fluid and solid regions. However, shape optimization cannot deal with the change of topology: *e.g.,* making new holes into an object. Topology optimization is the most flexible optimization method, which can not only modify the shape of an object but also allow the connectedness of the object to change.

Topology optimization has been applied to a variety of engineering optimization problems such as structural mechanics problems, heat transfer problems, and acoustic problems since Bendsøe and Kikuchi first proposed the so-called homogenization design method [1]. However, the application to flow problems is still limited to low-to-moderate Reynolds numbers due to nonlinearity in governing equations.

The basic concept of topology optimization is replacement of the optimization problem with a material distribution problem in a fixed simulation domain using the characteristic function which indicates material exists or not. However, conventional topology optimization tends to suffer from numerical instabilities such as grayscale material and checkerboard pattern. The level set method is one of the approaches to avoid such instabilities. The level set method introduces a signed scalar function and distinguishes solid and fluid regions according to the sign of the function. Thus, zero-contours indicate the boundaries of the regions.

Conventional topology optimization generally explores the optimal solution by the gradient-based method according to the sensitivity of an objective function. However, the gradient-based method tends to find the local optima rather than the global optimum. On the other hand, Evolutionary Algorithm (EA) is one of the metaheuristic optimization methods, which is more capable to explore the global optimum. However, EA requires numerous function evaluations to realize population-based multipoint simultaneous exploration. Thus, EA is not efficient to solve the optimization problems with expensive calculations (*e.g.* Computational Fluid Dynamics (CFD)) for function evaluation if EA is employed solely. Moreover, topology optimization involves a large design space due to a high degree of freedom for shape and topology representation. Thus, it requires much expensive computational cost (i.e., large population and many generations) to obtain competitive solution. Surrogate models are effective to reduce computational cost required for function evaluation. This model approximates the response of each objective or constraint function to design variables in an algebraic expression. This model is derived from the sample points with real values of the objective or constraint function given by expensive numerical simulations. Thus, it can promptly give estimates of function values at arbitrary design variable values.

To validate the global topology optimization methods applied to flow problems, this research works on the optimization of flow channels to minimize their pressure loss. The level set method based on the Poisson equation is employed to relax the simulation domain. The pressure loss of the channels is evaluated by the Building-Cube Method (BCM), which is a Cartesian-mesh CFD approach. A genetic algorithm (GA) assisted by the Kriging surrogate model [2] is employed for efficient global optimization.

## 2. Computational Methods

The boundaries between fluid and solid regions are represented by the level set method that introduces a signed scalar function (level set function) $\phi(x)$ where $x$ represents the location in the simulation domain. This research sets the range of $\phi(x)$ as $|\phi(x)| \leq 1$, and assumes $x$ is in the fluid region if $|\phi(x)| > 1$ or in the solid region if $|\phi(x)| < 1$. At the outer boundary of the simulation domain, $\phi(x)$ is given as the step functions corresponding to the width of the inlet and outlet of the channel. Given $\phi(x)$ at several discrete points inside the simulation domain (which are treated as design variable and stated in the next section), the Poisson equation is solved in the entire domain to obtain the distribution of $\phi(x)$.

In order to evaluate the pressure loss of the channels, CFD simulations are conducted by BCM. The governing equations of BCM are the 2D incompressible Navier-Stokes equations. The convection terms are evaluated by a third-order upwind differencing, and the viscous terms are evaluated by a second-order central differencing. Time integration is conducted by the Crank-Nicolson method, and the coupling of velocity and pressure is conducted by a fractional step method. For high accuracy computation, the Immersed Boundary

Corresponding author: Mitsuo Yoshimura
*E-mail address*: yoshimura@edge.ifs.tohoku.ac.jp

Method (IBM) using ghost cell and image point is employed at the wall boundary.

For efficient global optimization, the Kriging surrogate model is employed together with GA. The Kriging model is based on Bayesian statistics, and can adapt well to nonlinear functions. In addition, the Kriging model estimates not only the function values themselves but also those uncertainties. Based on these uncertainties, the expected improvement (EI) of an objective function, which may be achieved on the Kriging model by adding a new sample point, is evaluated. Furthermore in the present optimization with a constraint, the probability of satisfying the constraint, which may be achieved on the Kriging model, is also evaluated and multiplied by the original EI value. Maximizing this value, the location of an additional sample point is determined for global search while satisfying the constraint.

## 3. Optimization Problems and Results

In this research, two cases with different layouts of channel inlets and outlets, as shown in Fig. 1, are considered as topology optimization problems. The design variables are the values of $\phi(x)$ given at 9 red points as shown in Fig. 2. At the outer boundary of the simulation domain, a fixed value (0.5 or -0.5) is given to represent inlets and outlets of the channels. The wall boundaries of the channels are then obtained by solving the Poisson equation in the entire simulation domain. This domain is discretized as a 240×240 uniform Cartesian grid. The Reynolds number based on the width of inlet is 100. At the inlets, velocity is set as the Dirichlet boundary condition (parabolic profile with the reference velocity of 1) and pressure is set as the Nuemann condition. At the outlets, on the other hand, velocity is set as the Nuemann condition and pressure is set as the Dirichlet condition (zero pressure). The objective function is to minimize pressure loss. Three constraints are considered; 1) flow channels go from inlets to outlets without dead ends, 2) the area of flow channels is less than 40% of the simulation domain, and 3) pressure loss is less than a threshold value. The third constraint aims to avoid aberrant flow channels involving excessive pressure loss.

Case 1 sets the threshold value of pressure loss to 1.0, and uses 128 initial sample points satisfying all constraints to construct the Kriging model. GA identifies the solution, which maximizes the EI value on the Kriging model, as an additional sample point. The Kriging model is reconstructed after adding this new

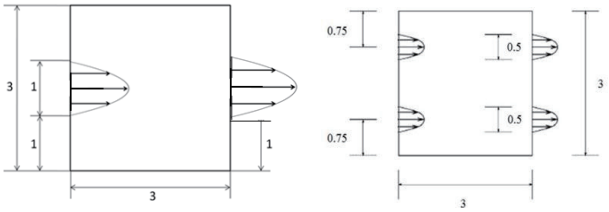


Fig. 1 Layouts of channel inlets and outlets (left: Case1, right Case2)

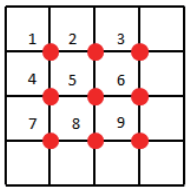


Fig. 2 Points where $\phi(x)$ is gives as design variables

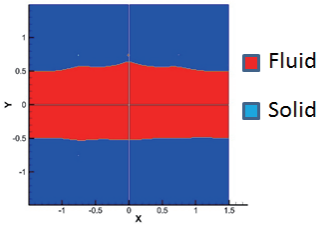


Fig. 3 Optimal flow channel (Case1)

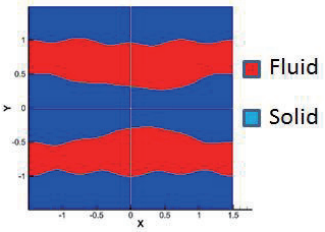


Fig. 4 Optimal flow channels (Case2)

sample point. In Case1, the Kriging model is reconstructed 18 times. Figure 3 shows the optimal flow channel and it is similar to a straight pipe, which is considered to minimize the pressure loss theoretically.

Next, Case 2 sets the threshold value of pressure loss to 3.0, uses 198 initial sample points to construct the Kriging model, and reconstructs the Kriging model 20 times. Figure 4 shows the optimal flow channels in Case 2. These two isolated channels achieve lower pressure loss than the channels with confluence. The previous optimization [3] resulted in two exactly straight channels. Although the present optimization shows just a qualitative agreement with the previous one, it is reasonable to confirm the capability of topology search using the present optimizer.

## 4. Concluding Remarks

Global topology optimization was conducted in flow channel design problems that minimize pressure loss using a Kriging-surrogate-based genetic algorithm. The results agreed with the previous study qualitatively. Thus the proposed method showed its capability to explore global optima in flow topology optimization problems.

## References

[1]. M. P. Bendsøe, N. Kikuchi, *Computer Methods in Applied Mechanics and Engineering*, 71, (1988), 197-224.
[2]. D. R. Jones, M. Schonlau, and W. J. Welch, *J. Global Optim.*, 13, (1998), 455-492.
[3]. V. J. Challis, J. K. Guest, *International Journal for Numerical Methods in Engineering*, 79, (2009), 1284-1308.

Eleventh International Conference on Flow Dynamics
October 8-10, 2014, Sendai, Miyagi, Japan

# Effect of blade wake by means of interference with propeller slipstream on low Reynolds number condition

Satoru Hattori[1], Kotaro Watanabe[1], Hiroki Nagai[1]
[1]Department of Aerospace Engineering, Graduate School of Engineering, Tohoku University
6-6-01 Aramaki Aoba, Aoba-ku, Sendai, Miyagi, 980-8579 JAPAN

**ABSTRACT**

It has been investigated that the drag and lift force is affected by interference between propeller slipstream and wingtip vortex in low Reynolds number condition. The objective of this paper is to verify the effect of wing character and behind the wing wake by means of interference with propeller slipstream in case of change aspect ratio and propeller advance ratio. The experiment is measuring the lift and drag force and behind wing wake. In case of changing aspect ratio of the wing, it was observed that the stall angle of attack becomes larger in running propeller condition.

## 1. Introduction

It is planned to use aircraft for Mars exploration [1] as an important purpose of space development project in Japan. Exploration by means of aircraft is expected to be able to investigate more large area than rover on ground. In addition, Martian surface has big mood swings, so it is required three-dimensional exploration. Therefore it is expected to innovate at Mars exploration. Mars airplane is planning to propeller propulsion system which is tractor configuration. The density of Mars atmosphere is one-hundredth that of the Earth, therefore Mars airplane flies in low Reynolds number condition. Although many study on the propeller -wing interference of some aircrafts have been reported, but the case in low Reynolds number condition is still not clear, so it needs to understand the wing characteristic which is affected by interference of the propeller slipstream in low Reynolds number condition. It has been investigated that wing character affected by change propeller advance ratio and propeller rotation direction in case of the tractor configuration and the propeller located at wingtip in low Reynolds number condition [2].

The objective of this paper is to verify the effect of wing characteristics and behind wing wake by means of interference with propeller slipstream in case of the propeller at wingtip, based on that study. In this experiment, changing parameter of wing aspect ratio and propeller advance ratio, the aerodynamic performance of the wing is investigated.

## 2. Test models and experimental set up

### 2.1 Test models and propeller

The airfoil of test model used NACA0012 airfoil in this experiment. The dimension of the test model used in this experiment shows in Table 1. Symbol of in Table 1 defines as follows, *AR*: Aspect Ratio, *c*: Cord length of test model, *L*: Span length of the test model.
The propeller used in this experiment a two-blade propeller for Radio Control model airplane. In this experiment used reverse pitch and forward pitch propeller, both pitch is 6 inches (152.4mm) and both diameters are 8 inches (203.2mm). These propellers are made of Landing Products.

The propeller is driven by a 50 W brushless DC motor, which the maximum revolution speed is 10,000rpm.

Table 1. Dimensions of test model

| No. | *AR* | *c*(mm) | *L*(mm) |
|---|---|---|---|
| 1 | 3 | 50 | 150 |
| 2 | 6 | 50 | 300 |

### 2.2 Five holes Pitot tube

In this experiment was carried out measuring the behind the wing wake using Five holes Pitot tube (yaw meter).The Five holes Pitot tube is designed for Air Data Sensor of Mars Airplane, and this experiment used it to measure behind the wing wake. Five holes Pitot tube was calibrated by Wright method [3].This method is estimate yaw meter the character which is velocity, angle of flow, static pressure changing only yaw direction angle. So, it is easy to estimate character of yaw meter than other method.

### 2.3 Experimental set up and conditions

The experiments were carried out using the frontier wind tunnel which is located at the Institute of Fluid Science, Tohoku University.
The aerodynamic force was measured by three components load cell, which is a product of Nissho electric works. The experimental set-up shows in Fig 1.
The parameters of propeller configuration were defined by changing propeller pitch direction and the propeller advance ratio. The propeller was located at in front of the wing as tractor configuration. The propeller position of span-wise direction was set at the wingtip.
The propeller advance ratio is following equation.

$$J = \frac{U}{nD} \qquad (1)$$

Where, *U*: flow velocity of wind tunnel, *n*: revolutions per second, *D*: the propeller diameter. The propeller was run at *J*=0.6, 0.8. The Reynolds number set at *Re*=40000 without the effect of propeller induced flow and the angle of attack was tested from -4 degree to

Corresponding author: Hiroki Nagai
*E-mail address*: nagai.hiroki@aero.mech.tohoku.ac.jp

20degree changing by each 1 degree in all conditions.

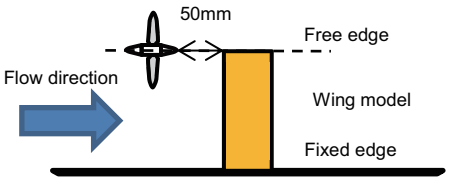


Fig. 1 Outline of experimental set-up

## 3. Results and Discussion

Figure 2 shows lift curve, which is affected by propeller slipstream changing propeller advanced ratio in an aspect ratio *AR*=3 condition.
This graph was shifted $C_L$ direction in order to easy to compare without propeller condition.

From this figure, it can observe that the stall angle of attack is larger than without propeller condition.
The reason is that a separation bubble broken-down by means of affected by propeller slipstream. It said that separation bubble break-down because the lift curve is linearity when near 0degree in propeller running condition [1].

Figure 3 and 4 shows the lift curve, which is affected by propeller slipstream changing aspect ratio in propeller advanced ratio *J*=0.6 condition. From these figures, it is seen that the effect of propeller slipstream is larger than the smaller wing aspect ratio.
This phenomenon is thought that it is related to the ratio of between area of wing interference propeller slipstream and other area.

## 4. Conclusions

From this experiment, obtained knowledge following:
(1) Stall angle of attack is larger than without propeller condition. This is because the separation bubble is broken down by propeller slipstream.
(2) It has become clear that the effect of lift force coefficient is large when the wing aspect ratio is small. It is caused by different wing area of the effect of propeller slipstream.

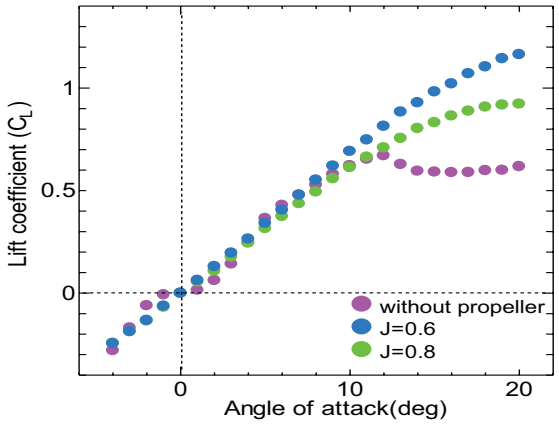


Fig. 2 Lift curve of changing propeller advanced ratio

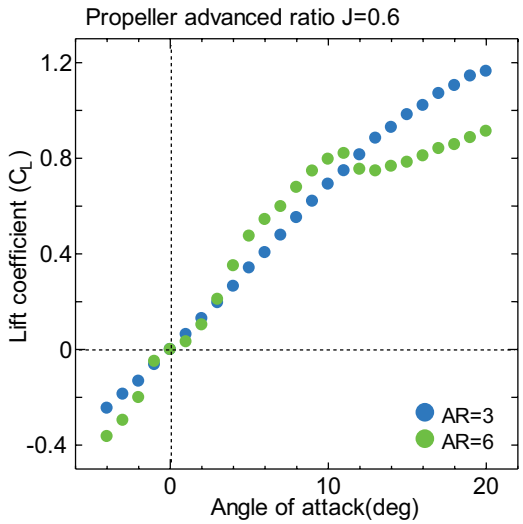


Fig. 3 Lift curve of changing wing aspect ratio in propeller advanced ratio *J*=0.6 and reverse pitch condition

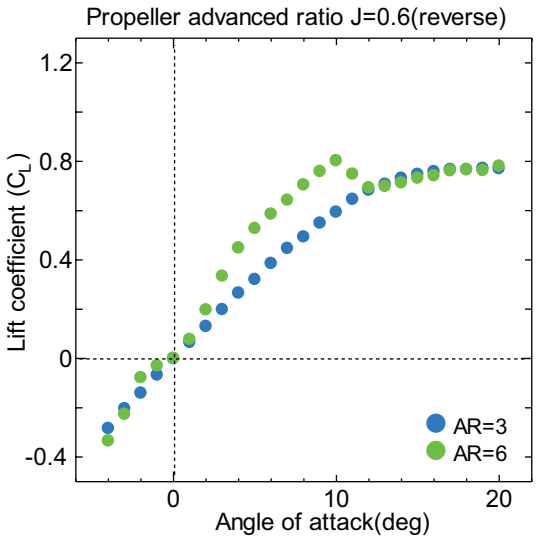


Fig. 4 Lift curve of changing wing aspect ratio at propeller advanced ratio *J*=0.6

## References

[1]F. Makino, H. Nagai, *52nd Aerospace Sciences Meeting*, (2014), AIAA 2014-0744.
[2] S. Ushiyama, M. Okamoto, *45th Annual Meeting*,(2014),JSASS 2014-1052.
[3]Wright, *Journal of Physics E. Scientific Instruments,Vol. 3* (1970), 356-362.

# Analysis of High-Speed Projectile Dispersion Using a Ballistic Range

Ko Miyakoshi[1], Takahiro Ukai[1], Toshihiro Ogawa[1], Kiyonobu Ohtani[1], Shigeru Obayashi[1], Chul Park[2]
[1]Institute of Fluid Science, Tohoku University
2-1-1 Katahira, Aoba-ku, Sendai, Miyagi, 980-8577, Japan
[2]Korea Advanced Institute of Science and Technology
Guseong-dong, Daejeon, 305-701, Korea

**ABSTRACT**

To predict the damages by the meteoric explosion in the atmosphere, it is important to understand the mechanism of a meteoric breakup such as fragmentation, ablation and deceleration. This paper reports the preliminarily experimental and numerical results of high-speed projectile dispersion behavior. In an experimental investigation performed using a ballistic range, the projectile flew leaving a spreading trail with the small particles behind it. The numerical results confirmed that the projectile breaks up by the pressure difference between the backward and forward of it.

## 1. Introduction

On February 15, 2013, a huge meteor exploded above the Chelyabinsk region in central Russia and injured over 1,500 people. In this way, meteor fall has a high risk to damage the earth's surface and humans. Therefore, it is a significant issue to understand the phenomenon such as fragmentation, deceleration and shock wave interaction producing a repulsive force.

About the dispersion behavior of meteor, Park performed experimental investigation to launch the high-speed projectile made of graphite at a speed of 4 km/s using of a ballistic range at NASA Ames Research Center[1-2]. Also he developed the model, called “Medusa’s head”, for the configuration of meteor fragmentation, and performed numerical simulation. However, it is not reached to clarify closely about these phenomena.

This study aims to clarify dynamics of fragmentation of meteor. As the first step, high-speed projectile dispersion behavior evaluated experimentally and numerically in this paper. An experimental investigation was performed in a ballistic range. Furthermore, a numerically investigation is calculated using hydrocode ANSYS AUTODYN. This paper discusses the result of comparing experimental and numerical analysis.

## 2. Experiment

### 2. 1 Method

The experiments were conducted in a ballistic range which is a single-stage powder gun mode at the Institute of Fluid Science, Tohoku University. It consists of a propellant chamber, a launch tube and a test section of 1.66 m in inner diameter and 12 m in length. A projectile is usually stored in a support called sabot and then the sabot which contains the projectile launched. The sabots are separated from the projectile by aerodynamic force and picked up by the sabot stopper plate, so only the projectile flies freely in downstream area.

An experimental setup in the test section is illustrated in Fig. 1. Direct photography was conducted using the high-speed video camera (HPV-X, Shimadzu Corp., 128 frames at 400 x 250 pixel resolution,

Corresponding author: Ko Miyakoshi
*E-mail address*: miyakoshi@edge.ifs.tohoku.ac.jp

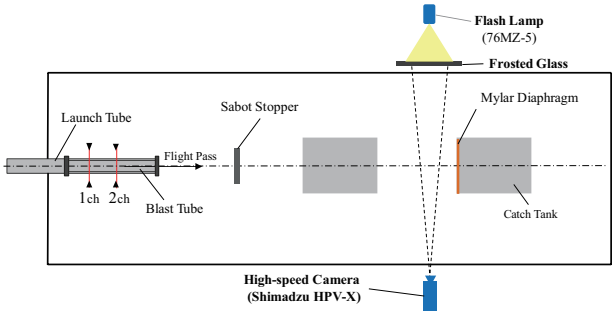


Fig. 1 The experimental setup in the test section.

maximal framing rate 10,000,000 frame/sec) with the camera zoom lens (AF ASPHERICAL LD MACRO 285D, TAMRON Corp., AF28-300 mm, F/3.5-6.3). As a background, frosted glass exposed by a stroboscopic lamp (76MZ-5, Kenko Tokina Corp.,) was used.

The cylindrical projectile was made by pressing the brayed sugar powder containing water, using a hydraulic press machine. This projectile was 8.0 mm in diameter, 7.0 mm in length and 0.52 g in mass. The sabot was made of polycarbonate and shaped cylinder of 15mm in diameter and 5.45 g in mass. The launching projectile velocity was set at 1.6 km/s.

### 2. 2 Result

Fig. 2 shows the sequential images of high-speed photography. Exposure time was 500 ns and inter-frame time was 10 μs. The recording time of Fig. 5 (a) is set as

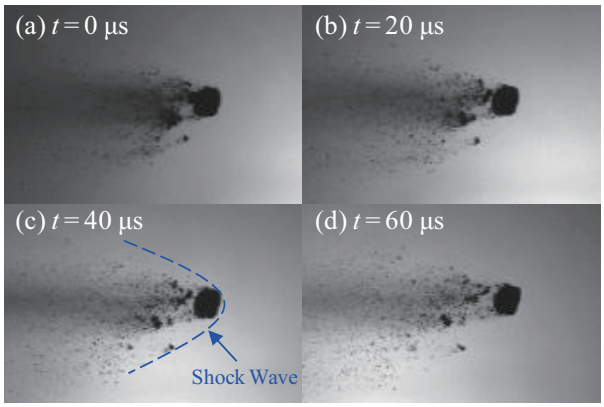


Fig. 2 The sequential images of the high-speed projectile behavior.

0 μs, and the images are showed at 20 μs intervals.

The pressed projectile flied breaking up from the rear side, meanwhile the front of the projectile hardly broke up. The observed trail consists of the cloud, which is composed of the very small particle, and relatively large fragments. The width of the cloud does not change very much, but surrounding fragments have also the velocity in a vertical direction to the axis of flight. The shock wave generated from the mother body of fragments is confirmable, and the surrounding fragments seem to be flying to the direction with the Mach angle. It is considered that shock waves contribute largely to dispersion behavior.

## 3. Numerical Analysis

### 3. 1 Method

A numerically investigation of high-speed projectile dispersion behavior was calculated using hydrocode ANSYS AUTODYN ver.14.5. Fig. 3 shows the two-dimensional analysis model. This analysis was set up as along with the experiment conditions, so in this analysis, pressed sugar powder model flied freely at high-speed in the atmosphere. The analytical area was 20 mm x 700 mm and applied the Euler solver of 1 mm/cell. The pressed sugar model was cylindrical shape of 6.0 mm in diameter, 7.0 mm in length and applied the Lagrange solver of 0.05 mm/cell.

This pressed sugar model was applied the linear state equation, Drucker-Prager constitutive model and tensile failure model by reference to the material model of a brittle materials such as a rock or a concrete. Additionally, the air area was applied the equation of state for perfect gas of $\rho$ = 1.225 x $10^{-2}$ g/cm$^3$ in density, $\gamma$ = 1.4 in ratio of specific heat.

### 3. 2 Result

Fig. 4 shows the result of numerical analysis. The air surrounding the pressed sugar model is described as pressure contour. In Fig. 4, the breakup behaviors of the model were showed at interval of 80 μs from 10 μs after the beginning of calculation. The initial velocity of the model was set up to 1.55 km/s.

There is a high-pressure area at the front side of model and a negative-pressure area at the backward of model. The pressed sugar model began to deform from the backward of it, after that it flied splitting into a number of the fragments. In this analysis the destroyed sugar model is not described due to the setting, so the trail as the experimental results is not showed in these results.

Fig. 5 shows the model position and lengthways

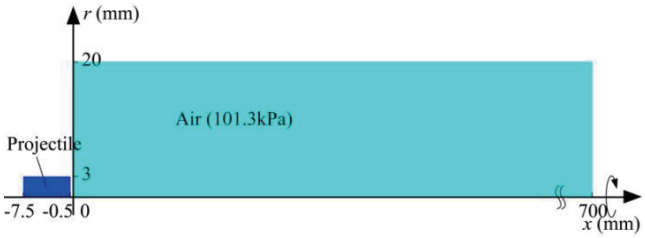


Fig. 3 Numerical analysis model.

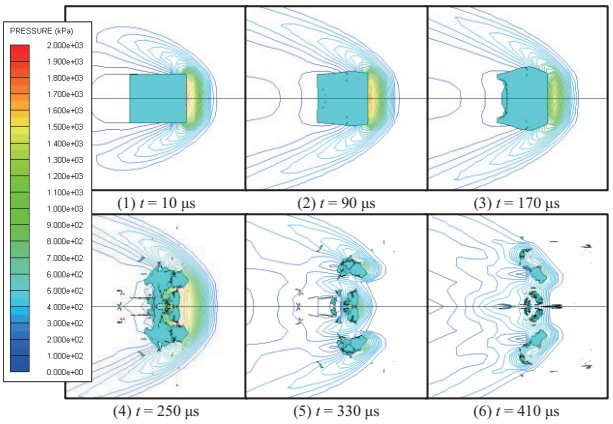


Fig. 4 The result of numerical analysis of the pressed sugar model.

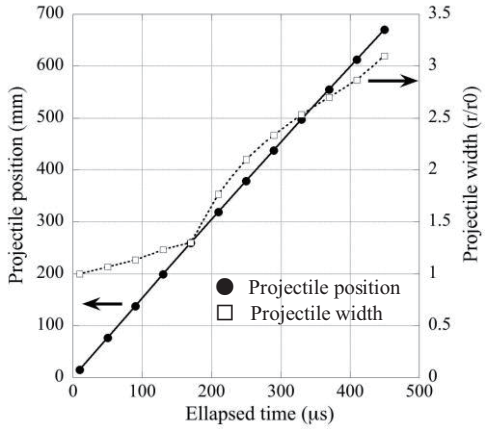


Fig. 5 The model position and spreading width by the time history.

spreading width by the time history observed from the numerical analysis results. Deceleration by dispersion was not confirmed. Lengthways spreading width had grown little by little until 180 μs and after that it grew exponentially, so fragmentation of this model started at this point.

## 4. Conclusion

Dispersion behavior of high-speed projectile was evaluated experimentally and numerically. In the experimental investigation, a pressed sugar projectile was launched using a ballistic range and high-speed photography of the flying projectile was observed. The way of spreading between the cloud of small particle and surrounding large fragments were different.

Numerically investigation of the pressed sugar model was performed. Due to the difference of pressure at model anteroposterior, the model began to deform little by little and then broke up exponentially. However, analysis results still show differences with experiment, so further research is required.

## References

[1] C. Park, *AIAA Paper,* (2013), 0904.
[2] C. Park, J.D. Brown, *The Astronomical Journal*, (2012), 144－184.

# Aerodynamic performance of optimized airfoil for Mars Airplane using Multi-objective generic algorithm

Kentaro Yamahara[1], Hiroki Nagai[1], Takaya Sato[2] and Masahiro Kanazaki[2]
[1]Tohoku University
6-6-01, Aramaki-Aza-Aoba, Aoba-ku, Sendai 980-8579, JAPAN
[2]Tokyo Metropolitan University
6-6, Asahigaoka, Hino-shi, Tokyo, 191-0065 Japan

**ABSTRACT**

The objective of this study is to evaluate the aerodynamic characteristics of the airfoils in low Reynolds number region. We measured the aerodynamic forces using wind tunnel which can simulate Mars atmosphere. In this study, we used the airfoils optimized by multi-objective generic algorithm. The result shows that this airfoils show better characteristics than the previous NACA airfoils or Ishii airfoil characteristics.

## 1. Introduction

Currently, Mars aircraft has been considered as a new method for exploring Mars. Mars aircraft can explore without dependence on Mars surface. So, the aircraft can get larger and clearer data than the rovers which are used now.

When the aircraft cruises in Mars, there thin atmosphere become an issue to solve. Mars air pressure is 1/100 of the earth. That means that the aircraft cruises in low Reynolds number region. In low Reynolds number region, the aerodynamic characteristics of NACA airfoils turn worse, because the previous NACA airfoils are easy to cause laminar separation, and this region have high dependences on airfoil. So, we need to improve the method of airfoil expression.

The objective of this study is to evaluate the aerodynamic characteristics of the optimized airfoils using multi-objective generic algorithm.

## 2. Multi-objective optimization

### 2-1. Method

To design airfoil for Mars aircraft, PARametric SECtion(PARSEC) airfoil representation was used. PARametric SECtion(PARSEC) airfoil representation is one of the promising method for automated airfoil/wing design for this small parameterization. However, this small parameterization makes the worse for the airfoil representation in low Reynolds number region. So, this method divides the thickness parameters and camber parameters of airfoil. This modification makes camber parameters have new representation at leading edge. In this study, we set five design parameters for camber, and six design parameters for airfoil thickness.

Also, as the analytical method, we solved the next Navier-Stokes equation for an aerodynamics evaluation calculation.

$$\frac{\partial}{\partial t}\int_{\Omega}\Phi\, dV + \oint_{\partial\Omega} F\cdot nds = 0 \qquad (1)$$

In this equation, Φ is the sum of the conservation in the domain, and F is the sum of the conservation which go in and out of the domain. We applied to LU-SGS (Lower- Upper Symmetric Gauss- Seidel) implicit method for time integration, and third-order accuracy windward differential with MUSCL method for a flux evaluation. Also, we applied to Baldwin-Lomax model for turbulence calculation. Also, we used structured meshes method for spatial discretization, so generate CH type grid automatically around wing by algebraic method

This modified method is applied to airfoil design using Multi-Objective Genetic Algorithm (MOGA) to obtain optimal airfoil for Mars aircraft. The objective functions are to maximize maximum lift-to-drag ratio, to minimize drag at maximum lift-to-drag ratio, and to do maximum wing thickness to 7%

### 2-2. the result of optimization

Fig. 1 means the result of optimization. In Fig. 1, red points mean non-inferior solutions. We chose the test

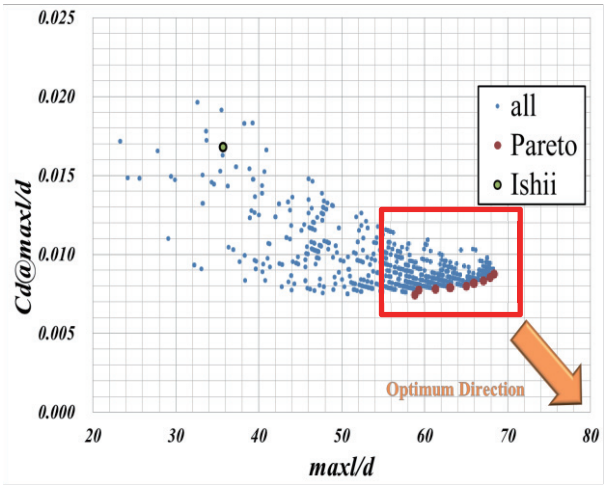


**Fig. 1 the result of optimization**

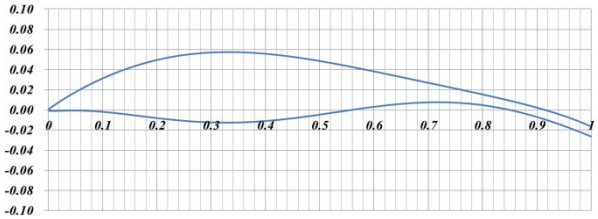


**Fig. 2 the optimized airfoil shape**

Corresponding author: Kentaro Yamahara
*E-mail address*: Yamahara.kentaro@aero.mech.tohoku.ac.jp

airfoil in these non-inferior solutions.

### 2-3. airfoil

We used the optimized airfoil as test model. Fig. 2 shows the cross-section of the airfoil.

## 3. Experimental Setup

### 3-1. Mars Wind Tunnel

Fig. 3 is the schema of Mars Wind Tunnel. The MWT is composed of a vacuum chamber, an induction-type wind tunnel and a buffer tank. The induction-type wind tunnel is located inside the vacuum chamber where the pressure condition of Martian atmosphere can be simulated. The test gas is dry air in usual tests, but can be replaced with carbon dioxide. Currently, the MWT is being operated at ambient temperature only.

### 3-2. Two-component Balance System

A two-component balance system was used to measure aerodynamic force. This balance system is composed of two load cells and has a sufficient sensibility and accuracy to measure lift and drug at reduced pressure.

### 3-3. Experimental Condition

As most important condition, Mach number and Reynolds number are fixed at 0.2 and 20000.In addition, the angle of attack was changed from -5(deg) to 15(deg).

## 4. Result

### 4.1 CL-α

Fig. 4 means Lift curve of the optimized airfoil and Ishii airfoil. This graph shows that Lift force of the optimized airfoil is superior to Ishii airfoil at the degree of all. In the outline of the optimized airfoil, the nonlinearity which is said well in low Reynolds number region appears. Also, the stall angle of the optimized airfoil moves to upper angle than Ishii airfoil, and the stall of this airfoil is smooth.

### 4.2 CD-α

Fig. 5 means Drag curve of the optimized airfoil and Ishii airfoil. This graph shows that Lift force of the optimized airfoil is superior to Ishii airfoil at the degree of all. Especially, within the range of degrees 7 to 12, a difference is reflected on the drag coefficient. On the other hand, at other angles, both drag coefficients is nearly equal. As the reason of this graph, it is thought that the movement of the boundary layer and the laminar separation is same. Especially, at the angle that is bigger than 12 degrees, it is thought that the laminar separation bubble bursts. Therefore in Lift curve, Fig. 4, a sudden and significant reduction of the lift coefficient is shown.

As the result, the burst of the laminar separation bubble was improved by the optimization and the modification of PARSEC airfoil representation, especially the leading edge.

## 5. Summary

The force characteristic of the optimized airfoil was investigated experimentally in low Reynolds number region. The Lift curve and the Drag curve show that the optimized airfoil is superior to Ishii airfoil.

## References


[1] T. Sato, M. Kanazaki , MC thesis, Tokyo Metropolitan University, 2014.

[2] T. Sato, T. Yotsuya, M. Kanazaki, K. Matsushima , JSASS-2012-4367, 2012.

[3] Ryan Gerakopulos, Michael S. H. Boutilier, and Serhiy Yarusevych,"Aerodynamic Characterization of a NACA 0018 Airfoil at Low Reynolds Numbers", AIAA 2010-4629, 2010.


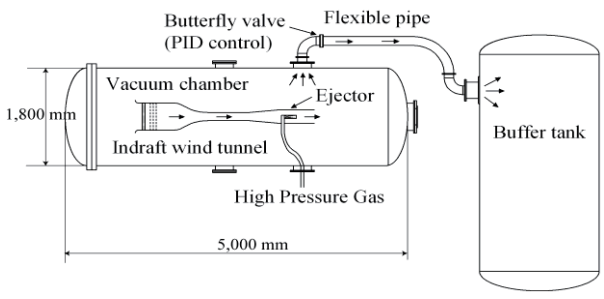


**Fig. 1 Mars Wind Tunnel**

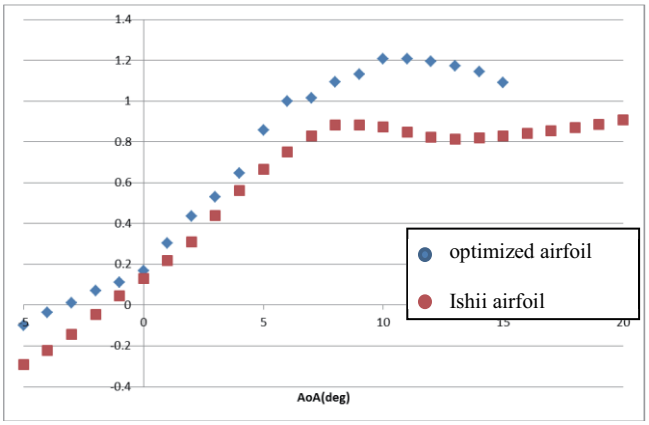


**Fig. 4 Lift curve**

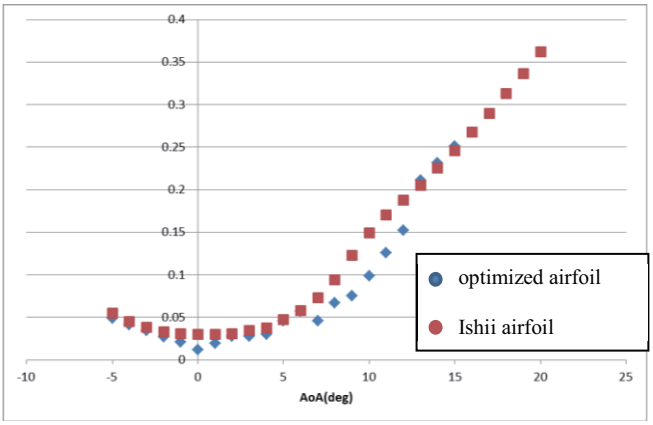


**Fig. 5 Drag curve**

Eleventh International Conference on Flow Dynamics
October 8-10, 2014, Sendai, Miyagi, Japan

# Numerical Analysis of Behavior of Cavitation Bubble in Liquid Droplet Impingement

Hirotoshi Sasaki[1], Naoya Ochiai [2] and Yuka Iga [2]
[1] Graduate School of Engineering, Tohoku University
6-6-01 Aramaki Aza Aoba Aoba-ku Sendai, Miyagi 980-8579, Japan
[2] Institute of Fluid Science, Tohoku University
2-1-1 Katahira Aoba-ku Sendai, Miyagi 980-8577, Japan

**ABSTRACT**

When the droplet impinges on the material surface at a high speed, the pressure wave propagates inside the droplet as a compression wave. The compression wave propagates inside the droplet and reflects as an expansion wave in the gas-liquid interface because of the difference in acoustic impedance. The expansion wave converges and generates low-pressure area inside the droplet. When the pressure of liquid decreases locally, cavitation bubble occurs in the low-pressure area inside the droplet. In this study, behavior of this cavitation bubble is discussed in liquid droplet impingement.

## 1. Introduction

When droplet impinges on the material surface at a high speed, which is called liquid droplet impingement (LDI), the pressure wave propagates inside the droplet as a compression wave and reflects as an expansion wave in the gas-liquid interface because of the difference in acoustic impedance. By the expansion waves converge, low-pressure area is generated inside the droplet. When the pressure of liquid decreases locally, cavitation bubble is known to occur in the low-pressure area[1]. Because this cavitation bubble is collapsed by propagating compression wave inside droplet, the high collapse pressure is generated and the material may be influenced by the collapse pressure. The purpose of this study is aimed at obtaining knowledge for the cavitation bubble generated inside droplet in LDI by using an original numerical analysis method which is fluid/material coupling.

## 2. Numerical Method

### Governing Equation in Fluid

In this study, the locally homogeneous model[2] of simulation of compressible gas-liquid two-phase medium is used for simulation of the liquid droplet in gas phase. The governing equations are the equation of continuity, the Navier-Stokes equations and the energy conservation equation of the compressible gas-liquid two phase, and the mass conservation equation of gas phase. Phase change term due to the evaporation and condensation rate is modeled by using the equation for vapor-liquid mixture based on the theory of evaporation/condensation on a plane surface[3]. In this study, threshold of evaporation/ condensation is assumed to take place at saturated vapor pressure, this pressure of water is calculated by the empirical formula given by Sugawara[4].

### Governing Equation in Material

For a simulation of stress wave propagation in material, it is assumed that material is elastic and the density is constant because the density change is very small in material. The equation of motion and the time-differential constitutive equations of homogeneous isotropic elastic medium[5] are solved.

Corresponding author: Hirotoshi Sasaki
*E-mail address*: hsasaki@cfs.ifs.tohoku.ac.jp

### Numerical Scheme

The cell centered finite volume formulation is used to discretize the governing equations in both fluid and material. The AUSM type scheme is used for the evaluation of numerical flux in the fluid side. In the material side, Godunov method is used for upwind scheme. The conservative variables are interpolated at the cell interfaces by using the 3rd-order MUSCL-TVD method with a minmod limiter. The 4th-order Runge-Kutta method is used for the time integration.

The algorithm of two-way coupling method at fluid/material interface[6] is applied as follows: fluid surface pressure and normal stress of vertical direction on material surface are obtained by considering reflection and transmission of pressure and stress waves with acoustic impedance[7]. Nonslip condition is adopted on fluid/material surface, where the vertical speed has the values obtained by considering reflection and transmission and the tangential speed of fluid has the same speed of solid which is calculated by material analysis.

## 3. Results and Discussion

### Calculation Condition

The initial temperature and pressure of water droplet in air are 293.15K and 0.1 MPa, respectively. The material phase is assumed to be carbon steel and the initial stress is compressive stress of 0.1 MPa. The material properties for carbon steel are set as follows: density $\rho_s$= 7800kg/m$^3$, Young's modulus $E$ = 200 MPa and Poisson's ratio $\nu_s$ = 0.3. The equivalent stress $\sigma_{eq}$ is the von Mises's equivalent stress. In this study, impingement velocity $V$ is 200 m/s, droplet diameter $d$ = 0.1 mm and $t_0$ is the time of first contact of the droplet to the material surface.

### Cavitation Bubble Generated by LDI

The simulation of vertical droplet impingement on the flat material surface has been performed. The time variation of images made schlieren imaging process is shown in Fig.1. The propagating pressure waves inside the droplet are seen after droplet impingement on material surface. (Fig.1(a)). These pressure waves reach the gas-liquid interface as compression waves and these pressure waves reflect as expansion waves due to the difference in acoustic impedance. (Fig.1(b)). By converging these

expansion waves with each other in the top of droplet, low-pressure area is locally generated and cavitation bubble begins to occur. (Fig.1(c)). After cavitation bubble is expanding inside droplet, cavitation bubble is shrinked and collapsed by the compression waves which propagate inside the droplet from the bottom again. (Fig.1(d)).

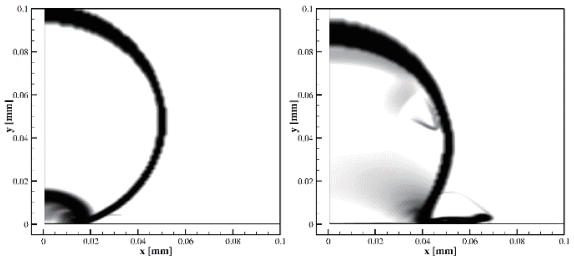

(a) $t = t_0$+0.010 μs (b) $t = t_0$+0.061 μs

(c) $t = t_0$+0.145 μs (d) $t = t_0$+0.184 μs

Fig.1 Time variation of schlieren images inside and outside the droplet ($d$ = 0.1mm, $V$=200 m/s)

The time variation of pressure and equivalent stress is shown in Fig.2, where the black line indicates the gas-liquid interface at void fraction $\alpha$ = 0.1. High pressure caused by the impingement was observed in the early stages of the impingement and the variation is not seen of void fraction inside the droplet. (Fig.2(a)). When the impingement advances, high pressure by droplet impingement is attenuated and the occurrence of cavitation bubble inside the droplet has been observed. In addition, the occurrence position of cavitation bubble locates 0.056 mm upper from the material surface. (Fig.2(b)). Afterward the cavitation bubble collapses by compression wave and high pressure is generated. The collapse pressure is about 80 MPa. However the cavity collapse pressure has little effect for LDI because the pressure is lower than droplet impingement pressure and the pressure wave from the collapse pressure attenuates before reaching the material surface. (Fig.2(c)).

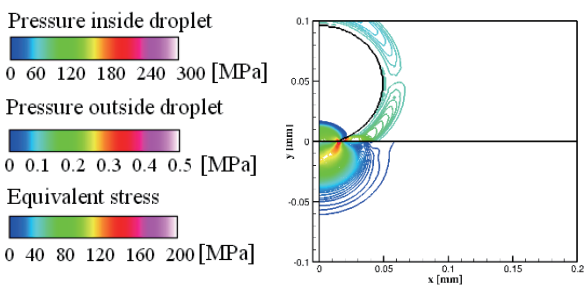


(a) $t = t_0$+0.010 μs

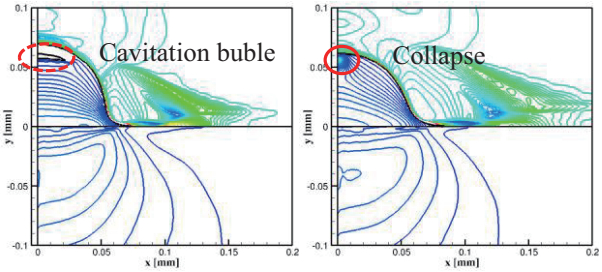


(b) $t = t_0$+0.145 μs (c) $t = t_0$+0.184 μs

Fig.2 Time variation of pressure distribution in fluid and equivalent stress distribution in material ($d$ = 0.1mm, $V$=200 m/s)

## 4. Conclusions

Our original fluid/material coupled numerical method which considers reflection and transmission of pressure waves on the fluid/material interface was used to simulate the liquid droplet impingement on material surface. The simulation of vertical droplet impingement on the material surface was carried out and behavior of cavitation bubble inside the droplet was investigated from the occurrence to collapse. The obtained results can be summarized as follows:

(1) Cavitation bubble occurs inside the droplet because of interface of expansion wave which is generated by reflection of compression wave by impingement pressure.

(2) The place of cavitation bubble occurrence is 0.056 mm upper from the material surface and center inside droplet in the case of droplet diameter 0.1 mm and impingement velocity 200 m/s.

(3) Because the value of maximum pressure of cavitation bubble collapse is about 80 MPa, which is lower than the pressure of droplet impingement and the collapse position is away from the material surface, the cavitation bubble collapse is considered to have little effect on erosion of the material in the present impingement condition.

## References


[1] J.H.,Brunton, J.J.,Camus, *Proc. 9th Int. Congress on High Speed Photography,* (Denver, CO), (1970).

[2] Ochiai, N., Iga, Y., Nohmi, M., and Ikohagi, T., 2010, J. Fluid Sci. Technol., 5(3), pp. 416–431.

[3] Fujikawa, S., and Akamatsu, T., *J. Fluid Mech.*, Vol.97 (1980), 481-512.

[4] Sugawara, S. New Steam Tables, *JSME*, Vol.35 (1932), 999-1004, (in Japanese).

[5] Takano, Y., Goto, T. and Nishino, S., *Trans. JSME, Ser.A*, Vol. 64 (1998), 2471-2476.

[6] Sasaki, H., Iga, Y., and Ikohagi, T., *Proc. Joint International Conference on Supercomputing in Nuclear Applications and Monte Carlo 2010 (SNA + MC2010)*,10189.pdf

[7] Ysuda, K , Mechanical Acoustics (2004), CORONA, (in Japanese).

Eleventh International Conference on Flow Dynamics
October 8-10, 2014, Sendai, Miyagi, Japan

# Aerodynamic Forces Measurements of a Corrugated Thin Airfoil at Very Low Reynolds Number

Keita Ebina[1],Masato Okamoto[2]
[1]Graduate School of Kanazawa Institute of Technology
Ogigaoka 7-1, Nonoichi, Ishikawa, 921-8501, Japan
[2] Kanazawa Institute of Technology
Ogigaoka 7-1, Nonoichi, Ishikawa, 921-8501, Japan

**ABSTRACT**

The aerodynamic forces and moment acting on the corrugated thin airfoil like the wing section of a wings dragonfly were measured at low Reynolds number between 1,000 and 10,000 by conducting the low pressure wind tunnel. These results were compared with those of thin flat plate in the same Reynolds number. When the corrugation was inserted in a profile of thin airfoil at an appropriate position, the minimum drag coefficient decreased and the maximum lift-to-drag ratio increased. It was found that the vortices in the concaves of airfoil were effective at very low Reynolds number.

## 1. Introduction

The wing section of a dragonfly that has thin and corrugated profile is known to perform well at very low Reynolds number less than 10,000 [1]. The thick airfoil consisting of a stream line shape with leading edge radius like an airfoil used at large aircraft is unavailable at such low Reynolds number. Hidaka and Okamoto[2] showed that the thin angular airfoils are effective by comparing with the thick triangular airfoil at very low Reynolds number. The purpose of the present study is to ascertain the aerodynamic characteristics of the corrugated thin airfoil made in imitation of the wing section of a dragonfly at very low Reynolds numbers between 1,000 and 10,000 by using a low pressure wind tunnel developed by authors.

## 2. Experimental setup

The low pressure wind tunnel used in this study is very small, which test section is 160mm×100mm with 200mm long, and its wind tunnel is installed in the vacuum desiccator. The wide range of Reynolds number based on the chord length of a model wing is able to be set up by changing the wind velocity in the test section from 6 to 10m/s in the pressure between 10kpa and the atmospheric pressure of about 100kPa, and the turbulent intensity in the flow velocity is less than 0.3%. The three components balance system comprises a load measuring device and the stepping motor for changing the angle of attack. The load measuring device was made from some aluminum blocks on which attached the strain gauges; the lift, the drag and the pitching moment acting on the wing model were measured.

Figure 1 shows the wing section profiles used in this study: airfoil 1 called thin corrugated airfoil made in imitation of the outboard wing of a dragonfly (*Anax parthenope*), airfoil 2 and 3 made by deforming the airfoil 1, airfoil 4 called thin angular airfoil that shows a good performance in the low Reynolds number range, and the flat plate of which thickness is 1.5% of the chord. Here, airfoils 1- 4 have the same height of 5%*c*, and airfoil 4 and the flat plate were applied to compare the aerodynamic characteristics at the present Reynolds number. These airfoils were made of the thin aluminum plate having thickness of 1%*c* for airfoil 1-4 and 1.5%*c* for the flat plate.

Corresponding author: Keita Ebina
*E-mail address*: b6400262@planet.kanazawa-it.ac.jp

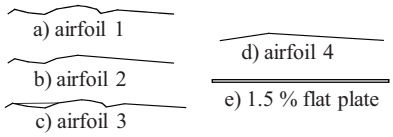


Fig. 1 Airfoils tested in this study

## 3. Results and discussion

### 3.1 Aerodynamic characteristics of airfoil 1

Figure 2 shows the aerodynamic coefficients $C_l$, $C_d$, $C_{m,0.25c}$ versus angle of attack $\alpha$ of airfoil 1 obtained by changing the Reynolds number between 1,000 and 10,000. As seen in the lift curve at $Re$=10,000, the non-linearity of the lift slope is remarkable, that is $C_l$ increases with the increases at 0deg < $\alpha$ < 3deg, however $C_l$ increases largely beyond the theoretical lift slope of 2π at 3deg < $\alpha$ < 4deg, and it reaches maximum value of $C_{l\max}$ at $\alpha$=7deg. The lift slope decreases and the angle of attack of the $C_{l\max}$ is increase as the Reynolds number decreases; specifically, at $Re$=1000, $\alpha$ of $C_{l\max}$ is very large of 18deg and $C_{l\max}$ is larger than that of higher Reynolds number. The minimum drag coefficient $C_{d\min}$ is provided at $\alpha$ of $C_l$=0 and $C_{d\min}$ gradually increases with the decrease of Reynolds number due to the increase of friction drag. $C_d$ increases as $C_l$ increases and the ratio of increase in $C_d$ increases after decreases momentarily as the lift slope increases largely. The maximum lift-to-drag ratio $(l/d)_{\max}$ is obtained just before the large increase of $C_d$. The pitching moment coefficient $C_{m,0.25c}$ indicates the negative value due to the positive camber at small $\alpha$. As the lift slope increases largely, $C_m$ begins to decrease and reaches nearly -0.1 at $\alpha$=20deg.

### 3.2 Effect of the corrugated profile

Figure 3 shows the comparison between airfoil 1 and modified airfoils 2 and 3 at $Re$=5000. The large $C_l$ was obtained in the airfoil 2 that lower surface was smooth,

and $C_l$ in the airfoil 3 that has flat surface near the leading-edge was flat was slightly small in comparison with airfoil 1. Because $C_d$ in airfoil 1was small, largest $(l/d)_{max}$ was obtained at airfoil 1. From these results, it is considered that minimum $C_d$ of airfoil 1 is obtained by being convex profile of its lower surface, and large $(l/d)_{max}$ of airfoil 1 is obtained by being concave profile of the upper surface near the leading-edge. However, $C_l$ of airfoil 2 is more large by the smooth lower surface.

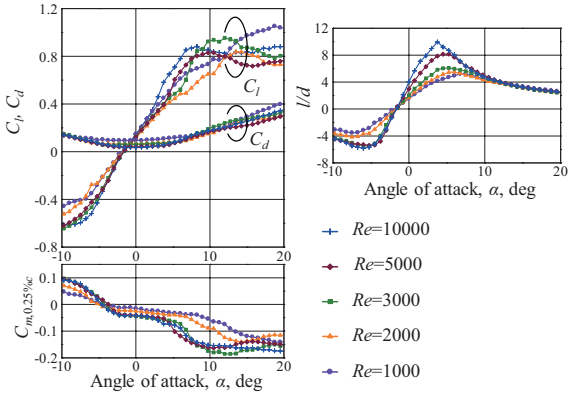


Fig. 2 Aerodynamic characteristics of airfoil 1

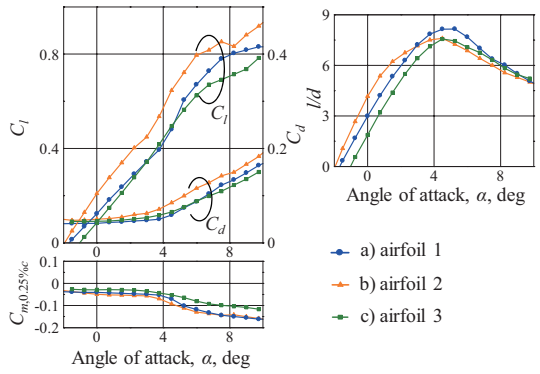


Fig. 3 Comparison between airfoil 1 and modified airfoils

### 3.3 The Reynolds number effects on the main aerodynamic characteristics

Figure 4 shows the main aerodynamic characteristics of all airfoils at each Reynolds number from 1,000 to 10,000. The difference in the maximum lift coefficient $C_{l\max}$ caused by the Reynolds number in comparatively small in any airfoil at $Re \geqq 2{,}000$, whereas $C_{l\max}$ is large at $Re$=1,000. This is because the lift slope is small at $Re$=1,000 and $C_l$ gradually increases as the angle of attack increases as shown in Fig. 2.

The minimum drag coefficient $C_{d\min}$ of the thin triangular airfoil was largest and that of airfoil 1 was smallest in the present airfoils. Specifically, it should be noted that $C_{d\min}$ of the corrugated airfoil (airfoil 1) is smaller than that of the thin flat plate.

The largest maximum lift-to-drag ratio $(l/d)_{max}$ is obtained for thin triangular airfoil at $Re$=10,000, and the difference in $(l/d)_{max}$ of the corrugated airfoil is small as the Reynolds number decreases.

### 3.4 Flow Visualization around the corrugated airfoil

The streak line visualizations around the corrugated airfoils were conducted by the water channel tests. For details of the water channel tests, please refer to the ref [2]. Figure 5 is the comparison in photographs of the streak lines between airfoil 1 and airfoil 2 at $\alpha$=0deg of $C_l$=0. As seen in the flow patterns of the each airfoil, the separation vortex were seen in the concave part of both upper and lower surfaces of the airfoil. In the lower surface, although the vortex of airfoil 1 was fixed in the concave part, the vortex of airfoil 3 was shedding to the trailing-edge. It is considered that the reverse flow of the fixed vortex causes the minimum drag coefficient.

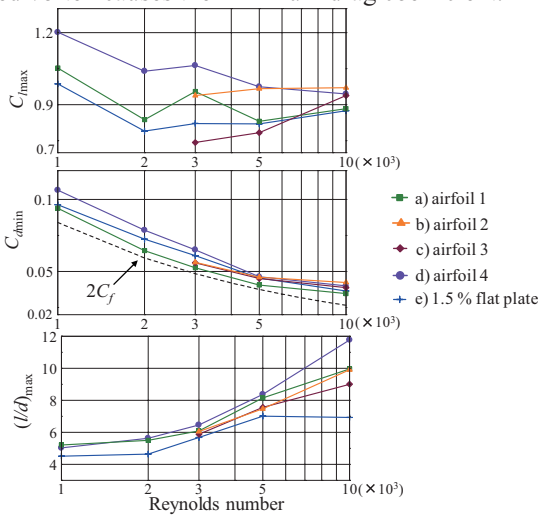


Fig. 4 Main aerodynamic characteristics of the airfoils

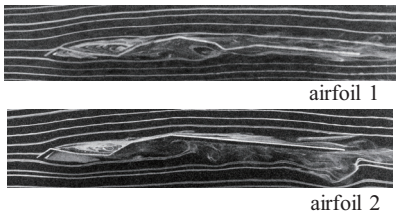


Fig. 5 Flow visualization of the airfoil 1 and 2

### 4. Conclusions

Following results were obtained through the low pressure wind tunnel tests conducted at very low Reynolds number.

1) The corrugated thin airfoil such as dragonfly wings shows a good performance in $C_{l\max}$ and $(l/d)_{max}$ at Reynolds number less than 5,000.
2) The minimum drag coefficient of the corrugated a airfoil is small in comparison with that of the thin flat plate.
3) The separation vortex seen in the concave of the airfoil surface is effective to obtain a good performance at very low Reynolds number.

### References


[1] M. Okamoto, K. Yasuda, and A. Azuma, *J. Exp. Biology*, *Vol.199*, pp. 281-294, 1999

[2] T. Kuroda, M. Okamoto, *2013 Asia-Pacific International Symposium on Aerospace Technology*, 2013

Eleventh International Conference on Flow Dynamics
October 8-10, 2014, Sendai, Miyagi, Japan

# Efficient Aeroacoustic Analysis of Jet Noise

Yuma Fukushima[1], Shigeru Obayashi[1], Daisuke Sasaki[2], Kazuhiro Nakahashi[3]
[1]Institute of Fluid Science, Tohoku University
Sendai, 980-8577, Japan
[2]Kanazawa Institute of Technology
Nonoichi, 921-8501, Japan
[3]Japan Aerospace Exploration Agency
Chofu, 182-8522, Japan

**ABSTRACT**

An efficient jet noise prediction procedure is constructed. The proposed stochastic noise generation and radiation model consists of the Building-Cube Method solvers and a synthetic eddy method. The present method is applied to the noise prediction of subsonic round jet. The prediction result of jet noise shows good quantitative agreement with experiment up to 6,000 Hz.

## 1. Introduction

Broadband noise generated from the complicated jet flows is still main noise source of aircraft. By using large eddy simulation (LES) or direct numerical simulation (DNS) to compute near-field turbulent structure, an accurate noise prediction can be made [1]. However these approaches are too time consuming for industrial and design purposes. Therefore, computationally efficient and accurate methods of modeling turbulence are needed in order to study designs that reduce broadband noise of jet flows. From this background, various stochastic methods to generate the turbulent velocities are presented. These methods are computationally efficient and also provide time dependent turbulent fields which have prescribed flow features. In practical, these turbulence generation methods are employed in combination with Reynolds-averaged Navier-Stokes (RANS) and linearized Euler equations (LEE) simulations. This combined method is called stochastic noise generation and radiation (SNGR) model [2].

The objective of this research is the development of a fast and accurate broadband noise prediction method. The target is the far-field noise generated from a round jet. To achieve the computationally efficient process, RANS and LEE simulations are solved on the framework of block-structured Cartesian mesh method called Building-Cube Method (BCM) [3]. Furthermore, the synthetic eddy method (SEM) [4] is employed for stochastic turbulence generation.

## 2. Computational Method

Figure 1 shows the flowchart of the SNGR model. First, RANS simulation with a turbulence model provides a time-averaged flow field. The simple low-dissipative AUSM (SLAU) scheme is implemented to compute the inviscid flux. For time integration, the lower-upper symmetric Gauss-Seidel (LU-SGS) implicit method is employed. Chien's standard $k$-$\varepsilon$ turbulence model is used to close the equations. Second, turbulent velocity fluctuations are generated by SEM procedure using the flow information obtained from the RANS simulation.

Corresponding author: Yuma Fukushima
*E-mail address*: fukushima@edge.ifs.tohoku.ac.jp

The SEM is based on a superposition of a synthetic velocity signal which can be written as a sum of a finite number of eddies convecting with constant velocity. Third, LEE with unsteady source terms computed from turbulent velocity fluctuations is solved. The spatial derivative is computed by fourth-order dispersion relation preserving (DRP) scheme. Time integration is performed by fourth-order low dissipation and dispersion Runge-Kutta (LDDRK) scheme.

## 3. Results and Discussion

The present SNGR model is applied to the noise prediction of a subsonic round jet [5]. The noise generated from a jet flow is computed and compared with experiment and other's computational result. The jet Mach number $M_{jet} = 0.72$ and the diameter of the nozzle $D = 80$ mm are considered. The computation is conducted with the background flow of $M_\infty = 0.01$ because a flow into quiescent air is numerically difficult to solve with the present RANS solver. Reynolds number based on the diameter of the nozzle is $Re = 5{,}601$. Turbulent kinetic energy and the dissipation rate of RANS computation are used to generate the velocity fluctuation. The flow field is used as the background flow of LEE computation. Figure 2 shows the $u$ velocity and turbulent kinetic energy distribution of the cross-section surface. The jet flow spreads in the radial direction toward the downstream. Turbulent kinetic energy increases at the shear flow region.

The sound source of LEE simulation is the velocity fluctuation generated by the SEM procedure. Figure 3 shows the computational domain of LEE computation. Computational domain is bounded by $400D \times 50D \times 50D$, the number of Cubes are 1,544, total number of cells are 50.6 million and minimum cell size is $9.76 \times 10^{-2}D$. Figure 4 shows the pressure distribution generated from SEM procedure with turbulent kinetic energy contours of RANS computation. The sound source is located in the shear flow. The SEM successfully simulates the sound source of a jet flow. The generated noise propagates to far-field.

Figure 5 shows the power spectral density (PSD) of the $r = 10D$ radius. The PSD at 45 and 60 deg are compared with experiment and Lafitte's computational

results [5]. Frequency is normalized by jet velocity $V_{jet}$ = 244.8 m/s and reference length $D$ = 80 mm. PSD is also normalized by Strouhal number, $St$. $St$ = 1 corresponds to 3,060 Hz. At 60 deg, the PSD of present method shows good agreement with experiment up to 6,000 Hz quantitatively. Highest PSD near $St$ = 0.4 and negative slope near $St$ = 1 are shown. However, the result at 45 deg is slightly overestimated compared with experiment and Lafitte's computational results. The sampling point of 45 deg is closest to sound source in the sampling points, and PSD is overestimated. This result is able to be improved by the modification of turbulence model because the standard $k$-$\varepsilon$ turbulence model tends to estimate the peak of turbulent kinetic energy downstream compared with experiment in the jet flow computation.

## 4. Conclusion

In this research, an efficient jet noise prediction procedure is constructed. The present SNGR model is employed to predict the turbulent noise generated from jet flow. RANS and LEE simulations are conducted on the BCM framework. The SEM is introduced to generate the velocity fluctuation.

The broadband noise generated from a round jet is predicted and compared with experimental and Lafitte's computational results. The predicted PSD shows good agreement with experiment at two angles of $r$ = 10$D$ radius. Highest PSD near $St$ = 0.4 and negative slope at $St$ = 1 are shown. However, the result at 45 deg is slightly overestimated. This result can be improved by the modification of a turbulence model.


## Acknowledgements

The computation in this research was conducted by SGI AltixUV2000 of Institute of Fluid Science, Tohoku University.


## References


[1] U. Paliath, H. Shen, R. Avencha, C. Shieh, AIAA Paper 2011-2881, 2011.

[2] C. Bailly, D. Juve, AIAA Paper 99-1872, 1999.

[3] K. Nakahashi, *Computational Fluid Dynamics 2002,* (2003) 77-81.

[4] N. Jarrin, S. Benhamadouche, D. Laurence, R. Prosser, *International Journal of Heat and Fluid Flow*, **27**(2006) 585-593.

[5] A. Lafitte, T. L. Garrec, C. Bailly, E. Laurendeau, AIAA Paper 2012-2149, 2012.


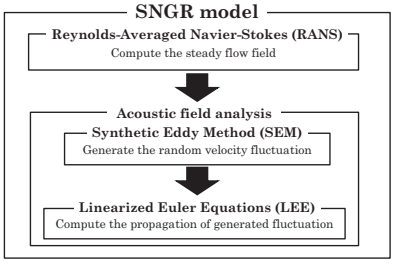


Fig. 1 Flowchart of aeroacoustic analysis based on SNGR approach.

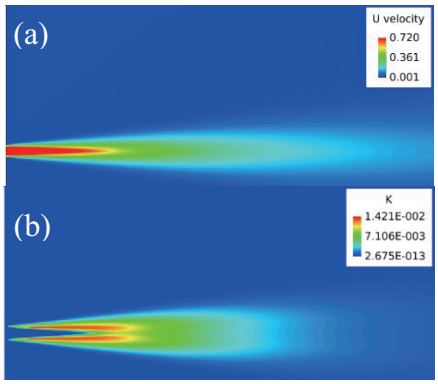


Fig. 2 Results of RANS simulation. (a) $u$ velocity, (b) Turbulent kinetic energy.

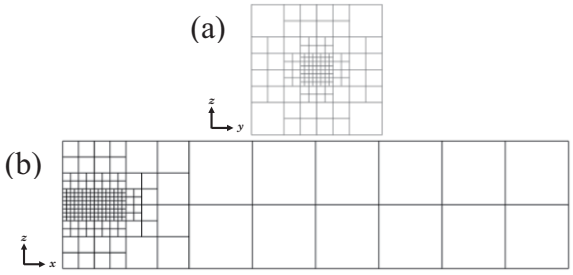


Fig. 3 Computational domain of LEE computation. (a) From +$x$ direction, (b) From –$y$ direction.

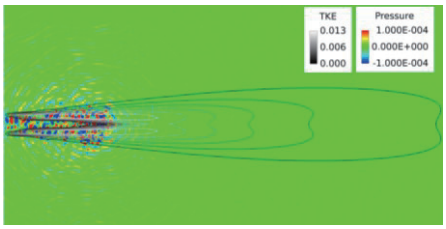


Fig. 4 Pressure distribution with turbulent kinetic energy contours.

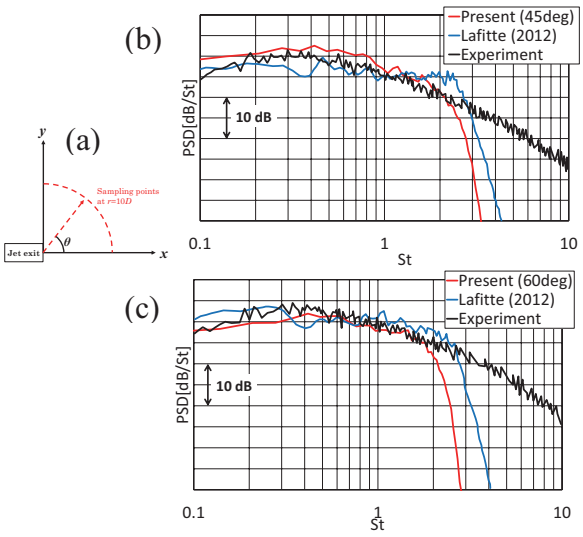


Fig. 5 PSD distribution at $r$ = 10$D$ radius. (a) The definition of sampling points, (b) 45deg, (c) 60deg.

Eleventh International Conference on Flow Dynamics
October 8-10, 2014, Sendai, Miyagi, Japan

# Numerical Simulation of a Bubble Crash by Underwater shock

Yusuke Sato[1], Mingyu Sun[1]
Tohoku University
2-1-1 Katahira, Aoba-ku, Sendai,980-8577, Japan

**ABSTRACT**

This study focuses on underwater shock and bubble by numerical simulation. The CFD method is useful for these type problems because underwater bubble collapsing that can create very high temperature and pressure in a small space that can be hardly measured in experiments. In this study, shock wave relations are derived from exact Riemann solvers for water of the Tait equation of state. The bubble collapsing is successfully resolved on a coarse grid using a multiphase flow solver with subgrid-scale modeling [1].

## 1. Introduction

Bubble crash or bubble collapse is a subject of study not only in hydraulic engineering but also in many other fields, for example, volcanology and applied medicine [2]. However two-phase flow is still a challenge for numerical prediction of such a phenomenon. In this research, we calculate numerical simulation of a bubble collapse by underwater shock. This simulation is similar to shock tube problems. A shock wave in water placed in the left side of calculating domain moves to the right side, and then it interacts with a bubble interface. In order to set up the primitive variables of water shock, Rankine-Hugoniot relations for gases cannot be used as shock wave relations if the water obeys Tait equation of state. Then we introduced the exact Riemann solver for Tait equation of state [3] as post shock relations. Riemann solver is the solution of Riemann problems, that is, shock tube problems [4].

## 2. Method

In this study, the simulation is conducted with an explicit Lagrange-Remap method. In the Lagrange step, it solves primitive quantities of pressure and velocity in theLagrangian frame. The equation of continuity and the equation of motion,

$$\frac{Dp}{Dt} = -\rho c^2 \nabla \cdot \vec{u} \tag{1}$$

$$m\frac{D\vec{u}}{Dt} = -\nabla p \quad , \tag{2}$$

then discretized as follows,

$$\frac{\left(p_i^*\right)^{n+1} - \left(p_i^*\right)^n}{\Delta t} = -\frac{I_i^2}{m_i}\sum\left(\left(u_i^*\right)^n S_{xij} + \left(v_i^*\right)^n S_{yij}\right) \tag{3}$$

$$m_i \frac{\left(u_i^*\right)^{n+1} - \left(u_i^*\right)^n}{\Delta t} = -\sum\left(\left(p_i^*\right)^n S_{xij}\right) \tag{4}$$

$$m_i \frac{\left(v_i^*\right)^{n+1} - \left(v_i^*\right)^n}{\Delta t} = -\sum\left(\left(p_i^*\right)^n S_{yij}\right) \quad , \tag{5}$$

where $m$ is mass at cell number $i$, $S_{xij}$ and $S_{yij}$ are outward normal vectors. Superscript (*) indicates values in the Lagrangian coordinate. Acoustic impedance is given by

$$I_i = \rho_i c_i \quad . \tag{6}$$

The conservative quantities are then calculated from the pressure and velocity at the boundary of the particle. They are remapped to the Eulerian coordinate, as a finite volume method.

On the other hand, the exact solution to the Riemann problem using the Tait equation of state is obtained by solving a single non-linear equation for the density. Tait equation written as

$$P = B\left[\left(\frac{\rho}{\rho_0}\right)^n - 1\right] \tag{7}$$

where $B,n$ is a constant. The density of the liquid at atmospheric pressure is denoted by $\rho_0$ .

About shock wave relations, the Rankine-Hugoniot conditions that hold across it required [3]. These can be written as

$$\rho_R w_R = \rho_* w_* \tag{8}$$

$$\rho_R w_R^2 + k\rho_R^n = \rho_* w_*^2 + k\rho_*^n \tag{9}$$

Where subscript R represents the right side of the shock, and star (*) represents the region of the shock wave. $k = B/\rho_0$ . $w$ is the particle velocity in a reference moving with the shock of speed $S_R$,

$$w_R = u_R - S_R, w_* = u_* - S_R \tag{10}$$

now

$$Q_R = -\rho_R w_R = -\rho_* w_* \tag{11}$$

substituting this into (9) gives

$$Q_R = \frac{k(\rho_*^n - \rho_R^n)}{w_R - w_*} = \frac{k(\rho_*^n - \rho_R^n)}{u_R - u_*} \tag{12}$$

and eliminating w from equations (9)-(12) gives

$$Q_R = \left[\frac{k(\rho_*^n - \rho_R^n)\rho_R\rho_*}{(\rho_* - \rho_R)}\right]^{1/2} \tag{13}$$

this is rearranged to define $g_R$

$$u_* = u_R + g_R \tag{14}$$

where the right function, $g_R$ is given by

$$g_R = \frac{k(\rho_*^n - \rho_R^n)}{Q_R} = \left[\frac{k(\rho_*^n - \rho_R^n)(\rho_* - \rho_R)}{\rho_R\rho_*}\right]^{1/2} \tag{15}$$

then, the density and velocity of the shock wave region

Corresponding author: Yusuke Sato
*E-mail address*: sato@shock.ifs.tohoku.ac.jp

are regarded as function of the pressure of it.

## 3. Results and Discussion

We calculate a underwater shock moving to the right, and the bubble collapse induced by the interaction of an incident shock. Fig.1 shows the initial computational grid.

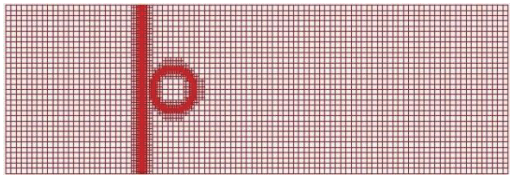

Fig. 1 Initial computational grid
(Initial grid number is 9540)

In calculations, the adaptive mesh refinement is used and the level of mesh adaptation is 5. The liquid is water and the gas is air. The water obeys the Tait equation of state and the gas is the equation of state for ideal gases. The viscosity is not considered. And Volume of fluid (VOF) method is used to tracing the interface.

Initial pressure of shock wave region is set as 3[GPa], and then the other primitive variables, density and velocity, are respectively given by equation (7) and (14). The results of the simulations of a bubble crash by the underwater shock are recorded in Fig.2

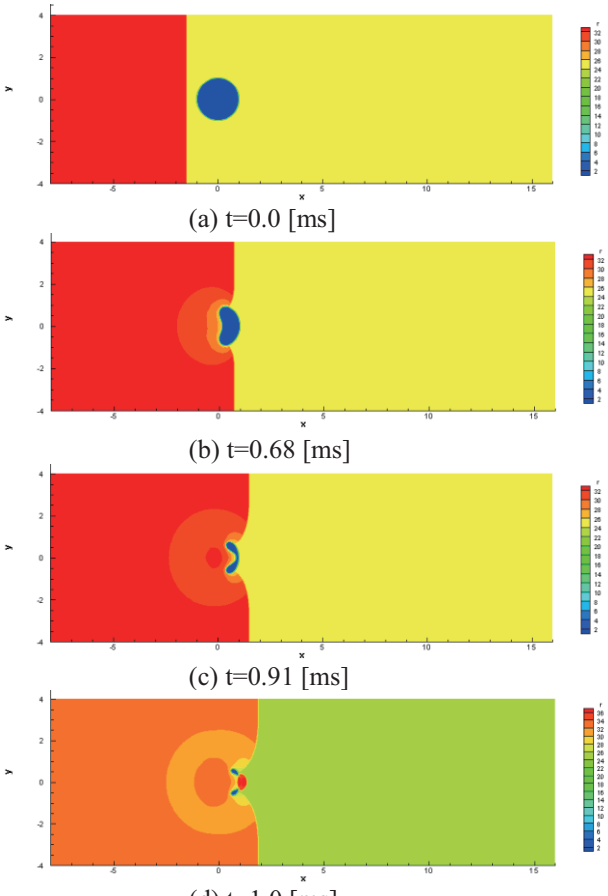

(a) t=0.0 [ms]

(b) t=0.68 [ms]

(c) t=0.91 [ms]

(d) t=1.0 [ms]

Fig. 2 Density contours in the interaction of underwater shock and an air bubble

At t=0.68[ms] and 0.91[ms], it shows that underwater shock interacts the bubble and forms instability on the interface of the bubble. At t=1.0 [ms], the shock wave crash the bubble and the bubble is divided into two bubbles. This phenomenon is caused by water jet occurring at the interface of the bubble. Fig.3 is the contour of the pressure at t=1.0[ms], and Fig.4 shows enlarged contours of pressure and velocity near the bubble of Fig.3.

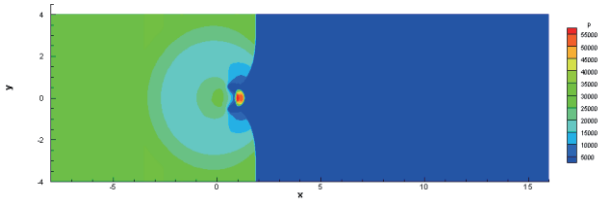

Fig. 3 Contour of the pressure at the same time of Fig.2 (d)

The maximum pressure of the water jet is about 5.5[GPa] and maximum velocity is about 3000[m/s]. But the maximum pressure area is different from the maximum velocity area.

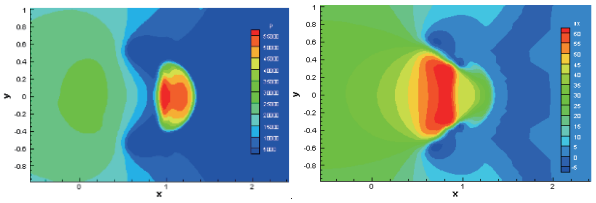

(a) pressure contour (b) velocity contour

Fig. 4 Enlarged figure near the bubble of the contours at t=1.0[ms]

## 4. Concluding Remarks

The planar underwater shock is exactly specified using the exact Riemann solver for the Tait EOS. Numerical simulation of a bubble crash by water shock is analyzed. The bubble collapse and water jet after shock loading is properly simulated.

## References


[1] M.Sun, *Symposium on Computational Fluid Dynamics (2010), A8-2*

[2] K.Kobayashi, Y.Jinbo, H.Takahira, *transaction of the JSME No.10-610 (2011)*

[3] M.J.Ivings, D.M.Causon, E.F.Toro, *Int.J.Numer. Meth. Fluids 28:395-418(1998)*

[4] E.F.Toro, *Springer, Berlin (1997)*

# Aerodynamic force oscillation of the wing with leading-edge flap at low Reynolds number

Yasuhiro Takata[1], Masato Okamoto[2]
[1]Graduate school of Kanazawa Institute of Technology
[2]Kanazawa Institute of Technology
[1, 2]Ogigaoka 7-1, Nonoichi, Ishikawa 921-8501, Japan

**ABSTRACT**

The thin flat plate attached at the leading-edge of the airfoil which we called LEF (leading-edge flap) improves the aerodynamic characteristics of the airfoil at low Reynolds number. However, it was found that aerodynamic forces acting on the airfoil with LEF oscillate at the specific angle of attack due to the leading-edge separation bubble. In case of dragonfly, the thin chin seen at the leading-edge of the wing has a thick vein. We found that the vein attached on the tip of LEF reduced the oscillation of the forces acting on the wing.

## 1. Introduction

The stream lined airfoil with leading-edge radius having large thickness shows a poor performance at very low Reynolds number less than 10,000 that corresponds to an insect wing. Because the wings of small creatures like insects are thin[1)], we proposed the leading-edge flap (hereafter, it is called LEF) attached on the leading-edge of the airfoil for improving the performance of stream lined airfoil in the low Reynolds number flow[2)], it is considered that the leading-edge separation bubble generated at the thin leading-edge is able to prevent the laminar separation at low Reynolds number[2)]. However, as seen in detail of the dragonfly wing, there is a vein, which is rather longitudinal profile, at its leading-edge as shown in Fig. 1. The purpose of the present study is to ascertain the effects of the vein attached on the tip of LEF in the aerodynamic force and moment acting on the airfoil having LEF.

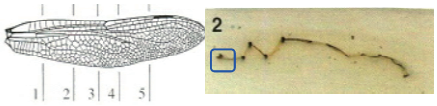


Fig. 1 The wing section of dragonfly

## 2. Experimental setup

It is known by computational fluid dynamics (CFD) and experiments of the flat plate that there are large oscillations caused by the leading-edge separation bubble in the forces acting on the flat plate at certain angle of attack[3)]. In the present study, the fluid dynamic forces and pitching moment acting on the airfoil were studied through the water channel tests at very low Reynolds number as shown in Fig. 2, because it is easy to get the oscillation of the forces and moment due to small frequency. The three components balance system comprised of a load measuring device and the stepping motor for changing the angle of attack was installed on the wing model set in the water flow. The load measuring device was made from some aluminum blocks on which attached the strain gauge; the lift $l$, the drag $d$, and the pitching moment $m$ acting on the wing model were measured. For details of the water channel tests, please refer to the ref. 4. Further, the streak line around the airfoil was visualized by using the comb having thin teeth on which the aqueous paint was painted, and it was photographed with the shutter speed of 1/160 of a second.

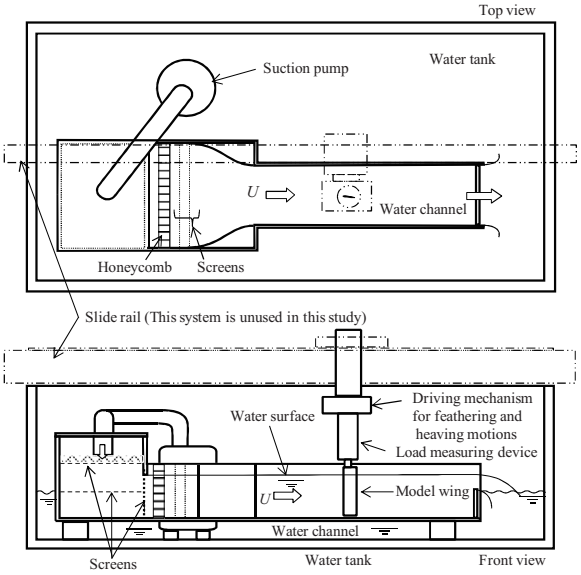


Fig. 2 Water channel experimental equipment

Figure 3 shows the wing section profile used in this study: airfoil 1 called Ishii airfoil made for the hand launch glider, airfoil 2 having LEF at the leading-edge of airfoil 1, airfoil 3, 4 and 5 having LEF with the vein of various diameters. The wing models were made of the synthetic resin, LEF were made of thin aluminum plates with 0.3mm (0.43%$c$) thick and 4mm (5.7%$c$) long, and the veins were made of piano wires with diameters of 1mm (1.4%$c$), 2mm (2.8%$c$) and 3mm (4.2%$c$).

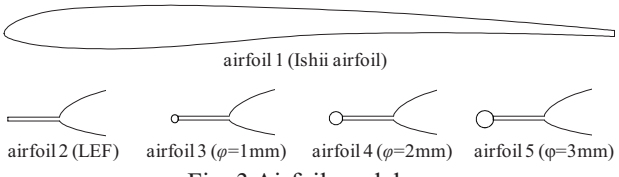


Fig. 3 Airfoil models

## 3. Results and discussion

Figure 4 shows the aerodynamic coefficients of lift, drag and pitching moment at 25%$c$, which are expressed as $C_l$, $C_d$ and $C_{m,0.25c}$ respectively, versus angle of attack

Corresponding author: Yasuhiro Takata
*E-mail address*: b6301572@planet.kanazawa-it.ac.jp

$\alpha$ of all tested airfoils at $Re$=5,600, and the straight line in the figure shows the theoretical life slope of 2π. $C_l$, $C_d$ and $C_{m,0.25c}$ of every airfoil are similar at $\alpha$<6deg. The lift slope is larger than 2π at $\alpha$>6deg, it then gradually decreases and $C_l$ reaches maximum as $\alpha$ increases largely. The non-linearity lift slope seems to be caused by the separation vortex generated at the leading-edge. Although these lift curves were seen in all airfoils, the non-linearity of the lift curve decreased as the diameter of vein attached at the tip of LEF increased. As seen in the curves of the lift-to-drag ratio $l/d$ in Fig. 4, $(l/d)_{max}$ was obtained at the angle of attack where the lift slope increases. Although $(l/d)_{max}$ of airfoil 1 increased by attaching LEF and LEF with appropriate vein, it of airfoil 5 which has vein of largest diameter decreased.

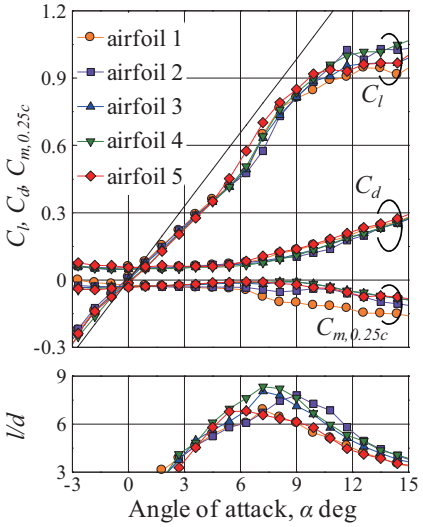


Fig. 4 Aerodynamic characteristics of the airfoils

Figure 5 shows the time histories of $C_l$ of each airfoil. Here, the time of x-axis represents the non-dimensional time as shown in the following equation:

$$t^* = \frac{U}{c}t \qquad (1)$$

where, $U$ is the flow velocity and $t$ is the time. The oscillation of $C_l$ with small amplitude of 0.1 was seen in every airfoil at $\alpha$=4.5deg, whereas the oscillation with large amplitude of 0.4 appeared in airfoil 2 at $\alpha$=9deg; the frequency was 1.6Hz that corresponds to the Strouhal number of $St$=0.22. $St$ was obtained by defining the following equation:

$$St = \frac{fc\sin\alpha}{U} \qquad (2)$$

The oscillations with the same frequency of $C_d$ and $C_{m,0.25c}$ were also seen in airfoil 2. However, these periodic oscillations were not seen in airfoil 1 and 3-5.

From these results, it was found that the thin LEF vibrated the aerodynamic forces and moment, although the LEF was effective to obtain large $C_l$ and $(l/d)_{max}$, and the vein having an appropriate diameter attached on the tip of LEF reduced without lowering the performance of the wing.

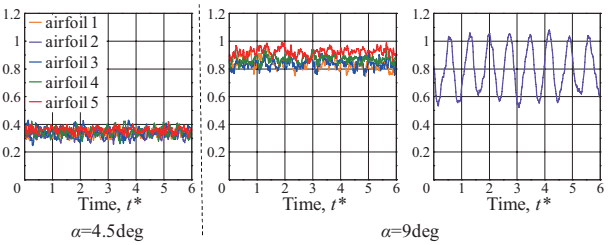


Fig. 5 Time histories of $C_l$

## 4. Flow visualization around the airfoil

Figure 6 is the comparison in the flow visualization between airfoil 2 and airfoil 4 at $\alpha$=9deg. As seen in the flow patterns of each airfoil, the small vortices were observed behind the leading-edge separation bubble. The large vortex which gathered the small vortices appeared at the rear of the airfoil 2 with the frequency similar to the oscillation of the aerodynamic forces acting on the wing, whereas in the case of airfoil 4, the large vortex with the periodic oscillation was not seen at the rear of the wing. It is considered that the vein is effective to diffuse the large vortex, which is caused by the oscillation of the aerodynamic forces acting on the wing, in the three dimensional flow.

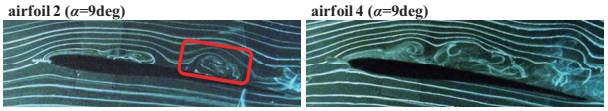


Fig. 6 Flow visualization for the airfoil

## 5. Conclusions

Following results were obtained though the water channel tests.

1) LEF attached on the leading-edge of Ishii airfoil is effective to improve the lift coefficient $C_l$ and maximum lift to drag ratio $(l/d)_{max}$, whereas the aerodynamic forces and moment have a periodic oscillation.

2) The vein with appropriate diameter attached on the LEF reduced the oscillations of the aerodynamic forces and moment.

3) The large vortex is seen on the rear upper surface of the wing, which is caused by the oscillations, and the vein makes the vortex diffused in the three dimensional flow.

## References


[1] M. Okamoto, K. Yasuda and A. Azuma, J. Exp. Biology, Vol. 199, 1996, pp. 281-294

[2] Y. Takata and M. Okamoto, The 45th JSASS Annual Meeting, 2014 (in Japanese)

[3] H. Eda and M. Okamoto, 44th Fluid Dynamics Conference/ Aerospace Numerical Simulation Symposium 2012 (in Japanese)

[4] T. Kuroda and M. Okamoto, The 2013 Asia-Pacific International Symposium on Aerospace Technology, 2013

# Numerical Analysis of the Sirocco Fan with a Small Number of Blades

Kazuki Hasuike[1], Kazuyuki Takata[1], Kiyoshi Kawaguchi[1] and Daisuke Watanabe[1]

[1] University of Toyama
3190, Gofuku, Toyama-shi, Toyama, 930-8555 Japan

**ABSTRACT**

Although the sirocco fan has the characteristics of high pressure and high quantity flow, there is a problem with the noise which easily becomes loud. The purpose of this study is to clarify the effect of the number of blades on the flow field of the sirocco fan at the design point, using numerical analysis and the tested sirocco fans which have 22 and 11 blades. As a result of the LES, for the vortex structure at $\theta$ =0, the blade tip vortex in case of $N$=22 is generated significantly when passing through the scroll tongue, but the blade tip vortex is decreasing in the case of $N$=11.

## 1. Introduction

Recently, fans have been used in order to cool the interior of electronic equipment. Especially the sirocco fan has been used in a narrow place. But the noise of the fan becomes loud easily so it's very important to reduce the noise of the fan. So far, there were a lot of attempts to reduce the noise of the fan by performing experiments. In spite of that, it didn't obtain enough knowledge about the internal flow in the sirocco fan.

On the other hand, there were attempts to examine the internal flow of the sirocco fan using numerical analysis[(1)]. The number of blades of this tested sirocco fan were 40. Moreover, K. Oe and K. Kawaguchi have examined the internal flow of the fan with 80 blades by LES (large eddy simulation)[(2)]. However, there is little knowledge regarding the sirocco fan with a small number of blades. There is an advantage that it can reduce the production cost of the sirocco fan if it has a small number of blades.

Therefore, in this study, fans used for testing have a small number of blades ($N$=22, 11). The effect of the number of blades on the flow field of the sirocco fan at the design point was found using numerical analysis (LES). This study reports it.

## 2. Tested Fan

Fig.1 shows the definition of the rotation angle and the appearance of the tested sirocco fans with 22 and 11 blades respectively. Table 1 shows the specification of the tested sirocco fan.

## 3. Method of Calculation

In this study, the FrontFlow/Blue which was developed by the Institute of Industrial Science of the University of Tokyo as software for numerical analysis was used. Therefore, the DSM was used as the SGS model.

Fig.2 shows the computational model which has an inlet, fan and outlet area. In the inlet area, there is a constant pressure with the value 0Pa. And in the outlet area, air flow was kept at a constant velocity which was obtained by performing the experiment.

Corresponding author: Kazuki Hasuike[1]
*E-mail address*: kawaguti@eng.u-toyama.ac.jp

Fig.3 shows the computational grid around the blade and the scroll tongue.

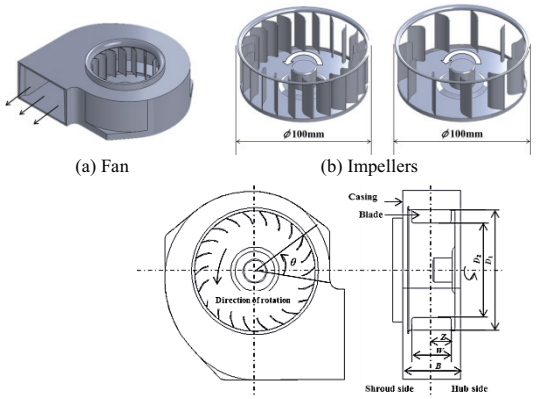


(a) Fan (b) Impellers

(c) Definition of the parameter

Fig.1 Tested fan and impellers

Table 1 Specification of tested fan

| | |
|---|---|
| Fan diameter $D_1$ | 100mm |
| Fan internal diameter $D_2$ | 76mm |
| Height of scroll $B$ | 44.5mm |
| Height of blade $W$ | 33mm |
| Number of blades $N$ | 22 |
| Rotational speed $n$ | 2400rpm |
| Maximum static pressure $P_{max}$ | 294Pa |
| Maximum flow rate $Q_{max}$ | 1.94 $m^3$ / min |
| SPL (1m) | 56dB(A) |

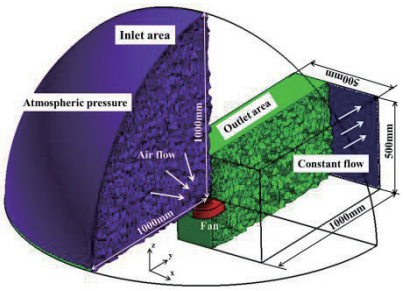


Fig.2 Computational model

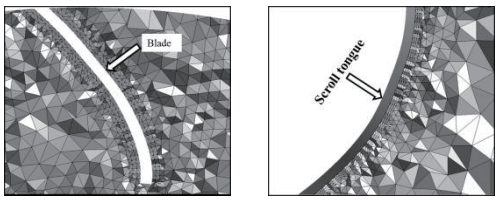


(a) Mesh around the blade (b) Mesh around the scroll tongue

Fig.3 Computational grid

## 4. Verification of the Accuracy of the Calculated Results

Fig.4 shows the comparison of the experiment with the calculation. The errors of the *P-Q* curve of the experimental values compared with the calculated values show that it is within the 10% of each graph. Therefore, it can be determined that the result of this calculation is almost accurate and can be trusted. This study considers the design points (dp22, dp11).

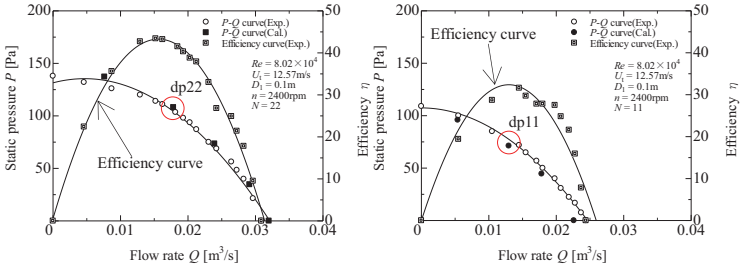


(a) *N*=22 (b) *N*=11

Fig.4 Comparison of the experiments and the calculations

## 5. Results and Discussion

From Fig.4, it could be acquired that the maximum efficiency value in the case of *N*=11 became lower from 45% to 35% compared with *N*=22.

Fig.5 and 6 show the difference of the vortex structure and the distribution of pressure at the scroll tongue and the suction side surface of each fan. In visual observation, there are no significant differences for the vortex structure at the scroll tongue. For the distribution of pressure, the pressure of the blades and the scroll tongue in the case of dp11 was reduced generally compared with dp22. Fig.7 and 8 show the difference of the vortex structure and the distribution of pressure at the scroll tongue and the pressure side of each fan. In the visual observation, the blade tip vortex is generated significantly when passing through the scroll tongue, but the blade tip vortex is decreasing in the case of dp11. It would seem that there is little effect from the adjacent blade.

## 6. Conclusion

In order to clarify the effect of the number of blades on the flow field of the sirocco fan at the design point, the LES was conducted. From the results of the LES, the following conclusions were obtained:

(1) For the distribution of pressure at $\theta$ =0, the pressure of the blades and the scroll tongue in the case of dp11 was reduced generally compared with dp22.

(2) For the vortex structure at $\theta$ =0, the blade tip vortex in the case of dp22 is generated significantly when passing through the scroll tongue, but the blade tip vortex is decreasing in the case of dp11.

## References


[1] S. Sasaki, A. Kuroda, H. Hayashi, *Faculty of Engineering in University of Nagasaki reports*, 41(76), (2011) 7-12.

[2] K. Oe, K. Kawaguchi, *Turbo-machinery*, 41(4), (2013) 216-225.


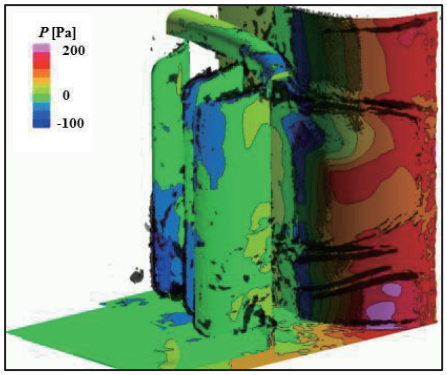


Fig.5 The vortex structure and the distribution of pressure of the scroll tongue and the suction side surface ($\theta$ =0, dp22)

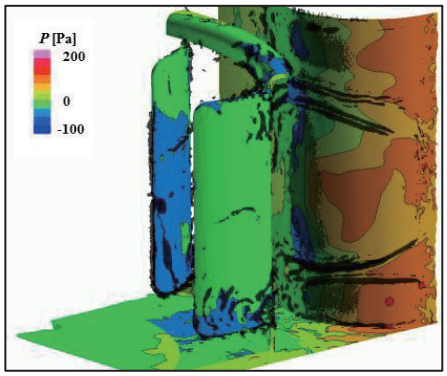


Fig.6 The vortex structure and the distribution of pressure of the scroll tongue and the suction side surface ($\theta$ =0, dp11)

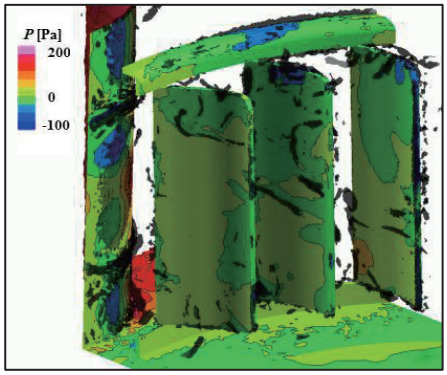


Fig.7 The vortex structure and the distribution of pressure of the scroll tongue and the pressure side surface ($\theta$ =0, dp22)

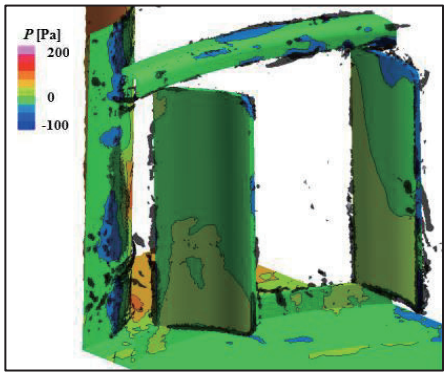


Fig.8 The vortex structure and the distribution of pressure of the scroll tongue and the pressure side surface ($\theta$ =0, dp11)

# Decomposition of Acetic Acid using Multiple Bubble Jets with Nanosecond Pulsed Discharge

Kazuma Ishihata[1], Hideya Nishiyama[2]
[1]Graduate School of Engineering, Tohoku University
6-6-01,Aramaki, Aza Aoba, Aoba-ku, Sendai, Miyagi, 980-8579, Japan
[2] Institute of Fluid Science, Tohoku University
2-2-1, Katahira, Aoba-ku, Sendai, Miyagi, 980-8577, Japan

**ABSTRACT**

Advanced water treatment technologies using OH and O radicals have been studied. The radicals can decompose persistent organic substance such as dioxins since they have strong oxidation potential. In this study, acetic acid decomposition experiments are carried out by using multiple bubble jets with nanosecond pulsed discharge. In order to obtain optimum conditions, parametric experiments are carried out for various applied voltages, frequencies, and anode geometry from the view of decomposition rate and energy efficiency.

## 1. Introduction

Recently, the polluted water treatment has become an important problem. Especially, the persistent organic pollutants such as dioxins are difficult to be decomposed by conventional water treatment process. The advanced oxidation process (AOP) using OH and O radicals which have strong oxidation potential is an effective way to decompose these substances [1]. The direct injection of OH and O radicals produced by streamer discharge inside bubbles into treated solution is very effective way to improve the decomposition efficiency of solution.

In this study, acetic acid decomposition experiments are conducted using OH and O radicals generated by multiple bubble jets with nanosecond pulsed discharge. The purpose of this study is to obtain decomposition rate and energy efficiency for various applied voltages, frequencies, and anode geometry.

## 2. Experimental setup

Figure 1 shows the schematic of experimental setup. This system consists of a nanosecond pulsed high power supply, a water reactor, electrodes, and a gas feeding tube. The gas feeding tube is set vertically in the central region of the reactor. There are five holes with 0.5 mm diameter with 10 mm space in a line along both the opposite tube side walls to produce electrically discharged multiple gas bubbles. A grounded tungsten cathode rod is centered inside the tube. A stainless plate anode is placed at the bottom of reactor and a cylindrical mesh anode is placed enclosing gas feeding tube. The flow rate of feeding Ar gas is 2.0 S*l*/min, and the volume of acetic acid solution is 200 mL and 550 mL with the initial concentration of 100 mg/L. The applied nanosecond pulsed voltage and frequency are 6-9 kV and 1000-2000 Hz respectively.

## 3. Results and discussion

Figure 2 shows the photo of Ar bubble jets with streamer discharge at applied voltage $V$ = 6 kV, frequency $f$ = 1000 Hz, flow rate $Q_{Ar}$ = 2.0 S*l*/min and solution volume is 550 mL. Figure.2(a) is a picture of streamer discharge using plate anode. This picture shows that intensity of streamer discharge increases toward the bottom of reactor. On the other hand, for cylindrical mesh anode, intensity is approximately uniform regardless of the positions of holes. These differences are caused by the difference of the distance between anode and cathode. The distance between them is uniform at Fig.2(b), hence electric field strength is also uniform.

Figure 3 shows time evolution of acetic acid concentration at $V$ = 6 kV, $f$ = 1000Hz, $Q_{Ar}$ = 2.0 S*l*/min and solution volume is 550 mL. The decomposition rate of acetic acid solution for the cylindrical mesh anode is larger than that for the plate anode, since the distance between anode and cathode is more uniform and much

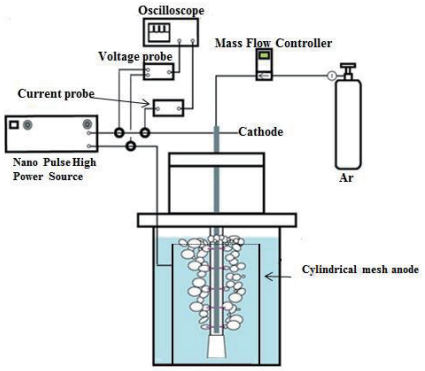


Fig.1 Schematic of experimental setup.

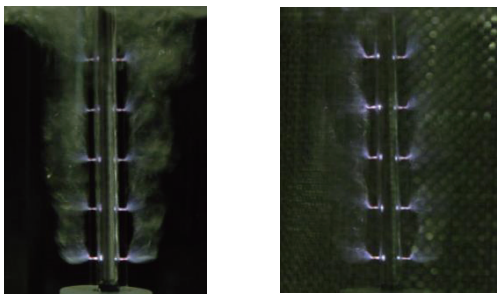

(a) (b)

Fig.2 Photo of Ar bubble jets with streamer discharge.
(a) Plate electrode, (b) Cylindrical mesh electrode.

Corresponding author: Kazuma Ishihata
*E-mail address*:ishihata@paris.ifs.tohoku.ac.jp

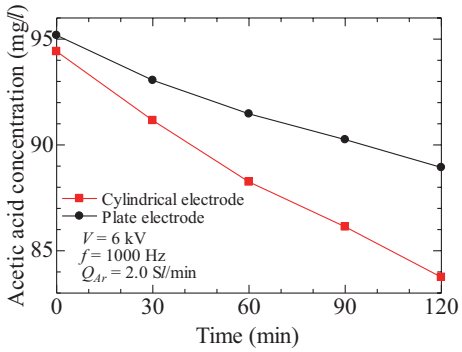


Fig.3 Time evolution of acetic acid concentration.

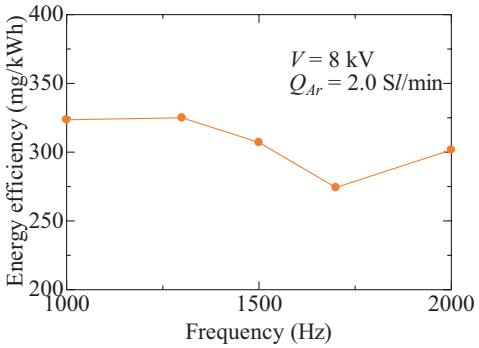


Fig.4 Dependence on frequency of energy efficiency.

power is applied. The process of decomposing acetic acid is shown in Eqs. (1)-(3). OH radicals are generated by electron impact with water molecules. Acetic acid is decomposed to $H_2O$ and $CO_2$ by OH radicals at the end of the process.

$$H_2O+e^- \rightarrow \cdot H+ \cdot OH+e^- \quad (1)$$

$$CH_3COOH+\cdot OH \rightarrow CH_3C(O)O\cdot+H_2O \quad (2)$$

$$\rightarrow CO_2+\cdot CH_3+H_2O \quad (3)$$

Figure 4 shows dependence on frequency of energy efficiency at $V$ = 8 kV, $f$ = 1000-2000 Hz, $Q_{Ar}$ = 2.0 S*l*/min. The solution volume is 200 mL, and the solution concentration is 95 mg/*l*. In this study, energy efficiency is evaluated at 50% conversion of the pollutant. Although the energy efficiency slightly decreases as frequency increases, the influence of frequency on energy efficiency is small. This result shows that self-quenching reaction of OH radicals as shown in Eq. (4) is not so enhanced in our experimental condition.

$$OH + OH \rightarrow H_2O_2 \quad (4)$$

Figure 5 shows the dependence on applied voltage of energy efficiency at $V$ = 5-9 kV, $f$ = 2000 Hz, $Q_{Ar}$ = 2.0 S*l*/min. The solution volume is 200 mL, and solution concentration is 95 mg/*l*. Energy efficiency is highest when the applied voltage is 5 kV in this study. More OH radicals are generated as the applied voltage increases. This enhances simultaneously self-quenching reaction shown in Eq. (4). Then, energy efficiency decreases with increasing the applied voltage.

Figure 6 shows time evolution of decomposed acetic acid with nanosecond pulse power source and microsecond pulse power source at $V$ = 6 kV, $f$ = 1000

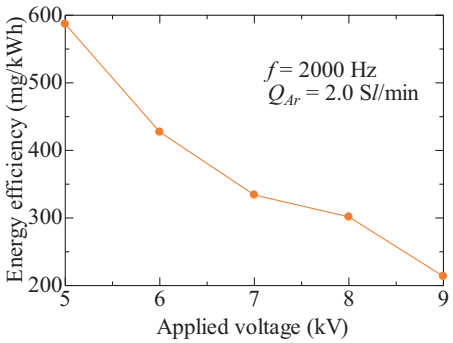


Fig.5 Dependence on applied voltage of energy efficiency.

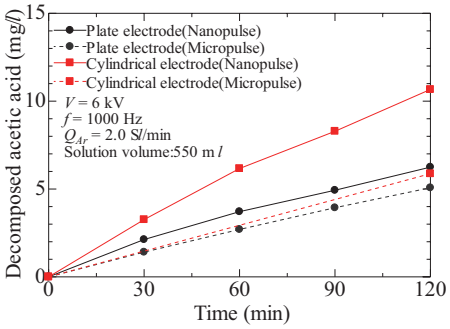


Fig.6 Time evolution of decomposed acetic acid with nanosecond pulse power source and microsecond pulse power source.

Hz, $Q_{Ar}$ = 2.0 S*l*/min. The solution volume is 550 mL, and the solution concentration is 95 mg/*l*. Plate electrode and cylindrical mesh electrode are used as anode. The decomposition rate increases when nanosecond pulse power source is used. It is because that high current flows and more OH radicals are generated by using nanosecond pulsed discharge.

## 4. Conclusions

Acetic acid decomposition experiments are carried out by using multiple bubble jets with nanosecond pulsed discharge. The conclusions are summarized as follows.

1. The intensity of streamer discharge is uniform and decomposition rate increases by using cylindrical mesh anode compared with plate anode.
2. The effect of frequency on energy efficiency is relatively small in this study.
3. The energy efficiency decreases with applied voltage. In this study, optimum applied voltage for energy efficiency is 5 kV.
4. The decomposition rate is larger for nanosecond pulsed discharge than that for microsecond pulsed discharge.

## Reference

[1] K. Sato, K. Yasuoka and S. Ishii, *IEEJ Transactions on Fundamentals and Materials,* Vol.128, 6 (2008), 401-406.

# Operating Characteristics of Electromagnetic Energy Conversion Device for Advanced Wind Energy Utilization

Akira Tanida[1] and Hidemasa Takana[2]
[1]Graduate School of Engineering, Tohoku University
2-1-1 Katahira, Aoba-ku, Sendai, Miyagi 980-8577, Japan
[2]Institute of Fluid Science, Tohoku University
2-1-1 Katahira, Aoba-ku, Sendai, Miyagi 980-8577, Japan

**ABSTRACT**

An innovative energy conversion device has been developed for efficient wind energy utilization. This device has co-axial configuration and the rotational speed of the wind turbine can be kept constant by controlling rotational torque with electrical power generation. For large magnetic field intensity, rotational torque increases by interaction between electromagnetic field and liquid metal flow. On the other hand, rotational torque decreases by lowering the interaction with decreasing magnetic field intensity. Therefore, even when torque increases with wind velocity, the turbine can be operated at a constant rotational speed by controlling magnetic field intensity.

## 1. Introduction

The growing attention has been paid to the renewable energy without $CO_2$ emission for establishes the low carbon society. Among other renewable energy sources, the demands for wind energy have been increasing worldwide [1].

In the conventional wind turbines, a constant power output is obtained by controlling the pitch angle of the turbine blades to decrease the angle of attack in the case of excessive wind velocity [2]. Therefore, if this excessive wind energy can be utilized at a constant rotational speed without changing the pitch angle, the rated power operation can be possible with enhanced efficiency. In order to realize further utilization of wind energy during rated power operation even with increasing wind velocity, an innovative electromagnetic energy conversion device has been proposed in this study.

This device has co-axial configuration and the rotational speed of the turbine can be kept constant by controlling rotational torque with electrical power extraction from excessive wind energy. In this study, the power generation and torque controlling characteristics of the developed prototype have been experimentally clarified in detail.

## 2. Experimental Systems

Figure 1 shows the cross sectional view of the developed co-axial electro-magnetic energy conversion device for wind turbine. The U-alloy as a liquid metal is filled between 60 mm diameter of rotational shaft and 80 mm inner diameter of outer ring electrode, both made of copper. The liquid metal in the device is driven in the azimuthal direction by the electronically insulated propellers attached to the rotating shaft at every 90°. The U-alloy is the alloy mainly composed of tin and bismuth, and it has very low melting point of 289 K. The electrical conductivity and the viscosity are $2.31 \times 10^6$ S/m and 22.4 mPa·s, respectively. The axial magnetic field is externally applied by the azimuthally located neodymium magnets. The applied magnetic field is non-uniform in azimuthal direction and the maximum magnetic flux density between disk walls can be set to either 200 mT or 360mT in the channel by changing permanent magnets. According to the Faraday's law, the electromotive force of $\boldsymbol{u}\times\boldsymbol{B}$ is generated in the radially

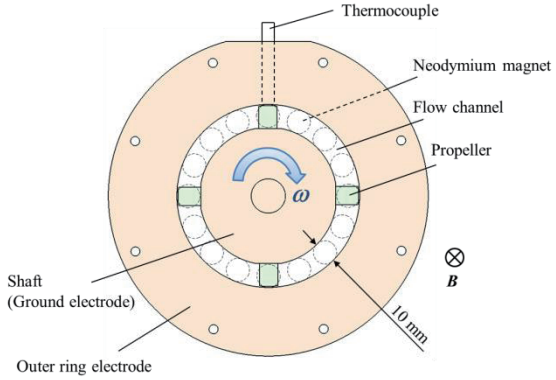


Fig. 1 Cross sectional view of the developed co-axial energy conversion device for wind turbine.

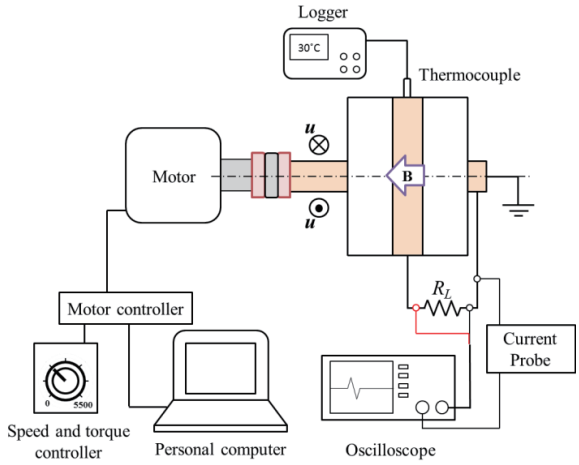


Fig. 2 Experiment systems with co-axial energy conversion device.

Corresponding author: Hidemasa Takana
*E-mail address*: takana@paris.ifs.tohoku.ac.jp

outward direction. The generated electric power is extracted by connecting an external load resistance between the rotational shaft and outer ring electrode. During power generation, the rotational torque increases due to the Lorentz force acting against the liquid metal flow. The electric power output and rotational torque can be controlled by magnetic field.

Figure 2 shows experimental systems with co-axial energy conversion device. The systems mainly consist of DC motor as a driving source, motor controller, and electric load resistance. The shaft is connected to the motor through flexible coupling. The motor and shaft are both grounded. The load voltage and current were measured for the output power. The rotational torque is obtained from motor current using current-torque characteristics.

## 3. Results and Discussion

Figures 3 (a) and (b) show the electric output power against load resistance for 200 mT and 360 mT, respectively. The output power increases with rotational speed due to increase in electromotive force for both conditions. The optimum load resistance for electric output power clearly exists. The optimum load resistance is decided by the matching between internal load resistance of liquid metal and external load resistance. The output power also increases with magnetic flux density. The optimum load resistance shifts to higher value for higher magnetic flux density. This is because the eddy current inside the liquid metal also increases with applied magnetic field and then the effective internal resistance increases. In this study, the maximum output power of 73 mW was obtained at 3.8 mΩ for 360 mT and 2000 rpm.

Figure 4 shows rotational torque with or without applied magnetic field for the rotational speed of the shaft. The load resistances are set to the optimum resistances; 1.6 mΩ for 200 mT and 3.8 mΩ for 360 mT, respectively. The required rotational torque increases by applying magnetic field and the torque becomes larger for higher applied magnetic field. The increase in the required rotational torque is due to the increase in by Lorentz force attributed to the output current (radial electric current) acting against the liquid metal flow in the azimuthal direction as a body force and also due to the increase in wall friction by Lorentz force attributed to the eddy current.

## 4. Conclusions

The results obtained in the present study can be summarized as follows.

(1) The optimum load resistance exists for electric power generation regardless of the rotating speed of the shaft. The maximum electric power output of 73 mW was obtained at 3.8 mΩ and 2000 rpm under 360 mT.

(2) The required rotational torque for a given rotational speed increases with applied magnetic field.


## Acknowledgment

Part of this work was carried out under the Collaborative Research Project of the Institute of Fluid Science, Tohoku University. Authors would like to thank Professor Hideya Nishiyama from Tohoku University for his valuable discussions.


## References


[1] GWEC, Global Wind Report 2013, http://www.gwec.net/wp-content/uploads/2014/04/GWEC-Global-Wind-Report_9-April-2014.pdf, (2014).

[2] K.E. Kathryn, L.J. Fingersh, *45th AIAA*, (2007), 1023.


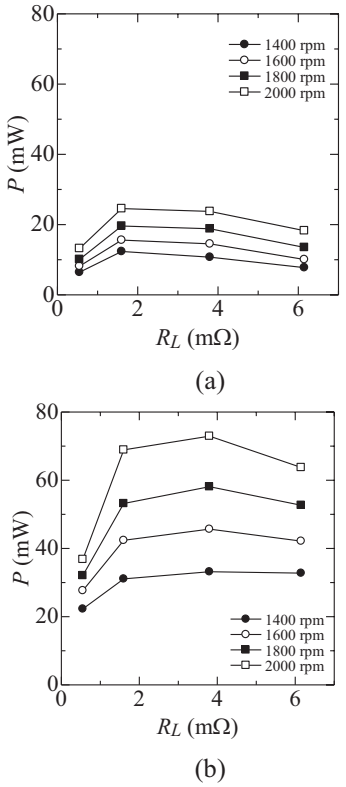


Fig. 3 Output power as a function of external load resistance for various rotational speeds under (a) 200 mT and (b) 360 mT.

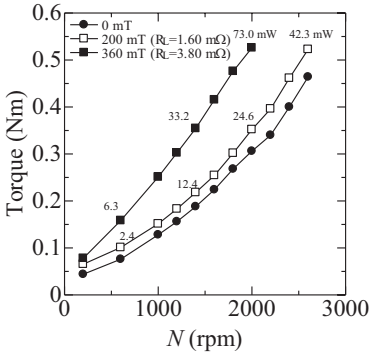


Fig. 4 Rotational torque with or without applied magnetic field for rotational speeds.

# A Comparison of One and Two Temperature Models in Cavitation Flow

Shintaro Oda[1], Mingyu Sun[2],
[1]Graduate School of Engineering Tohoku University,
6-6 Aoba, Aramaki aza, Aoba-ku, Sendai 980-8577, Japan
[2]Institute of Fluid Science Tohoku University
2-1-1 Katahira, Aoba-ku, Sendai 980-8578, Japan

**ABSTRACT**

This work compares the temperature change in the cavitation flows using two-temperature and one-temperature assumptions based on the two-fluid compressible model. The two-temperature model assumes both vapor and water have their own temperature; for the one-temperature model, the single temperature is enforced for the mixed cell using the state of thermal equilibrium. It is found that the numerical oscillations associated with the two-temperature model can be suppressed by assuming the instantaneous thermal equilibrium.

## 1. Introduction

In the analysis of multi-phase flow including a cavitation flow, some problems still exist. Concerning the cavitation analysis, the thermodynamic and the temperature non-equilibrium effects are not well-investigated. Thermodynamic effects play an important role in the cavitation dynamics, especially for cryogenic fluids. Such flows are characterized by strong variations in fluid properties with the temperature. A compressible, two-phase formulation that accounts for the energy balance and variable thermodynamics properties of the fluid is often necessary.

In this study, paying attention to the temperature change of a cavitation flow, the two temperature model, which takes individual temperature of vapor and liquid phases, is compared with the one-temperature model that uses the mean temperature of the two phases.

## 2. Method

### 2.1 Lagrange Remap method

In this study, cavitating flow is calculated with the inviscid 2-pressure 2-velocity two-fluid compressible model based on the Euler equation, Calculation is performed based on the Lagrange-Remap method [1]. In Lagrange-Remap method, the state in the Euler coordinate system is assumed to be the initial state in the Lagrange coordinate system. The speed and pressure in an interface use all speed acoustic Riemann solver [1], and the value calculated by this serves as space secondary accuracy by the MUSCL method. After calculating the primitive equation in a Lagrange coordinate system using the ILU-GMRES iteration method, the conservative quantity is integrated and remapped back to the Euler coordinate system. The dynamic non-equilibrium state of two-phase flow is evaluated by following the subgrid model [2]. The equilibrium cavitation model was used. By this technique, since the two-fluid compressible model was adopted, realistic equations of state can be readily introduced. In this work the vapor phase uses the equation of state of ideal gas, and the Tait type equation of state was used for the liquid.

Corresponding author: Shintaro Oda
*E-mail address*: oda@shock.ifs.tohoku.ac.jp

### 2.2 Two and One temperature models

In the program used by this research, two-temperature of the vapor phase and the liquid phase is treated fundamentally. It was made into the two temperature model this time, temperature was equalized as follows to it, and one temperature model was built.

$$\bar{T} = \frac{m_{vapor}C_{vapor}T_{vapor} + m_{liquid}C_{liquid}T_{liquid}}{m_{vapor}C_{vapor} + m_{liquid}C_{liquid}}, \qquad (1)$$

where, C is the specific heat under constant volume of respective phase. It carried out twice in one time step. One is before calculating the initial state of a cell for the Lagrange step, and the other is conducted for the conservative state of the Lagrangian cell after one step, but before the cavitation model is applied.

## 3. Results

### 3.1 Numerical condition

Working fluid is water with flow velocity of 8 m/s at the temperature of 293 K. The NACA0015 hydrofoil at the AoA of 8deg is tested. The cavitation numbers 0.4, 0.6, and 0.8 are tested. The nearly steady non-cavitation flow was computed first, and then the result was used as the initial condition for starting the cavitation computation.

### 3.2 History of Cl and Cd

Comparison of the lift and drag coefficients for Cavitation number of σ = 0.4, 0.6, 0.8 are shown in Figs. 1-3 respectively for two temperature models.

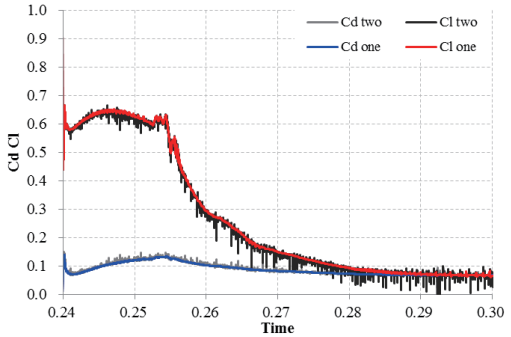


Fig. 1 History of Cl and Cd (t = 0.24-0.30 s, σ = 0.4).

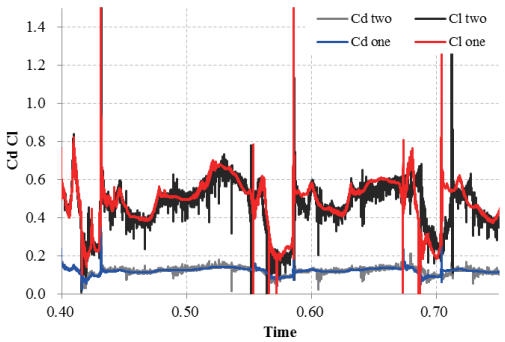


Fig. 2 History of Cl and Cd (t = 0.4-0.75 s, σ = 0.6).

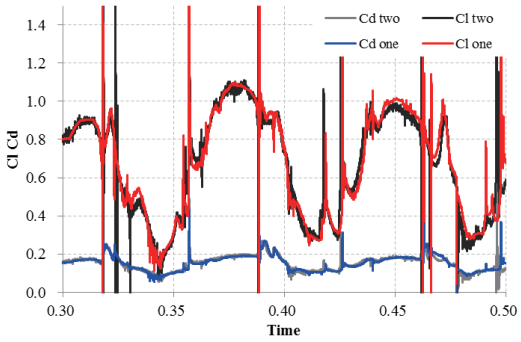


Fig. 3 History of Cl and Cd (t = 0.3-0.5 s, σ = 0.8).

### 3.2 Two temperature model

The void fraction distributions of the two-temperature model are shown in Fig. 4 for σ = 0.8. Vapor phase temperature distribution is shown in Fig. 5, and liquid phase temperature distribution is shown in Fig. 6.

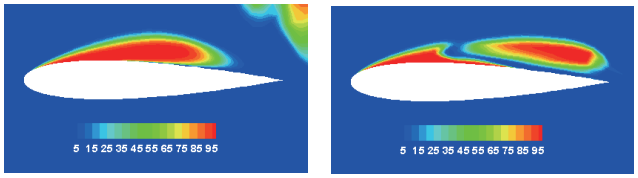


Fig. 4 Void fraction (t = 0.42 s, 0.46 s, σ = 0.8).


Fig. 5 Temperature distribution of vapor (t = 0.42 s, 0.46 s, σ = 0.8).


Fig. 6 Temperature distribution of liquid (t = 0.42 s, 0.46 s, σ = 0.8).

### 3.2 One temperature model

The void fraction distributions of one-temperature model for the same cavitation number σ = 0.8 are shown in Fig. 7, and averaged temperature distributions are shown in Fig. 8.

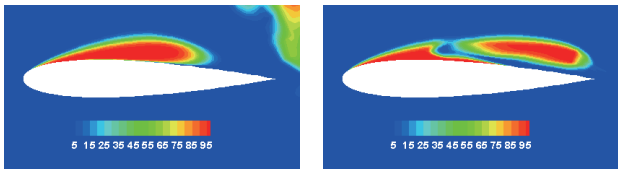


Fig. 7 Void fraction of one-temperature model (t = 0.42 s, 0.46 s, σ = 0.8).

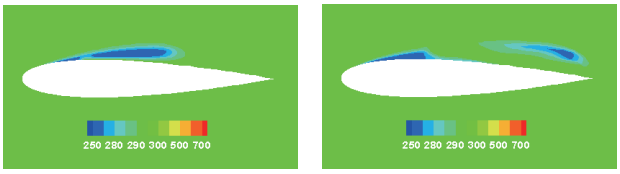


Fig. 8 Averaged temperature distribution of water and vapor (t = 0.42 s, 0.46 s, σ = 0.8).

As seen from these results, the oscillations of small amplitude observed in two-temperature model are suppressed when one-temperature model was applied. This is considered that the temperature dependency of sound speed. In the vapor phase specially, temperature dependency is high, and the difference in the temperature between the vapor phase and the liquid phase causes numerical vibration. In a two temperature model, there is a tendency for vapor temperature to change a lot, and the difference of vapor phase temperature is large compared with liquid temperature. this is because that this program not taking into consideration change of the maximum vapor pressure by a temperature change, so temperature continued risen or descending by adiabatic change in the cavity compressed or expanded. However, this influence was reduced by introducing an one temperature model that equalize the temperature of the liquid phase and the vapor phase.

## 4. Concluding Remarks

Vibrations of the lift coefficient and the drag coefficient observed in the two-temperature model is significantly suppressed in the one-temperature model, and the history of Cl and Cd become smooth. The range of temperature change in the vapor phase in the two temperature model reduces from about 400K to about 20K in the one temperature model.

## References

[1] M. Sun. An implicit cell-centered Lagrange-Remap scheme for all speed flows. : Computers & Fluids, 2013.

[2] M. Sun. A thermodynamic and dynamic subgrid closure model for two-material cells. : International Journal for Numerical Methods in Fluids, 73, 2013.

Eleventh International Conference on Flow Dynamics
October 8-10, 2014, Sendai, Miyagi, Japan

# Experimental Investigation of Interaction between Normal Shock Wave and Energy-Deposited Counter Flow

Takahiro Tamba[1], Tatsuya Harasaki[1], Nguyen Manh Tuan[1], Kenji Takeya[1], Takeshi Osuka[1], Atsushi Toyoda[1], Akira Iwakawa[1] and Akihiro Sasoh[1]
[1]Department of Aerospace Engineering, Nagoya University
Furo-cho Chikusa-ku Nagoya 464-860, Japan

**ABSTRACT**

Experimental study of the interaction between a normal shock wave and a bubble column generated by laser energy depositions was conducted on the Counter-Driver Shock Tube (CD-ST). The strength of the normal shock wave and the flow velocity where the energy is deposited were controlled independently. The strong shock wave and the dense low density column was successfully interacted, however the deformation of the normal shock wave has not been observed yet.

## 1. Introduction

One of the biggest problems to develop the next generation supersonic transport is the reduction of its operating cost. A shock wave generated in front of an aircraft flying at supersonic produces large wave drag which causes poor fuel consumption rate. In recent researches, the method to change the flow field around an aircraft by energy deposition to reduce wave drag has been investigated. Especially, laser energy deposition is an effective method since it can deposit the energy at the desired location.

Previous studies of drag reduction using laser energy deposition were investigated with single pulse and repetitive pulse lasers. Kim et al. [1] investigated the interaction between hot bubbles generated by high repetitive pulse laser and a bow shock in front of a blunt model at $M$=1.92. The deformation of the bow shock reduced the drag 21%. The results also indicated the distance between bubbles strongly affect the amount of drag reduction.

Kremeyer et al. [2] conducted a numerical study of the interaction between the hot elongated region generated by the energy deposition and the bow shock in front of models. This elongated region can be assumed as a very dense bubble column. In the simulation, the interaction generated the precursor shock and as a result the drag was reduced up to 96%.

Takeya et al. [3] investigated the deformation of a normal shock wave. The hot bubble column generated by a repetitive pulse laser was interacted with the normal shock wave in the shock tube. However, the deformation of the normal shock wave was not observed since a strong enough shock wave could not be formed for the experiment because of the facility limitation.

The objective of this paper is to investigate the deformation of the normal shock wave by the interaction with the bubble column. Therefore, a Counter-Driver Shock Tube which enables the interaction between a strong shock wave and a bubble column has been developed.

Corresponding author: Takahiro Tamba
*E-mail address*: tamba@fuji.nuae.nagoya-u.ac.jp

## 2. Counter-Driver Shock Tube (CD-ST)

Figure 1 shows the schematic of the CD-ST. The CD-ST has two Driver section at the each end of the driven section (Fig. 1a). The distinctive characteristic of the CD-ST is that it can generate Left-incident shock wave (L-iSW) and Right-incident shock wave (R-iSW) independently. Also, Left- and Right-post shock flow (L-PSF and R-PSF) are induced behind each shock wave (Fig. 1b). After the head-on collision of two incident shock waves, two transmitted shock waves are formed as the new shock wave, L-tSW and R-tSW. Subsequently they interact with the post shock flows (Fig. 1c). The transmitted shock wave and the post shock flow against the shock wave are generated by different incident shock wave, thus the interacted shock wave and the flow can be controlled independently.

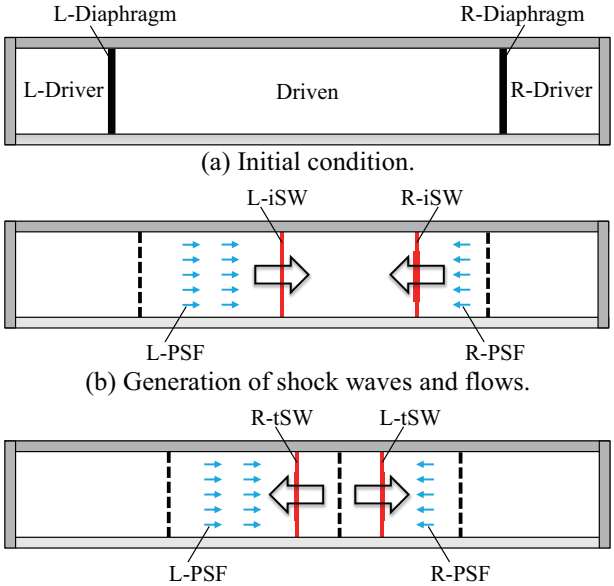


(a) Initial condition.

(b) Generation of shock waves and flows.

(c) Interactions between shock waves and flows.

Fig. 1 The schematic of Counter-Driver Shock Tube.

## 3. Experimental Setup

Figure 2 shows the experiment schematic on the CD-ST. Nd:YLF laser [wavelength, 1064 nm; repetition frequency, 10 kHz maximum; average power, 80 W maximum] is used for generating a hot bubble column in this experiment. The bubble column is generated in

Left-post-shock flow behind Left-incident shock wave by the laser pulse energy deposition (Fig. 2a). After the collision of shock waves, Right-transmitted shock wave propagates to left and interacts with the bubble column in Left-post shock flow (Fig. 2b).

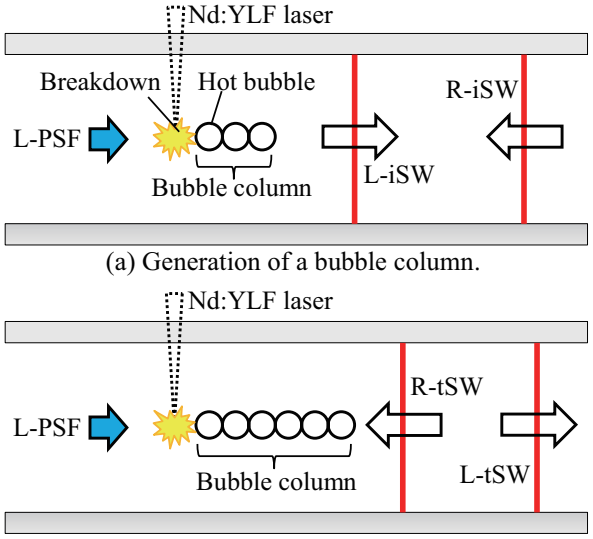


(a) Generation of a bubble column.

(b) Interaction between R-tSW and the bubble column.

Fig. 2 The interaction in CD-ST.

## 4. Experimental Result

Table 1 shows the experimental condition. By using the CD-ST, the Mach number of Right-transmitted shock wave could be raised to 1.27 while Left-post shock flow remained at 11.9 m/s. In this flow, the bubble column was generated by the laser pulse (repetitive frequency $f$=4 kHz, pulse energy $E$=7.0 mJ).

Figure 3 shows the Schlieren images of the experiment. At $t$=216 μs, the bubble column was formed by laser energy deposition. The distance between bubbles is calculated as 3.0 mm by the flow velocity of Left-post shock flow and the frequency of repetitive pulse laser. Since the distance is calculated shorter than the diameter of a bubble which is 1.8 mm, the dense bubble column was generated. Also, the bubbles deformed before Right-transmitted shock wave reached the bubble column.

From $t$=216 μs, Right-transmitted shock wave propagated to left while interacting with the bubble column. However, the deformation of the Right-transmitted shock wave was not observed. The deformation did not occur since the shock Mach number of the Right-transmitted shock wave is too small.

Table 1 Experimental condition.

| | |
|---|---|
| $M_{\text{R-tSW}}$ [-] | 1.27 |
| $u_{\text{L-PSF}}$ [m/s] | 11.9 |
| $P_{\text{L-PSF}}$ [kPa] | 60.5 |
| $f$ [kHz] | 4.000 |
| $E$ [mJ/pulse] | 7.0 |

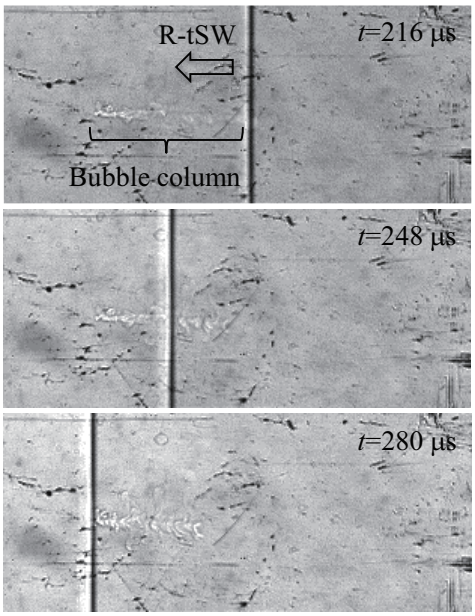


Fig. 3 Schlieren images.

## 4. Conclusion

The experiment of the interaction between a normal shock wave and a bubble column was conducted on CD-ST. The dense bubble column was generated by a repetitive pulse laser, however the deformation of the normal shock wave has not been observed yet.


## Acknowledgement

The authors would like to thank Mr. Akira Saito, Mr. Yukihiro Nakanishi, and Mr. Naoyasu Shiraki from the Technical Division, Nagoya University. This work was supported by Japan Society for the Promotion of Science (JSPS) “KAKENHI” through a Grant-in-Aid for Scientific Research, (S) 22226014, and that for Challenging Exploratory Research No. 25630390. The cellophane diaphragms was provided from Futamura Chemical Co., Ltd.


## Reference


[1] Kim, J. H., Matsuda, A., Sakai, T., and Sasoh, A., *AIAA J.* 49, 2076–2078 (2011).

[2] Kremeyer, K., Sebastian, K., and Shu, C. W., *AIAA J.* 44, 1720–1731 (2006).

[3] Takeya, K., Yokota, S., Sasoh, A., *Proceedings of 44th Fluid Dynamics Conference*, 1A12 (JSASS–2012–2015–F/A) (in Japanese).

Eleventh International Conference on Flow Dynamics
October 8-10, 2014, Sendai, Miyagi, Japan

# Premixed $CH_4/O_2/Xe$ Cellular and Tubular Flames in Slot-jet Counterflow Field

Koichi Takase, Hisashi Nakamura, Kaoru Maruta
Institute of Fluid Science, Tohoku University
Katahira, Aoba, 2-1-1, Sendai, Miyagi, 980-8577, Japan

**ABSTRACT**

The numerical investigation of the formation of premixed $CH_4/O_2/Xe$ cellular and tubular flames in slot-jet counterflow field was conducted for near-limit, low stretch rate conditions. With the isothermal wall of 300 K, wrinkled flame was obtained at the stretch rate of 3.2 $s^{-1}$ and equivalence ratio of 0.40. The wrinkled flame changed to twin tube-like flames and then a single tube-like flame with the decrease of equivalence ratio. At the stretch rate of 0.70 $s^{-1}$, a single tube-like flame which has a similarity with a flame ball in the tendency between diameter and equivalence ratio was obtained.

## 1. Introduction

The usage of oxy-fuel combustion (the combustion with $O_2/CO_2$ mixture) technology with carbon capture and storage is considered as the effective method for combustion with no exhaust of $CO_2$. However, when lean $CH_4/O_2/CO_2$ mixture is used as reactants, the Lewis number, *Le*, of mixture decreases to lower than unity. Thus, the knowledge on flammability limit of low-*Le* mixture is required for the controlling of practical oxy-fuel combustors. For considering the flammability limit of low-Lewis-number mixture, the formation of cellular flames due to the imbalanced diffusions of mass and heat becomes an important factor. Joulin and Clavin [1] theoretically predicted that cellular flames occur before the extinction. Furthermore, they indicated that the cellular instability is enhanced when the flame is suffered from the heat loss. For considering heat loss by radiation, the formation of spherical premixed flame in the quiescent mixture, "Flame ball" [2], was observed at near-limit low-*Le* mixture. However, the flammability limit theory of flame ball was investigated dependently from that of planar propagating flame. For the construction of more detailed flammability limit theory, the unified flammability limit theory between planar propagating flame and flame ball is required. For the research of unified flammability limit theory, the method using low-speed counterflow flame is considered to be effective. The transition from planar flame to ball-like flame has been obtained experimentally and numerically for $CH_4/O_2/Xe$ counterflow premixed flames at the stretch rate lower than 3.2 $s^{-1}$ [3]. Furthermore, the use of a slot-jet counterflow burner is effective method for the research because 2-D flow is available for reduced computational cost. Daou and Linan [4] theoretically predicted the formation of a single tube-like flame in the center of slot-jet counterflow field when the *Le* of the mixture is sufficiently small ($Le \leqq 0.5$). Kaiser et al. [5], observed the formation of tube-like flames and the transition from twin tube-like flames to a single tube-like flame with decrease of equivalence ratio in the slot-jet $H_2$/air (*Le*~0.3) counterflow field. This study focused on the low-*Le* counterflow flame under interaction of convective, diffusive and radiative effects by numerical computation.

Corresponding author: Koichi Takase
*E-mail address*: takase@edyn.ifs.tohoku.ac.jp

The objective of this study is the clarification on the characteristics of $CH_4/O_2/Xe$ counterflow premixed slot-jet burner flames.

## 2. Method

To identify the limits of counterflow premixed flame at low stretch rate, three-dimensional steady computations of slot-jet $CH_4/O_2/Xe$ counterflow premixed flames were conducted.

Figure 1 shows configuration of a slot-jet counterblow burner. The distance between two nozzles of counterflow, *L*, was fixed to 3.0 cm. The stretch rate of counterflow, *a*, was calculated by $2u/L$, where *u* shows the flow velocity at the inlet of mixture. Slip-wall conditions at boundary walls ($y = \pm 1.5$ cm) were adopted. At the walls, two kinds of thermal boundary conditions were adopted; adiabatic wall condition and the isothermal wall, $T_w$, of 300 K, which is the same value with the temperature of unburned mixture, and the effect of wall heat loss on the formation of cellular flame was investigated. As a diluent of mixture, Xe was selected in the present study to obtain the mixture with $Le < 1$. The ratio of molar fraction of $O_2$ to that of Xe was fixed to 0.141 (*Le*~0.5). FLUENT 14.5 were used for the 3-D computations. The one-step overall irreversible reaction proposed by Westbrook and Dryer [6] was used. Discrete ordinate method and Weighted Sum of Gray-Gas Model was used for the calculation of radiative heat transfer.

## 3. Results and Discussion

At the equivalence ratio, $\phi$, of 0.40 and $a = 3.2$ $s^{-1}$, as shown in Fig. 2, planar flames is obtained in the adiabatic wall case. Whereas, wrinkled flame is obtained in the case of $T_w = 300$ K. This difference indicates that the formation of cellular flame is enhanced by heat loss. Thus, the discussion below is focused on the case of $T_w = 300$ K.

At the case of $T_w = 300$ K, the flame shape changed with the decrease of equivalence ratio, as shown in Fig 3. At $a = 3.2$ $s^{-1}$, wrinkled flames were obtained at $\phi = 0.40$, as described previously. However, the wrinkled flame separated into twin tube-like flames at $\phi = 0.38$ and a single tube-like flame was obtained at $\phi = 0.37$.

At lower stretch rate condition ($a = 0.70$ $s^{-1}$), a single tube-like flame was obtained. The diameter of tube-like flame in the *y* direction decreased with the decrease of

equivalence ratio, as shown in Fig 4. At lower equivalence ratio, the smaller diameter of tube-like flame was obtained. This flame response corresponds qualitatively that the radius of flame ball decreases with the decrease of equivalence ratio. Therefore, a tube-like flame obtained at low-stretch-rate region is considered to have the relationship with flame ball.

## 4. Concluding Remarks

The numerical investigations about the low-speed $CH_4/O_2/Xe$ ($Le$~0.5) slot-jet counterflow premixed flames have been conducted. The findings are as follows.

1. At $\phi$ = 0.40 and $a$ = 3.2 $s^{-1}$, the cellular flame shape was obtained when the heat loss through the burner walls were considered.
2. At $T_w$ = 300 K and $a$ = 3.2 $s^{-1}$, the shape of flame changed from wrinkled flames to twin tubular flames and then a single tubular flame with decrease of equivalence ratio from 0.40 to 0.37.
3. The single tube-like flame obtained at $a$ = 0.70 $s^{-1}$ has qualitative correspondence with the flame ball in the point of diameter.

## References


[1] G. Joulin, P. Clavin, *Combust. Flame,* 35 (1979) 139–153.
[2] P. Ronney, *Combust. Flame*, 82 (1990) 1–14.
[3] K. Takase, X. Li, H. Nakamura, T. Tezuka, S. Hasegawa, M. Katsuta, M. Kikuchi, K. Maruta, *Combust. Flame*, 160 (2013), 1235–1241.
[4] J. Daou, A. Linan, *Combust. Flame*, 118 (1999) 479–488.
[5] C. Kaiser, J-B. Liu, P. Ronney, paper 2000–0576. *Aerospace Sciences Meeting and Exhibit*, 38 (2000).
[6] C. K. Westbrook, F. L. Dryer, *Combust. Sci. Technol*, 27 (1981) 31–43.


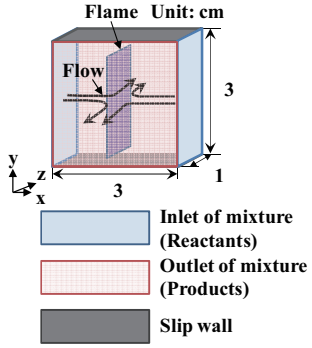


Fig. 1 Configurations of computational slot-jet counterflow burner.

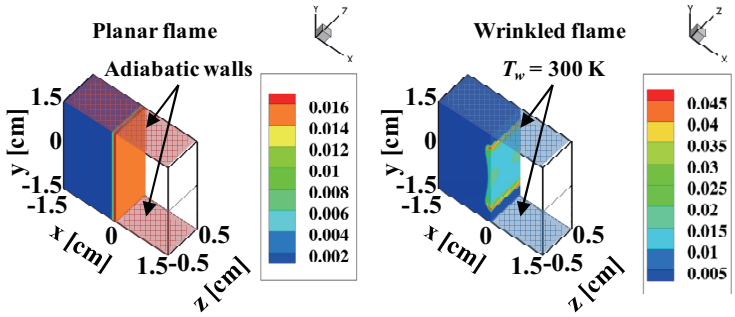


Fig. 2 Computational reaction rate contours [kmol/($m^3$·s)] in two wall boundary conditions at $\phi$ = 0.40 and $a$ = 3.2 $s^{-1}$.

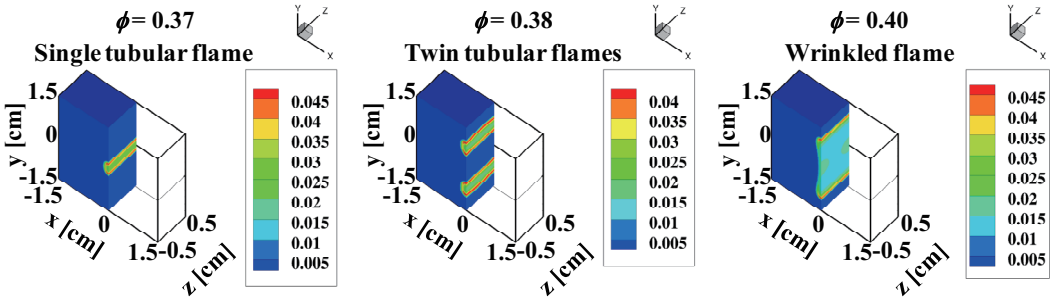


Fig. 3 Computational reaction rate contours [kmol/($m^3$·s)] in various equivalence ratios at $T_w$ = 300 K and $a$ = 3.2 $s^{-1}$.

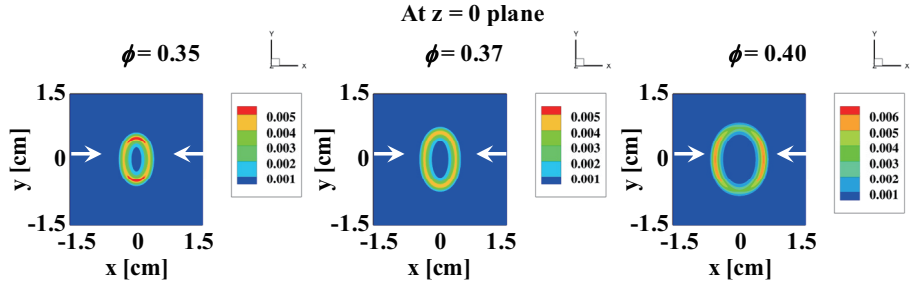


Fig. 4 Computational reaction rate contours of single tube-like flames [kmol/($m^3$·s)] at $T_w$ = 300 K, $a$ = 0.70 $s^{-1}$ and $z$ = 0.

# Effect of Oscillation frequency on $NO_X$ and Nanoparticle Emissions in High-Pressure Pulse Spray Combustion

Shota Sugawara[1], Satoki Yokoi[1], Yasuhiro Saito[1], Yohsuke Matsushita[1], Hideyuki Aoki[1], Masakazu Shoji[2]
[1]Department of Chemical Engineering, Graduate School of Engineering, Tohoku University,
6-6-07 Aoba, Aramaki, Aoba-ku, Sendai, Miyagi 980-8579, Japan
[2] Shizenkankyosangyo Co. Ltd.,
1-7-21 Hinodemachi, Miyagino-ku, Sendai, Miyagi 983-0035, Japan

**ABSTRACT**

Combustion experiments in high-pressure pulse spray were conducted to investigate the effect of oscillation frequency on OH chemiluminescence, $NO_X$ concentration, and particle size distribution. The results show that combustion reaction occurs intermittently at 100 Hz in oscillation frequency. Although the oscillation frequency of injection did not affect $NO_X$ concentration greatly, the effect of oscillation frequency on particle size distribution of PM was significant. At lower oscillation frequency, the particle number concentration increased and the size of particles shifted to larger sizes.

## 1. Introduction

In a stationary combustor (e.g., boiler), environmental pollutants such as nitrogen oxides, $NO_X$ and particulate matters, PM have been reduced by a combination of combustion technology (e.g., two-stage combustion and rich-lean combustion) and exhaust gas treatment equipments such as denitrification plant and electrostatic precipitator[1]. However, to introduce exhaust gas treatment equipments is not suitable for small combustors in terms of cost and space, and the combustion technology for small ones is disired to reduce environmental pollutants without any equipment. In diesel engines, common rail system leads to reduction of $NO_X$ and PM emissions by accurately controlling fuel injection pressure, time, and quantity. Appllying this common rail system to a stationary combustor, fuel concentration distribution of the fuel-air mixture can be controlled by high-pressure injection and injection time. Concequentry, it enables us to controll combustion behavior and can reduce $NO_X$ and PM emissions. In this study, combustion experiments in high-pressure pulse spray were conducted to investigate the impact of oscillation frequency, which is the number of injections per second with common rail injector, on OH radical chemiluminescence, $NO_X$ concentration, and particle size distribution.

## 2. Experimental

Figure 1 shows a schematic diagram of experimental apparatus. The experimental apparatus was composed of a furnace, a blower, and a common-rail system. Table 1 shows the experimental conditions. In this study, the fuel flow rate was fixed regardless of oscillation frequency by controlling injection time. The fuel sprays were ignited by thermal radiation from the furnace wall. OH radical chemiluminescence was monitored at axial distance of 308 mm from the injector nozzle tip, using a photomultiplier tube (H10721–110, Hamamatsu photonics). The $NO_X$ and $O_2$ concentrations in the exhaust gas were also measured by a portable gas analyzer (testo350, TESTO INC.). The $NO_X$ concentration was corrected at 0% $O_2$ concentration to eliminate the effect of dilution by the excess air. Combustion gas temperatures were measured by a suction pyrometer with B-type thermocouples. The combustion gas temperature and exhaust gas concentration were recorded for a period of 20 s. For each condition, the measurements were performed three times, and the maximum values of each measurement were averaged. The particle size distribution at the exhaust was analyzed by the Scanning Mobility Particle Sizer (SMPS 3936, TSI INC.).The sheath and sample flow rates were 1.5 and 0.5 L/min, respectively. The analyzed particle size was ranged from 6.0 to 220 nm.

Corresponding author: Yohsuke Matsushita
*E-mail address*: matsushita@tranpo.che.tohoku.ac.jp

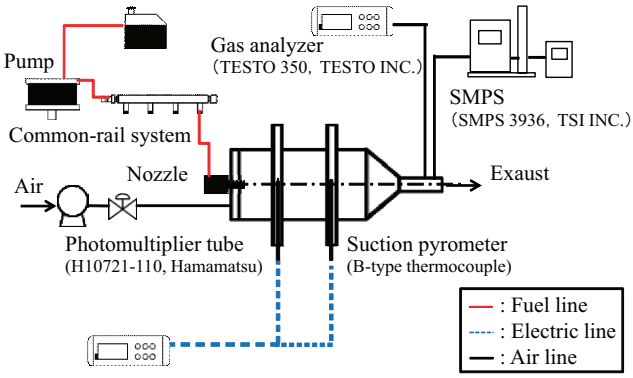


Fig.1 Experimental apparatus.

Table 1 Experimental conditions.

| Fuel | | | Diesel | |
|---|---|---|---|---|
| Fuel flow rate | [L/min] | | 0.05 | |
| Injection pressure | [MPa] | | 40 | |
| Nozzle diameter | [mm] | | 0.21 | |
| Oscillation frequency | [Hz] | 100 | 175 | 250 |
| Injection time | [ms] | 1.32 | 0.63 | 0.36 |
| Air ratio | [–] | | 1.2 | |

## 3. Results and Discussion

To investigate the effect of oscillation frequency on combustion reaction, OH radical chemiluminescence intensities were measured. Figure 2 shows OH radical

chemiluminescence from high-pressure pulse spray combustion. The detection time of OH radical chemiluminescence tended to be shorter with a decrease in oscillation frequency. When the oscillation frequency is low, the fuel quantity per injection and injection interval of fuel increase. Consequently, OH radical chemiluminescence was detected intermittently because combustion reaction occurred intermittently due to an increase in injection interval.

The effects of oscillation frequency on the maximum combustion gas temperature and $NO_X$ concentration are shown in Table 2. The maximum temperatures for each condition were 1500°C or lower in which thermal $NO_X$ was not formed. Hence, it is suggested that most $NO_X$ formed in the present experiment is prompt $NO_X$. Although the effect of oscillation frequency on $NO_X$ concentration was small, $NO_X$ concentration was slightly reduced at 250 Hz in oscillation frequency. This is because mixing of fuel and air was enhanced due to reducing the amount of fuel per injection at 250 Hz. Therefore, prompt $NO_X$ produced in the fuel-rich region was inhibited.

Figure 3 shows particle size distributions in the exhaust gas. The peak of the particle size distribution appeared around 10 and 80 nm in diameter regardless of oscillation frequency. In general, particles around 10 nm in diameter are called volatile particles, and the particles are formed by the condensation of unburnt fuel vapor in sampling. As described in Kittelson [2], particles around 80 nm in diameter are mainly soot produced from pyrolysis of fuel vapor. The number concentration of particle around 80 nm in diameter increased at lower oscillation frequency. This is attributed the fact that fuel-rich region was formed because the amount of fuel per injection increased with a decrease in oscillation frequency. In addition, when oscillation frequency is low, the particle diameter was large. This is because particles aggregated frequently as particle number concentration increased with a decrease in oscillation frequency. The peak of the particle number concentration was detected within 20–30 nm at 100 Hz in oscillation frequency, and a little peak was observed within 40–60 nm at 175 and 250 Hz. This results from intermittent fuel injection. As can be seen in Fig. 2, combustion reactions occur continuously at 250 Hz in oscillation frequency but that occurs intermittently at 100 Hz. At 250 Hz in oscillation frequency, soot particles could be formed and grew continuously with combustion reactions. Hence, the size of soot particle becomes relatively uniform and the peak of the particle size distribution becomes sharply. On the other hand, the production of soot with combustion reactions was intermittent at 100 Hz in oscillation frequency. Consequently, the particle size distribution becomes complicated within 20–30 nm in diameter because soot is composed of large particles produced in fuel-rich region during fuel injections and small particles produced in fuel-lean region during no fuel injections.

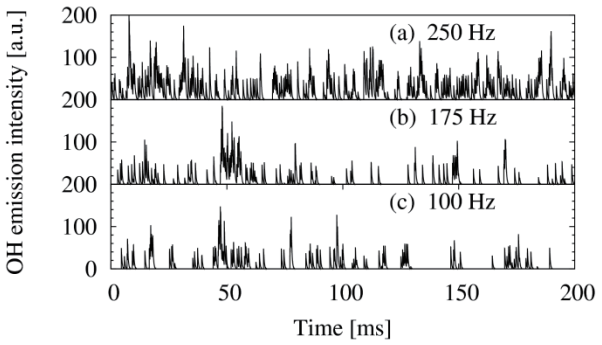


Fig. 2 Time series of OH radical chemiluminescence at axial distance of 308 mm from the injector nozzle tip.

Table 2 The effects of oscillation frequency on combustion characteristics.

| Oscillation frequency | [Hz] | 100 | 175 | 250 |
|---|---|---|---|---|
| Maximum temperature | [°C] | 1380 | 1373 | 1332 |
| $NO_X$ concentration | [ppm] | 37.0 | 38.8 | 33.4 |

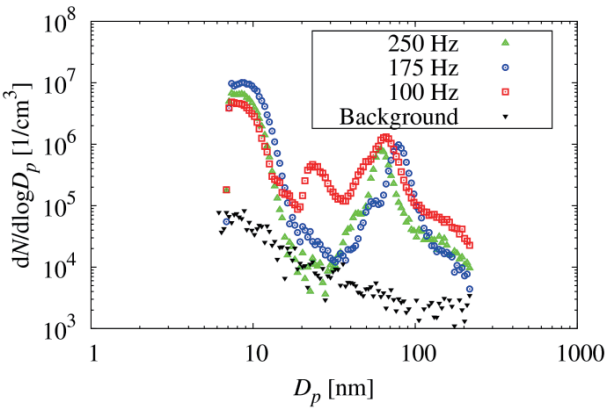


Fig. 3 Particle size distributions for each oscillation frequency.

## 4. Concluding Remarks

In this study, combustion experiments in high-pressure pulse spray were conducted, and the effects of oscillation frequency on OH radical chemiluminescence, $NO_X$ concentration, and particle size distribution were discussed. The results indicate that OH radical chemiluminescence is detected intermittently at low oscillation frequency. Although the effect of oscillation frequency on $NO_X$ concentration is not significant, particle number concentration is reduced with increasing oscillation frequency.


## Acknowledgements

This work was supported by Naito Taisyun Science and Technology Foundation, JSPS KAKENHI Grant Number 22360318, and JST Research Seeds Quest Program.


## References


[1] Okubo *et al.*, *J. Plasma Fusion Res.*, 89 (2013), 152–157.
[2] David B. Kittelson, *J. Aerosol Sci.*, 29 (1998), 575–588.

Eleventh International Conference on Flow Dynamics
October 8-10, 2014, Sendai, Miyagi, Japan

# Wide-Angle Solar Selective Absorbers Using Multilayer Structures

Makoto Yamada[1] and Atsushi Sakurai[2]

[1]Graduate School of Science and Technology, Niigata University
Niigata 950-2181, Japan
[2]Department of Mechanical and Production Engineering, Niigata University
Niigata, 950-2181, Japan

**ABSTRACT**

The purpose of this study is to clarify the phenomena inside the cermet-based solar selective absorbers using the rigorous coupled wave analysis (RCWA). We computed the reflectance of W-$SiO_2$ solar selective absorber and the power dissipation profiles. The predicted radiative properties showed good solar performance, i.e., solar absorptance levels are successfully high with wide angular range. The power dissipation profiles showed that how solar energy is absorbed in the cermet layer. This study provides the valuable guidance for designing solar selective absorbers.

## 1. Introduction

The solar selective absorber is considered a good structure for receiver of solar thermal power system. The design of high performance absorbers is possible by wavelength control, i.e., wavelength-selective absorber.

Sergeant et al. [1] and Chester et al. [2] designed dielectric-metal multilayer structures as absorbers and showed good performance. Sakurai et al. [3] designed for wide-angle and high temperature absorber.

However, physical mechanisms for solar energy absorption have not been well understood. Therefore, the purpose of this study is to clarify the phenomena inside solar selective absorbers. We compute power dissipation profiles of solar selective absorbers in each layer to investigate the behaviors of electromagnetic wave inside the cermet layer. This study provides the valuable guidance for designing solar selective absorbers.

## 2. Method

Figure 1 shows a schematic of the solar selective absorber with cermet. The structure consists of 3 types of layers, i.e., an anti-reflection (AR) coating, wavelength selective cermet layers and a highly reflective back layer. Each layer can play roles of enhancement of the light absorption for a visible light and reflecting an infrared light.

The computational condition is shown in Table 1. The silica ($SiO_2$) is selected as dielectric and tungsten (W) is selected as metal. Therefore, the cermet consists of tungsten-silica (W-$SiO_2$). The volume fraction and thickness of cermet and AR coating were optimized value by Sakurai et al. [3].

As for $SiO_2$, the dielectric function is set to 2.25 for the full spectrum, and we use the Lorentz-Drude model at 1000 K for W. The dielectric function of the cermet at each volume fraction is given by Bruggeman approximation.

To compute the structures, we employ the $S^4$ software that is developed for solving the Maxwell equation using the rigorous coupled wave analysis (RCWA) [4] method. The incident waves are assumed the transverse magnetic (TM) plane waves, and the magnitude of electric field is set to unity. In the calculation, a total of 101 Fourier components are used to represent dielectric functions, and we have confirmed these are appropriate numbers.

Corresponding author: Atsushi Sakurai
*E-mail address*: sakurai@eng.niigata-u.ac.jp

Table 1. Computational condition [3].

| Layer | Material | Volume fraction | Thickness [nm] |
|---|---|---|---|
| AR Coating | $SiO_2$ | 0.0 | 51.9 |
| Cermet 1 | W-$SiO_2$ | 0.177 | 48.8 |
| Cermet 2 | W-$SiO_2$ | 0.495 | 51.1 |
| Reflective Back | W | 1.0 | 300 |

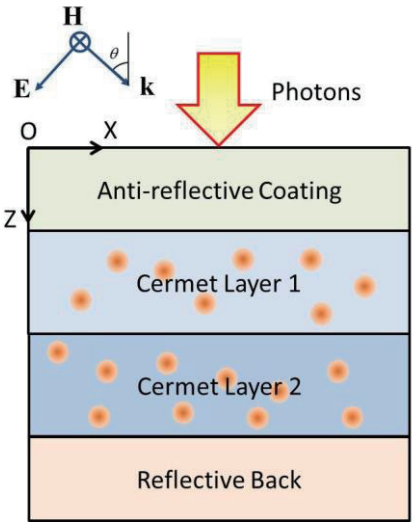


Fig. 1 Schematic of cermet-based solar selective absorber.

## 3. Results and Discussion

The first step is to check the computational validity of the present work, i.e., RCWA. As shown in Fig. 2, the result is compared with the reference [3]. The present result shows good agreement over full spectrum, hence, computational accuracy is acceptable. Furthermore, the result is near to an ideal absorber performance, which is low reflectance at visible light range and high

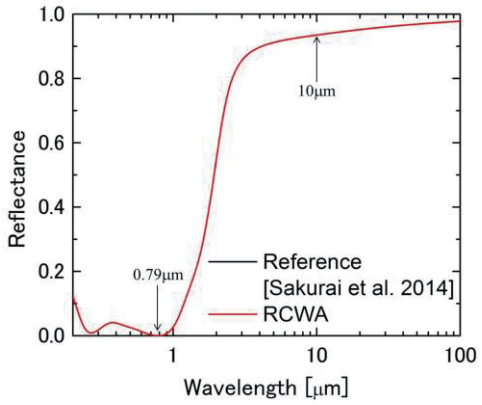


Fig. 2 Validation test of spectral normal reflectance.

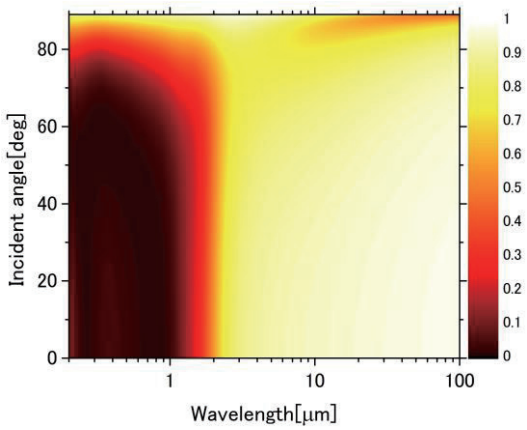


Fig. 3 Spectral directional reflectance of W-$SiO_2$ 2 layer cermet-based solar selective absorber.

reflectance at infrared light range.

The directional dependence of the reflectance for 2 layer cermet-based solar selective absorber at 1000 K is shown in Fig. 3. The angle is varied from 0 to 90 deg. This structure shows good spectral selectivity over a wide angular range.

The power dissipation profiles of 2 layer cermet-based solar selective absorber at 1000 K are shown in Fig. 4 in order to investigate the phenomena inside the cermet layers in details. Here, the power dissipation density $P$ can be expressed as [5]

$$P = \frac{1}{2}\varepsilon_0 \varepsilon'' \omega |\boldsymbol{E}|^2 . \quad (1)$$

where $\varepsilon_0$, $\varepsilon''$ and $\omega$ are the permittivity of free space, imaginary part of permittivity of materials, and angular frequency, respectively. The power dissipation density is related to the absorbed power per unit volume [W/$m^3$] or local Joule heating. Figs. 4(a) and (b) show the power dissipation profiles at 0.79 μm and 10 μm, respectively.

In the case of 0.79 μm (Fig. 4(a)), the result shows that the power dissipation is large in cermet layers. Especially, it is observed that the strong light absorption occurs at cermet layer 2. It is considered that the energy loss in cermet layers is large, therefore, the reflectance is low. On the other hand, in the case of 10 μm (Fig. 4(b)),

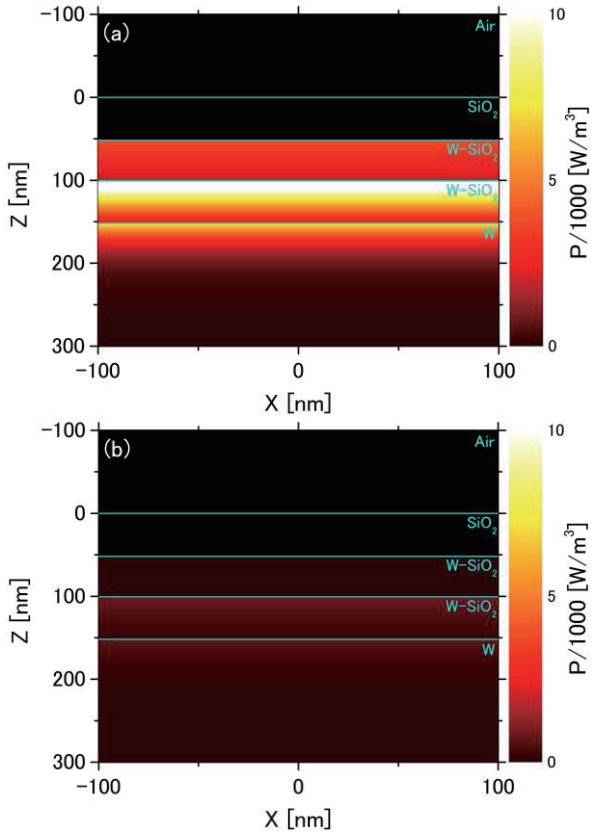


Fig. 4 Power dissipation profiles for 2 layer cermet-based solar selective absorber. (a) 0.79 μm. (b) 10 μm.

the result shows that the power dissipation is not large over all layers. Therefore, it is considered that the energy loss is little, so that the reflectance is high.

## 4. Concluding Remarks

Our conclusions are summarized as follows:

1. The present was validated by comparing it with the reference.
2. The 2 layer cermet-based solar selective absorber showed the good spectral selectivity over a wide angular range.
3. For the power dissipation profiles, strong light absorption occurred at cermet layer 2 at 0.79 μm and the energy loss in cermet layers was large, on the other hand, the energy loss was little over all layers at 10 μm.

## References

[1] N. P. Sergeant *et al.*, *Optics Express*, 17 (2009) 22800–22812.
[2] D. Chester *et al.*, *Optics Express*, 19 (2011) A245–A257.
[3] A. Sakurai *et al.*, *Journal of Quantitative Spectroscopy & Radiative Transfer*, 132 (2014) 80–89.
[4] V. Liu *et al.*, *Computer Physics Communications*, 183 (2012) 2233–2244.
[5] J. Hao *et al.*, *Phis Rev B*, 83 (2011) 165107.

Eleventh International Conference on Flow Dynamics
October 8-10, 2014, Sendai, Miyagi, Japan

# Analysis of Control Problems for Two-dimensional Model of Wave Scattering

Alexey Lobanov[1], Valeriy Sosnov[2]
[1]Institute of Applied Mathematics FEB RAS
7, Radio St., Vladivostok, PrimorskyKrai, 690041, Russia
[2]Far Eastern Federal University
8, Suhanova St., Vladivostok, PrimorskyKrai, 690950, Russia

**ABSTRACT**

Control problems for 2-D Helmholtz equation under mixed boundary conditions for total field are considered in unbounded domain with partially coated boundary. These problems are associated with acoustic cloaking. Dirichlet boundary condition is given on one part of the boundary and the impedance boundary condition is given on another part of the boundary. The role of control in control problem under study is played by surface impedance. Solvability of control problem is proved and optimality system is derived.

## 1. Introduction. Statement and solvability of the boundary value problem

In this paper we consider time-harmonic acoustic waves in an infinitely long cylindrical waveguide with bounded cross section $\Omega$. It is assumed that domain $\Omega$ is subset of $R^2$ and the boundary $\Gamma$ of the domain $\Omega$ is Lipshitz and consists of two parts $\Gamma_D$ and $\Gamma_I$ whichare disjoint, relatively open subsets on $\Gamma$. We also assume that boundary conditions of Dirichlet and impedance type are specified on uncoated part $\Gamma_D$ and coated part $\Gamma_I$ of the boundary $\Gamma$, respectively. Let $\nu$ denote the unit outward normal vector defined almost everywhere on $\Gamma$. It is well known that the two-dimensional direct scattering problem in this situation is described by the 2-D Helmholtz equation

$$\Delta u + k^2 u = 0 \quad \text{in} \quad \Omega, \tag{1}$$

with mixed boundary conditions

$$u = 0 \quad \text{on} \quad \Gamma_D, \quad \frac{\partial u}{\partial \nu} + ik\lambda u = g \quad \text{on} \quad \Gamma_I. \tag{2}$$

Here $\lambda$ is a surface impedance on the part $\Gamma_I$ of the boundary $\Gamma$, $k$ is a positive wave number, $g$ is a function defined on $\Gamma_I$. Boundary condition on $\Gamma_I$ implies that the normal component of vibrational velocity is proportional to acoustic pressure. We shall refer to problem defined by (1) and (2) as Problem 1.

The goal of this paper is analysis of control problems connecting with solving cloaking problems for electromagnetic or acoustic fields. Beginning with pioneering paper by J. Pendry et al. [1] the large number of publications was devoted to solving of problems of constructing cloaking shells (see, e.g., [2, 3] and references therein). In cited papers cloaking effect is achieved due choice of parameters of medium filling cloaking shell by solving respective inverse problems for Maxwell equations or Helmholtz equation with variable coefficients. We emphasize that technical realization of solutions obtained in these papers is connected with substantial technical difficulties.

Corresponding author: Aleksey Lobanov
*E-mail address:* alekslobanov1@mail.ru

There are several approaches of overcoming these difficulties. The first approach consists of approximation of solutions of "exact" cloaking problem by approximate solutions which admit simple technical realization. Alternative approach consists of replacing the exact cloaking problem by approximate cloaking problem of constructing "approximate" cloaking shell. This approach is based on introducing the cost functional under minimization which adequately corresponds to inverse problem of constructing approximate cloaking shell. Just this idea is used in this paper. Moreover, unlike cited papers the cloaking effect in the paper is achieved due choice of surface impedance $\lambda$ entering into the second boundary condition in (2). The details of this approach can be found in [4, 5, 6, 7]. For realization of this purpose we formulate and study control problem for model (1).

We shall use Sobolev space $H^1(\Omega)$. Denote by $X$ the subspace $H^1(\Omega)$ of which consists of functions $v$ from $H^1(\Omega)$ which satisfy first boundary condition from (2). Now we study briefly solvability and uniqueness of solutions of direct boundary value problem defined by (1) and (2). To this purpose we multiply (1) by a function $v^*$ where $v$ is element of $X$ (we denote complex conjugate of $v$ as $v^*$ for any function or functional), then integrate over $\Omega$ and apply Green's formula. We obtain

$$a_0(u,v) + ik(\lambda u, v)_{\Gamma_I} = (g,v)_{\Gamma_I}. \tag{3}$$

Where

$$a_0(u,v) = (\nabla u, \nabla v) - k^2(u,v),$$

$$(u,v) = \int_\Omega u v^* dx, \quad (g,v)_{\Gamma_I} = \int_{\Gamma_I} g v^* d\sigma. \tag{4}$$

We call a solution $u$ of problem (3) a weak solution of Problem 1. Using the theory developed in [7] we can prove the following theorem.

Theorem 1. Let $\lambda$ be an element of $L^\infty(\Gamma_I)$ and $\lambda(x) \geq \lambda_0, \quad \lambda_0 > 0$ Then for any function $g$ from $L^2(\Gamma_I)$ problem (3) has a unique solution $u$ which is an element of $X$.

## 2. Statement and solvability of the control problem

The control problem under study consists of

minimization of certain cost functional depending on the state u and an unknown function (control) satisfying the state (1) and (2). As the cost functional we choose one of the following:

$$I_1(u)=\int_Q |u-u_d|^2\,dx,\quad I_2(u)=\int_{\Gamma_r} |u-u_d|^2\,d\sigma.$$

Here $u_d$ is an element of $L^2(Q)$ (or $u_d$ is an element of $L^2(\Gamma_r)$) which models the acoustic field measured in some subdomain $Q$ of domain $\Omega$ or on the boundary $\Gamma_r$ of the disc $B_r$ of the radius $r$ such that $B_r$ is subdomain of $\Omega$.

Now we are able to state and study our control problem. We shall assume that control $\lambda$ is changed over certain set $K$. More precisely, it is assumed that the following conditions are satisfied:

(j) $\Gamma$ belongs to $C^{0,1}$, $\Gamma_I$ belongs to $C^{1,1}$; $\alpha_0>0$; $K$ is subset of $H^s_{\lambda_0}(\Gamma_I)$ which contains functions $\lambda$ which satisfy $\lambda(x)\ge\lambda_0$; $K$ is non-empty convex closed set where $s>1/2,\ \lambda_0>0$.

Rewrite the weak formulation of Problem 1 in the form of the operator equation $G(u,\lambda,g)=0$. We consider the following constrained minimization problem:

$$J(u,\lambda)=\frac{\alpha_0}{2}I(u)+\frac{\alpha_1}{2}\|\lambda\|^s_{\Gamma_I}\to\inf,$$
$$G(u,\lambda)=0,\ (u,\lambda)\in X\times K. \qquad (5)$$

Using the mathematical theory of [7] one can prove the following theorems.

Theorem 2. Let under assumptions (j), $\alpha_1>0$ or $\alpha_1\ge 0$ and $K$ be bounded set. Then control problem (5) has at least one solution $(u,\lambda)$ which is an element of $X\times K$ for $I=I_m$, $m=1,2$.

## 3. The optimality system

The following stage of analysis of control problem (5) consists of derivation of the optimality system which describes the first–order necessary conditions of extremum for our control problem. On this way the following theorem can be proved.

Theorem 3. Let under assumptions (j) an element $(u_1,\lambda_1)\in X\times K$ be a solution of problem (5) and let $I(u)$ be continuously Frechet differentiable functional with respect to the state $u$ in a point $u_1$. Then there exists a unique non-zero Lagrange multiplier $p$ which is an element of $X$ that satisfies the Euler-Lagrange equation

$$a_0(v,p)+ik(\lambda_1 v,p)_{\Gamma_I}=-(\alpha_0/2)\overline{\left\langle I'_u(u_1),v\right\rangle}\ \ \forall v\in X, \qquad (6)$$

and following variational inequality holds

$$\alpha_1(\lambda_1,\lambda-\lambda_1)_{s,\Gamma_I}+k\,\mathrm{Re}[i((\lambda-\lambda_1)u_1,p)_{\Gamma_I}]\ge 0\ \forall\lambda\in K. \qquad (7)$$

The direct problem (3), identity (6) which has the sense of an adjoint problem for adjoint state and variational inequality (7) constitute the optimality system for control problems under study. It describes necessary conditions of an extremum for control problem (5).

## 4. The numerical algorithm

Optimality system derived above can be used to design effective numerical algorithms for solving control problem (5). The simplest numerical algorithm can be obtained by applying simple iteration method for solving the optimality system. The n-th iteration of this algorithm consists of finding values $u^n$, $p^n$ and $\lambda^{n+1}$ by sequentially solving following problems:

$$a_0(u^n,v)+ik(\lambda^n u^n,v)_{\Gamma_I}=(g,v)_{\Gamma_I}\ \ \forall v\in X,$$
$$a_0(v,p^n)+ik(\lambda^n v,p^n)_{\Gamma_I}=-(\alpha_0/2)_{\Gamma_I}\left(\left\langle I'_u(u^n),v\right\rangle\right)^*$$
$$\forall v\in X,$$
$$\alpha_1(\lambda^{n+1},\lambda-\lambda^{n+1})_{s,\Gamma_I}+k\,\mathrm{Re}[i((\lambda-\lambda^{n+1})u^n,p^n)_{\Gamma_I}]\ge 0$$
$$\forall\lambda\in K. \qquad (8)$$

Direct and adjoint problems in (8) can be solved by finite element method. The authors plan to devote separate paper to study of the algorithm and to analysis of results of numerical experiments.


## 5. Acknowledgements

This work was financially supported by the Russian Foundation for Basic Research (project no. 13-01-00313-a) and by the Ministry of Education and Science of the Russian Federation (project 14.Y2.31.0003).


## References


[1] J.B. Pendry, D. Schurig and D.R. Smith, *Science*, 312 (2006), 1780.

[2] G.V. Alekseev, V.G. Romanov, *J. of Applied and Industrial Mathematics*,6 (2012), 1.

[3] A.E. Dubinov, L.A. Mytareva, *Physics-Uspekhi*, 53 (2010), 455.

[4] G.V. Alekseev, *Doklady Physics*,58 (2013), 147.

[5] G.V. Alekseev, *Computational Mathematics and Math. Physics*, 53 (2013), 1853.

[6] G.V. Alekseev, *Doklady Physics*, 58 (2013), 482.

[7] G.V. Alekseev, *Applicable Analysis*, 93 (2014), 254.

# Dynamics of Liquid Film during Phase Change in a Microchannel

Yuta Aizawa[1], Junnosuke Okajima[2], Atsuki Komiya[2], Shigenao Maruyama[2]
[1]School of Engineering, Tohoku University
6-6-04, Aramaki Aza Aoba Aoba-ku, Sendai, Miyagi 980-8579, Japan
[2]Institute of Fluid Science, Tohoku University
2-1-1, Katahira, Aoba-ku, Sendai, 980-8577, Japan

**ABSTRACT**

Achieving high heat flux cooling by evaporation in a microchannel, the liquid film dynamics was evaluated by numerical analysis with VOF (Volume Of Fluid) method in this study. Using this simulation method, dynamics of liquid film and relationship between liquid film thickness and heat transfer characteristics during bubble expansion by phase change inside a microchannel was analyzed. As a result, as bubble head speed was accelerated by phase change, liquid film became thicker and average heat transfer coefficient also became larger.

## 1. Introduction

Recently a cooling problem has been one of the bottlenecks in the improvements of electrical devices. The cooling devices with high heat flux have been expected to improve the computation performance. Most of conventional cooling devices have been utilized the forced convection of air or liquid and the natural convection of air. However, these cooling methods have limitations on the cooling performance. On the other hand, phase change heat transfer has high heat transfer coefficient of about 100 times compared with air forced convection like a fin or fan. While boiling phenomenon can evidently offer higher heat transfer coefficient, difficulty of flow boiling control makes it to be seldom used in the normal electronic device. Concertedly, miniaturization of cooling device is important object because electronic device gets small. For the reasons described above, effective utilization of microchannel is studied frequently.

In this study, a phenomenon suppressing nucleate boiling and cooling by only evaporation from liquid film was applied cooling. Liquid film thickness was determined from empirical formula of bubble growth velocity by phase change and condition suppressing nucleate boiling was reviewed by Okajima et al [1]. Additionally, using the VOF (Volume Of Fluid) method, heat flow phenomenon with bubble dynamics inside a microchannel was studied [2]. However, this numerical simulation evaluate only temperature distribution around bubble in a microchannel without acceleration derived from bubble growth. Therefore, using the VOF method considering phase change, evaporation heat transfer phenomenon is investigated in this study. By using this numerical simulation method, an influence of bubble and liquid film dynamics on heat transfer characteristics was evaluated.

## 2. Numerical Analysis

### 2.1 Analysis Method

In this study, numerical simulation program which was programmed by Kunkelmann et al. was used [3]. In this simulation code, gravity effect was neglected because the diameter of microchannel was 200 μm in this study.

Corresponding author: Yuta AIZAWA
*E-mail address*: aizawa@pixy.ifs.tohoku.ac.jp

Accordingly, governing equations are as below

$$\nabla \cdot (\rho \boldsymbol{u}) = \dot{\rho}\,, \tag{1}$$

$$\frac{\partial(\rho \boldsymbol{u})}{\partial t} + \nabla \cdot (\rho \boldsymbol{u}\boldsymbol{u}) = -\nabla p + \nabla \cdot \boldsymbol{\tau} + \sigma\kappa\nabla\alpha\,, \tag{2}$$

$$\frac{\partial(\rho c_p T)}{\partial t} + \nabla \cdot (\rho c_p T \boldsymbol{u}) = \nabla \cdot (k\nabla T) + \dot{\rho} h_{LV}\,, \tag{3}$$

where $\rho$, $\boldsymbol{u}$ and $\dot{\rho}$ are density, velocity and source term in Eq. (1). In Eq. (2), $p$, $\boldsymbol{\tau}$, $\sigma$, $\kappa$ and $\alpha$ are pressure, viscosity tensor, surface tension, curvature and ratio of air and liquid in computational grid. In Eq. (3), $t$, $c_p$, $T$, $k$, and $h_{lv}$ are time, specific heat at constant pressure, temperature and thermal conductivity, and latent heat, respectively. Then, evaporation mass during phase change is calculated as below

$$j_{\mathrm{evap}} = \frac{T_{\mathrm{int}} - T_{\mathrm{sat}}}{R_{\mathrm{int}} h_{lv}}\,. \tag{4}$$

Where $T_{\mathrm{int}}$, $T_{\mathrm{sat}}$ and $R_{\mathrm{int}}$ are temperature on bubble interface, saturation temperature, and thermal resistance on bubble interface, respectively. Evaporative mass flux $j_{\mathrm{evap}}$ was transformed to volumetric source term $\dot{\rho}$.

Equations mentioned above are solved using PISO method. The VOF method is used for interface tracking. The VOF function is advected according to advection equation.

$$\frac{\partial \alpha}{\partial t} + \nabla \cdot (\alpha \boldsymbol{u}) = \frac{\dot{\rho}}{\rho}\alpha\,. \tag{5}$$

Additionally, the CSF (Continuum Surface Force) model suggested by Brackbill is used for surface tension [4].

### 2.2 Analysis Model

Analysis of bubble growth is explained as below. Microchannel diameter and length has 200 μm and 3 mm, respectively. Then the initial bubble which has diameter of 180 μm is put on near the inlet region. The calculation domain was two-dimensional axi-symmetry and divided into 150 grids in radial direction and 1125 grids in axial direction. The boundary conditions on temperature field were uniform heat flux on the channel wall and adiabatic on the other side. Water of saturation condition at 0.1 MPa flows from inlet at 3.1 mm$^3$/s flow rate and no-

slip on the wall. Initial conditions of temperature and velocity were fully-developed temperature and velocity field, respectively. Bubble expands by given initial temperature distribution and heating by channel wall. The channel wall was assumed to completely wet condition. Heat flux is attempted 0.05, 0.075, and 0.1 MW/m$^2$. Calculation is continued until bubble head reaches outlet.

## 3. Results and Discussion

### 3.1 Bubble Dynamics in Microchannel

Figure 1 compares the bubble shape between initial state in Fig. 1(a) and expanded state by phase change in Fig. 1(b). The larger a bubble grows, the faster the bubble head speed becomes. This causes that bubble gets heat because of increasing surface area by bubble growth. As a result, bubble is expanded in short time. Then, liquid film formed between bubble and wall as shown in Fig. 1(b). Evaporation from this liquid film enhanced bubble growth and heat transfer.

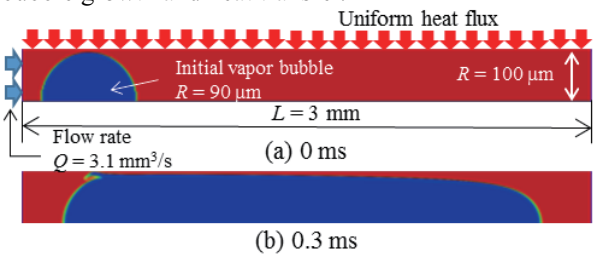


Fig. 1 Simulation results of bubble growth in a microchannel.

Figure 2 plots the temporal variations of liquid film thickness at several condition of heat flux. Horizontal axis is dimensionless time as below.

$$t/\tau = \frac{4q}{\rho_v h_{lv} D} t, \qquad (6)$$

where $D$ is microchannel diameter. In this study, the area of liquid film was determined that the gradient of bubble interface was less than 0.01. Here, interface is that ratio of air and liquid in computational grid is 0.5. When using this definition, influence of temporal change of liquid film thickness was obtained.

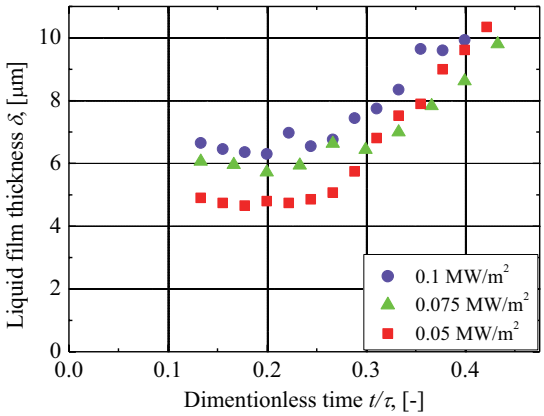


Fig 2 Relationship between liquid film thickness and time at several condition of heat flux.

As shown in Fig. 2, the variations of liquid film thickness for dimensionless time show almost same tendency in all cases. The trend is divided into two regions. Initially, liquid film thickness kept constant value. As the time advanced, it became thicker drastically. As mentioned in section 3.1, bubble head speed became faster exponentially. According to Bretherton [5], liquid film thickness depends on bubble velocity. The faster a bubble head speed, the larger viscous force become. Hence, liquid film thickness becomes thick drastically as shown in Fig. 2.

### 3.2 Heat Transfer Characteristics

Figure 3 shows relationship between average heat transfer of whole wall and time. Typically, thinner liquid film enhances heat transfer characteristics. However, this figure indicates that the average heat transfer coefficient became larger in spite of thicker liquid film. Hence, average heat transfer coefficient depends on not only liquid film thickness but also bubble length. It shows that the effect of the channel diameter on liquid film has to be considered to achieve higher heat flux cooling.

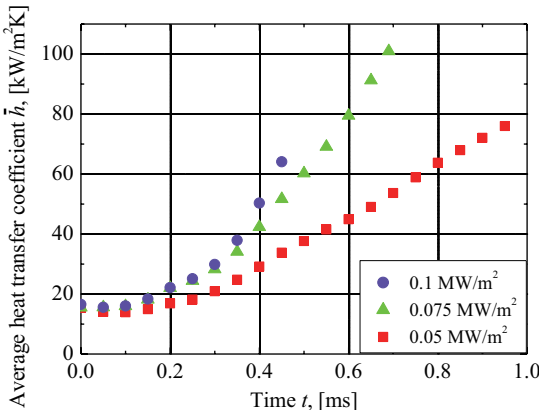


Fig. 3 Relationship between average heat transfer coefficient and time at several condition of heat flux.

## 4. Concluding Remarks

For the investigation of efficient cooling device using evaporation, dynamics of liquid film and influence on heat transfer characteristics were evaluated. The obtained results in this study are as follows:

1. Bubble head speed increased drastically because of increasing surface area.
2. Liquid film thickness has flat region at initial state and increasing region exceeding initial state.
3. Heat transfer coefficient became higher gradually.

## References


[1] J. Okajima, A. Komiya, S. Maruyama, *JSTS*, 7 (2012), 740－752.

[2] J. Okajima, K. Hou, Y. Iga, S. Maruyama, *Proc. Thermal Eng. Conference*, 12 (2012), 131－132.

[3] C. Kunkelmann, P. Stephan, *Numer. Heat Transfer, Part A*, 56 (2009), 631－646.

[4] J. U. Brackbill, D. B. Kothe, C. Zemach, *J. Comput. Phys*, 39 (1992), 335－254.

[5] F. P. Bretherton, *J. Fluid Mech.*, 10 (1961) 166－188.

# Pressure Drop Reduction and Heat Transfer Deterioration of Slush Nitrogen Flow in Horizontal Triangular Pipes

Kizuku Kurose, Jun Okuyama, Yutaro Saito, Koichi Takahashi, Katsuhide Ohira
Institute of Fluid Science, Tohoku University
2-1-1 Katahira, Aoba-ku Sendai, Miyagi 980-8577, Japan

**ABSTRACT**

Cryogenic slush fluids such as slush hydrogen are solid-liquid, two-phase fluids. There are high expectations as a functional thermal fluid. Experiments were performed using slush nitrogen to elucidate flow and heat transfer characteristics in horizontal triangular pipes. In experiments, the pressure drop reduction and heat transfer deterioration of slush nitrogen emerged in every case of different vertex orientation in pipe cross section. The velocity range for the pressure drop reduction occurrence is almost the same as that for the heat transfer deterioration occurrence.

## 1. Introduction

Today, a variety of technical fields such as space, superconductive, and energy technology has utilized advantage of cryogenic fluids. But, the cryogenic fluids have two major problems. First, low density of the fluids requires larger size of storage tanks. Secondly, low evaporative latent heat of the fluids causes easy vaporization of the liquid.

Our laboratory therefore has proposed the utilization of cryogenic solid-liquid two-phase slush fluids, which have superior properties of high-density and high cooling capacity. Furthermore, our laboratory has proposed a high-efficiency hydrogen energy system as shown in Fig. 1[1, 2]. This system is expected synergetic effects by using slush hydrogen (14K) that performs two roles in transportation of hydrogen energy and refrigerant for super conducting power transmission. For development of this system, a study of slush flow properties in triangular pipe, which has larger heat transfer area and is superior in channel integration compared to circular pipe, has been advanced.

In this paper, we report the flow properties and heat transfer characteristics of slush nitrogen (63K) flow in horizontal triangular pipes.

## 2. Experimental apparatus and procedures

Figure 2 shows the test apparatus used in this study. The apparatus is composed of a run tank, a test section and a catch tank. Slush nitrogen produced in the run tank was transferred into the test section by pressurization with helium gas. Figure 3 shows details of the test section. The cross section of the flow channel is equilateral triangular. A side length of the triangle is 20 mm and the wall thickness is 1.2 mm. The pipe is 1025 mm in length and made of oxygen-free copper. The heated section by heater wires is 800 mm in length. Experiments were performed in three patterns of pipe cross section for different vertex orientation as shown in Fig. 3 (Type-A, Type-B, Type-C).

For the measurement of pressure drop, two pressure taps were installed in the test section with length of 550 mm. Wall and bulk temperatures were measured, respectively, at six points and two points in the test section for the measurement of heat transfer coefficient.

In the experiment, liquid nitrogen (63K) flow was also examined for comparison with the slush flow. Experimental conditions are as follows: flow velocities of 0.9–4.1 m/s, solid fractions of 7–23 wt.% and a heat flux of 10 kW/m$^2$.

## 3. Results and Discussion

Figure 4 shows the measured pressure drop per unit length and the measured local heat transfer coefficient against mean flow velocity. The solid mass fraction

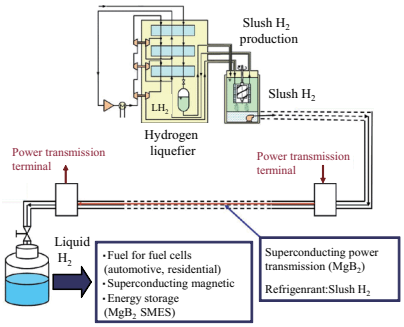


Fig. 1 High-efficiency hydrogen energy system using slush $H_2$.

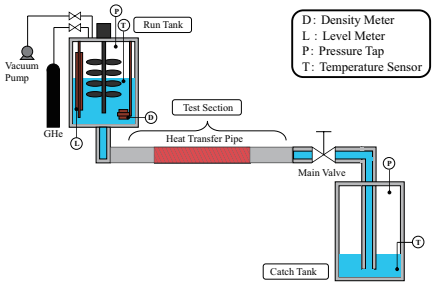


Fig. 2 Experimental apparatus for slush $N_2$ flow test.

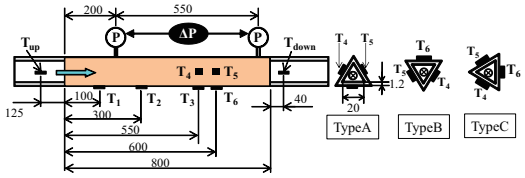


Fig. 3 Details of the test section.

Corresponding author: Kizuku Kurose
*E-mail address*: kurose@luna.ifs.tohoku.ac.jp

range of the data plotted in the figure is 7–23%. The data of subcooled liquid nitrogen is also plotted in Fig. 4. In the figure, the local heat transfer coefficient measured at the point of the temperature sensor $T_6$ is shown as an example. Equation (1) shows the definition of the local heat transfer coefficient.

$$h = q / (T_{wall} - T_{bulk}). \quad (1)$$

The solid fraction and heat flux have little effect on the pressure drop characteristic for each vertex orientations. The pressure drop for liquid nitrogen flow shows the same tendency of the Blasius equation.

Pressure drop ratio $r_{dp}$, and heat transfer ratio $r_{dh}$ defined as

$$r_{dp} = \Delta P_{sl} / \Delta P_{sub}, \quad (2)$$
$$r_{dh} = \Delta h_{sl} / \Delta h_{sub}, \quad (3)$$

are plotted against mean flow velocity in Fig. 5 and Fig. 6, respectively.

When the pressure drop ratio and the heat transfer ratio fall below unity ($r_{dp}$, $r_{dh} < 1$), the pressure drop and heat transfer coefficient of slush flow are less than those of liquid flow, which shows that the pressure drop reduction and heat transfer deterioration occur.

As shown in Fig. 5, for each velocity range of over 1.8 m/s in a case of Type-A, and over 1.6 m/s in cases of Type-B and Type-C, the pressure drop reduction is confirmed. Pressure drop ratio reduces up to 18% for Type-A, and up to 20% for Type-B and Type-C.

With the increase of mean velocity, solid particles are uniformly distributed through the pipe cross section and the flow pattern becomes a pseudo-homogeneous flow. And then solid particles migrated to the cross-sectional center of the pipe with the increased flow velocity may decrease the interference between solid particles and the pipe wall, and suppress turbulence generation within the liquid layer near the wall.

As shown in Fig. 6, in each velocity range of over 1.8 m/s for Type-A, over 1.5 m/s for Type-B and over 1.6 m/s for Type-C, the heat transfer deterioration is confirmed. Heat transfer coefficient ratio reduces up to 13% for Type-A, 21% for Type-B and 22% for Type-C. This feature was also observed at the point of the temperature sensor $T_{3\text{-}5}$.

For each vertex orientation, the velocity range for the heat transfer deterioration occurrence is almost the same as that for the pressure drop reduction occurrence. Therefore, the same mechanism as the pressure drop reduction may cause the heat transfer deterioration. However, there are differences in the velocity range among the three vertex orientation. The differences are possibly caused by the correlation between the vertex orientation and gravitational acceleration, but it is not still clear.

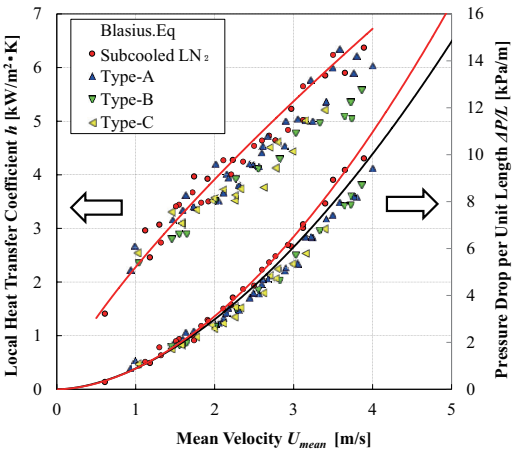


Fig. 4 Pressure drop and local heat transfer coefficient vs. mean velocity of slush $N_2$.

## 4. Conclusions

Pressure drop reduction and heat transfer deterioration in slush nitrogen flow for horizontal triangular pipes were examined and clarified in this study. For each vertex orientation, the velocity range for the heat transfer deterioration occurrence was almost the same as that for the pressure drop reduction occurrence.

## References

[1] K. Ohira, *TEION KOGAKU*, 41 (2006), 61–72.
[2] K. Ohira, *Cryogenics*, 51 (2011), 389–396.

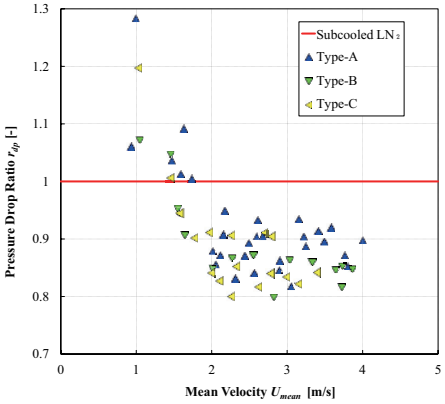


Fig. 5 Pressure drop ratio vs. mean velocity of slush $N_2$.

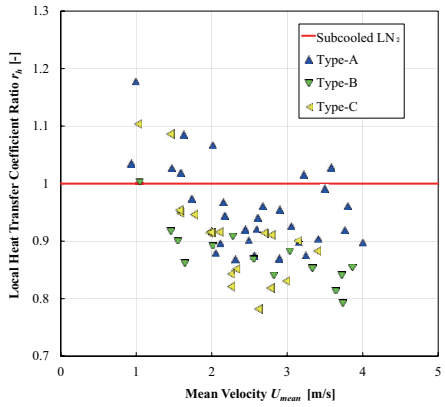


Fig. 6 Heat transfer ratio vs. mean velocity of slush $N_2$.

Eleventh International Conference on Flow Dynamics
October 8-10, 2014, Sendai, Miyagi, Japan

# Effects of Intermediate Species on Flame Instability in Turbulent Premixed Flames of Propanol Isomers at High Pressure

Shun Nakajima[1], Tomohiro Uchida[1], Syungo Soyoshi[1] , Taku Kudo[1],
Akihiro Hayakawa[1], Satoshi Kadowaki[2], Hideaki Kobayashi[1]
[1]Institute of Fluid Science 2-1-1 Katahira, Aoba-ku, Sendai, Miyagi 980-8577, Japan
[2]Nagaoka University of Technology 1603-1 Kamitomioka, Nagaoka, Niigata ,940-2188, Japan

**ABSTRACT**

Observations of turbulent premixed flame structure and numerical simulations for propane/air, n-propanol/air and iso-propanol/air flame at high pressure were performed to reveal the effect of intermediate species in flame zone. Differences of local flame surface density shown by experiments and profiles of intermediate species by numerical simulation among these mixtures indicated that $C_2H_2$ and $C_2H_4$ in flame zone constrain the intrinsic flame instability.

## 1. Introduction

Propanol and butanol are considered as next generation bio fuels because they have some advantages including their higher energy density and less $CO_2$ emission compared to ethanol, the widely used bio fuel. Although combustion characteristics are important for the usage in the practical combustors, few studies on premixed turbulent combustion of propanol and butanol at high pressure have been conducted.

In addition to its importance for bio fuel, propanol has two isomers whose thermal properties are almost identical. Veloo and Egolfopoulos[1] recently reported that the reaction process of propanol isomers are different including thermal dissociations, leading to different profiles of intermediate species in flame zone. The difference is expected to affect the intrinsic flame instability, though the Lewis number, predominant number for diffusive-thermal instability, of the mixture is almost the same.

The purpose of this study is to investigate the fundamental characteristics of turbulent premixed flames of propanol isomers at high pressure and to elucidate the effects of intermediate species on flame structure and instability. OH-PLIF method was exploited to measure local flame surface density. A numerical simulation using a two-step reaction model was used to evaluate the effect of intermediate species.1-D flame model analysis was also performed to determine which intermediate species affect the combustion characteristics in terms of flame instability.

## 2. Experimental and numerical methods

The high-pressure combustion test facility in Institute of Fluid Science at Tohoku University was used for combustion experiments at high pressure. Fuel evaporator and an air heater were installed in the high pressure chamber. Fuel was supplied through a mass flow controller. A stainless steel nozzle-type burner with an outlet diameter of 20 mm was placed in the high-pressure chamber. All tubes and the burner in the chamber were heated by flexible heaters to maintain the temperature of 343±10 K. Turbulence was generated by a perforated plate and Bunsen-type turbulent premixed flames were stabilized under constant pressure of 0.5 MPa.

In this experiment, OH-PLIF method was used to obtain instantaneous flame cross section images. These images are used to estimate mean progress variable, <c> and local flame surface density, Σ local. Here, <c> is defined as frequency that certain point was included in the burned region during certain time. Σ local is defined as flame length in 10×10 pixels in size centered at certain point assuming isotropy of the flame front structure.

The characteristics of the unburnt mixtures estimated by the numerical simulation using CHEMKIN-Ⅱ[2] based on the detail mechanism developed by Johnson[3] are shown in table 1.

Table 1. Thermal Properties of mixtures. (P = 0.5 MPa, T = 343 K, $\phi$ = 0.9)

| | Kinematic viscosity $\nu$ [$cm^2/s$] | Thermal diffusivity $\alpha$ [$cm^2/s$] | Diffusion coefficient $D_{fuel}$ [$cm^2/s$] | Lewis number $Le_{fuel}$ | Laminar burning velosity $S_L$ [cm/s] |
|---|---|---|---|---|---|
| n-Prpanol/air | 0.0361 | 0.0503 | 0.0237 | 2.12 | 24.0 |
| iso-Propanol/air | 0.0361 | 0.0504 | 0.0237 | 2.13 | 20.5 |
| Propane/air | 0.0376 | 0.0519 | 0.0285 | 1.82 | 24.8 |

The numerical simulation using a two-step-model adopts compressible two-dimensional Navier-Stokes equations with non-dimensional parameters. 1-D numerical analysis was also performed using CHEMKIN-PRO[4] with Johnson's mechanism[3] under the same condition as the combustion experiments.

## 3. Results and Discussion

The profiles of Σ local are shown in Fig. 1 for different non-dimensional turbulence intensity, $u'/S_L$. In Fig. 1a, the peak value of Σ local is in the order of iso-propanol/air, n -propanol/air and propane/air mixture. On the other hand, the difference of Σ local among the three mixtures is smaller in Fig. 1b, implying that the effect of $u'/S_L$ is more predominant in flow with stronger turbulence. The higher Σ local means that the flame surface has more finely wrinkled structure. Thus, it can be said that the magnitude of intrinsic flame instability is largest for iso-propanol/air flame followed by n-propanol/air and propane/air. These results indicate that the intrinsic flame instability of n- and iso-propanol/air

Corresponding author: Shun Nakajima
*E-mail address*: nakajima@flame.ifs.tohoku.ac.jp

flames are not equivalent, while their Lewis numbers are almost identical.

Regarding the differences mentioned above, numerical simulation using a two-step reaction model was conducted to reveal the relationship between flame instability and intermediate species. As the result of the simulation, it was indicated that certain intermediate species which has larger peak value of its mole fraction in front of reaction zone can restrain the growth rate of disturbance. Those intermediate species should have large chemical enthalpy, leading to constrain the flame instability.

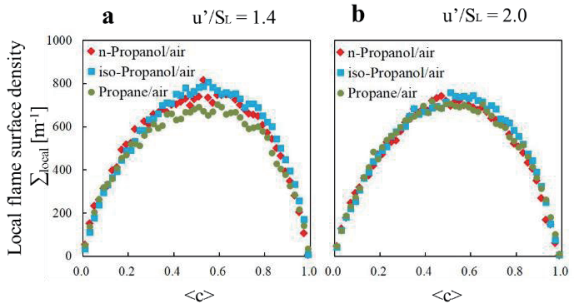


Fig. 1 Profiles of flame surface density, Σ, and mean progress variable, <c>.

Figure 2 shows the profiles of intermediate species in the three mixtures calculated by 1-D flame model simulation using detail chemistry. In this figure, origin of x coordinate is the position where flame temperature rises 1.0% against the maximum flame temperature. The vertical solid line indicates the position of the maximum heat release rate of the flames. It is seen clearly that the mole faction of $C_2H_4$ is larger in propane/air and n-propanol/air mixtures. Nevertheless, mole fraction of $C_3H_6$ in iso-propanol/air mixture is notably larger compared to other two mixtures, indicating profiles of intermediate species vary greatly in each mixture. Thus, $C_2H_4$ and $C_3H_6$ can be the intermediate species which correspond to the flame stability analysis mentioned above.

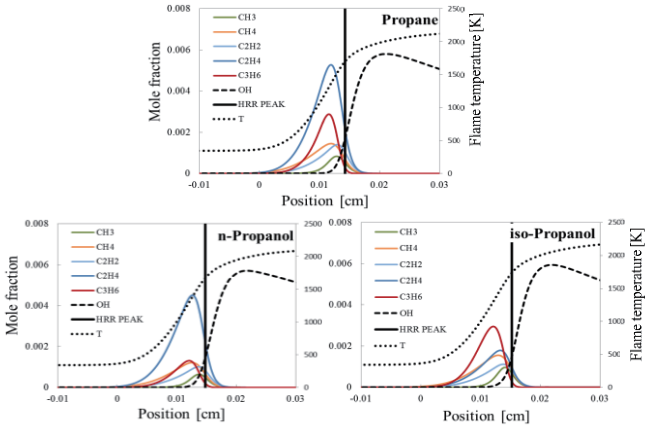


Fig. 2 Profiles of intermediate species in flame zone of the three kinds of mixtures.

To deal with the chemical enthalpy of the intermediate species, nominal heat release, $H_c$, for each species was evaluated. In this study, $H_c$ is defined as the product of mole fraction shown in Fig. 2 and enthalpy of formation of each intermediate species. It was found that $H_c$ by C2 species, i.e., $C_2H_2$ and $C_2H_4$, is remarkably larger in all mixtures. The comparison of $H_c$ by C2 species is shown in Fig. 3. It was also confirmed that the peak value of $H_c$ shown in Fig. 3 is largest for propane/air flame, followed by n-propanol/air and iso-propanol/air flames. It is of great interest that this order is the opposite order of the magnitude of Σ local, which is an indicator of the strength of intrinsic flame instability.

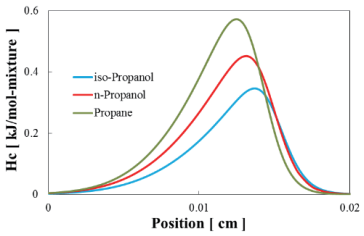


Fig. 3 Comparison of $H_c$ profiles for C2 species.

These findings reinforce the idea that different profiles of intermediate species in flame zone affect the intrinsic flame instability, leading to different flame structures including wrinkled laminar flames.

## 4. Concluding remarks

Propane/air, n-propanol and iso-propanol/air premixed flames at high pressure were experimentally investigated and numerically analyzed. The obtained findings are as follows.

1. The difference of local flame surface density of propanol isomer flames was observed. Iso-propanol/air flame has more finely wrinkled flame region than that of n-propanol/air flame. For stronger turbulence intensity, the effect of turbulence becomes predominant resulting in smaller difference between the two isomer flames.
2. Numerical simulation using a two-step reaction model revealed the effect of intermediate species on intrinsic flame instability. The intermediate species with larger peak value of its mole fraction upstream of the heat release zone highly affects the growth rate of disturbances.
3. 1-D numerical analysis using detail chemistry clarified that heat release by $C_2H_2$ and $C_2H_4$ in the flame zone contributes toward suppressing flame instability in the three mixtures.

## References


[1] P.S Veloo, F.N.Egolfopoulos, *Combust. Flame* 160 (2011) 501-510.
[2] R.J.Kee, Sandia Rep.,SAND (1983) 85-8240.
[3] M.V. Johnson, et.al, *Energy Fuels* 23 (2009) 5886-5898.
[4] CHEMKIN-PRO, Release 15101, Reaction Design, (2010).

Eleventh International Conference on Flow Dynamics
October 8-10, 2014, Sendai, Miyagi, Japan

# OH-PLIF Measurements of GH2/GO2 Diffusion Flames Using Higher Electron Excitation Bands

Kiyonori Takeuchi[1], Yoshio Nunome[2], Takeo Tomita[2], Taku Kudo[1], Akihiro Hayakawa[1], Hideaki Kobayashi[1]
[1]Institute of Fluid Science, Tohoku University
2-1-1 Katahira, Aoba-ku, Sendai, Miyagi 980-8577, Japan
[2]Japan Aerospace Exploration Agency
1 Koganezawa, Kimigaya, Kakuda, Miyagi 981-1525, Japan

**ABSTRACT**

OH-PLIF measurements using higher electron excitation bands such as OH (A-X) (2,0) and OH(3,0) were conducted to observe OH fluorescence for the GH2/GO2 diffusion flames intensely emitting chemiluminescence from OH(0,0) band. In the case of OH(2,0) band excitations, the fluorescence from OH(1,0) band was successfully collected and the chemiluminescence from OH(0,0) band was completely eliminated showing the possibility of OH-PLIF for rocket engines.

## 1. Introduction

The GH2/GO2 combustion has been used for the general liquefied bi-propellant rocket engines. This combustion generates much higher temperature comparing with ordinary flames. However, the optical measurement technique of species for the rocket combustion, i.e., high pressure GH2/GO2 combustion, has not been established. Recently, various laser diagnostics have been tried to measure the rocket engine combustion, and OH-Planer Laser induced Fluorescence (OH-PLIF) is one of the techniques [1]. OH-PLIF is used frequently to observe flame structures, flame temperature and radical mole concentrations. The fluorescence emitted by excited OH radical, OH $A^2\Sigma^+ \rightarrow X^2\Pi$ (0,0) is usually collected in this technique. Nevertheless, H2/O2 flames intensely emit the chemiluminescence from OH(0,0) band. When the chemiluminescence is much stronger than the fluorescence, it is difficult to collect fluorescence emitting in same bands as the chemiluminescence. The purpose of this study is to realize the OH-PLIF measurement which is unaffected by the chemiluminescence from OH(0,0) band in GH2/GO2 diffusion flames prior to GH2/LOX flame study.

## 2. Experimental Method

A schematic of the experimental apparatus is shown in Fig. 1. The laser assembly was composed of a Nd:YAG laser, a dye laser, and a frequency doubler. The dye laser was tuned around wave length 262 nm and 245 nm, which excite the Q1(4) transition in OH $A^2\Sigma^+ \leftarrow X^2\Pi$ (2,0) and (3,0) bands, respectively [2]. The energy of the laser beam emerging out of a doubler was about 12 mJ with a pulse duration of 10 ns in both excitations. The laser beam was formed in a sheet of 70 mm in hight and less than approximately 1 mm in thickness through a convex lens and cylindrical lenses and then introduced into the flame center vertically. Thus, the 2-dimentional spatial distributions of the OH fluorescence could be measured. The OH fluorescence was collected by an ICCD camera (Andor Technology, USB-iStar) through a UV lens. This camera ran with 50 ns using the gate input. Two kinds of filter, Type-A and Type-B were fitted to the UV lens.

Corresponding author: Kiyonori Takeuchi
*E-mail address*: takeuchi@flame.ifs.tohoku.ac.jp

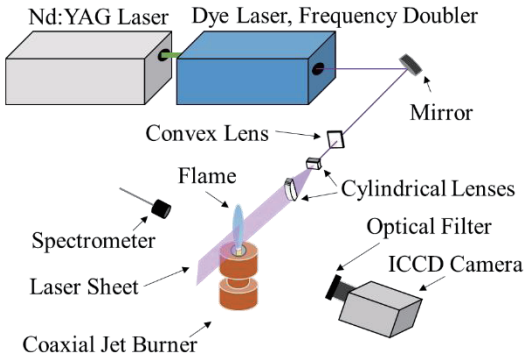


Fig. 1 Experimental apparatus.

Type-A and Type-B were composed of UG11 (SCHOTT) + HQBP0280-UV (ASAHI SPECTRA) and UG11 + UG5, respectively. These filters were used to eliminate interferences from scattered laser light. The Type-A fileter was possible to collect fluorescence from only OH(1,0) band around the wavelength of 280 nm. The Type-B filter was possible to collect fluorescence in wide band from 270 nm to 380 nm. In addition, chemiluminescence spectrum from GH2/GO2 flame was measured by spectrometer (StellarNet, Blue-Wave).

GH2/GO2 diffusion flames was stabilized by a coaxial jet burner at atmospheric pressure. The inner tube (inner diameter of 2 mm) and outer tube (inner diameter of 20 mm) used to inject GH2 and GO2, respectively. Mass flow rate ratio of GO2 to GH2 (O/F) was about 8.8.

## 3. Results and Discussion

### 3.1 OH Chemiluminescence

The spectrum of the chemiluminescence emitted from the GH2/GO2 flame is shown in Fig. 2. The broken line indicates the spectrum which is emitted from the GH2/Air diffusion flame formed by the same experimental setup. Compared to the GH2/Air flame, the GH2/GO2 flame intensely emitted the chemiluminescence from OH(0,0) band. The intensity is almost twenty five times higher than that for the GH2/Air flame.

These differences are explained mainly by the difference in flame temperatures between the GH2/GO2 and GH2/Air flames. The temperature of GH2/GO2 flame is higher than that of the GH2/Air flame. The

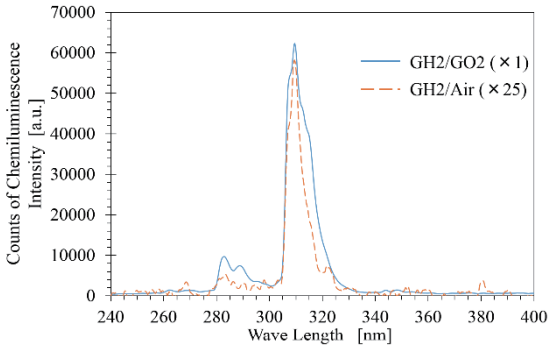


Fig. 2 OH chemiluminescence spectrum.

radiation is more enhanced for the GH2/GO2 flame. As these results, Type-A filter is effictive to measure the GH2/GO2 flame, because it is possible to eliminate intense chemiluminescence from OH(0,0) band.

### 3.2 OH-PLIF Measurements

Figure 3 shows a single shot OH-PLIF image using OH(2,0) band excitation. In this figure, the fluorescence from OH(1,0) band appeared from the burner lip to downstream. Near the burner lip, the fluorescence is located at the boundary between GH2 and GO2. In the downstream region, OH radicals observed widely due to mixing of fuel and oxidizer. Although the fluorescence intensity was weak, the flame structure was observed and chemiluminescence from OH(0,0) band was thoroughly eliminated.

The OH-PLIF image using Type-A filter for OH(3,0) band excitation is shown in Fig. 4 (a). In this figure, almost no signal of a single shot fluorescence from OH(1,0) band was obtained, while in the case of OH(2,0) band excitation could be detected. This difference is due to the differences of vibrational relaxation processes and the transition probabilities between OH(2,0) and OH(3,0) band excitations. In contrast, Fig. 4 (b) shows the result using Type-B filter for the same excitation. A weak signal could be obtained. Type-B filter collects signal over wide wave length range, thus the signal indicates fluorescence emitted from those including OH(1,0) and OH(0,0) bands.

The fluorescence intensity was commonly weak for both OH(2,0) and OH(3,0) band excitations compared to OH(1,0) band excitation. One reason for this is the absorption intensity. OH absorption lines simulated by LIFBASE [3] are shown in Fig. 5. The simulation was performed by setting the temperature to 3000 K, pressure to 0.1 MPa and using standard population value. In this figure, the vertical axis indicates absorption intensity normalized by maximum intensity within OH(0,0). The intensity of OH(2,0) and OH(3,0) band excitations are much weaker than OH(1,0) band excitations which are used typical OH-PLIF measurements. LIF is composed of two processes; first process is absorption, second process is emission. When absorption intensity is weak, LIF intensity is also weak. Although, it was difficult to collect high intensity fluorescence for a single shot OH(2,0) and OH(3,0) band excitations, multi shot integration of OH-PLIF is feasible and the experiments will be performed soon.

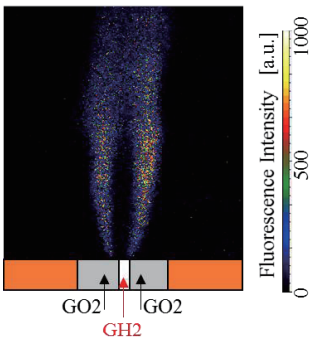


Fig. 3 OH-PLIF image for OH(2,0) excitation.

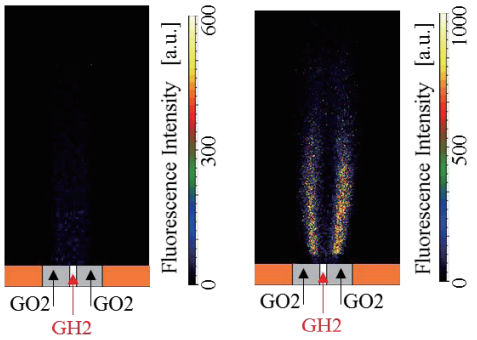


Fig. 4 OH-PLIF images for OH(3,0) excitations; (a) Using Type-A filter, (b) Using Type-B filter.

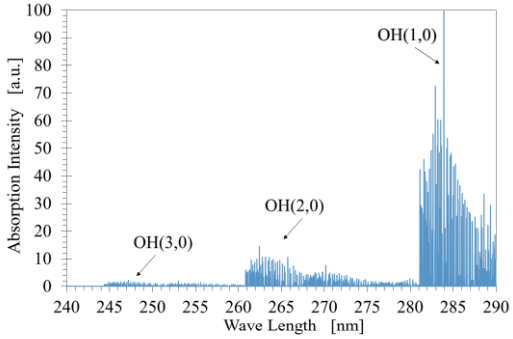


Fig.5 OH absorption spectrum.

### 4. Concluding Remarks

(1) OH chemiluminescence from the GH2/GO2 flame is almost twenty five times stronger than that from the GH2/GO2 flame.

(2) A single shot OH-PLIF signal for OH(3,0) band excitation for GH2/GO2 flame was weak, while that for OH(2,0) band excitation could be successfully detected. These indicates the possibility to use higher excitation band especially using multi shot integration.

### References

[1] G. Singla, P. Scouflaire, C. Rolon, S. Candel, *Combust. Flame*, 144 (2006) 151–169.

[2] K. L. Steffens, J. Luque, J. B. Jeffries, D. R. Crosley, *Journal of Chemical Physics*, 106 (1997) 6262–6227.

[3] J. Luque, D. R. Crosley, *SRI International Report*, 96–001(1996).

Eleventh International Conference on Flow Dynamics
October 8-10, 2014, Sendai, Miyagi, Japan

# Calculation of Turbulent Characteristic of Natural Convection in Parallel Heated Plates at High Rayleigh Number by Large Eddy Simulation

Takuma Kogawa[1], Junnosuke Okajima[2], Atsuki Komiya[2], Yuka Iga[2], Shigenao Maruyama[2]
[1]Graduate School of Engineering, Tohoku University
6-6 Aoba, Aaramaki, Aaoba-ku, Sendai, Miyagi, 980-8578, Japan
[2]Institute of Fluid Science, Tohoku Unievrsity
2-1-1Katahira, Aoba-ku, Sendai, Miyagi, 980-8577, Japan

**ABSTRACT**

The turbulent boundary layer of natural convection in the vertical parallel plates at high Rayleigh number was analyzed by Large Eddy Simulation. Modified Rayleigh number of the vertical parallel plates was from $8.8\times10^2$ to $3.6\times10^6$. When the width of the vertical parallel plates become shorter, the interaction of the turbulent thermal boundary layer was observed. By calculating the turbulent heat flux and Reynolds stress, it was revealed that interaction of the turbulent thermal boundary layer caused a decreasing of heat transfer and stabilized a turbulent flow.

## 1. Introduction

Natural convection has been widely used as cooling method. Some researches for the laminar natural convection in the vertical parallel plates were conducted by experiment and numerical simulation. Aihara [1] investigated the thermal boundary layer by using Schlieren method. Aihara and Maruyama [2] calculated the laminar natural convection of the vertical parallel plates with considering the variable thermal physical properties and derived the empirical formula of heat transfer rate by adopting the dimensionless numbers.

The turbulent natural convection of the vertical parallel plates observed in large scale is used in not only cooling method but also producing of electricity and artificial upwelling of deep sea-water [3]. Compared to the laminar natural convection, the turbulent natural convection of parallel plates has not been investigated adequately. Especially, the influence of the turbulent boundary layer developing from parallel plates was not evaluated.

In this study, to investigate the turbulent boundary layer of the turbulent natural convection in the vertical parallel plates, turbulent heat flux and Reynolds stress were calculated by Large Eddy Simulation (LES).

## 2. Calculation Method

Figure 1 shows computational domains, schematic and the coordinate systems of the present solution. To make the flow developing to the turbulent, the heated plates length were set to 1.5 m. The width of parallel plates was changed with $1\times10^{-2}$ m, $2\times10^{-2}$ m and $4.5\times10^{-2}$ m, calculated modified Rayleigh ($Ra^*$) numbers of each width were $8.8\times10^2$, $1.4\times10^4$ and $3.6\times10^6$. The $Ra^*$ is defined as follows:

$$Ra^* = \frac{g\beta(T_w - T_\infty)b^3}{\nu\alpha}\cdot\frac{b}{L}, \tag{1}$$

where $g$ [m/s$^2$] is the gravity acceleration, $\beta$ [1/K] is the volumetric thermal expansion coefficient, $L$ [m] is the length of heated plate, $\nu$ [m$^2$/s] is the kinematic viscosity, $\alpha$ [m$^2$/s] is the thermal diffusivity. Pure water was used as the working fluid. The temperature of heated plate was set to 299.7 K. The inlet temperature of the fluid was 288.2 K.

Governing equations used in this calculation are the continuity equation, the Navier-Stokes equation and the energy equation. These governing equations are written in Eqs. (2)–(4),

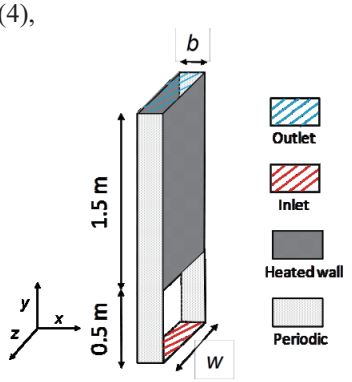


Fig. 1 Calculation domain of the vertical parallel plates.

$$\frac{\partial\bar{u}_k}{\partial x_k} = 0, \tag{2}$$

$$\frac{\partial\bar{u}_i}{\partial t} + \frac{\partial}{\partial x_i}(\bar{u}_j\bar{u}_i) - \frac{\partial}{\partial x_j}\left\{\frac{\mu}{\rho_0}\left(\frac{\partial\bar{u}_i}{\partial x_j} + \frac{\partial\bar{u}_j}{\partial x_i}\right) - \tau_{ij}\right\} = -\frac{\partial\bar{p}}{\partial x_i} + g_i\beta\left(\bar{T} - T_0\right), \tag{3}$$

$$\frac{\partial\bar{T}}{\partial t} + \frac{\partial}{\partial x_j}\left(\bar{T}\bar{u}_j\right) - \frac{\partial}{\partial x_k}\left(\frac{\lambda}{\rho_0 c_0}\frac{\partial\bar{T}}{\partial x_k} + q_t\right) = 0, \tag{4}$$

where $u_i$ [m/s] is the velocity in i-direction, $x$ [m] is the coordinate in i-direction, $t$ [s] is the time, $\mu$ [Pa·s] is the viscosity, $\rho$ [kg/m$^3$] is the density, $\tau$ [m$^2$/s$^2$] is the turbulent stress, $p$ [m$^2$/s$^2$] is the modified pressure, $T$ [K] is the temperature and $q_t$ [K·m/s] is the turbulent heat flux. The properties with subscript 0 represent the properties evaluated by inlet temperature. The Boussinesq approximation was applied for the variation of density of water with temperature. The temperature dependency of thermal properties of water must be considered. In order to consider the temperature dependency of thermal properties of water, linear

Corresponding author: Takuma Kogawa
*E-mail address*: takuma@pixy.ifs.tohoku.ac.jp

approximations were adopted. To assume the linear approximation for the volumetric thermal expansion coefficient, the non-linearity of variation of density for water can be considered.

The Vreman model [4] was used as a LES Sub Grid Scale (SGS) model. The turbulent viscosity calculated by Vreman model is written as,

$$\nu_t = C_v \sqrt{\frac{B_\beta}{a_{ij}a_{ij}}}, \tag{5}$$

$$B_\beta = \beta_{11}\beta_{22} - \beta_{12}^2 + \beta_{11}\beta_{33} - \beta_{13}^2 + \beta_{22}\beta_{33} - \beta_{23}^2, \tag{6}$$

$$\beta_{ij} = \Delta_m^2 a_{mi} a_{mj}, \tag{7}$$

where $C_v$ [-] is the constant number, $a_{ij}$ [1/s] is the velocity gradient tensor and $B_\beta$ is the scalar value calculated by $\beta_{ij}$. $\beta_{ij}$ is the value calculated by the velocity gradient tensor and filter width $\Delta_m$ in $m$ direction. This model calculates the turbulent dissipation dynamically. The turbulent flux of SGS is calculated by turbulent Prandtl number ($Pr_t$) of 0.4.

The finite volume formulation was employed to discretize the governing equations. Second order Total Variation Diminishing (TVD) was applied to the convective term in order to calculate stably. The second order central difference was used to the diffusive term. The calculation of the flow field was advanced with the implicit method. To reduce the numerical diffusion, the Crank-Nicholson scheme was adopted in the difference of the time. In order to predict the pressure and velocity field, the Pressure Implicit with Splitting Operator (PISO) method was used. The convective boundary condition [5] was adopted in the outlet. The inlet pressure was set to a constant.

## 3. Results and Discussion

Figure 2 shows the temperature contour plot in each region at $Ra^*$ of $1.4\times10^4$. In the laminar region, the thermal boundary layers were not interacted. On the other hand, the turbulent thermal boundary layer started to become thicker drastically in the transition region and it had an interaction of thermal boundary in the developed region. This interaction of thermal boundary layer caused the reduction of heat transfer from the heated plate.

Figures 3 and 4 show the profile of Reynolds stress and turbulent heat flux in the developed region, respectively. Both turbulent profiles had not symmetrical distribution because of the difference of direction of horizontal velocity. Additionally, the amplitude of these values became lower with shortening of the width of the parallel plates. Especially, the amplitude at $Ra^*$=$8.8\times10^2$ were almost zero. This result shows that the influence of turbulence was reduced by the interaction of thermal boundary layer drastically. Therefore, in the vertical parallel plates at high Rayleigh number, it was revealed that the interaction of thermal boundary layer made the flow from the turbulent flow to the laminar flow.

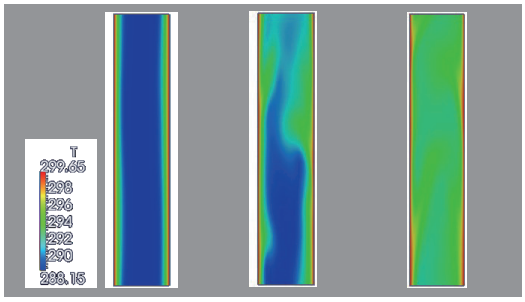


Fig. 2 Temperature contour plots in each region ($Ra^* = 1.4\times10^4$).

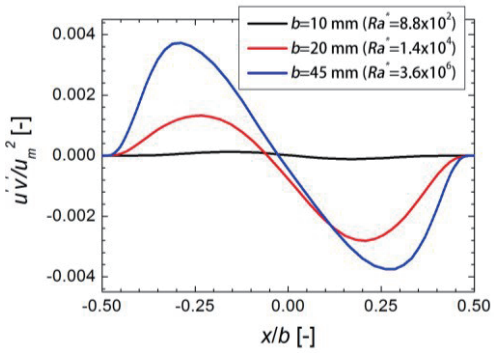


Fig. 3 Profile of the Reynolds stress in the developed region ($Ra_y$ =$4\times10^{11}$).

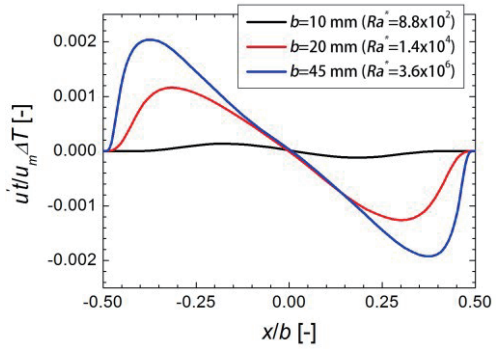


Fig. 4 Profile of the turbulent heat flux of the horizontal direction in the developed region ($Ra_y$ =$4\times10^{11}$).

## 4. Conclusion

(1) Turbulent thermal boundary layer developing from each heated plates was interacted each other.

(2) Interaction of thermal boundary layer caused the stabilization of the flow from the turbulent to the laminar in the developed area.

## References


[1] T. Aihara, *Transactions of the JSME*, 29 (1963), 903.

[2] T. Aihara, S. Maruyama, J.S. Choi, *IHTC-6* (1985), 1581.

[3] S. Maruyama, K. Tsubaki, K. Taira, S. Sakai, *J. Oceanogr.*, (2004), 563.

[4] Vreman, *Phys. Fluids*, 16 (2004), 3670.

[5] Akselvoll K, Moin P, *J. Fluid Mech.*, 315 (1996), 387.

# Improvement of Mini-Channel Gas Separator Utilizing Soret Effect

Tomohiro Higurashi[1] , Yuya Yoshikawa[1], Souhei Matsumoto[2] and Naoki Ono[1]
[1]Shibaura Institute of Technology
3-7-5, Toyosu, Koto-ku, Tokyo, 135-8548, Japan
[2]Advanced Industrial Science and Technology
1-2-1, Namiki, Tsukuba-shi, Ibaraki, 305-8564, Japan

**ABSTRACT**

Soret effect is a phenomenon in which temperature gradient gives rise to concentration gradient. In this study, we proposed a channel to separate hydrogen from mixture gas utilizing Soret effect. However, concentration difference by one separation was very small. Therefore, we produced multistage channel utilizing MEMS technology. To impose much bigger difference of temperature, we plan to build all-metal channel.

## 1. Introduction[1][2]

These days, a new energy source is being demanded. Above all, hydrogen is expected as a new energy because it is eco-friendly and has high energy conversion efficiency. However, the establishment of the hydrogen production technology is essential. Current main hydrogen manufacturing method is raised steam reforming method, However, this technique emitts hydrogen and carbon dioxide. Therefore, The technique to separate hydrogen and carbon dioxide is necessary to raise purity of hydrogen. Therefore, gas separation technology utilizing Soret effect that a concentration difference occurrs only due to temperature difference is paid attention. In addition, heat source is assumed to be, for example, exhaust cold heat at the time of reforming LNG. Furthermore, as for the separation by the Soret effect, it is thought that space-saving can greatly contribute to energy saving in terms of process time. However, repeated separation is necessary because only several percent is improved by one separation. We proposed the channel using the MEMS(Micro Electro Mechanical Systems) technology to prevent enlargement of the channel size and to increase the separation number of times. In addition, we plan to make new channel with metal material to improve durability and heat-resistance.

## 2. Theory[2][3]

The principle of the Soret effect is illustrated in Fig.1. The mass flux is occurred by the temperature gradient when heating temperature $T_1$ and cooling temperature $T_2$ are given in domain one or two, respectively. This phenomenon is called Soret effect. A characteristic of this phenomenon is that the concentration gradient increases with the increase of the temperature gradient. On the other hand, the mass flux based on the concentration gradient, i.e. Fick's law influences to relieve concentration gradient when the system with the concentration gradient. In the system of two ingredients (chemical species A and B), Soret effect and Fick's law is expressed to (1) and (2), respectively.

$$j_i^{(T)} = -\frac{c^2}{\rho} M_A M_B D_{AB} \frac{k_T}{T} \frac{dT}{dz}. \quad (1)$$

$$j_i^{(x)} = -\frac{c^2}{\rho} M_A M_B D_{AB} \frac{dx_i}{dz}. \quad (2)$$

In those equations, $c$ and $\rho$ are the molar density and mass density, respectively, $M$ is the molecular weight, $D_{AB}$ is the diffusion coefficient, $x$ is the molar fraction. $k_T$ is the thermal diffusion ratio, $T$ is the temperature, and $L$ is the separation distance. The subscripts $i$ indicates chemical species A and B. When these two mass fluxes are balanced, it is in a condition that species was completed. The separation density difference is expressed as: (3).

$$\Delta x_i = x_{i2} - x_{i1} = k_T \ln \frac{T_2}{T_1}. \quad (3)$$

Between two ingredients, the value of $k_T$ takes a positive value with light molecules and takes a negative value with the heavy molecules. In the system of $H_2$-$CO_2$, the value of $k_T$ is 0.0899. This value is detected by Bastick[4].

Therefore, the light molecules move to the high temperature domain, and the heavy molecules move to the low temperature domain, respectively.

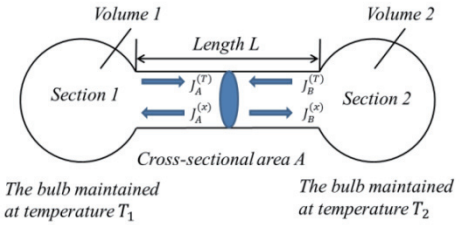


Fig.1 Steady-state binary thermal diffusion.

## 3. The outline of the experiment

The channel for two-step experiments was performed by two sets of channel in parallel. This channel have named multistage mini-channel. The photograph of the multistage mini-channel is shown in Fig.2.

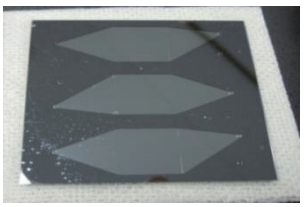

Fig.2 Photograph of multistage mini-channel.

Corresponding author: Naoki Ono
*E-mail address*: naokiono@shibaura-it.ac.jp

As an experiment, at first, mixed gases flowed into the both ends of the channel from gas cylinder (The flow rate to each channel becomes half of the input flow rate). Next, separated high concentration gas or low concentration gas was collected and flowed to central channel. Finally, high concentration gas and low concentration gas was measured with a gas chromatograph and confirmed improvement of hydrogen concentration. Combining two outflow from both ends of the first stage gave the same inflow rate at the second stage as at the first stage. The flow ratio of outlet of the channel is shown in Table 1. The flow rate from two exits was measured at the same ambient pressure. Separated gases was measured by a mass flow meter(FCSTM38V-4F9-F100, Fujikin).

The duct shape in the channel and each condition is shown in Table 2. Experimental apparatus including a channel is shown in Fig.2.

Table 1. Flow quantity ratio of outlet

| Flow rate [ml/min] | High side [ml/min] | Low side [ml/min] |
|---|---|---|
| 50 | 25 | 24.3 |
| 100 | 50 | 49.2 |
| 200 | 99.6 | 98.4 |

Table 2. Experimental Condition

| | |
|---|---|
| Thickness of the channel[mm] | 0.2 |
| Width of the channel[mm] | 15 |
| Flow rate[ml/min] | 20~200 |
| Heating/Cooling temperature[℃] | 80/0 |
| $H_2$:$CO_2$ | 47.5:52.5 |

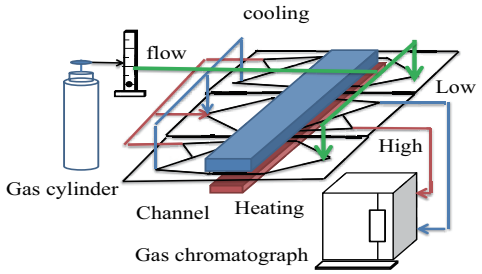


Fig.2 Experimental apparatus.

## 4. Result and Discussion

Experimental result is shown in Fig. 3. A blue plot is the first stage result. A red plot is the second stage result. Horizontal axis is flow rate. Vertical axis is hydrogen concentration. The center line is hydrogen concentration of gas cylinder, Higher than center line means high concentration, lower than center line means low concentration. In less than flow rate 25[ml/min], data were scattered. In more than flow rate 30[ml/min], data was converged. In flow rate 50, 100[ml/min], hydrogen concentration was improved because gas was separated by two stages.

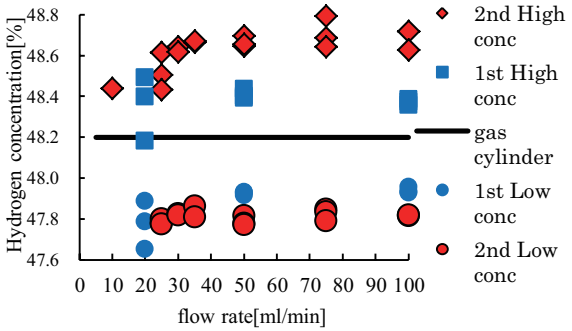


Fig.3 Experimental result.

## 5. Improvement of channel

The tube connector of outlet and inlet had a heat-resistant problem. Moreover, it had durable problem because it was made by glass and silicon material. The new channel will adopt SUS304 as its body material. The tube connector of outlet and inlet will be connected to a metal tube of SUS304. Thus, heat-resistance and durability of the channel will be much improved. Channel image of SUS304 is shown in Fig. 4.

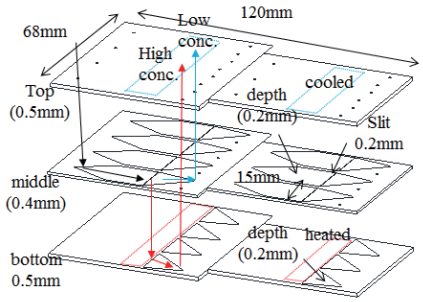


Fig.4 Channel image (SUS304).

## 6. Conclusion

1) Hydrogen concentration was improved because gas was separated by two stages.

2) Multistage mini-channel had heat-resistance and durability problem.

## 7. Future plan

We will impose much bigger difference of temperature at the channel. We will perform an experiment with three steps.

### References

[1] K.Yamaji, Hydrogen Energy Society, JSER, (2008), pp.136－143

[2] T.Wako, International Conference on Flow Dynamics, Sendai International Center, Paper No.GS1-19 (2013)

[3] R.Byron Bird , Watten E. Stewart, Edwin N. Lightfoot Transport phenomena, John Wiley & Sons, (1976), pp.554-575.

[4] R.E.Bastick, H. R. Heath, T. L. Ibbs, The molecular fields of carbon dioxide and nitrous oxide , *Proc.Roy.Soc, A173*, (1939), pp.543－546.

Eleventh International Conference on Flow Dynamics
October 8-10, 2014, Sendai, Miyagi, Japan

# Development and Performance Evaluation of High Temperature Electromagnetic Acoustic Transducer Using Air-cored Pulsed Electromagnet

Shohei Ogata[1], Tetsuya Uchimoto[2], Toshiyuki Takagi[2], Gerd Dobmann[3]
[1]Graduate School of Engineering, Tohoku University, 6-6 Aramaki Aza Aoba, Aoba-ku, Sendai, Miyagi, Japan
[2]Institute of Fluid Science, Tohoku University, 2-1-1 Katahira, Aoba-ku, Sendai, Miyagi, Japan
[3]Saarland University, 66123 Saarbrücken, Germany

**ABSTRACT**

Monitoring techniques in high temperature environment is demanded in various industrial plants and energy plants. Electromagnetic Acoustic Transducer (EMAT) provides non-contact measurements, and it is suitable for measurements in high temperature. This paper proposes to use air-cored coil as the bias magnetic source of EMAT to increase maximum working temperature. The pulse-echo waveforms of aluminum alloy and carbon steel specimens are measured by the present EMAT and shear wave velocity at each temperature are evaluated. Back-echo signals can be identified up to 400℃ with aluminum alloy and 450℃ with carbon steel.

## 1. Introduction

In steel plants and large energy plants, there are many components which are operated at high temperature more than 500℃. Nevertheless, sensing techniques in such high temperature has not been treated as critical research targets very much so far. To improve the quality of the product, increase the reliability of components, and save energy, development of monitoring sensors working in high temperature environment is highly required. Electromagnetic Acoustic Transducer (EMAT) can provide non-contact measurements, and it is suitable for measurements in high temperature [1]. Conventional EMAT uses rare-earth based magnets such as Nd or Sm-Co base ones for its bias magnetic sources, but the operation temperature of these types of magnets are limited by their Curie points [2]. Recently, pulsed electromagnet EMAT which uses iron yoke is developed [3], and it is confirmed that this EMAT can work up to 600℃. However, to use it in higher temperature, the Curie point of iron yoke may become a problem. To overcome this limitation, we propose to apply an air-cored coil for bias magnet of EMAT.

In this paper, we design the air-cored electromagnet which can apply sufficient magnetic field, and fabricate prototype EMAT using high temperature materials. To evaluate performance of present EMAT, pulse-echo waveforms are measured under high temperatures by using magnetic material and non-magnetic material.

## 2. Experimental method

The pulsed electromagnet EMAT proposed in this study consists of an air-cored solenoid coil and RF coil. Pulsed current is fed to the air-cored coil to generate bias magnetic field. At the same time, Pulsed RF current is fed to the RF coil which is located between bias electromagnet and specimen. The RF coil induces eddy current in the specimen, and interaction between the eddy current and the bias magnetic field makes Ampère force and the oscillation propagates into specimen as ultrasonic wave. When the reflected wave reaches near the surface, it is measured by the RF coil.

Corresponding author: Tetsuya Uchimoto
*E-mail address*: uchimoto@ifs.tohoku.ac.jp

In the case of magnetic materials such as carbon steels, ultrasonic waves are generated and received by not only Ampère mechanism but also magnetostrictive effect, and sensitivity is high at room temperature. On the other hand, when the temperature increases up to the Curie point, materials become paramagnetic and the sensitivity decreases.

The schematic of pulsed EMAT fabricated in this study is shown in Fig. 1. A multilayered solenoid coil is used for pulsed electromagnet. A copper wire (ϕ1.0 mm) is wound 100 times. To make peak of the magnetic field broad, the coil is connected to another coil in series to increase the inductance. RF coil is a flat spiral coil located under bias magnetic coil. It is wound by a copper wire (ϕ0.2 mm) and the number of turns is 30. In order to overcome the coil's insulation constraints at high temperatures, wire of the two coils are wound leaving behind a uniform gap in between the turns, and insulated by magnesia-based ceramic adhesive.

Pulsed current generator which can provide the maximum current of 2000 A drives the electromagnet together with a trigger signal for the pulser/receiver system. The trigger signal is adjusted so that pulse-echo signals can be acquired when the magnetic field becomes maximum. Direction of generated Ampère force is parallel to surface of the specimen, therefore, shear wave propagates to the vertical direction of the surface. As specimens, an aluminum alloy plate (JIS A7075) and a carbon steel plate (JIS SS400) are used. Thicknesses of two specimens are 20 mm and 10 mm respectively. EMAT and specimen are set in an electric furnace and heated up to the target temperature, and back-wall echo signals are measured at every 50℃. The signals are averaged 16 times to remove the noise.

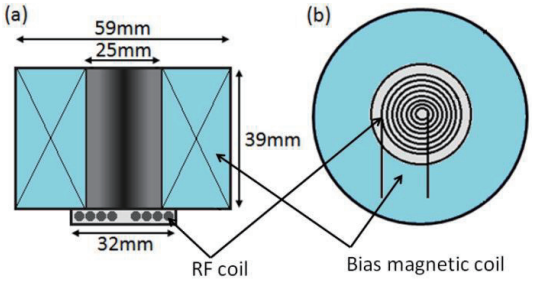


Fig. 1 Schematic diagram of air-cored pulsed EMAT. (a) side view (b) bottom view

## 3. Results

### 3.1 Experiments for aluminum alloy specimen

First, EMAT testing on the aluminum alloy specimen was conducted. Center frequency is set to 3.5 MHz. The obtained pulsed-echo signals are shown in Fig. 2. Clear echo signals were confirmed at the range of temperatures from RT to 400℃.

Shear wave velocity at each temperatures are calculated by the time of flight of echoes and the thickness of specimen. To consider the thermal expansion in high temperatures, the thickness of specimen is calculated by

$$L = L_o[1 + \alpha(T - T_o)], \qquad (1)$$

where, $L_o$, $\alpha$, $T$ and $T_o$ are the thickness of specimen at RT, the expansion coefficient, RT, and temperature at measurement of echoes, respectively. The estimated wave velocity as function of temperature is shown in Fig. 3. The shear wave velocity decreases with temperature rise. Generally, the elastic coefficient decreases with temperature rise, which leads decrease of the shear wave velocity. This result supports that the present EMAT works properly at elevated temperature.

Melting temperature of aluminum alloy is about 470℃~630℃, and it is supposed that partial melting of the specimen affected decreasing of echo signals over 400℃.

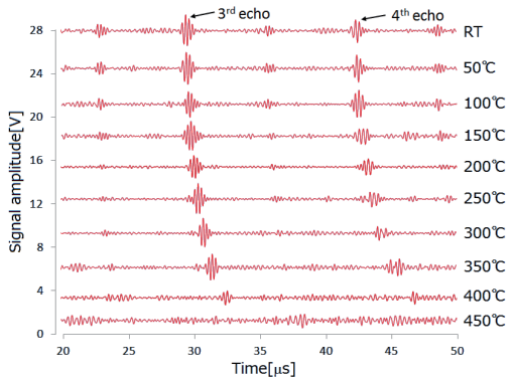


Fig. 2 Back-wall echo signals at elevated temperature (A7075).

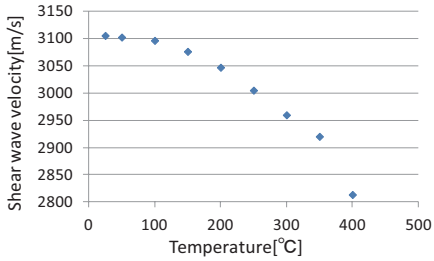


Fig. 3 Shear wave velocity of aluminum alloy at a range of temperatures from RT to 400℃.

### 3.2 Experiments for carbon steel specimen

Experiments on carbon steel specimen were also conducted. Center frequency is set to 6 MHz. The obtained pulsed-echo signals are shown in Fig. 4. Signal amplitudes are much larger than that of aluminum alloy, and echo signals were successfully obtained up to 450℃.

Shear wave velocities are calculated like a case of aluminum alloy. The estimated wave velocity as function of temperature is shown in Fig. 5. Monotonous reduction of shear wave velocity with temperature rise was confirmed.

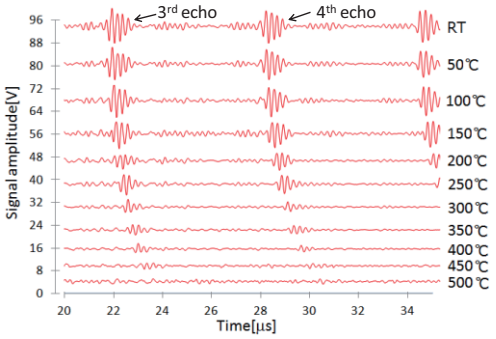


Fig. 4 Back-wall echo signals at elevated temperature (SS400).

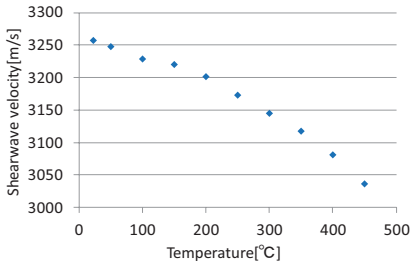


Fig. 5 Shear wave velocity of carbon steel at a range of temperatures from RT to 450℃.

## 4. Summary

In this study, we designed the pulsed electromagnet EMAT with air-cored solenoid coil for high temperature measurements over 600℃. EMAT was fabricated with copper wire and high temperature ceramic adhesive. Pulse-echo signals of magnetic material and non-magnetic material at elevated temperatures were measured. As a result, the echo signals were successfully obtained from RT to 400℃ with aluminum alloy and up to 450℃ with carbon steel, and the decrease of shear wave velocity with temperature rise was confirmed. In order to observe echo signals at 500℃ or higher, we are going to improve the bias magnetic coil to get larger magnetic field.


## Acknowledgements

This study is supported by the Grant-in-Aid for Challenging Exploratory Research (24656080) of Japan Society for the Promotion of Science (JSPS), and the JSPS Core-to-Core Program, A. Advanced Research Networks, “International research core on smart layered materials and structures for energy saving”.


## References


[1]R. Murayama, *Non-destructive inspection*, Vol.51, No.2, (2002) 62－67.

[2]R. Urayama, T. Takagi, T. Uchimoto, and S. Kanemoto, *EJAM*, Vol.5, (2013) 155－164.

[3]F. Hernandez-valle and S. Dixon, *Insight*, Vol.43, No.2, (2011) 96－99.

Eleventh International Conference on Flow Dynamics
October 8-10, 2014, Sendai, Miyagi, Japan

# OH-LIF Measurement of $H_2/O_2/N_2$ Flames in a Micro Flow Reactor with a Controlled Temperature Profile

Takashige Shimizu[1], Hisashi Nakamura[1], Takuya Tezuka[1], Susumu Hasegawa[1], Kaoru Maruta[1]
[1]Institute of Fluid Science, Tohoku University
2-1-1 Katahira, Aoba-ku, Sendai, Miyagi, 980-8577, Japan

**ABSTRACT**

Combustion characteristics of $H_2/O_2/N_2$ flames were investigated in a micro flow reactor. OH-LIF measurement was applied to capture flame images in this study. Three kinds of flame response; normal flame; FREI; and weak flame were observed. Computations with four kinds of mechanism were conducted to compare with experimental flame locations of weak flame. It was found that results with GRI3.0 mech. showed good agreement with measured flame locations.

## 1. Introduction

Hydrogen which can be produced by renewable energies attracts attentions as one of alternate fuels for petroleum fuels. Hydrogen has huge energy per unit mass and its combustion never exhausts carbon dioxide because it contains no carbon atom. However, it is important to investigate combustion characteristics to apply hydrogen for practical combustion devices such as gas turbines because the present knowledge on hydrogen combustion is not sufficient.

We employed a micro flow reactor with a controlled temperature profile [1] in this study. A narrow channel, whose diameter is smaller than the ordinary quenching diameter, was heated by external heat source and a stationary wall temperature gradient was formed. In our previous study for $H_2/O_2/N_2$ mixture using this reactor, two kinds of flame responses were observed experimentally by the measurement of OH chemiluminescence using an UV CCD camera and image-intensified high-speed camera [2]. One is the stable flat flame (Normal flame) which was observed in the high flow velocity region. Another is the unstable flame called *flames with repetitive extinction and ignition* (FREI) [1] which was observed in the intermediate flow velocity region. However, a stable flame with weak luminescence (Weak flame), which was observed in low velocity conditions for hydrocarbon fuels in our past studies [1,3], could not be observed for $H_2/O_2/N_2$ mixture at the low flow velocity[2]. Thus, the existence of weak flame of $H_2/O_2/N_2$ mixture is still open question. The investigation of weak flames is important because weak flame can be applied to examine detailed oxidation process[1] and be reproduced by 1-D steady computation quantitatively. In this study, OH-LIF measurement was conducted to investigate the existence of $H_2/O_2/N_2$ weak flames for variable inlet flow velocity, $U$.

## 2. Experimental and computational method

### 2.1 Experiment

A schematic of experimental setup is shown in Fig. 1. A quartz tube with an inner diameter of 2 mm was used as a reactor channel and was heated by a $H_2$/air flat-flame burner to obtain a stationary temperature profile from 300 K to 1300 K. A $H_2/O_2/N_2$ mixture was supplied to the reactor at equivalence ratio, $\phi$, of unity and atmospheric pressure. Two kinds of dilution ratios of the mixture ($H_2/O_2/N_2$ = 2:1:7 and 2:1:9) were chosen in this study. Flame responses for variable inlet flow velocity were observed by OH-LIF measurement. Wave length of 283 nm by DYE-Laser (FINE ADJUSTMENT, 0312P043) which was converted from 532 nm of Nd:YAG-Laser (LOTIS TII, LS-2137/3) was chosen to excite OH radicals. A laser beam was run through a pinhole with diameter of 2 mm after concentrated by convex and concave lens. The laser was introduced from the downstream side of the reactor. An image-intensified CCD camera (ANDOR, DH334T-18-E3) with UV lens, an OH band-pass filter (center wavelength: 313 nm; half value width: 10 nm; and transmissivity > 60%) and two 300 nm high-pass filters were used to capture flame images. 10 and 50 signals are accumulated for normal flame and weak flame images respectively. On the other hand, extinction and ignition temperature of FREI were identified from the upstream and downstream edge of more than 50 instantaneous OH-LIF images which constitute FREI. Background subtraction image processing was done for captured images.

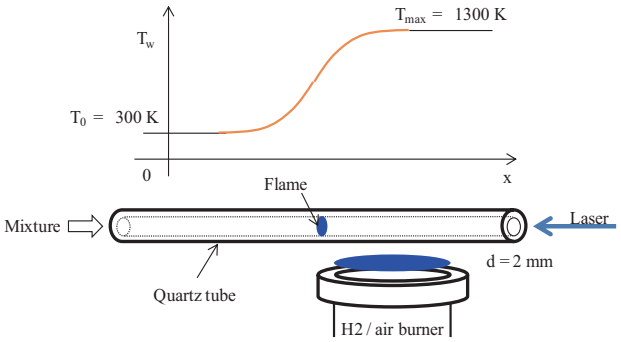


Figure 1. Schematic of experimental setup and provided wall-temperature profile.

### 2.2 Computation

One-dimensional steady-state flame code based on PREMIX was used. The energy equation includes convective heat transfer between gas and wall. Four kinds of mechanism (GRI 3.0[4], San Diego Mech.[5], Princeton $H_2$-$O_2$ Model[6] and Aramco Mech. 1.3[7].) were used to examine their performance in the present

Corresponding author: Takashige Shimizu
*E-mail address*: shimizu@edyn.ifs.tohoku.ac.jp

reactor. Computations were conducted for the same conditions as that of the present experiments.

## 3. Results and Discussion

Three kinds of flame response; normal flame in the high velocity; FREI in the intermediate velocity; and weak flame in the low velocity, were observed in each flow velocity region with dilution ratio of $O_2$:$N_2$=1:9. Obtained flame images were shown in Fig. 2.

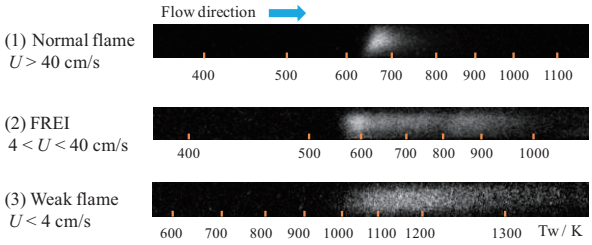


Fig. 2 Flame responses captured by OH-LIF measurement in each inlet flow velocity region at $\phi$ =1 and $O_2$:$N_2$=1:9.

As shown in Fig. 2, normal flame was observed in $U$ > 40 cm/s, FREI in 4 < $U$ < 40 cm/s and weak flame in $U$ < 4 cm/s. Weak flame shows broader distribution in OH-LIF signal than normal flame because OH radicals were diffused more strongly at low flow velocity. All measured flame locations were shown in Fig. 3. The flame positions of normal flame shifted to upstream with decreasing $U$ and weak flame shifted to downstream with decreasing $U$. These tendencies correspond to computational heat release rate (HRR) peak which correspond to the flame position. (A figure of the position of HRR peaks is not shown here.) Brightness peak positions of the OH-LIF images were used for identifying normal flame locations since the location of the HRR peak corresponds to that of OH mole fraction peak for normal flames in the computation. On the other hand, location of the half maximum in OH profile rise was used for that of weak flame. Because the rising edge of OH mole fraction profile agrees with that of HRR peak for weak flames in the computation.

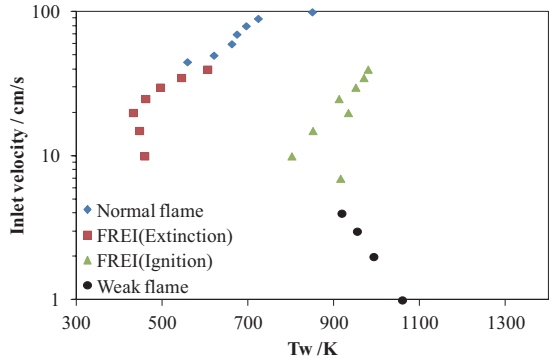


Fig. 3 Measured flame position and extinction and ignition points of FREI in variable flow velocities at $\phi$ =1 and $O_2$:$N_2$=1:9.

Further examination of weak flames at $O_2$:$N_2$ = 1:7 was conducted between experiment and computation. Comparisons of weak flame locations between computation and experiment is shown in Fig. 4. All mechanisms predicted that computational weak flame locations shifted to the high temperature region with the decrease of $U$. On the other hand, experimental weak flame locations shifted to the high temperature region with the decrease of $U$ down to 1 cm/s, and then shifted to low temperature region. Computational weak flame location using GRI3.0 mech. showed good agreement with that of experiment compared with the other mechanisms employed.

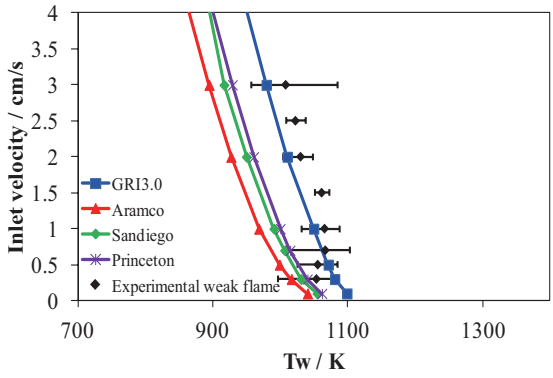


Fig.4 Comparison for weak flames between the rising edge of measured OH profile and that of computational OH mole fraction at $\phi$ =1 and $O_2$:$N_2$=1:7.

## 4. Conclusions

For $H_2$/$O_2$/$N_2$ mixture, three kinds of flame response; normal flame in the high velocity; FREI in intermediate velocity; and weak flame in low velocity, were observed by OH-LIF measurement in a micro flow reactor with a controlled temperature profile. In detailed investigation of weak flame, experimental weak flame locations were compared with that of computation. As a result, experimental results shift to higher temperature region as the decrease of the inlet flow velocity, $U$, down to 1 cm/s, however, results of $U$ < 1 cm/s showed different tendency. Comparison between experiment and computation shows that results of GRI3.0 mech. had good agreement with experimental results in $U$ > 1 cm/s in this study.

## References


[1] K. Maruta, et al., Proc. Combust. Inst. 30 (2005) 2429–2436.

[2] K. Saruwatari, H. Nakamura, T. Tezuka, S. Hasegawa and K. Maruta, ICFD (2012), OS11.

[3] Y. Tsuboi, T. Yokomori and K. Maruta, Proc. Combust. Inst. 32 (2009) 3075–3081.

[4] GRI Mech 3.0, http://www.me.berkeley.edu/gri-mech/.

[5] The San Diego Mechanism, http://web.eng.ucsd.edu/mae/groups/combustion/mechanism.html.

[6] Princeton H2/O2 Model, http://www.princeton.edu/mae/people/faculty/dryer/homepage/kinetic_models/h2-o2-model-update/.

[7] Aramco Mech1.3, http://www.nuigalway.ie/c3/Mechanism_release/frontmatter.html.

Eleventh International Conference on Flow Dynamics
October 8-10, 2014, Sendai, Miyagi, Japan

# Linear Analysis of Thermal-diffusive Stability in Divergent Gas Flow

Sergey Mokrin[1], Roman Fursenko[1, 2]
[1]Far Eastern Federal University
Sukhanova str., 8, Vladivostok, 690950, Russia
[2]Khristianovich Institute of Theoretical and Applied Mechanics SB RAS
Institutskaya str., 4/1, Novosibirsk, 630090, Russia

**ABSTRACT**

A two-dimensional linear stability of counterflow premixed flames was analytically and numerically investigated. Results show that three types of the instability exist. It is shown that two types of instability can lead to the flame quenching and the third one can be related with the cellular flame formation. Flammability limits and the region of cellular flames existence has been established.

## 1. Introduction

Understanding of propagation and stability of counterflow premixed flames is required for the development of new combustion technologies such as: combustion with low-NOx emission, combustion of lean mixtures, micro-scale combustion and material synthesis. The only stable combustion regimes can be used to obtain materials with homogeneous properties. Recent experimental and theoretical studies on combustion using stationary counterflow premixed flames found existence of multiple flame regimes [1, 2]. Despite the fact that the stability problem of various combustion regimes is important, previously only one-dimensional thermal-diffusive stability of counterflow flames was considered [3]. The main objective of this work is a two-dimensional linear stability analysis of the stationary solutions.

## 2. Method

The scheme of counterflow premixed flames is shown in Fig. 1. The symmetry plane is defined at $x = 0$. We restrict stationary solutions in the area $x > 0$. By employing the conventional assumptions of constant density, constant thermal properties, potential flow and localized reaction zone the governing equations for temperature and fuel concentration are:

$$\frac{\partial T}{\partial t} - ax\frac{\partial T}{\partial x} = \frac{\partial^2 T}{\partial x^2} + (1-\sigma)W - Q, \qquad (1)$$

$$\frac{\partial C}{\partial t} - ax\frac{\partial C}{\partial x} = \frac{1}{Le}\frac{\partial^2 C}{\partial x^2} - W, \qquad (2)$$

where

$$W = \exp\left(\frac{N}{2}\left(1-\frac{1}{T_f}\right)\right)\delta(x - x_f), \qquad (3)$$

is the chemical reaction rate, $t$, $x$, $T$, $C$, $N$ and $\delta$ are dimensionless time, streamwise coordinate, temperature, fuel mass fraction, the activation energy normalized by the adiabatic flame temperature and Dirac $\delta$-function.

Corresponding author: Roman Fursenko
*E-mail address*: roman.fursenko@gmail.com

The stretch rate is defined by $a = V_0 / L$, where $V_0$ is the burner inlet gas velocity and $L$ is the half distance between burners. Subscript $f$ denotes variables on the flame front and the stationary solutions are marked by subscript $s$. For simplicity, the radiative heat losses $Q(T)$ is approximated by a linear function of temperature $Q = h(T - \sigma)$, where $\sigma = T_0 / T_{ad}$.

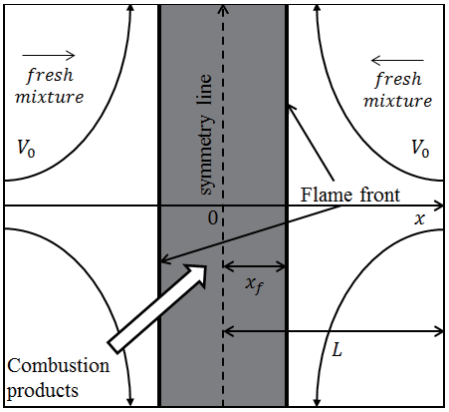


Fig. 1 Schematic of counterflow flames.

Using the method described in paper [3] we can obtain the stationary solutions of (1)-(2).

For 2D linear stability analysis we find solutions of linearized non-stationary equations

$$\frac{\partial T}{\partial t} - ax\frac{\partial T}{\partial x} = \frac{\partial^2 T}{\partial x^2} + \frac{\partial^2 T}{\partial y^2} - h(T - \sigma), \qquad (4)$$

$$\frac{\partial C}{\partial t} - ax\frac{\partial C}{\partial x} = \frac{1}{Le}\left(\frac{\partial^2 C}{\partial x^2} + \frac{\partial^2 C}{\partial y^2}\right), \qquad (5)$$

in the form of $T = T^s + \widetilde{T}e^{\Omega t + iky}$, $C = C^s + \widetilde{C}e^{\Omega t + iky}$, $T_f = T_f^s + \widetilde{T}_f e^{\Omega t + iky}$, $x_f = x_f^s + \widetilde{x}_f e^{\Omega t + iky}$, where known stationary solutions are marked by subscript $s$. Here $\widetilde{T}, \widetilde{C}, \widetilde{x}_f, \widetilde{T}_f$ are small perturbations. The solutions of linearized equations (1)-(2) were described in [3], therefore

following the same method we can obtain the dispersion equation:

$$(\beta-\alpha)\left(\frac{2(T_f^s)^2}{N}\left(ax_f^s Le+\gamma\right)+\frac{dT_1^s}{dx}\right)+ \\ +\left(\frac{(1-\sigma)}{Le}\left(\left(1-Le\right)ax_f^s+\beta-\gamma\right)\right)\frac{dC^s}{dx}=0, \quad (6)$$

where $\alpha,\beta,\gamma=f(\Omega,k)$ are known functions.

### 3. Results and Discussion

The equation (6) was solved numerically focusing on search of unstable solutions for which Re[Ω]≥0. The analysis of equation (5) allows to distinguish three typical dependencies of growth rate perturbations Ω on wave number $k$ corresponding to different types of instability:

1) Re[Ω]>0, Im[Ω]=0 at $k$=0 – corresponds to unstable flame and this instability leads to flame quenching;

2) Re[Ω]>0, Im[Ω]≠0 at $k$=0 – flame front pulsations. The development of such pulsations can also lead to flame quenching [3];

3) Re[Ω]>0, Im[Ω]=0 at $k$≠0 – this type of instability is pertinent to cellular flame.

This conclusion is supported by results of direct numerical simulations performed in paper [4]. The typical dependencies of growth rate on wave number are shown in Fig. 2. The dependencies were calculated both for symmetrical and asymmetrical cases.

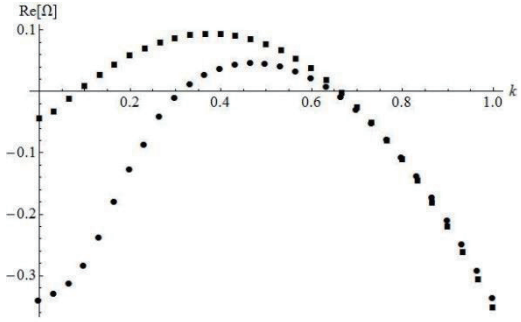


Fig. 2 Real part of growth rate dependencies on wave number for $Le$ = 0.3, σ = 0.25 and $a$ = 0.1. Squares correspond to asymmetrical and circles correspond to symmetrical perturbations.

The wave number associated with maximal growth rate allows to estimate the characteristic cell size of the flame surface. One can assume that this instability is responsible for the flame tubes formation observed in experiments [5].

All combustion regimes and flammability limits could be plotted at the diagram.

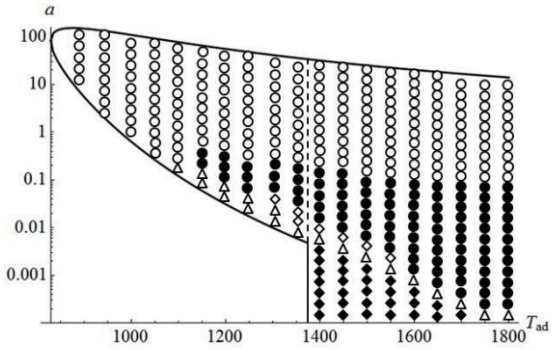


Fig 3. Flammability limits at the plane (non-dimensional stretch rate vs adiabatic temperature). The hollow circles mark stable NF, solid circles are cellular NF, hollow rhombs are pulsating flame, triangles are stable WF and solid rhombs are unstable slow burning flow.

### 4. Concluding Remarks

A two-dimensional stability of various combustion regimes of stretched counterflow flames is theoretically investigated. The present analysis gives out a dispersion equation describing growth rate of small spatial perturbations of the flame front. The stability diagram is obtained and the region of instability is distinguished. Analysis of two-dimensional stability of various combustion regimes reveals three types of instability. It was suggested that two types of instability can lead to the flame quenching and the third type of instability can be related with formation of cellular flame. The establishing of flammability limits and the region of cellular flames existence can be useful for practical applications related with counterflow flame-synthesis methods of new material production.

### 5. Acknowledgment

This work was supported by The Ministry of Education and Science of Russian Federation (project №14.Y26.31.0003) and Far Eastern Federal University.

### References

[1] Y. Ju, H. Guo, K. Maruta, F. Liu, *J. Fluid Mech.*, 342 (1997) 315.

[2] J.D. Buckmaster, *Combust. Theory Modelling*, 1 (1997) 1 – 11.

[3] S. Minaev, R. Fursenko, Y. Ju, C.K. Law, *J. Fluid Mech.*, 488 (2003) 225 – 244.

[4] R. Fursenko, et.al., *Proceedings of Combustion Institute,* 34 (2013) 981–988.

[5] C. Kaizer, J.-B. Liu, P.D. Ronney, *38th Aerospace Sciences Meeting&Exhibit*, (2000) 1 – 14.

# Numerical Research of Cooling Performance for Work-piece in Hot Stamping

Chenguang Lai, Chao Man, Kaiping Wen, and Hao Sun
College of Vehicle Engineering, Chongqing University of Technology
No. 69, Hongguang Road, Banan District, Chongqing, Chongqing, 400054, China

**ABSTRACT**

Two different cooling tunnels were set in hot stamping mold, one was smooth inner wall, and another added triangle backup bars. Cooling performance for blanking in the two cases, the flow and heat transfer situation of cooling water in two different tunnels were obtained after the numerical simulation. The result shows that, the cooling effect of inner backup bars tunnel is advantageous than smooth tunnel, and also the heat transfer ability is stronger. For backup bars tunnel, the average temperature of work piece is 12 K lower than that of smooth tunnel while holding time is 10 s.

## 1. Introduction

The application of high strength steel (HSS) is an effective approach to achieve automotive lightweighting. To get HSS, hot stamping integrated heating, forming and quenching in one process. This could effectively soften the blank and prevent it from cracking and wrinkling. After heating the blank to austenite, it should be cooled down quickly through the suitable cooling tunnels in mold. If the blank phase transfers from austenite to martensite evenly, it could acquire substantial high tensile and yield strength. Hence, cooling the high temperature blank rapidly is a key point in hot stamping process.

According to the field synergy theory [1], the heat transmission of flowing fluid whether has been enhanced depends on the intersection angle $\theta$ between velocity direction and temperature gradient direction. Decrease $\theta$ is an effective approach to enhance convection heat transfer ability. This paper adds the triangle backup bars (calls bars tunnel in brief blow) in the smooth tunnel to decrease the synergy angle between velocity field and temperature field. After simulation for these two kinds of cooling tunnels, the mechanization of heat transfer enhancement in bars tunnel had been analyzed deeply. Hence, this research provides important references for designing of cooling tunnels in hot stamping.

## 2. Method

The computational model includes feature dies, cooling tunnels and vehicle blanking. The main purpose of this paper is to compare the cooling effective between bars tunnel and smooth tunnel; hence, part of the blanking is used for this simulation. The thickness of blanking is 2 mm, and the other sizes are $200\,\text{mm}\times164\,\text{mm}\times50\,\text{mm}$ . The diameter of the tunnel is 8 mm. See Fig. 1.

This paper applied two cooling cases to compare the cooling effect. Smooth cooling tunnels were installed in the die for case 1, and bars tunnels for case 2. Nine bars were added in the smooth tunnel. The diameter is 8 mm. Tooth spacing is 20 mm. Depth of tooth is 1 mm. Tooth angle is 90° . See right of Fig. 1.

Corresponding author: Chao Man
*E-mail address*: chaoman2008@yahoo.com

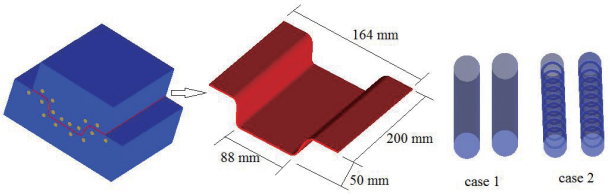


Fig. 1 Computational model.

The mesh interfaces were created at the tunnel surfaces so that the heat could transfer normally between fluid and solid. The heat transfer equation at these interfaces shows as below,

$$-\lambda(\frac{\partial T}{\partial n})_w\Big|_{solid} = h(T_w - T_f)\Big|_{fluid} \quad . \qquad (1)$$

Where, $q_w$ means the thermal density on the interface ($W/m^2$); $n$ means outer normal of the wall; λ means the thermal conductivity of the mold ($W/(m\cdot K)$); $h$ means the coefficient of convection heat transfer surface ($W/(m^2\cdot K)$); $T_w$ , $T_f$ mean the temperature of interface and temperature of fluid near wall (K).

In this paper, the mold material is H13. And the blanking material is BR1500HS. For the initial temperature, mold is 423 K. Blanking is 1173 K. Cooling water is 300 K.

## 3. Results and discussion

The cooling time is 10 s. Figures 2 and 3 show the changes of maximum temperature and average temperature of blanking alone the time in two cases.

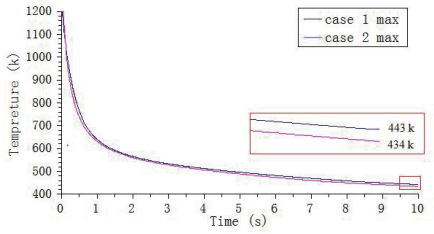


Fig. 2 Maximum temperature curve of blanking.

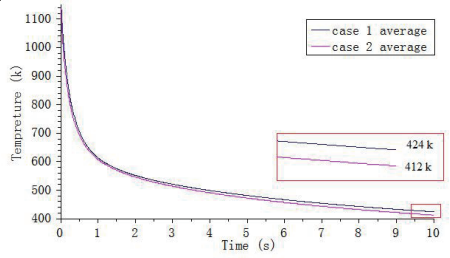


Fig. 3 Average temperature curve of blanking.

Whether from the view of average temperature or maximum temperature, the cooling effect of blanking in case 2 is better than case 1. At the point of 10 s, the maximum blanking temperature in case 2 is 9 K lower than case 1. The average temperature in case 2 is 12 K lower than case 1. It shows more obvious advantage of cooling effect.

In the situation of convection heat transfer, the thinness thermal boundary layer would be created near the wall for the temperature difference between fluid and solid wall. Fluid temperature changes extreme heavily in this boundary layer and it would creates thermal resistance. The temperature distribution of cooling water in tunnel, see Fig. 4, show that, the solid wall temperature in case 2 is easier to disperse in fluid, because the bars could disturb the thermal boundary layer. Compared with case 1, the distance of the flow water is shorter in case 2 if cooling water rise to the same temperature. Conversely, for the same distance of the flow water, the temperature on the axle center in case 2 is higher than case 1. Hence, it could take more quantity of heat away. As cooling time goes on, the temperature difference between fluid and solid wall becomes small, reducing the heat transfer coefficient, and decreasing the heating-up of tunnel outlet.

The velocity of cooling water in laminar sub-layer is almost zero as the viscous of fluid. Most of the thermal resistance concentrates in the low velocity domain [2]. Because the cooling tunnel wall is smooth in case 1, the flow regime in tunnel is laminar, see Fig. 5. Therefore, for smooth tunnel, the thermal resistance is large. It is not beneficial for the process of heat transfer. The bars were added in the smooth tunnel in case 2. The flow regime changes obviously in tunnel, causing low pressure areas behind the bars. It will create vortices under the action of pressure difference. The laminar near the wall would be destroyed by these vortices. Therefore, it will reduce the thermal resistance in these areas and enhance the heat transfer capability.


Fig. 4 Counter of temperature in tunnel at each time.

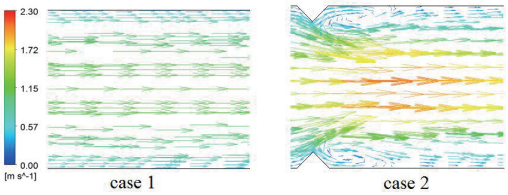


Fig. 5 Velocity vectors.

Dimensionless *Nu* (Nusselt) number is an important norm to evaluate the heat transfer ability in heat convection. The bigger *Nu* value means stronger ability of heat transfer. And the value of *Nu* could compute through formula (2),

$$Nu = h \cdot L/k \quad (2)$$

Where, $h$ means the convection heat transfer coefficient (W/(m$^2$ · K)); $L$ means character length of geometry (m); $k$ is thermal conductivity (W/(m · K)).

At the moment of 10 s, the *Nu* distribution of cooling tunnel in both case 1 and case 2 shows as Fig. 6. For smooth tunnel, the temperature difference between fluid and solid wall near the inlet is big, which would increase the value of heat transfer coefficient $h$. So the Nusselt number is big in this area. With the cooling water flows to the end of tunnel, temperature difference decreases. The Nu number becomes smaller. For the bars tunnel, as the bars would destroy the laminar state of cooling water and enlarge the turbulence intensity, the Nu number would rise again at each bar. Hence, the reduction of Nu number is small. Especially at the end of tunnel, the Nu number is much bigger than that of smooth tunnel. The average Nu number for smooth tunnel is 71.18, and for bars tunnel is 83.96. Therefore, it is proved that the heat transfer capability of bars tunnel is stronger than that of smooth tunnel. In the process of hot stamping, the cooling effect of bars tunnel is advantageous than smooth tunnel.

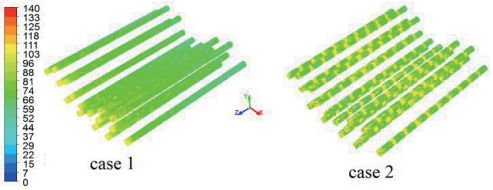


Fig. 6 Distribution of Nusselt number.

## 4. Conclusions

In the simulation of cooling effect for blanking in hot stamping process, these conclusions could be obtained by comparing the cooling performance between smooth tunnel and bars tunnel:

(1) The cooling performance for mold of bars tunnel is better than smooth tunnel. Therefore, it could improve the cooling effect for blanking further. It is beneficial to achieve the cooling requirement in hot stamping.

(2) By adding the inner backup bars in the smooth tunnel, the turbulence intensity in tunnel becomes stronger. The cooling water temperature could get higher in the tunnel axis center. It can enhance the heat transfer capability of cooling tunnel. This heat transfer enhancement technology also could apply to other heat exchangers.


## Acknowledgements

This research is supported by Natural Science Foundation Project of CQ CSTC (CSTC, 2011BB6113).


## References


[1] S.W. Xiong, X.P. Luo, G.L. Gao. Review on Field Synergy Theory for Heat Transfer Enhancement [J]. *Petro-chemical Equipment*, 36 (2007) 50-54.

[2] S.W. Qian, D.S. Zhu, Q.L. Li et al. Technology of Heat Transfer Enhancement in Tube heat exchanger [M]. *Chemical Industry Press*, Beijing, (2003)

Eleventh International Conference on Flow Dynamics
October 8-10, 2014, Sendai, Miyagi, Japan

# Hydrodynamic Instability of Flame Propagating in Premixture with Fuel Drops

Nikolay S. Belyakov
Far Eastern Federal University
Sukhanova str. 8, Vladivostok, 690000, Russia

**ABSTRACT**

This thesis is a theoretical study of the hydrodynamic instability of a plane wave premixed combustion with fuel particles. In this paper we analyzed the effect of the density of droplets in the fresh mixture, the coefficient of expansion and other characteristics of gasdroplet environment on the stability of the flame front. Was investigated by the limiting transition to the theory of hydrodynamic instability Darrieus-Landau conventional flame. Modes of combustion in which the flame front observed oscillations detected experimentally.

## 1. Introduction

Process of combustion of mixture consisting of a premixture with fuel microdroplets is of interest to researchers, such as this type of fuel used in gas turbines, diesel engines, internal combustion engines, boilers. Experimental studies [1] showed that the surface of the divergent spherical flame gas-droplet mixtures has intensively cellular structure, and in some cases, oscillation of flame front.

## 2. Method

In this paper we made the assumption that the observed pulsations of the flame front, as well as its cellular structure caused by hydrodynamic instability. The theory of hydrodynamic instability of the flame front premixed gases was proposed by Landau [2]. In this classic work has been shown that the flame front is unstable with respect to small perturbations, the development of which can cause cells on the flame front. At the same time, this model is capable of describing the pulsation of the flame, which are sometimes observed in the gas-droplet mixture.

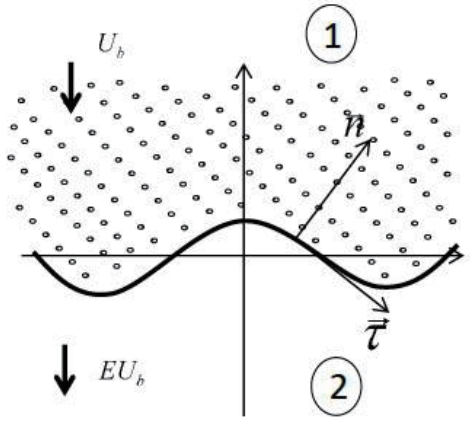


Fig. 1. Scheme of considered process

Figure 1 schematically shows the studied process. The area 1 contain the fresh mixture (air, fuel gas and fuel droplets), the region 2 – products of combustion. To describe this process uses a coordinate system associated with the front surface, the combustible mixture is incident on the flame front at a rate equal to the normal flame propagation velocity $U_b$, and combustion product s are entrained at a speed $EU_b$, where $E$ - the coefficient of expansion.

Mathematical model describing the flow in the fresh mixture, based on the idea of two interacting interpenetrating continua. Flame front is seen as an interface between the unburned mixture with drops of fuel and products of combustion. It is believed that the normal velocity of the combustion wave is dependent on the density of the fuel droplets near the flame front and the local curvature of the surface.

In fresh mixture area:

$$div\ v_1 = 0, \tag{1}$$

$$\frac{\partial v_1}{\partial t} + v_1 \nabla v_1 = -\frac{\nabla P_1}{\rho_1}, \tag{2}$$

$$\frac{\partial \rho_d}{\partial t} + div\ \rho_d v_d = 0, \tag{3}$$

$$\frac{\partial v_d}{\partial t} + v_d \nabla v_d = -\alpha (v_d - v_1), \tag{4}$$

In products of combustion area:

$$div\ v_2 = 0, \tag{5}$$

$$\frac{\partial v_2}{\partial t} + v_2 \nabla v_2 = -\frac{\nabla P_2}{\rho_2}, \tag{6}$$

where v – velocity, ρ – density, α – coefficient of drops transportable by gas flow, indexes 1 – fresh mixture, 2 – products of combustion, d – droplets.

The flow of combustible mixture containing fuel drops described by equations (1–4), of which (1,2) describe the movement of the gas phase, and (3,4) - droplets. Equations (5,6) describe the flow of combustion products.

Boundary conditions on the flame front are following:

$$\rho_1 + \rho_d = E\rho_2, \tag{7}$$

$$D_n - v_{2n} = EU_b(1 + \sigma f_{xx}), \tag{8}$$

$$\rho_1(D_n - v_{1n}) + \rho_d(D_n - v_{dn}) = \rho_2(D_n - v_{2n}), \tag{9}$$

Corresponding author: Nikolay S. Belyakov
*E-mail address*: N.S.Belyakov@gmail.com

$$\rho_1\left(D_n - v_{1n}\right)\bar{v}_1 + \rho_d\left(D_n - v_{dn}\right)\bar{v}_d - P_1\bar{n} = \\ = \rho_2\left(D_n - v_{2n}\right)\bar{v}_2 - P_2\bar{n}, \quad (10)$$

where σ – Markstein number, *f* – flame front, D – flame front velocity, index n – normal component, x – derivative with respect to coordinate.

It is assumed that the flame velocity depends on the concentration: $U_b = U_b(\phi)$, where concentration $\phi$ have the following form:

$$\phi = \frac{\rho_F v_1 + \rho_d v_d}{\rho_1 v_1}, \quad (11)$$

where $\rho_0$ – air density in fresh mixture, $\rho_F$ – combustible gas density in fresh mixture, $\rho_1 = \rho_0 + \rho_F$.

In the unperturbed state, according to the chosen coordinate system, the flame front is given by the equation $z = 0$, the velocity of the fresh mixture coincides with the velocity of the droplets and equal $U_b$, and the velosity of the combustion products is $EU_b$.

## 3. Results and Discussion

For perturbations of the form $\tilde{Y}\exp(\Omega t + ikx)$ obtained dispersion equation:

$$\bar{\Omega}^2 + \frac{2(1+\sigma k)}{1+E}\bar{\Omega} + \frac{2\sigma k}{1+E} + \frac{(1-E)}{E(1+E)} + \\ + \frac{\rho_d}{\rho_1}\frac{\dfrac{\alpha}{EU_b^0 k}}{\bar{\Omega} + \dfrac{\alpha}{EU_b^0 k} + \dfrac{1}{E}}\left(\frac{1}{1+E}\bar{\Omega}^2 + \frac{(1+\sigma k)}{1+E}\bar{\Omega} + \frac{2\sigma k}{1+E} + \frac{(1-E)}{E(1+E)}\right) = \\ = \frac{U_b'}{U_b^0}\frac{\rho_d}{\rho_0}\frac{\rho_1+\rho_d}{\rho_1}\frac{1-E}{1+E}\left(\bar{\Omega}^2 + 2\bar{\Omega} + \frac{1}{E}\right), \quad (12)$$

where $\bar{\Omega} = \dfrac{\Omega}{EU_b^0 k}$.

Denote $C = \dfrac{U_b'}{U_b^0}\dfrac{\rho_d}{\rho_0}\dfrac{\rho_1+\rho_d}{\rho_1}\dfrac{1-E}{1+E}$. Region with negative numbers C corresponds to a lean mixture, positive values C - rich mixture, and C = 0 - stoichiometry.

In the absence of droplets ($\alpha = 0$ and $\rho_d = 0$) the dispersion equation becomes an equation obtained by Markstein [2] for the premixed gases into account the curvature of the flame front.

Dependence of increment on the wave number is more complicated than in the classical theory of hydrodynamic instability

## 4. Concluding Remarks

In this paper we analyzed the effect of the density of droplets in the fresh mixture, the coefficient of expansion and other characteristics of gas-droplet mixture on the stability of the flame front. Was investigated by the limiting transition to the Darrieus-Landau theory of hydrodynamic instability planar flame. We investigated the modes of combustion in which was observed oscillations of the flame front which was detected experimentally [1].

**Acknowledgement**

This work was supported by the Ministry of Education and Science of the Russian Federation (contract no. 14.Y26.31.0003) and Far Eastern Federal University.

**References**

[1] F. Atzler, F.X. Demoulin, M. Lawes and Y. Lee, // Combustion Science and Technology–Volume 178, Issue 12, 1 June 2006, Pages 2177-2198.

[2] Zeldovich, Ya. B., Barenblatt, G. I., Librovich, V. B., and Makhviladze, G. M., *The Mathematical Theory of Combustion and Explosions*, (1985), 597.

# Catalytic Effect on Combustion in Heated Micro Channel

Shogo Onishi[1], Hisashi Nakamura[1], Takuya Tezuka[1], Susumu Hasegawa[1],
Kaoru Maruta[1], Nozomi Yokoo[2], Koichi Nakata[2]
[1]Institute of Fluid Science, Tohoku University, 2-1-1 Katahira Aoba-ku, Sendai, Miyagi, 980-8577, Japan
[2]Toyota Motor Corporation, Higashifuji Technical Center, 1200 Mishuku, Susono, Shizuoka, 410-1193, Japan

**ABSTRACT**

The effects of catalytic reactions on combustion were examined using a micro flow reactor with a controlled temperature profile. Pure platinum, platinum alloy and silica were used as samples and PRF90 was used as a fuel. Flame images were taken at various maximum wall temperatures on the inner surface of the reactor, $T_{w,max}$, and ignition temperature, which is the value of $T_{w,max}$ when normal flames or FREI were formed, was measured. Results showed that pure platinum showed the highest ignition temperature, indicating strongest suppression of the flame formation.

## 1. Introduction

Appropriate ignition control is an essential feature of spark ignition engines (SI engines). Since various kinds of materials which are supposed to reveal catalytic effects are used in electrodes of spark plugs, effects of catalytic or surface reactions on combustion must be investigated to avoid an undesirable ignition. However, there are few studies regarding this area.

In this study a micro flow reactor with a controlled temperature profile [1] was used. The micro flow reactor consists of a quartz tube with an inner diameter smaller than the ordinary quenching diameter which is heated by an external heat source providing a stationary temperature profile. This reactor was able to observe combustion and ignition characteristics of given fuels in the simple system and our previous study showed multi-stage oxidation as stable weak flames [2]. In this study, a gasoline primary reference fuel (PRF) was used as a fuel to consider SI engines and several samples from electrodes were employed, and then effects of catalytic reactions on gas-phase combustion were examined.

## 2. Experimental method

Figure 1 shows a schematic of the experimental setup. A quartz tube was used as a reactor channel and its inner diameter, $d$, was chosen to be 2.0 mm. The quartz tube was heated by a $H_2$/air flat-flame burner to obtain a stationary temperature profile along the inner surface of the tube in the axial direction. By controlling the equivalence ratio of the $H_2$/air flat-flame burner, the maximum wall temperature on the inner surface of the reactor, $T_{w,max}$, was changed. A sample from electrodes was placed in the region where maximum wall temperature was attained. Pure platinum, platinum alloy and silica were used as a sample. Note that silica is expected to have no catalytic reaction and used in insulators of spark plugs. For the platinum alloy and the silica, length of samples was 5 mm and diameter was 1 mm. Two kinds of pure platinum samples, one with total length of 30 mm for U =140 cm/s and another with total length of 15 mm for U = 7 cm/s were used. Both samples were folded in thirds and diameter was 0.3 mm.

PRF90 (*iso*-octane:*n*-heptane=90:10) was used as a fuel mixing pure $O_2$ and a heated PRF90/$N_2$ mixture which were supplied using mass flow controllers. The equivalence ratio was set to be 0.7. Two inlet mean flow velocities, $U$, of 7 and 140 cm/s were employed. To prevent condensation of the fuel, the fuel line was heated with an electric heater and controlled to be 373 K. Images of flames were captured using a digital camera with an optical band-pass filter (transparent wavelength: 431.4 nm; half bandwidth: 6.4 nm) for better observation of chemiluminecsence from hydrocarbon flames. Temperature measurement on the inner surface was made by a K-type themolcouple inserted from the exit of the reactor. Experiments were conducted at various $T_{w,max}$ and "ignition temperature" was defined as the value of $T_{w,max}$ when propagating flames (normal flames or FREI, discussd later) were formed.

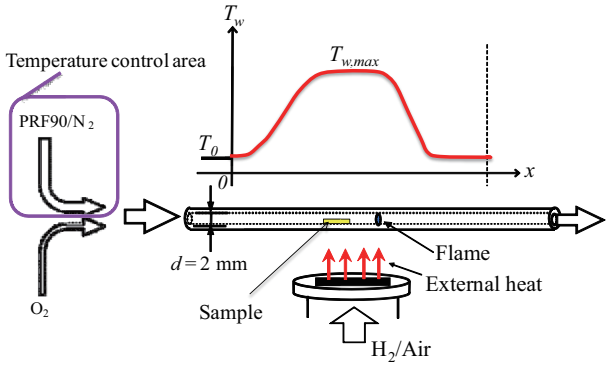


Fig. 1 Schematic of experimental setup and provided wall temperature profile.

## 3. Results and discussion

Figure 2 shows flame images in the cases with and without samples at $U$ = 7 cm/s. Two kinds of flames were obtained in all conditions; blue flames and FREI (Flames with Repetitive Extinction and Ignition) [3]. Blue flame is the second stage of the three-stage oxidation process of large hydrocarbons [4]. With the increase of $T_{w,max}$, blue flame was formed at first and then FREI was formed above a certain $T_{w,max}$ in all conditions. The extinction point of FREI for the silica sample is close to the upstream side of the sample while that with the platinum alloy sample is close to the downstream side of the sample. It implies that flame propagation was prevented by catalytic reactions on the surface of the platinum alloy sample. In the case of pure platinum, the ignition point

Corresponding author: Shogo Onishi
*E-mail address*: s.onishi@edyn.ifs.tohoku.ac.jp

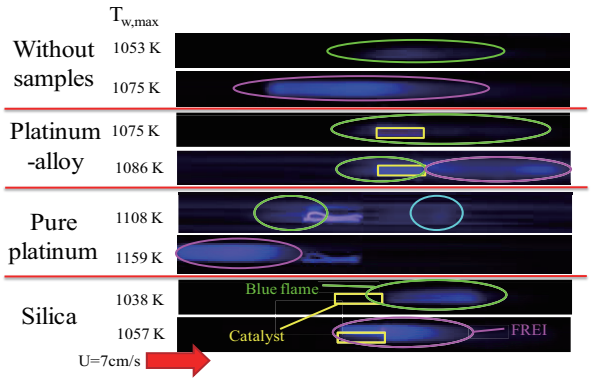


Fig. 2 Images of blue flame and FREI with and without samples at $U$ = 7 cm/s.

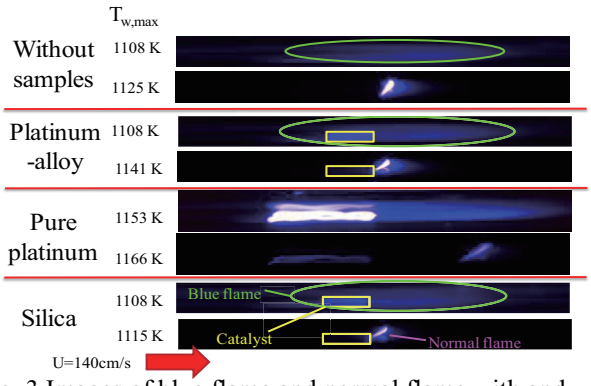


Fig. 3 Images of blue flame and normal flame with and without samples at $U$ = 140 cm/s.

of FREI was not formed in the downstream side of the sample and it was formed in the upstream side of the sample at very high $T_{w,max}$. The thermal radiation from the surface of pure platinum became strong when the mixture was supplied to the reactor. Such strong thermal radiation on the sample surface was not observed in the cases with platinum alloy and silica. Therefore, catalytic reactions on the pure platinum surface must occur and these suppressed ignition of FREI.

Figure 3 shows flame images in the cases with and without samples at $U$ = 140 cm/s. With the increase of $T_{w,max}$, blue flame was formed at first and then normal flame was formed above a certain $T_{w,max}$ in all conditions. In the cases of platinum alloy and silica, normal flames are formed close to the downstream side of the samples. In the case of pure platinum, on the other hand, normal flames are formed far downstream side of the sample. As in $U$ = 7 cm/s, the thermal radiation from the sample surface became strong only in the case of pure platinum when the mixture was supplied to the reactor. It implies that the some catalytic reactions on the pure platinum occur and these reactions would result in flames with lower flame speed.

Figure 4 shows ignition temperatures at $U$ = 7 cm/s and 140 cm/s. Ignition temperature at 140 cm/s is higher than that at 7cm/s. It must be due to the shorter residence times of the mixture at 140 cm/s than those at 7 cm/s. Ignition temperatures for pure platinum at both flow velocities are higher than those with the other samples. Figure 5 shows the difference in ignition temperatures

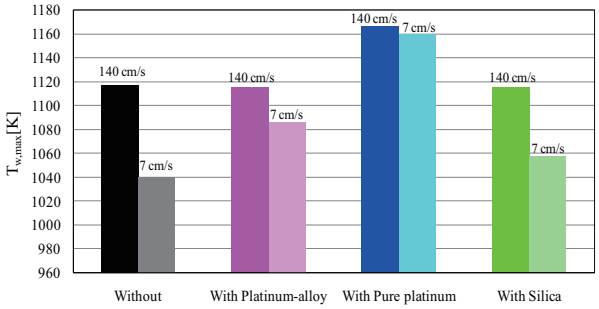


Fig. 4 Ignition temperatures at $U$ =7.0 and 140 cm/s with and without samples.

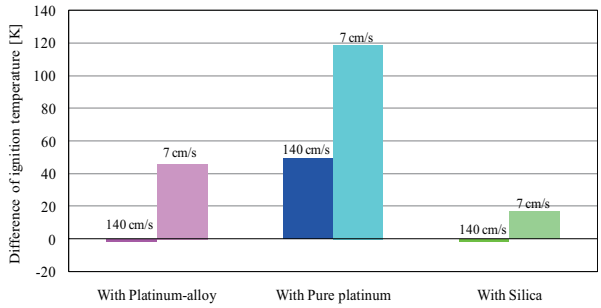


Fig. 5 Difference of ignition temperature between the cases with and without samples.

between the cases with and without samples (ignition temperature difference due to the existence of catalysis). At 7 cm/s, only pure platinum shows larger ignition temperature difference. At 140 cm/s, both pure platinum and platinum alloy show large ignition temperature differences. Ignition temperature difference in the case with pure platinum is larger than that in the case with platinum alloy. These results indicate that pure platinum showed the strongest flame suppression effect and platinum alloy follows.

## 4. Conclusions

The effects of pure platinum, platinum alloy and silica on ignition temperature were examined using a micro flow reactor with temperature gradient for PRF90/air mixtures. From the flame images obtained, catalytic reaction on the surface of platinum alloy inhibited flame propagation of FREI. Ignition temperature with pure platinum was higher than that without platinum. Catalytic reaction on the surface of platinum would suppress ignition in the conditions studied.

## References

[1] K. Maruta, T. Kataoka, N. I. Kim, S. Minaev and R. Fursenko, Proc. Combust. Inst. **30** (2005) 2429–2436.

[2] H. Oshibe, H. Nakamura, T. Tezuka, S. Hasegawa, K. Maruta,Combust. Flame **157** (2010) 1572–1580.

[3] Y. Tsuboi, T. Yokomori and K. Maruta, Proc. Combust. Inst. **32** (2009) 3075–3081.

[4] A. Yamamoto, H. Oshibe, H. Naamura, T. Tezuka, S. Hasegawa, K. Maruta, Proc. Combust. Inst. **33** (2011) 3259-3266.

Eleventh International Conference on Flow Dynamics
October 8-10, 2014, Sendai, Miyagi, Japan

# Investigation of Dispersion of Nano-sized $TiO_2$ Particle in CFRP by using VaRTM

Asuka Konno[1], Hiroyuki Kosukegawa[2], Hiroyuki Miki[3], Toshiyuki Takagi[2]
[1] Graduate School of Engineering, Tohoku University, 6-6 Aramaki Aza Aoba, Aoba-ku, Sendai, Miyagi, Japan
[2] Institute of Fluid Science, Tohoku University, 2-1-1 Katahira, Aoba-ku, Sendai, Miyagi, Japan
[3] Frontier Research Institute for Interdisciplinary Sciences, Tohoku University, 6-3 Aramaki Aza Aoba,Aoba-ku, Sendai, Japan

**ABSTRACT**

It is suggested to add nanoparticles in matrix of CFRP to improve mechanical properties such as ductility. In this study, CFRP including nano-sized $TiO_2$ is prepared by vacuum assisted resin transfer molding, and the dispersion of nanoparticles is investigated with SEM and EDS in terms of dispersive coefficient of resin/$TiO_2$ solution.

## 1. Introduction

Carbon fiber reinforced plastic (CFRP) is a composite material made of polymeric resin and carbon fibers. Because it has some remarkable features such as high strength and lightweight properties, CFRP is expected as structural material to replace metals such as aluminum and steel. There are, however, some issues in use of CFRP as structural material; e.g., low ductility to induce interlayer delamination.

Recently, to improve interlayer toughness, adding nanoparticles like carbon nanotube approch is proposed [1]. In addition, to add nanoparticles such as $TiO_2$ in resin can increase mechanical properties [2]. However, there are few studies to evaluate the distribution of nanoparticles in CFRP.

The objective of this study is to investigate the diffusion in CFRP and the relationship between dispersion and diffusion characteristics. Addition of nano-sized $TiO_2$ particles in CFRP is performed with vacuum assisted resin transfer molding technique (VaRTM). Observation of $TiO_2$ particles in CFRP is performed with scanning electron microscope (SEM) and energy dispersive X-ray spectrometry (EDS).

## 2. Experiments

### 2.1 Materials

Epoxy resin used in this study is two-liquid mixing type purchased from ThreeBond Co., Ltd. The main agent is TB2023 with viscosity at 25ºC of 0.9 Pa・s, and cure agents are TB2163 and TB2131D, their viscosities at 25ºC of 1.15 Pa・s and 0.01 Pa・s, respectively.

Carbon cloth with UT-60S (Toray Industries Inc.). The warp yarn is T700SC (number of filaments = 24000) and the weft yarn is glass fiber. The thickness of UT-60S is 1 mm.

$TiO_2$ particles are Super Titania, G-1 and F-6A purchased from Showa Denko K.K. The particle diameters of G-1 and F-6A are 250 nm and 15 nm respectively.

### 2.2 Preparation of Epoxy Resin including $TiO_2$

Main agent and cure agent of epoxy resin were mixed with rotation-revolution mixer. 4.4 wt% of $TiO_2$ particle was added in the epoxy solution, and was homogeneously dispersed with rotation-revolution mixer; agitation was conducted for three minutes with rotation/revolution = 800/2200 rpm, and defoaming was performed for one minute with rotation/revolution = 0/2000 rpm. The epoxy resin including $TiO_2$ was impregnated into carbon cloth in one hour since dispersion.

To evaluate influence of diffusion characteristics of epoxy/$TiO_2$ solution on the dispersion of nanoparticles in resulting CFRP, diffusion coefficient ($D$) is calculated by the formula of Stokes-Einstein (1):

$$D = k_B T / 6\pi r\eta, \tag{1}$$

where $k_B$ is Boltzmann constant, $T$ is temperature of the epoxy/$TiO_2$ solution, $r$ is radius of $TiO_2$ particles, and $\eta$ is viscosity of epoxy/$TiO_2$ solution.

### 2.3 Preparation of CFRP including $TiO_2$

As shown in Fig. 1, carbon cloth was cut by 130 × 150 mm$^2$ and was laminated on aluminum board. Fiber direction of laminates was in one direction to be parallel to the flow of epoxy solution. Flow path of epoxy solution and carbon laminates were covered with a vacuum bag. Inside of the bag was evacuated with vacuum pump from outlet side of the flow path. By vacuuming, the epoxy solution was impregnated into carbon cloth laminates from inlet side of the flow path. After impregnation, the inlet and outlet of the flow paths were closed, and the inside of the bag was sealed. After sealing, the vacuumed set including CFRP was heated in oven at 100ºC for two hours.

With different cure agents and $TiO_2$, two combinations of epoxy/$TiO_2$ solution were prepared. Table 1 shows characteristics of the specimen 1 and 2.

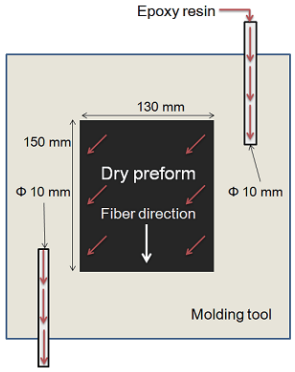


Fig. 1 Top view of VaRTM method.

Corresponding author: Hiroyuki Kosukegawa
*E-mail address*: kosukegawa@wert.ifs.tohoku.ac.jp

Table 1. Characteristics of CFRP including $TiO_2$ particles.

| Test specimen number | Diameter of $TiO_2$ (nm) | Viscosity of cure agent (Pa·s) | Viscosity of main agent (Pa·s) | Diffusion coefficient ($m^2/s$) |
|---|---|---|---|---|
| 1 | 250 | 1.15 | 0.9 | $8.7 \times 10^{-16}$ |
| 2 | 15 | 0.01 | 0.9 | $9.7 \times 10^{-14}$ |

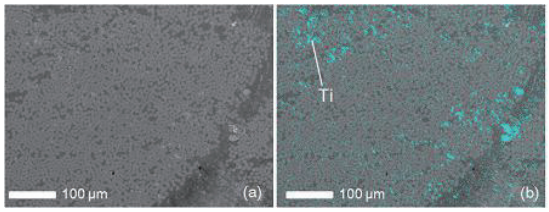

Fig. 2 (a) SEM image of tow and (b) Ti mapping on SEM image at the inlet section.

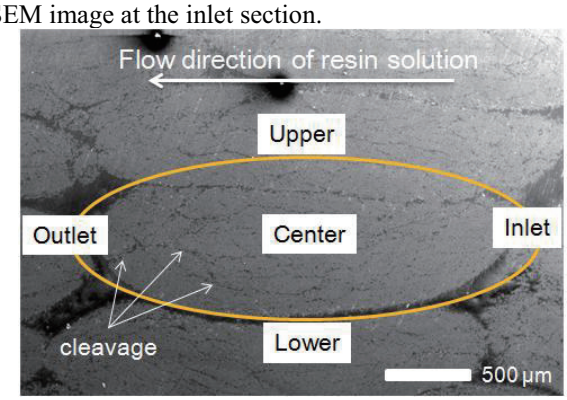

Fig. 3 A full SEM image of one tow in CFRP. The dispersion of $TiO_2$ at the five sections of a tow was investigated.

### 2.4 Observation of $TiO_2$ in CFRP

The prepared CFRP was cut in direction perpendicular to the fiber direction, and the cross section was polished. As shown in Fig. 2, the dispersion of $TiO_2$ on the cross section was observed with SEM (JSM6530、Japan Electron Optics Laboratory Ltd.) and EDS (Ultra Dry, Thermo Fisher Scientific Inc.). The tow of CFRP, which is a bundle of carbon fibers, was observed in particular. The observed area on a tow was separated into five sections: i.e., inlet, outlet, upper, lower and center (Fig. 3). The area ratio of picture elements for Ti per entire elements of EDS image was calculated by image processing with a software package (ImageJ, NIH). The condition of SEM was unified as the magnification ratio was 350, the electron accelerating voltage was 15 kV, and the spot size was fixed. The spectrum of characteristic X-ray of three tows for each specimen was observed to determine the mean and standard deviation of the area ratio of Ti in a tow.

## 3. Results and Discussion

From the SEM image of Fig. 3, the carbon filaments of a tow cleave in a horizontal direction due to pressure from upper side in VaRTM technique. Fig. 4 shows the area ratio of Ti of specimen 1 and 2. The area ratio of Ti at the inlet and outlet sections in both specimen 1 and 2 are larger than at the upper and lower sections. The reason is that the cleavages at the inlet and outlet sections are larger than those at the upper and lower

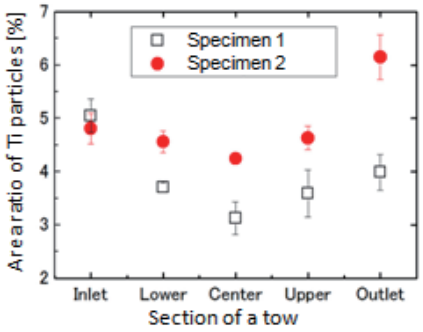

Fig. 4 Area ratio of Ti particles in a tow of test specimen 1 and 2.

sections. Therefore, $TiO_2$ nanoparticles easily flow into the inlet and outlet sections. The area ratio of Ti at the center is smaller than other sections as shown in Fig. 4.

In addition, by comparing specimen 1 and 2 in Fig. 4, specimen 2 has a high percentage of the area ratio of Ti in the four sections with the exception of the inlet. With the comparison of diffusion coefficients of the specimens in Table 1, specimen 2 shows a larger value of about 100 times than that of specimen 1. Therefore, it is suggested that diffusion coefficient is related to the dispersion of $TiO_2$ nanoparticles in CFRP. Diffusion coefficient is the parameter which indicates diffusing capacity of particles and which does not depend on influence of advection. Because the inlet section is subjected to the flow of solution, the other sections are considered to be less influence of advection of the resin. This condition and Fig. 4 indicated that diffusing capacity of $TiO_2$ nanoparticles influences on the dispersion of the particles.

From these results, it is considered that diffusion coefficient of nanoparticles influences on dispersion of the particles in tows. As other causes of influence on dispersion of nanoparticles, shape of tow and cleavages of filaments are to be considered.

## 4. Summary

CFRP including nano-sized $TiO_2$ particles is prepared with the VaRTM, and the dispersion of nanoparticles is evaluated with SEM and EDS. The dispersion of nanoparticles is influenced by diffusion coefficient of resin/$TiO_2$ solution.


## Acknowledgement

This work was partly supported by a Grant-in-Aid for Young Scientists (Start-up) Grant Number 25889008 and the JSPS Core-to-Core Program, A. Advanced Research Networks, “International research core on smart layered materials and structures for energy saving”.


## References


[1] Y. Li, N. Hori, M. Arai, N. Hu, Y. Liu, H. Fukunaga, *Composites: Part A,* 40 (2009) 2004－2012.

[2] C.B. Ng, L.S. Schadler, R.W. Siegel, *Nanostructured Materials*, 12 (1999) 507－510.

Eleventh International Conference on Flow Dynamics
October 8-10, 2014, Sendai, Miyagi, Japan

# Combustion Enhancement by Ozone Addition in Supersonic Flow

Junya Kurasawa, Ko Murata, Taku Kudo, Akihiro Hayakawa and Hideaki Kobayashi
Institute of Fluid Science, Tohoku University
2-1-1 Katahira, Aoba-ku, Sendai 980-8577, Japan.

**ABSTRACT**

Numerical simulations were conducted to explore the combustion enhancement by ozone addition in supersonic flow. Ozone was injected perpendicular to the main flow 15 mm or 45 mm upstream of the fuel injection slot. By ozone addition, mole fraction of OH radical increased more than that in the conditions without ozone. This is because O radical generated from ozone was supplied to combustion area. When ozone was injected near the fuel injection slot, O radical of high concentration was supplied to combustion area.

## 1. Introduction

Scramjet engine is one of the most efficient propulsion system for hypersonic flight, while it is difficult to hold a steady flame because of the short residence time of a fuel in supersonic flow. Therefore, to complete the combustion in short time is the key technology for the development of scramjet engine. There are two ways to keep stable combustion:

1. Forming a recirculation zone in supersonic flow for mixing fuel and air.
2. Increasing the rate of a chemical reaction.

In the past, several studies to mix fuel and air have been performed, which include cavity, strut and so on. However, a pressure loss is high by using such aerodynamic devices. On the other hand, there are no such problems in a way that promotes chemical reaction. Above all, ozone, which can be easily generated from oxygen by using dielectric barrier discharge (DBD) device, is a strong oxidizer and has been studied as a combustion enhancement matter recently [1,2]. However, quantitative measurement of the amount of generation of the ozone by DBD device in supersonic flow is not performed and it is not clear what quantity of ozone contributes to the enhancement of combustion.

The purpose of this study is to examine the combustion intensification by ozone addition in supersonic flow using numerical simulation.

## 2. Method of the numerical simulation

The governing equations were the two-dimensional Reynolds averaged Navier-Storkes (RANS) equations with Wilcox's $k$-$\omega$ two-equation turbulence model [3] and species conservation equations. These equations were solved using finite volume method. The convection terms were evaluated by AUSM-DV method [4] with the third-order MUSCL approach. The viscous terms were evaluated by the second-order central differential scheme. The Matrix Free Gauss-Seidel (MFGS) method was used for the time integral. Muller's $H_2$-$O_2$ kinetic mechanism [5] together with Wang's $O_3$ kinetic mechanism [2] involving 16 elementary reactions was composed.

The summary of free-stream, fuel injection and ozone injection conditions are given in Table 1. The fuel injection gas was pre-burned hydrogen/air gas whose equivalence ratio is 3.6. The total temperature of the pre-burned injection gas was estimated by a chemical equilibrium calculation using CHEMKIN PSR. The ozone injection gas was premixed $N_2/O_3$ gas which is assumed that oxygen in the air has changed in all ozone. In addition, the conditions where air injected instead of $N_2/O_3$ gas for comparison were also considered.

The calculation area is shown in Fig. 1. The set of grid points was a structured grid having 116,000 cells. Both of two injection holes are 0.5 mm in width, and inject gas vertically from the surface of the wall. The surface of the wall was no-slip adiabatic wall. Although the distance between the ozone injection and fuel injection is 45 mm in Fig. 1, 15 mm case was also calculated for comparison.

Table 1. Summary of main flow, fuel injection and ozone injection.

| | | |
|---|---|---|
| Main flow | Ma | 2.5 |
| | Tt (K) | 673 |
| | Pt (MPa) | 0.5 |
| Fuel (Pre-burned $H_2$/air) | Ma | 1 |
| | Tt (K) | 1635 |
| | Pt (MPa) | 0.5 |
| Ozone ($N_2/O_3$) | Ma | 1 |
| | Tt (K) | 300 |
| | Pt (MPa) | 0.1 |

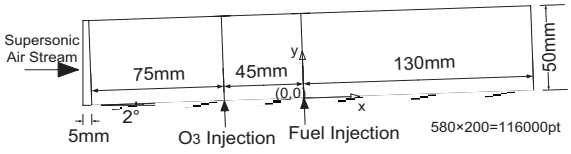


Fig. 1 The calculation area.

Corresponding author: Junya Kurasawa
*E-mail address*: kurasawa@flame.ifs.tohoku.ac.jp

## 3. Results and discussion

Two-dimensional numerical simulations with the fuel injection and ozone injection were conducted under the four conditions. Figure 2 shows OH radical mole fraction distributions in four conditions:

(a) Air injection 15 mm upstream of the fuel injection slot.

(b) $N_2/O_3$ injection 15 mm upstream of the fuel injection slot.

(c) Air injection 45 mm upstream of the fuel injection slot.

(d) $N_2/O_3$ injection 45 mm upstream of the fuel injection slot.

In Fig. 2, the OH radical was rarely seen in the two conditions of no ozone addition. However, the OH radical mole fraction increased near the fuel injection slot and in downstream area by ozone addition. It suggests that combustion was enhanced by ozone addition. It is reported that the reaction R1 contributes to the mechanism of this combustion enhancement by ozone [2].

$$O_3+N_2=O_2+O+N_2 \qquad (R1)$$

In brief, O radical is generated by three body reaction of $O_3$ and $N_2$. Therefore, $H_2/O_2$ branched-chain reactions are promoted by extra O radical. In order to verify this regard, the O radical mole fraction distributions of the two conditions are shown in Fig. 3. In air injected condition, O radical was rarely seen in the whole calculation area. On the other hand, under the condition of the ozone addition, the O radical mole fraction increased in the three areas, which include the vicinity of fuel injection, downstream area and the vicinity of ozone injection. The increase of the O radical mole fraction in the former two regions was due to combustion considering OH radical mole fraction distribution. However, the O radical mole fraction increase in the vicinity of ozone injection was not match OH mole fraction distribution, so it is due to decomposition reaction including R1 rather than $H_2/O_2$ combustion reactions.

By comparing the conditions (b) with (d), the OH mole fraction in the condition (b) was more than that of condition (d). Due to long distance between two injections, the O radical dispersed. Therefore, high concentration O radical was not supplied to combustion area and combustion enhancement was limited.

## 4. Concluding remarks

In this study, the combustion enhancement by ozone addition was investigated by numerical simulations. By ozone addition, the O radical concentration increased and combustion was enhanced. The effect of ozone was remarkable when ozone was injected near the fuel injection.

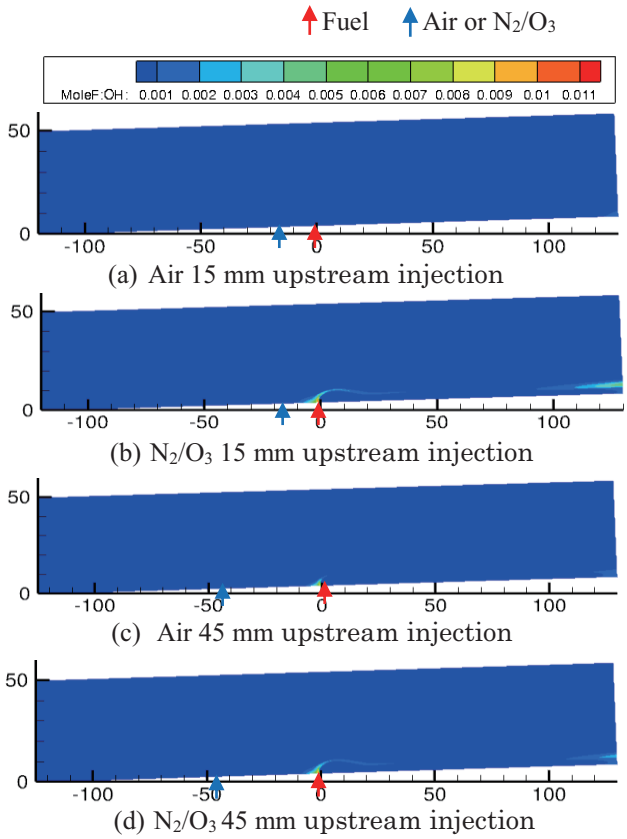


Fig. 2 OH mole fraction distribution.

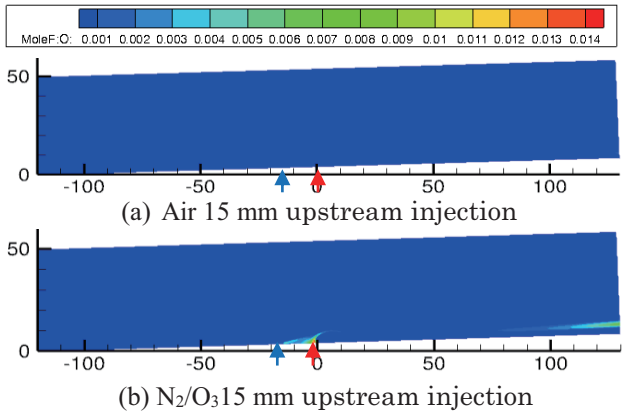


Fig. 3 O mole fraction distribution.

## References

[1] Y. Matsubara, K. Takita, G. Masuya, *Proceedings of the Combustion Institute*, Vol. 34 (2012), 3287–3297.

[2] Z. H. Wang, L. Yang, B. Li, Z. S. Li, Z. W. Sun, M. Alden, K. F. Cen, A. A. Konnov, *Combustion and Flame,* Vol. 159 (2011), 120–129.

[3] D. C. Wilcox, *Turbulence Modeling for CFD 2nd ed., DCW Industries*, 1998.

[4] Y. Wada, M. S. Liou, *AIAA Paper* (1994), 94–0083.

[5] M. A. Mueller, T. J. Kim, R. A. Yetter, F. L. Dryer, *International Journal of Chemical*, 31 (1999), 113–125.

# Visualization of Laminar to Turbulent Transition on Re-entry Capsule using TSP in High Enthalpy Shock Tunnel

Takehiro Nagayama[1], Takehito Horagiri[1], Hiroki Nagai[1], Hiroyuki Tanno[2], Tomoyuki Komuro[2]
[1]Department of Aerospace Engineering, Tohoku University
6-6-01, Aramaki-Aza Aoba, Aoba-ku, Sendai-shi, Miyagi, 980-8579, Japan
[2]Japan Aerospace Exploration Agency
1 Koganezawa, Kimigaya, Kakuda-shi, Miyagi, 981-1525, Japan

**ABSTRACT**

A visualization experiment was performed in a high-enthalpy shock tunnel (HIEST). The test model was the re-entry capsule model HRV. This study visualized the hypersonic boundary-layer transition on the side of the model using Temperature-Sensitive Paint (TSP). Temperature distribution on the model's surface was successfully visualized, though the heat flux could not be calculated due to self-illumination. Additionally, the increase in temperature measured by TSP agreed with the data obtained from thermocouples installed in the model; the difference between them was within 2.5%.

## 1. Introduction

When a space vehicle re-enters the atmosphere, an intense shock wave generates on the front face of the vehicle, causing its aerodynamic heating. To calculate the amount of aerodynamic heating in wind tunnel test, temperature sensor such as thermocouples is used [1]. However, the method measures only discrete "points" data. In contrast, by using Temperature-sensitive Paint (TSP) it's possible to get a full-field image of temperature distribution on the model surface [2]. Because the turbulence region of the boundary layer developed on the model has a greater heat transfer coefficient than the laminar region, a difference in the recovery temperature is also observed. However, the boundary-layer transition on a model has never been measured using a TSP in a high-enthalpy shock tunnel (HIEST), which is capable of simulating the re-entry in the atmosphere. In such a HIEST experiment, optical measurement is difficult because of the self-illumination of dissociating oxygen and nitrogen molecules. Other challenges are the responsiveness of the TSP and the exposure time of the camera while it is used to shoot photos during the test.

Considering those background, this study developed a highly luminescent and sensitive TSP, which can be applied to wind tunnels for short tests. The TSP was applied in the HIEST at Japan Aerospace Exploration Agency to visualize the boundary-layer transition of a re-entering capsule.

## 2. Experimental Setup and Conditions

Figure 1 shows the sketch of the test model used for the experiment. The model was used to align the transition measurement region parallel to the flow. At the measurement region, seven trips were inserted to force a laminar-to–turbulent transition and five coaxial thermocouples were also installed: one on the upstream of the trips and four on the downstream.

A high-power blue laser diode was used to excite the TSP with which the model was coated. The luminescent

Corresponding author: Takehiro Nagayama
*E-mail address*: nagayama.takehiro@aero.mech.tohoku.ac.jp

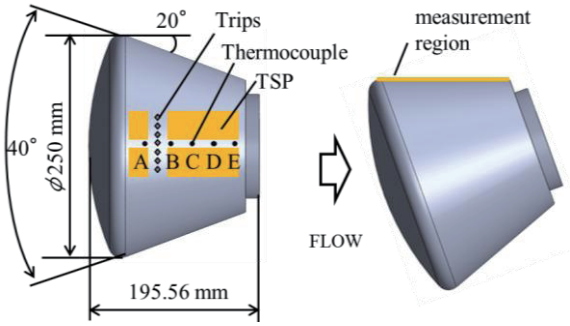


Fig. 1 Sketch of the test model.

of the TSP was detected by 12-bit high-speed camera. A 105-mm lens was mounted on the camera, and the *f* value was set at 2.8. A 560-nm, high-pass filter was attached to the camera to block light other than that emitted by the TSP. The sampling rate and exposure time of the camera were set to 10 kHz and 1/10342 s, respectively.

The material of test model SUS303 had relatively high heat conductivity. Thus, it was primed with a white paint to improve the insulation under the TSP coating. A summary of the TSP coating is given in Table 1. Table 2 lists the test conditions. Nitrogen ($N_2$) was used as the test gas.

Table 1 Summary of TSP coating.

| TSP | Ru(phen)-TSP |
|---|---|
| Mixture | Calcium silicate |
| Mixing ratio | 50% |
| TSP Thickness | 14±6 μm |

Table 2 Experimental conditions.

| | | | |
|---|---|---|---|
| $P_0$ [MPa] | 18.5 | $\rho_\infty$*10$^3$ [kg/m$^3$] | 26.9 |
| $H_0$ [MJ/kg] | 2.62 | $u_\infty$ [km/s] | 2.20 |
| $T_\infty$ [K] | 184 | $Re/10^6$ | 3.31 |

## 3. Data acquisition

Dark images ($I_{dark}$), wind-off images ($I_{ref}$), and wind-on images ($I$) are necessary to analyze the TSP

images. Therefore, dark images were captured before turning on the light, and wind-off images were shot with the excitation light turned on. Subsequently, wind-on images were acquired at the same time when the flow started.

## 4. Results and Discussion

### 4.1 Temperature distribution

Figure 2 shows the time history of rise in the temperature of the thermocouples. This result revealed that there was an approximate difference of 10°C in the temperatures at the front and back of the trips ('A' and 'B', respectively); however, the differential between points 'B' and 'E' was as low as 0.5°C.

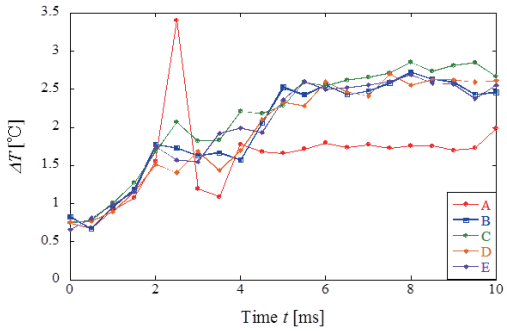


Fig. 2 Time history of rise in the temperature of thermocouples.

Figure 3 shows the image of temperature distribution. This image revealed that the temperature rises by approximately 10°C between the front and back of the trip, but changes little downstream of the trips. A longitudinal, vortex-like flow occurred immediately behind the trips; this subsequently transitioned into turbulence and contributed to a rise in the temperature.

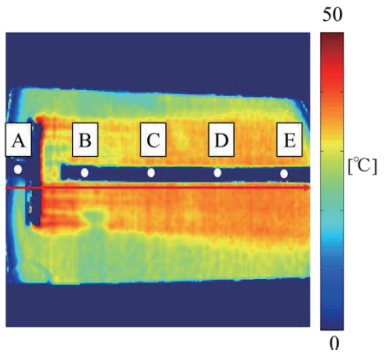


Fig. 3 Temperature distribution calculated from the intensity distribution image.

In Fig. 4, the temperature rise ratio of the thermocouples and TSP are compared. Horizontal axis indicates the normalized values of the length of the image, while vertical axis indicates the normalized values of the temperature at point 'B'. From this result, the difference in the temperature rise ratio in the front and back of the trips is found to be 1.27% and 2.5%, respectively.

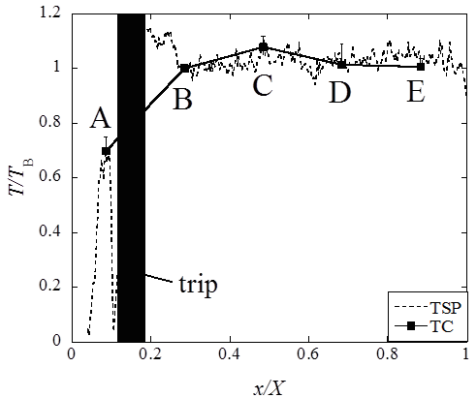


Fig. 4 Normalized values of the length of the image.

### 4.2 Spreading angle of region of turbulence

Figure 5 is an image that was normalized by the maximum temperature, and the counter lines of the normalized values 0.80, 0.85 and 0.90 were drawn. Both the horizontal and vertical axes were normalized by 350 pixels. The contour lines confirmed that the turbulence region became broader downstream.

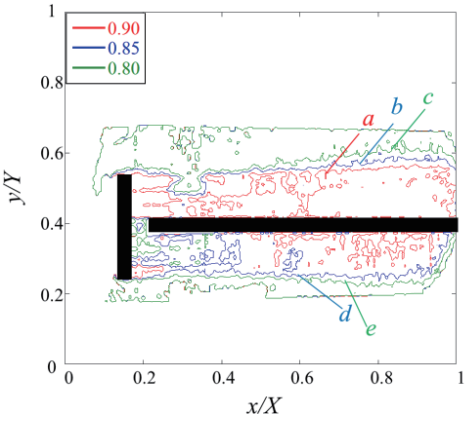


Fig. 5 Counter lines of maximum temperature.

## 5. Conclusion

The developed TSP was applied in the HIEST to visualize the laminar-to-turbulent transition location. The findings of the study are as follow:

1. The boundary-layer transition on the HTV-R model was visualized using the TSP.
2. From the comparison of between the TSP results and thermocouples, the difference in the temperature rise ratio in the front and the back of the trips and downstream was found to be 1.27% and within 2.5%, respectively, indicating a consistent qualitative direction.
3. The spreading angle was found to rage between 0.9° and 5.76° in the downstream direction

## References


[1] T. Hashimoto, T. Komuro, M. Takahashi, K. Sato, K. Itoh, G. Jadadeesh, K. P. J. Reddy, *43rd National Heat Transfer Symposium, 2006*.

[2] T. Liu, J. P. Sullivan, *Springer, Berlin, 2005.*

# Evaluation of Mixing Performance in a Hypermixier Scramjet Combustor

Noritsugu Kubo[1], Sadatake Tomioka[2]
[1]Department of Aerospace Engineering, Tohoku University
Aoba Aramaki-Aza-Aoba 6-6-01, Sendai, 980-8579, Japan
[2]Kakuda Space Center, Japan Aerospace Exploration Agency
Kimigaya Koganezawa 1, Kakuda, 981-1525, Japan

**ABSTRACT**

To improve the performance of the scramjet combustor with a modification of the injector, two kinds of injectors which have different shapes, i.e. a physical ramp injector (Hyper-Mixer) and an application of aeroramp in place of its injector wedge, were investigated experimentally. In this study, experiments were conducted under "cold flow." As a result, the difference of flow filed between Aeroramp and Hyper-Mixer was observed in the pitot pressure distribution, on the other hand we could not find the difference from schlieren photographs.

## 1. Introduction

Supersonic mixing and combustion control is the key technology for the development of the scramjet engine. Especially, the mixing and combustion enhancement is one of the problems that must be solved to develop the scramjet engine. In the supersonic flow, generation of turbulent eddies and entrainment of the supersonic mixing layer decline by the compressibility effect, hence the mixing performance of the engine is significantly reduced. Therefore, a technique of diminishing the compressibility effect and promoting of the mixing of air and fuel is required. Usage of the streamwise vortices is one of the promising ideas for enhancement of fuel/air mixing in supersonic flow. The fuel injectors which introduce streamwise vortices in the mainstream, is proposed in the past few. For example, it is "Hyper-mixer" and "Aeroramp." The purpose of this study was made to evaluate and improve on the performance of the scramjet combustor by a modification of the injector.

## 2. Experimental Setup

In this study, experiments were conducted under cold flow. "Cold flow" means no enthalpy release by chemical reactions. Figure 1 shows the test section using current work. The flow path of this is the similar shape to scramjet combustor which was used in previous combustion tests. However, this test section has the lower half of the duct in comparison with the combustor for the combustion tests. The top wall of the test section was in a gradient of 1/100 to diminish the effect of developed boundary layer on the top wall, because such boundary layer does not exist in combustion tests and may cause unexpected static pressure raising and trigger the generation of unexpected shock wave by the boundary layer separation. The test section was connected to an intermittent suction-type wind tunnel through an adjustable back pressure chamber. A throttling valve is placed downstream of the back pressure chamber, to simulate the blockage effects of heat release in parallel section. Thus, a flow structure in combustion tests can be reproduced in cold flow [1].

Corresponding author: Noritsugu Kubo
*E-mail address*: n.kubo@scrj.mech.tohoku.ac.jp

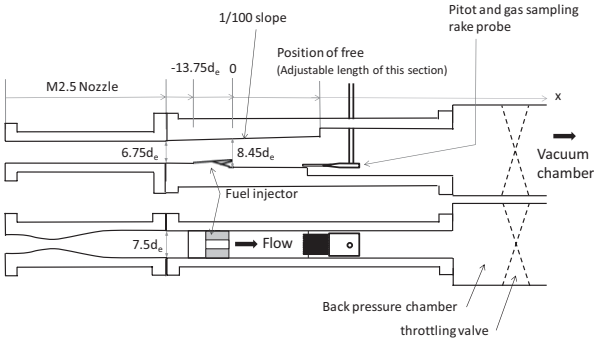


Fig. 1 Schematic image of test section.

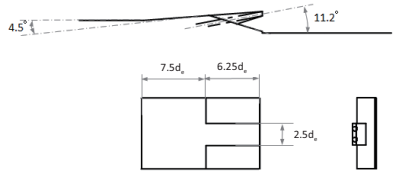


(a) Hyper-Mixer injector

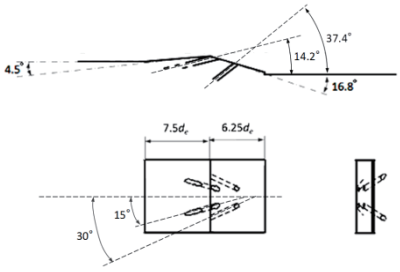


(b) Aeroramp injector

Fig. 2 Outline of design for injectors.

Fuel gaseous was simulated by helium gas of room temperature and pressure. To obtain the corresponding combustion and cold flow test, the wall pressure distribution was matched. In this study, two kinds of injectors which have different mechanism of generating streamwise vortices were investigated. The first model is physical ramp injector which was called "Hyper-Mixer", the other model is "Aeroramp" injector. Hyper-Mixer injector tested in the present experiments is based on the design concept introduced by Sunami et al. Hyper-mixer

injector was consisted of a two-dimensional compression ramp at upstream side, and a following generating streamwise vortices section. At this section, wedges were formed by extended compression ramp from the upstream side, and wedges and expansion ramps were arranged alternately in the span width direction. Moreover, the cavity at under the compression wedge exists. Figure 2 (a) shows a schematic of the injector model used in the current work. The injector can introduce a pairs of large-scale counter-rotating streamwise vortices in a spanwise row configuration. Fuel was injected into such vortices through circular orifices locate at the trailing edge of wedges. A second injector model is simulated by an application of Aeroramp proposed by Schetz and Jacobsen et al [2]. in place of injector wedges of Hyper-mixer. The aeroramp was located on a two-dimensional expansion ramp, which was composed of four flush-wall jets. The physical wedge effect on flow field was imitated by the exclusion effect due to four flush-wall jets. Figure 2 (b) shows a schematic of the injector model used in the current work.

## 3. Results and Discussion

In Fig. 3, flow field in the four conditions which were visualized by the schlieren method were compared. One condition of without back pressure rise was simulated the flow field of nearby injectors with non-combustion and low combustion pressure in combustion tests. The other is conditions of with fuel injection and back pressure rise. This condition was simulated the flow field of nearby injectors with high combustion pressure in combustion tests. Both conditions were set for each injector, respectably. From these figures, a large difference in the flow field between using Aeroramp and Hyper-Mixer injectors is not observed. On the other hand, the flow field is significantly changed by the control of back pressure. The flow field under without back pressure was clearly generated streamwise vortices in injector wake flow, but in the flow field with high back pressure, streamwise vortices was not generated much. The figures show that the boundary layer on injector compression ramp is separated at the leading edge of the injector expansion ramp and become a separated shear layer. This flow structure indicates that the injector wedges are covered with a large separation bubble. Figure 4 shows the Pitot pressure distribution. In this figure, the difference of flow filed between Aeroramp and Hyper-Mixer were observed in the Pitot pressure distribution, in spite of we could not find the difference from Schlieren photograph. In more detail, the fuel plume of Hyper-Mixer is growth in height direction, on the other hand, that of Aeroramp is a shape that was stretched to the span direction.

## 4. Concluding Remarks

The cold flow tests were conducted for the fuel mixing in a scramjet combustor. As a result, the difference of flow filed between Aeroramp and Hyper-Mixer was observed in the pitot pressure distribution, on the other hand we could not find the difference from schlieren photographs. In future, we will evaluate the mixing efficiency from fuel distribution by the gas sampling and component analysis.

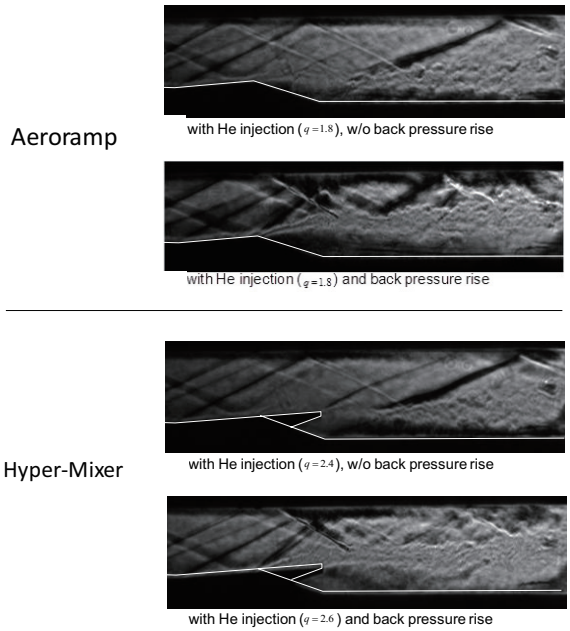


Fig. 3 Schlieren visualization which were comparison of wake flow field between Aeroramp (top 2 figures) and Hyper-Mixer (bottom 2 figures).

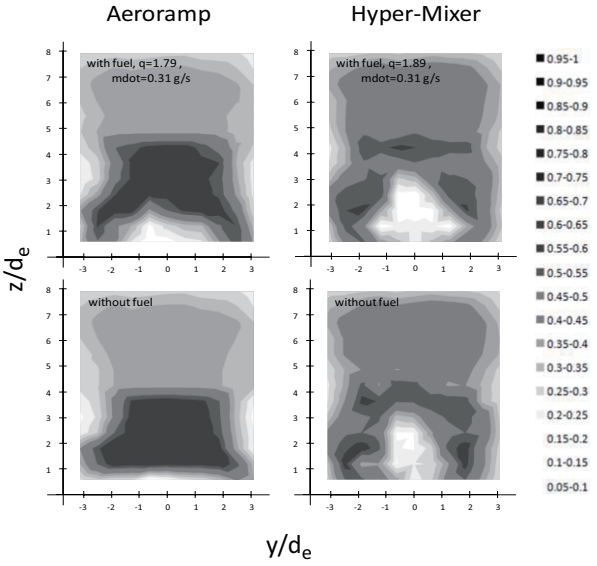


Fig. 4 Pitot pressure distributions which were comparison between Aeroramp (left) and Hyper-Mixer (right) / with fuel (top) and without fuel (bottom).

## References

[1] F. S. Billig, *Journal of Propulsion and Power,* Vol. 9, no. 4, 1993.

[2] L.S. Jacobsen, S.D. Gallimore, J.A. Schetz, W.F. O'Brien, L.P. Goss, *Journal of Propulsion and Power,* Vol. 19, no. 4, 2003.

# Hydro-thermal-mechanical Coupled Simulation of Fluid Flow in Fracture at Depths for Geothermal Development

Kosuke Kaneta[1], Yusuke Mukuhira[2], Takatoshi Ito[2]
[1]Graduate school of Environmental Studies, Tohoku University
6-6-20 Aza Aoba, Aramaki, Aoba-ku, Sendai, Miyagi, 980-8579, Japan
[2]Institute of Fluid Science, Tohoku University
2-1-1 Katahira, Aoba-ku, Sendai, Miyagi, 980-8577, Japan

**ABSTRACT**

We investigated the effect of thermal contraction of rock mass on fracture permeability. We simulated the change of fracture permeability when low temperature fluid was injected into single fracture within high temperature rock mass subjected to confining stress. The results showed that fracture permeability increased due to thermal contraction of rock mass in case that the temperature difference was larger than a critical value.

## 1. Introduction

In geothermal development, reinjection is an important tool for field management [1]. The reinjection may help with the recharge of the geothermal reservoir. However, reinjection may also cause cooling of the reservoir. Therefore, it is important to consider optimum condition of the reinjection.

It has been known from the field tests that cold fluid injection results in improvement of the injectivity comparing the hot fluid injection [2]. Such improvement is interpreted as the effect of thermal contraction of the rock mass around fractures. However, the in-situ compressive stress should suppress the fracture opening. It is uncertain whether the thermal contraction of rock mass causes the fracture opening which affects change in fracture permeability. In consideration of that, Ito et al. [3, 4] investigated the effect of thermal contraction on fracture opening by conducting 2D FEM simulation for cold fluid flow in a fracture network within high temperature rock mass. As a result, it has been found that fracture permeability increased drastically. That phenomenon occurred when the difference in temperature between the rock mass and injected fluid was larger than a critical value. The critical value is given as a function of confining stress, fluid pressure in fracture and elastic properties of rock mass.

In this study, we examined in more detail the problem whether the thermal contraction of rock mass causes increase of fracture permeability. We focused on a single fracture and investigated the effect of thermal contraction of rock mass on change in fracture permeability by numerical simulation.

## 2. Methodology of analysis

All calculations were carried out by using a 2D Finite Element Modeling code of Geocrack2D, which was developed by Swenson et al. [5]. This code can treat the coupled problem of fluid flow in fractures, thermal/elastic deformation of rock mass and heat transfer by fluid flow and conduction.

Figure 1 shows the model of a 5x5 $m^2$ rock mass subjected to uniform confining stress $S$ ($=S_x=S_y$). A single horizontal fracture of 1 m long was located at the center. Considering the symmetry of the model and loading conditions, a half part of the rock was discretized using triangular elements. The initial temperature of rock mass was 300°C. Constant temperature fluid flowed through the fracture in the direction vertical to the figure. In order to investigate the effect of thermal contraction, the fluid pressure was set at zero. Young's modulus, $E$, Poisson's ratio, $\nu$, and linear expansion coefficient of rock mass, $a$, were 60 GPa, 0.2 and $7.5\text{x}10^{-6}$°$C^{-1}$. The simulation was stopped when temperature changed at the boundary of the rock mass model.

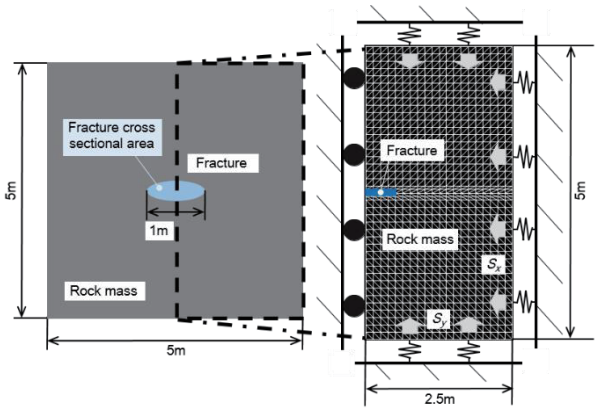


Fig. 1 Configuration of the model.

## 3. Results of analysis

Figure 2 shows the change of fracture cross sectional area with time obtained by the numerical simulations, where the confining stress $S$ was 20 MPa. $\Delta T$ is the difference in temperature between rock mass and injected fluid. Fracture cross sectional area did not increase for the cases of $\Delta T$ = 50 and 100°C, however, for the case of $\Delta T$ = 150°C, the fracture cross sectional area began to increase obviously at around 40000 sec. The fracture cross sectional area increased earlier and more steeply for the case of $\Delta T$ = 200°C. These results suggest that thermal contraction due to cold fluid injection causes fracture opening. We also found that the effective normal stress acting on the fracture decreased

Corresponding author: Kosuke Kaneta
*E-mail address*: kaneta@geo.ifs.tohoku.ac.jp

with time. The time when effective normal stress at the fracture center became zero was almost coincident with the time when the fracture began to open. From these results, the time for the effective normal stress to be zero is defined as the fracture opening time in this study.

Furthermore, we conducted the numerical simulations for $S$ was 10 and 30 MPa. The $\Delta T$ was set at between 50°C and 200°C. The results were summarized in the relationship between the fracture opening time and the temperature difference $\Delta T$ as shown in Figure 3. The fracture opening time increased exponentially when $\Delta T$ was small in all case of the confining stress. When $\Delta T$ was smaller than certain value, the fracture did not open. These results indicate the existence of a critical value of $\Delta T$ which is the minimum value of $\Delta T$ required for the fracture opening. The critical values of $\Delta T$ were changed with the confining stress and the critical values can be estimated actually to be around 55, 105 and 165°C for the cases of $S$ = 10, 20 and 30 MPa, respectively.

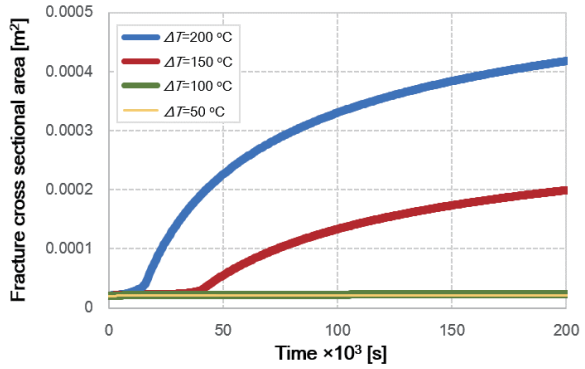


Fig. 2 Change of fracture cross sectional area with time for $\Delta T$ (50, 100, 150, 200°C) where the constant confining stress of $S$ was 20 MPa.

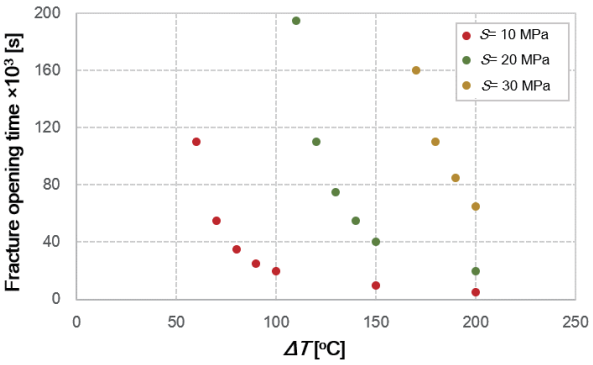


Fig. 3 Change of the fracture opening time with $\Delta T$ for $S$ (10, 20, 30 MPa).

## 4. Discussion and conclusions

The results of our simulation can be interpreted that cooling of rock mass by cold fluid injection into single fracture caused thermal contraction of rock mass. When the $\Delta T$ was larger than a critical value, effective normal stress acting on a fracture became zero and fracture began to open. Therefore, increase of fracture permeability is implicated although confining compressive stress was subjecting to the rock mass.

Rock mass subjected to confining stress strains compressively. In case that large confining stress existed, thermal contract required for fracture opening was large because compressive strain was also large. Therefore, when confining stress was large, the critical values of $\Delta T$ became large.

Ito et al. [3, 4] evaluated theoretically the critical value of $\Delta T$ assuming a thermo-elastic deformation of rock mass caused by cooling of circular region around the injection point. Ito et al. [3, 4] described theoretically the critical value, $\Delta T_c$ as follows;

$$\Delta T = \frac{2(1-\nu)}{\alpha E}\left(S_{avg} - P\right) \equiv \Delta T_c. \qquad (1)$$

where $P$ is the fluid pressure, $S_{avg}$ is the average magnitude of the confining stress. When the parameter values used for the simulations of Figure 3 were substituted in Eq. (1), the values of $\Delta T_c$ were estimated to be 36, 71 and 107°C. These were smaller than those $\Delta T_c$ estimated from Figure 3 for all cases. Large region has to be cooled for fracture opening. Larger cooled region is available for the case of fracture network than a single fracture. Thus, larger $\Delta T$ was required for single fracture opening.


## Acknowledgements

We used Geocrack2D for the simulations in this paper and appreciate discussions and support by Dr. Daniel Swenson, the developer of the simulator.


## References


[1] E. Kaya, S. J. Zarrouk, M. J. O'Sullivan, *Renew. Sustain. Energy Rev*., 15 (2011) 47−68.

[2] K. Araki, K. Hatakeyama, *J. Geotherm. Res. Soc. Japan* (in Japanese), 19 (1997) 197−208.

[3] T. Ito, D. Swenson, K. Sekine, K. Hayashi, Geothermal Resources Council *Transactions*, 27 (2003) 695−698.

[4] T. Ito, H. Watanabe, D. Swenson, K. Hayashi, *J. Geotherm. Res. Soc. Japan* (in Japanese), 27 (2005) 101−113.

[5] D. Swenson, R. DuTeau, T. Sprecker, *Proc. World Geoth. Cong*., Florence, (1995) 2553−2558.

Eleventh International Conference on Flow Dynamics
October 8-10, 2014, Sendai, Miyagi, Japan

# Interaction between Incident Shock Wave and Pre-combustion Gas Injection from a Ramp Injector in Supersonic Flow

Tatsuya Yamaguchi, Yoshitaka Iwamura, Taku Kudo, Akihiro Hayakawa, Hideaki Kobayashi
Institute of Fluid Science, Tohoku University
2-1-1 Katahira, Aoba-ku, Sendai, Miyagi, 980-8577, Japan

**ABSTRACT**

Experiments and numerical simulations were conducted to explore the interaction between an incident shock wave and pre-combustion gas injection from a ramp injector. Combustion region was visualized by Schlieren method and wall pressure measurement was conducted to investigate the effects of incident shock wave quantitatively. Numerical simulations for a three-dimensional flow field were performed to understand the flow-field features and examine the phenomena observed in the experiments.

## 1. Introduction

A SCRAMJET engine is expected as a propulsion system for a hypersonic airplane. Because of short residence time of inlet air, mixing and combustion should be completed in the combustor within millisecond time scale. In addition, the interaction between shock waves and combustion region must be revealed. Ramp injector is expected as a promising injection method which can introduce streamwise vortices for mixing enhancement and reduce the total pressure loss. The aim of this study is to investigate the interaction between pre-combustion gas injection from a ramp injector and an incident shockwave in supersonic flow by experiments and numerical simulations.

## 2. Experimental Setup and Procedure

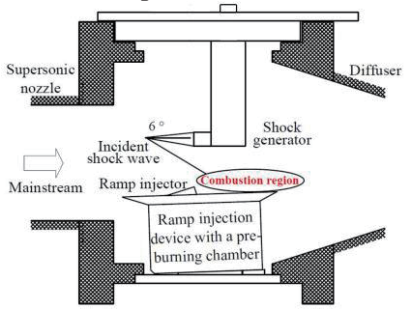


Fig.1 A schematic of the test section.

In this study, supersonic combustion wind tunnel was used for a supersonic combustion test. This wind tunnel introduce supersonic air flow into a test section from a high pressure tank for 20 seconds. A ramp injector, a shock generator, and a pre-combustion chamber are installed in the test section. A schematic of the test section is shown Fig. 1. A single unswept-type ramp injector was selected in this study. The injection surface geometry is 10-mm-square. It has a $d$ = 3.57 mm circular injection hole. The injection hole is designed to inject pre-combustion gas at sonic speed. $H_2$/air mixture with equivalence ratio of 3.6 is ignited in the pre-combustion chamber before injection. The incident shockwave is formed by the shock generator, which has turning angle of 6 degrees, and introduced into region downstream of the ramp injector. The Mach number and total pressure of the inlet air are 2.5 and 0.5 MPa, respectively.

Combustion region was visualized by the Schlieren method to figure out the interaction between incident shock wave and combustion region. The light source was a Xenon flash lamp and the test section was taken by a digital camera during the combustion test.

To investigate the flow structure near the wall and the effects of incident shock wave quantitatively, wall pressure measurement was conducted. There are 11 static holes downstream of the injection surface at 10 mm intervals. Pressure transducers (PA-20-302R, NIDEC COPAL) were used for the measurement.

## 3. Method of the numerical simulation

Numerical simulations for a three-dimensional flow field were performed using FLUENT 14.0. Three-dimensional compressible Reynolds Averaged Navier-Stokes (RANS) equations were solved by the finite volume method. Wilcox's $k$-$\omega$ two-equation turbulence model was used [1]. In order to fit to the actual experimental conditions, the mach number, total pressure and total temperature of the inlet air were set to 2.5, 0.5 MPa and 673 K, respectively. Those properties of injection gas, which is high-temperature air as an ideal gas, are 1.0, 0.6 MPa and 1500K, respectively.

## 4. Results and Discussion

### 4.1 Results of Schlieren method

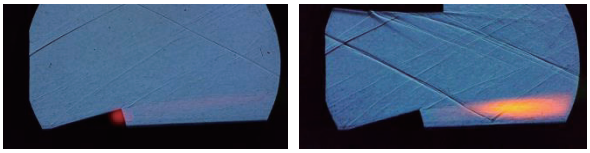

(a)Without shock wave (b)With shock wave

Fig.2 Schlieren images.

Figure 2 shows a shock wave visualized by Schlieren method and combustion region. Red luminescence is emitted by superheated water vapor contained within the combustion gas. In the case without the shockwave, no apparent red luminescence was observed, while in the case with the shock wave, red luminescence was observed clearly downstream of the shock wave. It is

Corresponding author: Tatsuya Yamaguchi
*E-mail address*: yamaguchi@flame.ifs.tohoku.ac.jp

thought to be due to reaction rate enhancement caused by increase of pressure and temperature downstream of the shock wave.

### 4.2 Numerical results

Three-dimensional numerical simulations with an air injection at high-temperature were conducted and the phenomena observed in the experiment were analyzed based on these numerical results in terms of the flow field.

Figure 3 shows profiles of $x$-vorticity on the 3 surfaces perpendicular to the $x$-axis. The shock wave incident point is $x = 40$ mm. It is indicated that $x$-vorticity was strengthened downstream of the incident shock wave and mixing was facilitated by the generated $x$-vorticity. A possible reason for this is effect of the baroclinic torque induced by the pressure gradient of incident shock wave and the density gradient between inlet air and injection gas [2].

Figure 4 shows mass fraction profile of injection gas. Injection gas is diluted by air downstream of the incident shock wave compared to the case without shock wave, indicating that mixing was enhanced due to strengthened $x$-vorticity. Figure 4 also shows that the injection gas is distributed near the wall in the case without shock wave, while it lifted up and completely away from the wall in the case with shock wave. This phenomenon is caused by high pressure region near the wall downstream of the incident shock wave.

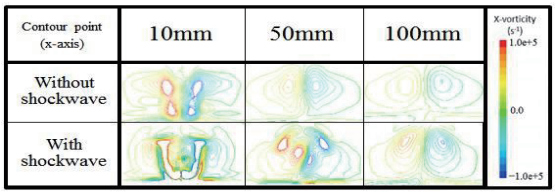


Fig. 3 Profiles of x-vorticity.

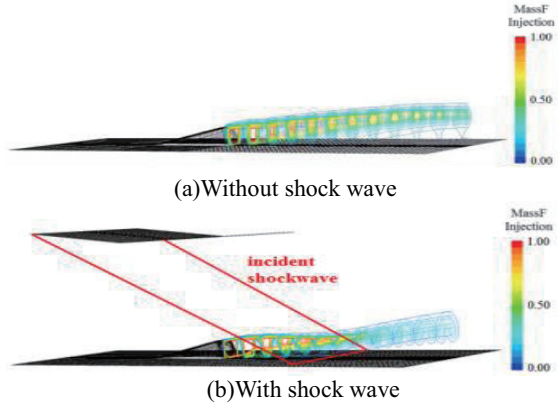


(a)Without shock wave

(b)With shock wave

Fig. 4 Profiles of mass fraction on injection gas.

### 4.3 Results of wall pressure measurement

Figure 5 shows profiles of wall pressure. Vertical axis and horizontal axis represent pressure non-dimensionalized by atmospheric pressure and distance from the injection surface non-dimensionalized by the injection surface size, respectively. In the case without the shock wave, the wall pressure measured in the combustion test slightly greater than those measured in the non-combustion test, which indicates pressure increase caused by combustion. In the case with shock wave, great pressure rise was observed near the shock wave incident point in both combustion and non-combustion test. It turns out that pressure rise caused by the incident shock wave is stronger than pressure rise caused by combustion. This indicates that the strong high pressure region induced by the incident shock wave can uplift the injection gas. In the combustion test, the pressure rising point moved forward compared to the non-combustion test. This is due to the difference in temperature of injection gas. Hot pre-combustion gas was injected in the combustion test, while common temperature air was injected in the non-combustion test. Pre-combustion gas injection decreases the Mach number in the injection gas region. According to the relational equation among turning angle, shock angle, and Mach number, the angle of the oblique shock wave increases in the low Mach number region like a combustion region.

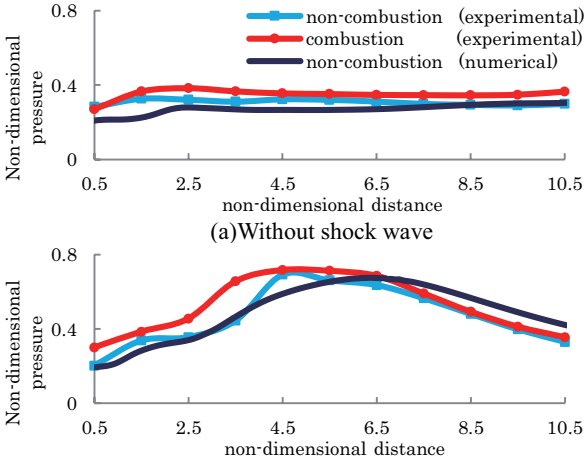


(a)Without shock wave

(b)With shock wave

Fig. 5 Profiles of wall pressure.

## 5. Concluding Remarks

In this study, the interaction between incident shock wave and pre-combustion gas injection from a ramp injector was investigated experimentally and numerically. The following conclusions were drawn:

1) Pressure and temperature increase in the region downstream of the incident shockwave facilitate combustion by raising reaction rate.
2) Balocllinic torque induced by the incident shock wave facilitates mixing of inlet air and injection gas caused by increasing $x$-vorticity.
3) Uplifted jet is cause by high pressure region near the wall downstream of the incident shock wave which is stronger than pressure increase by combustion.
4) An oblique shock wave entering into high temperature zone like a combustion region changes the shock angle to satisfy the relational equation among tuning angle, shock angle, and Mach number.

## References

[1] D. C. Wilcox, Turbulence Modeling for CFD, 2nd ed., DCW Industries (1998).
[2] I.A. Waitz, F.E. Marble, E.E. Zukoski, AIAA paper 91–2265 (1991).

Eleventh International Conference on Flow Dynamics
October 8-10, 2014, Sendai, Miyagi, Japan

# Development on Microwave Nondestructive Testing of a Wall Thinning inside a Pipe by Optimizing the Frequency Range of Incident Microwaves

Kota Sasaki[1], Noritaka Yusa[1], Hidetoshi Hashizume[1]
[1]Department of Quantum Science and Energy Engineering, Graduate School of Engineering, Tohoku University, 6-6-01-2, Aramaki Aza Aoba, Aoba-ku, Sendai, Miyagi 980-8579, Japan

**ABSTRACT**

This study reports the development of a microwave nondestructive testing for wall thinning inside metal pipes through optimizing a sweeping frequency range. Three-dimensional finite element simulations are carried out to evaluate effects of the frequency range on reflected signals from the wall thinning. The simulation results show that detected signals have a relatively larger signal-to-noise ratio and influence of dispersion on propagating microwave is quite small in higher frequency range.

## 1. Introduction

Piping system is one of the important components in many industries. Maintenance of piping system is essential to keep reliable service and periodical inspections are therefore required [1],[2]. However, existent major nondestructive inspections of flaws on inner pipe wall, such as ultrasonic and eddy current testing, have a long inspection time because of requirement of surface scanning, although these techniques possess high degree of accuracy. Therefore, a new method that can efficiently inspect long pipes is required.

A nondestructive testing (NDT) using microwaves is proposed as one of the efficient inspection methods because microwaves can propagate along inside metal pipes with small attenuation and with little leakage of microwave energy outside pipes [3],[4]. In this method, microwaves are generated and detected by a network analyzer in frequency domain, and then time domain response is obtained by imposing inverse fast Fourier Transform on detected signals. This method has a potential to detect wall thinning locations based on the flight time and velocity of microwaves propagating inside pipe.

Earlier studies demonstrated that this method can detect not only wall thinning locations but also conditions by analyzing the reflected microwave signals propagating inside pipe [5], and then confirmed an optimization method of profiles of microwave exciting probes, which are connection point between coaxial cables and inspected pipes, for application to arbitrary diameter pipes [6]. Furthermore, a previous study discussed optimization of sweeping frequency range, which strongly affects spatial resolution of microwave NDT [7]. Spatial resolution is product of the velocity of microwaves propagating inside a pipe and time resolution of reflected signals, which is determined by difference between maximum and minimum sweep frequency. Therefore, optimization of the frequency range is important to improve detection accuracy of microwave NDT. However, concrete optimization methods of the frequency range, especially for long-range and arbitrary diameter pipes, have not sufficiently discussed yet.

Corresponding author: Kota Sasaki
*E-mail address*: ksasa@karma.qse.tohokuoku.ac.jp

Therefore, this study proposes an optimization method of sweeping frequency range, which is based on evaluations of the effects of sweeping frequency range on reflected signals caused by wall thinning inside pipes in time domain with the aid of numerical simulations modeling detection tests. Experimental verifications are consequently carried out.

## 2. Numerical simulations

Axisymmetric numerical configuration is illustrated in Fig.1. The coaxial cable, microwave exciter probe, pipe and wall thinning were modeled to analyze reflections caused by the wall thinning. The probe has a plate-structure profile and a coaxial cable core wire protruding into the pipe whose length is 7 mm. All of the geometric parameters are shown in Fig. 1. The internal dielectric was Teflon with relative permittivity of 1.687, relative permeability of 1.000, and conductivity of 0.000 S/m. The absorbing boundary condition, perfectly matched layer, was placed at the end of the pipe, thereby preventing any reflected microwaves being generated, thereby emulating a pipe of sufficient length. Reflection signals were calculated in frequency domain, and consequently transformed into signals in the time domain as the reflection due to a wall thinning when the probe emitted microwave as a pulse. Cut-off frequencies for the propagating modes are listed in Table 1.

The two-dimensional axisymmetric finite element simulations were carried out using commercial COMSOL Multiphysics with its RF module (v4.4) software applying the following governing equation:

$$\nabla \times \mu_{\mathrm{r}}^{-1}(\nabla \times \boldsymbol{E}) - k_0^2[\varepsilon_{\mathrm{r}} - \mathrm{j}\sigma/(\omega\varepsilon_0)]\boldsymbol{E} = \boldsymbol{0} \quad (1)$$

$$k_0 = \omega\sqrt{\varepsilon_0\mu_0} \quad (2)$$

where $\boldsymbol{E}$ denotes the electric field, $\varepsilon_0$ and $\mu_0$ are respectively the permittivity and permeability in a vacuum, $\varepsilon_{\mathrm{r}}$ and $\mu_{\mathrm{r}}$ are respectively the relative permittivity and permeability, $\sigma$ is the electrical conductivity and $\omega$ denotes the angular frequency. Because brass pipes and probes were used in experiments, the following material constants were used: 1.000 for relative permittivity, 1.000 for relative permeability, and $2.558\times10^7$ S/m for conductivity of pipe wall. Since the skin depth of brass is quite small for microwaves at

frequencies of several to tens of GHz, the pipe wall and the outer conductor of the coaxial cable were not meshed in the simulations. Imposed on their surfaces were the impedance boundary condition:

$$\sqrt{\mu_0\mu_r \Big/ \left(\varepsilon_0\varepsilon_r - \mathrm{j}\frac{\sigma}{\omega}\right)}\,\boldsymbol{n}\times\boldsymbol{H} + \boldsymbol{E} - (\boldsymbol{n}\cdot\boldsymbol{E})\boldsymbol{n} = \boldsymbol{0} \qquad (3)$$

where $\boldsymbol{n}$ is an inward-looking normal vector to the pipe wall surface and $\boldsymbol{H}$ denotes the magnetic field.

In all simulations, the transverse electro-magnetic (TEM) mode was excited at the entry ports of the coaxial cable. Second-order tetrahedral elements were used for discretization.

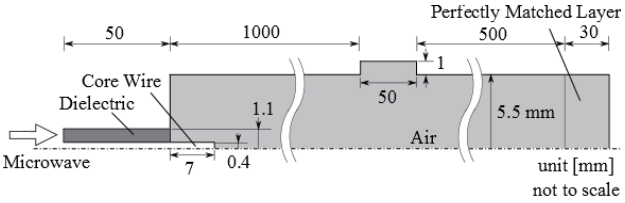


Fig. 1 Numerical Configuration

Table 1. Mode dependence of cut-off frequencies for pipe of 11.0 mm diameter

| Mode | Cut-off frequencies [GHz] |
|---|---|
| $TM_{01}$ | 20.88 |
| $TM_{11}$ | 33.27 |
| $TM_{02}$ | 47.92 |

## 3. Results and Discussion

Simulation results with frequency range of 21.00-31.00 GHz and 30.00-40.00 GHz are shown in Fig. 2 (a) and (b), respectively. The reflections at 0-5 ns are caused by the microwave exciter probe and reflections at 8-15 ns are caused by the wall thinning. In order to compare voltages of the signals from the wall thinning, detected signals were normalized by each voltage of the reflection from the microwave probe. According to results, with frequency range of 30.00-40.00 GHz, signals from the wall thinning are largest and the effect of a dispersion is quite small. Therefore, improvement of the detection accuracy of this method for a wall thinning can be expected by optimizing the sweeping frequency range. Furthermore, detailed evaluations imposing signal processing which compensates dispersion are performed.

## 4. Concluding Remarks

This study evaluated the effects of sweeping frequency ranges on detected signals caused by a wall thinning in NDT using microwave. The simulation results showed that detected signals with higher frequency range are larger and sharper than those with lower frequency range. On the basis of the numerical simulations, the experimental verifications and further evaluations of effects of frequency range are performed and will be presented at the conference.

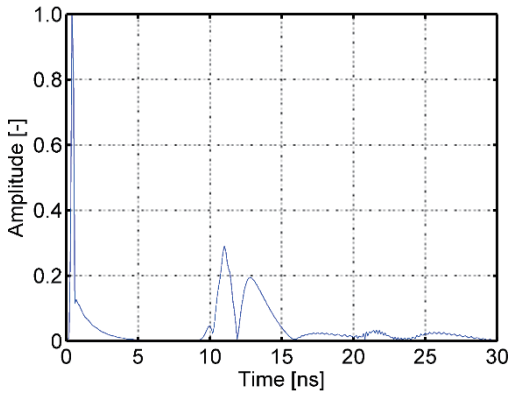


(a) Frequency range of 21.00-31.00 GHz

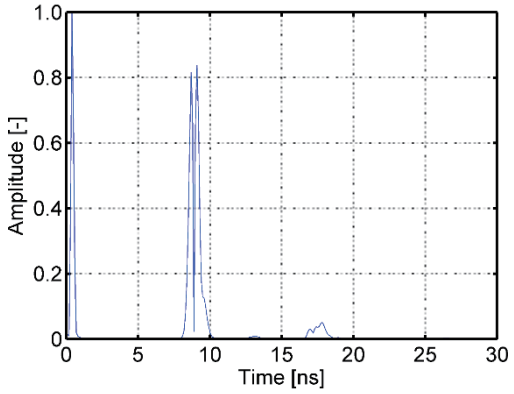


(b) Frequency range of 30.00-40.00 GHz

Fig. 2 Reflections of microwave caused by a wall thinning


## Acknowledgements

This work was supported in part by Grants for Excellent Graduate Schools "World Center of Education and Research for Trans-disciplinary Flow Dynamics", MEXT, Japan, supported by Grant-in-Aid for JSPS Fellows and supported by MEXT KAKENHI Grant Number 25750181.


## References


[1] I. Nishiguchi, F. Inada, M. Takahashi, B. Ogawa, T. Inagaki, T. Ohira, K. Iwahara, K. Yamakami, *EJAM*, 2 (2010) 14－24.

[2] T. Knook, M. Persoz, S. Trevin, S. Friol, M. Moutrille, L. Dejoux, *EJAM*, 2 (2010) 1－13.

[3] K. Sugawara, H. Hashizume, S. Kitajima, *JSAEM Studies in Applied Electromagnetics and Mechanics*, 10 (2001) 313－316.

[4] H. Hashizume, T. Shibata, K. Yuki, *International Journal of Applied Electromagnetics and Mechanics*, 20 (2001) 171－178.

[5] Y. Sakai, N. Yusa, H. Hashizume, *Nondestructive Testing and Evaluation*, 27 (2012) 171－184.

[6] K. Sasaki, N. Yusa, T. Wakai, H. Hashizume, *Maintenology*, 12 (2013) 81－86.

[7] L. Liu, Y. Ju, M. Chen, *NDT&E International*, 57 (2013) 52－57.

Eleventh International Conference on Flow Dynamics
October 8-10, 2014, Sendai, Miyagi, Japan

# Friction Properties of $MoS_2$ Dispersed Cu-based Composite Materials Formed by Compression Shearing Method at Room Temperature

Sho Takeda[1], Hiroyuki Miki[2], Noboru Nakayama[3], Hiroyuku Takeishi[4], Toshiyuki Takagi[5]
[1]Graduate School of Engineering, Tohoku University, 6-6 Aramaki aza Aoba, Aoba-ku, Sendai, Miyagi, 980-8579, Japan
[2]FRIS, Tohoku University, 6-3 Aramaki aza Aoba, Aoba-ku, Sendai, Miyagi, 980-8578, Japan
[3]Shinshu University, 4-17-1 Wakasato, Nagano, Nagano, 380-8553, Japan
[4]Chiba Institute of Technology, 2-17-1 Tsudanuma, Narashino, Chiba, 275-0016, Japan
[5]Institute of Fluid Science, Tohoku University, 2-1-1 Katahira, Aoba-ku, Sendai, Miyagi, 980-8577, Japan

**ABSTRACT**

To clarify the relationship between mechanical properties of matrix materials and friction properties of composite materials, the microstructures and the friction properties of Cu/$MoS_2$ formed by a compression shearing method at room temperature are investigated. The samples with five different $MoS_2$ concentrations between 0 to 20 vol.% were prepared. $MoS_2$ is homogeneously dispersed between Cu grains and was not aggregated. With increasing $MoS_2$ concentration, the coefficients of friction of Cu/$MoS_2$ was decreased, and that of Cu/$MoS_2$ with 10 vol.% $MoS_2$ was 0.18.

## 1. Introduction

Today, many slide members of machines are lubricated by lubricant oils, greases or sputtering films of solid lubricant. Molybdenum disulfide ($MoS_2$) is known as a representative of the solid lubricants. $MoS_2$ is widely used as an additive agent in lubricant oils or greases. In addition, $MoS_2$ shows very low friction in the vacuum. However, these lubricants lose lubricating properties by the depletion or abrasion with long-term use, so that regular maintenance is necessary to keep performance. However, the maintenance is difficult in the extreme environment such as outer space, a new maintenance-free lubricating method is required.

Recently, we investigated friction properties of composite materials, focusing on the method of dispersing $MoS_2$ into the matrix material[1]. Considering practical use, metal is desirable to be used as a matrix material. A powder metallurgy technique has been proposed in general to fabricate composite materials from materials that have different melting point. However, since the melting points of almost all metals are higher than the oxidation temperature of $MoS_2$, friction property of the composite material becomes worse under the conventional techniques which need high temperature treatment. Thus, the new method for forming composite materials which prevent oxidation process of $MoS_2$ is required.

The new powder metallurgy method, which was developed by our research group; compression shearing method at room temperature (COSME-RT) has been employed. COSME-RT is a method for forming a thin metal plate by applying a shearing strain and a compression stress to a metal powder simultaneously at room temperature and in the atmosphere[2].

In the solidification process of COSME-RT, it is considered that the bonding of each matrix powder particle was improved by the deformation of particles[3], but Ti cannot be solidified when $MoS_2$ concentration is more than 2 vol.% and the friction coefficient of Ti/$MoS_2$ is high[1]. It seems that since $MoS_2$ prevents the stiff contact of each matrix powder particle, because of its lubricity, deformation of the matrix powder particles is insufficient. On the other hand, the study by Miki et al. indicated that Al-Si-Cu-Mg/$MoS_2$ composite material which contains 5 vol.% $MoS_2$ can be solidified and it has excellent friction property[4]. It seems that Al-Si-Cu-Mg can be solidified even if $MoS_2$ concentration is increased because the tensile strength of Al-Si based alloy is 290 MPa[5], relatively lower than that of Ti(330 MPa)[1] and it can be deformed more easily. It seems that the differences of friction properties of composite materials are caused by the mechanical properties of the matrix materials, but these two examples is not sufficient to clarify this phenomenon and further study is required.

In this study, to clarify the relationship between mechanical properties of matrix materials and friction properties of composite materials, Cu which tensile strength is 275 MPa[5], lower than Ti and Al-Si based alloy is chosen as the matrix material. Then, the microstructures and the friction properties of Cu/$MoS_2$ samples are investigated.

Corresponding author: Hiroyuki Miki
*E-mail address*: miki@fris.tohoku.ac.jp

## 2. Method

### 2.1 Materials

The materials used in this study are powder of 99.9% purity Cu and 98.0% purity $MoS_2$. The average particle size of the Cu and $MoS_2$ were 35 and 6 μm, respectively. Mixed powders of which $MoS_2$ concentration $r$ is varied to 0, 1.0, 5.0, 10, and 20 vol.% were prepared.

### 2.2 Forming conditions

Fig. 1 shows a schematic illustration of solidification process of COSME-RT equipment (DIP Co., Ltd., DRD-NNK-002). First, Cu/$MoS_2$ mixed powder is placed between the stationary plate and the moving plate, and the compression stress $\sigma_N$ is applied to the moving plate and maintained during forming process. Then, the shearing strain $\gamma$ is added to a mixed powder by

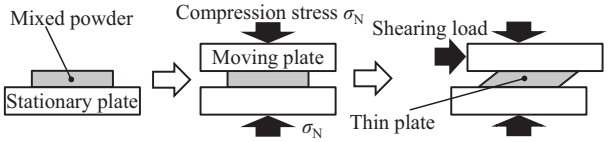


Fig. 1 Schematic illustration of COSME-RT.

displacing the moving plate, and a thin plate sample is solidified. The shearing strain is determined from $\gamma = L_S / t_P$, where $L_S$ is the shearing distance ($L_S$ = 4 mm) and $t_P$ is the sample thickness ($t_P$ = 0.25 mm). The target size is 20 × 20 × 0.25 mm$^3$, $\sigma_N$ = 1250 MPa, $\gamma$ = 20, and the shear rate was 5 mm/min. All samples are fabricated at room temperature and in the atmosphere.

## 3. Results and Discussion

To investigate the homogeneity of variance of $MoS_2$ in the microstructure of the samples, the cross-section of the samples were observed by Electron Back Scatter Diffraction. Fig. 2 shows the inverse pole figure map of cross-section of $r$ = 0 and 10 vol.% samples. It seems that the black regions that are not identified as Cu are $MoS_2$. These regions distribute in wide area. It is indicated that $MoS_2$ is homogeneously dispersed between Cu grains and was not aggregated.

A ball-on-disk friction test was carried out to investigate the friction properties of the samples. The test was also performed for the rolled Cu samples for comparison. Normal load, sliding distance, and sliding velocity were programmed in this experiment to 1 N, 130 m, and 12 mm/s, respectively. A SUJ2 ball with a diameter of 6 mm was used for the test, and the test was carried out at room temperature and in the atmosphere. The average values of the coefficients of friction were determined by averaging from sliding distance $L$ = 100 to 130 m in each sample. Fig. 3 shows the relationship between $MoS_2$ concentration and the average coefficients of friction of the samples. With increasing $MoS_2$ concentration, the coefficient of friction of the samples was decreased, and that of $r$ = 10 vol.% sample were 0.18. It is suggested that friction properties of the sample is improved by dispersed $MoS_2$.

To investigate the wear of the SUJ2 balls used in the friction tests, elemental analysis on the wear tracks was carried out by Energy Dispersive X-ray Spectrometry (EDS) analysis. Fig. 4 shows SEM images and mapping images on the wear tracks of the SUJ2 balls used in the friction tests of $r$ = 1.0 and 10 vol.% samples by EDS. There were adhesive materials on both of them. Although Mo did not exist on the SUJ2 ball used in the friction test of $r$ = 1.0 vol.% sample, it existed on the ball used in the friction test of $r$ = 10 vol.% sample. From these results, it seems that the coefficient of friction of $r$ = 10 vol.% sample was decreased because of the lubrication of $MoS_2$ which transferred to the SUJ2 ball. It is clarified that the friction property of the Cu/$MoS_2$ is improved by dispersed $MoS_2$ in Cu, compared with that of COSME-RT processed Cu and rolled Cu. From these results, it is indicated that the material which has relatively lower strength is more desirable as a matrix material because $MoS_2$ worsens the formability of the composite material.

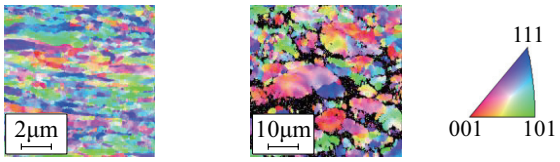


(a) $r$ = 0 vol.% sample (b) $r$ = 10 vol.% sample

Fig. 2 Inverse pole figure map of cross-section of samples.

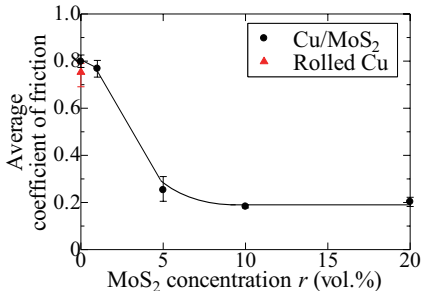


Fig. 3 Relationship between $MoS_2$ cocentration $r$ and average coefficient of friction of samples.

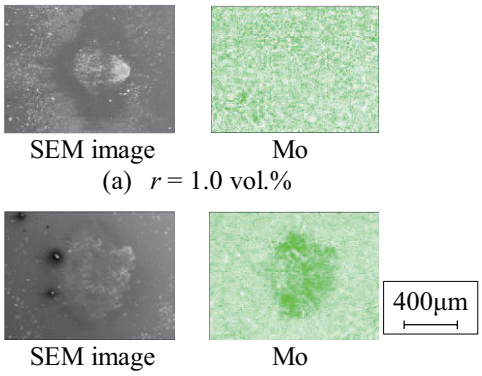


(a) $r$ = 1.0 vol.%

(b) $r$ = 10 vol.%

Fig. 4 SEM images and mapping images on wear tracks of SUJ2 balls used in friction test by EDS.

## 4. Concluding remarks

In this study, Cu/$MoS_2$ composite materials were formed by a COSME-RT, and the microstructures and the friction properties of them were investigated. The results are as follows.

1) $MoS_2$ is homogeneously dispersed between Cu grains and was not aggregated.
2) With increasing $MoS_2$ concentration, the coefficients of friction of the samples are decreased, and that of the samples with 10 vol.% $MoS_2$ is 0.18. This is due to the lubrication of $MoS_2$ which transferred to the SUJ2 ball.


## Acknowledgement

This work was partly supported by the JSPS Core-to-Core Program, A. Advanced Research Networks, "International research core on smart layered materials and structures for energy saving". Part of the work was carried out under the Collaborative Research Project of the Institute of Fluid Science, Tohoku University.


## References


[1] S. Takeda, et al., *Proc. ICFD2013*, (2013) 738-739.
[2] H. Takeishi, et al., *J.Soc. Mat. Sci., Jpn*, 54-3 (2005) 233-238.
[3] M. Horita, et al., *Journal of JSTP*, 54-625 (2013) 186-190.
[4] H. Miki, et al., *38th Leeds-Lyon Symposium on Tribology, Lyon, France*, (2011).
[5] J. Kaneko, et al., "Kaitei Shinban Kiso Kikai Zairyo Gaku", Asakura Publishing Co., Ltd., (2010) 176-180.

# Plasma Characteristics of Discharge in a Culture Medium

Yusuke Sato[1], Tomoki Nakajima[2], Takehiko Sato[2], Daisuke Yoshino[2]
[1] Department of Bioengineering and Robotics, Graduate School of Engineering, Tohoku University
6-6-01 Aramaki-Aoba, Aoba, Sendai, Miyagi, 980-8579, Japan
[2]Institute of Fluid Science, Tohoku University
2-1-1 Katahira, Aoba, Sendai, Miyagi, 980-8577, Japan

**ABSTRACT**

Generation of plasma in a culture medium and investigation of its characteristics are important to improve the effect of plasma stimuli on cell responses since most of researches generate plasma in a gas phase and the plasma stimuli transfer through surrounding liquids of cells/tissues. In this study, plasma characteristics of discharge in a culture medium were investigated by comparing with results of ionic solution. The spectra analysis showed little difference between the culture medium and the ionic solutions. $H_2O_2$ concentration and the liquid temperature increased with the discharge time.

## 1. Introduction

Plasma medicine, which is medical treatment using plasma, has been received much attention recently [1, 2]. It has been reported that a skin treatment [1] and an induction of apoptosis to tumor cells by direct irradiation of plasma [2]. In these reports, plasma generated in a gas-phase was used. Generation of plasma in liquid is important to improve the effect of plasma stimuli for medical treatments, because previous methods generally applied to cells and tissues covered with body fluids.

Plasma in liquid has been studied in the field of a transformer and electrical discharge machining for long time. In these cases, the liquids are generally dielectric oil [3]. Recently, plasma in water has been also remarked since it has high potential for environmental treatments [4]. However, conventional underwater plasma is not suitable for medical treatments because cells cannot survive in these water such as distilled water or tap water. Although generation of plasma in a saline solution has been reported [5], it is also unsuitable for medical treatments because saline solution does not contain amino acid, vitamin and so on needed for cell life activities. To apply underwater plasma to medical treatment, it is necessary to generate plasma in a culture medium and to reveal the plasma characteristics such as generation of chemical species, thermal flow fields, discharge process and light emissions.

In this study, we aimed at generation of plasma in a culture medium and revealing the plasma characteristics, such as emission spectrum, changes of temperature, pH and $H_2O_2$ concentration. Characteristics of plasma in an ionic solution were also investigated from the point of view of effect of various components in the culture medium.

## 2. Experimental methods

The platinum wire electrode of 0.3 mm in diameter was coated by glass and the end face was exposed. As grounded electrode, a cylindrical aluminum electrode of 4 mm in diameter was set at outside of the glass coated platinum electrode as shown in Fig. 1 (a). Grounded electrode was position 1.5 mm from the end face of the glass coated platinum electrode. Electrodes were immersed in the culture medium as shown Fig. 1 (b).

The Dulbecco's Modified Eagle Medium (Gibco, REF.11054-020) which does not contain phenol red was used as the culture medium. A plasma emissions by a single-shot pulse was taken by a digital camera (Nikon, D4) with a microscope lens (Mitutoyo, M Plan Apo 5 ×). Emission spectra from plasma were measured by a multichannel spectroscope (HAMAMATSU, PMA-12). Temperature and pH in the culture medium were measured by thermocouple (OMRON) and pH meter (ASONE) respectively. $H_2O_2$ concentration was measured by a digital water quality meter with chemical agents (KYORITSU CHEMICAL-CHECK Lab, WAK-H2O2). Applied voltage was +6 kV with 10Hz. The ionic solution contains typical inorganic salts which are NaCl (110 mM), KCl (5.3 mM) and $CaCl_2$ (1.8 mM), and these concentration are same with the using culture medium.

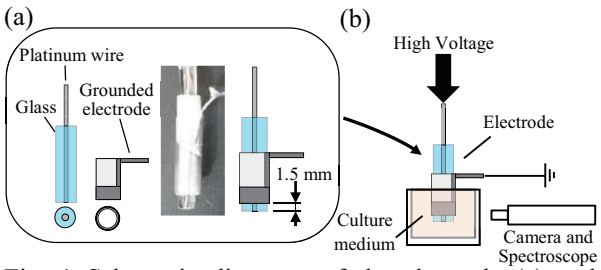


Fig. 1 Schematic diagrams of the electrode (a) and experimental setup (b).

## 3. Results and Discussion

Fig. 2 (a) shows photographs of the discharge in the culture medium and in the ionic solution. The shapes of bright regions in both cases were semispherically with many filaments. These result imply that discharges occur in the bubble generated at the tip of the electrode because the bright region correspond to the shadow region of the shadowgraph visualization. These bubbles were formed by the joule heating due to the high current density at the end face of the wire electrode [4].

The spectrum of the plasma emission in the culture medium showed similar trend as the spectrum in the ionic solution as shown Fig. 2 (b). Emission lines of Na, K, Ca, OH, H and O bands were observed in both cases. These result suggest that various components such as

Corresponding author: Yusuke Sato
*E-mail address*: satoy@plasma.ifs.tohoku.ac.jp

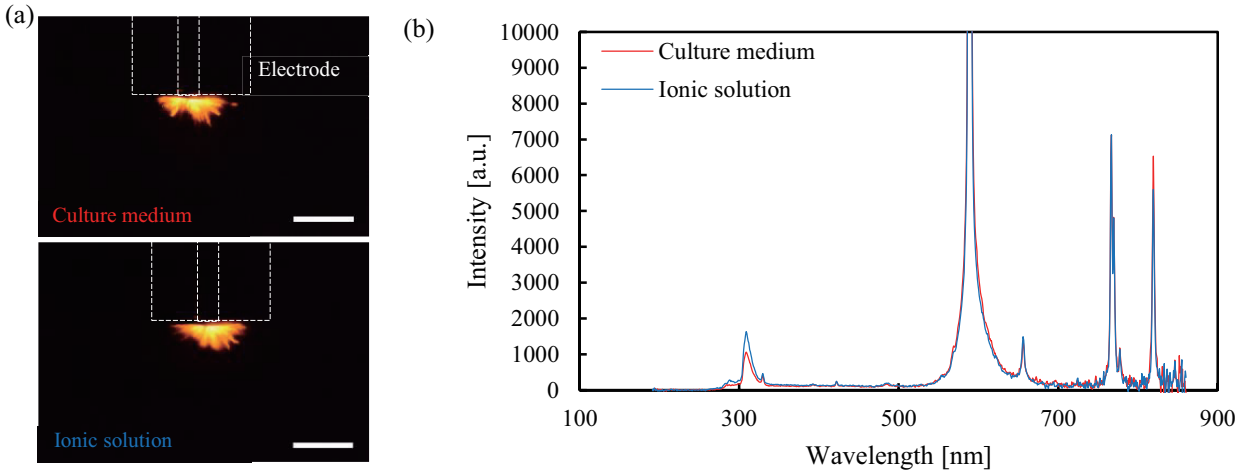


Fig. 2 Photographs of the discharge in the culture medium (upside) and the ionic solution (bottom side) (a) and spectrum analysis (b). Scale bar: 1 mm.

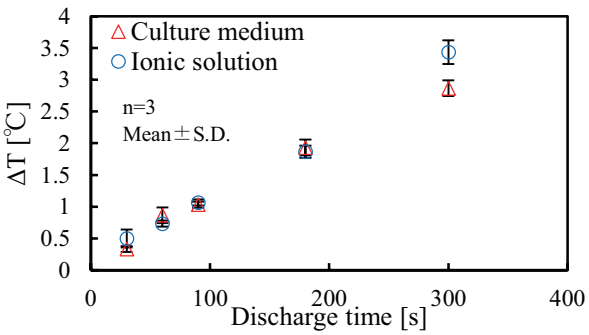


Fig. 3 Changes in temperature in the case of the culture medium and ionic solution.

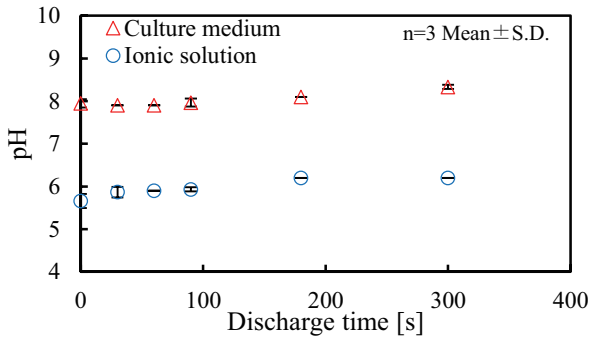


Fig. 4 Changes in pH in the case of the culture medium and ionic solution.

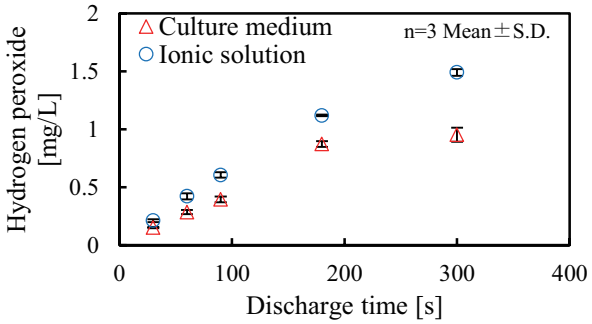


Fig. 5 Changes in the hydrogen peroxide concentration in the case of the culture medium and the ion solutions. Red triangle: in the culture medium. Blue circle: in the ion solution.

amino acid in the culture medium have little effect on plasma-generated species and emission intensities.

Changes in temperature are shown in Fig. 3. The temperature increased with the discharge time in both cases, and the increasing rate was approximately $1\times10^{-2}$ K/s. Changes in pH are shown in Fig. 4. The changes of pH of the solutions were little for 300 s.

$H_2O_2$ concentration against the discharge time are shown in Fig. 5. The concentration in the case of the ionic solution increased with the discharge time and it was greater than that of the culture medium. It's seems that generated $H_2O_2$ in the culture medium react to some molecules in the culture medium.

## 4. Conclusions

In this study, we generated plasma in the culture medium and investigated plasma characteristics in the culture medium and in the ionic solution.

By spectrum analysis, emission lines were similar in both cases. This result suggests that various molecules in the culture medium have little effect on plasma-generated species and emission intensities. By the measurements of changes in temperature and pH, the temperature increased with the discharge time and pH changed little. By the measurement of $H_2O_2$ concentration in the solutions, the concentration in the culture medium was smaller than the case of the ionic solution.

## References

[1] G. Fridman, *et.al.*, *Plasma Process. Polymers*, 5 (2008), 503-533.
[2] G. Fridman, *et.al.*, *Plasma. Chem. Plamsa. Process,* 27 (2007), 163-176.
[3] J.F. Kolb, *et.al.*, *J. Phys. D: Appl. Phys.* 41 (2008), 234007.
[4] B. Sun, *et.al.*, *J. Phys. D: Appl. Phys.* 32 (1999), 1908.
[5] L. Schaper, *et.al.*, *Plasma Sources Sci. Technol*. 20 (2011), 034004.

Eleventh International Conference on Flow Dynamics
October 8-10, 2014, Sendai, Miyagi, Japan

# One-way Shape Memory Effect on Ferromagnetic Ni-Mn-In Based Alloy Solidified by Compression Shearing Method at Room Temperature

Eijiro Abe[1], Makoto Ohtsuka[2], Hiroyuki Miki[3] and Toshiyuki Takagi[4]
[1]Graduate School of Engineering, Tohoku University, Aramaki aza Aoba 6-6, Aoba-ku, Sendai, Miyagi, Japan
[2]IMRAM, Tohoku University, Katahira 2-1-1, Aoba-ku, Sendai, Miyagi, Japan
[3]FRIS, Tohoku University, Aramaki aza Aoba 6-3, Aoba-ku, Sendai, Miyagi, Japan
[4]IFS, Tohoku University, Katahira 2-1-1, Aoba-ku, Sendai, Miyagi, Japan

**ABSTRACT**

As a powder metallurgy technique for solidifying Ni-Mn-In based alloy thin plate, a compression shearing method at room temperature (COSME-RT) is proposed. The powder used for COSME-RT is made by grounding the films deposited by a dual magnetron sputtering apparatus using $Ni_{45}Mn_{40}In_{15}$ and Co targets. The solidified plate is annealed to crystallize, and the plate after annealing shows the good crystalline order, good magnetic property, and one-way shape memory effect is induced by heating.

## 1. Introduction

Ferromagnetic shape memory alloys (FSMAs) are attractive functional materials, since FSMAs show the martensitic transformation (MT) which is controlled by not only temperature and stress, but also magnetic field. Therefore, FSMAs have been expected in terms of quick response and remote control ability assisted by the applied magnetic field [1]. In FSMAs, the large magnetic-field-induced strain (MFIS) resulting from rearrangement of twin variants in martensite was reported [2]. Ni-Mn-*X* (*X* = In, Sn, Sb) based FSMAs have been found and they show the MT from ferromagnetic austenitic (A) phase to antiferromagnetic or paramagnetic martensitic (M) phase [3]. It was reported for Ni-Mn-In bulk samples that the MT temperature decreases by an applied magnetic field [4], and the magnetic field induced reverse MT from paramagnetic M phase to ferromagentic A phase, which is called metamagnetic phase transition. These alloys show both metamagnetic phase transition and MT induced by heating. In addition, those are expected to apply to a high performance actuator due to their shape memory effect (SME) associated with the conventional MT induced by heating, and the reverse MT induced by a magnetic field.

Our research group have much attention to Ni-Mn-*X* (*X* = In, Sn), based FSMAs and had fabricated these films by sputtering. However these sputtered films are insufficient in terms of power due to their thinness and brittleness, compared to bulk samples. Recently, we proposed a compression shearing method at room temperature (COSME-RT) [5] as a new way for making FSMAs plate. The COSME-RT is one of the powder metallurgy techniques performed related to the severe plastic deformation processes, the way for forming a thin metal plate by applying compression stress and shearing strain simultaneously at room temperature in the atmosphere. Target thickness of the plate is 50 ~ 100 μm, which is difficult to deposit by sputtering. In addition, since the plate solidified by COSME-RT shows grain refinement and preferred orientation [5], it is expected to improve mechanical and magnetic properties, and the MFIS better than sputtered films.

The purpose of this study is to solidify Ni-Mn-In based alloy plate by COSME-RT, and to investigate its performance for a magnetic- field-driven actuator.

## 2. Method

In order to make the powder for COSME-RT processing, Ni-Mn-In films containing Co are deposited on polyvinyl alcohol (PVA) substrate using the dual magnetron sputtering apparatus which has radio-frequency (RF) and direct current (DC) power sources. The RF power for Ni-Mn-In target and the DC power for Co target are set to 200 and 8 W, respectively. The composition of Ni-Mn-In target is $Ni_{45}Mn_{40}In_{15}$. The thickness of the sputtered film is 5 μm. Sputtered Ni-Co-Mn-In alloy films are grounded after removed from the substrate. Fig. 1 shows scanning electron microscopy (SEM) image of the Ni-Co-Mn-In alloy powder. The average size of the powder is 10 to 30 μm, and the thickness is 5 μm, which is the thickness of sputtered film.

The forming process by COSME-RT is as follows. At first, grounded powder is placed between the stationary plate and moving plate. Then compression stress $\sigma_N$ is applied to moving plate. Keeping the compression stress, the shearing strain $\gamma$ is added to moving plate. In this way, the plate is solidified. The $\gamma$ is determined from $\gamma = L_s/t_p$. $L_s$ and $t_p$ are shearing distance (mm) and film thickness (mm), respectively. The weight of the powder is 0.02 g, the target size of the plate is 10 mm × 5 mm × 0.05 mm, $\sigma_N$ = 1.2 GPa, $L_S$ = 0.1 mm, $\gamma$ =

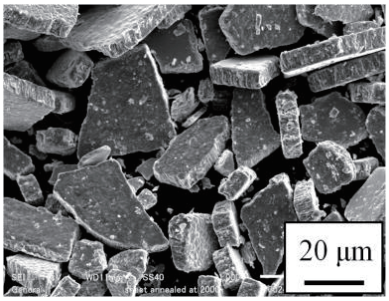


Fig.1 SEM image of Co added Ni-Mn-In powder.

Corresponding author: Hiroyuki Miki
*E-mail address*: miki@fris.tohoku.ac.jp

2, and shearing speed is 5 mm/min. After solidification, the plate is annealed at 1173 K for 36 ks to remove internal stress and crystallize the plate.

## 3. Results and Discussion

The chemical composition of the plate was determined to $Ni_{48.2}Co_{3.3}Mn_{35.9}In_{12.6}$ by the inductively coupled plasma (ICP) method. Fig. 2 shows the X-ray diffraction (XRD) profiles at room temperature for the as-solidified and the annealed plates. As for the as-solidified plate, the weak diffraction peak was observed, at 42°, but its half width showed crystallization was insufficient. However, the XRD pattern of the annealed plate showed the distinct diffraction peaks due to good crystalline order and the diffraction peaks from modulated M phase (14M) [6] were observed.

In order to measure the MT temperatures and Curie temperature ($T_c$), thermomagnetization curve was measured using a super conducting quantum interference device (SQUID) magnetometer. Fig. 3 shows the temperature dependence of the magnetization measured in magnetic fields of 0.05 and 1 T for the annealed plate. As the result in magnetic field of 0.05 T, the $T_c$ is 379 K and the MT temperatures are close to the $T$c. The MT starting and finishing temperatures, $M_s$ and $M_f$, are 362 and 346 K, respectively. The reverse MT starting and finishing temperatures, $A_s$ and $A_f$, are 361 and 368 K, respectively. The thermal hysteresis is estimated to be 15 K. This thermal hysteresis is equivalent with that of practical NiTi-Cu alloy [7]. It is also found that $M_s$ decreases by 1.5 K under the magnetic field of 1 T. This result indicates the MT temperatures decrease by applying magnetic field, and it is expected to show the metamagnetic phase transition due to this MT temperatures decrease.

The annealed alloy plate shows one-way SME by heating (Fig. 4). Heating speed was 0.5 K/s. The dimensions of the plate are 7 mm × 3.5 mm × 0.05 mm. From this behavior, apparent reverse MT starting and finishing temperatures, $A_s$* and $A_f$* are estimated to be 372 and 389 K, respectively. Those are higher than the reverse MT temperatures measured by SQUID. This difference was attributed to the heating speeds, and as for one-way SME, current heating speed is too high for homogenous temperature distribution.

The annealed alloy plate shows M phase at room temperature and the reverse MT to A phase by heating. Since the MT temperatures decrease by applying magnetic field, it is expected to show the metamagnetic phase transition. In addition, one-way SME is found by heating. These results indicate the possibility for metamagnetic SME.

## 4. Summary

In this study, Ni-Mn-In alloy plates containing Co were fabricated by COSME-RT using the powder grounded from the sputtered films. The MT and one-way SME induced by controlling the temperature were observed, and the MT temperatures decreased with increasing magnetic field. They show the possibility of metamagnetic SME and the possibility for a magnetic-field-driven actuator is also indicated.

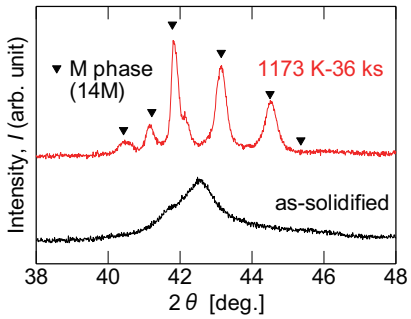


Fig. 2 XRD profiles of $Ni_{48.2}Co_{3.3}Mn_{35.9}In_{12.6}$ plates.

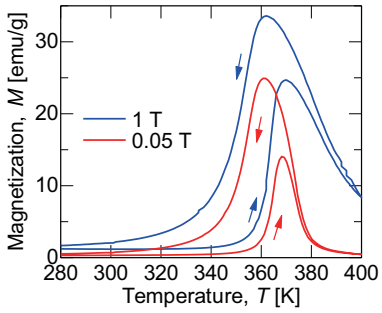


Fig. 3 Thermomagnetization curves of annealed $Ni_{48.2}Co_{3.3}Mn_{35.9}In_{12.6}$ plate.

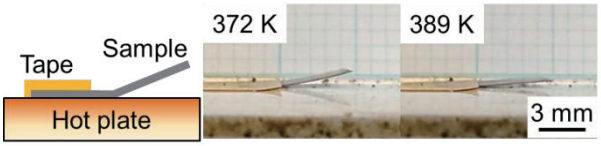


Fig. 4 Shape memory effect on annealed $Ni_{48.2}Co_{3.3}Mn_{35.9}In_{12.6}$ plate.


## Acknowledgement

This work was partly supported by the JSPS Core-to-Core Program, A. advanced Research Networks, "International research core on smart layered materials and structures for energy saving".


## References


[1] K. Ullakko, J. K. Huang, V. V. Kokorin, R. C. Handley, *Scr. Mater.,* 36 (1997) 1133-1138.

[2] A. V. Vasil'ev, V. D. Buchelnikov, T. Takagi, V. Khovailo, E. I. Estrin, *Phys. Uspekhi,* 46 (2003) 559-588.

[3] Y. Sutou, Y. Imano, N. Koeda, T. Omori, R. Kainuma, K. Ishida, K. Oikawa, *Appl. Phys. Lett.,* 85 (2004) 4358-4360.

[4] K. Oikawa, W. Ito, Y. Imano, Y. Sutou, H. Morito, S. Okamoto, O. Kitakami, T. Kanomata, *Appl. Phys. Lett.,* 88 (2006) 122507-122509.

[5] H. Takeshi, N. Nakayama, H. Miki, *J. Soc. Mater. Sci., Jpn*, 54 (2005) 233-238.

[6] V. V. Khovaylo, T. Kanomata, T. Tanaka, M. Nakashima, Y. Amako, R. Kainuma, R. Y. Umetsu, H. Morito, H. Miki, *Phys. Rev. B,* 80 (2009) 144409-144415.

[7] T. Sakuma, U. Iwata, *Trans. JSME (in Japanese)*, *A* 63 (1997) 1320-1326.

Eleventh International Conference on Flow Dynamics
October 8-10, 2014, Sendai, Miyagi, Japan

# Solving the Impedance Cloaking Problems Using the Boundary Elements Method

Andrei Baydin[1], Olga Larkina[1]
[1]Far Eastern Federal University
8 Sukhanova str., Vladivostok, 690950, Russia

**ABSTRACT**

The cloaking problem is considered for a 2-D wave scattering model in an unbounded homogenous medium with impedance boundary condition. The problem is reduced to the inverse extremal problem of choosing the surface impedance. The solvability of the original scattering problem for 2-D Helmholtz equation and of the extremal problem is proved. Optimality system describing the necessary extremum conditions is derived. The algorithm for numerical solving of the control problem based on the optimality system and boundary element method is designed.

## 1. Introduction

It was proposed that perfect invisibility cloaking shells can be constructed for hiding objects from electromagnetic illumination [1]. Even though numerical simulations and further theoretical analysis [2] confirmed the efficiency of this method, experimental demonstrations have proven to be more challenging. The difficulty in fabricating such shells stems from the requirements on the material that composes it: such cloaking shells have anisotropic, spatially varying optical constants with infinite values at the interior surface of the cloak. However, approximations were made that significantly reduced the scatter reduction performance of the shell. Another approach in cloaking material bodies consists of coating theirs outer boundaries with special material having the certain value of surface impedance. In this case, the cloaking problem is reduced to choosing the impedance such that the wave scattered by the object have certain properties [3]. We mention papers [4-6] devoted to development of methods of solving impedance cloaking problems based on optimization approach of solving inverse problems for the wave equations.

## 2. Formulation and Solvability of the Original Scattering Problem

Let $\Omega$ be bounded region in $R^2$ with a connected complement $\Omega^c = R^2 \setminus \Omega$ and with a boundary $\Gamma$. It is well known that the problem of scattering waves in a homogenous medium containing an impermeable obstacle $\Omega$ with a covered boundary is reduced to finding a function $u = u^{inc} + u^s$ in $\Omega^c$ that satisfy the Helmholtz equation

$$\Delta u + k^2 u = 0 \qquad \text{in } \Omega^c, \tag{1}$$

and obey the impedance boundary condition and the Sommerfield radiation condition in $R^2$

$$\partial u / \partial n + i k \lambda u = 0 \qquad \text{on } \Gamma,$$
$$\lim_{r \to \infty} \sqrt{r} (\partial u^s / \partial r - i k u^s) = 0 \text{ as } r = |x| \to \infty. \tag{2}$$

Here $u^{inc}$ is the incident wave, $u^s$ is the scattered wave, $\lambda$ is the surface impedance on boundary $\Gamma$, $k$ is the wave number, $i$ is the imaginary unit, $n$ is the outward (relative to $\Omega$) unit normal vector.

The following conditions are assumed below to hold:

(i) $\Omega$ is a bounded domain in $R^2$ with a connected complement $\Omega^c$ and with a boundary $\Gamma$ in $C^{0,1}$.

Let $B_R$ be a disk of radius $R$ containing $\Omega$, and let $\Omega_e = \Omega^c \cap B_R$. Clearly, $\Omega_e$ is a bounded domain in $R^2$ with the boundary $\partial\Omega_e$ consisting of two parts: $\Gamma$ and $\Gamma_R$ where $\Gamma_R$ is a boundary of $B_R$. For any open subset Q of $B_R$, we use the Sobolev space $H^1(Q)$ of complex or real scalar functions defined in Q. We also use the trace spaces $H^{1/2}(\partial Q)$ and in particular $H^{1/2}(\Gamma)$ and $H^{1/2}(\Gamma_R)$. Let $H^{-1/2}(\partial Q)$ denote the dual of the space $H^{1/2}(\partial Q)$ with respect to $L^2(\partial Q)$. The norms in $H^1(Q)$, $H^{1/2}(\partial Q)$, and $H^{-1/2}(\partial Q)$ are denoted by $\|\cdot\|_{1, Q}$, $\|\cdot\|_{1/2, \partial Q}$, $\|\cdot\|_{-1/2, \partial Q}$ respectively. The inner products and norms in $L^2(Q)$ and $L^2(\partial Q)$ are designated as $(\cdot, \cdot)_Q$, $\|\cdot\|_Q$ and $(\cdot, \cdot)_{\partial Q}$, $\|\cdot\|_{\partial Q}$.

In order to reduce the problem (1)-(2) to the equivalent problem considered in the bounded domain $\Omega_e$ we define a Dirichlet-to-Neumann mapping $T: H^{1/2}(\Gamma_R) \to H^{-1/2}(\Gamma_R)$ that maps every function $g$ in $H^{1/2}(\Gamma_R)$ to a function $\partial v / \partial n$ where $v$ is a solution of the exterior Dirichlet problem for Helmholtz equation with boundary condition $v|_{\Gamma R} = g$. It is well known that problem (1)-(2) is equivalent to equation (1) in $\Omega_e$ and impedance boundary condition from (2) with the following boundary condition:

$$\partial u^s / \partial n = T u^s \qquad \text{on } \Gamma_R. \tag{3}$$

For brevity this problem will be referred to as problem 1.

Let $u^{inc}$ be in $H^{inc}(\Omega_e) = \{u \text{ in } H^1(Q): \Delta u + k^2 u = 0 \text{ as a distribution}\}$. We multiply (1) by $\varphi^*$ where $\varphi$ in $H^1(\Omega_e)$ is a test function, $\varphi^*$ means the complex conjugate of $\varphi$, integrate over $\Omega_e$ and apply Green formula. We have

$$\int_{\Omega e} (\mathbf{grad}\, u \cdot \mathbf{grad}\, \varphi^* - k^2 u \varphi^*)\, dx = -\int_\Gamma \varphi^* \partial u / \partial n \, d\sigma + \int_{\Gamma R} \varphi^* \partial u / \partial n \, d\sigma. \tag{4}$$

Taking into account boundary conditions (2) and (3) we rewrite (4) in the form

$$a_0(u, \varphi) - i k (\lambda u, \varphi)_\Gamma = \langle f, \varphi \rangle \quad \forall \varphi \text{ in } H^1(\Omega_e), \tag{5}$$

where $a_0(\cdot, \cdot)$, $(\lambda \cdot, \cdot)$ and $\langle f, \cdot \rangle$ are the following sesquiliniear and linear forms:

$$a_0(u, \varphi) := \int_{\Omega e} (\mathbf{grad}\, u \cdot \mathbf{grad}\, \varphi^* - k^2 u \varphi^*)\, dx - \int_{\Gamma r} \varphi^* T u \, d\sigma,$$
$$(\lambda u, \varphi)_\Gamma := \int_\Gamma \lambda u \varphi^* \, d\sigma,$$
$$\langle f, \varphi \rangle := \int_{\Gamma R} \varphi^* (\partial u^{inc} / \partial n - T u^{inc}) \, d\sigma. \tag{6}$$

The solution of (5) is called the weak solution of problem 1. Using the properties of forms $a_0(\cdot, \cdot)$, $(\lambda \cdot, \cdot)$ and $\langle f, \cdot \rangle$ we can prove the following theorem.

Corresponding author: Andrei Baydin
*E-mail address*: thulfm@gmail.com

**Theorem 1.** Under conditions (i) let $\lambda$ in $L^{\infty}_{\lambda 0}(\Gamma) = \{\lambda \text{ in } L^{\infty}(\Gamma)\colon \lambda(x) \geq \lambda_0\}$ be an arbitrary function where $\lambda_0 > 0$. Then for every incident wave $u^{inc}$ in $H^{inc}(\Omega_e)$ there exist a unique solution $u_\lambda$ to (5) that satisfies the following estimate with a constant $C_\lambda$ that depends on $\lambda$ and is independent of $u^{inc}$:

$$\|u_\lambda\|_{1,\,\Omega e} \leq C_\lambda \, \|u^{inc}\|_{1,\,\Omega e}. \quad (7)$$

Assuming that the impedance $\lambda$ belongs to a nonempty bounded subset K of $L^{\infty}_{\lambda 0}(\Gamma)$ we can prove the following theorem.

**Theorem 2.** Under conditions (i) let $\lambda$ in K where K is a nonempty bounded subset of $L^{\infty}_{\lambda 0}(\Gamma)$, $\lambda_0 > 0$. Then for every $u^{inc}$ in $H^{inc}(\Omega_e)$ a unique solution $u$ to (5) satisfies the following estimate:

$$\|u\|_{1,\,\Omega e} \leq C_0 \, \|u^{inc}\|_{1,\,\Omega e}, \quad (8)$$

with constant $C_0$ independent of $\lambda$.

## 3. Control Problem and Optimality System

Now we are able to formulate the control problem for model (1), (2). This problem is to minimize a certain cost functional depending on the state (wave field) $u$ and the unknown function (control), which satisfy the equations of state in the form of (5) of problem 1. The control is specified by the impedance $\lambda$, while the cost functional is either one the following two:

$$I_1(u) = \|u - u^d\|^2_Q = \int_Q |u - u^d|^2 \, dx,$$
$$I_2(u) = \|u - u^d\|^2 = \int_{\Gamma q} |u - u^d|^2 \, d\sigma. \quad (9)$$

Here Q is a subdomain of $\Omega_e$, $\Gamma_q$ is a continuous cycled curve in $\Omega_e$. When $u^d = u^{inc}$ the functional $I_1$ (or $I_2$) is the squared mean square integral norm of the scattered field $u^s$ over Q (or over $\Gamma_q$). Assume the following conditions hold:

(j) $\Gamma$ belongs to $C^{1,\,1}$; $\alpha_0 > 0$; and K is a nonempty convex closed subset of $H^s_{\lambda 0}(\Gamma) = \{\lambda \text{ in } H^s(\Gamma)\colon \lambda(x) \geq \lambda_0\}$, where $s > 1/2$ and $\lambda_0 > 0$.

Introducing the operator $G\colon H^1(\Omega_e) \times K \times H^{inc}(\Omega_e) \to H^1(\Omega_e)^*$ by $\langle G(u, \lambda, u^{inc}), \varphi\rangle = a_0(u, \varphi) - i\,k\,(\lambda u, \varphi)_\Gamma - \langle f, \varphi\rangle \;\forall\; \varphi$ from $H^1(\Omega_e)$, where $H^1(\Omega_e)^*$ is a dual space to $H^1(\Omega_e)$, we rewrite (5) in the form $G(u, \lambda, u^{inc}) = 0$. Consider the constrained minimization problem

$$J(u, \lambda) := (\alpha_0 / 2)\, I(u) + (\alpha_1 / 2)\, \|\lambda\|^2_{s,\,\Gamma} \to \inf,$$
$$G(u, \lambda, u^{inc}) = 0, \quad (u, \lambda) \text{ in } H^1(\Omega_e) \times K. \quad (10)$$

Here $I = I_k$, $k = 1, 2$. Proceeding as in [4] we arrive to the following theorem.

**Theorem 3.** Under conditions (i), (j) let $\alpha_0 > 0$, $\alpha_1 \geq 0$ and let K be a bounded set and $u^{inc}$ in $H^{inc}(\Omega_e)$. Then control problem (11) has a least one solution $(u, \lambda)$ in $H^1(\Omega_e) \times K$ for $I = I_k$, $k = 1, 2$.

The further analysis of problem (10) consists in using the extremum principle in smooth convex extremum problems [4]. It allows us to derive the necessary extremum conditions and leads to the following theorem.

**Theorem 4.** Under conditions (i), (j) let $(u, \lambda)$ in $H^1(\Omega_e) \times K$ be a solution of problem (10) at $I = I_k$, $k = 1, 2$. Then there exists a unique Lagrange multiplier $p$ in $H^1(\Omega_e)$ that satisfies the Euler-Lagrange equation

$$a_0(\varphi, p) - i\,k\,(\lambda\,\varphi, p)_\Gamma = -(\alpha_0 / 2)\,\langle I'_u(u), \varphi\rangle^* \quad \forall\, \varphi \text{ in } H^1(\Omega_e), \quad (11)$$

and the following minimum principle holds:

$$\alpha_1\,(\lambda, \mu - \lambda)_{s,\,\Gamma} - \mathrm{Re}[i\,k\,((\mu - \lambda)\,u, p)_\Gamma] \geq 0 \quad \forall\, \mu \text{ in K}. \quad (12)$$

Here $I'_u$ is a Fréchet derivative of the functional I.

The weak formulation of problem 1, (5), problem (11), which is interpreted as an adjoint problem for the adjoint state $p$ in $H^1(\Omega_e)$, and variational inequality (12) form an optimality system of problem (10). This system describes the necessary extremum conditions of (10).

## 4. Numerical Algorithm for Control Problem

In order to find the numerical solution of the optimality system we suggest the following algorithm based on the idea of simple iteration. Assume that for any step of the algorithm we know some approximation $\lambda_n$. Using the $\lambda_n$ we find $\lambda_{n+1}$ by sequential solving the following problems

$$a_0(u_n, \varphi) - i\,k\,(\lambda_n u_n, \varphi)_\Gamma = \langle f, \varphi\rangle \quad \forall\, \varphi \text{ in } H^1(\Omega_e), \quad (13)$$

$$a_0(\varphi, p_n) - i\,k\,(\lambda_n \varphi, p_n)_\Gamma = -(\alpha_0 / 2)\,\langle I'_u(u_n), \varphi\rangle^* \quad \forall\, \varphi \text{ in } H^1(\Omega_e), \quad (14)$$

$$\alpha_1\,(\lambda_{n+1}, \mu - \lambda_{n+1})_{s,\,\Gamma} - \mathrm{Re}[i\,k\,((\mu - \lambda_{n+1})\,u_n, p_n)_\Gamma] \geq 0 \quad \forall\, \mu \text{ in K}. \quad (15)$$

Thus, each step of the algorithm consists of finding the solutions $u_n$ and $p_n$ of (13) and (14), which are the weak formulations of some external boundary value problems. Using the boundary element approach we can reduce these problems to boundary integral equations. Boundary element method gives direct numerical values of $u_n|_\Gamma$ and $p_n|_\Gamma$ which are used in (15) and the way to find $u_n$ and $p_n$ in any subdomain of $\Omega_e$.

## 5. Summary

We have analyzed the direct scattering impedance problem and the inverse extremal problem of choosing the surface impedance. The solvability of direct and inverse problems is derived. The optimality system constructed. Numerical algorithm of solving the control problem based on optimality system and boundary element method is proposed. The results of numerical simulations will be published in separate authors' work.

This work was financially supported by the Russian Science Foundation (project no. 14-11-00079).

## References

[1] J.B. Pendry, D. Schurig, D.R. Smith, *Science*, 312 (2006), 1780-1782.
[2] H. Chen, B.-I. Wu, B. Zhang, J. A. Kong. *Phys. Rev. Lett.* 99 (2007), 063903.
[3] Yu. I. Bobrovnitskii, *Doklady Physics*, 57 (2012), 18-22.
[4] G.V. Alekseev, *Doklady Physics*, 58 (2013), 147-151.
[5] G.V. Alekseev, *Computational Mathematics and Math. Physics*, 53 (2013), 1853-1869.
[6] G.V. Alekseev, *Doklady Physics*, 58 (2013), 482-486.

# Characterization of vortical flow structures within swirling jet in an unconfined isothermal environment

Dilip Sanadi[1], Saptarshi Basu [1],
[1]Department of Mechanical Engineering, Indian Institute of Science,
CV Raman Road, Bangalore, Karnataka -560012, India

## Abstract

This work reports the response of isothermal co-annular swirling flow field subjected to a co-axial central air jet emanating from a nozzle. 2D-PIV measurements were carried out to understand the topology of swirling flow field in response to center jet, structure of internal recirculation zones and its transition to cone-type breakdown. This time-mean transition was studied by varying the jet Reynolds number ($Re_c$) while maintaining constant Reynolds number for the annular swirling stream ($Re_s$).

## 1. Introduction

Swirling flows at different intensities have been employed efficiently in plethora of industrial applications. This includes both reacting (combustion systems) and non-reacting flows which underlines its immense practical utility. In particular, aero-engines, internal combustion engines, industrial boilers, refineries are a few examples of combustion systems that employ swirl. This is also pertinent in non-reacting flow systems such as cyclone separators, jet pumps and pharmaceutical drug nebulizers. The imperative flow structure formed in swirl flows is the internal recirculation zone (IRZ) which acts as an effective aerodynamic flame holder. The principal reason for the flow reversal leading to IRZ is the decay of radial pressure gradient in the axial direction introducing a negative axial pressure gradient [1]. This IRZ exhibits toroidal patterns which can be observed at supercritical swirl strengths (~swirl number $S \geq 0.6$) [2]. Further, vortex breakdown observed in swirl flows characterized by sudden deceleration of the axial flow leading to a bifurcation at the stagnation point is identified as absolute instability [3]. The distinctive types of vortex breakdown detailed in literature primarily include spiral, axisymmetric bubble and double helix configurations [4, 5-7]. In addition to these states, Billant et al. [8] observed two new states namely conical sheet and asymmetric cone type disturbance. The present study aims at transition of recirculation structures in isothermal swirling field from axisymmetric vortex breakdown bubble (VBB) to conical sheet by injecting central air jet from a nozzle with stepwise increase in $Re_c$. This is aimed as a precursor study to thoroughly understand the underlying fluid dynamics of swirl-hollow cone spray interaction.

## 2. Experimental approach

The experimental test facility utilizing an axial-flow, pressure swirl nozzle to form a central air jet is illustrated schematically in Fig.1.

Corresponding author: Saptarshi Basu
*E-mail address*: sbasu@mecheng.iisc.ernet.in

This standard co-annular assembly comprises an inline arrangement of three main sections: (1) a settling chamber supplying compressed air (4 bar gauge) to the swirler end piece, (2) guided vane swirler (3) honeycomb flow conditioners. In order to ensure an equal distribution of co-axial air supply, air flow was delivered into a settling chamber (placed upstream of the guided vane swirler) through two diametrically opposite apertures. Honeycombs (3mm holes) are placed inline inside the settling chamber at 40mm and 60mm upstream of the swirler exit plane to breakdown the large scale eddies. The guided vane swirler has a blade angle of $\emptyset$=45° ($S_G$=0.8) and equipped with 9 flat vanes that are periodically arranged around the central hub. The corresponding geometrical swirl number ($S_G$) is given by the expression [2].

$$S_G = \frac{2}{3}\left[\frac{1-\left(\frac{d_h}{d}\right)^3}{1-\left(\frac{d_h}{d}\right)^2}\right]\tan\emptyset \qquad (1)$$

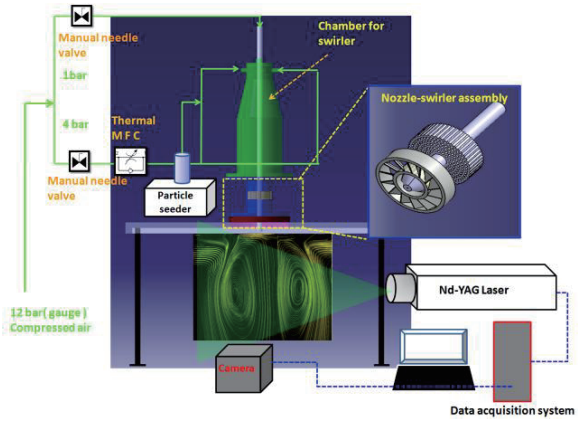


Fig.1 Schematic of the experimental test facility.

Where $d_h$ is annulus inner hub diameter (52mm) and $d$ is outer hub diameter (92mm). 2D-PIV technique was employed to characterize the structure of recirculation zone. The imaging sub-system

consists of (a) Dual pulsed Litron nano PIV Nd:YAG solid-state laser ( pulse energy: 70 mJ/pulse and 532 nm) which illuminates the flow field laden with DEHS (Di-ethyl-hexyl-sebacat) tracer particles and (b) sheet making optics to produce 1mm thick laser sheet. Image acquisition system comprises of a CCD camera (pixel resolution: 1376 × 1040) (c) a programmable timing unit (PTU) which acts as a master timing device and Davis 7.2 is used as the software interface from which the time-averaged vector field was obtained. A window size of 64×64 and 50% overlap are used as post-processing parameters.

### 3. Results and discussion

This section outlines the time-mean transition in disruptive vortex core from an open-bubble type axisymmetric breakdown state to classical cone breakdown as $Re_c$ was varied in the range $600 \leq Re_c < 1200$ (at a fixed $Re_s = 3200$). 2D velocity vector field and streamlines plots of this sequential transition are shown in Fig.2. This transition was initiated by first introducing the annular swirling stream without centre jet. This leads to the formation of an IRZ (Fig.2a) with vortex core centers (VCC) located at $y/R_0$=1.5 downstream of the exit plane. Next, as the centre jet was injected into the recirculation field it is observed that the IRZ swells volumetrically to form a toroidal structure. This was substantiated by the radial expansion to the breakdown bubble (also seen by the radial outward shifting of the VCC and the reverse flow boundary). Further increment in the axial flow rate of the inner jet causes more bulging of the IRZ until it breaks down at a critical $Re_c$ to form a wide angle conical sheet. This was characterized by disruption of the vortex core (i.e. extreme fanning-out of the flow field). Fig.2d shows this cone type break down with typical wake like velocity profile in its interior signifying near stagnant zone in the cone interior or very low velocity axial flow recirculation of the entrapped fluid. Flow visualization images of this time-mean transition are shown subset in Fig. 2. In general this transition features a downstream shifting of the VCC in increments of $y/R_0$=0.25 (where $R_0$ is swirler radius). Further at $Re_c$ = 800 similar topological changes were observed with a further downstream shift of the vortex core center (corresponding to $y/R_0$=0.45) and more widening of recirculation zone as shown in Fig. (2c). This represents a metastable state that marks the onset of transition to the cone type breakdown. In this state it was observed that prior to conical breakdown at $Re_c$ = 1200 the IRZ's distorts and exhibits large scale oscillations as the shear layer vortices rolls-up and shed vigorously.

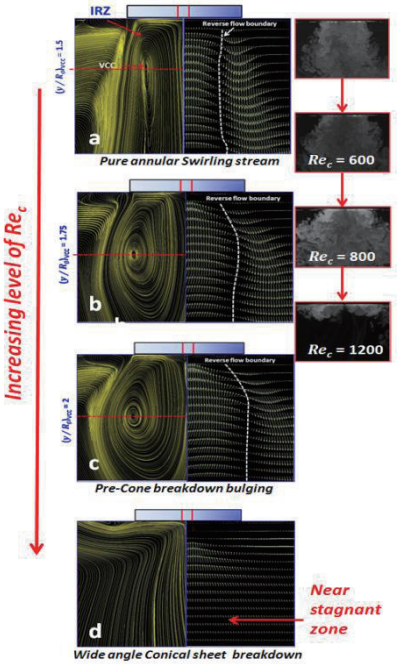


Fig. 2 Schematic of time-mean transition from IRZ to cone-type breakdown depicting streamline plots (left) and 2D velocity vector field with reverse flow boundaries.

### 4. Conclusion

Effect of central air jet (emanating from a centre nozzle) on the internal recirculation zone (IRZ) established due to vortex breakdown in an isothermal (non-reacting) swirling flow field was investigated. The present fluid dynamical study bears a direct connection with reacting flow experiments involving hot flow in the sense that the dynamic flow field behavior inherently present in cold flow may contribute significantly in deciding the complex flame dynamics. Similar transition was also observed at high $Re_s$=1600 and 4800 and has not been reported for brevity.

### References


[1] N. Syred, *Progress in Energy and Combustion Science*. **32,**93 (2006).

[2] A.K. Gupta, D.G. Lilley, N. Syred, *(Abacus Press.* 1984).

[3] N.Syred, J.M. Beer, *Combustion and Flame*. **23,** 143 (1974).

[4] O. Lucca-Negro, T. O Doherty, *Prog. Energy Combust. Sci.* **27**, 431 (2001).

[5] T. Sarpkaya, *J. Fluid Mech*. **45**, 545 (1971).

[6] S. Leibovich, *Annual Review of Fluid Mechanics*. **10,** 221 (1978).

[7] M.G. Hall, *Annual Review of Fluid Mechanics*, 4, 195 (1972).

[8] P. Billant , J.M. Chomaz, P. Huerre, *J. Fluid Mech,* **376**,183 (1998).

Eleventh International Conference on Flow Dynamics
October 8-10, 2014, Sendai, Miyagi, Japan

# The Helical Behavior of the Single-Square Grid-Generated Turbulence

Yi Zhou[1], Kouji Nagata[1], Yasuhiko Sakai[1], Yasumasa Ito[1], Toshiyuki Hayase[2]

[1]Department of Mechanical Science and Engineering, Nagoya University
Furo-cho, Chikusa-ku, Nagoya, Aichi, 464-8603, Japan
[2]Institute of Fluid Science, Tohoku University
1-1-2 Katahira, Aoba-ku, Sendai, Miyagi, 980-8577, Japan

**ABSTRACT**

Single-square grid-generated turbulence is studied via direct numerical simulations (DNSs). The results demonstrate that owing to large wake-interactions, the turbulent flow generated by the single square grid acquires the alignment of the velocity $\boldsymbol{u}$ and vorticity $\boldsymbol{\omega}$. In the fully turbulent region, the probability density functions (PDFs) of $\cos(\theta)$ remain unchanged and are fairly flat, where $\theta$ is the angle between $\boldsymbol{u}$ and $\boldsymbol{\omega}$. In the downstream region i.e., at $X/X_*$=1.4 greater alignment of the fluctuating velocity $\boldsymbol{u}'$ and vorticity $\boldsymbol{\omega}'$ is found in the high dissipation or enstrophy regions.

## 1. Introduction

In our previous studies [1, 2], DNSs were performed to investigate the turbulence generated by the single square grid. Our previous results suggested that fluid points along the centerline undergo three different stages, e.g., irrotational region ($X/X_* < 0.1$), transition region ($0.1 \le X/X_* \le 0.4$), and fully turbulent region ($X/X_* > 0.4$). Here, the wake-interaction length scale $X_*$ is defined as $L_0^2/t_0$, where $t_0$ is the thickness of the grid bar and $L_0$ is the mesh size of the single square grid [3].

This study mainly focuses on the helical behavior of single-square grid-generated turbulence. Helicity $H$ is given by

$$H = \boldsymbol{u} \cdot \boldsymbol{\omega}, \tag{1}$$

where $\boldsymbol{u}$ and $\boldsymbol{\omega}$ are the velocity vector and the vorticity vector, respectively.
And the helicity density $h$ is given by

$$h = \cos(\theta) = H/(|\boldsymbol{u}| \cdot |\boldsymbol{\omega}|), \tag{2}$$

where $\theta$ is the angle between $\boldsymbol{u}$ and $\boldsymbol{\omega}$. For helical structures or swirling motion, $h$ takes the value of ±1. The relationship $h$=0 indicates that $\boldsymbol{u}$ is perpendicular to $\boldsymbol{\omega}$, which is observed in the two-dimensional flow.

## 2. Flow conditions

Figures 1 and 2 show the schematics of the single square grid and the computational domain, respectively. This single square grid is placed near the inlet of the computational domain. The inlet Reynolds number $\mathrm{Re}_{L0} = U_{in} L_0 / \nu$, which is based on the inlet velocity $U_{\mathrm{in}}$ and the kinematic viscosity $\nu$, is 20,000. For more numerical details, refer to [1, 2].

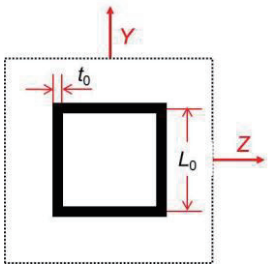


Fig. 1 Schematic of the single square grid used in this study. The dotted lines represent periodic boundary conditions in the vertical and spanwise directions.

Corresponding author: Yi Zhou
*E-mail address*: zhou.yi@b.mbox.nagoya-u.ac.jp

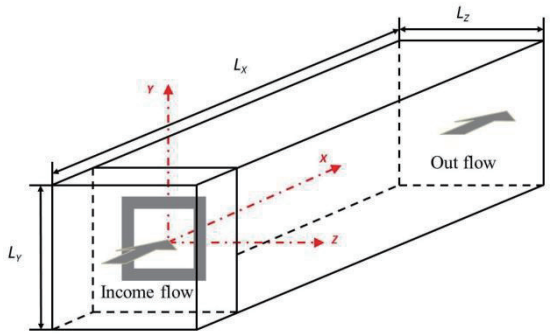


Fig. 2 Schematic view of the computational domain.

## 3. Results and Discussion

The streamwise evolution of the variance $\langle h^2 \rangle$ (not shown here) is examined to study the alignment of $\boldsymbol{u}$ and $\boldsymbol{\omega}$ along the centerline, where $\langle\ \rangle$ denotes an ensemble average. Note that $\langle h^2 \rangle$ takes the value of 0.333 for a uniformly distributed PDF profile of $h$. The variance $\langle h^2 \rangle$ with a value much smaller than 0.333 implies that $\boldsymbol{u}$ and $\boldsymbol{\omega}$ are more likely to be orthogonal, whereas a much larger value of $\langle h^2 \rangle$ means a greater alignment (parallel or antiparallel of $\boldsymbol{u}$ and $\boldsymbol{\omega}$). In the irrotational region, the value of $\langle h^2 \rangle$ is considerably small (< 0.05). This observation reveals that at $X/X_* < 0.1$, fluid motions show a strong tendency to local two-dimensionalization. The value of $\langle h^2 \rangle$ increases sharply in the transition region ($0.1 \le X/X_* \le 0.4$). In contrast, in the fully region $X/X_* > 0.4$, the value of $\langle h^2 \rangle$ remains constant and is close to 0.333.

The PDFs of $h$, $P(h)$, at four streamwise locations $X/X_*$= 0.00, 0.26, 0.40, and 1.40 are plotted in Fig. 3 to investigate further details of $h$. Note that the profile of $P(h)$ is only determined by the alignment of $\boldsymbol{u}$ and $\boldsymbol{\omega}$ at different turbulent states. In the upstream region, as seen in Figs. 3(a) and (b), $P(h)$ has a distinct peak at $h$=0, which indicates less helical behavior. Figs. 3(c) and (d), in contrast, demonstrate that the profiles of $P(h)$ are fairly flat and no discernible peaks at $h$=0 can be observed. Hence, there is no preferred tendency for $\boldsymbol{u}$ and $\boldsymbol{\omega}$ to be orthogonal.

We also examine the PDFs of $h' = \cos\theta'$ (see Fig. 4)

at $X/X_*$= 0.00, 0.26, 0.40, and 1.40, where $\theta'$ is the angle between $\boldsymbol{u}'$ and $\boldsymbol{\omega}'$, where the prime $'$ denotes the fluctuating variable. Note that $\theta'$ is Galilean invariant, whereas $\theta$ is not.

The main difference between the profiles of $P(h)$ and $P(h')$ is that at $X/X_* \leq 0.26$, the profiles of $P(h')$ are much boarder than those of $P(h)$. However, the shapes of $P(h)$ and $P(h')$ at $X/X_* \geq 0.40$ are quite similar.

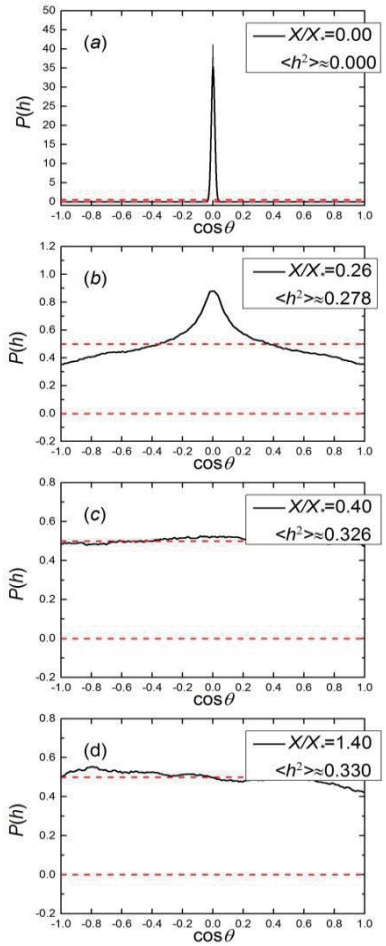


Fig. 3 PDFs of $h$ at $X/X_*$ =0.0, 0.26, 0.40 and 1.40.The two dashed lines represent $P(h)$ = 0.0 and 0.5.

The $P(h')$ (conditioned on $S'_{ij}S'_{ij} \geq 2 < S'_{ij}S'_{ij} >$ and $\Omega'_{ij}\Omega'_{ij} \geq 2 < \Omega'_{ij}\Omega'_{ij} >$) are also investigated (the corresponding profiles are not presented, due to volume limitation), where $S'_{ij} = 1/2(\partial u'_i/\partial x_j + \partial u'_j/\partial x_i)$ and $\Omega'_{ij} = 1/2(\partial u'_i/\partial x_j - \partial u'_j/\partial x_i)$. One interesting finding is that the conditional profiles of $P(h')$ conditioned on either high dissipation or high enstrophy levels are roughly flat at $X/X_*$=0.40 and the corresponding conditional values of $<h'^2>$ is approximately equal to the unconditional value, whereas more alignment between $\boldsymbol{u}'$ and $\boldsymbol{\omega}'$ is found when conditioned on high dissipation or enstrophy levels at $X_*$=1.4. Note that Choi *et al.* [4] has already demonstrated that for the forced isotropic turbulence greater alignment is found in the high enstrophy region.

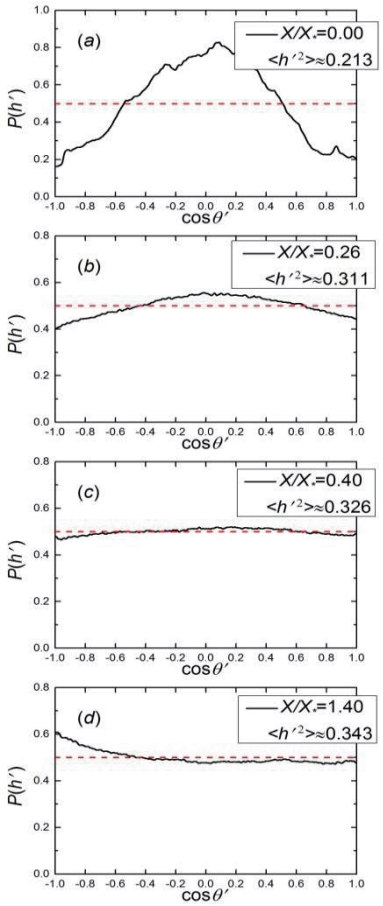


Fig. 4 PDFs of $h'$ at $X/X_*$ =0.0, 0.26, 0.40 and 1.40.The dashed line is $P(h')$ = 0.0.

## 4. Concluding Remarks

The rapid increase in the alignment of $\boldsymbol{u}$ and $\boldsymbol{\omega}$ is due to the wake interactions, indicating the existence of a transition process from a two dimensional state to a three dimensional state. In the energy decay region i.e., at $X_*$=1.4, when conditioned on high dissipation or high enstrophy levels, $\boldsymbol{u}'$ and $\boldsymbol{\omega}'$ become more aligned compared with the unconditional PDF profile. However, this conclusion does not hold in the upstream region i.e., at $X_*$=0.4.


**Acknowledgements**

Part of the work was carried out under the Collaborative Research Project of the Institute of Fluid Science, Tohoku University and supported by Grants-in-Aid (Nos. 2528930 and 2528931) from the Japanese Ministry of Education Culture, Sports, Science and Technology.


**References**


[1] Y. Zhou, K. Nagata, Y. Sakai, H. Suzuki, Y. Ito, O. Terashima, T. Hayase, *Phys. Fluids*, 26(2014) 1－17.

[2] Y. Zhou, K. Nagata, Y. Sakai, H. Suzuki, Y. Ito, O. Terashima, T. Hayase, *Phys. Fluids*, *Phys. Fluids*, 26(2014) 1－12.

[3] N. Mazellier and J. C. Vassilicos, *Phys. Fluids*, 22(2010) 1－25.

[4] Y. Choi, B. Kim, C. Lee, *Phys. Rev. E*, 80(2009) 1－4.

Eleventh International Conference on Flow Dynamics
October 8-10, 2014, Sendai, Miyagi, Japan

# Non-destructive Evaluation of Creep Damage Based on Magnetic Incremental Permeability

Takanori Matsumoto[1], Tetsuya Uchimoto[2], Toshiyuki Takagi[2], Gerd Dobmann[3], Shigeru Takaya[4]
[1]Graduate School of Engineering Tohoku University
2-1-1 Katahira, Aoba-ku, Sendai, Miyagi, 980-8577, Japan
[2]Institute of Fluid Science, Tohoku University
2-1-1 Katahira, Aoba-ku, Sendai, Miyagi, 980-8577, Japan
[3]Saarland University
66123 Saarbrücken, Germany
[4]Japan Atomic Energy Agency
4002 Narita-cho, Oarai-machi, Higashiibaraki-gun, Ibaraki, 311-1393, Japan

**ABSTRACT**

The aim of this study is to estimate microstructure change by creep damage in mod. 9Cr-1Mo steels by electromagnetic nondestructive evaluation method. For the purpose, magnetic incremental permeability is measured in creep and isothermal aging specimens. Featured parameters of magnetic incremental permeability are discussed in relation to structure change by creep damage.

## 1. Introduction

In fossil fuel power plants, mod. 9Cr-1Mo steels are used as high temperature materials. Time to rupture of long term creep tests in mod. 9Cr-1Mo steel is shorter than that based on accelerated creep tests [1]. Therefore, microstructure change due to creep damage should be evaluated in nondestructive way.

In this study, to establish electromagnetic nondestructive evaluation of microstructure change by creep damage in mod. 9Cr-1Mo steel, magnetic properties of creep specimens are systematically investigated. For the purpose, magnetic incremental permeability of creep and isothermal aging specimens is measured. Featured parameters of incremental permeability are extracted and discussed in relation with incremental permeability.

## 2. Mod. 9Cr-1Mo steel samples

In this study, samples of mod. 9Cr-1Mo steels were prepared. Creep specimens were made by different temperature and stress. In isothermal aging specimens, temperature condition is 500, 550, 600 and 650 degrees for each test time (600, 1400, 4000 and 7520 hours). Larson-Miller Parameter, LMP which is one of time-temperature parameters, is defined as LMP=$T$(20+log$t$), where $T$ is absolute temperature [K] and $t$ is time [h]. The specimens have columnar shape with diameter of 3mm and length of 30 mm.

## 3. Incremental permeability method

Incremental permeability $\mu_\Delta$ is defined as $\mu_\Delta = \Delta B/\mu_0 \Delta H$, where $\mu_0$ is the permeability of free space, $\Delta B$ is the incremental magnetic flux density, and $\Delta H$ is the incremental magnetic field [2]. In this study, incremental permeability was estimated during the magnetization process. Figure 1 shows the experimental setup for measuring of incremental permeability. A sinusoidal magnetic field is applied to a columnar specimen uniformly by the electromagnet. The magnetic field of specimen is measured by the hall element. In order to measure the incremental permeability, the exciting and pickup coils are wound concentrically to the specimen. Incremental magnetic field $\Delta H$ is applied by sinusoidal current flowing in the exciting coil, and voltage of pickup coil, which is proportional to incremental flux density, was measured by the lock-in amplifier.

The amplitude and frequency of magnetic field are 21 kA/m, and 0.5 Hz, respectively. The incremental magnetic field was applied at the frequency of 4 kHz and 50 kHz, and discussed the effect of exciting frequency on the incremental permeability.

## 4. Results

Figure 2 shows the incremental permeability as function of magnetic field for the isothermal aging specimens with different LMP values. The waveforms have butterfly shape which changes depending on LMP values. For the quantitative evaluation, full width at half maximum (FWHM), peak-to-peak distance, and magnitude of pickup signal were extracted as featured

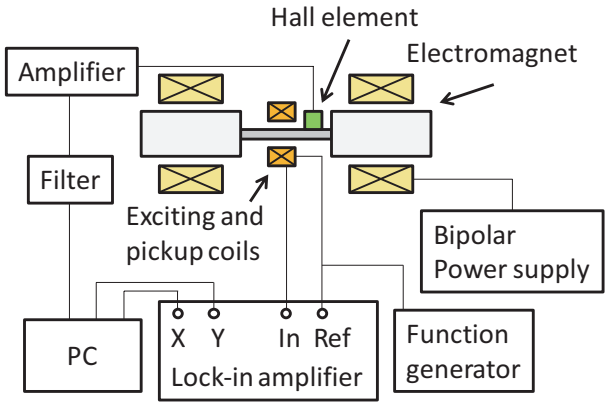


Fig. 1 Experimental setup of incremental permeability method.

Corresponding author: Tetsuya Uchimoto
*E-mail address*: uchimoto@ifs.tohoku.ac.jp

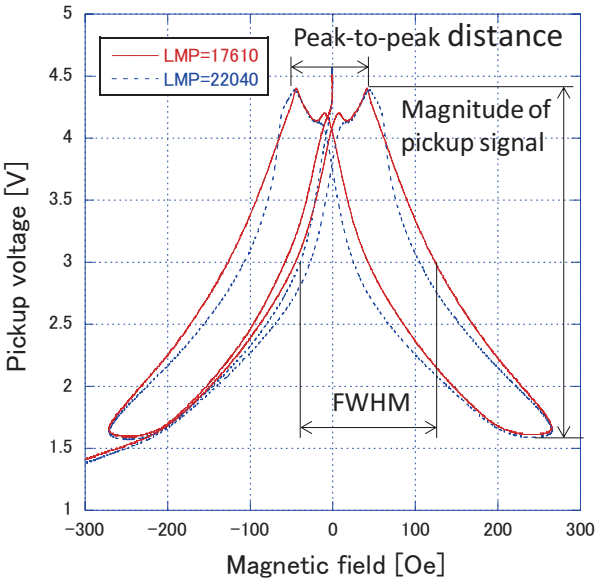


Fig. 2 Incremental permeability profile curves of isothermal aging specimens with different LMP values.

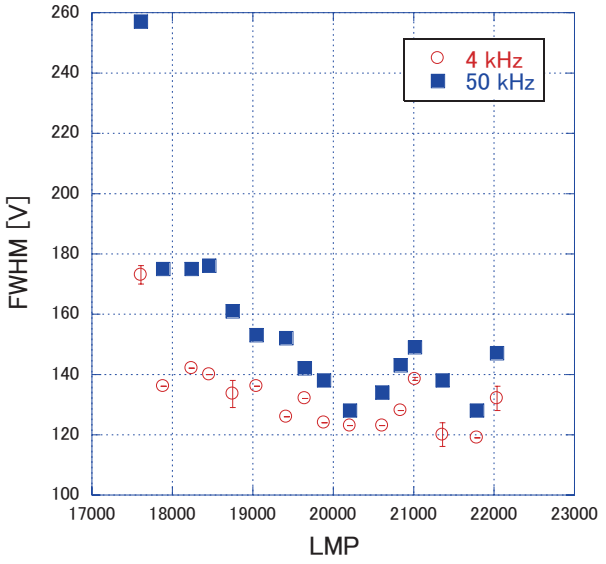


Fig. 3 Relationship between Larson-Miller Parameter and FWHM in mod. 9Cr-1Mo steels.

parameters. Figure 3 shows the plots of the FWHM as the function of LMP at the frequencies of 4 kHz and 50 kHz. The FWHM decreases with increase of LMP, and the FWHM at the frequency of 50 kHz is larger than at that of 4 kHz. Figure 4 shows the plots of the peak-to-peak distance as the function of LMP. The linear relationship between LMP and the peak-to-peak distance is obtained at the frequency of 50 kHz. The microstructure observation by SEM shows that precipitations such as M23C6 coarsen with increase of LMP value [3], and change in the FWHM and the peak-to-peak distance is due to the precipitation coarsening. From Figs. 3 and 4, incremental permeability depends on the frequency of the excitation, and evaluating the peak-to-peak distance at high frequency can estimate precipitation coarsening by isothermal aging.

For evaluation of creep damage, the parameters of incremental permeability of waveforms in creep specimens are evaluated. The results of creep specimens will be presented at the conference.

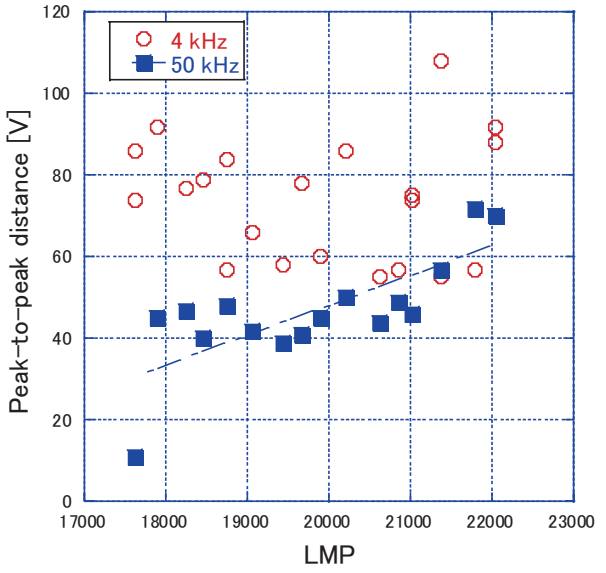


Fig. 4 Relationship between Larson-Miller Parameter and peak-to-peak distance in isothermal aging samples.

## 5. Summary

Incremental permeability method is applied to evaluate microstructure change in mod. 9Cr-1Mo steels, and featured parameters of incremental permeability are extracted and discussed. The relationship between change of incremental permeability and microstructure change by creep or isothermal aging will be investigated in future.


## Acknowledgement

This work was partly supported by the JSPS Core-to-Core Program, A. Advanced Research Networks, “International research core on smart layered materials and structures for energy saving”.


## References


[1] K. Kimura, H. Kushima, F. Abe, *The Society of Materials Science, Japan*, 52 (2003) 57-62.

[2] A. Yashan. G. Dobmann, *Electromagnetic Nondestructive Evaluation (VI)*, (2002) 150-157.

[3] S. Ueno, *Proceedings of 44th annual meeting of The Japan Society of Mechanical Engineers Tohoku Branch*, (2009), 76.

Eleventh International Conference on Flow Dynamics
October 8-10, 2014, Sendai, Miyagi, Japan

# A New Concept for Measuring Rock Stress at Depth Using a Core Obtained by Drilling

Hiroshi Mikami[1], Akio Funato[2], Takatoshi Ito[3]
[1]Graduate School of Environmental Studies, Tohoku University,
6-6-20 Aoba, Aza, Aramaki, Aoba-ku, Sendai, Miyagi 980-8579, Japan
[2]Fukada Geological Institute, 2-13-12 Honkomagome, Bunkyo-ku, Tokyo 113-0021, Japan
[3]Institute of Fluid Science, Tohoku University, 2-1-1 Katahira, Aoba-ku, Sendai, Miyagi 981-0933, Japan

**ABSTRACT**

We considered theoretically a problem how a core of an anisotropic rock expand in response to the relief of anisotropic in-situ stresses. Finally we succeeded to have a closed forma solution to give the circumferential distribution of the core diameter, and we demonstrated considerable effects of the anisotropic elasticity on the core deformation.

## 1. Introduction

Differential Core Deformation Analysis (DCDA) is a new method to estimate the in-situ stress using cores, i.e. cylindrical rock samples obtained by drilling. Magnitude and azimuth of the in-situ stress are evaluated from the cross-sectional shape of the core. DCDA was originally proposed by Funato et al. (2012) assuming isotropic rocks. We have been improving the method to be applicable for anisotropic rocks. In the present study, we proposed a closed form solution for the relationship between the cross-sectional shape of the core and the state of in-situ stress taking account of anisotropic elasticity of rocks. By using the solution, we demonstrated the effect of the anisotropy on the cross-sectional shape of the core.

## 2. Basic concept of DCDA

In order to obtain core samples of rocks at depth, a hollow cylindrical core tube is used. A core bit is pushed to the exposed surface of rock at the bottom of the borehole with a rotating motion. As a result, a column of rock is carved out and stored in a core tube. A cross section of the carved column at the moment of drilling should be perfectly circular, since the column is carved out by a rotating bit. However, a portion of the column away from the drill bit must expand elastically in response to the relief of in-situ stress. The expansion should occur in an asymmetric manner under the relief of anisotropic in-situ stress field as shown in Fig. 1.

Based on such a phenomenon, we can determine the azimuths of the maximum and minimum horizontal stresses, $S_H$ and $S_h$ from the azimuths of the maximum and minimum diameter of the core, $d_{max}$ and $d_{min}$. Also the deviatoric stress ($S_H$ - $S_h$) can be determined from the ratio of ($d_{max}$ - $d_{min}$)/ $d_{min}$. If the rock is isotropic, and deforms elastically by the stress relief, the deviatoric stress in the plane perpendicular to the axis of the core will be related to the difference of diameters of the core as follows:

$$S_H - S_h = \frac{d_{\max} - d_{\min}}{d_0} \cdot \frac{E}{1+\nu} \approx \frac{d_{\max} - d_{\min}}{d_{\min}} \cdot \frac{E}{1+\nu} \qquad (1)$$

where $E$ and $\nu$ are the Young's modulus and the Poisson's ratio of the rock respectively, and $d_0$ is the original diameter of the core. While $d_0$ is actually unknown, the core deformation by stress relief is very minute and $d_0$ could be assumed almost equal to $d_{min}$.

Corresponding author: Hiroshi Mikami
*E-mail address*: h.mikami@geo.ifs.tohoku.ac.jp

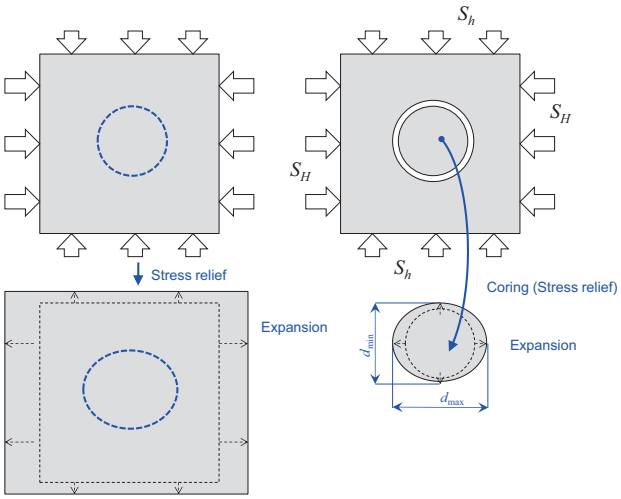


Fig. 1 Basic concept of DCDA.

## 3. Modelling of deformation of anisotropic rock core

The concept of Diametrical Core Deformation Analysis, DCDA, has originally proposed by Funato et al. (2012) assuming isotropic rocks. We improve the method to be applicable for anisotropic rocks.

To this end, we consider first a problem how a core of an anisotropic rock expand in response to the relief of anisotropic in-situ stresses.

Fig. 2 illustrates the anisotropic rock subjected to the anisotropic in-situ stresses of $S_H$ and $S_h$. It is assumed here that the rock is homogeneous and orthotropic and one of the orthotropic axis is coincident with the core axis, in other words, the borehole axis. The rock has the maximum and minimum Young's moduli of $E_H$ and $E_h$ respectively in orthogonal directions in a plane perpendicular to the core axis. The angle between the axes of $S_H$ and $E_h$ is denoted by $\phi$.

The problem is here broken down into two subsets of Problems A and B as illustrated in Fig. 3 (a) and (b) respectively. In Problem A, the anisotropic rock is subjected to an isotropic component $S_0$ which is equal to the mean value of $S_H$ and $S_h$, and the core is carved out from the rock to be free from $S_0$. On the other hand, in Problem B, an isotropic rock is subjected to deviatoric components of in-situ stresses, $S_H$ - $S_0$ and $S_h$ - $S_0$, and the

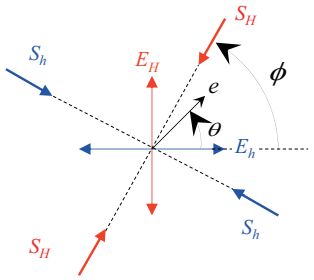


Fig. 2 Geometrical relationship between axes of the maximum and minimum Young's moduli of rock, $E_H$ and $E_h$, and those of the maximum and minimum in-situ stresses, $S_H$ and $S_h$.

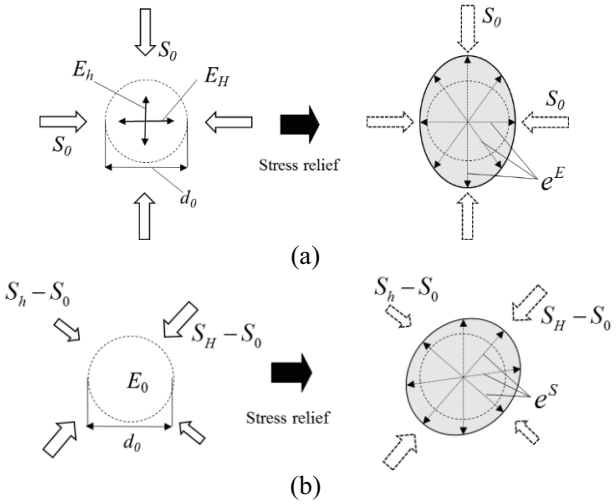


Fig. 3 Definitions of Problems (a) A and (b) B.

core is carved out from the rock to be free from $S_H$ - $S_0$ and $S_h$ - $S_0$. The isotropic rock has a Young's modulus of $E_0$ which is equal to the mean value of $E_H$ and $E_h$. The Poisson's ratio of the rock is assumed isotropic for both cases of Problems A and B, and it is denoted by $\nu$. We can have closed form solutions of radial strain in the core for each problem.

Finally, the diameter $d(\theta)$ of the core carved out from the anisotropic rock subjected to the anisotropic in-stress stresses is given as follows:

$$d(\theta) = \{e^E(\theta) + e^S(\theta) + 1\} d_0 \qquad (2)$$

where $\theta$ is circumferential angle taken from the direction of $E_h$ (see Fig. 2), and $e^E(\theta)$ and $e^S(\theta)$ are the radial strains in the core for the cases of Problems A and B respectively.

## 4. Effect of anisotropic elasticity on core deformation

By using Eq. (2), we estimated the deformation of anisotropic rock core in response to the relief of anisotropic in-situ stresses. The parameters assumed for the estimation are summarized in Table 1, where $S_v$ is the in-situ stress in the direction of core axis.

Fig. 4 shows the estimated circumferential variation of the core diameter. For the case assuming the isotropic rock with $E_H = E_h = 10$ [GPa], the core diameter became maximum to be $d_{max}$ at the circumferential angle of 60° which is consistent with the direction of $S_H$. However, the

Table 1. Model parameters.

| | |
|---|---|
| $d_0$ [mm] | 60 |
| $E_h$ [GPa] | 10 |
| $E_H$ [GPa] | 10, 12, 14, 16, 18, 20 |
| $\nu$ | 0.2 |
| $S_h$ [MPa] | 20 |
| $S_H$ [MPa] | 30 |
| $\phi$ [deg.] | 60 |
| $S_v$ [MPa] | 45 |

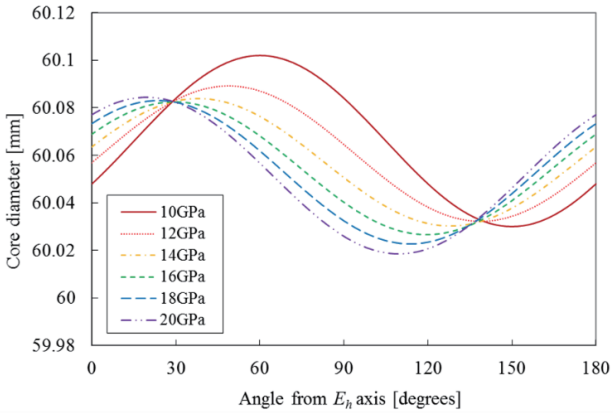


Fig. 4 Estimated circumferential variation of the core diameter.

circumferential angle of $d_{max}$ decreased with increasing $E_H$, while $E_h$ was fixed to be 10 GPa. When $E_H$ became twice of $E_h$, i.e. $E_H = 20$ [GPa], the circumferential angle of $d_{max}$ was apart from the direction of $S_H$ by 40°. On the other hand, the difference between the maximum and minimum diameters, $d_{max}$ - $d_{min}$, was about 0.07 mm for the case of $E_H = E_h = 10$ [GPa], and it was about 0.06 mm for the case of $E_H = 20$ [GPa] and $E_h = 10$ [GPa]. Thus the effect of anisotropic elasticity on the value of $d_{max}$ - $d_{min}$ is relatively small compared with the effect on the direction of $d_{max}$.

## 5. Conclusion

The effect of anisotropic elasticity on the value of $d_{max}$ - $d_{min}$ is relatively small compared with the effect on the direction of $d_{max}$. In the method of DCDA, the value of $d_{max}$ - $d_{min}$ is used to determine the magnitude of the deviatoric stress ($S_H$ - $S_h$), and the direction of $d_{max}$ is used to determine the direction of in-situ stresses. Those results suggest that we should pay more attention to the effect of anisotropic elasticity for determining the direction of in-situ stresses rather than the magnitude of the deviatoric stress ($S_H$ - $S_h$).


## Acknowledgement

This work was partly supported by Grants - in - Aid for Scientific Research 21107006 (Ministry of Education, Culture, Sports, Science and Technology, MEXT), Japan.


## References


[1] Funato, A, Ito, T. and Shono, T., Proc. of 46th US Rock Mechanics / Geomechanics Symp., Chicago, 24-27 June, ARMA 12-588, 2012.

Eleventh International Conference on Flow Dynamics
October 8-10, 2014, Sendai, Miyagi, Japan

# Short Time and 2D Thickness Measurement by Phase-shifting Technique and Ellipsometry

Shingo Nakamura[1], Atsuki Komiya[2], Junnnosuke Okajima[2], Shigenao Maruyama[2]
[1]Graduate School of Engineering, Tohoku University, Sendai, Miyagi, 980-8579, Japan
[2]Institute of Fluid Science, Tohoku University, Sendai, Miyagi, 980-8577, Japan

**ABSTRACT**

In this study, a phase-shifting ellipsometry is developed to measure the nano-scale order thickness of thin film within a short time. A phase-shifting ellipsometry integrates the features of a phase-shifting interferometry with conventional ellipsometry. By using phase-shifting technique, two-dimensional thickness distribution of the thin film could be obtained precisely. The experimental results verified the capability and the performance of phase-shifting ellipsometry on precise two-dimensional measurement of thickness distribution.

## 1. INTRODUCTION

A study concerning surfaces and thin films has been carried out for several years, recently has become increasingly important in several academic and industrial fields. With such interest, a conventional and powerful optical method for the study of thin film has been further developed and applied to various fields. The method has been called by "Ellipsometry" and is based on the classic theory of P. Drude [1,2]. Ellipsometry is a noninvasive, surface sensitive and well-developed optical method widely employed for characterizing the optical properties of a thin film, such as the thickness, refractive index and extinction coefficient of the film.

Generally, ellipsometry is the method of one-point thickness measurement. To obtain a two-dimensional thickness distribution, a complicate control is required for scanning of sample stage and light source, and a sophisticate signal processing software has been employed. Thus, conventional ellipsometry can't be applied to dynamic phenomena due to a limitation of the measurement time for generating two-dimensional information.

In this study, we introduce a phase-shifting technique [3] to conventional ellipsometry. To overcome this disadvantage, by using phase-shifting technique, two-dimensional thickness distribution can be obtained without scanning within a short time measurement.

## 2. MEASUREMENT PRINCIPLE

### 2.1 Ellipsometry

In the ellipsometry measurement, the optical properties of thin film, such as the thickness and refractive index, can be characterized on the basis of the change in the polarization state of a monochromatic plane wave that is reflected by the surface of the test sample at oblique incidence. The change in polarization state after reflection can be determined by measuring the ratio $\rho$ of the complex reflective coefficients, namely $r_P = |r_P|\exp(i\phi_P)$ and $r_S = |r_S|\exp(i\phi_S)$, of parallel ($P$) and perpendicular ($S$) polarized components of the monochromatic plane wave with respect to the incident plane using the equation

$$\rho = \frac{r_P}{r_S} = \frac{|r_P|}{|r_S|}\exp\left[i\left(\phi_P - \phi_S\right)\right] = \tan(\psi)\exp(i\Delta) \qquad (1)$$

where $(|r_P|, |r_S|)$ and $(\phi_P, \phi_S)$ are the absolute amplitude reflectance and phase shifts of $r_P$ and $r_S$ respectively. The angles $\psi = \arctan(|r_P|/|r_S|)$ and $\Delta = \phi_P - \phi_S$ are thus defined as the ellipsometric parameters. The change of the polarization state can be deduced from the Fresnel equations via the complex amplitude reflectance, which are fully interpreted by $(\psi, \Delta)$ simultaneously [2]. Therefore the thic2kness of the thin film can be calculated in terms of $(\psi, \Delta)$ and the incident angle by using the three phase model.

### 2.2 Phase-shifting technique

The phase-shifting technique is an image processing technique, which converts the interferogram to ellipsometric parameters $(\psi, \Delta)$ distribution images.

The symbol $(\psi, \Delta)$ are obtained from three interferograms in different polarization state expressed as

$$\psi = \arctan\left(A \pm \sqrt{A^2 - 1}\right), \qquad (2.a)$$

where,

$$A = \frac{I_0 + I_{120} + I_{240}}{\sqrt{2\left\{\left(I_0 - I_{120}\right)^2 + \left(I_{120} - I_{240}\right)^2 + \left(I_{240} - I_0\right)^2\right\}}}, \qquad (2.b)$$

$$\Delta = \arctan\left\{\frac{\sqrt{3}\left(I_{120} - I_{240}\right)}{I_{120} - 2I_0 + I_{240}}\right\}, \qquad (3)$$

the symbol $I$ is the intensity of the beam, which is detected by the CCD sensor in each pixel, the subscript is the polarization angle of the beam. In this technique, three interferograms are collected sequentially by CCD sensor with respect to three pre-determined polarization angle of a rotating polarizer during measurement. By introducing the rotating polarizer, polarization modulation can be produced sequentially.

## 3. THICKNESS MEASUREMENT

### 3.1 Measurement system

Figure 1 shows the schematic of the phase-shifting ellipsometry. In this system, the incident angle was set to 70° to obtain high measurement sensitivity. However, this optical system had a distinct limitation of the measurement area in captured image due to a defocus effect. In case that the imaging lens

Corresponding author: Shingo Nakamura
*E-mail address*: shingo@pixy.ifs.tohoku.ac.jp

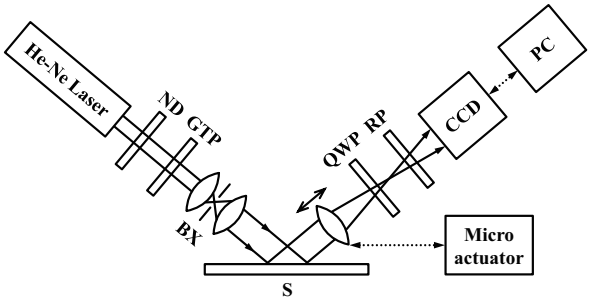


ND: ND filter, GTP: Glan-Thompson calcite polarizer, BX: Beam expander, QWP: Quarter wave plate, RP: Rotating polarizer, S: Sample.

Fig. 1 Schematic of phase-shifting ellipsometry.

after reflection is focused of the center of the test surface, the defocus occurs in the near and far side due to shallow depth of field (DOF) of the imaging lens and oblique incidence. To overcome the effect of defocus, the focus stacking technique was employed for extending the DOF of captured image. In this technique, the imaging lens was slide by a microactuator, and some captured images were synthesized into an image with extended DOF by the image processing [4].

### 3.2 Measurement method

In this measurement, the optical intensity distributions $I_0, I_{120}, I_{240}$ were measured by CCD sensor. Additionally, by substituting $I_0, I_{120}, I_{240}$ into Eqs. (2), (3) in each pixel, $(\psi, \Delta)$ were obtained. Finally, the thickness distribution was calculated by applying the three phase model. To verify the ability and the performance of the measurement system, The thin films of silicon dioxide formed on silicon wafer by thermal oxidation were used. The calibrated thickness values were measured by spectroscopic ellipsometry (HORIBA Co., UNIVERSEL). Moreover, the 50 nm step-shaped wafer was fabricated, and the surface shape measurement was conducted.

### 3.3 Measurement results

Figure 2 shows the measured results with the calibration data for the various test samples. From these results, good agreement was obtained. In case that thickness value was about 100 nm, the difference between the measured data and calibration data became larger due to the measurement condition. By changing the measurement condition including incident angle and wavelength of the optical source, the measurement accuracy will be improved in this case.

Figure 3 shows the measured thickness distribution of the 50 nm step-shaped wafer. From this result, the height of the step could be measured precisely. Also, asperity due to the noise of the CCD sensor and the contamination of the optical elements could be measured. The measurement error is estimated about 1 nm.

## 4. CONCLUSIONS

In this study, the phase-shifting ellipsometry was developed and nano-scale thickness measurement was

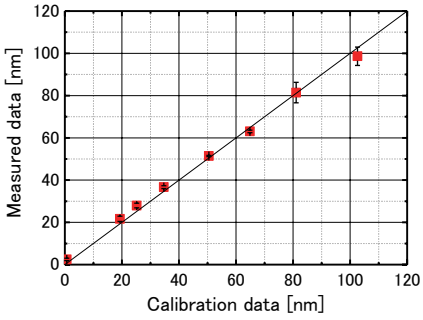


Fig. 2 Comparison between calibration and measured data.

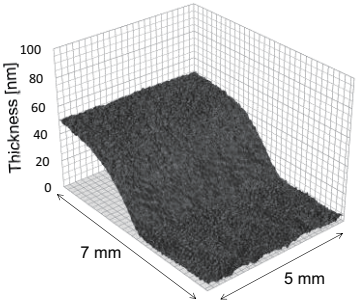


Fig. 3 (a) Thickness distribution of step-shaped wafer.

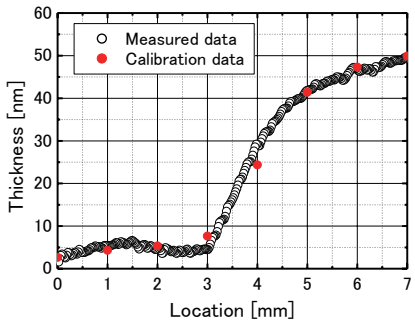


Fig. 3 (b) One-dimensional thickness distribution of step-shaped wafer.

conducted using the optical system. The following conclusions were obtained.

1. The phase-shifting ellipsometry was developed to obtain the two-dimensional thickness distribution.
2. The focus stacking technique was employed for extending the depth of field of captured image by scanning the imaging lens after reflection.
3. In the thickness measurement, good agreement was obtained with calibration data.
4. The surface shape measurement could be measured.

## REFERENCES

[1] P. Drude, Ann. Physik. 272, 532（1889）; ibid. 272, 865（1889）; ibid. 275, 481（1890）.
[2] R. M. Azzam, N. M. Bashara, Ellipsometry and Plarized Light, North–Holland, Amsterdam, 1980.
[3] S.Maruyama, T.Shibata, K.Tsukamoto, *Exp Therm Fluid Sci*, 19 (1999) , pp.34-48.
[4] N. Mizoguchi, H. Oku, M. Ishikawa, High-speed variable-focus optical system for extended depth of field, ISIE 2009, 1668-1673.

# Formation of Microjet by Plasma Generated Underwater Shock Wave

Tomoya Minami[1], Takehiko Sato[2], Tomoki Nakajima[2], Daisuke Yoshino[2], Toshiro Kaneko[3]
[1]Graduate School of Engineering, Tohoku University
6-6-01 Aoba, Aramaki, Aoba, Sendai, Miyagi, 980-8579, Japan
[2]Institute of Fluid Science, Tohoku University
2-1-1 Katahira, Aoba, Sendai, Miyagi, 980-8577, Japan
[3]Graduate School of Engineering, Tohoku University
6-6-05 Aoba, Aramaki, Aoba, Sendai, Miyagi, 980-8579, Japan

**ABSTRACT**

Behavior of cavitation bubbles generated by an underwater shock wave was visualized by a high-speed camera. Some of those cavitation bubbles formed microjets in the collapse process. The direction of the microjets was investigated in this study.

## 1. Introduction

Cavitation bubbles are known as a main factor to reduce performance of fluid machines [1]. A plenty of studies have been reported to prevent cavitation. Recently, biomedical applications using cavitation bubbles have been remarked [1]. For Drug Delivery System (DDS), bubbles are used to introduce a drug into cells. Because microjets which are generated at collapse of bubbles are capable of performing a micropore and injecting a drug into cells. As microjets are known as micro meter size and micro second phenomena, the behaviors of microjets have not been clarified enough. Therefore, understanding of microjets dynamics and control of microjets behaviors are very important to apply to biomedical applications.

In this study, to understand generation mechanism of microjets, we aim at visualizing microjets using shock waves and measuring the directions of the microjets.

## 2. Experimental method

### 2.1. Acoustic impedance

Acoustic impedance is a physical quantity which is a density in a medium multiplied by speed of sound. When a shock wave propagates from one medium to another, it is reflected when the difference of the acoustic impedances between those two media is great. On the other hand, it transmits when the difference of the acoustic impedance between them is enough small. In the case of the propagation of a shock wave from a medium of higher acoustic impedance to that of lower one, the reflected shock wave changes from a compression wave to an expansion wave. As the acoustic impedance of water is $1.5\times10^6$ kg/(m$^2$·s) and the acoustic impedance of air is $4.3\times10^2$ kg/(m$^2$·s) [2], underwater shock wave is reflected at water-air boundary surface and converted to an expansion wave. Therefore, the reflected expansion shock wave is used in this study. To obtain the reflected expansion shock wave at the bottom of the vessel, polydimethyl-siloxane (PDMS) whose acoustic impedance is $1.4\times10^6$ kg/(m$^2$·s) was used as a bottom of the water vessel. As the PDMS has a similar property in acoustic impedance, an expansion shock wave can be generated after the reflection.

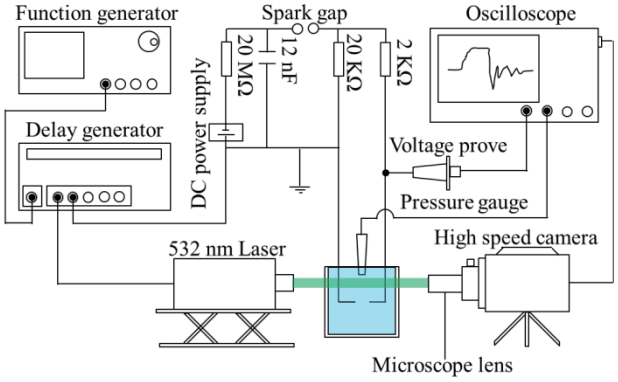


Fig. 1 Schematic of the experimental setup.

### 2.2. Experimental setup

Figure 1 shows a schematic diagram of the experimental setup. An underwater shock wave was generated by a spark. A pulsed high-voltage circuit was composed of a DC power source (HJPQ-30P1, MATSUSADA Precision Inc.), spark gap switch, registers, and capacitors, as shown in Fig. 1. A trigger signal from a function generator was sent to a delay generator (DG645, STANFORD RESEARCH SYSTEMS) and it controlled to synchronize the timings

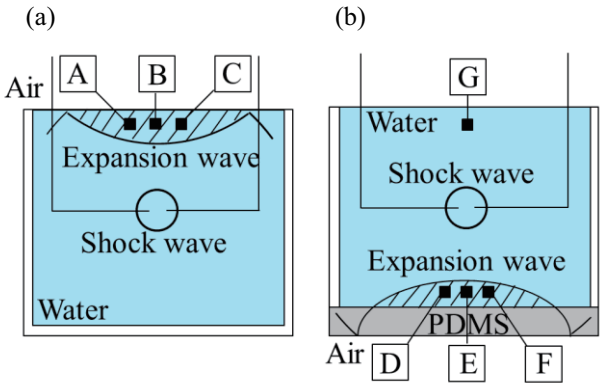


Fig. 2 Schematic model of reflection of shock wave at the water surface (a) and at the PDMS film (b).

Corresponding author: Tomoya Minami
*E-mail address*: minami@plasma.ifs.tohoku.ac.jp

of the spark and the back light laser (SSL-532-5000-10TM-D, SANCITTY LASER.). The applied voltage was measured by a high-voltage probe (PHV4-3577, LeCroy) with an oscilloscope (LeCroy, WaveSurfer 104MXs-B). The trigger signal to an ultra high-speed camera (ULTRA Neo, NAC Image Technology Co. Ltd.) was sent by the oscilloscope. Pressure change was measured by a pressure gauge (Müller-Platte Needle Probe, Müller Instruments.). Figure 2 shows water vessels which can generate expansion shock waves at the water surface and at the bottom of vessel. A stainless steel needle electrode of 0.5 mm in diameter was set in the center of the vessel. Those electrodes were set at 5 mm below the water surface shown in Fig. 2 (a) and above the bottom of the vessel shown in Fig. 2 (b). The thickness of the PDMS film was 0.25 mm. The pressure was measured at 10 mm above the electrode at G shown in Fig. 2 (b).

## 3. Experimental results

Figure 3 shows the microjet images at A (a), at B (b), at C (c), at D (d), at E (e), and at F (f). The locations at A, B, C, D, E, and F are shown in Fig. 2. The distances from an A to B and C to B were 1 mm, respectively. The distances from D to E and F to E were 1 mm, respectively. The directions of microjets showed approximately the same directions of the propagation of the compression shock wave. Figure 4 shows the time history of the pressure. The indicated as a region I shown in Fig. 4 shows the compression wave of 2 MPa at a maximum and a region II shown in Fig. 4 shows the reflected expansion wave of -1.5 MPa at a maximum for the case of the use of the bottom reflection. The time difference between the compression wave and the expansion wave corresponded to the estimation from the sound speed.

## 4. Discussion

Generally, the microjet is generated in the area where there is a pressure gradient. And the microjet is generated towards lower pressure area [3, 4]. It is also reported that the microjets were generated in the directions of shock wave propagation when the shock wave passed a bubble [5]. The results obtained in this study shows the same trend of these reported phenomena, though any visible bubbles were not observed before generation of the shock wave. These results imply two hypotheses: (1) bubble nuclei exist in the water because newly formation of bubble nuclei requires much large pressure, and (2) the characteristics of the bubble nuclei are similar to micro-size bubbles.

## 5. Conclusion

In this study, we succeeded to form microjets using the expansion wave generated by reflection at the interface of air-water and air-PDMS sheet. We found that the directions of the microjets were the same directions of the compression wave propagation. In addition, these results suggest the possibility of controlling microjets directions.


## Acknowledgements

This study was partly supported by JSPS Grant-in-Aid for Scientific Research.


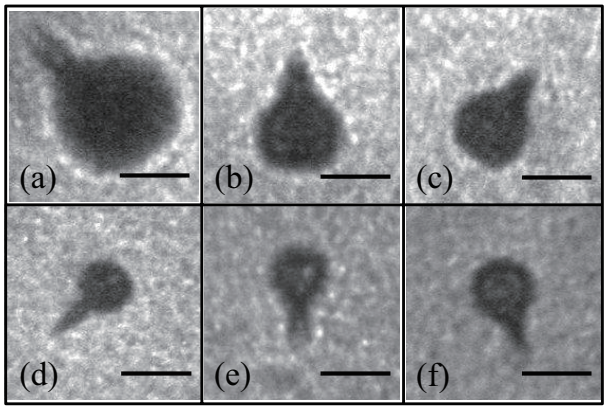


Fig. 3 Microjet images at A (a), B (b), C (c), D (d), E (e), and F (f). The locations at A, B, C, D, E, and F are shown in Fig. 2. (Exposure time: 20 ns, Scale bar: 50 μm)

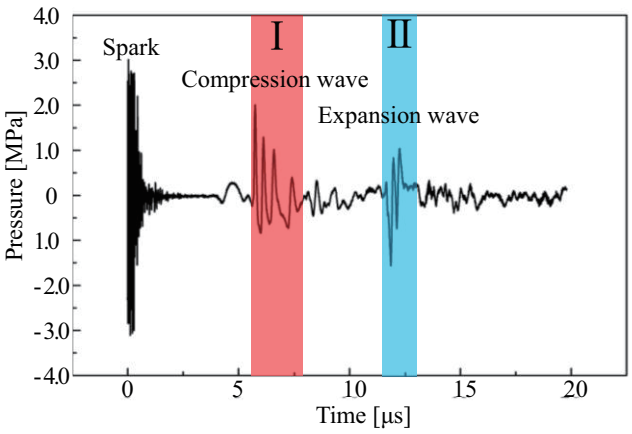


Fig. 4 Time history of the pressure at G shown in the Fig. 2 (b).

## References


[1] Hideki Tsuge, The state of the art in microbubbles and nanobubbles, *CMC* (2007) [in Japanese].

[2] Ryo Tachikawa, Akira Tsukamoto, Keiichi Nakagawa, Tatsuhiko Arfune, Hongen Liao, Etsuko Kobayashi, Takashi Ushida, Ichiro Sakuma, *Advanced Biomedical Engineering*, 1 (2012), 68-73.

[3] B.Gerold, P. Glynne-Jones, C. Mcdougall, D. Mcgloin, S. Cochran, A. Melzer, P. Prentice, *Appl.Phys.Lett.*, 100 (2012), 024104-1-024104-3.

[4] D. Obreschkow, M.Tinguely, N. Dorsaz, P. Kobel, A. de Bosset, M. Farhat, *Phys.Rev.Lett.*, 107 (2011), 204501-1-204501-5.

[5] Claus-Dieter Ohl, R. Ikink, *Phys. Rev. Lett.*, 90 (2003), 214502-1-214502-4.

# Numerical Study of Discharged Bubble based on Experiment for Water Purification

Taketo Hayashi[1], Satoshi Uehara[2], Hideya Nishiyama[2]
[1]Graduate school of Engineering, Tohoku University
2-1-1, Katahira, Aoba, Sendai, Miyagi 980-8577, Japan
[2]Institute of Fluid Science, Tohoku University
2-1-1, Katahira, Aoba, Sendai, Miyagi 980-8577, Japan

**ABSTRACT**

In this study, an experiment on pulsed discharge inside bubbles was conducted to evaluate discharge characteristics for water purification. Based on the experiment, a zero-dimensional simulation model was developed for the analysis of chemical reactions in a bubble. Our model has two phases (gas and liquid) and the carrier gas is argon including water vapor. It was shown that OH radicals were generated during discharge and diffused into the liquid. OH concentration in the liquid increased as water vapor concentration increased.

## 1. Introduction

Persistent organic pollutants in wastewater such as dioxin are considered to accumulated and affect the environment. They require high oxidation potential to be decomposed. Conventionally, ozone is used to decompose organic pollutants. However, its oxidation potential is not strong enough to decompose persistent pollutants. Therefore, it is necessary to utilize stronger oxidizer such as OH radicals. Since OH radicals have short life time, they need to be generated near water surface. OH radicals were generated by pulsed discharge inside bubbles in water and applied to decomposition of Methylene blue [1]. However, OH radical generation process is not clarified in detail because the discharge occurs within short time and in small space.

In this study, an experiment on discharge inside a bubble is carried out to evaluate discharge characteristics. Then, a zero-dimensional numerical model for chemical reaction analysis is developed based on the experiment.

## 2. Experiment

Fig. 1(a) shows the schematic illustration of the experimental setup. The setup consists of reactor, power source, gas supply tube and electrodes. A 3 kΩ resistance is set to protect the power source. The inner diameter of the gas supply tube and the diameter of the electrode are 3.5 mm and 3 mm, respectively. The thickness of the tube is 1.25 mm. Argon gas was fed at a flow rate of 100 Sml/min to a pore with the diameter of 0.5 mm. The solution is 1.1 l of pure water. Assuming water as a dielectric, the reactor is considered as an electric circuit with capacitors and resistances as shown in Fig. 1(b). When pulsed voltage was applied, streamer propagated along the bubble surface. The applied voltage, the voltage drop at the resistance and the current were measured in order to evaluate the discharged voltage at the bubble.

Fig. 2 shows the applied voltage $V_a$ the discharged voltage at the bubble $V_g$ and the current $I_a$. The voltage rising time was about 100 ns. The maximum discharge current was 1.3 A and continued for about 400 ns.

Corresponding author: Taketo Hayashi
*E-mail address*:hayashi@paris.ifs.tohoku.ac.jp

The discharged voltage was calculated as following

$$V_g = V_a - V_r - (1/C_w)\int I_a dt \quad (1)$$

where $C_w$ and $V_r$ denote the capacitance of the water and the voltage drop at the resistance, respectively. The maximum discharged voltage was approximately 2 kV.

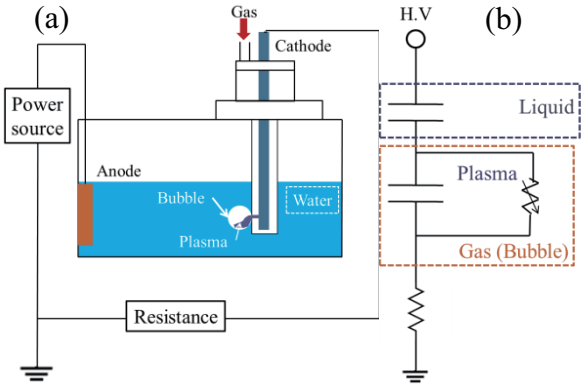


Fig.1(a) Schematic of the setup (b) equivalent circuit

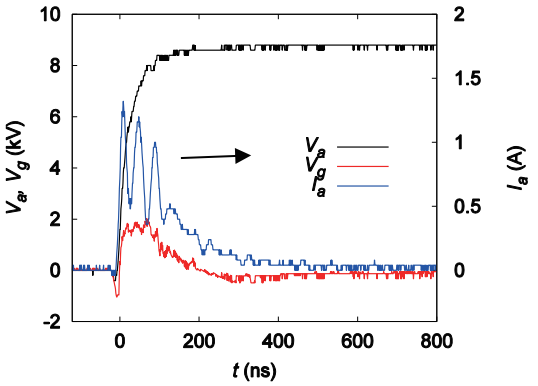


Fig.2 Applied voltage, discharged voltage and current

## 3. Numerical model

The simulation model is zero-dimensional, but two phases (gas and liquid) are considered. The model is developed based on the model described in Matsui's paper [2]. The bubble diameter is 2 mm. The gas and the water temperature are assumed to be constant at 295K, which corresponds to the water temperature in the experiment. The pressure inside the bubble is 1 atm. The

carrier gas is argon including water vapor. The gas phase contains 18 species including electron and the liquid phase contains 3 species. The simulation was performed in two steps. In the first step the reactions in the gas phase and the liquid phase were calculated. The reaction processes were calculated by solving the rate equations for each species. In the second step, the interaction between the gas and the liquid phase was calculated by using Henry's law for OH, $HO_2$, and $H_2O_2$. The Henry's law constants, $H$ is used in following equations [3].

$$\frac{dC_{liq}}{dt} = k_{mt}C_{gas} - k_{mt}\frac{1}{HRT_g}C_{liq} \quad (2)$$

$$\frac{dC_{gas}}{dt} = -k_{mt}W_L C_{gas} + k_{mt}W_L \frac{1}{HRT_g}C_{liq} \quad (3)$$

where $C$ (mol/l) is the concentration of the species and $R$ (0.0821 atm·l/K/mol) is the gas constant. The mass transport coefficient $k_{mt}$ is determined by the bubble form. $W_L$ is the ratio of the liquid volume to the bubble volume to take account of the effect of the volume differences.

The discharged voltage measured in the experiment $V_g$ was approximated by a linear function. The function was used to calculate the reduced electric field.

Fig. 3 shows the reduced electric field and the time evolution of species in gas phase during one discharge cycle, 500 μs. The water vapor concentration was 3 percent in this case. OH was generated during the discharge period through the dissociation of $H_2O$ by electron impact. $H_2O_2$ increased after the discharge mainly through the equation as below.

$$OH_{gas} + OH_{gas} \rightarrow H_2O_{2gas} \quad (4)$$

OH, $H_2O_2$ and $HO_2$ started to decrease at around 40 μs by diffusions to the liquid phase as well as reactions. $H_2$ and $O_2$ were produced by the recombination of H and O generated by dissociation of $H_2O$.

In liquid phase, OH was supposed to decrease because only equation (5) and (6) were considered. However, OH increased as shown in Fig. 4. This implies that the diffusion process was more dominant than reactions in OH production in liquid phase.

$$OH_{liq} + OH_{liq} \rightarrow H_2O_{2liq} \quad (5)$$

$$OH_{liq} + H_2O_{2liq} \rightarrow HO_{2liq} \quad (6)$$

Fig. 5 shows OH concentration in liquid phase with 3 different water vapor concentrations in carrier gas. The more water vapor was included, the more OH was generated in liquid phase. It is because that more OH is generated as water vapor concentration increases.

## 4. Concluding Remarks

1. The discharged voltage applied to the bubble was evaluated by the experiment. The maximum discharged voltage was calculated to be 2 kV when applied voltage was 9 kV.
2. The zero-dimensional numerical model was developed to clarify the chemical reactions. In the gas phase, OH was generated during the discharge and $H_2O_2$ was produced by consuming OH after the discharge. In the liquid phase, each species increased with time by the diffusions from the gas to the liquid phase. Considering the increase in OH in the liquid phase, the diffusion process was dominant.
3. The OH in the liquid phase showed the dependence on the water vapor concentration in the carrier gas. More OH was produced in the liquid phase for high vapor concentration.

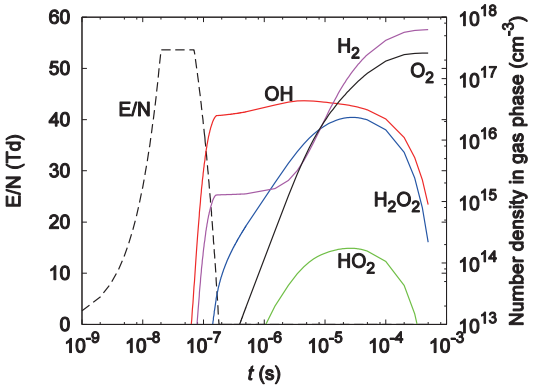


Fig. 3 Time evolution of the species in gas phase

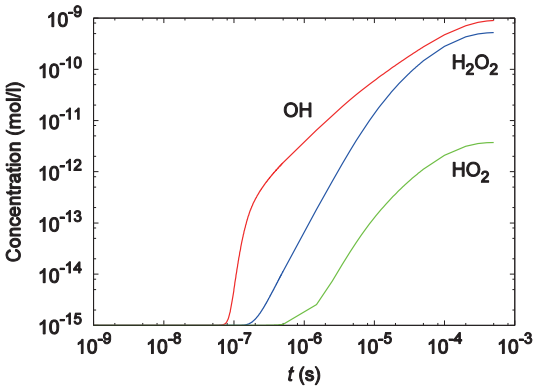


Fig. 4 Concentration of species in liquid phase

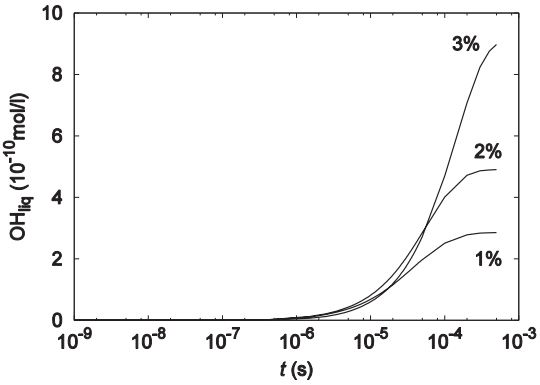


Fig. 5 OH in the liquid phase with 3 different water vapor concentrations

## References


[1] H. Nishiyama et al, *J. Fluid Sci. Technol.*, 8, 1 (2013) 65-74.

[2] Y. Matsui et al, *Plasma sources Sci. Technol.*, 20 (2011) 034015.

[3] S.N. Pandis and J.H. Seinfeld, *J. Geophys. Res.*, 94 (1989) 1105–1126.

Eleventh International Conference on Flow Dynamics
October 8-10, 2014, Sendai, Miyagi, Japan

# Influence Evaluation of Stress-induced Martensite for Fatigue Cracks in Austenitic Steels using Eddy Current Testing

Hao Feng[1], Ryoichi Urayama[2], Tetsuya Uchimoto[2] and Toshiyuki Takagi[2]
[1]Graduate School of Engineering, Tohoku University,
2-2-1 Katahira, Aoba-ku, Sendai, Miyagi, 980-8579, Japan
[2]Institute of Fluid Science, Tohoku University,
2-2-1 Katahira, Aoba-ku, Sendai, Miyagi, 980-8577, Japan

**ABSTRACT**

This study investigates the influence of stress-induced martensite in austenite stainless steels on eddy current signals of fatigue crack in austenite stainless steels. Several fatigue cracks were created under the four-point bending method using different loads. In the crack tip section, stress concentration creates a plastic zone. The plastic deformation will transform the austenite to α'-martensite (stress-induced martensite), and this transformation changes the magnetic property of the material. The influence of magnetic phase on ECT signals is investigated. At the same time the relationship between load and martensite transformation is qualitatively derived.

## 1. Introduction

Fatigue is a type of material degradation caused by fluctuating stress. In the plant operation environment, the metal parts and components suffer harsh environments which accelerate the metal degradation process. SCC (stress corrosion cracking) is formed under stress and corrosive media. Creep damage is a chronic diffusion process under high temperature and stress. Metal degradation inevitably creates cracks in the material and threatens the integrity of the structure. The eddy current nondestructive testing method is used in the power plant industry for maintenance to make sure the normal operation and avoid accident. In order to accurately detect and examine cracks, it is important to evaluate property change in the materials which will influence eddy current signals. During the fatigue crack propagation process, there will be a plastic zone in the crack tip section because of the stress concentration [1]. The metastable high alloyed austenite stainless steel will transform to magnetic stress-induced martensite (α'-martensite) under deformation at room temperature. This α'-martensite is a metastable phase and reverts to austenite at high temperatures [2]. The magnetic property change caused by martensite transformation will have an effect on eddy current testing signals because of the electromagnetic origin.

The purpose of this paper is to evaluate the influence of martensite transformation on ECT signal when examining fatigue cracks, and derive the relationship between martensite transformation and fatigue testing load qualitatively.

## 2. Specimens and experimental procedures

The profile of specimen used in this experiment is shown in Fig.1. There is an upper convex section with a height 10 millimeters. A triangular notch with 60° is fabricated using EDM with a height of 5 millimeters as a concentration locus to introduce the fatigue crack using the four-point bending method.

The material of specimen used in this experiment is AISI316L austenite stainless steels. The chemical composition of the material is listed in Table 1. The carbon content is very low, and about 0.024 weight percent. The chemical composition of material will affect the yield strength, so it will affect the plastic zone around the fatigue crack tip, and in a further step affect the martensite transformation of austenite.

The stress induced α'-martensite will revert back to austenite when heating under high temperature. From Harries [3] the effects of annealing for 20 hours at 600℃ on α'-martensite in 50% cold worked 18Cr-8Ni steel will revert over 75% of α'-martensite to austenite. In this experiment, the specimen will undergo annealing process for 24 hours under 600℃to stimulate the reversion of α'-martensite. Before and after the annealing process, the crack will be scanned for two times separately. Through comparing the signal change before and after the heating process to get the idea about the effect of magnetic α'-martensite on the ECT signals. In the last, using numerical simulation to verify the influence of magnetic α'-martensite. Also by changing the load when creating fatigue crack, so as to change the stress intensity factor in the crack tip, the relationship between load and magnetic α'-martensite formation is derived.

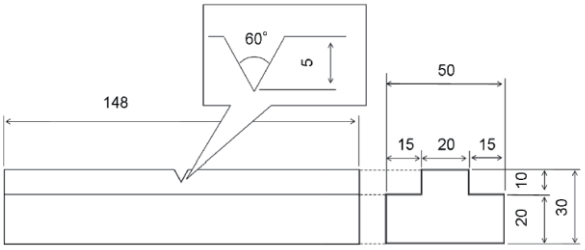


Fig.1 Profile of the specimen (Unit: mm)

## 3. Results and discussion

Three different fatigue cracks are created under three different load using the four-point bending method, 30kN, 40kN and 49kN, respectively. The depths of the cracks are evaluated by destructive test. The numerical simulation is conducted for the three different fatigue cracks to examine the intensity of the magnetic phase using reduced *A*, and the edged finite element method [4]. The model used in the simulation is shown in Fig.2. There is a magnetic layer situated around the crack section. This layer has a slightly higher relative permeability than the bulk austenite stainless steels which is 1.0. The parameters for simulations of three different cracks are listed in Table 2. The crack widths and magnetic layer widths in the simulation are the same in order to examine the intensity of magnetic property.

The experiment and simulation results for the specimen under 49kN are shown in Fig.3. From this result, the ECT signal of experiment after the heating treatment under 600 ℃ for 24 hours is changed toward the vertical axis comparing with signal before the heating process. Through comparing with numerical simulation results, this phenomenon is

Corresponding author: Toshiyuki Takagi
*E-mail address*: takagi@ifs.tohoku.ac.jp

Table 1. Chemical composition of the material used for specimen (wt%)

| C | Si | Mn | P | S | Cu | Ni | Cr | Mo | N |
|---|---|---|---|---|---|---|---|---|---|
| 0.024 | 0.56 | 1.03 | 0.022 | 0.001 | 0.26 | 10.56 | 16.19 | 2.07 | 0.0566 |

Table 2. Parameters used in the simulation

| Load | Crack depth | Simulation depth of magnetic layer | Simulation width of crack | Simulation width of magnetic layer | $\mu_r$ range of magnetic layer |
|---|---|---|---|---|---|
| 30kN | 4.2mm | 5mm | 0.04mm | 0.6mm | 1.0-1.4 |
| 40kN | 4.8mm | 6mm | 0.04mm | 0.6mm | 1.0-1.4 |
| 49kN | 3.7mm | 4.5mm | 0.04mm | 0.6mm | 1.0-1.4 |

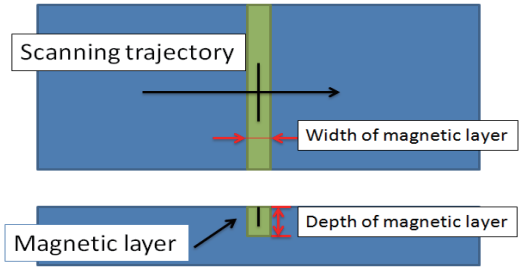


Fig.2 Simulation model

explained by the decreasing of relative permeability of magnetic layer. This is exactly shown what was happened before and after heating treatment. Before the heating process the relative permeability of magnetic layer is higher because of the magnetic α'-martensite. After the heating treatment, the relative permeability is decreasing from 1.3 to almost 1 because the reversal of magnetic α'-martensite phase.

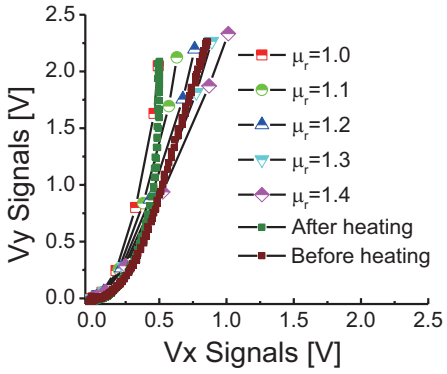


Fig.3 ECT signal of the specimen under load 49kN

The results of two other specimens also have the same tendency as those shown in Fig.3. The relative permeability after heat treatment is decreasing from 1.15 to 1.0 for specimen under load 30kN, and 1.2 to 1.1 for specimen under load 40kN separately. By comparing the relative permeability of magnetic layer before heat treatment of the above three specimens, the increasing of relative permeability of magnetic layer along with the load is observed as shown in Fig.4.

**4. Summary**

In this paper, the influence of martensite transformation in the plastic deformation zone of the fatigue crack is evaluated qualitatively. This magnetic phase will slightly influence the magnitude and phase of the ECT signals. Also as we increase the load when creating the fatigue crack, the stress induced martensite phase will have larger volume which is may be caused by the larger plastic deformation zone.

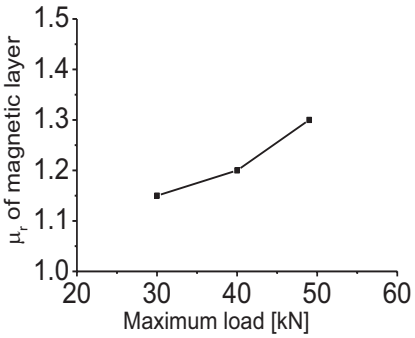


Fig.4 Relationship between load and $\mu_r$ of magnetic layers

**5. Acknowledgement**

This work was partly supported by the JSPS Core-to-Core Program, Advanced Research Networks, "International research core on smart layered materials and structures for energy saving" and also a part of this study was performed in "Aging Management Program Development on System Safety of Nuclear Power Plant in Japan", supported by Nuclear Regulation Authority, Japan.

**References**

[1]R.I. Stephens, John Wiley & Sons, Inc., (2001) 133-136.
[2]P. Marshall, Springer Science & Business Media (1984) 408-417.
[3]D.R. Harries, Int. Conf. Mech. Behaviour and Nuclear Applications of Stainless Steels at Elevated Temperatures, Varese, London, Metals Society (1981) 238-242.
[4]H. Fukutomi, H.Y. Huang, IEEE Trans. Magn, 34, 5 (1998) 2893-2896.

# Thickness Evaluation of Pipe Walls with Different Bottom Shapes Using Electromagnetic Acoustic Transducers

Shoichiroh Hara[1], Ryoichi Urayama[2], Tetsuya Uchimoto[2], Toshiyuki Takagi[2]
[1] Graduate School of Engineering, Tohoku University
2-1-1 Katahira Aoba-ku, Sendai, Miyagi 980-8577, Japan
[2]Institute of Fluid Science, Tohoku University
2-1-1 Katahira Aoba-ku, Sendai, Miyagi 980-8577, Japan

**ABSTRACT**

The electromagnetic acoustic resonance (EMAR) method provides accurate and stable evaluation of thickness of pipes. The authors have proposed an EMAR technique with a signal processing method, called the superposition of n-th compression (SNC) method, to estimate thickness of pipes based on EMAR spectral response data. This paper presents application of EMAR with SNC method to the evaluation of pipe wall thinning with R-shaped bottom. Results of inspection using EMAR show the good accuracy for two specimens with different R-shaped dent.

## 1. Introduction

In nuclear and thermal power plants, it is necessary to perform maintenance of piping for safe operation. Piping maintenance is based on residual lifetimes estimated by periodic measurements of thickness. Currently, it is expected to establish nondestructive evaluation techniques that are more reliable and convenient.

Electromagnetic acoustic transducer (EMAT), which is one of ultrasonic measurement methods, provides non-contacting measurements, since ultrasonic waves are transmitted and received in electromagnetic way [1].

The drawback of the EMAT is its low electromechanical conversion efficiency, which leads to low sensitivity and low SN ratio. Then, electromagnetic acoustic resonance method (EMAR) method is proposed based on the resonant phenomenon of ultrasonic wave propagating in the thickness direction. It is possible to improve the SN ratio with the amplified received signals. Further, it hardly depends on the state of the inspection surface and also can be applied to wall thickness measurement at high temperatures [2,3].Since the thickness varies in a complex way, thickness evaluation of pipe walls is difficult.

The authors have proposed a signal processing method, called the superposition of n-th compression (SNC) method, to extract thickness of pipes with wall thinning from EMAR spectral response data. This method was applied to a measurement of pipe wall cut from the mock-up test loop, and high capability of evaluating thickness was confirmed [4].

If the bottom shape is changed greatly by the thinning progresses, it can affect the measurement signal to the evaluation thickness.

This study evaluates the effect of the measurement signal to the wall thickness in measuring plates with different bottom shapes based on EMAR.

## 2. Method

Specimens are made of carbon steel plates SS400 with a simulated wall thinning. The bottom surface of a plate with the length of 150 mm, the width of 50 mm, and the thickness of 10 mm was machined two-dimensionally to form a different R-shaped dent as a simulated thinned wall. Figure1 shows the schematic drawing of specimens. Table1 shows a list of different R-shaped specimens.

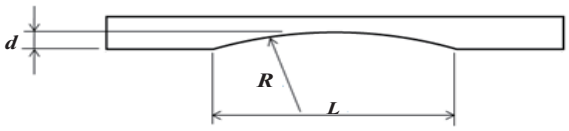


Fig.1 R-shaped surface as bottom specimens.

Table 1. List of R-shaped specimens.

| Test specimen number | *L*(length) [mm] | *R*(radius) [mm] | *d*(depth) [mm] |
|---|---|---|---|
| 1 | 70 | 300 | 2 |
| 2 | 76 | 150 | 5 |

The SNC method is a signal processing method based on the resonance frequencies of cyclic appearance at integral multiples. This means that by reducing the frequency measurement results obtained by the EMAR method by a factor of $n$, the intensity of $n^{th}$ order frequency $f_n$ can be superimposed on the intensity of the fundamental resonance frequency.

The fundamental resonance frequency $f_1$ and thickness $d$ are obtained from following equation.

$$f_1 = \arg\max_f \left\{ \sum_n x\left(\frac{f}{n}\right) \Big/ m \right\} \quad (1)$$

$$d = \frac{v}{2f_1} \quad (2)$$

where $x(f)$ is SNC spectrum intensity, arg max (argument of the maximum) is the frequency at which the SNC spectrum intensity is maximum, and $m$ is the number of superimposed resonance orders. Then, conversion from sound velocity to specimen thickness is conducted using Eq. (2). The maximum spectrum intensity so obtained is treated as the peak SNC value.

Corresponding author: Toshiyuki Takagi
*E-mail address*: takagi@ifs.touhoku.ac.jp

Peak of SNC spectrum is normalized by the peak value of the SNC results obtained by measuring the calibration test specimens with thickness of 10 mm thick made of the same material. Full width half maximum (FWHM) is also extracted as a featured parameter of spectra.

### 3. Results and Discussion

Figures 2 and 3 show the measurement results. The maximum error was 0.15 mm and 0.04 mm, respectively speciments1 and 2.

Figures 4 and 5 show the results of analysis SNC at locations 10 mm and 25 mm distant from the center of the R-shape of specimen 2. Dotted line is the FWHM. The bottom angle of the coil center is 4 degree in terms of 10 mm, the peak value is 0.13 mm, the half width was 0.23 mm. The bottom angle of the coil center is 10 degree in terms of 25 mm, the peak value is 0.10 mm. The half width could not be determined, because the half value was reduced to less than noise level.

### 4. Summary

This study evaluates the effect of the measurement signal to the wall thickness by measuring different bottom shapes based on EMAR. Result show that it is possible to evaluate the thickness with a high accuracy of 0.15 mm or less error.

FWHM may not be able to be determined with the inclination angle more than 10 degree. The peak values of signals also decrease with larger gradient. Hence the bottom surface geometry may be evaluated with FWHMs and peak values.

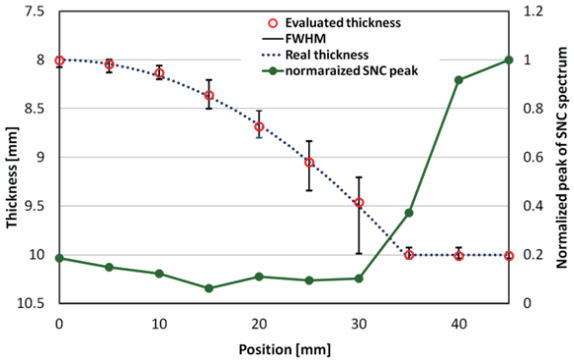


Fig.2 Wall thickness evaluation (specimen 1).

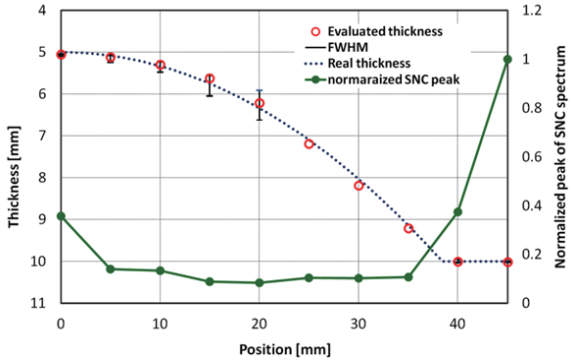


Fig.3 Wall thickness evaluation (specimen 2).

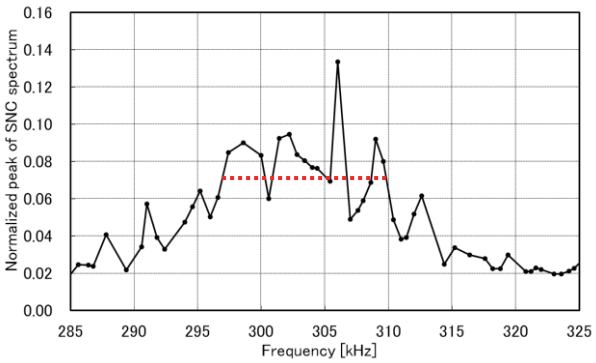


Fig.4 SNC signal of R-shaped bottom (10 mm).

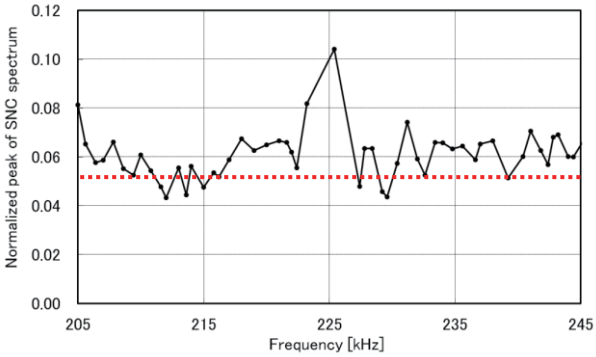


Fig.5 SNC signal of R-shaped bottom (25 mm).


### Acknowledgment

The authors thank the JSPS Core-to-Core Program, A. Advanced Research Networks, “International research core on smart layered materials and structures for energy saving”.


### References


[1] N. Yamagata, M. Takahashi and N. Ahiko, *Toshiba Review* (*in Japanese*), 63 (2008)46-49.

[2] R. Urayama, T. Uchimoto, T. Takagi, *International Journal of Applied Electromagnetics and Mechanics*, 33 (2010)1317-1327.

[3] F. Hermandez-Valle and S. Dixon, *INSIGHT*, 53 (2011)96-99.

[4] R. Urayama, T. Uchimoto, T. Takagi, S. Kanemoto, *E-Journal of Advanced Maintenance,* 2 (2010/2011)25-33.

Eleventh International Conference on Flow Dynamics
October 8-10, 2014, Sendai, Miyagi, Japan

# Quantitative Measurement of Pulse Waves Using PVDF Film Sensor and Cuff

Yuta Wakabayashi[1], Atsushi SHIRAI[2]
[1]Graduate School of Engineering, Tohoku University
6-6-01 Aramaki Aza Aoba, Aoba-ku, Sendai, Miyagi, 980-8579, Japan
[2]Institute of Fluid Science, Tohoku University
2-1-1 katahira, Aoba-ku, Sendai, Japan

**ABSTRACT**

In the pulse diagnosis, the doctor indents radial arteries of a patient by fingers and diagnoses illness from tactile sense of pulse waves detected on the arteries. The authors have proposed a system to mimic the diagnosis using a PVDF film sensor to detect the pulse waves and a cuff to indent the artery for the purpose of measuring the tactile force of the pulse waves. In this study, relationship between the cuff pressure and the sensor signal was measured to show that amplitude of the pulse waves had the maximum at a certain cuff pressure and the tendency matched with that obtained by the cuff.

## 1. Introduction

The pulse diagnosis is one of the traditional Chinese medicine in which the doctor diagnoses illness from characteristics of tactile sense of pulsation of a patient detected on the radial arteries at the wrists while indenting the vessel. The diagnostics result by the pulse diagnosis, however, varies with doctors because the diagnosis is subjective depending on skill and experience of the doctor[1]. Systematic observation to associate each illness and the detected pulse waves is essential to objectify the diagnosis and there are many researches to objectify the pulse diagnosis[2]-[6], but quantitative relationship between the tactile sense and the pulse waves has not been elucidated yet.

The authors have proposed a system which measures the pulse waves using a PVDF film sensor on the radial artery and a cuff to indent the vessel mimicking the pulse diagnosis for the purpose of measuring tactile force in the diagnosis. The PVDF film sensor is a very sensitive strain gauge to be able to detect subtle pulse waves via skin but it does not respond to a steady strain. Therefore, in the present study, change in the sensor signal by the indentation of the vessel and the correlation with the cuff pressure were quantitatively investigated for validation of this system.

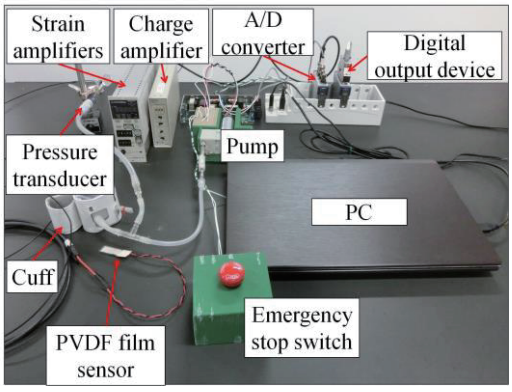


Fig. 1 Experimental system.

Corresponding author: Yuta Wakabayashi
*E-mail address*: wakabayashi@reynolds.ifs.tohoku.ac.jp

## 2. Experimental setups

### 2.1 System constitution

Figure 1 shows the experimental system to measure the pulse waves with indenting the radial artery. This system is composed of a PVDF film sensor, a charge amplifier, a cuff, a pump to supply air to the cuff, a pressure transducer to measure the cuff pressure, a strain amplifier, an A/D converter, a digital output device, and a PC. The PVDF film sensor (DT1-028K/L, Tokyo sensor) is held on the radial artery at the wrist by a fixture which is explained in the next section, and the cuff (separated from EW-BW50-S, Panasonic) is worn so as to be put around the wrist over the fixture.

LabVIEW 2012SP (National Instruments) is used in order to control the pump and to acquire and analyze the data. The cuff expands in a stepwise, and the pulse waves are measured for 10 s both by the PVDF film sensor and the pressure transducer from 5 s after the every cuff expansion. The expansion of the cuff is controlled by the driving period of the pump using the digital output device. An emergency stop switch is prepared to ensure the safety of test subjects.

### 2.2 Mounting of PVDF film sensor

Mounting arrangement of the PVDF film sensor at the wrist by a fixture is shown in Fig. 2. The PVDF film sensor is set perpendicular to the radial artery to detect the pulse signal effectively. The fixture is a rubber sheet of 0.13 mm in thickness to hold the sensor tight on the skin and to prevent the sensor to slide during being pressed by the cuff.

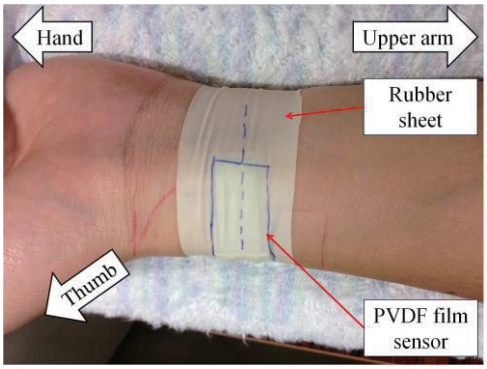


Fig. 2 Mounting arrangement of PVDF film sensor with fixture.

In the pulse diagnosis, there are some theories in the measurement position of the pulse waves. Today in Japan, it is common to consider the length of the forearm, distance from striation of the elbow to that of the wrist, as 1 che (= 10 sun) and to diagnose on the radial artery at the position of the 1.9 sun from the wrist[7]. In the present study, however, the PVDF film sensor was set at 1 sun from the striation of the wrist taking into consideration the procedure in the literature[7].

## 3. Experimental results and discussion

The experiment was performed with a 24 years old healthy male volunteer under permission (#26-1) of the ethics committee of Inst. Fluid Sci., Tohoku Univ. His mean, systolic and diastolic blood pressure were 13.1, 16.7 and 11.3kPa, respectively, and the pulse rate was 57 BPM before the experiment, which were measured by the automated sphygmomanometer (HEM-9000AI, OMRON). Number of the expansion step of the cuff was 22.

Figure 3 shows time variation of the signal of the PVDF film sensor and the cuff pressure. Amplitude of the signal of the PVDF film sensor changes with the increase in the cuff pressure, showing the maximum around 250 s. Comparing waveform of the pulse waves between the PVDF film sensor and the cuff at each indentation step, it was confirmed that the PVDF film sensor could reproduce the waveform more clearly than the cuff in a low cuff pressure region, while the frequency which gave the maximum power spectrum was the same between them in the FFT analysis of the signals.

Figure 4 shows the comparison of amplitude of the pulse waves with respect to mean cuff pressure, together with the standard deviation of the amplitude of the pulse waves. In this figure, the both amplitudes show the similar trend having the maximum at the mean cuff pressure of 14.5 kPa which is about 10% higher than the measured mean blood pressure. It implies that the PVDF film sensor detected volumetric change of the vessel, taking into consideration the principle of the oscillometric method. It is also clear that the standard deviation of the signal amplitude of the PVDF film sensor is smaller than that of the cuff though the signal intensity is low in the range of low amplitude. Together with the fact that signal of the PVDF film sensor well reproduced the waveform, it can be said that the sensor is effective to detect subtle tactile sense of the pulsation. This system, however, has a problem that the cuff presses not only the radial artery but also the ulnar artery because the cuff was wrapped around the wrist. It is necessary to indent only the radial artery to reproduce the pulse diagnosis. The authors are designing the indentation mechanism of the artery to improve the system.

## 4. Conclusion

The authors have proposed a system which measures the pulse waves using a PVDF film sensor and a cuff for

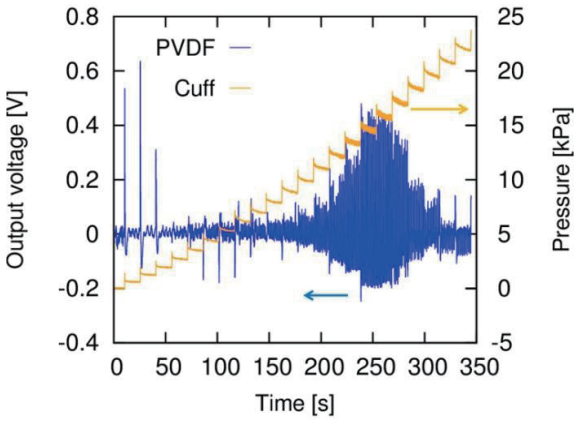


Fig. 3 Time variation of signal of PVDF film sensor and cuff pressure.

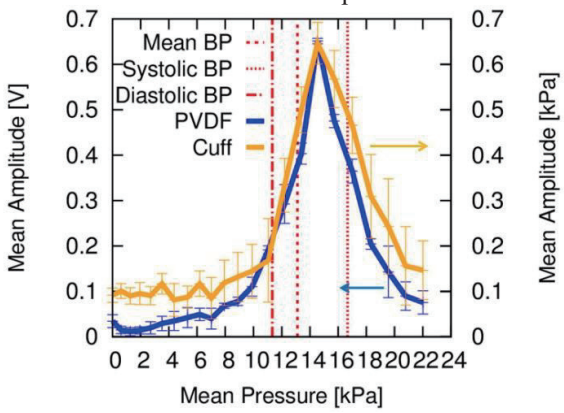


Fig. 4 Relationship between mean cuff pressure and amplitude of pulse waves.

the purpose of measuring the tactile force. Change in the sensor signal by the indentation of the radial artery and the correlation with the cuff pressure were quantitatively investigated. The obtained signal of the PVDF film sensor agreed well with the cuff pressure with respect to the relationship between amplitude of the pulsation and the mean cuff pressure. In addition, the PVDF film sensor well reproduced the pulse waveform even in the range of low mean cuff pressure.

## References

[1] K. Kawakita, M. Fujiki, T. Ogawa, M. Kido, M. Maruyama, E. Chihara, *Journal of the Japan Society of Acupuncture and Moxibustion*, 57, 2 (2006), 110-123. (in Japanese)

[2] K. Narumi, T. Nakanishi, A. Shirai, T. Hayase, *Trans. JSME*, Ser. B, 74, 737 (2008), 142-147. (in Japanese)

[3] F. Sirota, H. Mitsufuji, H. Igarashi, *Kampo Med.*, 22, 2 (1972), 201-209. (in Japanese)

[4] M. Takashima, K. Nagaya, T. Kikuna, K. Matsuta, *Kampo Med.*, 47-4 (1997), 635-643. (in Japanese)

[5] R. Fujita, *Kampo Med.*, 28, 2 (1977), 81-84. (in Japanese)

[6] M. Onaka, *Oriental Med. Pain Clin.*, 31, 1~4 (2001), 34-40.

[7] M. Kido, H. Hikarisawa, A. Mutou, *Method for Acquiring Myakushin*, Ishiyaku Publishers, Inc., (2013). (in Japanese)

Eleventh International Conference on Flow Dynamics
October 8-10, 2014, Sendai, Miyagi, Japan

# Kriging Surrogate Model Enhanced by Coordinate Transformation of Design Space

Nobuo Namura, Koji Shimoyama, and Shigeru Obayashi
Institute of Fluid Science, Tohoku University
2-1-1 Katahira, Aoba-ku, Sendai, Miyagi, 980-8577, Japan

**ABSTRACT**

The Kriging surrogate model with coordinate transformation of design space is proposed to improve the approximation accuracy of objective functions with correlated design variables. To identify suitable coordinates, significant trends in the objective function are extracted through its gradients. Comparing with the ordinary Kriging model, the proposed method shows higher accuracy in the approximation of a two-dimensional test function and reduces the computational cost to achieve the global optimization.

## 1. Introduction

Optimization in real-world problems is usually time consuming and computationally expensive in the evaluation of objective functions. Surrogate models are often useful to solve this difficulty. Surrogate models are constructed to promptly estimate the values of the objective functions at any point from sample points where real values of the objective functions are obtained by expensive computations. Therefore, it is very important that accurate models can be constructed even with only a small number of sample points.

The most common surrogate model is the polynomial regression (PR). In construction of the PR model, users give the polynomial order arbitrarily and then compute the coefficients of each term in the polynomial so as to fit the sample points by the least-squares method. The accuracy of the PR model significantly depends on the polynomial order, which corresponds to the number of local maxima and/or minima in an objective function. However, it is not always possible to achieve sufficient accuracy by adjusting the order because the real shape of the objective function is usually not known.

To approximate complex functions, radial basis function (RBF) networks [1] and the Kriging model [2] are often used. Both of them can adapt well to complex functions because they approximate a function as a weighted superposition of basis functions such as Gaussian function. Thus, the model complexity can be controlled by changing the weight coefficients and variance of each basis function. Gaussian basis functions in the Kriging model have independently different variance values along each design variable direction while those of RBF have the same values. In addition, the Kriging model gives not only estimated function values but also approximation errors, which help users determine the locations of the additional sample points to improve the accuracy of the surrogate model.

Some design variables can be correlated with each other in the real-world problems although the only PR model takes account of it as the cross-terms among different variables. However, the PR model does not approximate the complex function accurately for the reason described above. In this study, we propose modified Kriging models suitable for the problems with correlated design variables by focusing on the anisotropy of Gaussian basis functions. It means finding out the suitable coordinates representing significant trends in the objective function from its gradients (Fig. 1(a)) and then defining the variance of basis functions along each coordinate in the transformed system (Fig. 1(b)). The proposed method and the ordinary Kriging (OK) model are applied to a test function to investigate the feature of the proposed method.

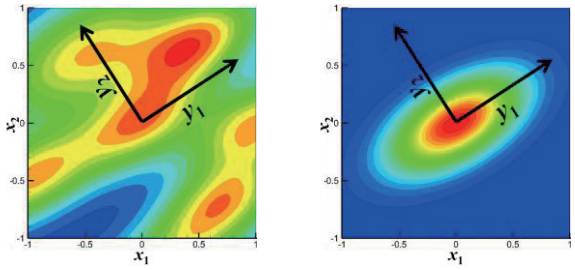


(a) Objective function (b) Basis function

Fig. 1 Extraction of suitable coordinates

## 2. Enhanced Kriging Model

The Kriging model is expressed by the superposition of the following Gaussian basis function

$$\prod_{i=1}^{m} \exp\left[-\theta_i \left(x_i - x_i^k\right)^2\right], \tag{1}$$

where $m$ is the number of design variables, $\theta_i$ $(0 \le \theta_i \le \infty)$ is an inverse of variance along the $i$-th variable direction, $x_i$ is the $i$-th design variable, and $x_i^k$ is the value of $x_i$ at the $k$-th sample point. The final form of the Kriging model is obtained by summing all basis functions and constant term after the weight coefficients are multiplied by each basis function. If the accuracy of the current surrogate model is insufficient, it is necessary to reconstruct a new surrogate model by including additional sample points. Accuracy improvement in the present Kriging model is accomplished by iteratively adding points with a maximum value of "expected improvement (EI)," which corresponds to the probability that the function approximation may achieve a new global optimum on a reconstructed surrogate model with consideration of an additional point.

Corresponding author: Nobuo Namura
*E-mail address*: namura@edge.ifs.tohoku.ac.jp

In order to identify the suitable coordinates and improve the approximation accuracy, gradients of objective function to each design variable are employed as is the case in Ref. [3]. First, the $m \times m$ covariance matrix $\boldsymbol{C}$, whose ($i$, $j$) entry is $\left(\partial \hat{f}/\partial x_i\right)\left(\partial \hat{f}/\partial x_j\right)$, is defined. $\hat{f}$ is the objective function estimated by the Kriging model in this study while gradients of real objective function are used in Ref. [3]. This study calculates $\boldsymbol{C}$ at 10,000 points in the design space, which are randomly sampled by the Monte Carlo method, and averages them. Second, eigenvalue decomposition is performed to the averaged $\boldsymbol{C}$, and eigenvectors $\mathbf{v}_i$ which represent the suitable coordinates are obtained. Third, the design variable vector in the new coordinate system $\mathbf{y}$ is calculated from the original vector $\mathbf{x}$ as

$$\mathbf{y} = \left[\mathbf{v}_1 \quad \cdots \quad \mathbf{v}_m\right]^{\mathrm{T}} \mathbf{x} . \tag{2}$$

Finally, the Kriging model is reconstructed in the transformed design space of $\mathbf{y}$.

## 3. Test Function Definition

The enhanced Kriging (EK) model and the OK model are applied to a two-dimensional minimization test function defined as

$$f(x_1, x_2) = (1 - y_1)^2 + 100\left(y_2 - y_1^2\right)^2,$$
$$\begin{bmatrix} y_1 \\ y_2 \end{bmatrix} = \begin{bmatrix} \cos\phi_1 & -\sin\phi_1 \\ \sin\phi_1 & \cos\phi_1 \end{bmatrix} \begin{bmatrix} x_1 \\ x_2 \end{bmatrix}, \quad \phi_1 = 30\,[\mathrm{deg}], \tag{3}$$
$$-1 \le x_1, x_2 \le 1.$$

Figure 2 shows the shape of this function. The initial sample points are generated by the Latin hypercube sampling (LHS) method [4] and additional sample points are employed one after another at the location where the EI value becomes a maximum. To compare the accuracy of two models, root mean square error (RMSE) between the surrogate model and the real function is calculated at $41 \times 41$ validation points. 100 independent trials with different initial sample points are performed and their averaged RMSE is evaluated for comparison.

## 4. Results and Discussion

Figure 3 shows the histories of averaged RMSE obtained by the OK and EK models. The EK model has lower RMSE than the OK model when the number of sample points is over 12, which means the EK model can approximate the function more accurately. In general, sample points are added until the surrogate model converges. From this point of view, the EK model requires only 23 sample points to achieve the global optimization while the OK model requires 31 sample points.

Typical shapes of the OK and EK models with 20 sample points are shown in Fig. 4 in which black dots denote the sample points. A comparison of Figs. 2 and 4 indicates that the EK model approximates the entire function shape exactly although the OK model has a slightly distorted shape along the original coordinates. Therefore, the EK model is useful for the optimization problems with correlated design variables.

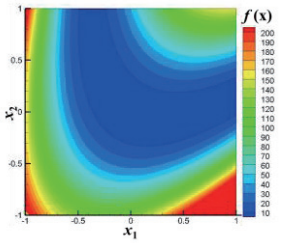


Fig. 2 Shape of test function

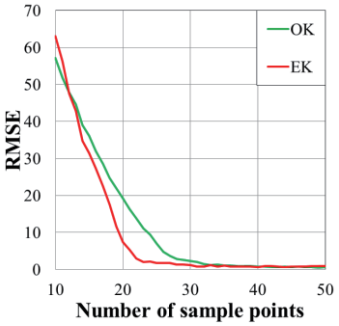


Fig. 3 Histories of averaged RMSE

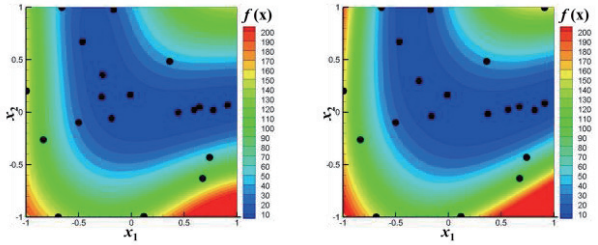


(a) OK model (b) EK model

Fig. 4 Surrogate models with 20 sample points

## 5. Concluding Remarks

The Kriging surrogate model enhancing its accuracy by the coordinate transformation of design space was proposed and validated in a two-dimensional test function with correlated design variables. Eigenvalue decomposition was applied to the covariance matrix of objective function gradients to each design variables to identify suitable coordinates. The ordinary Kriging model was distorted along the original coordinates. The proposed method approximated the entire function shape exactly and successfully reduced the number of function evaluations for efficient global optimization.

## References


[1] D.S. Broomhead, D. Lowe, *Complex Systems*, 2 (1988) 321-355.

[2] D.R. Jones, M. Schonlau, W.J. Welch, *J. of Global Optimization*, 13 (1998) 455–492.

[3] T. Lukaczyk, F. Palacios, J.J. Alonso, P.G. Constantine, *AIAA-Paper 2014-1171*, (2014).

[4] M.D. McKay, R.J. Beckman, W.J. Conover, *Technometrics*, 21 (1979) 239-245.

Eleventh International Conference on Flow Dynamics
October 8-10, 2014, Sendai, Miyagi, Japan

# Performance Improvement of a Closed-Conduit UV Reactor by Asymmetric Lamp Positioning using CFD

Tipu Sultan[1], Leesang Cho[2], Jinsoo Cho[1]
[1]Department of Mechanical Engineering, Hanyang University,
Haengdang-dong, Sungdong-gu, Seoul 133-791, Republic of Korea
[2]Department of Mechanical system Engineering, Hansung University,
Seoul 136-792, Republic of Korea

**ABSTRACT**

The performance of a closed-conduit ultraviolet (UV) reactor was improved by changing the lamp positions from symmetric to asymmetric. This goal was achieved by incorporating the performance factor reduction equivalent dose (RED). The fluence rate modeling was performed by using UVCalc3D. The results of the four asymmetric cases were compared with the symmetric one. The asymmetric lamp presented can be useful for UV reactor design and optimization. The simulation results provide detailed information about the model configuration and RED. The RED value was increased by approximately 15% for the UVCalc3D model.

## 1. Introduction

Millions of people are affected each year from dirty water. Public health data shows that 85% of child and 65% of adult diseases are due to waterborne pathogens and this rate is increasing [1]. This systemic problem calls for more stringent standards on the microbiological pollution of water effluents. Several approaches are used for the water disinfection including ozonation, membrane filtration, advanced oxidation processes (AOP), chlorination and ultraviolet (UV) irradiation [2].

The UV treatment has an advantage over other treatment processes is the absence of toxicity and by-product formation with comparable costs. UV treatment does not alter water chemically; nothing is added except energy. This property has paved the way for the development of a UV disinfection technology. The first drinking water disinfection application took place in Marseilles, France in 1910 [3].

The performance of the UV reactor was analyzed by using several computational fluid dynamics techniques. Blatchley et al. [4] studied the performance of the UV reactor through geometric modifications made at the walls for pathogens inactivation. Sozzi and Taghipour [5] studied the UV reactor performance by employing Eulerian and Lagrangian approaches. They found a good agreement between them at high flow rates. Pan and Orava [6] evaluated the performance of UV reactor by employing the concept of UV disinfection efficiency. Kelly et al. [7] found key design parameters for close vessel UV reactor performance. Qualls et al. [8] found that the proximity of the lamps to the walls and to each other causes UV energy loss due to light absorption. Furthermore, excessively close lamp spacing results in a reduction of the performance.

In addition few studies, have examined the performance of the UV reactor by considering different parameters. But the effects of asymmetric lamp positioning on the UV reactor performance are not mentioned in the literature.

Corresponding author: Prof. Jinsoo Cho
*E-mail address:* jscho@hanyang.ac.kr

Therefore, in this research work, four asymmetric lamp positionings are compared to one symmetric lamp positioning in order to achieve a better UV reactor performance.

## 2. Method

The CFD modeling of the UV reactor consists of three processes flow modeling, fluence rate modeling and kinetic modeling that results in UV water disinfection. UV reactor installed at the ECOSET drinking water treatment plant in Seoul, Republic of Korea, was used as system for the model evaluation. The relevant computational model of the UV reactor involves the integration of a number of distinct computational parameters and components. The geometric modeling was performed using three-dimensional modeling software CATIA V5R20. The computational meshes were constructed using the ICEM CFD commercially available tool of ANSYS 14.5. The grid independence test was conducted by evaluating several computational meshes. The velocity field within the UV reactor was computed using the standard k-ε model available in the ANSYS FLUENT 14.5, a commercial CFD tool. This CFD software apply a finite volume method (FVM) to solve the steady state Reynolds averaged Navier Stokes (RANS) equation. These are Eqs. (1) and (2).

$$\frac{\partial \bar{u}_i}{\partial x_i} = 0 \qquad (1)$$

$$\frac{\partial \bar{u}_i}{\partial t} + \frac{\partial}{\partial x_j}(\bar{u}_i \bar{u}_j) = -\frac{1}{\rho}\frac{\partial \bar{p}}{\partial x_j} + \frac{\partial}{\partial x_j}[\nu(\frac{\partial \bar{u}_i}{\partial x_j} + \frac{\partial \bar{u}_j}{\partial x_i}) - \overline{u_i' u_j'}] \qquad (2)$$

In this research four asymmetric lamp positions were compared with one symmetric position. The hydrodynamics and movement of the pathogens in UV reactor was considered predominant idea for the entire model selection. First case was selected by providing double UV intensity focused at one point near the inlet and at a distance on the tail. In second case at the inlet region two lamps were placed at smaller vertical distances so that it can retard the flow at start and more

time will be available for disinfection. Furthermore, two lamps near the outlet were kept at large distances in order to irradiate the pathogens that pass close to the wall. In the third case the lamps were positioned the shape of a rhombus in order to check the angular position irradiation effects. In the fourth case the lamps were positioned diagonally and the diagonal was maintained at $45^0$ to inactivate the pathogens diagonally.

### 3. Results and Discussion

The fluence rate is location dependent, when lamps are placed close to each other, it will confine all UV irradiance in a small area, and that will magnify the loss of the fluence rate. Furthermore, dose is also affected by the residing time of the pathogens as explained earlier in the method Section 2. Four asymmetric cases were analyzed to validate the results.

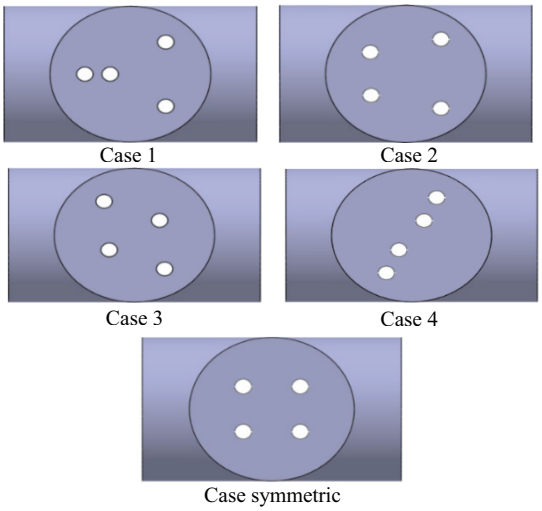


Fig. 1 Diagrammatic layout of the lamp positioning

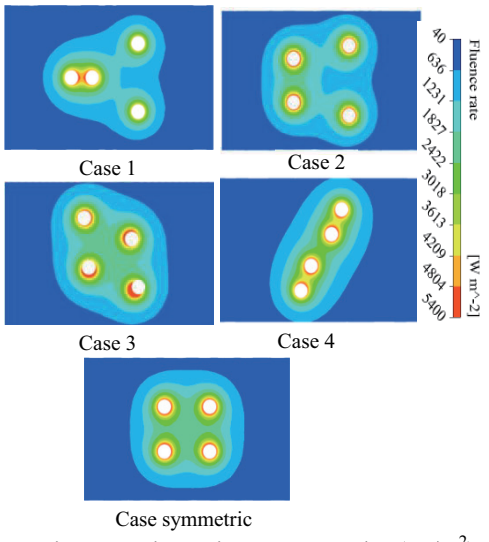


Fig. 2 UV intensity contours plot ($W/m^2$)

The increase in RED was significant for all asymmetric cases ranging from 8% to 15% for UVCalc3D. Thus it was inferred that lamp position within the UV reactor is an important criteria. The RED was improved through asymmetric lamp positionings. It should be noted that this study has been concerned with the asymmetric lamp positioning effects for better reactor performance. The performance improvement was carried out by considering four cases, although other potentially more favorable lamp positions cannot be ruled out.

| Case | Flow rate [Kg/s] | Simulated RED [$mJ/cm^2$] | % increase in RED [(Increase/Original)x100] |
|---|---|---|---|
| Symmetric | 3 | 12.13 | N/A |
| 1 | 3 | 13.19 | 8.74% |
| 2 | 3 | 12.79 | 5.44% |
| 3 | 3 | 13.62 | 12.29% |
| 4 | 3 | 13.94 | 14.93% |

Table1. RED by using UVCalc3D

In future work, the authors are currently extending UV reactor studies along several dimensions for the investigation of optimized lamp position criteria for UV reactor that will optimize the UV reactor performance.

### References


[1] K. A. Reynolds, K. D. Mena, and C. P. Gerba, *Reviews of environmental contamination and toxicology*. vol. 192, ed: Springer, (2008), pp. 117-158.

[2] V. Lazarova, P. Savoye, M. L. Janex, E. R. Blatchley Iii, and M. Pommepuy, *Water Science and Technology,* vol. 40, (1999) pp. 203-213.

[3] USEPA, Washington DC NOV (2006).

[4] K.-p. Chiu, D. A. Lyn, P. Savoye, and E. R. Blatchley III, *Journal of environmental engineering,* vol. 125,( 1999) pp. 459-469.

[5] D. A. Sozzi and F. Taghipour, *Environmental science & technology,* vol. 40, (2006) pp. 1609-1615.

[6] H. Pan and M. Orava, *Journal of Water Supply: Research and Technology—AQUA,* vol. 56, (2007) pp. 181-189.

[7] R. Kelly, B. Ferran, and S. Jin, *Proceedings of the Water Quality Technology Conference*, (2004).

[8] R. G. Qualls and J. D. Johnson, ," *Water Research,* vol. 19, (1985) pp. 1039-1046,.

Eleventh International Conference on Flow Dynamics
October 8-10, 2014, Sendai, Miyagi, Japan

# Analysis of Diffraction Effect on Sonic Boom Propagation Using the KZK Equation

Junpei Takeno, Takashi Misaka, Koji Shimoyama, and Shigeru Obayashi
Institute of Fluid Science, Tohoku University
2-1-1, Katahira, Aoba-ku, Sendai, Miyagi, 980-8577, Japan

**ABSTRACT**

In this study, sonic boom propagation is simulated by the Khokhlov-Zabolotskaya-Kuznetsov (KZK) equation. The KZK equation accounts for the effects of diffraction, thermoviscous absorption, relaxation, geometrical spreading, inhomogeneity of the medium and nonlinearity. The diffraction effect considered in the KZK equation is confirmed by the propagation of N-wave with sinusoidal perturbations. This result indicates that the diffraction effect mitigates the perturbations while the wave propagates through the turbulent and inhomogeneous atmosphere.

## 1. Introduction

The Concorde supersonic transport had started commercial flights in 1976, and retired in 2003. Since then several problems have prevented commercial supersonic aircrafts. The most significant problem is a sonic boom, which is generated from shock waves and causes a big sound noise like a close lightning strike. Supersonic flights of the Concorde were prohibited above the ground because of a sonic boom. This limited the advantage of supersonic transport, i.e., short flight time. In order to realize the next generation supersonic transport, sonic boom reduction techniques must be developed. Moreover, a tool to simulate sonic boom propagation considering the effects of atmosphere is required to evaluate the magnitude of sonic boom on the ground accurately.

Currently, the waveform parameter method[1] and the augmented Burgers equation[2] have been used for the numerical prediction of sonic boom. The waveform parameter method is based on geometric acoustics to estimate the amplitude and utilizes isentropic wave theory to take account of nonlinear waveform distortion. This method is able to express the effects of nonlinearity, geometrical spreading, and the change of the medium in which waves propagate, and estimate the peak pressure level and duration time of the sonic boom. The augmented Burgers equation is able to take account of thermoviscous absorption and molecular relaxation in addition to the effects handled by the waveform parameter method, and estimate the peak pressure, duration time, and rise time of the sonic boom. However, these methods cannot consider the effect of wave front distortion when the waves propagate through inhomogeneous media such as atmospheric turbulence. On the other hand, the Khokhlov-Zabolotskaya -Kuznetsov (KZK) equation,[3] which is originally derived for the description of nonlinear acoustic beams, is able to express the three-dimensional nature of sonic boom described above. Thus, it is more promising to analyze the sonic boom propagation based on the KZK equation.

This study aims to construct the sonic boom analysis tool based on the KZK equation and confirm its capability. Currently we consider the effects of diffraction, thermoviscous absorption, relaxation, geometrical spreading, inhomogeneity of the medium and nonlinearity in the sonic boom analysis tool. In this paper, the diffraction effect considered in the KZK equation is investigated based on the propagation analyses of N-wave with sinusoidal perturbations.

Corresponding author: Junpei Takeno
*E-mail address*: takeno@edge.ifs.tohoku.ac.jp

## 2. Numerical Method

### A. KZK equation

The KZK equation, which accounts for the effects of diffraction, thermoviscous absorption, relaxation, geometrical spreading, inhomogeneity of the medium, and nonlinearity, is expressed as

$$\frac{\partial p}{\partial z} = \frac{c_0}{2}\int_{-\infty}^{t}\left(\frac{\partial^2 p}{\partial x^2}+\frac{\partial^2 p}{\partial y^2}\right)d\tau' + \frac{\beta}{2\rho_0 c_0^3}\frac{\partial p^2}{\partial t} + \frac{D}{c_0^4}\frac{\partial^2 p}{\partial t^2} + \sum_i \frac{(\Delta c)_i \tau_i}{c_0^2}\left(1+\tau_i\frac{\partial}{\partial t}\right)^{-1}\frac{\partial^2 p}{\partial t^2} - \frac{1}{2A}\frac{\partial A}{\partial z}p + \frac{1}{2\rho_0 c_0}\frac{\partial(\rho_0 c_0)}{\partial z}p \quad (1)$$

where $p$ is the acoustic pressure, $t$ is the retarded time, $c_0$ is the ambient sound speed, $\rho_0$ is the ambient density of the medium, $\beta$ is the coefficient of nonlinearity, $D$ is the diffusivity of sound, $A$ is the ray tube area, $z$ is the propagation coordinate, $x$ and $y$ are the transverse coordinates, $i$ is the relaxation process, $\tau_i$ is the relaxation time, and $(\Delta c)_i$ is the increment in sound speed. The difference between this KZK equation and the augmented Burgers equation is the diffraction term, which is included in the former and expresses the three-dimensional nature of sonic boom.

### B. Analysis procedure

The KZK equation is solved by the operator splitting method. Analysis procedure of the proposed tool is summarized in Fig. 1. First, a near-field pressure profile, which is usually obtained by computational fluid dynamics simulation or pressure measurement in experiment, is used as an input. Second, a sonic boom propagation path is calculated under the flight conditions of the analyzed model and the atmospheric conditions through which the sonic boom propagates. Third, Eqs. (2)-(6) are solved in the following order: diffraction, thermoviscous absorption, relaxation, geometrical spreading and inhomogeneity of the medium, and nonlinearity. The analysis procedure of the proposed tool follows that of Xnoise.[2] The steps from the definition of a sonic boom propagation path to the calculation of nonlinearity effect shown in Fig. 1 are iterated until the sonic boom reaches to the ground.

Diffraction
$$\frac{\partial p}{\partial z} = \frac{c_0}{2}\int_{-\infty}^{\tau}\left(\frac{\partial^2 p}{\partial x^2} + \frac{\partial^2 p}{\partial y^2}\right)d\tau' \quad (2)$$

Thermoviscous absorption
$$\frac{\partial p}{\partial z} = \frac{D}{c_0^4}\frac{\partial^2 p}{\partial \tau^2} \quad (3)$$

Relaxation
$$\frac{\partial p}{\partial z} = \sum_i \frac{(\Delta c)_i \tau_i}{c_0^2} \times \left(1 + \tau_i \frac{\partial}{\partial t'}\right)^{-1} \frac{\partial^2 p}{\partial t'^2} \quad (4)$$

Geometrical spreading and Inhomogeneity of the medium
$$\frac{\partial p}{\partial z} = -\frac{1}{2A}\frac{\partial A}{\partial z}p + \frac{1}{2\rho_0 c_0}\frac{\partial(\rho_0 c_0)}{\partial z}p \quad (5)$$

Nonlinearity
$$\frac{\partial p}{\partial z} = \frac{\beta}{2\rho_0 c_0^3}\frac{\partial p^2}{\partial t} \quad (6)$$

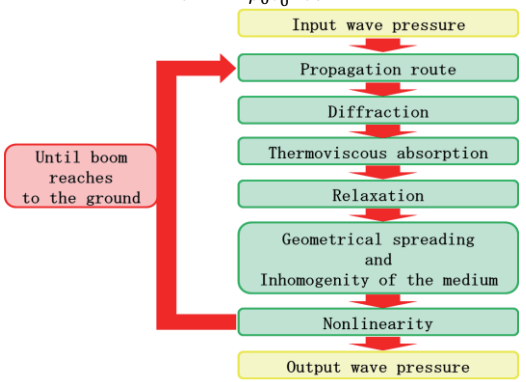


Fig 1. Analysis procedure of the proposed tool

## 3. Results and Discussion

The propagation of N-wave with sinusoidal perturbations is analyzed with and without a diffraction term to compare the resulting wave form. Input wave is planer N-wave whose wave front is located in $x$ = -25 to 25 [m] and $y$ = -25 to 25 [m]. N-wave propagates in $z$-direction and has sinusoidal amplitude of 0.3 along the $y$-direction. Figure 2(a) shows the input wave monitored at $x$ = 0 [m]. The speed of wind is 0 [m/s], the temperature is 15 [℃] and the relative humidity is 0 [%]. Propagation from the altitude of 5,000 [m] to the ground is analyzed with and without the diffraction term.

Figures 2(b) and (c) show the resulting N-waves without and with diffraction effect, which are monitored at $x$ = 0 [m] on the ground. The output wave in Fig. 2(b) has the sinusoidal perturbation along $y$-axis as in the input wave. Perturbations included in the input wave remain during the propagation if the diffraction effect is not considered. On the other hand, such perturbations disappear and pressure amplitudes are constant in the output wave in Fig. 2(c). This is because contiguous pressure waves interact with each other by diffraction effect and perturbations in input wave decrease during the propagation. Furthermore, the maximum pressure of the analysis with diffraction effect is smaller than that without diffraction effect. Therefore, the peak pressure level on the ground is likely to change by the diffraction effect, which cannot be considered in the conventional methods.

## 4. Conclusions

In this study we developed a sonic boom analysis tool based on the KZK equation by considering the effects of diffraction, thermoviscous absorption, relaxation, geometrical spreading, inhomogeneity of the medium and nonlinearity. The three-dimensional diffraction effect expressed by the proposed method was confirmed by the propagation of N-wave with sinusoidal disturbances. The results showed the peak pressure level on the ground was likely to change due to the diffraction effect, which was not able to be considered in the conventional methods.


## Acknowledgements

The authors would like to thank JAXA for providing the augmented Burgers equation solver, Xnoise.


## References


[1] Thomas, C, L., NASA TN D-6832, (1972).

[2] Yamamoto, M., Hashimoto, A., Murakami, K., Aoyama, T., and Sakai, T., *42nd Fluid Dynamics Conference/ Aerospace Numerical Simulation Symposium 2010*, 2B11, (2010), (in Japanese).

[3] Anna, R, P., preprint of Laboratory Jaques-Louis, Paris 6, (2006).


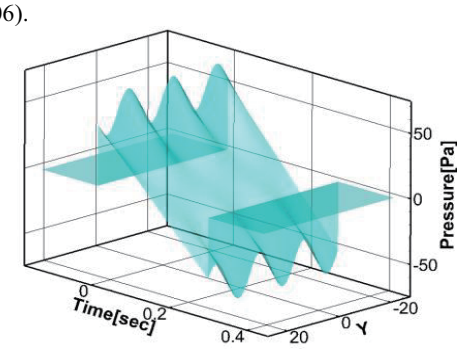


(a) Input N-wave

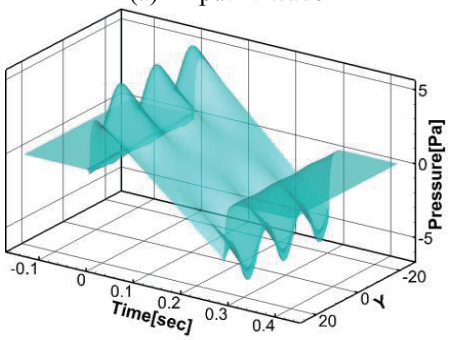


(b) Resulting N-wave without diffraction term

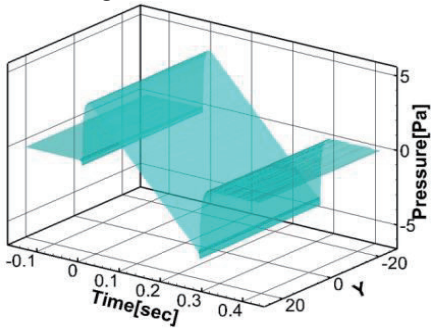


(c) Resulting N-wave with diffraction term

Fig 2. Propagation analyses of N-wave with sinusoidal perturbations

# Computational Modeling and Simulation on Cone Formation in Ionic Liquid Electrospray

Shohei Shinoki[1] and Hidemasa Takana[2]
[1] Graduate School of Engineering, Tohoku University
2-1-1 Katahira, Aobaku, Sendai, Miyagi, 980-8577, Japan
[2] Institute of Fluid Science, Tohoku University
2-1-1 Katahira, Aobaku, Sendai, Miyagi, 980-8577, Japan

**ABSTRACT**

The computational modeling of cone formation in the ionic liquid electrospray has been established. Interface tracking of the liquid interface is performed using Volume-of-Fluid (VOF) method and the advection of the liquid interface is solved using Volume/Surface Integrated Average based Multi-Moment Method (VSIAM3). Surface tension is evaluated as a body force acting on the interface using Continuum Surface Force (CSF) model. With coupling the above methods to solve liquid-gas two phase fluid flow equations and the electrostatic equations, the cone formation in ionic liquid electrospray is successfully simulated.

## 1. Introduction

Electrospray is a promising technology to form an ultra-fine spray from the capillary tip by supplying conductive liquid including ions to the capillary and applying high voltage to the capillary [1]. When high voltage is applied between the capillary and the grounded plate electrode, the conical gas-liquid interface called Taylor cone is formed at the capillary tip and then fine droplets start ejecting from the tip of Taylor cone. In an electrospray, multivalent charged droplets and polyatomic ions are generated in the gas phase. It is also possible to generate the charged droplets containing excessive positive ions in the case of a positive applied voltage and to generate the negatively charged droplets including excessive negative ions just by changing the polarity of the applied voltage.

Recently, the applications of electrospray using ionic liquid to surface treatment, secondary ion mass spectroscopy and space propulsion have been drawn attention as innovative technologies because of the great feature of ionic liquid generating ionic species with large mass. In addition, it is possible to generate well focused spray even in a vacuum. However, electrospray process with an ionic liquid has not yet made clear, and in a detailed analysis of ionic liquid electrospray process including the cone formation is essential for the further improvement of ionic liquid electrospray.

Therefore, in this study, the Taylor cone formation in the ionic liquid electrospray has been clarified by two-dimensional numerical simulation by establishing electrostatic modeling on electrospray with ionic liquid.

## 2. Governing equations and numerical conditions

Figure 1 shows the schematic illustration of the electrospray systems and the computational domain used in this study. Ionic liquid is supplied to the micro capillary of which inner diameter and length are both 0.2 mm at $Q$ = 2.83 ml/min. Positive voltage is applied between the capillary and the grounded plate electrode. In this numerical calculation, an axisymmetric two-dimensional model is applied. The computational domain is 0.6 mm along axis and 0.4 mm in radial direction. The distance between the tip of capillary and the grounded plate electrode is set to 0.4 mm.

Corresponding author: Hidemasa Takana
*E-mail address*: takana@paris.ifs.tohoku.ac.jp

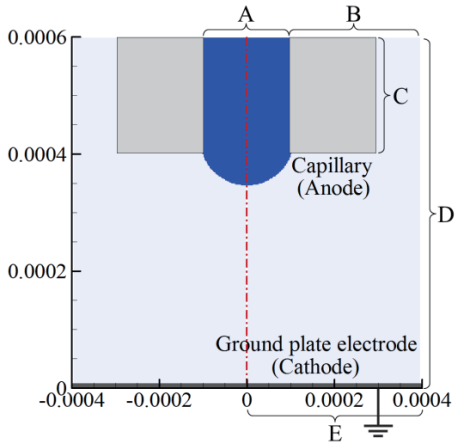


Fig. 1 Schematic illustration of computational domain.

Table 1. Boundary conditions.

| | Velocity | Pressure | Potential |
|---|---|---|---|
| A | $v = Q/A$ | pressure in velocity field | $\partial\phi/\partial n = 0$ |
| B | $\partial u/\partial n = 0$, $\partial u/\partial n = 0$ | Atmosphere | $\partial\phi/\partial n = 0$ |
| C | $u = 0$, $v = 0$ | $\partial p/\partial n = 0$ | $\phi = 56$ V |
| D | $\partial u/\partial n = 0$, $\partial u/\partial n = 0$ | $\partial p/\partial n = 0$ | $\partial\phi/\partial n = 0$ |
| E | $\partial u/\partial n = 0$, $\partial u/\partial n = 0$ | $\partial p/\partial n = 0$ | $\phi = 0$ V |

Table 2. Physical properties of ionic liquid.

| Density (kg/m$^3$) | Viscosity (Pa · s) | Surface tension (N/m) | Permittivity (F/m) |
|---|---|---|---|
| 1200 | 0.3 | 0.4 | 1200 |

The governing equations consist of mass and momentum conservation equations and they are shown below [2].

Mass conservation equation:

$$\nabla \cdot \boldsymbol{u} = 0. \quad (1)$$

Momentum conservation equation:

$$\frac{\partial \boldsymbol{u}}{\partial t} + \nabla \cdot (\boldsymbol{uu}) = -\frac{1}{\rho}\nabla p + \frac{1}{\rho}\nabla \cdot \tau + \boldsymbol{g} + \frac{1}{\rho}\boldsymbol{F}_b, \quad (2)$$

where $\boldsymbol{u}$ is the velocity vector, $\rho$ is the liquid density, $p$ is

the pressure, $\tau$ is the stress tensor, $\boldsymbol{g}$ is the gravitational constant and $\boldsymbol{F_b}$ is body force. Flow field is obtained by solving equation (1), (2). These equations were solved by VSIAM3 method with excellent stability.

Based on the flow field in the computational domain obtained from solving equations (1) and (2), the VOF method is used to advect the interface location. In this method, a volume fraction $\gamma$ is defined as the fraction of a cell volume occupied by liquid. $\gamma$ can take values within the range $0 \leq \gamma \leq 1$. $\gamma = 1$ and $\gamma = 0$ is defined as the liquid phase and the gas phase, respectively. The interface is present in cells with $\gamma$ values of $0 < \gamma < 1$, and the isosurface of $\gamma = 0.5$ is considered as the gas-liquid interface. The advection equation for volume fraction is shown below.

$$\frac{\partial \gamma}{\partial t} + \nabla \cdot (\boldsymbol{u}\gamma) = 0. \tag{3}$$

Surface tension $\boldsymbol{F_{sv}}$ acting on the interface is evaluated as a body force in the CSF model as shown in equation (4). The curvature $\kappa$ and the normal vector of the surface are obtained by constructing a distant function $\psi$.

$$\boldsymbol{F_{sv}} = \sigma \kappa \nabla \psi, \tag{4}$$

where $\sigma$ is the surface tension coefficient.

Electrostatic force $\boldsymbol{F_e}$ acting on the gas-liquid interface is given by the following equation using the surface charge density $\rho_c$.

$$\boldsymbol{F_e} = \rho_c \boldsymbol{E} - \frac{1}{2}\boldsymbol{E} \cdot \boldsymbol{E} \nabla (\varepsilon \varepsilon_0). \tag{5}$$

Then, the electric field intensity $\boldsymbol{E}$ is expressed as the gradient of the electric potential $\phi$. The electric potential is given by Poisson equation for the electric potential shown below.

$$\nabla \cdot (-\varepsilon \varepsilon_0 \nabla \phi) = \rho_c. \tag{6}$$

$\rho_c$ is calculated as

$$\rho_c = \nabla \cdot (\varepsilon \varepsilon_0 \boldsymbol{E}). \tag{7}$$

The boundary conditions are summarized in table 1. Also, the physical properties of ionic liquid used in this study are listed in table 2.

## 3. Results and Discussion

Figure 2 shows the electric potential distribution at $t = 0$ s. Because of high permittivity of ionic liquid, the potential in the ionic liquid inside the capillary is equipotential. The axial gradient of electric potential is high in the vicinity of the meniscus tip, showing that the electric field concentrates on the meniscus tip to form the Taylor cone.

Figure 3 shows the surface charge density and electrostatic force vectors. The maximum charge density appears at the meniscus tip due to the concentration of electric field as shown in Fig. 2. The electrostatic force also becomes higher at the meniscus tip according to the concentration of electric field.

Figure 4 shows the interface and velocity flow field at $t = 11.1$ μs. Ionic liquid inside the capillary is successfully extracted to the outside of the capillary due to the strong electrostatic force even for the high viscosity of the ionic liquid.

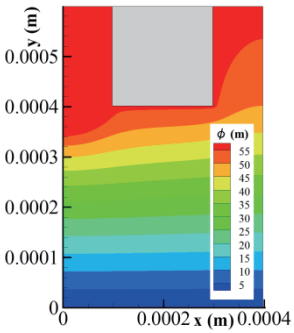


Fig. 2 The electric potential distribution in the computational domain.

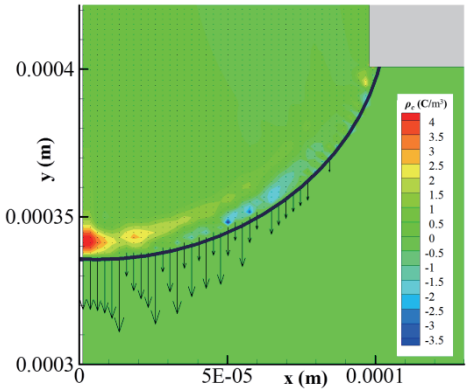


Fig. 3 Distribution of surface charge density and electrostatic force vectors around the meniscus. (The solid line represents the liquid interface.)

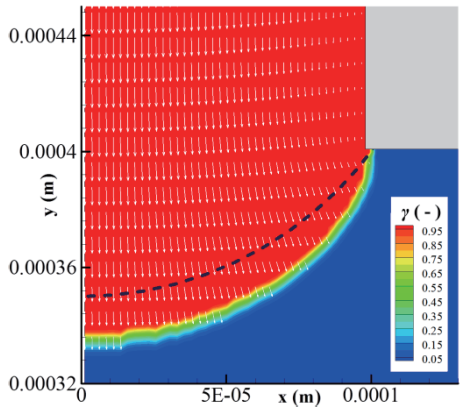


Fig. 4 The interface and velocity vectors at $t = 11.1$ μs. (The dashed line represents the initial liquid interface.)

## 4. Concluding Remarks

In this study, the computational modeling of cone formation in the ionic liquid electrospray has been established. It was clarified from the computational simulation that the ionic liquid is successfully extracted from the micro capillary by the electrostatic force acting on the ionic liquid interface. The surface charge density becomes highest at the tip of the meniscus due to the concentration of electric field.

## References

[1] A. K. Sen. J. Darabi and D. R. Knapp, *Microfluidics and Nanofluidics* , 3, 3 (2007) 283－298.

[2] M. P. Fard, M. Rahimzadeh and S. Pooyan, *ESDA2010*, 25034 (2010).

Eleventh International Conference on Flow Dynamics
October 8-10, 2014, Sendai, Miyagi, Japan

# Calibration of the Model Position and Attitude Sensor System in the 0.3-m Magnetic Suspension and Balance System

Shuhei Taniguchi, Takumi Ambo, Daiju Noguchi, Daiju Numata, Keisuke Asai
Department of Aerospace Engineering, Tohoku University
6-6-01 Aramaki Aza Aoba, Aoba-ku, Sendai, Miyagi, 980-8579 JAPAN

**ABSTRACT**

The objective of this research is to calibrate a model position and attitude measurement sensor system for 0.3-m Magnetic Suspension and Balance System (MSBS). Highly-accurate sensing system is indispensable for MSBS. We constructed sensing system using CCD line sensors and evaluated the performance of this system. As the result of evaluation, although adjustment is necessary, the sensor system has enough potential for levitation of a model in MSBS.

## 1. Introduction

In a wind-tunnel testing, there is a problem of support interference that sting to support a model adversely affects air flow. Particularly, the problem grows big in the dynamic wind-tunnel testing (DWT) which is made to measure dynamic aero force, because a sting is made to vibrate with a model in wind tunnel in DWT.

Magnetic Suspension and Balance System (MSBS) is one of the methods to solve this problem. MSBS can support a model in airflow by non-contact using magnetic force between a permanent magnet in a model and coils located around measurement section [1].

The 0.3-m MSBS is under development in Tohoku-University. This research reports about the present state of the development of a model position and attitude sensor system which is necessary for model control.

## 2. Outline of 0.3-m MSBS

The 0.3-m MSBS is under development for use in Tohoku-University Basic aerodynamic Research Tunnel (T-BART) which has a 0.3m x 0.3m square test section. 0.3-m MSBS is constructed five components that are model, sensor, control, power and coil systems. Figure1 shows configuration of a model levitation procedures.

## 3. Sensing system

### 3.1 Principle of the sensing system

Sensor system using CCD line sensors was adopted in 0.3-m MSBS [2]. The levitation model is painted white and center of gravity part is painted black marker. By line sensors read edges and the marker of the model, the position and attitude of the model are measured.

This system consist of five line sensors (TAKEX, TL-7450S), four red LEDs (Shott Moritex, MSPP-CR42), four blue LEDs (Shott Moritex, MSPP-CB42), one half mirror, two dichroic color filters (red and blue), two plano-convex lens (f=80, f=100). Magnification of the lens is set 0.67. Figure2 shows a configuration of sensor system.

Three line sensors are located side of the measurement section using a half mirror and two line sensors are located upper of the measurement section. Five line sensors are driven by synchronized signal. Figure 3 shows the position of the edge of the model and the marker, which line sensors read. In this research, the levitation model is axial symmetry for simple. Sensor system measures five-axis without roll.

The edges and marker are converted voltage signals by line sensors. This signals converted count number by counter board in DOS-PC. Count number correspond to line sensor's element number. The position and attitude of the model is calculated by following equations based on count number.

$$x_{count} = \frac{X_{\#1}^{+} - X_{\#1}^{-}}{2} - r\psi_{\mathrm{count}} \quad (1)$$

$$y_{count} = \frac{1}{2}\left(\frac{Y_{\#4}^{-} + Y_{\#4}^{+}}{2} + \left(Y_{\#5}^{max} - \frac{Y_{\#5}^{-} + Y_{\#5}^{+}}{2}\right)\right) \quad (2)$$

$$z_{count} = \frac{1}{2}\left(\frac{Z_{\#2}^{-} + Z_{\#2}^{+}}{2} + \left(Z_{\#3}^{max} - \frac{Y_{\#3}^{-} + Y_{\#3}^{+}}{2}\right)\right) \quad (3)$$

$$\theta_{count} = \frac{1}{\frac{2u}{m}}\left(\frac{Z_{\#2}^{-} + Z_{\#2}^{+}}{2} - \left(Z_{\#3}^{max} - \frac{Y_{\#3}^{-} + Y_{\#3}^{+}}{2}\right)\right) \quad (4)$$

$$\psi_{count} = \frac{-1}{\frac{2u}{m}}\left(\frac{Y_{\#4}^{-} + Y_{\#4}^{+}}{2} - \left(Y_{\#5}^{max} - \frac{Y_{\#5}^{-} + Y_{\#5}^{+}}{2}\right)\right) \quad (5)$$

$u$ is distance between the element of line sensor #2 and #3, #4 and #5. $m$ is magnification of the lens.

Displacement of the model position are calculated using change quantity of count number and resolution.

$$x = \Delta x \times (x_{count} - x_{count_0}) \quad (6)$$

$$y = \Delta y \times (y_{count} - y_{count_0}) \quad (7)$$

$$z = \Delta z \times (z_{count} - z_{count_0}) \quad (8)$$

$$\theta = \Delta\theta \times (\theta_{count} - \theta_{count_0}) \quad (9)$$

$$\psi = \Delta\psi \times (\psi_{count} - \psi_{count_0}) \quad (10)$$

Where $\Delta x, \Delta y, \Delta z, \Delta\theta$ and $\Delta\psi$ are resolutions and $x_{count_0}$, $y_{count_0}, z_{count_0}, \theta_{count_0}$ and $\psi_{count_0}$ are initial value of count number.

### 3.2 The method of evaluation of the sensing system

Sensor system was evaluated using a calibration device to show in figure 4. This device has the calibration model which is size same as the levitation model.

Sensor system evaluated by reading the movement of the model which is moved by the device exactly. In the evaluation test, sensor systems measure five-axis without roll for simple. The quantity of the $x$, $y$, $z$-axis movement are 3 mm, $\theta$, $\psi$,-axis movement are 3 degree.

Corresponding author: Shuhei Taniguchi
*E-mail address*:
taniguchi.shuhei@aero.mech.tohoku.ac.jp

## 4. Result and Discussion

Following figure 5 and 6 are the result of evaluation test. Figure 5 shows relationship between movement of the model by each 1 axis and change of count number. (a), (b), (c), (d) and (e) is about x, y, z, θ, ψ-axis movement each other. The vertical axis is the position of the model. The horizontal axis is the count number. Figure6 shows change of RMS value when the model move in a condition same as Figure 5. RMS value indicates dispersion edges and marker on the line sensor elements.

Figure 5 shows that movement of the model and change of the count number are linear relations, and there is no interference to other axes. Figure6 shows that RMS value is under about 2. It means this sensor system resolution is about 9μm because line sensor element size is 4.7μm×4.7μm. This resolution is enough to levitate a model stable. And it is revealed that RMS value improves by coordinating light distribution of the LED, so resolution improvement is anticipated.

## 5. Conclusion

We constructed and evaluated the model position and attitude sensor system for 0.3-m MSBS in Tohoku-University. As the result of evaluation test, it is evaluated that sensor system resolution is about 9μm and the relation between model movement and change of the count number is linear. It is enough performance for levitate a model stable in MSBS.

## References


[1] H.Sawada, T.Kunimas, JOURNAL OF THE JAPAN SOCIETY FOR AERONAUTICAL AND SPACE SCIENCES, Vol.50, No.580, (2002) 188-195

[2] H.Sawada, H.Kanda and H.Suenaga, AIAA Paper 91-0397, January, (1991)


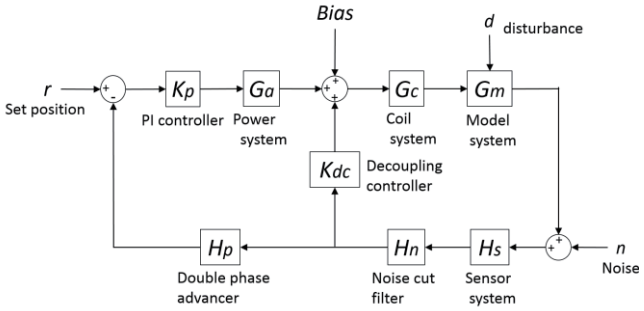


Fig.1 Control procedures to levitate a model stable

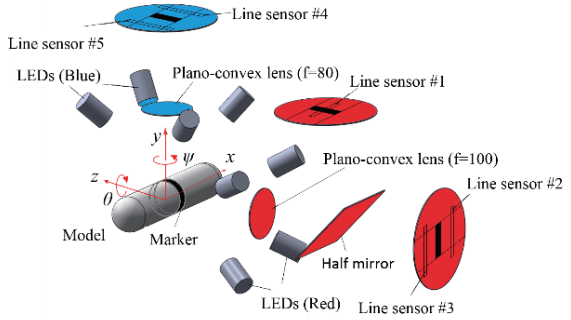


Fig.2 Configuration of the sensing system

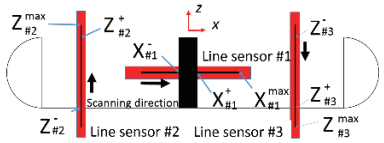


(a) Side line sensors of measurement section (x, z, θ)

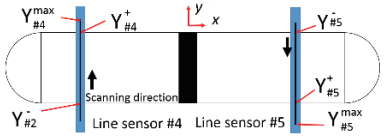


(b) Upper line sensors of measurement section (y, ψ)

Fig.3 The position of the edges and markers read by line sensors at surface of the model

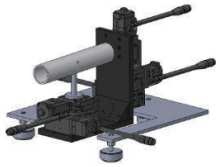

Fig.4 Configuration of the calibration device

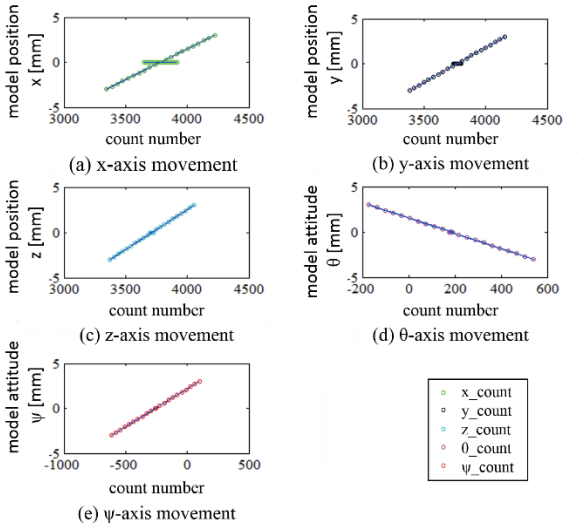


Fig.5 change of the count number for the model movement of each axis

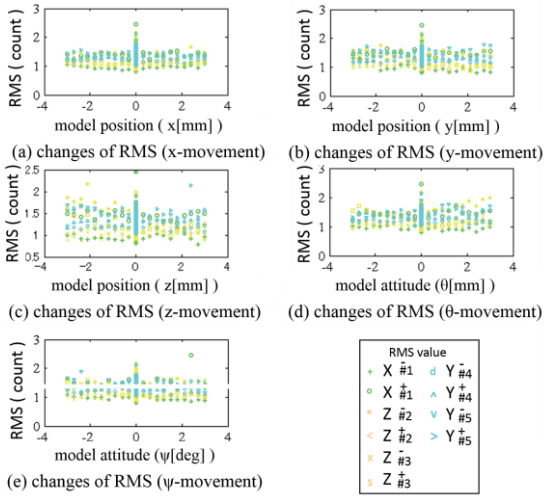


Fig.6 Change of RMS value for the model movement of each axis

Eleventh International Conference on Flow Dynamics
October 8-10, 2014, Sendai, Miyagi, Japan

# Experimental Study on Effects of Korteweg Force on Miscible Viscous Fingering

Fu Wei Quah, Yu Qi, Yuichiro Nagatsu
Department of Chemical Engineering, Tokyo University of Agriculture and Technology
2-24-16 Naka-cho, Koganei, Tokyo, 184-8588, Japan

**ABSTRACT**

We experimentally investigate effects of Korteweg force on miscible viscous fingering (VF). To do so, we prepare two liquid systems in which the viscosity contrast is the same but the effective interfacial tension (EIT). We confirm that the viscosity is the same in the both system but EIT is different by means of the measurement of viscosity and EIT. We performed VF experiment by using a Hele-Shaw cell. We find that the typical width of the fingers is larger for larger EIT system. This experimental result has a good agreement with recent numerical studies of the related issue.

## 1. Introduction

When a more viscous fluid is displaced by a less viscous one in porous media and in Hele-Shaw cells, the boundary of the two fluids becomes unstable and forms a finger-like pattern. This phenomenon is referred to as viscous fingering (VF). VF can be divided into two categories, namely immiscible VF and miscible VF depending on whether two fluids are immiscible or miscible. In both the cases, viscosity contrast between two fluids is the most important parameter. In the former case, effects of an interfacial tension between two immiscible fluids also have an important role on VF dynamics.

It is known that a stress acts in the region having a steep concentration gradient between the two miscible liquids, which mimics an interfacial tension acting on two immiscible fluids. The stress is referred to as Korteweg stress. Recently, it has been reported by numerical study that the Korteweg stress suppress instability of miscible viscous fingering [1].

If the miscible VF experiments are conducted by varying the concentration gradient between the two miscible liquids under the same viscosity contrast, it will be possible to experimentally investigate the effects of the Korteweg stress on miscible VF. The present study has developed an experimental system which enables such an investigation.

## 2. Experiment

### 2.1 Liquids

We need to prepare two liquid systems in which the viscosity contrast is the same but the effective interfacial tension (EIT). We used 99 wt% glycerin solution - pure water system which is expected to have larger EIT because of a high concentration gradient. In contrast, we used 8.2 wt% hydroxyethyl cellulose (HEC) solution - pure water system which is expected to have smaller EIT because of a low concentration gradient. We confirmed that the viscosity is the almost same as mentioned in detail.

### 2.2 Viscosity measurement

Viscosity of 99 wt% glycerin solution and 8.2 wt% HEC solution was measured by a rheometer (AR-G2, TA instruments). The viscosity measurement was done at room temperature.

Corresponding author: Yuichiro Nagatsu
*E-mail address*: nagatsu@cc.tuat.ac.jp

### 2.3 Measurement of EIT

We measured EIT by using Spinning Drop Tensiometer (SDT). The SDT is totally controlled by computer and calculate the EIT by the following equation,

$\sigma = \Delta\rho\omega^2 r^3/4$,

where $\sigma$ is EIT [mN/m], $\Delta\rho$ is the density difference between two liquids, $\omega$ is rate of rotation, and $r$ is the radius of the drop.

### 2.4 VF experiment

We used a radial Hele-Shaw cell (Fig.1) for VF experiments.

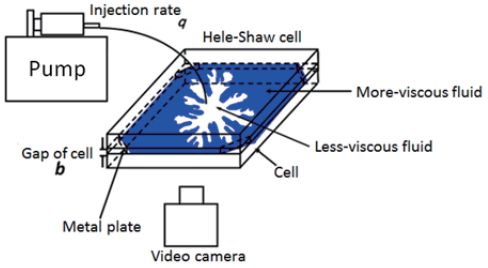


Fig. 1 VF experimental apparatus

## 3. Results and Discussion

### 3.1 Viscosity measurement

Fig. 2 shows the results of the viscosity measurement. 99 wt% glycerin solution is a Newtonian fluids. Thus, the viscosity is independent of shear rate. On the other hand, HEC is polymer solution. We, however, find that dependence of the viscosity of 8.2 wt% HEC solution on shear rate is very small. As a result, characteristics of viscosity of the both solution is the almost same.

### 3.2 Measurement of EIT

Figs. 3~5 show the results of EIT measurement when a rotational speed is 2000, 4000, and 6000 rpm, respectively. Figs. 3~5 shows that HEC-water system

possesses a lower EIT compared to glycerin-water system.

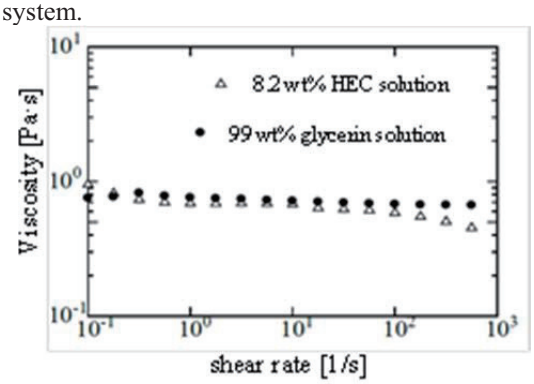


Fig.2 Viscosity measurement

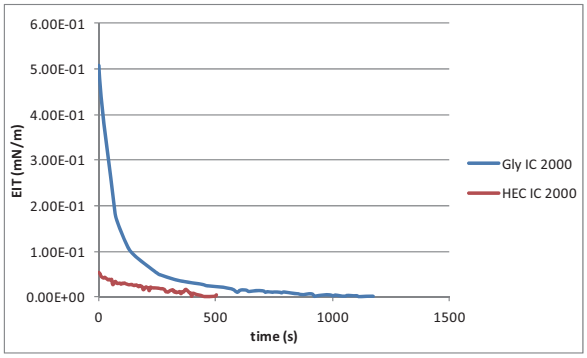


Fig.3 EIT measurement with 2000 rpm

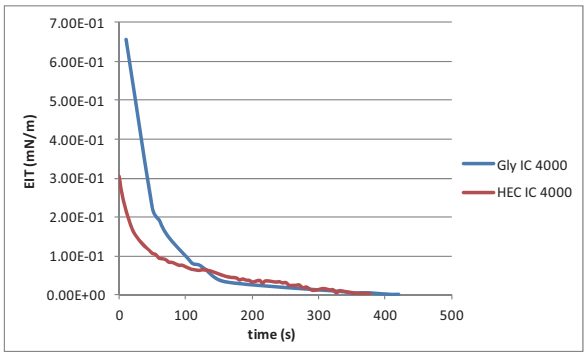


Fig.4 EIT measurement with 4000 rpm

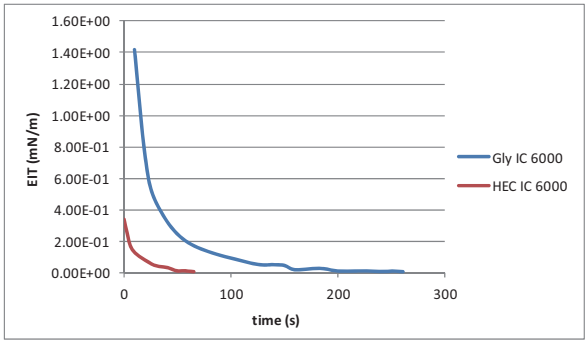


Fig.5 EIT measurement with 6000 rpm

### 3.3 VF experiment

Fig. 6 shows the results of VF experiment. VF pattern of (a) is more stable than (b) and we suggest that Korteweg Force (or EIT) plays a role in giving this result.

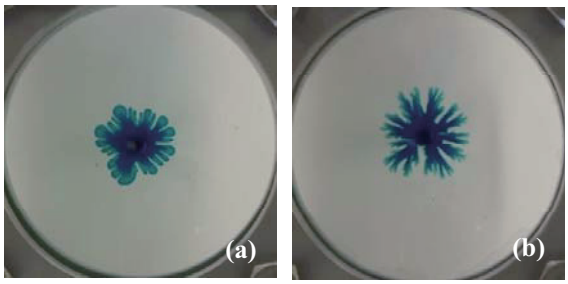


Fig.6 VF pattern at $t$ = 80 s (a) 99 wt% glycerin (b) 8.2 wt% HEC

## 4. Conclusion

By the EIT measurement, we proved that the system with higher concentration gradient possesses a higher Korteweg force. A system with higher concentration gradient (glycerin-water) gives a more stable VF pattern. These results show Korteweg force make VF instability more stable. This experimental result has a good agreement with recent numerical studies of the related issue [1].

### References

[1] S. Pramanik, M. Mishra, *Phys. Fluids*, 25 (2013) 074104

Eleventh International Conference on Flow Dynamics
October 8-10, 2014, Sendai, Miyagi, Japan

# Surrogate-Based Probability Density Function Modeling for Efficient Particle Filter

Ryota Kikuchi[1], Takashi Misaka[1] , Shigeru Obayashi[1]
[1]Institute of Fluid Science, Tohoku University
Katahira 2-1-1, Sendai, Miyagi, 980-8577, Japan

**ABSTRACT**

The efficient algorithm of a particle filter for data assimilation that uses the RBF networks (PF-RBF) is proposed and the capability is demonstrated by numerical experiments. RBF networks give the estimated values, which produce approximated particles from the estimated function. PF-RBF is able to provide the approximated particles from the estimated function, therefore, PF-RBF realizes a better estimation than PF. By using PF-RBF, it is confirmed that more accurate estimation is possible using a smaller number of particles.

## 1. Introduction

Data assimilation is employed to reduce the uncertainty of a numerical model by assimilating observations into the numerical simulation. Various data assimilation approaches have been applied in the fields of meteorological and oceanic researches [1], because they can determine unknown inputs, such as the boundary and initial conditions and other parameters by assimilating observations. There are several types of data assimilation. Even among them, we focus on sequential data assimilation method that is able to update the estimation of the numerical simulation at each observation time.

The possibility of solving various problems without the limitations of the observation and the simulation by the particle filter (PF) has attracted a great deal of attention [2]. PF approximates the probability density functions (PDFs) of a state vector by a large number of particles that are represented by each numerical simulation case. However, there is a problem of particle degeneration where the variety of each particle is lost by assimilating observation into simulation. The problem does not occur in other data assimilation methods. The problem of particle degeneration is solved by using a sufficiently large number of particles. However, the use of large number of particles requires massive computational resources, and is therefore impractical for applying high dimensional models. Therefore, there has been extensive research to reduce the number of particles while maintaining the accuracy. Unfortunately, these methods do not always guarantee reduction of the computational cost and stability of the estimation.

Here, we propose the efficient algorithm of PF that uses the surrogate model based on the radial basis function (RBF) networks [3]. RBF networks give the estimated values, which produce approximated particles from the estimated function. Therefore, a distribution of PDF is expressed properly by using the approximated particles, and the required number of particles can be reduced.

In this paper, we investigate the difference of the performance between PF and PF-RBF. Here the Lorenz 63 model [4] is employed for conducting the numerical experiment.

Corresponding author: Ryota Kikuchi
*E-mail address*:rkikuchi@edge.ifs.tohoku.ac.jp

## 2. Method

### 2.1 Particle Filter

The nonlinear state space model used is given as:

$$\boldsymbol{x}_t = f_t(\boldsymbol{x}_{t-1}, \mathbf{v}_t), \quad \boldsymbol{y}_t = h_t(\boldsymbol{x}_t, \mathbf{w}_t), \tag{1}$$

where the vectors $\boldsymbol{x}_t$ and $\boldsymbol{y}_t$ indicate the state vector of a system and observation values at time $t$, and the vectors $\boldsymbol{v}_t$ and $\boldsymbol{w}_t$ are the system noise and the observation noise, respectively. The operator $f_t$ represents the simulation model. The operator $h_t$ is the projection matrix from the model space to the observation space. Particle represents an approximation of probability density functions as follows:

$$p(\boldsymbol{x}_t|\boldsymbol{y}_{1:t-1}) \cong \frac{1}{N}\sum_{i=1}^{N} \delta\left(\boldsymbol{x}_t - \boldsymbol{x}_{t|t-1}^{(i)}\right), \tag{2}$$

$$p(\boldsymbol{x}_t|\boldsymbol{y}_{1:t}) \cong \frac{1}{N}\sum_{i=1}^{N} \delta\left(\boldsymbol{x}_t - \boldsymbol{x}_{t|t}^{(i)}\right), \tag{3}$$

where $\left\{\boldsymbol{x}_{t|t-1}^{(i)}\right\}_{i=1}^{N}$ is the ensemble of $\boldsymbol{x}_{t|t-1}^{(i)}$, $y_{1:t} = \{y_1, y_2, \cdots, y_t\}$ represents the observation values, and $N$ is the number of particles. $p(\boldsymbol{x}_t|\boldsymbol{y}_{1:t-1})$ is predictive PDFs, which is obtained from each particle of the forecast ensemble $\boldsymbol{x}_{t|t-1}^{(i)} = f_t\left(\boldsymbol{x}_{t-1|t-1}^{(i)}, v_t\right)$. The filtered PDFs $p(\boldsymbol{x}_t|\boldsymbol{y}_{1:t})$ are obtained from $p(\boldsymbol{x}_t|\boldsymbol{y}_{1:t-1})$ and the observations $\boldsymbol{y}_t$ by using Bayes' theorem. The procedures of PF consist of two steps, the prediction and the filtering steps, which are repeated alternatively.

### 2.2 RBF networks

This study employs RBF networks to obtain the approximated particles from the estimated function. Estimated function $\hat{y}_{RBF}(\mathbf{x})$ is expressed as follows:

$$\widehat{\boldsymbol{y}}_{RBF}(\boldsymbol{x}) = w_0 + \sum_{i=1}^{n} w_i h_i(\boldsymbol{x}), \tag{4}$$

where $w_0$ is the mean value of sample points, $w_i$ is the weight of the $i$-th basis function, $h_i(\mathbf{x})$, and the number of basis functions is the same as the number of sample points, $n$. In general, $h_i(\mathbf{x})$ is expressed as

$$h_i(\boldsymbol{x}) = exp\left(\frac{\left\|\boldsymbol{x} - \mathbf{c}^i\right\|}{r_i}\right)^2, \tag{5}$$

where $\varphi$ represents the function used, $\mathbf{c}^i$ is the center, and $r_i$ is the width (design variables should be normalized). In this study, the Gaussian function $\varphi(z) = \exp(-z^2)$ is used and $\mathbf{c}^i$ is placed at the sample

point, $\mathbf{c}^i = \mathbf{x}^i$. The value of $r_i$ controls the superposition of basis functions and must be tuned.

$$E = \sum_{i=1}^{n} \left( y(\mathbf{x}^i) - \hat{y}_{RBF}(\mathbf{x}^i) \right)^2 + \sum_{i=1}^{n} \lambda_i w_i^2 \qquad (6)$$

where $\lambda_i$ is a regularization parameter of $w_i$. In this study, each basis function has the same width and regularization parameter ($r$ and $\lambda$) which are determined by minimizing leave-one-out cross-validation (LOOCV) using a genetic algorithm.

In RBF networks, design variables in PF-RBF are realization values of the particles immediately after data assimilation and objective functions are defined by the value of the particles just before data assimilation. Therefore, the predictive PDFs are constructed by sampling from the estimated function values of RBF.

## 3. Results and Discussion

We use the Lorenz 63 model in the numerical experiment to investigate the performance of PF-RBF. Time integration of the Lorenz 63 model is performed by the fourth-order Runge-Kutta method, and one time step size is set to be 0.01. As for the observations, all of the components of the Lorenz 63 model are used every 20 time step by PF and PF-RBF. Details of data assimilation setting are described in Ref. 2.

First, we perform the numerical experiment that uses the particles of 32 in PF and PF-RBF. PF-RBF generates the estimated function from RBF, and the approximated particles of 1024 are sampled from the estimated function. Figure 1 shows the result of x-component of the Lorenz 63 model estimated by PF and PF-RBF. In Fig. 1, the estimated value of PF deviates considerably from the true value. On the other hand, it is confirmed that PF-RBF is able to estimate correctly in comparison of PF.

Next, we perform the numerical experiment that changes the number of particles in PF and PF-RBF. In PF-RBF, the number of approximated particles is 1024 in all cases. Figure 2 shows the root mean square error (RMSE) of all components between the PF/PF-RBF estimations and the true values over 50,000 time steps. With the number of particles from 16 to 128, it is confirmed that the estimate accuracy of PF-RBF are superior in comparison of that of PF. In other cases, the estimation accuracy of PF-RBF is similar to that of PF.

## 4. Concluding Remarks

An efficient algorithm of PF that uses the RBF networks (PF-RBF) was proposed. The proposed method reproduces the approximated particles by the surrogate model. The capability of the proposed method was investigated by numerical experiments employing the Lorenz 63 model.

PF-RBF was able to provide the approximated particles from the estimated function. Therefore, PF-RBF realizes a better estimation than PF, because the PDF of PF-RBF was generated adequately. With the number of particles from 16 to 128, it was possible to greatly improve the prediction accuracy. By using PF-RBF, it was confirmed that more accurate estimation was possible using a small number of particles.

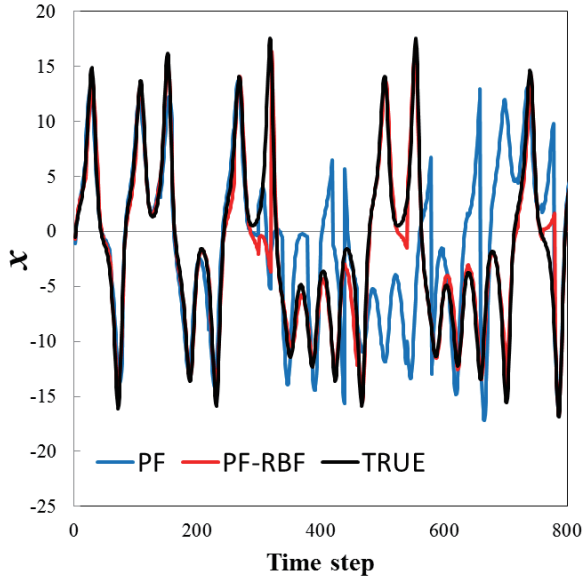


Fig. 1 A model state obtained by PF and PF-RBF from time step 0 to time step 800 for the $x$-component.

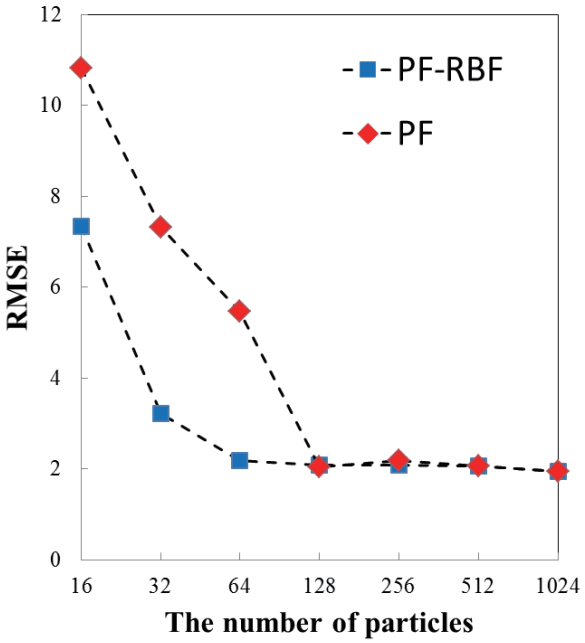


Fig. 2 RMSE of PF and PF-RBF against the true state over 50,000 time steps.

## References

[1] W. A. Lahoz, Q. Errera, R. Swinbank, D. Fonteyn, *Atmospheric Chemistry and Physics*, 7 (2007) 5745-5773.

[2] S. Nakano, G. Ueno, T. Higuchi, *Nonlinear Processes in Geophysics*, 14 (2007) 395-408.

[3] M. J. L. Orr, *Tech. Report*, Edinburgh University (1996).

[4] E. N. Lorenz, *Journal of the Atmospheric Sciences*, 20 (1963) 130-141.

# CS1: The Second International Workshop on Fluid and Material Sciences in Cooperation between Tohoku University and KTH

Eleventh International Conference on Flow Dynamics
October 8-10, 2014, Sendai, Miyagi, Japan

# Turbulent Channel Flow of Suspensions of Neutrally-Buoyant Particles

Francesco Picano[1], Luca Brandt[1]
[1] Linné FLOW Centre and SeRC, Royal Institute of Technology KTH
100 44 Stockholm, Sweden

**ABSTRACT**

The present study investigates the turbulent flow of a Newtonian fluid laden with solid neutrally-buoyant spheres at relatively high volume fractions in a plane channel. The results show that the mean velocity profiles are significantly altered by the presence of a solid phase with a decrease of the von Karman constant in the log-law while the overall drag is found to increase with the volume fraction. At the highest volume fraction here investigated, the velocity fluctuations and the Reynolds shear stress decrease.

## 1. Introduction

Fluids with a suspended solid phase frequently occur in environmental processes and in industrial applications. Sometimes laminar flow conditions take place as in magmatic flows, but often turbulent regimes appear as in the sediment transport in rivers. In industrial processes, the flow is usually turbulent to achieve high flow rates. When the suspended phase is not that dilute, its effect on the flow characteristics is not negligible.

In this context, many studies dealt with the rheological properties of laminar suspensions from the dilute to the dense cases, see e.g. [1]. It is well known that the presence of particles induces an increase of the effective viscosity of the suspension [2] and may generate normal stress differences in the denser cases. Indeed, it has been observed that, at high shear rates and fixed volume fraction, the viscosity may increase with the shear rate, i.e. the so-called shear-thickening [2-3].

Turbulent and transitional flows are usually characterized by field of shear rate that intermittently fluctuates in space and time. This feature, in combination with the peculiar rheological features of semi-dilute/dense suspensions, lead to new effects in these chaotic flow regimes. As an example, it has been found in pipe flow [4] that, for relatively large particles, the critical Reynolds number at which transition to turbulence occurs, cannot be simply rescaled considering the increase of the effective viscosity due to the presence of the solid phase.

The aim of the present work is to understand how the presence of a solid particulate phase at high volume fraction alters the turbulence features in channels flows. The turbulent drag appears to increase with the volume fraction, but no simple rescaling in terms of effective viscosity has been found. As discussed below, we document a deep change in the structure of the turbulence that already strongly alters the mean flow profile.

## 2. Method

Direct numerical simulations have been performed by using an algorithm that fully describes the coupling between the solid and fluid phases.

Corresponding author: Luca Brandt
*E-mail address*: luca@mech.kth.se

The incompressible Navier-Stokes equations are discretized by second order finite differences on a staggered mesh. The particles are evolved by a Lagrangian algorithm that solves the linear and angular momentum equations. The coupling between the two phases is directly achieved by using an Immersed Boundary Method. Lubrication models are also used to correctly reproduce the interaction between particles when their gap distance is smaller than the mesh size. The code was fully validated against several test cases, see [5] for more details.

Simulations of turbulent channel flow were performed in a domain of length 6h, 2h and 3h in the streamwise, wall-normal and spanwise directions, respectively. Periodic boundary conditions are enforced in the streamwise and spanwise directions with no-slip velocity at the wall. The bulk velocity $U_0$ is kept constant by adjusting the pressure gradient; fix the bulk Reynolds number $Re_h = U_0 h/\nu = 2650$ (with $\nu$ the kinematic viscosity). The domain is discretized by a cubic mesh with 864x288x432 points in the streamwise, wall-normal and spanwise directions. We study non-Brownian spherical particles with same density as the fluid with the particle radius 1/18 of the channel half-width. Three different volume fractions, $\phi$= 0.05; 0.1; 0.2, are considered.

## 3. Results and Discussion

The mean fluid velocity profiles are shown in figure 1. In general, the mean velocity more closely resembles the laminar parabolic profile when increasing the volume fraction: the velocity increases in the centre of the channel at higher volume fractions, whereas it decreases near the wall. The higher the volume fraction the more intense this effect is. The velocity profiles are scaled in inner units in the log-lin scale, using the friction velocity and viscous length scale. The progressive decrease of the profiles with the volume fraction indicates that the overall drag increases. Analysing the flow in terms of the canonical classification of wall turbulence, we can still recognize for all cases a region where the mean profile follows a log-law, enabling us to fit the von Karman constant and the additive coefficient B. Interestingly, the friction Reynolds number computed from the simulation data differs from what can be estimated using the rheological

properties of the suspension, that is using the relative viscosity of the suspension.

To analyse the solid phase behaviour, we report the mean local volume fraction in figure 2. The mean local volume fraction shows a first local maximum around y=0.06-0.1, a value slightly larger than a particle radius (y=1/18). Increasing the bulk volume fraction the intensity of the peak grows, while a local minimum appears at y=h/9. As also observed in dense laminar regimes, a particle layer forms at the wall and becomes more intense when increasing the bulk volume fraction. It should be noted however that these near-wall maxima are smaller or similar to the bulk concentration, hence they are not related to the turbophoretic drift typically observed in dilute suspensions when particles are heavier than the fluid. Instead, these near-wall layers are induced by the planar symmetry of wall and the excluded finite volume of the solid spheres. We also note that solid and fluid phases flow with the same mean velocity across the whole channel with the exception of the first particle layer near the wall, where particles have a mean velocity larger than the surrounding fluid.

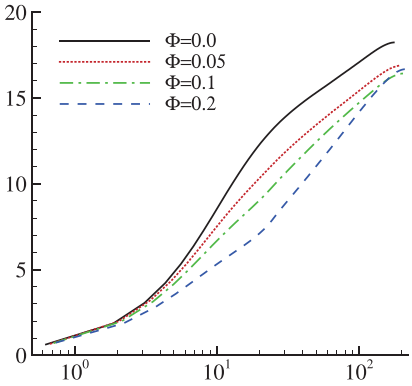


Fig. 1 Mean fluid velocity profiles for the different volume fractions under investigation in inner units, $U_f^+=U_f/U^*$ vs $y^+=y/\delta^*$

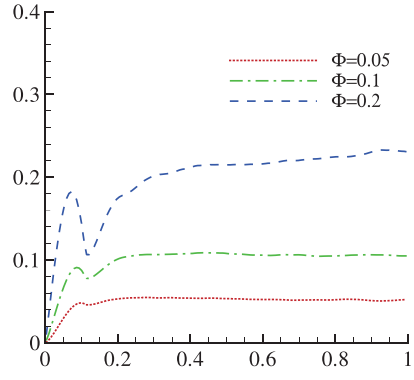


Fig. 2 Particle statistics: mean local volume fraction ϕ vs y/h for the volume fractions under investigation.

## 4. Concluding Remarks

We report data from the numerical simulations of turbulent channel flow laden with finite-size particles at high volume fractions. The finite-size particles interact with the turbulent motions altering the near-wall turbulence regeneration process. For the two lowest volume fractions considered, $\Phi<0.1$, we still observe the classic behaviour of near-wall turbulence, modulated however by the particle presence. At $\Phi = 0.2$ the solid phase is so dense that several aspects of turbulent wall flows are lost: the mean velocity profile is strongly altered, the turbulent fluctuations decrease, the velocity auto-correlations show streamwise elongated structures twice as large as in single-phase channel flows and the absence of a negative correlation of the wall-normal velocity, in addition to a more isotropic distribution of the velocity fluctuations.

The law of the wall is modified by the presence of a solid phase but can still be recognized at the Reynolds number of our simulations for all the volume fractions investigated. The von Karman and additive constants, k and B, assume therefore different values. In particular, increasing the volume fraction we report a reduction of k, increase of the slope, and a strong decrease of B, increased near-wall dissipation. The reduction of k usually denotes turbulent drag reduction. These results suggest that further increasing the Reynolds number while keeping constant the particle size in inner units may lead to an overall drag reduction in dense cases as those studied here.

For the final contribution, we shall evaluate the streamwise momentum balance for the flows under investigations and show that the additional stress due to the presence of the particles becomes more and more relevant when increasing the particle volume fraction. As expected the Reynolds transport term dominates at zero and low ϕ□□while at ϕ = 0.2 the particle stress becomes of the same order of magnitude.

*Acknowledgements*: This work was supported by the European Research Council Grant No. ERC-2013 -CoG-616186, TRITOS. Computer time is provided by SNIC (Swedish National Infrastructure for Computing)

## References

[1] É. Guazzelli and J.F Morris. *A Physical Introduction to Suspension Dynamics.* Cambridge Univ Press, (2011).

[2] J.J. Stickel and R.L. Powell. *Annu. Rev. Fluid Mech.*, 37 (2005) 129–149.

[3] F. Picano, W.-P. Breugem, D. Mitra and L. Brandt, *Phys. Rev. Lett.*, 111, (2013) 098302.

[4] J.-P. Matas, J. F. Morris, and É. Guazzelli. *Phys. Rev. Lett.*, 90, (2003) 014501.

[5] W.-P. Breugem. *J. Comp. Phys.*, 231 (2012) 4469 – 4498.

Eleventh International Conference on Flow Dynamics
October 8-10, 2014, Sendai, Miyagi, Japan

# Cavity Noise Suppression by Placing a Small Bar on the Cavity Wall

Yu Fukunishi[1], Yoichiro Nishi[1], Yu Nishio[1] and Seiichiro Izawa[1]
[1]Tohoku University
6-6-01 Aramaki-Aoba, Aoba-ku, Sendai, Miyagi, 980-8579, Japan

**ABSTRACT**

Experimental and numerical studies are performed to investigate the feasibility to suppress the noise emitted from a separating flow over a cavity using a small bar on the cavity wall. Two types of cavity flows, shallow and deep, are studied. For noise reduction in the shallow cavity case, the most effective location to place a small bar is found to be the bottom of the cavity, while in the deep cavity case, it is the downstream-side cavity wall. In both cases, the small bar induces flow separations which affect the vortex structures in the shear layer over the cavity.

## 1. Introduction

Flows past open cavities induce self-sustained oscillations, often accompanying acoustic resonances. Such an interaction between a separating shear layer and an acoustic resonator is utilized in music instruments such as flutes and pipe organs, however, from an engineering point of view, periodic and intense acoustic vibrations of the cavity flows are major problems and may also lead to dangerous structural fatigues.

A number of methods have been proposed to control the cavity flows, some active and some passive. Cattafesta and Sheplak [1] provided a review of fundamentals of actuators including their advantages and drawbacks. For the passive control methods, for example, Levasseur et al. [2] investigated the influence of a rod and a spoiler located in the upstream boundary layer on the growth of downstream shear layer.

The series of experiments for noise control carried out by our group, both active and passive, are overviewed in Izawa [3]. The present work focuses on the passive control method using a small rod placed at the wall of a cavity. The relation between the separating shear flow and the recirculating flow inside the cavity is studied both experimentally and numerically.

## 2. Experimental and Numerical Methods

The experiments were carried out using a wind tunnel of the Institute of Fluid Science (IFS), Tohoku University. It has an octagonal cross-section nozzle of 121.36 mm on a one side and an open test section of 911 mm in length. The freestream velocity $U$ was set to 26 m/s, where the turbulence level in the freestream was about 0.5 % of the freestream velocity at the test section.

Figure 1 shows the model with a deep cavity used in the experiment. The model was horizontally mounted in the test section. The trailing edge was slightly tilted upward to prevent a flow separation at the leading edge. The model was 750 mm long and 250 mm wide. The cavity of 50 mm in streamwise length was 300 mm downstream of the leading edge. The depth was 27.5 mm for the shallow cavity, 128 mm for the deep cavity model. The origin of coordinate system is at the center of the upstream edge of the cavity, where $x$, $y$ and $z$ axes denote the streamwise, the wall-normal and the spanwise directions, respectively. A rectangular bar of 250 mm in length was placed at various locations attached to the walls of the cavity, parallel to either the upstream and downstream edges. The dimensions of the square cross section of the rectangular bar were 0.5 mm × 0.5 mm or 2 mm × 2 mm. The noise was measured 700 mm above the cavity using a condenser microphone. A single hotwire probe was used to measure the flow field, and ensemble averaged flow fields were obtained.

Three-dimensional numerical simulations were also carried out under the same conditions as the experiments. The incompressible Navier-Stokes equations were solved by a fractional step method together with a multi-directional scheme. The convection term was discretized by the third-order upwind scheme and the second-order central difference scheme was used for the other terms. The time integration was given by the second-order

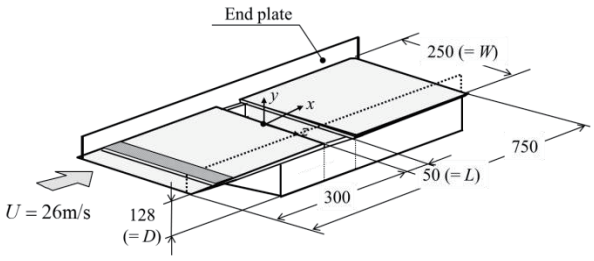


Fig. 1 Model for deep cavity experiment.

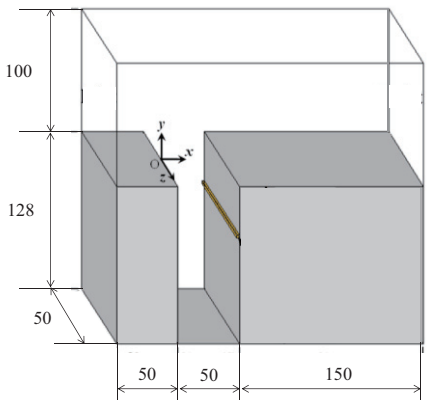


Fig. 2 Computational domain for deep cavity simulation.

Corresponding author: Yu Fukunishi
*E-mail address*: fushi@fluid.mech.tohoku.ac.jp

Adams-Bashforth method for the convection term and the second-order Crank-Nicolson method for the viscous term.

Figure 2 shows the schematic view of the computational domain when a square bar of 2 mm on a side was placed on the downstream sidewall. In the computations, the origin of the coordinate system is at the upstream edge of the cavity. The domain corresponds to $x$ = -50 mm ~ 200 mm, $y$ = -128 mm ~ 100 mm and $z$ = -25 mm ~ 25 mm. The Blasius velocity profile was given at the inlet and the Neumann condition was used at the outlet. The velocity at the upper boundary of the computational domain was fixed to the freestream velocity. The no-slip condition was given on the wall surfaces. Periodic boundary condition was used in the spanwise direction. The grids were concentrated near the wall and at the shear layer. The number of grid points was 181×211×81 in total, including 88×146×81 points inside the cavity. The freestream velocity $U$ was assumed to be 26 m/s, which was same as the experiments. The thickness of upstream laminar boundary layer $\delta$ at the inlet was 2.4 mm. The Reynolds number defined by $Re = UL/\nu$ was 85,979.

## 3. Results and Discussion

Figure 3 shows the variation of the dominant peak level of the cavity noise measured in the deep cavity experiment when the location of the bar was changed. The smaller square bar of 0.5 mm had almost no effect on the cavity noise, while the square bar of 2 mm on the downstream sidewall(DS) reduced the cavity noise. It is found that bar at $y/D$ = -0.2 ~ 0.4 on the downstream sidewall reduced the cavity noise by 20 dB, or the peak level was reduced to half. The square bar on the upstream sidewall(US) increased the sound.

For the shallow cavity case, the small bar in the cavity bottom floor efficiently reduced the noise.

The results of numerical simulations are shown in Fig. 4. The figure shows the isosurface of the rms velocity fluctuations with and without a bar on the sidewalls. The agreement between the experiments and the simulations was satisfactory in most cases. For the case without the square bar, the region where the velocity fluctuation is high coincides with the area where the vorticity is high, which is the main shear layer over the cavity. A part of the shear layer can be found traveling downward along the downstream sidewall of the cavity. This way, the circulation is supplied into the cavity, which maintains the large recirculating flow around the center of the cavity. When the bar was put on the downstream side, the downward moving flow separated from the wall at the bar location, $y/D$ = -0.31. The large circulating flow inside the cavity changed its size and location. The circulating pattern became more compact and its location became closer to the shear layer. It can be assumed that the interaction between the two may have increased. In this case, the rolled-up vortices in the shear layer occasionally passed above the downstream edge of the cavity without colliding to it. This phenomenon should weaken the feedback loop reducing the noise. However, details of the mechanism are yet to be studied.

## 4. Concluding Remarks

Experimental and numerical studies were carried out to investigate the effect of a small bar on the cavity wall to the aerodynamic noise generation. In the shallow cavity case, the bottom of the cavity was found to be the best location to place a small bar, while in the deep cavity case, it was the downstream-side cavity wall. In both cases, the small bar induced flow separations which affected the vortex structures in the shear layer over the cavity. Further investigation is needed to find out the detailed mechanism of the phenomena.

## References


[1] L. N. Cattafesta, M. Sheplak, *Ann. Rev. Fluid Mech.* 43(2011) 247-272.

[2] V. Levasseur, P. Sagaut, M. Mallet, F.R.S. Chalot, *J. Fluids and Structures,* 24 (2008) 1204-1215.

[3] S. Izawa, *Wind Tunnels and Exp. Fluid Dyn. Res., InTech.* 17 (2011) 369-394.


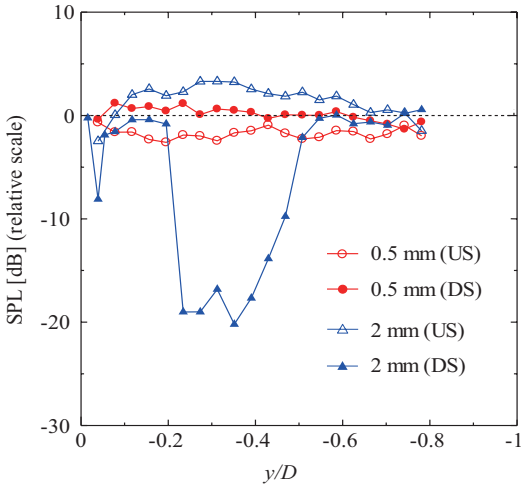


Fig. 3 Change in sound peak level by square bar.

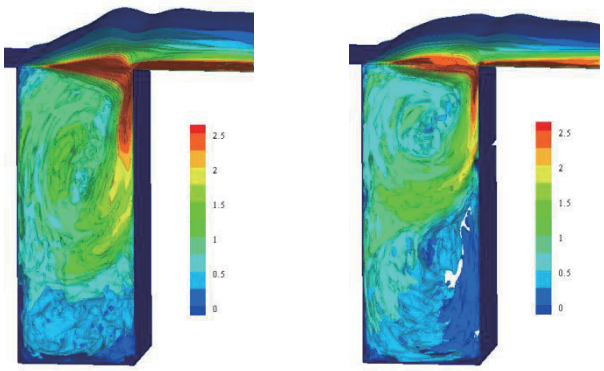

(a) Without bar (b) On downstream sidewall

Fig. 4 Isosurface of rms values of velocity fluctuations with/without a 2 mm square bar at $y/D$ = -0.31.

Eleventh International Conference on Flow Dynamics
October 8-10, 2014, Sendai, Miyagi, Japan

# Adaptive Control of Finite-Amplitude 3D Disturbances in 2D Boundary Layer Flows

Nicolo Fabbiane, Shervin Bagheri and Dan Henningson
Department of Mechanics
Linné FLOW Centre
Royal Institute of Technology KTH
Stockholm S-10044, Sweden

**ABSTRACT**

The control of growing three-dimensional (3D) disturbances in two-dimensional (2D) boundary-layer flows is addressed. An adaptive FXLMS compensator is used to process the information of the flow gathered from two rows of wall-bounded sensors. The FXLMS algorithm computes the control signal for a row of localized actuators in order to minimize the amplitude of the disturbances in the flow and eventually delay the transition from a laminar to a turbulent state. LES simulations are used to evaluate and analyze the performance of the controller.

## 1. Introduction

Being able to reduce the friction drag in boundary-layer flows may reduce the energy required for transportation, such as trains and airplanes. Since the laminar state is characterized by a smaller friction drag than the turbulent one, avoiding or delaying the laminar-turbulent transition will reduce the overall drag. In a low-turbulence environment, the transition is dominated by local instabilities of the flow -- Tollmien-Schlichting waves -- that exponentially grow, eventually breakdown and lead to turbulence [1].

We have previously used reactive flow-control techniques for skin-friction drag [2] using a model-based framework. The work by [2] however focused on controlling a single wave-packet and, although a clear transition to turbulence was observed, the disturbance environment is more complex in reality, where many 3D disturbances interact with each other. We model a distributed 3D disturbance field using a span-wise row of independent random forcings (figure 1). Each input has a localised spatial support inside the boundary layer. The inputs generate a complex 3D random pattern of disturbances, which is more realistic than previous studies.

## 2. Method

The control action is performed by a row of localized, equispaced actuators forcing the flow in the proximity of the wall. The action of each actuator is computed based on the measurements obtained by a row of sensors upstream of the actuators: for this set-up, the number of sensors is equal to the number of actuators and they are positioned aligned respect the flow direction (Fig.1).

We assume a linear control law and an equal number *(M)* of sensors and actuators. As a consequence, the number of transfer function between the *M* sensors and the *M* actuators is M^2. This imposes a computation constraint when M is large, which is the case when covering a large spanwise width with the controller.

Corresponding author: Shervin Bagheri
*E-mail address*: shervin@mech.kth.se

However, since the flow is spanwise homogeneous, a single transfer function (from all the sensors to one actuator) is replicated for each actuator, as shown in figure 2.

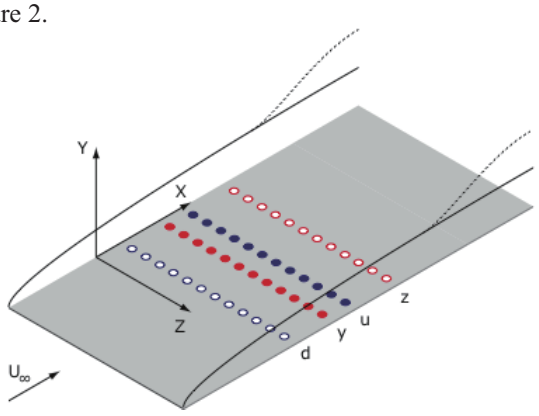


Fig. 1 Control configuration. Random 3D disturbances are generated by a row of localised independent forcings *d*. The measurements from the sensors *y* and *z* are used by an adaptive FXLMS algorithm to compute the actuation signal for the actuators *u* in order to reduce the amplitude of the detected disturbances.

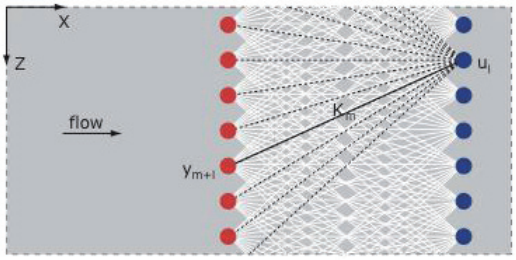


Fig. 2 Compensator structure. The action of each actuator is computed by filtering the signals from all the sensor via a linear filter *K*. An adaptive FXLMS filter is responsible of computing the response in order to maximize in real time the control performances measured by the error sensors.

This assumption reduces the number of transfer function to be designed from *M* squared to *M*. The design of the compensator consists in computing the

time-discrete convolution kernel $K$ [3]. In this work, an FXLMS algorithm is used to dynamically design the compensator: the algorithm uses the real-time measurements from the downstream sensors (*error sensor*) and it adapts the kernel $K$ in order to minimize the amplitude of the error signals

In order to analyze the control algorithm, LES simulations are performed using a pseudo-spectral code [4]. Periodicity is assumed in the spanwise and streamwise directions: a fringe-region is placed in the last 20% of the domain to enforce the periodicity in the streamwise direction. The flow is expanded over 1536 x 384 Fourier modes in the $XZ$ plane and 101 Chebyshev's polynomials in the wall-normal direction. All the spatial dimensions are non-dimensionalized by the boundary-layer displacement thickness in the beginning of the domain. The computational domain is 2000 units long, 30 units high and 250 units wide. The resulting Reynolds number is 1000. For the time-integration a Crank-Nicholson/Runge-Kutta method is used.

### 3. Results and Discussion

Inputs and outputs are configured as follows: *25* equispaced objects are considered for each row of sensors/actuators/disturbances, resulting in a spanwise separation $dZ = 10$. The disturbance inputs are fed by 25 independent white noise signals with variance 0.0003 each.

The transition delay performed by the compensator is shown in figure 3. The friction-trace of the TS-waves generated by the disturbance source in the beginning of the domain is visible in figure 3a-b, where the instantaneous skin friction fluctuations with respect to the laminar solution are reported. The disturbances exponentially grow while travelling downstream and lead to transition in the uncontrolled case. In figure 3b, it can be observed that the compensator is able to attenuate disturbances and move the transition point out of the computational box. In particular, friction fluctuations decay downstream the actuators, they reach minimum amplitude where error sensors are positioned and they grow again without triggering the transition. This can be observed also in figure 3c, where the spanwise average of the streamwise shear stress is shown. In conclusion, the employed adaptive control technique is able to delay the transition point in a realistic scenario, as shown by the results reported in this short overview.

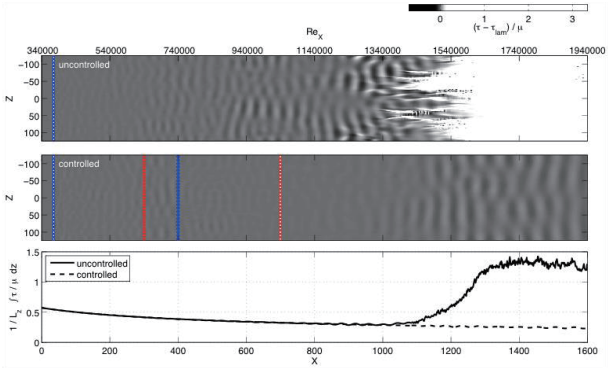

Fig. 3 Transition delay. In (a) and (b) the skin friction fluctuations respect to the laminar solution are shown at t = 4000. In the uncontrolled case (a) the disturbances grow and lead to transition to turbulent state in the end of the domain. In the controlled case (b), instead, the disturbances are attenuated by actuators action and transition is delayed. In (c), the mean skin friction with and without control is compared.

### References

[1] Saric, W. S., Reed, H. L. & Kerschen, E. J. *Ann. Rev. Fluid Mech.,* 34 (2002) 291–319.

[2] Semeraro, O., Bagheri, S., Brandt, L. & Henningson, D. S. *J. Fluid Mech.* 731 (2013) 288–311

[3] Aström, K. J. & Wittenmark, B. *Adaptive Control*, 2nd edn. Addison Wesley (1995).

[4] Chevalier, M., Schlatter, P., Lundbladh, A. & Henningson, D. S. *Tech. Rep. TRITA-MEK KTH Mechanics, Stockholm, Sweden, 07 (2007)*

Eleventh International Conference on Flow Dynamics
October 8-10, 2014, Sendai, Miyagi, Japan

# Spin Torque and Spin Hall Effect Nano-Oscillators

Randy. K. Dumas[1], Sohrab. R. Sani[2], Majid Mohseni[2] , Ezio Iacocca[1], Sunjae Chung[2], Philipp Dürrenfeld[1], Mohammad Haidar[1], Ahmad Awad[1], Mojtaba Ranjbar[1], and Johan Åkerman[1,2]
[1]Department of Physics, University of Gothenburg
Fysikgränd 3, 41296 Gothenburg, Sweden
[2]Materials and Nanophysics, School of ICT, Royal Institute of Technology KTH
Isafjordsgatan 22, 164 40 Kista, Sweden

**ABSTRACT**
We review our most recent results on nano-contact spin torque oscillators and spin Hall effect oscillators.

## 1. Introduction

Nano-contact spin torque oscillators (NC-STOs) are broadband microwave signal generators where a dc current enters an extended ferromagnetic layer through a constriction with dimensions on the order of 100 nm and generates a microwave response via the spin transfer torque (STT) effect [1]. Typically, the magnetically active portion of the extended layer consists of a ferromagnet/spacer/ferromagnet (FM/S/FM) trilayer pseudo spin valve (PSV) structure. One of the FM layers is considered "free" and easily susceptible to the influence of STT. The other FM layer is considered "fixed", either by pinning to an adjacent magnetic layer, an intrinsically high anisotropy, or simply by virtue of being thicker. The primary role of the fixed layer is to spin polarize the initially unpolarized electron current and act as a reference layer to create magnetoresistance.

NC-STOs are not only of fundamental interest but have particular potential as nanoscale wideband frequency-tunable and rapidly modulated microwave oscillators for telecommunication, vehicle radar, and microwave spectroscopy applications.

It was very recently shown how the spin Hall effect can also be used to sustain similar magnetodynamics in so-called spin Hall nano-oscillators (SHNOs) [2]. The SHNO has the additional experimental advantage that its active area is free to probe with e.g. optical means and hence allows for detailed microscopic studies of the generated spin wave modes.

In this work we review our most recent NC-STO and SHNO results and discuss where this highly active research field is heading.

## 2. Method

Fig.1 shows the basic device geometry of NC-STOs and SHNOs. All layers are sputtered onto 4" Si substrates terminated with a 1 um thick $SiO_2$ layer. The active magnetic layer is typically 4-5 nm thick and extends laterally several microns to avoid boundary effects on the fundamental spin wave (SW) modes.

Measurements are then performed in a custom probe station allowing for characterization under variable current and magnetic (angle and magnitude) fields. The induced magnetodynamics result in a time varying voltage over the device via the giant magnetoresistance (GMR) effect. This voltage is then amplified using low noise broadband microwave amplifiers and analyzed in the frequency domain using a spectrum analyzer or time domain using an oscilloscope.

Corresponding author: Johan Åkerman
*E-mail address*: akerman1@kth.se

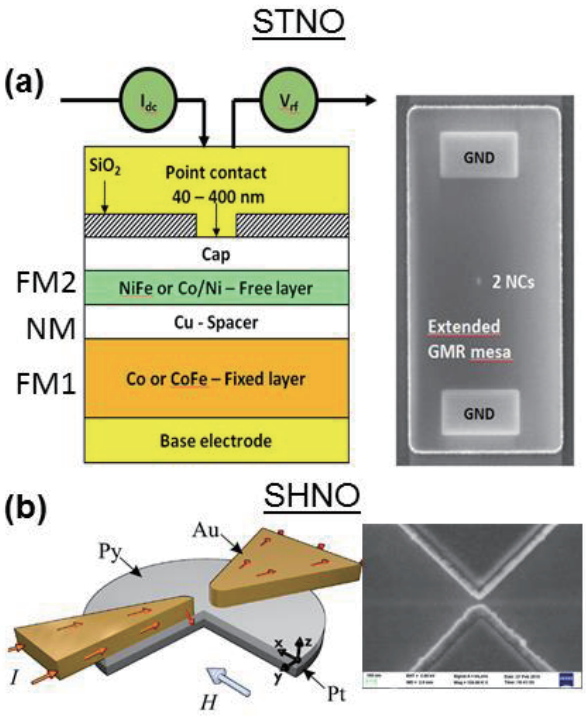


Fig. 1 Device Geometries (a) Nano-contact spin torque nano-oscillator (NC-STO) and (b) spin Hall nano-oscillator (SHNO).

## 3. Results and Discussion

The angular dependence of the generated NC-STO SW mode frequencies is shown in Fig. 2(a). For $\theta > 60^{o}$ only one frequency, significantly above the ferromagnetic resonance (FMR) frequency of the extended NiFe film, is found in the spectrum, corresponding to the propagating SW mode. However, for $\theta < 60^{o}$ a second, much weaker, signal begins to appear and lies well below the FMR frequency. This low frequency mode corresponds to the solitonic bullet mode which is stable only for angles less than the critical angle [3] namely $60^{o}$ for these experimental conditions. Interestingly, a very broad, signal ($f < 3$ GHz) accompanies the critical angle and is associated with the much slower mode-hopping

dynamics that are dominant for this range of angles. For $\theta < 45^{o}$ this low frequency mode hopping feature disappears, signaling the beginning of mode-coexistence. It is especially interesting to note that the angle at which the low frequency mode-hopping frequency disappears coincides with the angle at which the propagating mode frequency becomes less than the FMR frequency and therefore becomes localized. This localization of both modes at low angles is one of the key factors promoting mode-coexistence [4].

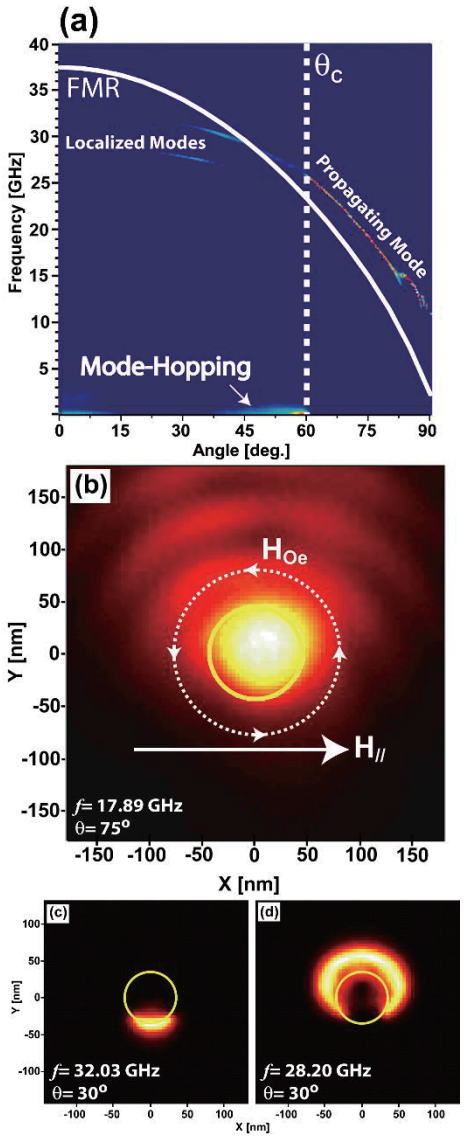


Fig. 2 Experimentally measured frequency response of an in-plane NC-STO with a NC diameter of 90 nm as a function of the applied field angle. The simulated spatial profiles of the (b) propagating mode (applied field angle of 75°), and (c, d) localized modes (applied field angle of 30°) highlight the critical role played by the Oersted field.

Dramatic changes in the magnetodynamical processes are found when the free layer is changed to a Co/Ni ML with perpendicular magnetic anisotropy (PMA).The measured microwave response of a PMA based NC-STO with a NC diameter of 105 nm in a perpendicularly applied field of 0.2 T is shown in Fig. 3(a). The observed behavior is consistent with a small precession FMR-like mode. In a moderate field of 0.8 T, Fig. 3(b), the oscillator behavior changes dramatically. As similarly shown in low fields the FMR-like mode is present at small drive currents. However, at a critical current of approximately -12.4 mA there is a dramatic drop in frequency and increase in oscillator power, both of which are consistent with the formation of a magnetic droplet soliton [5].

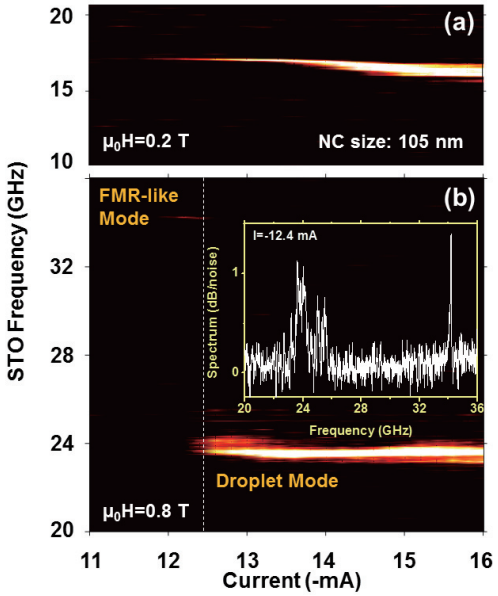


Fig 3 The frequency response of PMA based NC-STO with a NC diameter of 105 nm in perpendicularly applied fields of (a) 0.2 T and (b) 0.8 T is shown as a function of drive current. At low fields (a) only the FMR-like mode is found while droplet nucleation can occur at higher fields (b) at a critical current of approximately -12.4 mA.

### 3. Conclusions

Spin Torque Oscillators remain a vibrant research field with a wealth of dynamical phenomena that will continue to inspire theoretical and experimental work, and provide new insights into the magnetodynamics of these devices.

### References

[1] R. K. Dumas, *et al.*, IEEE Trans. Magn. 50, (2014) 4100107
[2] V. E. Demidov, *et al*., Nature Mater. 11, (2012) 1023
[3] S. Bonetti *et al*, Phys. Rev. Lett. 105, (2010) 217204
[4] R. K. Dumas, *et al.*, Phys. Rev. Lett. 110, (2013) 247202
[5] S. M. Mohseni, et al., Science 339, (2013) 1295

Eleventh International Conference on Flow Dynamics
October 8-10, 2014, Sendai, Miyagi, Japan

# Three-Terminal Spintronics Devices for Nonvolatile Memory and Logic

Shunsuke Fukami[1,2], Samik DuttaGupta[3], Chaoliang Zhang[3], Hideo Ohno[1,2,3,4]
[1]Center for Spintronics Integrated Systems, Tohoku Univ.
[2]Center for Innovative Integrated Electronic Systems, Tohoku Univ.
[3]Laboratory for Nanoelectronics and Spintronics, Research Institute of Electrical Communication, Tohoku Univ.
[4]WPI-Advanced Institute for Materials Research, Tohoku Univ.
2-1-1, Katahira, Aoba, Sendai, Miyagi 980-8577 Japan

**ABSTRACT**

Spintronics devices are expected to be a key enabler for future ultralow-power and high-performance memories and logic circuits. Three-terminal spintronics device can achieve high-speed and high-reliability operation owing to its cell circuit structure. We study a current-induced domain wall motion, which is used for the write operation in the three-terminal device, and discuss the operation speed, reliability, and scalability. We confirm that the domain wall motion device with a Co/Ni multilayer has promising potential from these aspects.

## 1. Introduction

In spintronics devices, digital information is stored as a magnetization direction in a ferromagnetic recording layer. Employing them instead of currently-used semiconductor-based devices, one can design ultralow-power and high-performance memories and logic circuits owing to their unique features such as scalability, *i.e.*, their size can be in principle reduced down to less than 10 nm, nonvolatility, *i.e.*, no power is needed to retain the information, and high endurance, *i.e.*, there is no limit of the number of read/write operation, and thus they have been intensively developed [1,2]. The spintronics devices fall into two categories: two-terminal device (Fig. 1(a)) and three-terminal device (Fig. 1(b)); in this paper we focus on the latter. We first describe the structure and characteristics of the three-terminal spintronics devices, in particular the devices utilizing current-induced magnetic domain wall (DW) motion. After that, we review our recent studies on the magnetic domain wall motion with a Co/Ni multilayer.

## 2. Three-Terminal Spintronics Devices

In Figs. 1(a) and (b), typical structure of two-terminal and three-terminal spintronics devices are depicted. The two-terminal cell consists of one magnetic tunnel junction (MTJ) and one cell transistor. It utilizes spin-transfer torque magnetization switching for the write operation. Since its cell size is relatively small, it can be used for large capacity memories like dynamic random access memories. On the other hand, the three-terminal cell consists of one MTJ and two cell transistors. For the write operation, it can utilize current-induced magnetic DW motion [3-5] or spin-orbit-torque-induced magnetization switching [6-8]. Since the read and write current paths are separated from each other at the cost of cell size, the three-terminal device makes high-speed and high-reliability operation possible, which are necessary to be applied to cache memories and registers [9].

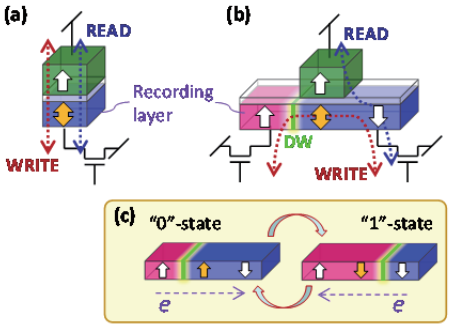


Fig. 1: Structures of (a) two-terminal and (b) three-terminal spintronics devices. (c) Magnetic configuration of recording layer of DW-motion device.

Figure 1(c) illustrates the magnetic configuration of recording layer of the three-terminal spintronics device with the current-induced DW motion. Bidirectional electric current drags a DW back and forth through the spin-transfer torque and thus changes the stored information. It was found that a Co/Ni multilayer with perpendicular easy axis is a promising material system for the realization of current-induced DW-motion [10,11]. For the practical use, ability to accurately control the position of DW within a few nanosecond and scalability down to deep sub-100 nm are required. In the following sections, we will show the experimental results regarding the DW depinning probability from a potential well by nanosecond current pulses and device size dependence of DW-motion and retention properties down to 20 nm.

## 3. Depinning Probability of Magnetic Domain Wall

We study the depinning probability of DW trapped in an artificially-prepared pinning site in a 160-nm-wide Co/Ni nanowire by the application of nanosecond current pulses with various current densities and durations [12]. The DW depinning is measured 100 or 10,000 times repeatedly for each pulse condition. Figure 2(a) shows the DW depinning probability as a function of current density and pulse duration. The critical current density is about $6.5\times10^{11}$ A/m$^2$ and it does not increase with respect to the pulse duration down to less than 2 ns. This indicates that one can reduce the pulse

Corresponding author: Shunsuke Fukami
*E-mail address*: s-fukami@csis.tohoku.ac.jp

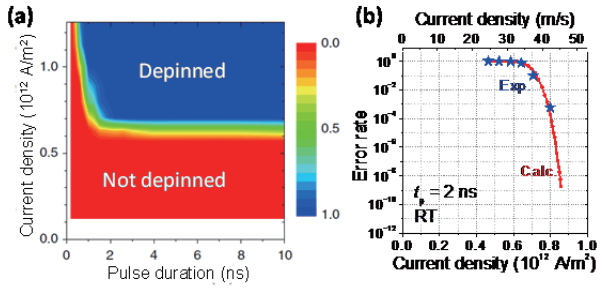


Fig. 2: (a) Depinning probability of DW as a function of current density and pulse duration. (b) Depinning error rate as a function of current density. Red curve denotes numerical calculation result.

duration down to less than 2 ns without the increase in the write current in the DW-motion device. Next we fix the pulse duration to 2 ns and measure the depinning error rate as a function of current density. As shown in Fig. 2(b), the error rate steeply decreases with respect to the current density above a certain threshold. In Fig. 2(b) the numerical calculation results in which thermal fluctuation of DW is considered are also shown. The calculation results agree well with the experimental result. The steep decrease of error rate indicates that the extremely small error rate, which is indispensable for logic applications, can be obtained by slightly increasing the current density above the threshold. We find that these promising properties are attributed to the mechanism of DW depinning where the adiabatic spin-transfer torque governs the dynamics. As described here, we confirm that the DW-motion device with Co/Ni multilayer has attractive properties in terms of high-speed and high-reliability operation.

## 4. Scalability of Domain Wall Motion Device

We also fabricate the DW-motion devices made of Co/Ni multilayer with various wire widths, and evaluate their write current, write time and retention property [13]. The write time is calculated from the DW-motion velocity and depinning time; the former is measured in actual devices and the latter is calculated numerically. The retention property, which is represented by the thermal stability factor $E/k_BT$ where $E$ is the energy barrier, $k_B$ the Boltzmann constant, and $T$ the absolute temperature, is evaluated by measuring the retention time under the application of dc magnetic field. Figure 3 shows the evaluated write current, write time, and thermal stability factor as functions of device size. Note here that the write current shown in Fig. 3(a) is not the critical current but the current by which one can obtain both the write time shown in Fig. 3(b) and the depinning error rate of less than $10^{-12}$. The write current and time linearly scale with the device size. This is quite a natural result since the cross section and length of the DW-motion wire linearly scales along with the device size. On the other hand, it is notable that the thermal stability factor does not decrease with decreasing the size. The required value for the thermal stability factor to ensure

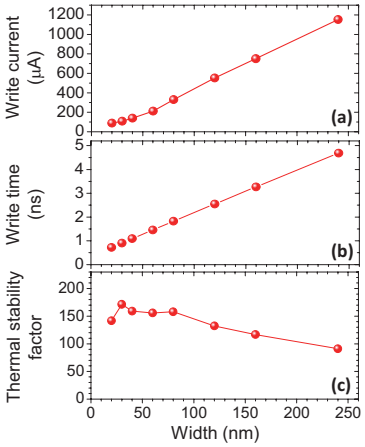


Fig. 3: (a) Write current, (b) write time, and (c) thermal stability factor as functions of device width.

10-years retention is more than about 70, which is satisfied for the whole range we study here. These results indicate an excellent scalability of the DW-motion device, *i.e.*, by reducing the device size, one can obtain low-power and high-speed write operation while maintaining sufficient retention property.

## 5. Concluding Remarks

In this paper, we describe the three-terminal spintronics device with current-induced DW motion and show experimental results regarding the depinning probability of DW and the scaling property of DW-motion and retention properties. We confirm that the DW-motion device has high capability in terms of operation speed and reliability, and scalability down to 20 nm.


## Acknowledgements

This work was supported by the FIRST program of JSPS, R&D Project for ICT Key Technology to Realize Future Society of MEXT, and the R&D Subsidiary Program for Promotion of Academia-industry Cooperation of METI.


## References


[1] H. Ohno et al., *in 2010 IEEE Int. Elect. Dev. Meeting (IEDM)*, (2010) 9.4.1.
[2] N. Sakimura et al., *in 2014 IEEE Int. Solid-State Cir. Conf. (ISSCC)*, (2014) 184.
[3] A. Yamaguchi et al., *Phys. Rev. Lett.*, 92, (2004) 077205.
[4] M. Yamanouchi et al., *Nature*, 428, (2004) 539.
[5] S. Fukami et al., *in 2009 Symp. on VLSI Tech.*, (2009) 230.
[6] I. M. Miron et al., *Nature*, 476, (2011) 189.
[7] L. Liu et al., *Science*, 336, (2012) 555.
[8] C. Zhang et al., *J. Appl. Phys.*, 115, (2014) 17C714.
[9] S. Fukami et al., *IEEE Trans. Magn.*, *in-press*.
[10] S. Fukami et al., *J. Appl. Phys.*, 103, (2008) 07E718.
[11] S. Fukami et al., *Appl. Phys. Lett.*, 95, (2009) 232504.
[12] S. Fukami et al., *Nat. Commun.*, 4, (2013) 2293.
[13] S. Fukami et al., *in 2013 IEEE Int. Elect. Dev. Meeting (IEDM)*, (2013) 3.5.1.

Eleventh International Conference on Flow Dynamics
October 8-10, 2014, Sendai, Miyagi, Japan

# Material Design and Crystal Growth of High Performance Scintillators and Their Applications

Akira Yoshikawa[1,2], Kei Kamada[2], Shunsuke Kurosawa[1,2] , Yuui Yokota[2] , Yuji Ohashi[1] , Martin Nikl[3]
[1] Institute for Materials Research (IMR), Tohoku University, Sendai 980-8577, Japan
[2] New Industry Creation Hatchery Center (NICHe), Tohoku University, Sendai, 980-8579, Japan
[3]Institute of Physics AC CR, Cukrovarnicka 10, 16253 Prague, Czech Republic

**ABSTRACT**

Ce: $\{Gd,RE\}_3(Ga,Al)_5O_{12}$ (RE=Y, Lu) (Ce:GAGG)single crystals shows high light yield and high energy resolution. Though the lattice constant, volume and emission wavelength changes linearly, LY has maxima at the specific ratio. This is explained as the result of suitable BGE. Psude-binary system $Gd_2O_3$ - $Al_2O_3$, $GdAlO_3$ (perovskite) is congruent, however, $Gd_3Al_5O_{12}$ (garnet) is incongruent. 2 inch diameter Ce:GAGG single crystal is available.

Czochralski growth of 2inch Ce: Ce:La-GPS crystals was succeeded. LY~42,000ph/MeV, ER~7% are obtained at the x=0.01, y=0.24. As it shows high temperature stability, Ce :La-GPS can be the promising scintilaltor for high temp. use.

## 1. Introduction

Scintillation detectors are used for detection of ionizing radiation such as X-rays, gamma rays or elementary particles. They consist of a scintillation material, which converts the energy of the ionizing radiation into visible or UV light, and a photodetector, which detects the emitted visible/UV scintillation light. Radiation detectors are used in X-ray computed tomography, positron emission tomography and other medical imaging techniques, high energy and nuclear physics applications, and natural resource surveys [1].

## 2. Development of high performance scintillators

### A) Ce:GAGG

Multicomponent garnet is the typical example. Recently, it is found that Ce: $\{Gd,RE\}_3(M,Al)_5O_{12}$ (RE=Y, Lu, M=Sc, Ga) single crystals shows high light yield and high energy resolution [2]. Thuogh the lattice constant, volume and emission wavelength changes linearly, LY has maxima at the specific ratio (Fig.1). The is explained as the result of suitable BGE. Tranport efficiency will be changed depending on the position between the botom of conduction band of the host lattice and the level of 5d of $Ce^{3+}$[3].

In order to investigate BGE, consideration of phase diagram is also very important. For example, in the psude-binary system $Gd_2O_3$ - $Al_2O_3$, $GdAlO_3$ (perovskite) is congruent, however, $Gd_3Al_5O_{12}$ (garnet) is incongruent. In order to get garnet phase as initial phase, either the dodecahedral site must be smaller or the octahedral one bigger.

The maximum emission wavelength of GAGG was 520 nm, which is in the high-detection efficiency region of Si detectors, such as photodiode, avalanche photodiode (APD) and gaiger mode APD. This emission is ascribed to the 5d–4f transition of $Ce^{3+}$, and the decay time was around 80-90 ns.

The light yield was characterized as 56,00ph/MeV. It is remarkably higher than that of LYSO, which is regarded as the best scintillator (Fig. 2).

Corresponding author: Akira Yoshikawa
*E-mail address*: yoshikawa@imr.tohoku.ac.jp

Using a GAGG scintillator, a novel dosimeter was The GAGG is especially advantageous for application in a Compton camera consisting of a Compton scatter part and a scattered gamma-ray absorber, because the angular resolution of a Compton camera depends on the energy resolution of the absorber. The scintillator could be used as the absorber due to its superior detection efficiency over semi-conductors. Additionally, due to the lack of an intrinsic background, a Compton camera mounted with a GAGG scintillator would obtain high quality images. Recently, a national project supported by JST has been started with Univ. of Tokyo, JAEA and Furukawa Co.Ltd., in order to develop a GAGG Compton camera. Pollution mapping in the Fukushima area could be conducted by a GAGG Compton camera mounted on an unmanned helicopter.

Fig.1 (a)GAGG single crystal grown by the CZ method. (b)GAGG mounted dosimeter “gamma spotter”.

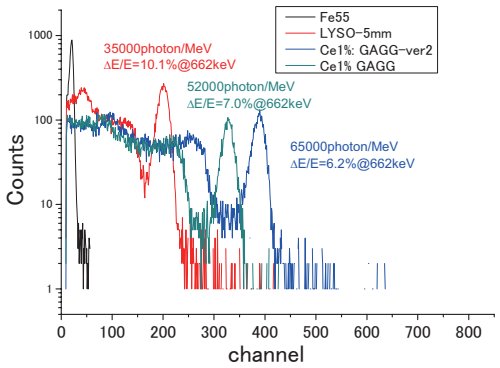


Fig.2. Pulse height spectra of GAGG and LYSO.

Though the light yield is high, LYSO shows higher timing resolution than that of GAGG. The reason is relatively long decay time in GAGG. Recently, we

found that the small amount of divarent co-doping accerarate decay time of GAGG. Favorable effects of $Mg^{2+}$ codoping are explained by creation of the stable $Ce^{4+}$ centers in the GAGG structure (Fig.3). Such centers create another fast radiative recombination pathway working in parallel with the classical mechanism based on the stable $Ce^{3+}$ centers. Such optimization strategy can be used also in other scintillation materials whenever the $Ce^{3+}$ scintillation spectrum does not overlap with charge transfer absorption of $Ce^{4+}$ centers. As a result, 39ns is obtained in the case of Ce:Mg:GAGG. This makes timing resolution of GGG shorter than that of LYSO. Therefore, the fast type GAGG can be the promising scintillator for positron emission tomography (PET) application.

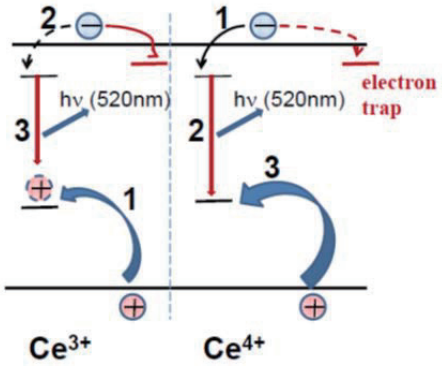


Fig. 3. Sketch of the scintillation mechanism at the stable $Ce^{3+}$ (left) and $Ce^{4+}$ (right) emission centers.

**B) Ce:La-GPS**

Recently, $(Gd,RE)_2Si_2O_7$ is also considered from similar point of view. $Gd_2Si_2O_7$ itself is incongruent. When larger cation such as La or Ce is partially substitute Gd, then it turned to be congruent. Scintillation performance is depend on the La concentration [4,5]. 2inch bulk Ce:La-GPS is shown in Fig.4.

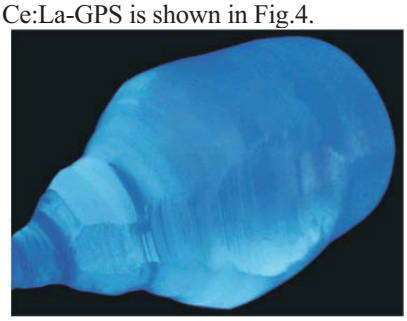

Fig.4 La-GPS single crystal grown by the CZ method.

In order to investigate high temperature stability, $Ce^{3+}$ nanosecond decay times temperature dependences for LPS:Ce and GPSLa48%:Ce are displayed in Fig. 5a and 5b, respectively and the latter dependence for the GPSLa48%:Ce is extended up to 700 K. The onset of nanosecond decay times shortening, regardless its origin, for all studied pyrosilicates lies well above room temperature around 380 K (LPS:Ce) and 440 K (Ce: La30%GPS and Ce: La48%GPS). In earlier studies the onset of this process in LPS:Ce was reported at 470 K [6] and 400 K [7]. The variation in reported values might be due to actual concentration of $Ce^{3+}$ in the crystals since the concentration quenching can effectively shift the onset temperature to lower values [8].

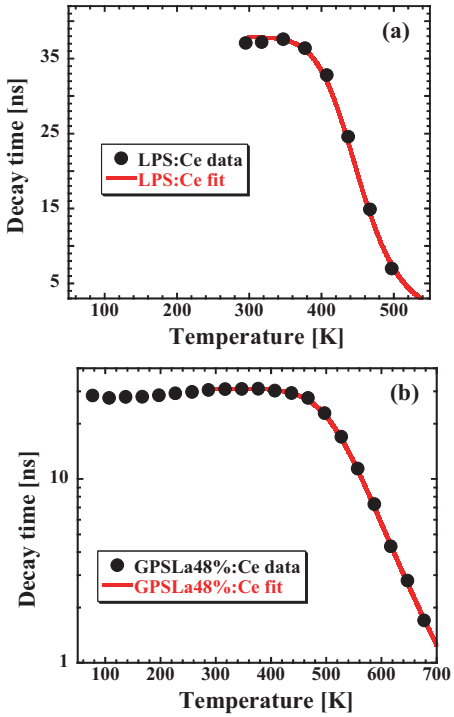


Fig. 5. Nanosecond decay time temperature dependence of the $Ce^{3+}$ emission in LPS (a) and GPSLa48%:Ce (b) ($\lambda_{ex}$ = 339 nm, $\lambda_{em}$ = 380 nm).

**3. Results and Discussion**

We study $Ce^{3+}$ luminescence and scintillation characteristics in novel, high performing host among the oxide single crystal scintillators. The light yield of GAGG was characterized as 56,00ph/MeV. It is remarkably higher than that of LYSO. We found Mg co-doping improved the timing resolution of GAGG. This suggests the potential of GAGG for PET application.

We observed higher quenching temperature of La-GPS. High scintillation efficiency, low afterglow and the onset of $Ce^{3+}$ excited state ionization appearing well above room temperature indicate a large potential of La-GPS in a high temp. scintillating applications.

**References**


[1] A. Yoshikawa, V. Chani, M. Nikl, ACTA PHYSICA POLONICA A 124 (2) (2013) 251-264

[2] K. Kamada, M. Nikl, A. Yoshikawa, et al. Cryst. Growth Des. 11, (2011) 4484-4490.

[3] M. Fasoli, A. Vedda, M. Nikl et al., Phys. Rev. B 84, (2011) 081102.

[4] A. Suzuki, S. Kurosawa, A. Yoshikawa et al., Appl. Phys. Express 5 (2012) 102601.

[5] S. Kurosawa, A. Suzuki, A. Yoshikawa et al., Nucl. Instr. & Methods Phys. Res. A 744 (2014) 30 – 34.

[6] L. Pidol, P. Dorenbos, C. W. E. van Eijk et al., J. Phys.: Condens. Matter 15 (2003) 2091–2102.

[7] H. Feng, D. Ding, H. Li, S. Lu, S. Pan, X. Chen, G. Ren, J. Alloys Comp. 509 (2011) 3855–3858.

[8] V. Bachmann, C. Ronda, A. Meijerink, Chem. Mater. 21 (2009) 2077–2084.

Eleventh International Conference on Flow Dynamics
October 8-10, 2014, Sendai, Miyagi, Japan

# Importance of Surface Structure for Dynamic Wetting

Jiayu Wang[1], Yoshinori Nakamura[1], Andreas Carlson[2], Feng Yue[1], Yuji Suzuki[1], Gustav Amberg[2],
Junichiro Shiomi[1,3], Minh Do-Quang[2],
[1]Department of Mechanical Engineering, The University of Tokyo,
7-3-1 Hongo, Bunkyo-ku, Tokyo 113-8656, Japan
[2]Department of Mechanics, Linné Flow Center,
Royal Institute of Technology KTH, S-100 44 Stockholm, Sweden.
[3]Japan Science and Technology Agency, CREST,
Chiyoda, Tokyo, 102-0075, Japan.

**ABSTRACT**

The importance of the nanoscopic and microscopic structure of the surface for dynamic wetting is studied using molecular dynamics, continuum simulations, and experiments. For nanoscopically rough surfaces with Lennard-Jones interactions, it is found that spreading is slowed down by elimination of the slip that is present on a perfectly flat (L-J) surface. For real liquids on $SiO_2$ it is found that the presence of micron-size structures slow down the spreading by increasing the contact line friction.

## 1. Introduction

Wetting phenomena are omnipresent in nature and play an important role in many engineering processes such as lubrication, spray printing, inkjet printing, etc. In addition to these classical applications we may add the recent interest in nano inkjet printing as a flexible and inexpensive technique to fabricate nanostructures. In all of these processes the dynamic wetting behavior comes in as a crucial phenomenon. A droplet wetting a flat surface is a representative case of such, where the high system symmetry allows us to probe the fundamental physics of wetting.

Although the capillary spreading of a drop on a dry substrate is well studied, understanding and describing the physical mechanisms that govern the dynamics remain challenging.

Several different mechanisms that determine the dynamic spreading have been proposed. In the Molecular Kinetic Theory [1] it is assumed that the dominant resistance to spreading is in the form of a localized contact line friction, which can be linked to atomistic properties of the system. In slow spreading approaching equilibrium, viscous dissipation in the bulk liquid may dominate [2]. It has also been found that under appropriate conditions the spreading may be analogous to droplet coalescence and that the surface then has a surprisingly small influence [3].

Our long term aim is to identify when and how the nanoscopic and microscopic properties of the surface and the fluid influence dynamic wetting.

## 2. Method

In this presentation we will use information from MD simulations, continuum simulations and experiments to show how the peculiarities of the surface may influence the spreading speed.

Corresponding author: Gustav Amberg
*E-mail address:* gustava@kth.se

In our MD simulations [4] we focus on the simplest possible molecules, i.e. a Lennard-Jones (L-J) fluid, with L-J interactions also between the solid substrate and the fluid molecules. The surface is either an atomistically flat crystalline surface, or one with a prescribed periodic shape.

We study the dynamics of spreading of partially wetting nano-droplets, see fig. 1, by combining molecular dynamics simulations and continuum phase field simulations. The phase field simulations account for all the relevant hydrodynamics, i.e. capillarity, inertia and viscous stresses. By coordinated continuum and molecular dynamics simulations, the macroscopic model parameters are extracted [5]. To avoid violating the no-slip condition, this method describes the movement of the contact line by a diffusive interfacial flux.

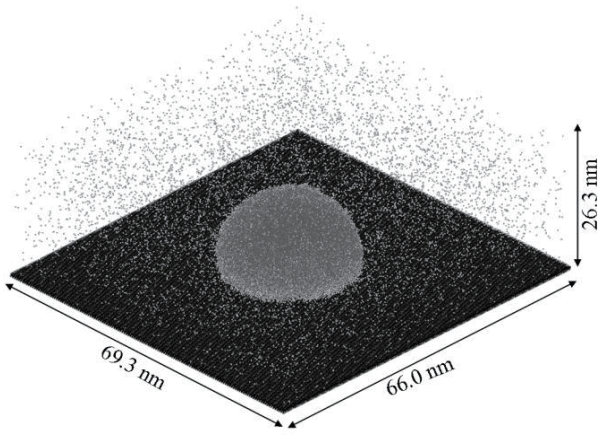


Fig. 1 Nanoscopic droplet studied using MD.

Droplet wetting experiments were performed on flat and microstructured surfaces. The microstructures are periodic arrays of pillars with square cross sections of side length $a$, spacing $b$, and height $h$, see fig. 2. The height of the pillars is kept constant at 1.6 $\mu$m while $a$

is varied from 0.5 to 5 $\mu$m, and $b$ from 1 to 45 $\mu$m. The surfaces of the flat and microstructured substrates are uniformly covered with native oxide layers. Wenzel wetting is realized by using a mixture of water and ethanol as working fluid, and the viscosity may be varied by adding glycerol. The initial droplet radius is fixed to 0.5 mm. The dynamic spreading of the droplet was captured by filming the evolution from the instant when the droplet is brought into contact with the substrate with a high speed camera through a microscope.

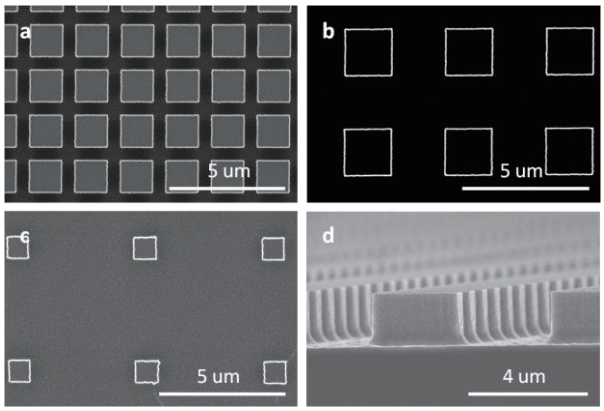


Fig. 2 Examples of microstructure geometries. (a) $b/a$=1/3, (b) $b/a$=1, (c) $b/a$=4, and (d) the side view of the pillars. Here, $a$ is the width of pillar and $b$ is the distance between the neighboring pillars.

### 3. Results and Discussion

For a Lennard-Jones fluid spreading on an atomically planar surface, the liquid slip at the solid substrate is found to be significant, and crucial for the motion of the contact line. Evaluation of the different contributions to the energy transfer shows that the liquid slip generates dissipation of the same order as the bulk viscous dissipation or the energy transfer to kinetic energy, and that the contact line friction is negligible.

To investigate the importance of nanoscale roughness we also performed MD simulations for a sinusoidally shaped substrate. It was found that the spreading scaled similarly as the spreading on flat surfaces, but was generally about 30% slower. A corresponding continuum simulation was found to give a spreading rate similar to that obtained with MD for the rough surface, if the slip length was reduced to zero, i.e. a no-slip condition. One possible interpretation of this is that the main effect of the nano-scale roughness is to destroy the order in the fluid that is associated with fluid slip.

The experiments on real surfaces show a somewhat different behavior. For spreading on a flat oxidized Si-surface the contact line friction is found to be significant. As shown in Fig. 3, spreading on the substrates with denser patterns tend to be slower, which indicates that the microstructures inhibit the spreading process. Further investigation on the influence of the liquid viscosity, droplet radius, and contact angles are also carried out and will be discussed in the presentation.

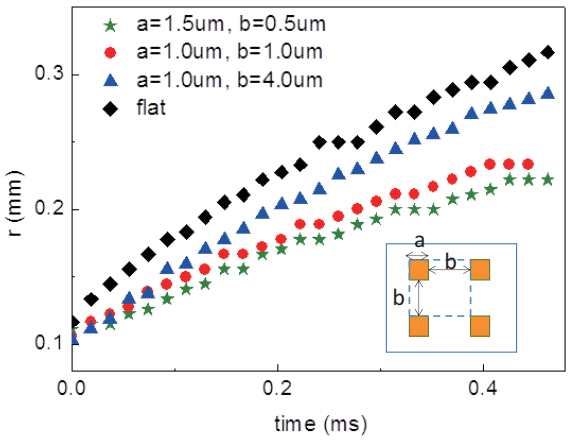


Fig. 3 Time history of the spreading radius r of droplets on different microstructured substrates.

### 4. Concluding Remarks

We have established that the surface structure, whether it is nanoscopic or microscopic, can have a significant influence on the wetting speed. An atomically flat surface generally shows the fastest spreading. The mechanisms of how and why the structures hinder the spreading depend on the nature of the liquid and surface material, and the scale and pattern of the surface structure.

### 5. References

[1] Blake, T. D., *J. Colloid Interface Sci.* 299 (2006) 1-13.
[2] Tanner, L. H., *J. Phys. D: Appl. Phys.* 12 (1979) 1473-1484.
[3] Biance, A. L., Clanet, C. & Quere, D., *Phys. Rev. E* 69 (2004) 016301.
[4] Nakamura, Y.; Carlson, A.; Amberg, G.; Shiomi, J., *Phys. Rev. E,* 88 (2013) 033010.
[5] Carlson, A., Bellani, G. & Amberg, G., *Europhysics Lett.* 97 (2012) 44004.

Eleventh International Conference on Flow Dynamics
October 8-10, 2014, Sendai, Miyagi, Japan

# Modeling of Cortical Bone and Bone Marrow

Makoto Ohta[1], Wataru Sakuma[2], Yuta Muramoto[3], Hitomi Anzai[1], Toshio Nakayama[1]
[1]Institute of Fluid Science, Tohoku University,
2-1-1 Katahira Aoba-ku Sendai, 980-8577, Japan
[2]School of Engineering, Tohoku University
6-6-04 Aramaki Aza Aoba, Aoba-ku Sendai, 980-8579, Japan
[3]School of Biomedical Engineering, Tohoku University
6-6-05 Aramaki Aza Aoba, Aoba-ku Sendai, 980-8579, Japan

**ABSTRACT**

Bone consists of cortical bone and cancellous bone. In cancellous bone, bone marrow flowed and the bone marrow harvest is, recently, attractive because the hematopoietic cells will be a key role of regenerative medicine. However, efficient transplantation is not developed and the donor's problem occurs. The bone marrow can be modeled using a realistic geometry or Darcy's law. On the other hand, artificial joint or implantation using three dimensional printing are also recently focused in the field of cortical bone, because of necessity of tailor made implantation. In this study, we introduce hot topics of biomedical flows in these bones.

## 1. Introduction

A super-aging society has come and the preparation for the society is an emergent field. Medical devices such as artificial joint, bone screw, bone plate, bone saw, ultrasound cut, or puncture needle for bone marrow could be necessary for the society. Especially, the society pays an attention to regenerative medicine or tailor made medicine. Medical devices will support these medicine fields.

Bone consists of cortical bone and cancellous bone. The cortical bones support their body weight, whereas the bone marrow in cancellous bone is a fluid with the hematopoietic cells for use in regenerative medicine. To help the treatments, development of a novel medical device should be progressed.

Modeling bone from the viewpoint of mechanical engineering or biomedical fluid could evaluate the recent developed medical device fields. Previously, the evaluations of mechanical properties of bone were performed with animal bones. However, such animal tests have large standard deviation and should be reduced. Then, the importance of bone model increases. Also the education of tactile feedback using a bone model should be necessary. Young-Kyun Kim et al., performed implant drilling test using one of bone models called as SAWBONES[1] made of Polyurehane [2]. However, the sawbones were, firstly, developed as a cancellous bone. On the other hand, although a model for cortical bone from SAWBONES is similar mechanical properties to a list of bone properties, the thrust force of drill was extremely high and the tactile feedback also showed too high. Then, we developed a cortical bone model with good tactile feedback with mucosa.

## 2. Cortical Bone Model

Figure 1 shows examples of bone models used for evaluation of medical devices by dentists. A cortical bone model and performing implantation are shown Fig. 1 (a). A good tactile feedback of implantation is reported after the evaluation. Figure 1 (b) shows a bone model with oral mucosa, which one is performing drill on the bone [3]. Thrust force was measured and the highest force and the time dependency are similar to a

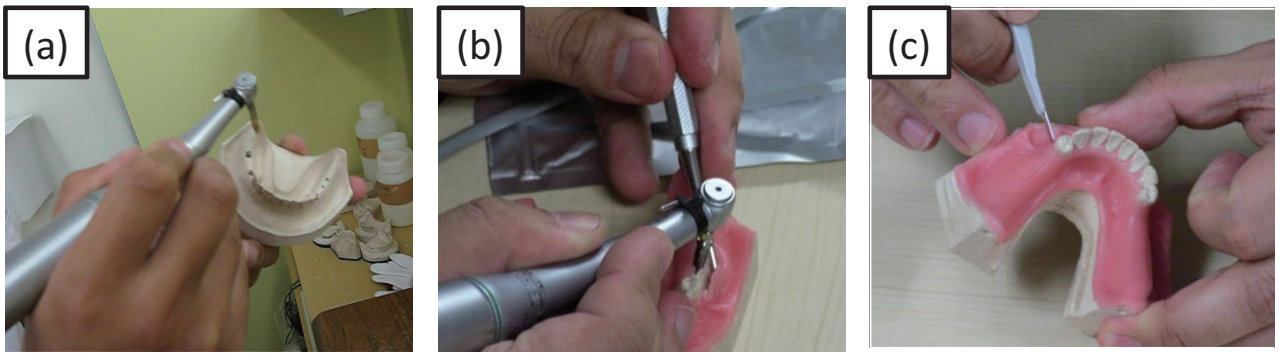


Fig. 1 Bone models for evaluation of medical devices by dentists. (a) implantation, (b) drilling, (c) cutting oral mucosa

Corresponding author: Makoto Ohta
*E-mail address*: ohta@biofluid.ifs.tohoku.ac.jp

porcine bone. Figure 1 (c) shows cutting mucosa made of Poly (vinyl alcohol)-Hydrogel (PVA-H) and a good tactile feedback of this mucosa is reported. However, the mechanical properties such as Young's modulus [4] and the strength are very small under the comparison with a porcine bone.

### 3. Numerical Modeling for Cancellous Bone

Modeling of cancellous bones could be described using porous media. The permeability of porous media will be assumed using Darcy's law [5].

### 3.1 Darcy's Law

The flow in the porous medium was modeled based on the addition of a momentum source term to the standard fluid flow equations. This term was composed of a viscous resistance term and inertial resistance term as following equations.

$$\Delta p = \left( \frac{\mu}{\alpha} v_i + C_2 \frac{1}{2} \rho v_i^2 \right) \Delta e \,. \qquad (1)$$

$$\Delta p = av^2 + bv \qquad . \qquad (2)$$

where $i$ is the $i$th ($x$, $y$, or z) coordinate, $v$ is the velocity, $\alpha$ is the permeability, $C_2$ is the inertial resistance factor, $\mu$ is the viscosity, and $\rho$ is the density. $\Delta e$ is the porous medium thickness. If the pressure drop is approximated as eq. (2), we can obtain two pressure coefficient, $1/\alpha$ and $C_2$. Fluent (ANSYS Inc.) was used to construct a model to apply the law.

### 3.2 Numerical Model with a Realistic Geometry of Cancellous Bone

CFD analysis was performed using a realistic geometry of cancellous bone similar to Thomas R. Coughlin et al. [6]. A geometry of cancellous bone was scanned using Micro-CT (Comscantecno Co.,Ltd). Reconstruction and smoothing of (Standard Triangulated Language (STL) were performed using Osirix [7], Pro/E (PTC Inc.), and Magics (Materialise HQ). Numerical Simulations were performed with Fluent. Figure 2 shows streamline and speed distribution. The flow volume depending on pressure is similar to experimental results of permeability [8].

### 4. Concluding Remarks

Cortical bone is modeled using composite materials and bone marrow in cancellous bone is modeled using permeability based on Darcy's law with the purpose of both performances for evaluation or development of medical devices. The Modeling will be useful for equivalency, efficacy, and usability.


### Acknowledgements

This project is partially supported by, Collaborative Research Project (IFS, JSPS), and project of development of international standardization "Development of International Standardization of Bone Model for Mechanical Safety Test" by Ministry of Economy, Trade and Industry. We are also thankful for a support from JIMRO Co., Ltd.


### References


[1] http://www.sawbones.com

[2] Young-Kyun Kim, Yoon-Ji Kim, Pil-Young Yun, Jong-Wan Kim, *Angle Orthodontist*, 79 (2009) 908-914.

[3] Kei Ozawa, Yuji Katakura, Yukihiko Shibata, Philippe Kapsa, Vincent Fridrici, Gaetan Bouvard, Makoto Ohta, *9th ICFD* (2012) 584-585.

[4] Kei, Ozawa, Koji Yamaguchi, Yukihiko Shibata, Toshio Nakayama, Yoko Hashida, Makoto Ohta, *6th WCB*, (2010) 537-537.

[5] Bone Mechanics Handbook, Edt. Stephan C. Cowin, *Informa Healthcare, (*2009).

[6] Thomas R. Coughlin, Glen L. Niebur, *J. Biomech.* 45 (2012) 2222-2229.

[7] http://www.osirix-viewer.com

[8] Wataru Sakuma, Makoto Ohta, Toshio Nakayama, Syuji Nakamura, Katsuyuki Sado and Hirokazu Takagawa, *Proc. Conf. Comput. Eng. Sci.*, 19, (2014) CD-ROM (Japanese).


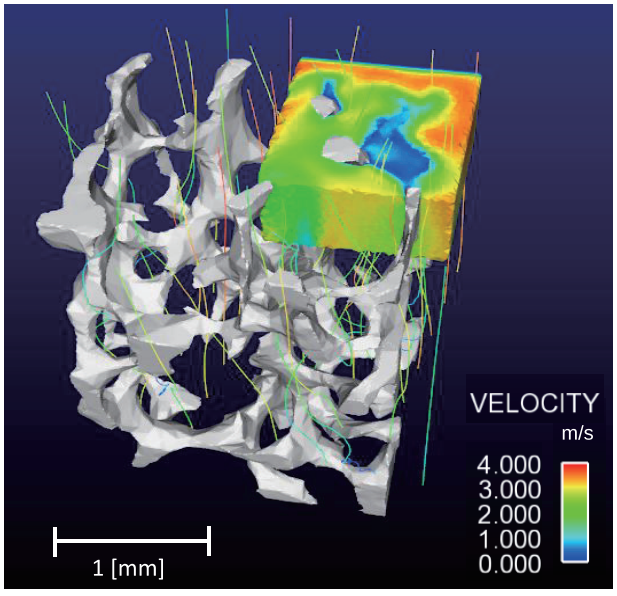


Fig. 2 Streamlines and velocity distribution of bone marrow in cancellous bone.

Eleventh International Conference on Flow Dynamics
October 8-10, 2014, Sendai, Miyagi, Japan

# Flow Manipulation of Nano-Fibrillated Cellulose: a Key Technology for New Bio-Based Materials

Karl Håkansson, Fredrik Lundell, Lisa Prahl-Wittberg, Daniel Söderberg
Wallenberg Wood Science Centre and Linné FLOW Centre
KTH Mechanics, Royal Institute of Technology KTH, SE-100 44 Stockholm, Sweden
Fredrik@mech.kth.se

**ABSTRACT**

Nano-fibrillated cellulose (NFC) is obtained by disintegrating cellulose fibres from paper pulp into fibrils. The fibrils have a thickness of about 20 nm and length around a micron and is a promising commodity for high performance bio-based materials. Here, we show how the nano-structure and fibril alignment of NFC can be manipulated in flow systems. Furthermore, we show how the fibrils can be assembled to a filament with good mechanical properties. The flow and filament is evaluated by x-ray diffraction, polarized light and tensile testing.

## 1. Introduction

Nano-fibrillar cellulose (NFC) is obtained by disintegrating cellulose fibres extracted from wood (usually used for paper production) into near crystalline nano-fibrils, which have a diamter around 2 nm and a length on the order of a micrometer. The highest reported values of the strength (specific stiffness and ultimate strength) for cellulose fibres extracted from wood are considerably higher than the strength that has been reported for filaments produced by NFC. This could be interpreted so that the full potential of NFC has not been reached yet. Here, an assembly process that combines hydrodynamic alignment of surface-charged nano-fibrils with a controlled dispersion-gel transition is presented [1]. It is demonstrated that the process can produce cellulose filaments from nano-fibrillated cellulose (NFC) with a preferential fibril orientation along the filament direction.

## 2. Materials and Methods

The filaments are produced in a flow focusing setup (see Fig. 1), where a central flow containing NFC is focused by two outer flows. In this flow setup, the fibrils are aligned and later assembled, so that a thread isformed. After drying, a dry filament is obtained. The process and filament are investigated with small- and wide-angle X-ray scattering (at the P03 beamline at PETRAIII in Hamburg, Germany), tensile testing, polarized light and SEM microscopy.

In addition to experimental determination of fibril alignment, simulations have been performed. The simulations consists of two stages. First, the velocity is determined. The second step is a calculation of fibril orientation in this flowfield by mean of a Smoluchowski equation.

The flowfield is calculated in a 2D geometry designed to capture the key aspects of the channel system. This is obtained in a cylindrical geometry with a central flow and an annular inflow. The velocity along the centerline is used as the basis for the orientation calculation. This velocity shows first a decceleration directly after the beginning of the side injection. This deceleration is followed by a strong acceleration due to the increase of total flow.

The orientation along the central streamline is calculated based on the assumption that there are two mechanisms that affect the orientation. The first is that the fibrils rotate due to the gradients of the flow based on the rotational velocities of inertia free spheroids[2]. The second effect is a diffusion towards an isotropic fibril distribution due to Brownian motion[3]. The magnitude of the latter diffusion has to be fitted to experimental data. Polarized light visualizations have

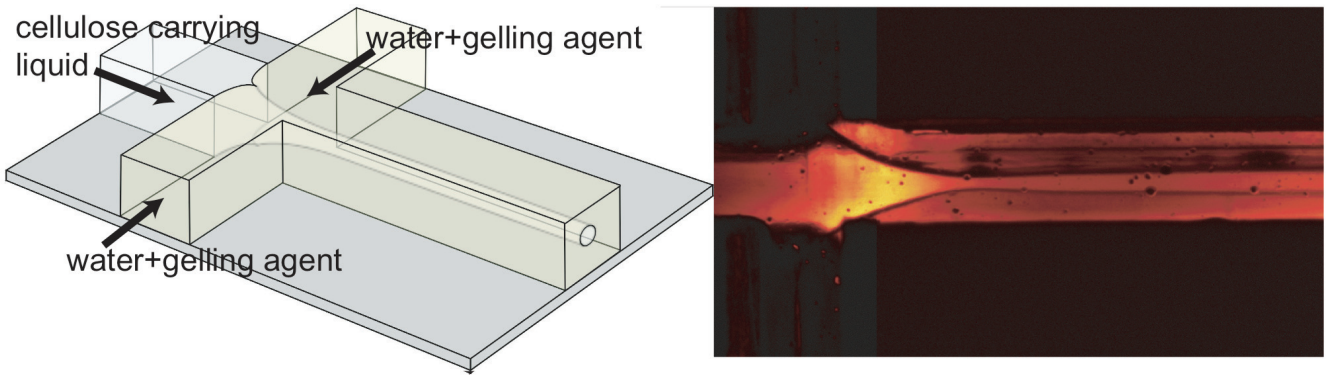


Fig. 1: Flow focusing setup (left) and visualization with polarized light (right). The visualization shows that the fibrils are aligned by the focusing.

Corresponding author: Fredrik Lundell
*E-mail address*: fredrik@mech.kth.se

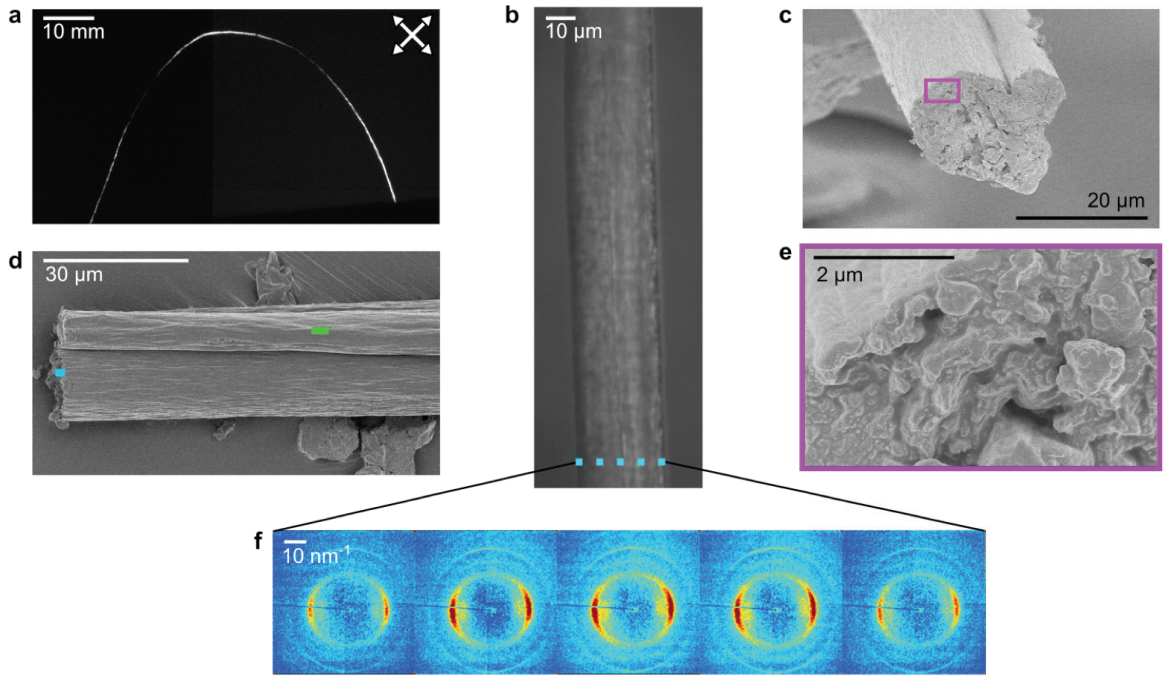


Fig. 2: Picture of the filament in polarized light demonstrating fibril alignment, SEM images of the filament and wide-angle X-ray scattering images showing alignment of Cellulose 1 crystals.

been used for this purpose.

### 3. Results and Discussion

The filament is shown in Fig. 2. The results show that the specific ultimate strength and stiffness of the filaments are in line with the strongest cellulose pulp fibres extracted from wood with the same degree of fibril alignment. Furthermore, the specific ultimate strength and stiffness of the filaments are considerably higher than previously reported filaments made from NFC as well as regenerated cellulose fibers such as viscose or lyocell. The scattering measurements show that these excellent properties are achieved by creating a controlled nanostructure of free fibrils before the structure is locked. This is achieved in a process that is highly controllable, parallelizable and scalable.

The controllability of the process opens up for reverse engineering of NFC filaments: first, a desired nano-structure is determined by micro-mechanical modelling and analyses. The process would then be tuned a-priori so that this particular nanostructure is created. Thus, the results envisage industrial production of highly specialised filaments made form NFC.

The orientation calculations show decent agreement with the polarized light visualization. They indicate that higher alignment can be achieved as long as hydrodynamic instabilities does not set in and destroy the filament.

### 4. Conclusions

Homogeneous cellulose filaments with a high degree of fibril alignment have been produced by flow focusing. The alignment is characterized by polarized light and x-ray diffraction. Furthermore, the alignment is modeled with a Smoluchowski equation and agrees well with polarized light visualizations. The process offers a possibility to create filaments with a controllable nano structure.

[1] K.M.O. Håkansson, A. Fall, F. Lundell, S. Yu, S. Roth, G. Santoro, C. Krywka, M. Kvick, L. Prahl-Wittberg, L. Wågberg & L. D. Söderberg, Nature Comm. **5** 4018 (2014)
[2] G. B. Jeffery, Proc. Roy Soc., Serie A **102** (715) pp. 161-179 (1922)
[3] M. Doi & S. Edwards, The theory of polymer dynamics. Oxford University Press (1986)

# Fundamental Characteristics on Electromagnetic Energy Conversion Device for Efficient Wind Energy Utilization

Hidemasa Takana[1] and Akira Tanida[2]
[1] Institute of Fluid Science, Tohoku University
2-1-1 Katahira, Aoba-ku, Sendai, Miyagi 980-8577, Japan
[2] Graduate School of Engineering, Tohoku University

**ABSTRACT**

An innovative electromagnetic energy conversion device has been developed for efficient wind energy utilization. This device has co-axial configuration with liquid metal filled inside under applied magnetic field. The rotational speed of the turbine can be kept constant even for increasing wing power by controlling rotational torque using electromagnetic interaction with electrical power generation. The characteristics of electric power generation and torque control have been experimentally investigated with DC motor as a driving source.

## 1. Introduction

The growing attention has been paid to the renewable energy without $CO_2$ emission for the establishment of low carbon society. Among other renewable energy sources, the demand for wind energy has been increasing worldwide.

In the conventional wind turbines, a constant power output is obtained by controlling the pitch angle of the blades to decrease the angle of attack in the case of excessive wind velocity [1,2]. Therefore, if this excessive wind energy can be utilized at a constant rotational speed without changing the pitch angle, the rated power operation can be possible with enhanced efficiency.

Therefore, with aiming for efficient utilization of wind energy, an innovative energy conversion device for rotational torque control by electro-magnetic interaction in liquid metal has been developed based on the insights from the previous theoretical and experimental researches of liquid metal magnetohydrodynamic (MHD) technologies such as MHD power generator [3] and MHD viscous coupler. This device has co-axial configuration and the rotational speed of the turbine can be kept constant by controlling rotational torque with electrical power extraction from excessive wind energy. In this study, the power generation and torque controlling characteristics of the developed prototype have been experimentally clarified in detail.

## 2. Experimental Systems

Figure 1 shows the cross sectional view of the developed co-axial electromagnetic energy conversion device for wind turbine. The U-alloy as a liquid metal is filled between 60 mm diameter of rotational shaft and 80 mm inner diameter of outer ring electrode, both made of copper. The liquid metal in the device is driven in the azimuthal direction by the electronically insulated propellers attached to the rotating shaft at every 90°. The U-alloy is the alloy mainly composed of tin and bismuth, and the U-alloy has very low melting point of 289 K. The electro conductivity and the viscosity are 2.31x10[6] S/m and 22.4 mPa·s, respectively. Because the axial magnetic field is externally applied by the azimuthally located neodymium magnets, the applied magnetic field is non-uniform in azimuthal direction. The maximum magnetic flux density between disk walls in the channel is either 200 mT or 360 mT by changing permanent magnets. According to the Faraday's law, the electromotive force of $\boldsymbol{u}\times\boldsymbol{B}$ is generated in the radially outward direction. The generated electric power is extracted by connecting an external load resistance between the rotational shaft and outer ring electrode. During power generation, the rotational torque increases due to the Lorentz force acting against the liquid metal

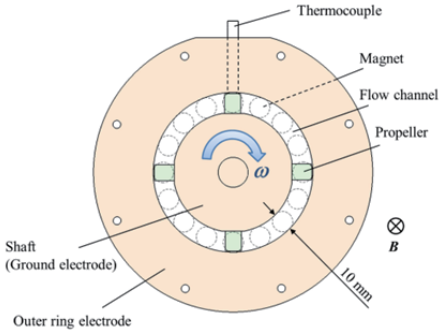


Fig. 1 Cross sectional view of the developed co-axial energy conversion device for wind turbine.

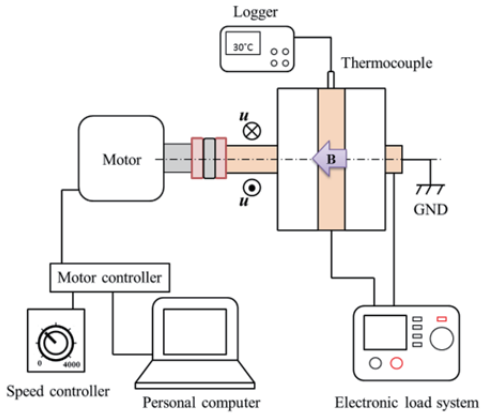


Fig. 2 Experiment systems with co-axial energy conversion device.

Corresponding author: Hidemasa Takana
*E-mail address*: takana@paris.ifs.tohoku.ac.jp

flow. The electric power output and rotational torque can be controlled by operating conditions of load resistance and magnetic field.

Figure 2 shows experimental systems with co-axial energy conversion device. The systems mainly consist of DC motor as a driving source, motor controller, and electric load resistance. The shaft is connected to the motor through flexible coupling. The motor and shaft are both grounded. The load voltage and current were measured for the output power. The rotational torque was obtained from motor current using current-torque characteristics.

## 3. Results and Discussion

Figure 3 shows the output voltage and current characteristics for 360 mT. As the voltage and current characteristics show, the output voltage increases as the current decreases for higher load resistances. The decrease in output current shows that the eddy current inside the liquid metal increases as the external load resistance approaches open circuit conditions. The output power increases with rotational speed of the shaft at every external load resistances. The highest output power of 73 mW was obtained at 3.8 mΩ. The output power decreases for the off-matching load resistances.

Figure 4 shows the ratio of rotational torque with magnetic field to the torque without magnetic field for rotational speeds under 200 mT and 360 mT. The load resistances are set to be the optimum resistance. The ratio is rather small for 200 mT due to the week electro-magnetic interaction, and the ratio is ~1.2 for the rotational speed higher than 1000 rpm. On the other hand, the ratio of 1.7-2.1 can be obtained under 360 mT and the ratio decreases with rotational speeds. This result shows that the rotational torque for a given rotational speed can be controlled by the external magnetic field and torque control range is wider for lower rotational speed.

Figure 5 shows the motor torque as a function of external load resistance for various rotational speeds at 360 mT. The torque becomes lowest at the optimum load resistance for every rotational speed. The increase in the torque results from the Lorentz force by output current and eddy current. The torque becomes higher when the load resistance is higher or lower than the optimum resistance, i.e. off-matching condition. This is because eddy current dominantly increases for higher load resistance, while the output radial current increases for lower load resistance.

## 4. Concluding Remarks

The fundamental characteristics of developed electromagnetic energy conversion device for efficient utilization of wind energy have been experimentally clarified. The operation of wind turbine at the constant rotational speed can be realized even for the increasing wind input power through adjustment of rotational torque with electric power extraction by applied magnetic field and load resistance.

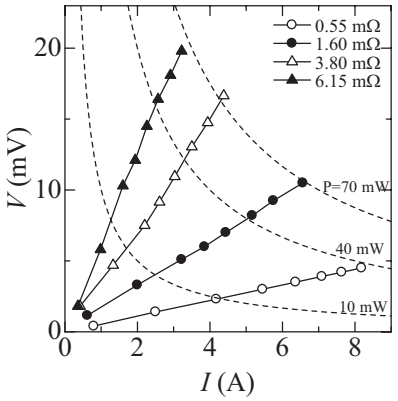


Fig. 3 Output voltage and current characteristics under 360 mT.

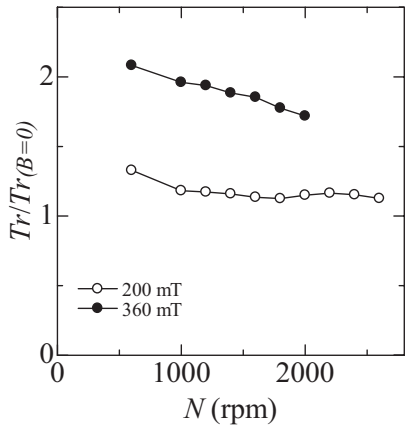


Fig. 4 Ratio of rotational torque with magnetic field to the torque without magnetic field for rotational speed under 200 mT and 360 mT.

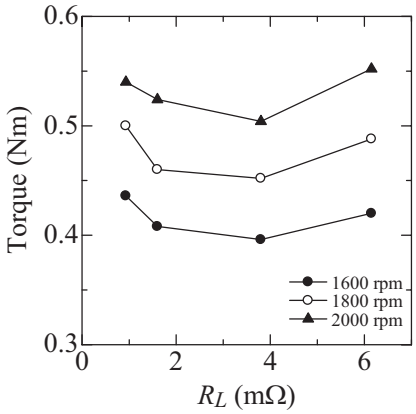


Fig. 5 Rotational torque as a function of external load resistance for various rotational speed under 360 mT.

## References


[1] E.J. Kathryn, and E.J. Lee, *Journal of Solar Energy Engineering*, 130-3 (2008) 031012.

[2] E. Muljadi, and C.P. Butterfield, *IEEE Transaction on Industry Applications*, 37 (2001) 240-246.

[3] J.C.R Hunt, and R. Moreau, *Journal of Fluid Mechanics*, 78-2 (1976) 261-288.

# CS2: Heat and Fluid Flow

Eleventh International Conference on Flow Dynamics
October 8-10, 2014, Sendai, Miyagi, Japan

# Effect of Rub Mushrooming Damage on the Leakage Flow Characteristics of Labyrinth Seal

Xin Yan[1], Kun He[2], Jun Li[1,3]
[1]Institute of Turbomachinery, Xi'an Jiaotong University, Xi'an 710049, China
[2] MOE Key Laboratory of Thermo-Fluid Science and Engineering, Xi'an Jiaotong University Xi'a 710049, China
[3] Collaborative Innovation Center of Advanced Aero-Engine, Beijing 100191, China

**ABSTRACT**

Numerical computations were performed to investigate the effect of the rub mushrooming damage on the sealing performance of the labyrinth seal. It is found that the leakage rate is almost proportionally increased with the increase of effective sealing clearance. As to the mushroomed labyrinth seal, the leakage rate increases with the increase of mushrooming radius if the effective sealing clearance is fixed. Among the studied damages, the large mushrooming damage with unbent fin has the largest leakage rate.

## 1. Introduction

The labyrinth seal is widely used in turbomachinery to control leakage between the rotating and stationary parts. In practice, the labyrinth seal not only significantly affects the aerodynamic performance [1], but also influences the operation safety and the interval of overhaul of the turbomachinery [2]. Some critical problems due to the failure of labyrinth seals still remains in the turbomachinery during the running process especially in the transient periods of startup, shutdown and hot restart [3]. In these cases, the interference of seal rotor and stator often occurs and leads primarily to damage the labyrinth fin (for instance, bending and mushrooming) or opposite stator surface (for instance, rub groove), thus significant affects the overall performance of the labyrinth seal in contrast to the original design [1].

Figure 1 provides the photos of common rub damages in labyrinth fin when seal rotor and stator contacts each other. Notice that the seal structure varies a lot compared to the original design, especially in the fin tip. The change in the labyrinth fin will significantly influence the jet speed across the tip and induce subsequent loss of aerodynamic performance. The deformation of the labyrinth fins changes the area of the chamber which determines the dissipation effect of the leakage jet [3].

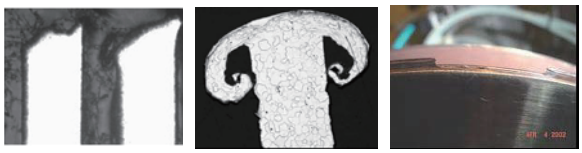

(a) wear-off (b) mushrooming (c) break-off
Fig. 1 Photos of the damaged labyrinth fin [3]

Among the leakage characteristic research of the labyrinth seal in publications, almost all of the researchers aimed towards the leakage rates and flow pattern for the original design in the last decades. The most representative research carried out by Wittig et al [4] shows that the pressure ratios and geometrical parameters, such as gap width, pressure ratio and fin number, are the main influence factors to determine the leakage rate and flow pattern in the labyrinth seal. Although above study [4] is very helpful for the labyrinth seal design and installation, it still not well suited for the sealing performance evaluation during the running process. The reason is, in the realistic operation process, the labyrinth seal geometry may change with time due to the pressure gradient, thermal stress, rotor-stator contact and so on.

With such background, Whalen et al [5] systematically analyzed the geometry deformation characteristics in typical metallic labyrinth seals during the rub process. Collins and Teixeira [6] experimentally and numerically investigated the sealing performance degradation for the labyrinth seal with worn honeycomb land. In the present paper, the leakage rates and flow pattern of the labyrinth seal with rub mushrooming damage were illustrated and discussed.

## 2. Method

In the present paper, a labyrinth seal with three fins was selected as the research objective. The original design geometry of the seal is depicted in Figure 2(a), and the geometrical parameters and dimensions are listed in Table 1. The shaft radius is 250.152mm, and the rotational speed is 10000rpm. For the mushrooming case, as shown in Figure 2(b), the geometry of the labyrinth fin is determined by the unbent height $U$ and mushrooming radius $R_m$.

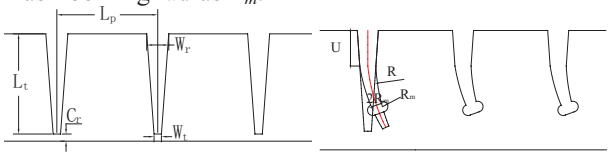


(a) Original case (b) Mushrooming case
Fig. 2 Geometrical parameters for the labyrinth seal without and with mushrooming damage

Table 1. Geometries of the original case (*mm*)

| $L_t$ | $L_p$ | $C_r$ | $W_r$ | $W_t$ |
|---|---|---|---|---|
| 3.556 | 3.556 | 0.254 | 0.76 | 0.26 |

Figure 3 illustrates the computational meshes for the original design and different degrees of bending and mushrooming damages. For all computations, the multi-block structured grids were generated. In the current study, the commercial CFD software ANSYS-CFX11.0 was adopted to solve the three-dimensional Reynolds-Averaged Navier-Stokes (RANS) equations. For the spatial discretization, high resolution scheme was selected, and the turbulence model was selected to be the standard $k$-$\varepsilon$ with scalable

Corresponding author: Jun Li
*E-mail address*: junli@mail.xjtu.edu.cn

wall function treatment. The detailed boundary conditions and numerical methods for the present study were listed in Table 2.

Table 2. Boundary conditions and numerical methods

| *Numerical methods* | *Property* |
|---|---|
| Seal length (*mm*) | 13.984 |
| Shaft radius (*mm*) | 250.19 |
| Shaft speed (rpm) | 10000 |
| Inlet turbulence intensity | 5% |
| Inlet pressure (MPa) | 1.379 |
| Inlet temperature (K) | 394 |
| Outlet pressure (MPa) | 1.149 |
| Discretization scheme | High resolution |
| Computational method | Time marching |
| Turbulence model | *k-ε*, scalable wall function |
| Fluid | Air ideal gas |
| Wall properties | Adiabatic, smooth, non-slip |

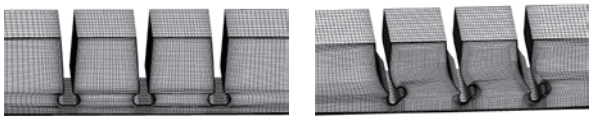

Fig. 3 The computational mesh of the labyrinth seal with simple and bending mushrooming damage

## 3. Results and Discussion

The effect of mushrooming damage on the leakage flow characteristics of the labyrinth seals is investigated. Figure 4 shows the leakage rate versus effective sealing clearance $C_r^*$ for the original design and three mushrooming damage cases. Figure 5 plots the streamline distribution of the mushrooming labyrinth seal with different size. The similar leakage flow pattern of the mushrooming labyrinth seal with different size is captured according to the Figure 5. To reveal the leakage flow pattern in the mushrooming labyrinth seal, Figure 6 illustrate the turbulence kinetic energy contours distributions on the meridian plane. The turbulence effect as well as the carry-over effect increase with the increase of effective sealing clearance at the same mushrooming radius. It is seen that more turbulence flow enters the chamber than the unbent case at the same effective sealing clearance. This indicates that less jet flow, which carried high turbulence kinetic energy, flows to the downstream. Therefore, the leakage rate for the mushroomed seal with bent fins is smaller than that of simple mushroomed damages.

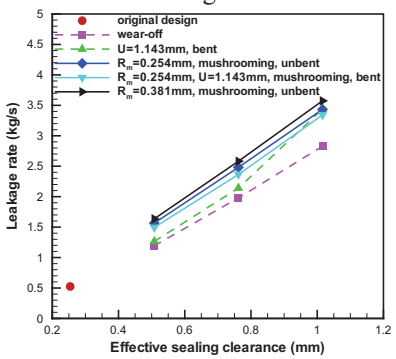


Fig. 4 Leakage rate versus $C_r^*$

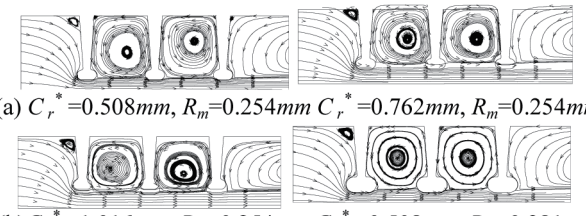

(a) $C_r^*$=0.508*mm*, $R_m$=0.254*mm* $C_r^*$=0.762*mm*, $R_m$=0.254*mm*

(b)$C_r^*$=1.016*mm*, $R_m$=0.254*mm* $C_r^*$=0.508*mm*, $R_m$=0.381*mm*

Fig. 5 Streamline distribution of the mushrooming labyrinth seal

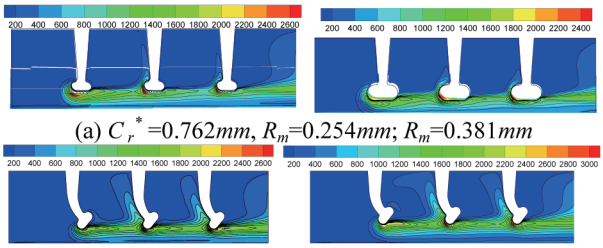

(a) $C_r^*$=0.762*mm*, $R_m$=0.254*mm*; $R_m$=0.381*mm*

(b) $U$=1.143*mm*, $C_r^*$=0.762*mm*, $R_m$=0.254*mm*; $C_r^*$=1.016*mm*

Fig. 6 Turbulence kinetic energy contours distributions

## 4. Concluding Remarks

Three-dimensional RANS solution was utilized to investigate the effect of mushrooming damage on the leakage flow characteristics in the labyrinth seals. The leakage rate and the meridian flow field were obtained with a range of mushrooming radius and pressure ratios. As to the unbent seal, the leakage rate increases with the increase of mushrooming radius if the effective sealing clearance $C_r^*$ is kept the same. The largest mushrooming radius without bent on the labyrinth fin has the largest leakage rate.


## Acknowledgement

This work is supported by the National Natural Science Foundation (No. 51106122) and Fundamental Research Funds for the Central Universities of China.


## References


[1] R.E. Chupp, R.C. Hendricks, S.B. Lattime, et al, Sealing in turbomachinery, *Journal of Propulsion and Power* 22(2) (2006) 313-349.

[2] J. Vance, F. Zeidan, B. Murphy, *Machinery Vibration and Rotordynamics, John Wiley & Sons,* New York, USA, (2010).

[3] F. Ghasripoor, N. A. Turnquist, M. Kowalczyk, et al, Wear prediction of strip seals through conductance, *Proceedings of ASME Turbo Expo 2004: Power for Land, sea and Air*, Vienna, Austria. (2004) GT2004-53297.

[4] S. Wittig, K. Jacobsen, U. Schelling, et al, Heat transfer in stepped labyrinth seals, *Gas Turbine Conference and Exhibition,* California, USA. (1987) 87-GT-92.

[5] J.K. Whalen, E. Alvarez and L.P. Palliser, Thermoplastic labyrinth seals for centrifugal compressors, *Proceedings of the Thirty-Third Turbomachinery Symposium*, (2004)113-126.

[6] D. Collins and J. Teixeira, The degradation of abradable honeycomb labyrinth seal performance due to wear, *Sealing Technology*, 2008(8)(2008)7-10.

Eleventh International Conference on Flow Dynamics
October 8-10, 2014, Sendai, Miyagi, Japan

# Vortical Structures in Film Cooling Induced by Shaped Holes and Slots

Wei-Siang Chao, Shang-Hong Chen, Wu-Shung Fu

EE306, Department of Mechanical Engineering, 1001 Ta Hsueh Road, Hsinchu, Taiwan

**ABSTRACT**

Vortical structure in the wake of a film cooling jet is studied numerically. The compressibility of working fluid are taken into consideration. Methods of the Roe scheme, preconditioning, and dual time stepping matching with MUSCL are adopted to solve governing equations. Results show that the shape of the film cooling hole have large influence on the vortical structure, By controlling the geometry of the film cooling hole the film cooling effectiveness can be improved.

## 1. Introduction

In order to improve efficiency of a gas turbine engine, increasing the temperature of the inlet working fluid is a great method. But increasing the temperature of the working fluid means the component of the gas turbine engine to be necessarily operated under hazardous conditions, as a consequence the life of the component will be decreased dramatically. One of the important component is the turbine blade, so in order to protect the turbine blade using film cooling is necessary.

Therefore, a problem of investigation of behaviors of the cooling fluid mentioned above flowing through the gas turbine blade becomes important and worthy investigated deeply.

## 2. Physical model

A compressible forced convection flow in a three dimensional converging channel is investigates and the model is shown in Fig. 1.

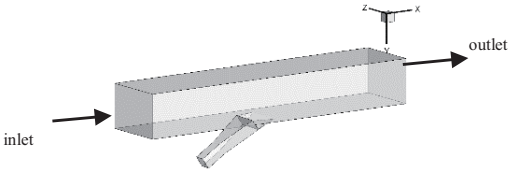


Fig. 1. Physical model

The density ratio is 1.86. The boundary of the inlet is forced convection condition, the outlet is the non-reflection condition, the top and bottom wall is no-slipping condition, ant the side wall is periodic condition. The length, width, and height of the channel are shown in Fig. 2.

The governing equations in which the parameters of viscosity and compressibility of the fluid and gravity are considered simultaneously are shown in the following equations.

Corresponding author: Wei-Siang Chao

*E-mail address*: huchihauuu@livemail.tw

$$\frac{\partial U}{\partial t}+\frac{\partial F}{\partial x}+\frac{\partial G}{\partial y}+\frac{\partial H}{\partial z}=S \qquad (1)$$

$$P=\rho RT \qquad (2)$$

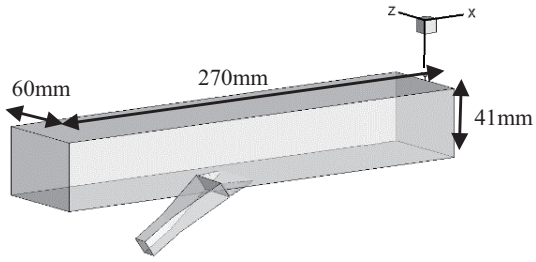


Fig. 2.

## 3. Method

Schemes of Roe, preconditioning[1] for resolving compressible flow under a low Mach number situation, dual time stepping and MUSCL (Monotonic Upstream-Centered Scheme for Conservation Laws) coordinating LUSGS[2] (Lower-Upper Symmetric Gauss Seidel) are adopted to resolve 3-D Navier–Stokes equations. Methods of algebraic grid generation and a non-reflecting boundary condition are used to execute coordinates transformation and decrease the computational domain, respectively. Furthermore, Boussinesq assumption is no longer used and the compressibility of fluid is considered instead

## 4. Results and Discussion

Initially, the present numerical results are validated with the numerical data presented by Ki-Don Lee and Kwang-Yong Kim[1]. Fig. 3 shows the film cooling effectiveness distribution in the present numerical result. Fig. 4 shows the effect of blowing ratio on the fan shaped holes compare to the reference data.

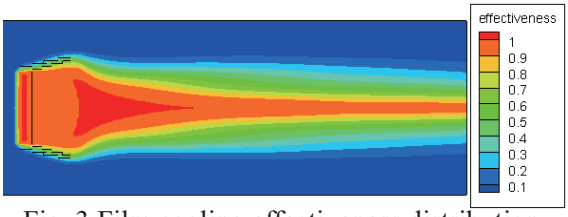


Fig. 3 Film cooling effectiveness distribution with fan shaped hole. (L/D=10)

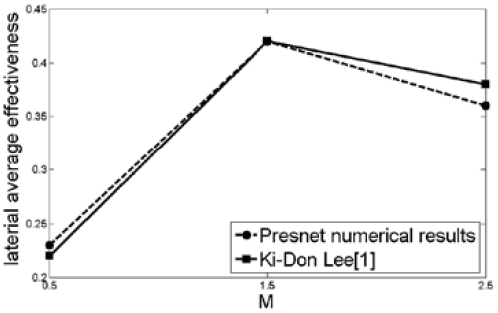


Fig. 4 Effect of blowing ratio on the fan shaped holes.

In order to compare the difference between slots and fan shaped holes, a constant coolant mass flow rate had been set for both two case. Fig. 5 shows the film cooling effectiveness distribution with the slots and Fig. 6 shows the streamline on the y-z plane.

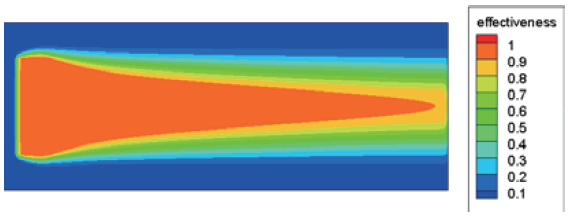


Fig. 5 Film cooling effectiveness distribution with slots.

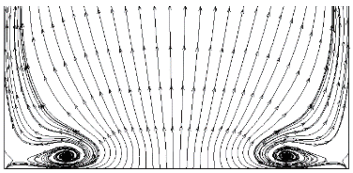

Fig. 6 Stream line on the y-z plane. (slot, X/D=2)

In Fig. 6 we can find that there are two small vortices which initially arising from the sidewalls of the slot passage. Compare to the fan shaped hole case, we can see in Fig. 7, obviously, the two vortices become larger and more close to each other. And because the rotating direction of the two vortices each of which will induce an upward velocity on the other, so the coolant ejected from the fan shaped holes will tend to lift-off, so the film cooling effectiveness on the wall will decrease.

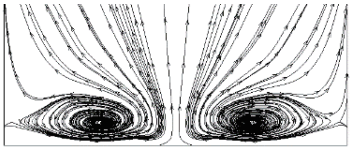

Fig. 7 Stream line on the y-z plane. (fan shaped hole, X/D=2)

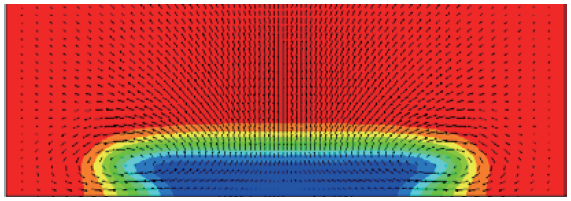

Fig. 8 vector on the y-z plane. (slot, X/D=6)

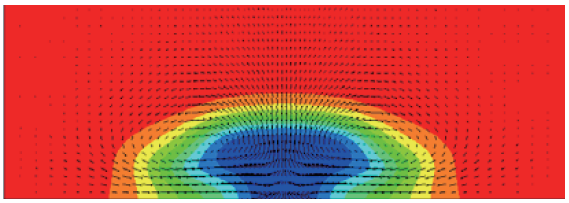

Fig. 9 vector on the y-z plane. (fan shaped hole, X/D=6)

From Fig.8 can find the two sidewall vortices decrease with X/D increase, and the coolant jet tend to stay near the wall. The lateral average effectiveness with slot is 0.49. And from the Fig.9, the film cooling with fan shaped holes, we can see the jet lift-off and separated from the Wall, the lateral average film cooling effectiveness is 0.35 which is smaller than the film cooling with slots.

In present numerical results, the lateral average film cooling effectiveness with slots is better than the film cooling with fan shaped hole. The main reason to explain this situation is that, the distance between two vortices which initially arising from the side walls has a significant influence on whether the jet will stay near the wall or not. The vortices generated from the fan shaped hole very close to each other, and because the vortices will induce an upward velocity in the other, so the jet tend to develop into the mainstream. On the other hand, the vortices generated from the slot have larger distance between two vortices, so the sidewall vorticity would not be affected by the other one, and the jet tend to stay near the wall. With the jet stay near the wall, achievement of the larger film cooling effectiveness is reasonable.

## 5. Concluding

The main points may be concluded as follows.

1. With same coolant mass flow rate film cooling with slots is better than the fan shaped holes.
2. The size of the sidewall vortices and the distance between two side wall vortices have signification effect on film cooling effectiveness.

## 6.References

[1] Ki-Don Lee and Kwang_Yong Kim, 2010, “Shape Optimization of a Fan-Shaped Hole to Enhance Film-Cooling Effectiveness,” J. Heat and Mass Transfer, Vol. 53.

Eleventh International Conference on Flow Dynamics
October 8-10, 2014, Sendai, Miyagi, Japan

# Heat Transfer and Friction Performance of Plate Heat Exchangers Having Hexagonal Dimples

Chun-Long Wang, Kun-Hao Lee, Chi-Chuan Wang*
Hsinchu, Department of Mechanical Engineering, National Chiao Tung University,
30010, Taiwan

**ABSTRACT**

In this paper presented pressure drop and heat transfer characteristics in four channel of hexagonal plate heat exchanger by numerical analysis. In addition, it also compare with the result of v shape plate heat exchanger in the study. The calculations indicate that the fluid on the part of front of dimple would enhance heat transfer. Both side of cavity formed lateral vortex which cause poor heat transfer in the region. The fluid was uplifted by wall and enhanced heat transfer again. Consider to the performance of heat transfer and pressure drop, v shape both better than hexagonal dimple.

## 1. Introduction

Plate heat exchanger had been used in different industries such as chemical, food, pharmaceutical process, and refrigeration. The traditional plate heat exchanger used the corrugations on successive plates and good contact between each other to provide a mechanical support. This can be made available through the plate pack and a large number of contact points. This results in a quite narrow flow passages and a highly interrupted and tortuous structure so that will enhance the heat transfer and flow mixing to promote the level of turbulence. At the same time, the structure yields a higher pressure drop. In addition to a better flexibility and cost concern of the design phase of the plate heat exchanger. An existing plate heat exchanger can very easily be extended or modified to meet the variable demand of the heat transfer duty.

Some commonly used plat patterns are dimple or V shape. For V shape structure, the commonly used chevron angle varies between 30 to 60°. The V shape design had already been verified by many researchers according to experimental and simulations results.

In the study, we proposed a different dimple design which is of hexagonal configuration rather than conventional round dimple design. The associated heat transfer and pressure drop characteristics of hexagonal dimple on the plate heat exchanger are presented by numerical analysis. Its performance is compared to conventional V shape plate heat exchanger. In the simulation model, standard k-ε turbulence model is adopted for analysis.

## 2. Method

Simulation is performed using a commercially available software – flow simulation embedded in Solidwork. The dimension of this plate was 125 mm in width, and 715 mm in length. The plate thickness was 0.5 mm. As seen from Fig. 1, the test section is installed with horizontal direction.

For the V shape plate heat exchanger, the corrugated plate corresponds to a herringbone corrugation pattern with a sine shape with a 30 degree chevron angle. The plate material is copper.

Corresponding author: Chi-Chuan Wang*
*E-mail address* : ccwang@mail.nctu.edu.tw

The geometry of the heat Exchanger and analysis conditions of the experiments are given in Table 1. For the hexagonal dimple plate exchanger, it has 137 hexagonal dimple and 26 half hexagonal dimple. The depth and diameter ratio is 0.2.The dimple dimension is shown in Fig.3. Note those half dimple were in order to enhance mechanical strength as depicted from Fig.2. In the simulation, dimple's arrangement is staggered arrangement. The simulations are made with five plate and four channel. The working fluid is water and its inlet velocity is 0.25 m/s. The inlet temperature of the hot stream is 50 °C and the cold stream is 20 °C. The simulation is at room temperature and atmospheric pressure condition

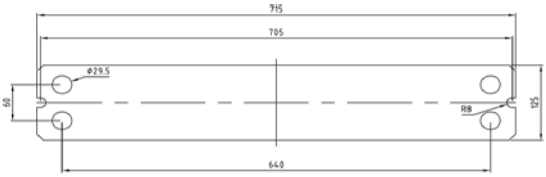


**Fig. 1 Plate shape and dimension**

**Fig. 2 hexagonal dimple shape plate**

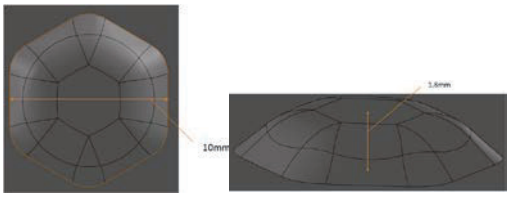


**Fig. 3 hexagonal dimple shape and dimension**

**Table 1. Geometry and analysis conditions**

| Parameter | value |
|---|---|
| Plate length | 715 mm |
| Plate width | 125 mm |
| Temp. of hot stream | 50 °C |
| Temp. of cold stream | 20 °C |

## 3. Results and Discussion

In this section the simulation results are presented.

According to Fig.4, by observing fluid trajectory, we could find that when fluid just entering the hexagonal dimple, it impacted the wall to cause phenomenon of separation. At the same time, it would product stronger vertex result in enhancing heat transfer. On both side of dimple, it products lateral vortex. However, this lateral vortex couldn't enhance plate heat transfer. In the latter half of hexagonal dimple, fluid was uplifted by wall. This zone also has stronger heat transfer.

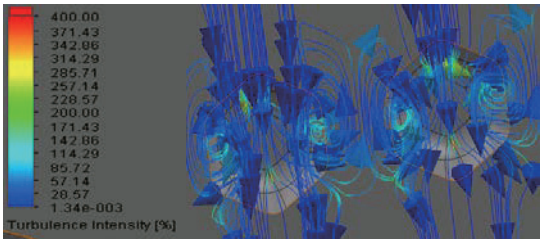

Fig.4 trajectory of fluid and turbulent intensity

For further examination about the fluid flow acroos the dimples, the corresponding trajectory of fluid flow and the variation of local heat transfer coefficients is shown in Fig. 4 and Fig.5. Apparently, stronger turbulent intensity exists in the cavity, leading to a higher heat transfer coefficient. However, it should be noted that part of cavity (around corner) has poor heat transfer coefficient due to there is lateral vortex zone and less fluid is able to flow across it.

In addition to cavity, the flip side of the surface is actually a dimple (protrusion). As can be seen in Fig. 6, the water impinges in front of the dimple. Hence very high heat transfer occurs. In the latter half of hexagonal dimple, fluid separated from the wall and formed a wake region which exhibits very poor heat transfer performance in general.

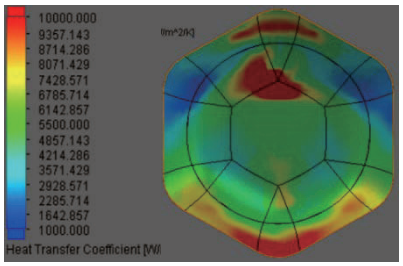

Fig. 5 hexagonal cavity - HTC distribution

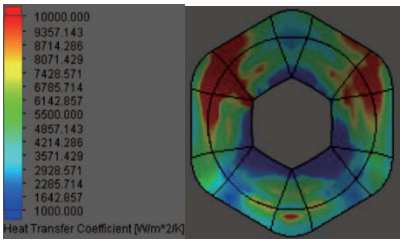

Fig. 6 hexagonal dimple - HTC distribution

Comparison of the dimple design and conventional V shape is shown in Fig.7. It appears that v shape is better than hexagonal dimple in general. The difference is about 6~10%. On the pressure drop, the pressure drop of v shape is lower than that of hexagonal dimple by about 30%. It is show in Fig.8 and Fig.9. The higher pressure drop for the dimple shape design is because its complex staggered arrangement and numerous dimples.

## 4. Concluding Remarks

This study examines the heat transfer performance of hexagonal dimple plate heat exchanger and comparisons are made with the conventional v shape plate. The calculations indicate that the fluid on the part of front of dimple would separate to form longitudinal vortex. It could enhance heat transfer. Both side of cavity formed lateral vortex which cause poor heat transfer in the region. Finally, the fluid was uplifted by wall and enhanced heat transfer once again. Consider to the performance of heat transfer and pressure drop, v shape both better than hexagonal dimple.

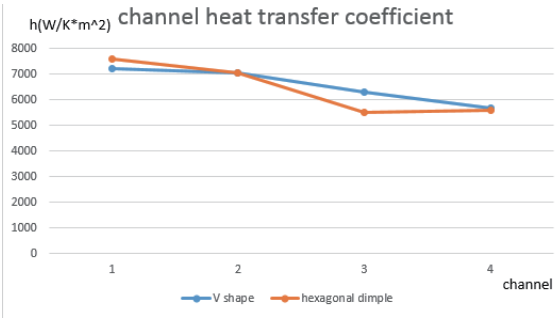

Fig.7 channel heat transfer coefficient

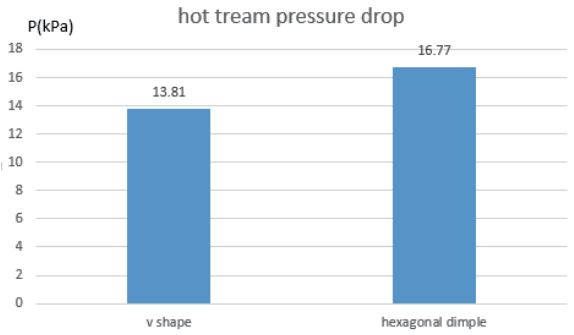

Fig. 8 hot stream pressure drop

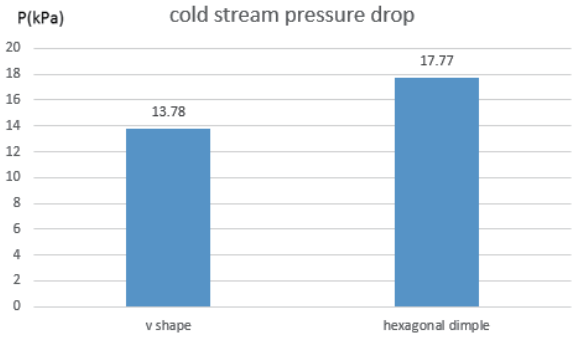

Fig. 9 cold stream pressure drop

## References

[1] S.W. Chang, K.F. Chiang, T.L. Yang, C.C. Huang, *J. Exp. Thermal Fluid Sci.,Italic*. 33 (2008) 23–40.

Eleventh International Conference on Flow Dynamics
October 8-10, 2014, Sendai, Miyagi, Japan

# Heat Transfer in a Developing Region of a Boundary Layer Affected by a Wake of a Square Bar

Yasumasa Ito[1], Xia Shuang[1], Kouji Nagata[1], Yasuhiko Sakai[1], Toshiyuki Hayase[2]
[1]Dept. Mechanical Science and Engineering, Nagoya University
Furocho, Chikusa-ku, Nagoya, 464-8603, Japan
[2]Institute of Fluid Science, Tohoku University
Katahira 2-1-1, Aoba-ku, Sendai, Miyagi, 980-8577, Japan

**ABSTRACT**

Direct numerical simulation (DNS) is carried out to investigate the flat plate boundary layer with heat transfer affected by a wake of a square bar. The bar is installed parallel to the plate and normal to the flow direction at the beginning of the boundary layer. The results show that the thermal boundary layer in the small-gap case is strongly suppressed by the large negative vortices shed from the upper side of the bar. This results in the larger temperature gradient and more active heat transfer with respect to the large-gap case.

## 1. Introduction

A boundary layer with heat transfer is one of the classical research themes in fluid mechanics and it has been studied by a number of researchers. In practice, there are many situations that the free-stream is not laminar and the turbulence structure and heat transfer are modified by the disturbances. Marumo et al.[1] carried out a set of experiments on heat transfer in a flat plate boundary layer disturbed by cylinder wakes and showed that the ratio between the diameter of the cylinder and the gap between the cylinder and the plate strongly affects the turbulence structure in the boundary layer. Further investigations by Suzuki et al.[2] has clarified that large dissimilarity between momentum and heat transfer in the boundary layer can exist just after the cylinder and it is caused by the intensification of the cold wallward and hot outward interactions. Baskaran and Bradshaw[3] studied a boundary layer under the influence of wakes of circular and square bars with different sizes. In the present study, heat transfer in a developing region of a boundary layer affected by a wake of a square bar was investigated by a direct numerical simulation.

## 2. Direct Numerical Simulation (DNS)

The governing equations are the continuity equation, incompressible Navier-Stokes equations, and the scalar transfer equation. Those equations are solved by the fractional step method. A semi-implicit Runge-Kutta scheme with a fully conservative second-order finite difference scheme are employed for the time advancement and spatial discretization for the convective term, respectively, while the viscous and diffusion terms along the wall-normal direction are advanced implicitly by the Crank-Nicolson scheme. On the other hand, the viscous and diffusion terms along the streamwise and wall-normal directions are discretized by the second-order central difference scheme, while the fourth-order central difference scheme is adopted for the discretization of the viscous and diffusion terms along spanwise direction. The resulting Poisson equation for pressure is solved at each sub-step by the Bi-CGstab iterative method.

Figure 1 shows the computational domain. A square bar is placed horizontally at a location of 3$d$ downstream from the inlet. Here $d$ is the side length of the bar. The gap between the square bar and the bottom wall, $C$, is set to $C/d$=0.25 (referred to as the small-gap case) and $C/d$=3.0 (the large-gap case). The computational domain is $L_x \times L_y \times L_z = 48d \times 8d \times 8d$ and the mesh number is $N_x \times N_y \times N_z = 624 \times 200 \times 160$, respectively. Note that the mesh spacing is non-uniform in the streamwise and wall-normal directions with refined mesh in the vicinity of the square bar and the wall.

Reynolds number, $\mathrm{Re}_d = U_\infty d/\nu$, is set to 1667 and Prandtl number is set to 0.71 in this study. With respect to the boundary condition, a uniform flow with a 1/7 power law near the wall is employed at the inlet. The convective outflow boundary conditions are applied at the exit for velocity and temperature. The non-slip and constant temperature boundary conditions ($T$=0) are imposed on the wall, while the slip and constant temperature boundary conditions ($T$=1) are applied to the upper boundary. The periodic boundary condition is applied in the spanwise direction. On the surface of the square bar, the velocity is set to zero by interpolation.

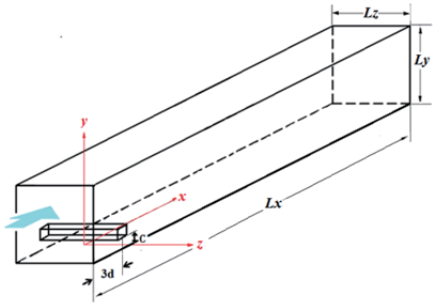


Fig. 1 Schematic of the computational domain.

## 3. Results and Discussion

Figure 2 shows the instantaneous velocity field along with the velocity vector on the $x$-$y$ plane at $z$=0. It is confirmed that the boundary layer is triggered and interact with the wake. In the small-gap case, the wake

Corresponding author: Yasumasa Ito
*E-mail address*: yito@nagoya-u.jp

merges with the boundary layer immediately after shedding from the square bar because the shear layer generally generates downward movements. On the other hand, in the large-gap case, the wake starts to merge with the boundary layer some distance downstream. It is known that the merging distance depends on the propagation speed of the wake, the boundary layer growth rate, and the gap between the square bar and the bottom wall. Comparing to the large-gap case, large recirculating regions are observed in the small-gap case particularly in the upstream region. This results in the thicker boundary layer in the small-gap case.

The mean temperature profiles for both cases at different streamwise locations are plotted in Fig. 3. It shows that the temperature gradient in the small-gap case is larger than that in the large-gap case, especially in the upstream region. This is attributed to that the thermal boundary layer in the small-gap case is strongly suppressed by the large negative vortices in comparison with the large-gap case. Consequently, hot fluid is entrained more from the outer region into the near-wall region, which results in the larger temperature gradient in the small-gap case.

Figure 4 shows the streamwise development of the Stanton number, *St*. *St* in the small-gap case is larger than that in the large-gap case, especially in the upstream region. In other words, heat transfer is more active in the small-gap case. This is due to the existence of the large negative vortices. As shown previously, such vortices suppress the thermal boundary layer strongly (Fig. 2) and makes the temperature gradient larger (Fig. 3).

## 4. Concluding Remarks

The development of a boundary layer with heat transfer under the effects of a wake of a square bar has been investigated. The results are summarized as follows.

- In the large-gap case (*C/d*=3.0), the negative and positive vortices shed from the bar alternatively perturb the boundary layer by advecting the fluid wallward and outward in turn.
- In the small-gap case (*C/d*=0.25), the negative vortices are large and occupy almost the entire region. They induce the strong backward sweep motions of fluid near the wall.
- The thermal boundary layer in the small-gap case is strongly suppressed by the large negative vortices. This results in the larger temperature gradient and more active heat transfer in comparison with the large-gap case.


## Acknowledgements

Part of the work was carried out under the collaborative research project with the Institute of Fluid Science, Tohoku University. Financial support by Grants-in-Aid (Nos. 25289030 and 25289031) from the Japanese Ministry of Education, Culture, Sports, Science, and Technology are also gratefully appreciated.


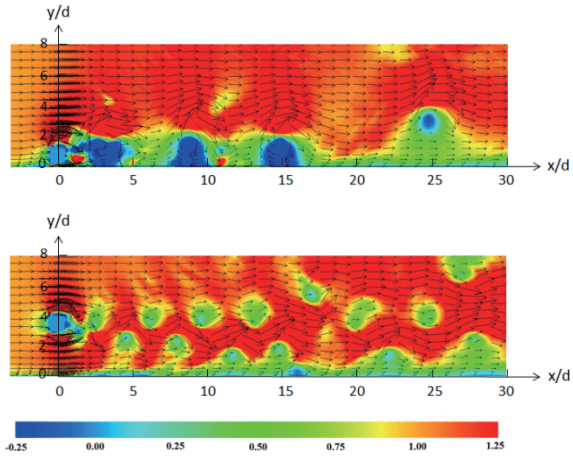


Fig. 2 Instantaneous velocity field for the small-gap (upper image) and large-gap (lower image) cases.

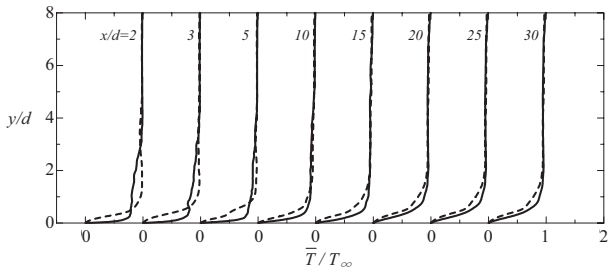


Fig. 3 Mean temperature profile for the small-gap (solid line) and large-gap (dash line) cases.

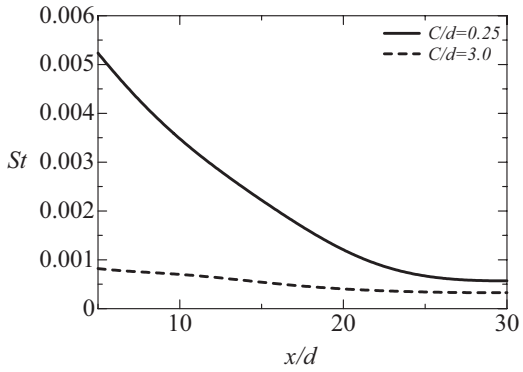


Fig. 4 Streamwise development of Stanton number.

## References


[1] Marumo, E., Suzuki, K. and Sato, T., *Int. J. Heat Fluid Flow*, 6, (1985) 241-248.

[2] Suzuki, H., Suzuki, K. and Sato, T., *Int. J. Heat Mass Transfer*, 31, (1988) 259-265.

[3] Baskaran, V. and Bradshaw, P., *J. Wind Eng. Ind. Aerod.*, 49, (1993) 269-278.

Eleventh International Conference on Flow Dynamics
October 8-10, 2014, Sendai, Miyagi, Japan

# Air-Water Two-Phase Flow Distribution in Multi-Plates Heat Exchanger

Yen-Shuo Tseng, Chien-Yuh Yang and Fu-Chen Lin
Department of Mechanical Engineering, National Central University
No.300, Jhongda Rd. Jhong-Li, Taoyuan, 32001, Taiwan

**ABSTRACT**

This study provides an experimental observation of air-water flow through a transparent multi-plate heat exchanger with various flow header designs. Two different types of baffle plates were inserted in the inlet port to block the upper or lower part of the water flow in the header. The experimental results showed that the flow distribution in the channels of a plate heat exchanger was determined by the flow pattern in the inlet port. Baffle plates cannot improve the distribution of the air flow in a plate heat exchanger but may reduce the pressure drop of air-water flow through the heat exchanger.

## 1. Introduction

While applying plate heat exchanger as an evaporator in an air-condition system, the entering two-phase refrigerant is generally at a vapor quality of around 0.25. Due to the momentum difference between liquid and vapor, the higher inertia liquid will flow mostly through the passages far away the entering port and vice versa for the vapor flow. This will cause a mal-flow distribution of the two-phase refrigerant in the plate heat exchanger and degrade it heat transfer performance.

This study provides an experimental observation of two-phase flow through a transparent multi-plate heat exchanger with various flow header designs. It is aims to further understand the two-phase flow mechanism in the entering port and looking for the methods to improve the uniformity of the flow distribution.

## 2. Experimental Method

The test heat exchanger was made of 59 transparent plastic plates and two end plates to form a 60 channels plate heat exchanger as shown in Fig. 1(a). The thickness of the plates and the spaces of the flow channels are at 2 mm. Air-water mixture was used as working fluid to simulate the two-phase refrigerant flowing through the heat exchanger. The inlet vapor quality of the air-water mixture is 0.02 which provides the same void fraction as the two-phase refrigerant R-41-A does at vapor quality of 0.25. Two different types of baffles were inserted in the inlet port to block part of the water flow in the header as shown in Figure 1(b). One is for blocking the upper part of the inlet port and the other one is for blocking the lower part. An enlarged view of the baffle plate is shown in Fig. 2.

Fig. 3 shows the schematic diagram of the test system. Water was pumped from a storage tank through a set of flow meters to the mixing chamber prior to the inlet port of the heat exchanger. Air was compressed through a flow meter to the mixing chamber and combined with water to be air-water mixture. The flow pattern of the air-water mixture flowed inside the transparent heat exchanger was recorded by a high speed camera.

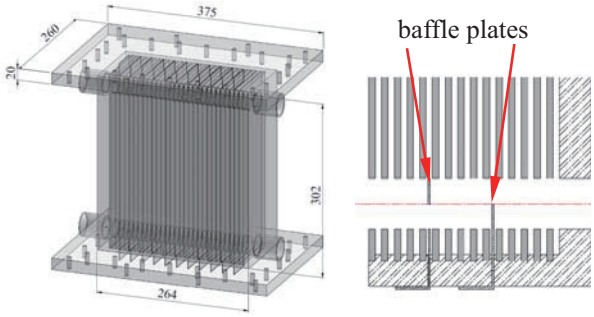


(a) test heat exchanger (b) inlet port

Fig. 1 Schematic diagram of the test section

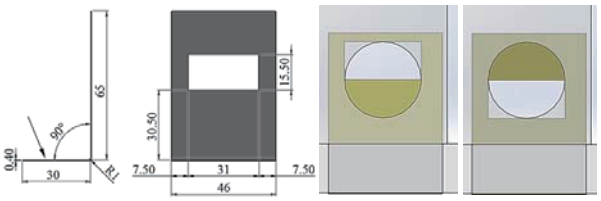


(a) dimensions (b) lower part (c) upper part

Fig. 2 Size and positions of the baffle plates

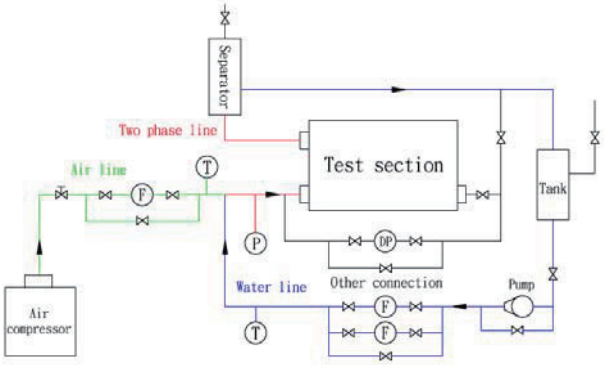


Fig. 3 Schematic diagram of the test system

## 3. Results and Discussion

3.1 Effect of flow rate on flow distribution

Fig. 4 shows the flow distribution in the test heat exchanger at Reynolds number varied from 50 to 250. At low Reynolds number (Re=50), since the flow inertia is low, it is observed that air flowed at the upper part of the header and up directly through the passages near the inlet port. Most of the air accumulated in the top portion of the heat exchanger but not flowed out with water.

Corresponding Author: Chien-Yuh Yang
*E-mail address:* cyyang@ncu.edu.tw

While flow rate increased (Re=150), the region of air penetration increased. Air-water mixture flowed through almost half of the passages. The amount of air accumulated on the top of the heat exchanger reduced. At the highest flow rate condition (Re=250), air-water mixture flowed evenly through all of the flow passages beside very few passages in the right part of the heat exchanger. There is no air accumulated in the top of the heat exchanger.

The flow pattern in the inlet port was observed and evaluated by the Taitel-Dukler [1] flow pattern transition criteria. It was found that while the flow pattern in the inlet port is stratified or wavy, since air was distributed in the upper part of the header, it tended to flow up directly right after it entering the inlet header. It caused that air flowed through the channels in the left part only. While the flow patterns in the inlet port is annular or churn, air-water mixture was uniformly distributed in each channels.

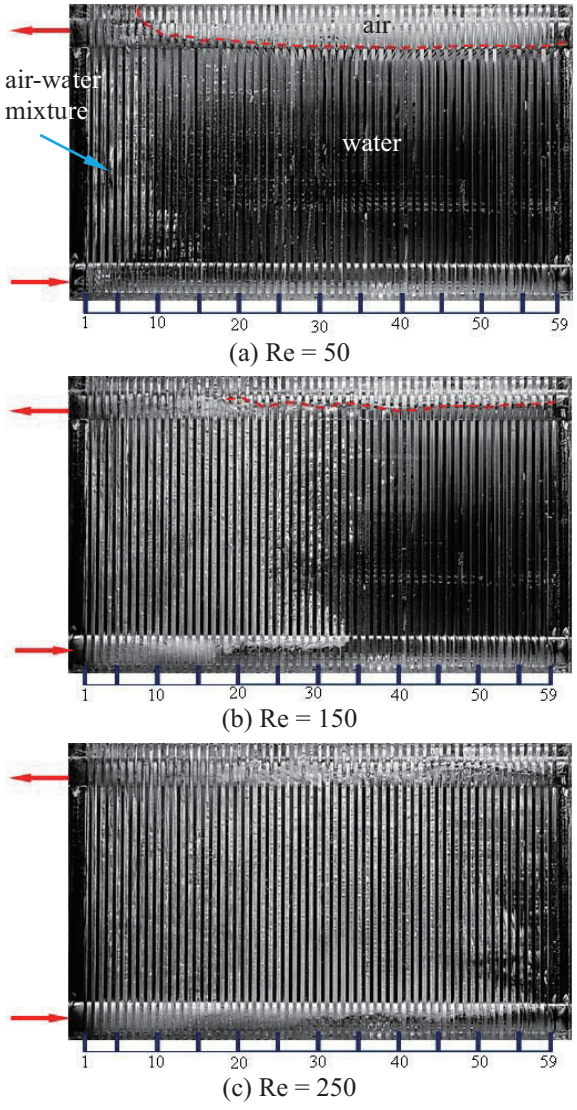


(a) Re = 50

(b) Re = 150

(c) Re = 250

Fig. 4 Effect of Reynolds number on flow distribution

3.2 Effect of baffle position on the flow distribution.

Aluminum baffle plates were used to block part of the flow cross-section area of the inlet header. The baffle plates was inserted through the bottom of the header every five channels. Two different types of baffles were inserted in the inlet port to block part of the water flow in the header. One is for blocking the upper part of the inlet port and the other one is for blocking the lower part. Fig. 5 shows the effect of baffle blocking positions on flow distribution at various Reynolds. While the upper of the inlet header was blocked, the flow distribution is similar to that without baffle plates. However, while the lower part was blocked, the air flow was limited in the few channels near the inlet port. The flow distribution was less evenly than that of the upper part blocked conditions.

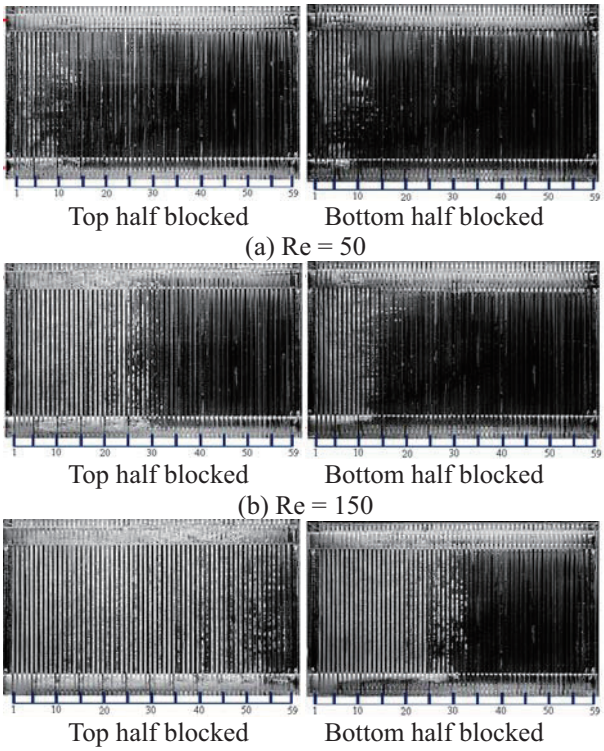

Top half blocked Bottom half blocked

(a) Re = 50

Top half blocked Bottom half blocked

(b) Re = 150

Top half blocked Bottom half blocked

(c) Re = 250

Fig. 5 Effect of baffle position on the flow distribution

**4. Conclusions**

From the previous stated experimental observation, we may conclude that:

1. The flow distribution in the channels of a plate heat exchanger was determined by the flow pattern in the inlet port.
2. Baffle plates cannot improve the distribution of the air flow in a plate heat exchanger. But it may reduce the pressure drop of air-water flow through the heat exchanger.

**Reference**

[1] Y. Taitel and A.E. Dukler, *AIChE Journal*, 22 (1976) 47 - 55.

Eleventh International Conference on Flow Dynamics
October 8-10, 2014, Sendai, Miyagi, Japan

# Experimental Studies on Self-assembled Ferrofluid Drops in a Rotating Field

Ching-Yao Chen, Sheng-Yan Wang, Hao-Chung Hsueh
Department of mechanical Engineering, National Chiao Tung University
1001 University Road, Hsinchu City 300, Taiwan

**ABSTRACT**

We experimentally investigate the motion of a ferrodrop array in a rotating magnetic field. Magnetized and driven by the external field, the ferrodrops are stretched and self-align to form a drop array along the field orientation. An interesting planet-like dual rotation, including local self-spins of individual drops and a global revolution of the drop array, is newly identified. While the drops spin nearly synchronized with the external field, the revolution always lags behind the field and appears a forth and back movement.

## 1. Introduction

The dynamics of slender magnetic structures in a dynamical field, such as a chain consisted of magnetic beads in a rotating or an oscillating field, have been intensively studied in recent years [1-5]. Inspired by these researches, a close resemblance is forming such a slender device by arraying ferrofluid drops, instead of chaining superparamagnetic beads. Nevertheless, motion of multiple drops aligned as an array, which is crucial for their manipulations in practical applications, has not yet drawn much attention. In addition, even the magnetic interactions between the magnetized drops mimic to the magnetic particles, the deformable surface would lead to a new phenomenon. This study intends to realize the motion of such a deformable drop array subjected to a rotating field. An interesting phenomenon of dual rotation, including the local self-spin and the global revolution, is reported. Sample experiments are also presented to demonstrate the capability as an effective active fluid mixer.

The experimental apparatus includes two pairs of coils powered by AC power sources and placed perpendicularly, designated as x- and y-axis. Two identical sinusoidal field components along the x- and y-axis are generated by the coils associated with a frequency of $f$=1 Hz. The overall external field ($\boldsymbol{H}$) composed by the two dynamical components is given by $\boldsymbol{H}=H_m\sin(2\pi ft+\triangle\theta_H)\boldsymbol{i}+H_m\sin(2\pi ft)\boldsymbol{j}$, where $\triangle\theta_H$ is the phase difference between $\boldsymbol{H}_x$ and $\boldsymbol{H}_y$. $H_m$ is the reference field strength.

## 2. Results and Discussion

If multiple drops are placed in an array and subjected to the same field condition. Under such a condition, the interactions between magnetized drops would expect to play an important role. Shown in Fig. 1 are the snapshots of a three-drop array under field configurations of $\triangle\theta_H=50^o$, $70^o$ and $90^o$. Similar to the case of a single drop, all the drops undergo local motions of self-spins. Nevertheless, an interesting global phenomenon of array revolution can also be identified. Contrary to the local self-spins which appear almost synchronized with the rotating field, this global revolutionary motion of the array does not follow the orientation of external field consistently. The drop array in a uniform rotating field of $\triangle\theta_H=90^o$ undergoes an apparent overall revolution with the external field, i.e. counter-clockwise, but lagging behind greatly. On the other hand, the drop array in a strongly non-uniform rotating field of $\triangle\theta_H=50^o$ merely shows a local oscillation. For the condition in a milder non-uniform rotating field of $\triangle\theta_H=70^o$, the array appears forth and back with a net counter-clockwise revolutionary movement within the period. Because of the inconsistent global revolution, the drop array usually does not align toward the same orientation with the overall field, so that full elongations of drops are allowed toward the simultaneous orientation of the overall field, e.g. examples shown the bottom row of Fig. 1. Nevertheless, when the alignment of the array is collateral to the simultaneous field, e.g. t=0.47s and 0.93s shown in the top row of Fig. 1, only the outward sides of the most outer drops can be stretched freely to form elliptical fronts. The shapes appear flatter at the sides adjacent to the neighbor drops. It is also interesting to notice that no drop coalescences occur between the adjacent drops in the present experimental condition. It is noticed that the drops can be in contact for sufficient strong field strength. Nevertheless, in the most commonly observed cases under the present experimental fluids, the drops retain separated if the field is turned off. An ongoing effort is devoted to explore the possibility of drop coalescences under different experimental conditions.

According to the experimental observations described in the above paragraph, a ferrodrop array driven by a rotating field undergoes an interesting motion of dual rotation, such as the local self-spin of individual drops and the global revolution of the array. Understandings of the local self-spins are straightforward, in which the orientation of elongation tends to follow along the orientations of the rotating field. On the other hand, the global revolution of the drop array is attributed by the interactions between the magnetized drops, whose mechanism can be analogized to the magnetic bead chain subjected to rotational or oscillating fields [1-5]. By this analogy, the ferrofluid drops and array resemble the magnetic beads and the chain, respectively. Based on the assumption of point dipoles, the torque (T) generated by the external field to the magnetized chain or array can be approximated as $T \sim \sin(2\triangle\theta_L)$, where $\triangle\theta_L$ stands for the simultaneous phase difference between the external field and the alignment of drop array. This torque is driving source to the global revolution. To

Corresponding author: Ching-Yao Chen
*E-mail address*: chingyao@mail.nctu.edu.tw

further understand this driving force, the trajectories of both the overall fields and drop arrays within one period of rotation for three field configurations are demonstrated in Fig. 2. For a uniform rotating field of $\triangle\theta_H$=90°, the angular speed of the field is constant, so that the field trajectory is a straight line as shown in the figure. On the contrary, for the configurations of non-uniform fields, their trajectories appear wavering with variant angular speeds within rotation. At an earlier time stage, the fields move well ahead of the arrays for all three conditions and generate effective torques toward the orientations of the rotating fields, i.e. counter-clockwise, so that the arrays are driven to undergo global revolutions. Nevertheless, due to the significant hydrodynamic drags to resist the revolutionary motion, the phase lags ($\triangle\theta_L$) continue to grow. At a certain extent, the phase lags would exceed a critical value of $\triangle\theta_L$ > 90°, and leads to a sign change of torque, i.e. T ~ sin(2$\triangle\theta_L$). Similar phenomenon had also been reported in a superparamegnatic chain, and was referred to as trajectory shift [5]. Then, the revolutionary movement of the drop array would be reversed. This reversed revolution would proceed till the direction of torque is changed again at $\triangle\theta_L$ > 180°. Similar scenarios would proceed continuously afterward at the times when the phase lag exceeds the multiples of 90°. The continuous alternation of torques explains the forth and back motion of the global revolutions. More detailed dynamics regarding the trajectory shift is referred to Ref.[5]. In addition, it is realized that the simultaneous angular speed of the external field at an early stage is the greatest for the most non-uniform rotating field of $\triangle\theta_H$=50°, as shown in Fig. 2, so that a largest phase lag is resulted at the early time interval. As a result, the first reversed revolution occurs the earliest for $\triangle\theta_H$=50°, as the vertical line marked by A1 shown in Fig. 2. By the same token, the first reversed revolutions for $\triangle\theta_H$=70 ° and 90°, marked by B1 and C1 respectively, will happen at later times subsequently. Fig. 2 shows that the trajectory of array has been shifted 4 times, e.g. A1~A4, for $\triangle\theta_H$=50°, while there are only 3 shifts for $\triangle\theta_H$=70 ° and 90°, e.g. B1~B3 and C1~C3, respectively. The later and fewer occurrences of the reversed revolutions for more uniform rotating field conditions are the reasons of greater net revolutionary movements.

### 3. Concluding Remarks

Driven by a rotating field, an interesting phenomenon of dual rotations is identified in arrayed ferrofluid drops, including a local self-spin of individual drops and the global revolution of the array. Because of the simultaneous realignments of the induced poles in the magnetized ferrofluids, the ferrodrops are elongated and spin nearly synchronized to the field. On the other hand, the global revolution of the drop array is resulted by the interactions between the magnetized drops, and might undergo a wave-like forth and back movement. The wavering behaviors of array revolutions are realized by the alternative magnetic torques acting to the array, which change sign when the phase lag between the orientations of the external field and the alignment of the array reaches multiples of π/2.

Financial support by the National Science Council of Republic of China (Taiwan) through Grant NSC 102-2221-E-009-051-MY3 is acknowledged.

**References:**

[1] Biswal, Gast, *Phys. Rev. E* 69 (2004), 041406.
[2] Cebers, Javaitis, *Phys. Rev. E* 69 (2004), 021404.
[3] Li, Sheu, Pai, Chen, *J. Appl. Phys.* 111 (2012), 07A924.
[4] Li, Chen, Sheu, Pai, *Microfluid Nanofluid* 13 (2012), 579.
[5] Li, Lin, Chen, *Microfluid Nanofluid* 14 (2013), 831.

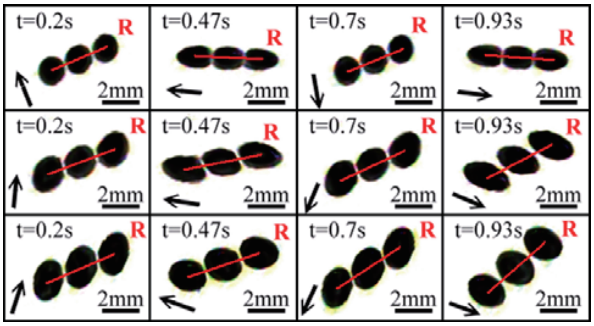


Fig. 1: Motion of a three-drop array at different times subjected to an overall field strength of $H_m$ = 47 Oe and (top row) $\triangle\theta_H$=50°; (middle row) $\triangle\theta_H$=70° ; (bottom row) $\triangle\theta_H$=90°. The drop on the right and the axis of array revolution are marked by letter "R" and red lines, respectively, to demonstrate the global revolution of the array.

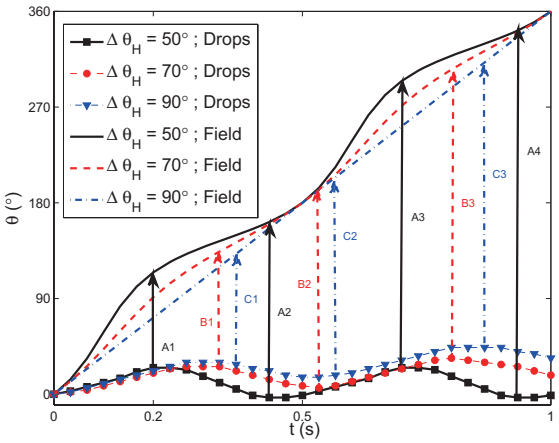


Fig. 2: Corresponding phase trajectories of the external fields and the drop arrays. The vertical lines, marked by letters "A" , "B" and "C" to represent the configurations of $\triangle\theta_H$=50°, 70° and 90° respectively, indicate the timings when the phase lags of the arrays to their corresponding fields reach the multiples of 90°.

Eleventh International Conference on Flow Dynamics
October 8-10, 2014, Sendai, Miyagi, Japan

# Calculation of Normal Modes and Natural Frequencies of a Wave Tank with Hinged Side Walls

Po-Hsun Chen, Tian-Shiang Yang
Department of Mechanical Engineering
National Cheng Kung University
1 University Road, Tainan, Taiwan 70101

**ABSTRACT**

As a simple model system for water-wave energy harvesting and storage, here we consider a wave tank with hinged side walls. In the present work, system forcing temporarily is omitted, and two-dimensional potential flow theory and standard analytical techniques are used to calculate the linear normal modes and the corresponding natural frequencies of the model system. The mathematical formulation and the results of calculations are discussed here, which form the basis for future work that will take into account system forcing and thus examine energy harvesting/storage efficiency.

## 1. Introduction

Water-wave energy utilization may not be the most important option of alternative energy technologies at present (see [1] for a recent review). But it still has significant practical value, and surely is worth studying for theoretical reason. As a first step in our projected series of theoretical studies of water-wave energy harvesting and storage, here we consider the simple model system of a wave tank with hinged side walls. In particular, we omit the system forcing for now, and use two-dimensional (2-D) potential flow theory and standard analytical techniques to calculate the linear normal modes and the corresponding natural frequencies of the model system. Note that this configuration is relevant in practical wave energy converters [2].

Some previous works related to the present pursuit are briefly discussed below. In 1929, Havelock [3] studied a simple wave generator. In that work, linear waves generated by small oscillations of a vertical wavemaker (say, at $x=0$) with radiation condition at infinity (i.e., out-going waves only as $x\to\infty$) were calculated. More recently, in 1976 Hyun [4] studied the performance of plunger-type wavemakers, for which waves are generated by periodic vertical motion of a thin triangular wedge. In that work the total hydrodynamic force on the wedge was calculated, which then was used to explain the performance of the wavemaker from mechanical perspectives. Moreover, Wu [5] numerically investigated the dynamics of an inclined-plate wave generator by use of the boundary collocation method to deal the kinematic boundary condition on the inclined plate.

A nontrivial difference between the present work and the previous works discussed above is that, instead of considering wave generators, here we shall think of wave-energy conversion systems. Technically, the radiation condition at infinity no longer is appropriate, and that is why we consider a wave tank with two hinged side walls; see Fig. 1. The mathematical formulation will be detailed in Section 2. Then, the main results will be discussed in Section 3, before we conclude this paper in Section 4.

Corresponding author: Tian-Shiang Yang
*E-mail address*: tsyang@mail.ncku.edu.tw

## 2. Mathematical Formulation

The schematic of the model system, which consists of a 2-D wave tank with hinged side walls, is shown in Fig. 1. In the sequel we shall use dimensionless variables. The length $L$ and equilibrium depth $h$ of the wave tank are used to normalize the horizontal and vertical coordinates, respectively. Time is scaled by $\sqrt{h/g}$, $g$ being the gravitational acceleration. Moreover, the amplitude of the side-wall oscillations is scaled by a small dimensionless parameter $\varepsilon$ (with $0<\varepsilon<<1$). The free-surface elevation is scaled by $\varepsilon h$, and the velocity potential by $\varepsilon h\sqrt{gh}$.

Then, in terms of dimensionless variables, the velocity potential $\phi(x,z,t)$ satisfies the Laplace's equation

$$\frac{\partial^2\phi}{\partial z^2}+\mu^2\frac{\partial^2\phi}{\partial x^2}=0, \tag{1}$$

where $\mu=h/L$ is the aspect ratio of the wave tank. Moreover, $\phi(x,z,t)$ is subjected to the bed condition

$$\frac{\partial\phi}{\partial z}=0 \quad (z=-1), \tag{2}$$

and the kinematic and dynamic boundary conditions on the free surface ($z=0$):

$$\frac{\partial\phi}{\partial z}=\frac{\partial\eta}{\partial t} \quad (z=0), \tag{3}$$

$$\frac{\partial\phi}{\partial t}+\eta=0 \quad (z=0). \tag{4}$$

Meanwhile, we also impose the side-wall kinematic boundary conditions:

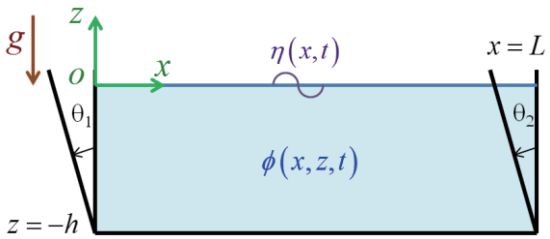


Fig. 1 Schematic of the wave tank model system studied here.

$$\frac{\partial \phi}{\partial x} = -\mu^{-1}(z+1)\dot{\theta}_1 \quad (x=0), \tag{5a}$$

$$\frac{\partial \phi}{\partial x} = -\mu^{-1}(z+1)\dot{\theta}_2 \quad (x=1), \tag{5b}$$

and the dynamic boundary conditions:

$$I\ddot{\theta}_1 + K\theta_1 = -\int_{-1}^{0} \left.\frac{\partial \phi}{\partial t}\right|_{x=0} (z+1)\,dz, \tag{6a}$$

$$I\ddot{\theta}_2 + K\theta_2 = \int_{-1}^{0} \left.\frac{\partial \phi}{\partial t}\right|_{x=1} (z+1)\,dz, \tag{6b}$$

Note also that (6a) and (6b) are balances of inertial, angular elastic spring, and pressure forces in essence; $I$ and $K$ are dimensionless parameters characterizing the inertia of the side walls and the stiffness of the angular springs, respectively.

## 3. Results and Discussion

Using standard analytical techniques, we then calculate the natural frequencies of the wave tank. For the purpose of demonstration, both the inertia and stiffness parameters are set at unity value, i.e., $I=1$ and $K=1$. Moreover, the aspect ratio of the wave tank is set as $\mu = 0.5$.

With the aforementioned parameter setting, the first few calculated natural frequencies are plotted in Fig. 2. It is interesting, but by no means surprising, that there are two different sets of natural frequencies, one with the two side walls oscillating in phase (denoted by $\omega_n^+$ here), and the other with the two side walls oscillating $\pi$ out of phase (denoted by $\omega_n^-$).

The corresponding mode shapes of the free-surface oscillation corresponding to the first three sets of natural frequencies are plotted in Figs.3. It is seen that the in-phase modes have anti-symmetric (with respect to the mid-plane) free-surface oscillations, while the out-of-phase modes have symmetric free-surface oscillations. This observation, of course, makes perfect physical sense.

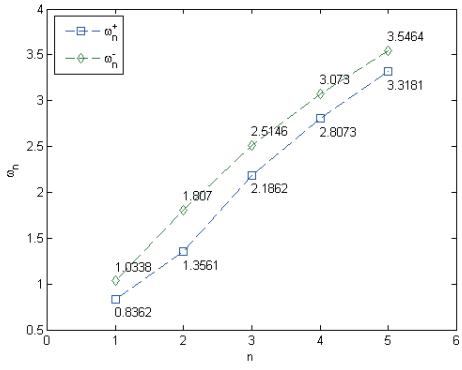


Fig. 2 The first few calculated natural frequencies of the wave tank. Here $\omega_n^+$ are the natural frequencies for modes having the two side walls oscillating in phase, and $\omega_n^-$ are for those with the two side walls oscillating $\pi$ out of phase.

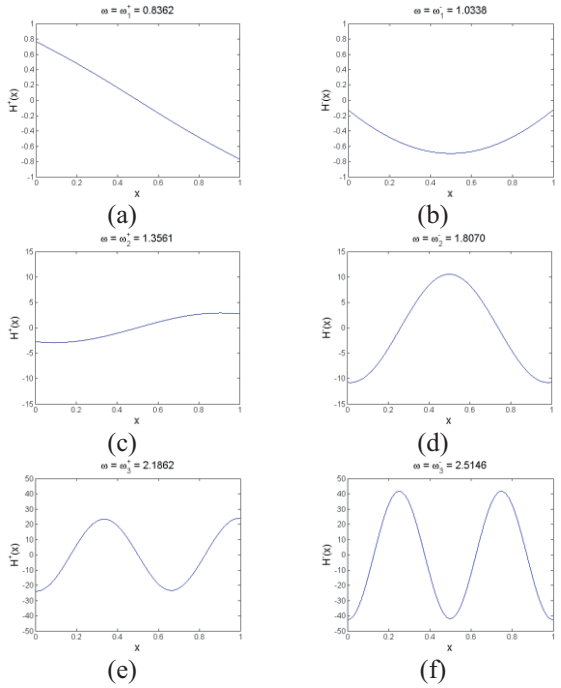


Fig. 3 The mode shapes corresponding to (a) $\omega_1^+$, (b) $\omega_1^-$, (c) $\omega_2^+$, (d) $\omega_2^-$, (e) $\omega_3^+$ and (f) $\omega_3^-$. Here $H_n^{\pm}$ are the free-surface deformation distributions corresponding to $\omega_n^{\pm}$.

## 4. Concluding Remarks

Here we have briefly discussed the normal modes and the corresponding natural frequencies of a 2-D wave tank with hinged side walls. This works differs from previous ones in that waves can propagate both ways, and thus is more directly relevant to water-wave energy harvesting/storage applications.

In future work, we shall incorporate forcing into the problem, and then study its wave-energy harvesting and storage characteristics. Also, some experiments will be attempted. Meanwhile, as we gain insights into the analytical technicalities, we will also try to impose even more realistic end-wall conditions to the problem, and see how substantially such conditions affect the results, and if such effects are important when comparing theoretical and experimental results.

## References


[1] A.F. de O. Falcão, *Renewable and Sustainable Energy Reviews*, 14 (2010) 899–918.

[2] S. Hazra, S. Bhattacharya, K.K. Uppalapati, J. Bird, In: Proceedings of the *2012 IEEE Energy Conversion Congress and Exposition*, (2012) 407–413.

[3] T.H. Havelock, Philosophical Magazine, 8 (1929) 569–576.

[4] J.M. Hyun, *Journal of Hydronautics*, 10 (1976) 89–94.

[5] Y.C. Wu, *International Journal for Numerical Method in Fluid*, 8 (1988) 803–811.

# An Investigation of the Applications of the Immersed Boundary and Grid Deformation Method in Compressible Flow Field

Kun-Rung Huang[1], Wu-Shung Fu[1], Chung-Gang Li[2]
[1] National Chiao Tung University
Ta Hsueh Road, HsinChu, HsinChu, 30010, Taiwan
[2] RIKEN, Advanced Institute for Computation Science
2-1 Hirosawa, Wako, Saitama 351-0198, Japan

**ABSTRACT**

In this study, the complex geometry compressible flow field in Roe scheme was investigated by using the immersed boundary method and grid deformation technology. Case one is the heat transfer phenomena of two dimensional wavy channel by using grid deformation technology. The other is the process of compressed gas discharging through a high pressure tank. Two different cases was examined and compared with experimental data, the result showed that both of them have good agreements.

## 1. Introduction

In order to calculate the complex geometry problem in CFD, a lot of numerical methods were tested and released for now. The most popular code is the SIMLPE algorithm base on the unstructured grid. The above method can handle the complex geometry flow field problem smoothly, but the results have to base on the fine mesh that some can made. In this study, the method of Roe scheme [1] was applied and deduced to curvilinear coordinate, and therefore the same problem can be solved with less grid. The construction of the grid bases on structured grid, it means that the accuracy of the results are higher than unstructured grid in the same grid number. Two different cases was investigated: the two dimensional wavy channel and the process of high pressure gas discharging by using two different technology: the grid deformation technology and immersed boundary method [2].

## 2. Physical Model

Two cases model were listed as following:

**1. Two dimensional wavy channel:**

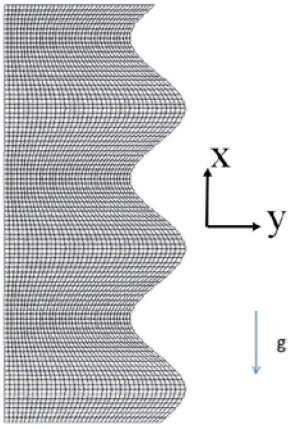


Fig. 1 Physical model of wavy channel

In Fig.1, the structure can be divided to three parts: left vertical adiabatic wall, wavy heating area and bottom and top open boundaries. The length of wavy channel, the aspectratio and the wavelength are 3λ, *a* and λ, respectively. The width of the top and bottom open boundaries is λ.

**2. Transient process of gas discharging:**

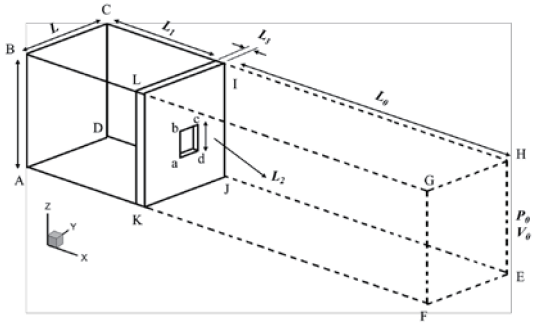


Fig. 2 Physical model of vessel and surroundings

The physical model was divided to two parts: the high pressure vessel and open boundary zone. In the inside region, highly compressed gases is filled in the beginning and surrounded by solid wall with a small opening. The pressure and temperature at the outside zone is set as 1atm and 298K.

The boundary of the top and bottom of the wavy channel and the outside region of the vessel were set as non-reflection boundary condition [3].

## 3. Numerical Method

The governing equations are continuity, momentum and energy equations and written as general partial form also shown in Eq. 1. The ideal gas condition and body force such as gravity or immersed boundary force are also considered in the above Navier - Stokes equations.

$$\Gamma\frac{\partial U_p}{\partial \tau}+\frac{\partial \tilde{U}}{\partial t}+\frac{\partial \tilde{F}}{\partial x}+\frac{\partial \tilde{G}}{\partial y}+\frac{\partial \tilde{H}}{\partial z}=S' \qquad (1)$$

In Eq.1 the symbol $U_p$, $\tau$, $U$, and $S'$ are the preconditioning, artificial time, time dependant, and source term. The symbol $F$, $G$, and $H$ are the convection accompanied with viscous part in x, y, and z derivative form.

The Roe scheme matching preconditioning method and grid deformation technology are adapted to resolving the governing equations. Then the 3th order

Corresponding author: Wu-Shung Fu
*E-mail address*: wsfu@mail.nctu.edu.tw

MUSCL proposed by Abalakin et al. [4] is used to compute inviscid terms. Viscid terms are solved by a second order central difference. Finally, the LUSGS [5] is used to solve temporal advancements.

The immersed boundary method was proposed by Peskin, and further Ye et.al. [6] deduced the method into Cartesian coordinate. In their study, Ye et.al. [6]. also derived the interpolation equations for structured gird and shown in Eq. 2, and 3.

$$\begin{bmatrix} C_1 \\ C_2 \end{bmatrix} = \begin{bmatrix} x_1 & 1 \\ x_2 & 1 \end{bmatrix}^{-1} \begin{bmatrix} \phi_1 \\ \phi_2 \end{bmatrix} \tag{2}$$

$$\phi_R = x_R C_1 + C_2 \tag{3}$$

Eq. 2 is the one dimensional interpolation method, the $x_i$ and $C_i$ are the coordinate of the $\phi_i$ and interpolation constant, the Eq. 3 is the interpolation equation for node "*R*".

## 4. Results and Discussion

The result are divided by the type of the method that been used.

### 1. Grid Deformation:

In order to confirm the flow and temperature field the result of the Bhavnani [7] proposed the experiment with wavy heating vertical wall of natural convection. The boundary condition of three flat sides are opened space i.e. $P$ = 100kPa $T$ = 298K and the waved wall is 328K, the periodic boundary was set in z-direction; the comparisons are shown in Fig. 3.

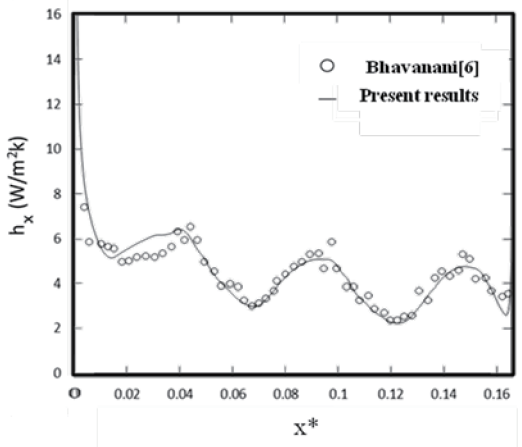


Fig. 3 Heat transfer coefficient distribution along the streamwise, $\lambda$ = 50.8mm, $a$ = 5.08, $Ra$ = $3\times10^5$

### 2. Immersed boundary method:

For verifying the accuracy of the immersed method, two different situation are investigated and compared with compared with Perry and Chilton [8]. The pressure in the vessel of the two cases are 1.5atm and 1.8atm, respectively, the density of the two cases are also 1.5 and 1.8 times than air density in 298K. The wall with a small opening immersed in the computational domain, The results are the mass flow rate through the opening and shown in Fig. 4. Both two simulation results have good agreements with the experience equation [8]. The data of mass flow rate accompanied with a little vibration because of the pressure fluctuation at the inside region.

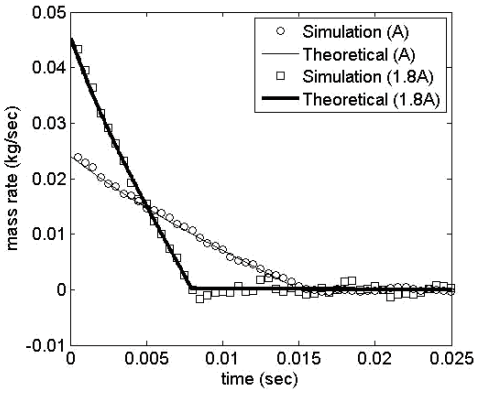


Fig. 4 The comparison of variations of mass flow rates of different cases

## 5. Concluding Remarks

Due to the comparisons of two methods, both results have good agreement with experimental studies [7, 8]. The two methods were added to Roe scheme solver completely, also the grid number of both two cases were not too much.

The two methods work smoothly in Roe scheme with structured grid but they also complicated the original program. The calculation time for an iteration is 1.5 times than the situation without grid deformation technology and immersed boundary method. The calculation booster technology must be applied such as OpenMP or CUDA.

In order to generate the ideal mesh for the grid deformation method, the Algebraic Grid Generation Techniques, Partial Differential Equation Techniques, and Coordinate System Control should be considered. Sometimes the ideal grid generator software such as Gambit or ANSYS are better than above technologies but have to possess the ability of handling the software output data.

The immersed boundary method is powerful but pre-process are complicated, the inverse coordinate matrix (Eq. 2) of each interpolation point has to be calculated. If the mesh scale of the immersed body is too large or small than calculation grid scale the iteration could lead to blow up. And finally, the proper immersed body mesh scale should be tested before the calculation.

## References


[1] P. L. Roe, *J. Comput. Phys.*, 43 (1981) 357-372.
[2] C.S. Peskin, *J. Comput. Phys.*, 10 (1972) 252-271.
[3] T.J. Poinsot, S.K. Lele, *J. Comput. Phys.*, 101 (1992) 104-129.
[4] I. Abalakin, A. Dervieux, T. Kozubskaya, *INRIA.*, (2002) No4459.
[5] S. Yoon, A. Jameson, *AIAA.*, 26 (1988) 1025-1026.
[6] T. Ye, R. Mittal, H.S. Udaykumar, W. Shyy, *J. Comput. Phys.*, 156 (1999) 209–240.
[7] Bhavanani S.H., Bergles A.E, *Int. J. heat and mass trans.*, 33(5) (1990) 965-981.
[8] Perry, Chilton, *Chemical engineers handbook 5 ed.*, (1973).

# Numerical Simulation on Displacement of Immiscible Layers

Hanni Maksum Ardi[1], Yu-Shang Huang[1], Ching-Yao Chen[1]
Department of Mechanical Engineering, National Chino Tung University
1001 University Road, City, Hsinchu, 30010, Taiwan, ROC

**ABSTRACT**

The influences of viscous fingering due to difference between the viscosities of displacing fluids and followed by effect of different parameters are investigated. We present numerical simulations using a diffuse-interface model for this immiscible displacement with variety of the layers. The qualitative and quantitative results obviously presented the viscous fingering structures in this paper. The Péclet number parameter didn't provide much different effects in viscous fingering patterns. Otherwise, capillary number *Ca* and Atwood number *A* being the main control parameters here.

## 1. Introduction

Viscous fingering is representation of an unstable displacement process form in which a more viscous fluid is displaced by a less viscous fluid. This phenomenon is commonly used in the enhanced oil production process which is implemented to increased oil recovery (EOR) performance.

The phenomenon of instability between two parallel plates in a two dimensional flow in porous media have been investigated carefully by numerous investigators since Saffman and Taylor [1] published their fundamental study in 1958. Recently, Kang et al [2] used a lattice Boltzmann multiphase/multi-component model to study the flow of two immiscible displacement fluids with different viscosities in a channel for two dimensional layered flows. They clearly investigated the effect of viscosity ratio, capillary number, and wettability displacing fluid.

Chen and Wang [3] presented the miscible displacement of a layer by high accuracy numerical simulation in porous media. They observed the structures of fingering patterns and found that the growth of fingers is suppressed by another fingers have caught up the stable front. The fingering on the miscible displacement in porous media never break through the stable leading front.

In this study, we intend to systematically investigate the effects of the viscosity ratio, capillary number at high *Pe* of fluids on incompressible displacement of immiscible layers in porous media. We focus on the behavior of the fingers for single-layer and multi-layers displacement.

## 2. Method

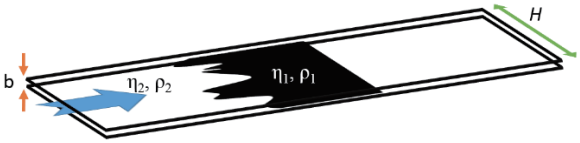


Fig.1 Sketch of immiscible layer displacement in porous media. The width of gap is b, the concentration and viscosity of the fluids are donated as c and $\mu$. The less viscous is displaced by more viscous on the displacement with uniform velocity U.

Corresponding author: Ching-Yao Chen
*E-mail address*: chingyao@mail.nctu.edu.tw

This study established by numerical simulations which focus on displacement method to investigate the instability of immiscible fluids flow in porous media. The less-viscous fluid displaced in porous media with a uniform velocity U. Which a less viscous fluid has density $\rho_1$ and viscosity $\eta_1$ and the more viscous fluid has density $\rho_2$ and viscosity $\eta_2$. Correlations of viscosity $\eta$ and density $\rho$ with the phase field variable c are required by:

$$\eta(c) = \eta_1 e^{[\mathbb{R}(1-c)]}, \quad \mathbb{R}=\ln\left(\frac{\eta_2}{\eta_1}\right), \tag{1}$$

The dimension governing equation can be provided using:

$$\nabla \cdot \vec{\mathbf{u}} = 0, \tag{2}$$

$$\nabla p = -\frac{\mu}{h^2}\vec{\mathbf{u}} - \varepsilon\nabla^2 c, \tag{3}$$

$$\rho\left(\frac{\partial c}{\partial t} + \vec{\mathbf{u}}\cdot\nabla c\right) = \alpha\nabla^2\mu, \tag{4}$$

$$f_0 = f^* c^2 (1-c)^2, \tag{5}$$

Where **u** is the velocity of fluid, c denotes the concentration of fluid layer, p the pressure and μ is chemical potential. The mobility coefficient represented by α. In addition, approaching the dimensionless to derive the equation use characteristic parameters, as given by Length H, velocity $U_0$, time $\frac{H}{U_0}$, viscosity $\eta_1$, pressure $\eta_1 U\frac{H}{K}$, and energy $f^*$.

Furthermore, we also need the governing equations dimensionless, so that we take the vertical extent H domain as the characteristic length scale and K as permeability in a homogeneous porous medium.

$$\nabla^* \cdot \overrightarrow{U^*} = 0, \tag{6}$$

$$\nabla . p^* = -\eta^* \overrightarrow{U^*} - \frac{Ca}{Cahn}\nabla^* \cdot \left[\left(\nabla^* c\right)\left(\nabla^* c\right)^T\right], \tag{7}$$

$$\frac{\partial c}{\partial t^*} + \overrightarrow{U^*}\cdot\nabla^* c = \frac{1}{Pe}\nabla^{*2} c, \tag{8}$$

The constants ε and c represent the coefficient of capillarity and concentration of fluid viscosity.

To simulate the immiscible displacement, we have some main control parameters in numerical code. Which are the Péclet number *Pe*, the Capillary number *Ca* represent the relative effect of viscous forces versus

surface tension between two immiscible liquids. The Cahn number *Cahn* describes process of separation of fluids, and the viscosity contrast Atwood number *A*. As given by:

$$Pe = \frac{\rho U_0 H}{\alpha f^*}, Ca = \frac{\rho U_0 H}{K f^*}, \quad Cahn = \frac{\varepsilon}{H^2 f^*}, A = \frac{(\mu_1 - \mu_2)}{(\mu_1 + \mu_2)} \tag{9}$$

In the model, the dimensionless momentum equation can be rearrange into a vorticity ω and streamfunction ψ, is given by:

$$\nabla^2 \psi = -\omega, \tag{10}$$

The boundary conditions are prescribed as follows;

$$u = \frac{\partial \psi}{\partial y}, v = \frac{\partial \psi}{\partial x}, \tag{11}$$

Finally, according to the definitions of the new formula of the dimensionless governing equatios can be expressed as:

$$\omega = \mathbb{R}\left( u\frac{\partial c}{\partial x} - v\frac{\partial c}{\partial y} \right) + \frac{E}{\eta}\left\{ \begin{matrix} \frac{\partial c}{\partial x}\left[ \frac{\partial^3 c}{\partial x^2 \partial y} + \frac{\partial^3 c}{\partial y^3} \right] - \\ \frac{\partial c}{\partial y}\left[ \frac{\partial^3 c}{\partial x \partial^2} + \frac{\partial^3 c}{\partial x^3} \right] \end{matrix} \right\}, \tag{12}$$

## 3. Results and Discussion

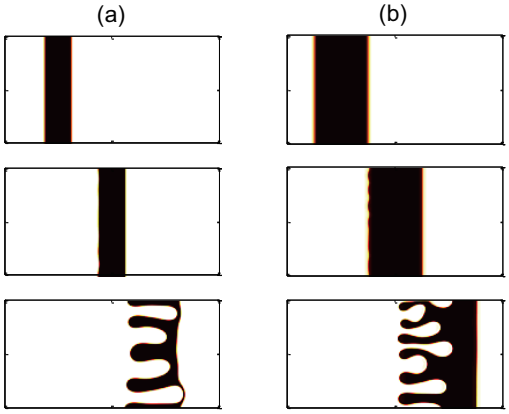


Fig.2 Pattern of fingering by concentration plot (a) layer width = 0.125 (b) layer width = 0.25.

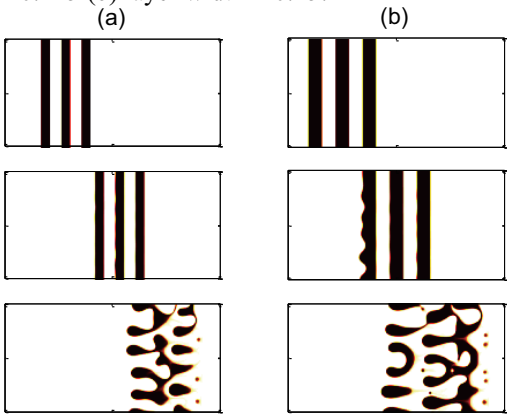


Fig.3 Pattern of fingering by concentration plot (a) layer width = 0.125 (b) layer width = 0.1875

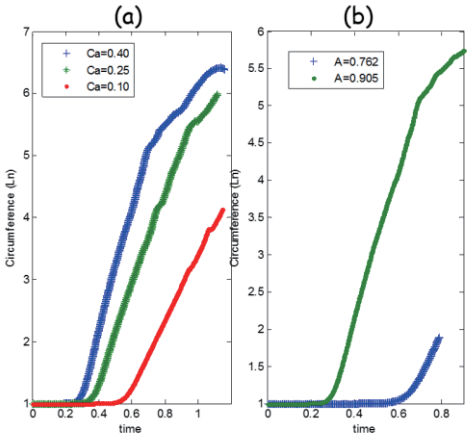


Fig.4 Circumference conditions of Pe=$10^4$, A=0.905, Cahn=$10^{-5}$ on immiscible single-layer (a) for diff. *Ca*, (b) for diff. of *A*.

In this section, results for displacement flows for immiscible layer are presented. We begin by presenting data related to various numerical simulations for single layer, which have control parameter: Pe = $10^4$, A = 0.762, Ca = 0.40, Cahn = $10^{-5}$ for total layer width is 0.125; 0.25. Figure 1 showed that the first fluids has concentration c = 0 and the second fluid c = 1 is immiscible fluid flows when the first fluid is injected to second fluid. Figure 2 displayed the concentration at different time distribution conditions. From top to bottom, respectively the time t = $10^{-6}$, 0.5, 1.0. For multi-layer concentration of immiscible displacement has shown in Figure 3. Which have control parameter Pe = $10^4$, A = 0.762, Ca = 0.40, Cahn = $10^{-5}$ for total layer width is 0.125; 0.1875. In order to understand the effects of capillary number Ca, we present the result in Figure 4 as the quantitative data in this simulation. It showed the condition of fluid flow between the perimeter of different Ca vs. time (a), and comparing the ratio of circumference of different A vs. time (b) for single layer.

## 4. Concluding Remarks

Our analysis considered for the single layer and multi-layer behaviors at high Pe on immiscible displacement. The result revealed that the Ca and A affect the pattern of viscous fingering on immiscible displacement. Furthermore, we found that at the time bottom the fingering have high possibilities to breakthrough for single layer and multi-layer.

## References


[1] Saffman, P.G. and Taylor, G.I., *Proc R Soc London A*, 245(1958)321-29.

[2] Kang, Q. Zhang, D. and Chen, S., *Advances in Water Resources*, 27(2004)13-22.

[3] Chen, C.-Y. and Wang, S.-W., *Fluid Dyn*, Vol. 11(2001)8.

Eleventh International Conference on Flow Dynamics
October 8-10, 2014, Sendai, Miyagi, Japan

# An Investigation of Transitional Phenomena from Laminar to Turbulent Natural Convection using Compressible Direct Numerical Simulation

Chung-Gang Li[1], Makoto Tsubokura[1], Keiji Onishi[1], Wu-Shung Fu[2]
[1]Advanced Institute for Computational Science, RIKEN
7-1-26, Minatojima-minami-machi, Chuo-ku, Kobe, Hyogo, 650-0047, Japan
[2] Department of Mechanical Engineering, National Chiao Tung University
1001 Ta Hsueh Road, Hsinchu, 30056, Taiwan

**ABSTRACT**

The complete transition from laminar to turbulent natural convection is investigated by compressible direct numerical simulation (DNS). Numerical methods of Roe scheme with precontioning and dual time stepping are used for addressing the flow field which is low speed but the density is variable. During the transient process, there are four stages which are laminar, unstable process, relaminarization and turbulence can be obviously identified. Finally, the laminar, transition and turbulence coexist and the statistics are in good agreement with the experimental data.

## 1. Introduction

The transition from laminar to turbulent natural convection is one of the most important subjects for heat transfer applications. In order to understand above phenomena, a physical model of an open-ended finite length channel with heat on the wall has been investigated for several decades. Experimentally, Miyamoto et al. [1] is a pioneer about this topic. He set a constant heat flux on the wall to observe the transition and obtain the turbulence quantity profiles. One of the most important contributions in this paper was that the transition points can be identified very clearly and the position is just the same with the peak of the temperature distribution. For the numerical simulations, owing to numerical complexities, the simulation for the complete transition process has been limited. Lau et al. [2] adopted the same physical model with Miyamoto et al. [1] to investigate the transitional phenomena. The transition point can be accurately captured using weakly compressible Navier-Stokes equation and large eddy simulation (LES) with the Vreman subgrid-scale (SGS) model. Subsequently, he compared the Vreman SGS model with Smagorinsky, dynamic and approximate localized dynamic models and concluded that the Vreman model is more suited to this kind of phenomena. From the above, it can be known that there are three major challenges to simulating this kind of flow, which are the availability of using compressible program on low speed regions, the appropriate boundary conditions at inlet and outlet, and the accuracy of capturing turbulent motions in small scales.

Because of the inapplicability of Bossinesq assumption under the high temperature difference, adopting the compressible program at very low Mach numbers is necessary. Owing to the different orders between acoustic and flow speeds, Weiss and Smith [3] proposed a preconditioning matrix matching with Roe scheme and dual time stepping to simulate a natural convection in a two dimensional concentric circles.

For the boundary conditions, in incompressible flows, generally, methods of matching a mass conservation or based on Bernoulli's equation are used. However, the above methods are not suited to the compressible flows. Fu et al. [4] combined the Non-reflection and absorbing boundary conditions and extended them to low Mach numbers to be suited to the problem of the channel flow with natural convection.

To compare with the numerical turbulent solvers of the Reynolds-averaged Navier-Stokes equations (RANS) and LES, DNS has the merit of the reliability.

The aim of this study is thus to investigate the transitional phenomena from laminar to turbulent natural convection using compressible DNS. The physical model is a long channel with constant heat flux on the wall that the air can be sucked from the inlet and developed to turbulence at outlet. The transient stats are separated to four stages according to the flow field. Finally, the statistics data is compared with Miyamoto et al. [1].

## 2. Physical model and Governing equation

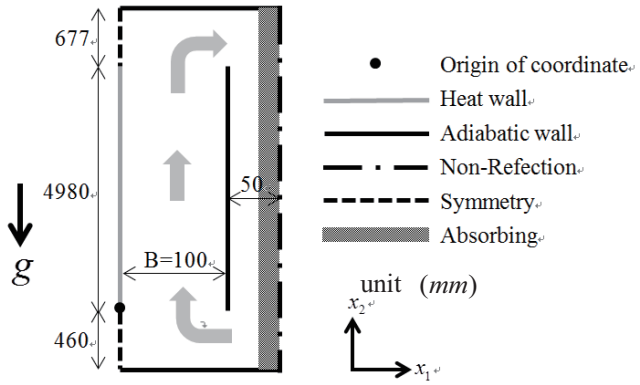


Fig. 1 Physical model

The channel flow with constant heat flux $Q = 104W/m^2$ on the heat wall shown in Fig. 1. The streamwise, vertical and spanwise directions are denoted $x_1$, $x_2$ and $x_3$, respectively, and the corresponding velocities are $u_1$, $u_2$ and $u_3$, respectively. The length, height and width are $l_1$, $l_2$ and $l_3$, respectively.

The governing equation is

$$\frac{\partial U}{\partial t}+\frac{\partial F_1}{\partial x_1}+\frac{\partial F_2}{\partial x_2}+\frac{\partial F_3}{\partial x_3}=0. \quad (1)$$

Corresponding author: ChungGang Li
*E-mail address*: chung-gang.li@riken.jp

## 3. Numerical method

At extremely low Mach numbers, the fluid speed is several orders of magnitude lower than the sound speed. The Roe scheme with a preconditioning method is then adopted to resolve the governing equation. Additionally, curvilinear coordinates are derived to strengthen the resolution near the wall, and dual time stepping is added to correct the temporal term.

For the boundary conditions, at the inlet, the flow should be sucked automatically instead of imposing a velocity and at the outlet, the flow should leave the computational domain without any reflection to pollute the flow field. Therefore, the hybrid boundary condition at low Mach numbers [4] which combines non-reflection and absorbing boundary conditions is adopted.

## 4. Results and Discussion

The computations are implemented at an extremely low Mach numbers using the compressible DNS method. The total resolution is $4000\times192\times150$. In the right hand side of the channel, an extra computational domain and absorbing zone are added.

Figure 2 shows the temperature distribution contour for four stages during the whole transient processes. In the early stage of $t=3.2s$, the distribution is quite ordered and the high temperature zone appearing only near the heat wall is very thin. In the second stage of $t=12.8s$, owing to the violent heat transfer between the cold and heated fluid, the distribution starts to be distorted. Accompanying with more and more heat from the wall to the fluid, the high temperature zone is gradually spread to the whole channel. Thus, the fluctuation source, coming from the natural convection by temperature gradient, continuously decreases, so the unstable process in the second stage couldn't be maintained. The flow field then laminarized again in third stage of $t=16.0s$. However, because the fluctuation velocity is continuously sucked from the inlet of the channel, finally, the flow develops to the turbulence at the upper part of the channel at $t=17.6s$.

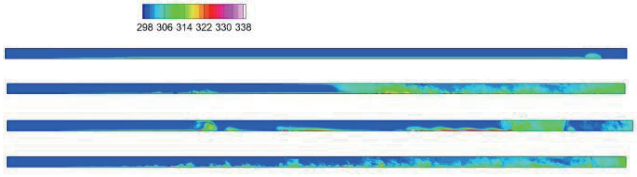


Fig. 2 temperature distribution contour

After reaching the quasi-steady state, the flow develops from laminar to turbulent natural convection can be identified very clearly in Figure 3.

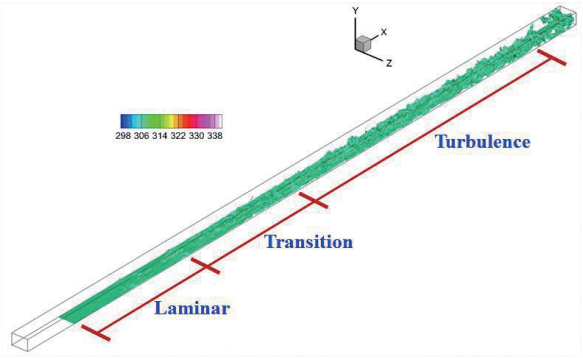


Fig. 3 temperature isothermo-surface ( $T=310K$ )

Figure 4 shows the comparison between the present and experimental wall temperature excess distribution along heated and adiabatic wall. Although the discrepancy is around $6K$, the trend is still well consistent with the experimental data. Moreover, the transition point which is located around $2.25m$ can be accurately captured.

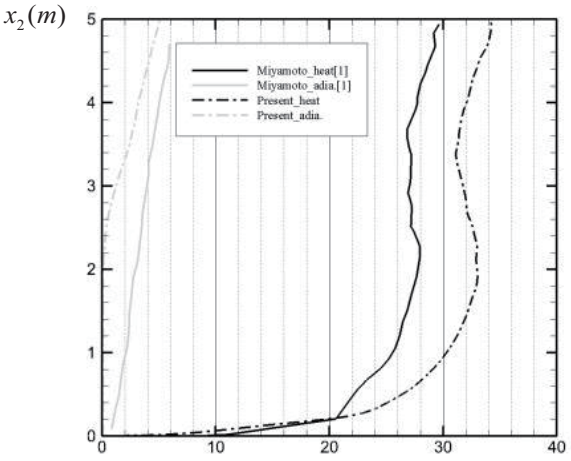


Fig. 4 Temperature excess distribution

## 5. Conclusion

The compressible DNS is used to simulate the transition from laminar to turbulent natural convection in a long channel. There are four stages, which are laminar, unstable process, relaminarization and turbulence, can be clearly identified. After reaching the quasi-steady state, it can be observed that the laminar, transition and turbulence coexist in the same flow field. Finally, the transition point can be accurately captured.

## References

[1] M. Miyamoto ,Y. Katoh, J. Kurima, H. Sasaki, *Proceedings of the eighth international heat transfer conference*, (1986) 1593.
[2] GE. Lau, GH. Yeoh, V. Timchenko, JA. Reizes, *Computers & Fluids*, 59 (2012) 101.
[3] M. Weiss, A. Smith, *AIAA*, 33 (1995) 2050.
[4] WS. Fu, WH. Wang and CG. Li, *International Journal of Thermal Sciences*, 84 (2014) 48.

Eleventh International Conference on Flow Dynamics
October 8-10, 2014, Sendai, Miyagi, Japan

# Numerical Analysis in a Directional Solidification System

Ting-Kang Lin, Ching-Yao Chen
Department of Mechanical Engineering, National Chiao Tung University
1001 University Road, Hsinchu City 300, Taiwan, R.O.C.

**ABSTRACT**

Manufactures of multi-crystalline silicon ingots by means of the directional solidification system (DSS) is important to the solar photovoltaic (PV) cell industry. The quality of the ingots, including the grain size and morphology, is highly related to the shape of the crystal-melt interface during the crystal growth process. We performed numerical simulations to analyze the thermo-fluid field and shape of the crystal-melt interface for a transient process. Accuracy of the results is supported by comparing the evolutions of crystal heights with the experimental measurements.

## 1. Introduction

The multi-crystalline-silicon based solar cell has the highest market share in the worldwide production of photovoltaic cells. Advanced manufacturing procedure of the multi-crystalline silicon ingot is strongly desired to reduce the costs, and to enhance the quality of the photovoltaic cells. The performance of the photovoltaic cell can be affected by the grain size and the morphology of the multi-crystalline silicon. Larger and more uniform grains of the multi-crystalline silicon improve the conversion efficiency of the solar cell [1]. It has been understood that the formation of the grains is highly related to the shape of the crystal-melt interface. Directional solidification system (DSS) is a cost-effective method for the production of the multi-crystalline silicon ingot [2]. In this study, we aim to carry out more challenging simulations of transient crystal growth processes in the DSS furnace by means of the software package of CGSim. To achieve the aims, steady simulations are first performed to realize the detailed distributions of flows and temperatures as well as the profile of crystal-melt interface. To improve the accuracy of transient simulations, results of steady simulations at early times are taken as initial conditions. The numerical simulations are validated by the corresponding experimental measurements.

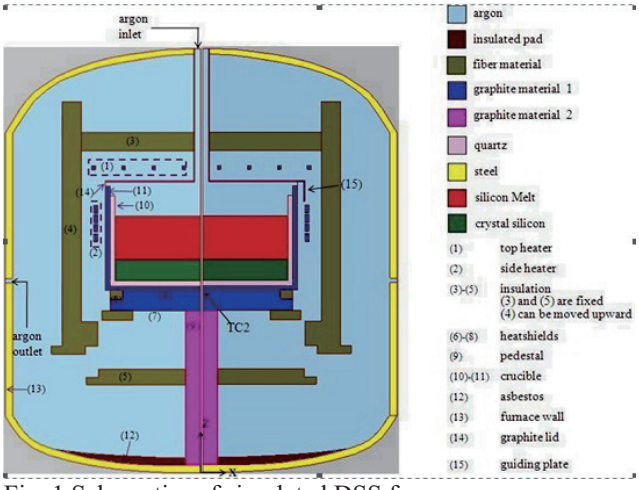


Fig. 1 Schematics of simulated DSS furnaces.

## 2. Results and Discussion

A steady simulation in a furnace, as shown in the left of Fig. 1, is first performed. Detailed flow patterns and the temperature distributions in the entire fluid region, including the argon gas and silicon melts, for a representative case of H = 105mm are depicted in the left of Fig. 2. To illustrate the entire thermo-fluid field, four main regions are categorized, such as (I) the outer argon flow between the furnace wall and the insulators, (II) inner argon flow between the insulators and crucible, (III) argon flow within the crucible and (IV) the crystal melt inside the crucible. In the region I, argon trends to flow clockwise when argon exits the furnace body through the opened gap. A large vortex (or a vortex ring in a three-dimensional configuration) is observed. Due to the insulation, the temperature is significantly lower in region I. Since the main function of this region is a vent, the effects to the growth of crystal are generally less important. The temperature is much higher in region II, where the heaters are placed. Even the overall pattern of argon flow is downward to exit from the gap between the insulators and crucible, local circulations are induced around the heaters by the natural convection. This region II is directly adjacent the crucible wall and cover across the solid-fluid interface, so that the flow field as well as its effects of heat transfer are expected to be crucial to the phenomenon of solidification. More detailed discussion regarding the local fields in this region II is emphasized in a latter paragraph. In region III, the argon gas enters/exits through the central inlet/upper-corner outlet. A reverse circulation of argon flow occurs due to a sudden expansion in space. The temperature is lower in this reverse circulation area because of continuous supply of cooler argon flow and farther away from the heaters. Another region influences the processes of crystal growth importantly is the region IV of melt flow. Affected by coupled factors, such as (1) the higher temperature generated by the heaters on the side, (2) lower temperature on the bottom caused by the lift of insulators and no-slip velocity by the solid crystal, and (3) heat convention and induced shear by the argon flow on the top, two counter-rotating vortexes are observed. The formation of such vortexes plays a direct role in determining the profile the crystal interface, as well as the distributions of relevant chemical components, which are not considered in the present study. Affected by the vortex, interface between crystal and melt appears convex and concave near the central

Corresponding author: Ching-Yao Chen
*E-mail address*: chingyao@mail.nctu.edu.tw

region and wall of crucible, respectively. The overall patterns of the simulations are generally consistent with results presented in Ref. [3]. To further validate the simulated results, direct comparisons with the experimental measurements of temperature at a position beneath the crucible [4] for different silicon height of H = 105 mm, 204 mm, and 248 mm are shown in Table 1. Excellent agreements are obtained, which the errors are well limited around 3 percents, to ensure the credibility of simulations.

After reliable steady simulations are achieved as presented in the previous section, more practical simulations of transient growth processes are performed. To start the transient simulations, initial conditions are required. The steady state solution of H = 105 mm, as the whole condition shown in the left of Fig. 2, is taken as the initial condition as $t=t_0$, and the unsteady governing equations will be solved numerically and advanced in time. Two distinct control mechanisms are applied to analyze the transient growth processes; condition (A): a fixed crystallization rate, and condition (B): a fixed temperature at point TC2 shown in Fig. 1. The transient phenomena regarding the profiles of crystal-melt interface and the flow fields within the melts are focused. Furthermore, evolutions of the average crystal heights will be compared with the actual experimental measurements. The heights of crystal are compared with the experiments as shown in Fig. 3. The position measured in the experiments is at the center of the interface. The prediction by condition (A) agrees excellently with the experiments, while slightly over-growth is obtained by condition (B). The good agreements vindicate the applicability of numerical simulations even to practical problems of transient crystal growth processes.

## 3. Concluding Remarks

The crystallization rate and the interface shape, which are crucial factors in the productions of multi-crystalline silicon ingot by the DSS furnace, are highly related to the dissipation of heat. Detailed understandings of the thermo-fluid fields in the furnace are essential for better processes of crystal growth. In the present study, direct numerical simulations in the DSS furnace are performed by CGSim, a specialized numerical package for crystal growth. A practical task to simulate the transient processes in the whole DSS furnace is performed. The transient simulations are capable to capture detailed melt flows at different times, which lead to distinct features of the crystal-melt interfaces. The credibility of the transient simulations is also supported by the good agreements in predicting the evolution of crystal heights with the experimental measurements.

**References:**


[1] K. Fujiwara, W. Pan, K. Sawada, *Journal of Crystal Growth* 292 (2006) 282-285.

[2] R. C. Newman, *Materials Science and Engineering: B* 36 (1996) 1–12.

[3] Y. Y. Teng, Ph. D thesis, National Central University, Taiwan, 2011.

[4] Private communications.


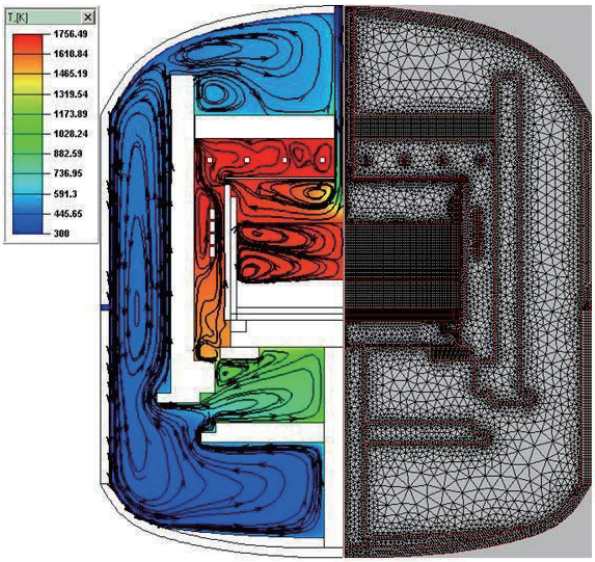


Fig. 2 Shown in the right is the mesh applied to simulate the furnace without a guiding plate at a crystal height of H = 105mm. Correspondent distributions of temperate and flow fields in all fluid regions, i.e. including gases and melts, are demonstrated in the left. Silicon crystal inside the quartz crucible is displayed in blank, where temperature is lower than 1685K. Interface between crystal and melt appears convex and concave near the central region and wall of crucible, respectively.

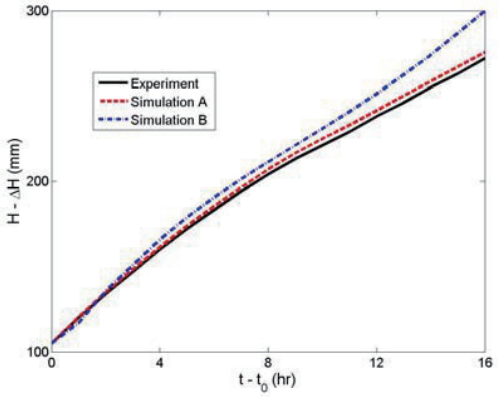


Fig. 3 Evolutions of crystal height predicted by the transient simulations and the experimental measurement. The starting time t0 of simulations is at H = 105 mm. Simulations A and B are under conditions of fixed crystal growth rate and temperature at TC2 position (displayed in Fig. 1), respectively. Excellent predictions are obtained in both simulations.

Table 1. Comparisons of temperatures by the present simulations and the experimental measurements at various silicon crystal heights

| silicon crystal height (H) | H=105 mm | H=204 mm | H=246 mm |
|---|---|---|---|
| measured temperature [29] | 1411.85K | 1368.05K | 1357.85K |
| calculated temperature | 1367.6K | 1326.9K | 1318.4K |
| error | 3.13% | 3% | 2.91% |

Eleventh International Conference on Flow Dynamics
October 8-10, 2014, Sendai, Miyagi, Japan

# An Investigation of Swing Phenomena of Natural Convection in Parallel Square Plates by a Hybrid Boundary Condition

Wei-Hsiang Wang[1], Hsuan-Lun Lin [1], Wu-Shung Fu [1]
[1] EE306, Department of Mechanical Engineering, National Chiao Tung University,
Hsinchu 30010, Taiwan, ROC

**ABSTRACT**

Swing phenomena of natural convection in parallel square plates are investigated numerically. For solving the swing phenomena occurring in the pates, a hybrid boundary condition composed of the absorbing boundary condition and modified LODI method is then adopted in artificial buffer zones. Results show that swing behaviors are concentrated in the upper region of the plates, and both results of the present study and an existing literature have the same trend.

## 1. Introduction

Natural convection in parallel square plates is complex and interesting because of geometric characteristics and broad applications in industry and academy. Multiple open boundaries included in the parallel square plates is a main feature that causes the fully developed boundary conditions usually used in an extended boundary to be difficultly held. An appropriate method of the absorbing boundary condition was then adopted [1] and successfully to reveal phenomena of natural convection in the parallel square plates. However, the Rayleigh numbers used in [1] were relatively small, and then steady phenomena were revealed exclusively. The absorbing boundary condition is suitable to treat this steady flowing problem. Furthermore, accompanied with increment of the Rayleigh number, an unstable flowing situation has possibility to occur that causes swing behaviors of fluids to be observed in the parallel square plates. Therefore, the usage of the absorbing boundary condition is no longer suitable to treat this unstable problem. A combination of the absorbing boundary condition and modified LODI method [2] is adopted to investigate swing phenomena of natural convection in the parallel square plates with a heated bottom wall numerically. The fifth-order of the MUSCL scheme [3], Roe scheme, preconditioning [4], and dual time stepping matching the LUSGS method are adopted. The results show that accompanied with increment of the Rayleigh number, swing behaviors of fluids are indicated in the parallel square plates.

## 2. Physical model and Numerical method

A physical model of three dimensional parallel square plates is indicated in Fig. 1. The absorbing boundary is used and the artificial buffer zone is added to the original domain. The modified LODI method is adopted at the outside boundary of artificial buffer zone. The heated bottom square is *cdhg*, and the top square *abfe* is adiabatic. The modified Rayleigh number $Ra^* = Ra \times (l_1/l_2)$ equal to $3.26\times10^7$ is considered.

The governing equations of the original domain in which the parameters of viscosity and compressibility of the fluid are considered are shown in the following equation.

$$\frac{\partial U}{\partial t}+\frac{\partial F_1}{\partial x_1}+\frac{\partial F_2}{\partial x_2}+\frac{\partial F_3}{\partial x_3}=S \tag{1}$$

The artificial convection and damping terms are newly adopted to Eq. and the general form of the governing equations in the artificial buffer zone can be described as Eq. (2).

$$\frac{\partial U}{\partial t}+\frac{\partial \widetilde{F}_1}{\partial x_1}+\frac{\partial \widetilde{F}_2}{\partial x_2}+\frac{\partial \widetilde{F}_3}{\partial x_3}+\widetilde{\sigma}=0 \tag{2}$$

where $\widetilde{F}_1$, $\widetilde{F}_2$, $\widetilde{F}_3$ and $\widetilde{\sigma}$ are indicated in [1].

Methods of the Roe scheme, preconditioning and dual time stepping matching LSUGS scheme are used to solve the situation of a low speed compressible flow.

The modified LODI method is adopted at the outer surfaces of artificial boundary zone. The equations of the magnitude of wave amplitude along $x_1$ direction of NSCBC are shown as follow.

$$L=\begin{pmatrix}L_1\\L_2\\L_3\\L_4\\L_5\end{pmatrix}=\begin{pmatrix}u_1\dfrac{\partial T}{\partial x_1}+\dfrac{1}{\rho\gamma}\left(\dfrac{\partial P}{\partial x_1}-\gamma\dfrac{\partial P}{\partial x_1}\right)\\ u_1\dfrac{\partial u_3}{\partial x_1}\\ u_1\left(-\dfrac{\partial u_2}{\partial x_1}\right)\\ (u_1'+c')\left[\dfrac{\partial P}{\partial x_1}-\rho(u_1'-c'-u_1)\dfrac{\partial u_1}{\partial x_1}\right]\\ (u_1'-c')\left[\dfrac{\partial P}{\partial x_1}-\rho(u_1'+c'-u_1)\dfrac{\partial u_1}{\partial x_1}\right]\end{pmatrix} \tag{3}$$

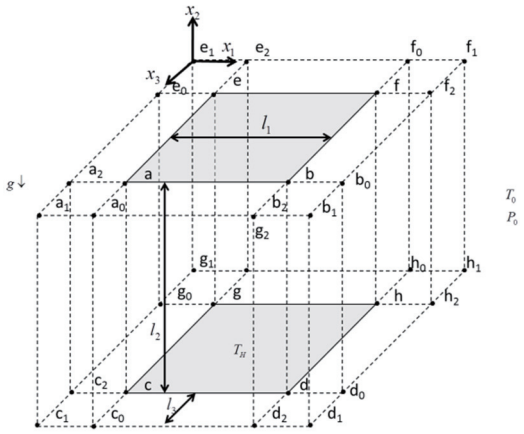


Fig. 1 Physical model of three dimensional parallel square plates

Corresponding author: Wei-Hsiang Wang
*E-mail address*: flyman.me98g@g2.nctu.edu.tw

## 3. Results and Discussion

Figure 2 indicates the three dimensional iso-surfaces of temperatures of T = 360K, 410K and 460K at the dimensionless time $4.3\times10^{-1}$, respectively. In Fig. 2(a), the swing phenomena occur in the top region. However, in Figs. 2(b) and (c), the iso-surfaces remain stable.

In Fig. 3, distributions of streamlines at four different dimensionless times are indicated, respectively. At the time of $2.76\times10^{-1}$, the distribution of streamlines is approximate to a symmetrical shape. Accompanied with increment of the time, the symmetrical distribution of streamlines gradually collapses near the top surface region.

In Fig. 4, the time-averaged Reynolds number at the center line from bottom to top plate is shown. At the location of non-dimensional coordinates $Y \approx 0.75$, $\overline{\mathrm{Re}_t}$ increased to a large value about 1000, which makes the fluids unstable. Besides, it explains the swing phenomena occur in Fig. 2 and Fig. 3 as well.

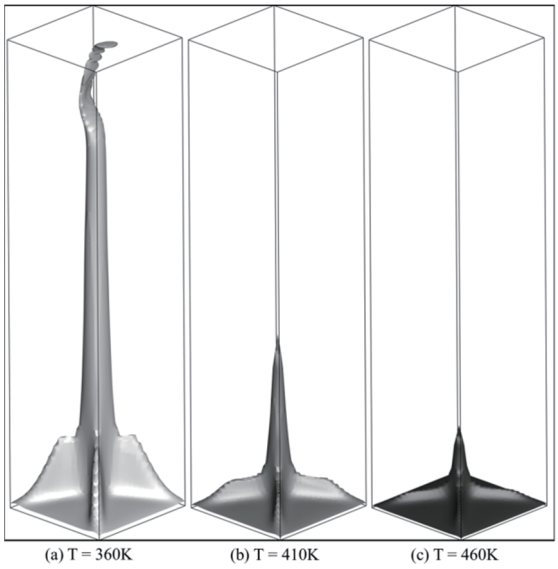


Fig. 2 Iso-surface temperatures of T = 360K, 410K and 460K at dimensionless time $4.3\times10^{-1}$.

Therefore, these results imply that the slight swing of the high temperature fluids is caused by the instability of the flow. The high temperature fluids are surrounded by low temperature fluids, which are composed of surrounding fluids sucked by the upward stream. Then behaviors of the surrounding fluids around the upward stream are easily affected by the slight swing of the upward stream and become drastic.

## 4. Concluding Remarks

Both the absorbing boundary condition and modified LODI method are adopted successfully to investigate behaviors of the swing of natural convection occurring in parallel square plates. Several conclusions are drawn as follows.

1. The usage of the hybrid boundary condition is absolutely necessary to investigated behaviors of swing phenomena.
2. The swing phenomena are caused by the instability of high Reynolds number fluids due to natural convection.

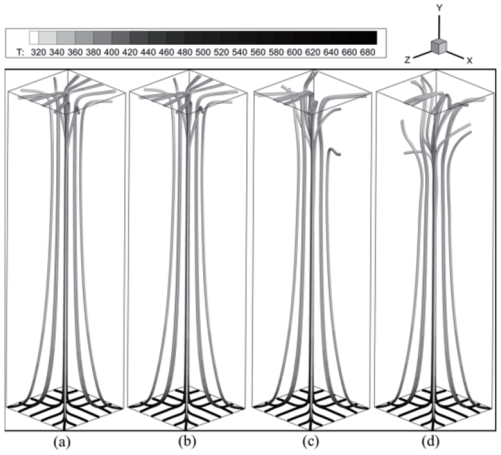


Fig. 3 Distributions of streamlines at dimensionless times of (a) $2.76\times10^{-1}$, (b) $3.1\times10^{-1}$, (c) $3.61\times10^{-1}$ and (d) $4.23\times10^{-1}$.

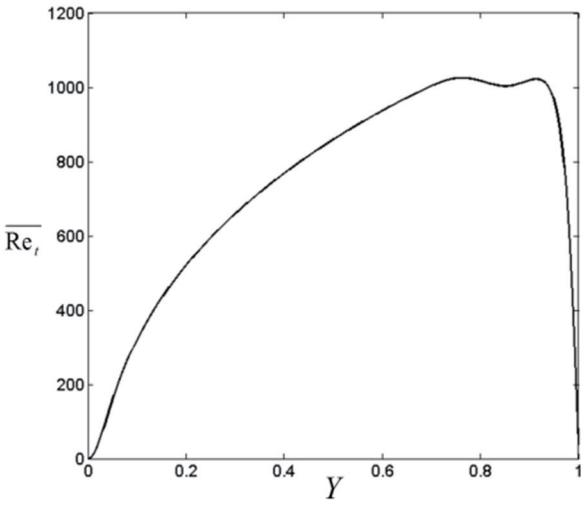


Fig. 4 Time-averaged Reynolds number at $X = 0.5$ and $Z = 0.5$


## Acknowledgements

The authors gratefully acknowledge the support of the Natural Science Council, Taiwan, ROC under Contact NSC102-2221-E-009-53-MY2.


## References


[1] W. S. Fu, W. H. Wang, C. C. Li and S. H. Huang, *Int. J. Heat Mass Transfer*, 56 (2013) 35-44.

[2] W. S. Fu , C. G. Li, C. C. Tseng, *Int. J. Heat Mass Transfer*, 53 (2010)1575-1585.

[3] I. Abalakin, A. Dervieux, and T. Kozubskaya, *INRIA*, (2002) No4459.

[4] J. M. Weiss and W. A. Simth, *AIAA*, 33 (1995) 2050-2056.

Eleventh International Conference on Flow Dynamics
October 8-10, 2014, Sendai, Miyagi, Japan

# Manipulation of an Oscillating Superparamagnetic Micro-bead Chain: Effect of Frequency

He-Ching Lin, Ching-Yao Chen
Department of Mechanical Engineering, National Chiao Tung University
EE321, 1001 TA HSUEH ROAD, HSINCHU, TAIWAN 30010,ROC

**ABSTRACT**

Issues concerning the structural instability of an oscillating micro-bead chain are addressed based on systematic experiments. The chains are first formed by a static directional field, and then manipulated by an additional dynamical perpendicular field(different frequency). The effects of key parameter, such as frequency, is thoroughly analyzed. Distinct behaviors, from rigid body oscillations and bending distortions to rupture failures, are observed by increasing the value of frequency.

## 1. Introduction

A magnetorheological (MR) suspension is an artificial and functionalized fluid containing paramagnetic solid particles suspended in a non-magnetic solvent. MR suspension has been actively applied in the so-called magnetofluidics [1].

A popular application is chaining the micro-sized particles as micro-devices to be effectively manipulated by external fields, such as micromechanical sensors [2,3], micro-swimmers [4,5,6], micro-mixers [7,8,9]. The aggregation processes and the dynamics of micro-chains in motion subjected to different field configurations, e.g., an oscillating field [5,6,10,11], have also been subjects of intensive studies.

Driven by the external fields, a magnetic chain in a rotating field either remains in its chaining formation or is ruptured into multiple sub-chains (ruptured segments). A flexible chain can be bent and rotates synchronously with the overall external field under the critical frequency. When an excessive frequency is applied, the dynamics become asynchronous, with back-and-forth motions. It is well understood that the mechanism for chaining instability in a dynamical field involves competition between the induced viscous torque ($M^v$) and the magnetic torque ($M^m$), which define the dimensionless Mason number (Mn).

When a chain composed of N beads is exposed to an overall external field strength H, the magnetic torque, the induced viscous torque and the corresponding Mason number are given as [7]

$$M^m = \frac{\mu_0}{4\pi}\frac{3m^2N^2}{2(2a)^3}\sin(2\Delta\theta_L) \quad (1)$$

$$M^v = \frac{4\pi a^3 N}{3}\frac{2N^2}{\ln(N/2)}\eta\omega \quad (2)$$

$$Mn = \frac{32\eta\omega}{\mu_0\chi^2H^2} \quad (3)$$

where $\mu 0$ and a represent the vacuum permeability and the radius of beads, respectively. The magnetic susceptibility of the magnetic beads and the viscosity of solvent fluid are denoted as $\chi$ and $\eta$, respectively. The dipolar moment, m, of a single bead is given by $m = (4\pi a^3/3)\chi H$ The instantaneous angular speed of the chain is expressed as $\omega$, and $\Delta\theta$ L is phase lag of the chain to the external field.

Corresponding author: Ching-Yao Chen
*E-mail address*: chingyao@mail.nctu.edu.tw

## 2. Experimental setups

A sketch of the experimental apparatus is shown in Fig. 1. In order to form a micro-chain, micro-sized superparamagnetic beads are initially dispersed in a solvent fluid. The solvent fluid used in the experiments is a mixture of distilled water and sodium dodecyl sulfate (SDS) surfactants. The viscosity of this solvent fluid is $\eta$ = 1.75 cp. One type of superparamagnetic bead is used, with a mean diameter of d = 4.5 $\mu$m whose susceptibilities are $\chi$ = 1.6

A static directional magnetic field, denoted as $H_d$, is applied to chain the micro-beads. An additional dynamical field ($H_v$) is applied perpendicularly, to oscillate the bead chain. This dynamical field is sinusoidal, given by $H_v = H_p\sin(2\pi ft)$, with a maximum field strength $H_p$ and a frequency f. It results in an overall external field of $H = H_d\,i + H_v\,j$, in which i and j are unit vectors in the directional (x-direction) and perpendicular (y-direction) axis, respectively. Under the present configuration, the trajectory of the phase angle of the overall external field, denoted as $\theta_f$, is prescribed as $\theta_f(t) = \tan^{-1}[(H_p/H_d)\sin(2\pi ft)]$. The motion of the microchain is recorded using an optical microscope that is connected to a digital camera (Silicon Video 643C), whose maximum shooting rate is 200 frames/s. Representative snapshot images, which are modified from the original recorded movies by improving their contrast and resolution, are presented in the following sections to identify the distinct behaviors of micro-chains.

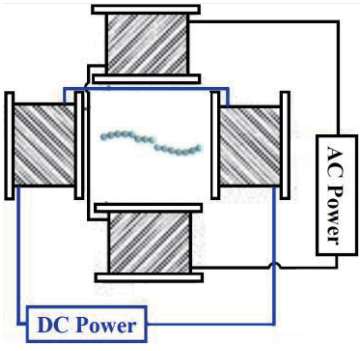


Fig. 1 Principle sketch of experimental setup (left) and relevant notations (right). A static directional magnetic field provided by DC power is applied to form the chain.

An additional sinusoidal dynamical field powered by AC source is applied perpendicularly to oscillate the chain.

### 3. Results and Discussion

The effect of the controlling parameter, such as the frequency, is analyzed to obtain more insights in manipulating the chain. A complete series of experiments, in which the lengths of the chains vary from P3 to P18, are firstly performed using the same manipulating field, i.e. a constant chaining field of $H_d$ =24.15 Oe and an dynamical field strength of $H_v$ =18.73 Oe that is subjected to an increasing oscillating frequency. Increase the frequency 1 to 7Hz is observed to result in a stable oscillating chain to break up then restore stable oscillating chain show in Fig. 2.

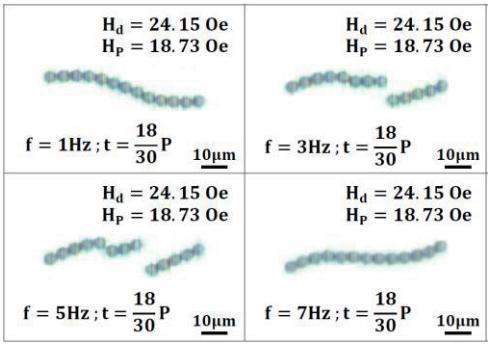


Fig. 2 Sequential images of a chain consisted of 13 beads (P13 chain) subjected to an increasing frequency of f=1-7 Hz, at same time t = 18P/30, within a period (P = 1 s in the experiments). The directional field strength and dynamical field strength of the oscillating field are $H_d$ = 24.15 Oe and $H_p$ = 18.73 Oe, respectively. Increase the frequency 1 to 7Hz is observed to result in a stable oscillating chain to break up then restore stable oscillating chain.

A shorter chain results in an oscillation that is more synchronized with the overall external field and not affected by various frequency. Because of a shorter chain (P3) and a higher instantaneous angular speed ($\omega$), a reduction in hydrodynamic drags is easily understood by referring to Eq. (2). The higher instantaneous angular speed is a result of the much higher amplitude within the same period, which can be seen by comparing the images shown in Fig. 3. On the other hand, the higher frequency due to smaller amplitudes ($\theta_{Amax}$).

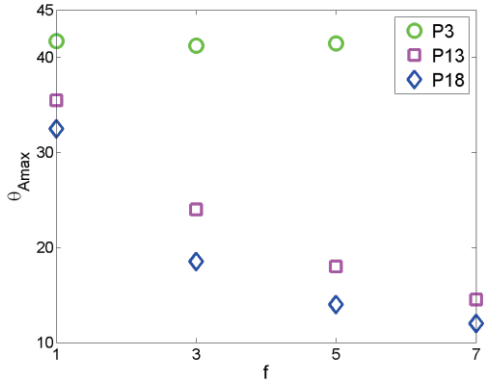


Fig. 3 Amplitudes ($\theta_{Amax}$) of chains with various frequency, Subjected to the same directional field strength and dynamical field strength, a shorter chain oscillating in larger amplitude is expected due to its smaller induced drag. On the other hand, less pronounced oscillations of chains subjected to a high frequency due to the strong transient phenomena.

### 4. Concluding Remarks

In this study, distinct behaviors, from rigid body oscillations and bending distortions to rupture failures, are observed by increasing the value of frequency, which depend strongly on the viscosity of the solvent fluid. In order to analyze these phenomenas, systematic experiments in a more viscous mixture are first investigated. Because of the smaller induced drag, the shorter chain results in an oscillation that is more synchronized with the overall external field and not affected by various frequency

### References


[1] Nguyen NT., *Microfluidics and Nanofluidics*, 12,(2012)1.

[2] Goubault C., Jop P., Fermigier M., Baudry J., Bertrand E., and Bibette J., *Physical Review Letters,* 91(2003) 260802.

[3] Cebers A., *Journal of Colloid and Interface Science,* 10(2005)167.

[4] Dreyfus R., Baudry J., Roper M. L., Fermigier M., Stone H. A., and Bibette J., *Nature,* 437.7060(2005) 862-865.

[5] Li Y.-H., Sheu, S.-T., Pai, J.-M., Chen, C.-Y., *Journal of Applied Physics,* 111(2012)07A924.

[6] Li, Y.-H., Lin, H.-C., and Chen, C.-Y., *IEEE Transactions on Magnetic,* 49.7(2013)4120.

[7] Biswal S., and Gast A., *Analytical chemistry,* 76.21(2004)6448-6455.

[8] Kang TG., Hulsen M., Anderson P., den Toonder J. M. J., and Meijer H., *Physical Review E,* 76.6(2007) 066303.

[9] Roy T., Sinha A., Chakraborty S., Ganguly R., and Puri I. K., *Physics of Fluids,* 21(2009)027101.

[10] Li, Y.-H., Chen, C.-Y., Sheu, S.-T., and Pai, J.-M., *Microfluidics and Nanofluidics,* 13(2012)579-588.

[11] Li, Y.-H., Lin, H.-C., and Chen, C.-Y., *Microfluidics and Nanofluidics,* 14(2013)831-838.

Eleventh International Conference on Flow Dynamics
October 8-10, 2014, Sendai, Miyagi, Japan

# Thermal Behavior and Electrical Characterization of Paralleled GaN HEMTs Power Module

Stone Cheng, Po-Chien Chou, Hsin-Ping Chou
Dept. of Mechanical Engineering National Chiao-Tung University
Hsinchu, Taiwan

**ABSTRACT**

In this paper we present the heat generation behavior and electrical analysis of paralleled AlGaN/GaN high electron mobility transistors (HEMTs) with power module packages. Since thermal management is extremely important for these high power packaging, a hybrid integration of the HEMTs onto an AlN carrier substrate is proposed. We investigate the temperature performance for 24 paralleled AlGaN/GaN HEMTs integrated onto AlN substrate by thermal simulations in combination with experimental results using infrared thermography and electrical dc-analysis.

## 1. Introduction

AlGaN/GaN High Electron Mobility Transistors (HEMTs) have the advantages of wide bandgap, high breakdown voltage, and high electron mobility. Therefore, many applications of HEMTs had been developed. GaN HEMTS fabricated on large diameter Si substrates have emerged as promising candidates for high-voltage power management applications. A great concern with these devices is current collapse or dynamic ON-resistance phenomenon. To enhance the voltage handling ability of GaN devices, multiple field-plate structures are used. Their effectiveness at high voltage operation to prevent current collapse is unclear. In this work, we investigated the field plate structure in GaN for > 600 V operation.

To validate the use of GaN technology in high power applications, such as motor driver of automobile, variable-frequency air conditioners and refrigerators, there is a need to demonstrate a power module that has multiple paralleled GaN HEMT devices. In this work, an all-GaN power module is fabricated. The individual GaN device was presented at a lower current rating of 2 A per cell. The design requirements for this particular module were focused on thermal distribution of parallel operation.

## 2. Electric Characteristic Simulation

We used Silvaco Atlas to simulate the electric performance of GaN device. Due to the scale difference, chip was simplified for simulation. The cross-section structure is as shown in Fig. 1. The 80 mm GaN device with 500 μm (gate width) of 160 HEMTs on silicon substrate was simplified to one gate formed as 2×5000 $\mu m^2$ (length×width). Individual cells were tested to verify on-state characteristics, voltage blocking, and to measure gate leakage current. The gate voltage (Vg) was set from -3 V to 0 V and the drain voltage (Vd) was set from 0 V to 1000 V. Figure 2 shows the forward blocking characteristics at a breakdown voltage of 870 V and a drain current can rise up to 2 A. In our GaN device, the design of appropriate field plate structures for the reliable high-voltage operation distribute the electric field in the channel more equally and by that improve the device performance. In this case the electric field is reduced in critical volumes such as under the gate's drain side and under the drain's gate side. Figure 3 shows the simulated electric field in GaN device. The peak value of electric field locates at drain side of the gate bottom, where the value was only a little higher than the area near the edge of field plate. This figure indicates that electron energy is the highest at this area, and the hot spot area is under the gate and slightly near the drain [1,2]. Hence, it can be observed that electric field and temperature of the device have a reciprocal effect.

Corresponding author: Stone Cheng
*E-mail address*: stonecheng@mail.nctu.edu.tw

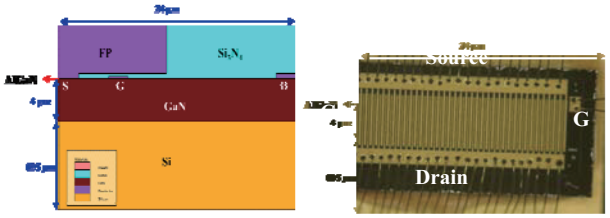


Fig. 1. Structure of AlGaN/GaN HEMTs that was simplified to simulate the I-V curve.

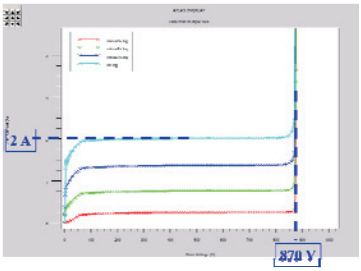


Fig. 2. The simulated I-V curve of GaN device.

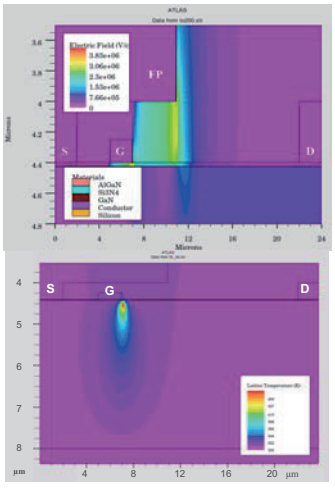


Fig. 3. The simulated electric field and hest spot distribution of GaN device ($V_{DS}$=200 V).

## 3. Thermal Analysis of AlGaN/GaN HEMTs Module

Boundary-related issues related to heat-sinking and to the conditions to be applied at the lateral and bottom edges of the simulation region are complicated [3]. In the actual device, the Joule heat is sunk largely through a metal baseplate upon which the chip sits, with very little heat flowing out of the GaN device topside contacts. Complete treatment of mathematical modeling the chip, its packaging, an inherently three-dimensional problem are not pursued here because, in addition to being computationally intensive, it does not seem likely that such an analysis would yield new insights into the thermomechanics of GaN devices. To simulate thermal management of packaged GaN device, the location of main heat source of working device should be known first. We attribute the peak temperature appeared at the area under drain side of gate. Therefore, the heat source takes place in a narrow region right under the edge of the outermost field plate at the drain side of the device.

The explosion drawing of designed module packaging is shown in Fig. 4. The housing wall is built on the base plate. The chips are bonded to the DBC board with sintering of silver nano-particles and then wire-bonded to the electrical interconnect board. The DBC material provides good coefficients of thermal expansion (CTE) matching and an efficient heat transfer path for removing heat from GaN HEMTs. There are 8 chips attached on each DBC. Every chip consists of 3 multi-finger GaN HEMTs (3 cells), i.e. there are 24 cells on one each DBC and 72 cells in total formed the power module. Finally, protective coating is used to shield chips from environment.

Prior to device processing we have demonstrated the heat transfer of parallel AlGaN/GaN HEMTs devices on using Ansys Icepak simulation, and the thermal resistance was calculated. Thirty heat sources are set above the GaN layer for each chip. The thickness of silver adhesive is 100 μm. Fig. 5(a) shows the total structure of simulated model with referred values of thermal conductivities [4]. The cross section view of a single chip is shown in Fig. 5(b).

## 4. Simulation and Experiment results

The simulated temperature distribution of GaN-on-Si AlN-DBC board is shown in Fig. 6. The highest temperature (red) is 382 K situated at heat sources as expected. From the simulation results, the thermal resistances of metal plate, silver adhesive, and AlN PCBs are 1.51 K/W, 0.21 K/W, and 0.23 K/W, respectively. And that of silicon substrate and GaN are 4.87 K/W and 0.15 K/W. The total thermal resistance is from junction of case about 6.97 K/W, most of the thermal resistance came into being in Si substrate. Figure 7 illustrates IR images of GaN devices on DBC AlN substrate with 200W heat disspation. A comparison of these corresponding temperatures with simulation results indicates the effectiveness of designed module packaging.

## 5. Conclusion

The simulations of electric performance and thermal distribution of GaN power devices in parallel operation are presented. To predict the electric performance of paralleled GaN chip, numerical simulation to a GaN device was used to study the I-V curve, breakdown voltage, and electric field for the design of appropriate field plate structures. We also investigate the thermal distribution of packaged power module by Finite Element Method and IR imaging, which consists of parallel-connected GaN chips. The highest temperature of operating module is 382 K when the power efficiency is 90 % and the output power is 4 kW, these results agree well with IR experimental data. The understanding derived here suggests that the thermal resistance of the packaging is 6.97 K/W.

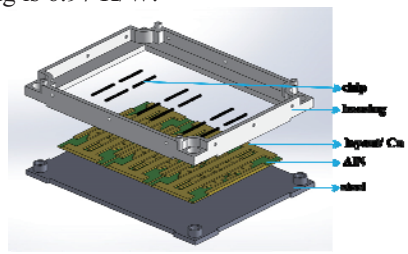

Fig. 4. Designed module packaging.

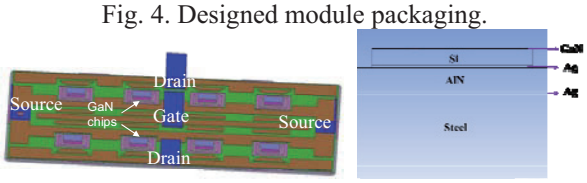


(a) (b)

Fig. 5. Model of simulation. (a)A GaN-DBC AlN substrate structure. (b)Cross sectional view of a single chip.

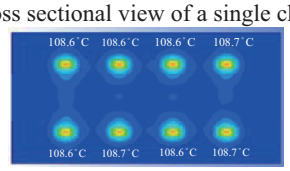


Fig. 6. Simulation results of temperature distribution . Red: 382K; dark blue: 329 K.

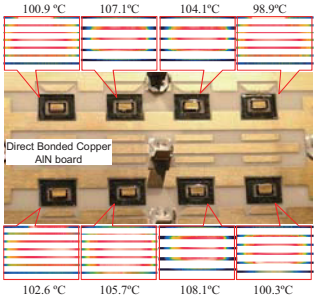


Fig. 7. Temperature measurement of GaN on DBC AlN board by IR camera with 200W heat disspation. IR images shown maximum temperature area and value.

## References


[1] M. G. Ancona, S. C. Binari, and D. J. Meyer, *Journal of Applied Physics,* vol. 111, 074504-1~16, 2012.

[2] B. Benbakhti, M. Rousseau, and J. C. De Jaeger, *Microelectronics Journal,* vol. 38, pp. 7-13, 2007.

[3] S. Russo, V. d'Alessandro, M. Costagliola, G. Sasso, and N. Rinaldi, *Materials Science and Engineering: B,* vol. 177, pp. 1343-1351, 2012.

[4] S. K. Bose, *Solid State Communications,* vol. 159, pp. 102-105, 2013.

Eleventh International Conference on Flow Dynamics
October 8-10, 2014, Sendai, Miyagi, Japan

# Influence of Boundary Implementation with Lattice Boltzmann Method on the Prediction of Lid-driven Cavity Flow on Graphics Processor Unit

You-Hsun Lee, Chao-An Lin
Department of Power Mechanical Engineering,
National Tsing Hua University, Hsinchu 30013, Taiwan

**ABSTRACT**

The focus of the present study is to investigate the influence of the boundary condition on the prediction of lid-driven cavity flow using lattice Boltzmann method. The computing platform is based on the graphic processing unit. Different boundary implementations are explored, namely bounce-back, equilibrium and non-equilibrium schemes.

## 1. Introduction

A successful LBM simulation rests on the correct implementation of the boundary conditions, where unknown distribution functions originated from the undefined nodes external to the flow domain are encountered during the streaming operation. In order to solve the problems on boundary, many schemes had been proposed. In this paper, four commonly adopted schemes were examined, namely:

1. Bounce-back scheme on the node: the bounce-back boundary condition only gives first order accuracy.
2. Halfway bounce-back scheme: boundary condition is employed with the wall located at half-grid-spacing between a flow node and a bounce-back node, the scheme is shown to produce second-order accuracy [1]. Compared with bounce-back scheme, the advantage of this scheme is the better mass conservation. Non-zero velocity boundary condition was proposed by Ladd [2,3].
3. Equilibrium scheme on the node: This scheme assigns the equilibrium distribution function on the boundary [4].
4. Bounce back rule for non-equilibrium distribution function on the node: This scheme could be used for pressure, velocity, and stationary conditions [5].

In order to examine the applicability of schemes demonstrated above, the two dimensional (2-D) lid-driven cavity is chosen as a target problem, which has been studied by many. Hou et al. [4] simulated square cavity with bounce-back scheme and equilibrium scheme for stationary wall and moving wall, respectively. The results compared favorably with benchmark solution from Ghia et al. [8]. Patil et al. [6] studied the 2-D lid-driven cavity at different aspect ratio. The boundary treatment is similar to that in [4]. However, the vortex structure for the four cavity width depth geometry at Reynolds number 1000 differs from that predicted by Lin et al. [7] using the MRT-LBM, where the former and latter studies produced three and four primary vortices within the cavity, respectively.

There is no detailed evaluation of the influences of the boundary condition on predicting the lid-driven cavity at different depth width aspect rations, which is the focus of the present study. The numerical simulation is conducted on the graphics processor unit: nVidia Titan.

Corresponding author: Chao-An Lin
*E-mail address*: calin@pme.nthu.edu.tw

## 2. Numerical Method

For this study, multiple relaxation time (MRT) lattice Boltzmann method (LBM) with D2Q9 model is adopted.

Macroscopic density $\rho$ and velocity $\vec{u}$ of lattice Boltzmann models are defined by particle distribution function $f$ as,

$$\sum_i f_i = \rho \quad , \quad \sum_i f_i \vec{e_i} = \rho \vec{u}$$

$\vec{e_i}$ is the particle speed and is defined as,

$\vec{e_0} = 0$

$\vec{e_i} = \left(Cos\left[\pi(i-1)/2\right] , \mathrm{Sin}\left[\pi(i-1)/2\right]\right)c \ , \quad i = 1, 2, 3, 4$

$\vec{e_i} = \left(Cos\left[\pi(i-4-1/2)/2\right] , \mathrm{Sin}\left[\pi(i-4-1/2)/2\right]\right)c \ , \quad i = 5, 6, 7, 8$

where the weighting factors are $\omega_0 = 4/9$, $\omega_{1,2,3,4} = 1/9$, and $\omega_{5,6,7,8} = 1/36$.

The particle equilibrium distribution functions are shown as,

$$f_i^{eq} = \omega_i \rho \left[ 1 + \frac{3\vec{e_i}\cdot\vec{u}}{c^2} + \frac{9\left(\vec{e_i}\cdot\vec{u}\right)^2}{2c^4} - \frac{3\vec{u}\cdot\vec{u}}{2c^2} \right]$$

where dx is lattice length, dt is the time step, and $c = \mathrm{dx}/\mathrm{dt}$ is the lattice speed. Here, dt is chosen to be equal to dx, thus $c = 1$.

The MRT LBM is expressed as:

$$f_i^+\left(\vec{x}, t\right) = f_i\left(\vec{x}, t\right) - \mathbf{M}_{il}^{-1} S_{lj} \left[ m_j - m_j^{eq}\left(\vec{x}, t\right) \right]$$

$$f_i\left(\vec{x} + \vec{e_i}\Delta t, t + \Delta t\right) = f_i^+\left(\vec{x}, t\right)$$

**M** is matrix transforming from $f$ to the moment $\mathrm{m} = \mathbf{M}\mathrm{f}$, and S is the relaxation matrix.

$$m = \begin{bmatrix} \rho \\ e \\ \varepsilon \\ j_x \\ q_x \\ j_y \\ q_y \\ p_{xx} \\ p_{xy} \end{bmatrix} = \begin{bmatrix} 1 & 1 & 1 & 1 & 1 & 1 & 1 & 1 & 1 \\ -4 & -1 & -1 & -1 & -1 & 2 & 2 & 2 & 2 \\ 4 & -2 & -2 & -2 & -2 & 1 & 1 & 1 & 1 \\ 0 & 1 & 0 & -1 & 0 & 1 & -1 & -1 & 1 \\ 0 & -2 & 0 & 2 & 0 & 1 & -1 & -1 & 1 \\ 0 & 0 & 1 & 0 & -1 & 1 & 1 & -1 & -1 \\ 0 & 0 & -2 & 0 & 2 & 1 & 1 & -1 & -1 \\ 0 & 1 & -1 & 1 & -1 & 0 & 0 & 0 & 0 \\ 0 & 0 & 0 & 0 & 0 & 1 & -1 & 1 & -1 \end{bmatrix} \begin{bmatrix} f_0 \\ f_1 \\ f_2 \\ f_3 \\ f_4 \\ f_5 \\ f_6 \\ f_7 \\ f_8 \end{bmatrix} = \mathbf{M}\mathrm{f}$$

Also, the equilibrium of moments $m^{eq}$ are,

$$m^{eq} = \left( \rho , -2\rho + \left(u^2 + v^2\right) , \rho - 3\left(u^2 + v^2\right) , \rho u , -u , \rho v , -v , u^2 - v^2 , uv \right)^T$$

Besides, the speed of sound is $C_s = c/\sqrt{3}$, and then the kinetic viscosity can be expressed as $\nu = (\tau - 0.5)C_s^2 dt$.

The relaxation matrix **S** is a diagonal matrix, i.e.,

$$S = diag\left[s_0, s_1, s_2, s_3, s_4, s_5, s_6, s_7, s_8\right]$$

where $s_7 = s_8 = 1/\tau$, . And, $s_0 = s_3 = s_5 = 0$ ensures mass and momentum conservation before and after collision step.

Table 1. Different boundary conditions of moving and stationary wall for BC 1, 2, 3, and 4

| | Moving wall | Stationary wall |
|---|---|---|
| **BC1** | Halfway bounce-back | Halfway bounce-back |
| **BC2** | Equilibrium scheme [4] | Non-equilibrium scheme [5] |
| **BC3** | Non-equilibrium scheme [5] | Non-equilibrium scheme [5] |
| **BC4** | Equilibrium scheme [5] | Bounce-back scheme |

As shown in Table 1, there are four c boundary conditions combinations to examine the influence of boundary condition on the predictions of cavity flows.

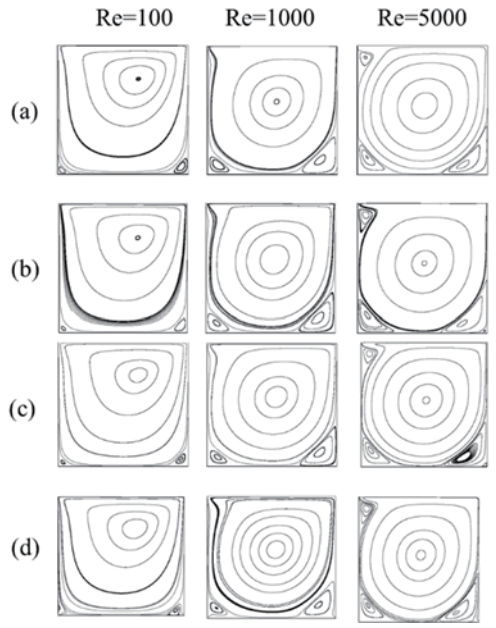


Fig. 1 The stream function contours for square cavity at Re=100, 1000, 5000 using different boundary implementations (a) BC1, (b) BC2 , (c) BC3, (d) BC4

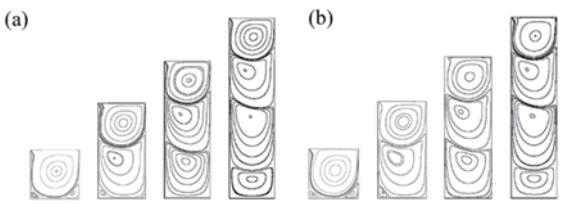


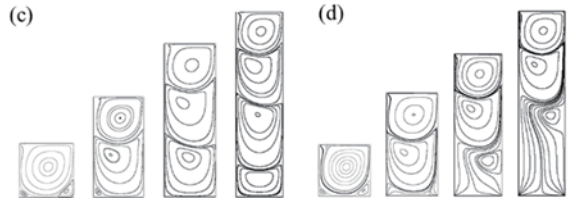


Fig. 2 Stream function contours of cavity with aspect ratio being 1, 2, 3, and 4 at Re=1000 using different boundary implementations (a) BC1, (b) BC2 , (c) BC3, (d) BC4

**3. Results and Discussion**

First, attention is directed to the lid-driven flows for square cavity. The contours of streamline for Re= 100, 1000, and 5000 are shown in Fig 1. By increasing the Reynolds number, the location of primary vortex approaches the geometric center. All results are consistent with that observed in Ghia et al. [8].

Computations are further extended to deep cavity at aspect ratio (K) 2, 3, 4. Fig 2 shows the predicted stream function contours of cavities (K=1, 2, 3, 4) at Re=1000. Similar results are obtained for BC1, 2 and 3. But the contours of BC4 shows dramatically different behavior, especially for deep cavity K=3 and 4.

**4. Concluding Remarks**

- For square cavity, BC1, 2, 3, and 4 show similar results.
- For deeper cavities (K = 3 and 4, simulations with bounce-back scheme for stationary wall show erroneous results.

**References**


[1] D.P. Ziegler, *J Stat Phys*, 71 (5–6) (1993) 1171–1177.
[2] A.J.C. Ladd, *J Fluid Mech*, 271 (1994) 285–309.
[3] A.J.C. Ladd, *J Fluid Mech*, 271 (1994) 311– 339.
[4] S. Hou, Q. Zou, S. Chen, G. Doolen, A.C. Cogley, *J Comput Phys*, 118 (1995) 329–347.
[5] Q. Zou and X. He, *Phys. Fluids*, (1997) 1591-1598.
[6] D. Patil, K. Lakshmisha, B. Rogg, *Comput Fluids,* 35 (2006) 1116-1125.
[7] L.S. Lin, Y.C. Chen, C.A. Lin, *Comput Fluids*, 45 (2011) 233-240.
[8] U. Ghia, K.N Ghia, C.T Shin, *J Comput Phys*, 48 (1982) 387– 411.

Eleventh International Conference on Flow Dynamics
October 8-10, 2014, Sendai, Miyagi, Japan

# A Numerical Study of Shock-bubble Dynamics based on the Multi-Equation Model

Yang-Yao Niu, Po-Jen Shih, and Hong-Wei Wang
Department of Aerospace Engineering, Tamkang University,
New Taipei City, Taiwan (ROC)

**ABSTRACT**

In this paper, a algebraic type Approximated Riemann solver is proposed to compute the compressible cavitated liquid-gas flows. As we know. an accurate resolution of multi-scale phenomena such as material interfaces, contact surfaces and discontinuities due to the interaction among multi-phase flows which is still an unsolved problem. In this work, a six equation two-fluid approach with the stratified flow model are selected to model liquid-gas flows based on individual equation of state. Benchmark test including 2D shock-bubble interaction problem demonstrates accurate capturing of interfaces, shock waves and contact discontinuity.

## 1. Introduction

A series of numerical methods exist for solving the two-phase flow problems, including the volume of fluid method [1], the interface capturing methods [2] and the arbitrary Lagrangian-Euler method [3], etc. In general, most two-phase flow models are derived from the ensemble average procedure, Stewart and Wendroff [4] showed that the model could also be derived through the stratified flow model. However, the stratified flow model gives a clearer view of the mathematical and physical characteristics of the two-phase flow. Because the stratified flow model defines fluids in individual regions, we can apply the conservation laws to each range and obtain the governing equations in conservative form. The present work will demonstrate that a proper incorporation of this concern in the numerical scheme proposed herein can alleviate these problems.

In order to capture the shock wave within the water flows, we also employed AUSMD type Approximated Riemann Solver to solve two fluid models consisting of mass, momentum and energy conservation equations as well as an EOS for each phase [5]. A 2D shock-bubble interaction problem is chosen for the bechmark test.

In this work, we shall focus on single pressure six-equation models to solve two-phase flows, written in the general form [5], The gas and liquid fluid are governed by the perfect gas model and stiffened gas model, respectively. The stiffened gas model was seen in [5]

## 2. Results of 2D Shock-bubble interaction problem

The interaction of underwater shock and the air bubble is studied. The initial condition is basically follows the case used by Nourgaliev [6]. The air bubble with diameter 6.0 mm is immersed in the water pool with its center in the origin. The incoming shock is initially located in x = −4.0mm. The initial condition is shown in fig.10. The fluid states before the shock is

$p = 1.013250 \times 10^5\ Pa$ , $u_i = v_i = 0$ m/s , $T_i = 292.98$ K

and the states behind of the shock are:

$p = 1.6 \times 10^9\ Pa$ , $u_i = 661.81$ m/s , $v_i = 0$ m/s , $T_i = 595.14$ K

The Mach number of the shock wave is M = 1.509. The time evolution of the simulation result is presented in Fig.1 We observe that, after the water shock wave hits the bubble, a strong reflection rarefaction wave is developed and a relatively small shock is transmitted into the air (t = 1.2 ~ 3.6 $\mu$ sec) as shown in Fig. 2. The strength of the shock in air is relatively small (no more than 0.1% the strength of the incoming shock), we find it's difficult to identify it in the pressure contours without confusion. However, the shock wave can be clearly seen in the Mach contour which is not shown here. A water jet generated by the rarefaction wave continuously pushes the bauble into a crescent shape. The bubble finally breakups and the water jet collides with the still water behind the bubble (t = 3.6 $\mu$ sec). The collision generates several shock waves propagating in all direction radially. In the same time, the separated air bubbles are compressed into very small volume due to the extremely high pressure opposed on it (t = 4.8 $\mu$ sec).

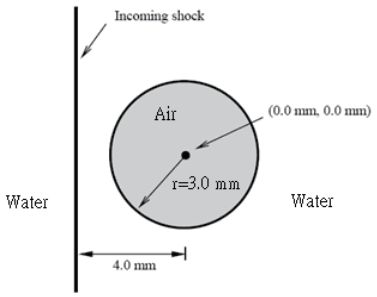


Fig. 1 Illustration of the Shock-bubble interaction problem.

Corresponding author:Yang-Yao Niu
*E-mail address*:yyniu@mail.tku.edu.tw

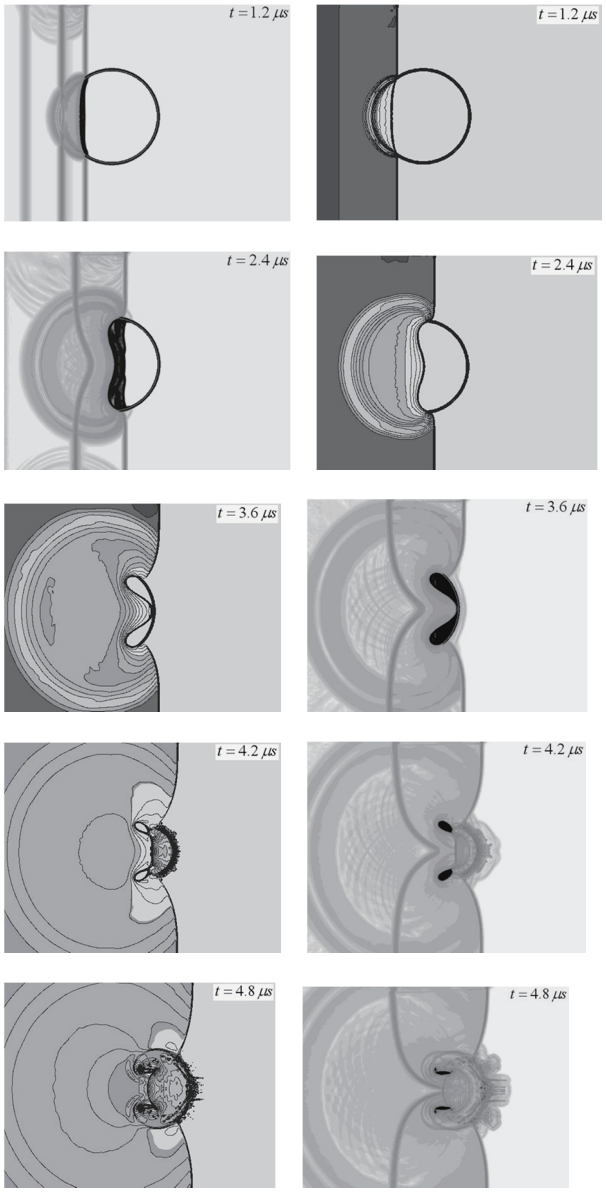


Fig. 2 Time evolution of the shock-bubble interaction problem. Left: contours of pressure and void fraction; Right: contours of function $(1+\alpha_g^2)\log(|\nabla\rho_{avg}|+1)$ (schlieren photo). (computed by the six-equation 2 fluid model)

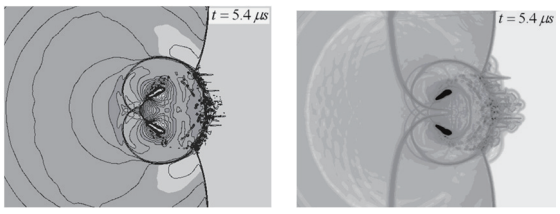


Fig. 3 Time evolution of the shock-bubble interaction problem. Left: Langseth's data, Right: numerical ($t = 4.8\ \mu s$)

### 3. Concluding Remarks

In this work, we use the current numerical model to solve a liquid fluid flow described by the stiffened gas model. This scheme was demonstrated to be robust and accurate enough to capture the pressure wave within the liquid flow. In the real situation, the liquid under a strong expansion wave will be vaporized into the gas phase if the pressure is dropped under the saturation pressure as compared with the validated data as in Fig. 3. Our numerical results after t = 4.8 $\mu$ sec look unsatifactory.However, the pressure, which is derived from the conservation variables, may become negative if we still use stiffened gas model in this situation It indicates that a more precise equation of state is necessary for realistic applications.

### References

[1] Hirt, W. and Nichols, B. D., *Journal of Computational Physics*, 39, (1981) 201-225.
[2] Y. Y. Niu, *Numerical Heat Transfer*, Part B, 38 No.2, (2000) 203-222.
[3] Luo, H., Baum and J. D., and Lohner, R., *Journal of Computational Physics*, 194, (2004) 304-328.
[4] H. B. Stewart, B. Wendroff, *Journal of Computational Physics*, 56, (1984) 363-409.
[5] . Chang CH, Liou MS. *J Comput Phys* 225, (2007) 840-73.
[6] R. R. Nourgaliev, T. N. Dinh, T. G. Theofanous, *Journal of Computational Physics*, 213,(2006) 500-529.

Eleventh International Conference on Flow Dynamics
October 8-10, 2014, Sendai, Miyagi, Japan

# Relationships Between Symmetry of Vortical Flow and Pressure Minimum Feature Derived from Flow Kinematics in Local Approach

Katsuyuki Nakayama[1], Yasumasa Ohira[2], Hideki Hasegawa[1]
[1]Department of Mechanical Engineering, Aichi Institute of Technology
Yakusa-cho, Toyota, Aichi, 470-0392, Japan
[2]Graduate School of Engineering, Aichi Institute of Technology
Yakusa-cho, Toyota, Aichi, 470-0392, Japan

**ABSTRACT**

The present investigation introduces an invariant to represent symmetry of vortical flow geometry specified by velocity gradient tensor, and investigates relationships between the features of the symmetry and of pressure minimum in terms of flow kinematics, in isotropic homogeneous turbulence. It shows that the local pressure minimum features represented by $Q$- and $\lambda_2$- definitions in local approach require a certain symmetry of the local vortical flow geometry, and that the transition of the pressure features is associated with that of the symmetry.

## 1. Introduction

The detail analysis of the vortical flow geometry (topology) is important for the elucidation of vortical phenomena and for the control or suppression of vortices in many engineering fields. Although the universal definition of a vortex has not been established, many definitions are proposed in local or non-local approach, with respect to several physical characteristics of a vortex.

The Δ-, $Q$-, and $\lambda_2$- definitions [1-3] are popular definitions which are used frequently [4], and they are definitions in the local approach that expresses a (finite-scale) vortex as a vortical region where an applied definition is satisfied. The Δ- definition [1] is based on the invariant local flow geometry specified by the velocity gradient tensor $\nabla \boldsymbol{v}$, and focuses on the invariant swirling or vortical motion. On the other hand, the $Q$- and $\lambda_2$- definitions focus on the pressure characteristics in terms of flow kinematics. $Q$ and $\lambda_2$ denote the second invariant of $\nabla \boldsymbol{v}$ and the second biggest pressure Hessian ignoring unsteady strain and viscous terms, respectively. The $Q$-definition [2] specifies the positive Laplacian of the pressure ($0<Q$), and the $\lambda_2$-definition [3] requires the pressure minimum induced by the vortical flow ($\lambda_2<0$). Although the physical points of view in these definitions are different, relationships of these popular definitions and their universal representation are investigated [4], and their universal definition has also been proposed [5].

The important vortices or vortical regions to be identified in many engineering fields may be required to be stable to exhibit significant effect for a certain time period, and may have pressure minimum characteristics induced by the swirling motion or high symmetry that is associated with the stability of vortices [6].

Nakayama investigated the detail flow geometry, and clarified the physical interpretation of the complex eigenvalues of $\nabla \boldsymbol{v}$ and derived the symmetry properties represents symmetry of the vortical flow in itself terms of the complex eigenvectors, and this invariant represents symmetry of the vortical flow in itself.

Corresponding author: Katsuyuki Nakayama
*E-mail address*: nakayama@aitech.ac.jp

The present study applies this invariant, and investigates the relationships between the symmetry of the vortical flow and the pressure minimum feature in terms of flow kinematics represented by the $Q$- and $\lambda_2$-definitions, in local approach. We analyze the transient features of the symmetry and the pressure minimum in a homogeneous isotropic turbulence analyzed by DNS (Direct Numerical Simulation).

## 2. Local Flow Geometry Specified by $\nabla \boldsymbol{v}$

We show the invariant representing the symmetry of the vortical flow geometry [7]. In three dimensional velocity field, if $\nabla \boldsymbol{v}$ in a point has complex eigenvalues $\lambda_R \pm i\phi$ ($i$: imaginary number) and eigenvectors $\boldsymbol{\xi}_p \pm i\boldsymbol{\eta}_p$, and a real eigenvalue $\lambda_a$ and its eigenvectors $\boldsymbol{\xi}_a$, the local flow pattern around the point can be expressed in terms of these eigenvalues and eigenvectors:

$$\boldsymbol{x} = 2\exp(\lambda_R t)\{\cos(\phi t)\boldsymbol{\xi}_p - \sin(\phi t)\boldsymbol{\eta}_p\} + \exp(\lambda_a t)\,\boldsymbol{\xi}_a. \quad (1)$$

It is noted that $\boldsymbol{\xi}_p$ and $\boldsymbol{\eta}_p$ can be orthogonal. Different to the real eigenvectors, $\boldsymbol{\xi}_p$ and $\boldsymbol{\eta}_p$ has a restriction in terms of the ratio of the norms (lengths) of these vectors in order to satisfy the eigenequation, and a ratio $c$ of the lengths is specified as an invariant, i.e.,

$$c = |\boldsymbol{\xi}_p|/|\boldsymbol{\eta}_p| \text{ or } |\boldsymbol{\eta}_p|/|\boldsymbol{\xi}_p| \quad (0<c\leq 1). \quad (2)$$

Even though the complex eigenvalues are the same, the flow topology differs according to $c$. The vortical flow is symmetric if $c$ is equal to 1, and the skewness increases as $c$ is close to 0, as shown in Fig 1.

## 3. Results and Discussion

The vortices are analyzed in a decaying isotropic homogeneous turbulence analyzed with the pseudo spectral method in the region $(2\pi)^3$ composed of $256^3$ nodes with $|k_i| < 85$ ($i$=1,2,3) of wavenumber vector $\boldsymbol{k} = (k_1, k_2, k_3)$ and time step 0.001. An energy spectrum $E(k) = (k/k_p)^4 \exp\{-2(k/k_p)^2\}/2$ ($k=|\boldsymbol{k}|$, $k_p$=4) gives the initial velocity field with random phases of $\boldsymbol{k}$, where the Taylor Reynolds number $Re_\lambda$ =154, the Taylor microscale $\lambda_T$ =0.58, the Kolmogorov length $\eta$=0.021, and the eddy turnover time $t_e$=0.064. The time $t$, and $Q$ and $\lambda_2$ are non-dimensionalized by an eddy turnover time and root

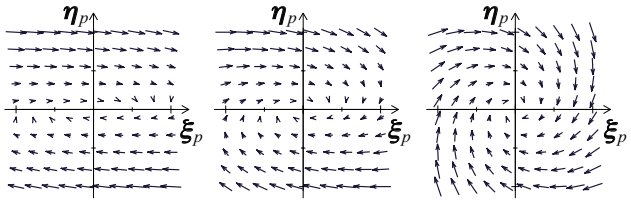


(a) $c$ = 0.25 (b) $c$ = 0.5 (c) $c$ = 1.0

Fig. 1 flow geometries in swirl plane, with same complex eigenvalues ($\lambda_R$=-1, $\phi$=2) and different $c$.

mean squares of respective properties at the relevant time, respectively.

Figure 2 shows a joint probability density function (JPDF) of $\lambda_2$ and $c$. It indicates that the local pressure minimum requires a certain symmetry of the vortical flow, and that $c$ should be over 0.1-0.2. Figure 3 shows contours of $\lambda_2$ and $c$ in a vortex in the turbulence. In a section of the tubular vortex, the contours of $\lambda_2$ = -2 is inside that of $\lambda_2$ = -0.8, and the contours of $c$ = 0.75, 0.85 are inside those of $\lambda_2$, which indicates that the core region of a vortex has high symmetry.

Figures 4 and 5 show JPDFs of $\partial c/\partial t$ and $\partial Q/\partial t$, and $\partial c/\partial t$ and $\partial \lambda_2/\partial t$, respectively. Both figures indicate that the development or decay of $Q$ and $\lambda_2$ is statistically associated with that of $c$, in spite that $Q$ and $\lambda_2$ do not require the symmetry in their definitions. $Q$ can be expressed as $Q = \phi^2 - 3\lambda_R^2$ [4], where $c$ is not involved. It implies that the progress of the symmetry is associated with that of the intensity of swirling, i.e., $\phi$ which is defined as swirlity representing the geometrical average of rotating components of $\nabla \boldsymbol{v}$ in swirl plane [7].

## 4. Concluding Remarks

A symmetry property of local vortical flow geometry is applied in vortices in an isotropic homogeneous turbulence. The local pressure minimum characteristics ($Q$- and $\lambda_2$- definitions) require a certain vortical flow symmetry, and the development or decay of the pressure minimum has a correlation with that of the symmetry.

## References


[1] M. S. Chong, A. E. Perry, B. J. Cantwell, *Phys. Fluids*, A2(5) (1990) 765－777.

[2] J. C. R. Hunt, A. A. Wray, P. Moin, *Center for Turbulence Research*, CTR-S88 (1988) 193－208.

[3] J. Jeong, F. Hussain, *J. Fluid Mech.*, 285 (1995) 69－94.

[4] P. Chakraborty, S. Balachandar, R. J. Adrian, *J. Fluid Mech.*, 535 (2005) 189－214.

[5] K. Nakayama, K. Sugiyama, S. Takagi, *Fluid Dyn. Res.*, (in press).

[6] T. S. Lundgren, *Phys. Fluids*, 25(12) (1982) 2193－2203.

[7] K. Nakayama, *Fluid Dyn. Res.*, 46 (2014) 055502.


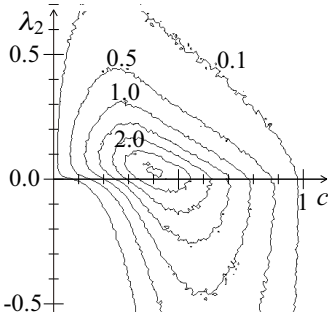


Fig. 2 JPDF of $\lambda_2$ and $c$.

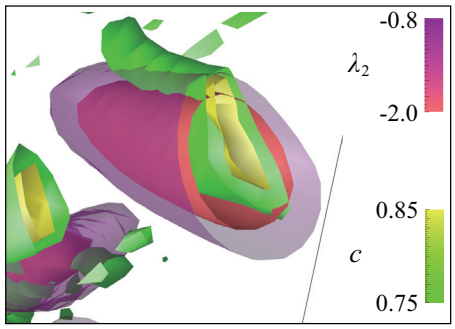


Fig. 3 Contour of $\lambda_2$ and $c$ in a vortex in the isotropic turbulence. ( $\lambda_2$ = -0.8, -2; $c$ = 0.75, 0.85)

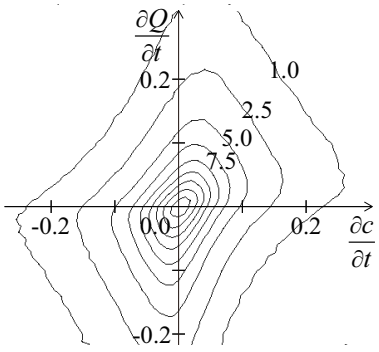


Fig. 4 JPDF of $\partial c/\partial t$ and $\partial Q/\partial t$.

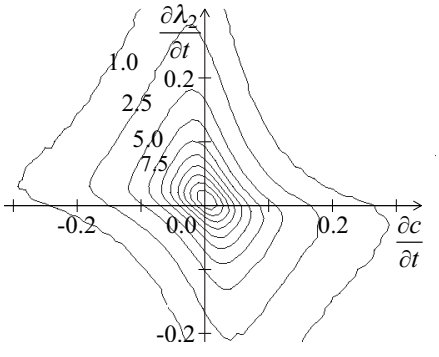


Fig. 5 JPDF of $\partial c/\partial t$ and $\partial \lambda_2/\partial t$.

Eleventh International Conference on Flow Dynamics
October 8-10, 2014, Sendai, Miyagi, Japan

# Flow Reversal of Natural Convection in Vertical Parallel Plates with Asymmetrically Heating

Chung-Jen Chen, Shang-Hao Huang, Wu-Shung Fu
National Chiao Tung University
1001 Ta Hsueh Road, Hsinchu, Taiwan

**ABSTRACT**

An unsteady flow reversal of natural convection in vertical parallel plates with an asymmetrically heated wall is investigated numerically. Numerical methods of the Roe scheme, preconditioning and dual time stepping are adopted for solving governing equations of a low speed compressible flow. The results show the modified Rayleigh number is smaller than the critical Rayleigh number, the total mass flow rate increases with the modified Rayleigh numbers. When the modified Rayleigh number is larger than the critical Rayleigh number, the total mass flow rate is almost equal to the critical mass flow rate.

## 1. Introduction

The subject of natural convection in vertical parallel plates still attracts lots of experimental and numerical studies. In some situations of this subject, a special phenomenon called flow reversal in which surrounding fluids through the outlet flow into the vertical parallel plates is found when the ratio of the width to the length of the plates exceeds a certain threshold. A low-speed compressible fluid flow is taken into consideration instead of Boussinesq assumption in high temperature difference [1]. In those past studies, the effect of distance between vertical parallel plates that is very important and the phenomena of natural convection varying from a steady to an unsteady situation in a heating process are hardly studied. Therefore, the aim of this study investigates of natural convection between vertical parallel plates with asymmetric heating numerically.

## 2. Physical Model

A physical model of three dimensional vertical parallel plates is indicated in Fig.1. The length, height and width are $h$, $b$ and $w$, respectively. The temperature of the heated surface is $T_h(400K)$, and the other regions are adiabatic. The gravity is downward and the temperature and pressure of the surroundings are $T_0(298K)$ and $P_0(101300Pa)$, respectively.

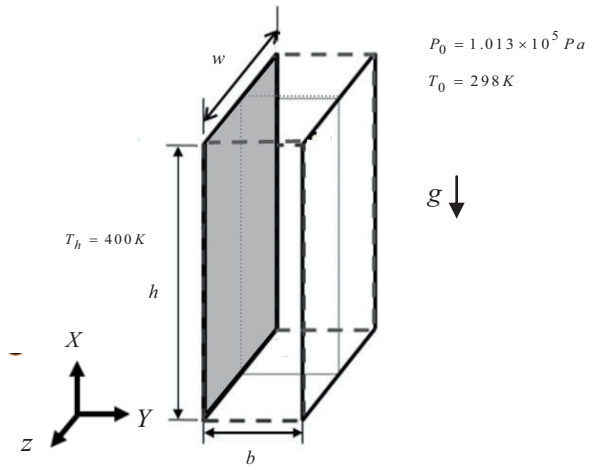


Fig. 1 Physical model

Corresponding author: Shang-Hao Huang
*E-mail address:* shhuang.me98g@g2.nctu.edu.tw

## 3. Numerical Method

For the investigation of the heat transfer with high temperature difference, the numerical method of compressible flow without Boussinesq assumption is considered. The governing equations of a compressible flow can be divided into two parts. One is the inviscid term and the other is the viscous term. The Roe scheme with $3^{rd}$ order MUSCL proposed by Abalakin et al. [2] are used to compute the inviscid terms. The method of dual time stepping is added to calculate the transient state. And a second order central difference method is adopted to calculate the magnitudes of the viscous terms. Finally, the LUSGS was modified by [3] to suitable for preconditioning in solving temporal term. The non-reflecting boundary conditions are used at the apertures of the vertical parallel plates in order to avoid a low speed compressible flow to be polluted by the reflections of acoustic waves. And both sides of the width are periodic conditions.

And governing equations can be obtained.

$$\Gamma\frac{\partial U_p}{\partial \tau}+\frac{\partial U}{\partial t}+\frac{\partial F}{\partial x}+\frac{\partial G}{\partial y}+\frac{\partial H}{\partial z}=S \qquad (1)$$

where $\tau$ is the artificial time, $t$ is the physical time . $\Gamma$ is a preconditioning matrix proposed by Weiss and Smith[4]

## 4. Results and Discussion

In Fig.2, streamlines are indicated under the $Ra = 8.35\times10^4$ situation. The heated fluids with light density exerted by the buoyancy force ascend to the aperture. And then ascending fluids along the heated wall continuously accumulate and start to form rotation behaviors. In the low modify Rayleigh number situation, the shear force is dominant, and then recirculation cell length $l$ decreases.

In the $Ra = 1.31\times10^6$ situation. The boundary layer flow is found along the heated surface and the reverse flow is formed on the opposite side from the outlet of the channel. The reverse flow from the outlet forms an eight-shaped structure with two main recirculation cells. The flow field of the top half region begins to swing unsteadily. An unsteady flow reversal revealed by the present work is shown, several circulations are observed. The flow visualization of the existing result [5] is shown. The sizes and locations of

circulations and the entrance length of the flow reversal of both results are similar.

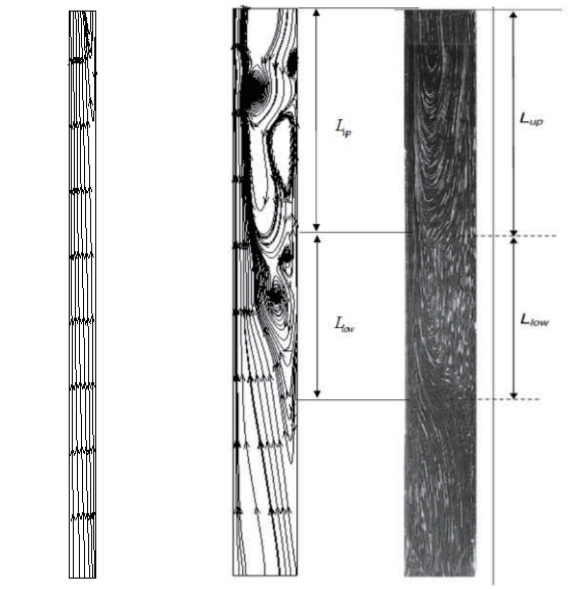


Fig. 2 Comparison of flow field for $Ra = 8.35\times10^4$ and $Ra = 1.31\times10^6$

In Fig. 3, local Nusselt numbers at four different locations varied with the dimensionless time are shown for $Ra^* = 1.31\times10^6$, respectively. In this situation, the quantity of the fluids via the outlet sucked into the plates is larger than that via the inlet sucked into the plates that causes the impingement between both downward and upward mass flow rates to be drastic. As a result, the distributions of local Nusselt numbers are no longer smooth. Accompanied with the increment of the X, the variation of the distribution becomes more drastic. At the location of X=0.875, because the location is close to the outlet, and the amplitude of the variation becomes large.

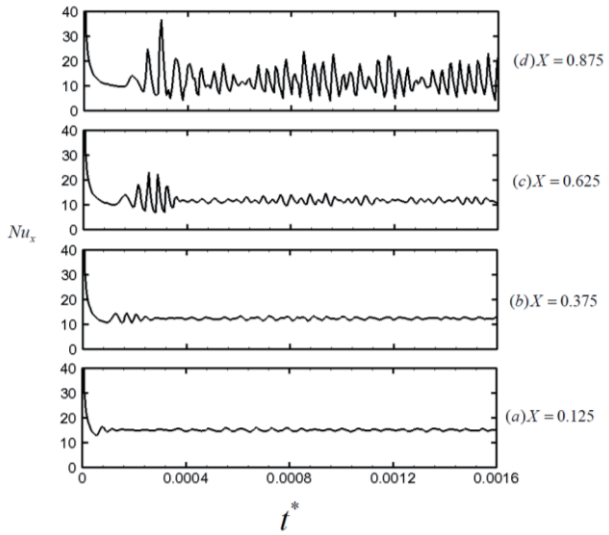


Fig. 3 Local Nusselt numbers at four different locations varied with the dimensionless time for $Ra^* = 1.31\times10^6$

In Fig. 4, the variation of the total mass flow rate $\overline{M}_y$ with the modified Rayleigh number is shown. The total mass flow rate, which includes both mass flow rates via the inlet and outlet flowing into the plates. The results show the modified Rayleigh number is smaller than the critical Rayleigh number, the total mass flow rate increases with the modified Rayleigh numbers. When the modified Rayleigh number is larger than the critical Rayleigh number, the total mass flow rate is almost equal to the critical mass flow rate.

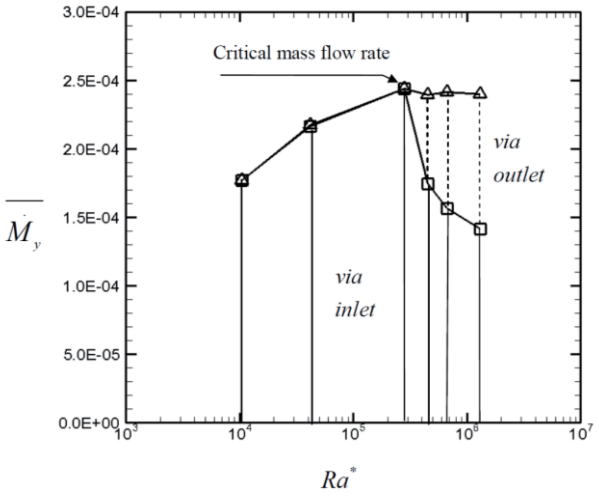


Fig. 4 Variation of the total mass flow rate with the modified Rayleigh number

## 5. Concluding Remarks

Several conclusions are summarized as follows.

1. Thermal and flow fields incline to a steady or unsteady situation that is connected with Rayleigh number and aspect ratio.
2. The modified Rayleigh number is smaller than the critical Rayleigh number, the total mass flow rate increases with the modified Rayleigh numbers. When the modified Rayleigh number is larger than the critical Rayleigh number, the total mass flow rate is almost equal to the critical mass flow rate.

## References


[1] D.D. Gray, A. Giorigini, *Int. J. Heat Mass Transfer*, 19 (1976) 545–551.

[2] I. Abalakin, A. Dervieux, T. Kozubskaya, *INRIA* (2002) 4459.

[3] W. S. Fu, C. G. Li, W. F. Lin and Y. H. Chen, *Int. J. Nume. Meth. Fluids*, 61 (2009) 888–910.

[4] J. M. Weiss and W. A. Smith, *AIAA*., 33 (1995) 2050–2056.

[5] D. Ospir, C. Popa, C. Chereches, G. Polidori and S. Fohanno, *Int. Comm. Heat Mass Transfer*, 39 (2012) 486–493.

Eleventh International Conference on Flow Dynamics
October 8-10, 2014, Sendai, Miyagi, Japan

# Heat Transfer Measurement in Rotating Internal Cooling Channels Using Liquid Crystal Thermography

Yao-Hsien Liu, Szu-Chi Huang, Chi-Wei Yen
Department of Mechanical Engineering, National Chiao-Tung University
1001 Ta-hsueh Road, Hsinchu, 30010, Taiwan

**ABSTRACT**

Liquid crystal thermography was used to obtain the heat transfer coefficient in rotating internal cooling channels. Stroboscope was used as the illumination device and CCD camera was used to record the images. The aspect ratio of the rectangular channel was 4:1, with two opposite walls roughened with pin-fins. The diameter and height of the pin fins were 5mm and 5mm height, respectively. The Reynolds number from 10000 to 20000 and the rotation number ranged from 0 to 0.195 in this study. Results showed that rotation altered the wake flow behind the pin-fins.

## 1. Introduction

Cooling of the gas turbine blade can reduce the thermal load and improve operational safety. Proper cooling lowers the blade temperature and prevents blade failure. Gas turbine blades are cooled internally by sending the compressed air through the internal cooling passages. In order to increase the cooling efficiency, the cooling passage is roughened with turbulence promoters to enhance convective heat transfer.

Pin-fins are widely applied to the trailing edge of the turbine blades to increase heat transfer and improve structural support. Metzger et al. [1] investigated heat transfer in a rectangular channel with circular pin-fins. They observed an initial rise in Nusselt number encompassing the first three to five rows followed by a subsequent gradual decline in Nusselt number through the reminder of the pin-fin array. Pandit et al. [2] tested partial pin-fin arrays of circular, triangular, hexagonal, and diamond shapes on the walls of a rectangular channel. Results showed that the diamond pin fins perform the best in enhancing heat transfer.

Heat transfer in the cooling passages of the rotor blades are influenced by the Coriolis force and rotating buoyancy force, which shift the core flow and alter the heat transfer distribution. Heat transfer increases on the trailing surface and decreases on the leading surface in a radially-outward flow channel [3, 4]. Experimental studies of heat transfer in the rotating channels have been done extensively by thermocouples. However, the point measurement can only provide local or regionally averaged data in limited locations. Liquid crystal thermography is a technique of measuring the surface temperature distribution by obtaining the reflected color of the coating. This technology is able to provide a detailed heat transfer distribution over the rough surface [5]. The objective of the current study was to use the liquid crystal technique for investigating heat transfer distribution in a rectangular rotating internal cooling channel. This technique is able to obtain the temperature distribution in the flow channels under rotating condition. Nusselt number distribution influenced by rotation and pin fins was studied.

Corresponding author: Yao-Hsien Liu
*E-mail address*: yhliu@mail.nctu.edu.tw

## 2. Method

The heat transfer measurement was conducted in a rotating facility as shown in **Fig. 1**. The coolant flow was from an air compressor and the flow rate was measured by a thermal mass flow meter (Tokyo KEISO TF 4000). The test section was connected to the rotating arm and the rotational speed was controlled by a frequency controller. A slip ring was used to transfer thermocouple signals and heater currents during the rotating condition. A stroboscope with the CCD camera was used to record the color change of the liquid crystal coating under rotating condition.

The rectangular test section was shown in **Fig. 2**. It was made from garolite materials. Color of the liquid crystal coating on the heater surface was captured by viewing through a quartz sight glass. The channel width and height were 50 mm and 12.5 mm, respectively. Staggered pin fin arrays were applied to the leading and trailing surfaces. The diameter and height of the pin fins were 5mm and 5mm, respectively. The pitch-to-diameter ratio was 2 in both streamwise and spanwise directions.

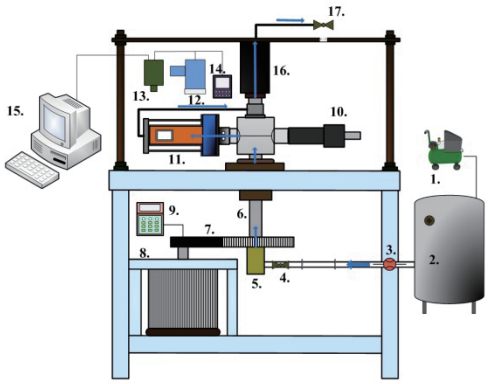


Fig. 1 Rotating facility

Heat transfer coefficient (h) was determined from the Newton's law of cooling:

$$h = \frac{\dot{Q}_{in} - \dot{Q}_{loss}}{A(T_{w,x} - T_{b,x})} \quad (1)$$

Heat input ($\dot{Q}_{in}$) was determined from the voltage and current through the resistance heater. The heat loss ($\dot{Q}_{in}$) test was performed by supplying power to the heater until the wall temperature reached predetermined temperature. Meanwhile the test section was filled with insulation materials to eliminate natural convection. Heat supplied to the test section and was recorded to determine the heat loss. Wall temperature ($T_{w,x}$) was obtained from the liquid crystal coatings and the bulk temperature ($T_{b,x}$) was determined from the thermocouples placed at the inlet and exit of the test section. A Nusselt number ratio was calculated based the Dittus-Boelter/McAdams correlations developed for fully-developed turbulent flow in a smooth tube:

$$\frac{Nu}{Nu_o} = \frac{hD_h/k}{0.023\,\mathrm{Re}^{0.8}\,\mathrm{Pr}^{0.4}} \quad (2)$$

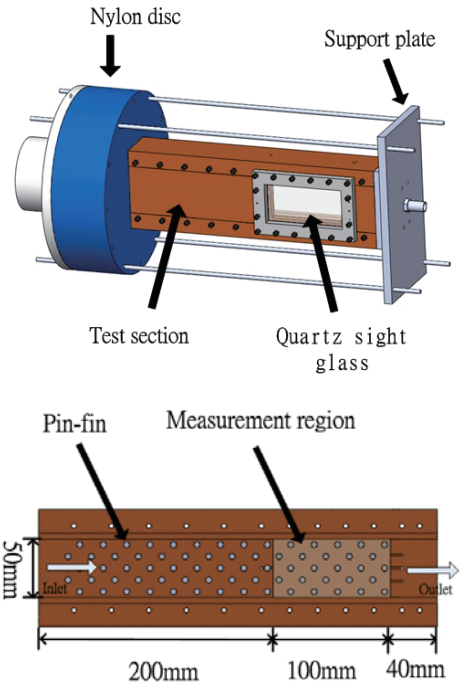


Fig. 2 Test Section

## 3. Results and Discussion

Nusselt number distribution in a stationary channel was shown in **Fig. 3**. The white regions in front of the pin fins have high heat transfer rates, resulting in low temperature that was not within the temperature range of the narrow-band liquid crystal (2°C). The Nusselt number gradually decreased along the streamwise direction. Higher heat transfer can be observed behind the pin fins due to wake flow. Effect of rotation on heat transfer distribution was shown in **Fig. 4**. It can be observed that the Nu contours were altered due to rotation.

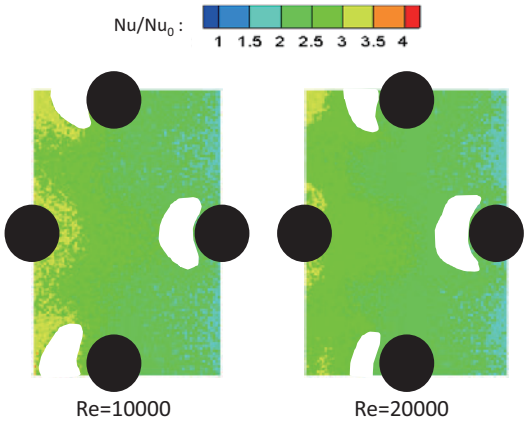


Fig. 3 Nusselt number in the stationary channel

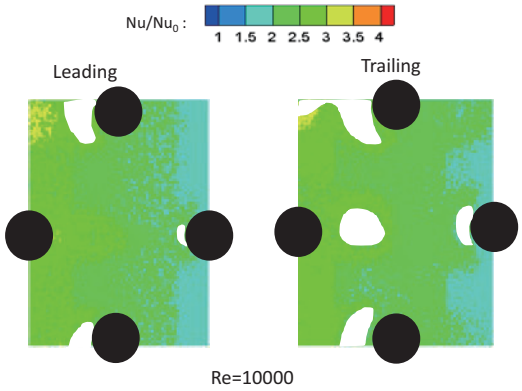


Fig. 4 Nusselt number in the rotating channel with a rotational speed of 360 rpm

## 4. Concluding Remarks

Liquid crystal thermography was used to obtain the heat transfer distribution in a rotating rectangular cooling channel. This technique was able to obtain detailed heat transfer distributions on the surface. High rotation number effect on heat transfer can be further investigated in this channel.


## Acknowledgements

This research was funded by the National Science Council, Taiwan (NSC 101-2221-E-009-040 -MY2).


## References


[1] D.E. Metzger, R.A. Berry, J.P. Bronson, *Journal of Heat Transfer*, 104 (1982) 700－706.

[2] J. Pandit, M. Thompson, S. V. Ekkad, S. T. Huxtable, *International Journal of Heat and Mass Transfer*, 77 (2014) 359－368.

[3] J. H. Wagner, B.V. Johnson, T. J. Hajek, *Journal of Turbomachinery*, 113 (1991), 42–51.

[4] W.L. Fu, L.M. Wright, J.C. Han, *Journal of Thermophysics and Heat Transfer*, 20 (2006), 569–582.

[5] Y.H. Liu, S.J Song, Y.H. Lo, *International Journal of Heat and Mass Transfer*, 58 (2013) 292–299.

# Optical Skin Friction Measurement in Hypersonic Flow Utilizing LCCs

Xing Chen, Dapeng Yao, Shuai Wen, Jian Gong, Zhixian Bi
China Academy of Aerospace Aerodynamics
Yungang West Road, Beijing, BJ 10, China

**ABSTRACT**

Shear-sensitive liquid-crystal coatings (SSLCCs) have an optical property that they are sensitive to the applied shear stress. Images of spatial reflection spectrum of the LCC with illumination of white light can be processed to get the surface shear stress vector distribution on the coating. Based on this theory, experimental investigations on skin friction measurement using the LCCs have been done, both in low speed jet flow and hypersonic flow. In the Ma=5 hypersonic wind tunnel experiment, distribution of skin friction on a sharp leading edge flat plate is obtained.

## 1. Introduction

In the high-speed flight, friction takes a larger proportion of total drag on the vehicle, not only affects the aircraft's aerodynamic performance, but also has a great influence on the aerodynamic heating. As a fundamental research of fluid dynamics, friction measurement has been paid great attention. Research institutions and universities all over the world have invested great efforts in studying friction. In 2009, the United States set up a hypersonic science center, whose task is the development of new measurement techniques, which includes friction measurement. As the friction varies with the flow states, especially in hypersonic transition flow field, the prediction of friction is rather difficult by both wind tunnel experiments and numerical simulations. These difficulties are due to the small absolute value of the friction and the complexity of the flow.

On friction measurements, there are varieties of techniques and methods, such as friction gauge measurement, optical measurement, displacement measurement, hot wire measurement, Preston tube measurement and measurement based on MEMS technology [1-5]. The LCC optical measurement is an optical non-contact technique, which can quantitatively measure both the magnitude and direction of the shear stress [6,7]. In the past 20 years, NASA Ames Research Center, Niigata University of Japan and other institutions have made a thorough study on this technique [8]. But those studies are focused on subsonic and supersonic conditions. There has not been friction measurement research in hypersonic condition using the LCCs. Here, we aim to explore an experimental method for skin friction measurement using the LCCs in hypersonic wind tunnel.

## 2. Principle and Method

Color-change response of a LCC depends on both the magnitude of the applied shear vector and its direction. When a certain shear stress is applied on the LCCs, the most obvious color change of any point on the coating can only be observed along the stress direction, while observing reversely, almost no color change could be seen, as shown in Fig.1.

Corresponding author: Xing Chen
*E-mail address*: chenxing0234@sina.com

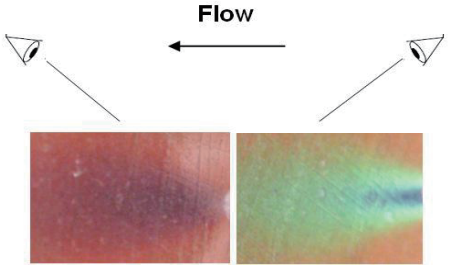


Fig.1 LCC color-change properties

Utilizing the optical properties of the LCCs, shear stress vector distribution can be quantitatively measured. Spraying the liquid-crystal material onto the model surface to form a coating, the wall does not change its shape. Using the friction gauge for calibration of the LCCs, the relationship between hue and stress, Hue ~ τ curve, could be obtained, as shown in Fig.2. For quantitative measurement, images of the LCC color-change response to the shear field are recorded from multiple in-plane view angles encompassing all shear vector directions. After image processing, hues at all points of the coating gained from different angles are obtained. For each physical point on the test surface, a Gaussian curve to the variation in measured colors (hues) with the changing in-plane view angles could be fitted. The in-plane view angle corresponding to the maximum hue value represents the shear direction. And the hue value could be processed to get the magnitude of the stress through the calibration curve. Distribution of surface shear stress vectors can be obtained by this image processing method.

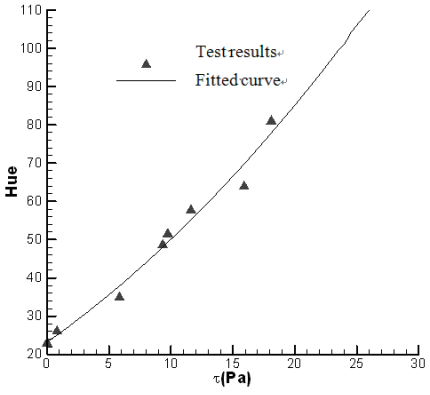


Fig. 2 Calibration curve of liquid crystal CN/R2

## 3. Experiments and results

Based on the optical properties of the LCCs, shear stress vector distribution can be quantitatively measured. In order to carefully study the characteristics of the shear-sensitive liquid crystals, a low-speed jet test platform is designed to carry out a series of experiments. And a distribution of surface shear stress vectors on the flat plate beneath tangential jet is gained in the experiment, which presents a good symmetry with respect to the centre line, as shown in Fig.3.

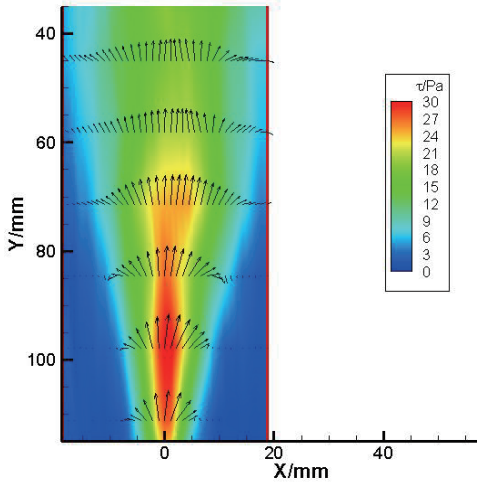


Fig.3 Presentation of shear stress distribution on flat plate in a jet flow

Skin friction measurements on a shear-sensitive liquid crystal coated flat plate in hypersonic flow are conducted in wind tunnel FD-07 of CAAA. FD-07 is a conventional free stream blow down hypersonic wind tunnel, equipped with a series of contoured nozzles, with 500mm exit diameter. A 400mm×160mm sharp leading-edge flat plate made of anodized ultralumin is employed as test model. For local monitoring, a friction gauge is installed at the position 300mm after the leading edge. Before the experiment, a uniform coating of the LCC CN/R2 is sprayed onto the model surface. And the test condition would be determined by the valid applying region of the LCC which resulted from calibration. The free stream parameters are as follows: total pressure $P_0$=0.65Mpa, total temperature $T_0$=339K, and unit Reynolds number Re=1.53×$10^7$/m. The same light source as that in low-speed jet experiment is used for illumination. A BASLER camera which can provide 30 pictures of a resolution of 1608×1208 per second is used for image acquisition. Images are captured along the centre line of the plate.

Friction coefficients calculated using both the LCC and the friction gauge results along the centre line are obtained from a series of wind tunnel tests. A computational result is also taken as reference and plotted in Fig.4. The repeat accuracy is good by noting that the deviations of the 3 sets of test data are less than 10%. The measurement values of $C_f$ begin to increase at x=80mm, and remain nearly constant between 0.0011 and 0.0013 after x=210mm, corresponding with the computational result of turbulent flow. It is evident that the boundary layer transition is completed at x=210mm for Ma=5, Re=1.53×$10^7$/m. The measurement value of friction gauge installed at x=300mm also shows an agreement with that of LCC by a 17% relative deviation.

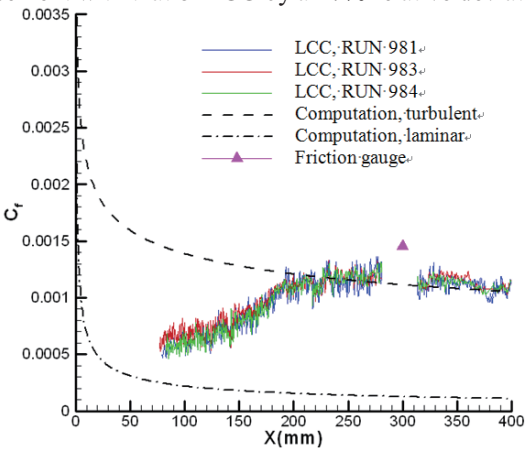


Fig. 4 Distribution of skin friction coefficient on the centre line of the flat plate

## 4. Conclusions

The spectrum of the shear-sensitive liquid crystal coatings with normal illumination of white light contains the information of shear stress vector. Low-speed jet experiment gives a symmetric distribution of shear stress on the model surface with the tangential jet flow applied. In the Ma 5 wind tunnel experiment, the measurement values of the LCCs show an agreement with those of friction gauge and computational results. Additionally, the variation of shin friction along the center line indicates the transition onset location, which gives a new method for flow analysis and transition research. The most important, the experiment proves that the LCCs can be used for skin friction measurement in a hypersonic flow condition.

## References


[1] C. P. Goyne, A. Paull, R. J. Staller, *AIAA*, (1995) 95-3152.

[2] P. Reddeppa, G. Jagadeesh, M. S. Bobji, *AIAA*, (2005) 2005-1412.

[3] E. R. Keener, E. J. Hopkins, *AIAA*, (1969) 69-345.

[4] T. Liu, & J. P. Sullivian, *AIAA*, (1997) 97-2216.

[5] J. W. Naughton, M. Sheplak, *AIAA*, (2000) 2000-2521.

[6] D. C. Reda, J. J. Muratore, *AIAA*, (1994) 94-0729.

[7] D. C. Reda, M. C. Wilder, *AIAA*, (1998) 98-2717.

[8] N. Fujisawa, A. Aoyama, S. Kosaka, *Measurement Science and Technology*, Vol. 9. Sep. (2003) 1655～1661.

Eleventh International Conference on Flow Dynamics
October 8-10, 2014, Sendai, Miyagi, Japan

# Heat-Flux Measurement of Flat-Plate with Cylinder using Phosphor Thermography Technique

Jian GONG[1], Zhixian BI[1], Shuguang HAN[1] , Chaohua WU[1], Jianming FU[2]
[1]China Academy of Aerospace Aerodynamic
Beijing, 100074, China
[2]Shanghai Electro-Mechanical Engineering Institute
Shanghai, 200000, China

**ABSTRACT**

Phosphor Thermography Technique is a new optical heat-flux measurement method. Phosphor thermography system based on the temperature-sensitivity material has been developed in China Academy of Aerospace Aerodynamics (CAAA). A series of experiments of flat-plate with cylinder is performed in FD-20 gun tunnel of CAAA. Results are discussed in detail, the distribution of heat-flux around the cylinder shows complicated flow structures. a brief mechanism analysis and an evaluation on phosphor thermography technique have been made.

## 1. Introduction

Phosphor thermography is a global heat-flux measurement techniques, the phosphor material fluoresce when excited by ultraviolet radiation, and their emission intensity is dependent on environment temperature. Contrasted with the traditional heat-flux measurement methods (e.g., thin-film heat-transfer sensors, the thermal couples), thermography technique can quantitatively obtain the global distribution without placing the gauge on the model surface.

Began from 2006, phosphor thermography system was developed in CAAA, heat flux distributions of simple shape models were measured in gun tunnel in CAAA[1,2] .

## 2. Method

A) Basic Theory and System

The phosphor material based on the lanthanum, prior to excitation, the material's electronic levels are populated in the ground state, and the excitation sources (ultraviolet) deposit the energy in the material, so that the higher electronic state is reached. This is accomplished by exposure to electromagnetic radiation; usually the radiation includes visible light. The atomic configuration won't remain permanently excited but will return to its ground state or assume an intermediate level. With the change of environment temperature, the intensity of visible light changes in inverse proportion. Base on this phenomenon, the temperature distribution of model surface can be calculated out by the transformation which relies on the intensity-temperature relationship [3].

Phosphor thermography system was shown in Fig.1, before the test, model coated with phosphor material is fixed in the wind tunnel, the radiant visible light from the phosphor coating was excited by the UV light source, and the visible light is received by the CCD camera placed at the optic window. During the test, the intense change of visible light caused by aeroheating is captured by the high speed camera, and the images are switched to the surface heat flux distribution after the test.

Corresponding author: Shuguang Han
*E-mail address*: shuguang1987@126.com

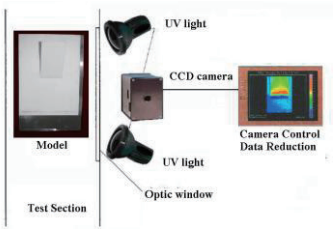


Fig.1 Phosphor thermography system

B) Phosphor Material

The phosphor material belongs to the lanthanum. Before the test it is mixed with the binder with a certain proportion and is sprayed uniformly on the model surface in the test. Diameter of the granules in the material is about 1 micron; thickness of the phosphor coating is about 20-30 microns observed by electron microscope (Fig.2). Figure 3 is phosphor powder's behavior with and without UV light irradiation.

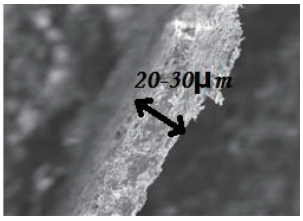


Fig.2 Coating side section Fig.3 Phosphor powder

C) Calibration

The light intensity-temperature relationship is obtain by calibration (Fig.4), a ceramic plate with phosphor coating is heated by a temperature controller, then the light intensity is captured by CCD camera, repeat this step at different temperature points selected, then a relationship of temperature and light intensity can be fitting out.

D) UV Light

Short duration of gun tunnel requires high intensity UV light to keep the coating emission stable during the test, the intensity of UV light is 14000 μ w/cm$^2$(distance:15 inches) . The wavelength of the UV light is 365 nm. The power of the UV light is 35W.

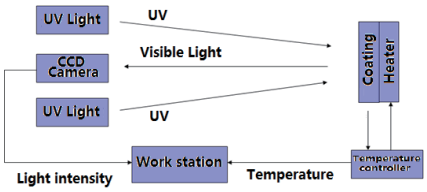


Fig.4 Calibration system

E) Image Acquisition

Light intensity change on the surface of the model is recorded by the image acquisition system in the tests. The frame rate of the system should fast enough for the short run time of the wind tunnel. This system is composed of a high-speed video camera with a zoom lens, a work station with a digitizer.

Frame Rate: 300 fps

Resolution: 512x512 pixels

Data Format: 12 bit

F) Data Reduction

Assuming the model is a semi-infinite flat plate, the transient one dimensional heat conduction can be used as the surface temperature govern equation in isotropic, homogeneous material.

The heat flux at time t can be expressed with T(t) in Equation (1)[4]:

$$q(t)=\sqrt{\frac{\rho ck}{\pi}}\sum_{i=1}^{m}\frac{T(i)-T(i-1)}{(t_m-t_i)^{1/2}+(t_m-t_{i-1})^{1/2}} \qquad (1)$$

## 3. Experiment Setup

A) Facility

Experiments are performed in FD-20 gun tunnel, an impulse hypersonic wind tunnel at CAAA. The facility has a nozzle exit of 480mm in diameter, typical stable flow period varies from 25 to 60 milliseconds. The detail test condition is shown in Table.1.

Table 1. Nominal tunnel flow conditions

| $M_\infty$ | $Re_\infty$(1/m) | $P_0$(MPa) | $T_0$(K) |
|---|---|---|---|
| 8.04 | $2.21\times10^7$ | 18.18 | 1066 |

B) Model

In order to obtain higher measurement accurate, the change of visible light intense from the coating should be larger, models need to be made of the material with lower thermal diffusivity properties. Ceramic material whose thermal diffusivity lower than the stainless steel was chosen, model used in the phosphor experiments was fabricated by silica ceramic models (Fig.5).

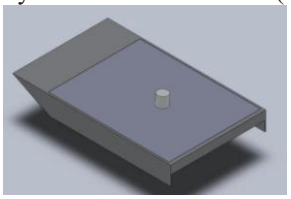

Fig.5 Flat-plate with Cylinder

## 4. Results and Discussion

About the flow structure of flat-plate with cylinder, studies have been made by former researchers which shown in Fig.6[5].

In Fig.7, a high heat-flux line is shown at the upstream of cylinder, it's very close to the side-wall and extended to the lateral back of the cylinder, a possible explain for the entity of high heat-flux line is the shockwave/boundary layer interaction. The low heating area behind the cylinder is also can be explained that caused by the two vortexes, an evident separation line at far upstream of the obstacle can be observed, it caused the heat-flux varies evidently.

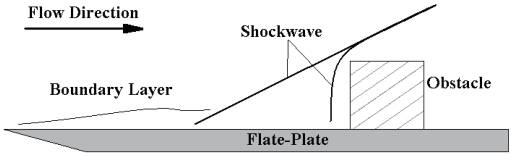


Fig.6 Schematic of small protuberance in turbulent boundary layer

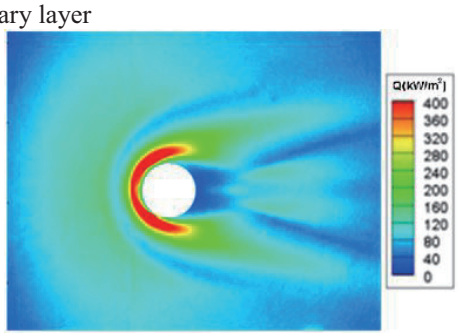


Fig.7 Heat-flux distribution of flat-plate with cylinder

## 5. Conclusions

Flow structure information can be obtained not only from the flow visualizing technique, but also the heat-flux measurement method. Thermography technique avoids some traditional measurement methods' limits, it do without damage to the model surfaces, all need just a thin coating, and this technique's most important advantage is that can obtain far more heat-flux information than heat-flux gauges.

## References

[1] S.G. Han, Z. X. Bi, C. H. Wu, R. Q. Li, C. Y. Li. *PSP & TSP Workshop,*(2010)78.

[2] C. H. Wu, S.G. Han, Z. X. Bi, J. Gong, R. Q. Li. *Sino-Italian Conference on Space Aerothermodynamics and Hot Structures*, (2011)97-100.

[3] T. Liu, J.P. Sullivan. *Springer Berlin Heidelberg, New York,* (2011)16.

[4] W. J. Cook, E. J. Felderman. *AIAA Journal,* 4, 3, (1966) 561-562.

[5] R. Sedney, C. W. Kitchens Jr. *AIAA Journal,* 15, 4, (1976) 546-552.

Eleventh International Conference on Flow Dynamics
October 8-10, 2014, Sendai, Miyagi, Japan

# Non-Intrusive Polynomial Chaos based Uncertainty Quantification of Heat Transfer Performance of High Temperature Blade

Jun Nie[1], Yinjie Song[1], Liming Song[1], Jun Li[1]
[1] Institute of Turbomachinery, Xi'an Jiaotong University
No.28, Xianning West Road, Xi'an, 710049, China

**ABSTRACT**

An uncertainty quantification (UQ) method for heat transfer prediction of high temperature blade was proposed by coupling non-intrusive polynomial chaos based probabilistic collocation method with conjugate heat transfer analysis. Taking four uncertain operating condition parameters into account, Mark-II blade was selected to demonstrate this UQ method. The statistics of maximum metal temperature and maximum temperature gradient were calculated, along with probability of failure and reliability. The results also show which uncertainty mostly affects heat transfer performance.

## 1. Introduction

Uncertainty quantification (UQ) is concerned with quantifying uncertainty characteristics of system output resulted from model input uncertainties and model uncertainties propagated through computational simulation [1]. Several methods for uncertainty quantification, including Monte Carlo simulation and its improved methods, Perturbation techniques, Polynomial Chaos expansion based methods and so on [2], have been developed and been successfully applied in many research filed, such as civil engineering, aerospace engineering, etc. As for uncertainty quantification of high temperature blade, there emerges increasing interest and research in recent years [3].

Among those UQ methods, polynomial chaos (PC) expansion is a promising one. In the generalized PC expansion framework, stochastic solutions are expressed as orthogonal polynomials of input uncertainties, and in theory, exponential convergence rates can be obtained with the optimal polynomial basis [4]. In non-intrusive polynomial chaos (NIPC), simulations are used as black boxes and the calculation of chaos expansion coefficients for stochastic outputs of interest is based on a set of simulation response evaluations. To calculate these response PC coefficients, two primary classes of approaches have been proposed: spectral projection and linear regression [5].

The rest of the paper is organized as follows. In section 2, the proposed UQ method is presented. The results and discussion of UQ of heat transfer performance of Mark-II are in Section 3. Concluding remarks are included in Section 4.

## 2. Uncertainty Quantification Method

### 2.1 Non-Intrusive Polynomial Chaos

A stochastic response $Y$ can be expressed in terms of its polynomial chaos expansion as

$$Y = \sum_{j=0}^{\infty} \alpha_j \Psi_j(\xi) \tag{1}$$

where each of $\Psi_j$ is a multivariate polynomial obtained as product of one-dimensional orthonormal polynomials, $\xi$ is uncertain variables vector for the chaos expansion.

The summation in Eq.(1), in practice, is truncated as

$$Y = \sum_{j=0}^{p} \alpha_j \Psi_j(\xi) \tag{2}$$

The total number of terms $N_t$ is given by

$$N_t = 1 + P = \frac{(n+p)!}{n!\,p!} \tag{3}$$

where $p$ is the total order of expansion, $n$ is the number of random variables. In this paper, $n$ is 4, $p$ is set at 2.

To calculate PC coefficients, spectral projection approach or linear regression approach can be adopted, details of these two methods could be referred to [5]. Here linear regression was adopted.

Mean and variance of the polynomial chaos expansion can be evaluated in the following forms:

$$\mu_Y = E\left(\sum_{j=0}^{P} \alpha_j \Psi_j(\xi)\right) = \alpha_0 \tag{4}$$

$$\sigma_Y^2 = E\left[(Y-\mu_Y)^2\right] = \left\langle \left(\sum_{j=1}^{P} \alpha_j \Psi_j(\xi)\right)^2 \right\rangle = \sum_{j=1}^{P} \alpha_j^2 < \Psi_j^2 > \tag{5}$$

Latin Hypercube Sampling (LHS) is employed on the PC expansion of response $Y$ to calculate all possible values of $Y$ and perform reliability analysis. If a critical value of $Y$, $Y_c$, is given, then the reliability can be calculated. The probability of failure $P_f$, defined as the probability of $Y$ being greater than $Y_c$, can be calculated:

$$P_f = P\{Y < Y_c\} \tag{6}$$

Then reliability R is calculated

$$R = 1 - P_f \tag{7}$$

### 2.2 Conjugate Heat Transfer Analysis

Mark II blade [6] is selected to demonstrate the proposed UQ method. CHT analysis has been carried out using ANSYS CFX. Turbulent eddy viscosity is obtained from SST turbulence mode; $\gamma$-$Re_\theta$ transition model is used to simulate boundary layer transition. Structured mesh is chosen for all regions and mesh on boundary layer is refined to ensure the maximum value of $y^+$ is below 1. Mesh with 1.3 million elements is adopted after a grid independency analysis.

No.4311 operating condition (Table 1) is simulated. Pressure and temperature distribution at midspan for both numerical results and experiment measurements are illustrated in Fig.1 and Fig. 2, respectively. It is evident that there is a satisfactory agreement between numerical results and experiment measurements, which verifies the accuracy and reliability of the CHT analysis used here.

Corresponding author: Liming Song
*E-mail address*: songlm@mail.xjtu.edu.cn

Table 1 No.4311 operating condition

| | Parameter | Value |
|---|---|---|
| Inlet | $T_t$ [K] | 803.0 |
| | $P_t$ [kPa] | 276.5 |
| | Turbulence Intensity | 6.5 % |
| Outlet | $P_s$ [kPa] | 254.170 |
| | Ma | 0.90 |
| | Re | $1.56\times10^6$ |

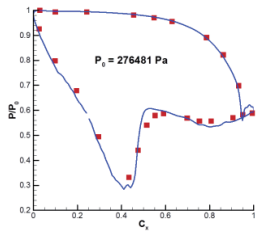


Fig. 1 Pressure distribution at midspan

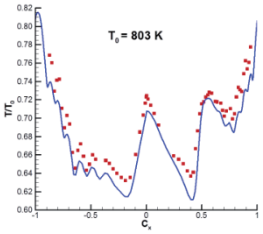


Fig. 2 Temperature distribution at midspan

### 2.3 Input Uncertainties and Stochastic Output

Four operating condition parameters, including stagnation pressure (Pt), inlet total temperature (Tt), turbulence intensity (Tu) for mainstream inlet and stagnation pressure (Pt) for coolant inlet, are chosen as input uncertainties. All input uncertainties have been assumed as normal distribution, detailed statistics are summarized in Table 2.

Maximum metal temperature (Max T) and maximum temperature gradient (Max TG) are chosen as stochastic output quantities of interest. Under the deterministic condition, nominal value of Max T is 689.6 K, and 20.53 K $mm^{-1}$ for Max TG. As the increase of Max T and Max TG could significantly reduce life of blade, in this paper, the critical value of Max T is defined as 710 K, and 22.0 K $mm^{-1}$ for Max TG, which is much greater than the nominal value.

Table 2. Probability distribution of the uncertainties

| Input Uncertainties | | Interval | Mean | Std deviation |
|---|---|---|---|---|
| Mainstream inlet | Tu [%] | 3 - 10 | 6.5 | 1.1667 |
| | Tt [K] | 773 - 833 | 803 | 10.0 |
| | Pt [kPa] | 246.5 - 306.5 | 276.5 | 10.0 |
| Coolant inlet | Pt [kPa] | 234.0 - 286.0 | 260.0 | 8.6667 |

### 3. Results and Discussion

The histogram of the uncertain Max T and that of uncertain Max TG are presented in Fig. 3 and Fig. 4, respectively, and the statistics of Max T and Max TG are given in Table 3. Compared to nominal value, the Max T under the uncertain operating condition can increase as much as 40.2 K, which is a great increase that could sharply reduce the life of the blade. The probability of failure calculated for Max T is 5.4%, implying there is a probability of 5.4% for Max T to be over the defined critical value to be vulnerable to failure. So the reliability for Max T is 94.6%.

Under the uncertain operating condition, the maximum increase of the Max TG can reach to 2.17 K $mm^{-1}$, which is a great increase that could significantly reduce the life of the blade. The probability of failure calculated for Max TG is 3.1%, indicating the probability of Max TG to surpass the defined critical value is 3.1%. Therefore the reliability in term of Max TG is 96.9%.

When four input uncertainties separately exists, uncertain total temperature of mainstream inlet has the greatest impact on Max T which is about one order of magnitude more important than the other uncertainties.

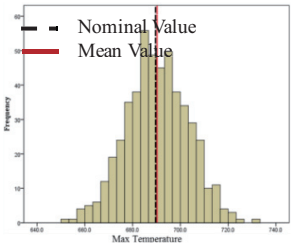


Fig. 3 Histogram of Max T

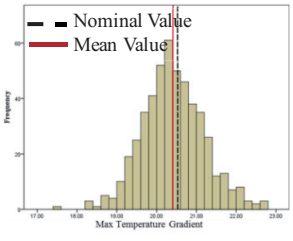


Fig. 4 Histogram of Max TG

Table 3. Statistics of Max T and Max TG

| Stochastic Output | Nominal | Mean | Std Deviation | Minimum | Maximum |
|---|---|---|---|---|---|
| Max T [K] | 689.6 | 689.9 | 12.54 | 651.2 | 729.8 |
| Max TG [K $mm^{-1}$] | 20.53 | 20.43 | 0.7736 | 17.59 | 22.70 |

### 4. Concluding Remarks

Through coupling non-intrusive polynomial chaos based probabilistic collocation method with conjugate heat transfer analysis, an uncertainty quantification method for heat transfer performance of high temperature blade was proposed. Latin Hypercube Sampling was carried out on the PC expansion to calculate probability of failure and reliability. UQ was carried out on Mark II, considering four uncertain operating conditions parameters. Input uncertainties can result in an increase of 40.2 K in maximum temperature of blade, and a raise of 2.17 K $mm^{-1}$ in maximum temperature gradient of blade. The reliability in term of Max T and Max TG is 94.6% and 96.9%, respectively. The uncertain parameter with the greatest effect on heat transfer performance and blade life is total temperature of mainstream inlet.

### References


[1] W. Yao, X.Q. Chen. W.C. Luo, M. Tooren. *Progress in Aerospace Sciences*, 47 (6) (2011) 450-479.

[2] Walters, R. W., Huyse, L. *NASA CR* 2002-211449, (2002).

[3] Ronald S. Bunker. *ASME Journal of Turbomachinery*, 131 (4) (2009) 041018.

[4] Xiu, D. and Karniadakis, G. M. *SIAM J. Sci. Comput.*, Vol.24, No.2, (2002) 619-644.

[5] M. Eldred. *50th AIAA/ASME/ASCE/AHS/ASC Structures, Structural Dynamics, and Materials Conference*, (2009).

[6] L. Hylton, M. Mihelc. *NASA CR 168015*, (1983).

Eleventh International Conference on Flow Dynamics
October 8-10, 2014, Sendai, Miyagi, Japan

# Effect of Pressure on Adsorption/Desorption of Zeolite 4A

Yu-Cheng Chu[1], Ling-Chia Weng[2], Pen-Chang Tseng[2], Neng-Chieh Chang[1], Chi-Chuan Wang[1]
[1] National Chiao Tung University,
Daxue Rd, Hsinchu, 30010, Taiwan
[2]Industrial Technology Research Institute,
Zhongxing, Zhudong 31053, Taiwan

**ABSTRACT**

This study focuses on the heat and mass transfer performance of the dehumidification system under periodic change of environmental pressure. Based on some available literatures, high environmental pressure enhance the performance of absorption, but prolong the time of desorption regeneration. Hence, for a better performance, the concept of adsorption in high environmental pressure, and desorption in atmospheric pressure is numerically investigated. The present study examines the relevant parameters of changing environmental pressure to optimize the performance of this system.

## 1. Introduction

Since the invention of the "heatless dryer", there has been significant process in the design and modeling of air drying based on pressure swing adsorption (PSA). Based on some literatures, a high environmental pressure enhance the performance of absorption dehumidification, but prolong the time of desorption regeneration. In this study, we try to optimize the performance of the system in this study. Some related references in connection with the present numerical modeling is described as follows.

Pesaran & Mills [1] investigated the diffusion mechanism of silica gel particles, then proposed a model for heat and mass transfer in packed bed of desiccant particles. Gorbach et al. [2], Hughes et al. [3], Kwapinski & Tsotas [4] compared the result of experiment and simulation and developed an empirical correlation for formulation of the model of desiccant. In this study, we employ a 2-D model to examine the relevant parameters of changing environmental pressure, this is because Sphaier & Worek [5, 6] had shown that there are some difference between 1-D and 2-D model.

In this study, the most important part is operating pressure. According to the study of Golubovic & Worek [7]. Generally, a high environmental pressure promotes the performance of adsorption and a low environmental pressure is favorable during desorption. Hence, a numerical study is performed with adsorption in high environmental pressure, and desorption in atmospheric environmental pressure. The effect of periodic changing of environmental pressure to optimize the performance of this system is further investigated.

## 2. Method

In order to realize how the changing environmental pressure affect the performance of the dehumidification system, we construct a desiccant micro channel model which use zeolite 4A as the desiccant. In this study, a commercially available simulation package (COMSOL4.0) had been use. The simulation models contain different physics, such as free and porous medium flow, fluid in porous media and heat transfer

Corresponding author: Chi-Chuan Wang
*E-mail address*: ccwang@mail.nctu.edu.tw

The geometry of the micro channel is shown in the Fig.1, and it is a single channel system.


Fig. 1 Schematic of the modeling

Fig.1 is a 2-D schematic diagram of the model use in this paper. The corresponding size for simulation is:
Channel length is 0.3m
Channel width is 0.1m
Air side height is 0.005m
Desiccant height is 0.0007m.

To build such a model, we have to define characteristics and properties of zeolite 4A. The characteristics is tabulated in Table 1.

Table 1. Properties of zeolite 4A

| | |
|---|---|
| Density | 777 kg/m$^3$ |
| Particle diameter | 0.0005m |
| Specific heat capacity | 910kJ/kg |
| Porosity | 0.30 |

For other physical properties of zeolite 4A such as diffusivity for desiccant particles with different diameter is shown in [4]. During desorption process, desiccant temperature will increase, hence concerns about how desiccant temperature affecting diffusivity must be taken into account. From [4], Kwapinski & Tsotas also derived the associated correlation about this effect and its correlation is used in the present modeling.

Kwapinski & Tsotas [4] had presented the water vapor isotherms on zeolite 4A. Their experimental data is taken and fitted to arrive an empirical formula of relative humidity in desiccant ($\varphi$), which can be relate to temperature ($T_d$) and desiccant loading (X).

With relative humidity, we can define Water vapor partial pressure ($P_w$) in desiccant too. With water vapor partial pressure, we can derive the air mixing ratio on the interface between desiccant and air. Also, we can define concentration different between air and desiccant.

## 3. Results and Discussion

In this section, we first explain operating conditions, then show the data.

With the present model, we first compare the adsorption/de-sorption performance in different pressures. In this paper, a high pressure is 7.5 atm. The inlet velocity of air in atmospheric pressure is 0.1667 m/s, and in high pressure is 0.0223 m/s, because the inlet air flow should be the same during comparison.

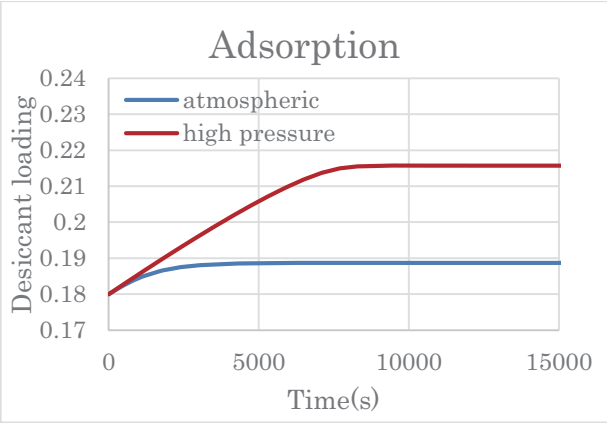


Fig. 2 this figure shows that zeolite 4a could have better adsorption performance in high pressure.

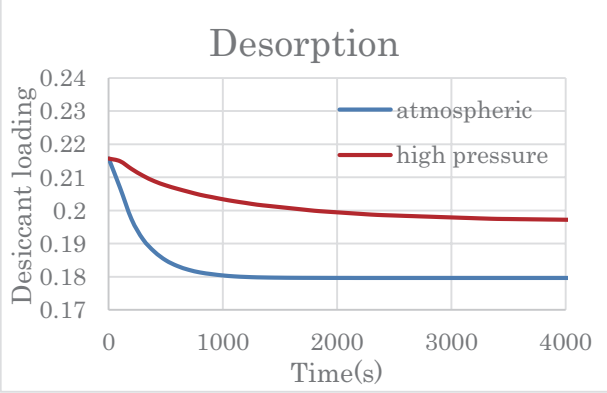


Fig.3 this figure shows that zeolite 4a could have better desorption performance in high pressure. The regeneration heat is 100W/m$^2$ on each desiccant side.

As shown in Fig. 2 and Fig. 3, a better operation is made available in a high pressure adsorption and an atmospheric pressure desorption. To combine these two part, we had defined a time to turn to desorption from adsorption. In drying industry, the dew point temperature of the outlet air is an important part to characterize the performance of a system, hence a dew point temperature of -30 °C is regarded as the turning point. If the dew point temperature of the outlet air is higher than -30 °C, the system will turn to desorption. In this case, the time required to reach the turning point is 6800 s.

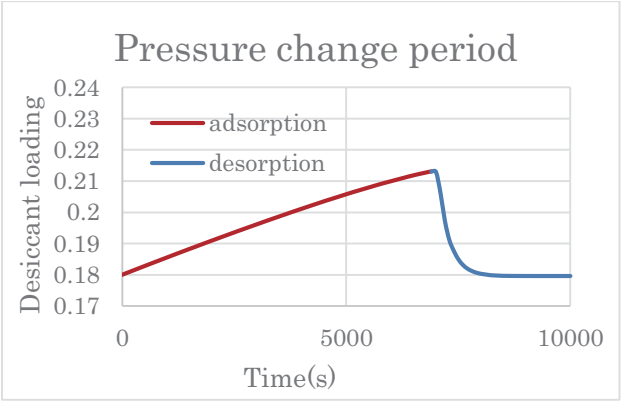


Fig.4 this figure show a period of high pressure adsorption and atmospheric desorption. The turning point is 6800s. There are 200s for changing pressure after the turning point.

Result of Fig.4 shows that it is possible to define an optimized operating condition for each case of desiccant channel by PSA, and the most important part is to defined an appropriate turning point such as Fig.4 shows.

## 4. Concluding Remarks

This study is focus on how the changing environmental pressure affect the performance of the dehumidification system. It is found that a high pressure adsorption can enhance the performance of this system. Conversely, a low pressure de-sorption can assist the system performance. The related time to reach the turning point is about 6800 s.

## References


[1] A.A. Pesaran, A.F. Mills, *Int. J. of Heat and Mass transfer*, 30 (6) (1987) 1037-1049.

[2] A. Gorbach, M.Stegmaier & G. Eigenberger, *adsorption*, 10(1) (2004) 29–46.

[3] P.D.M. Hughes, P.J. McDonald, N.P. Rhodes, J.W. Rockliffe, E.G. Smith and J. Wills, *Phys. Rev.*, 51 (1995) 11332.

[4] W. Kwapinski, E. Tsotsas, *Chem. Eng. Technol.*, 27 (2004) 681–686.

[5] L.A. Sphaier, W.M. Worek, *Int. J. of Heat and Mass transfer*, 47(2004) 3415-3430.

[6] L.A. Sphaier, W.M. Worek, *Numerical Heat Transfer*, Part B, 49(2006) 223-237.

[7] M.N. Golubovic, W.M. Worek, *Numerical Heat Transfer*, part A 45 (2004) 869-886.

Eleventh International Conference on Flow Dynamics
October 8-10, 2014, Sendai, Miyagi, Japan

# Numerical Study of Pressure Drop Influenced by Pitch Length Inside Multiple Thread Spiral-Grooved Tube

Gao Xiao-fei, Qian Jin-yuan, Jin Zhi-jiang, Liu Bu-zhan
Institute of Process Equipment, Zhejiang University
Zheda Street 38, Hangzhou, 310027, China

**ABSTRACT**

Coaxial heat exchanger is a highly efficient heat exchanger, and its core component is the spiral-grooved tube. The tube side study shows that the multiple thread spiral-grooved tube has an increasing pressure drop of the tube side compared with the smooth round tube. In the present study, pressure drop performances inside multiple thread spiral-grooved tube have been studied numerically with a high Reynolds number. The result reveals that there is the mixing flow result from the influence of centrifugal force and the pressure drop increase with the decreasing pitch length P.

## 1. Introduction

Coaxial tube heat exchanger is a highly efficient heat exchanger, which is widely used in many regions, such as refrigeration, chemical engineering, medicine, etc. From the point of energy saving, it is very necessary to improve the efficiency of heat transfer of heat exchanger by using heat transfer enhancement techniques. The core components of the coaxial tube heat exchanger is spiral grooved tube, which caused great attention and widely study all over the world because of its good double-sided heat transfer. The spiral grooved tube studied by this paper is made from smooth copper tube through special technology. The spiral grooved tube studied by this paper has advantages of resistant to vibration, pressure fluctuation, thermal shock, etc, and it has self-cleaning ability. Although many scholars had studied lots of spiral grooved tubes, the model of this paper has not been studied in detail.

In this paper, pressure drop performance influenced by pitch length inside six thread multiple spiral grooved tube was studied numerically. 3D numerical simulation on single-phase convective heat transfer performance and turbulent flow characteristics in tube-side was researched based on Fluent 6.3.26 for spiral grooved tube. The tube-inside flow and heat transfer of six thread spiral grooved tube was simulated exactly.

## 2. Model and Numerical Simulation

### 2.1 Model and Operating Conditions

The internal structure of common coaxial spiral grooved tube heat exchanger is a spiral grooved tube jacketed with a smooth tube. The external view and sketch of the spiral grooved tube are shown in Fig.1. The geometric parameters of Analysis model in this paper are as follows: Inner diameter 30mm; On the purpose of getting the effects of P on pressure drop performances of the spiral grooved tube , screw pitch series size was selected five groups: 50mm, 60mm, 70mm, 80mm, 90mm, tube length 560mm. Operating conditions [1] is illustrated in Table 1.

### 2.2 Modeling Process

Since the structure of the spiral groove tubes is a bit of complex, it is difficult to model with preprocessing software Gambit, so model was built by UGS NX 7.0 which is a more powerful three-dimensional modeling software. Here, the model of spiral groove tube is shown in Fig. 2.

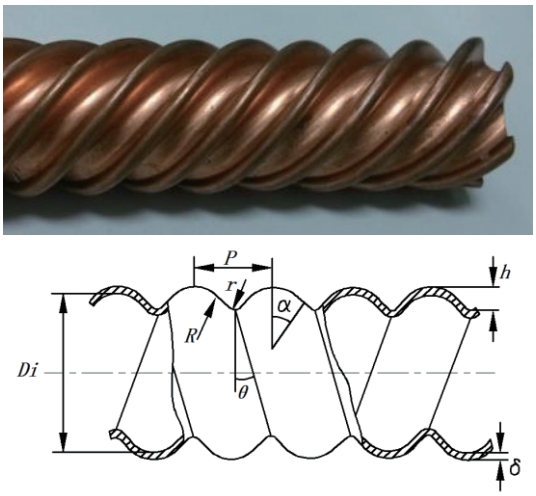


Fig. 1 The external view and sketch of six thread spiral grooved tube. [1]

Table 1. Operating conditions [1]

| Fluid | Velocity of inlet | Temperature of inlet | Temperature of wall |
|---|---|---|---|
| water | 1.5 m/s | 303 K | 313 K |

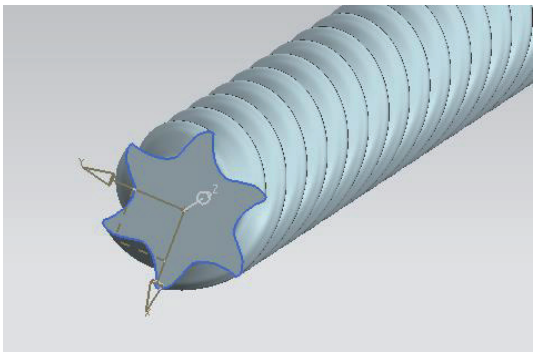

Fig. 2 The model of spiral grooved tube.

Corresponding author: Jin Zhi-jiang
*E-mail address*: jzj@zju.edu.cn

### 2.3 Numerical Simulation

The three-dimensional model of tubes drawn by Pro/Engineer was imported into Gambit to mesh grid. As the surface of spiral grooves tube is uneven and rough spiral shape, characteristics near the wall is rather complex, in order to capture the flow characteristics and heat transfer characteristics near wall region fluid of tubes more accurately, so mesh must be enough dense in the near wall region. Because the model is distorted, structured mesh is more difficult, so unstructured mesh was used to mesh. Through the net unrelated check, the number of grid was controlled in about 1.1 million.

In the simulation, the Realizable $k-\varepsilon$ model [2] was chosen. Boundary conditions are as follow:

The working medium is water in the tube, its properties was assumed to be constant, details are:

$\rho$ =998.2kg/m$^3$, $Cp$ =4182W • m$^{-1}$ • K$^{-1}$

$\mu = 1.003 \times 10^{-3}$Pa · s, $\lambda = 0.6$W/(m · k)

Inlet boundary condition:

$u_i = 0$, $v_i = 0$, $w_i = 1.5$m/s, $k_i$=constant ,

$\varepsilon_i$= constant. $T_i$ = 303K

Wall boundary condition:

$u_w = 0$, $v_w = 0$, $w_w = 0$, $T_w$ = 313K

Pressure outlet for export conditions, and outlet pressure are set to 0Pa; hydraulic diameter d is 20mm; Velocity of inlet was set to 1.5m / s, so the Reynolds number is 29886.29.

Standard k-ε model was used in this paper. During defining solver, pressure-based implicit, 3D, steady-state solver was chosen, so all the governing equations are solved with pressure-based coupled algorithm. Simple algorithm is employed to solve the flow and pressure equations. Convergence condition is defined that calculated residual value of mass is less than 1 × 10$^{-6}$, the residual value of the energy is less than 1 10$^{-7}$.

### 3. Results and Discussions

Length of spiral groove tube Model is 560mm, the middle 200mm of model was taken for analysis. First, the weighted average of import and export pressure was solved, and then pressure drop of import and export was obtained. The result is shown in Table 2.

As it can be seen from the simulation results, the multiple thread spiral-grooved tube has an increasing pressure drop of the tube side compared with the smooth round tube, and pressure drop of spiral grooved tube decreases gradually with the increasing P, indicating that the shorter pitch is, the greater the pressure drop are in the same conditions. As smaller pitch cause larger resistance to flow, selection of pumps, compressors and other power equipment must be taken into consideration in the design and installation of the unit.

In addition, the intermediate interface of model was cut out, and the pressure and the transverse velocity vector distribution are shown in Fig. 3. As shown in the figure, there is also a spiral motion in the same rotating direction of the spiral grooved tube except along the main direction of flow. As centrifugal effect caused by the spiral motion, pressure in the tube groove is greater than the pressure at the center of the tube.

Table 2. Influence of P on pressure drop performance.

| P/mm | 50 | 60 | 70 | 80 | 90 |
|---|---|---|---|---|---|
| Pressure drop/Pa | 1254 | 1007 | 841 | 721 | 632 |
| Pressure drop of 200mm smooth tube is 95 Pa | | | | | |

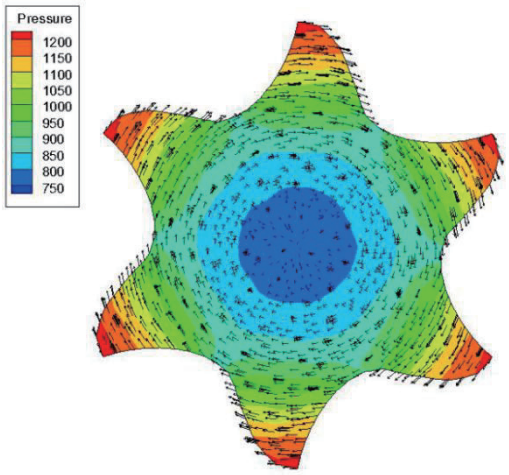


Fig. 3 Secondary flow and pressure distributions of the middle section of the model

### 4. Concluding Remarks

Spiral grooved tubes have many advantages in terms of heat transfer enhancement, as a result that it is widely used in coaxial tube heat exchanger. In this investigation, the relationship between flow resistance and pitch length of six thread spiral grooved tube has been studied, The effects of the pitch length on pressure drop performance of the spiral grooved tube is analyzed. The numerical results show that pressure drop reduces with the increasing pitch length. The emergence of spiral in the spiral grooved tubes causes secondary flow, and this secondary flow changes the velocity and temperature distributions in the spiral grooved tubes. With the development of computer technology and computational methods, it will bring a lot of convenience for research related to the spiral grooved tubes to combine numerical simulation with experiment combined.

### Acknowledgements

This work is supported by the National Natural Science Foundation of China (NSFC) through Grant No.51175454, the Science and Technology Department of Zhejiang Province through Grant No.2012C11018-1 and No. 2012C11002, and China Scholarship Council.

### References

[1] J.Z. Shi, K.K. Zhao, J.W. Bai, *Refrigeration and Air-conditioning*, 11(4) (2009, 8) 116-120.

[2] T.H. Shih, W.W. Liou, A. Shabbir, Z.G. Yang, J. Zhu, A new $k-\varepsilon$ eddy viscosity model for high Reynolds number turbulent flows, *Computers & Fluids* 24 (3) (1995)227–238.

Eleventh International Conference on Flow Dynamics
October 8-10, 2014, Sendai, Miyagi, Japan

# Simulation of Droplet Resting on Micro-structured Surface by Lattice Boltzmann Method

Yu-Tang Ju, Yi-Ting Lin, Tzu-Chun Huang, Chao-An Lin
Department of Power Mechanical Engineering
National Tsing Hua University, Hsinchu 30013, Taiwan

The steady-state interface profile of a liquid droplet resting on micro-structured pillar surface is simulated with lattice Boltzmann method incorporating the Cahn-Hilliard equation. Two Simulations are conducted with the same area fractions but with different pillar heights, i.e. surface roughness at Cassie state. Three different boundary implementation strategies focusing on edges and corners are explored to find out the most correct way for dealing with the boundary conditions with pillars.

## 1. Introduction

Considerable success in simulating hydrodynamic problems has been achieved using Lattice Boltzmann method (LBM) [1]. Here, a three-dimensional LBM methodology [2] is adopted to simulate liquid droplet resting on micro-structures surface at different roughness. This is based on the high density model of Zheng et al. [3] combined with partial wetting boundary method proposed by Briant et al. [4]. Water droplet rests on hydrophobic surfaces exhibits a high contact angle, and surface hydrophobicity can be further enhanced by the presence of surface roughness, which can be created by micro geometric structure on surface. The simulated contact angles are contrasted with the theoretical predictions and experimental results [5] to examine its capability.

Further, different implementation of boundary conditions will be investigated to obtain the most appropriate way by contrast with the experiment results under the same situation.

## 2. Method

To describe the binary fluids and the interface between them, the free energy function is chosen as [6]

$$\Phi = \int \left\{ \psi(\phi) + \frac{\kappa}{2}(\nabla\phi)^2 + \frac{n \ln n}{3} \right\} dV \qquad (1)$$

where $n=(\rho_H+\rho_L)/2$, and $\kappa$ is a coefficient which is related to the surface tension ($\sigma$) and the thickness of the interface layer (W). $\rho_H$ and $\rho_L$ mean the high and low density fluids, respectively. The bulk free energy density $\psi(\varphi)$ is chosen as a double-well form [6],

$$\psi(\phi)=A\left(\phi^2-\phi^{*2}\right)^2 \qquad (2)$$

where $\phi^*=(\rho_H-\rho_L)/2$, and A is an amplitude parameter to control the energy between the two phases.

Thus, the chemical potential $\mu_\varphi$ depending on the free energy function can be derived as

$$\mu_\phi=\frac{\partial\Phi}{\partial\phi}=\frac{\partial\psi}{\partial\phi}-\kappa\nabla^2\phi \qquad (3)$$

Also, the $\sigma$ and W are related to the A and $\kappa$ i.e. $A=3\sigma/(4W\varphi^{*4})$ and $\kappa = 3W\sigma/(8\varphi^{*2})$.

The Cahn-Hilliard equation is used to capture the interface of binary fluid, where $\theta_M$ is mobility.

$$\frac{\partial\phi}{\partial t}+\nabla\cdot(\phi u)=\theta_M\nabla^2\mu_\phi \qquad (4)$$

Corresponding author: Chao-An Lin
*E-mail address*: calin@pme.nthu.edu.tw

To Solve the multiphase fluid flow, $f_i$ and $g_i$, are introduced in the Lattice Boltzmann equations [2],[7]

$$f_i(\vec{x}+\vec{e}_i\Delta t,t+\Delta t)-f_i(\vec{x},t)=\frac{-1}{\tau_n}\left[f_i(\vec{x}t)-f_i^{e9-}(\vec{x},t)\right]+F_i^f \qquad (5)$$

$$g_i(\vec{x}+\vec{e}_i\Delta t,t+\Delta t)-g_i(\vec{x},t)$$
$$=\frac{-1}{\tau_\phi}\left[g_i(\vec{x},t)-g_i^{eq}(\vec{x},t)\right]+(1-q)\left[g_i(\vec{x}+\vec{e}_i\Delta t,t)-g_i(\vec{x},t)\right] \qquad (6)$$

and $F_i^f$ is defined as in [8], i.e.,

$$F_i^f=\left(1-\frac{1}{2\tau_n}\right)\frac{\omega_i}{c_s^2}\left[(\vec{e}_i-\vec{u})+\frac{\vec{e}_i\cdot\vec{u}}{c_s^2}\vec{e}_i\right]\cdot\left(\mu_\phi\nabla\phi+\vec{F_b}\right)\Delta t \qquad (7)$$

where $f_i$ and $g_i$ are used to calculate the velocity $\boldsymbol{u}$ and the $\phi$. The relaxation time $\tau_n$ is related to viscosity and the constant $q = 1/(\tau_n + 0.5)$ [2] in eq. (6) [7] allows to control the propagation rate between neighboring sites.

The distribution functions satisfy the conservation laws as,

$$n=\sum_i f_i \ , \ n\vec{u}=\sum_i f_i\vec{e}_i+\frac{\Delta t}{2}\left(\mu_\phi\nabla\phi+\vec{F_b}\right), \ \phi=\sum_i g_i \qquad (8)$$

By minimizing the surface free energy [1], the contact angle can be related to the gradient of the surface order parameter, i.e.,

$$\cos\theta_w=\frac{(1+\tilde{\omega})^{\frac{3}{2}}-(1-\tilde{\omega})^{\frac{3}{2}}}{2} \qquad (9)$$

where $\tilde{\omega}=\omega/(\sqrt{2\kappa}A\ (\phi^{*}\ )^2\ )$ , and

$$-\omega-\kappa\left(\frac{d\phi}{dz}\right)_{wall}=0 \qquad (10)$$

where $\omega=-\frac{d\Phi}{d\phi_{wall}}$ , and $\left(\frac{d\Phi}{dz}\right)_{wall}=\lim_{z\to 0}\frac{d\Phi}{dz}$

Therefore, the above equation can be used to deal with the gradient of the order parameter in the equilibrium distribution function as suggested by Briant et al. [1]

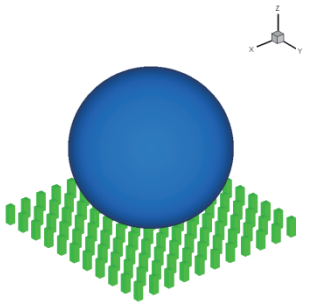

Fig. 1 Droplet on pillar structured surface

## 3. Results and Discussion

Simulations of a liquid droplet are presented. The predicted contact angles are contrasted with measurements [5] and theoretical results based on Cassie-Baxter theory [9]. The geometry of the pillar

structure is shown in Figure. 1, where the pillar is regularly spaced. The surface roughness (r) and area fraction (f) are defined as,

$r=\frac{4ah+(a+b)^2}{(a+b)^2}$, $f=\frac{a^2}{(a+b)^2}$

which describes the fraction of actual area of rough surface and the geometric projected area. a, b, and h are pillar width, spacing, and height, respectively.

The settings of two simulations are shown in Table 1, where D =Da+b and Bo=Δ σ. flat contact angle θw is 114◦. Area fractions for cases 1 and 2 are the same, and they differ only on their pillar heights.

In the simulations, the lattice size adopted is 170 × 170 × 180. No-slip boundary conditions are applied at top and bottom boundaries, and periodic boundary conditions are applied at the other four boundaries. Other simulations parameters are: droplet radius (R = 62 lattice units), surface tension (σ = 0.1), interface width (W = 6 lattice units), mobility coefficient (Γ = 3000). Also, the pillar heights in cases 1 and 2 are respectively at 15 and 28 lattice units.

Table 1. The parameters of experiment and simulation

| | Exp 1 | SL 1 | Exp 2 | SL 2 |
|---|---|---|---|---|
| a-b -h | 50-100-150 μm | 5-10-15 unit | 50-100-282 μm | 50-10-28 μm |
| D | 0.00124 m | 124 unit | 0.00124 m | 0.00124 m |
| f | 0.111 | 0.111 | 0.1111 | 0.1111 |
| r | 2.32 | 2.32 | 3.51 | 3.51 |
| Bo | 0.2069 | 0.2069 | 0.2069 | 0.2069 |
| D | 8.27 | 8.27 | 8.27 | 8.27 |

Dealing with the wall grid, the gradient of order parameter ( $\nabla\phi$ ) within the forcing term and the Lapacian of order parameter ($\nabla^2\phi$), which represents the seperation force in two phase fluid flow, should be treated carefully. By using central,backward,and forward difference, we made three different strategies (BC1,BC2, BC3, respectively) as shown in Fig. 2.

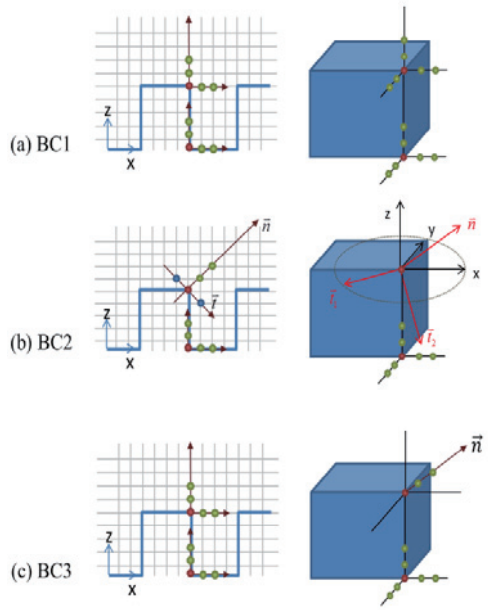


Fig. 2 The selected points in different treatments.

The results of three different treatments on edges and corners are shown in Fig. 3. We can see that BC2 is the most correct way for dealing with the boundary conditions with pillars..

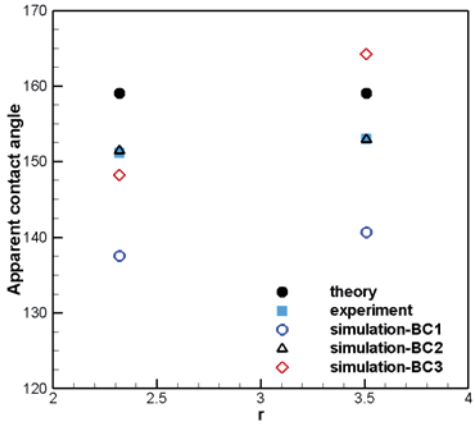


Fig. 3 Comparsion of Cassie and Baxter model experiment, and simulation.

## 4. Concluding Remarks

According to the Cassie-Baxter model [9], the apparent contact angle is at $\theta_{CB}$ =159◦. This is somewhat higher than the measurements, which are around 151 to 153◦ for r=2.32 and 3.51. Predictions, however, show much lower apparent contact angles and the deviations are around 15◦. This might be due to the inadequate treatment of wetting boundary condition of the pillar surface, and this is deserved to be further studied.

For our simulations of three treatments, it is observed that the simulation results using BC2 is well consistent with the experimental values rather than other two boundary treatments.

## References


[1] S. Chen, G.D. Doolen, *Annular review of fluid mechanics,* 30 (1998) 329-364.

[2] C.H. Shih, C.L. Wu, L.C. Chang, C.A. Lin, *Philos. Trans. R. Soc. A-Math. Phys. Eng. Sci,* 369 (2011) 2510-2518.

[3] H.W. Zheng, C. Shu, Y.T. Chew, *J. Comput. Phys.* 218 (2006) 353-371.

[4] A.J. Briant, P. Papatzacos, J.M. Yeomans, Phil. *Trans. Roy. Soc.A,* 360 (2002) 485-495.

[5] Z. Yoshimitsu, A. Nakajima, T. Watanabe, K. Hashimoto, Effects of Surface Structure on the Hydrophobicity and Sliding Behavior of Water Droplets, Langmuir 18 (2002) 5818-5822.

[6] D. Jacqmin, *J. Comput. Phys.* 155 (1999) 96-127.

[7] A. Lamura, S. Succi, *Int. J. Mod. Phys.*17 (2003) 145-148.

[8] Z.L. Guo, C.G. Zheng, B.C. Shi, *Phys. Rev. E,* 65 (2002) 046308.

[9] A.B.D. Cassie, S. Baxter, *Trans. Faraday Soc.* 40 (1944) 546-551.

Eleventh International Conference on Flow Dynamics
October 8-10, 2014, Sendai, Miyagi, Japan

# Numerical Simulations of the Immersed Boundary Formulation with a Parallel Iterative Solver for Flow with Moving Boundary

Wen-Wei Hsiao, Ting-Yu Lin, Chuan-Chieh Liao and Chao-An Lin
Department of Power Mechanical Engineering,
National Tsing Hua University, Hsinchu 30013, Taiwan

**ABSTRACT**

The immersed-boundary technique is adopted to simulate viscous incompressible flows interacting with moving solid boundaries. 2-D and 3-D test problems are simulated to examine the validity of the present immersed-boundary technique. In addition, two spheres sedimenting in a closed container filled with a viscous fluid are investigated. The above implementations are constructed on the parallel software PETSc.

## 1. Introduction

Immersed boundary methods were developed in 1972 by Peskin [1], where by using an external force field, the complex geometry within the Cartesian grid can be mimicked. In general, IBMs are categorized into feedback forcing and direct forcing approaches. The disadvantage of feedback forcing is the potential of smearing across the interface. For sharper interface, direct forcing is preferred. Mohd-Yusof [2] proposed a direct forcing method that introduces a body-force f, such that the desired velocity distribution is obtained at the boundary without adopting the Lagrangian markers. Fadlun et al. [3] further extended the Mohd-Yusof's approach by employing the direct forcing along the first Eulerian grid. Tseng and Ferziger [4] extended the idea of Fadlum et al. via a ghost cell approach. Liao et al. [5] adopted solid body forcing to eliminate the oscillating phenomenon due to the movement of embedded object.

The present study is an extension of Liao et al. [5] by simulating multiple moving objects and the parallel implementation is built on PETSc.

## 2. Method

The influence of the immersed boundary on the fluid is represented by forces exerted on the fluid and thus causing it to move under the influence of boundary motion. The prescribed velocity via the no-slip condition thus can predict and compute the fluid velocity around the immersed boundary in this domain. Considering the mass and momentum conservation, we have the following governing equations:

$$\nabla \cdot \mathbf{u} = 0 \tag{1}$$

$$\frac{\partial \mathbf{u}}{\partial t} + \nabla \cdot (\mathbf{uu}) = -\nabla p + \frac{1}{\mathrm{Re}} \Delta \mathbf{u} + \mathbf{f_M} \tag{2}$$

Note that the momentum forcing term $f_M(x, t)$ is applied to satisfy the no-slip condition on the immersed boundaries, as in [5].

Spatial derivatives are approximated using second-order central differencing, and a fractional-step (projection) method implemented with a combination of Adams-Bashforth and Crank-Nicholson methods for advective and diffusive terms, respectively, are used for temporal discretization.

The forcing must be determined in advance to satisfy the no-slip boundary condition on any immersed boundary at the advanced time level. This force is used to calculate the acceleration of any node nearby the immersed boundary of the solid body. Thus,

$$\mathbf{f^{n+1}} = \frac{\mathbf{u_F} - \hat{\mathbf{u}}}{\mathbf{\Delta t}} \tag{3}$$

where $\hat{u}$ is estimated with a simple, explicit Adams-Bashforth scheme where Eq. (2) is provisionally discretized explicitly in time and $\mathbf{u_F}$ is the velocity ( at the same location), when forcing is taken into account.

For the u velocity component at the point $\mathbf{x_F}$, with analogous computations used for other velocity components. Hence, we get the forcing point $\mathbf{x_F}$ and a direct forcing calculations of $\mathbf{f^{n+1}}$:

$$\mathbf{f^{n+1}} = \frac{\mathbf{u_F} - \mathbf{u^n}}{\Delta t} + \frac{3}{2}[\nabla_h \cdot (\mathbf{uu}) - \frac{1}{\mathrm{Re}} \Delta_h \mathbf{u}]^n - \frac{1}{2}[\nabla_h \cdot (\mathbf{uu}) - \frac{1}{\mathrm{Re}} \Delta_h \mathbf{u}]^{n-1} + \nabla_h p^n \tag{4}$$

The solid-body-forcing strategy is imposed within the solid region through the solid-body force calculated as:

$$\mathbf{f^{n+1}} = \frac{\mathbf{Umove} - \hat{\mathbf{u}}}{\mathbf{\Delta t}} \chi(\mathbf{x^{n+1}}) \tag{5}$$

where $\mathbf{U_{move}}$ represents the velocity of the moving object. It is clear that within the solid region $\mathbf{u_F} = \mathbf{U_{mov}}$. The parameter $\chi$ is merely a characteristic function for points of the solid, defined in the usual way as :

$$\chi(x^{n+1}) = \begin{cases} 1, & x^{n+1} \in \textit{solid region} \\ 0, & \textit{otherwise} \end{cases} \tag{6}$$

In the sedimentation problem, the collisions between particles are unavoidable. We use the collision model of Glowinski et al.[6].

## 3. Results and Discussion

The order of accuracy of the present technique is first scrutinized by computing two dimensional decaying vortex [7], where analytic solutions are available for comparisons. The grid arrangement was set to (10×10×6), (20×20×6), (40×40×6). The present numerical scheme was shown to be 2nd order convergence for both $l_2$ and $l_\infty$ norms.

Computations are further applied to flow within a circular cylinder that is placed asymmetrically inside a

Corresponding author: Chao An Lin
*E-mail address*: calin@pme.nthu.edu.tw

channel as reported by Schafer and Turek [8]. At Re=100, the flow becomes unsteady, and a periodic vortex shedding is observed. The predicted values of drag and lift coefficients and Strouhl number, i.e., $C_{D,max}$, $C_{L,max}$ and S,t at Re = 100 are summarized in Table 1. The oredictions show compatible results with the benchmark solutions of Schafer and Turek [8].

Table 1. Values of $C_{D,max}$, $C_{L,max}$ and St for 2-D flow over a cylinder asymmetrically placed in a channel with Re = 100.

| | $C_{D,max}$ | $C_{L,max}$ | $St$ |
|---|---|---|---|
| Schafer and Turek [39] | 3.22-3.24 | 0.99-1.01 | 0.295-0.305 |
| Present | 3.249 | 0.952 | 0.302 |

The technique is further applied to simulate flow of the in-line oscillating cylinder within a static fluid, as experimented using LDA by Dutsch et al. [9]. Fig. 1 shows the predicted axial and transverse velocity at four cross section, when the oscillating reaches the center of the channel at phase angle 180°. The presence of the cylinder can be clearly observed form the velocity distribution at x=0, where a solid body motion is observed in the cylinder, showing a constant positive velocity at this phase angle. Good agreements with the measurements are obtained, as shown in Fig. 1.

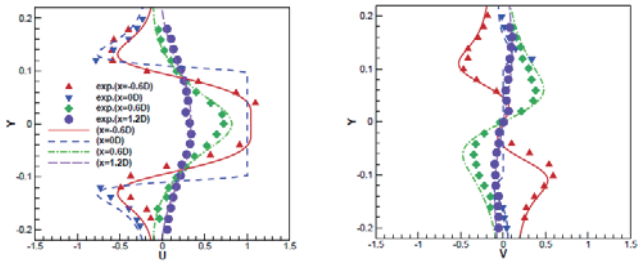


Fig. 1 Comparison of velocity profiles at four cross sections

Finally, two spheres sedimenting under gravity in a stagnant enclosure was studied, as shown in Fig. 2. It was found that when the sphere approaching a fixed wall, the repulsive forces will occur due to the squeezing motion of the fluid near the wall. At the same time, the gap becomes so small that cannot be resolved by the numerical grids, which produces over-accelerated flow near the bottom wall. This can be partly alleviated by introducing the lubrication force.

Since the sphere will collide with each other, so the collision force as proposed by Glowinski et al. [10] must be taken into account to prevent the two spheres from penetrating into each other. This is achieved through the prescription of collision free safe zone. The instantaneous vortical structures for two spheres sedimenting in the container are shown in Fig. 2, where the **drafting-kissing-tumbling** phenomenon can be clearly observed.

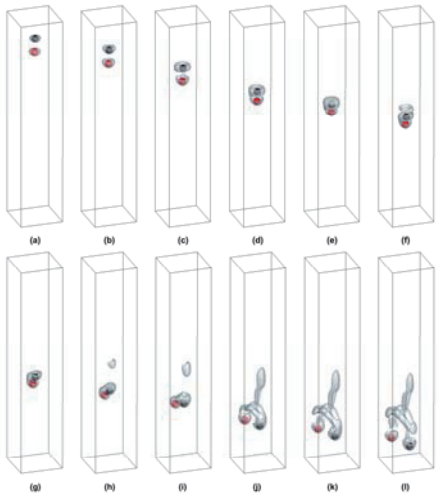

Fig. 2 Instantaneous vortical structures at different instants for two spheres sedimenting in a closed container.

## 4. Concluding Remarks

The accuracy of numerical scheme is first examined by decaying vortex case, where the analytical solution is available. The results of decaying vortex test indicate second-order accuracy of our implementation with respect to the $l_2$ norm and $l_\infty$ norm. Several test problems are also used to examine the validity of the present technique, namely 2-D flows over an asymmetrically-placed cylinder and in-line oscillating cylinder in fluid at rest. Finally, two spheres sedimenting under gravity in a stagnant enclosure was studied, where the drafting-kissing-tumbling phenomenon can be clearly observed from the simulation results. In general, all computed results are in good agreement with previous measurements and benchmark solutions, which indicate the capability of the present implementation to simulate flows with embedded moving objects.

## References


[1] C.S. Peskin, *J. Comp. Phys.*, (1972) 10:252.
[2] J. Mohd-Yusof, *NASA Ames/Stanford University*, (1997).
[3] E.A. Fadlum, R. Verzicco, P. Orlandi, J. Mohd-Yusof, *J. Comp. Phys.*, (2000) 161:30.
[4] Y.H. Tseng, J.H. Ferziger. *J. Comp. Phys.*, (2003) 192:593.
[5] C.C. Liao, Y.W. Chang, C.A. Lin , J.M. McDonough, *Computers & Fluids*, (2010) 39:152.
[6] R. Glowinski, T.W. Pan, T.I. Hesla, D.D. Joseph, J. Periaux, *J. Comp. Phys.*, (2001) 169:363.
[7] C.E. Pearson, *Sudbury (MA): Sperry Rand Reasearch Center*, (1964).
[8] M. Schafer, S. Turek, *Numerical Fluid Mechanics*, (1996) 52:547.
[9] H. Dutsch, F. Durst, S. Becker, H. Lienhart, *J. Fluid Mech.*, (1998) 360:249.
[10] R. Glowinski, T.W. Pan, T.I. Hesla, D.D. Joseph, J. Periaux, *J. Comp. Phys.*, (2001) 169:363.

Eleventh International Conference on Flow Dynamics
October 8-10, 2014, Sendai, Miyagi, Japan

# Numerical Simulation of Natural Convection in Vertical Parallel Plates at High Aspect Ratios

Tzu-En Peng, Shang-Hao Huang, Wu-Shung Fu
EE306, Department of Mechanical Engineering, National Chiao Tung University
1001 Ta Hsueh Road, Hsinchu, Taiwan

**ABSTRACT**

Natural convection between vertical parallel plates with asymmetric heating is numerically investigated in this research. Non-reflecting boundary condition is used at the inlet and outlet to consider the physical model as an infinite long channel. The results show the phenomena of the secondary flow and the mass flow rate of the inlet reversed flow, and the Nusselt number is affected by changing the aspect ratio. As the aspect ratio increases, the mass flow rate of the inlet reversed flow increases.

## 1. Introduction

Natural convection heat transfer between vertical parallel plates with asymmetric heating is a very important subject in both academic and industrial research. In practical applications, this subject can be observed in many thermal apparatuses, such as the solar panel, the liquid crystal growth chamber and the chimney. A low-speed compressible fluid flow is taken into consideration instead of Boussinesq assumption in high temperature difference [1]. In those past studies, the effect of distance between vertical parallel plates is very important and the phenomena of natural convection varying from a steady to an unsteady situation in a heating process are hardly studied. Therefore, the aim of this study is to investigate the natural convection between vertical parallel plates in different aspect ratios with asymmetric heating numerically.

## 2. Physical Model

A physical model of two dimensional vertical parallel plates is indicated in Fig. 1. The length and width are *b* and *w*, respectively. The gravity is downward and the temperature and pressure of the surroundings are $T_0(298K)$ and $P_0(101300Pa)$, respectively. The temperature of the heated surface is $T_h(400K)$, and the other regions are adiabatic.

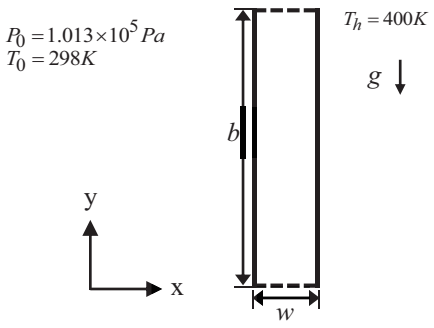


Fig. 1 Physical model

## 3. Numerical Method

For the investigation of the heat transfer with high temperature difference, the numerical method of compressible flow without Boussinesq assumption is considered. The governing equations of a compressible flow can be divided into two parts. One is the inviscid term and the other is the viscous term. The Roe scheme with $3^{rd}$ order MUSCL proposed by Abalakin et al. [2] is used to compute the inviscid terms. The method of dual time stepping is added to calculate the transient state. A second order central difference method is adopted to calculate the magnitudes of the viscous terms. Finally, the LUSGS was modified by [3] to suitable for preconditioning in solving temporal term. The non-reflecting boundary conditions are used at the apertures of the vertical parallel plates in order to avoid a low speed compressible flow to be polluted by the reflections of acoustic waves. Both sides of the width are periodic conditions.

The governing equations can be obtained as follows.

$$\Gamma\frac{\partial U_p}{\partial \tau}+\frac{\partial U}{\partial t}+\frac{\partial F}{\partial x}+\frac{\partial G}{\partial y}+\frac{\partial H}{\partial z}=S \quad (1)$$

Where $\tau$ is the artificial time, *t* is the physical time. $\Gamma$ is a preconditioning matrix proposed by Weiss and Smith[4]. *U*, *F*, *G*, *H* and *S* are defined in [5].

## 4. Results and Discussion

In Fig. 2, thermal fields and streamlines are under $Ra = 2.26\times10^6$ and $Ra = 6.69\times10^5$ situations. In the thermal field, the heated fluids with lighter density exerted by the buoyancy force ascend to the aperture. Then ascending fluids along the heated wall continuously accumulate and start to form rotation behaviors. In the flow field, the secondary flow from the outlet forms circles structure with three main recirculation cells. The flow field of the top half region begins to swing unsteadily. Between these two different aspect ratios, in the higher aspect ratio case, there are more disturbances in both thermal field and streamlines.

Corresponding author: Tzu-En Peng
*E-mail address*: patrick7659.me02g@nctu.edu.tw

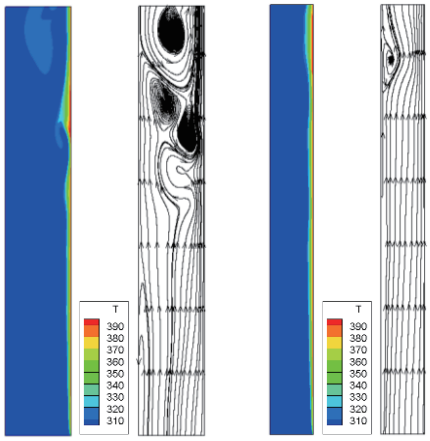


Fig. 2 Thermal fields and streamlines under $Ra = 2.26\times10^6$ (left) and $Ra = 6.69\times10^5$ (right) at *t=7.9s*.

In Fig. 3, thermal field and streamlines are under $Ra = 5.35\times10^6$ situation. Due to the high aspect ratio of the model, the buoyancy force is not large enough to drag up the fluids which away from the heated side. At the inlet of the physical model, the fluids flows out of the physical model.

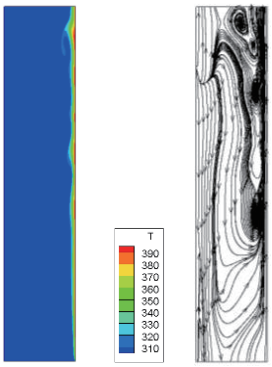


Fig. 3 Thermal field and streamlines under $Ra = 5.35\times10^6$ at *t=7.9s*

In Fig. 4, it shows the amounts of mass flow rate flows out of the inlet in different Rayleigh numbers cases. It can be easily observed that higher Rayleigh number is, the more mass flow rate flows out of the inlet of the physical model.

In Fig. 5, the distributions of variations of area average Nusselt numbers with time under different Rayleigh numbers are shown. For the case of $Ra = 6.69\times10^5$, the average Nusselt numbers fluctuates within *t=2s*, and then stabilizes after *t=4s*. But for the case of $Ra = 5.35\times10^6$, the average Nusselt numbers oscillate and never become a steady state.

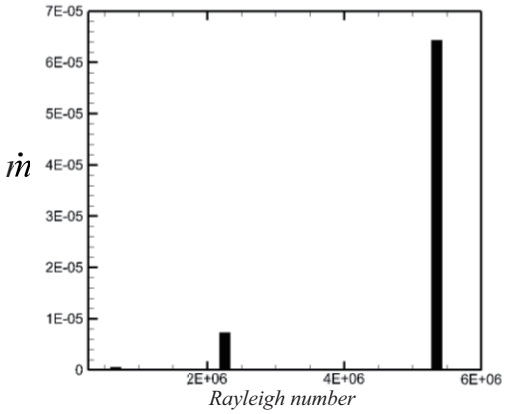


Fig. 4 Amounts of mass flow rate with different Rayleigh numbers.

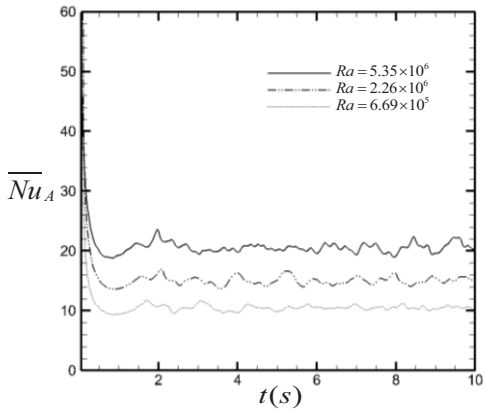


Fig. 5 Distributions of variations of area average Nusselt numbers with time under different Rayleigh numbers.

## 5. Concluding Remarks

The main conclusions are summarized as follows.

1. Higher aspect ratio case causes more unsteadiness, and the area average Nusselt number is large which indicates a better heat transfer situation.
2. There are more secondary flow and reversed flow in the high aspect case.

## References

[1] D.D. Gray, A. Giorigini, *Int. J. Heat Mass Transfer*, 19 (1976) 545-551.

[2] I. Abalakin, A. Dervieux, T. Kozubskaya, *INRIA* (2002) No4459.

[3] W. S. Fu, C. G. Li, W. F. Lin and Y. H. Chen, *Int. J. Nume*. Meth. Fluids (2008).

[4] J. M. Weiss and W. A. Smith, *AIAA. 33* (1995) 2050-2056.

[5] W. S. Fu, C. G. Li, C. C. Tseng, *Int. J. Heat Transfer*, 53 (2010) 1575-1585.

Eleventh International Conference on Flow Dynamics
October 8-10, 2014, Sendai, Miyagi, Japan

# The Optimization of Mixed Convection Heat Transfer by an Adjustable Inlet Condition

Yu-Ming Lin, Wei-Siang Chao, Wu-Shung Fu
EE306, Department of Mechanical Engineering, National Chiao Tung University,
Hsinchu City 300, Taiwan (R.O.C.)

**ABSTRACT**

Mixed convection heat transfer of compressible flow in a three-dimensional straight square channel with adjustable inlet condition is studied numerically. The inlet comprises a forced convection area in the middle and an open area at the annular part. The result shows that the ratio between the calibers of the open area and the whole inlet affects the inlet velocity in the open area and the heat transfer coefficient near the wall. Therefore, an optimization of the ratio has been done in this research.

## 1. Introduction

With the increasing of the heat generation of electronic devices, pure natural convection is no longer enough for the heat dissipation systems. Therefore, mixed convection is widely used in the electronic devices nowadays. Fu et al. [1] conducted simulations of pure natural convection and aiding mixed convection in a vertical square channel and found out that if the inlet velocity of mixed convection were smaller than the maximum inlet velocity of pure natural convection can generate, the Nusselt number of mixed convection would be smaller than the one of pure natural convection. In that case, the cooling method using mixed convection would be useless. However, the inlet velocity of pure convection is hard to be predicted beforehand. This research adds an open area at the annular part and sets a constant velocity condition in the middle of the inlet. With the open area, the flow at the inlet can modify itself automatically by sucking in the air from the outside. The results shows that the ratio between the calibers of the open area and the whole inlet can affect the heat transfer coefficient near the wall. Therefore, the aim of this study is to optimize this ratio.

## 2. Physical Model

A compressible mixed convection flow in three-dimensional vertical square channel is investigated and the model is shown in Fig. 1.The length of the channel is $l_0$ (0.4 m). The cross section of the channel is square and the width is $l_1$ (0.04 m). The caliber of the force convection part in the middle of the inlet is $l_2$ (0.16 m) and the Reynolds number, defined in Eq. (1), is 500.

$$\mathrm{Re} = \frac{\rho_0 u_f l_2}{\mu_0} \tag{1}$$

In Eq. (1), $u_f$ is the inlet velocity of the force convection part, $\mu_0$ is the viscosity of the air, and $\rho_0$ is the density of the air.

The temperature of the four heated wall surfaces are $T_h$ (398 $K$) and the other surfaces are adiabatic. The direction of gravity g is downward and parallel to the vertical channel, and the temperature and pressure of the surroundings are $T_0$ (298 $K$) and $P_0$ (101300$Pa$) .An open ratio α is defined as the ratio between the calibers of the open area ( $l_3$ ) and the cross section of the channel ( $l_1$ ) here. By this definition, the open ratio is adjustable by adding no-slip condition wall of which the length is $l_4$ between the force convection area and the open area.

Corresponding author: Yu-Ming Lin
*E-mail address*: highca0709@hotmail.com

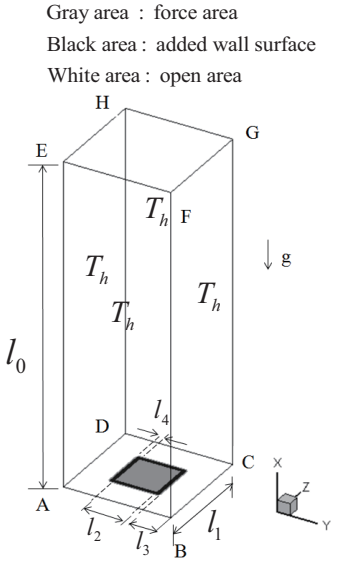


Fig. 1 Physical model

## 3. Numerical Method

Due to the high temperature difference, the Boussinesq assumption is no longer suitable. The viscosity and compressibility of the fluid are also considered. The Roe scheme with MUSCL (Monotonic Upstream-Centered Scheme for Conservation Laws) [2], preconditioning [3], dual time stepping and LUSGS (Lower-Upper Symmetric Gauss Seidel) [4] are used in solving the three-dimensional Navier Stokes equations. The non-reflecting boundary conditions [5] are used at the outlet and the annular part of inlet of the channel in order to avoid a low speed compressible flow to be polluted by the reflections of pressure waves.

The governing equation is shown below:

$$\Gamma \frac{\partial Up}{\partial \tau} + \frac{\partial U}{\partial t} + \frac{\partial F}{\partial X} + \frac{\partial G}{\partial Y} + \frac{\partial H}{\partial Z} = S \tag{2}$$

In Eq. (2), the Γ is the preconditioning matrix, τ is the artificial time, and t is the physical time. $U_p$ , $U$ , $F$ ,

$G$, and $H$ are fluxes of different directions.

## 4. Results and Discussion

In Fig. 2 and Fig. 3, the velocity fields with different αs are indicated. In the case of which α is 0.3, there is not any wall surface added at the inlet yet. Due to the buoyancy and the viscous effect from the force convection, the velocity of the junction of the force convection and open areas is larger. When α is reduced to 0.25, although the velocity at the newly added wall surface area is small, the velocity at the open area is still increasing because of the reason that the open area is smaller in this case and still affected by the two forces mentioned above.

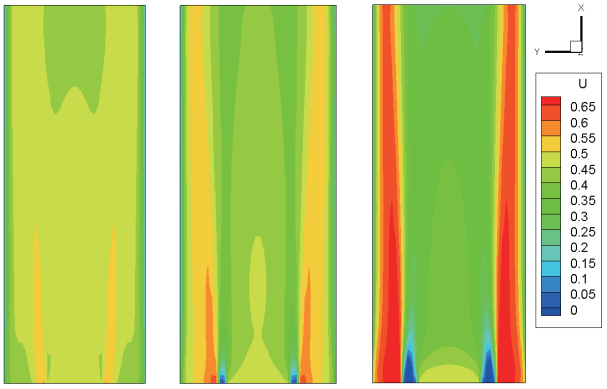


α=0.3 α=0.25 α=0.2

Fig. 2 Velocity fields of $\alpha$=0.3、0.25、0.2 under Re= 500 at t= 10 s

Then α is further reduced to 0.2, and the velocity at the open area is even larger. Because of the increasing of the added wall surface, there are small vortexes generated. In this case, the vortexes are not large enough to affect the whole flow field yet.

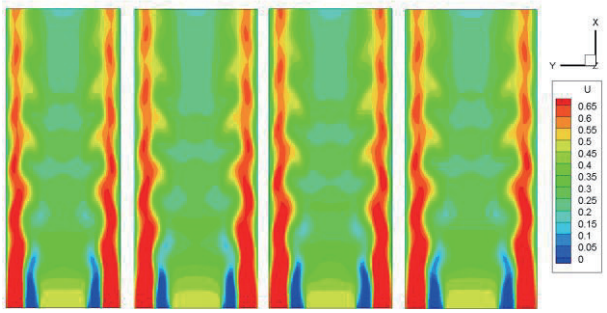


t=9.55 s t=9.70 s t=9.85 s t=10.00 s

Fig. 3 Velocity field of α=0.175 under Re=500 at t= 9.55 s~ 10.00 s

Finally, α is reduced to 0.175, and the inlet velocity of the open area still sticks to the trend. With the further incrementing of the added wall surface, the vortexes near the wall become large disturbances. These disturbances make the flow field fluctuate periodically as shown in Fig. 3 and affect the heat transfer near the wall.

The distribution of variations of area-averaged Nusselt numbers with time is shown in Fig. 4. It can also be observed in Fig. 4 that the area-averaged Nusselt numbers increase while α is decreased. When α is 0.175, the increasing of inlet velocity is not that clear as before. Even though the higher inlet velocity of α=0.175 can improve the heat transfer near the wall, the mixing of the flows at the open area and the force area due to the fluctuation can make the near wall flow velocity at the downstream of the flow field slower and weaken the heat transfer near the wall. The combined effect of these two opposite influences make the area-averaged Nusselt number slightly increase in the case of α=0.2.

Although the heat transfer of the case of α=0.175 is slightly better than the one that of 0.2, the fluctuation may cause some thermal stress and harm the electronic device. As a result, α=0.2 is the best choice in this research, which has the highest heat transfer ability without harmful thermal stress.

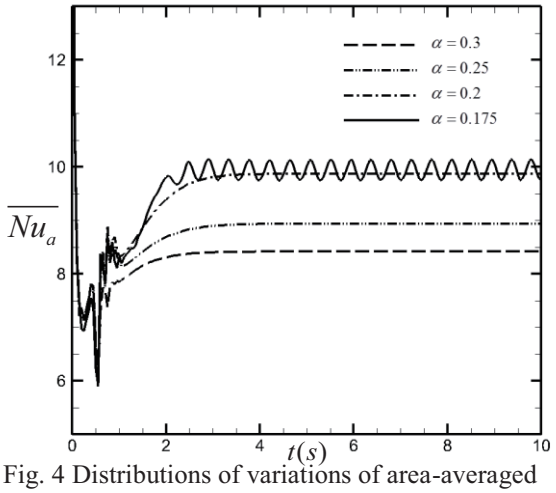


Fig. 4 Distributions of variations of area-averaged Nusselt numbers with time under different open ratio

## 5. Concluding Remarks

Several conclusions are summarized as follows.

1. The velocity of the open area increases with the decreasing of the open ratio α, which also enhances the heat transfer near the heated wall.
2. There are small disturbances generated while α is decreased.
3. The fluctuation of α=0.175 only slightly enhances the heat transfer near the heated wall, but it may cause thermal stress on the heated wall.
4. The open ratio of 0.2 is the best choice in this research.

## References


[1] W.S. Fu, Y.C. Lai, Y. Huang, K.L. Liu, *Int. J. Heat Mass Transfer.* 64 (2013) 636-646.

[2] I. Abalakin, A. Dervieux, T. Kozubskaya, *INRIA* (2002) No.4459.

[3] J. M. Weiss and W. A. Smith, *AIAA.* 33 (1995) 2050-2056.

[4] S. Yoon, A. Jameson, *AIAA.* 26 (1988) 1025-1026.

[5] W.S. Fu, C.G. Li, C.P. Huang, J.C. Huang, *Int. J. Heat Mass Transfer* 52 (2009) 2571–2580.

Eleventh International Conference on Flow Dynamics
October 8-10, 2014, Sendai, Miyagi, Japan

# Numerical Simulations on Viscous Fingering in Radial Hele-Shaw Flows

Yu-Sheng Huang[1], Pei-Yu Yan[1], Herry Yu[1], Ching-Yao Chen[1], Jose A. Miranda[2]
[1]Department of Mechanical Engineering, National Chiao Tung University, Taiwan
1001 University Road, Hsinchu City 300, Taiwan, R.O.C.
[2] Departamento de Fisica, Universidade Federal de Pernambuco
Av. Prof. Moraes Rego, 1235 - Cidade Universitária Recife, Pernambuco 50670-901 Brazil

**ABSTRACT**

We study the development of intricate, fully nonlinear immiscible interfacial patterns in the injection- and suction-driven radial Hele-Shaw problems. The complex-shaped, contracting (expanding) fluid-fluid interface arises when an initially circular blob of more (less) viscous fluid, surrounded by less (more) viscous one, is drawn into an eccentric point sink (source). We present sophisticated numerical simulations, based on a diffuse interface model, that capture the most prominent interfacial features revealed by existing experimental studies of the problem.

## 1. Introduction

We investigate the interfacial instability between two fluids in a radial Hele-Shaw flow. The plate spacing is represented by h. A more viscous fluid drop with an initial diameter of $D_0$ is surrounded by another less viscous fluid. The suction proceeds for a time period of $t_f$, when the diameter of the more viscous drop reduces to $D_c$. The governing equations of such a diffuse interface based on the model of the Boussinesq Hele-Shaw-Cahn-Hilliard model can be written as [1,2]

$$\nabla \cdot \mathbf{u} = 0, \tag{1}$$

$$\nabla p = -\frac{12\eta}{h^2}\mathbf{u} - \epsilon\rho\nabla\cdot\left[(\nabla c)(\nabla c)^T\right], \tag{2}$$

$$\rho\left(\frac{\partial c}{\partial t} + \mathbf{u}\cdot\nabla c\right) = \alpha\nabla^2\mu, \tag{3}$$

$$\mu = \frac{\partial f_0}{\partial c} - \epsilon\nabla^2 c. \tag{4}$$

Here, u, p and η denote the velocity vector, the pressure and the viscosity, respectively. The phase-field variables of the drop and the surrounding fluids are set as c=1 and c=0, respectively. The constants ε and α represent the coefficients of capillary and mobility, respectively. μ is the chemical potential, and $f_0$ is the classical part of the free energy (or the Helmholtz free energy).

Dimensionless parameters, such as the Atwood number A, the Peclet number Pe, the Cahn number C, the suction strength S and the terminal core diameter $D_c$ are defined as

$$\mathrm{Pe} = \frac{\rho D_0^2}{\alpha f^* t_f},\ A = \frac{e^R - 1}{e^R + 1},\ C = \frac{\epsilon}{D_0^2 f^*},$$

$$S = \frac{12\eta_1 D_0^2}{\rho f^* h^2 t_f},\ D_c = \frac{D_f}{D_0}.$$

An equilibrium Capillary number can be expressed by the Cahn number and the suction strength as

$$\mathrm{Ca} = \frac{3S}{\sqrt{C/2}}.$$

For the situation of an injection flow, all the conditions are identical, except the reverse of a suction source by a point sink. As a result, the suction strength S will be replaced by an injection strength I.

The numerical methods applied are largely identical to the Ref[2], in which the governing equations are recast into the well known streamfunction - vorticity formulation.

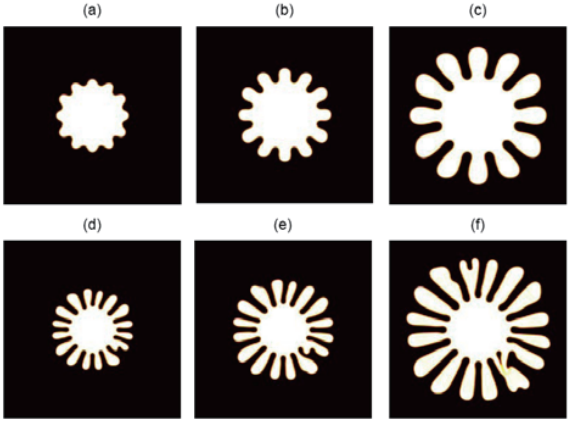


Fig. 1 Immiscible fingering patterns for $C=10^{-5}$ at t=0.33 (left column), 0.5 (middle column) and 1 (right column). Top row: a constant injecting rate of I=1. Middle row: a constant injecting rate of I=5. More vigorous fingering is triggered for a higher injecting number as shown in middle row.

## 2. Results and Discussion

A representative series of injection displacements are demonstrated first. Shown in Fig. 1 are constant injection, of I=1 and 5 at times t=0.33, 0.5 and 1 (terminal time), respectively. The patterns clearly show more unstable fingerings in higher values of the injection strength, which can be quantitatively judged by the more numbers of fingers. Several well-known non-linear features of the fingering patterns are recovered, such as finger spreading, branching and tip-splitting. In addition, fingering merging is also observed. This fingering merging behaviors had been commonly observed in the miscible condition, in which the effects of surface tension are minimized. Nevertheless, they are not commonly discussed in a radial immiscible displacement till recently, e.g. in a shrinking interface by suction presented in the latter paragraphs, even they were experimentally observed n a rectilinear displacement [3].

We now focus on the interfacial instability for a

Corresponding author: Ching-Yao Chen
*E-mail address*: chingyao@mail.nctu.edu.tw

suction flow. Shown in Fig. 2 are cases with variant Atwood number and capillary number. The breakthrough time is defined when the surrounding less viscous fluids reach the position the core at r=0.075. The patterns clearly show more unstable fingerings in higher values of the Atwood number and Capillary number, which can be quantitatively judged by the more numbers of fingers as well early breakthrough times. It is noticed that the breakthrough time is an important global measurement in particular applications, such as the enhanced oil recovery. After the breakthroughs, channels are forms for direct passages of the less viscous fluids to the sink, and suction of the more viscous fluids becomes very ineffective. As a result, considering the constant suction strength and characteristic time scale, the breakthrough time can be directly viewed as an approximated suction efficiency in the present situation.

Vigorous secondary fingering phenomena, such as shielding, merging and pinch-off, are observed to take place sequentially. These secondary behaviors had been commonly observed in the miscible condition, in which the effects of surface tension are minimized. Nevertheless, they are not commonly discussed in an immiscible interface. For more detailed presentations regarding these secondary behaviors, cases associated with extremely fingering are shown in Fig. 3 for even higher values of Ca=13416, 20125 and 26833, numerous fingers are observed to undergo competitions, shielding, merging and pinch-offs. For the extreme cases of Ca=20125, the early occurrences of pinch-off even generate many island drops of the outward fingers.

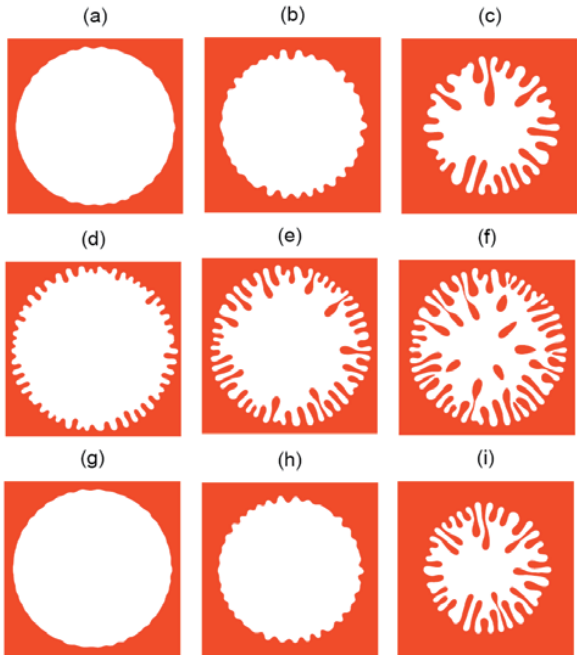


Fig. 2 Images for various Atwood numbers and Capillary numbers at t=0.5, 0.6 and at the breakthrough time $t_b$. (a~c) At=0.922 and Ca=2683 ; $t_b$ =0.75. (d~f) At=0.922 and Ca=6708 ; $t_b$ =0.67. (g~i) At=0.848 and Ca=6708 ; $t_b$ =0.79.

**Acknowledgement**

Financial support by the National Science Council of Republic of China (Taiwan) through Grant NSC 101-2221-E-009-033-MY3 is acknowledged.

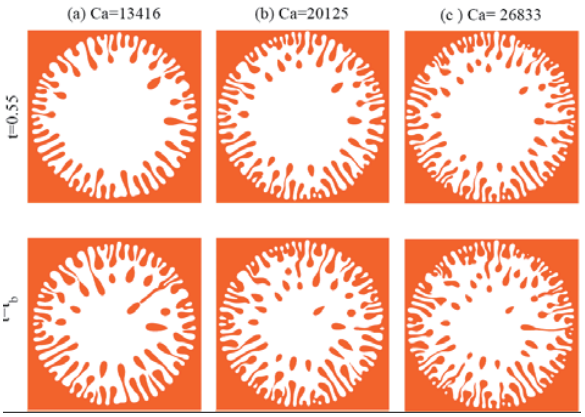


Fig. 3 Typical fingering patterns in the limit of high capillary numbers Ca and for A=0.922, exhibiting prominent nonlinear phenomena such as finger merging, shielding, and pinch-off at time t=0.55, and at the breakthrough time $t_b$: (a) Ca=13461 ($t_b$ =0.608), (b) Ca}=20125 ($t_b$ =0.598), and (c) Ca=26833 ($t_b$ =0.589).

## 3. Concluding Remarks

We have performed intensive numerical simulations in order to probe the advanced time pattern formation dynamics of the radial viscous fingering problem induced by injection and suction. By employing a diffuse interface model we have been able to generate complex patterns which contain the most important morphological and dynamic features detected by previous experimental investigations of the problem. In agreement with experimental observations we have identified patterns showing a strong competition among finger. Our numerical predictions regarding the velocity of both inward and outward fingers, as well as the ones describing as the number of fingers evolve with time are also in line with experiments. All these conclusions have been reached for a set of values for the capillary number. Moreover, at the large capillary number regime we unveiled some interesting phenomena that have not yet being analyzed experimentally, namely the occurrence of characteristic finger merging and pinch-off events. In this scenario, we predicted the possible uprising of both entrapped island drops of the less viscous fluid, and of satellite droplets of the more viscous fluid located at peripheral regions of the patterns.

## References

[1] H-G Lee, J. Lowengrub and J. Goodman, *Phys. Fluids*, 14 (2002) 492.
[2] C.-Y. Chen, Y.-S. Huang and J. Miranda, *Phys. Rev E*, 84 (2011) 046302.
[3] M. Moore, A. Juel, J. Burgess, W. McCormick, and H. L. Swinney, *Proceedings of the 7th Experimental Chaos Conference*, Springer-Verlag 676 (2003) 189.

# CS3: Global / Local Innovations for Next Generation Automobiles (Joint Session)

Eleventh International Conference on Flow Dynamics
October 8-10, 2014, Sendai, Miyagi, Japan

# Changing International Face of Transportation and Energy

Dr. Mark C. Williams,
Visiting Professor, Tohoku University
Morgantown, WV USA 26501

**ABSTRACT**

Energy and transportation are major world industries joined inextricably together. The world produces and consumes 80 million barrels per day of petroleum products. China and US are the enormous markets for automobiles and consume 40 percent of the world's production. In the future hydrogen, solar, natural gas and other renewable will dominate the transportation. Solar cars, battery vehicles, PHEV, hydrogen fuel cell vehicles, and natural gas vehicles, represent tomorrow's propulsion future.

## 1.Introduction

Reducing energy use and reducing the negative human impact on the environment in a constrained, highly populated state with frequent interactions with multiple consequences. It is critical to do as little damage as possible and intrude as little as possible on the environment. We are obviously in a transition period for energy and transportation as we search for new fuels and attempt to use now dominant fuels more efficiently. Energy and transportation are major world industries joined inextricably together.

## 2. Oil

The world is rapidly consuming the finite amounts of stored energy, especially petroleum. The world produces/consumes 80 million BBL per day petroleum products. China is now the world's largest importer of oil. Canada (2-3 million BBL per day - half from tar sands) and Middle East (1.5 million BBL per day) help supply USA petroleum. Canada tar sands contain 300 BBL, one of the world's largest resources ever known, would supply USA for 40 years. However, the USA is now the world's largest producer of oil and natural gas.

The USA has the opportunity with demand side management to even lower consumption through higher automobile fleet efficiency since 2/3 of the oil is used for transportation. The internal combustion engine hybrid, such as the Prius, has already made inroads to improve automotive efficiency. Opportunity for improvement in stationary power generation with fuel cells will result in greater efficiency and the opportunity for the USA to be energy independent.

## 3. Natural Gas

We benefit from the chemical energy, like natural gas, extracted from sunlight on this planet. As long as there is life and sunlight, we will always have renewable natural gas on this planet in the future. Methane from human (ADG) and plant and animal and plant residues and wastes captured from sunlight are available today and in the future.

Corresponding author: Mark C. Williams
*E-mail address*: Markcwilliams1@frontier.com

In addition, huge reserves of natural gas have been found and are being extracted with fracturing techniques. It has been estimated by Pennsylvania State University (PSU) that 4,400 trillion cubic feet of natural gas is located in the Marcellus Shale in the Eastern USA. In addition, huge reserves of gas some 50,000 TCF are believed to exist in methane hydrates in the United States alone.

The cost to convert vehicles to NG is estimated $12,500 to $22,500 depending on the vehicle, engine, size of CNG tanks needed, and who does the converting**.** Due to the short range operation of natural gas internal combustion engine vehicles, alternative electrical technology such as high-efficient solid oxide fuel cells operating directly on natural gas are being considered [1]. In addition, the fuel cell could be hybridized with a turbo-generator for additional performance [2].

## 4. Hydrogen

Hydrogen fuel cell vehicles will require a hydrogen infrastructure. Natural gas is currently the principle method to generate hydrogen. Fuel cell technology transforms electricity production in stationary and transportation applications because it is the most efficient way to convert chemical energy to electricity. While major, multi-billion dollar development world-wide has centered on polymer electrolyte fuel cells for the future of transportation, solid oxide fuel cells operating directly on natural gas are a definite possibility, as previously mentioned.

In the USA in California in 2014 many more efforts to introduce fuel cell cars by Toyota and others and to build many more hydrogen filling stations exist.

## 5. Solar

All the energy stored on the earth comes from the supernova of suns or from the Sun itself in direct incidence. Direct incidence is stored by lifeforms as chemical energy and powers many energy related events such as wind. In one year the incident energy of the sun equals that of all the stored energy on earth contained in uranium, coal, gas, and oil. With the solar electric vehicle (SEV) solar system, the Toyota Prius, for example, can operate up to 30 miles per day in electric mode thus improving fuel economy by up to 34-60%.

Power from a solar array is limited by the size of the vehicle and area that can be exposed to sunlight. While energy can be accumulated in batteries to lower peak demand on the array and provide operation in sunless conditions, the battery adds weight and cost to the vehicle.

**6. Stationary Power from Coal, Nuclear, Natural Gas, and Renewables for Transportation**

Primary non-renewable energy sources for stationary power – coal, nuclear, and natural gas nuclear - will continue to be used until unavailable or until environmental pressure curtails their usage. While direct propulsion in transportation with these fuels is limited, the use of this energy for transportation and especially plug-in hybrids is increasing.

However, the efficiency of stationary power generation is problematic. Greater use by plug-in hybrids will only shorten the long term availability of primary non-renewable fuels like coal and increase reliance on an inefficient system.

However, electrochemical technology – solid oxide fuel cells, particularly solid-oxide fuel cell turbine hybrids, and solid-state lighting have the opportunity to increase stationary power generation efficiency by an order of magnitude [3].

In the nuclear energy fuel cycle, the fuel rods will spend about 3 operational cycles (typically 6 years total) inside the reactor or generally until about 3% of their uranium has been fissioned. Then they are moved to a spent fuel pool where the short lived isotopes generated by fission can decay away. After about 5 years in a spent fuel pool the spent fuel is radioactively and thermally cool enough to handle, and it can be moved to dry storage casks or reprocessed. There is no storage facility for nuclear waste in USA. All our nuclear waste belongs to the American people.

The use of renewable biomass is questionable. While it has been estimated by Oak Ridge National Laboratory that 600 million to a billion tons/year may be available in the USA alone, a reliable source of biomass within a hundred miles of power generation sources is not always feasible. In addition, ethanol production impacts food prices.

**7. Electrochemical Storage Battery**

Today the energy for charging batteries must come from some currently dominate, primary energy sources – fossil and nuclear. Battery vehicles depend on electricity from the current electrical grid system and stationary power. However, the grid efficiency could be improved as we have seen and, in addition, the grid is changing and renewables could account for a greater and greater share of global power [4].

**8. Future of Energy and Transportation - Concluding Remarks**

Energy and transportation are major world industries joined inextricably together. When all practical oil, coal and nuclear energy is exhausted, transportation will have to rely on sunlight and natural gas. Natural gas ICE's and natural gas solid oxide fuel cells, which can use natural gas directly as a fuel unlike other fuel cells, will provide bulk and long haul transportation needs. Battery vehicles will dominate personal and local travel.

**9. References**


[1] Wachsman, E. et al., Science, "Lowering the Temperature of Solid Oxide Fuel Cells," Science, Volume 334, (2011) 935-36.

[2] Bossel, U., European Fuel Cell Forum, "Efficiency of Hydrogen Fuel Cell, Diesel-SOFC-Hybrid and Battery Electric Vehicles," (2003) 34-36.

[3] Gemmen, R., Tucker, R., M. C. Williams, M.C., Winkler, W and Nehter, P., Journal of Power Sources, "General Fuel Cell Hybrid Synergies and Hybrid System Testing Status," Volume 159, (2006) 656-666.

[4] Jacobson, M. and Delucchi, M., Energy Policy, "Providing all global energy with wind, water, and solar power," Volume 39, (2011) 1170–1190.


**About the Author**


Dr. Mark C. Williams is Director of Research for URS Corporation and Visiting Professor at Tohoku University, Sendai Japan. He is the author of over 200 papers and editor of twenty-five handbooks and books. He is a Fellow of the Electrochemical Society. He can be reached at: markcwillams1@frontier.com

# Chinese Automobile Industry

Noriko Hikosaka Behling
Author
McLean, Virginia, 22101 USA

**ABSTRACT**

China enjoys the world's fastest growing economy. Its GNI per capita has been growing by double digits for the past ten years and China's automobile industry has been expanding along with the economy. Indeed, China's automobile production levels surpassed US production in 2009. One result is that China has the world's worst air pollution problems. In response, China's government has initiated a series of counter air pollution measures, which could lead to major opportunities for automakers with advanced clean vehicle technologies.

## 1. Introduction

China is the fastest growing economy in the world. It is currently the second largest global economy, only second to the United States. The US GDP was $16.8 trillion in 2013 with China being $9.24 trillion. China's GDP is forecast to surpass the US in 2019 at about $20 trillion.

Japan's GDP, in contrast, has been contracting in recent years. It was $4.9 trillion in 2013, half China's GDP and a third of US.

At the same time, China's population is growing robustly. The rate of growth was between 0.6-0.5 percent per annum for the period 2005-2010. Although growth has been stable at about 0.5 percent for the past 5 years, it is still robust. China's population was 1.357 billion in 2013. In contrast, the Japanese population was 127.3 million in 2013--less than one tenth China's population. Moreover, Japan's population is gradually declining.

Chinese life expectancy in 2013 was 75 years while Japanese life expectancy is 83.

Meanwhile, China's GNI per capita also has been growing by double digits for the past ten years. China's GNI per capital was $6,560 in 2013 while Japan's was $46,140.

## 2. Rapidly Increasing China's Automobile Market

Against this backdrop of strong population growth and rapidly increasing disposable incomes, China's automobile industry is vigorously expanding. In 2013, China's automobile production exceeded 22 million, more than double the level in 2008. China's car market surpassed the US in 2009 as the biggest in the world. In 2014, China's production is expected to approach 25 million vehicles.

Of automobiles sold in 2013, more than 80 percent or 18 million were passenger cars, with the rest commercial vehicles, including trucks and buses. Of the passenger cars, 47 percent were sedans, 39 percent SUVs, and 16 percent multiple purpose vehicles and cross vehicles.

SUVs are the fastest growing category of vehicles.

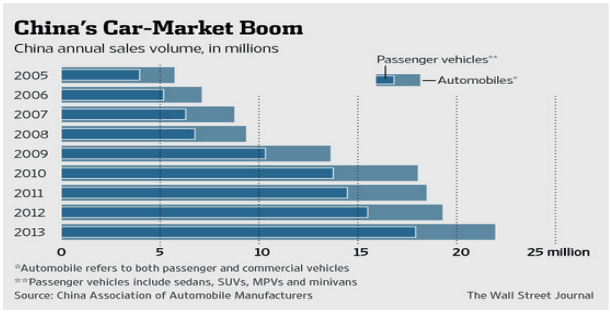


Fig. 1 China's Car-Market Boom, by the Wall Street Journal, April 18, 2014.

During the last five years, SUV sales in China have grown five-fold. In the first ten months of 2013, the accumulative total sale of SUVs reached 2.2 million, up 53.8 percent year-on-year, according to the China Association of Automobile Manufacturers. SUV sales are predicted to be over 4 million in 2020. China's middle-class consumers see SUVs as a status symbol which also provides more space, better road positioning, and an increased sense of safety. The popularity of SUVs is also partly due to China's vehicle regulations. SUVs are bigger and heavier and, like trucks, are treated more leniently by government rules on fuel efficiency and emissions, thus making them less expensive to produce.

In addition to SUVs, luxury vehicles have achieved an impressive growth rate in the last several years. Sales also have grown five-fold in the past five years. Although the Chinese automobile market grew only marginally in 2011, the luxury segment nonetheless grew 54.5 percent. By the end of 2013, the segment was still enjoying double-digit growth of 18.4 percent, reaching sales of 1.4 million units. China is expected to surpass the US in luxury sales by 2016. The Chinese consumers like luxury cars because such cars are seen to reflect the prestige and status of the owners. China's population of affluent consumers is quickly expanding, both in volume and in age range. Younger first time buyers have increasing buying power, and the result has been rapidly growing sales of luxury cars.

Beginning in 2014, a new trend has been emerging. Minivan sales in China have risen 11 percent to 1.41 million during the first five months of the year, according to the China Association of Automobile

Corresponding author: Noriko Hikosaka Behling
*E-mail address*: behlingn@msn.com

Manufacturers. Minivans are popular because they can seat more passengers at a relatively low price. In China, extended families live under the same roof and a minivan is a practical conveyance.

**3. China's Automobile Industry Faces Intense Competition from Foreign Automakers**

Of the 18 million passenger cars sold in China in 2013, 40 percent were Chinese brands, and 60 percent foreign, including 19 percent German, 17 percent Japanese, 12 percent US, 9 percent Korean, and 3 percent French.

China has been promoting domestic automakers, particularly those with no foreign joint venture partners, to create high-wage jobs and local employment. The government has been providing them with subsidies and incentives promoting, but their market share has been declining and this trend has accelerated in 2014. Poor quality, uninspired marketing, and an inefficient industry structure are viewed as the root causes. In addition, foreign automakers and their Chinese joint-venture partners are increasingly looking to produce low-cost cars, increasing head-to-head competition with other domestic automakers. Many small independent domestic automakers could face extinction.

Meanwhile, foreign automakers are thriving. The top ten best selling automobile brands in 2013 included Volkswagen, GM, Hyundai Renault/Nissan, Changan, Toyota, Ford, BAIC, Donfeng, and Honda. Many foreign automakers, witnessed double-digit growth in 2013. They are expecting record sales in 2014 as China's consumers look West for quality and affordability.

Japan's share of China's passenger car market, on the other hand, has declined over the past several years. Japan had a 25 percent share in 2009, 23 percent in 2010, and 22 percent in 2011, according to the China Association of Automobile Manufacturers. The decline was attributed to the increasing competition from European and US manufacturers who have more vigorously invested in China and brought newer brands into China when Japanese automakers remained complaisant. Also in August 2012, anti-Japan protests erupted in China cities after a Japanese group landed on an island that both countries claim, causing Japan's market share in 2012 and 2013 to plunge to 18 percent. German car makers saw their share of China's passenger car market increase to 21.4 from 19.3 percent over the same period.

Japan's automobile sales have recovered and stabilized since the August 2012 crisis. Still, the share is well below the roughly 20 percent share before the territorial dispute. Japan's car makers face an uphill battle given intensifying competition. The mid-sized sedan market, where Japanese brands had a strong position, are now flooded with new models from competitors. In addition, rivals from the U.S. and Germany have been much more agile in focusing on China's less wealthy central and western regions, where demand for cars is growing fast.

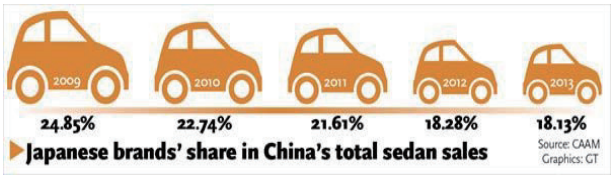


Fig. 2 Japanese Brand's Share in China's Total Sedan Sales by the China Association of Automobile Manufacturers

**4. Chinese Air Pollution Worsening to Crisis Levels**

China's three-decade neglect of environmental concerns at the expense of economic development multiplied by the rapid growth of automobiles on the road have led to alarming pollution levels in some of the most populated regions. According to China's environment ministry, levels of airborne PM2.5—particulate matter measuring less than 2.5 micrometers in diameter—measured on average 76 micrograms per cubic meter across 74 large urban areas in China from January through the end of June in 2014. That's more than seven times the World Health Organization's recommended exposure over the course of a year. Emissions from vehicles and coal-fired Chinese power plants are blamed for more than a million premature deaths a year, for producing acid rain that damages the nation's agriculture, for driving away tourists and even for encouraging the brightest students to study abroad. Scientists in early 2014 compared the conditions to a "nuclear winter."

Now, China's leaders have acknowledged environmental clean-up as one of the country's highest priorities and initiated a series of anti-pollution measures. This has prompted an unprecedented outpouring of candor and criticism from state-run media, an implicit acknowledgment by the government that the problem has reached crisis levels and threatens a political backlash.

In February 2013, China's State Council said it will ratchet up national fuel standards to levels similar to those currently found in the U.S. and Europe by the end of 2017. In September 2013, it announced limits on the concentration of sulfur in gasoline to 50 parts per million from 150 parts per million before the end of 2014. At the same time, it China rolled out a new subsidy program for new energy vehicles aiming to have 500,000 hybrid and electric vehicles on the roads by 2014 and five million by 2020. In July 2014, the Chinese government revealed a new mandate requiring at least 30 percent of all automobiles purchased by the government to be electric or "new energy" vehicles by 2016.

The Chinese government's strong interest in a clean environment and its new initiatives for new energy vehicles could create new opportunities for Japan's automakers that possess leading edge technologies for low emission vehicles.

Eleventh International Conference on Flow Dynamics
October 8-10, 2014, Sendai, Miyagi, Japan

# Advanced NDT To Monitor Friction Stir Welding

Gerd Dobmann
Chair for NDT and Quality Assurance, Saar University
Campus E 3 1, 66123, Saarbrücken, Germany

**ABSTRACT**

The challenge to produce cars with reduced weight in order to reduce then also fuel consumption and waste was in the last two decades always a driver for innovations in materials design and production. So far new materials were developed or conventional-ones were optimized there was also always the question to answer: Do we have proper NDT-technologies to characterize the quality of the optimized material components and to detect – may be now new type of irregularities – coming-up with the new materials and/or the new production technologies? Whereas the 2013 contribution [1] has presented an overview with many case studies, the actual paper will concentrate only on one topic: The on-line monitoring of the friction stir welding process of AL-alloys.

## 1. Introduction

The author of the here presented contribution is a co-author of the handbook to "lightweight constructions" which was published 2011 by the HANSER publishing house [2] where he has described in a wider format standardized as well as enhanced NDT technology to be applied on lightweight materials and structures. The handbook chapter covers the full range of NDT based on mechanical vibration and ultrasonic wave propagation, electromagnetic fields and waves, heat transfer and diffusion and irradiation of X-rays and computing tomography. The emphasis was to present an overview about the spectrum of applications. In contrast to this the here presented material is focused on one special process monitoring technology of an advanced manufacturing process, i.e. friction stir welding.

## 2. NDT-Monitoring of the FSW-process

The continuously increasing usage of friction stir welding (FSW), mainly of safety relevant components in automotive and aerospace applications ask for a comprehensive understanding of the development of nonconformities/irregularities occurring in the weld during welding.

Jene [3] has studied friction stir welding of the Al-alloy AA5454. Examined micrographs of FSW joints (Fig. 1) show the mixture of Al-hydroxides and Al-oxy-hydroxides arranged along characteristic lines. The oxide particles, often referred to as 'RootFlaw', 'Kissing Bond' or 'Joint Line Remnant', are arranged along a characteristic pattern transversely and longitudinally to the weld. The formation of the pattern is influenced by the welding parameters welding force as well as by the design of the FSW-tool.

Wrought Al-alloy AA5454 (300x125 mm$^2$ with a thickness of 3.5 mm were friction stir welded on a milling machine from the type Deckel Maho DMU80T, DMG Germany. The tool shoulder possesses a 14 mm diameter and a M3.5 pin and was tilted by 2° during the process. The ratio of the welding parameters, feed rate and rotational speed per revolution, FPR, ranges from 50 µm/R to 200µm/R.

Corresponding author: Gerd Dobmann
*E-mail address*: gerd.dobmann@t-online.de

The machine is equipped with a force measurement system which allows recording the welding forces in x-, y-, and z-direction emerging during the welding process. For microscopic investigations the cuts of the welded sheets were etched in hydrofluoric acid for 10 s.

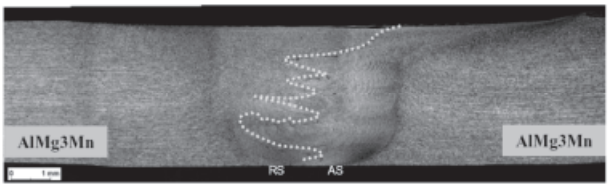


Fig. 1 Cross section of a FSW joint (y-z-plane), the oxide particle distribution is highlighted.

The typical distribution of the oxide segments in a FSW-AlMg3Mn/AlMg3Mn-joint is shown in a cross section in Fig. 1. A differing pattern only appears if other welding flaws like pores occur as a result of the welding process.

A further pronounced feature of the oxide fragments can be seen in Figure 2 cross section of the y-z-plane. A zigzag structure is superposed to the fragment line with an inclination of approximately 10° to 15° to the horizontal. In regular the oxide lines possess a thickness of 1 to 5 µm, but regions with a shift in y-direction show a significantly more distinctive oxide area.

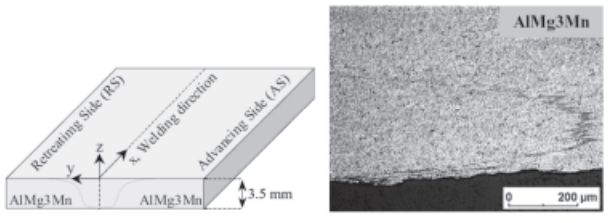


Fig. 2 Co-ordinate system within the weld and cross section with zig-zag oxide structure

In a surface section along the welding seam (Fig. 3) a running of the oxide lines through the whole weld is visible. Hence a description of the oxide fragments as oxide bands is more appropriate.

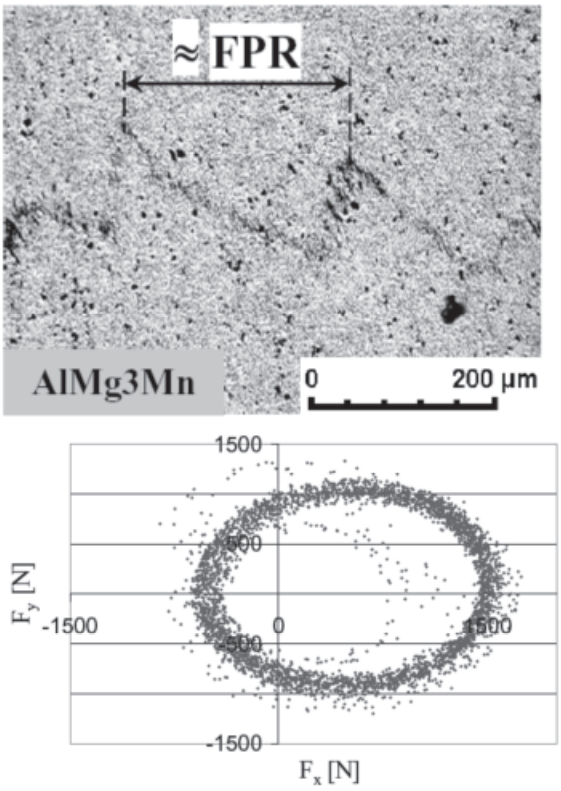


Fig. 3 Surface section in the x-y-plane with oxide fragment distribution and plot of the welding forces.

Furthermore a recurrent oscillating trace of the oxide particles can be detected, which clearly relates to the oscillating welding forces during the FSW-process. FPR is an important indicator for the oxide fragment distribution in the seam and a linear correlation between this welding parameter and the weld face, which is described by the groove spacing Psm . Due to the linear correlation between the periodical lengths of the oscillating welding forces and Psm the appearing welding forces in x- and y-direction are depending on the welding parameter ratio FPR. An analogue periodic oxide structure is observed in the x-z-plane displaying the oscillating forces in the z-direction. The analysis of the welding forces can be used to predict tool breakage and the formation of elongated cavities inside the weld. This showed that by monitoring the welding forces, the ability to change the welding variables in real-time could prevent the formation of flaws in friction stir welds. This analysis is performed by a short-time Fourier transformation (STFT) of the welding forces (Fig.4).

### 3. Results and Discussion

By analyzing the oxide particle distribution in micrographs the influence of the process parameters can be studied. An accurate validation of wormholes and an early warning of tool break are possible by using the online process monitoring analysis. These are promising results to enhance weld quality and to reduce component rejections in industrial friction stir welding applications.

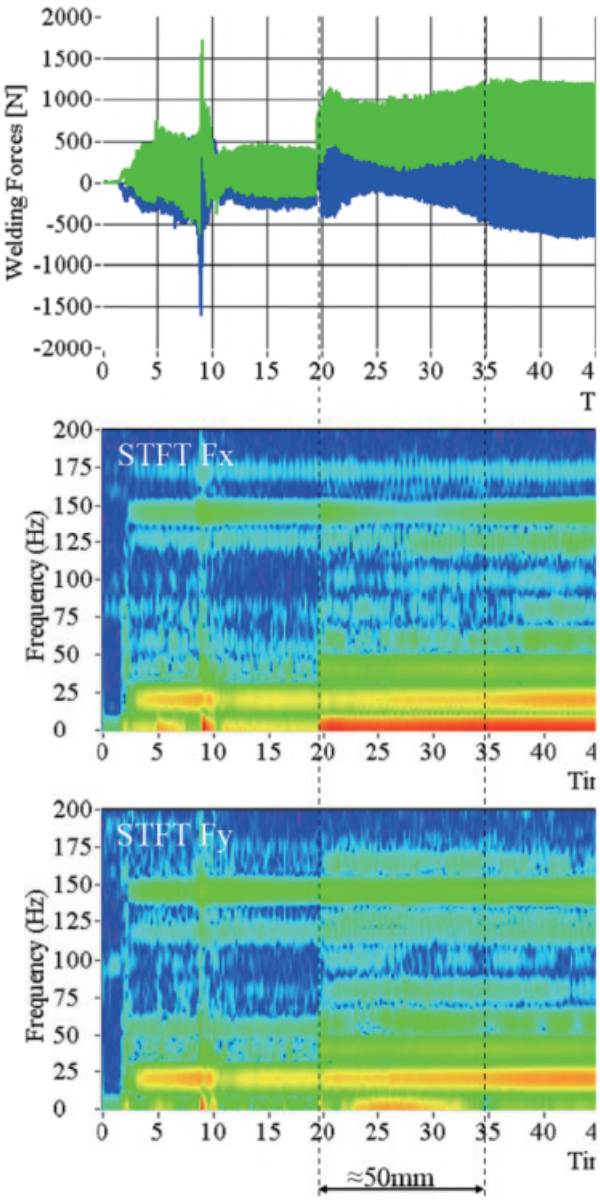


Fig. 4 Force plots and STFT spectrogram (Fx and Fy) of a FSW joint of a 50mm warmhole

### References

[1] G. Dobmann, NDT-Innovations In The Automotive Industrial Sector And to Light-Weight Materials, Proceedings of the ICFD2013, Sendai, Japan

[2] G. Dobmann, NDT for light-weight constructions, in the handbook to “light-weight constructions”, ISBN 978-3-446-42267-4, 2011

[3] T. Jene, G. Dobmann, G. Wagner, D. Eifler, Monitoring of the friction stir welding process to describe parameter effects on joint quality, Welding in the World, Volume 52 - 2008

# CS4: IFS Collaborative Research Forum

For details, please refer to the separate volume.

# Author Index

# Author Index